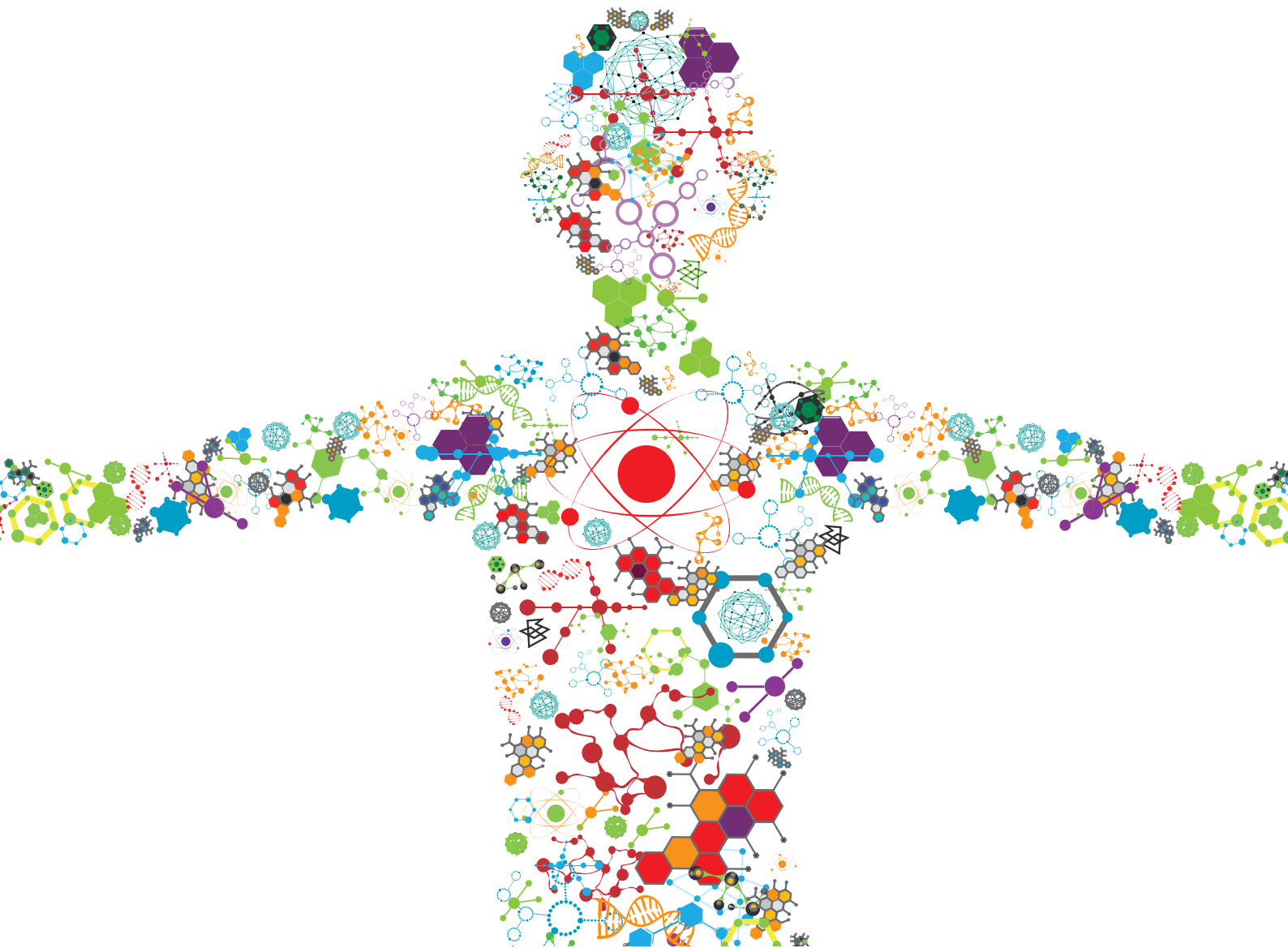


ISOLATION, MODIFICATION, AND CHARACTERIZATION OF THE CONSTITUENTS (CELLULOSE, HEMICELLULOSE, LIGNIN, ET AL.) IN BIOMASS AND THEIR BIO-BASED APPLICATIONS

EDITED BY: Caoxing Huang, Chunlin Xu, Xianzhi Meng, Lei Wang and Xin Zhou
PUBLISHED IN: *Frontiers in Bioengineering and Biotechnology*





frontiers

Frontiers eBook Copyright Statement

The copyright in the text of individual articles in this eBook is the property of their respective authors or their respective institutions or funders. The copyright in graphics and images within each article may be subject to copyright of other parties. In both cases this is subject to a license granted to Frontiers.

The compilation of articles constituting this eBook is the property of Frontiers.

Each article within this eBook, and the eBook itself, are published under the most recent version of the Creative Commons CC-BY licence.

The version current at the date of publication of this eBook is CC-BY 4.0. If the CC-BY licence is updated, the licence granted by Frontiers is automatically updated to the new version.

When exercising any right under the CC-BY licence, Frontiers must be attributed as the original publisher of the article or eBook, as applicable.

Authors have the responsibility of ensuring that any graphics or other materials which are the property of others may be included in the CC-BY licence, but this should be checked before relying on the CC-BY licence to reproduce those materials. Any copyright notices relating to those materials must be complied with.

Copyright and source acknowledgement notices may not be removed and must be displayed in any copy, derivative work or partial copy which includes the elements in question.

All copyright, and all rights therein, are protected by national and international copyright laws. The above represents a summary only. For further information please read Frontiers' Conditions for Website Use and Copyright Statement, and the applicable CC-BY licence.

ISSN 1664-8714

ISBN 978-2-88976-277-4

DOI 10.3389/978-2-88976-277-4

About Frontiers

Frontiers is more than just an open-access publisher of scholarly articles: it is a pioneering approach to the world of academia, radically improving the way scholarly research is managed. The grand vision of Frontiers is a world where all people have an equal opportunity to seek, share and generate knowledge. Frontiers provides immediate and permanent online open access to all its publications, but this alone is not enough to realize our grand goals.

Frontiers Journal Series

The Frontiers Journal Series is a multi-tier and interdisciplinary set of open-access, online journals, promising a paradigm shift from the current review, selection and dissemination processes in academic publishing. All Frontiers journals are driven by researchers for researchers; therefore, they constitute a service to the scholarly community. At the same time, the Frontiers Journal Series operates on a revolutionary invention, the tiered publishing system, initially addressing specific communities of scholars, and gradually climbing up to broader public understanding, thus serving the interests of the lay society, too.

Dedication to Quality

Each Frontiers article is a landmark of the highest quality, thanks to genuinely collaborative interactions between authors and review editors, who include some of the world's best academicians. Research must be certified by peers before entering a stream of knowledge that may eventually reach the public - and shape society; therefore, Frontiers only applies the most rigorous and unbiased reviews. Frontiers revolutionizes research publishing by freely delivering the most outstanding research, evaluated with no bias from both the academic and social point of view. By applying the most advanced information technologies, Frontiers is catapulting scholarly publishing into a new generation.

What are Frontiers Research Topics?

Frontiers Research Topics are very popular trademarks of the Frontiers Journals Series: they are collections of at least ten articles, all centered on a particular subject. With their unique mix of varied contributions from Original Research to Review Articles, Frontiers Research Topics unify the most influential researchers, the latest key findings and historical advances in a hot research area! Find out more on how to host your own Frontiers Research Topic or contribute to one as an author by contacting the Frontiers Editorial Office: frontiersin.org/about/contact

ISOLATION, MODIFICATION, AND CHARACTERIZATION OF THE CONSTITUENTS (CELLULOSE, HEMICELLULOSE, LIGNIN, ET AL.) IN BIOMASS AND THEIR BIO-BASED APPLICATIONS

Topic Editors:

Caoxing Huang, Nanjing Forestry University, China

Chunlin Xu, Åbo Akademi University, Finland

Xianzhi Meng, The University of Tennessee, Knoxville, United States

Lei Wang, Ocean University of China, China

Xin Zhou, Nanjing Forestry University, China

Citation: Huang, C., Xu, C., Meng, X., Wang, L., Zhou, X., eds. (2022). Isolation, Modification, and Characterization of the Constituents (Cellulose, Hemicellulose, Lignin, et al.) in Biomass and Their Bio-based Applications.

Lausanne: Frontiers Media SA. doi: 10.3389/978-2-88976-277-4

Table of Contents

- 07 Editorial: Isolation, Modification, and Characterization of the Constituents (Cellulose, Hemicellulose, Lignin, et al.) in Biomass and Their Bio-Based Applications**
Caoxing Huang, Chunlin Xu, Xianzhi Meng, Lei Wang and Xin Zhou
- 11 Inactivation of Inulinase and Marination of High-Quality Jerusalem Artichoke (*Helianthus tuberosus* L.) Pickles With Screened Dominant Strains**
Li Zhang, Wei Liu, Jiahong Ji, Lina Deng, Qian Feng, Wujian Shi and Jian Gao
- 22 Co-production of Xylooligosaccharides and Xylose From Poplar Sawdust by Recombinant Endo-1,4- β -Xylanase and β -Xylosidase Mixture Hydrolysis**
Qi Li, Yunpeng Jiang, Xinyi Tong, Linguo Zhao and Jianjun Pei
- 35 Using Carboxymethyl Cellulose as the Additive With Enzyme-Catalyzed Carboxylated Starch to Prepare the Film With Enhanced Mechanical and Hydrophobic Properties**
Can Liu, Shijiao Qin, Jin Xie, Xu Lin, Yunwu Zheng, Jing Yang, Huan Kan and Zhengjun Shi
- 46 Using Cellulose Nanocrystal as Adjuvant to Improve the Dispersion Ability of Multilayer Graphene in Aqueous Suspension**
Haiqiao Zhang, Yan Wu, Feng Yang, Huiling Dong, Yuqing Bian, Huanliang Jia, Xuqin Xie and Jilei Zhang
- 56 Guanidino-Acetic Acid: A Scarce Substance in Biomass That Can Regulate Postmortem Meat Glycolysis of Broilers Subjected to Pre-slaughter Transportation**
Bolin Zhang, Ning Liu, Zhen He, Peiyong Song, Meilin Hao, Yuxiao Xie, Jiahui Li, Rujie Liu and Zewei Sun
- 68 Aerobic and Anaerobic Biodegradability of Organophosphates in Activated Sludge Derived From Kitchen Garbage Biomass and Agricultural Residues**
Xingfeng Yang, Deling Fan, Wen Gu, Jining Liu, Lili Shi, Zhi Zhang, Linjun Zhou and Guixiang Ji
- 82 Extraction and Application of Natural Rutin From *Sophora japonica* to Prepare the Novel Fluorescent Sensor for Detection of Copper Ions**
Shilong Yang, Lu Sun, Zhiwen Song and Li Xu
- 91 Engineered Polyploid Yeast Strains Enable Efficient Xylose Utilization and Ethanol Production in Corn Hydrolysates**
Lulu Liu, Mingjie Jin, Mingtao Huang, Yixuan Zhu, Wenjie Yuan, Yingqian Kang, Meilin Kong, Sajid Ali, Zefang Jia, Zhaoxian Xu, Wei Xiao and Limin Cao
- 102 Pilot Scale Elimination of Phenolic Cellulase Inhibitors From Alkali Pretreated Wheat Straw for Improved Cellulolytic Digestibility to Fermentable Saccharides**
Ikram ul Haq, Ali Nawaz, Badar Liaqat, Yesra Arshad, Xingli Fan, Meitao Sun, Xin Zhou, Yong Xu, Fatima Akram and Kankan Jiang

- 110** *Changes in the Leaf Physiological Characteristics and Tissue-Specific Distribution of Ginsenosides in Panax ginseng During Flowering Stage Under Cold Stress*
Tao Zhang, Changbao Chen, Yuqiu Chen, Qinghe Zhang, Qiong Li and Weichen Qi
- 128** *MgO Nanoparticles-Incorporated PCL/Gelatin-Derived Coaxial Electrospinning Nanocellulose Membranes for Periodontal Tissue Regeneration*
Wenzao Peng, Shuangshuang Ren, Yibo Zhang, Ruyi Fan, Yi Zhou, Lu Li, Xuanwen Xu and Yan Xu
- 141** *Cellulose Isolated From Waste Rubber Wood and Its Application in PLA Based Composite Films*
Zhiqiang Ou, Qi Zhou, Xin Rao, Haifeng Yang, Chunqing Huo and Xueyu Du
- 154** *Using the Major Components (Cellulose, Hemicellulose, and Lignin) of Phyllostachys praecox Bamboo Shoot as Dietary Fiber*
Jinlai Yang, Liangru Wu, Huimin Yang and Yanhong Pan
- 162** *The in vitro and in vivo Antioxidant and Immunomodulatory Activity of Incomplete Degradation Products of Hemicellulosic Polysaccharide (Galactomannan) From Sesbania cannabina*
Yuheng Tao, Ting Wang, Chenhuan Lai, Zhe Ling, Yanmin Zhou and Qiang Yong
- 174** *Selective Production of Xylooligosaccharides by Xylan Hydrolysis Using a Novel Recyclable and Separable Furoic Acid*
Jianglin Zhao, Xiaotong Zhang, Xin Zhou and Yong Xu
- 182** *Valorization of Enzymatic Hydrolysis Residues from Corncob into Lignin-Containing Cellulose Nanofibrils and Lignin Nanoparticles*
Rui Xu, Haishun Du, Hui Wang, Meng Zhang, Meiyang Wu, Chao Liu, Guang Yu, Xinyu Zhang, Chuanling Si, Sun-Eun Choi and Bin Li
- 192** *A Novel Inulin-Mediated Ethanol Precipitation Method for Separating Endo-Inulinase From Inulinases for Inulooligosaccharides Production From Inulin*
Xin Li, Qiannan Zhang, Wei Wang and Shang-Tian Yang
- 202** *A Novel Biosorbent From Hardwood Cellulose Nanofibrils Grafted With Poly(m-Aminobenzene Sulfonate) for Adsorption of Cr(VI)*
Yong Ho Yu, Liangliang An, Jin Ho Bae, Ji Won Heo, Jiansong Chen, Hanseob Jeong and Yong Sik Kim
- 213** *Bio-Based Hydrogels With Ion Exchange Properties Applied to Remove Cu(II), Cr(VI), and As(V) Ions From Water*
Julio Sánchez, Daniel Dax, Yesid Tapiero, Chunlin Xu and Stefan Willför
- 225** *Isolating High Antimicrobial Ability Lignin From Bamboo Kraft Lignin by Organosolv Fractionation*
Jinyan Yun, Liao Wei, Wei Li, Duqiang Gong, Hongyu Qin, Xiuqing Feng, Guojiang Li, Zhe Ling, Peng Wang and Baishuang Yin
- 236** *Preparation of Lignin-Based Magnetic Adsorbent From Kraft Lignin for Adsorbing the Congo Red*
Lingyan Fang, Hao Wu, Yuxuan Shi, Yuheng Tao and Qiang Yong

- 247 Application of Ethanol Extracts From *Alnus sibirica* Fisch. ex Turcz in Hair Growth Promotion**
Eun Ju Ha, Jang-Hyuk Yun, Chuanling Si, Young Soo Bae, Young-Hwan Jeong, Kwang-Hyun Park and Sun-Eun Choi
- 258 20-Hydroxy-3-Oxolupan-28-Oic Acid, a Minor Component From *Mahonia bealei* (Fort.) Carr. Leaves Alleviates Lipopolysaccharide-Induced Inflammatory in Murine Macrophages**
Xiaojun Yang, Jing Zhou, Yang He, Lingyun Lv, Yufeng Cao and Weicheng Hu
- 269 Recent Developments and Applications of Hemicellulose From Wheat Straw: A Review**
Ling-Zhi Huang, Ming-Guo Ma, Xing-Xiang Ji, Sun-Eun Choi and Chuanling Si
- 283 Multifunctional Lignin-Based Composite Materials for Emerging Applications**
Chang Ma, Tae-Hee Kim, Kun Liu, Ming-Guo Ma, Sun-Eun Choi and Chuanling Si
- 295 Genetic Diversity, Chemical Components, and Property of Biomass *Paris polyphylla* var. *yunnanensis***
Nong Zhou, Lingfeng Xu, Sun-Min Park, Ming-Guo Ma, Sun-Eun Choi and Chuanling Si
- 303 Improved Production of Xylanase in *Pichia pastoris* and Its Application in Xylose Production From Xylan**
Ting Miao, Abdul Basit, Junquan Liu, Fengzhen Zheng, Kashif Rahim, Huiqiang Lou and Wei Jiang
- 310 Transcriptomic and Metabolomic Differences Between Two *Saposhnikovia divaricata* (Turcz.) Schischk Phenotypes With Single- and Double-Headed Roots**
Tao Zhang, Yuqiu Chen, Qinghe Zhang, Peng Yu, Qiong Li, Weichen Qi and Changbao Chen
- 325 Improvement of Nicotine Removal and Ethanol Fermentability From Tobacco Stalk by Integration of Dilute Sulfuric Acid Presoak and Instant Catapult Steam Explosion Pretreatment**
Hongsen Zhang, Chenqing Fu, Tianbao Ren, Hui Xie, Guotao Mao, Zhimin Wang, Fengqin Wang and Andong Song
- 335 Synthesis of pH-Sensitive and Self-Fluorescent Polymeric Micelles Derived From Rosin and Vegetable Oils via ATRP**
Juan Yu, Chaoqun Xu, Chuanwei Lu, Qian Liu, Jifu Wang and Fuxiang Chu
- 346 Structural Characterization of Sulfated Polysaccharide Isolated From Red Algae (*Gelidium crinale*) and Antioxidant and Anti-Inflammatory Effects in Macrophage Cells**
Yu Pei, Shengtao Yang, Zhenbang Xiao, Chunxia Zhou, Pengzhi Hong and Zhong-Ji Qian
- 359 The Effect of Ball Milling Time on the Isolation of Lignin in the Cell Wall of Different Biomass**
Guangrong Yang, Xueying An and Shilong Yang
- 369 Thermostable Cellulases / Xylanases From Thermophilic and Hyperthermophilic Microorganisms: Current Perspective**
Samaila Boyi Ajeje, Yun Hu, Guojie Song, Sunday Bulus Peter, Richmond Godwin Afful, Fubao Sun, Mohammad Ali Asadollahi, Hamid Amiri, Ali Abdulkhani and Haiyan Sun

- 388** *Improved Release of Monosaccharides and Ferulic Acid Using Enzyme Blends From Aspergillus Niger and Eupenicillium Parvum*
Zhenghui Liu, Enze Shi, Feng Ma, Xin Zhou and Kankan Jiang
- 397** *Metabolic and Evolutionary Engineering of Diploid Yeast for the Production of First- and Second-Generation Ethanol*
Yang Sun, Meilin Kong, Xiaowei Li, Qi Li, Qian Xue, Junyan Hou, Zefang Jia, Zhipeng Lei, Wei Xiao, Shuobo Shi and Limin Cao
- 409** *Effects of Microwave-Assisted Liquid Hot Water Pretreatment on Chemical Composition and Structure of Moso Bamboo*
Jie-Yu Cui, Ning Zhang and Jian-Chun Jiang
- 416** *Biochemical and Molecular Dynamics Study of a Novel GH 43 α -L-Arabinofuranosidase/ β -Xylosidase From Caldicellulosiruptor saccharolyticus DSM8903*
Md. Abu Saleh, Shafi Mahmud, Sarah Albogami, Ahmed M El-Shehawi, Gobindo Kumar Paul, Shirmin Islam, Amit Kumar Dutta, Md. Salah Uddin and Shahriar Zaman
- 428** *Enhanced Mechanical Properties of Polyvinyl Chloride-Based Wood-Plastic Composites With Pretreated Corn Stalk*
Tao Shen, Minghui Li, Bo Zhang, Lingxia Zhong, Xiran Lin, Pengpeng Yang, Ming Li, Wei Zhuang, Chenjie Zhu and Hanjie Ying



Editorial: Isolation, Modification, and Characterization of the Constituents (Cellulose, Hemicellulose, Lignin, et al.) in Biomass and Their Bio-Based Applications

Caoxing Huang^{1*}, Chunlin Xu², Xianzhi Meng³, Lei Wang⁴ and Xin Zhou¹

¹Co-Innovation Center for Efficient Processing and Utilization of Forest Resources, College of Chemical Engineering, Nanjing Forestry University, Nanjing, China, ²Laboratory of Natural Materials Technology, Åbo Akademi University, Turku, Finland, ³Department of Chemical and Biomolecular Engineering, University of Tennessee, Knoxville, TN, United States, ⁴College of Food Science and Engineering, Ocean University of China, Qingdao, China

Keywords: cellulose, hemicellulose, lignin, biotechnology, bio-applications

Editorial on the Research Topic

Isolation, Modification, and Characterization of the Constituents (Cellulose, Hemicellulose, Lignin, et al.) in Biomass and Their Bio-Based Applications

Lignocellulosic biomass is an abundant renewable biomaterial that is mainly composed of cellulose, hemicellulose, lignin, and extractives in different proportions (**Figure 1**). The constituents of cellulose and hemicellulose have been widely used as the precursors to prepare bio-materials, dietary fibers, and intermediates, which can be applied in the areas of biomedical therapy, food preservation, food additives, and cosmetics. Lignin is the most naturally abundant aromatic polymer that can be used to prepare bioactive components. Due to the natural recalcitrance of lignocellulosic biomass, an isolation approach should be carried out to obtain these constituents with high purity. In addition, various modification technologies are often applied to these constituents to improve their reactive activation or tailor the polymers with specific functions. Hence, seeking the appropriate approaches to isolation and modification is essential for the effective utilization of these biomass components.

To obtain the different constituents in biomass, physical, chemical, and combined methods have been widely investigated. Despite the tremendous progress that has been made in the development of these isolation technologies, there still exist some problems, such as bulk chemical consumption, low isolation yield, low purity for final products, and harsh extraction conditions. Hence, seeking environmentally friendly, sustainable, and industrialized technologies to obtain the constituents in different biomass is still quite challenging to a large extent. In addition, due to the structural diversities of cellulose, hemicellulose, and lignin in different biomass, the modified constituents can be explored to prepare the diversified bio-materials and bio-chemicals for application in undiscovered bio-applications. Combining the new isolation, modification, and characterization technologies with novel applications will be the key steps to ultimately unlocking the integrated, economically viable, and multi-product biorefinery process.

The topic “*Isolation, modification, and characterization of the constituents (cellulose, hemicellulose, lignin, et al.) in Biomass and Their Bio-based Applications*” covers new pretreatment/fraction technologies for different biomass to achieve their valorization and bio-application of different substances in biomass. Here we sincerely thank all the contributors for their wonderful works on this topic. Following are the highlights drawn from their contributions to this special topic.

OPEN ACCESS

Edited and reviewed by:

Manfred Zinn,
HES-SO Valais-Wallis, Switzerland

*Correspondence:

Caoxing Huang
hcx@njfu.edu.cn

Specialty section:

This article was submitted to
Bioprocess Engineering,
a section of the journal
Frontiers in Bioengineering and
Biotechnology

Received: 31 January 2022

Accepted: 31 March 2022

Published: 13 May 2022

Citation:

Huang C, Xu C, Meng X, Wang L and
Zhou X (2022) Editorial: Isolation,
Modification, and Characterization of
the Constituents (Cellulose,
Hemicellulose, Lignin, et al.) in Biomass
and Their Bio-Based Applications.
Front. Bioeng. Biotechnol. 10:866531.
doi: 10.3389/fbioe.2022.866531

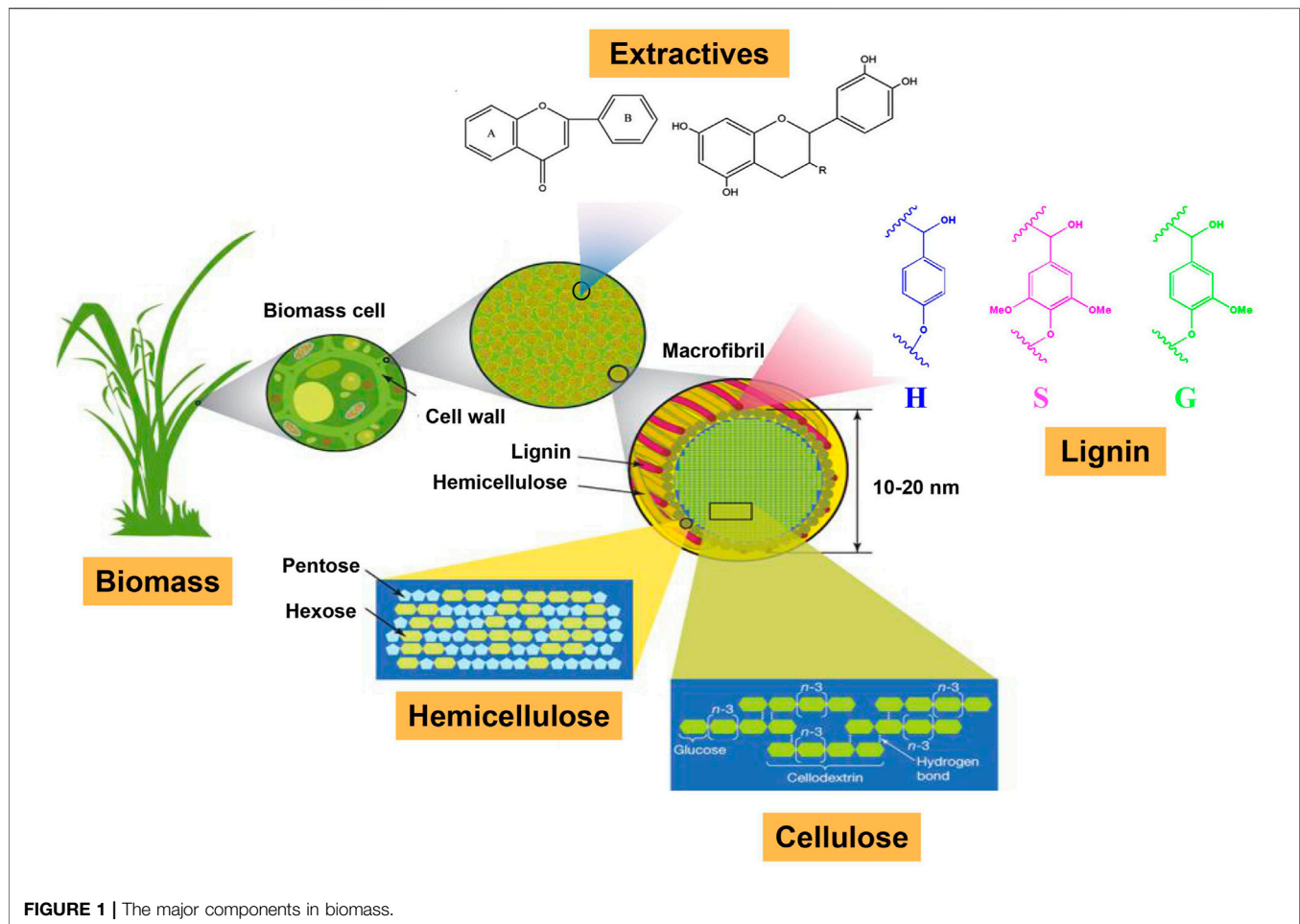


FIGURE 1 | The major components in biomass.

NEW METHODS TO PREPARE THE CELLULOSE DERIVATIVES FROM DIFFERENT BIOMASS AND THEIR POTENTIAL APPLICATIONS

Liu et al., used carboxymethyl cellulose as the additive to improve the hydrophobicity and strength of carboxylated starch film, which is prepared from starch catalyzed by bio- α -amylase. They found that the addition of 15% carboxymethyl cellulose improved the mechanical properties of the prepared film with maximum tensile strength of 44.8 MPa. Carboxymethyl cellulose effectively improved the hydrophobicity of the starch film with the addition amount of 10%–30%, while hydrophobic property was stable at 66.8° when the addition amount was exceeded to 35%. Ou et al., isolated cellulose with high purity from waste rubber wood (RW) and further processed this into cellulose nanocrystals. They demonstrated that, compared with pure polylactic acid (PLA) film, the addition of acetylated RW cellulose reinforced the thermal properties of PLA composite films. The acetylated RW cellulose nanocrystals reinforced PLA composite films exhibited more enhanced performance in mechanical properties, in which highest tensile strength (55.0 MPa) and Young's modulus (3.9 GPa) were achieved with

5% acetylated rubber wood cellulose nanocrystals. Yu et al., prepared a novel biosorbent from cellulose nanofibrils grafted with poly(m-aminobenzene sulfonate) (PABS) for effective detoxification and adsorption of Cr(VI) in an aqueous medium of 6,6-tetramethylpiperidine-1-oxyl (TEMPO)-oxidized cellulose nanofibrils (TOCNF). They demonstrated that the biosorbent from TOCNF-grafted PABS could detoxify and adsorb Cr(VI) synchronously.

ENVIRONMENTALLY FRIENDLY, SUSTAINABLE, AND INDUSTRIALIZED TECHNOLOGIES TO PREPARE BIO-PRODUCTS FROM DIFFERENT BIOMASS

Zhang et al., studied the inactivation of inulinase and marination of high-quality Jerusalem Artichoke (*Helianthus tuberosus* L.) pickles with screened dominant strains. They found that the enzymes in Jerusalem artichoke pickles were inactivated using a combination of NaCl and ultrasound exhibited better flavor than those exposed to NaHCO₃. Further, this combination reduced the inulinase activity of the Jerusalem artichokes to 2.50 U/ml, which

could maintain the inulin content at 61.22%. Yang et al., extracted and purified the natural rutin in *Sophora japonicato* to prepare fluorescent-responding sensor systems intended to recognize copper ions with both strong selectivity as well as appropriate sensitivity. They found that when rutin and (2-hydroxypropyl)- β -cyclodextrin were introduced within buffer solution, fluorescent emission intensity was significantly increased, in which the minimum detection limit can be 3.5×10^{-8} mol/L. Yang et al., prepared a powder consisting of the main components of bamboo shoots (cellulose, hemicellulose, and lignin) from fresh *Phyllostachys praecox* shoots as the supplement in the diet of mice, and aimed to evaluate the potential utility of these components as a dietary fiber supplement. They demonstrated that the major components of bamboo shoot powder (cellulose, hemicellulose, and lignin) could be used as beneficial natural additives in the food industry. Liu et al., used an enzyme at a 0.5% (w/w) loading dosage with the addition of ferulic acid esterase (1 U/g substrate) to obtain monosaccharides and ferulic acid from wheat bran autohydrolysis residues. The obtained hydrolysis yields were desirable, including 84.98% of glucose, 84.74% of xylose, 80.24% of arabinose, and 80.86% of ferulic acid. They demonstrated that a combination of autohydrolysis and enzymatic hydrolysis can achieve a satisfying yield of enzymatic saccharification and ferulic acid production from wheat bran. Cui et al., investigated the effects of microwave assisted liquid hot water (MA-LHW) pretreatment on the chemical composition of moso bamboo and the fiber structure of pretreated residues. They demonstrated that MA-LHW pretreatment increased the removal of hemicellulose, lignin, and other non-crystalline parts in bamboo materials, and more cellulose with crystalline structure was retained, which increased the CrI value of moso bamboo by 14.84%. Sun et al., developed a yeast strain of *Saccharomyces cerevisiae* A31Z for 2G bioethanol production from biomass. They found that this strain competed better than its ancestors in xylose utilization and subsequent ethanol production. In addition, this yeast strain manifested higher tolerance against common inhibitors from lignocellulosic hydrolysates, and it lowered the production of glycerol by-product. They provided a promising path for improving 2G bioethanol production in industries using *Saccharomyces cerevisiae*.

UPGRADING OF APPLICATIONS OF LIGNIN

Yun et al., prepared the lignin fraction with a suitable structure to tailor excellent biological activities by sequentially organosolv fractionation with anhydrous acetone, 50% acetone, and 37.5% hexanes. They demonstrated that the lignin with high functional groups showed the ability to ameliorate *Escherichia coli*-induced diarrhea damage of mice to improve the formation of intestinal contents *in vivo*. Overall, this work demonstrated that a lignin fraction with a tailored structure can be used as a novel antimicrobial agent in the biomedical field. Fang et al., prepared magnetic lignin nanoparticles (MLN) from kraft lignin with Fe_3O_4 via Mannich reaction. They demonstrated that in terms of environmental protection and adsorption

efficiency, MLN can act as an ideal adsorbent for Congo red dyes due to its simple preparation, superior performance, and convenient recovery. Yang et al., carried out different ball milling times on hardwood (poplar sawdust), softwood (larch sawdust), and gramineous material (bamboo residues) to understand the optimum condition to isolate the representative milled wood lignin (MWL) in these different biomass species. They demonstrated that milling time with 3 and 7 h were sufficient to isolate the representative lignin (with yield over 30%) in the cell wall of bamboo residues and poplar sawdust, respectively, while more than 7 h should be carried out to isolate the representative lignin in larch sawdust.

BIOLOGICAL TECHNOLOGIES TO OBTAIN THE CONSTITUENTS IN DIFFERENT BIOMASS

Li et al., focused on enzymatic hydrolysis of poplar sawdust xylan for production of XOS and xylose by a GH11 endo-1,4- β -xylanase MxynB-8 and a GH39 β -xylosidase Xln-DT. MxynB-8 showed the excellent ability to hydrolyze hemicellulose of broad leaf plants of poplar. Their results showed that the enzymatic hydrolysis yield of poplar sawdust xylan was improved by adding Xln-DT, and a xylose-rich hydrolysate could be obtained with the xylose yield of 89.9%. In addition, the enzymatic hydrolysis yield was higher (32.2%) by using MxynB-8 and Xln-DT together. Zhang et al., investigated the effects of short- and long-term cold stress (5°C) on the physiological characteristics, tissue-specific ginsenoside distributions, and ginsenoside synthesis gene expressions of 3-year-old *Panax ginseng* during the flowering period. They demonstrated that short-term cold stress can stimulate membrane lipid peroxidation, in turn stimulating the antioxidant enzyme system to alleviate oxidative damage and increase the expression of key enzyme genes involved in ginsenoside biosynthesis. Haq et al., reported dephenoliphication of wheat straw using various alkalis of $\text{Ca}(\text{OH})_2$ and NH_3 , acids of H_2O_2 , H_2SO_4 , and H_3PO_4 , and combinations of $\text{NH}_3 + \text{H}_3\text{PO}_4$ and $\text{H}_3\text{PO}_4 + \text{H}_2\text{O}_2$ at pilot scale to increase enzymatic saccharification yield. They found that upon subsequent saccharification of dephenoliphied substrate, the hydrolysis yield was recorded as 46.88%. Optimized conditions such as using 1% + 5% concentration of $\text{NH}_3 + \text{H}_3\text{PO}_4$ for 30 min at 110°C temperature reduced total phenolic content (TPC) to 48 mg GAE/g DW. Zhao et al., proposed a recyclable and separable organic acid of furoic acid for hydrolyzing xylan to optimize XOS production by the response surface methodology. Their results indicated that the predicted maximum yield of XOS was 49.0% with 1.2% furoic acid at 167°C for 33 min, being close to the experimental value (49.2%). The results indicated that the fitted models were in good agreement with the experimental results to obtain the XOS. Liu et al., reported that *Saccharomyces cerevisiae* strain F106 could utilize xylose for ethanol production. Their results showed that the strains of F106-KR and diploid produced an ethanol yield of 0.45 and 0.48 g/g total sugars, respectively, in simulated corn hydrolysates within 36 h. Using non-detoxicated corncob

hydrolysate as the substrate, the ethanol yield with the triploid was approximately seven-fold more than that of the diploid at 40°C. Zhang et al., used dilute sulfuric acid pretreatment for tobacco stalk to enhance the performance of instant catapult steam explosion (ICSE). They found that the optimized 0.8% sulfuric acid (w/w) presoak-integrated ICSE pretreatment resulted in 85.54% nicotine removal from tobacco stalk. In addition, the total sugar concentration from enzymatic hydrolysis of pretreated tobacco stalk increased from 33.40 to 53.81 g/L; ethanol concentration increased 103.36% from 5.95 to 12.10 g/L in flask. They achieved the expected purpose of efficient utilization of discarded tobacco stalk. Boyi Ajeje et al., aimed to give an overview of the most recent thermostable cellulases and xylanases isolated from thermophilic and hyperthermophilic microbes. They emphasized on recent advancements in manufacturing these enzymes in other mesophilic hosts and the enhancement of catalytic activity as well as thermostability of thermophilic cellulases and xylanases, using genetic engineering as a promising and efficient technology for its economic production.

CELLULOSE, HEMICELLULOSE, AND LIGNIN-BASED BIO-MATERIALS

Zhang et al., used the cellulose nanocrystal (CNC) suspensions with different concentrations (0.4%, 0.6%, and 0.8%) as the adjuvant to improve the dispersion ability of multilayer graphene (MLG) in aqueous suspension, which is easy to be aggregated by van der Waals force between layers. They found that CNC suspension with 0.8% concentration showed the highest ability to disperse 1.0 wt% MLG with the most stable performance in suspension. Sánchez et al., used the hemicellulose of O-acetyl galactoglucomannan (GGM) as the precursor material to prepare the hydrogels with ion exchange properties to remove Cu(II), Cr(VI), and As(V) ions. They found that the poly-GGM-glycidyl methacrylate-2-acrylamido-2-methyl-1-propanesulfonic acid hydrogel reached an absorption capacity of 90 mg/g for Cu(II). The poly-GGM-glycidyl methacrylate-(3-acrylamidopropyl)trimethylammonium chloride hydrogel reached values of 69 and 60 mg/g for Cr(VI) and As(V) oxyanions, respectively. Peng et al., used coaxial electrospinning technique to fabricate magnesium oxide

(MgO) nanoparticles-incorporated PCL/gelatin core-shell nanocellulose periodontal membranes. They demonstrated that the incorporation of MgO nanoparticles barely affected the morphology and mechanical property of nanocellulose membranes and MgO nanoparticles-incorporated coaxial electrospinning PCL-derived nanocellulose periodontal membranes might have great prospects for periodontal tissue regeneration. Xu et al., used enzymatic hydrolysis residues (EHRs) of corncob residues to produce high lignin-containing cellulose nanofibrils (LCNFs) and lignin nanoparticles (LNPs) through a facile approach. They investigated morphology, thermal stability, chemical and crystalline structure, and dispersibility of the resultant LCNFs and LNPs. This work demonstrated that the lignocellulose-based nanomaterials with excellent properties could be achieved by coupling LCNFs and LNPs from EHRs. Huang et al., reviewed the recent developments and various applications of hemicellulose from wheat straw, including the hemicellulose-based derivatives and composites. In addition, they discussed the microstructure and molecule of hemicellulose extracted by different methods. Overall, this review will contribute to the development and high-value applications of hemicellulose from wheat straw.

AUTHOR CONTRIBUTIONS

All authors listed have made a substantial, direct, and intellectual contribution to the work and approved it for publication.

Conflict of Interest: The authors declare that the research was conducted in the absence of any commercial or financial relationships that could be construed as a potential conflict of interest.

Publisher's Note: All claims expressed in this article are solely those of the authors and do not necessarily represent those of their affiliated organizations, or those of the publisher, the editors and the reviewers. Any product that may be evaluated in this article, or claim that may be made by its manufacturer, is not guaranteed or endorsed by the publisher.

Copyright © 2022 Huang, Xu, Meng, Wang and Zhou. This is an open-access article distributed under the terms of the Creative Commons Attribution License (CC BY). The use, distribution or reproduction in other forums is permitted, provided the original author(s) and the copyright owner(s) are credited and that the original publication in this journal is cited, in accordance with accepted academic practice. No use, distribution or reproduction is permitted which does not comply with these terms.



Inactivation of Inulinase and Marination of High-Quality Jerusalem Artichoke (*Helianthus tuberosus* L.) Pickles With Screened Dominant Strains

Li Zhang, Wei Liu, Jiahong Ji, Lina Deng, Qian Feng, Wujian Shi and Jian Gao*

School of Marine and Bioengineering, Yancheng Institute of Technology, Yancheng, China

OPEN ACCESS

Edited by:

Caoxing Huang,
Nanjing Forestry University, China

Reviewed by:

Chi Cheng,
Dalian University of Technology, China
Shang-Tian Yang,
The Ohio State University,
United States

*Correspondence:

Jian Gao
gaojian@ycit.edu.cn

Specialty section:

This article was submitted to
Bioprocess Engineering,
a section of the journal
Frontiers in Bioengineering and
Biotechnology

Received: 07 November 2020

Accepted: 18 December 2020

Published: 20 January 2021

Citation:

Zhang L, Liu W, Ji J, Deng L, Feng Q, Shi W and Gao J (2021) Inactivation of Inulinase and Marination of High-Quality Jerusalem Artichoke (*Helianthus tuberosus* L.) Pickles With Screened Dominant Strains. *Front. Bioeng. Biotechnol.* 8:626861. doi: 10.3389/fbioe.2020.626861

Freshly harvested Jerusalem artichoke tubers contain inulinase, an enzyme that requires inactivation, because of its ability to hydrolysis inulin into fructose, which can be consumed by microorganism during marination. As the traditional pickling process takes 6 months, and involves the addition of a large amount of salt (18–20%), this production strategy is uneconomical and increases the nitrite intake. Additionally, miscellaneous bacteria produced during pickling affect the product taste. In this study, the enzyme inactivation effects of NaCl, NaHCO₃, and ultrasound were evaluated. NaHCO₃ treatment results in the highest degree of enzyme inactivation; however, the quality and flavor of the obtained Jerusalem artichoke pickles were not ideal. The Jerusalem artichoke pickles in which the enzymes were inactivated using a combination of NaCl and ultrasound exhibited better flavor than those exposed to NaHCO₃; further, this combination reduced the inulinase activity of the Jerusalem artichokes to 2.50 U/mL, and maintained the inulin content at 61.22%. The strains LS3 and YS2, identified as *Enterococcus faecalis* and the salt-tolerant yeast *Meyerozyma guilliermondii*, respectively, were the dominant microorganisms isolated from the pickle juice. Jerusalem artichokes with inactivated inulinase were pickled with microbial powder, separated, purified, and dried to remove the natural Jerusalem artichoke sauce. This process shortened the fermentation cycle and improved product quality.

Keywords: Jerusalem artichoke pickles, inulinase, enzyme inactivation, microbial powder, inulin

INTRODUCTION

The Jerusalem artichoke, also known as *Helianthus tuberosus* L., belongs to the *Compositae* family and the sunflower genus. The artichokes are widely cultivated and distributed, owing to their ecological adaptability and fertility under harsh conditions, such as salinity, alkalinity, cold, drought, and wind (Shao et al., 2019). As a non-grain raw material that has a high yield as well as soil-improving and environment-beautifying attributes, the Jerusalem artichoke can provide many ecological and economic benefits (Guo et al., 2018). Jerusalem artichoke tubers have a fine texture, a crisp, sweet taste, and they are rich in nutrients, including inulin, vitamins, minerals, amino acids, and trace elements (Guo et al., 2018; Judprasong et al., 2018). Importantly, the Jerusalem artichokes serves as an ideal raw material for high-quality pickles (Lv et al., 2019).

Pickled vegetables undergo a traditional microbial fermentation process that employs the preservative effect of salt to prolong the shelf life of the vegetable. The popularity of pickled vegetables has been steadily rising, owing to their unique color, aroma, and low cost (Behera et al., 2020). For instance, the unique sensory properties (i.e., flavor and mouthfeel) and the potential health benefits associated with lactic acid fermentation in the Paojiao produced in Yunnan—considered the most authentic—have made it popular in China (Ye et al., 2020). Another pickled product, Kimchi is world-renowned for being rich in vitamin A, thiamine, riboflavin, calcium, iron, and lactic acid-producing bacteria. In addition, several studies have reported that fermented soybean products possess beneficial properties, including antioxidant, antimicrobial, blood pressure-lowering, and antidiabetic activity (Hwang et al., 2017).

Jerusalem artichoke pickles are crisp, fragrant, slightly sweet, and tender; further, they are easy to store, which is why they are favored by consumers. Healthier and low-salt pickles are being prepared to match the improved living standards. Moreover, Jerusalem artichoke tubers are rich in inulin, which is the second most-common plant storage carbohydrate after starch and accounts for ~50–70% of the Jerusalem artichoke tuber stem weight (Rubel et al., 2018). Inulin is a linear polysaccharide in which D-fructofurans are linked by a β (1→2) bond, with a D-glucose residue—typically residing at the end of individual fructose chains—being linked to fructose by an α (1→2) bond (Zhu et al., 2020). The average molecular weight of inulin is ~5,500 Da, and the molecular formula is G_nF_n , as shown in **Figure 1**, where G represents the terminal glucose, F represents fructose, and n represents the number of fructose units. Inulin is used as a healthcare product as it has been shown to regulate blood sugar, reduce fat and weight, improve the intestinal environment, promote mineral absorption, and prevent constipation (Shoaib et al., 2016; Wang et al., 2016; Yu et al., 2018). Thus, the development of Jerusalem artichoke pickled products is of economic importance; however, the enzymes involved in the pickling process may alter the flavor and texture of the product.

One problem that is encountered during the pickling of Jerusalem artichokes is the presence of inulinase. During the pickling of fresh Jerusalem artichokes, inulin present in these vegetables can be acted on by inulinase. Inulinase can hydrolyze the β (1→2) glycoside bonds between the fructose moieties of inulin, and this process is widely used in the production of oligosaccharides and high-fructose syrup (Singh et al., 2020). Inulin can be degraded by inulinase into fructose, which is consumed by microorganism during pickling. Furthermore, inulinase can alter the quality of pickled products, so it is necessary to take appropriate measures to check inulinase activity in Jerusalem artichoke pickles during the curing process. This not only preserves the beneficial health properties of inulin, but also protects Jerusalem artichokes from putrefaction and deterioration, and inhibits discoloration, flavor change, and nutrient content reduction due to enzyme activity (Makroo et al., 2020).

Another problem in the processing of Jerusalem artichoke pickles is the long curing period, during which a large amount

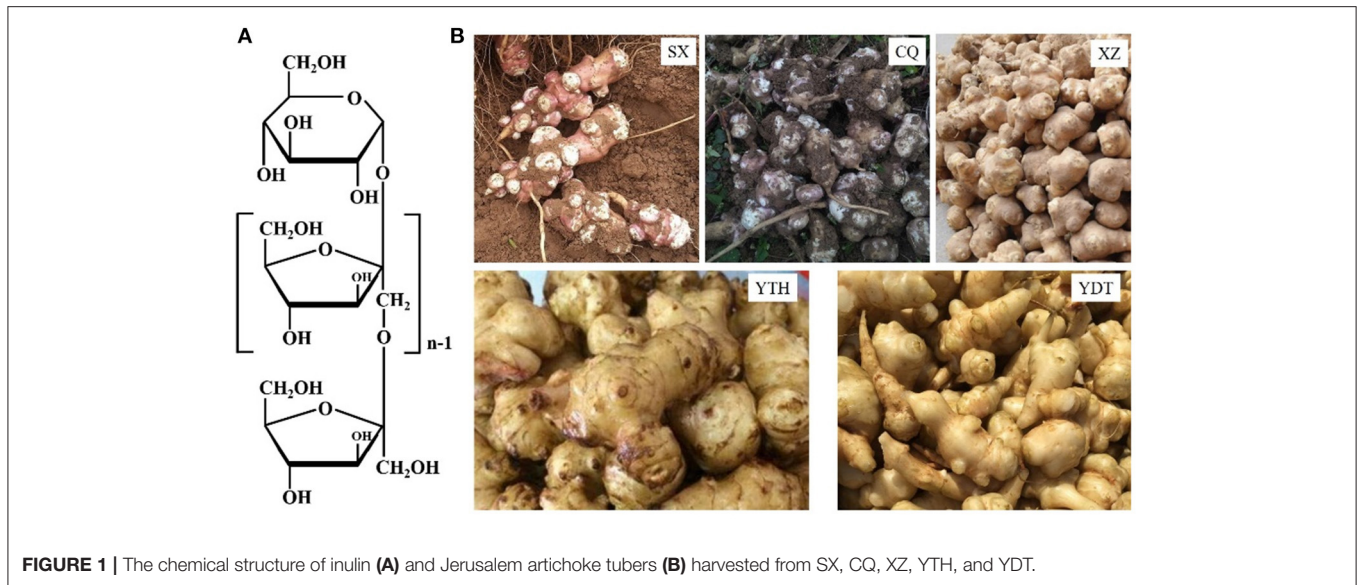
of salt is added (18–20%) and the pickles are exposed to an environment with high nitrite levels and infectious microbes. Notably, the procedure is uneconomical, and the high levels of nitrite and miscellaneous microorganisms produced during the pickling process affect the taste of the product. In this study, dry powders of lactic acid bacteria and yeast strains were separated from pickle juice samples that had been obtained from a pickle factory and used as experimental strains. Microorganisms (mainly lactic acid bacteria and yeasts) play a pivotal role in pickling and affect the quality and safety of the final product (Behera et al., 2020). The inulin and nitrite contents of the Jerusalem artichokes subjected to traditional and improved pickling processes were determined, with the goal of screening and identifying naturally-brewed strains and shortening the pickling period.

Inulinase inactivation in Jerusalem artichoke pickles presents many challenges, including the prevention of inulin degradation and preservation of the taste of pickles, while ensuring the production of high-quality Jerusalem artichoke pickles. To our knowledge, no method has been developed to inactivate the inulinase—to ensure inulin preservation—during the production of Jerusalem artichoke pickles. Therefore, it is necessary to prepare high-quality pickles with the raw material of Jerusalem artichoke tubers and explore inulinase inactivation, so as to maintain the inulin content of Jerusalem artichokes during curing, thereby preserving the health benefits associated with artichokes. Specifically, the aim of this study was to investigate the effects of enzyme inactivation during the pickling of Jerusalem artichokes. The effect of three different treatments, i.e., NaCl, NaHCO_3 , and ultrasound on inulinase inactivation during Jerusalem artichokes pickling were evaluated; their effects on the sensory qualities of the pickles were studied. Then, Jerusalem artichokes with inactivated inulinase were pickled using microbial powder, which had been separated, purified, and dried from the natural Jerusalem artichoke sauce. This process shortened the fermentation cycle and improved the product quality. Efforts are underway to develop nutritious, therapeutic, low salt, and naturally preserved vegetables.

MATERIALS AND METHODS

Raw Materials and Crude Inulin Extract

Jerusalem artichoke tubers that were fresh, shiny, even in size, and free from decay and mechanical damage were purchased from Shan Xi (SX), Chong Qing (CQ), Xu Zhou (XZ), Yancheng Ting Hu (YTH), and Yancheng Dong Tai (YDT). The tubers were washed, dried, peeled, and weighed. Inulinase activity was determined by preparing inulinase crude extract from 10 g of fresh Jerusalem artichoke tuber. The remaining Jerusalem artichoke tubers were cut into thin slices and then heated in boiling water at 100°C for 5–10 min to inactivate polyphenol oxidase (PPO), which is responsible for browning in most vegetables (Makroo et al., 2020). Then, the artichoke slices were dried in an oven at constant temperature, and the weight was recorded. Jerusalem artichoke powder (ground using a grinder and then sifted through a 40-mesh sieve) was mixed with distilled water at a ratio of 1:8 and incubated in a 70°C water bath



for 2 h. The pH was adjusted to 10.0 with lime milk, and the solution was then incubated in an 80°C water bath for 1 h. Inulin extract was obtained after removing the filter residue using eight layers of gauze. The total sugar and reducing sugar content were determined to calculate the inulin content of the Jerusalem artichoke tubers.

Inulinase Inactivation

Salt Stress

Fresh Jerusalem artichoke tubers were washed, dried, sliced into 5 mm-thick slices weighing 100 g, placed in 600 mL pickle jars, and salted with NaCl. The fresh Jerusalem artichoke tubers contained ~80% water. After salt was added, the Jerusalem artichoke slices exuded water to dissolve the salt, and the exudate covered all of the pickled Jerusalem artichoke slices. The taste of Jerusalem artichoke pickles can change in the presence of excessive salt and nitrite, and the traditional pickle marinade of 18–20% (w/w) salt is not healthy. Therefore, the concentration of salt was reduced to 10–16% (w/w) in this study, which is cost-effective and benefits the green economy. Jerusalem artichoke slices (10 g) pretreated with salt were blended with 50 mL chilled phosphate buffer. The supernatant was collected after centrifugation at 5,000 r/min for 10 min and treated as a crude enzyme to determine inulinase activity.

NaHCO₃ Treatment

Fresh Jerusalem artichoke tubers were washed, dried, sliced into 5 mm thick slices weighing 100 g, placed in 600 mL pickle jars, and salted with NaHCO₃. The concentration of NaHCO₃ was reduced to 10–16% (w/w), and inulin content and inulinase activity were determined.

Ultrasonic Treatment

Jerusalem artichoke slices (100 g) were weighed accurately and then layered in a 500 mL beaker containing 150 mL distilled water. Then, inulinase was inactivated in an ultrasonic cleaning

machine at room temperature with the following parameters: ultrasonic frequency, 40 KHz; ultrasonic power, 480 W for 20–70 min; gradient, 10 min. Inulin content and inulinase activity were then determined.

Microbial Powder Preparation

Screening for *Lactobacillus* in Pickle Juice

The Jerusalem artichoke pickle juice was diluted to the optimum concentration and plated onto LB agar medium. After incubating at 30°C for 2–3 d, bacteria with different growth potentials were selected and cultured repeatedly on LB medium, and pure bacteria were obtained. The pure bacteria were stored in 30% glycerin in a –20°C refrigerator for later use. The preserved strains were lined up and cultured in sterilized MRS solid medium, at 37°C for 3–4 d. Bacteria that were able to grow on MRS medium and exhibited melt-calcium rings were observed and recorded. The pure bacteria that grew on MRS culture medium were Gram-stained and observed using oil immersion microscopy (Zheng et al., 2020). The gram-positive bacteria were suspected to be *Lactobacillus* strains and were cultured on an inclined plane and preserved. *Lactobacillus* strains were identified by 16S rDNA sequencing (Won et al., 2020).

Saccharide fermentation tests were conducted as follows. Saccharide fermentation tubes were prepared, and inverted tubules were inserted to identify whether gas was generated. The tubes were marked and sterilized. The name of the fermentation medium and the number of lactic acid bacteria to be inoculated were marked on the outer wall of each tube with a marker pen. Different *Lactobacillus* strains were inoculated into corresponding labeled sugar fermentation tubes, which were shaken gently to blend and prevent bubble generation in the inverted tubes. An uninoculated sugar fermentation tube was used as a blank control. The sugar fermentation tubes and blanks were inoculated for 24–48 h at 37°C. The color change in each test

tube was examined to determine whether bubbles had formed in the Duchenne tubules.

Screening for Yeast in Pickle Juice

The Jerusalem artichoke pickle juice was pretreated, diluted to different concentrations, plated onto PDA medium, labeled, and incubated at 30°C for 2–3 d to observe culture growth. The best culture concentrations were selected, and the selected strains were lined on sterilized PDA medium and cultured at 30°C for 2–3 d. The growth states were compared and observed on the medium. The suspected strains were selected and lined on the medium to isolate single colonies. The purified single colonies were cultured on chloramphenicol-supplemented YPD, Czapek-Dox Medium, and Malt Extract Agar medium at 28°C for 3–4 d to observe growth. The suspected strains were isolated and purified on Malt Extract Agar medium and stored in glycerol for later use (Liu et al., 2018). Primers against D1/D2 region of the 26S rDNA were designed, and PCR was performed to identify yeast based on the amplification.

Procedure for Microbial Powder Preparation

The screened and purified strains were cultured for 48 h and centrifuged at 8,000 rpm for 5 min, after which the supernatant was discarded. The collected sediment was added to the protective agent in proportion and mixed using an oscillator to prepare the microbial suspension. The suspension was then placed in the freezer, pre-cooled at 4°C for 30 min, transferred to the –30°C refrigerator for 60 min, placed in a –80°C refrigerator for 60 min, and freeze-dried for 14 h in a freeze-vacuum drying machine (the temperature of the freeze-drying chamber was –60 to –70°C with a pressure of 0.1 Pa). The powder was sealed and stored in a refrigerator at 4°C, with 10% skim milk as the protective agent.

Brewing of High-Quality Artichoke Pickles

Curing after inulinase inactivation was performed as follows: the selected dominant microbial powder was obtained by screening and purifying the natural pickle juice. A solution of 10% (w/w) salt was added to the jar containing Jerusalem artichoke pieces with inactivated inulinase. The brine seeped out after 1–2 d, and 2% (w/w) salt was added until the top layer of the Jerusalem artichoke pieces was covered. Then, the dry bacterial powder was added. During the curing process, inulin, salt, and nitrite contents were measured every 4 d.

Analytical Methods

Determination of Inulin

3,5-Dinitrosalicylic acid (7.5 g), NaOH (14 g), sodium potassium tartrate (216.0 g), and sodium sulfite (6.0 g) were dissolved separately and mixed sequentially. Finally, 5.5 mL phenol was fully dissolved in 1,000 mL of distilled water, which had been pre-boiled for 10 min. The prepared 3,5-dinitrosalicylic acid colorimetry reagent (DNS) was stored in a 4°C refrigerator away from light, and the solution was used for a period of 1 month after allowing to stand for 5 d. Crude inulin extract (1 mL) was mixed with DNA reagent (3 mL), and incubated in a boiling water bath for 5 min to allow color development. The cooled solution was

diluted to an appropriate concentration with distilled water, and the absorbance was determined at 520 nm. The reducing sugar content was calculated using a standard curve.

Crude inulin extract (2 mL) was mixed with 6% phenol solution (1 mL), and then concentrated sulfuric acid (5 mL) was added rapidly, and the solution was left to cool for 10 min and then shaken well. After allowing solution to stand at room temperature for 20 min, the absorbance was measured at 490 nm. The total sugar content was calculated using a standard curve, and the inulin content was equal to the total sugar content minus the reducing sugar content.

Determination of Inulinase Activity

Crude inulinase solution (1 mL) was reacted with of 2% inulin (4 mL) prepared in an acetate buffer (pH 4.5) in a constant-temperature water bath (set at 55°C) for 30 min, and the reaction was terminated immediately by shifting the contents to a boiling water bath for 5 min. Pre-inactivated inulinase was used as a blank. DNS was used to measure reducing sugar content, and 1 mL of the sample was thoroughly mixed with 3 mL DNS reagent, and incubated in a boiling water bath for 5 min to allow color development. Then, the solution was diluted with distilled water to an appropriate concentration, and the absorbance was measured at a wavelength of 520 nm.

Under certain conditions, enzyme activity (U/mL) was defined as the amount of enzyme required to hydrolyze substrates to 1 g of fructose/min in a volume of 1 mL and calculated as follows.

$$E = \frac{1000 \times C \times N}{T \times V}$$

E, inulinase activity (U/mL); C, fructose content (mg/mL) corresponding to the average absorption value of the sample aligned with the standard curve; N, dilution of crude inulinase solution; T, reaction time (min); V, crude enzyme volume involved in the reaction (mL).

Detection of Salt Content

Samples (5–10 g) were added to a 250 mL volumetric bottle, to which 50 mL distilled water, 1 mL potassium chromite (50 g/L), and 25 mL sample liquid were added. Another conical bottle was used as a blank control, wherein instead of the sample, distilled water was used. A silver nitrate standard solution (0.1 mol/L) was titrated to the end point (orange red), and the volume of consumption of the silver nitrate standard solution was recorded.

$$X = (V1 - V0) \times C \times 0.0585 / (m \times 25/250) \times 100\%$$

X, content of salt (NaCl) in the sample (%); V1, dilution of the sample used for determination of silver nitrate volume (mL) with the standard titration solution; V0, blank control of the volume of the standard titrated solution of consumed silver nitrate (mL); C, concentration of the standard titrated solution of silver nitrate (mol/L); M, mass of sample (g); 0.0585, the mass of sodium chloride that is equivalent to 1.00 mL of the silver nitrate standard solution (g).

TABLE 1 | Sense grade of Jerusalem artichoke pickles with inulinase inactivation and microbial powder.

Scores	Items		
	Color and lustre	Fragrance	Brittleness
4.5~5.0	Bright yellow, glossy without browning	Heavy flavor	Very crispy
4.0~4.5	Light yellow without obvious tan	Intense flavor	Crispy
3.5~4.0	Pale brownish yellow with partial browning of the epidermis	Light fragrance	Brittle
3.0~3.5	Epidermis of the plant with obvious browning	None	Soft
<3.0	All brown and black	Taint	Rot

Detection of Nitrite in the Samples

Pickle samples in the juicer were squeezed into a paste, and 100 g of the pickle paste was placed in the middle of a 250 mL beaker. The pickle paste—along with distilled water (80°C)—was placed in a 250 mL volumetric flask, and 2 g of carbon powder was added to remove the pigment and organic matter. Potassium ferrocyanide (2 mL) and zinc sulfate (2 mL) were used to precipitate proteins. Finally, distilled water was used to measure the volume, and a colorless transparent solution was obtained by vacuum pump filtration.

The filtrate (40 mL) was weighed and poured into a 50 mL volumetric flask, and 2 mL of paminophenesulfonic acid was added. After allowing to stand for 3 min, 1 mL naphthalene ethylenediamine hydrochloride was added, and distilled water was added to the scale. The solution was shaken and allowed to stand for 15 min, and then, the absorbance was determined at a wavelength of 540 nm using distilled water as the reference. Finally, the nitrite content in the pickles was calculated using a standard curve according.

Sensory Evaluation

Sensory evaluation of the Jerusalem artichoke pickles with inactivated inulinase was conducted, and the criteria and scoring matrices are shown in **Table 1**. The quality—measured based on taste, flavor, and color—varied depending on the manufacturing process. Here, the score was mainly based on color, flavor, and crispness, with 5 point score for each, as shown in **Table 1** (de Matos et al., 2019). Sixty members of the laboratory and related major students were selected for the test, and the total score was calculated as follows: total score = color × 30% + crispness × 30% + fragrance × 40%.

RESULTS AND DISCUSSION

Comparison of Inulin Content and Inulinase Activity in Jerusalem Artichokes From Different Habitats

The inulin content and inulinase activity of artichokes from different habitats, SX, CQ, XZ, YTH, and YDT, are shown in

TABLE 2 | Comparison of inulin content and inulinase activity in Jerusalem artichokes from different habitats.

	SX	CQ	XZ	YTH	YDT
Inulin content (%)	68.85	67.08	64.02	62.93	53.31
Inulinase (U/mL)	5.17	3.98	4.02	4.51	4.45

Table 2. Depending on the region of origin, the outer skin of the tuber was either red, yellow, or white; the shape was an irregular tumor or spindle; and the roots were fibrous, as shown in **Figure 1**. In the Jerusalem artichokes from different production areas, inulin content also differed due to different soil, water, light, temperature, and wind conditions and other external factors (de Matos et al., 2019; Lv et al., 2019). Therefore, in order to obtain higher quality Jerusalem artichoke pickles with inulin—more conducive to human health—the total sugar and reducing sugar contents of Jerusalem artichokes from SX, CQ, XZ, YTH, and YDT were measured to calculate the inulin content. The inulin content of Jerusalem artichokes ranged from 50 to 70%, which is close to the values published in literature (Lv et al., 2019). The inulin content was the highest in artichokes from SX—accounting for 68.85% of the dry Jerusalem artichoke weight—while those from YDT had the lowest inulin content (53.31%).

Further, the Jerusalem artichokes from SX exhibited the highest inulinase activity (5.17 U/mL), followed by those from YTH and YDT. The inulinase activity of Jerusalem artichokes harvested from XZ and CQ was only slightly lower than that of artichokes from other regions. Plants secrete far lower amounts of inulinase than microorganisms (Yuan et al., 2012; Singh et al., 2020). For instance, optimization of the parameters for inulinase production during *Rhizopus oryzae*-mediated fermentation using a statistical approach, resulted in maximum inulinase activity and specific activity of 348.36 EU/mL and 3621.78 EU/mg, respectively (Yazici et al., 2020).

Effect of Different Inactivation Processes on Inulin Content and Inulinase Activity

Jerusalem artichoke inulinase is a biocatalyst regulating inulin turnover, resulting in the production of low poly fructose or high-fructose syrup. However, inulin hydrolysis by inulinase should be avoided; as loss of inulin would result in low-quality Jerusalem artichoke pickles. The inulinase activity of Jerusalem artichokes can be affected, to different degrees, by the physical and chemical properties of Jerusalem artichokes, the microorganisms present during the pickling process, and human intervention.

Salt Stress

NaCl is an abiotic stress that reduces the inulinase activity during pickling process of Jerusalem artichoke. The soil environment, osmotic stress, and ion poisoning due to salt could also inhibit inulinase activity. As shown in **Figure 2**, a solution of 10–16% NaCl was used to inactivate inulinase during the pickling of Jerusalem artichokes. Higher salt concentrations were correlated with greater ability to inactivate the enzyme, but the variation in inulinase activity was limited among samples treated with

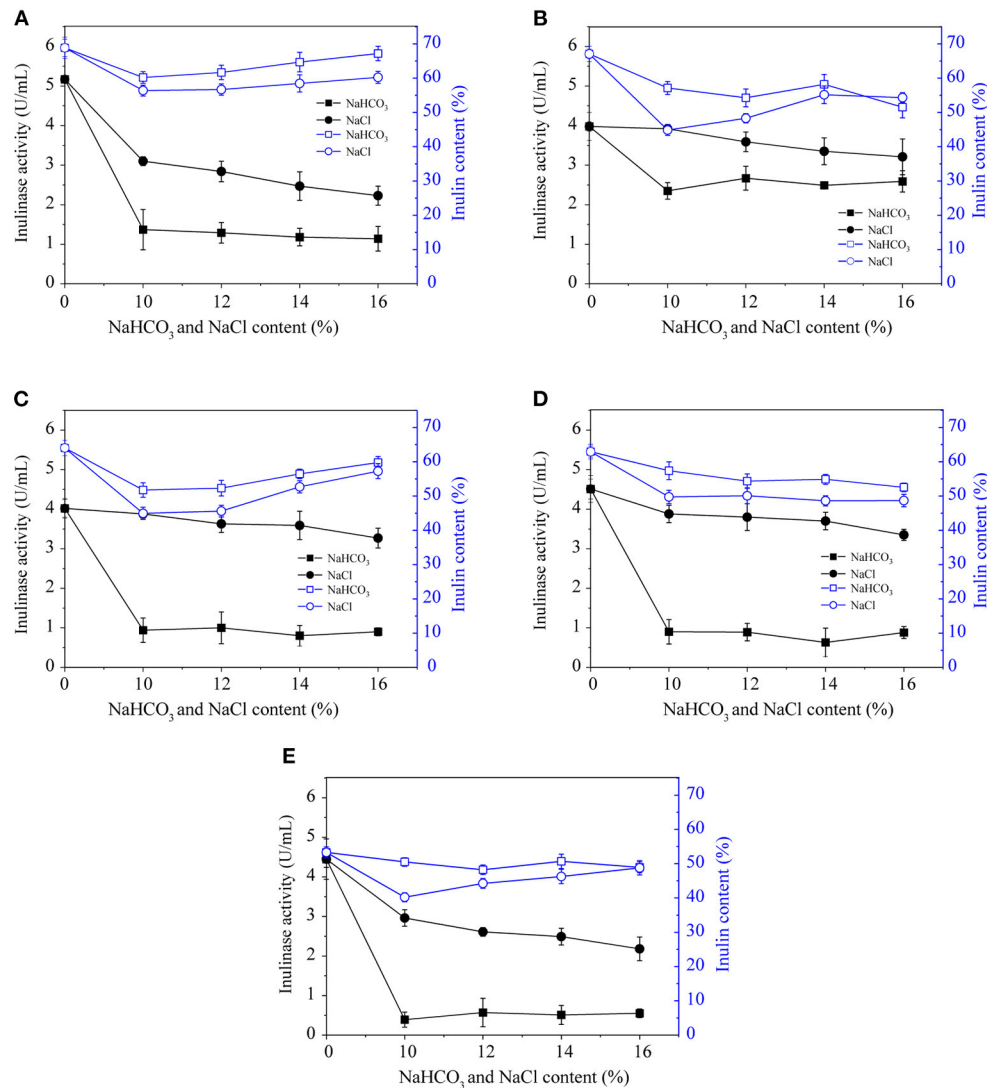
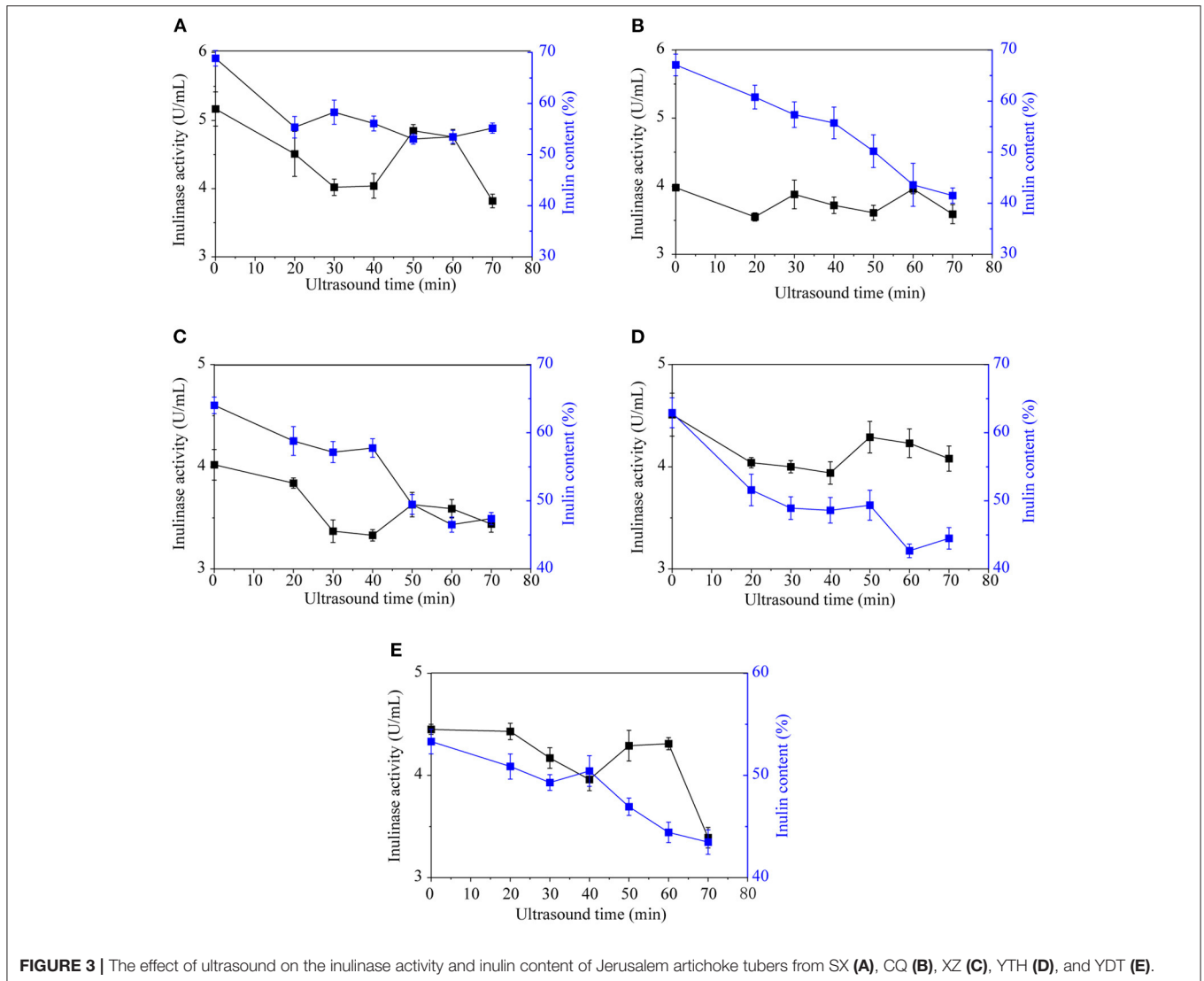


FIGURE 2 | The effects of NaHCO₃ and NaCl on the inulinase activity and inulin content of Jerusalem artichoke tubers from SX (A), CQ (B), XZ (C), YTH (D), and YDT (E).

varying concentrations of NaCl (10–16%) according to **Figure 2**. Therefore, in response to the increasing adaption of low-salt lifestyles, 10–12% NaCl is considered to be good choice for inactivating inulinase in Jerusalem artichokes. When NaCl was used to inactivate inulinase, the artichokes initially exhibited a flaxen appearance; only slight browning and softening occurred over time, and the flavor was considerable (Luo et al., 2018). According to feedback from the Jerusalem artichoke brewing plant, the Jerusalem artichoke acquired after maturation can be washed and pickled with only 10% NaCl in the middle of October every year. This might be due to the low temperature in winter, leading to reduced activity of various mixed bacteria compared with that in spring and summer (Li et al., 2015); thus, less salt is used.

Treatment With NaHCO₃

NaHCO₃ has been widely used in analytical, synthetic, pharmaceutical, medical, and food fermentation. It does not alter the dry weight of the cells in the fermentation system during vegetable curing, but it significantly increases the rate of glucose consumption (Zhang et al., 2019). According to **Figure 2**, a 10–16% solution of NaHCO₃ can inactivate inulinase during Jerusalem artichoke pickling. The inulinase activity of Jerusalem artichokes from CQ, after NaHCO₃ treatment, was ~2.5 U/mL. After Na₂HCO₃ treatment, the inulinase activity of Jerusalem artichokes from the remaining four regions was similar, ~0.5–1.5 U/mL. However, the Jerusalem artichoke tubers exhibited browning and became soft during marination. Furthermore, artichoke appearance, taste, and sensory qualities



were unsatisfactory when inactivation was performed using NaHCO_3 . In conclusion, Jerusalem artichoke tubers were damaged by NaHCO_3 stress to a much greater extent than they were in response to NaCl stress, as evidenced by the oxidative damage in mulberry seedling leaves (Zhang et al., 2019, 2020).

Ultrasonic Treatment

Ultrasonic waves are mechanical vibrations that can alter or accelerate changes in material performance, state, structure, and organization (Soria and Villamiel, 2010; Shoaib et al., 2016). Currently, ultrasonic processing is widely used as a new non-thermal technology for enzyme inactivation. Jerusalem artichoke inulinase could be inactivated by ultrasound, with an optimum effect at an ultrasonic time of 30–40 min (Figure 3). Ultrasonic treatment was most effective against inulinase from Jerusalem artichoke tubers from SX, with the inulinase activity decreasing from 5.17 to 4.02 U/mL. When the ultrasonication time was extended to 50–60 min, enzyme activity increased slightly

because the temperature approached the optimum temperature (55°C) required by Jerusalem artichoke inulinase for its activity. As the ultrasonic time continues to extend, high levels of energy are generated through extremely high-density shock waves, leading to extreme physical effects such as high temperature, high pressure, etc. This may alter the molecular structure and conformation of inulin, and enzyme activity might be reduced by the strong shear force and shock waves.

Ultrasound can damage the activity of enzymes, thereby affecting normal cells as well as energy metabolism, and even leading to cell death. Several studies have shown that the activity of ATP and catalase decreased after ultrasonic treatment, and ultrasonic treatment has also enhanced enzymatic browning (Soria and Villamiel, 2010). Various effects of ultrasonic waves, such as increased temperature, increased pressure, and vibration, can accelerate molecular movement, thus accelerating inulinase secretion into the medium and promoting the hydrolysis of Jerusalem artichoke inulin. The Jerusalem artichoke tubers

from different regions are irregular, with corners unwashed. Ultrasound can be used to deeply clean Jerusalem artichokes and inactivate inulinase, and it can be integrated with PPO enzyme inactivation, thereby reducing browning in the pickling process.

Combination of Salt and Ultrasonic Treatment

As shown in **Figure 2**, NaHCO_3 or salt stress was able to inactivate the inulinase of Jerusalem artichokes. NaHCO_3 achieved significantly better enzyme inactivation and inulin levels than NaCl. Further, 10–16% NaHCO_3 exhibited potent inulinase inactivating ability but resulted in bad flavor; thus, this treatment is not suitable for inactivating inulinase during the pickling of Jerusalem artichokes. In conditions of salt stress, higher concentrations of NaCl are correlated with a greater degree of enzyme inactivation and improved sensory qualities of Jerusalem artichokes. Under room temperature conditions, the frequency of the ultrasonic cleaner was fixed at 40 kHz, the ultrasonic power at 480 W, and the ultrasonic treatment at 30 min for Jerusalem artichokes purchased from SX. Then, 10% NaCl was added for enzyme inactivation. The Jerusalem artichoke with the highest inulin content was selected, and the inulinase was inactivated via ultrasound and NaCl. In response to this combined treatment, the inulinase activity was reduced to 2.50 U/mL, and the inulin percentage was 61.22%. Therefore, this strategy of using a combination of ultrasound and NaCl to inactivate inulinase could preserve the inulin content of Jerusalem artichokes during curing and maintain the beneficial health effects of these pickles (Shoaib et al., 2016; Yu et al., 2018).

Preparation of Microbial Powder Physiological, Biochemical, and Molecular Identification of Suspected Strains

In accordance with procedure 2.3, eight suspected *Lactobacillus* strains (labeled LS1–8) and seven yeast strains (labeled YS1–7) were selected from the pickle juice samples obtained from pickle factories as experimental strains. The eight suspected *Lactobacillus* strains were gram-positive. LB medium was used in the anaerobic test tube, and 0.1% CaCO_3 was added to solidify the sample. LS3 and LS6 grew well under anaerobic conditions, showing milky white and generally linear growth (Contreras-Hernández et al., 2018), while the growth of LS1 and LS8 was extremely poor. Lactic acid bacteria are commonly identified in pickles because of their ability to produce high levels of lactic acid and survive under highly acidic conditions (Zokaeifar et al., 2012). Indeed, pickles fermented by lactic acid bacteria have a distinctive flavor and exhibit positive effects on health (Irkin and Songun, 2012). The seven suspected yeast strains were molded into water immersion tablets and observed under a microscope. YS1 grew slightly worse, while YS2 and YS5 grew well compared with the other strains. The surface of the colony was white and smooth, the individual shape of the species was spherical or elliptical, and the flavor was strong.

Growth Curves of Microbial Species Under Different Salinity Conditions

Of the 15 strains (LS1–8 and YS1–7), four strains (LS3, LS6, YS2, and YS5) with good growth status were selected for salt tolerance

experiments. As shown in **Figure 4A**, in response to 1% NaCl, the growth of the four strains was relatively fast initially and then flattened or decreased over 16 h. When the NaCl concentration was increased to 4% (**Figure 4B**), the growth of LS3 ($\text{OD}_{620} = 2.96$) and YS2 ($\text{OD}_{620} = 3.14$) was relatively fast in the first 16 h. After 16 h, LS6 ($\text{OD}_{620} = 1.95$) and YS5 ($\text{OD}_{620} = 2.87$) still exhibited slow growth that did not decline until 32 h later. When the NaCl concentration increased to 7% (**Figure 4C**), the growth of LS3 ($\text{OD}_{620} = 2.65$) and YS2 ($\text{OD}_{620} = 3.42$) was faster within the first 16 h, but flattened or declined after 16 h, while LS6 and YS5 grew slowly within the first 8 h. The growth of all four strains in the first 8 h was rather slow in the presence of high salinity (10% NaCl) (**Figure 4D**). LS3 and YS2 exhibited a higher growth rate from 8 to 32 h, indicating that LS3 and YS2 were more resilient to 10% NaCl and could maintain high density for a long time. To summarize, YS2 and LS3 exhibited greater salt tolerance compared with strains YS5 and LS6, which could adapt to the salt concentration over a short time as the flora reproduced, thereby inhibiting the growth of other hybrid strains. Therefore, yeast YS2 and lactic acid bacteria LS3 were found to be Jerusalem artichoke brewing, and a dry powder made of YS2 and LS3, according to procedure 2.3.3, was added into the curing pot to reduce the curing period.

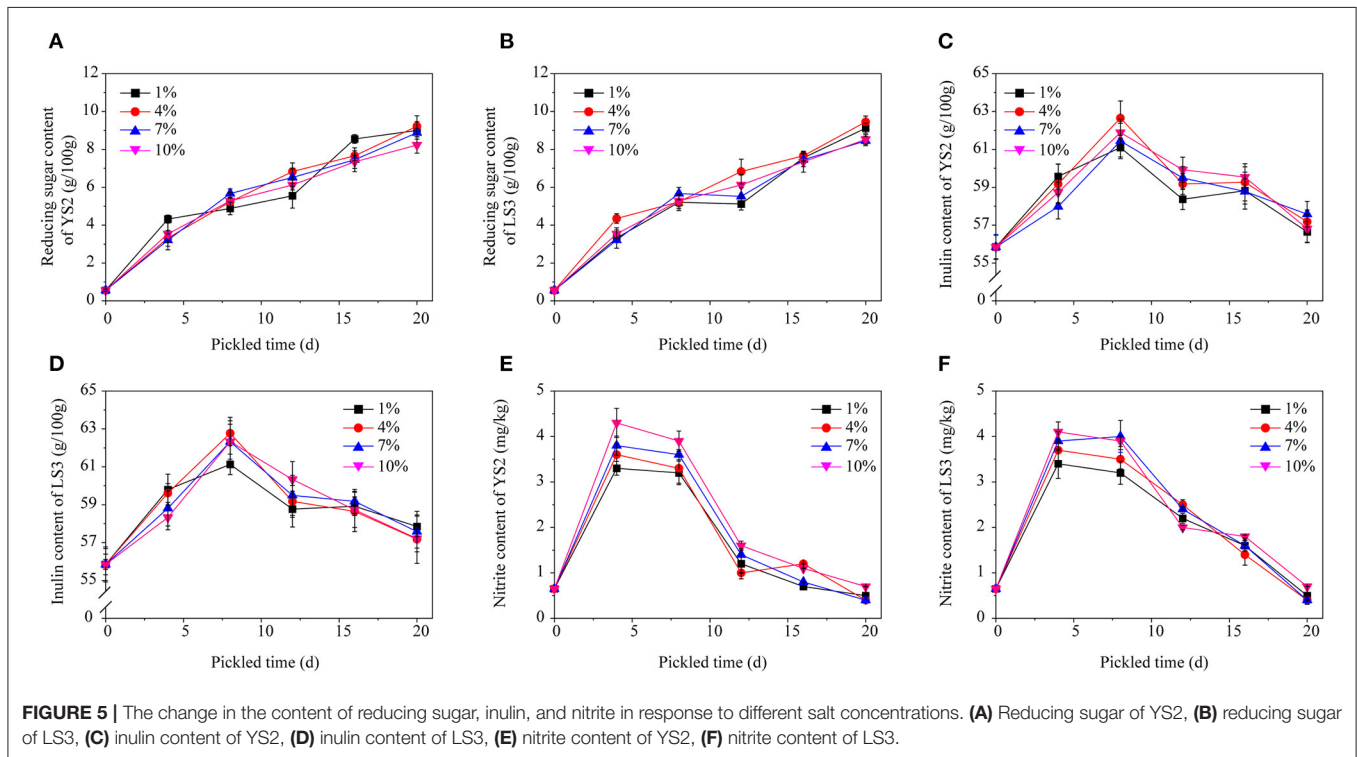
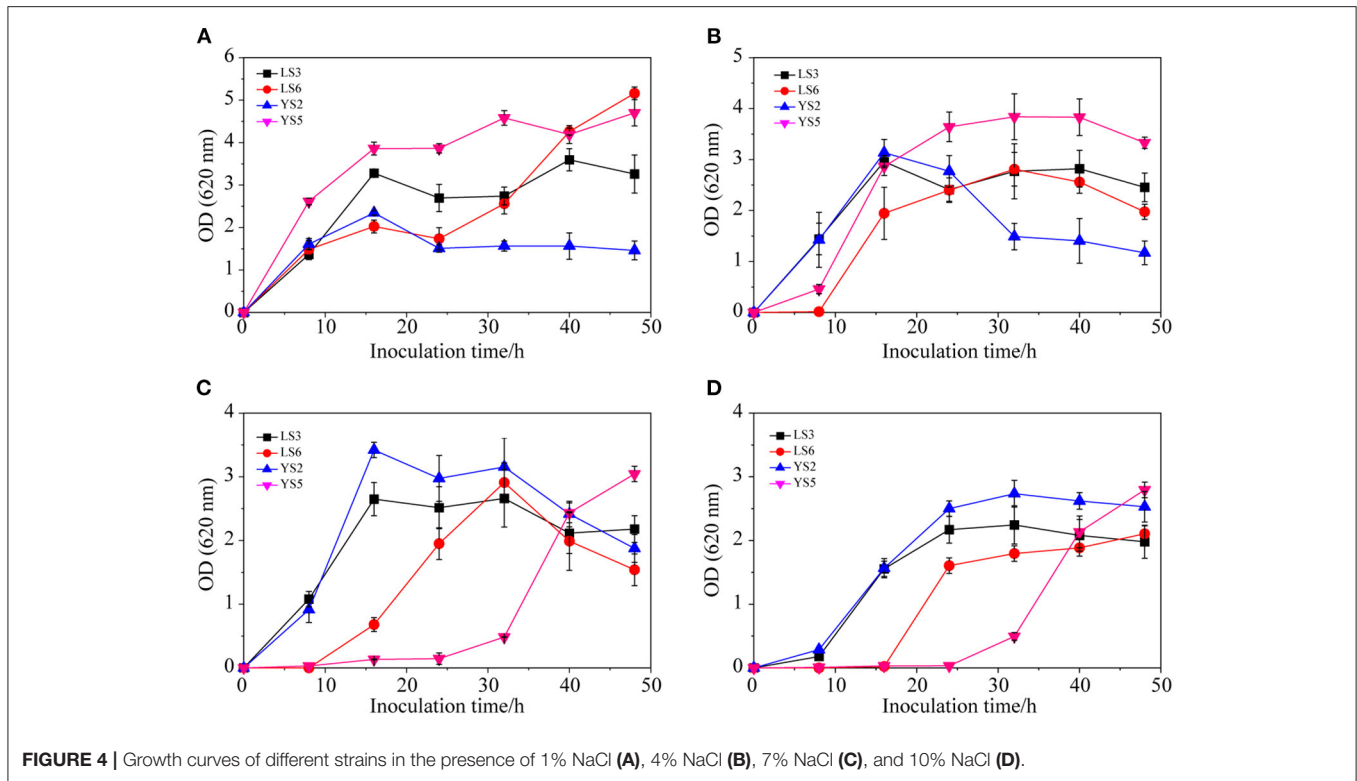
Alterations in Jerusalem Artichoke Pickle Components in Response to Different Salt Concentrations With Screened Strains

In contrast to the traditional pickling methods, in this study, we employed the strategy of adding a dry powder composed of the dominant strains YS2 and LS3 during the curing process, and measured the inulin and nitrite contents.

Microbial powders made of YS2 and LS3 were independently added to four salt concentrations (1, 4, 7, and 10%). The change in reducing sugar content is shown in **Figures 5A,B**. Initially, the reducing sugar content of the Jerusalem artichokes was low (0.78/100 g), but it gradually increased to 9.42/100 g. There was no significant change in the reducing sugar content between the two strains or between different salt concentrations. The reason for the gradual increase in the reducing sugar content was that the high salt concentration outside of the Jerusalem artichokes caused loss of water from the artichokes, resulting in the hydrolysis of polysaccharides into monosaccharides.

The change in inulin content is an important index to ensure the curing quality of Jerusalem artichokes. The inulin content exhibited an upward trend in the first 8 d and a downward trend until 12 d (**Figures 5C,D**). After curing for ~20 d, the inulin generally decreased to ~55/100 g. The trend of increasing inulin concentrations during the early stage may be attributed to the loss of water from Jerusalem artichoke tissues, while the decrease in inulin content in the later stage indicates inulin partially degradation.

It can be seen from **Figures 5E,F** that the nitrite content on the fourth day was relatively high, and even exceeded the national standard of 4 mg/kg, which was higher than the initial nitrite content. In the early pickling stage, nutrients oxidize the nitrate in vegetables into nitrite via the action of microorganisms. At the



same time, phenolic compounds in vegetables also reduce nitrite; however, the degree of nitrite generation is much higher than the degree of nitrite reduction, so the nitrite content in the early

stage increases dramatically. However, the salts and sugar present in Jerusalem artichokes inhibit the growth of microorganisms as well as the consumption of oxygen. Meanwhile, the nitrate

content in vegetables reduces owing to oxidation, so the nitrite level drops to a relatively stable value (Hou et al., 2013; Kandasamy et al., 2018).

The 16S rDNA universal primer was designed to identify LS3, and the whole genomic DNA of strain LWFQ2048 was used as the template. A target fragment of ~1,468 bp was obtained, which was purified and sent for sequencing. The sequencing results were used to construct phylogenetic trees using SPSS data analysis software for molecular identification, as shown in **Supplemental Figure 1**, and the strain LS3 was further identified as *Enterococcus faecalis*. Primers against D1/D2 region of the 26S rDNA were designed, and PCR was performed to identify strain YS2 based on the amplification of a target fragment of ~538 bp. The sequencing results were used to construct phylogenetic trees using SPSS data analysis software for molecular identification, as shown in **Supplemental Figure 2**, and the strain YS2 was further determined to be the salt-tolerant yeast *Meyerozyma guilliermondii*. The isolation of more lactic acid bacterial and yeast strains from the pickling juice has been under investigation. It's possible to develop a defined mixed culture for the pickling process based on the in-depth study.

In this study, sixty members of the laboratory and related major students were selected for sample evaluation. The total score was calculated as: total score = color × 30% + crispness × 30% + fragrance × 40%. The taste of the Jerusalem artichoke pickles significantly improved after adding LS3 and YS2 microbial powders. Notably, the sensory evaluation score of inulinase-inactivated Jerusalem artichoke pickles tubers with the microbial powder was 4.15 ± 0.27 (color was 4.03 ± 0.42 , crispness was 4.18 ± 0.36 , and fragrance was 4.23 ± 0.36), whereas that of naturally pickled artichokes was 3.75 ± 0.36 (color was 3.60 ± 0.48 , crispness was 3.79 ± 0.47 , and fragrance was 3.83 ± 0.68), and significance ($p < 0.001$) was evaluated by SPSS. The new method greatly shortens the fermentation cycle, reduces the amount of salt, and ensures that the nitrite content is lower than the national standard.

CONCLUSIONS

In this study, we identified a feasible strategy for inactivating of Jerusalem artichoke inulinase. The inulinase in Jerusalem

artichoke pickles was inactivated by employing a combination of salt stress and ultrasonic treatment, without any pronounced deterioration or color changes. Ultrasound for 30–40 min combined with 10% NaCl was found to be the best treatment to effectively deactivate inulinase while still producing a high-quality and flavorful pickle. Furthermore, two Jerusalem artichoke pickling strains were identified. A dry powder composed of lactic acid bacteria and yeast strain isolated from pickle juice samples obtained from a pickle factory were used to pickle Jerusalem artichokes with inactivated inulinase, which reduced the fermentation time to ~20–30 d and improved the quality of the final product.

DATA AVAILABILITY STATEMENT

The original contributions presented in the study are included in the article/**Supplementary Material**, further inquiries can be directed to the corresponding author.

AUTHOR CONTRIBUTIONS

All authors listed have made a substantial, direct and intellectual contribution to the work, and approved it for publication.

FUNDING

This work was financially supported by China Post-doctoral Science Foundation (2019M661727), Talent Introduction Project of Yancheng Institute of Technology (XJ201722), and North Jiangsu Science and Technology Special Project-Enriching Civilization and Enhancing the County (SZ-YC2018015).

ACKNOWLEDGMENTS

We would like to thank Editage (www.editage.cn) for English language editing.

SUPPLEMENTARY MATERIAL

The Supplementary Material for this article can be found online at: <https://www.frontiersin.org/articles/10.3389/fbioe.2020.626861/full#supplementary-material>

REFERENCES

- Behera, S. S., Sheikha, A. F. E., Hammami, R., and Kumar, A. (2020). Traditionally fermented pickles: How the microbial diversity associated with their nutritional and health benefits? *J. Funct. Foods* 70:103971. doi: 10.1016/j.jff.2020.103971
- Contreras-Hernández, M. G., Ochoa-Martínez, L. A., Rutiaga-Quíñones, J. G., Rocha-Guzmán, N. E., Lara-Ceniceros, T. E., Contreras-Esquivel, J. C., et al. (2018). Effect of ultrasound pre-treatment on the physicochemical composition of *Agave durangensis* leaves and potential enzyme production. *Bioresour. Technol.* 249, 439–446. doi: 10.1016/j.biortech.2017.10.009
- de Matos, A. D., Marangon, M., Magli, M., Cianciabella, M., Predieri, S., Curioni, A., et al. (2019). Sensory characterization of cucumbers pickled with verjuice as novel acidifying agent. *Food Chem.* 286, 78–86. doi: 10.1016/j.foodchem.2019.01.216
- Guo, X., Xie, Z., Wang, G., Zou, Q., and Tang, R. (2018). Effect on nutritional, sensory, textural and microbiological properties of low-fat yoghurt supplemented with Jerusalem artichoke powder. *Int. J. Dairy Technol.* 71, 167–174. doi: 10.1111/1471-0307.12404
- Hou, J. C., Jiang, C., and Long, Z. (2013). Nitrite level of pickled vegetables in Northeast China. *Food Control* 29, 7–10. doi: 10.1016/j.foodcont.2012.05.067
- Hwang, J., Kim, J., Moon, H., Yang, J., and Kim, M. (2017). Determination of sodium content in traditional fermented foods in Korea. *J. Food Compos. Anal.* 56, 110–114. doi: 10.1016/j.jfca.2016.11.013
- Irkin, R., and Songun, G. E. (2012). Applications of probiotic bacteria to the vegetable pickle products. *Sci. Rev. Chem. Commun.* 2, 562–567. Available online at: <https://www.tsijournals.com/articles/applications-of-probiotic-bacteria-to-the-vegetable-pickle-products.pdf>

- Judprasong, K., Archeepsudcharit, N., Chantapiriyapoon, K., Tanaviyutpakdee, P., and Temviriyankul, P. (2018). Nutrients and natural toxic substances in commonly consumed Jerusalem artichoke (*Helianthus tuberosus* L.) tuber. *Food Chem.* 238, 173–179. doi: 10.1016/j.foodchem.2016.09.116
- Kandasamy, S., Kavitha, D., and Shetty, P. H. (2018). "Lactic acid bacteria and yeasts as starter cultures for fermented foods and their role in commercialization of fermented foods," in *Innovations in Technologies for Fermented Food and Beverage Industries*, eds S. Panda, and P. Shetty (Cham: Springer), 25–52. doi: 10.1007/978-3-319-74820-7_2
- Li, W., Zhang, J., Yu, C., Li, Q., Dong, F., Wang, G., et al. (2015). Extraction, degree of polymerization determination and prebiotic effect evaluation of inulin from Jerusalem artichoke. *Carbohydr. Polym.* 121, 315–319. doi: 10.1016/j.carbpol.2014.12.055
- Liu, K.-F., Li, X.-H., and Hui, F.-L. (2018). *Yarrowia brassicae* f.a., sp. nov., a new yeast species from traditional Chinese sauerkraut. *Int. J. Syst. Evol. Microbiol.* 68, 2024–2027. doi: 10.1099/ijsem.0.002783
- Luo, R., Song, X., Li, Z., Zhang, A., Yan, X., and Pang, Q. (2018). Effect of soil salinity on fructan content and polymerization degree in the sprouting tubers of Jerusalem artichoke (*Helianthus tuberosus* L.). *Plant Physiol. Biochem.* 125, 27–34. doi: 10.1016/j.plaphy.2018.01.025
- Lv, S., Wang, R., Xiao, Y., Li, F., Mu, Y., Lu, Y., et al. (2019). Growth, yield formation, and inulin performance of an on-food energy crop, Jerusalem artichoke (*Helianthus tuberosus* L.), in a semi-arid area of China. *Ind. Crops Prod.* 134, 71–79. doi: 10.1016/j.indcrop.2019.03.064
- Makroo, H. A., Rastogi, N. K., and Srivastava, B. (2020). Ohmic heating assisted inactivation of enzymes and microorganisms in foods: a review. *Trends Food Sci. Technol.* 97, 451–465. doi: 10.1016/j.tifs.2020.01.015
- Rubel, I. A., Iraporda, C., Novosad, R., Cabrera, F. A., Genovese, D. B., and Manrique, G. D. (2018). Inulin rich carbohydrates extraction from Jerusalem artichoke (*Helianthus tuberosus* L.) tubers and application of different drying methods. *Food Res. Int.* 103, 226–233. doi: 10.1016/j.foodres.2017.10.041
- Shao, T., Gu, X., Zhu, T., Pan, X., Zhu, Y., Long, X., et al. (2019). Industrial crop Jerusalem artichoke restored coastal saline soil quality by reducing salt and increasing diversity of bacterial community. *Appl. Soil Ecol.* 138, 195–206. doi: 10.1016/j.apsoil.2019.03.003
- Shoib, M., Shehzad, A., Omar, M., Rakha, A., Raza, H., Sharif, H. R., et al. (2016). Inulin: properties, health benefits and food applications. *Carbohydr. Polym.* 147, 444–454. doi: 10.1016/j.carbpol.2016.04.020
- Singh, R. S., Singh, T., Hassanb, M., and Kennedy, J. F. (2020). Updates on inulinases: Structural aspects and biotechnological applications. *Int. J. Biol. Macromol.* 164, 193–210. doi: 10.1016/j.ijbiomac.2020.07.078
- Soria, A. C., and Villamiel, M. (2010). Effect of ultrasound on the technological properties and bioactivity of food: a review. *Trends Food Sci. Technol.* 21, 323–331. doi: 10.1016/j.tifs.2010.04.003
- Wang, Z., Hwang, S. H., Lee, S. Y., and Lim, S. S. (2016). Fermentation of purple Jerusalem artichoke extract to improve the α -glucosidase inhibitory effect in vitro and ameliorate blood glucose in db/db mice. *Nutr. Res. Pract.* 10, 282–287. doi: 10.4162/nrp.2016.10.3.282
- Won, S.-M., Chen, S., Park, K. W., and Yoon, J.-H. (2020). Isolation of lactic acid bacteria from kimchi and screening of *Lactobacillus sakei* ADM14 with anti-adipogenic effect and potential probiotic properties. *Food Sci. Technol.* 126:109296. doi: 10.1016/j.lwt.2020.109296
- Yazici, S. O., Sahin, S., Biyik, H. H., Geroglu, Y., and Ozmen, I. (2020). Optimization of fermentation parameters for high-activity inulinase production and purification from *Rhizopus oryzae* by Plackett–Burman and Box–Behnken. *J. Food Sci. Technol.* doi: 10.1007/s13197-020-04591-3
- Ye, Z., Shang, Z., Li, M., Qu, Y., Long, H., and Yi, J. (2020). Evaluation of the physicochemical and aromatic qualities of pickled Chinese pepper (Paojiao) and their influence on consumer acceptability by using targeted and untargeted multivariate approaches. *Food Res. Int.* 137, 109535–109545. doi: 10.1016/j.foodres.2020.109535
- Yu, Q., Zhao, J., Xu, Z., Chen, Y., Shao, T., Long, X., et al. (2018). Inulin from Jerusalem artichoke tubers alleviates hyperlipidemia and increases abundance of bifidobacteria in the intestines of hyperlipidemic mice. *J. Funct. Foods* 40, 187–196. doi: 10.1016/j.jff.2017.11.010
- Yuan, B., Hu, N., Sun, J., Wang, S.-A., and Li, F.-L. (2012). Purification and characterization of a novel extracellular inulinase from a new yeast species *Candida kutaonensis* sp. nov. KRF1T. *Appl. Microbiol. Biotechnol.* 96, 1517–1526. doi: 10.1007/s00253-012-4108-y
- Zhang, H., Li, X., Guan, Y., Li, M., Wang, Y., An, M., et al. (2020). Physiological and proteomic responses of reactive oxygen species metabolism and antioxidant machinery in mulberry (*Morus alba* L.) seedling leaves to NaCl and NaHCO₃ stress. *Ecotoxicol. Environ. Saf.* 193:110259. doi: 10.1016/j.ecoenv.2020.110259
- Zhang, H., Shi, G., Shao, J., Li, X., Li, M., Meng, L., et al. (2019). Photochemistry and proteomics of mulberry (*Morus alba* L.) seedlings under NaCl and NaHCO₃ stress. *Ecotoxicol. Environ. Saf.* 184:109624. doi: 10.1016/j.ecoenv.2019.109624
- Zheng, X.-F., Yang, Z., Zhang, H., Jin, W.-X., Xu, C.-W., Gao, L., et al. (2020). Isolation of virulent phages infecting dominant mesophilic aerobic bacteria in cucumber pickle fermentation. *Food Microbiol.* 86:103330. doi: 10.1016/j.fm.2019.103330
- Zhu, P., Zeng, Y., Chen, P., Meng, Y., Yang, J., Yue, X., Zhang, J., Zhu, Y., and Sun, Y. (2020). A one-pot two-enzyme system on the production of high value-added D-allulose from Jerusalem artichoke tubers. *Proc. Biochem.* 88, 90–96. doi: 10.1016/j.procbio.2019.10.006
- Zokaeifar, H., Balcázar, J. L., Kamarudin, M. S., Sijam, K., Arshad, A., and Saad, C. R. (2012). Selection and identification of non-pathogenic bacteria isolated from fermented pickles with antagonistic properties against two shrimp pathogens. *J. Antibiot.* 65, 289–294. doi: 10.1038/ja.2012.17

Conflict of Interest: The authors declare that the research was conducted in the absence of any commercial or financial relationships that could be construed as a potential conflict of interest.

Copyright © 2021 Zhang, Liu, Ji, Deng, Feng, Shi and Gao. This is an open-access article distributed under the terms of the Creative Commons Attribution License (CC BY). The use, distribution or reproduction in other forums is permitted, provided the original author(s) and the copyright owner(s) are credited and that the original publication in this journal is cited, in accordance with accepted academic practice. No use, distribution or reproduction is permitted which does not comply with these terms.



Co-production of Xylooligosaccharides and Xylose From Poplar Sawdust by Recombinant Endo-1,4- β -Xylanase and β -Xylosidase Mixture Hydrolysis

Qi Li^{1,2†}, Yunpeng Jiang^{2†}, Xinyi Tong², Linguo Zhao^{2,3*} and Jianjun Pei^{1,2}

¹ Jiangsu Co-Innovation Center for Efficient Processing and Utilization of Forest Products, Nanjing Forestry University, Nanjing, China, ² College of Chemical Engineering, Nanjing Forestry University, Nanjing, China, ³ Co-innovation Center for Sustainable Forestry in Southern China, Nanjing Forestry University, Nanjing, China

OPEN ACCESS

Edited by:

Lei Wang,
Jeju National University, South Korea

Reviewed by:

Xiao Jiang,
North Carolina State University,
United States
Jingcong Xie,
Chinese Academy of Forestry, China

*Correspondence:

Linguo Zhao
njfu2304@163.com

[†] These authors have contributed
equally to this work

Specialty section:

This article was submitted to
Bioprocess Engineering,
a section of the journal
Frontiers in Bioengineering and
Biotechnology

Received: 03 December 2020

Accepted: 21 December 2020

Published: 01 February 2021

Citation:

Li Q, Jiang Y, Tong X, Zhao L and
Pei J (2021) Co-production of
Xylooligosaccharides and Xylose From
Poplar Sawdust by Recombinant
Endo-1,4- β -Xylanase and
 β -Xylosidase Mixture Hydrolysis.
Front. Bioeng. Biotechnol. 8:637397.
doi: 10.3389/fbioe.2020.637397

As is well-known, endo-1,4- β -xylanase and β -xylosidase are the rate-limiting enzymes in the degradation of xylan (the major hemicellulosic component), main functions of which are cleaving xylan to release xylooligosaccharides (XOS) and xylose that these two compounds have important application value in fuel, food, and other industries. This study focuses on enzymatic hydrolysis of poplar sawdust xylan for production of XOS and xylose by a GH11 endo-1,4- β -xylanase MxynB-8 and a GH39 β -xylosidase Xln-DT. MxynB-8 showed excellent ability to hydrolyze hemicellulose of broadleaf plants, such as poplar. Under optimized conditions (50°C, pH 6.0, dosage of 500 U/g, substrate concentration of 2 mg/mL), the final XOS yield was 85.5%, and the content of XOS₂₋₃ reached 93.9% after 18 h. The enzymatic efficiency by MxynB-8 based on the poplar sawdust xylan in the raw material was 30.5%. Xln-DT showed excellent xylose/glucose/arabinose tolerance, which is applied as a candidate to apply in degradation of hemicellulose. In addition, the process and enzymatic mode of poplar sawdust xylan with MxynB-8 and Xln-DT were investigated. The results showed that the enzymatic hydrolysis yield of poplar sawdust xylan was improved by adding Xln-DT, and a xylose-rich hydrolysate could be obtained at high purity, with the xylose yield of 89.9%. The enzymatic hydrolysis yield was higher (32.2%) by using MxynB-8 and Xln-DT together. This study provides a deep understanding of double-enzyme synergetic enzymolysis of wood polysaccharides to valuable products.

Keywords: poplar sawdust, xylooligosaccharide, synergetic enzymolysis, endo-1,4- β -xylanase, β -xylosidase

INTRODUCTION

Hemicellulose is a structural polysaccharide that constitutes agricultural and forestry plant cell wall, which is often cross-linked with cellulose and lignin to form lignocellulose (Yang et al., 2020). As one of the richest and cheapest renewable resources on earth, hemicellulose is mainly composed of pentose (D-xylose, L-arabinose) and (or) hexose (D-glucose, D-mannose, D-galactose) and other monosaccharide groups (xylose is the most abundant) (Lahtinen et al., 2019; Qi et al., 2020). The

side chain may also contain a small amount of glucuronic acid (D-glucuronic acid, 4-O-methyl-D-glucuronic acid, and D-galacturonic acid) groups (Sun et al., 2013). Therefore, hemicellulose has tremendous latent capacity in the production of biofuels, feeds, and other chemicals, which contribute to the development of a circular economy (Ordonsky et al., 2015; Wang et al., 2020). Poplar is a kind of fast-growing and high-yield tree species, which has become an important industrial raw material and is used for civil construction, pulp and paper making, wood board processing, etc. (Christersson, 2008; Kiara et al., 2014; Dong et al., 2020). With the processing and utilization of poplar wood resources, a large number of wood residues and sawdust have been produced. These poplar sawdust residues contain 20–35% hemicellulose, which xylosyl group accounted for 30–40% of total sugar (Yan et al., 2015). Obviously, poplar sawdust has become one of the potential raw materials for efficient utilization of hemicellulose.

Xylan, as the most abundant hemicellulose in nature, is linked with xylopyranosyl group through β -1,4-glycosidic bond and may be replaced by glucuronic acid, arabinose, and acetic acid at the C2 and C3 positions of xylose (Li et al., 2020b). The main way to produce xylooligosaccharides (XOS) and xylose is from the degradation of xylan. XOS can selectively promote the proliferation of bifidobacteria and other probiotics, promote calcium absorption, and resist dental caries in human intestinal tract, among which the most effective components are xylobiose, xylotriose, and xyloetraose (Vázquez et al., 2000; Hsu et al., 2004). Moreover, compared with other functional oligosaccharides, XOS have good thermal stability and are not easy to degrade in the range of pH 2.0–7.0. In the biomass industry, XOS and xylose can be converted into ethanol, furfural, and other valuable fuels or chemicals (Zhang et al., 2015; Li et al., 2020a; Wang and Fang, 2020). At present, various pretreatment methods, such as self-hydrolysis, enzymatic hydrolysis, acid hydrolysis, microwave-assisted method, and enzymatic acid hydrolysis can be used to degrade xylan to obtain XOS with different polymerization degrees (Wei et al., 2018; Li et al., 2019b; Wen et al., 2019; Jun et al., 2020). Among these methods, through the self-hydrolysis of lignocellulose, the yield is low, and the by-products are multiple; the acid hydrolysis method using sulfuric acid or hydrochloric acid brings great burden to the environment. Compared with them, enzymatic hydrolysis is a powerful tool to convert hemicellulose into value-added products in an environmental friendly way because of its mild reaction conditions, being pollution-free, and high conversion efficiency (Menezes et al., 2009; Li et al., 2019a). Enzymatic degradation of xylan into XOS, disaccharides, monosaccharides, and other simpler components usually requires the combined use of a variety of relatively specific enzymes. Endo-1,4- β -xylanase and β -xylosidase are important components of enzyme cocktails for hydrolysis of xylan. Endo-1,4- β -xylanase can cut off the β -1,4-xyloside bonds in the main chain of xylan randomly to produce XOS, but not produce too many xyloses. Subsequently, β -xylosidase can continue to degrade the terminal, non-reducing β -D-xylosyl residues to release xylose, thus alleviating the inhibition of endo-1,4- β -xylanase by XOS (Blake et al., 2018). The synergy among endo-1,4- β -xylanase, β -xylosidase, and other

side-chain enzymes leads to that the hydrolysis efficiency of xylan can be significantly accelerated, thus reducing the cost of enzyme. Zhuo et al. (2018) reported a xylanase and β -xylosidase from white rot fungi and their application in synergistic hydrolysis of lignocellulose, in which the two enzymes could efficiently improve the hydrolysis rate of cornstalk pretreated by sodium hydroxide. Jamaldeen et al. (2019) optimized two-step enzymatic saccharification of hemicellulose part of the pretreated finger millet straw for production of xylose using endo-1,4- β -xylanase and exo-1,4- β -xylosidase with the percentage conversion yield of 24.7%.

From the source, endo-1,4- β -xylanase and β -xylosidase can be produced by many organisms, such as fungi, bacteria, plant, and archaea (Li et al., 2017, 2020c; Shi et al., 2018; Zhang et al., 2019b). Nowadays, the hot spot of research is still microbial source endo-1,4- β -xylanases and β -xylosidases. According to the amino acid sequence homology comparison, endo-1,4- β -xylanase was distributed in the glycoside hydrolases GH5, GH8, GH10, GH11, and GH43 (Vincent et al., 2014). Among them, endo-1,4- β -xylanases from GH11 family are widely used in lignocellulose degradation and food additives because of their high specificity, low molecular weight, and high catalytic efficiency (Juturu and Wu, 2012). At present, endo-1,4- β -xylanases from GH11 family are mainly distributed in *Aspergillus*, *Trichoderma*, and *Penicillium* (Collins et al., 2010). Generally, the expression level of endo-1,4- β -xylanases from filamentous fungi was much higher than that of bacterial endo-1,4- β -xylanases (Li et al., 2012). However, the optimum temperature and temperature stability of filamentous fungi endo-1,4- β -xylanases are far less than those of bacteria (Li et al., 2017). Merely, the thermostability of endo-1,4- β -xylanases from filamentous fungi can be improved by genetic engineering; thereby, the application scope of the filamentous fungi endo-1,4- β -xylanases is greatly extended (Li et al., 2019c). All the β -xylosidases are mainly divided into GH1, GH3, GH30, GH39, GH43, GH52, GH54, and GH120 (Rohman et al., 2019). However, most β -xylosidases, especially the β -xylosidases belonging to GH3, are sensitive and inhibited to xylose by feedback, which limits its practical application. The reported K_i values of β -xylosidases from *Penicillium oxalicum*, *Humicola insolens* Y1, *Thermotoga petrophila*, and *Dictyoglomus turgidum* were in the range of 1.857–28.09 mM (Yang et al., 2014; Ye et al., 2017; Zhang et al., 2019b; Li et al., 2020c). Along with a growing number of β -xylosidases discovered, β -xylosidases from GH39 family with high xylose tolerance (K_i values of 210–3,300 mM) are gradually recognized (Corrêa et al., 2012; Bhalla et al., 2014; Li et al., 2018). Thus, the application efficiency of GH39 family β -xylosidases in xylan hydrolysis was greatly improved.

In this article, a GH11 family endo-1,4- β -xylanase MxynB-G116C-Y135C-S58H-D76R-N28H-N29D-Y45M-N47L (MxynB-8) from *Aspergillus niger* NL-1, which has been modified by heat resistance (Li et al., 2019c), and a GH39 family β -xylosidase Xln-DT from *Dictyoglomus thermophilum* (Li et al., 2018) were used to hydrolyze poplar sawdust. At the same time, the enzymolysis conditions were optimized. In addition, the effect and mode of enzymatic hydrolysis of poplar sawdust xylan were also studied by MxynB-8 and Xln-DT. All the results will lay a foundation for the high-value application of poplar sawdust

xylan and determine its potential applicability to lignocellulosic bioethanol production.

MATERIALS AND METHODS

Materials and Reagents

The recombinant plasmids pTrc-99a-*mxynB*-G116C-Y135C-S58H-D76R-N28H-N29D-Y45M-N47L, pET-20b-*xynB-DT*, pET-28a-*xln-DT*, and pET-20b-*dt-xyl3* were constructed and preserved by Microbial Technology Research Laboratory (Nanjing Forestry University, China). *Escherichia coli* BL21 (DE3) was the expression host, which were preserved in Microbial Technology Research Laboratory. The bacterial strains were grown overnight at 37°C in Luria-Bertani (LB) medium containing kanamycin or ampicillin (100 µg/mL).

Poplar sawdust was purchased from Fukang wood processing plant (Jiangsu, China). The analysis of chemical components of poplar sawdust was carried out according to the National Renewable Energy Laboratory Standard (Abbas et al., 2020). The moisture content of milled poplar sawdust was ~9.8%. The results showed that the cellulose content of poplar sawdust was 38.91%, followed by hemicellulose (26.93%) and lignin (18.22%). Poplar sawdust xylan was extracted by alkali method. The optimum extraction conditions were as follows: the mass fraction of alkali solution was 10%, the ratio of solid to liquid was 1:10 (wt/vol), and the temperature was 120°C, whereas the yield of poplar xylan could reach 20.7% after 3 h. According to infrared radiation, acid hydrolysis, and high-performance liquid chromatography (HPLC) results, it showed that xylose was the main component of poplar sawdust xylan, accounting for 88.69%, and containing 4.76% cellobiose and 6.62% glucose (Supplementary Figure 1). The structure of xylan was mainly composed of β-configuration pyran ring (Supplementary Figure 2).

The substrate *p*-nitrophenyl-β-D-xylopyranoside (*p*NPX), *p*NP-β-D-glucoside (*p*NPG), *o*NP-β-D-glucoside (*o*NPG), *p*-nitrophenyl-β-D-galactopyranoside (*p*NPGal), *p*-nitrophenyl-α-L-rhamnopyranoside (*p*NPR), *p*NP-α-L-arabinofuranoside (*p*NPA), beechwood xylan, birchwood xylan, oat spelt xylan, D-glucose, D-xylose, D-galactose, D-mannose, and L-arabinose were purchased from Sigma-Aldrich (USA). Xylobiose (X_2), xylotriose (X_3), xyloetraose (X_4), xylopentaose (X_5), and xylohexaose (X_6) were purchased from Megazyme (Ireland), and were used as standards. All other conventional chemical reagents were of analytic grade and obtained from general commercial sources.

Protein Expression, Purification, Sodium Dodecyl Sulfate–Polyacrylamide Gel Electrophoresis Assay, and Enzyme Assay

The four recombinant expression plasmids were transformed into *E. coli* BL21 (DE3) and grown in LB kanamycin or ampicillin (100 µg/mL) medium at 37°C overnight. Then, the transformants were induced to express the recombinant MxynB-8, XynB-DT, Xln-DT, and Dt-xyl3, respectively, to an absorbance at OD₆₀₀ ~0.8 before being induced with 0.01 mM of isopropyl-β-D-thiogalactopyranoside (IPTG), and then the bacteria were

further incubated at 28°C for 6–14 h. Each cultures were harvested by centrifugation at 10,000 revolutions/min for 10 min at 4°C, and then the pellets were resuspended in 20 mM Tris-HCl buffer (pH 7.9) and broken up by ultrasonication (Ultrasonic Cell Pulverizer, China). The cell lysate after ultrasound was centrifuged at 10,000 revolutions/min for 20 min at 4°C to remove inclusion bodies. The crude endo-1,4-β-xylanase MxynB-8, XynB-DT and β-xylosidase Xln-DT, Dt-xyl3 were purified by an immobilized metal affinity column (Novagen, USA). Finally, the pure endo-1,4-β-xylanase and β-xylosidase proteins were collected by eluting with 1 M imidazole, 0.5 M NaCl, and 200 mM Tris-HCl buffer (pH 7.9), respectively.

Purities of the target proteins were performed by sodium dodecyl sulfate–polyacrylamide gel electrophoresis (SDS-PAGE) on a 12.5% gel, visualized by staining with Coomassie brilliant blue R-250, and the protein bands were analyzed by density scanning with Bio-Rad Analysis System (USA). The purified protein concentrations of the samples were determined by the Bradford method with bovine serum albumin as a standard (Chen et al., 2015).

Endo-1,4-β-xylanase activity was measured with a 3,5-dinitrosalicylic acid assay by using 1% solubilized beechwood xylan as a substrate in a 200 µL of reaction mixture containing 100 µL of 50 mM sodium citrate buffer (pH 6.0), 50 µL of beechwood xylan, and 50 µL of purified enzyme at the optimal temperature for 30 min. The activity of the enzyme without preincubation was defined as 100%. One unit of endo-1,4-β-xylanase activity was defined as the amount of enzyme that releases 1 µmol of reducing xylose from the substrate solution per minute. All measurements were performed in triplicate.

β-Xylosidase activity was assayed using *p*NPX as a substrate in a 200 µL of reaction mixture containing 180 µL of 50 mM sodium phosphate buffer (pH 6.0), 10 µL of 20 mM substrate *p*NPX, and 10 µL of purified enzyme. After incubation at the optimal temperature for 5 min, the reaction was stopped by adding 600 µL of 1 M Na₂CO₃. The absorbance of the released *p*NP was immediately measured at 405 nm. One unit of β-xylosidase activity was defined as the amount of enzyme releasing 1 µmol of *p*NP from the substrate solution per minute under the assay conditions. All measurements were performed in triplicate.

The substrate specific activities and kinetic constant (K_m and V_{max}) of the purified enzymes Xln-DT and Dt-xyl3 were tested by using *p*NPX, *p*NPG, *o*NPG, *p*NPGal, *p*NPR, and *p*NPA ranging from 0.2 to 8 mM under standard reaction conditions. The effects of various xylose, arabinose, and glucose concentrations (20, 50, 100, and 500 mM) on the β-xylosidase activity of purified enzyme Xln-DT and Dt-xyl3 were measured. Production of xylose and glucose from xylobiose and cellobiose (0.2, 0.5, 1.0, 2.0, 3.0, 5.0, 8.0, and 10.0 g/L), respectively, by the purified enzyme Xln-DT and Dt-xyl3 was examined. The activity of the enzyme without the sugar was defined as 100%. All experiments were performed in triplicate.

Enzymatic Hydrolysis of Beechwood, Birchwood, Oat Spelt, and Poplar Sawdust Xylan

Endo-1,4-β-xylanase MxynB-8 and XynB-DT were used by hydrolysis of 2 mg/mL beechwood, birchwood, oat spelt, and

poplar sawdust xylan, respectively, in 1.5 mL 50 mM sodium phosphate buffer (pH 6.0), which were carried out by incubating the reaction at 50 and 75°C (according to the optimum temperature of the enzyme to be determined, data were not shown), respectively, and 180 r/min in a bath shaking incubator. After 6 h, the supernatant of the reaction was collected to analyze the hydrolysate products. XOS were determined by HPLC (Dionex ICS-5000) equipped with a CarboPac PA-200 as the anion-exchange column using 100 mM NaOH and 500 mM NaOAc as the mobile phase at a flow rate of 0.3 mL/min and column temperature of 30°C. Standard four-potential-pulse amperometer was used for detection. The XOS yield and enzymatic efficiency were calculated according to the following equation:

$$\text{XOS yield (\%)} = \frac{\text{sum of all XOS } (X_2 - X_6) / \text{xylan in raw material} \times 100\%}{(1)}$$

where, $X_2 - X_6$ is the sum of mass concentrations of xylobiose, xylotriose, xyloetraose, xylopentaose, and xylohexaose (mg/mL).

$$\text{Enzymatic hydrolysis rate (\%)} = \frac{\text{the mole number of xylose in the enzymatic hydrolysate}}{\text{the mole number of xylose in the raw material}} \times 100\% \quad (2)$$

Optimization of Endo-1,4- β -Xylanase MxynB-8 Hydrolysis of Poplar Sawdust Xylan

The effects of several hydrolysis parameters (temperature, pH, enzyme dosage, and hydrolysis time) on XOS yield from poplar sawdust xylan were determined in batch systems. All reactions were incubated in a shaking water bath using the purified endo-1,4- β -xylanase MxynB-8, setting the poplar sawdust xylan concentration as 2 mg/mL. With the XOS yield as the evaluation index, the effects of different temperature (30, 40, 50, 60, 70, 80, and 90°C), pH (5.0, 5.5, 6.0, 6.5, 7.0, 7.5, and 8.0), enzyme dosage (50, 100, 200, 300, 400, 500, 600, and 800 U/g), and hydrolysis time (3, 6, 9, 12, 15, 18, 21, 24, and 28 h) were optimized. Three groups of parallel tests were set for all conditions. The best MxynB-8 hydrolysis conditions optimized were further used for MxynB-8 and Xln-DT mixture reaction optimization.

Optimization of Xylose Production From XOS by β -Xylosidase Xln-DT

Endo-1,4- β -xylanase MxynB-8 hydrolysate was used as substrate; further hydrolysis of XOS to produce xylose was carried out by β -xylosidase Xln-DT. For optimization of xylose production, the temperature, pH, and enzyme dosage were optimized. The ranges for the factors were as follows: temperature (30, 40, 50, 60, 70, 80, and 90°C), pH (5.0, 5.5, 6.0, 6.5, 7.0, 7.5, and 8.0), and enzyme dosage (50, 100, 200, 300, 400, and 500 U/g). The xylose concentrations were determined by HPLC (Agilent 1260, USA) equipped with a refractive index detector and Aminex Bio-Rad HPX-87H column using 50 mM H₂SO₄ at a flow rate of 0.6 mL/min and column temperature of 55°C.

Enzymatic Hydrolysis Model of Poplar Sawdust Xylan

Under the optimal conditions, the mode of enzymatic hydrolysis of poplar sawdust xylan by endo-1,4- β -xylanase MxynB-8 and β -xylosidase Xln-DT was studied; the specific design scheme was as follows: (1) only endo-1,4- β -xylanase MxynB-8; (2, 3) simultaneous enzymolysis by MxynB-8 and β -xylosidase Xln-DT; (4) the double-enzyme step hydrolysis: MxynB-8 was added first, and then the suitable temperature was adjusted, and Xln-DT was added; (5) the double-enzyme step hydrolysis: Xln-DT was added first, and then the suitable temperature was adjusted, and MxynB-8 was added; (6) only Xln-DT.

RESULTS AND DISCUSSION

Expression, Purification, and Characterization of Endo-1,4- β -Xylanase and β -Xylosidase

Under the optimal culture conditions, the endo-1,4- β -xylanases MxynB-8 and XynB-DT belonging to GH11 were heterologously expressed in *E. coli* BL21 (DE3) after incubation with 0.1 mM IPTG for 6 h, whereas the β -xylosidase Xln-DT belonging to GH39 and Dt-xyl3 belonging to GH3 were heterologously expressed in *E. coli* BL21 (DE3) after incubation with 0.01 mM IPTG for 14 h. After sonication, almost all the recombinant MxynB-8, XynB-DT, Xln-DT, and Dt-xyl3 were found in the soluble fraction, and the activities of the recombinant endo-1,4- β -xylanase and β -xylosidase were 563.1, 13.7, 5.6, and 5.3 U/mL, respectively. From the initial expression level of enzyme, the MxynB-8 from *A. niger* NL-1 was significantly higher than that of XynB-DT from *D. thermophilum*, ~41.1-fold, which indicated that the industrial application of MxynB-8 was more promising. Then, the soluble fractions were heat-treated in 75°C for 30 min and followed by a Ni²⁺-NTA affinity chromatography. The specific purification steps and yield were shown in **Table 1**. Finally, the purified endo-1,4- β -xylanase MxynB-8/XynB-DT and β -xylosidase Xln-DT/Dt-xyl3 showed a single band on the SDS-PAGE gel and a molecular mass of ~24, 50, 55, and 80 kDa, respectively, without undesired bands (**Figure 1**).

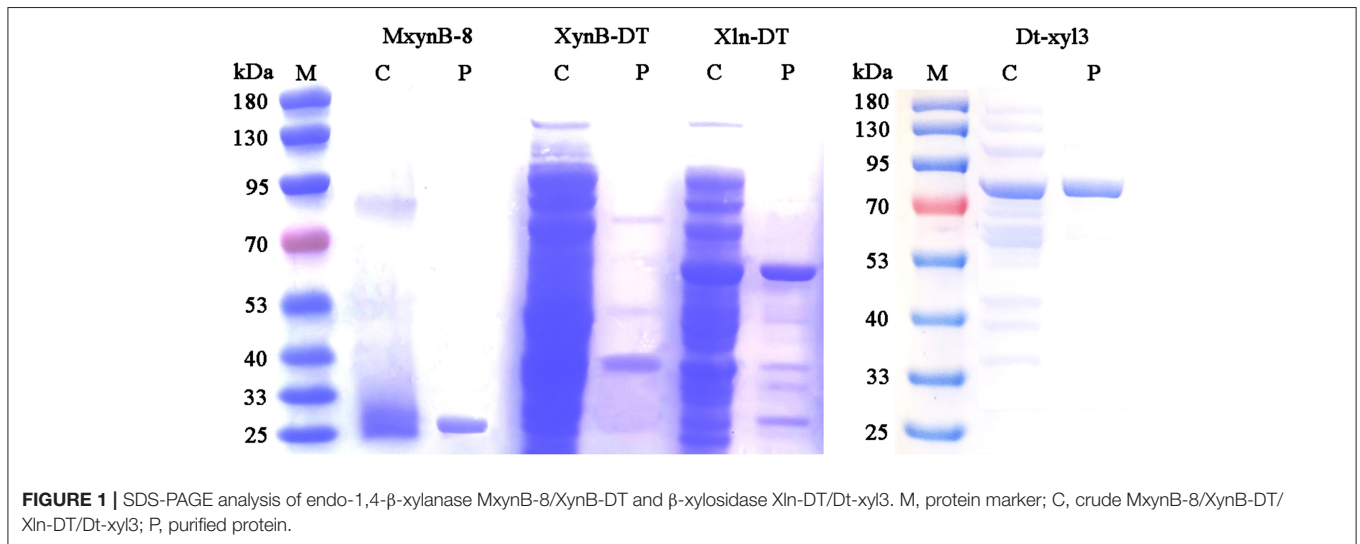
Enzymatic Specificity of MxynB-8 and XynB-DT to the Substrate

The endo-1,4- β -xylanase MxynB-8 and XynB-DT were tested for the specific activities to the different substrates and showed preference for xylan from birchwood, followed by beechwood xylan, poplar sawdust xylan, and oat spelt xylan (**Table 2**). Compared with the xylan from Gramineae (oat spelt xylan), these two endo-1,4- β -xylanases were more suitable for the degradation of xylan from broadleaf plants (68.4, 65.5, and 63.8% XOS yields for birchwood, beechwood, and poplar sawdust xylan, respectively, by MxynB-8, whereas 51.9, 45.9, and 54.4% XOS yields for birchwood, beechwood, and poplar sawdust xylan, respectively, by XynB-DT). Moreover, MxynB-8 and XynB-DT showed very low affinities for carboxymethylcellulose (CMC), which suggests that these two endo-1,4- β -xylanases do not have

TABLE 1 | Purification of recombinant protein MxynB-8, XynB-DT, Xln-DT, and Dt-xyI3.

Enzyme	Culture extract			Ni affinity chromatography			Yield (%)	Fold purification
	Total activity (U)	Total protein (mg)	Specific activity (U/mg)	Total activity (U)	Total protein (mg)	Specific activity (U/mg)		
MxynB-8	56,312.8	97.7	576.38	43,923.9	48.2	910.68	78.1	1.58
XynB-DT	13,766.1	2,935.2	4.69	9,553.7	352.2	27.12	69.4	5.78
Xln-DT	560.4	190.5	2.94	318.3	37.2	8.56	56.8	2.91
Dt-xyI3	532.4	287.9	1.85	285.4	46.3	6.16	53.4	3.35

Substrate for MxynB-8 and XynB-DT was beechwood xylan, while substrate for Xln-DT and Dt-xyI3 was p-nitrophenyl- β -D-xylopyranoside.

**FIGURE 1** | SDS-PAGE analysis of endo-1,4- β -xylanase MxynB-8/XynB-DT and β -xylosidase Xln-DT/Dt-xyI3. M, protein marker; C, crude MxynB-8/XynB-DT/Xln-DT/Dt-xyI3; P, purified protein.**TABLE 2** | Enzymatic hydrolysis of different xylans and other substrates in 6 h by MxynB-8 and XynB-DT.

Source	MxynB-8							XynB-DT						
	XOS yield (%)	Distribution of X1-X6 (%)						XOS yield (%)	Distribution of X1-X6 (%)					
		X1	X2	X3	X4	X5	X6		X1	X2	X3	X4	X5	X6
Birchwood xylan	68.4	10.2	41.1	2.9	—	2.3	43.4	51.9	14.0	68.9	14.6	—	—	2.5
Beechwood xylan	65.5	9.6	37.8	3.0	—	2.4	47.2	45.9	15.8	67.5	2.9	10.3	3.4	—
Oat spelt xylan	42.6	19.1	62.6	14.7	—	3.5	—	32.8	17.2	72.9	4.1	—	—	5.8
Poplar sawdust xylan	63.8	5.2	36.4	6.0	6.9	2.2	43.2	54.4	1.8	46.0	11.3	8.6	2.8	29.5
CMC		ND							ND					

X1, xylose; X2, xylobiose; X3, xylotriose; X4, xylotetraose; X5, xylopentaose; X6, xylohexaose; XOS, xylooligosaccharides; CMC, carboxymethylcellulose; ND, not detected.

cellulose degradation function, as is the case of endo-1,4- β -xylanase of *Streptomyces* sp. (Georis et al., 2000) and *Caulobacter crescentus* (Jacomini et al., 2020). Cellulose-free endo-1,4- β -xylanase can remove hemicellulose compounds selectively with minimal cellulose loss, which is more profitable industrial processes, such as pulp bleaching, textile biorefining treatment, and food industry (Belfaqui et al., 2002).

In consideration of beechwood and birchwood, xylans are commercially difficult to obtain by most suppliers, or else the cost of the available products is very high. In addition, the

composition and structure of these substrates derived from broadleaf are similar, so the performance of the endo-1,4- β -xylanases against these compounds is also equivalent. In the later experiments, poplar sawdust xylan was used as substrate to investigate the hydrolysis efficiency of these two endo-1,4- β -xylanases. After 6-h hydrolysis, MxynB-8 and XynB-DT both could degrade the poplar sawdust xylan into XOS, with the XOS yield of 63.8 and 54.4%, respectively (Figure 2). Xylobiose and xylohexaose are the main components in the hydrolysate, with a small amount of xylose, xylotriose, xylotetraose, and

xylopentaose. Similar results were obtained for endo-1,4- β -xylanases from *Streptomyces* sp. (Kholis et al., 2015) and *Massilia* sp. (Xu et al., 2016), which degrade beechwood and wheat xylan specifically, and showed no detectable enzyme activity to other polysaccharides with different compositions. As the endo-1,4- β -xylanase MxynB-8 from *A. niger* has excellent expression capacity, its protein expression is significantly higher than that of XynB-DT from *D. thermophilum*, which is 41.1-fold of its expression. Considering the cost of enzyme, the application of endo-1,4- β -xylanase MxynB-8 from *A. niger* in hemicellulose degradation is more suitable.

Substrate Specificity and Effect of Sugar on Xln-DT and Dt-xy13 Activity

In addition to xylosyl recognition ability, β -xylosidase also has different catalytic ability to other types of glycosyl, such as

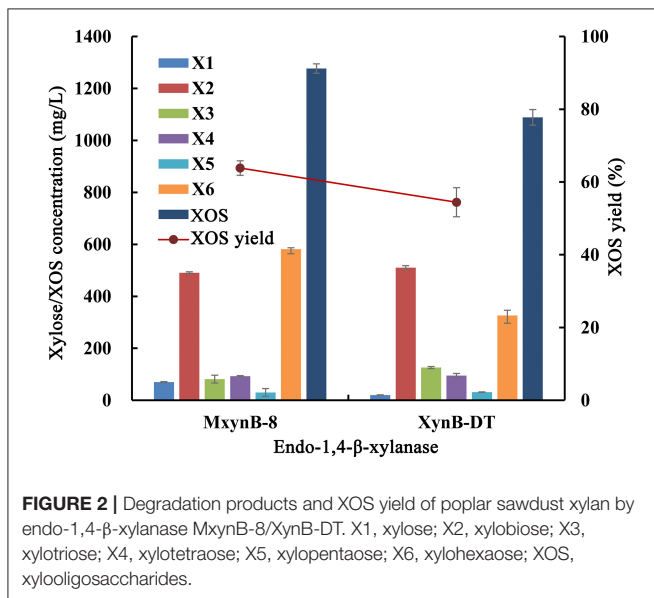


FIGURE 2 | Degradation products and XOS yield of poplar sawdust xylan by endo-1,4- β -xylanase MxynB-8/XynB-DT. X1, xylose; X2, xylobiose; X3, xylotriose; X4, xylo-tetraose; X5, xylopentaose; X6, xylohexaose; XOS, xylooligosaccharides.

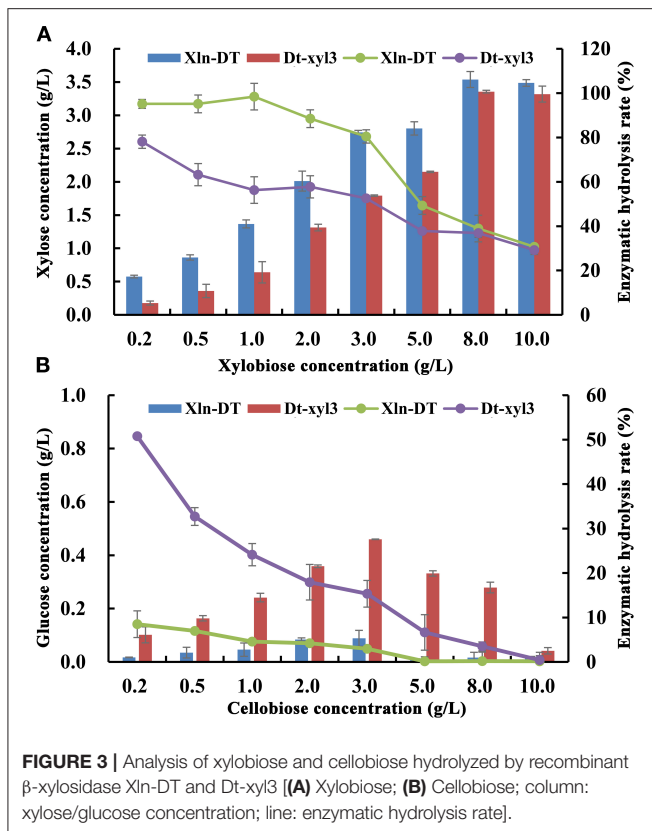
glucosyl, arabinopyranosyl, galactosyl, etc. Shi et al. (2013) cloned a GH3 β -xylosidase from *Thermotoga thermarum*, which could hydrolyze not only xylose but also arabinose. Zhang et al. (2019b) reported a GH3 β -xylosidase from *T. petrophila* could hydrolyze not only xylosyl, but also glucose and arabinopyranosyl groups. In order to further analyze the substrate specificity and kinetic constant (K_m and V_{max}) of two β -xylosidases, the enzyme activities of the purified enzymes Xln-DT and Dt-xy13 were detected, respectively, by using *p*NPX, *p*NPG, *o*NPG, *p*NPGal, *p*NPR, *p*NPA, cellobiose, xylobiose, and CMC. As shown in **Table 3**, both the enzyme Xln-DT and Dt-xy13 were able to hydrolyze *p*NPX and xylobiose with excellent efficiency and had few ability to hydrolyze *p*NPG and *p*NPA, whereas no activity was detected upon *o*NPG, *p*NPGal, *p*NPR, and CMC. *p*NPG was hydrolyzed at 25.9 and 21.6% of that of *p*NPX by Xln-DT and Dt-xy13, respectively, whereas for *p*NPA the relative activities were 44.4 and 30.8%, respectively. The dependence of the rate of the enzymatic reaction on the substrates concentration followed Michaelis–Menten kinetics, with K_m and V_{max} values of 1.66 mM and 13.58 U/mg for Xln-DT, respectively, and 0.83 mM and 19.05 U/mg for Dt-xy13, respectively, using the *p*NPX as the substrate. For xylobiose, the K_m and V_{max} values were 0.93 mM and 714.29 U/mg for Xln-DT, respectively, which were higher than that of Dt-xy13. Thus, the degradation efficiency of XOS by Xln-DT is higher than that by Dt-xy13.

Production of xylose and glucose from different concentrations of xylobiose and cellobiose by the purified Xln-DT and Dt-xy13 were determined. With the increase of the xylobiose concentration, xylose was also accumulated (**Figure 3**). When the concentration of xylobiose was below 3 g/L, the yield of Xln-DT enzymatic hydrolysis xylose could be maintained 80.5%, whereas the yield of Dt-xy13 enzymatic hydrolysis xylose could be only maintained 52.6%. In addition, the hydrolysis ability of cellobiose by Xln-DT was significantly lower than that by Dt-xy13. When 0.2 g/L of cellobiose was used as substrate, the enzymatic hydrolysis yield of Dt-xy13 was 50.7%, whereas that of Xln-DT

TABLE 3 | Kinetic parameters and specific activities of recombinant Xln-DT and Dt-xy13.

Substrate	Xln-DT			Dt-xy13		
	K_m (mM)	V_{max} (U/mg)	Relative activity (%)	K_m (mM)	V_{max} (U/mg)	Relative activity (%)
<i>p</i> NPX	1.66	13.58	100.0	0.83	19.05	100.0
<i>p</i> NPG	3.67	6.03	25.9	2.39	10.90	21.6
<i>o</i> NPG		ND			ND	
<i>p</i> NPGal		ND			ND	
<i>p</i> NPR		ND			ND	
<i>p</i> NPA	1.02	3.89	44.4	2.04	28.68	30.8
Cellobiose	11.00	217.39	—	2.28	277.78	—
Xylobiose	0.93	714.29	—	4.18	666.7	—
CMC		ND			ND	

*p*NPX, *p*-nitrophenyl- β -D-xylopyranoside; *p*NPG, *p*NP- β -D-glucoside; *o*NPG, *o*NP- β -D-glucoside; *p*NPGal, *p*-nitrophenyl- β -D-galactopyranoside; *p*NPR, *p*-nitrophenyl- α -L-rhamnopyranoside; *p*NPA, *p*NP- α -L-arabinofuranoside; CMC, carboxymethylcellulose; ND, not detected. Values shown are the mean of duplicate experiments, and the variation about the mean is below 5%.



was 8.5%. Therefore, compared with Dt-xy13, Xln-DT is more suitable for hemicellulose hydrolysis, which only hydrolyzed β -1,4-xyloside bond, but the hydrolysis rate of β -1,6-glucoside bond is very low, thus can reduce the hydrolysis loss of cellulose.

Glycoside hydrolases, such as β -glucosidase, β -xylosidase, and α -rhamnosidase, are sensitive to sugars. Only a few of the reported glycoside hydrolases are sugar tolerant and stimulated (Liu et al., 2017; Zhang et al., 2019a). In previous studies, β -xylosidases with sugar tolerance and stimulation can improve the efficiency of hemicellulose degradation, which are more suitable for industrial application. In the process of hemicellulose hydrolysis, xylose, glucose, and arabinose are the main monosaccharides, high concentrations of which would inhibit β -xylosidase activity. Therefore, we investigated the inhibitory effects of xylose, glucose, and arabinose on the activities of two β -xylosidases Xln-DT and Dt-xy13 at different concentrations (Figure 4). As shown in Figure 4, the GH39 β -xylosidases Xln-DT had excellent glucose and xylose tolerance, which the relative enzyme activity of Xln-DT increased by 25.4 and 75.2%, respectively, in the presence of xylose and glucose of 500 mM. And the arabinose had no inhibitory effect within 500 mM to Xln-DT. However, the three monosaccharides had obvious inhibitory effect on the GH3 β -xylosidases Dt-xy13. Among them, xylose had the most obvious inhibitory effect on Dt-xy13. When the xylose concentration was 20 mM, the relative activity of Dt-xy13 was only 51.7%,

whereas when the xylose concentration was 500 mM, Dt-xy13 was completely inhibited. Then there was the inhibition of glucose on Dt-xy13, which the relative enzyme activity of Dt-xy13 was reduced to 51.7 and 19.2% in 50 and 500 mM of glucose, respectively. Arabinose had the least inhibitory effect, and its residual enzyme activity of Dt-xy13 reached 51.3% at 500 mM. These results were also close to the reported literature, which shows the β -xylosidases from GH3 family had very poor tolerance to xylose or glucose (Zhang et al., 2019b). All the results above suggested that Xln-DT was more beneficial and suitable to hemicellulose degradation or other industrial applications without the product feedback inhibition than Dt-xy13.

Optimization of Hydrolysis Conditions of Poplar Sawdust Xylan by MxynB-8

Xylan, as the second most plentiful polysaccharide in plant cell walls, accounts for 20–30% of the secondary cell wall of the dicots. With the processing and utilization of poplar wood resources, a large number of wood residues, sawdust, and other residues are produced with a global yield 0.8 tons per m^3 of poplar wood (Yan et al., 2015). Also, the poplar sawdust is a by-product of poplar wood with a high hemicellulose content of 20–35%, of which xylosyl accounts for 30–40% of the total sugar. Poplar sawdust used in this study contained 23.93% of xylan. Poplar sawdust xylan was extracted by alkali method; 17.97 ± 0.12 g alkaline extractive with a xylan content of $88.69 \pm 0.52\%$ was obtained from 100 g dried poplar sawdust, resulting in an extraction rate of $66.61 \pm 0.28\%$.

As is well-known, endo-1,4- β -xylanase is a key enzyme for xylan hydrolysis and eventually for XOS production. The composition of endo-1,4- β -xylanases from different microorganisms are different, which lead to the difference of xylan hydrolysis ability. In order to understand the effect and suitable conditions of enzymatic hydrolysis of poplar sawdust xylan by MxynB-8, the effects of key parameters, such as temperature, pH, enzyme dosage, and hydrolysis time on enzymatic hydrolysis efficiency were studied, and the products after enzymatic hydrolysis were analyzed (Figure 5).

The effect of temperature on the enzymatic hydrolysis of poplar sawdust xylan was obvious. In a certain range (30–50°C), with the increase of temperature, it could accelerate the conversion rate of enzyme substrate intermediate into products, while the high temperature would affect the stability of the enzyme and reduce the enzymatic hydrolysis rate. As shown in Figure 5A, the optimum temperature for enzymatic hydrolysis of poplar sawdust xylan by MxynB-8 was 50°C. It is quite different from the reported optimal temperature of endo-1,4- β -xylanase XynB-DT from *D. thermophilum* (Tong et al., 2020) for enzymatic hydrolysis of poplar sawdust xylan, which indicated that temperature has great influence on the enzymatic hydrolysis efficiency, and such temperature difference is related to the source and structure of the enzyme. Considering the cost of the enzyme used in the industrial application, the temperature of the degradation should be minimized.

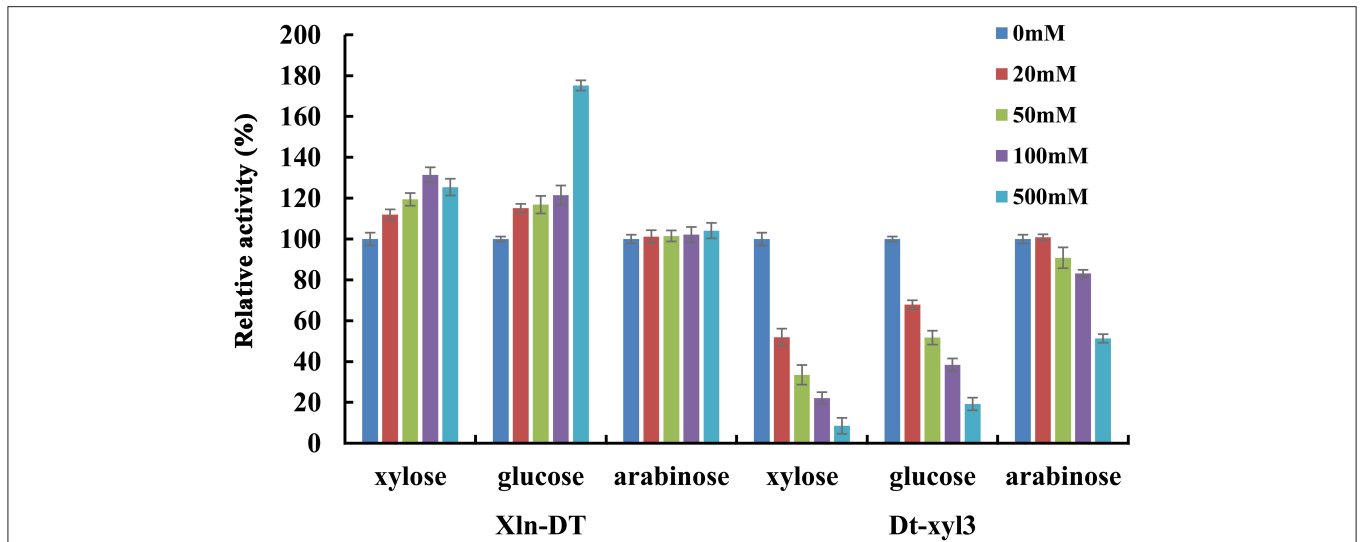


FIGURE 4 | The effects of xylose/glucose/arabinose on the activities of recombinant β -xylosidase Xln-DT and Dt-xyI3 (column: 0, 20, 50, 100, or 500 mM concentration of sugar). The activity of β -xylosidase enzyme without xylose/glucose/arabinose was defined as relative 100%. Influence of xylose/glucose/arabinose on enzyme activity with *p*-nitrophenyl- β -D-xylopyranoside.

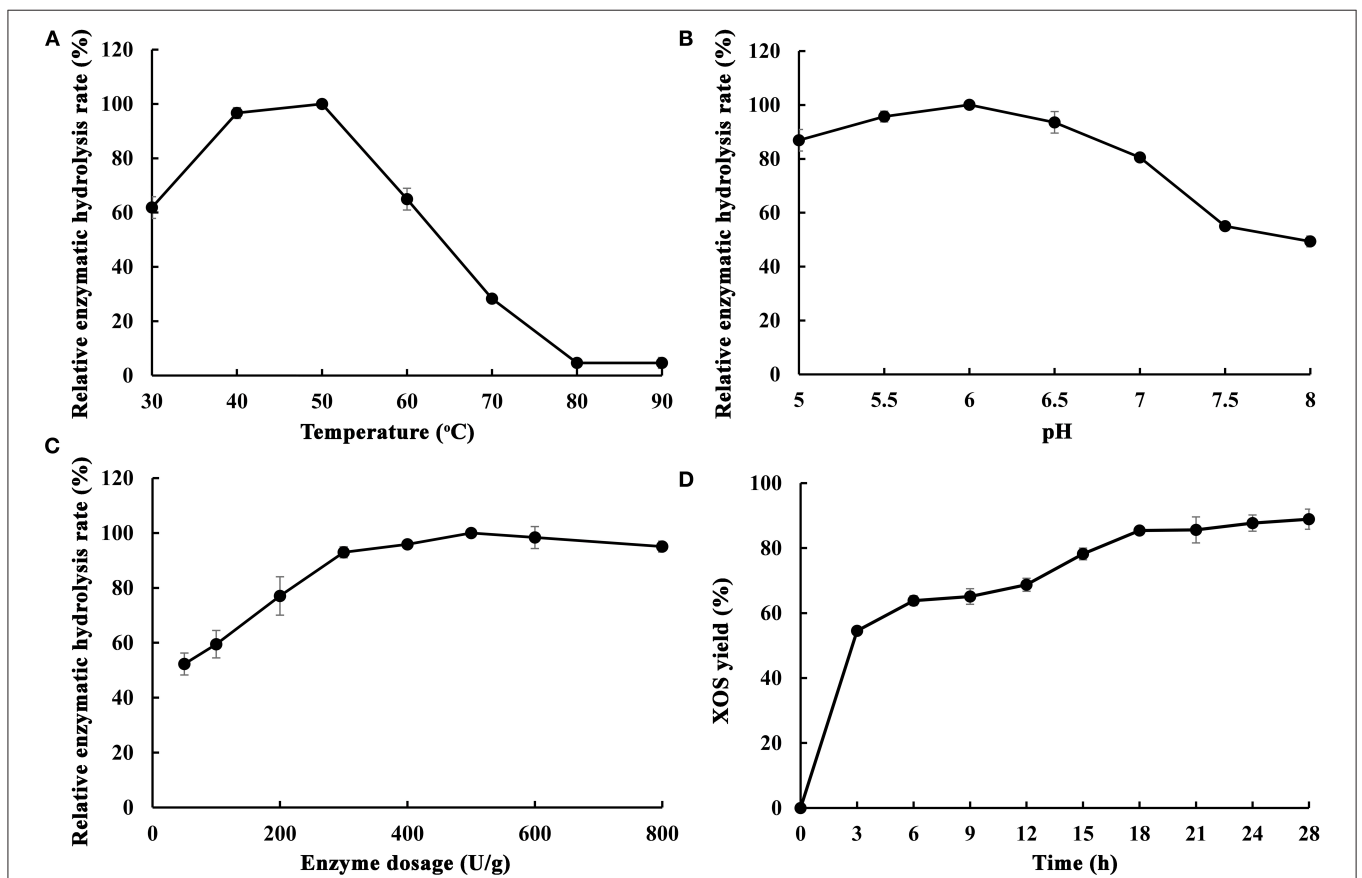


FIGURE 5 | Optimization of different enzymatic hydrolysis conditions of poplar sawdust xylan by recombinant endo-1,4- β -xylanase MxynB-8 [(A) The effect of temperature on the enzymatic hydrolysis rate; (B) The effect of pH on the enzymatic hydrolysis rate; (C) The effect of enzyme dosage on the enzymatic hydrolysis rate; (D) The effect of time on the enzymatic hydrolysis rate]. The maximum hydrolysis rate measured at a certain temperature/pH/enzyme dosage was defined as relative 100%.

To investigate the optimal pH of MxynB-8, at the optimum temperature of 50°C, the substrate concentration of poplar sawdust xylan was set to 2 mg/mL and hydrolyzed for 12 h in different pH values, and the maximum enzymatic yield is defined as relative 100%. The optimal pH of enzymatic reaction is shown in **Figure 5B**. With the increase of pH values, the enzymatic hydrolysis of xylan was first increased (pH 5–6) and then decreased (pH 6–8). When the pH was 6.0, the hydrolysis efficiency of poplar sawdust xylan by MxynB-8 was the highest, which was also consistent with the optimal pH of the enzyme in beechwood degradation. Moreover, when the pH value is too low, the self-hydrolysis effect of xylan is enhanced, and if the pH value is too high, the activity of endo-1,4- β -xylanase MxynB-8 will be affected. Considering the above results, pH 6.0 was selected as the optimal pH for poplar sawdust xylan degradation.

The enzyme dosage has a great influence on the enzymatic hydrolysis efficiency. If the enzyme dosage is too low, it is easy to cause insufficient enzymatic hydrolysis, and if the enzyme dosage is too large, the cost will increase. Therefore, it is very important to select the appropriate amount of enzyme. Setting the concentration poplar sawdust xylan as 2 mg/mL and the enzymolysis temperature and pH at 50°C and 6.0, respectively, the optimal enzyme dosage of MxynB-8 is shown in **Figure 5C**. Under the given conditions, with the increase of enzyme dosage of MxynB-8, the hydrolysis efficiency gradually increased. When the enzyme dosage of MxynB-8 exceeded 500 U/g, the enzymatic hydrolysis efficiency remained unchanged. The reason may be that the number of binding sites between xylan and MxynB-8 is limited. At the beginning of enzymatic reaction, with the increase of MxynB-8 amount, the long chain of poplar sawdust xylan was rapidly hydrolyzed, resulting in a large number of XOS. However, when all these binding sites are occupied by MxynB-8, further increase of enzyme dosage will only increase the invalid adsorption of enzyme and substrate. As a result, the enzymatic hydrolysis of MxynB-8 was inhibited. Therefore, the optimal enzyme dosage of MxynB-8 was 500 U/g.

Endo-1,4- β -xylanase preferentially acts on long-chain xylan to produce XOS and then hydrolyzes the XOS into mainly xylobiose and xylotriose and finally to monosaccharide by adding β -xylosidase. If the hydrolysis time is too short, the enzymolysis is not sufficient. Because of the limitation of the temperature stability of the enzyme, excessive extension of the enzymatic hydrolysis time is not conducive to the production of appropriate XOS. Therefore, in order to obtain as many XOS as possible, the enzymolysis time must be optimized. Samples were taken after 3, 6, 9, 12, 15, 18, 21, 24, and 28 h at the optimum temperature, pH, and enzyme dosage; the results are shown in **Figure 5D**. When the enzymolysis time was <18 h, the enzymolysis efficiency of MxynB-8 increased rapidly with the increase of time. In 3–12 h enzymatic hydrolysis time, xylobiose, xylotriose, xylotriose, and xylohexaose were the main XOS detected. In 12–18 h, the amount of xylobiose and that of xylotriose continued to increase, whereas the content of xylohexaose decreased slowly, which indicates that endo-1,4- β -xylanase hydrolyzed xylan into XOS continuously. The results confirmed that hydrolysis pattern of MxynB-8 was due to cleaving of the inner β -1,4-xyloside bonds randomly, which was as similar as the endoxylanases from

Streptomyces ipomoeae (Xian et al., 2019) and *Trichoderma reesei* (Oliveira et al., 2018). When the enzymolysis time was more than 18 h, the growth rate of enzymatic hydrolysis efficiency obviously slowed down and even had a downward trend. This is because the enzyme activity of endo-1,4- β -xylanase MxynB-8 decreased after fully combining with the substrate, and with the extension of time, some XOS would also be self-hydrolyzed, resulting in the break of β -1,4-xyloside chain. Therefore, the optimal enzymolysis time of MxynB-8 was 18 h. After optimization, XOS yield of MxynB-8 was 85.5%, which was higher than the values (between 72.5 and 73.9%) reported by acid hydrolysis (Huang et al., 2019). Among the hydrolysates, xylobiose and xylotriose were the main hydrolysates, accounting for 75.5% (with a concentration of 1.29 g/L in hydrolysate) and 24.3% (with a concentration of 0.42 g/L in hydrolysate) of the total hydrolysates, respectively, and contained a small amount of xylose and xylohexaose. The ratio of xylobiose in the xylose-based sugars released by MxynB-8 was higher than the previously reported 19.56 and 51.6% (Azelee et al., 2016; Sepulchro et al., 2020) and lower than reported 85.99% (Xian et al., 2019). In addition, the enzymatic efficiency based on the poplar sawdust xylan in the raw material was 30.5%, which is slightly higher than or similar to other reported enzymatic hydrolysis results (Azelee et al., 2016; Jacomini et al., 2020; Sepulchro et al., 2020). These results indicate that MxynB-8 has a promising biotechnological potential to transform poplar sawdust xylan into XOS, which can contribute to valorization of underutilized agricultural and forestry wastes.

Optimization of Hydrolysis Conditions of XOS From Poplar Sawdust Xylan by Xln-DT

Generally, β -1,4-xylosidase can mainly degrade XOS from the non-reducing end to produce xylose. In fermentation processes, using xylose as a carbon source to produce ethanol and xylitol is of great industrial relevance (Sderling and Pienihkkinen, 2020). With deciding the optimal hydrolysis conditions of XOS from poplar sawdust xylan by Xln-DT, the effects of temperature, pH, and enzyme dosage were studied in the second stage treatment. The main hydrolysis product, xylose, the product of the reaction catalyzed by XOS, is similar to that previously reported. After extended incubation times, only a small amount of xylose was continued to release, which rendered the optimization of the hydrolysis time less necessary. The purified β -1,4-xylosidase Xln-DT showed a concentration of 100 U/g was added into the poplar sawdust xylan hydrolyzed with the concentration of 1.6 g/L. By using the xylose content in the hydrolysate as the detection index, the optimal temperature and pH of Xln-DT in degrading XOS are shown in **Figures 6A,B**. After 4-h hydrolysis time, the xylose concentration was increased within a temperature range of 30–80°C, optimal temperature of which was 80°C, and the optimal pH was 6.0. We set the temperature at 80°C and pH 6.0; the effect of Xln-DT dosage on the enzymatic hydrolysis efficiency was optimized (**Figure 6C**). The results showed that XOS (xylobiose, xylotriose, etc.) could be continuously hydrolyzed into D-xylose by adding a small amount of Xln-DT (0–100 U/g). When the Xln-DT dosage was 500 U/g, the xylobiose and xylotriose were hydrolyzed to D-xylose wholly, with the enzymatic hydrolysis

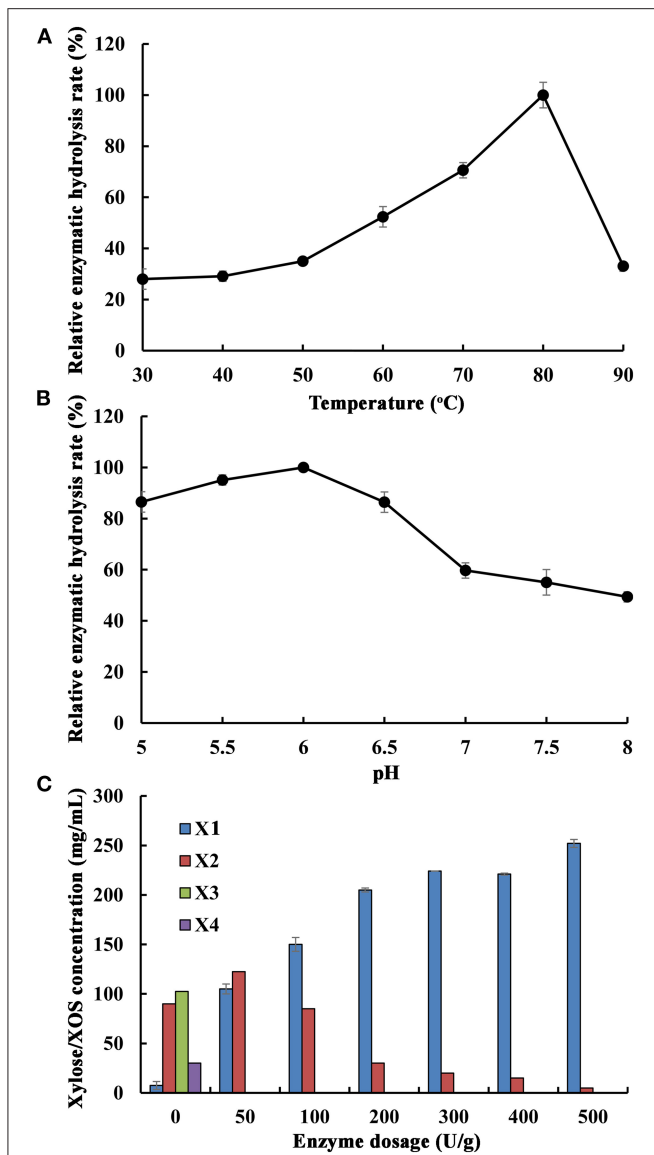


FIGURE 6 | Optimization of different enzymatic hydrolysis conditions of xylooligosaccharides from poplar sawdust xylan by recombinant β -xylosidase Xln-DT **(A)** The effect of temperature on the enzymatic hydrolysis rate; **(B)** The effect of pH on the enzymatic hydrolysis rate; **(C)** The effect of enzyme dosage on the enzymatic hydrolysis rate. X1, xylose; X2, xylobiose; X3, xylotriose; X4, xylotetraose. The maximum hydrolysis rate measured at a certain temperature and pH was defined as relative 100%.

rate reaching the maximum 32.2%, and D-xylose was the main component in the end-products. After that, the enzymolysis efficiency was basically unchanged by adding more Xln-DT, so the Xln-DT dosage was set as 500 U/g.

Synergistic Enzymatic Hydrolysis of Poplar Sawdust Xylan by MxynB-8 and Xln-DT

In addition, we used endo-1,4- β -xylanase MxynB-8 and β -1,4-xylosidase Xln-DT to synergetic degrade, the enzymolysis

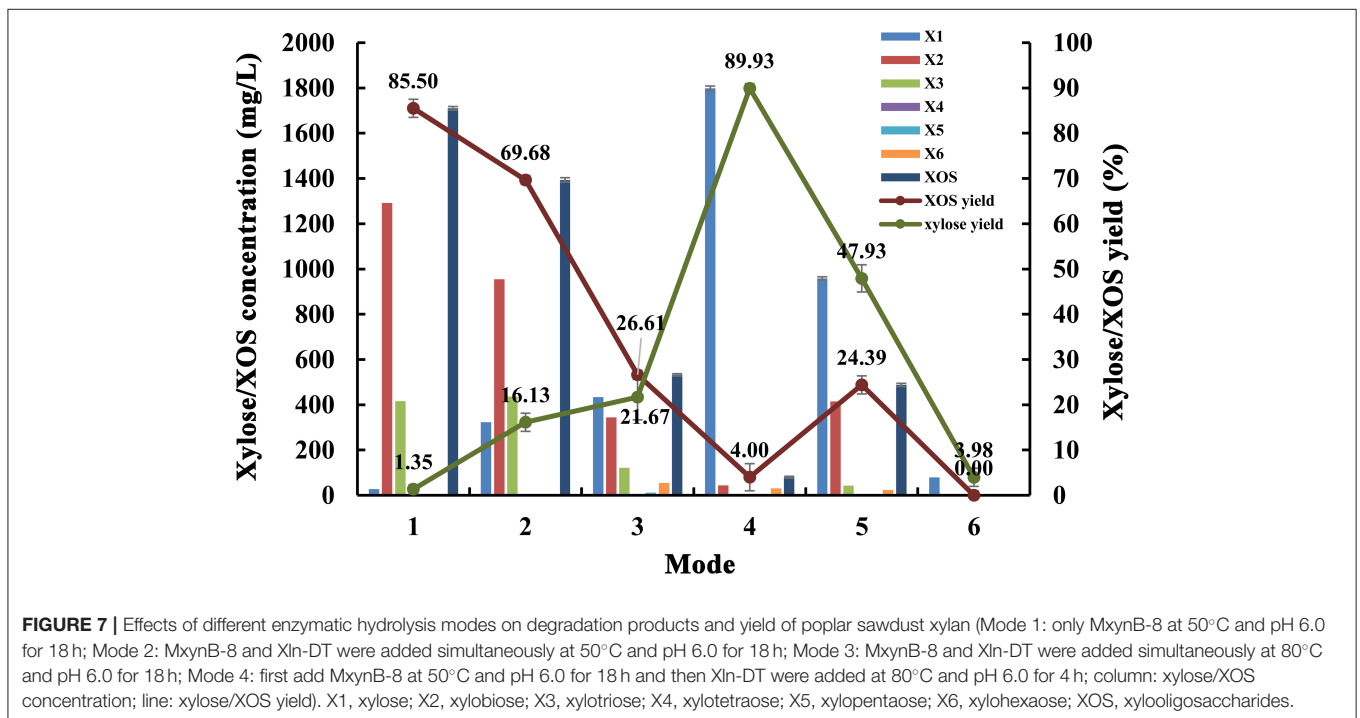
efficiency of which was evaluated by different enzymolysis modes. The degree of synergy was calculated as a means of assessing the synergistic activities in the context of poplar sawdust xylan degradation. Synergy of endo-1,4- β -xylanase and β -xylosidase against xylan could benefit for the enzymatic hydrolysis of xylan to xylose and further reduce cost. The synergistic effects between endo-1,4- β -xylanase MxynB-8 and β -xylosidase Xln-DT on poplar sawdust xylan degradation were determined by simultaneous or sequential addition, which is shown in **Table 4**. The yield of XOS and xylose from the degradation products under different enzymatic hydrolysis modes is shown in **Figure 7**. When adding MxynB-8 alone, XOS, mainly xylobiose, xylotriose, and xylohexaose, were the main hydrolysates of poplar sawdust xylan, with the XOS yield 85.5%, and low amounts of xylose were released. When employing MxynB-8 together with Xln-DT (Modes 2 and 3), the xylose yield of poplar sawdust xylan was increased by 91.6 and 93.8% for Modes 2 and 3, respectively. However, in Mode 3, the XOS yield (26.61%) was lower than those of Modes 1 (85.50%) and 2 (69.68%). The reason may be that MxynB-8 is a mesophilic enzyme; under high temperature, such as 80°C, the enzyme was easily inactivated, which leads to the decrease of enzymatic hydrolysis efficiency. At the double-enzyme step hydrolysis, first addition of MxynB-8 and then of Xln-DT at the suitable temperature, the xylose yield of poplar sawdust xylan was the highest (89.93%), which showed synergism effects between MxynB-8 and Xln-DT during hydrolysis, in which xylan was degraded to XOS by the endo-1,4- β -xylanase MxynB-8 and then effectively cleft to xylose by the β -xylosidase Xln-DT. The degree of synergy was calculated and showed that it was 15.89 in Mode 4, which was higher than that of Xyl43A from *H. insolens* (Yang X. et al., 2015) and Ac-Abf51A from *Alicyclobacillus* sp. (Yang W. X. et al., 2015). These results further underscore the mutual synergistic activity of endo-1,4- β -xylanase and β -xylosidase. At Mode 5, at which Xln-DT was added first, suitable temperature was adjusted, and MxynB-8 was added. The release of xylose (958.58 mg/L) was lower than that of Mode 4 (1,798.57 mg/L), which showed that xylan with a high degree of polymerization could not be affected by the first addition of Xln-DT. When endo-1,4- β -xylanase MxynB-8 was added, MxynB-8 hydrolyzed xylan macromolecules into XOS, and then Xln-DT could perform its function. This situation was also verified in Mode 6. When only Xln-DT was added, the yield of xylose from poplar sawdust xylan was very low, only 4.0%. To sum up, when only endo-1,4- β -xylanase MxynB-8 was added, XOS, such as xylobiose and xylotriose, were the main hydrolysates. In addition, xylose was the main component in the end-product after β -xylosidase Xln-DT was added. The greatest synergy degree (7.8-fold) was found in the simultaneous enzyme additions of MxynB-8 and Xln-DT, which suggested a pronounced synergistic effect of GH39 Xln-DT with the GH11 endo-1,4- β -xylanase on poplar sawdust xylan degradation. Moreover, as the optimal pH of MxynB-8 and Xln-DT was both 6.0, there was no need to change the pH value in the two-step hydrolysis system and adjusted only to the optimal temperature by each, which greatly reduced the cost of enzymatic hydrolysis. It is also suggested that MxynB-8 and Xln-DT have a good synergistic effect in bioconversion of xylan-rich lignocellulosic materials,

TABLE 4 | Simultaneous or sequential hydrolysis reactions by endo-1,4- β -xylanase MxynB-8 and β -xylosidase Xln-DT against poplar sawdust xylan substrate.

First reaction	Reaction conditions	Enzyme added		Poplar sawdust xylan	
		Second reaction	Reaction conditions	Xylose concentration (μ mol)	Synergy
MxynB-8	50°C, pH 6.0, dosage of 500 U/g, 18 h	None	—	26.94	—
MxynB-8+Xln-DT	50°C, pH 6.0, dosage of 500 and 100 U/g, 18 h	None	—	322.54	2.03
MxynB-8+Xln-DT	80°C, pH 6.0, dosage of 500 and 100 U/g, 18 h	None	—	433.48	3.07
MxynB-8	50°C, pH 6.0, dosage of 500 U/g, 18 h	Xln-DT	80°C, pH 6.0, dosage of 100 U/g, 4 h	1,798.57	15.89
Xln-DT	80°C, pH 6.0, dosage of 100 U/g, 4 h	MxynB-8	50°C, pH 6.0, dosage of 500 U/g, 18 h	958.58	8.01
Xln-DT	80°C, pH 6.0, dosage of 100 U/g, 4 h	None	—	79.50	—

Simultaneous or sequential reactions refer to the reactions with two enzymes added simultaneously or sequentially, respectively.

Synergy degree is defined as the ratio of xylose equivalents from simultaneous or sequential enzyme combinations to the sum of that released by the individual enzymes.



such as poplar sawdust to produce XOS and xylose and further reduce cost.

CONCLUSION

In this study, a GH11 endo-1,4- β -xylanase MxynB-8 and a GH39 β -xylosidase Xln-DT were used in degradation of poplar sawdust xylan. Compared with other characterized endo-1,4- β -xylanases, MxynB-8 showed excellent ability to hydrolyze hemicellulose of broadleaf plants, such as poplar. After 18 h, under 50°C, pH with the MxynB-8 dosage of 500 U/g, and substrate concentration of 2 mg/mL, the final XOS yield was 85.5%, and the content of XOS₂₋₃ reached 93.9%. The enzymatic efficiency based on the poplar sawdust xylan in the raw material was 30.5%. Moreover, Xln-DT showed excellent sugar tolerant, which is applied as a candidate to apply

in degradation of hemicellulose and the biotransformation of other natural active substances containing xylose. In addition, the process and enzymatic mode of poplar sawdust xylan with MxynB-8 and Xln-DT were investigated. The results showed that the enzymatic hydrolysis yield of poplar sawdust xylan was improved by adding Xln-DT, and the main product was D-xylose. The yield of enzymatic hydrolysis was higher when using MxynB-8 and Xln-DT together. This study provides a deep understanding of the double-enzyme combination hydrolytic conversion of wood polysaccharides to valuable products.

DATA AVAILABILITY STATEMENT

The datasets presented in this study can be found in online repositories. The names of the repository/repositories and

accession number(s) can be found at: <https://www.ncbi.nlm.nih.gov/>, HQ385274; <https://www.ncbi.nlm.nih.gov/>, CP001146.1; <https://www.ncbi.nlm.nih.gov/>, WP_012547134.1; <https://www.ncbi.nlm.nih.gov/>, ACK42995.1.

AUTHOR CONTRIBUTIONS

QL, YJ, and XT: investigation. QL, LZ, and JP: supervision. QL: writing—original draft. QL and LZ: writing—review and editing. All authors have read and approved the final manuscript.

REFERENCES

- Abbas, N., Wright, A., and Pao, L. Y. (2020). An update to the National Renewable Energy Laboratory baseline wind turbine controller. *J. Phys. Conf. Ser.* 1452:012002. doi: 10.1088/1742-6596/1452/1/012002
- Azelee, N. I. W., Jahim, J. M., Ismail, A. F., Fuzi, S. F. Z. M., Rahman, R. A., and Ilias, R. M. (2016). High xylooligosaccharides (XOS) production from pretreated kenaf stem by enzyme mixture hydrolysis. *Ind. Crops Products* 81, 11–19. doi: 10.1016/j.indcrop.2015.11.038
- Belfaquih, N., Jaspers, C., Kurzatkowski, W., and Penninckx, M. J. (2002). Properties of *Streptomyces* sp. endo- β -xylanases in relation to their applicability in kraft pulp bleaching. *World J. Microbiol. Biotechnol.* 18, 699–705. doi: 10.1023/A:1016810018859
- Bhalla, A., Bischoff, K. M., and Sani, R. K. (2014). Highly thermostable GH39 β -xylosidase from a *Geobacillus* sp. strain WSUCF1. *BMC Biotechnol.* 14:106. doi: 10.1186/s12896-014-0106-8
- Blake, A. D., Beri, N. R., Guttman, H. S., Cheng, R., and Gardner, J. G. (2018). The complex physiology of *Cellvibrio japonicus* xylan degradation relies on a single cytoplasmic β -xylosidase for xylo-oligosaccharide utilization. *Mol. Microbiol.* 107, 610–622. doi: 10.1111/mmi.13903
- Chen, M. X., Zhou, H. Z., Zhu, X. H., Tan, Z. L., and Li, X. D. (2015). Optimization of determination of protein in activated sludge by Bradford method. *Environ. Sci. Technol.* 38, 1–5.
- Christersson, L. (2008). Poplar plantations for paper and energy in the south of Sweden. *Biomass Bioenergy* 32, 997–1000. doi: 10.1016/j.biombioe.2007.12.018
- Collins, T., Gerday, C., and Feller, G. (2010). Xylanases, xylanase families and extremophilic xylanases. *FEMS Microbiol. Rev.* 29, 3–23. doi: 10.1016/j.femsre.2004.06.005
- Corrêa, J. M., Graciano, L., Abraho, J., Loth, E. A., Gandra, R. F., Kadowaki, M. K., et al. (2012). Expression and characterization of a GH39 β -xylosidase II from *Caulobacter crescentus*. *Appl. Biochem. Biotechnol.* 168, 2218–2229. doi: 10.1007/s12010-012-9931-1
- Dong, L. H., Widagdo, F. R. A., Xie, L. F., and Li, F. R. (2020). Biomass and volume modeling along with carbon concentration variations of short-rotation poplar plantations. *Forests* 11:780. doi: 10.3390/f11070780
- Georis, J., Giannotta, F., Buyl, E. D., Granier, B., and Frere, J. M. (2000). Purification and properties of three endo- β -1,4-xylanases produced by *Streptomyces* sp. strain S38 which differ in their ability to enhance the bleaching of kraft pulps. *Enzyme Microb. Technol.* 26, 178–186. doi: 10.1016/S0141-0229(99)00141-6
- Hsu, C. K., Liao, J. W., Chung, Y. C., Hsieh, C. P., and Chan, Y. C. (2004). Xylooligosaccharides and fructooligosaccharides affect the intestinal microbiota and precancerous colonic lesion development in rats. *J. Nutr.* 134, 1523–1528. doi: 10.1093/jn/134.6.1523
- Huang, K. X., Das, L., Guo, J. M., and Xu, Y. (2019). Catalytic valorization of hardwood for enhanced xylose-hydrolysate recovery and cellulose enzymatic efficiency via synergistic effect of Fe³⁺ and acetic acid. *Biotechnol. Biofuels* 12:248. doi: 10.1186/s13068-019-1587-4
- Jacomini, D., Bussler, L., Corrêa, J. M., Kadowaki, M. K., Maller, A., Silva, J. L. D. C., et al. (2020). Cloning, expression and characterization of *C. crescentus* xyn A2 gene and application of Xylanase II in the deconstruction of plant biomass. *Mol. Biol. Rep.* 47, 4427–4438. doi: 10.1007/s11033-020-05507-2
- Jamaldheen, S. B., Thakur, A., Moholkar, V. S., and Goyal, A. (2019). Enzymatic hydrolysis of hemicellulose from pretreated Finger millet (*Eleusine coracana*) straw by recombinant endo-1,4- β -xylanase and exo-1,4- β -xylosidase. *Int. J. Biol. Macromol.* 135, 1098–1106. doi: 10.1016/j.ijbiomac.2019.06.010
- Jun, M., Lin, W. F., Xu, L. B., Liu, S. H., Xue, W. L., and Chen, S. F. (2020). Resistance to long-term bacterial biofilm formation based on hydrolysis-induced Zwitterion material with biodegradable and self-healing properties. *Langmuir* 36, 3251–3259. doi: 10.1021/acs.langmuir.0c00006
- Juturu, V., and Wu, J. C. (2012). Microbial xylanases: engineering, production and industrial applications. *Biotechnol. Adv.* 30, 1219–1227. doi: 10.1016/j.biotechadv.2011.11.006
- Kholis, M. N., Yopi, Y., and Meryandini, A. (2015). Xylooligosaccharide production from Tobacco stalk xylan using xylanase *Streptomyces* sp. BO 3.2. *Makara J. Sci.* 19, 49–54. doi: 10.7454/mss.v19i2.4738
- Kiara, W., Joann, W., Alain, C., David, R., and Lisa, R. (2014). Soil carbon stocks in two hybrid poplar-hay crop systems in southern Quebec, Canada. *Forests* 5, 1952–1966. doi: 10.3390/f5081952
- Lahtinen, M. H., Valoppi, F., Juntti, V. K., Heikkinen, S., and Mikkonen, K. S. (2019). Lignin-rich PHWE hemicellulose extracts responsible for extended emulsion stabilization. *Front. Chem.* 7:871. doi: 10.3389/fchem.2019.00871
- Li, F., Yang, S. Y., Zhao, L. G., and Pei, J. J. (2012). Synonymous codon usage bias and overexpression of a synthetic *xynB* gene from *Aspergillus niger* NL-1 in *Pichia pastoris*. *Bioresources* 7, 2330–2343. doi: 10.15376/biores.7.2.2330-2343
- Li, H. L., Xiong, L., Chen, X. D., Luo, M., Chen, X. F., Wang, C., et al. (2019a). Enhanced enzymatic hydrolysis of wheat straw via a combination of alkaline hydrogen peroxide and lithium chloride/*N,N*-dimethylacetamide pretreatment. *Ind. Crops Products* 137, 332–338. doi: 10.1016/j.indcrop.2019.05.027
- Li, J., Zhang, M., and Wang, D. H. (2019b). High-solids hydrolysis of corn stover to achieve high sugar yield and concentration through high xylan recovery from magnesium oxide-ethanol pretreatment. *Bioresour. Technol.* 302:122838. doi: 10.1016/j.biortech.2020.122838
- Li, J. B., Feng, P., Xiu, H. J., Zhang, M. Y., Li, J. Y., Du, M., Zhang, X. F., et al. (2020a). Wheat straw components fractionation, with efficient delignification, by hydrothermal treatment followed by facilitated ethanol extraction. *Bioresour. Technol.* 316, 123882. doi: 10.1016/j.biortech.2020.123882
- Li, M., Sun, X. X., Chen, Y. J., Shen, T., Tan, Z. T., Tang, C. L., et al. (2020b). Effect of xylan sulfate on the responsive swelling behavior of poly(methacrylateoethyl trimethyl ammonium chloride)-based composite hydrogels. *Cellulose* 27, 8745–8756. doi: 10.1007/s10570-020-03402-4
- Li, Q., Chen, M. Z., and Zhao, L. G. (2017). Cloning and expression of a thermophile GH11 xylanase gene and its application in xylooligosaccharide production. *J. For. Eng.* 2, 63–69. doi: 10.13360/j.issn.2096-1359.2017.04.011
- Li, Q., Jiang, Y. J., Tong, X. Y., Pei, J. J., Xiao, W., Wang, Z. Z., et al. (2020c). Cloning and characterization of the β -xylosidase from *Dictyoglomus turgidum* for high efficient biotransformation of 10-deacetyl-7-xylosyltaxol. *Bioorg. Chem.* 94:103357. doi: 10.1016/j.bioorg.2019.103357
- Li, Q., Wu, T., Duan, Y. W., Pei, J. J., and Zhao, L. G. (2019c). Improving the thermostability and pH stability of *Aspergillus niger* xylanase by site-directed mutagenesis. *Appl. Biochem. Microbiol.* 55, 136–144. doi: 10.1134/S0003683819020108

FUNDING

This work was supported by the National Key Research Development Program of China National Key R&D Program of China (2017YFD0601001).

SUPPLEMENTARY MATERIAL

The Supplementary Material for this article can be found online at: <https://www.frontiersin.org/articles/10.3389/fbioe.2020.637397/full#supplementary-material>

- Li, Q., Wu, T., Qi, Z. P., Zhao, L.G., Pei, J. J., and Tang, F. (2018). Characterization of a novel thermostable and xylose-tolerant GH 39 β -xylosidase from *Dictyoglomus thermophilum*. *BMC Biotechnol.* 18:29. doi: 10.1186/s12896-018-0440-3
- Liu, Y., Li, R., Wang, J., Zhang, X. H., Jia, R., Gao, Y., et al. (2017). Increased enzymatic hydrolysis of sugarcanebagasse by a novel glucose-and xylose-stimulated β -glucosidase from *Anoxybacillus flavithermus* subsp. *yunnanensis* E13^T. *BMC Biochem.* 18:4. doi: 10.1186/s12858-017-0079-z
- Menezes, C. R. D., Silva, I. S., Pavarina, E. C., Dias, E. F. G., Dias, F. G., Grossman, M. J., et al. (2009). Production of xylooligosaccharides from enzymatic hydrolysis of xylan by the white-rot fungi *Pleurotus*. *Int. Biodeterior. Biodegrad.* 63, 673–678. doi: 10.1016/j.ibiod.2009.02.008
- Oliveira, S. M. D., Perez, S. M., Terrasan, C. R. F., Fernandez, M. R., Vieira, M. F., Guisan, J. M., et al. (2018). Covalent immobilization-stabilization of β -1,4-endoxylanases from *Trichoderma reesei*: production of xylooligosaccharides. *Process Biochem.* 64, 170–176. doi: 10.1016/j.procbio.2017.09.018
- Ordonsky, V., Khodakov, A., Nijhuis, T. A., and Schouten, J. C. (2015). Heterogeneously catalyzed reactive extraction for biomass valorization into chemicals and fuels. *Green Process. Synth.* 4, 369–377. doi: 10.1515/gps-2015-0037
- Qi, C. S., Hou, S. Y., Lu, J. X., Xue, W. W., and Sun, K. (2020). Thermal characteristics of birch and its cellulose and hemicelluloses isolated by alkaline solution. *Holzforschung* 74, 1099–1112. doi: 10.1515/hf-2019-0285
- Rohman, A., Dijkstra, B. W., and Puspangsih, N. N. T. (2019). β -Xylosidases: structural diversity, catalytic mechanism, and inhibition by monosaccharides. *Int. J. Mol. Sci.* 20:5524. doi: 10.3390/ijms20225524
- Sderling, E., and Pienihkinen, K. (2020). Effects of xylitol and erythritol consumption on mutans streptococci and the oral microbiota: a systematic review. *Acta Odontol. Scand.* 78, 599–608. doi: 10.1080/00016357.2020.1788721
- Sepulchro, A. G. V., Pellegrini, V. O. A., Briganti, L., Araujo, E. A. D., Araujo, S. S. D., and Polikarpov, I. (2020). Transformation of xylan into value-added biocommodities using *Thermobacillus composti* GH10 xylanase. *Carbohydr. Polym.* 247:116714. doi: 10.1016/j.carbpol.2020.116714
- Shi, H., Li, X., Gu, H. X., Zhang, Y., Huang, Y. J., Wang, L. L., et al. (2013). Biochemical properties of a novel thermostable and highly xylose-tolerant β -xylosidase/ α -arabinosidase from *Thermotoga thermarum*. *Biotechnol. Biofuels* 6:27. doi: 10.1186/1754-6834-6-27
- Shi, Z. L., Gong, W. L., Zhang, L. L., Dai, L., Chen, G. J., and Wang, L. S. (2018). Integrated functional-omics analysis of *Thermomyces lanuginosus* reveals its potential for simultaneous production of xylanase and substituted xylooligosaccharides. *Appl. Biochem. Biotechnol.* 187, 1515–1538. doi: 10.1007/s12010-018-2873-5
- Sun, S. L., Wen, J. L., Ma, M. G., and Sun, R. C. (2013). Successive alkali extraction and structural characterization of hemicelluloses from sweet sorghum stem. *Carbohydr. Polym.* 92, 2224–2231. doi: 10.1016/j.carbpol.2012.11.098
- Tong, X. Y., Li, Q., Chen, W. Q., and Zhao, L. G. (2020). Alkali extraction of xylan from poplar sawdust and preparation of xylooligosaccharide by enzymatic hydrolysis. *J. For. Eng.* 5, 61–68. doi: 10.13360/j.issn.2096-1359.201904030
- Vázquez, M. J., Alonso, J. L., Dominguez, H., and Parajó, J. C. (2000). Xylooligosaccharides: manufacture and applications. *Trends Food Sci. Technol.* 11, 387–393. doi: 10.1016/S0924-2244(01)00031-0
- Vincent, L., Hemalatha, G. R., Elodie, D., Coutinho, P. M., and Bernard, H. (2014). The carbohydrate-active enzymes database (CAZy) in 2013. *Nucleic Acids Res.* 42, 490–495. doi: 10.1093/nar/gkt1178
- Wang, S.S., Zou, C., Yang, H. P., Lou, C., Cheng, S. Z., Chao, P., Wang, C., et al. (2020). Effects of cellulose, hemicellulose, and lignin on the combustion behaviours of biomass under various oxygen concentrations. *Bioresour. Technol.* 320:124375. doi: 10.1016/j.biortech.2020.124375
- Wang, Y. T., and Fang, Z. (2020). Catalytic biomass to renewable biofuels and biomaterials. *Catalysts* 10:480. doi: 10.3390/catal10050480
- Wei, H., Chen, X. W., Joseph, S., Erik, K., Wang, W., Ji, Y., et al. (2018). Kinetic modelling and experimental studies for the effects of Fe²⁺ ions on xylan hydrolysis with dilute-acid pretreatment and subsequent enzymatic hydrolysis. *Catalysts* 8:39. doi: 10.3390/catal8010039
- Wen, P. Y., Zhang, T., Wang, J. Y., Lian, Z.N., and Zhang, J. H. (2019). Production of xylooligosaccharides and monosaccharides from poplar by a two-step acetic acid and peroxide/acetic acid pretreatment. *Biotechnol. Biofuels* 12:87. doi: 10.1186/s13068-019-1423-x
- Xian, L., Li, Z., Tang, A. X., Qin, Y. M., Li, Q. Y., Liu, H. B., et al. (2019). A novel neutral and thermophilic endoxylanase from *Streptomyces ipomoeae* efficiently produced xylobiose from agricultural and forestry residues. *Bioresour. Technol.* 285:121293. doi: 10.1016/j.biortech.2019.03.132
- Xu, B., Dai, L. M., Li, J. J., Deng, M., Miao, H. B., Zhou, J. P., et al. (2016). Molecular and biochemical characterization of a novel xylanase from *Massilia* sp. RBM26 isolated from the feces of *Rhinopithecus bieti*. *J. Microbiol. Biotechnol.* 26, 9–19. doi: 10.4014/jmb.1504.04021
- Yan, X. W., Lin, C., Zhang, L., Wang, F., and Chen, Q. W. (2015). Analysis on chemical components changes in preparation process of cellulosic ethanol from poplar wood. *J. Central South Univ. For. Technol.* 35, 119–122. doi: 10.14067/j.cnki.1673-923x.2015.02.023
- Yang, J., An, X., Liu, L., Tang, S., and Liu, H. (2020). Cellulose, hemicellulose, lignin, and their derivatives as multi-components of bio-based feedstocks for 3D printing. *Carbohydr. Polym.* 250:116881. doi: 10.1016/j.carbpol.2020.116881
- Yang, W. X., Bai, Y. G., Yang, P. L., Luo, H. Y., Huang, H. Q., Meng, K., et al. (2015). A novel bifunctional GH51 exo- α -1-arabinofuranosidase/endo-xylanase from *Alicyclobacillus* sp. A4 with significant biomass-degrading capacity. *Biotechnol. Biofuels* 8:197. doi: 10.1186/s13068-015-0366-0
- Yang, X., Shi, P., Huang, H., Luo, H., Wang, Y., Zhang, W., et al. (2014). Two xylose-tolerant GH43 bifunctional β -xylosidase/ α -arabinosidases and one GH11 xylanase from *Hemicola insolens* and their synergy in the degradation of xylan. *Food Chem.* 148, 381–387. doi: 10.1016/j.foodchem.2013.10.062
- Yang, X., Shi, P., Ma, R., Luo, H., Huang, H., Yang, P., et al. (2015). A new GH43 α -arabinofuranosidase from *Hemicola insolens* Y1: biochemical characterization and synergistic action with a xylanase on xylan degradation. *Appl. Biochem. Biotechnol.* 175, 1960–1970. doi: 10.1007/s12010-014-1416-y
- Ye, Y., Li, X., and Zhao, J. (2017). Production and characteristics of a novel xylose- and alkali-tolerant GH43 β -xylosidase from *Penicillium oxalicum* for promoting hemicellulose degradation. *Sci. Rep.* 7:11600. doi: 10.1038/s41598-017-11573-7
- Zhang, R., Li, N., Xu, S., Han, X., Li, C., Wei, X., et al. (2019a). Glycoside hydrolase family 39 β -xylosidases exhibit β -1,2-xylosidase activity for transformation of notoginsenosides: a new EC subclass. *J. Agric. Food Chem.* 67, 3220–3228. doi: 10.1021/acs.jafc.9b00027
- Zhang, S. S., Xie, J. C., Zhao, L. G., Pei, J. J., Su, E. Z., Xiao, W., et al. (2019b). Cloning, overexpression and characterization of a thermostable β -xylosidase from *Thermotoga petrophila* and cooperated transformation of ginsenoside extract to ginsenoside 20(S)-Rg3 with a β -glucosidase. *Bioorg. Chem.* 85, 159–167. doi: 10.1016/j.bioorg.2018.12.026
- Zhang, Y., Bi, P., Wang, J., Jiang, P., Wu, X., Xue, H., et al. (2015). Production of jet and diesel biofuels from renewable lignocellulosic biomass. *Appl. Energy* 150, 128–137. doi: 10.1016/j.apenergy.2015.04.023
- Zhuo, R., Yu, H. B., Qin, X., Ni, H. X., and Jiang, Z. (2018). Heterologous expression and characterization of a xylanase and xylosidase from white rot fungi and their application in synergistic hydrolysis of lignocellulose. *Chemosphere* 212, 24–33. doi: 10.1016/j.chemosphere.2018.08.062

Conflict of Interest: The authors declare that the research was conducted in the absence of any commercial or financial relationships that could be construed as a potential conflict of interest.

Copyright © 2021 Li, Jiang, Tong, Zhao and Pei. This is an open-access article distributed under the terms of the Creative Commons Attribution License (CC BY). The use, distribution or reproduction in other forums is permitted, provided the original author(s) and the copyright owner(s) are credited and that the original publication in this journal is cited, in accordance with accepted academic practice. No use, distribution or reproduction is permitted which does not comply with these terms.



Using Carboxymethyl Cellulose as the Additive With Enzyme-Catalyzed Carboxylated Starch to Prepare the Film With Enhanced Mechanical and Hydrophobic Properties

Can Liu¹, Shijiao Qin^{1,2}, Jin Xie¹, Xu Lin¹, Yunwu Zheng¹, Jing Yang¹, Huan Kan^{2*} and Zhengjun Shi^{1*}

OPEN ACCESS

Edited by:

Caoxing Huang,
Nanjing Forestry University, China

Reviewed by:

Ming-Guo Ma,
Beijing Forestry University, China
John Zhanhu Guo,
University of Tennessee, Knoxville,
United States

*Correspondence:

Zhengjun Shi
shizhengjun1979@swfu.edu.cn
Huan Kan
13700650213@163.com

Specialty section:

This article was submitted to
Bioprocess Engineering,
a section of the journal
Frontiers in Bioengineering and
Biotechnology

Received: 07 December 2020

Accepted: 05 January 2021

Published: 02 February 2021

Citation:

Liu C, Qin S, Xie J, Lin X, Zheng Y,
Yang J, Kan H and Shi Z (2021) Using
Carboxymethyl Cellulose as the
Additive With Enzyme-Catalyzed
Carboxylated Starch to Prepare the
Film With Enhanced Mechanical and
Hydrophobic Properties.
Front. Bioeng. Biotechnol. 9:638546.
doi: 10.3389/fbioe.2021.638546

¹ The Key Laboratory of State Forestry and Grassland Administration on Highly-Efficient Utilization of Forestry Biomass Resources in Southwest China, Southwest Forestry University, Kunming, China, ² College of Life Science, Southwest Forestry University, Kunming, China

Carboxymethyl cellulose, a hydrophobic derivative from cellulose that can be prepared from different biomass, has been widely applied in food, medicine, chemical, and other industries. In this work, carboxymethyl cellulose was used as the additive to improve the hydrophobicity and strength of carboxylated starch film, which is prepared from starch catalyzed by bio- α -amylase. This study investigated the effects of different bio- α -amylase dosages (starch 0.5%, starch 1%) and different activation times (10, 30 min) on starch to prepare the carboxylated starch. The effects of different carboxymethyl cellulose content on the carboxylated starch film were investigated by analysis viscosity, fourier-transform infrared spectroscopy, thermogravimetric analysis, differential scanning calorimetry, x-ray powder diffraction, scanning electron microscope, and contact angle. The results showed that preparing carboxylated starch using activated starch increased the carboxyl content, which could improve the effectiveness of the activated enzyme compared to prolonging the activation time. The carboxyl starch prepared by enzyme catalysis had a lower gelatinization temperature, and enzyme activation destroyed the crystallization area of the starch, thus facilitating the carboxylation reaction. The addition of 15% carboxymethyl cellulose improved the mechanical properties of the prepared film with maximum tensile strength of 44.8 MPa. Carboxymethyl cellulose effectively improved the hydrophobicity of the starch film with the addition amount of 10–30%, while hydrophobic property was stable at 66.8° when the addition amount was exceeded to 35%. In this work, it can be found that carboxymethyl cellulose improve the mechanical and hydrophobic properties of starch film, laying the foundation for the application of carboxylated starch materials.

Keywords: carboxymethyl cellulose, amylase, carboxylated starch, composite film, hydrophobicity

INTRODUCTION

Cellulose has abundant reserves, low price, environmental protection, and wide application. Carboxymethyl cellulose (CMC), a derivative of cellulose, is a natural anionic water-soluble polysaccharide that is used in food, medicine, chemical, and other industries (Suriyatem et al., 2018; Xie et al., 2018; Biauou et al., 2020). A large number of functional groups, such as carboxyl and hydroxyl, make the technical requirements of the CMC modification process simple, and performance improvement can be achieved with low modification costs. Studies have shown that the addition of CMC can improve the mechanical properties, transparency, and thermal stability of the material (Tasaso, 2015; Huang et al., 2017; Mansur et al., 2017; Kontturi and Spirk, 2019). In the preparation of an electrode film, the addition of CMC can improve the plasticity of the composite film (Ekramulmahmud et al., 2005; Ampaiwong et al., 2019; Nazrin et al., 2020). The above research shows, the CMC has a long carbon chain and polyhydroxyl structure, and is a good scaffold material for hydrophilic material modification. In this paper, CMC is used as the basic material for performance improvement, and the starch film is modified to obtain better material performance.

Starch is the most accessible biomass resource, starch utilization has been a focus of ongoing research. Natural starch has the disadvantages of poor water solubility, low degree of emulsification and gelatinization, and low stability, which limits the application range of natural starch in various industries (Kim et al., 2017; Remya et al., 2018; Escobar-Puentes et al., 2020; Chen et al., 2021). Therefore, modified starches are prepared by introducing new or changing functional groups through physicochemical and biological modifications to equip starch with new characteristics (Sangian et al., 2018; Xiao et al., 2018; Li et al., 2020; Menzel, 2020; Torbica et al., 2020). Because of its strong hydrophilicity and polarity, carboxylated starch has been widely used in drug carriers, adsorbents, flocculants, and other applications (Shahriarpanah et al., 2016; Sarmah and Karak, 2020). Starch is a polycrystalline polymer composed of crystalline, amorphous, and crystalline transition regions (subcrystalline regions) (Sharmin et al., 2020; Wu et al., 2020; Xiao et al., 2020). The modification of starch mostly occurs in the amorphous area within the surface layer of the granules. The unique crystal structure of the crystallization zone makes it difficult for the reagent to penetrate into the starch granules, which limits the further occurrence of chemical reactions, thus resulting in low reaction efficiency and difficulty obtaining products with high substitution degrees (Achremowicz et al., 2000; Shogren, 2000; Cao et al., 2002; Paulik et al., 2019; Shi et al., 2019).

To improve the efficiency of the reaction, starch is often pretreated to destroy its crystalline structure, enhance the degree of reaction, and improve the performance of the modified starch. The current pretreatment methods include physical, chemical, and biological methods (Gong et al., 2017; Zhang et al., 2017; Chang et al., 2019; Holck et al., 2019; Lee et al., 2019). Compared with the other two methods, biological methods are environmentally friendly and mild in response. Based on the characteristics of α -amylase hydrolysis, it was deduced

that α -amylase has higher hydrolysis efficiency (Souto et al., 2017; Ozdemir et al., 2018; Wang et al., 2019). Therefore, in the preparation of carboxylated starch, the use of amylase to change the structure of starch granules and reduce the starch crystallization area to improve the reaction efficiency of starch has important theoretical and practical significance. The unique structure of carboxylated starch facilitates water absorption, but the mechanical properties of the material are poor. Therefore, other supportive materials are needed to help improve the performance of carboxylated starch, such as carboxymethyl cellulose.

In order to prepare high value-added carboxylated starch, α -amylase was used to pretreat starch, and then carboxylated starch was prepared. Hope to destroy the crystalline structure of starch to a greater extent. Films were prepared using carboxylated starch, Carboxymethyl cellulose was used to improve the hydrophobicity and mechanical properties of the carboxylated starch films. The carboxyl content, Fourier-transform infrared spectroscopy (FTIR), thermogravimetric analysis (TGA), differential scanning calorimetry (DSC), x-ray powder diffraction (XRD), scanning electron microscope, contact angle, mechanical properties, and other parameters were used to characterize the prepared carboxylated starch and film. For the first time, the effect of enzyme pretreatment on the performance and application of carboxylated starch was studied. At the same time, the effect of CMC on starch film was discussed to establish a foundation for the industrial application of carboxylated starch film.

MATERIALS AND METHODS

Experimental Materials

Starch-Unmodified was purchased from Sigma-Aldrich, USA. Sodium hypochlorite, active chlorine $\geq 7.5\%$, AR grade, purchased from China Shanghai Titan Technology Co., Ltd. Potassium iodide test paper was purchased from China Shanghai Sanaisi Reagent Co., Ltd, and copper sulfate pentahydrate was purchased from China Shanghai Titan Technology Co., Ltd., AR grade. Sodium hydroxide was purchased from China Shanghai Titan Technology Co., Ltd., AR grade. Hydrochloric acid sodium hydroxide was purchased from China Shanghai Titan Technology Co., Ltd., AR grade, purity 36~38%. Carboxymethyl cellulose hydroxide was purchased from China Shanghai Titan Technology Co., Ltd., M.W.90000(DS = 0.7), AR grade. Sodium sulfite was purchased from Shanghai Titan Technology Co., Ltd., China, AR grade, $\text{SO}_2 \geq 98.0\%$. According to GB/ T601-2002 chemical reagent solution standard, 0.4% copper sulfate solution, 4% sodium hydroxide solution, 3% hydrochloric acid solution, 0.1 mol/L hydrochloric acid solution, 0.085 mol/L sodium hydroxide solution and 10% sodium sulfite were prepared.

Preparation Process

Amylase Pretreatment

According to the data and preliminary test results, the optimized process was: Take 60 g of native starch in a round bottom flask and added 90 g of water to make 4 groups of 40% starch milk, put the flask in a water bath and heated to 55°C and adjusted

pH = 6. This study investigated the effects of different bio- α -amylase dosages and different activation times on starch to prepare the carboxylated starch. After the enzymolysis reaction was completed, used sodium hydroxide to adjusted the pH=9 to kill the enzyme. After the sample is dried and crushed, waiting to be used in the next step. The samples 1: enzyme content 0 g, activation 0 min; sample 2: enzyme content 0.3 g, activation 10 min; sample 3: enzyme content 0.6 g, activation 10 min; sample 4: enzyme content 0.3 g, activation 30 min; sample 5: enzyme content 0.6 g, activation 30 min.

Preparation Process of Carboxylated Starch

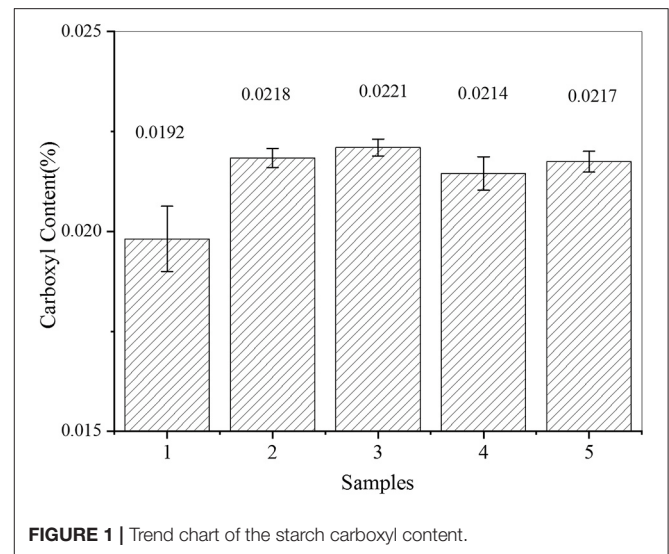
The starch milk pretreated by the first step enzyme was added into a round-bottom flask with agitator and temperature control device, and the pH was adjusted to 9 by 3% sodium hydroxide and 3% hydrogen chloride. Increased the temperature to 45°C, added 15 g NaClO (15% of dry starch), kept the constant temperature for reaction, after reaction for a period of time, determined the pH value in the reactor, and neutralized with 3% HCl, the reaction time was 6 h. After the reaction, potassium iodide test paper was used to determine whether the reaction of the modifier NaClO was complete. Added an appropriate amount of 10% sodium sulfite solution to stopped the reaction, took out the reaction flask, washed the product with distilled water for three times, then put it in the oven for 4 h at 45°C, and then grinded the carboxylated starch.

Preparation of Starch Film

Weighed 4 g carboxylated starch, preparation of 4% starch aqueous solution. and weighed 0 g, 0.2 g, 0.4 g, 0.6 g, 0.8 g, 1 g, 1.2 g, 1.4 g, 1.4 g, 1.4, g and 1.6 g carboxymethyl cellulose in conical flask (the addition amount of carboxymethyl cellulose was 0, 5, 10, 15, 20, 25, 30, 35, 40% of carboxylated starch), and dissolved with water. The solution was mixed in a conical flask and placed on a magnetic agitator. The rotating speed was adjusted to make the rotor rotate at a constant speed. After dissolution, vacuum degassing, and defogging were carried out. After completion, the solution was poured into the glass culture dish, drying in 45°C drying oven for 6 h to peel off the film.

Characterization and Analysis

Starch samples were prepared into 6% modified starch milk, heated in a water bath at 95°C for 15 min, and gelatinization temperature was measured by NDJ-5S rotary viscosimeter of Shanghai Pingxuan Scientific Instrument Co., LTD; FTIR used magnair 560E.S.P infrared spectrometer from Nicolet Company of The United States. The potassium bromide pressure plate/ATR method was adopted to scan the range of 4,000 to 400 cm^{-1} , and the number of scans was 64; DSC used DSC204 differential scanning calorimeter manufactured by NETZSCH, Germany. The sample was 3.5, and 5 mg of water was added with a micro sampler. The program was set at 5°C/min, 200°C was the termination temperature, and argon gas was blown and protected at 30 mL /min; TG-DTG was used by TGA209 F3, NETZSCH, Germany. The samples were dried in a drying oven at 50°C for 24 h, weighed 3~5 mg, and the heating rate was 10°C/min. Argon was used as protective gas, and thermogravimetric analysis



was performed on the samples at a gas flow rate of 30 ml/min; XRD test adopted Japanese Neo-D/MAX220, the optical tube was made by Philips and the target material was Cu. The sample was 120 mesh powder, dried at 100°C for 8 h. The test conditions were as follows: voltage 40 kV, current 30 mA, starting angle of 10°, termination angle of 60°, step width of 0.02°, curve fitting peak parting method was adopted for calculation (Chen et al., 2020); SEM was determined by Quanta200 SCANNING electron microscope from Dutch FEI Company. The observed environment was vacuum, the surface of the sample was treated with gold spray; The contact angle tester of Kruss DSA produced by Kruss DSA of Germany was used to test the surface wettability of the film sample; the carboxyl content was measured by the following method: 5 g samples were placed in a 150 mL beater, 25 mL 0.1 mol/L HCl solution was added, the samples were stirred for 30 min, filtered (filtered) with glass sand core funnel, washed with non-amino distilled water (distilled water cooled after boiling), and tested for chloride ion free with silver nitrate solution. The carboxylated starch after ash removal was transferred to a 600 mL beaker, 300 mL distilled water was added, heated and boiled (5~7 min), and NaOH solution was used for calibration.

RESULTS AND DISCUSSION

Enzyme's Effect on Carboxylated Starch

In this part of the experiment, five levels of experiments were designed using five samples. The carboxyl content was determined for each of the five samples. According to the analysis shown in **Figure 1**, the carboxyl group content of carboxylated starches prepared by the enzyme activation treatment was higher than that of native starch. The enzyme treatment effectively improved the carboxylation activity. On the basis of the same enzyme activation time, the amylase dosage increased the carboxyl content of modified starch. The rule was that with a greater amount of enzyme, the carboxyl content of modified

starch would be higher. Alpha-amylase is an endonuclease, but it is difficult to break the crystalline shell of starch granules. The activation may have been caused by the entry of amylase into the interior through the pores of starch granules and its reaction with the semi-crystalline soft shell, which increased the carboxyl content. Due to the limited pore quantity, the increased amount of enzyme only increased the carboxyl content for a limited time, it is unclear in what way the increase was limited (Ma et al., 2006; Salcedo-Mendoza et al., 2018; Navia-Coarite et al., 2019; Zeng et al., 2019). Using the same enzyme dosage, prolonging the

activation time of amylase reduced the starch carboxyl content, but the degree of change was not significant.

Viscosity is an index of the molecular weight of carboxylated starch. The decrease in starch viscosity was caused by a decrease in the degree of polymerization and molecular weight of starch macromolecules due to the carboxylation agent, which led to a decrease on gelatinization viscosity. It can be seen from **Figure 2** that the viscosity of the sample after 30 min of enzyme activation

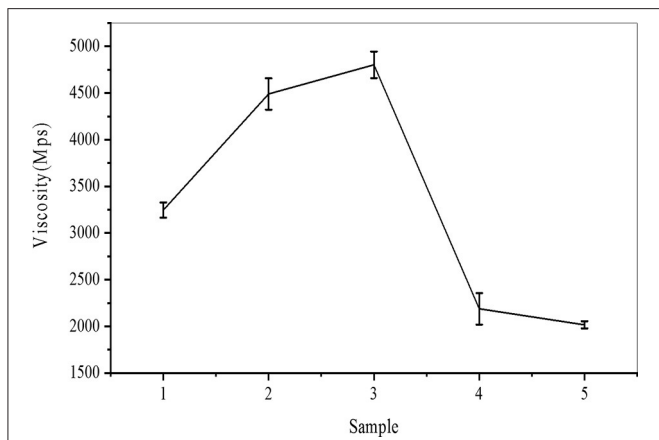


FIGURE 2 | Viscosity trend chart of carboxylated starch.

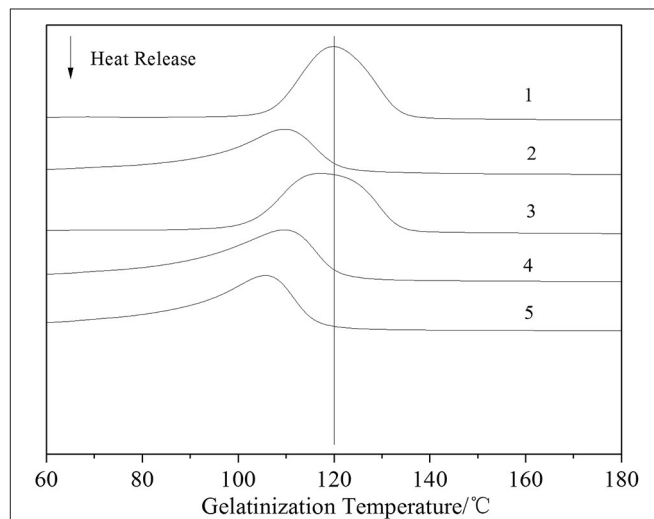


FIGURE 4 | DSC analysis of carboxylated starch.

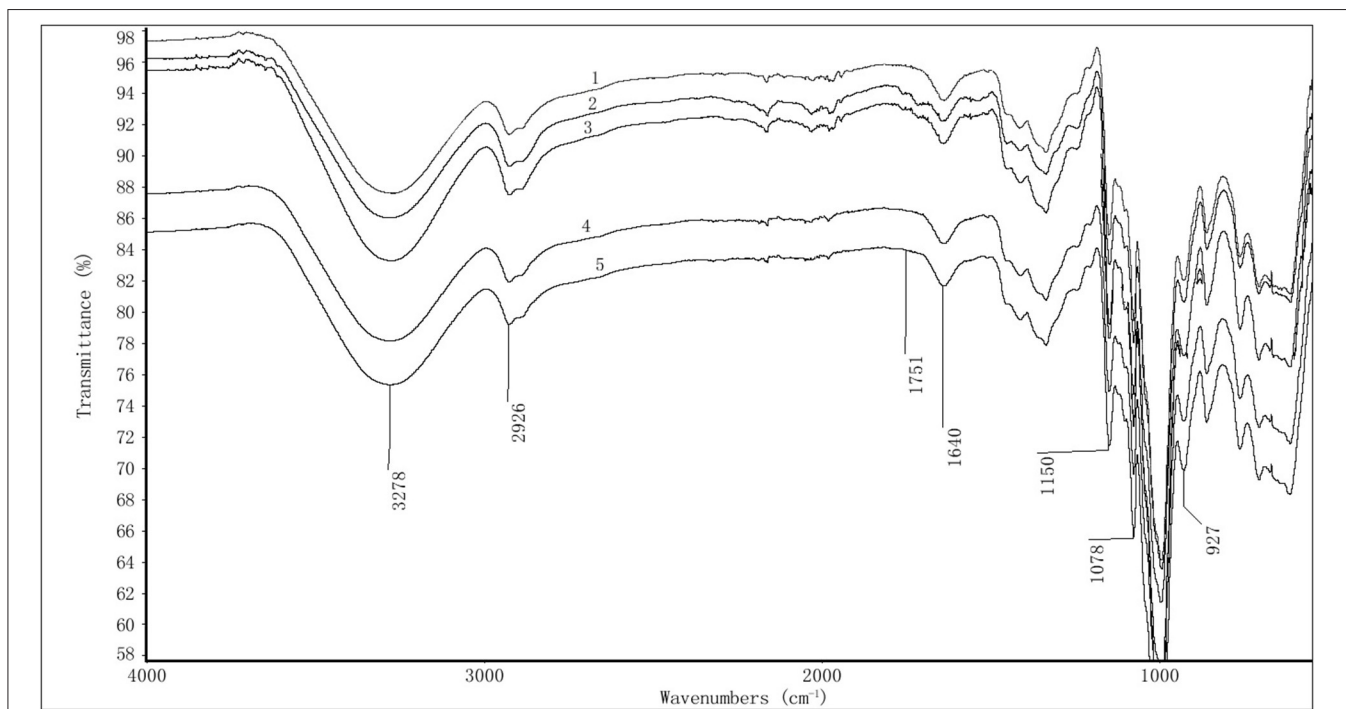
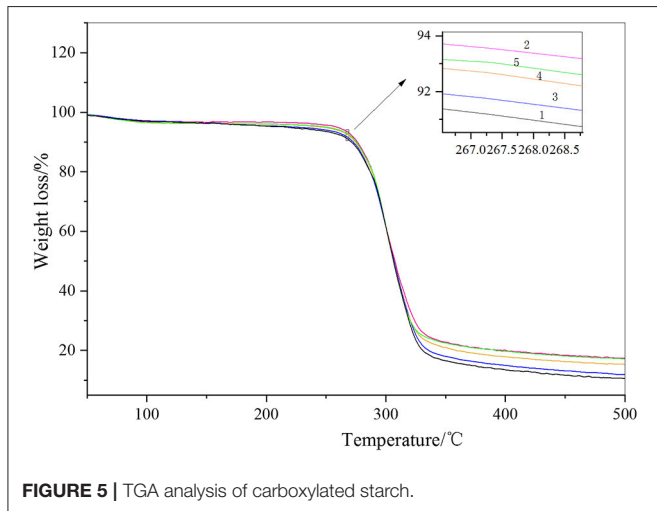


FIGURE 3 | FTIR diagram of carboxylated starch.

TABLE 1 | DSC analysis of carboxylated starch.

Sample	$T_p/^\circ\text{C}$	$T_o/^\circ\text{C}$	$T_c/^\circ\text{C}$	$\Delta H/\text{J}\cdot\text{g}^{-1}$
1	119.9	107.4	133.6	1368
2	109.7	94.2	120.7	973.8
3	117.2	103	133.4	1409
4	109.6	90.21	120.7	1252
5	105.8	90.4	116	1184

**FIGURE 5** | TGA analysis of carboxylated starch.

was lower than that of the other three samples, and sample five had the lowest viscosity. It can be seen that extending the enzyme activation time can effectively reduce the molecular weight of starch. At the same activation time, the amount of enzyme had little effect on the viscosity of starch, which may be due to the limited number of pores on the surface of starch granules. Therefore, once the maximum threshold is exceeded, the amount of enzyme added has little effect on the viscosity of the modified starch. Hence, the amount of enzyme has little effect on the molecular weight. Compared with the addition of the enzyme, the viscosity of modified starch was effectively reduced by prolonging the activation time.

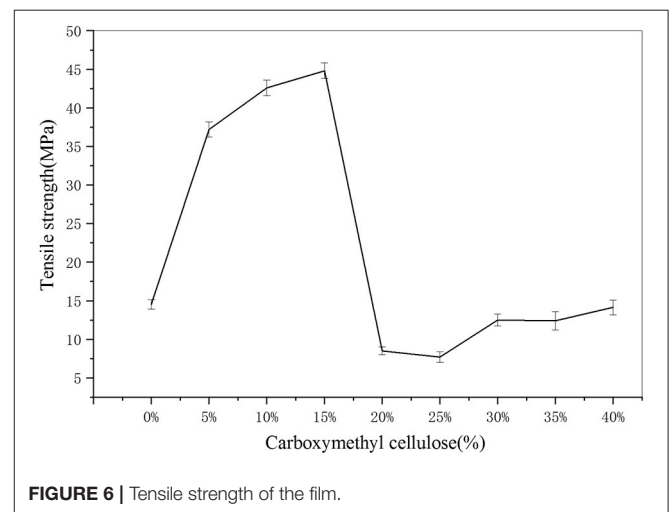
As shown in **Figure 3**, starch is composed of D-anhydroglucose units as basic units, and the most important characteristic groups are the hydroxyl groups on C_2 , C_3 , and C_6 . Among them, C_2 and C_3 were secondary alcoholic hydroxyl groups, and C_6 connected the primary alcoholic hydroxyl groups with a D-pyran ring structure. The positions of the infrared absorption peaks and structural assignments of these characteristic groups in the infrared spectrogram were as follows: The hydrogen-bonded O-H stretching vibration occurred near $3,278\text{ cm}^{-1}$; the O-H asymmetric stretching vibration occurred near $2,928\text{ cm}^{-1}$; the H-O-H bending vibration that occurred near $1,640\text{ cm}^{-1}$ was caused by water, and many scholars mistakenly believe via a starch analysis that it was the absorption peak of C=O; the C-O-C asymmetric stretching vibration peak occurred near $1,150\text{ cm}^{-1}$; the C-O stretching vibration of the D-glucopyranose band connected to the hydroxyl group occurred near $1,078\text{ cm}^{-1}$; and the glycosidic bond vibration

TABLE 2 | TGA analysis value of carboxylated starch.

Sample	Starting temperature ($^\circ\text{C}$)	End temperature ($^\circ\text{C}$)	Weight loss rate (%)
1	280.9	326.1	75.35
2	281.5	320.6	73.96
3	279.2	324.1	74.79
4	286.4	321.2	73.91
5	281.6	321.6	73.34

TABLE 3 | XRD analysis of carboxylated starch.

Sample	I (cps)	I_a (cps)	I_c (cps)	X_c (%)
1	51816.46	36856.46	14960.00	28.87
2	50683.36	37034.87	13648.50	26.93
3	49685.30	36698.13	12987.17	26.14
4	48677.63	35252.40	13425.24	27.58
5	49987.40	36944.26	13043.14	26.09

**FIGURE 6** | Tensile strength of the film.

occurred at 927 cm^{-1} as. Carboxylated starch not only contains the absorption peak of the above characteristic groups, but also a C=O absorption peak near $1,751\text{ cm}^{-1}$. Therefore, the occurrence or non-occurrence of a peak near $1,751\text{ cm}^{-1}$ determines whether the carboxylated starch contains carboxyl and carbonyl groups. It can be seen from **Figure 3** that the C=O absorption peak at $1,751\text{ cm}^{-1}$ can only be clearly observed in samples 2 and 3. However, this peak cannot be observed in the other levels. It can be seen that the degree of carboxylation of starch after enzyme activation was higher, and the FTIR data is consistent with the carboxyl content detection data.

Five starch samples were analyzed using DSC, the starch gelatinization start temperature ($T_o/^\circ\text{C}$), starch gelatinization peak temperature ($T_p/^\circ\text{C}$), gelatinization end temperature ($T_c/^\circ\text{C}$), and heat absorbed by gelatinization ($\Delta H/\text{J}\cdot\text{g}^{-1}$). It can be seen from **Figure 4** and **Table 1** that the gelatinization temperature of carboxylated starch was lower than that of native starch. The analysis showed that the activation of the enzyme

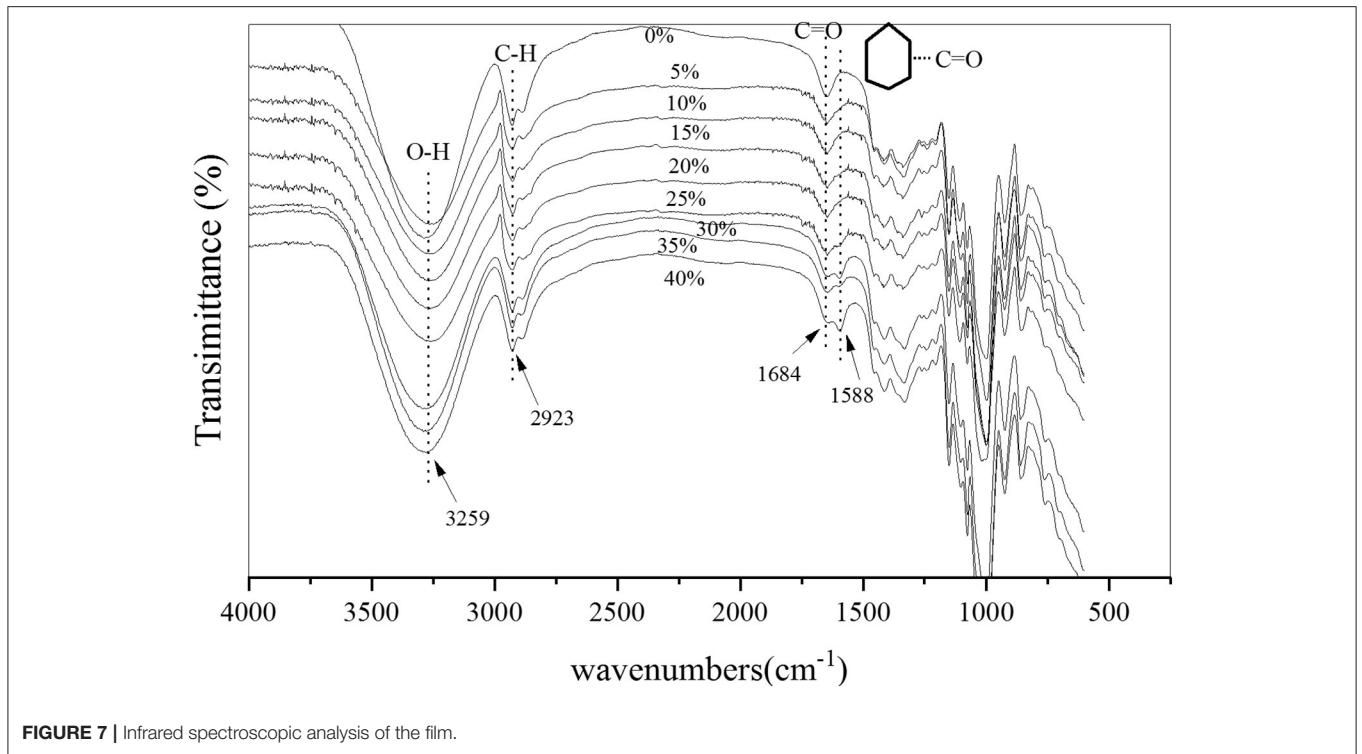


FIGURE 7 | Infrared spectroscopic analysis of the film.

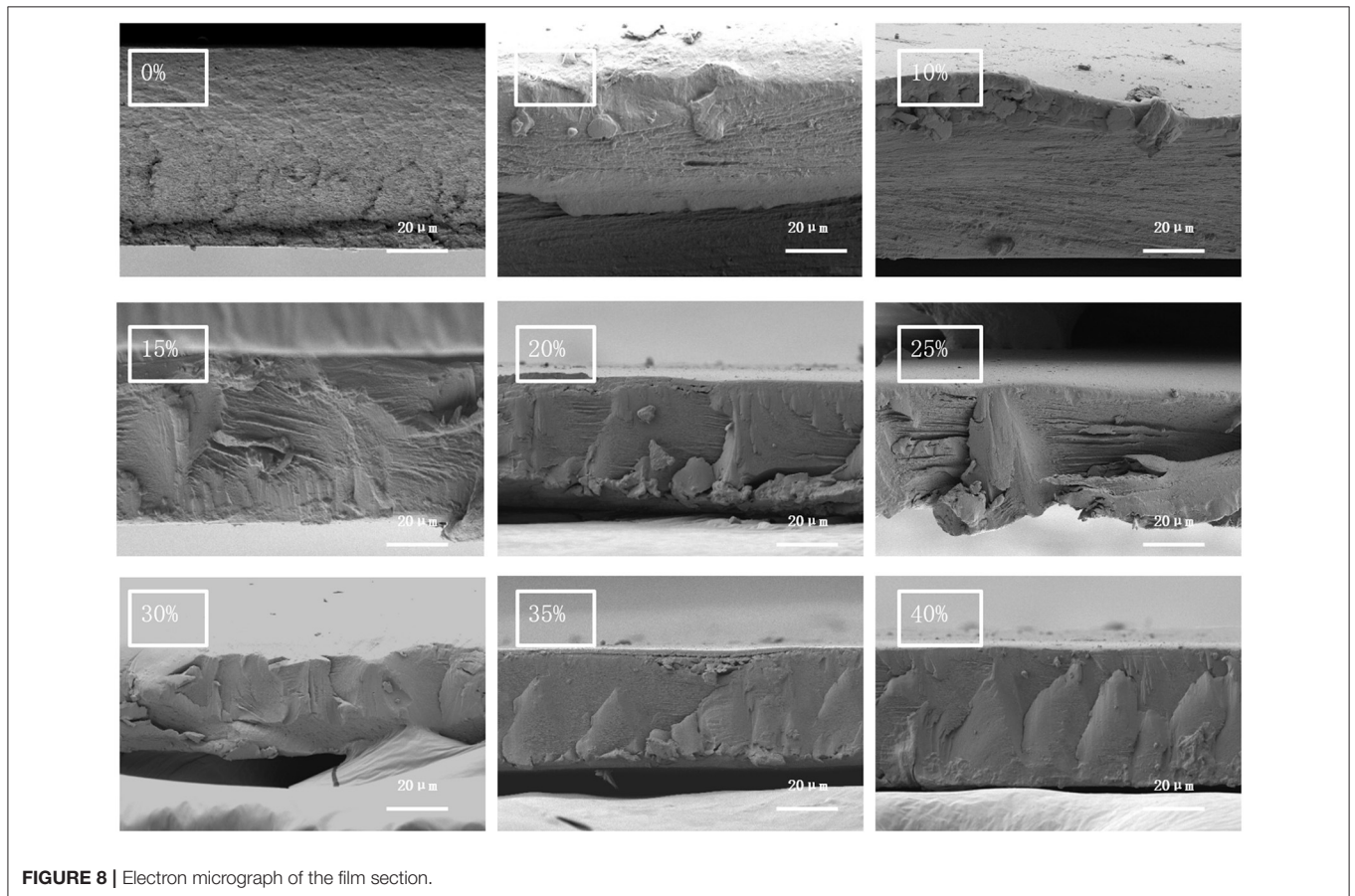


FIGURE 8 | Electron micrograph of the film section.

opened and expanded the pores leading to the inside of the starch granule. Thus, the crystallization area was destroyed during carboxylation preparation, which made it easier for water to enter the inside of the modified starch granule and, in turn, lowered the gelatinization temperature of the carboxylated starch compared to that of native starch. At the same time, the gelatinization enthalpy of the carboxylated sample decreased compared with that of the original starch. It is also proved that enzyme-activated starch was more easily destroyed by carboxylation.

It can be seen from **Figure 5** and **Table 2** that the TGA curves of the four carboxylated starch samples were essentially the same as those of the original starch. It can be clearly seen that the TGA curve of starch is divided into two stages of weight loss. The first weight loss stage occurred at $\sim 100^{\circ}\text{C}$, and the second weight loss stage occurred at $\sim 300^{\circ}\text{C}$. The first weight loss stage occurred due to the evaporation of water, and water in starch consists of two parts. The first part contains free water molecules, and the second part was the water that bound to the starch hydroxyl groups. The first part of water was easily lost, whereas the second part was difficult to lose. The free water in the starch sample started to volatilize at $\sim 60^{\circ}\text{C}$ and ended at $\sim 150^{\circ}\text{C}$. The second part contained less water, and the temperature when the loss occurred was generally above 200°C . Due to the low water content of the hydroxyl group, no obvious weight loss peak could be observed in the TGA analysis. It can be clearly seen that the weight loss rate of the original starch was higher than that of the other carboxylated starch samples. The bound water in carboxylated starch was destroyed during the oxidation reaction process, which resulted in the bound water of carboxylated starch being less than that of starch, which is one reason why the weight loss rate of carboxylated starch was less than that of starch. The thermal degradation temperature of the carboxylated starch sample increased slightly, and the unstable structure of the starch reduced in size during the oxidation reaction. The carboxylated starch sample was soluble in water during the washing process, and while the remaining structure was more compact and stable, the thermal stability performance was enhanced (Pei et al., 1985; Jha, 2020).

According to **Table 3**, the X-ray diffraction patterns of the five samples were essentially the same, with single peaks occurring near $15(2)$, $19(2)$, and $23(2)$, and a crystalline double peak occurring near $17(2)$ (**Supplementary Figure 1**). The carboxylated starch prepared by enzymatic activation has a similar pattern to that of natural starch. According to **Table 3**, the crystallinity of the four carboxylated starch samples was lower than that of the original starch, which indicates that enzyme activation promoted the carboxylation reaction of starch, destroyed the starch crystallization area, and reduced the crystallinity of starch. At the same activation time, the greater the amount of enzyme that was used, the more seriously the crystal zone was destroyed and, thus, the lower was the crystallinity. The relative activation time and enzyme dosage had a significant influence on the crystallinity of starch.

Preparation of Composite Films

As can be seen from **Figure 6**, with the increase of carboxymethyl cellulose, the tensile strength of the film first increased,

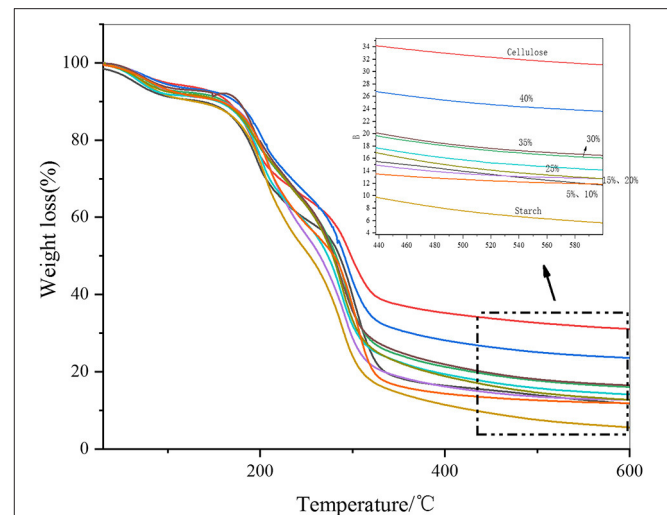


FIGURE 9 | Thermogravimetric analysis of the films.

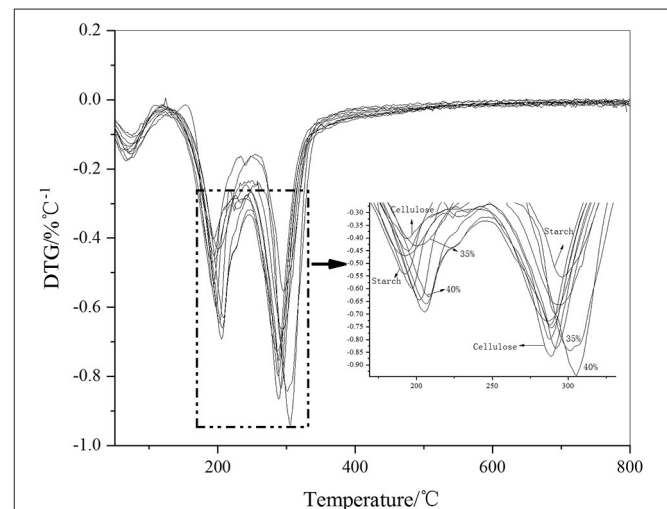


FIGURE 10 | DTG diagram of the film.

reaching its maximum tensile strength at 44.8 MPa when the cellulose content was 15%, and then decreased with further increases of cellulose, the mechanical properties of the films declined significantly.

It can be seen from **Figure 7** that the FTIR data showed more starch characteristics. The positions of the infrared absorption peaks and the structural assignments of these characteristic groups were, respectively, in the infrared spectrogram: The stretching vibration of hydrogen-bonded (O-H) occurred at $\sim 3,259\text{ cm}^{-1}$; the asymmetric stretching vibration of C-H occurred at $\sim 2,923\text{ cm}^{-1}$, and the absorption peak of C=O occurred at $\sim 1,684\text{ cm}^{-1}$. The asymmetric stretching vibration peak of C-O-C occurred at $\sim 1,148\text{ cm}^{-1}$; the C-O stretching vibration of the D-glucopyranose band connected to the hydroxyl group occurred at $\sim 1,075\text{ cm}^{-1}$; and the glycosidic

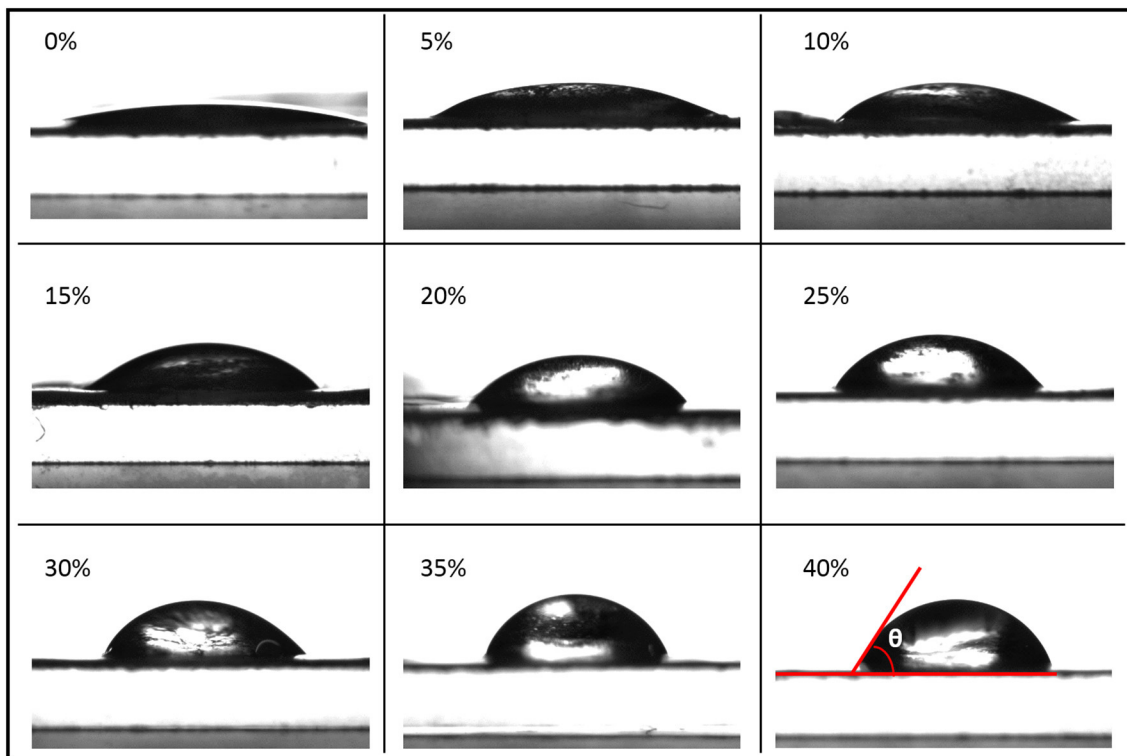


FIGURE 11 | Contact angle diagram of the film.

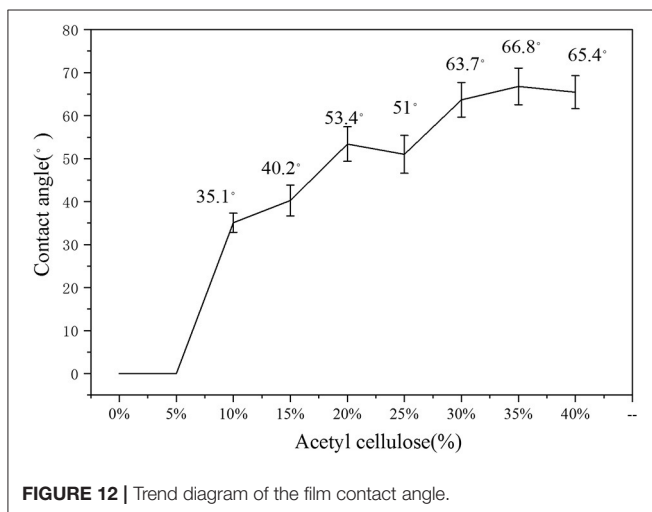


FIGURE 12 | Trend diagram of the film contact angle.

bond vibration occurred at $\sim 918 \text{ cm}^{-1}$. With the increase of cellulose $< 30\%$, the characteristic peaks at $\sim 3,259 \text{ cm}^{-1}$, $\sim 2,923 \text{ cm}^{-1}$, and $\sim 1,075 \text{ cm}^{-1}$ slightly deviated but did not change significantly. When the amount of cellulose was $> 30\%$, a new peak appeared at $\sim 1,588 \text{ cm}^{-1}$, and the peak increased with the increased amount of cellulose, which through analysis was determined to be the vibration of the aromatic C=O skeleton. With the increase of the amount of cellulose addition, the carboxyl content of cellulose increased along with its reaction

probability with the hydroxyl group in starch. Some starch and cellulose groups produced an esterification reaction and formed an aliphatic aromatic ring. Thus, the aromatic C=O skeleton vibration appeared in the FTIR diagram (Da Silva Filipini et al., 2020; Li and Wei, 2020; Zhou et al., 2020).

It can be seen from **Figure 8**, through the cross-sectional electron micrograph, it could be seen that the cross-section of the film was not smooth, and the graininess was particularly strong when the cellulose addition was zero. With the increase of the cellulose addition, the cross-sectional particle morphology of the film decreased and gradually showed fiber morphology. A blocky smooth section appeared when the addition amount was $> 20\%$, and a blocky break appeared in the film section when the addition amount was $> 30\%$. The analysis showed that as the addition amount increased, the fiber agglomerated and gradually separated from the starch. As carboxymethyl cellulose tends to be non-polar, phase separation occurred when the two materials were not closely bound, and the two materials were disconnected at the junction where they were not closely connected. Combined with the mechanical property analysis of the film, it was determined that when the additive amount exceeded 15%, the mechanical property of the film began to decline.

As shown in **Figure 9**, when the fiber additive amount was zero, the weight loss rate of the film was highest, and the residual carbon rate was the lowest at 5.6%. The highest carbon yield was 23.6% when 40% cellulose was added. With the increased cellulose content, the overall carbon yield of the film increased. The thermal properties of the two films were similar when the

additive amount was 5 and 10%. When the additive amount was 15 and 20%, the properties of the two materials were similar. In general, the addition of cellulose helped to improve the thermal stability of the film materials.

A derivative thermogravimetry (DTG) graph was developed to differentiate the TG data of the thin film materials. In **Figure 10**, two thermal decomposition peaks can be clearly seen. The first decomposition peak occurred at $\sim 200^{\circ}\text{C}$, which was the thermal decomposition peak of starch. The second peak occurred at $\sim 300^{\circ}\text{C}$, which was the thermal decomposition peak of cellulose. Because there is a large amount of high crystallinity amylose in starch, some of it was decomposed at 300°C . Similarly, the structure of non-oriented cellulose in cellulose was similar to that of starch, which decomposes at $\sim 200^{\circ}\text{C}$. However, from a general point of view, with the addition of cellulose, the 200°C decomposition peak of the film material was delayed, which indicated that the starch structure reacted with cellulose and the thermal stability was enhanced. Similarly, at $\sim 300^{\circ}\text{C}$, the thermal stability of cellulose was enhanced due to the highly crystallized starch, and the pyrolysis peak was also delayed. The thermal stability was highest when the additive amount reached $>35\%$, which exceeded the structural performance of the raw material itself. Combined with infrared analysis, it can be seen that due to the increased amount of cellulose, cellulose and starch formed an aromatic ring. Infrared data showed that an aromatic C=O skeleton vibration appeared at $\sim 1,588\text{ cm}^{-1}$. The thermal performance of the aromatic structure increased with respect to the temperature of the aliphatic structure.

It can be seen from **Figures 11, 12** that the film contact angle increased with the increase of cellulose addition. However, the film contact angles of 0 and 5% could not be measured. The analysis showed that starch, which is a water-absorbing material, and the carboxylated modified starch film had better water absorption, which caused water to be absorbed by the film in a short time, and the contact angle could not be measured. The film contact angle was improved when the additive amount was $>10\%$. It can be clearly seen from the data, that 10, 20, and 30% were the three turning points when the contact angle improved. When the added carboxymethyl cellulose was $>10\%$, the starch film was significantly improved. The analysis showed that because the hydroxyl groups on the starch structure were oxidized to the carboxyl groups, the water absorption of the starch film greatly improved. A small amount ($<5\%$) of the addition did not increase the distribution of cellulose on the surface, and it had a minor effect on the contact angle of the film. The addition of $>10\%$ significantly improving the contact angle. The increase in the contact angle was not significant when more than 30% cellulose was added. The analysis showed that the cellulose material was rich in hydroxyl groups and easily absorbed water. When $>30\%$ cellulose was added, the characteristics of the cellulose material limited further improvement to the hydrophobicity. The hydrophobic effect of the film was best when 35% cellulose was added, and the contact angle was 66.8%.

CONCLUSION

In conclusion, carboxymethyl cellulose was used as the additive to improve the hydrophobicity and strength of carboxylated starch film, which is prepared from starch catalyzed by bio- α -amylase. Activated enzyme was more effective at increasing the carboxyl content than was prolonging the activation time of the enzyme. Enzyme activation destroyed the crystalline structure of starch and effectively promoted the carboxylation reaction. Carboxymethyl cellulose effectively improved the hydrophobicity of the starch film with the addition of $>10\%$ carboxymethyl cellulose. The contact angle was 66.8° when the additive amount was 35%. The addition of carboxymethyl cellulose improved the mechanical properties of the membrane material, and the maximum membrane performance was 44.8 MPa when 15% was added. The addition of carboxymethyl cellulose can form an aliphatic aromatic structure partly through an esterification reaction, which can improve the thermal stability of thin film materials. The modified carboxylated starch film can be used at higher temperature and humidity, expanding the application range of the film.

DATA AVAILABILITY STATEMENT

The original contributions presented in the study are included in the article/**Supplementary Material**, further inquiries can be directed to the corresponding author/s.

AUTHOR CONTRIBUTIONS

CL, HK, and ZS conceived the project and contributed to the concept of the manuscript. SQ, JX, and XL synthesized and characterized the carboxylated starch, and performed experimental works. JY and YZ synthesized and characterized the composites. All authors contributed to the article and approved the submitted version.

FUNDING

This work was partially supported by the National Key Research and Development Program of China (No. 2019YFD1002404), the National Natural Science Foundation (No. 21961036), and the Applied Basic Research Programs of Science and Technology Department of Yunnan Province (Award No. 2018ZG004, 202002AA10007). The study also was supported by the Key Laboratory of State Forestry Administration for Highly-Efficient Utilization of Forestry Biomass Resources in Southwest China (2019-KF05).

SUPPLEMENTARY MATERIAL

The Supplementary Material for this article can be found online at: <https://www.frontiersin.org/articles/10.3389/fbioe.2021.638546/full#supplementary-material>

REFERENCES

- Achremowicz, B., Gumul, D., Bala-Piasek, A., Tomasik, P., and Haberko, K. (2000). Air oxidation of potato starch over Cu (II) catalyst. *Carbohydr. Polym.* 42, 45–50. doi: 10.1016/S0144-8617(99)00128-9
- Ampaiwong, J., Rattanawaleedirojn, P., Saengkiattiyut, K., Rodthongkum, N., Potiyaraj, P., Soatthyanon, N., et al. (2019). Reduced graphene oxide/carboxymethyl cellulose nanocomposites: novel conductive films. *J. Nanosci. Nanotechnol.* 19, 3544–3550. doi: 10.1166/jnn.2019.16120
- Biaou, O., O., Lallepak, L., Bianza, M. B., Saied, A. H., and Guang, Y. (2020). Combining silk sericin and surface micropatterns in bacterial cellulose dressings to control fibrosis and enhance wound healing. *Eng. Sci.* 10, 68–77. doi: 10.30919/es8d906
- Cao, Y., Qing, X., Sun, J., and Zhou, F. (2002). Graft copolymerization of acrylamide onto carboxymethyl starch. *Eur. Polym. J.* 38, 1921–1924. doi: 10.1016/S0014-3057(02)00077-0
- Chang, R., Ji, N., Li, M., Qiu, L., Sun, C., Xiong, L., et al. (2019). Green preparation and characterization of starch nanoparticles using a vacuum cold plasma process combined with ultrasonication treatment. *Ultrason. Sonochem.* 58:104660doi: 10.1016/j.ulsonch.2019.104660
- Chen, F. Q., Zhang, B. S., Huang, Q., and Lu, H. F. (2020). Research progress of determination crystallinity of starch granular by X-ray diffraction. *J. Sci. Technol. Food Ind.* 31, 432–435. doi: 10.13386/j.issn1002-0306.2010.01.079
- Chen, P., Zhang, Y., Qiao, Q., Tao, X., Liu, P., Xie, F., et al. (2021). Comparison of the structure and properties of hydroxypropylated acid-hydrolysed maize starches with different amylose/amylopectin contents. *Food Hydrocolloids* 110:106134. doi: 10.1016/j.foodhyd.2020.106134
- Da Silva Filipini, G., Romani, V. P., and Martins, V. G. (2020). Biodegradable and active-intelligent films based on methylcellulose and jambolão (*Syzygium cumini*) skins extract for food packaging. *Food Hydrocolloids* 109:106139. doi: 10.1016/j.foodhyd.2020.106139
- Ekrumulmahmud, H. N. M., Anuar, K., Zulkarnain, Z., and Wan, M. M. Y. (2005). Electrochemical formation of polypyrrole-carboxymethylcellulose conducting polymer composite films. *J. Mater. Sci. Technol.* 21, 661–665. doi: 10.3321/j.issn:1005-0302.2005.05.011
- Escobar-Puentes, A. A., García-Gurrola, A., Rincón, S., Zepeda, A., and Martínez-Bustos, F. (2020). Effect of amylose/amylopectin content and succinylation on properties of corn starch nanoparticles as encapsulants of anthocyanins. *Carbohydr. Polym.* 250:116972. doi: 10.1016/j.carbpol.2020.116972
- Gong, B., Xu, M., Li, B., Wu, H., Liu, Y., Zhang, G., et al. (2017). Repeated heat-moisture treatment exhibits superiorities in modification of structural, physicochemical and digestibility properties of red adzuki bean starch compared to continuous heat-moisture way. *Food Res. Int.* 102, 776–784. doi: 10.1016/j.foodres.2017.09.078
- Holck, J., Fredslund, F., Møller, M. S., Brask, J., Krogh, K. B. R. M., Lange, L., et al. (2019). A carbohydrate-binding family 48 module enables feruloyl esterase action on polymeric arabinoxylyan. *J. Biol. Chem.* 294, 17339–17353. doi: 10.1074/jbc.RA119.009523
- Huang, Z. W., Raghuvanshi, V. S., and Garnier, G. (2017). Functionality of immunoglobulin G and immunoglobulin M antibody physisorbed on cellulosic films. *Front. Bioeng. Biotechnol.* 5:41. doi: 10.3389/fbioe.2017.00041
- Jha, P. (2020). Effect of grapefruit seed extract ratios on functional properties of corn starch-chitosan bionanocomposite films for active packaging. *Int. J. Biol. Macromol.* 163, 1546–1556. doi: 10.1016/j.ijbiomac.2020.07.251
- Kim, H. Y., Oh, S. M., Bae, J. E., Yeom, J. H., Kim, B. Y., Kim, H. S., et al. (2017). Preparation and characterization of amorphous granular potato starches (AGPS) and cross-linked amorphous granular potato starches (CLAGPS). *Carbohydr. Polym.* 178, 41–47. doi: 10.1016/j.carbpol.2017.09.020
- Kontturi, E., and Spirk, S. (2019). Ultrathin films of cellulose: a materials perspective. *Front. Chem.* 7:488. doi: 10.3389/fchem.2019.00488
- Lee, D. J., Park, E. Y., and Lim, S. T. (2019). Effects of partial debranching and storage temperature on recrystallization of waxy maize starch. *Int. J. Biol. Macromol.* 140, 350–357. doi: 10.1016/j.ijbiomac.2019.08.128
- Li, S., Ma, Y., Ji, T., Sameen, D. E., Ahmed, S., Qin, W., et al. (2020). Cassava starch/carboxymethylcellulose edible films embedded with lactic acid bacteria to extend the shelf life of banana. *Carbohydr. Polym.* 248:116805. doi: 10.1016/j.carbpol.2020.116805
- Li, Z., and Wei, C. (2020). Morphology, structure, properties and applications of starch ghost: A Review. *Int. J. Biol. Macromol.* 163, 2084–2096. doi: 10.1016/j.ijbiomac.2020.09.077
- Ma, Y., Cai, C., Wang, J., and Sun, D. W. (2006). Enzymatic hydrolysis of corn starch for producing fat mimetics. *J. Food Eng.* 73, 297–303. doi: 10.1016/j.jfoodeng.2005.01.023
- Mansur, A. A. P., de Carvalho, F. G., Mansur, R. L., Carvalho, S. M., de Oliveira, L. C., Mansur, H. S., et al. (2017). Carboxymethylcellulose/Zn Cd S fluorescent quantum dot nanoconjugates for cancer cell bioimaging. *Int. J. Biol. Macromol.* 96, 675–686. doi: 10.1016/j.ijbiomac.2016.12.078
- Menzel, C. (2020). Improvement of starch films for food packaging through a three-principle approach: antioxidants, cross-linking and reinforcement. *Carbohydr. Polym.* 250:116828. doi: 10.1016/j.carbpol.2020.116828
- Navia-Coarite, N. A., Nina-Mollisaca, G. L., Mena-Gallardo, E. P., and Salcedo-Ortiz, L. (2019). Enzymatic hydrolysis in quinoa Y tarwi flour by α -amylase effect. *Biotechnol. Sector Agropecuario y Agroindustrial.* 17, 64–73.
- Nazrin, A., Sapuan, S. M., Zuhri, M. Y. M., Ilyas, R. A., Syafiq, R., et al. (2020). Nanocellulose reinforced thermoplastic starch (TPS), polylactic acid (PLA), and polybutylene succinate (PBS) for food packaging applications. *Front. Chem.* 8:213. doi: 10.3389/fchem.2020.00213
- Ozdemir, S., Fincan, S. A., Karakaya, A., and Enez, B. (2018). A novel raw starch hydrolyzing thermostable α -amylase produced by newly isolated *Bacillus mojavensis* SO-10: purification, characterization and usage in starch industries. *Braz. Arch. Biol. Technol.* 61:e18160399. doi: 10.1590/1678-4324-2018160399
- Paulik, S., Yu, W. W., Flanagan, B., Gilbert, R. G., Jekle, M., Becker, T., et al. (2019). Characterizing the impact of starch and gluten-induced alterations on gelatinization behavior of physically modified model dough. *Food Chem.* 301:125276. doi: 10.1016/j.foodchem.2019.125276
- Pei, G. W., Zhong, W. L., and Yue, S. B. (1985). *X-Ray Diffraction of Single Crystal, Polycrystalline and Amorphous Materials*. JINAN: Shandong University Press. 1985, 478–500.
- Remya, R., Jyothi, A. N., and Sreekumar, J. (2018). Effect of chemical modification with citric acid on the physicochemical properties and resistant starch formation in different starches. *Carbohydr. Polym.* 202, 29–38. doi: 10.1016/j.carbpol.2018.08.128
- Salcedo-Mendoza, J., Paternina-Urzola, S., Lujan-Rhenals, D., and Figueroa-Flórez, J. (2018). Enzymatic modification of cassava starch (Corpoica M-Tai) around the pasting temperature. *Dyna* 85, 223–230. doi: 10.15446/dyna.v85n204.66620
- Sangian, H. F., Telleng, R., and Aruan, I. (2018). The structural modification of cassava starch using a saline water pretreatment. *Food Sci. Technol.* 38, 215–220. doi: 10.1590/1678-457x.18517
- Sarmah, D., and Karak, N. (2020). Double network hydrophobic starch based amphoteric hydrogel as an effective adsorbent for both cationic and anionic dyes. *Carbohydr. Polym.* 242:116320. doi: 10.1016/j.carbpol.2020.116320
- Shahriarpanah, S., Nourmohammadi, J., and Amoabediny, G. (2016). Fabrication and characterization of carboxylated starch-chitosan bioactive scaffold for bone regeneration. *Int. J. Biol. Macromol.* 93, 1069–1078. doi: 10.1016/j.ijbiomac.2016.09.045
- Sharmin, E., Kafyah, M. T., Alzaydi, A. A., Fatani, A. A., Hazazzi, F. A., Hazazzi, F. A., et al. (2020). Synthesis and characterization of polyvinyl alcohol/corn starch/linseed polyol-based hydrogel loaded with biosynthesized silver nanoparticles. *Int. J. Biol. Macromol.* 163, 2236–2247. doi: 10.1016/j.ijbiomac.2020.09.044
- Shi, L., Zhang, B., Li, C., Fu, X., and Huang, Q. (2019). Annealing improves the concentration and controlled release of encapsulated ethylene in V-type starch. *Int. J. Biol. Macromol.* 141, 947–954. doi: 10.1016/j.ijbiomac.2019.08.244
- Shogren, R. L. (2000). Modification of maize starch by thermal processing in glacial acetic acid. *Carbohydr. Polym.* 43, 309–315. doi: 10.1016/S0144-8617(00)00178-8
- Souto, L. R. F., Caliar, M., Soares Junior, M. S., Fiorda, F. A., and Garcia, M. C. (2017). Utilization of residue from cassava starch processing for production of fermentable sugar by enzymatic hydrolysis. *Food Sci. Technol.* 37, 19–24. doi: 10.1590/1678-457x.0023
- Suriyatem, R., Auras, R. A., and Rachtanapun, P. (2018). Utilization of carboxymethyl cellulose from durian rind agricultural waste to improve

- physical properties and stability of rice starch-based film. *J. Polym. Environ.* 27, 286–298. doi: 10.1007/s10924-018-1343-z
- Tasaso, P. (2015). Optimization of reaction conditions for synthesis of carboxymethyl cellulose from oil palm fronds. *IJERA.* 6, 101–104. doi: 10.7763/IJCEA.2015.V6.460
- Torbica, A., Belović, M., and Popović, L., Čakarević, J. (2020). Heat and hydrothermal treatments of non-wheat flours. *Food Chem.* 334:127523. doi: 10.1016/j.foodchem.2020.127523
- Wang, K., Qi, T., Guo, L., Ma, Z., Gu, G., Xiao, M., et al. (2019). Enzymatic glucosylation of salidroside from starch by α -Amylase. *J. Agric. Food Chem.* 67, 2012–2019. doi: 10.1021/acs.jafc.8b06618
- Wu, Y., Huang, W., Cui, T., and Fan, F. (2020). Crystallization and strength analysis of amorphous maltose and maltose/whey protein isolate mixtures. *J. Sci. Food Agric.* doi: 10.1002/jsfa.10881. [Epub ahead of print].
- Xiao, H., Yang, F., Lin, Q., Zhang, Q., Zhang, L., Sun, S., et al. (2020). Preparation and characterization of broken-rice starch nanoparticles with different sizes. *Int. J. Biol. Macromol.* 160, 437–445. doi: 10.1016/j.ijbiomac.2020.05.182
- Xiao, L., Chen, J., Wang, X., Bai, R., Chen, D., Liu, J., et al. (2018). Structural and physicochemical properties of chemically modified Chinese water chestnut [*Eleocharis dulcis* (Burm. f.) Trin. ex Hensch] starches. *Int. J. Biol. Macromol.* 120, 547–556. doi: 10.1016/j.ijbiomac.2018.08.161
- Xie, S. Q., Zhang, X., Michael, P., W., and Lin, H. F. (2018). Cellulose nanocrystals (CNCs) applications: a review. *En. Sci.* 2, 4–16. doi: 10.30919/es.1803302
- Zeng, J., Guo, J., Tu, Y., and Yuan, L. (2019). Functional study of C-terminal domain of the thermoacidophilic raw starch-hydrolyzing α -amylase Gt-amy. *Food Sci. Biotechnol.* 29, 409–418. doi: 10.1007/s10068-019-00673-x
- Zhang, Y., Zhang, Y., Xu, F., Wu, G., and Tan, L. (2017). Molecular structure of starch isolated from jackfruit and its relationship with physicochemical properties. *Sci. Rep.* 7:13423. doi: 10.1038/s41598-017-13435-8
- Zhou, W., Zha, D., Zhang, X., Xu, J., Guo, B., Huang, Y., et al. (2020). Ordered long polyvinyl alcohol fiber-reinforced thermoplastic starch composite having comparable mechanical properties with polyethylene and polypropylene. *Carbohydr. Polym.* 250:116913. doi: 10.1016/j.carbpol.2020.116913

Conflict of Interest: The authors declare that the research was conducted in the absence of any commercial or financial relationships that could be construed as a potential conflict of interest.

Copyright © 2021 Liu, Qin, Xie, Lin, Zheng, Yang, Kan and Shi. This is an open-access article distributed under the terms of the Creative Commons Attribution License (CC BY). The use, distribution or reproduction in other forums is permitted, provided the original author(s) and the copyright owner(s) are credited and that the original publication in this journal is cited, in accordance with accepted academic practice. No use, distribution or reproduction is permitted which does not comply with these terms.



Using Cellulose Nanocrystal as Adjuvant to Improve the Dispersion Ability of Multilayer Graphene in Aqueous Suspension

Haiqiao Zhang^{1,2}, Yan Wu^{1,2*}, Feng Yang³, Huiling Dong^{1,2}, Yuqing Bian^{1,2}, Huanliang Jia⁴, Xuqin Xie⁴ and Jilei Zhang⁵

¹ College of Furnishings and Industrial Design, Nanjing Forestry University, Nanjing, China, ² Co-Innovation Center of Efficient Processing and Utilization of Forest Resources, Nanjing Forestry University, Nanjing, China, ³ Fashion Accessory Art and Engineering College, Beijing Institute of Fashion Technology, Beijing, China, ⁴ Dehua Tubao New Decoration Material Co., Ltd., Huzhou, China, ⁵ Department of Sustainable Bioproducts, Mississippi State University, Mississippi State, MS, United States

OPEN ACCESS

Edited by:

Lei Wang,
Jeju National University, South Korea

Reviewed by:

Tianyu Guo,
University of British Columbia,
Canada
Qian Li,
Zhejiang Agriculture and Forestry
University, China

*Correspondence:

Yan Wu
wuyan@njfu.edu.cn

Specialty section:

This article was submitted to
Bioprocess Engineering,
a section of the journal
Frontiers in Bioengineering and
Biotechnology

Received: 07 December 2020

Accepted: 06 January 2021

Published: 10 February 2021

Citation:

Zhang H, Wu Y, Yang F, Dong H, Bian Y, Jia H, Xie X and Zhang J (2021) Using Cellulose Nanocrystal as Adjuvant to Improve the Dispersion Ability of Multilayer Graphene in Aqueous Suspension. *Front. Bioeng. Biotechnol.* 9:638744. doi: 10.3389/fbioe.2021.638744

Cellulose nanocrystal (CNC) has been applied in various fields due to its nano-structure, high aspect ratio, specific surface area and modulus, and abundance of hydroxy groups. In this work, CNC suspensions with different concentrations (0.4, 0.6, and 0.8%) were used as the adjuvant to improve the dispersion ability of multilayer graphene (MLG) in aqueous suspension, which is easy to be aggregated by van der Waals force between layers. In addition, N-methyl-2-pyrrolidone, ethanol, and ultrapure water were used as control groups. Zeta potential analysis and Fourier transform infrared spectroscopy showed that the stability of MLG/CNC has met the requirement, and the combination of CNC and MLG was stable in aqueous suspension. Results from transmission electron microscopy, Fourier transform infrared spectroscopy, and absorbance showed that MLG had a better dispersion performance in CNC suspensions, compared to the other solutions. Raman spectrum analysis showed that the mixtures of 1.0 wt% MLG with 0.4% CNC had the least defects and fewer layers of MLG. In addition, it is found that CNC suspension with 0.8% concentration showed the highest ability to disperse 1.0 wt% MLG with the most stable performance in suspension. Overall, this work proved the potential application of CNC as adjuvant in the field of graphene nanomaterials.

Keywords: dispersion, ball-milling, multilayer graphene, cellulose nanocrystal, sedimentation analysis

INTRODUCTION

Graphene nanomaterials have been widely used as electrode materials for supercapacitors (Ouyang et al., 2013) and in composites with enhanced electrical (Gao et al., 2013), mechanical (Zhang et al., 2012), and thermal (Shahil and Balandin, 2012) properties because of their excellent properties. However, the large specific surface area and van der Waals forces (Atif and Inam, 2016) between layers induce graphene nanomaterial to agglomerate (Li et al., 2018) when dispersed into other materials as property enhancement agents, thereby causing lower performance of these nanomaterials as property-enhancement agents. Overcoming the agglomeration issue to fully take advantage of the superior properties of these nanomaterials becomes an important research topic.

The current method of dispersing graphene nanomaterial into a matrix is to disperse it in an aqueous surfactant solution first (Lotya et al., 2010). This is because the surfactant molecules attach onto the graphene nanomaterial surface through electrostatic repulsion or intermolecular forces, resulting in the uniform and high concentration dispersion of graphene nanomaterial in the solution. Surfactant aqueous solutions, such as ionic and non-ionic surfactants (Guardia et al., 2011), polymers (Wajid et al., 2012), organic salts (Du et al., 2013), and aromatic molecules (Geng et al., 2010; Zhang et al., 2010; Das et al., 2012), can be used both in organic and aqueous media to slow down reactions, maintain chemical balance, change surface tension, and prevent light and thermal decomposition or oxidative decomposition from happening. The direct exfoliation technique and stabilization of graphite in aromatic solvents or ionic liquids (Wang et al., 2010) suffer from low throughput and are a threat to human health and the environment (Yang et al., 2020). The aqueous surfactant solution has the advantages of low cost and being easily operated, but the concentration of the obtained graphene nanomaterial dispersion is relatively low. Some physical processes have also been applied to improve the dispersion of graphene nanomaterial in the solution mentioned above, like shearing (Knieke et al., 2010; Paton et al., 2014; Dong et al., 2018), microwave (Chiu et al., 2012), ball-milling (Zhao et al., 2010; León et al., 2014), and ultrasonic treatment (Nuvoli et al., 2011; Notley, 2012).

Herein, we demonstrated an approach to disperse multilayer graphene (MLG) in water with the cellulose nanocrystal (CNC) as adjuvant (Wu et al., 2019b). Cellulose, one of the most abundant, natural, and renewable biopolymers in the world, is widely present in biomasses like woods (Wu et al., 2019c, 2020a,b), corn stover (Zhao et al., 2020), and tunicate (Zhao et al., 2015), and can be metabolized by specific bacteria.

Cellulose is a long-chain polymer with repeated units of D-glucose, a simpler sugar form. The CNC is a nanomaterial that can be obtained by continuously peeling cellulose. The theoretical Young's modulus of CNC along its chain axis is 167.5 GPa (Wajid et al., 2012) and tensile strength is 7.5–7.7 GPa (Gray et al., 2018). Furthermore, the features of inherent renewability, biodegradability, and biocompatibility make it an eco-friendly green material. In general, extraction from natural fibers through sulfuric acid hydrolysis is usually used to prepare CNC (Wu et al., 2019b). The negative charged sulfate groups in the CNC surface prepared by this method make them repel each other and result in good stability (Jiang and Hsieh, 2013).

Herein, we demonstrated an approach to disperse MLG in water with the sulfuric acid hydrolysis CNC as adjuvant. The mechanism of CNC-assisted MLG dispersion in aqueous suspension is shown in **Figure 1**. The mechanism can be explained as the CNC aqueous suspension is sufficiently stable, and the MLG is attached to the “3D net” formed by CNC. In this study, MLG was ball-milled first. The ball-milling technology utilized the shear force generated by ball collision to offset the van der Waals force between the MLG layers (Guo and Chen, 2014), which can be physically peeled to reduce the size of MLG. Subsequently, through comparative experiments, the influence of CNC suspensions with different

concentrations as adjuvant on the dispersion ability of MLG in water was evaluated.

MATERIALS AND METHODS

Materials

The microcrystalline cellulose (MCC), N-methyl-2-pyrrolidone (NMP, AR), and ethanol absolute (AR) were purchased from Sinopharm Chemical Reagent Co., Ltd. (Shanghai, China). Sulfuric acid (AR, 98%) was obtained from Nanjing Chemical Reagents Co. (Nanjing, China). The ultrapure water was prepared by Plus-E3-10th (EPED, Nanjing, China). The MLG, a bio-MLG material (Yan et al., 2018), was provided by the Department of Sustainable Bioproducts, Mississippi State University.

Sample Preparation

Ball-Milling MLG

For ball-milling, some grinding balls with a diameter of 3 mm and a certain amount of MLG (the weight ratio of ball to powder was 5:1) were placed in a 25-ml tank of a Tehnica Millmix 20 homogenizer (DOMEL, Železniki, Slovenia), and the grinding time (10, 30, and 60 min) and oscillation frequency (20 Hz) were selected before running the machine. After ball-milling, the particle size of ground MLG was measured by a BT-90 nanoparticle size distribution analyzer (Bettersize, Dandong, China).

CNC Suspensions Preparation

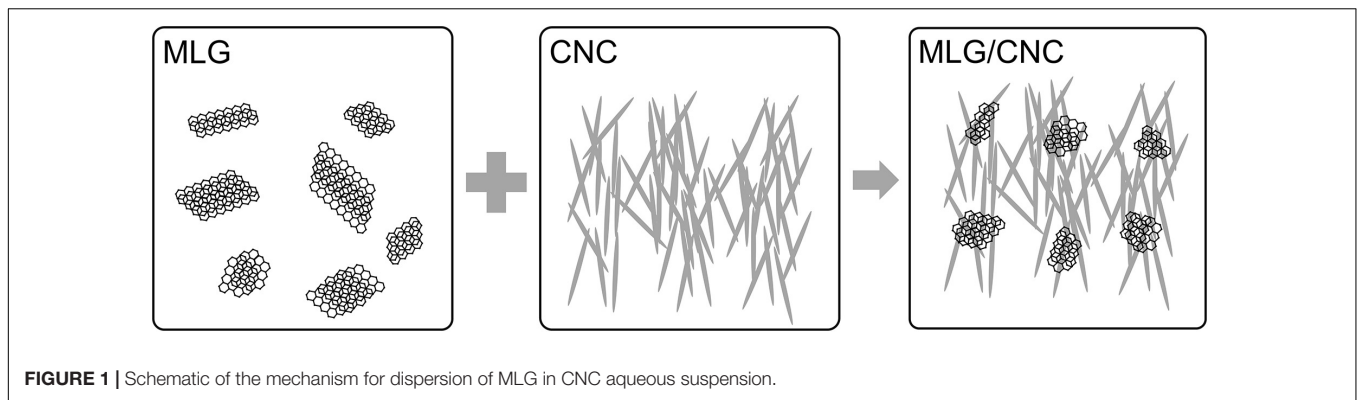
The CNC aqueous suspension was prepared through the sulfuric acid hydrolysis of MCC (Cranston and Gray, 2006). The procedure started with hydrolysis at 45°C for 60 min, followed by acid removal, dialysis, and ultrasonic treatment.

MLG/CNC and Control Group Preparation

The MLG/CNC and other control mixtures (mixture with NMP, ethanol, and ultrapure water) were prepared according to **Table 1**. The MLG/CNC mixing procedure started with adding ball-milled MLG (the amount added are 0.5 and 1.0 wt%) to CNC aqueous suspension (0.4, 0.6, and 0.8%), followed by performing the ultrasonic treatment for 10 min (Q700, QSonica, Newtown, CT, United States). The control groups also underwent magnetic stirring and ultrasonic treatment with the same power and time. The MLG/CNC and control groups were loaded into the sample bottles and kept for 135 days for sedimentation analysis.

Performance Testing

For particle size test, 0.01 g of ball-milled MLG was mixed with 20 ml of ultrapure water in a beaker, and the beaker was placed in a Q700 tip ultrasonicator for 2 min. After sonication, a total of 4 ml of suspension was loaded into a quartz cuvette for the test. This test used the automatic mode of nanoparticle size distribution analyzer. The zeta potential values of CNC aqueous suspension, MLG/CNC, MLG/NMP, MLG/ethanol, and MLG/ultrapure water were determined employing the Zetasizer Nano-ZS ZEN3600 (Malvern, Worcestershire, United Kingdom) provided with a 4-mW He-Ne (633 nm) laser. Except for 0.4,



0.6, and 0.8% CNC, all samples were diluted to 0.01 wt%, of which MLG/CNC samples 11–12 were diluted with the original dispersant. Samples 7–10 were diluted by ultrapure water due to their particularity (NMP will damage the inner wall of the sample cell, and the test results of alcohol do not meet the test quality requirement). The pH values of CNC aqueous suspension and MLG/CNC were around 3.0–3.5, and samples 7–12 were around 7.0. Using a syringe to transfer about 1 ml of the sample to the DTS1060 sample cell, after expelling the air bubbles, seal it with the stopper and perform the test. The sedimentation analysis of the MLG/CNC stored for 135 days was performed using the visual observation and microscopic characterization technique. The morphologies of CNC were observed by atomic force microscopy (Dimension Edge, Bruker, Germany) with a scan size of $1\ \mu\text{m} \times 1\ \mu\text{m}$. The transmission electron microscopy (TEM, JEM-1400, JEOL, Japan) was performed on the morphologies of MLG/CNC. As to TEM analysis, the diluted MLG/CNC was cast on copper grids for observation after drying. The absorbance analysis of the sample was performed using a U-3900 UV/vis/NIR spectrophotometer (Hitachi, Japan) at 660 nm. Use a “positioner” to get a certain height sample in the sample bottle, diluted at certain times to determine the absorbance. The sample was placed in the test cell, and the corresponding adjuvant was used as the reference. The Fourier transform infrared spectroscopy (FTIR)

of the dried sample was measured using a VERTEX 80V FTIR spectrometer (Bruker, Germany) with a wavenumber range of $4,000\text{--}400\ \text{cm}^{-1}$. The sample was dried in an oven and ground into powder and passed through a 200-mesh screen. Then, the powder was collected and mixed with potassium bromide (KBr) to make a transparent disk for testing. The dried MLG/CNC powder was put on a glass slide, and Raman spectra were carried out using DXR532 (Thermo Fisher Scientific, Asheville, NC, United States) with an excitation laser with $\lambda = 532\ \text{nm}$.

RESULTS AND DISCUSSION

Size Analysis of Ball-Milled MLG

Under the abovementioned conditions, the particle size distribution of ball-milled MLG at different treatment times is shown in **Figure 2**. The MLG size before ball-milling has reached the micron level, up to $2\ \mu\text{m}$ or more (measured by Adobe Photoshop CC 2015). After grinding for 10 min, the average particle size of MLG was 842 nm, the average particle size of MLG was 520 nm after grinding for 30 min, and the average particle was 790 nm after grinding for 60 min.

This result indicated that the 30-min treatment time has the smallest particle size. The reason may be insufficient grinding after 10 min of treatment. For 60 min of ball-milling, the ball mill machine has generated lots of heat, causing the separated MLG to agglomerate again.

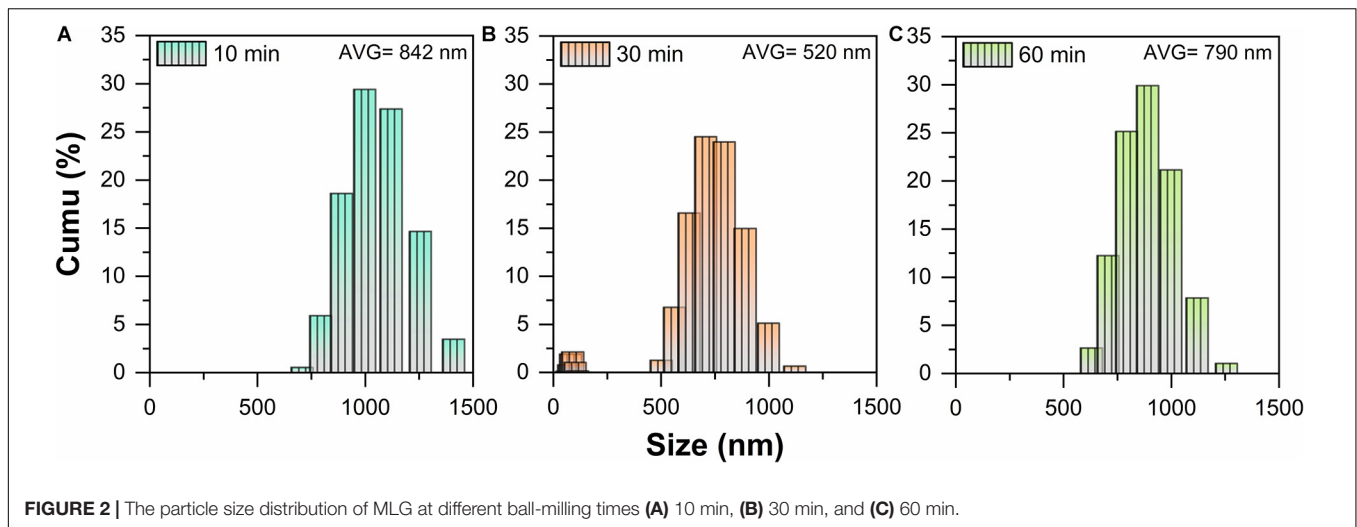
It can be known from **Figure 2B** that MLG has two size ranges. On the one hand, the reason was that MLG was wide and thin and not a sphere, and the nanoparticle size distribution analyzer detects its thickness and width, so there were two size ranges. On the other hand, the size of the MLG was not uniform, inducing the results concentrated in two size ranges. In view of this result, the MLG used later in this study was prepared with an oscillation frequency of 20 Hz and a ball-milling time of 30 min.

Zeta Potential Analysis

Zeta potential was usually used to evaluate the stability of the colloid (Zhong et al., 2012); a zeta potential value greater than 30 mV or less than $-30\ \text{mV}$ was considered solely stabilized (Cao et al., 2016). The zeta potential results of CNC, MLG/CNC, and control groups are shown in **Figure 3**. The zeta potential

TABLE 1 | The concentration of adjuvant or dispersant and the addition ratio of MLG in each sample.

Sample	Adjuvant or Dispersant (%)	MLG (wt%)
1	CNC	0.4
2		0.4
3		0.6
4		0.6
5		0.8
6		0.8
7	NMP	100
8		100
9	Ethanol	100
10		100
11	Ultrapure water	–
12		–



values of 0.4, 0.6, and 0.8% CNC aqueous suspension were -27.1 , -25.4 , and -24.4 mV, respectively. According to the results, the zeta potential of each group of samples after dispersion was around -30 mV, indicating that samples 1–11 can basically meet the requirements of stability. The surface of CNC was negatively charged due to the preparation process of sulfuric acid oxidation (Chatterjee et al., 2020). This result showed that as the concentration of CNC aqueous suspension increased, its zeta potential decreased; that is, the stability was worse. The reason was that with the concentration increased, the distance between colloidal particles was reduced, and the electrostatic double layer has been compressed, inducing the decrease in zeta potential (Hsiung et al., 2016). The zeta potential values of the MLG/CNC were higher than those of 0.4, 0.6, and 0.8% CNC aqueous suspensions. This was because MLG also showed a negative charge when dispersed in ultrapure water, which increased the negative charge of MLG/CNC. In general, MLG/CNC also showed a trend; that is, the higher concentration of the CNC aqueous suspension, the lower the zeta potential of MLG/CNC; the greater the amount of MLG added, the lower the zeta potential of MLG/CNC. As mentioned above, samples 7–12 were diluted with ultrapure water. When the dispersant was NMP and alcohol, the higher the amount of MLG, the higher the zeta potential, which was contrary to the trend of CNC aqueous suspension as the dispersant. Generally, the NMP has a similar surface energy to graphene, which could reduce the enthalpy and promote the stabilization of MLG/NMP suspension (Yang et al., 2020). Analysis of zeta results showed that CNC aqueous suspension was stabilized by the repulsion of negative charges on the particle surface, while MLG was also negatively charged. The two repel each other, making the MLG/CNC aqueous suspension stable without the sedimentation of MLG.

Sedimentation Analysis

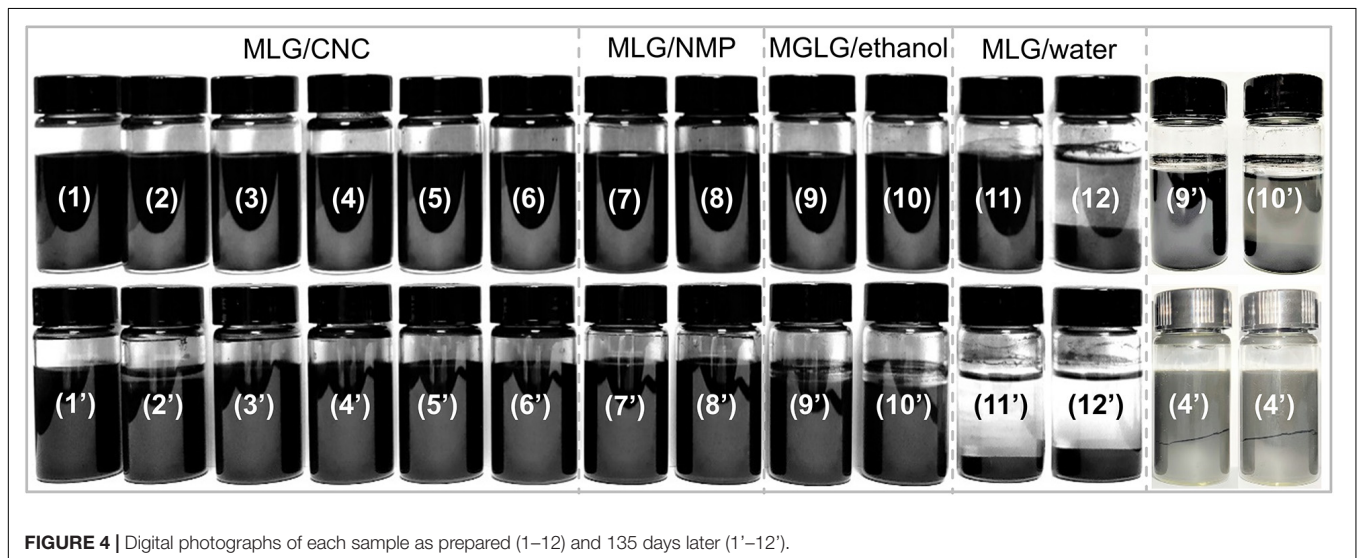
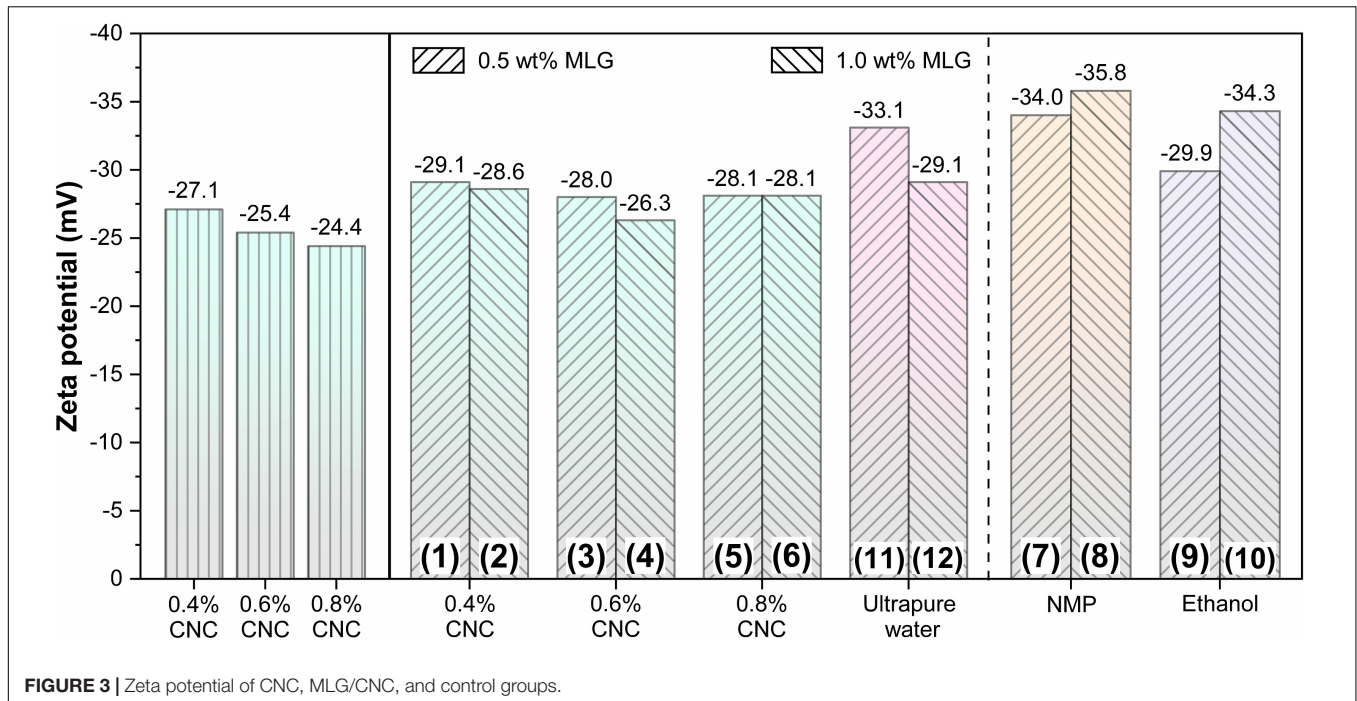
As shown in **Figure 4**, sample 12 (1.0 wt% MLG dispersed in ultrapure water) was the only sample that has sedimented at the beginning of its preparation, and according to the above

description, its zeta potential reached -29.1 mV. After 135 days of sedimentation experiment, most MLG/CNC (sample 1, 3–6) and all the MLG/NMP showed no visible sedimentation. MLG precipitation occurred in sample 2 (MLG/CNC), sample 10 (MLG/ethanol), and all the MLG/ultrapure water samples. Besides, sample 4 did not precipitate, but it was divided into two parts. This phenomenon was not found in other samples.

After 135 days, some of the alcohol in samples 9 and 10 (MLG/ethanol) evaporated, leaving a few circles of black MLG on the inner wall of the sample bottles. This result showed that CNC at an appropriate concentration can be used as an adjuvant to improve the dispersion ability of MLG in aqueous suspension.

AFM and TEM Analysis

The AFM image (**Figure 5A**) shows the morphology of the CNC with a typical rod-like structure, and **Figures 5F–I** show the length and diameter (measured by Adobe Photoshop CC 2015) distribution of CNC before and after dispersion. The size of CNC has not changed significantly before and after dispersion; the length was concentrated at 275 nm, and the largest proportion of diameter was 35 nm. The TEM images (**Figures 5B,C**) indicated that the size of non-ball-milled MLG was up to 2 μm or more. It can be known from **Figure 5J** that the size of the MLG dispersed in CNC aqueous suspension was concentrated in 50–150 nm, which was smaller than the particle size after ball-milling. This was because after dispersing the ball-milled MLG into the CNC aqueous suspension, sonicating it for 10 min will further reduce the size of the MLG. **Figure 5C** shows that relatively thin MLG has a wrinkled translucent structure. According to Zhu et al., the optical transmittance of single-layer graphene was almost 97% (Zhu et al., 2014), and the more layers, the lower the light transmittance. Wrinkles on the surface of graphene were not defects; they were a common phenomenon in two-dimensional membranes (Zhu et al., 2012). Wrinkles can be generated whether the graphene was peeled from three-dimensional highly oriented pyrolytic graphite to two-dimensional graphene or grown on the surface (Liu et al., 2011). **Figures 5D,E** show that countless CNCs

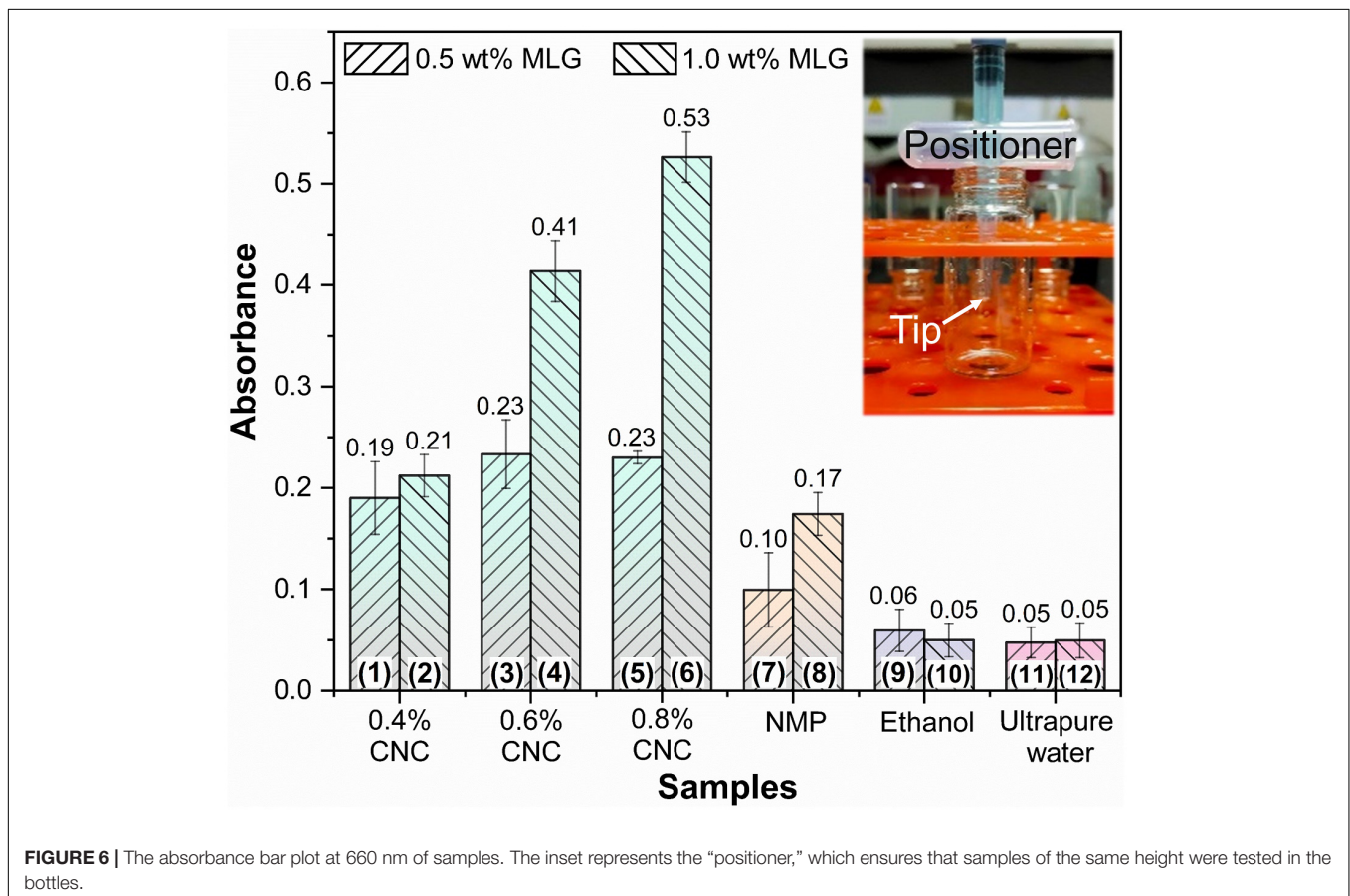
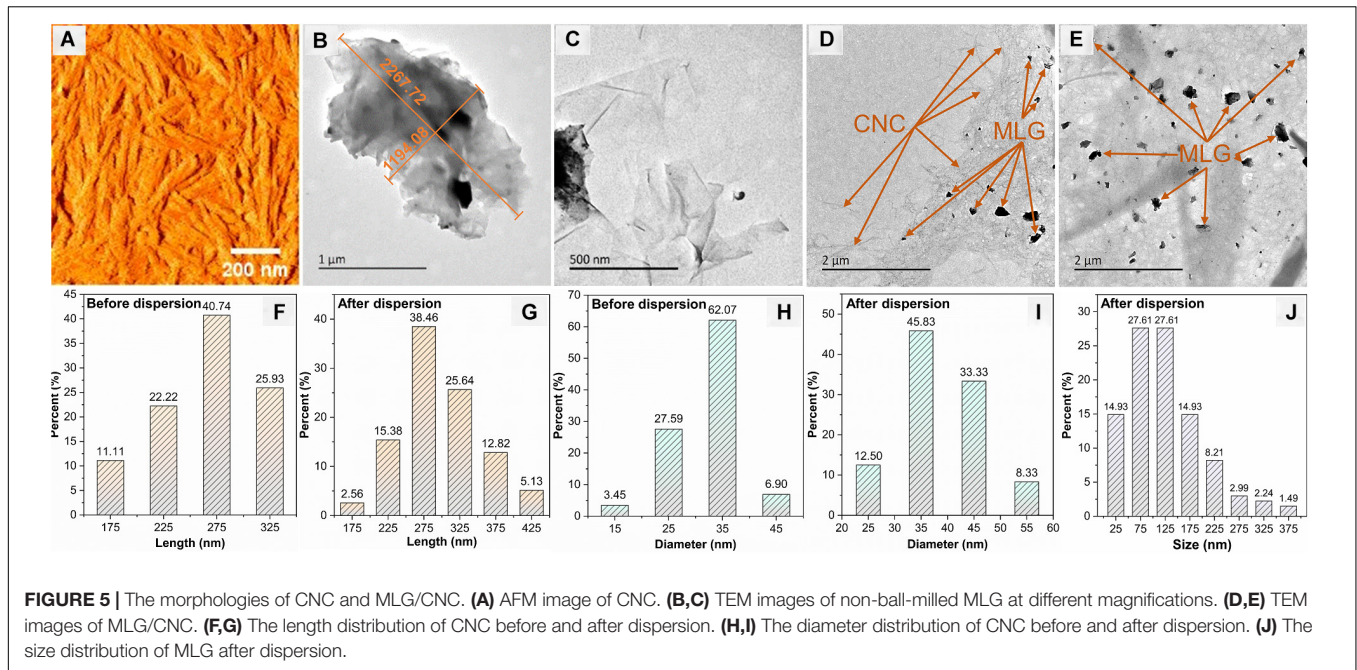


have formed a “3D net” with MLG attached. The size distribution of CNC and MLG before and after dispersion showed that neither CNC nor MLG was aggregated after dispersion, and CNC can be used as an adjuvant to disperse MLG in an aqueous suspension.

Absorbance Analysis

The absorbance at 660 nm is shown in **Figure 6**; the results of different adjuvants were significantly different. For the same adjuvant or dispersant (including the same concentration of CNC), except for MLG/ethanol, the absorbance of the sample containing 1.0 wt% MLG was higher than 0.5 wt%. Among them, the most significant difference was between sample 6 and sample 5. The absorbance of sample 6 was 2.3 times

than that of sample 5. The smallest difference was between sample 11 and sample 12, which were almost the same. For the samples of CNC as adjuvant, when the addition of MLG was 0.5 wt%, as the CNC concentration increased, the absorbance first increased and then remained unchanged. When the amount of MLG was 1.0 wt%, the absorbance increased with an increase of CNC concentration. In particular, when ethanol was used as dispersant, the absorbance of sample 10 (with 1.0 wt% MLG) was lower than that of sample 9 (with 0.5 wt% MLG). According to Lambert–Beer law, the higher the absorbance, the higher the concentration of MLG dispersion (Zhang et al., 2013), and the better the dispersion effect of the dispersant on MLG.



The absorbance of samples 9–12 was very close, but in **Figure 4**, it can be observed that the MLG in samples 11 and 12 has been significantly precipitated, and the upper

liquid has become transparent. The color of samples 9 and 10 was black; after adjusting the brightness of the digital photo, precipitation can only be observed in sample 10. This

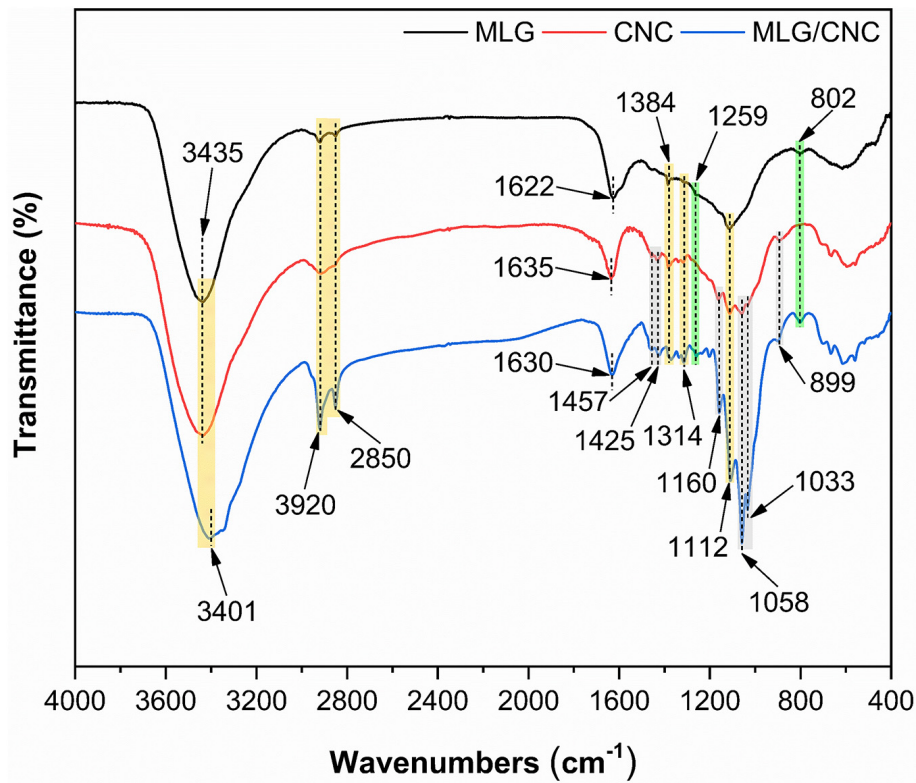


FIGURE 7 | The FTIR spectroscopy of dried MLG, CNC, and MLG/CNC.

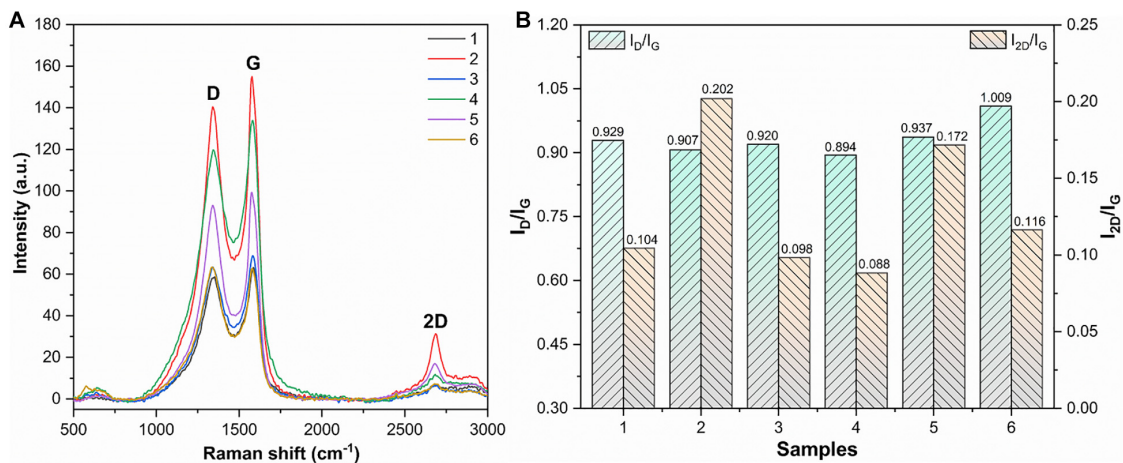


FIGURE 8 | Raman spectra, I_D/I_G , and I_{2D}/I_G of dried MLG/CNC. (A) The Raman spectra of dried MLG/CNC. (B) The I_D/I_G and I_{2D}/I_G bar plot of Raman spectra of dried MLG/CNC.

showed that the results obtained by visual observation were not accurate in this study.

FTIR Analysis

The FTIR spectra (Figure 7) of dried MLG and CNC were further compared with dried MLG/CNC. The peaks at 3,435 and 3,401 cm^{-1} were assigned to O–H stretching vibration.

The peaks at 3,920, 2,850, and 1,384 cm^{-1} were caused by the symmetrical stretching vibration, asymmetric stretching vibration, and bending vibration of C–H (Jin et al., 2016), respectively. The peaks of 1,425, 1,160, 1,112, 1,058, and 899 cm^{-1} were observed, which were associated with the typical feature groups of cellulose (Liu et al., 2017). The green area peaks showed obvious appearance on the spectra of MLG and

MLG/CNC but were not obvious or did not appear on the CNC spectrum. The peaks at 1,259 and 802 cm^{-1} indicated the C–H deformation (Leng et al., 2017). Correspondingly, the peaks in the gray area indicate that they appear on the spectra of CNC and MLG/CNC, but were not obvious on the MLG spectrum. The spectrum peaks at 1,457 and 1,033 cm^{-1} represented the $-\text{CH}_2$ symmetric bending vibration and C–O stretching vibration (Wu et al., 2019a), respectively. The characteristic peak at 1,622 cm^{-1} of MLG corresponded to C–C (aromatic ring) stretching vibration (Xiong et al., 2016). Other peaks at 1,635 cm^{-1} of CNC and 1,630 cm^{-1} of MLG/CNC belonged to the moisture that remained in the samples.

This result showed that the FTIR spectrum of MLG/CNC has special peaks in both the MLG and CNC spectrum, which showed that the two were closely integrated. This result also verified the conclusion of TEM analysis. In addition, the vibration peaks of C–H and O–H that appeared in MLG indicated that the MLG used in this study was not purified.

Raman Spectroscopy

Raman spectra were used to evaluate the structure and defects of MLG. As shown in **Figure 8A**, the MLG/CNC has the typical Raman characteristic peaks. One was the D peak located near 1,350 cm^{-1} , and the other was the G peak located near 1,580 cm^{-1} and the 2D peak around 2,670 cm^{-1} (Dresselhaus et al., 2010). In general, the D-band intensity represents the degree of disordered carbon in the composite and the intensity of the G-band represents the number of sp^2 hybridizations. The larger intensity ratio I_D/I_G means larger disorder and defect. The 2D band originated from a two-phonon double-resonance process, which was closely associated with the band structure of graphene layers; in single-layer graphene, I_{2D} is nearly twice as strong as I_G (Hu et al., 2019). If the number of graphene layers does not exceed five layers, the number of graphene layers can be determined directly based on the ratio of I_{2D}/I_G (Liu et al., 2013). The I_D/I_G and I_{2D}/I_G are shown in **Figure 8B**.

It was clearly known that the smaller the ratio of I_{2D}/I_G , that is, the fewer layers. **Figure 8B** shows that sample 4 (1.0 wt% MLG–0.6% CNC) has the smallest I_D/I_G value of 0.894; that is, it has the lowest defects and disorder. Sample 2 has the largest I_{2D}/I_G value (0.202), which was the minimum number of layers in the MLG/CNC. **Figure 8B** also shows that sample 4 has the smallest values of I_{2D}/I_G (0.088) and I_D/I_G (0.894) at the same time; that is, it has the lowest defects and disorder, but also has the largest number of layers, and graphene aggregation may have occurred. The highest I_{2D}/I_G value belonged to sample 2 (1.0 wt% MLG–0.4% CNC), and its I_D/I_G value was the second smallest (0.907), which can be used as the most preferred concentration and addition ratio among the MLG/CNC samples.

CONCLUSION

We demonstrated a simple, eco-friendly approach to improve the dispersion ability of MLG in aqueous suspension. After ball-milling, the MLG was dispersed into CNC aqueous

suspensions. In addition, NMP, ethanol, and ultrapure water were used as control groups. By observing the sedimentation experiment results of MLG/CNC and other control groups after storage of 135 days, as well as the characterization of zeta potential, AFM, TEM, absorbance, FTIR spectroscopy, and Raman spectroscopy, the effect of CNC as adjuvant to improve the MLG dispersion ability in aqueous suspension was studied. The zeta potential and FTIR results show that the stability of MLG/CNC meets the requirement and the combination of CNC and ball-milled MLG is stable in aqueous suspension. Results from AFM and TEM show that the size of CNC did not change after dispersion, but the size of MLG became smaller. The highest concentration of the samples is obtained by dispersing 1.0 wt% MLG into 0.8% CNC aqueous suspension. When the CNC concentration is 0.4% and the addition amount of MLG is 1.0 wt%, the MLG has the least defects and the thinnest thickness, which can be used as the best experimental parameters. Overall, CNC plays an obvious role in helping MLG disperse in aqueous suspension, while MLG does not agglomerate, which can provide a solution to the problem of MLG dispersion in aqueous suspension.

DATA AVAILABILITY STATEMENT

The original contributions presented in the study are included in the article/supplementary material, further inquiries can be directed to the corresponding author/s.

AUTHOR CONTRIBUTIONS

HZ, YW, and JZ: conceptualization. HZ and YW: writing—original draft preparation. HD, YB, and FY: investigation. HZ, HJ, and XX: methodology. HJ, XX, and YW: funding acquisition. All authors have read and agreed to the published version of the manuscript.

FUNDING

This study was supported by a foundation from the National Natural Science Foundation of China (32071687 and 32001382), the Project of Science and Technology Plan of Beijing Municipal Education Commission (KM202010012001), and the Special Scientific Research Fund of Construction of High-level teachers Project of Beijing Institute of Fashion Technology (BIFTQG201805). This work was also supported by Nan Taihu Lake Elite Plan project [(2018) No.2, Huzhou, Zhejiang province] and Eagle Plan project [(2020), Huzhou, Zhejiang province].

ACKNOWLEDGMENTS

We gratefully acknowledge the project funds and individuals who have contributed to this research, as well as the Modern Analysis Center of Nanjing Forestry University.

REFERENCES

- Atif, R., and Inam, F. (2016). Reasons and remedies for the agglomeration of multilayered graphene and carbon nanotubes in polymers. *Beilstein J. Nanotechnol.* 7, 1174–1196. doi: 10.3762/bjnano.7.109
- Cao, J., Zhang, X., Wu, X., Wang, S., and Lu, C. (2016). Cellulose nanocrystals mediated assembly of graphene in rubber composites for chemical sensing applications. *Carbohydr. Polym.* 140, 88–95. doi: 10.1016/j.carbpol.2015.12.042
- Chatterjee, S., Ke, W. T., and Liao, Y. C. (2020). Elastic nanocellulose/graphene aerogel with excellent shape retention and oil absorption selectivity. *J. Taiwan Inst. Chem. Eng.* 111, 261–269. doi: 10.1016/j.jtice.2020.04.020
- Chiu, P. L., Mastrogianni, D. D. T., Wei, D., Louis, C., Jeong, M., Yu, G., et al. (2012). Microwave-and nitronium ion-enabled rapid and direct production of highly conductive low-oxygen graphene. *J. Am. Chem. Soc.* 134, 5850–5856. doi: 10.1021/ja210725p
- Cranston, E. D., and Gray, D. G. (2006). Morphological and optical characterization of polyelectrolyte multilayers incorporating nanocrystalline cellulose. *Biomacromolecules* 7, 2522–2530. doi: 10.1021/bm0602886
- Das, S., Irin, F., Ahmed, H. S. T., Cortinas, A. B., Wajid, A. S., Parviz, D., et al. (2012). Non-covalent functionalization of pristine few-layer graphene using triphenylene derivatives for conductive poly (vinyl alcohol) composites. *Polymer* 53, 2485–2494. doi: 10.1016/j.polymer.2012.03.012
- Dong, L., Chen, Z., Zhao, X., Ma, J., Lin, S., Li, M., et al. (2018). A non-dispersion strategy for large-scale production of ultra-high concentration graphene slurries in water. *Nat. Commun.* 9:76. doi: 10.1038/s41467-017-02580-3
- Dresselhaus, M. S., Jorio, A., Hofmann, M., Dresselhaus, G., and Saito, R. (2010). Perspectives on carbon nanotubes and graphene Raman spectroscopy. *Nano Lett.* 10, 751–758. doi: 10.1021/nl904286r
- Du, W., Lu, J., Sun, P., Zhu, Y., and Jiang, X. (2013). Organic salt-assisted liquid-phase exfoliation of graphite to produce high-quality graphene. *Chem. Phys. Lett.* 568, 198–201. doi: 10.1016/j.cplett.2013.03.060
- Gao, K., Shao, Z., Wu, X., Wang, X., Li, J., Zhang, Y., et al. (2013). Cellulose nanofibers/reduced graphene oxide flexible transparent conductive paper. *Carbohydr. Polym.* 97, 243–251. doi: 10.1016/j.carbpol.2013.03.067
- Geng, J., Kong, B. S., Yang, S. B., and Jung, H. T. (2010). Preparation of graphene relying on porphyrin exfoliation of graphite. *Chem. Commun.* 46, 5091–5093. doi: 10.1039/c001609h
- Gray, N., Hamzeh, Y., Kaboorani, A., and Abdulkhali, A. (2018). Influence of cellulose nanocrystal on strength and properties of low density polyethylene and thermoplastic starch composites. *Ind. Crops Prod.* 115, 298–305. doi: 10.1016/j.indcrop.2018.02.017
- Guardia, L., Fernández-Merino, M. J., Paredes, J. I., Solís-Fernández, P., Villar-Rodil, S., Martínez-Alonso, A., et al. (2011). High-throughput production of pristine graphene in an aqueous dispersion assisted by non-ionic surfactants. *Carbon N. Y.* 49, 1653–1662. doi: 10.1016/j.carbon.2010.12.049
- Guo, W., and Chen, G. (2014). Fabrication of graphene/epoxy resin composites with much enhanced thermal conductivity via ball milling technique. *J. Appl. Polym. Sci.* 131:40565. doi: 10.1002/app.40565
- Hsiung, C. E., Lien, H. L., Galliano, A. E., Yeh, C. S., and Shih, Y. h (2016). Effects of water chemistry on the destabilization and sedimentation of commercial TiO₂ nanoparticles: role of double-layer compression and charge neutralization. *Chemosphere* 151, 145–151. doi: 10.1016/j.chemosphere.2016.02.046
- Hu, K. M., Xue, Z. Y., Liu, Y. Q., Long, H., Peng, B., Yan, H., et al. (2019). Tension-Induced Raman enhancement of graphene membranes in the stretched state. *Small* 15:1804337. doi: 10.1002/small.201804337
- Jiang, F., and Hsieh, Y. L. (2013). Chemically and mechanically isolated nanocellulose and their self-assembled structures. *Carbohydr. Polym.* 95, 32–40. doi: 10.1016/j.carbpol.2013.02.022
- Jin, E., Yang, F., Zhu, Y., Zhu, W., and Song, J. (2016). Surface Characterizations of Mercerized Cellulose Nanocrystals by XRD, FT-IR and XPS. *J. Cell. Sci. Technol.* 24, 1–6. doi: 10.16561/j.cnki.xws.2016.03.12
- Knieke, C., Berger, A., Voigt, M., Taylor, R. N. K., Röhr, J., and Peukert, W. (2010). Scalable production of graphene sheets by mechanical delamination. *Carbon N. Y.* 48, 3196–3204. doi: 10.1016/j.carbon.2010.05.003
- Leng, W., Barnes, H. M., Zhang, J., and Cai, Z. (2017). Effect of processing parameters on the synthesis of lignin-based graphene-encapsulated copper nanoparticles. *Wood Fiber Sci.* 49, 22–32.
- León, V., Rodríguez, A. M., Prieto, P., Prato, M., and Vázquez, E. (2014). Exfoliation of graphite with triazine derivatives under ball-milling conditions: preparation of few-layer graphene via selective noncovalent interactions. *ACS Nano* 8, 563–571. doi: 10.1021/nn405148t
- Li, Z., Chu, J., Yang, C., Hao, S., Bissett, M. A., Kinloch, I. A., et al. (2018). Effect of functional groups on the agglomeration of graphene in nanocomposites. *Compos. Sci. Technol.* 163, 116–122. doi: 10.1016/j.compscitech.2018.05.016
- Liu, C., Ma, Y., Li, W., and Dai, L. (2013). The evolution of Raman spectrum of graphene with the thickness of SiO₂ capping layer on Si substrate. *Appl. Phys. Lett.* 103:213103. doi: 10.1063/1.4832063
- Liu, N., Pan, Z., Fu, L., Zhang, C., Dai, B., and Liu, Z. (2011). The origin of wrinkles on transferred graphene. *Nano Res.* 4:996. doi: 10.1007/s12274-011-0156-3
- Liu, Y., Guo, B., Xia, Q., Meng, J., Chen, W., Liu, S., et al. (2017). Efficient cleavage of strong hydrogen bonds in cotton by deep eutectic solvents and facile fabrication of cellulose nanocrystals in high yields. *ACS Sustain. Chem. Eng.* 5, 7623–7631. doi: 10.1021/acssuschemeng.7b00954
- Lotya, M., King, P. J., Khan, U., De, S., and Coleman, J. N. (2010). High-Concentration, surfactant-stabilized graphene dispersions. *ACS Nano* 4, 3155–3162. doi: 10.1021/nn1005304
- Notley, S. M. (2012). Highly concentrated aqueous suspensions of graphene through ultrasonic exfoliation with continuous surfactant addition. *Langmuir* 28, 14110–14113. doi: 10.1021/la302750e
- Nuvoli, D., Valentini, L., Alzari, V., Scognamiglio, S., Bon, S. B., Piccinini, M., et al. (2011). High concentration few-layer graphene sheets obtained by liquid phase exfoliation of graphite in ionic liquid. *J. Mater. Chem.* 21, 3428–3431. doi: 10.1039/c0jm02461a
- Ouyang, W., Sun, J., Memon, J., Wang, C., Geng, J., and Huang, Y. (2013). Scalable preparation of three-dimensional porous structures of reduced graphene oxide/cellulose composites and their application in supercapacitors. *Carbon N. Y.* 62, 501–509. doi: 10.1016/j.carbon.2013.06.049
- Paton, K. R., Varrla, E., Backes, C., Smith, R. J., Khan, U., O'Neill, A., et al. (2014). Scalable production of large quantities of defect-free few-layer graphene by shear exfoliation in liquids. *Nat. Mater.* 13, 624–630. doi: 10.1038/NMAT3944
- Shahil, K. M. F., and Balandin, A. A. (2012). Thermal properties of graphene and multilayer graphene: applications in thermal interface materials. *Solid State Commun.* 152, 1331–1340. doi: 10.1016/j.ssc.2012.04.034
- Wajid, A. S., Das, S., Irin, F., Ahmed, H. S. T., Shelburne, J. L., Parviz, D., et al. (2012). Polymer-stabilized graphene dispersions at high concentrations in organic solvents for composite production. *Carbon N. Y.* 50, 526–534. doi: 10.1016/j.carbon.2011.09.008
- Wang, X., Fulvio, P. F., Baker, G. A., Veith, G. M., Unocic, R. R., Mahurin, S. M., et al. (2010). Direct exfoliation of natural graphite into micrometre size few layers graphene sheets using ionic liquids. *Chem. Commun.* 46, 4487–4489. doi: 10.1039/c0cc00799d
- Wu, Y., Tang, Q., Yang, F., Xu, L., Wang, X., and Zhang, J. (2019a). Mechanical and thermal properties of rice straw cellulose nanofibrils-enhanced polyvinyl alcohol films using freezing- and-thawing cycle method. *Cellulose* 26, 3193–3204. doi: 10.1007/s10570-019-02310-6
- Wu, Y., Wu, X., Yang, F., Xu, L., and Sun, M. (2019b). Study on the preparation and adsorption property of polyvinyl alcohol/cellulose nanocrystal/graphene composite aerogels (PCGAS). *J. Renew. Mater.* 7, 1181–1195. doi: 10.32604/jrm.2019.07493
- Wu, Y., Yang, L., Zhou, J., Yang, F., Huang, Q., and Cai, Y. (2020a). Softened wood treated by deep eutectic solvents. *ACS Omega* 5, 22163–22170. doi: 10.1021/acsomega.0c02223
- Wu, Y., Zhang, H., Yang, L., Wang, S., and Meng, Y. (2020b). Understanding the effect of extractives on the mechanical properties of the waterborne coating on wood surface by nanoindentation 3D mapping. *J. Mater. Sci.* 56, 1401–1412. doi: 10.1007/s10853-020-05347-2
- Wu, Y., Zhang, H., Zhang, Y., Wang, S., Wang, X., Xu, D., et al. (2019c). Effects of thermal treatment on the mechanical properties of larch (*Larix gmelinii*) and Red Oak (*Quercus rubra*) wood cell walls via nanoindentation. *BioResources* 14, 8048–8057. doi: 10.15376/biores.14.4.8048-8057

- Xiong, R., Hu, K., Grant, A. M., Ma, R., Xu, W., Lu, C., et al. (2016). Ultrarobust transparent cellulose nanocrystal-graphene membranes with high electrical conductivity. *Adv. Mater.* 28, 1501–1509. doi: 10.1002/adma.201504438
- Yan, Q., Zhang, X., Li, J., Hassan, E. B., Wang, C., Zhang, J., et al. (2018). Catalytic conversion of Kraft lignin to bio-multilayer graphene materials under different atmospheres. *J. Mater. Sci.* 53, 8020–8029. doi: 10.1007/s10853-018-2172-0
- Yang, B., Zhang, S., Lv, J., Li, S., Shi, Y., Hu, D., et al. (2020). Large-scale and green production of multi-layer graphene in deep eutectic solvents. *J. Mater. Sci.* 56, 4615–4623. doi: 10.1007/s10853-020-05209-x
- Zhang, M., Parajuli, R. R., Mastrogiovanni, D., Dai, B., Lo, P., Cheung, W., et al. (2010). Production of graphene sheets by direct dispersion with aromatic healing agents. *Small* 6, 1100–1107. doi: 10.1002/smll.200901978
- Zhang, X., Liu, X., Zheng, W., and Zhu, J. (2012). Regenerated cellulose/graphene nanocomposite films prepared in DMAC/LiCl solution. *Carbohydr. Polym.* 88, 26–30. doi: 10.1016/j.carbpol.2011.11.054
- Zhang, X. F., Liu, S., and Shao, X. (2013). Fluorescence of chemically derived graphene: effect of self-rolling up and aggregation. *J. Lumin.* 136, 32–37. doi: 10.1016/j.jlumin.2012.11.001
- Zhao, W., Fang, M., Wu, F., Wu, H., Wang, L., and Chen, G. (2010). Preparation of graphene by exfoliation of graphite using wet ball milling. *J. Mater. Chem.* 20, 5817–5819. doi: 10.1039/c0jm01354d
- Zhao, Y., Zhang, Y., Lindström, M. E., and Li, J. (2015). Tunicate cellulose nanocrystals: preparation, neat films and nanocomposite films with glucomannans. *Carbohydr. Polym.* 117, 286–296. doi: 10.1016/j.carbpol.2014.09.020
- Zhao, Z., Huang, C., Wu, D., Chen, Z., Zhu, N., Gui, C., et al. (2020). Utilization of enzymatic hydrolysate from corn stover as a precursor to synthesize an eco-friendly plywood adhesive. *Ind. Crop. Prod.* 152:112501. doi: 10.1016/j.indcrop.2020.112501
- Zhong, L., Fu, S., Peng, X., Zhan, H., and Sun, R. (2012). Colloidal stability of negatively charged cellulose nanocrystalline in aqueous systems. *Carbohydr. Polym.* 90, 644–649. doi: 10.1016/j.carbpol.2012.05.091
- Zhu, S. E., Yuan, S., and Janssen, G. C. A. M. (2014). Optical transmittance of multilayer graphene. *EPL (Europhysics Lett.)*. 108:17007. doi: 10.1209/0295-5075/108/17007
- Zhu, W., Low, T., Perebeinos, V., Bol, A. A., Zhu, Y., Yan, H., et al. (2012). Structure and electronic transport in graphene wrinkles. *Nano Lett.* 12, 3431–3436. doi: 10.1021/nl300563h

Conflict of Interest: HJ and XX were employed by the company Dehua Tubao New Decoration Material Co., Ltd., Huzhou, China.

The remaining authors declare that the research was conducted in the absence of any commercial or financial relationships that could be construed as a potential conflict of interest.

Copyright © 2021 Zhang, Wu, Yang, Dong, Bian, Jia, Xie and Zhang. This is an open-access article distributed under the terms of the Creative Commons Attribution License (CC BY). The use, distribution or reproduction in other forums is permitted, provided the original author(s) and the copyright owner(s) are credited and that the original publication in this journal is cited, in accordance with accepted academic practice. No use, distribution or reproduction is permitted which does not comply with these terms.



Guanidino-Acetic Acid: A Scarce Substance in Biomass That Can Regulate Postmortem Meat Glycolysis of Broilers Subjected to Pre-slaughter Transportation

Bolin Zhang^{1*}, Ning Liu¹, Zhen He¹, Peiyong Song¹, Meilin Hao¹, Yuxiao Xie¹, Jiahui Li¹, Rujie Liu¹ and Zewei Sun^{2*}

¹ Department of Biology and Agriculture, Characteristic Laboratory of Animal Resources Conservation and Utilization of Chishui River Basin, Zunyi Normal College, Zunyi, China, ² College of Animal Science and Technology, Jilin Agricultural University, Changchun, China

OPEN ACCESS

Edited by:

Caoxing Huang,
Nanjing Forestry University, China

Reviewed by:

Minmeng Zhao,
Yangzhou University, China
Wenhui Geng,
North Carolina State University,
United States

*Correspondence:

Bolin Zhang
zhangbolin@zync.edu.cn
Zewei Sun
sunzewei@jau.edu.cn

Specialty section:

This article was submitted to
Industrial Biotechnology,
a section of the journal
Frontiers in Bioengineering and
Biotechnology

Received: 19 November 2020

Accepted: 23 December 2020

Published: 10 February 2021

Citation:

Zhang B, Liu N, He Z, Song P,
Hao M, Xie Y, Li J, Liu R and Sun Z
(2021) Guanidino-Acetic Acid:
A Scarce Substance in Biomass That
Can Regulate Postmortem Meat
Glycolysis of Broilers Subjected
to Pre-slaughter Transportation.
Front. Bioeng. Biotechnol. 8:631194.
doi: 10.3389/fbioe.2020.631194

The different substances in biomass can regulate the metabolism and reproduction of broilers. Guanidino-acetic acid (GAA) is a natural feed additive that showed a potential application in dietary for broilers, while its amount is scarce in biomass. The objective of the present study was to investigate the effects of dietary supplemented with GAA on muscle glycolysis of broilers subjected to pre-slaughter transportation. A total of 160 Qiandongnan Xiaoxiang chickens were randomly assigned into three treatments, including a basal control diet without GAA supplementation (80 birds) or supplemented with 600 mg/kg (40 birds) or 1,200 mg/kg (40 birds) GAA for 14 days. At the end of the experiment, the control group was equally divided into two groups, thus resulting in four groups. All birds in the four groups aforementioned were separately treated according to the following protocols: (1) no transport of birds of the control group fed with the basal diet; (2) a 3-h transport of birds of the control group fed with the basal diet; (3) a 3-h transport of birds fed with diets supplemented with 600 mg/kg GAA; and (4) a 3-h transport of birds fed with diets supplemented with 1,200 mg/kg GAA. The results demonstrated that 3-h pre-slaughter transport stress increased corticosterone contents and lowered glucose contents in plasma ($P < 0.05$), decreased pH_{24h} ($P < 0.05$), and resulted in inferior meat quality evidenced by elevating the drip loss, cooking loss, and L* value ($P < 0.05$). Meanwhile, 3-h pre-slaughter transport stress decreased the contents of Cr and ATP in muscle ($P < 0.05$) and elevated the ratio of AMP:ATP and the glycolytic potential of muscle ($P < 0.05$). Moreover, 3-h pre-slaughter transport resulted in a significant elevation of mRNA expressions of LKB1 and AMPK α 2 ($P < 0.05$), as well as the increase in protein abundances of LKB1 phosphorylation and AMPK α phosphorylation ($P < 0.05$). However, 1,200 mg/kg GAA supplementation alleviated negative parameters in plasma, improved meat quality, and ameliorated postmortem glycolysis and energy metabolism through regulating the creatine-phosphocreatine

cycle and key factors of AMPK signaling. In conclusion, dietary supplementation with 1,200 mg/kg GAA contributed to improving meat quality via ameliorating muscle energy expenditure and delaying anaerobic glycolysis of broilers subjected to the 3-h pre-slaughter transport.

Keywords: guanidino-acetic acid, transport stress, postmortem glycolysis, AMPK signaling, broiler

INTRODUCTION

Pale, soft, and exudative (PSE)-like meat, characterized by lighter appearance, softer texture, lower water holding capacity, excessive yield losses, and formation of soft gels, has been recognized for decades and causes huge economic losses annually for modern poultry industry due to its inferior quality (Desai et al., 2016; Wang et al., 2017). In previous studies, it has been suggested that a 3-h pre-slaughter transport resulted in a significant decrease of glucose concentration in plasma and a sharp increase in plasma corticosterone level (Zhang et al., 2014, 2017), which are the two most sensitive indicators of transport stress. Moreover, pre-slaughter transportation accelerated energy consumption in muscle of broilers and resulted in a stress-induced increase in glycolysis, further inducing the accumulation of lactic acid in muscle (Hambrecht et al., 2005; Zhang et al., 2009). It has been well established that fast and excessive glycolysis, a rapid accumulation of lactic acid, and high temperature in muscle of early postmortem are the causes of PSE-like syndrome (Li et al., 2016). Therefore, pre-slaughter transport was considered to be one of the most important factors contributing to an increase in incidences of PSE-like chicken meat (Huang et al., 2018). Moreover, Xing et al. (2016) demonstrated that pre-slaughter transport induced a lower energy status in the early postmortem period, followed by an elevation of the concentration of lactic acid and an inferior meat quality. As a result, pre-slaughter transportation is one of the most important pre-harvest variables related to meat quality and should be regarded as a critical control point (Speer et al., 2001; Schwartzkopf-Genswein et al., 2012). Therefore, it is necessary to take a nutritional strategy to improve energy storage and alleviate the adverse effects of pre-slaughter transportation on meat quality of broilers.

Creatine (Cr) is heavily involved in energy metabolism through the Cr and phosphocreatine system, an important cellular energy source for rapid regeneration of ATP to meet the increased energy demands of intense activities of tissues, particularly muscle cells (Michiels et al., 2012; Zhang et al., 2017). It has been demonstrated that Cr, a natural regulator of energy homeostasis, could buffer energy concentration in tissues with significant and fluctuating energy demands, especially in muscles and brains (Ostojic et al., 2013). Guanidino-acetic acid (GAA) is the only immediate precursor of Cr in the body and is a naturally occurring compound in vertebrate animals (Dilger et al., 2013). Importantly, GAA is more chemically stable and more effective than Cr at enhancing tissue Cr storage (McBrearty et al., 2015). Accordingly, GAA was considered to be more suitable than Cr as a new natural feed additive. It has been demonstrated that dietary supplemented with GAA increased the contents of Cr and phosphorus creatine (PCr) in muscle

and improved the state of energy metabolism (Degroot, 2015). A previous study demonstrated that the increased concentrations of Cr and PCr and the higher ratio of PCr: Cr were observed by GAA supplemented in the diet (Liu et al., 2015). In addition to being involved in the regulation of energy metabolism, GAA also played an important role in improving meat quality. It has been reported that GAA supplementation increased postmortem muscle pH, lowered drip loss and cooking loss, and significantly reduced the shear force of meat (Wang et al., 2012). This may be due to the fact that dietary GAA supplementation increased available energy reserve such as PCr and ATP, which contributes to delaying the energy release of glycolysis and the accumulation of lactic acid, and consequently maintained a pH value postmortem. Moreover, Liu et al. (2015) suggested that GAA supplementation significantly decreased the activity of hexokinase, the rate-limiting enzyme in glycolysis, which means that GAA regulated the process of muscle energy metabolism through postmortem muscle glycolysis. However, the regulation mechanisms of GAA on postmortem glycolysis are still unknown.

Adenosine 5'-monophosphate (AMP)-activated protein kinase (AMPK), the downstream component of the protein kinase signal cascade pathway, is a key factor in sensing intracellular energy status and acts as a crucial component in regulating energy balance at both the cellular and whole body levels (Hardie, 2011). AMPK is an important energy sensor in the body, which is called the "energy regulator" of eukaryotic cells. AMPK was activated in response to stresses such as the exhaustion of ATP and the increase of the proportion of ADP/ATP, consequently accelerating postmortem glycolysis (Graeme and Hardie, 2014). Besides, postmortem glycolysis was inhibited in AMPK knockout mice, suggesting that AMPK could be a target to control postmortem glycolysis (Shen et al., 2008). Thus, we hypothesized that GAA regulated the postmortem glycolysis through the AMPK signaling pathway. Therefore, the objective of our study was to evaluate the effects of GAA supplementation on meat quality and intracellular energy metabolism of muscle, further determining the activities of key enzymes involved in glycolysis and gene or protein expressions of important components in the AMPK signaling pathway of broilers subjected to pre-slaughter transport.

MATERIALS AND METHODS

Animal Care, Diet, and Management

All the procedures including animal care and experiment treatments were in accordance with guidelines approved by the Institutional Animal Care and Use Committee of Zunyi Normal College. The basal diet was formulated to meet the nutrient requirements of Nutrient Requirements of Chinese Meat-Type

Yellow Feathered Chickens. The composition and nutritional level of the diet are as shown in **Table 1**.

One hundred and sixty Qiandongnan Xiaoxiang chickens (purchased from Guizhou Rongjiang Shannong Development Co., Ltd., China) 22 weeks old were randomly assigned into three treatments, including a basal control diet without GAA supplementation (80 birds) or supplemented with 600 mg/kg (40 birds) or 1,200 mg/kg (40 birds) GAA for 14 days. The source of GAA additive (>99% purity) was from Tianjin Tiancheng Pharmaceutical Co., Ltd. (Tianjin, China). Each treatment was consisted of 20 replicates and two broilers per cage, but the control group had 40 replicates and two broilers per cage. All birds were housed in an environmentally controlled facility and were *ad libitum* access to the feed in mash form and fresh water. At the end of the experiment, the body weight of the bird as the unit of pen was weighted after an 8-h feed deprivation. Average daily weight gain (ADG) and feed intake (ADFI) were calculated.

Transportation and Sample Collection

Before transportation treatment, all birds were tagged and fasted overnight without water withdrawal. The control group was averagely divided into two groups, thus resulting in four groups consisting of two control groups and two GAA supplementation groups. All birds in the four groups mentioned above were transported from the rearing house to the slaughterhouse according to the following protocols: (1) no transport of birds of the control group fed with the basal diet; (2) a 3-h transport of birds of the control group fed with the basal diet; (3) a 3-h transport of birds fed with diets supplemented with 600 mg/kg GAA; and (4) a 3-h transport of birds fed with diets supplemented with 1,200 mg/kg GAA.

No water or feed was provided during the transportation period. The transportation distance is about 240 km with an average speed of 80 km/h. After a 3-h transportation and rest for 1 h, 10 broilers with a body weight close to the mean body weight in each group were randomly selected for blood sampling. Blood samples were collected into 10-mL Eppendorf tubes coated with EDTA via wing vein puncture to collect plasma for subsequent analysis.

The left pectoralis major (PM) was taken from broilers within 10 min after slaughter and stored at 4°C for meat quality analysis. In addition, about 5 g of right PM was collected into the frozen tube and stored in liquid nitrogen for further analysis.

Growth Performance

At the beginning and end of the experiment, the body weights of broilers were separately recorded per pen. Feed consumption was recorded daily. Thus, the ADG, ADFI, and ratio of feed intake to the average daily weight gain (F:G) were calculated for each replicate pen of chicken.

Concentrations of Glucose and Corticosterone in Plasma

The concentration of glucose was analyzed using commercial test kits (Nanjing Jiancheng Bioengineering Institute, Nanjing, China) according to the protocols of manufacture. The

concentration of corticosterone was determined with commercial kits (Cusbio Biotech. Co., Ltd., Wuhan, China).

Meat Quality

Postmortem pH at 45 min (pH_{45min}) of the left PM were measured with PHBF-260 portable pH meter (Shanghai Instrument Electric Science Instrument Co., Ltd., Shanghai, China) and then were stored at 4°C to determine postmortem pH at 24 h (pH_{24h}). Each sample was measured at 3 locations. The probe of the pH meter was inserted into PM at an angle of 45° and was washed using ultrapure water between different samples. The values of meat color including a* (redness), b* (yellowness), and L* (lightness) at postmortem 24 h of the right PM were determined using a YS3010 portable spectrophotometer (Shenzhen San'enshi Technology Co., Ltd., Shenzhen, China). Drip loss, cooking loss, and shear force of PM were measured according to the protocols reported by the previous studies (Yue et al., 2010; Zhang et al., 2019).

Concentration of Cr, PCr, and Adenosine Nucleotides in Muscle

The concentrations of Cr, PCr, ATP, ADP, and AMP in muscle were determined by HPLC as previously reported with moderately modified (Wang et al., 2017; Zhang et al., 2017). Three hundred milligram frozen muscle samples were collected into tubes containing ice-cold perchloric acid and were homogenized for 1 min, followed by standing in an ice bath for 15 min. Then, the homogenates were centrifuged at 15,000 g at 4°C for 10 min to collect supernatants and further filtered through a 0.45-μm membrane. A 10-μL volume of each sample was injected into an Alliance HPLC system (Alliance HPLC system 2695, Water Corporation, Milford, MA, United States) equipped with a Waters SunFire C18 column (250 mm × 4.6 mm, 5 μm) at a temperature of 25°C for Cr and PCr determination, and at a temperature of 30°C for ATP, ADP, and AMP analysis. The ultraviolet wavelength for Cr and PCr determination and the analysis of ATP, ADP, and AMP were 210 and 245 nm, respectively. The mobile phase was a mixture of methyl cyanides and 29.4 mM KH₂PO₄ buffer (2:98, volume ratio) for Cr and PCr determination and was a mixture of methanol and phosphate buffer (13.5:86.5, volume ratio) for ATP, ADP, and AMP analysis, and the flow rate was 1 mL/min. The standards of creatine and phosphocreatine disodium salt, and 5'-ATP disodium salt, 5'-ADP sodium salt, and 5'-AMP sodium salt were all purchased from Sigma-Aldrich, Inc. (Sigma-Aldrich Inc., St. Louis, MO, United States).

Analysis of Activities of Glycolytic Key Enzymes

The activities of glycolytic key enzymes, including hexokinase (HK), pyruvate kinase (PK), and phosphofructokinase (PFK), were conducted with commercial kits (Nanjing Jiancheng Bioengineering Institute, Nanjing, China). All operation protocols were according to instructions of manufacture.

Determination of Glycogen, Lactic Acid, and Glycolytic Potential in Muscle

About 0.50 g (weighed exactly) frozen muscle sample was homogenized for 1 min in 4.5 mL ice-cold saline then was centrifuged for 10 min at 4,000 rpm at 4°C to collect supernatants for determining the concentration of lactic acid in muscle with a standard commercial kit (Nanjing Jiancheng Bioengineering Institute, Nanjing, China). Glycogen content was measured as previously reported (Zhang et al., 2009). Both lactic acid and glycogen contents were used to calculate the glycolytic potential (GP) according to the formula: $GP = 2 \times [\text{glycogen}] + [\text{lactic acid}]$, which was expressed as μmol of lactic acid equivalent per gram of wet muscle (Monin and Sellier, 1985).

RNA Extraction and Real-Time PCR Analysis

The mRNA expressions of the selected genes were evaluated by real-time PCR. Total RNA from muscle samples were extracted using RNAiso Plus reagent (catalog no. 9108, TaKaRa Biotechnology (Dalian) Co., Ltd., Dalian, China) according to the manufacturer's protocols. The purity of the total RNA was quantified by evaluating the OD₂₆₀/OD₂₈₀ ratio with a ND-1000 spectrophotometer (NanoDrop, Thermo Fisher Scientific). Samples with 260/280 ratios of 1.8–2.0 and 260/230 ratios of 2.0 to 2.2 were used for PCR reactions. Reverse transcription was conducted with the PrimeScript™ RT Master Mix (catalog no. RR037A, TaKaRa), and real-time RT-PCR was conducted using TB Green Premix Ex Taq (catalog no. RR420A). The PCR program was as follows: one cycle at 95°C for 30 s and 40 cycles at 95°C for 5 s, followed by 60°C for 30 s. The expression of target genes relative to the housekeeping gene (β -actin) was analyzed according to the method by Livak and Schmittgen (2000). All samples were processed in triplicate. The relative mRNA expression of each target gene was normalized to the control group (no transportation stress). The primer sequences for the target and housekeeping genes are shown in Table 2.

Western Blot

Approximately 10 mg frozen muscle samples was homogenized in tubes with 200 μL lysis buffer, then was centrifuged for 10 min at 12,000 rpm and 4°C to collect the supernatant, followed by protein quantification assay. Each muscle supernatant was mixed with an equal amount of 2 \times standard SDS sample loading buffer containing 0.5 M Tris-HCl (pH 6.8), 4.4% (w/v) SDS, 20% (v/v) glycerol, 2% (v/v) 2-mercaptoethanol, and 0.01% bromophenol blue and was boiled at 100°C for 5 min before electrophoresis. The extracted protein samples with equal amount (30 μg /lane) were loaded onto 10% sodium dodecyl sulfate polyacrylamide gel and transferred to a polyvinylidene difluoride membrane (Millipore, Billerica, MA, United States). Membrane blocking was conducted with 5% bovine serum albumin for 1 h and was incubated with primary antibodies (1:1,000) overnight at 4°C with gentle shaking. The membranes were washed three times with TBST (1 \times Tris buffered saline

TABLE 1 | Composition and nutrient levels of the basal diet (air-dry basis,%).

Items	Contents	Nutrient levels	Contents
Corn	68.50	² Crude protein (%)	16.00
Soybean meal	12.00	Metabolic energy (MJ/kg)	13.03
Corn gluten meal	3.60	Lysine (%)	0.85
Rapeseed meal	1.95	Methionine (%)	0.65
Soybean oil	3.93	Calcium (%)	0.81
L-Lysine HCl	0.32	Available phosphorus (%)	0.35
DL-Methionine	0.10		
Calcium monophosphate	1.30		
Limestone	0.85		
Salt	0.30		
1% Premix ¹	1.00		

¹Premix provided the following per kg of the diet: vitamin A 10,000 IU; vitamin D₃ 2,000 IU; vitamin E 25 mg; Vitamin K, 2.8 mg; thiamine 2.50 mg; riboflavin 7.5 mg; nicotinamide 40 mg; calcium pantothenate, 25 mg; pyridoxine-HCl, 3 mg; biotin, 0.20 mg; folic acid, 1.5 mg; vitamin B12, 0.015 mg; ferrous (as ferrous sulfate) 80 mg; copper (as copper sulfate) 8 mg; manganese (as manganese sulfate) 100 mg; zinc (as zinc sulfate) 60 mg; iodine (as potassium iodide) 0.35 mg; selenium (as sodium selenite) 0.3 mg.

²Nutrient content of the diets were the value of measurement.

including 0.1% Tween 20) and then were incubated with a second antibody of horseradish peroxidase-conjugated (1:3,000, Cell Signaling Technology Inc., Beverly, MA, United States) at room temperature. The primary antibodies for phosphor-LKB1 (Thr189, no. 3054s, 1:1,000), phosphor-AMK α (Thr172, no. 2531s, 1:1,000), and α -Tubulin (no. 2125s, 1:1,000) were purchased from Cell Signaling Technology Inc. (Beverly, MA, United States) and were validated previously for use with chicken samples (Zhang et al., 2017). The membranes were developed using ECL chemiluminescent reagents (Tanon Science and Technology Co., Ltd., Shanghai, China) and exposed to Kodak film. Band densities were quantified using Scion Image software (Scion Corporation, Frederick, MD, United States) and were normalized to α -tubulin and expressed as the relative values to those for the control group.

Statistical Analysis

All data were statistically analyzed with the SAS program (version 8.02, SAS Institute Inc., Cary, NC, United States). All data were normally distributed and were analyzed using analysis of one-way analysis of variance. Significant differences among treatment means were analyzed by Duncan's multiple-range test. The results were presented with mean values with their standard deviation, and a *P* value of less than 0.05 was considered statistically significant.

RESULTS

Growth Performance

The results of dietary supplemented with GAA on growth performance of Qiangdongnan Xiaoxiang chickens are shown in Table 3. Both 600 mg/kg GAA and 1,200 mg/kg GAA supplementation in diets did not affect ADG, ADFI, or F/G when compared with those fed with the control diet (*P* > 0.05).

TABLE 2 | Sequences used for real-time PCR primers.

Genes	Primers (5'→3')	Product size (bp)	Gene Bank ¹
LKB1	Sense: GTATGACGGCGGTGCCTTATCTG Antisense: ACCTGTCCTGGTACTGTGAAGTCC	121	NM_001045833.1
AMPK α 1	Sense: TGTGTATGTGCAGCAACCCG Antisense: AACAAACCAGCTATGCACCCC	195	NM_001039603.1
AMPK α 2	Sense: TCATCAGCACGCCAACAGACTTC Antisense: CGAGCCTCTGCCTCTTCAACAC	106	NM_001039605.1
β -actin	Sense: ATTGTCCACCGCAAATGCTTC Antisense: AAATAAAGCCATGCCAATCTCGTC	113	NM_205518.1

LKB1, liver kinase B1; AMPK α 1, adenosine 5'-monophosphate-activated protein kinase α 1; AMPK α 2, adenosine 5'-monophosphate-activated protein kinase α 2.
¹Genbank Accession Number.

TABLE 3 | Effect of dietary supplemented with GAA on growth performance of Qiandongnan Xiaoxiang Chicken.

Items	Control group	600 mg/kg GAA group	1,200 mg/kg GAA group	P value
ADG (g)	24.60 ± 1.34	25.09 ± 3.44	23.86 ± 3.77	0.850
ADFI(g)	110.0 ± 4.43	105.8 ± 3.98	108.1 ± 4.80	0.426
F/G(g/g)	4.49 ± 0.36	4.27 ± 0.57	4.65 ± 1.02	0.754

Results are expressed as the mean value and standard error. Means within the same row with different superscripts differ significantly ($n = 40$ per treatment, $P < 0.05$). Control, broilers fed the basal diet without transport stress; T 3h, broilers fed the basal diet and experienced a 3 h transport; T 3h + 0.06% GAA or T 3h + 0.12% GAA, broilers fed the basal diet supplemented with GAA at 600 or 1200 mg/kg and experienced a 3 h transport. GAA, guanidine acetic acid; ADG, average daily weight gain; ADFI, average daily feed intake; F/G, the ratio of feed to gain.

Similarly, there were no differences in ADG, ADFI, or F/G between 600 mg/kg GAA and 1,200 mg/kg GAA supplementation group ($P > 0.05$).

Plasma Parameters

The concentrations of glucose and corticosterone in plasma are shown in **Figure 1**. Compared with those in the control group (no pre-slaughter transport stress), the 3-h pre-slaughter transport significantly decreased the concentration of glucose and elevated the contents of corticosterone in plasma ($P < 0.05$, **Figures 1A,B**). However, dietary supplemented with 1,200 mg/kg GAA decreased the concentration of corticosterone of broilers induced by the 3-h pre-slaughter transport ($P < 0.05$). Moreover, there was no difference in the concentration of glucose or corticosterone between the control group and the 1,200-mg/kg GAA supplementation group ($P > 0.05$).

Meat Quality

As shown in **Table 4**, compared with broilers without transport stress, pH_{24h} values of broilers subjected to 3-h transport stress were significantly decreased ($P < 0.05$). In contrast, the drip loss, cooking loss, and L* value were all increased by 3-h transport stress ($P < 0.05$). However, the values of pH_{45min}, a*, b*, and shear force were not affected ($P > 0.05$). Diets supplemented with 600 mg/kg GAA or 1,200 mg/kg GAA similarly resulted in a higher value of pH_{24h} and the lower drip loss and L* of broilers in comparison with those subjected to 3-h transport stress ($P < 0.05$). Besides, compared with 3-h transport stress, the cooking loss was lowered by 1200 mg/kg GAA supplementation ($P < 0.05$). However, both 600 mg/kg GAA and 1,200 mg/kg GAA supplemented did not affect the values of pH_{45min}, a*, and b* ($P > 0.05$). Moreover, the drip loss of broilers fed with 1,200 mg/kg GAA was significantly lower than those fed with

600 mg/kg GAA diet ($P < 0.05$). No differences in parameters of meat quality measured in our study were observed between the 1,200-mg/kg GAA supplementation group and the control group ($P > 0.05$).

Concentrations of Cr, PCr, ATP, ADP, and AMP in Muscle

As shown in **Table 5**, compared with the control group, 3-h transport stress significantly decreased the contents of Cr and ATP in PM ($P < 0.05$) but elevated the contents of ADP, AMP, and the ratio of AMP:ATP ($P < 0.05$). However, no differences in the ratio of PCr:Cr and the concentration of PCr between 3-h transport stress and the control group were observed ($P > 0.05$). Compared with the 3-h pre-slaughter transport treatment, dietary supplemented with 600 mg GAA significantly increased the contents of Cr and PCr in PM ($P < 0.05$). However, the contents of ATP, ADP, and AMP and the ratio of PCr:Cr and AMP:ATP ($P > 0.05$) were not affected by dietary supplemented with 600 mg GAA when compared with 3-h transport stress. Notably, compared with 3-h pre-transport stress, dietary supplemented with 1,200 mg GAA exhibited significant increases in the contents of Cr, PCr, and ATP in muscle ($P < 0.05$). Furthermore, the contents of ADP and AMP and the ratio of AMP:ATP ($P < 0.05$) by 1,200 mg GAA supplementation were lower than those of 3-h transport stress. However, there were no differences in the ratio of PCr:Cr among four treatments ($P > 0.05$).

Glycolytic Potential of Pectoralis Major Muscle

The results of the glycolytic potential of PM muscle of Qiandongnan Xiaoxiang chickens fed with GAA are shown

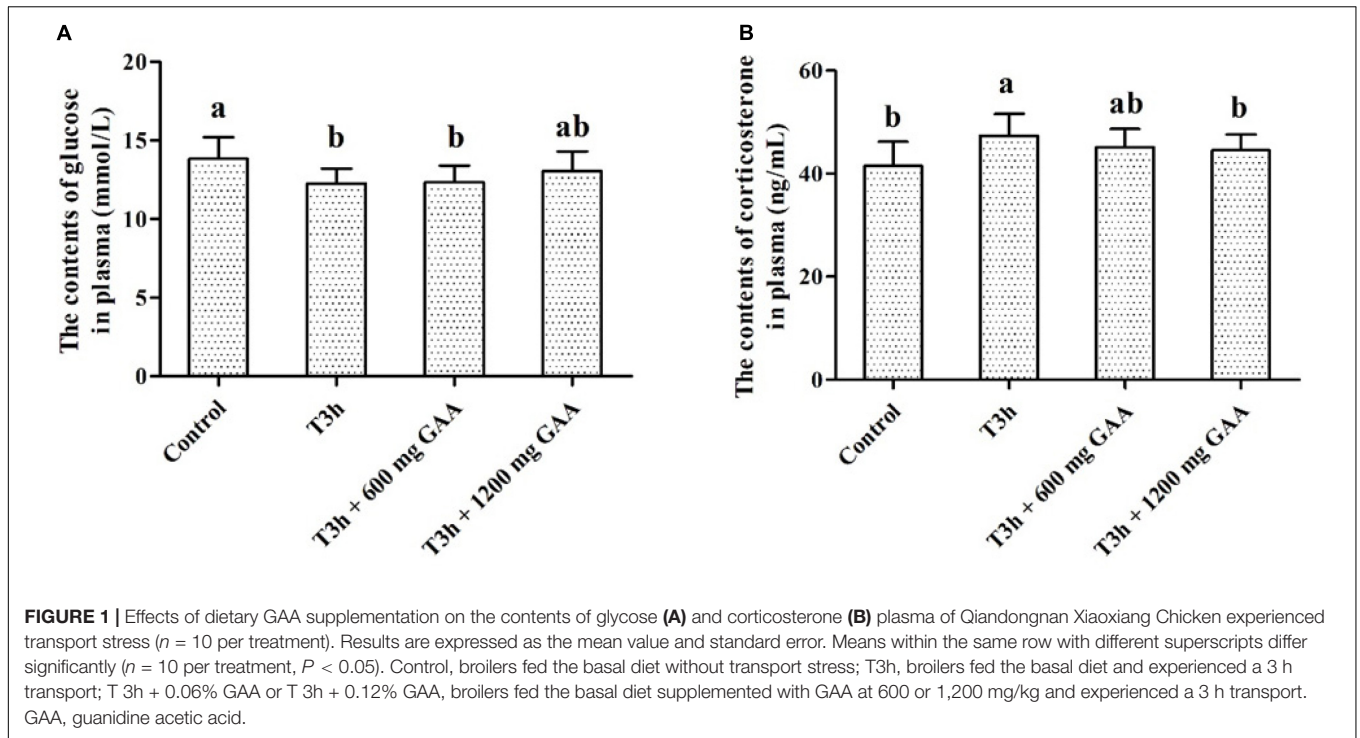


TABLE 4 | Effects of dietary supplementation with GAA on meat quality of the pectoralis major muscle of Qiangdongnan Xiaoxiang Chicken subjected to preslaughter transport stress.

Items	Control group	T 3h	T 3h + 600 mg GAA	T 3h + 1200 mg GAA	P value
pH _{45min}	6.40 ± 0.30	6.29 ± 0.22	6.34 ± 0.13	6.37 ± 0.07	0.720
pH _{24h}	5.88 ± 0.06 ^a	5.59 ± 0.05 ^b	5.86 ± 0.06 ^a	5.87 ± 0.09 ^a	<0.001
L*	51.5 ± 1.15 ^c	55.2 ± 1.61 ^a	53.4 ± 1.69 ^b	52.5 ± 1.60 ^{bc}	<0.001
a*	1.29 ± 0.11	1.21 ± 0.09	1.22 ± 0.18	1.25 ± 0.13	0.584
b*	5.08 ± 0.68	5.45 ± 0.28	5.06 ± 0.21	5.09 ± 0.33	0.220
Drip loss (%)	2.26 ± 0.21 ^c	2.75 ± 0.18 ^a	2.54 ± 0.12 ^b	2.30 ± 0.24 ^c	<0.001
Cooking loss (%)	16.6 ± 0.73 ^b	18.0 ± 1.18 ^a	17.2 ± 0.14 ^{ab}	16.8 ± 0.89 ^b	0.011
Shear force (N)	24.1 ± 0.86	25.1 ± 1.22	25.1 ± 0.92	24.3 ± 1.11	0.141

Results are expressed as the mean value and standard error. Means within the same row with different superscripts differ significantly ($n = 10$ per treatment, $P < 0.05$). Control, broilers fed the basal diet without transport stress; T 3h, broilers fed the basal diet and experienced a 3 h transport; T 3h + 0.06% GAA or T 3h + 0.12% GAA, broilers fed the basal diet supplemented with GAA at 600 or 1,200 mg/kg and experienced a 3 h transport. GAA, guanidine acetic acid; pH_{45min}, pH at 45 min postmortem; pH_{24h}, pH at 24 h postmortem; L*, lightness; a*, redness; b*, yellowness.

TABLE 5 | Effects of dietary supplementation with GAA on muscle energy status of the pectoralis major muscle of Qiangdongnan Xiaoxiang Chicken subjected to preslaughter transport stress.

Items	Control group	T 3h	T 3h + 600 mg GAA	T 3h + 1,200 mg GAA	P value
Cr	21.99 ± 1.36 ^b	19.79 ± 1.46 ^c	22.90 ± 1.60 ^{ab}	24.58 ± 1.70 ^a	0.001
PCr	2.24 ± 0.15 ^{ab}	2.10 ± 0.17 ^b	2.32 ± 0.16 ^a	2.41 ± 1.48 ^a	0.042
PCr: Cr	0.10 ± 0.01	0.11 ± 0.01	0.10 ± 0.01	0.10 ± 0.01	0.731
ATP	3.48 ± 0.16 ^a	3.03 ± 0.13 ^c	3.14 ± 0.20 ^{bc}	3.35 ± 0.17 ^{ab}	0.002
ADP	0.90 ± 0.03 ^b	1.04 ± 0.09 ^a	0.97 ± 0.06 ^{ab}	0.94 ± 0.01 ^b	0.009
AMP	0.32 ± 0.03 ^c	0.42 ± 0.03 ^a	0.38 ± 0.02 ^{ab}	0.35 ± 0.02 ^{bc}	0.001
AMP: ATP	0.09 ± 0.01 ^b	0.14 ± 0.02 ^a	0.12 ± 0.01 ^a	0.10 ± 0.01 ^b	<0.001

Results are expressed as the mean value and standard error. Means within the same row with different superscripts differ significantly ($n = 10$ per treatment, $P < 0.05$). Control, broilers fed the basal diet without transport stress; T3h, broilers fed the basal diet and experienced a 3 h transport; T3h + 0.06% GAA or T3h + 0.12% GAA, broilers fed the basal diet supplemented with GAA at 600 or 1,200 mg/kg and experienced a 3 h transport. GAA, guanidine acetic acid; Cr, creatine; PCr, phosphocreatine; ATP, adenosine triphosphate; ADP, adenosine diphosphate; AMP, adenosine monophosphate.

in **Figure 2**. Three-hour pre-slaughter transport stress resulted in lower glycogen contents and higher lactic acid ($P < 0.05$, **Figures 2A,B**), combined with higher glycolytic potential of PM muscle ($P < 0.05$, **Figure 2C**) in comparison with those of the control group. The content of lactic acid was decreased followed by 600 mg/kg GAA supplementation ($P < 0.05$); however, no differences were observed for glycogen content or glycolytic potential by 600 mg/kg GAA supplementation ($P > 0.05$). Compared with the 3-h pre-slaughter transport, however, 1,200 mg/kg GAA addition significantly elevated the glycogen content ($P < 0.05$) and markedly decreased glycolytic potential and the concentration of lactic acid ($P < 0.05$). Moreover, the content of lactic acid of broilers supplemented with 1,200 mg/kg GAA was lower than those fed with 600 mg/kg GAA ($P < 0.05$), but there were no differences in glycogen content or glycolytic potential between these two groups ($P > 0.05$). Additionally, no differences were observed for glycogen, lactic acid, or glycolytic potential between the 1,200-mg/kg GAA group and the control group ($P > 0.05$).

Activities of Glycolytic Key Enzymes

Data on the effects of transport stress on activities of glycolytic key enzymes are shown in **Figure 3**. Three-hour pre-slaughter transport stress increased the activities of PK and HK (**Figures 3A,B**), as well as the activity of 2,6-PFK ($P < 0.05$, **Figure 3C**). The activities of PK, HK, and 2,6-PFK were not significantly influenced by the 600-mg/kg GAA treatment compared to those treated with 3-h transport stress ($P > 0.05$). In contrast, compared with the 3-h transport stress group, the activities of PK, HK, and 2,6-PFK were all dramatically decreased by 1,200 mg/kg GAA supplementation ($P < 0.05$). Furthermore, compared to the control group, there were no differences in the activities of PK, HK, or 2,6-PFK of broilers supplemented with 1,200 mg/kg GAA ($P > 0.05$).

Related mRNA Expressions and Protein Abundances in the AMPK Signaling Pathway

The mRNA expressions and related protein abundances are shown in **Figure 4**. Three-hour pre-slaughter transport stress resulted in a significant elevation of mRNA expressions of LKB1 and AMPK α 2 ($P < 0.05$, **Figures 4A,B**), except for the mRNA expression of AMPK α 1 ($P > 0.05$, **Figure 4B**). Meanwhile, protein abundances of LKB1 phosphorylation and AMPK α phosphorylation were both increased by 3-h transport stress ($P < 0.05$, **Figures 4D,E**). On the contrary, compared to those treated by 3-h transport stress, the upregulated mRNA expressions of LKB1 and AMPK α 2, combined with the increased protein abundances of LKB1 and AMPK α , were all reversed by 1,200 mg/kg GAA supplementation ($P < 0.05$).

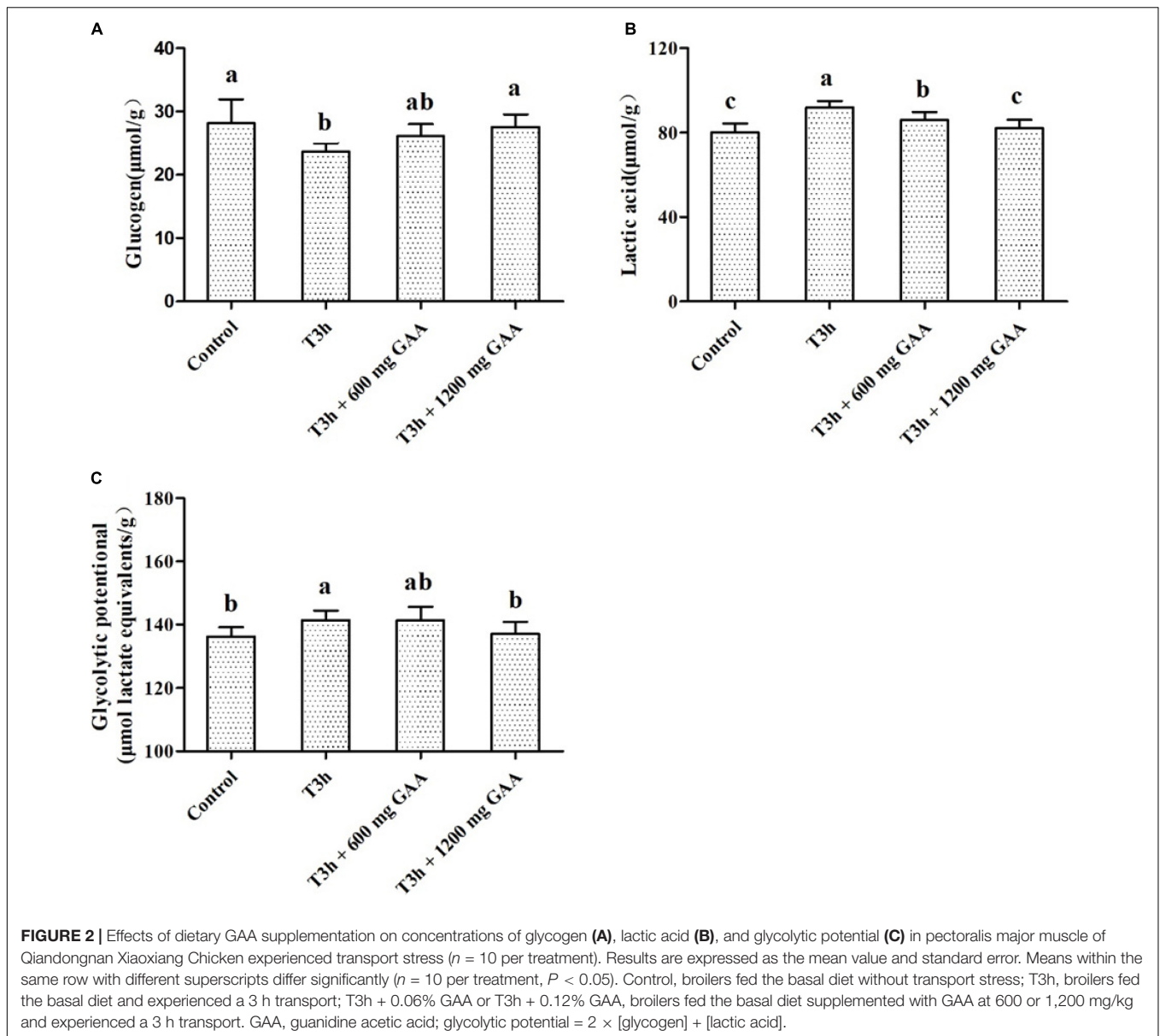
DISCUSSION

Several published studies have indicated that GAA supplementation could effectively increase creatine storage in tissues and accordingly positively affected the growth

performance, breast meat yield, and status of energy metabolism when GAA was supplemented with a dosage not higher than 600–800 mg GAA per kg feed for chicken (Michiels et al., 2012; Mousavi et al., 2013; Ostojic, 2015). Surprisingly, in our study, there were no differences in ADG, ADFI, or F/G of broilers supplemented with 600 or 1,200 mg/kg GAA, which was probably associated with the shorter experimental period (14 days before pre-slaughter transport). Similarly, Zhang et al. (2019) suggested that dietary supplemented with GAA prior to pre-slaughter for 14 days at a dosage of both 600 and 1,200 mg/kg did not affect ADG, ADFI, or feed efficiency of broilers. Moreover, a previous study conducted by Tossenberger et al. (2016) also demonstrated that 0.6% GAA supplementation did not affect the growth performance of broilers.

The plasma parameters such as glucose and corticosterone were considered to be a biochemical index in response to pre-slaughter transport stress (Zhang et al., 2009; Voslarova et al., 2011). In our present study, 3-h pre-slaughter transport stress decreased the concentration of glucose in plasma, accompanied by an increase of corticosterone contents when compared with the control group, indicating that a stress occurred in response to 3-h pre-slaughter transport stress. Consistent with our results, Zhang et al. (2019) suggested that 3-h transport stress exhibited higher plasma corticosterone concentration and lower plasma glucose concentration than the control group (0.5-h transport stress). However, compared with those exposed to 3-h pre-slaughter transport, dietary supplemented with 1,200 mg/kg GAA resulted in a decrease in the concentration of corticosterone, demonstrating that GAA addition could contribute to alleviating the negative effects induced by the 3-h pre-slaughter transport.

Pre-slaughter transport causes an acute response to broilers, resulting in an inferior meat. In our present study, 3-h transport stress decreased pH_{24h} values of broilers when compared with those in the control group. It was reported that the energy was generated from anaerobic glycolysis to maintain the metabolic activity of muscle cells during transport stress, resulting in the lactate and H⁺ accumulation, then followed by a lower pH (Xing et al., 2016). Moreover, the accumulation of lactate and protons from rapid anaerobic glycolysis induced by transport stress cannot be timely removed by postmortem meat, which may explain why pH at 24 h postmortem in the breast of 3-h transport broilers were still lower (Wang et al., 2017). In contrast, the drip loss, cooking loss, and L* value were all increased by 3-h transport stress. Similarly, Xing et al. (2016) demonstrated that the meat quality of broilers subjected to transport stress had higher drip loss, cooking loss, and L* value. Besides, Wang et al. (2017) also suggested that 3-h transport stress increased the L* value and drip loss of breast muscle at 24 h postmortem. Interestingly, in our present study, the broilers fed with both 600 mg/kg GAA and 1,200 mg/kg GAA for two weeks before slaughtering had a lower drip loss and L* value, combined with a higher value of pH_{24h} in comparison with those subjected to 3-h transport stress. It was reported that GAA supplementation before slaughtering could enhance the contents of available energy sources such as PCr and ATP, which contributes to delaying the conversion of glycogen to lactic acid and consequently maintains a pH value postmortem.



Accordingly, the higher pH value reduced muscle protein denaturation and increased muscle water holding capacity and meat tenderness, thus improving meat quality (Huff-Loneragan and Lonergan, 2005). Consistent with our results, Zhang et al. (2019) suggested that dietary addition of 1,200 mg/kg GAA reduced drip loss compared to 3-h pre-slaughter transport stress, which indicated that GAA supplementation prior to slaughtering could be an effective way to improve the meat quality of broilers subjected to transport stress.

It has been demonstrated that a lower ATP content and/or a higher AMP/ATP ratio in muscle were observed in broilers at the stage of pre-slaughter transport or heat stress (McKee and Sams, 1997; Savenije et al., 2002; Zhang et al., 2017). Similarly, our current study observed that 3-h transport stress decreased the contents of ATP, Cr, and PCr in muscle and

increased AMP and the ratio of AMP:ATP, indicating that 3-h transport stress accelerated muscle ATP exhaust accompanied by the activation of the Cr and phosphocreatine system. The primary physiological function of Cr is involved in the regulation of energy metabolism of cells, particularly muscle cells, through the Cr and phosphocreatine system (Michiels et al., 2012). The Cr and phosphocreatine system is described as a spatial energy buffer because it acts as an energy transport system that carries high-energy phosphates from mitochondrial production sites to energy utilization sites (Brosnan and Brosnan, 2007). In addition, it is a temporal energy buffer because it maintains energy homeostasis by buffering ADP and ATP ratios in order to store and mobilize energy when required on short notice, especially in muscle cells (Lemme et al., 2007). It has been demonstrated that supplemental GAA, a natural precursor of

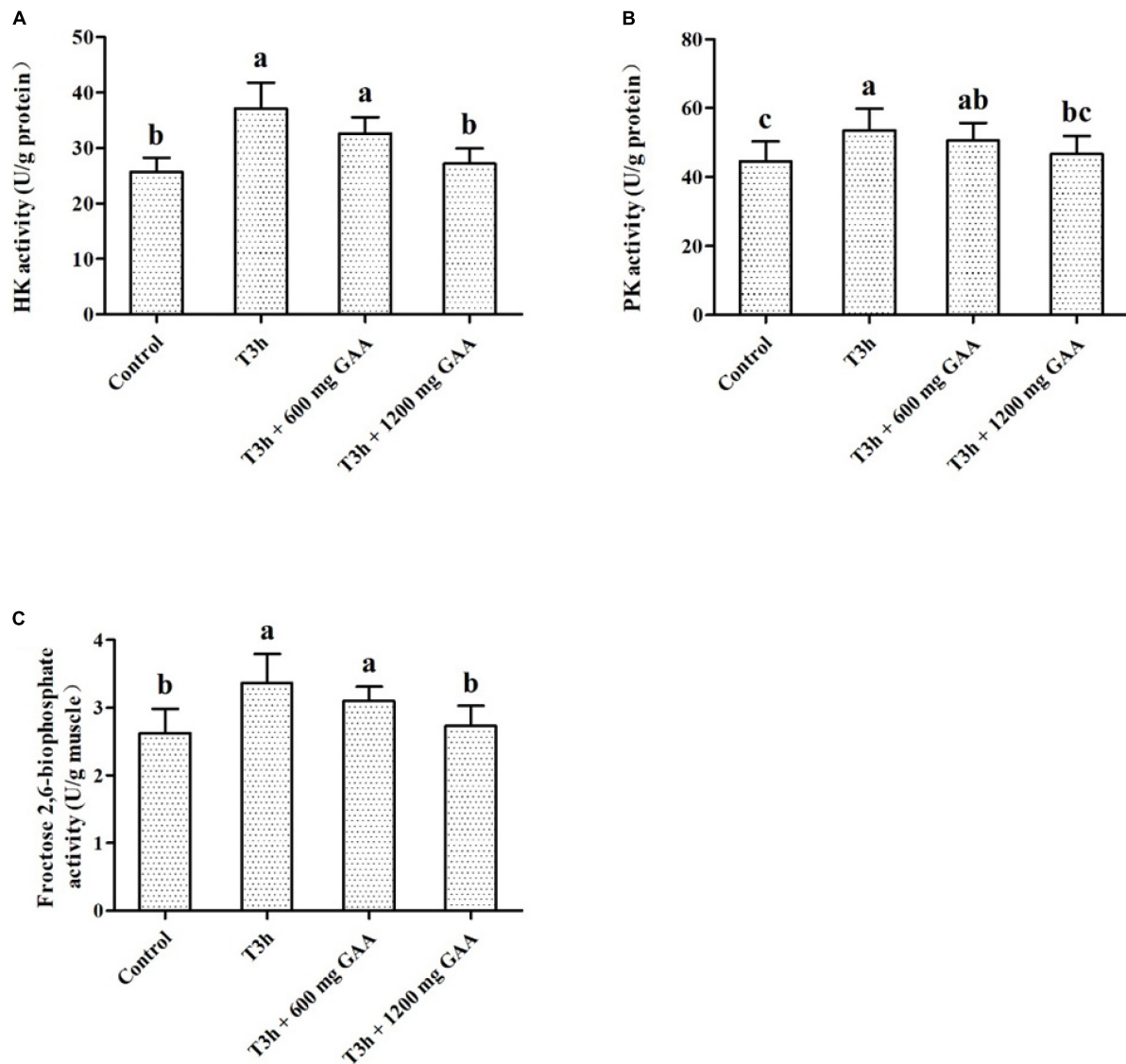


FIGURE 3 | Effects of dietary GAA supplementation on activities of HK (A), PK (B), and Fructose 2,6-niophosphate (C) in pectoralis major muscle of Qiandongnan Xiaoxiang Chicken experienced transport stress ($n = 10$ per treatment). Results are expressed as the mean value and standard error. Means within the same row with different superscripts differ significantly ($n = 10$ per treatment, $P < 0.05$). Control, broilers fed the basal diet without transport stress; T3h, broilers fed the basal diet and experienced a 3 h transport; T3h + 0.06% GAA or T3h + 0.12% GAA, broilers fed the basal diet supplemented with GAA at 600 or 1,200 mg/kg and experienced a 3 h transport. GAA, guanidine acetic acid; HK, hexokinase; PK, pyruvate kinase.

Cr, serves as an efficient Cr source improving the muscle energy metabolism (Lemme et al., 2007). In our study, dietary supplementation GAA at a dosage of 600 or 1,200 mg/kg GAA increased the concentration of Cr and PCr in muscle when compared with the 3-h transport group. Similar with this, Michiels et al. (2012) demonstrated that GAA supplementation enhanced the contents of Cr and PCr in muscle, indicating that GAA was an efficient Cr source to improve energy store in the forms of Cr and PCr.

It has been demonstrated that pre-slaughter stress exacerbated skeletal muscle energy consumption, evidenced by decreasing muscle ATP depletion and accelerating glycolysis metabolism,

which resulted in a decreased concentration of glycogen and an elevation of lactic acid (Yue et al., 2010; Zhang et al., 2017). Similar with the results of Zhang et al. (2019), in our present study, it showed that pre-slaughter transport stress increased the concentration of lactic acid and glycolytic potential of muscle, indicating that muscle cells switch from oxidative phosphorylation to glycolysis to produce enough ATP for increased muscle energy demands in response to the limited oxygen during pre-slaughter stress and anaerobic glycolysis then became the predominant energy source for the muscle ATP supply. It has been shown that HK, PK, and LDH are the rate-limiting enzymes involved in the glycolysis pathway, which

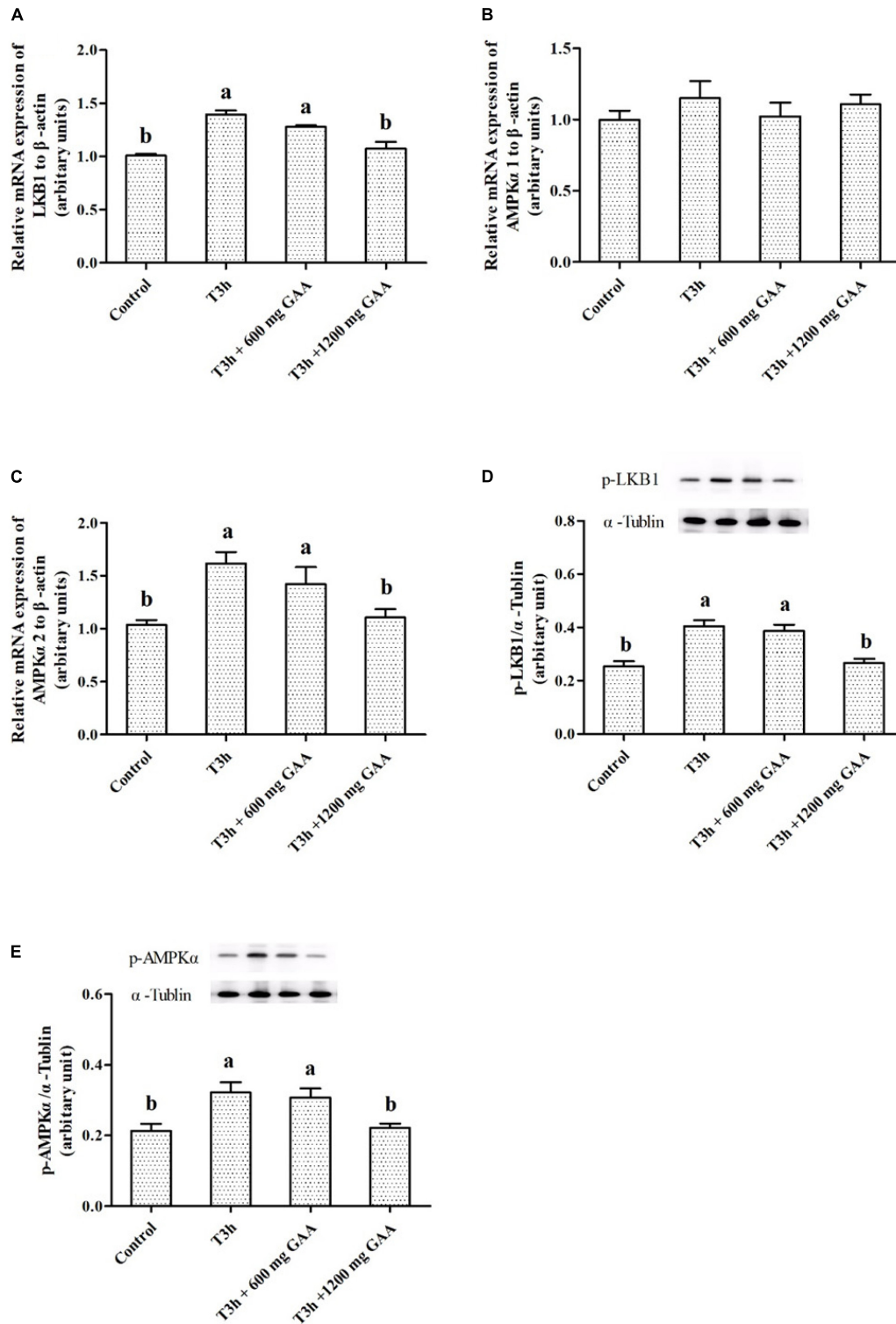


FIGURE 4 | Effects of dietary GAA supplementation on mRNA expressions of LKB1 (**A**), AMPK α 1 (**B**), AMPK α 2 (**C**), and protein abundances of phosphorylation LKB1 (**D**) and phosphorylation AMPK α (**E**) in pectoralis major muscle of Qianhongnan Xiaoxiang Chicken experienced transport stress ($n = 10$ per treatment). Results are expressed as the mean value and standard error. Means within the same row with different superscripts differ significantly ($n = 10$ per treatment, $P < 0.05$). Control, broilers fed the basal diet without transport stress; T3h, broilers fed the basal diet and experienced a 3 h transport; T3h + 0.06% GAA or T3h + 0.12% GAA, broilers fed the basal diet supplemented with GAA at 600 or 1,200 mg/kg and experienced a 3 h transport. GAA, guanidino acetic acid; LKB1, liver kinase B1; AMPK α 1, adenosine 5'-monophosphate-activated protein kinase α 1; AMPK α 2, adenosine 5'-monophosphate-activated protein kinase α 2; phosphorylation LKB1, phospho-liver kinase B1; phosphorylation AMPK α , phospho-adenosine 5'-monophosphate-activated protein kinase α (including α -1 and -2).

are responsible for converting glucose to glucose-6-phosphate, phosphoenolpyruvate to pyruvic acid, and pyruvic acid to lactic acid, respectively (Liu et al., 2015; Wang et al., 2017). In the present study, 3-h pre-slaughter transport stress elevated the activities of PK, HK, and LDH of breast, indicating that glycolysis may be triggered during 3-h pre-slaughter transport stress. However, 1,200 mg/kg GAA supplementation increased the concentration of glycogen and decreased lactic acid, glycolytic potential and the activities of PK, HK, and LDH of breast compared to 3-h transport stress, indicating that the rate of glycolysis reaction was downregulated because of GAA supplementation. Moreover, compared to 3-h transport stress, the increased Cr and PCr in muscle were observed by GAA supplementation, indicating that GAA supplementation may be beneficial for delaying rapid muscle anaerobic glycolysis induced by transport stress.

AMPK, which is mainly recognized as an important regulator of mitochondrial biogenesis in response to energy deprivation, is switched on by an increase in the AMP/ATP ratio via the phosphorylation of the α subunit at the Thr¹⁷² site by LKB1 (Du et al., 2005). AMPK is activated by stresses that deplete cellular ATP, when it acts to restore energy homeostasis by switching on catabolic pathways that generate ATP through accelerating the glycolysis process of muscle (Graeme and Hardie, 2014). However, a previous study in AMPK knockout mice demonstrated that postmortem glycolysis was inhibited (Shen et al., 2008), which suggested that AMPK played an important role in the postmortem glycolysis process in lack of oxygen. Moreover, AMPK is a heterotrimeric complex comprising α , β , and γ subunits, in which the α subunit is essential for the activation of AMPK signaling (Du et al., 2005; Graeme and Hardie, 2014). The α subunit of AMPK has two isoforms, $\alpha 1$ and $\alpha 2$. It was demonstrated that AMPK $\alpha 2$ but not AMPK $\alpha 1$ knockoff abolished the activity of AMPK in postmortem muscle. Besides, AMPK $\alpha 2$ knockoff reduced postmortem pH decline and the generation of lactate, while AMPK $\alpha 1$ knockoff had no significant effect, which suggested that the AMPK $\alpha 2$ catalytic subunit mainly regulates postmortem glycolysis in muscle (Liang et al., 2013). In our present study, it was observed that both LKB1 mRNA expression level and LKB1 protein abundances, combined with the phosphorylation abundance of AMPK α at Thr¹⁷², were all increased by 3-h transport stress, indicating that the energy metabolism of muscle under pre-slaughter transport stress was mediated by AMPK signaling. Similarly, it has been suggested that pre-slaughter transport stress accelerated the process of glycolysis, recognized by increasing an accumulation of lactate and subsequently an activation of the AMPK signaling pathway (Xing et al., 2016). Meanwhile, our study also indicated that AMPK $\alpha 2$ but not AMPK $\alpha 1$ was

elevated in response to 3-h transport stress. Nevertheless, dietary GAA supplementation downregulated the mRNA expressions of muscle LKB1 and AMPK $\alpha 2$, and the protein expression of LKB1 and the phosphorylation abundance of AMPK α Thr¹⁷², suggesting that dietary GAA addition may be an effective way in delaying anaerobic glycolysis via inhibiting the transport stress-induced activation of the AMPK pathway.

DATA AVAILABILITY STATEMENT

The original contributions presented in the study are included in the article/supplementary material, further inquiries can be directed to the corresponding author/s.

ETHICS STATEMENT

The animal study was reviewed and approved by Institutional Animal Care and Use Committee of Zunyi Normal College.

AUTHOR CONTRIBUTIONS

RL, JL, and NL participated in the animal trial and sample analysis together with BZ. BZ performed the data analysis and wrote the manuscript. ZH, PS, MH, and YX assisted in conducting the experimental analysis. BZ and ZS designed and supervised the study and revised the manuscript. All authors contributed to the article and approved the submitted version.

FUNDING

This work was financially supported by National Natural Science Foundation of China (No. 31760674), the Basic Project of Guizhou Provincial Natural Science Foundation [Qian Kehe (2017)1205], Zunyi 15851 Talent Project (2050020213#), Zunyi City-School Joint Fund [Zunshi Kehe (2018) No. 08], the Rural Industrial Revolution Project of Guizhou Province (Zunshi he Rural Industry 201905), and Zunshi Chi Shuihe Fund [Zunshi CSHKJ(2019)-01].

ACKNOWLEDGMENTS

We are grateful to Guizhou Rongjiang Shannong Development Co., Ltd. (China) for providing the Qiangongnan Xiaoxiang Chickens.

REFERENCES

- Brosnan, J. T., and Brosnan, M. E. (2007). Creatine: endogenous metabolite, dietary, and therapeutic supplement. *J. Annu. Rev. Nutr.* 27, 241–261. doi: 10.1146/annurev.nutr.27.061406.093621
- Degroot, A. A. (2015). *Efficacy of Dietary Guanidinoacetic Acid in Broiler Chicks. Master Degree*. Urbana IL: University of Illinois at Urbana-Champaign.
- Desai, M. A., Jackson, V., Zhai, W., Suman, S. P., Nair, M. N., Beach, C. M., et al. (2016). Proteome basis of pale, soft, and exudative-like (PSE-like) broiler breast (Pectoralis major) meat. *Poult. Sci.* 95, 2696–2706. doi: 10.3382/ps/pew213
- Dilger, R. N., Bryant-Angeloni, K., Payne, R. L., Lemme, A., and Parsons, C. M. (2013). Dietary guanidino acetic acid is an efficacious replacement for arginine for young chicks. *Poult. Sci.* 92, 171–177. doi: 10.3382/ps.2012-02425

- Du, M., Shen, Q. W., and Zhu, M. J. (2005). Role of beta-adrenoceptor signaling and AMP-activated protein kinase in glycolysis of postmortem skeletal muscle. *J. Agric. Food Chem.* 53, 3235–3239. doi: 10.1021/jf047913n
- Graeme, G. J., and Hardie, D. G. (2014). AMPK: a cellular energy sensor primarily regulated by AMP. *Biochem. Soc. Trans.* 42, 71–75.
- Hambrecht, E., Eissen, J. J., Newman, D. J., Smits, C. H., Verstegen, M. W., and den Hartog, L. A. (2005). Preslaughter handling effects on pork quality and glycolytic potential in two muscles differing in fiber type composition. *J. Anim. Sci.* 83, 900–907. doi: 10.2527/2005.834900x
- Hardie, D. G. (2011). Energy sensing by the AMP-activated protein kinase and its effects on muscle metabolism. *Proc. Nutr. Soc.* 70, 92–99. doi: 10.1017/S0029665110003915
- Huang, J., Yang, J., Huang, M., Zhu, Z., Sun, X., Zhang, B., et al. (2018). Effect of pre-slaughter shackling and wing flapping on plasma parameters, postmortem metabolism, AMPK, and meat quality of broilers. *Poult. Sci.* 97, 1841–1847. doi: 10.3382/ps/pey019
- Huff-Lonergan, E., and Lonergan, S. M. (2005). Mechanisms of water-holding capacity of meat: the role of postmortem biochemical and structural changes. *Meat Sci.* 71, 194–204. doi: 10.1016/j.meatsci.2005.04.022
- Lemme, A., Ringel, J., Sterk, A., and Young, J. F. (2007). “Supplemental guanidino acetic acid affects energy metabolism of broilers,” in *World Poultry Science Association, Proceedings of the 16th European Symposium on Poultry Nutrition*, Vol. 26–30, Strasbourg, 339–342.
- Li, Z., Li, X., Wang, Z., Shen, Q., and Zhang, D. (2016). Antemortem stress regulates protein acetylation and glycolysis in postmortem muscle. *Food Chem.* 202, 94–98. doi: 10.1016/j.foodchem.2016.01.085
- Liang, J., Yang, Q., Zhu, M. J., Jin, Y., and Du, M. (2013). AMP-activated protein kinase (AMPK) α 2 subunit mediates glycolysis in postmortem skeletal muscle. *Meat Sci.* 95, 536–541. doi: 10.1016/j.meatsci.2013.05.025
- Liu, Y., Li, J. L., Li, Y. J., Gao, T., Zhang, L., Gao, F., et al. (2015). Effects of dietary supplementation of guanidinoacetic acid and combination of guanidinoacetic acid and betaine on postmortem glycolysis and meat quality of finishing pigs. *Anim. Feed Sci. Technol.* 205, 82–89. doi: 10.1016/j.anifeeds.2015.03.010
- Livak, K., and Schmittgen, T. (2000). Analysis of relative gene expression data using real-time quantitative PCR and the $2^{-\Delta\Delta Ct}$ Method. *Methods* 25, 402–408. doi: 10.5897/AJB11.4117
- McBreairty, L. E., Robinson, J. L., Furlong, K. R., Brunton, J. A., and Bertolo, R. F. (2015). Guanidinoacetate is more effective than creatine at enhancing tissue creatine stores while consequently limiting methionine availability in Yucatan miniature pigs. *PLoS One* 10:e0131563. doi: 10.1371/journal.pone.0131563
- McKee, S. R., and Sams, A. (1997). The effect of seasonal heat stress on rigor development and the incidence of pale, exudative turkey meat. *Poult. Sci.* 76, 1616–1620. doi: 10.1093/ps/76.11.1616
- Michiels, J., Maertens, L., Buyse, J., Lemme, A., Rademacher, M., Dierick, N. A., et al. (2012). Supplementation of guanidinoacetic acid to broiler diets: effects on performance, carcass characteristics, meat quality, and energy metabolism. *Poult. Sci.* 91, 402–412. doi: 10.3382/ps.2011-01585
- Monin, G., and Sellier, P. (1985). Pork of low technological quality with a normal rate of muscle pH fall in the immediate post-mortem period: the case of the Hampshire breed. *Meat Sci.* 13, 49–63. doi: 10.1016/S0309-1740(85)80004-8
- Mousavi, S. N., Afsar, A., and Lotfollahian, H. (2013). Effects of guanidinoacetic acid supplementation to broiler diets with varying energy contents. *J. Appl. Poult. Res.* 22, 47–54. doi: 10.3382/japr.2012-00575
- Ostojic, S. M. (2015). Guanidinoacetic acid as a performance-enhancing agent. *Amino Acids* 48, 1867–1875. doi: 10.1007/s00726-015-2106-y
- Ostojic, S. M., Niess, B., Stojanovic, M., and Obrenovic, M. (2013). Creatine metabolism and safety profiles after six-week oral guanidinoacetic acid administration in healthy humans. *Int. J. Med. Sci.* 10, 141–147. doi: 10.7150/ijms.5125
- Savenije, B., Lambooj, E., Gerritzen, M., Venema, K., and Korf, J. (2002). Effects of feed deprivation and transport on preslaughter blood metabolites, early postmortem muscle metabolites, and meat quality. *Poult. Sci.* 81, 699–708. doi: 10.1093/ps/81.5.699
- Schwartzkopf-Genswein, K. S., Faucitano, L., Dadgar, S., Shand, P., Gonzalez, L. A., and Crowe, T. G. (2012). Road transport of cattle, swine and poultry in North America and its impact on animal welfare, carcass and meat quality: a review. *Meat Sci.* 92, 227–243. doi: 10.1016/j.meatsci.2012.04.010
- Shen, Q. W., Gerrard, D. E., and Du, M. (2008). Compound C, an inhibitor of AMP-activated protein kinase, inhibits glycolysis in mouse longissimus dorsi postmortem. *Meat Sci.* 78, 323–330. doi: 10.1016/j.meatsci.2007.06.023
- Speer, N. C., Slack, G., and Troyer, E. (2001). Economic factors associated with livestock transportation. *J. Anim. Sci.* 79(Suppl._E), E166–E170. doi: 10.2527/jas2001.79E-SupplE166x
- Tossenberger, J., Rademacher, M., Németh, K., Halas, V., and Lemme, A. J. P. S. (2016). Digestibility and metabolism of dietary guanidino acetic acid fed to broilers. *Poult. Sci.* 95, 2058–2067. doi: 10.3382/ps/pew083
- Voslárova, E., Chloupek, P., Vosmerova, P., Chloupek, J., Bedanova, I., and Vecerek, V. (2011). Time course changes in selected biochemical indices of broilers in response to pretransport handling. *Poult. Sci.* 90, 2144–2152. doi: 10.3382/ps.2011-01473
- Wang, L. S., Shi, B. M., Shan, A. S., and Zhang, Y. Y. (2012). Effects of guanidinoacetic acid on growth performance, meat quality and antioxidation in growing-finishing pigs. *J. Anim. Vet. Adv.* 11, 631–636. doi: 10.3923/javaa.2012.631.636
- Wang, X., Li, J., Cong, J., Chen, X., Zhu, X., Zhang, L., et al. (2017). Preslaughter transport effect on broiler meat quality and postmortem glycolysis metabolism of muscles with different fiber types. *J. Agric. Food Chem.* 65, 10310–10316. doi: 10.1021/acs.jafc.7b04193
- Xing, T., Xu, X., Jiang, N., and Deng, S. (2016). Effect of transportation and pre-slaughter water shower spray with resting on AMP-activated protein kinase, glycolysis and meat quality of broilers during summer. *Anim. Sci. J.* 87, 299–307. doi: 10.1111/asj.12426
- Yue, H. Y., Zhang, L., Wu, S. G., Xu, L., Zhang, H. J., and Qi, G. H. (2010). Effects of transport stress on blood metabolism, glycolytic potential, and meat quality in meat-type yellow-feathered chickens. *Poult. Sci.* 89, 413–419. doi: 10.3382/ps.2009-00550
- Zhang, L., Li, J. L., Gao, T., Lin, M., Wang, X. F., Zhu, X. D., et al. (2014). Effects of dietary supplementation with creatine monohydrate during the finishing period on growth performance, carcass traits, meat quality and muscle glycolytic potential of broilers subjected to transport stress. *Animal* 8, 1955–1962. doi: 10.1017/S1751731114001906
- Zhang, L., Li, J. L., Wang, X. F., Zhu, X. D., Gao, F., and Zhou, G. H. (2019). Attenuating effects of guanidinoacetic acid on preslaughter transport-induced muscle energy expenditure and rapid glycolysis of broilers. *Poult. Sci.* 98, 3223–3232. doi: 10.3382/ps/pez052
- Zhang, L., Wang, X., Li, J., Zhu, X., Gao, F., and Zhou, G. (2017). Creatine monohydrate enhances energy status and reduces glycolysis via inhibition of AMPK pathway in pectoralis major muscle of transport-stressed broilers. *J. Agric. Food Chem.* 65, 6991–6999. doi: 10.1021/acs.jafc.7b02740
- Zhang, L., Yue, H. Y., Zhang, H. J., Xu, L., Wu, S. G., Yan, H. J., et al. (2009). Transport stress in broilers: I. Blood metabolism, glycolytic potential, and meat quality. *Poult. Sci.* 88, 2033–2041. doi: 10.3382/ps.2009-00128

Conflict of Interest: The authors declare that the research was conducted in the absence of any commercial or financial relationships that could be construed as a potential conflict of interest.

Copyright © 2021 Zhang, Liu, He, Song, Hao, Xie, Li, Liu and Sun. This is an open-access article distributed under the terms of the Creative Commons Attribution License (CC BY). The use, distribution or reproduction in other forums is permitted, provided the original author(s) and the copyright owner(s) are credited and that the original publication in this journal is cited, in accordance with accepted academic practice. No use, distribution or reproduction is permitted which does not comply with these terms.



Aerobic and Anaerobic Biodegradability of Organophosphates in Activated Sludge Derived From Kitchen Garbage Biomass and Agricultural Residues

Xingfeng Yang^{1,2}, Deling Fan², Wen Gu², Jining Liu², Lili Shi², Zhi Zhang^{1*}, Linjun Zhou^{2*} and Guixiang Ji²

¹ College of Modern Agriculture and Ecological Environment, Heilongjiang University, Harbin, China, ² Nanjing Institute of Environmental Science, Ministry of Ecology and Environment, Nanjing, China

OPEN ACCESS

Edited by:

Xin Zhou,
Nanjing Forestry University, China

Reviewed by:

Wenhui Geng,
North Carolina State University,
United States
Yingwen Chen,
Nanjing Tech University, China

*Correspondence:

Zhi Zhang
dr_zhangzhi@163.com
Linjun Zhou
zhoulj@nies.org

Specialty section:

This article was submitted to
Bioprocess Engineering,
a section of the journal
Frontiers in Bioengineering and
Biotechnology

Received: 03 January 2021

Accepted: 25 January 2021

Published: 17 February 2021

Citation:

Yang XF, Fan DL, Gu W, Liu JN, Shi LL, Zhang Z, Zhou LJ and Ji GX (2021) Aerobic and Anaerobic Biodegradability of Organophosphates in Activated Sludge Derived From Kitchen Garbage Biomass and Agricultural Residues. *Front. Bioeng. Biotechnol.* 9:649049. doi: 10.3389/fbioe.2021.649049

Organophosphates (also known as organophosphate esters, OPEs) have in recent years been found to be significant pollutants in both aerobic and anaerobic activated sludge. Food waste, such as kitchen garbage and agricultural residues, can be used as co-substrates to treat the active sludge in sewage treatment plants (STPs). We investigated the biodegradability of nine OPEs derived from kitchen garbage biomass and agricultural residues under different conditions. Under anaerobic conditions, the rate of removal of triphenyl ester OPEs was significantly higher than that of chloride and alkyl OPEs. The addition of FeCl₃ and Fe powder increased the rate of degradation of triphenyl ester OPEs, with a DT₅₀ for triphenyl ester OPEs of 1.7–3.8 d for FeCl₃ and 1.3–4.7 d for Fe powder, compared to a DT₅₀ of 4.3–6.9 d for the blank control. Addition of an electron donor and a rhamnolipid increased the rate of removal of chlorinated OPEs, with DT₅₀ values for tris(2-carboxyethyl)phosphine (TCEP) and tris(1,3-dichloroisopropyl)phosphate (TDCPP) of 18.4 and 10.0 d, respectively, following addition of the electron donor, and 13.7 and 3.0 d, respectively, following addition of the rhamnolipid. However, addition of an electron donor, electron acceptor, surfactant, and Fe powder did not always increase the degradation of different kinds of OPEs, which was closely related to the structure of the OPEs. No treatment increased the removal of alkyl OPEs due to their low anaerobic degradability. Tween 80, a non-ionic surfactant, inhibited anaerobic degradation to some degree for all OPEs. Under aerobic conditions, alkyl OPEs were more easily degraded, chlorinated OPEs needed a long adaptation period to degrade and finally attain a 90% removal rate, while the rates of degradation of triphenyl ester OPEs were significantly affected by the concentration of sludge. Higher sludge concentrations help microorganisms to adapt and remove OPEs. This study provides new insights into methods for eliminating emerging pollutants using activated sludge cultured with kitchen garbage biomass and agricultural residues.

Keywords: organophosphates, biomass, biodegradation, aerobic, anaerobic, active sludge, kitchen garbage

INTRODUCTION

Sewage treatment plants (STPs) are the major secondary sources of emerging pollutants, which may not be completely removed or degraded (Styszko et al., 2020). Many pollutants pass through STPs owing to their persistence or continuous release or to the inefficient operation of STPs (Saxena et al., 2021).

The aerobic and anaerobic biodegradation of these pollutants are the major removal mechanisms employed in STPs. However, many full-scale STPs operate with low efficiencies, due to an unbalanced nutrient ratio, deficiencies in essential elements, an accumulation of volatile fatty acids, and the presence of process inhibitors (Tonanzi et al., 2020).

To overcome these problems, food waste, such as kitchen garbage with a high C/N ratio, is generally used as a co-substrate with municipal waste activated sludge. This method can overcome the difficulties associated with treating nutrient-deficient activated sludge, to adjust its unbalanced C/N ratio, and to increase buffer capacity, dilute toxic compounds, and adjust micro- and macro-nutrient availability (Z.-l. Zhang et al., 2013).

Organophosphoric acid esters (OPEs), one of the most commonly used organophosphorus flame retardants (Eede et al., 2012), have been used as plasticizers and flame retardants in plastics, electronic equipment, furniture, textiles, construction, and transport (Martínez-Carballo et al., 2007). **Table 1** lists the various types of OPEs and specific information related to them. OPEs have been confirmed to possess both acute and chronic toxicities, including eye and skin irritation, neurotoxicity, reproductive toxicity, endocrine disruptive effects, carcinogenicity (Castro-Jimenez et al., 2014), and environmental biological toxicity and risk (Kai, 2005). OPEs from urban, industrial, agricultural, street-flushed sewage, and atmospheric dry and wet depositions (Tappe et al., 2002; Ratola et al., 2012; O'Brien et al., 2015; Saini et al., 2016) all eventually end up in STPs.

Kim et al. (2017) compared the entry of OPEs into U.S. STPs with reported production and showed that the mass loads of triphenyl phosphate (TPHP), tris(1-chloro-2-propyl) phosphate (TCIPP), tris(1,3-dichloro-2-propyl) phosphate (TDCIPP), and tri(*n*-butyl) phosphate (TNBP) in STPs were 1.3–2.8% of the annual output. Anneli et al. (2005) showed that 15% of domestic OPE usage in Sweden is discharged into STPs. Therefore, the

study of OPE biodegradation in both aerobic and anaerobic processes in STPs is vitally important.

There are few studies that have examined the best conditions of oxygen availability for OPE degradation, and most have focused mainly on the investigation of the rate of removal of OPEs from STPs. Only a few studies have pointed out that the degradation of non-chlorine OPEs occurs mainly in aerobic aeration tanks. In addition, there was no obvious removal of alkyl OPEs under anaerobic conditions (Kawagoshi and Fukunaga, 1994). The study of suitable oxygen conditions for the degradation of different OPEs has practical significance for guiding the clean-up and maintenance of STPs.

The addition of electron donors and electron acceptors is also important for the biodegradation of organophosphate pollutants (Kieft et al., 1999; Gou et al., 2019). The biodegradation of chemicals depends largely on the availability of electron receptors and their respective energy yields. The removal of chemical substances can be improved by electron receptor species such as O₂, Fe³⁺, CO₂, CO, NO₃, NO₂, NO, N₂O, SO₄²⁻, and S (Hägglom and Young, 1999; Amend and Shock, 2001; Wu et al., 2017). In aerobic environments, microorganisms generally use oxygen as an electron receptor to accelerate the biodegradation process. In anaerobic degradation, however, because of the lack of oxygen as electron acceptor, microorganisms must use alternative electron receptors such as sulfate, nitrate, and trivalent iron, which are usually supplied more economically than oxygen (Varjani and Upasani, 2017).

In addition to the need for electron acceptors, methanogens rely on electron donors and matrixes to degrade these complex organic chemicals, such as H₂, Fe²⁺, H₂S, sulfide minerals, CH₄, various mono- and dihydroxyl carboxylic acids, alcohols, amino acids, and complex organic substrates (Grishchenkov et al., 2000). Electron donors, also known as co-matrixes, are added primarily as nutrients for anaerobic treatment, contaminants are generally removed by co-metabolism, sufficient nutrient substrates are made available, and anaerobic sludge can produce sufficient enzymes to degrade organic pollutants (Wei et al., 2010; Cao et al., 2012).

Zero-valent iron and surfactants can also be added to the anaerobic environment to promote anaerobic biodegradation. Because of its high reduction activity, zero-valent iron is often used to treat all kinds of pollutants in water. Zero-valent iron can provide electrons for microorganisms and keep the redox

TABLE 1 | Physicochemical properties of nine types of OPEs.

Compound	Abbreviation	CAS number	Chemical formula	Molecular weight	lg <i>K</i> _{oc}	lg <i>K</i> _{ow}
Tripropyl phosphate	TPrP	513-08-6	C ₉ H ₂₁ O ₄ P	224.23	2.58	1.87
Tri-isobutyl phosphate	TiBP	126-71-6	C ₁₂ H ₂₇ O ₄ P	266.31	3.14	3.60
Tributyl phosphate	TBP	126-73-8	C ₁₂ H ₂₇ O ₄ P	266.31	3.37	4.00
Tris(2-chloroethyl) phosphate	TCEP	115-96-8	C ₆ H ₁₂ Cl ₃ O ₄ P	285.49	2.58	1.44
Tris(1,3-dichloro-2-propyl) phosphate	TDCP	13674-87-8	C ₉ H ₁₅ Cl ₆ O ₄ P	430.9	4.04	3.65
Triphenyl phosphate	TPhP	115-86-6	C ₁₈ H ₁₅ O ₄ P	326.28	3.47	4.59
Tri- <i>o</i> -cresyl phosphate	<i>o</i> -TTP	78-30-8	C ₂₁ H ₂₁ O ₄ P	368.36	4.67	5.11
Tri- <i>m</i> -tolyl phosphate	<i>m</i> -TTP	563-04-2	C ₂₁ H ₂₁ O ₄ P	368.36	4.64	6.43
Tri- <i>p</i> -tolyl phosphate	<i>t</i> -TTP	78-32-0	C ₂₁ H ₂₁ O ₄ P	368.36	4.20	6.34

potential of the anaerobic environment low (Völker et al., 2017). Studies have shown that the presence of iron chips ($1 \text{ g}\cdot\text{L}^{-1}$) in water can significantly increase the anaerobic degradation of Chlorpyrifos and Bisphenol A (Shi et al., 2019b; Yang et al., 2019). Iron is also a major protein cofactor that is essential for most organisms and increases the production of degrading enzymes (Beauchene et al., 2015). Because of its advantages in accelerated hydrolysis, fermentation, and anaerobic digestion, zero-valent iron increases the abundance of methanogens and promotes methane production (Wei et al., 2018; Pan et al., 2019).

Surfactants can also increase the rate of degradation of organic pollutants, which can overcome the diffusion limitation of substrates to cells, reduce the tension and viscosity of the water interface effectively, and increase bioavailability. There are many kinds of surfactants, including biological, anionic, and non-ionic surfactants. Biosurfactants are produced mainly by microorganisms, which contribute to the desorption of soil pollutants and their migration to microbial cells, resulting in the reconstruction of their surfaces and a change in bioavailability of biodegradable compounds (Zdarta et al., 2018). The non-ionic surfactant Tween 80 and the rhamnolipid biosurfactant both enhance the enzyme activities of amylase, carboxymethyl cellulase, and xylanase effectively (Zeng et al., 2006), improving enzyme stability and increasing the enzymatic reaction rate (Mo et al., 2008).

Most studies in this area have examined the removal of emerging pollutants in unconditioned active sludge from STPs. However, there is a lack of information regarding the role of active sludge cultured with kitchen garbage and agricultural residues. In this study, the biodegradability of nine OPEs in both aerobic and anaerobic activated sludge derived from kitchen garbage biomass and agricultural residues was investigated under different conditions, including oxygen availability and addition of electron donors, electron acceptors, or surfactants, etc. The results were compared in order to determine the optimal degradation conditions, which will provide a new perspective on the effect of activated sludge cultured with kitchen garbage and agricultural residues to enable the elimination of emerging pollutants.

MATERIALS AND METHODS

Chemicals

The OPE standard substances, including trimethyl phosphate (TMP), tripropyl phosphate (TPrP), tri-isobutyl phosphate (TiBP), tributyl phosphate (TBP), Tris(2-chloroethyl) phosphate (TCEP), tris(1,3 dichloropropyl) phosphate (TDCPP), triphenyl phosphate (TPhP), *o*-trimethylphenol phosphate (*o*-TT), tri-*m*-cresyl phosphate (*m*-TTP), tri-*p*-cresyl phosphate (*p*-TTP), were purchased from Balinway Chemical Reagent Co., Ltd. (China). The physicochemical properties of the nine kinds of OPEs are listed in **Table 1**.

HPLC-grade *n*-hexane (Hex), ethyl acetate (EtAc), and acetone (ACE) were provided by Merck & Co. (Darmstadt, Germany).

NaSO_4 (AR), NaCl (GR), KH_2PO_3 (GR), $\text{Na}_2\text{HPO}_4\cdot 12\text{H}_2\text{O}$ (AR), NH_4Cl (GR), NaNO_3 (AR), $\text{CaCl}_2\cdot 2\text{H}_2\text{O}$ (GR), $\text{MgCl}_2\cdot 6\text{H}_2\text{O}$ (AR), Fe powder, Tween 80, FeCl_3 (GR), NaHCO_3 (GR), rhamnolipid, $\text{FeCl}_2\cdot 4\text{H}_2\text{O}$ (AR), $\text{Na}_2\text{S}\cdot 9\text{H}_2\text{O}$ (GR), HgSO_4 (GR), and resazurin ($\text{C}_{12}\text{H}_7\text{NO}_4$) were purchased from China National Pharmaceutical Group Corporation (Sinopharm, Beijing, China).

Sample Collection

Both aerobic and anaerobic activated sludges were collected from aerobic and anaerobic ponds of the Nanjing Chengdong STP. The treatment process was A^2/O and the volume of sewage was $350,000 \text{ m}^3$, serving approximately 500,000 people.

The kitchen garbage and agricultural residues obtained from school canteens were composed of rice, meat, and small quantities of vegetables. The garbage was chopped and then diluted to 82.75 g L^{-1} with tap water. A substrate blend of waste activated sludge and kitchen garbage was prepared in a ratio of 5:1 by volume. The blended sludges were cultivated under aerobic and anaerobic conditions at room temperature.

Biodegradation Experiments

The medium was prepared with deionized water, to which was added $0.27 \text{ g}\cdot\text{L}^{-1}$ anhydrous potassium dihydrogen phosphate (KH_2PO_4), $1.12 \text{ g}\cdot\text{L}^{-1}$ disodium hydrogen phosphate dodecahydrate ($\text{Na}_2\text{HPO}_4\cdot 12\text{H}_2\text{O}$), $0.53 \text{ g}\cdot\text{L}^{-1}$ ammonium chloride (NH_4Cl), $0.075 \text{ g}\cdot\text{L}^{-1}$ calcium chloride dihydrate ($\text{CaCl}_2\cdot 2\text{H}_2\text{O}$), and $0.10 \text{ g}\cdot\text{L}^{-1}$ magnesium chloride hexahydrate ($\text{MgCl}_2\cdot 6\text{H}_2\text{O}$).

The aerobic and anaerobic sludge cultures were dispersed in the medium so as to prepare sludge suspensions whose pH was adjusted to 7 with NaOH.

OPE Volatilization Experiments

A 3 L wash bottle was loaded with 1.5 L of deionized water. Nine types of OPEs listed in **Table 1** were added to a wash bottle to a final concentration of $1 \text{ mg}\cdot\text{L}^{-1}$. The air inlet of the wash bottle was connected to an aeration device set at a flow rate of $500 \text{ ml}\cdot\text{min}^{-1}$. The outlet of the aeration device was connected to a wash bottle containing methanol to absorb the volatile OPEs.

Aerobic Biodegradation

An OPE stock solution was added to an Erlenmeyer flask to a concentration of $0.5 \text{ mg}\cdot\text{L}^{-1}$ and the flask was placed in a fume hood to volatilize the acetone to dryness. The sludge suspension was added so that the sludge concentration was $1 \text{ g}\cdot\text{L}^{-1}$ for the low sludge concentration treatment and $10 \text{ g}\cdot\text{L}^{-1}$ for the high sludge concentration treatment, with 10 parallel treatments for each concentration. After the addition was complete, the rubber plug was covered and kept aerated and placed on a shaker for culture at 30°C . Samples were collected and analyzed intervals.

Anaerobic Biodegradation

The OPE stock solution was added to the prepared anaerobic fermentation bottle, the concentration was adjusted to $0.5 \text{ mg}\cdot\text{L}^{-1}$, and the bottle was then placed under the ventilation cabinet until the acetone was volatilized to dryness. The

configured medium was subjected to eight different treatments, designated b, c, d, e, f, g, h, and i. Then, the sludge and additional agents were added to each treatment, as given in **Table 2** (reducing iron powder, which is insoluble in water, was added separately to 12 vials). Each treatment had 12 bottles and a final volume of 100 mL. Following filling of each anaerobic fermentation bottle, nitrogen was blown through each one for 5 min to remove all traces of oxygen. Following this treatment, 0.04 g·L⁻¹ ferrous chloride (FeCl₂·4H₂O) and 0.20 g·L⁻¹ nine-water sodium sulfide (Na₂S·9H₂O) were added to each vial, and then 0.002 g·L⁻¹ resazurin was added as an oxygen indicator. Under abiotic control, the medium was heated to 100°C. Then, 1 g·L⁻¹ mercury sulfate was added after cooling to kill the microorganisms in the medium. All of the anaerobic fermentation bottles were then placed in an incubator at 35°C and shaken 1–2 times a day to release the gas produced by anaerobic fermentation. Samples were taken at regular intervals for analysis.

Analytical Methods

Samples of water (10 mL) were taken in the volatility experiments, to which were added 0.5 g of sodium chloride and 10 mL of organic solvents (*n*-hexane and ethyl acetate 1:1). The samples were then shaken for 3 min. The cap on the bottle was opened and the water and organic phases allowed to settle out. The upper organic phase was then sampled (10 mL) with a pipette, dehydrated with anhydrous sodium sulfate, and finally filtered through filter paper. Following filtering through a 0.22 μm microporous filter membrane, the samples were analyzed on a TSQ™ 9000 Triple Quadrupole

GC-MS/MS System (Thermo Fisher Scientific, Waltham, MA, United States). The methanol receiving tail gas was also analyzed by similar means.

The samples of aerobic and anaerobic biodegradation were poured into a separate funnel, to which 3 g of sodium chloride was added, and extracted twice with 20 mL of solvent (*n*-hexane and ethyl acetate 1:1). Following dehydration with anhydrous sodium sulfate and filtration through filter paper, the organic phase was adjusted to 50 mL with *n*-hexane. The sample was then analyzed by GC-MS/MS.

The chromatographic column was a HP-5MS (30 m × 0.25 mm × 0.25 μm). The heating procedure was as follows: the starting temperature was set at 50°C and maintained for 2 min, then heated to 150°C at a rate of 20°C min⁻¹ and maintained there for 4 min, then heated to 250°C at 25°C·min⁻¹, maintained there for 1 min, then heated to 280°C at rate of 5°C·min⁻¹ and maintained there for 3 min. Electron collision ionization (EI) sources and selected reaction monitoring (SRM) were employed. The carrier gas was high-purity helium gas, using pulse no shunt injection. The linear correlation between the standard curves of the nine OPEs was good, with an *R*² value above 0.993. The detection limits of the OPEs were in the range 0.01–1.5 μg·L⁻¹, and the quantitative limits were in the range 0.01–4.6 μg·L⁻¹.

Statistical Analyses

The data were collected and analyzed using Microsoft Excel 2010 (Microsoft Corporation, Redmond, WA, United States).

RESULTS

In the abiotic treatment, the OPE concentration remained basically unchanged, and degradation basically did not occur.

OPE Volatility Experiments

The volatility test results are shown in **Figure 1**. Under aeration conditions, the different types of OPEs in water showed different volatilities. The triphenyl ester OPEs (TPhP, *m*-TTP, *o*-TTP, and *p*-TTP) had a certain volatility, reaching 10–20% volatilization at 120 h. Alkyl and chlorinated OPEs were almost non-volatile.

Anaerobic Treatment

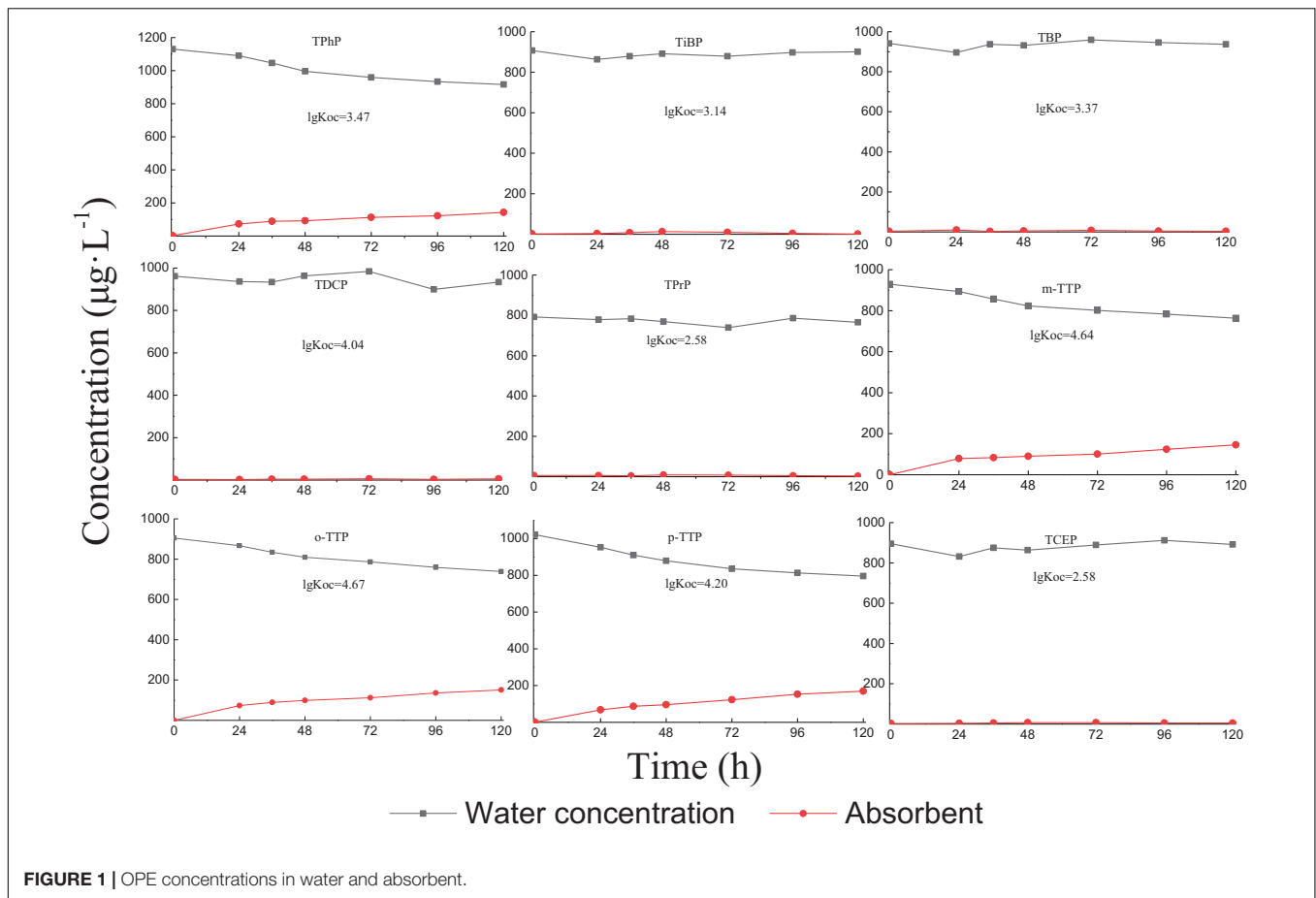
Resazurin was added as an oxygen indicator in the anaerobic treatment. During the test, none of the anaerobic fermentation bottles showed any color, so they met the conditions of complete anaerobic fermentation. When gas was released each day, a large volume of methane was released, which also indicated that the microorganisms were metabolically active and growing normally.

Degradation of Triphenyl Ester OPEs

Four triphenyl ester OPEs showed similar patterns of removal in the different treatments (**Figure 2**). Removal occurred mainly within 21 days of the start of the experiment. The rate of removal tended to be stable after 21 days. The triphenyl ester OPEs had high removal rates in the different treatments at 21 days; that for TPhP was 83–93%, that for *m*-TTP was 70–88%, that for

TABLE 2 | Test treatments.

Group	Treatment	Symbol	Sludge (g·L ⁻¹)	Addition of substances
Anaerobic	Biological control	b	3	–
	Electron donor	c	3	Sodium acetate: sodium propionate: sodium butyrate: sodium lactate = 1:1:1:1 (200 mmol·L ⁻¹)
	Electron receptor	d	3	NaNO ₃ = 20 mM
	Surfactants	e	3	Na ₂ SO ₄ = 20 mM, NaHCO ₃ = 20 mM
		f	3	FeCl ₃ = 20 mM, NaHCO ₃ = 20 mM
		g	3	Tween 80, CMC = 0.010 mM
	Reducing iron	h	3	Ribose glycolipid, CMC = 0.5 mM
		i	3	Reducing iron powder = 2 g·L ⁻¹
	Aerobic	Low sludge concentration	1 g·L ⁻¹	0.1
High sludge concentration		10 g·L ⁻¹	1	–
Abiotic control	–	AC	–	Mercury sulfate = 1 g·L ⁻¹



o-TTP was 55–75%, and that for *p*-TTP was 68–86%. When FeCl₃ (treatment f) and Fe (treatment i) were added, the degradation rate was increased compared with other treatments, and the final removal rate was also significantly higher than for the other treatments.

Kinetic curves for first-order degradation were used to fit the removal rates of the OPE (Table 3). The R^2 value was in the range 0.74–0.98. The DT₅₀ values of the triphenyl ester OPEs with added FeCl₃ (treatment f) were in the range 1.3–3.8 days, and with added Fe powder (treatment i) were 1.3–4.7 days, compare to a DT₅₀ of 4.3–6.9 days for the blank control (treatment b). The addition of either FeCl₃ or Fe powder increased the rate of degradation significantly. However, the other treatments did not have a significant effect on the degradation of the triphenyl ester OPEs.

Degradation of Chlorinated OPEs

Compared with the triphenyl ester OPEs, the degradation of chlorinated OPEs in the different treatments was slower under anaerobic conditions, and the removal of chlorinated OPEs failed to reach 80% even after 60 days. The results of these treatments are shown in Figure 3. Different treatments had significant positive or negative effects on the degradation of chlorinated OPEs. Among them, the final rate of degradation for TCEP and TDCP in rhamnolipid (treatment h) was increased by about 10%

compared to the control (treatment b). The removal rate of TCEP and TDCP was also significantly increased in treatment c of the electron donor (sodium acetate + sodium propionate + sodium butyrate + sodium lactate). At 60 days, the removal rate of TCEP was increased by 28%, and the removal rate of TDCP was increased by 31%. The effect of adding Na₂SO₄ (treatment e) on the removal of the two chlorinated OPEs was different: the removal rate of TCEP was increased by approximately 30%, but the removal of TDCP was inhibited.

First-order kinetic curves were used to fit the rates of degradation of chlorinated OPEs, and the results are given in Table 4. These results show that R^2 was in the range 0.84–0.99. In the blank control (treatment b), the DT₅₀ values of TCEP and TDCP were 38.2 and 12.3 days, respectively. In treatment c, the DT₅₀ value of TCEP and TDCP were reduced to 18.4 and 10.0 days, respectively. In treatment h, the DT₅₀ values of TCEP and TDCP decreased to 13.7 and 3.0 days, respectively. The results showed that the addition of an electron donor (treatment c) and rhamnolipid (treatment h) significantly increased the rate of degradation of chlorinated OPEs.

The addition of Na₂SO₄ (treatment e) had different effects on the two chlorinated OPEs. The DT₅₀ of TCEP was reduced to 33.9 days, while that of TDCP was increased to 33.3 days. Other treatments, including NaNO₃ as electron receptor (treatment d) and FeCl₃ as electron receptor (treatment f), non-ionic

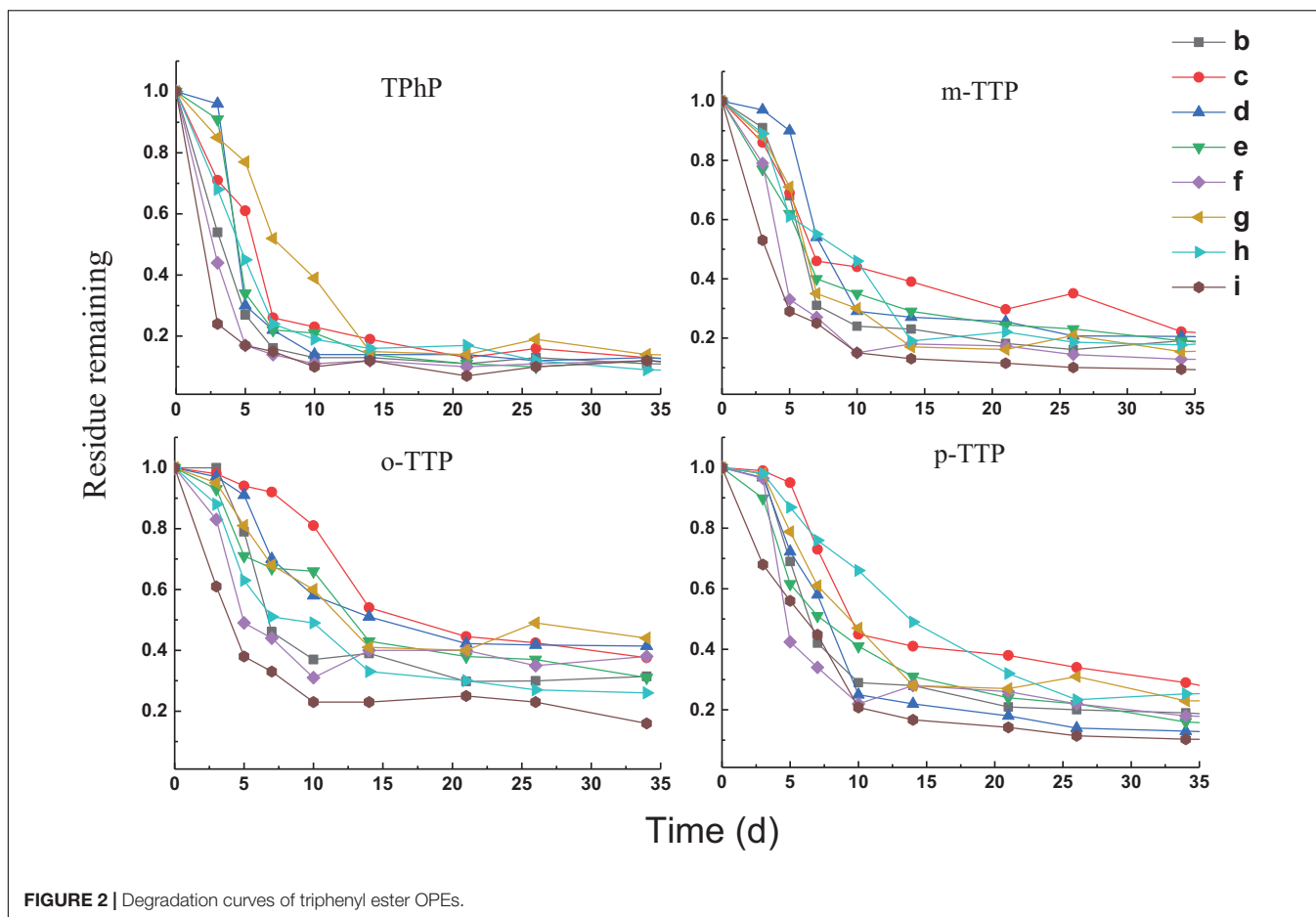


FIGURE 2 | Degradation curves of triphenyl ester OPEs.

TABLE 3 | Degradation rates and DT₅₀ values of triphenyl ester OPEs.

Treatment	TPhP			m-TTP			o-TTP			p-TTP			Promoting effect
	k (d ⁻¹)	R ²	DT ₅₀ (d)	k (d ⁻¹)	R ²	DT ₅₀ (d)	k (d ⁻¹)	R ²	DT ₅₀ (d)	k (d ⁻¹)	R ²	DT ₅₀ (d)	
b	0.16	0.74	4.3	0.11	0.77	6.0	0.15	0.87	4.8	0.10	0.78	6.9	/
c	0.21	0.89	3.4	0.13	0.92	5.3	0.05	0.94	14.2	0.11	0.77	6.3	±
d	0.20	0.84	3.4	0.11	0.89	6.2	0.10	0.94	6.9	0.11	0.93	6.1	±
e	0.24	0.80	2.8	0.16	0.96	4.3	0.09	0.97	7.9	0.13	0.93	5.5	±
f	0.40	0.98	1.7	0.22	0.92	3.1	0.26	0.86	2.6	0.18	0.86	3.8	+
g	0.15	0.81	4.6	0.18	0.83	3.9	0.13	0.91	5.4	0.13	0.79	5.2	±
h	0.20	0.97	3.4	0.14	0.93	5.1	0.14	0.97	5.0	0.08	0.90	9.2	±
i	0.55	0.96	1.3	0.24	0.98	2.9	0.25	0.98	2.7	0.15	0.98	4.7	+

surfactants (treatment g), and reduced Fe powders (treatment i), all inhibited the degradation of chlorinated OPEs, which was very pronounced.

Degradation of Alkyl OPEs

The degradation curves of the three alkyl OPEs subjected to different treatments are shown in Figure 4. At the end of the test (100 days), the removal percentage of the three alkyl OPEs were below 78%. The removal percentage in the blank control (treatment b) was 67–75%, while the removal percentage in the electron donor (treatment c) and electron acceptor (treatments

d, e, and f) were 24–74%. Therefore, all of the treatments with addition of electron donor and electron acceptor inhibited the removal of alkyl OPEs.

First-order kinetic curves were used to fit the degradation rates of the alkyl OPEs, and the results are given in Table 5. The values of R² were in the range 0.79–0.97. In the blank control (treatment b), the DT₅₀ of TiBP, TBP, and TPrP were 11.8, 8.4, and 9.7 days, respectively. The removal of alkyl OPEs under the different treatments was more complicated, and all of the treatments failed to significantly improve the degree of removal. Treatment c (sodium acetate + sodium propionate + sodium

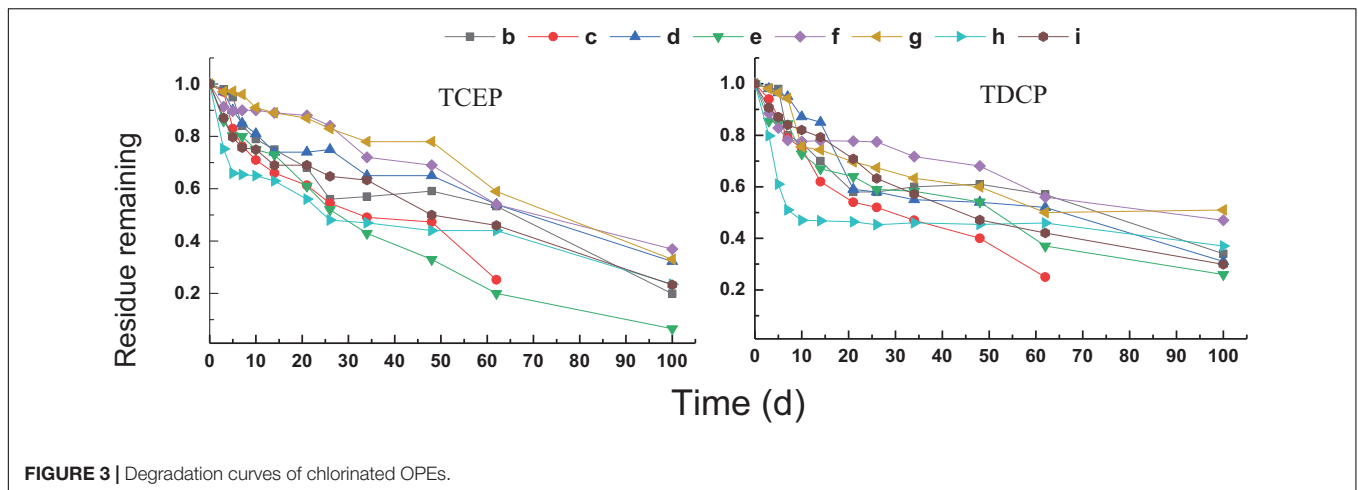


FIGURE 3 | Degradation curves of chlorinated OPEs.

butyrate + sodium lactate), treatment d (NaNO₃), and treatment e (Na₂SO₄) had an inhibitory effect on the removal of alkyl OPEs. The addition of FeCl₃ (treatment f) had an inhibitory effect on the removal of TiBP and TBP, but no inhibition of TPrP was observed. Tween 80 (treatment g) significantly inhibited the removal of TBP and TPrP, and the DT₅₀ increased to 36.7 and 43.7 days, respectively. However, the addition of the biological surfactant rhamnolipid (treatment h) had no significant effect on OPE removal. The addition of Fe powder (treatment i) inhibited the removal of TBP, increasing the DT₅₀ from 8.4 to 20.4 days, while Fe powder increased the removal of TiBP and TPrP slightly, reducing the DT₅₀ of TiBP from 11.8 to 6.8 days and that of TPrP from 9.7 to 5.8 days.

Aerobic Treatments

During the aerobic treatment, aeration was vigorous and the dissolved oxygen concentration was greater than 3 mg·L⁻¹, which met the requirements of aerobic degradation.

Aerobic Treatment of Triphenyl Ester OPEs

Figure 5 shows that the triphenyl ester OPEs were removed satisfactorily under aerobic conditions. The removal percentages of four OPEs were greater than 80% for both treatments at 35 days. The removal rate of OPEs in a sludge concentration

of 1 g·L⁻¹ was always higher than in a sludge concentration of 10 g·L⁻¹ up to 28 days. The removal of OPEs in a sludge concentration of 1 g·L⁻¹ was significantly greater than in a concentration of 10 g·L⁻¹, which may have been attributed to volatilization of the triphenyl ester OPEs. The higher sludge concentration resulted in more triphenyl ester OPEs being absorbed, and the removal by volatilization in the water phase was slowed down. With increasing hydrophobicity (sorption) of the OPE, the fraction of freely dissolved OPE present in the water phase available for degradation decreases, and therefore the overall rate constant should also decrease (Hansen et al., 2017).

In contrast, the removal percentage increased rapidly in the sludge concentration of 10 g·L⁻¹ after 28 days, and the removal percentage was higher than that in the sludge concentration of 1 g·L⁻¹. This may have been due to the fact that, after a period of adaptation, a high sludge concentration adapts to triphenyl ester OPEs faster than a low sludge concentration.

Aerobic Treatment of Chlorinated OPEs

The degradation curves of chlorinated OPEs in aerobic sludge are shown in Figure 6. The removal percentages of TCEP and TDCP were different from those of triphenyl esters OPEs. In the treatment of a sludge concentration of 1 g·L⁻¹, the removal percentages of the two chlorinated OPEs were low, with almost no removal occurring. In the sludge with 10 g·L⁻¹, there was almost no removal after 16 days. Thereafter, the residual concentration began to decrease, and the removal percentage reached 90% by 35 days, indicating that sludge acclimation had been completed and chlorinated OPEs had begun to biodegrade.

Aerobic Treatment of Alkyl OPEs

The degradation curves of the alkyl OPEs in aerobic sludge are shown in Figure 7. All of the alkyl OPEs showed similar removal behavior, and the aerobic sludge was able to remove alkyl OPEs efficiently. The degree of removal of the three alkyl OPEs reached 90% in the 10 g·L⁻¹ sludge concentration after 35 days. The removal percentages in the sludge concentration of 1 g·L⁻¹ were slightly lower, namely, 84% for TiBP, 76% for TBP, and 51% for TPrP.

TABLE 4 | Degradation rates and DT₅₀ values of chlorinated OPEs.

Treatment	TCEP			TDCP			Promoting effect
	k (d ⁻¹)	R ²	DT ₅₀ (d)	k (d ⁻¹)	R ²	DT ₅₀ (d)	
b	0.02	0.89	38.2	0.06	0.85	12.3	/
c	0.04	0.99	18.4	0.07	0.92	10.0	+
d	0.01	0.93	66.8	0.03	0.92	21.4	-
e	0.02	0.99	33.9	0.02	0.94	30.3	±
f	0.02	0.96	43.7	0.01	0.86	65.4	-
g	0.01	0.97	49.0	0.05	0.94	14.9	-
h	0.05	0.84	13.7	0.23	0.95	3.0	+
i	0.01	0.93	59.1	0.02	0.99	31.6	-

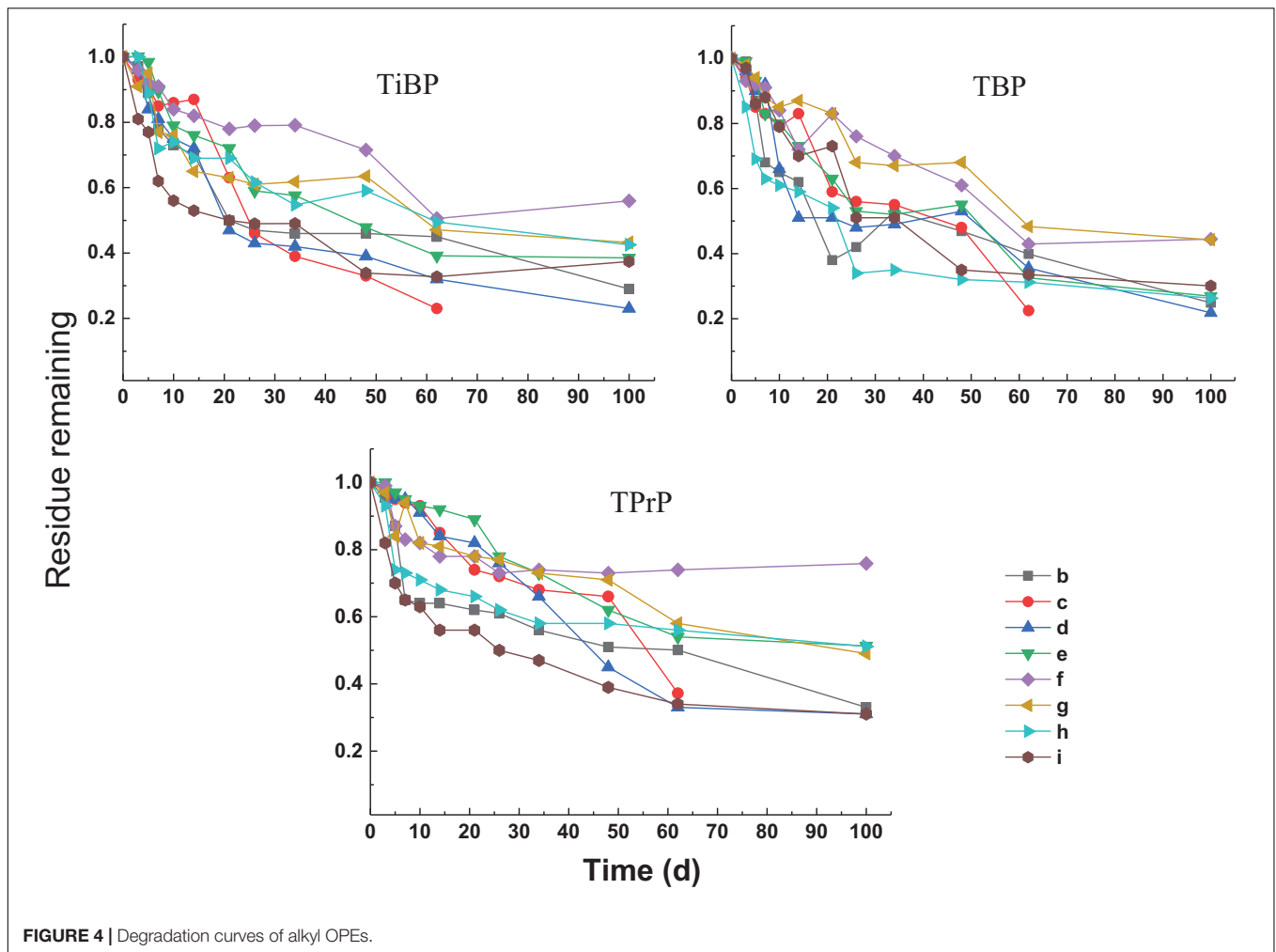


FIGURE 4 | Degradation curves of alkyl OPEs.

TABLE 5 | Degradation rates and DT₅₀ values of alkyl OPEs.

Treatment	TiBP			TBP			TPrP			Promoting effect
	<i>k</i> (d ⁻¹)	<i>R</i> ²	DT ₅₀ (d)	<i>k</i> (d ⁻¹)	<i>R</i> ²	DT ₅₀ (d)	<i>k</i> (d ⁻¹)	<i>R</i> ²	DT ₅₀ (d)	
b	0.06	0.95	11.8	0.08	0.87	8.4	0.07	0.83	9.7	/
c	0.02	0.94	32.1	0.02	0.93	46.0	0.02	0.93	38.4	–
d	0.05	0.97	14.7	0.06	0.86	11.8	0.03	0.87	26.2	–
e	0.04	0.97	19.7	0.03	0.95	21.5	0.02	0.96	39.4	–
f	0.02	0.88	34.1	0.02	0.91	37.8	0.09	0.79	7.8	–
g	0.06	0.88	11.7	0.02	0.94	36.7	0.02	0.91	43.7	–
h	0.06	0.89	11.9	0.07	0.94	9.7	0.11	0.91	6.4	±
i	0.10	0.93	6.8	0.03	0.96	20.4	0.12	0.88	5.8	±

DISCUSSION

Comparison of the Results Under Aerobic and Anaerobic Conditions

Under anaerobic conditions, the removal percentage of triphenyl ester OPEs was significantly higher than that of chlorinated and alkyl OPEs, indicating that triphenyl ester OPEs were more prone to anaerobic biodegradation. Facultative or specific anaerobes

can couple various electron receptors to mineralize aromatic compounds through anaerobic respiration and fermentation, with higher degrees of removal (Carmona et al., 2009; Grishchenkov et al., 2000). Margot et al. (2015)'s studies have also pointed out that triphenyl ester OPEs can be successfully removed (>70%) by anaerobic degradation in STPs. The removal percentage of chlorinated OPEs was low, which may have been due to the strong electron absorption effect of chlorine atoms,

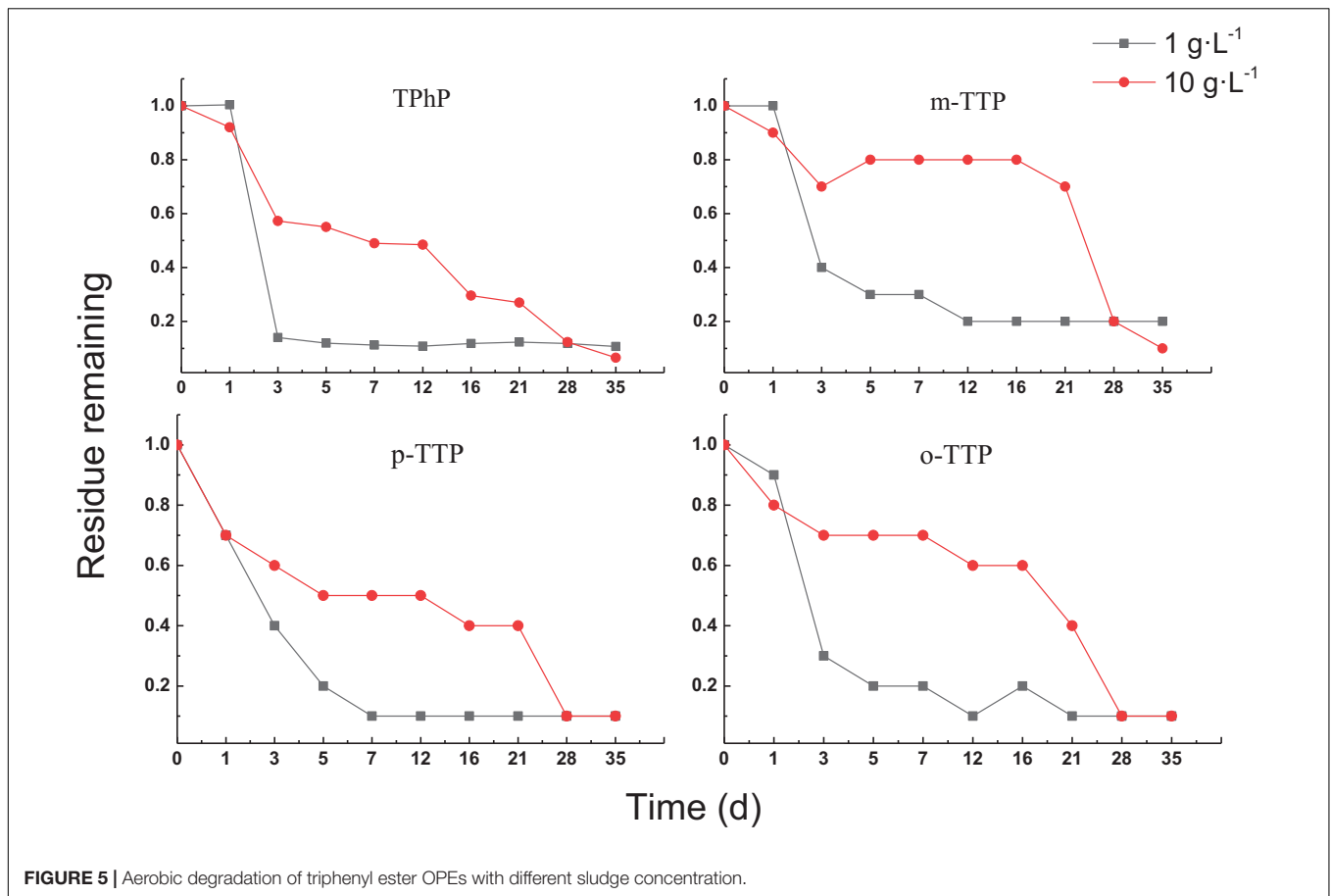


FIGURE 5 | Aerobic degradation of triphenyl ester OPEs with different sludge concentration.

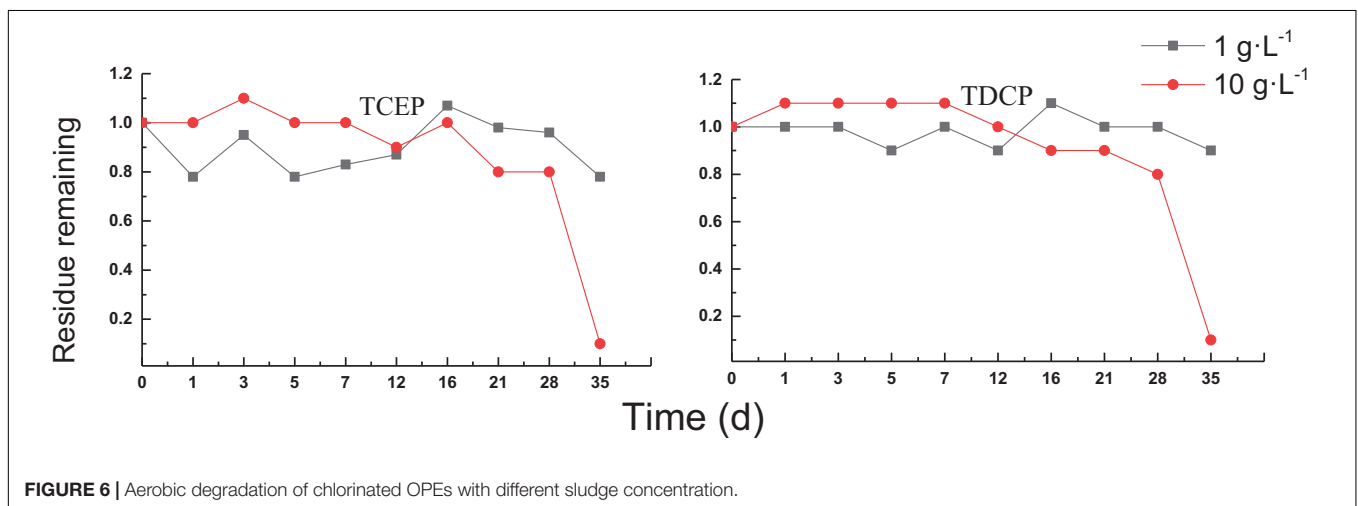


FIGURE 6 | Aerobic degradation of chlorinated OPEs with different sludge concentration.

which reduced the electrophilic properties of relevant enzymes (Pang et al., 2018). Studies have also shown that TCEP and TCEP in chlorinated OPEs are non-degradable and persistent in underground aquifers (Regnery et al., 2011). Kawagoshi and Fukunaga (1994) have also pointed out that there was no significant removal of alkyl OPEs under anaerobic conditions.

The removal percentages of the three types of OPEs in aerobic sludge were significantly higher than those in anaerobic

sludge, which may have been due to the easier removal of OPEs under aerobic reactions. Fries and Puttmann (2003) pointed out that aerobic removal of OPEs is greater than that of anaerobic removal. The most rapid and complete degradation of most pollutants is achieved under aerobic conditions (Mezzanotte et al., 2003; Fritsche and Hofrichter, 2005). The rate of degradation of chemicals under aerobic and anaerobic conditions is related mainly to enzymes and their

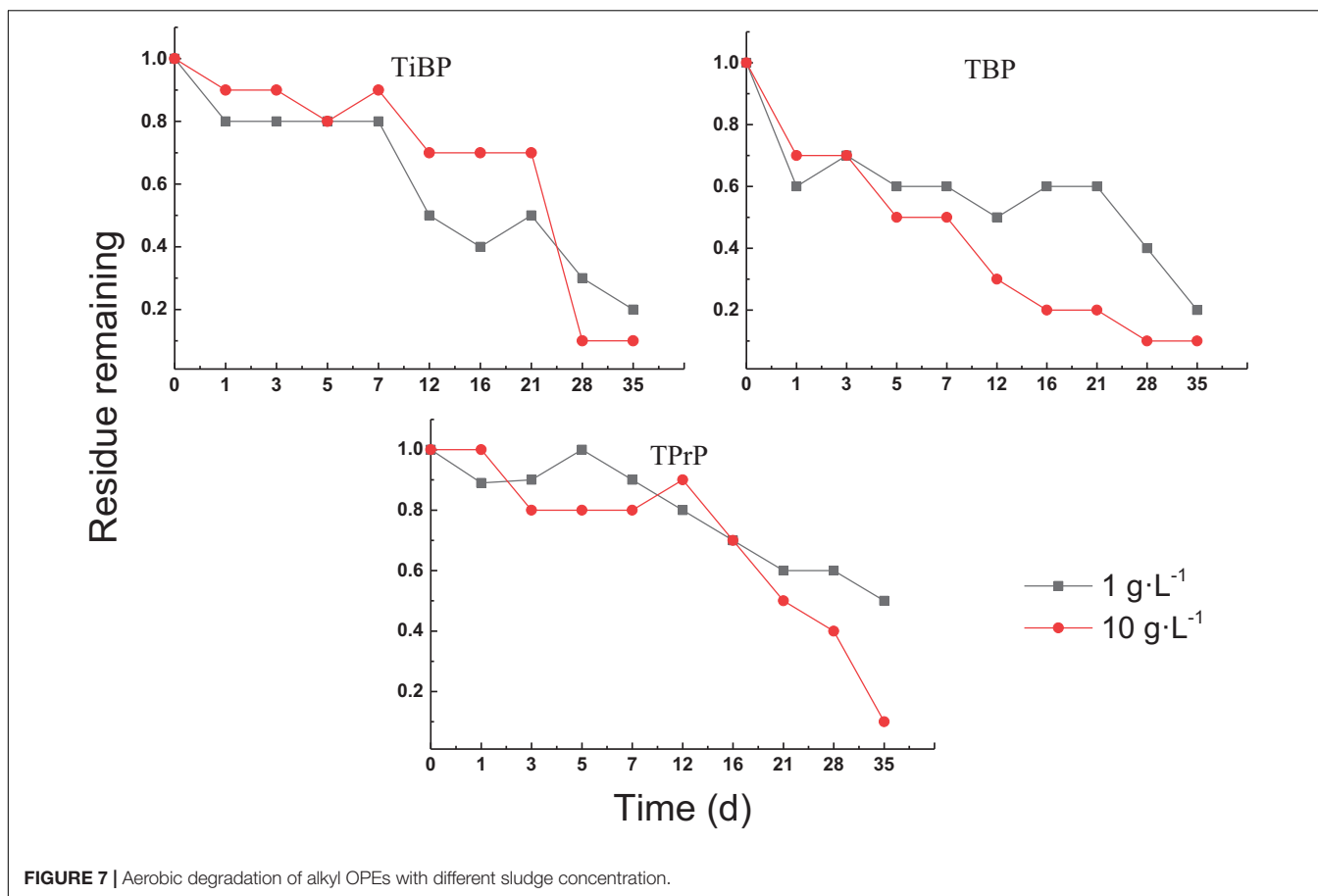


FIGURE 7 | Aerobic degradation of alkyl OPEs with different sludge concentration.

reactions. For example, under aerobic conditions, oxygenase activity is higher, and oxidation reactions occur more easily. Under anaerobic conditions, the enzyme activities of reductase and protease are 40–75% higher than under aerobic conditions, and dehydrogenase activity is about 40–60% higher, which is prone to hydrolysis and reduction (Goel et al., 1998). The removal of OPEs under aerobic conditions is greater than that under anaerobic conditions, probably because OPEs can be removed by volatilization under the former, while an anaerobic bottle is a sealed environment in the anaerobic treatment and OPEs, therefore, cannot be removed by volatilization.

Electron Donors

Addition of electron donors significantly increased the removal of chlorinated OPEs. Reduction dehalogenation is an important anaerobic biodegradation mechanism. Electron donors increase the reduction dehalogenation of chemical substances (Futagami et al., 2010), so the addition of electron donors to sludge may also increase the degradation of chlorinated OPEs. Moreover, organic pollutants can be removed by co-metabolism. For example, adding acetic acid as a co-substrate can increase the bacterial metabolism of triphenyl phosphate (TPP) (Hou et al., 2019), and adding lactic acid can significantly improve the efficiency of anaerobic removal of naphthalene (Cao et al., 2012). As a result, when the intermediate products, including

acetate + propionate + butyrate + lactate, are added as a co-matrix, the degradation of chlorinated OPEs is increased by co-metabolism. Studies have also shown that the addition of a common matrix increases the volume of methane production, while methanogenic organisms play an important role in the biodegradation of organic matter and increase the degradation of pollutants (Nazaries et al., 2013).

The removal of triphenyl ester OPEs in anaerobic sludge is relatively fast, so the addition of electron donors does not significantly increase their removal. Microorganisms need time to adapt to electron donors, the adaptation process needs to go through a lag period (Fischer and Majewsky, 2014), and the triphenyl ester OPEs are removed before the end of the lag period.

The addition of electron donors has an inhibitory effect on the removal of alkyl OPEs, which may be due to the fact that the metabolic pathway for removal of alkyl OPEs does not involve co-metabolism, but rather other degradation pathways. Studies of the anaerobic degradation of sediment have also shown that the addition of either acetic acid or lactic acid inhibited the rate of degradation of non-ylphenol (Chang et al., 2004).

Electron Acceptors

The rates of degradation of triphenyl ester OPEs were slightly accelerated by adding FeCl₃, but those of other OPEs were not significantly increased. Thus, the mechanism by which FeCl₃ acts

as an electron acceptor for OPEs is unclear. Moreover, FeCl_3 is also a flocculant, which can reduce the toxicity of wastewater and improve its biodegradability (Karthik et al., 2008). Flocculation can also increase the contact area between sludge and organic pollutants in sewage and accelerate the rate of degradation and increase the percentage removal of triphenyl ester OPEs.

Usually, NaNO_3 and Na_2SO_4 are added as electron receptors to increase pollutant degradation. The presence of NaNO_3 and Na_2SO_4 results in higher bacterial abundance and greater enrichment of functional genes during the nitrogen, carbon, sulfur, and phosphorus cycles (Dou et al., 2008; Xu et al., 2014; Zhang et al., 2019). In river sediments, the presence of nitrate and sulfate was found to accelerate the degradation of polycyclic aromatic hydrocarbons (PAHs) (Yang et al., 2020). However, due to the different reactions of different substances to electron acceptors (Schmidt et al., 2017), we came to different conclusions in our experiments. In this study, NaNO_3 and Na_2SO_4 did not significantly improve the anaerobic removal of triphenyl OPEs, and they inhibited the removal of chlorinated and alkyl OPEs. The concentration of added electron acceptors used in this study has been proven not to inhibit microorganisms (Dou et al., 2008; Guerrero-Barajas et al., 2014; Gou et al., 2019). Therefore, the inhibition of the removal of chlorinated and alkyl OPEs may have been due to the production of toxic intermediate products, which requires further study. Zhang et al. (2011) have also proposed that sulfate can stimulate sulfate-reducing bacteria to compete with methanogenic bacteria for electron utilization to produce sulfides that are toxic to microorganisms (Vogel et al., 1987). Nutrient salts such as magnesium sulfate and ammonium nitrate in the medium also negatively affect the biodegradation of chlorophenol (Sahoo et al., 2010). Nitrate can also reversibly block the metabolism of trimethyltrinitramine (Beller, 2002).

Surface-Active Agents

When organic matter is hydrophobic, adding surfactant can overcome the diffusion limitation of organic matter to cells, reduce the tension and viscosity of the water interface effectively (Zdarta et al., 2018), increase bioavailability, and thus increase the rate of removal (Varjani and Upasani, 2017). The biosurfactant rhamnolipid and the non-ionic surfactant Tween 80 can both usually increase the contact between microbial cells and the matrix. Previous studies have shown that rhamnolipid can significantly increase the rate of removal of phenanthrene, diesel, and pyrene. The addition of Tween 80 can also significantly increase the biodegradation ratio of phenanthrene (Burgess and Pletschke, 2008; Kang et al., 2019). Rhamnolipid and Tween 80 can also increase fungal biomass, the decomposition of hemicellulose and cellulose, and the rate of decomposition by 8.0 and 11.6%, respectively. They can also significantly affect the rate of carbohydrate and amino acid metabolism (Yin et al., 2019). In addition, they can also increase the maximum speed of enzyme reactions (Mo et al., 2008). However, the effect of surfactants on enzymes is not always positive (Veronika et al., 2018). Zeng et al. (2006) have pointed out that Tween 80 and rhamnolipid can increase the enzyme activity of amylase and xylanase, but have a negative effect on protease.

Addition of rhamnolipid had no significant effect on OPEs removal in this study, except for chlorinated OPEs. Tween 80 has an inhibitory effect on OPE degradation, possibly due to its ability to interact with microbial proteins and manipulate them to alter enzyme conformation, thereby altering enzyme activity, stability, and specificity, as well as its potential toxicity to microorganisms (Van Hamme et al., 2006; Tiehm and Schmidt, 2011).

Reduction of Fe Powder

Fe powder can significantly increase the rate of removal of OPE triphenyl esters. Zero-valent iron can provide electrons for microorganisms, and it has a high reduction activity that can maintain a low redox potential in the anaerobic environment (Völker et al., 2017) and significantly increase the anaerobic biodegradation of chlorpyrifos to reduce water poisoning (Shi et al., 2019a). Adding zero-valent iron can also increase anaerobic digestion in STPs as well as methane production (Wei et al., 2018). Fe can also significantly alter the bacterial and methanogenic community structure (Pan et al., 2019), is also an important protein cofactor (Kleemann and Meckenstock, 2011), and is essential for most organisms (Beauchene et al., 2015). Feng et al. (2014) have also pointed out that zero-valent iron as a reducing material is expected to enhance anaerobic processes, including hydrolytic acidification, which can help accelerate and improve anaerobic acid production and create good conditions for subsequent treatment (Liu et al., 2012).

Treatments of Different Aerobic Sludge Concentrations

A comparative study of the removal of OPEs from 1 to 10 $\text{g}\cdot\text{L}^{-1}$ sludge concentrations revealed that the removal percentages of OPEs were not proportional to the sludge concentration. In the early stages of the experiment, triphenyl ester OPEs had significantly higher removal percentages in 1 $\text{g}\cdot\text{L}^{-1}$ than in 10 $\text{g}\cdot\text{L}^{-1}$ sludge concentration, which may have been due to the greater contribution from the removal of triphenyl ester OPEs by volatilization. When the sludge concentration was high (10 $\text{g}\cdot\text{L}^{-1}$), the adsorption of OPEs was greater, which reduced the degree of removal in the early stage. After 16 days, the removal percentages of the three types of OPEs in the higher concentration of sludge (10 $\text{g}\cdot\text{L}^{-1}$) exceeded that of the low concentration (1 $\text{g}\cdot\text{L}^{-1}$), mainly because the higher sludge concentration ensured the diversity of microorganisms made the microorganisms more resistant to toxic pollutants. Currently, the European Union (ECHA, 2017) proposes the use of enhanced biodegradability tests to assess the biodegradability potential of chemicals, that is, by increasing the sludge concentration or increasing the volume of the test solution to ensure the test error caused by the heterogeneity of the dominant species when the sludge is added is reduced as much as possible.

CONCLUSION

The biodegradability of nine OPEs in both aerobic and anaerobic activated sludge derived from kitchen garbage biomass and agricultural residues under different conditions was investigated.

Under anaerobic conditions, the removal percentages of triphenyl ester OPEs were significantly higher than those of chlorinated and alkyl OPEs. The addition of electron donors, electron acceptors, surfactants, and Fe powder did not always increase the rate of degradation of the different kinds of OPEs, which is closely related to the structure of the OPEs. The addition of FeCl₃ and Fe powder increased the rate of degradation of triphenyl ester OPEs, with the DT₅₀ of triphenyl ester OPEs being in the range 1.7–3.8 days when FeCl₃ was added and 1.3–4.7 days when Fe powder was added, compared to a DT₅₀ of 4.3–6.9 days for the blank control. Addition of electron donors and rhamnolipid increased the removal of chlorinated OPEs, with the DT₅₀ values of TCEP and TDCP being 18.4 and 10.0 days, respectively, after electron donors were added, and 13.7 and 3.0 days, respectively, after rhamnolipid was added. No treatment increased the removal of alkyl OPEs as their low anaerobic degradability prevented that occurring.

The biodegradation rates of OPEs under aerobic conditions were significantly higher than those under anaerobic conditions. The sludge with the higher concentration had a lower rate of degradation for highly adsorbent chemicals at the beginning of the test. However, the sludge with the higher concentration helped the microorganisms present in the sludge to adapt and remove OPEs by the end of test.

REFERENCES

- Amend, J. P., and Shock, E. L. (2001). Energetics of overall metabolic reactions of thermophilic and hyperthermophilic Archaea and Bacteria. *FEMS Microbiol. Rev.* 25, 175–243. doi: 10.1111/j.1574-6976.2001.tb00576.x
- Anneli, M., Barbro, A., and Peter, H. (2005). Organophosphorus flame retardants and plasticizers in Swedish sewage treatment plants. *Environ. Sci. Technol.* 39, 7423–7429. doi: 10.1021/es0510131
- Beauchene, N. A., Myers, K. S., Chung, D., Park, D. M., Weisnicht, A. M., Keleş, S., et al. (2015). Impact of anaerobiosis on expression of the iron-responsive fur and RyhB regulons. *mBio* 6:e01947-15.
- Beller, H. R. (2002). Anaerobic biotransformation of RDX (hexahydro-1,3,5-trinitro-1,3,5-triazine) by aquifer bacteria using hydrogen as the sole electron donor. *Water Res.* 36, 2533–2540. doi: 10.1016/s0043-1354(01)00480-8
- Burgess, J. E., and Pletschke, B. I. (2008). Hydrolytic enzymes in sewage sludge treatment: a mini-review. *Water S.A* 34, 59–63.
- Cao, X. K., Qi, Y., and Hao, C. B. (2012). [Degradation kinetics of naphthalene by anaerobic sludge and analysis of the bacterial biodiversity]. *Huan Jing Ke Xue* 33, 3535–3541.
- Carmona, M., Zamarro, M. T., Blazquez, B., Duranterodriguez, G., Juarez, J. F., Valderrama, J. A., et al. (2009). Anaerobic catabolism of aromatic compounds: a genetic and genomic view. *Microbiol. Mol. Biol. Rev.* 73, 71–133. doi: 10.1128/mmb.00021-08
- Castro-Jimenez, J., Berrojalbiz, N., Pizarro, M., and Dachs, J. (2014). Organophosphate ester (OPE) flame retardants and plasticizers in the open mediterranean and black seas Atmosphere. *Environ. Sci. Technol.* 48, 3203–3209. doi: 10.1021/es405337g
- Chang, B. V., Yu, C. H., and Yuan, S. Y. (2004). Degradation of nonylphenol by anaerobic microorganisms from river sediment. *Chemosphere* 55, 493–500. doi: 10.1016/j.chemosphere.2004.01.004
- Dou, J., Liu, X., Hu, Z., and Deng, D. (2008). Anaerobic BTEX biodegradation linked to nitrate and sulfate reduction. *J. Hazardous Mater.* 151, 720–729. doi: 10.1016/j.jhazmat.2007.06.043
- ECHA (2017). *Guidance on Information Requirements and Chemical Safety Assessment Chapter R.7b: Endpoint Specific Guidance*. Helsinki: ECHA.
- Eede, N. V. D., Dirtu, A. C., Ali, N., Neels, H., and Covaci, A. (2012). Multi-residue method for the determination of brominated and organophosphate flame retardants in indoor dust. *Talanta* 89, 292–300. doi: 10.1016/j.talanta.2011.12.031
- Feng, Y., Zhang, Y., Quan, X., and Chen, S. (2014). Enhanced anaerobic digestion of waste activated sludge digestion by the addition of zero valent iron. *Water Res.* 52, 242–250. doi: 10.1016/j.watres.2013.10.072
- Fischer, K., and Majewsky, M. (2014). Cometabolic degradation of organic wastewater micropollutants by activated sludge and sludge-inherent microorganisms. *Appl. Microbiol. Biotechnol.* 98, 6583–6597. doi: 10.1007/s00253-014-5826-0
- Fries, E., and Puttmann, W. (2003). Monitoring of the three organophosphate esters TBP, TCEP and TBEP in river water and ground water (Oder, Germany). *J. Environ. Monit.* 5, 346–352. doi: 10.1039/b210342g
- Fritsche, W., and Hofrichter, M. (2005). *Aerobic Degradation of Recalcitrant Organic Compounds by Microorganisms*. Weinheim: Wiley-VCH Verlag GmbH & Co. KGaA.
- Futagami, T., Goto, M., and Furukawa, K. (2010). Biochemical and genetic bases of dehalorespiration. *Chem. Record* 8, 1–12. doi: 10.1002/tcr.20134
- Goel, R., Mino, T., Satoh, H., and Matsuo, T. (1998). Enzyme activities under anaerobic and aerobic conditions in activated sludge sequencing batch reactor. *Water Res.* 32, 2081–2088. doi: 10.1016/s0043-1354(97)00425-9
- Gou, Y., Yang, S., Cheng, Y., Song, Y., Qiao, P., Li, P., et al. (2019). Enhanced anoxic biodegradation of polycyclic aromatic hydrocarbons (PAHs) in aged soil pretreated by hydrogen peroxide. *Chem. Eng. J.* 356, 524–533. doi: 10.1016/j.cej.2018.09.059
- Grishchenkov, V. G., Townsend, R. T., McDonald, T. J., Autenrieth, R. L., and Boronin, A. M. (2000). Degradation of petroleum hydrocarbons by facultative anaerobic bacteria under aerobic and anaerobic conditions. *Process Biochem.* 35, 889–896. doi: 10.1016/s0032-9592(99)00145-4
- Gurrero-Barajas, C., Ordaz, A., Garibay-Orijel, C., García-Solares, S. M., Bastida-González, F., and Zárate-Segura, P. B. (2014). Enhanced sulfate reduction and trichloroethylene (TCE) biodegradation in a UASB reactor operated with a sludge developed from hydrothermal vents sediments: process and microbial ecology. *Int. Biodeterior. Biodegradation* 94, 182–191. doi: 10.1016/j.ibiod.2014.07.015

These results will provide a new perspective on the effect of activated sludge cultured with kitchen garbage biomass and agricultural residues in eliminating emerging pollutants.

DATA AVAILABILITY STATEMENT

The original contributions generated for this study are included in the article/supplementary material, further inquiries can be directed to the corresponding author/s.

AUTHOR CONTRIBUTIONS

LZ and ZZ proposed the idea. XY and WG did the experiments. JL, LS, and GJ analyzed the results. All authors contributed to the article and approved the submitted version.

FUNDING

This work was supported by the National Key Research and Development Program of China (No. 2018YFC1801504) and the Central Scientific Research Projects for Public Welfare Research Institutes (GYZX200102).

- Hägglom, M. M., and Young, L. Y. (1999). Anaerobic degradation of 3-halobenzoates by a denitrifying bacterium. *Arch. Microbiol.* 171, 230–236. doi: 10.1007/s002030050704
- Hansen, S. F., Sørensen, S. N., Skjolding, L. M., Hartmann, N. B., and Baun, A. (2017). Revising REACH guidance on information requirements and chemical safety assessment for engineered nanomaterials for aquatic ecotoxicity endpoints: recommendations from the EnvNano project. *Environ. Sci. Eur.* 29:14.
- Hou, R., Luo, X., Liu, C., Zhou, L., Wen, J., and Yuan, Y. (2019). Enhanced degradation of triphenyl phosphate (TPHP) in bioelectrochemical systems: kinetics, pathway and degradation mechanisms. *Environ. Pollut.* 254:113040. doi: 10.1016/j.envpol.2019.113040
- Kai, B. (2005). Comparison of TCPP concentrations in sludge and wastewater in a typical German sewage treatment plant—comparison of sewage sludge from 20 plants. *J. Environ. Monit.* 7, 509–513. doi: 10.1039/b502318a
- Kang, S., Kim, G., Choe, J. K., and Choi, Y. (2019). Effect of using powdered biochar and surfactant on desorption and biodegradability of phenanthrene sorbed to biochar. *J. Hazard. Mater.* 371, 253–260. doi: 10.1016/j.jhazmat.2019.02.104
- Karthik, M., Dafale, N., Pathe, P., and Nandy, T. (2008). Biodegradability enhancement of purified terephthalic acid wastewater by coagulation-flocculation process as pretreatment. *J. Hazard. Mater.* 154, 721–730. doi: 10.1016/j.jhazmat.2007.10.085
- Kawagoshi, Y., and Fukunaga, I. (1994). Levels and features of organophosphoric acid triesters at Osaka north port sea-based solid waste disposal site. *J. Environ. Chem.* 4, 797–804. doi: 10.5985/jec.4.797
- Kieft, T. L., Fredrickson, J. K., Onstott, T. C., Gorby, Y., and Gray, M. S. (1999). Dissimilatory reduction of Fe(III) and other electron acceptors by a thermus isolate. *Appl. Environ. Microbiol.* 65, 1214–1221. doi: 10.1128/aem.65.3.1214-1221.1999
- Kim, U., Oh, J., and Kannan, K. (2017). Occurrence, removal, and environmental emission of organophosphate flame retardants/plasticizers in a wastewater treatment plant in New York State. *Environ. Sci. Technol.* 51, 7872–7880. doi: 10.1021/acs.est.7b02035
- Kleemann, R., and Meckenstock, R. U. (2011). Anaerobic naphthalene degradation by Gram-positive, iron-reducing bacteria. *Fems Microbiol. Ecol.* 78, 488–496. doi: 10.1111/j.1574-6941.2011.01193.x
- Liu, Y., Zhang, Y., Quan, X., Li, Y., Zhao, Z., Meng, X., et al. (2012). Optimization of anaerobic acidogenesis by adding Fe₀ powder to enhance anaerobic wastewater treatment. *Chem. Eng. J.* 192, 179–185. doi: 10.1016/j.cej.2012.03.044
- Margot, J., Rossi, L., Barry, D. A., and Holliger, C. (2015). A review of the fate of micropollutants in wastewater treatment plants. *Wiley Interdiscip. Rev.* 2, 457–487. doi: 10.1002/wat2.1090
- Martínez-Carballo, E., González-Barreiro, C., Sitka, A., Scharf, S., and Gans, O. (2007). Determination of selected organophosphate esters in the aquatic environment of Austria. *Sci. Total Environ.* 388, 290–299. doi: 10.1016/j.scitotenv.2007.08.005
- Mezzanotte, V., Castiglioni, F., Todeschini, R., and Pavan, M. (2003). Study on anaerobic and aerobic degradation of different non-ionic surfactants. *Bioresour. Technol.* 87, 87–91. doi: 10.1016/s0960-8524(02)00211-0
- Mo, D., Yuan, X. Z., Zeng, G., and Liu, J. (2008). Effect of Tween 80 and rhamnolipid on enzymatic Hydrolysis of Straw. *Environ. Sci.* 29:14.
- Nazaries, L., Murrell, J. C., Millard, P., Baggs, L., and Singh, B. K. (2013). Methane, microbes and models: fundamental understanding of the soil methane cycle for future predictions. *Environ. Microbiol.* 15, 2395–2417. doi: 10.1111/1462-2920.12149
- O'Brien, J. W., Thai, P. K., Brandsma, S. H., Leonards, P. E., Ort, C., and Mueller, J. F. (2015). Wastewater analysis of Census day samples to investigate per capita input of organophosphorus flame retardants and plasticizers into wastewater. *Chemosphere* 138, 328–334. doi: 10.1016/j.chemosphere.2015.06.014
- Pan, X., Lv, N., Li, C., Ning, J., Wang, T., Wang, R., et al. (2019). Impact of nano zero valent iron on tetracycline degradation and microbial community succession during anaerobic digestion. *Chem. Eng. J.* 359, 662–671. doi: 10.1016/j.cej.2018.11.135
- Pang, L., Ge, L., Yang, P., He, H., and Zhang, H. (2018). Degradation of organophosphate esters in sewage sludge: effects of aerobic/anaerobic treatments and bacterial community compositions. *Bioresour. Technol.* 255, 16–21. doi: 10.1016/j.biortech.2018.01.104
- Ratola, N., Cincinelli, A., Alves, A., and Katsoyiannis, A. (2012). Occurrence of organic microcontaminants in the wastewater treatment process. A mini review. *J. Hazard. Mater.* 239, 1–18. doi: 10.1016/j.jhazmat.2012.05.040
- Regnery, J., Puttmann, W., Merz, C., and Berthold, G. (2011). Occurrence and distribution of organophosphorus flame retardants and plasticizers in anthropogenically affected groundwater. *J. Environ. Monit.* 13, 347–354. doi: 10.1039/c0em00419g
- Sahoo, N. K., Pakshirajan, K., and Ghosh, P. K. (2010). Enhancing the biodegradation of 4-chlorophenol by *Arthrobacter chlorophenolicus* A6 via medium development. *Int. Biodeter. Biodegradation* 64, 474–480. doi: 10.1016/j.ibiod.2010.05.008
- Saini, A., Thaysen, C., Jantunen, L., McQueen, R. H., and Diamond, M. L. (2016). From clothing to laundry water: investigating the fate of phthalates, brominated flame retardants, and organophosphate esters. *Environ. Sci. Technol.* 50, 9289–9297. doi: 10.1021/acs.est.6b02038
- Saxena, P., Hiwrale, I., Das, S., Shukla, V., Tyagi, L., Pal, S., et al. (2021). Profiling of emerging contaminants and antibiotic resistance in sewage treatment plants: an Indian perspective. *J. Hazard. Mater.* 408:124877. doi: 10.1016/j.jhazmat.2020.124877
- Schmidt, N., Page, D., and Tiehm, A. (2017). Biodegradation of pharmaceuticals and endocrine disruptors with oxygen, nitrate, manganese (IV), iron (III) and sulfate as electron acceptors. *J. Contam. Hydrol.* 203, 62–69. doi: 10.1016/j.jconhyd.2017.06.007
- Shi, J., Han, H., and Xu, C. (2019a). A novel enhanced anaerobic biodegradation method using biochar and Fe(OH)₃@biochar for the removal of nitrogen heterocyclic compounds from coal gasification wastewater. *Sci. Total Environ.* 697:134052. doi: 10.1016/j.scitotenv.2019.134052
- Shi, J., Xu, C., Han, Y., and Han, H. (2019b). Enhanced anaerobic biodegradation efficiency and mechanism of quinoline, pyridine, and indole in coal gasification wastewater. *Chem. Eng. J.* 361, 1019–1029. doi: 10.1016/j.cej.2018.12.162
- Styszko, K., Proctor, K., Castrignanò, E., and Kasprzyk-Hordern, B. (2020). Occurrence of pharmaceutical residues, personal care products, lifestyle chemicals, illicit drugs and metabolites in wastewater and receiving surface waters of Krakow agglomeration in South Poland. *Sci. Total Environ.* 768:144360. doi: 10.1016/j.scitotenv.2020.144360
- Tappe, W., Groeneweg, J., and Jantsch, B. (2002). Diffuse atrazine pollution in German aquifers. *Biodegradation* 13, 3–10.
- Tiehm, A., and Schmidt, K. R. (2011). Sequential anaerobic/aerobic biodegradation of chloroethenes—aspects of field application. *Curr. Opin. Biotechnol.* 22, 415–421. doi: 10.1016/j.copbio.2011.02.003
- Tonanzi, B., Braguglia, C. M., Gallipoli, A., Montecchio, D., Pagliaccia, P., Rossetti, S., et al. (2020). Anaerobic digestion of mixed urban biowaste: the microbial community shift towards stability. *New Biotechnol.* 55, 108–117. doi: 10.1016/j.nbt.2019.10.008
- Van Hamme, J. D., Singh, A., and Ward, O. P. (2006). Physiological aspects: part 1 in a series of papers devoted to surfactants in microbiology and biotechnology. *Biotechnol. Adv.* 24, 604–620.
- Varjani, S. J., and Upasani, V. N. (2017). A new look on factors affecting microbial degradation of petroleum hydrocarbon pollutants. *Int. Biodeter. Biodegradation* 120, 71–83. doi: 10.1016/j.ibiod.2017.02.006
- Veronika, B., Dan-kesson, Zamani, A., and Horváth, S. (2018). Anaerobic degradation of bioplastics: a review. *Waste Manag.* 80, 406–413. doi: 10.1016/j.wasman.2018.09.040
- Vogel, T. M., Criddle, C. S., and McCarty, P. L. (1987). Transformations of halogenated aliphatic compounds. *Environ. Ence Technol.* 21, 722–736. doi: 10.1021/es00162a001
- Völker, J., Vogt, T., Castronovo, S., Wick, A., Ternes, T. A., Joss, A., et al. (2017). Extended anaerobic conditions in the biological wastewater treatment: Higher reduction of toxicity compared to target organic micropollutants. *Water Res.* 116, 220–230. doi: 10.1016/j.watres.2017.03.030
- Wei, W., Cai, Z., Fu, J., Xie, G.-J., Li, A., Zhou, X., et al. (2018). Zero valent iron enhances methane production from primary sludge in anaerobic digestion. *Chem. Eng. J.* 351, 1159–1165. doi: 10.1016/j.cej.2018.06.160
- Wei, W., Han, H., Yuan, M., and Li, H. (2010). Enhanced anaerobic biodegradability of real coal gasification wastewater with methanol addition. *J. Environ. Sci.* 22, 1868–1874. doi: 10.1016/s1001-0742(09)60327-2
- Wu, Y., Sun, Q., Wang, Y., Deng, C., and Yu, C. (2017). Comparative studies of aerobic and anaerobic biodegradation of methylparaben and propylparaben in

- activated sludge. *Ecotoxicol. Environ. Saf.* 138, 25–31. doi: 10.1016/j.ecoenv.2016.12.017
- Xu, M., Zhang, Q., Xia, C., Zhong, Y., Sun, G., Guo, J., et al. (2014). Elevated nitrate enriches microbial functional genes for potential bioremediation of complexly contaminated sediments. *ISME J.* 8, 1932–1944. doi: 10.1038/ismej.2014.42
- Yang, C.-W., Liao, C.-S., Ku, H., and Chang, B.-V. (2019). Biodegradation of Tetrabromobisphenol-A in mangrove sediments. *Sustainability* 11:151. doi: 10.3390/su11010151
- Yang, X., Li, E., Liu, F., and Xu, M. (2020). Interactions of PAH-degradation and nitrate-/sulfate-reducing assemblages in anaerobic sediment microbial community. *J. Hazard. Mater.* 388:122068. doi: 10.1016/j.jhazmat.2020.12.2068
- Yin, Y., Gu, J., Wang, X., Zhang, Y., Zheng, W., Chen, R., et al. (2019). Effects of rhamnolipid and Tween-80 on cellulase activities and metabolic functions of the bacterial community during chicken manure composting. *Bioresour. Technol.* 288:121507. doi: 10.1016/j.biortech.2019.121507
- Zdarta, A., Pacholak, A., Galikowska, M., Smulek, W., and Kaczorek, E. (2018). Butylbenzene and tert-Butylbenzene-Sorption on sand particles and biodegradation in the presence of plant natural surfactants. *Toxins* 10:338. doi: 10.3390/toxins10090338
- Zeng, G., Shi, J., Yuan, X., Liu, J., Zhang, Z., Huang, G. H., et al. (2006). Effects of Tween 80 and rhamnolipid on the extracellular enzymes of *Penicillium simplicissimum* isolated from compost. *Enzyme Microb. Technol.* 39, 1451–1456. doi: 10.1016/j.enzmictec.2006.03.035
- Zhang, J., Zhang, Y., Quan, X., Liu, Y., An, X., Chen, S., et al. (2011). Bioaugmentation and functional partitioning in a zero valent iron-anaerobic reactor for sulfate-containing wastewater treatment. *Chem. Eng. J.* 174, 159–165. doi: 10.1016/j.cej.2011.08.069
- Zhang, Z., Wang, C., He, J., and Wang, H. (2019). Anaerobic phenanthrene biodegradation with four kinds of electron acceptors enriched from the same mixed inoculum and exploration of metabolic pathways. *Front. Environ. Ence Eng.* 13:80. doi: 10.1007/s11783-019-1164-x
- Zhang, Z.-L., Zhang, L., Zhou, Y.-L., Chen, J.-C., Liang, Y.-M., and Wei, L. (2013). Pilot-scale operation of enhanced anaerobic digestion of nutrient-deficient municipal sludge by ultrasonic pretreatment and co-digestion of kitchen garbage. *J. Environ. Chem. Eng.* 1, 73–78. doi: 10.1016/j.jece.2013.03.008

Conflict of Interest: The authors declare that the research was conducted in the absence of any commercial or financial relationships that could be construed as a potential conflict of interest.

Copyright © 2021 Yang, Fan, Gu, Liu, Shi, Zhang, Zhou and Ji. This is an open-access article distributed under the terms of the Creative Commons Attribution License (CC BY). The use, distribution or reproduction in other forums is permitted, provided the original author(s) and the copyright owner(s) are credited and that the original publication in this journal is cited, in accordance with accepted academic practice. No use, distribution or reproduction is permitted which does not comply with these terms.



Extraction and Application of Natural Rutin From *Sophora japonica* to Prepare the Novel Fluorescent Sensor for Detection of Copper Ions

Shilong Yang^{1*}, Lu Sun², Zhiwen Song² and Li Xu^{2*}

¹ Advanced Analysis and Testing Center, Nanjing Forestry University, Nanjing, China, ² College of Science, Nanjing Forestry University, Nanjing, China

OPEN ACCESS

Edited by:

Lei Wang,
Jeju National University, South Korea

Reviewed by:

Sukma Kusumah,
Indonesian Institute of Sciences,
Indonesia

Chuan-Ling Si,
Tianjin University of Science
and Technology, China

*Correspondence:

Li Xu
xuliqby@njfu.edu.cn
Shilong Yang
yshl6072@163.com

Specialty section:

This article was submitted to
Bioprocess Engineering,
a section of the journal
Frontiers in Bioengineering and
Biotechnology

Received: 15 December 2020

Accepted: 02 February 2021

Published: 22 February 2021

Citation:

Yang S, Sun L, Song Z and Xu L
(2021) Extraction and Application
of Natural Rutin From *Sophora
japonica* to Prepare the Novel
Fluorescent Sensor for Detection
of Copper Ions.
Front. Bioeng. Biotechnol. 9:642138.
doi: 10.3389/fbioe.2021.642138

Rutin (**R**), a representative flavonoid found in various biomasses, can be used to prepare different fluorescent sensors for environmental, biological and medical fields. In this work, the natural **R** in *Sophora japonica* was extracted and purified to prepare fluorescent-responding sensor systems intended to recognize copper ions with both strong selectivity as well as appropriate sensitivity. Results showed that neat **R** had no obvious fluorescent emission peak in PBS buffer solution. However, when **R** and (2-hydroxypropyl)- β -cyclodextrin (**CD**) were introduced within buffer solution, fluorescent emission intensity was significantly increased due to the resultant **R-CD** inclusion complex. In addition, the formed **R-CD** inclusion complex was shown to behave as the aforementioned fluorescent sensor for copper ions through a mechanism of quenched fluorescent emission intensity when **R-CD** became bound with copper ions. The binding constant value for **R-CD** with copper ions was 1.33×10^6 , allowing for quantification of copper ions between the concentration range of 1.0×10^{-7} – 4.2×10^{-6} mol·L⁻¹. Furthermore, the minimum detection limit was found to be 3.5×10^{-8} mol·L⁻¹. This work showed the prepared **R-CD** inclusion complex was both highly selective and strongly sensitive toward copper ions, indicating that this system could be applied into various fields where copper ions are of concern.

Keywords: rutin, (2-hydroxypropyl)- β -cyclodextrin, fluorescent sensor, copper ions, *Sophora japonica*

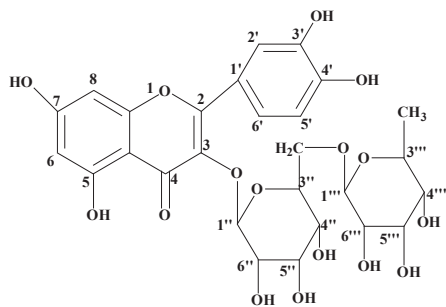
INTRODUCTION

As the shortage of oil resources and environmental pollution become more serious, biomass resources have attracted lots of attention as sustainable alternatives. Transformation of the constituents (cellulose, hemicellulose, lignin) into value-added products such as reinforcing materials, food additives, adhesive, and more continue to be extensively investigated (Du et al., 2019; Sun et al., 2019; Zhou and Xu, 2019; Zhou et al., 2019; Huang et al., 2020; Pei et al., 2020b; Zhao et al., 2020). Apart from the structural constituents of biomass, there is also potential value in the variously minor constituents present, specifically the flavonoids and polyphenols. The polyphenols can showed different physical and biological activity in bio-materials (Dong et al., 2020; Pei et al., 2020a; Zheng et al., 2021). Flavonoids are widely present in most plants. Biological activities of flavonoids are reported and reviewed frequently in the literature (Singh et al., 2014;

Zhao et al., 2016). Nevertheless, there are few reports about fluorescence properties of flavonoids. In one relevant work, the authors found that flavonoids isolated from bamboo residues were capable of detecting Fe^{3+} *in vitro* (Su et al., 2019). In a different work, the flavonoid quercetin was used to provide bioimaging in two applicable biological mediums (He et al., 2018). The key element of both of these works is that they demonstrate that flavonoids could play an important role as fluorescent chemicals from sustainable resources.

Rutin (**R**, **Scheme 1**) is a representative flavonoid that can be found in various plants. It has displayed many favorable biological activities, including anti-inflammatory, antiviral, and others (Nkpa et al., 2019; Huynh et al., 2020; Wani et al., 2021). However, there are few works which have sought to isolate **R** from biomass and use it as the fluorescent sensor for detection of metal ions. Therefore, this was the task of the present document. Thousands of ion-detective fluorescent sensors for ion have been reported upon in the literature (Zhang et al., 2018; Chen et al., 2019; Kan et al., 2020; Li et al., 2021). Importantly, the most common theme in these studies is that the fluorescent molecules investigated were often formed synthetically and their workup often included use of toxic reagents and solvents. Compared to these more traditional fluorescent sensors, **R** is easily extracted from plants with neat water or aqueous ethanol solutions. In addition, **R** is a dietary supplement and has excellent biocompatibility.

Sophora japonica is dried flower bud of *Sophora japonica* trees, which are planted in China widely for its ecological and economic benefits. However, the flowers of *Sophora japonica* trees fall and become waste. There is lots amount of **R** in the flowers, especially in the flower buds. To make full use of *Sophora japonica*, **R** is extracted from *Sophora japonica* and purified to prepare the novel fluorescent sensor for detection of different metal ions in this study. Isolated **R** was complexed with 2-hydroxypropyl- β -cyclodextrin (**CD**) in a buffer solution (pH = 7.40) to improve its emission fluorescence, and this resulting complex (**R-CD**) was then applied for detection and quantitation of metal ions. The mechanism of changes to fluorescence was also discussed to understand the ability of **R**-based fluorescent sensor. It is hoped that this work will shine light upon a new approach toward sensor molecules from the approach of utilization of secondary plant substance.



SCHEME 1 | Structure of the rutin.

MATERIALS AND METHODS

Reagents and Instruments

The different metal salts (AR) were provided by the Nanjing Reagent Co., Ltd. Methyl alcohol (HPLC) was produced by Tedia Company, Inc. **R** was extracted from *Sophora japonica* acquired from Bozhou Good health Food Co., Ltd. 2-Hydroxypropyl- β -cyclodextrin was purchased from Aladdin Reagent Co., Ltd. Next, phosphate buffer solution (PBS, pH = 7.40) were obtained from Beijing Solarbio Science & Technology Co., Ltd. Finally, sodium tetraborate, hydrochloric acid and calcium hydroxide were purchased by Sinopharm Chemical Reagent Co., Ltd. It is important to note that all solutions involving the above mentioned reagents were prepared freshly using ultrapure water produced by Milli-Q.

Fluorescence spectra and UV-visible absorption spectra were recorded on a PerkinElmer LS55 spectrophotometer and a Lambda 950 spectrophotometer, respectively. All ^1H NMR spectra were obtained via a Bruker AVANCE III HD 600 MHz spectrometer. Finally, FT-IR spectra were obtained by way of a Bruker VERTEX 80V.

Extraction and Purification of **R**

To begin extraction, dried *Sophora japonica* was added into a boiling aqueous solution of 0.4% sodium tetraborate. To reach a pH between 8 and 9, calcium hydroxide was added into the solution. After 0.5 h, the solution was filtered with gauze and filter paper, respectively. We observed that the temperature of the solution needed to remain above 60°C in order to avoid unwanted precipitation of **R**. Next, an appropriate amount of hydrochloric acid solution was added to the filtrate to render the solution at a pH between 2 and 3. After this adjustment, a mass of crude **R** precipitated from solution. Crude **R** was then re-dissolved in boiling water, and the hot solution was then quickly filtered again. From this filtrate, the **R** recrystallized while it cooled. The crystals (purified **R**) were then collected via vacuum filtration and allowed to dry.

The ^1H NMR spectra of purified **R** was shown in **Supplementary Figure 1**, and the data was as follows: ^1H NMR (DMSO- d_6 600 MHz): 12.594 (1H, s, 5-OH), 10.833 (1H, s, 7-OH), 9.670 (1H, s, 3'-OH), 9.176 (1H, s, 4'-OH), 7.548 (2H, m, 2'-H, 6'-H), 6.842 (1H, d, $J = 8.16$ Hz, 5'-H), 6.386 (1H, d, $J = 2.04$ Hz, 8-H), 6.195 (1H, d, $J = 2.04$ Hz, 6-H), 5.344 (1H, d, $J = 7.32$ Hz, 1''-H), 4.385 (1H, s, 1'''-H), 4.346–4.384 and 4.527–5.283 (6H, m, sugar moieties-OH), 3.058–3.714 (10H, m, sugar moieties-H), 0.991 (3H, d, $J = 6.18$ Hz, sugar moieties- CH_3). The results confirmed **R** was successfully extracted from *Sophora japonica* (Nam et al., 2015; Yingyuen et al., 2020).

Preparation of the Stock Solutions

Stock solutions (1×10^{-2} mol·L $^{-1}$) of different metal salts were prepared by dissolving appropriate amount of metal salts into ultrapure water. The stock solutions of **R** and **CD** were prepared by dissolving the appropriate amounts of **R** and **CD** into methyl alcohol and PBS solutions, respectively. The **R-CD**

solution was prepared by adding the **R** solution into the **CD** solution at a volumetric ratio 1:99. The concentration of **R** in **R-CD** solution was $1 \times 10^{-5} \text{ mol}\cdot\text{L}^{-1}$, while the concentration of **CD** varied by experiment.

Optimizing Concentration of CD

To study the effect of **CD** concentration on the fluorescence emission intensity, **R-CD** solutions with different concentrations of **CD** were measured via fluorescent spectrophotometry at the excitation wavelength 425 nm (**Supplementary Figure 2**). The concentrations corresponding to stronger fluorescence emission intensity were considered during these experiments.

Selectivity and Sensitivity of R-CD on Copper Ions

In order to evaluate the sensor system's selectivity for copper or other ions, stock solutions of different metal salts were added into individual **R-CD** solutions. And the fluorescence emission intensities were measured to study the changes after adding metal ions. For the mixed solutions, the concentration of copper ions was controlled at $1 \times 10^{-5} \text{ mol}\cdot\text{L}^{-1}$, the other metal ions was controlled at $2 \times 10^{-5} \text{ mol}\cdot\text{L}^{-1}$, or $5 \times 10^{-5} \text{ mol}\cdot\text{L}^{-1}$.

To evaluate the influence from other metal ions on the process of detecting copper ions, a pre-determined amount of copper ions was added into **R-CD** solutions to produce **R-CD-Cu(II)** complexes. Next, the other investigated metal ions were introduced into the **R-CD-Cu(II)** complex. And the fluorescence emission intensities of **R-CD-Cu(II)** complexes were measured.

In effort to evaluate the strength of correlation between fluorescence emission intensity and copper ions concentration, fluorescence titration experiments were performed. From this, fluorescence emission intensities of **R-CD** with various concentrations of copper ions were measured.

Stoichiometric Ratio

The stoichiometric ratio between the **R** and copper ions in **R-CD-Cu(II)** complex was determined by Job's method according to the literature (Facchiano and Ragone, 2003).

Detecting Copper Ions in Real Samples

The ability of **R-CD** to recognize copper ions in a real sample was verified by designing experiments to detect copper ions in various solutions prepared in our laboratory.

RESULTS AND DISCUSSION

Relationship Between CD Concentration and Fluorescent Intensity

To study how concentration of **CD** impacts fluorescence emission intensity of **R**, increasing amounts of **CD** were added to solution and respective fluorescence emission spectra of **R** were recorded (**Figure 1**). To begin, it is evident that **R** and **CD** had no obvious emission peaks between 510 and 700 nm. When adding **R** into buffer solution containing **CD**, the fluorescence emission peak at 535 of **R** became stronger when increasing [**CD**]. However, once the concentration of **CD** reached $10 \text{ g}\cdot\text{L}^{-1}$, no further increase to fluorescence emission intensity was observed.

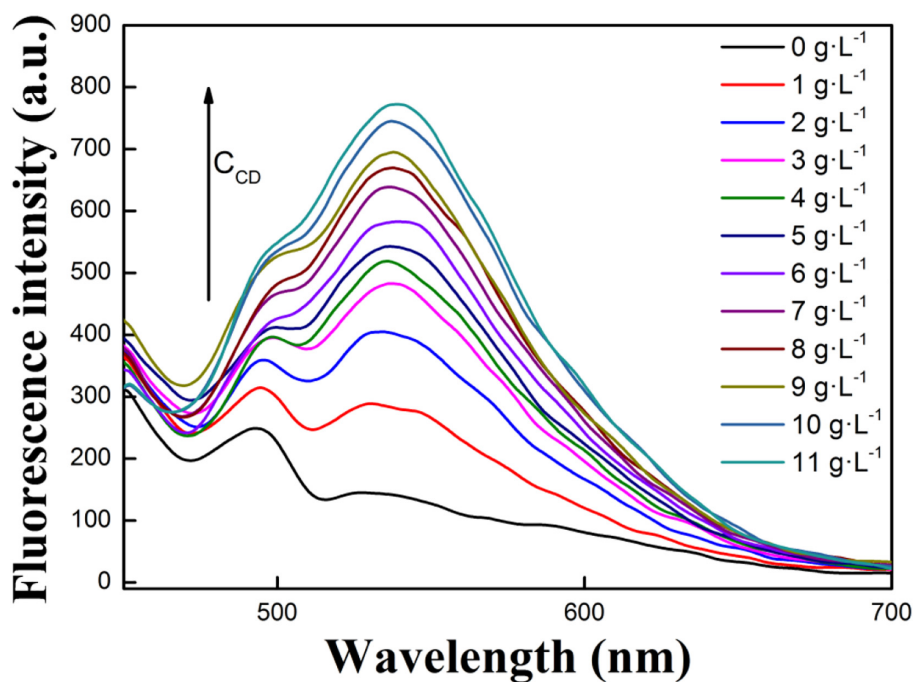


FIGURE 1 | Effects of **CD** concentration on the fluorescence intensity of **R** in buffer solution (1:99, V/V, pH = 7.40, [**R**] = $1.0 \times 10^{-5} \text{ mol}\cdot\text{L}^{-1}$).

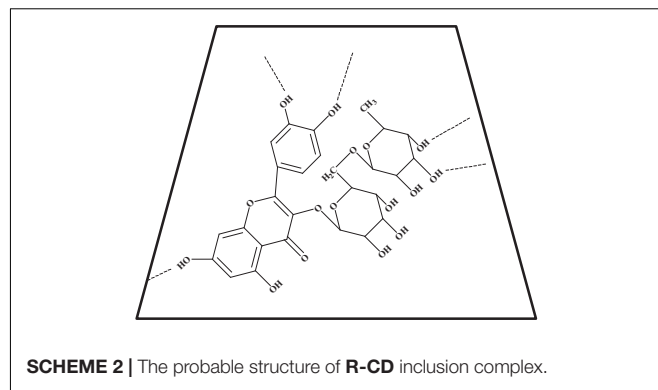
Thus, $10 \text{ g}\cdot\text{L}^{-1}$ was selected as an experimental condition for follow-up experiments. Overall, these spectra demonstrated that the interaction between **R** and **CD** occurs, and that the **R-CD** inclusion complex forms. To understand the interaction, FT-IR and ^1H NMR spectra of **R**, **CD**, and **R-CD** were studied.

When observing the acquired FT-IR spectra (**Supplementary Figure 3**), it was found that **R-CD** possessed all peaks that both **R** and **CD** had when alone. However, the absorption band of polyhydroxyl from **R-CD** became narrower compared to **R**. This change indicates that **R** interacts with **CD** through at least one of its multiple hydroxyl functional groups. Further evidence supporting the inclusion of **R** inside the cavity of **CD** was obtained by ^1H NMR. The ^1H NMR spectra of **R**, **CD** and **R-CD** can be found in **Supplementary Figure 4**. It is seen in the spectra that some peaks of **R** in **R-CD** either weakened or disappeared, along with broadening and up-field shifts of some peaks taking place (**Table 1**). These results supported the hypothesis regarding inclusion of **R** inside the cavity of **CD** via interaction around hydroxyl functionalities.

CD is cyclic oligosaccharides with cylindrical barrelled structures. It is reported in literature that **CD** can form inclusion complexes with **R** through the intermolecular forces of hydrogen bonding as well as hydrophobic interactions (Yan et al., 2006; Kellici et al., 2015; Savic et al., 2015). Depictions of some probable **R-CD** chemical structures can be found in **Scheme 2**. From these images, it can be hypothesized that molecular mobility and inter-molecular collisions between **R** molecules were reduced in frequency upon formation of the inclusion complexes. The decrease in these properties effectively prevents conveyance of energy amongst un-complexed **R** molecules. As a result of these changes, the intensity of fluorescence emission was elevated upon addition of **CD** (Zhang et al., 2011). In addition, the fluorescence emission intensity had no obvious change within 24 h (**Supplementary Figure 5**), which indicated that the **R-CD** was very stable.

Ion Detection Selectivity

To investigate the extent of the **R-CD** inclusion complex's selectivity toward a selection of various metal ions, a wide swath of



metal cations were doped into separate **R-CD** solutions. Effects of these various cations on fluorescence intensity are shown in **Figure 2**. The primary finding here was that the only cation which showed any differentiation was copper ions, which provided a sharp decrease to **R-CD**'s intensity of emission. All of the other tested cations rendered no significant changes to emission spectra, even at higher concentrations. This lack of variation clearly suggested that **R-CD** could clearly recognize copper ions, and only copper ions, with good selectivity.

The next set of experiments conducted was intended to investigate how the presence of non-copper cations impact recognition of **R-CD** to copper ions. All of the previously tested cations were again analyzed through addition into a solution containing **R-CD-Cu(II)**. Resultant fluorescence spectra from these new mixtures were shown in **Figure 3**. From these results, it can be seen that emission intensity of **R-CD-Cu(II)** was subject to fluctuation when in the presence of the testing cations. However, these fluctuations were deemed mostly minor with respect to relative percent change, resulting in our conclusion that suggested that the recognition process of copper ions by **R-CD** retains its notable selectivity toward copper ions even when in matrices containing all of the cations tested in this work.

Copper Detection Sensitivity With Respect to Changing $[\text{Cu}^{2+}]$

From the previous results, it was next decided to quantitatively define the system of **R-CD** toward detection of copper ions in solution. Results from these experiments are displayed in **Figure 4**. To begin, it was found that the intensity of fluorescence at 535 nm was subject to a gradual decrease when the concentration of copper ions ($[\text{Cu}^{2+}]$) began to rise. From the intensity values over the tested range, it was found that intensity was inversely proportional to $[\text{Cu}^{2+}]$ over the concentration range of 1.0×10^{-7} – $4.2 \times 10^{-6} \text{ mol}\cdot\text{L}^{-1}$. Within this range, a calibration curve could be constructed. Specifically, the linear regression equation was defined as $y = -10.41x + 723.77$ ($R^2 = 0.9974$), where y = fluorescence intensity and $x = [\text{Cu}^{2+}]$. The detection limit of copper ions was $3.5 \times 10^{-8} \text{ mol}\cdot\text{L}^{-1}$ (Gu et al., 2014). Based upon the relatively wide range of this regression, it can be concluded that the system is effectively sensitive to the presence of copper ions.

TABLE 1 | The chemical shifts of **R-CD** and **R**.

R/ppm	R-CD/ppm	R/ppm	R-CD/ppm
12.6096	12.5930	5.3660	5.3467
10.8489	–	5.3537	5.3344
9.6851	–	5.2987	5.2741
9.1910	–	5.1240	–
7.5653	7.5446	5.0938	–
7.5617	7.5306	4.5427	–
7.5484	7.5282	4.4005	–
6.8645	6.8444	4.3991	4.3812
6.8510	6.8307	4.3614	–
6.4028	6.3810	3.0738–3.7298	3.0368–3.7123
6.3994	6.1904	1.0113	0.9953
6.2118	6.1870	1.0009	0.9849
6.2084	5.9465		

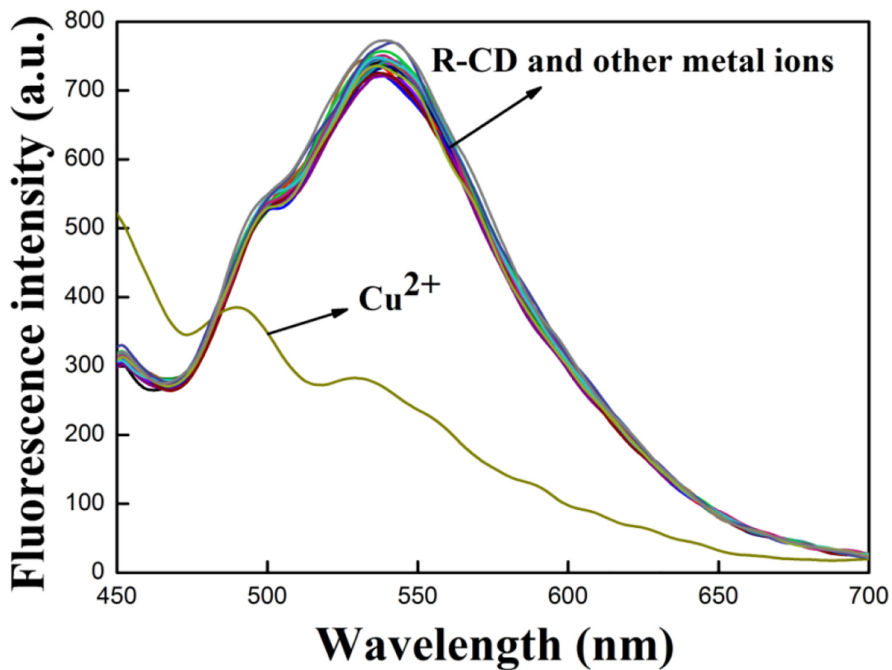


FIGURE 2 | Resultant emission spectra from different cations and R-CD in buffer solution.

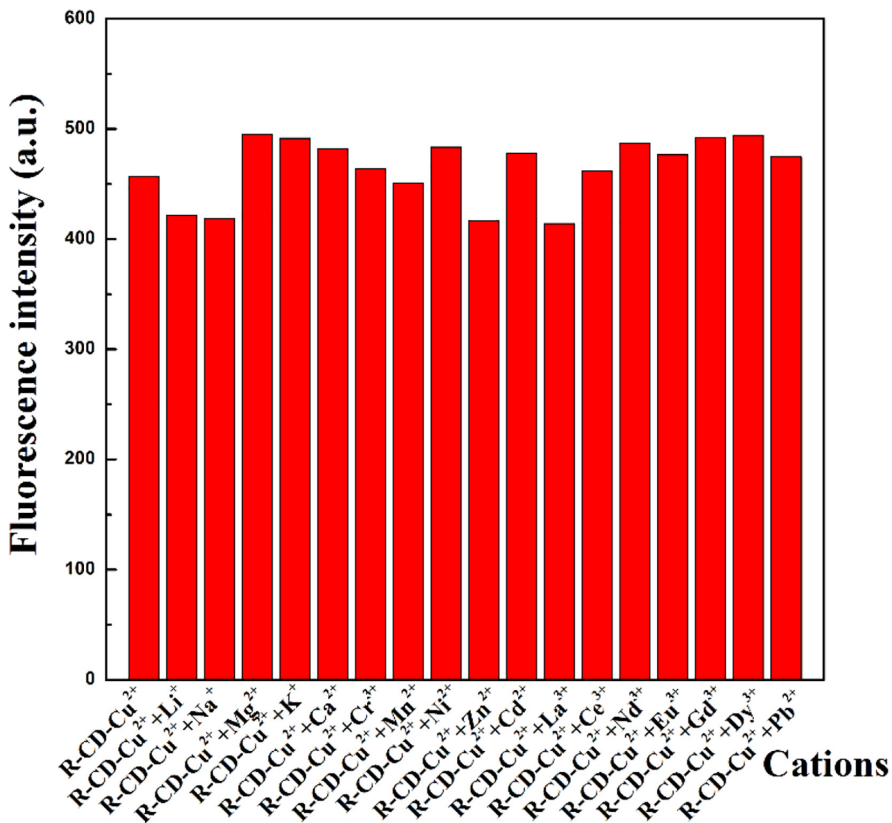


FIGURE 3 | Perturbations to fluorescent intensity of R-CD-Cu(II) through the presence of other cations.

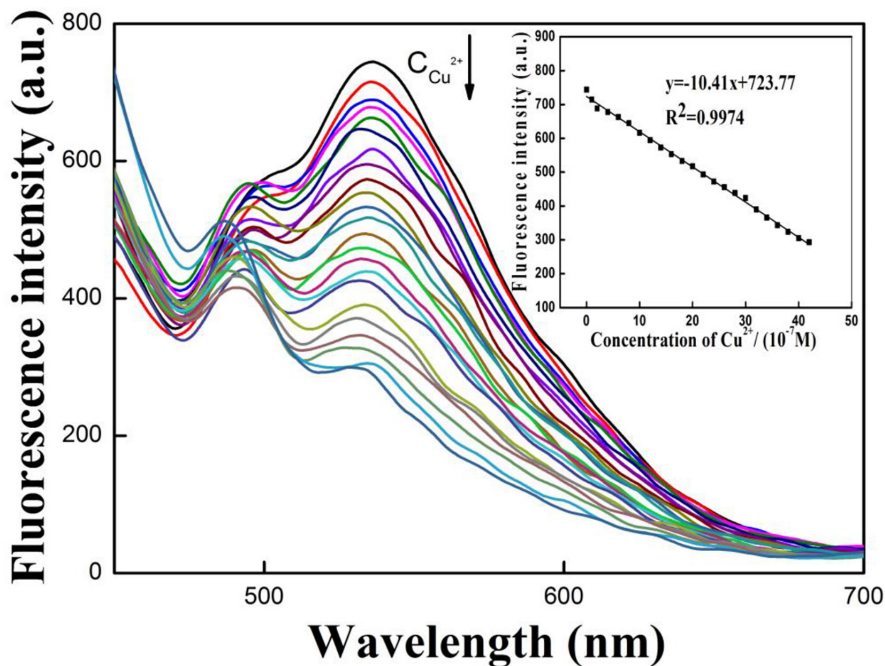


FIGURE 4 | Variance in wavelength emission at increasing copper ions concentrations; quantitative regression between varying concentrations of copper ions and emission intensity in buffer solution.

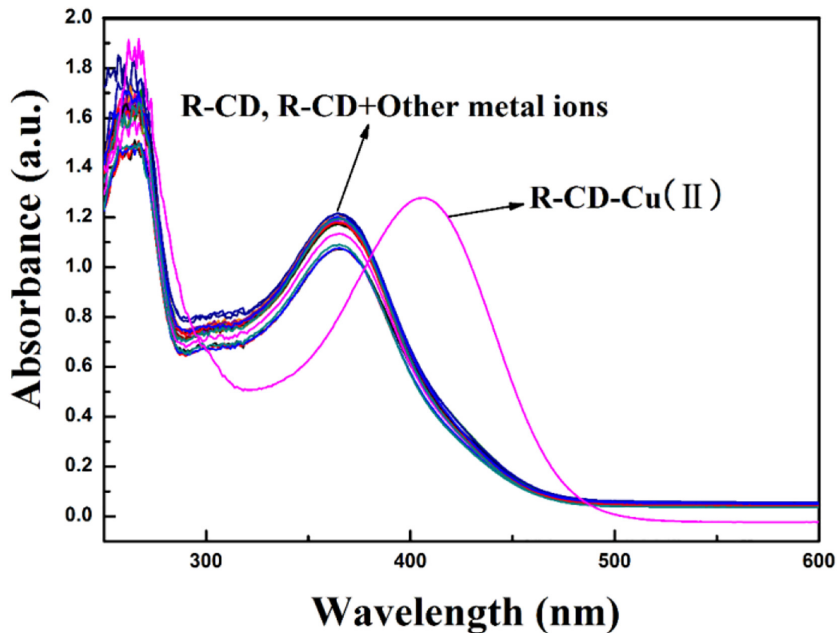


FIGURE 5 | Characteristic UV-visible absorption spectra of **R-CD** in buffer solution when in the presence of copper or other tested cations.

Evaluating Structural Properties of the Detectable Complex

With the previous results in hand, we began to ponder the components which drive the ability to quantitatively detect copper cations with the R-CD. It can be speculated that the first

step involved the occurrence of fluorescence quenching. In other words, copper cations engaged with R-CD in a way that yielded a R-CD-Cu(II) complex. With this final product in mind, the actual structure of the R-CD-Cu(II) complex was investigated via UV-visible spectrophotometry as well as Job's plots experiments.

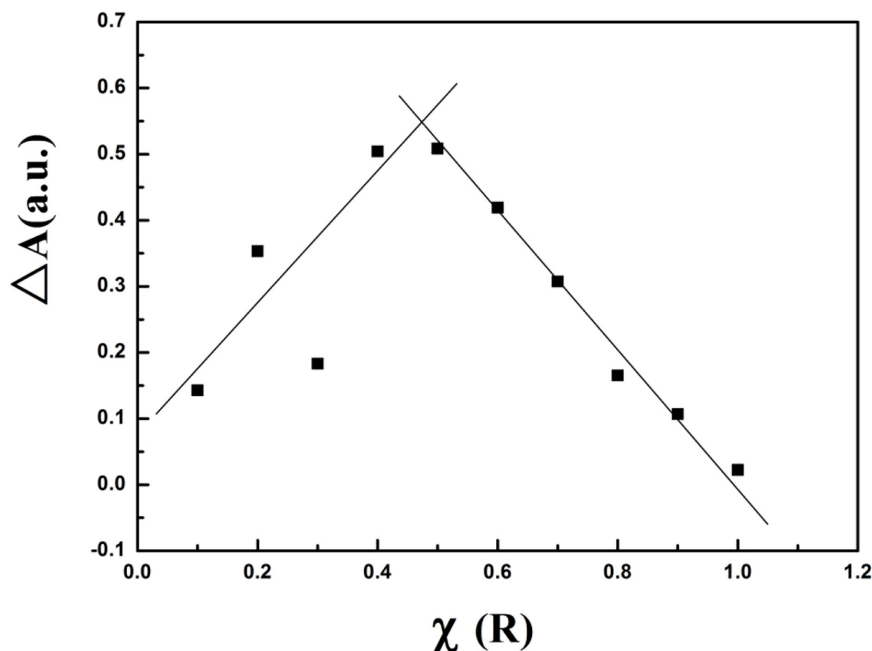


FIGURE 6 | Resultant Job's plot for **R-CD-Cu(II)** in buffer solution.

First, the UV-visible spectra of **R-CD** and **R-CD-Cu(II)** were acquired (**Figure 5**). For the UV-visible spectrum of **R-CD**, it was found that there were two spectra-defining absorption bands: 375 nm (band I) and 260 nm (band II). It is important to note that both of these bands were typical for flavonoids, and they can be related back to the B-ring cinnamoyl system and the A-ring benzoyl system, respectively (Uzasc and Erim, 2014). Comparing the copper inclusion complex with neat **R-CD**, it was noted that band I shifted to 419 nm. This bathochromic shift might be best understood by the new complex effectively extending the existing conjugated system defining **R-CD**. The fact that none of the other cations demonstrated this change further demonstrates that the complexation was more specific than overall cationic charge, and was instead driven by alignment of orbitals unique to copper and **R-CD**.

Based upon this unique configuration, we next endeavored to better understand the stoichiometry driving creation of

the **R-CD-Cu(II)** complex. We decided to conduct Job's plots experiments in order to achieve such results (**Figure 6**). For these experiments, changes to absorption band intensity at 419 nm was compared against molar fraction of **R** (χ) of the reactants. It was observed from the plot that maximum absorbance occurred when $\chi = 0.5$, which suggests that the stoichiometric ratio of **R** and copper cations was actually 1:1. Furthermore, a stability constant (K) for the resultant complex was calculated as 1.33×10^6 , indicating that the **R-CD-Cu(II)** complex's stability was relatively strong and largely resistant to reversion back to the individual components. This stability is most likely driven by the stability provided to the electrons via the extension of conjugation.

Spectra from FT-IR for **R-CD** and **R-CD-Cu(II)** are shown in **Supplementary Figure 2**. The key differentiator between the two spectra was a shift to 4-carbonyl. Specifically, 4-carbonyl stretching in **R-CD** was found at $1,653 \text{ cm}^{-1}$. For the **R-CD-Cu(II)** complex, the stretching peak was shifted to $1,629 \text{ cm}^{-1}$. This change suggests the 4-carbonyl functionality is involved in the complexation process. Based upon this clue, a hypothetical chemical structure for **R-CD-Cu(II)** complex has been included in this report as **Scheme 3**. In summary, it can

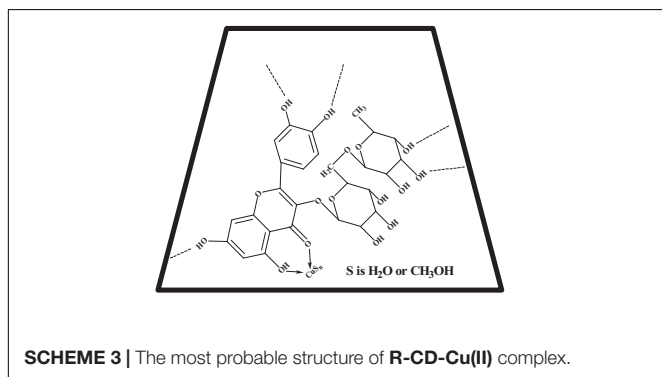


TABLE 2 | Quantification of Cu^{2+} in spiked samples using **R-CD** fluorescent sensor technology.

Samples	Adding concentration ($10^{-7}/\text{mol}\cdot\text{L}^{-1}$)	Measurement ($10^{-7}/\text{mol}\cdot\text{L}^{-1}$)	RSD (%)	Recovery (%)
1	22	22.03 ± 0.11	0.50	100.14
2	25	24.87 ± 0.06	0.24	99.48
3	36	35.57 ± 0.10	0.28	98.81

be said that formation of **R-CD-Cu(II)** complexes is initiated by an intramolecular charge transfer driven by the energy gain from extended molecular conjugation, subsequently allowing for fluorescence quenching take place (Parveen et al., 2015).

Determining Copper Cations Contents in Real Samples

To verify the feasibility of the quantification method described herein, we applied the approach to water samples spiked with copper. Varied amounts of copper cations were first added to pure water, and the quantification results were obtained by **R-CD** in **Table 2**. Compared with the content of copper cations added, the values obtained by this method were accurate. Specifically, Cu^{2+} recovery was 100.1, 99.5, and 98.8%, respectively. These promising values again demonstrated that the capability of the fluorescent sensor system developed in this work.

CONCLUSION

The investigated **R-CD** fluorescent sensor system was shown to selectively and accurately detect copper cations aqueous media, and was verified against spiked samples with near recovery around 100%. The mechanism for copper detection is driven by formation of the **R-CD-Cu(II)** complex, which is stabilized through an extension of the conjugated system present in **R-CD**. The resultant complex generated an ICT effect, causing fluorescence quenching. The findings of this work demonstrate that minor constituents of biomass, likely to be liberated during biorefinery processes, could be isolated in small quantities to produce materials with high-value application potential.

REFERENCES

- Chen, J. C., Jiang, W. N., Lu, W., Xu, L., Yang, S. L., Xue, H. Y., et al. (2019). A Study on the interaction between new indole amide compound and aluminum(III) ion. *Chem. Select.* 4, 4371–4375. doi: 10.1002/slct.201900217
- Dong, H. L., Zheng, L. M., Yu, P. J., Jiang, Q., Wu, Y., Huang, C. X., et al. (2020). Characterization and application of lignin-carbohydrate complexes from lignocellulosic materials as antioxidants for scavenging in vitro and in vivo reactive oxygen species. *ACS Sustain. Chem. Eng.* 8, 256–266. doi: 10.1021/acsschemeng.9b05290
- Du, H. S., Liu, W. M., Zhang, M. L., Si, C. L., Zhang, X. Y., and Li, B. (2019). Cellulose nanocrystals and cellulose nanofibrils based hydrogels for biomedical applications. *Carbohydr. Polym.* 209, 130–144. doi: 10.1016/j.carbpol.2019.01.020
- Facchiano, A., and Ragone, R. (2003). Modification of Job's method for determining the stoichiometry of protein-protein complexes. *Anal. Biochem.* 313, 170–172. doi: 10.1016/S0003-2697(02)00562-6
- Gu, L. Q., Wan, X. J., Liu, H. Y., Liu, T. Q., and Yao, Y. W. (2014). A novel ratiometric fluorescence sensor for Zn^{2+} detection. *Anal. Methods* 6, 8460–8463. doi: 10.1039/c4ay01483a
- He, T., Niu, N., Chen, Z. J., Li, S. J., Liu, S. X., and Li, J. (2018). Novel quercetin aggregation-induced emission luminogen (AIEgen) with excited-state intramolecular proton transfer for in vivo bioimaging. *Adv. Func. Mater.* 28:1706196. doi: 10.1002/adfm.201706196
- Huang, C. X., Dong, H. L., Zhang, Z. P., Bian, H. Y., and Yong, Q. (2020). Procuring the nano-scale lignin in prehydrolyzate as ingredient to prepare cellulose nanofibril composite film with multiple functions. *Cellulose.* 27, 9355–9370. doi: 10.1007/s10570-020-03427-9

DATA AVAILABILITY STATEMENT

The original contributions presented in the study are included in the article/**Supplementary Material**, further inquiries can be directed to the corresponding author/s.

AUTHOR CONTRIBUTIONS

SY, LS, and ZS did the experiments and analyzed the experimental data. LX designed the research. SY and LX wrote the manuscript. All authors contributed to the article and approved the submitted version.

FUNDING

This work was supported by the Natural Science Research of Jiangsu Higher Education Institutions of China (19KJB220005), the Innovation Fund for Young Scholars of Nanjing Forestry University (CX2017004), and the National Key Research and Development Program of China (2017YFD060070602).

SUPPLEMENTARY MATERIAL

The Supplementary Material for this article can be found online at: <https://www.frontiersin.org/articles/10.3389/fbioe.2021.642138/full#supplementary-material>

- Huynh, T., Wang, H. R., and Luan, B. Q. (2020). Structure-based lead optimization of herbal medicine rutin for inhibiting SARS-CoV-2's main protease. *Phys. Chem. Chem. Phys.* 22, 25335–25343. doi: 10.1039/d0cp03867a
- Kan, C., Wu, L. Y., Shao, X. T., Wang, X., Zhang, Y., Zhu, J., et al. (2020). A new reversible fluorescent chemosensor based on rhodamine for rapid detection of Al(III) in natural environmental water samples and living organisms. *Tetrahedron Lett.* 61:152407. doi: 10.1016/j.tetlet.2020.152407
- Kellici, T. F., Ntountaniotis, D., Leonis, G., Chatziathanasiadou, M., Chatzikonstantinou, A. V., Becker-Baldus, J., et al. (2015). Investigation of the interactions of silibinin with 2-hydroxypropyl- β -cyclodextrin through biophysical techniques and computational methods. *Mol. Pharmaceut.* 12, 954–965. doi: 10.1021/mp5008053
- Li, Z., Xu, Y. Q., Xu, H. D., Cui, M. Y., Liu, T. G., Ren, X. Y., et al. (2021). A dicyanomethylene-4H-pyran-based fluorescence probe with high selectivity and sensitivity for detecting copper (II) and its bioimaging in living cells and tissue. *Spectrochim. Acta A.* 244:118819. doi: 10.1016/j.saa.2020.118819
- Nam, T. G., Lee, S. M., Park, J. H., Kim, D. O., Baek, N. I., and Eom, S. H. (2015). Flavonoid analysis of buckwheat sprouts. *Food Chem.* 170, 97–101. doi: 10.1016/j.foodchem.2014.09.137
- Nkpaa, K. W., Onyeso, G. I., and Kponee, K. Z. (2019). Rutin abrogates manganese-induced striatal and hippocampal toxicity via inhibition of iron depletion, oxidative stress, inflammation and suppressing the NF-kappa B signaling pathway. *J. Trace Elem. Med. Bio.* 53, 8–15. doi: 10.1016/j.jtemb.2019.01.014
- Parveen, S. D. S., Kumar, B. S., Kumar, S. R., Khan, R. I., and Pitchumani, K. (2015). Isolation of biochanin A, an isoflavone, and its selective sensing of copper(II) ion. *Sensor. Actuat. B-Chem.* 221, 75–80. doi: 10.1016/j.snb.2015.06.060
- Pei, W. H., Chen, Z. S., Chan, H. Y. E., Zheng, L. M., Liang, C., and Huang, C. X. (2020a). Isolation and identification of a novel anti-protein aggregation activity

- of lignin-carbohydrate complex from chionanthus retusus leaves. *Front. Bioeng. Biotech.* 8:573991. doi: 10.3389/fbioe.2020.573991
- Pei, W. H., Shang, W. Q., Liang, C., Jiang, X., Huang, C. X., and Yong, Q. (2020b). Using lignin as the precursor to synthesize Fe₃O₄@lignin composite for preparing electromagnetic wave absorbing lignin-phenol-formaldehyde adhesive. *Ind. Crop. Prod.* 154:112638. doi: 10.1016/j.indcrop.2020.112638
- Savic, I. M., Nikolic, V. D., Savic-Gajic, I., Nikolic, L. B., Radovanovic, B. C., and Mladenovic, J. D. (2015). Investigation of properties and structural characterization of the quercetin inclusion complex with (2-hydroxypropyl)- β -cyclodextrin. *J. Incl. Phenom. Macro. Chem.* 82, 383–394. doi: 10.1007/s10847-015-0500-4
- Singh, M., Kaur, M., and Silakari, U. (2014). Flavones: An important scaffold for medicinal chemistry. *Eur. J. Med. Chem.* 84, 206–239. doi: 10.1016/j.ejmech.2014.07.013
- Su, Y., Dong, H. L., Li, M., Lai, C. H., Huang, C. X., and Yong, Q. (2019). Isolation of the flavonoid from bamboo residues and its application as metal ion sensor in vitro. *Polymers* 11:1377. doi: 10.3390/polym11091377
- Sun, S. J., Zhang, M., Umemura, K., and Zhao, Z. Y. (2019). Investigation and characterization of synthesis conditions on sucrose-ammonium dihydrogen phosphate (SADP) adhesive: Bond performance and chemical transformation. *Materials*. 12:4078. doi: 10.3390/ma12244078
- Uzasc, S., and Erim, F. B. (2014). Enhancement of native fluorescence intensity of berberine by (2-hydroxypropyl)- β -cyclodextrin in capillary electrophoresis coupled by laser-induced fluorescence detection: Application to quality control of medicinal plants. *J. Chromatogr. A.* 1338, 184–187. doi: 10.1016/j.chroma.2014.02.068
- Wani, T. A., Bakheit, A. H., Zargar, S., Alanazi, Z. S., and Al-Majed, A. A. (2021). Influence of antioxidant flavonoids quercetin and rutin on the in-vitro binding of neratinib to human serum albumin. *Spectrochim. Acta A.* 246, 118977. doi: 10.1016/j.saa.2020.118977
- Yan, C. L., Li, X. H., Xiu, Z. L., and Hao, C. (2006). A quantum-mechanical study on the complexation of β -cyclodextrin with quercetin. *J. Mol. Struct.-THEOCHEM.* 764, 95–100. doi: 10.1016/j.theochem.2006.02.008
- Yingyuen, P., Sukrong, S., and Phisalaphong, M. (2020). Isolation, separation and purification of rutin from Banana leaves (*Musa balbisiana*). *Ind. Crop. Prod.* 149:112307. doi: 10.1016/j.indcrop.2020.112307
- Zhang, M., Zhang, Y. H., and Ma, L. (2011). Studies and application of fluorescence of aflatoxin B-1 enhanced by synergetic effect of β -cyclodextrin and its derivatives and metalions. *Chinese J. Anal. Chem.* 39, 1907–1911. doi: 10.3724/SP.J.1096.2011.01907
- Zhang, X. L., Guo, X. H., Yuan, H. H., Jia, X., and Dai, B. (2018). One-pot synthesis of a natural phenol derived fluorescence sensor for Cu(II) and Hg(II) detection. *Dyes Pigments.* 155, 100–106. doi: 10.1016/j.dyepig.2018.03.037
- Zhao, Q., Zhang, Y., Wang, G., Hill, L., Weng, J. K., Chen, X. Y., et al. (2016). A specialized flavone biosynthetic pathway has evolved in the medicinal plant, *Scutellaria baicalensis*. *Sci. Adv.* 2:e1501780. doi: 10.1126/sciadv.1501780
- Zhao, Z. Y., Huang, C. X., Wu, D., Chen, Z., Zhu, N., Gui, C. S., et al. (2020). Utilization of enzymatic hydrolysate from corn stover as a precursor to synthesize an eco-friendly plywood adhesive. *Ind. Crop. Prod.* 152:112501. doi: 10.1016/j.indcrop.2020.112501
- Zheng, L. M., Yu, P. J., Zhang, Y. B., Wang, P., Yan, W. J., Guo, B. S., et al. (2021). Evaluating the bio-application of biomacromolecule of lignin-carbohydrate complexes (LCC) from wheat straw in bone metabolism via ROS scavenging. *Int. J. of Biol. Macromol.* 2021:103. doi: 10.1016/j.ijbiomac.2021.01.103
- Zhou, X., and Xu, Y. (2019). Integrative process for sugarcane bagasse biorefinery to co-produce xylooligosaccharides and gluconic acid. *Bioresource Technol.* 282, 81–87. doi: 10.1016/j.biortech.2019.02.129
- Zhou, X., Hua, X., Zhou, X. L., Xu, Y., and Zhang, W. X. (2019). Continuous co-production of biomass and bio-oxidized metabolite (sorbose) using gluconobacter oxydans in a high-oxygen tension bioreactor. *Bioresource Technol.* 277, 221–224. doi: 10.1016/j.biortech.2019.01.046

Conflict of Interest: The authors declare that the research was conducted in the absence of any commercial or financial relationships that could be construed as a potential conflict of interest.

Copyright © 2021 Yang, Sun, Song and Xu. This is an open-access article distributed under the terms of the Creative Commons Attribution License (CC BY). The use, distribution or reproduction in other forums is permitted, provided the original author(s) and the copyright owner(s) are credited and that the original publication in this journal is cited, in accordance with accepted academic practice. No use, distribution or reproduction is permitted which does not comply with these terms.



Engineered Polyploid Yeast Strains Enable Efficient Xylose Utilization and Ethanol Production in Corn Hydrolysates

Lulu Liu¹, Mingjie Jin², Mingtao Huang³, Yixuan Zhu¹, Wenjie Yuan⁴, Yingqian Kang⁵, Meilin Kong¹, Sajid Ali¹, Zefang Jia¹, Zhaoxian Xu², Wei Xiao^{1,6} and Limin Cao^{1*}

¹ Beijing Key Laboratory of Plant Gene Resources and Biotechnology for Carbon Reduction and Environmental Improvement, College of Life Sciences, Capital Normal University, Beijing, China, ² School of Environmental and Biological Engineering, Nanjing University of Science and Technology, Nanjing, China, ³ School of Food Science and Engineering, South China University of Technology, Guangzhou, China, ⁴ School of Bioengineering, Dalian University of Technology, Dalian, China, ⁵ Key Laboratory of Environmental Pollution Monitoring and Disease Control, School of Basic Medical Sciences, Guizhou Medical University, Guiyang, China, ⁶ Department of Biochemistry, Microbiology and Immunology, University of Saskatchewan, Saskatoon, SK, Canada

OPEN ACCESS

Edited by:

Xin Zhou,
Nanjing Forestry University, China

Reviewed by:

Wensheng Qin,
Lakehead University, Canada
Yucai He,
Changzhou University, China

*Correspondence:

Limin Cao
caolimin@cnu.edu.cn

Specialty section:

This article was submitted to
Bioprocess Engineering,
a section of the journal
Frontiers in Bioengineering and
Biotechnology

Received: 18 January 2021

Accepted: 08 February 2021

Published: 05 March 2021

Citation:

Liu L, Jin M, Huang M, Zhu Y,
Yuan W, Kang Y, Kong M, Ali S, Jia Z,
Xu Z, Xiao W and Cao L (2021)
Engineered Polyploid Yeast Strains
Enable Efficient Xylose Utilization
and Ethanol Production in Corn
Hydrolysates.
Front. Bioeng. Biotechnol. 9:655272.
doi: 10.3389/fbioe.2021.655272

The reported haploid *Saccharomyces cerevisiae* strain F106 can utilize xylose for ethanol production. After a series of *XR* and/or *XDH* mutations were introduced into F106, the *XR-K270R* mutant was found to outperform others. The corresponding haploid, diploid, and triploid strains were then constructed and their fermentation performance was compared. Strains F106-KR and the diploid produced an ethanol yield of 0.45 and 0.48 g/g total sugars, respectively, in simulated corn hydrolysates within 36 h. Using non-detoxicated corncob hydrolysate as the substrate, the ethanol yield with the triploid was approximately sevenfold than that of the diploid at 40°C. After a comprehensive evaluation of growth on corn stover hydrolysates pretreated with diluted acid or alkali and different substrate concentrations, ethanol yields of the triploid strain were consistently higher than those of the diploid using acid-pretreatment. These results demonstrate that the yeast chromosomal copy number is positively correlated with increased ethanol production under our experimental conditions.

Keywords: *Saccharomyces cerevisiae*, mutation, triploid, hydrolysate, ethanol

INTRODUCTION

The global corn yield has reached 1.1 billion tonnes in 2019, ranking first in all kinds of grain output. Due to their abundance, corn and corn stover have become popular feedstocks for the production of various industrial fuels and chemicals such as bioethanol and D-lactic acid (Wang et al., 2017). Bioethanol produced by microbes can be used as alternative fuel to alleviate the looming energy shortage and current environmental problems caused by fossil fuel combustion (Chen et al., 2018). *Saccharomyces cerevisiae* preferentially ferments glucose, and it cannot naturally metabolize xylose, the second most abundant carbohydrate in plant biomass hydrolysates (Xiong et al., 2013;

van Dijk et al., 2019). Therefore, maximizing ethanol production from xylose by metabolic engineering of *S. cerevisiae* has become a research hotspot (Kim et al., 2013).

Three xylose utilization pathways can be introduced to realize xylose catabolism, including the Dahms or Weimberg pathway, the X-1-P or R-1-P pathway and the classical XR-XDH or XI pathway (Li et al., 2019). The XR-XDH branch can support higher metabolic fluxes than the XI branch, which is limited by the low catalytic efficiency of isomerase. However, an unbalanced redox system due to different cofactor preferences of XR and XDH needs to be optimized to reduce xylitol accumulation and increase conversion of xylose to ethanol (Xiong et al., 2011; Jo et al., 2017). The redox balance can be approached by protein engineering, including K270R, K270M and R276H substitutions in XR, or the D207A/I208R/F209S triple substitution in XDH (Kostrzynska et al., 1998; Watanabe et al., 2005; Watanabe et al., 2007a,b).

Meanwhile, it has been reported that polyploidy can accelerate the evolutionary adaptation of yeast, which is often accompanied by chromosomal aneuploidy, concerted chromosome loss, and point mutations (Selmecki et al., 2015). Compared with haploid strains, diploid and triploid strains, including those obtained by mating two haploid strains with suboptimal xylose fermentation phenotypes, showed an improved xylose fermentation ability and increased ethanol yield, in addition to increased tolerance to heat, acid, ethanol and other inhibitors (Chen et al., 2012). Therefore, the development of polyploid strains with modified redox balance may enable a further enhancement of xylose utilization and ethanol production.

With an average annual yield of 10 tons/hectare, corn is one of the major starchy crops widely used for bioethanol production. However, the process requires pretreatment, liquefaction, saccharification, fermentation and distillation to produce ethanol (Chen et al., 2018; Cripwell et al., 2020). The common methods, such as pretreatment with dilute acid (DA), dilute alkali (AL) and ionic liquids, contribute to breaking down the rigid structure of lignin and hemicellulose to release cellulose for the enzymatic hydrolysis, producing sugars that are then converted to ethanol (Huang et al., 2020; Sankaran et al., 2020). Additionally, a promising amino pretreatment method based on urea was found to effectively improve the performance of enzymatic saccharification of corn stover (Wang et al., 2018). Therefore, it is desirable to make full use of corn hydrolysates, including corn flour and corn distiller's grains, corn stover hydrolysates with/without urea and corncob fermentation broth, for the evaluation of polyploid strains.

In this study, we attempted to address the redox imbalance for improved xylose conversion capability by constructing different XR and/or XDH mutant strains. Previous studies have constructed haploid strains with relevant favorable mutations (Xiong et al., 2013; Jo et al., 2017). Here we constructed diploid and triploid strains based on the above work, and evaluated their fermentation performance in comprehensive corn hydrolysates. Our results demonstrate that an increase of ploidy can improve yeast fermentation efficiency, which lays a ground for the development of yeast-based cellulosic ethanol.

MATERIALS AND METHODS

Construction of Yeast Strains S15 and S16

The *S. cerevisiae* strains and plasmids used in this study are listed in **Supplementary Tables 1, 2**. To cross yeast strains, equal amount of two mating type yeast cells were mixed in a centrifuge tube (containing aseptic water). A proper amount of mixed liquid was cultivated on YPD solid medium (20 g/L glucose, 20 g/L peptone, 10 g/L yeast extract, 20 g/L agar) at 30°C for 2 days. Single colonies were used to inoculate a sporulation medium (1% potassium acetate, 1.5% agar) and incubated at 28°C for 2–3 days. The diploid strains were identified by observing sporulation and mating-type confirmation by PCR (Tani et al., 1993). The triploid strains were obtained by similar methods, mainly using a mixed culture of diploid (*MATa/a*) and haploid (*MAT α*) cells, followed by strain confirmation.

Construction of Plasmids YEp-CAS and YEp-KCAS

Plasmid YEp-CAS has two mutant sites: (1) The DNA sequence of the first one is "TCCAGATTCTCCGACGAATA C" corresponding to position + 286 bp to + 306 bp concerning the ATG start codon of the *XYL2* gene, whose sequence was changed to "TG TAGATTCTGTGACGAATGT"; (2) The DNA sequence of the second one is "GACATTTTCGACAAC" corresponding to position + 619 bp to + 633 bp, covering the ATG start codon of the *XYL2* gene, whose sequence was changed to "GCTAGATCCGACAGA".

The plasmid YEp-CAS was constructed as follows: (1) The two DNA fragments C4-1 and C4-2 were amplified by PCR from plasmid YEp-3X using the primer pairs *XYL2-U/XYL2C4-D* and *XYL2C4-U/XYL2 KPN-D* and digested with *DpnI* (**Supplementary Table 2**; Xiong et al., 2011; Xiong et al., 2013). (2) A fragment of approximately 400 bp was amplified by PCR using primers *XYL2-U* and *XYL2-D* with C4-1 and C4-2 as templates, digested with *SalI* and *XbaI*, and inserted into the corresponding sites of plasmid pUC18 to form pUC18-C4. (3) *ARS-1* and *ARS-2* were amplified by PCR using primer pairs *XYL2KPN-U/XYL2 ARS-D* and *XYL2ARS-U/XYL2-D* with plasmid YEp-3X as the template, and digested with *DpnI* (**Supplementary Table 3**). (4) A fragment of approximately 700 bp was amplified by PCR using primers *XYL2 KPN-U* and *XYL2-D* with *ARS-1* and *ARS-2* as templates, digested with *KpnI* and *XbaI*, and inserted into the corresponding sites of plasmid pUC18-C4 to form pUC18-CAS. The resulting plasmid pUC18-CAS was confirmed by sequencing. (5) The mutant *XYL2* gene was cleaved from pUC18-CAS by using *SalI* and *XbaI*, and inserted into plasmid pUC18-PXYL2 to form pUC18-PXYL2 (CAS). (6) The wild-type sequence of PXYL2 in the plasmid YEp-3X was replaced by the corresponding sequence of pUC18-PXYL2 (CAS) to form plasmid YEp-CAS. YEp-CAS was the shuttle plasmid expressing *XYL1*, *XYL2* (CAS) and *XKS1* (Xiong et al., 2011). To construct the plasmid YEp-KCAS, the wild-type sequence of PXYL2 in the plasmid YEp-KR was replaced with the corresponding sequence of pUC18-PXYL2 (CAS) to form

plasmid YEp-KCAS. All other plasmids were constructed in a similar manner (Supplementary Table 2).

Synthetic Sugar Medium

Yeast cells cultured in YPD with shaking at 200 rpm for 16 h were collected by centrifugation, washed, and used to inoculate a 500-mL flask containing fresh YPDX medium (200 mL, 10 g/L yeast extract, 20 g/L peptone, 50 g/L or 80 g/L or 100 g/L glucose and 50 g/L xylose) to an initial OD₆₀₀ of 1 (Nambu-Nishida et al., 2018). The fermentation was performed at 30°C and 150 rpm shaking for 72 h under anaerobic conditions.

Hydrolysates With Added Urea

The seed cultures were obtained as described above, washed with saline and re-suspended in the corn stover hydrolysate containing 1 g/L urea before inoculation (provided by the company), then fermented it at 30°C in a 500-mL flask (Mataffo et al., 2020).

Pretreatment of Corn Flour (CF)

Using aseptic CF as substrate (30%, calculated by solid mass), sterile filtered α -amylase (0.064% of corn concentration) was added to liquefy at 85°C for 4 h (pH 5.7). Then, the amyloglucosidase (0.1% of CF concentration) used for saccharification and Novisin cellulase (0.6% of CF concentration) were added for the pre-degradation within 0.5 h at 50°C (pH 4.8), which was transferred to a flask used for yeast fermentation, seeded to an OD₆₀₀ of 1.0 and grown at 30°C and 150 rpm shaking for 72 h. The initial pH was set to 4.6.

Treatment of Corn Distiller's Grains

The distiller's grains stored at 4°C for 24 h were fermented for 96 h and treated with dilute acid (95°C, 1% dilute sulfuric acid, 90 min). The material was weighed and made up with sterile water to the previous quantity. After pre-treatment, rotary vacuum steam treatment (−0.09 MPa, 85°C, 30 min) was used to remove the remaining ethanol from the distiller's grains. After steaming, the dry matter concentration was kept constant by adding water (Biener et al., 2012). The pH of the system was adjusted to 4.8–5.0. Afterward, the distiller's grains were hydrolyzed with 0.6% cellulase and 1.5% xylanase at 50°C and 250 rpm shaking for 24 h (Hu et al., 2015; Xiao et al., 2019). Yeast cells were then used for fermentation at pH 4.6, 30°C and 150 rpm shaking (initial OD₆₀₀ of 1).

Preparation of Corncob Hydrolysates

A mixture of 0.5% (w/w) H₂SO₄ and 1.5% (w/w) H₃PO₄ was added to the crushed corncob set aside after drying at 105°C for 4 h at a solid-liquid ratio of 1:3, followed by treatment at 128°C for 1 h. Subsequently, the solid-liquid ratio and pH value were adjusted to 1:8 and 5, respectively, followed by adding 2 g/L peptone and 5 g/L yeast extract, and sterilization at 115 °C for 15 min. Seed cultures obtained by activation, amplification and culture (30°C, 150 rpm) were added to the resulting non-detoxicated hydrolysate (initial OD₆₂₀ of 2). Then, the mixtures were subjected to two-stage simultaneous saccharification co-fermentation (SSCF) at 40°C and 200 rpm shaking for 60 h in

500-mL flask, in which cellulose (20 FPU/g) was added after first stage fermentation and fermented for 36 h sequentially (Du et al., 2020).

Dilute Acid (DA) and Dilute Alkali (AL) Treatment of Corn Stover (CS)

The dilute acid (DA) pretreatment of corn stover was carried out in a 2-L high-pressure reactor with 10% (w/w) biomass and 1% (w/w) H₂SO₄ at 160°C for 10 min, and the CS slurry was neutralized with NaOH to pH 7.0 (Avci et al., 2013). The neutralized biomass was washed until the filtrate was clear, and dried at 60 °C until the moisture of CS after treatment was 10–20%. The dilute alkali (AL) pretreatment was performed in a 1-L flask containing 2% (w/w) sodium hydroxide, and 10% (w/w) biomass at 121°C for 20 min. After pretreatment, the pH of the CS slurry was adjusted to 7.0 with HCl, and the neutralized biomass was washed until the filtrate was clear, and dried at 60°C until the moisture of CS after treatment was 10–20%. All the pretreated CS was stored at 4°C until further use.

The enzymatic hydrolysis of pretreated biomass at different substrate concentrations (20 and 30%) was carried out at pH 4.8, 50°C, and 250 rpm shaking for 72 h. The total enzyme dosage was 40 mg protein/g polysaccharides, and the cellulase to xylanase ratio was 7:3. When the substrate concentration was 20 and 30%, the biomass and enzyme was fed at a ratio of 1:1 and 2:1, respectively. Sugar concentrations of the hydrolysates are shown in Supplementary Figure 2.

Quantitative Measurements During Fermentation

Microscopy was utilized to examine whether bacteria contaminated the yeast cultures and observe the germination or mortality rate of *S. cerevisiae* after staining it with methylene blue. During the experiment, cells from both the logarithmic phase and the initial cell volume needed to be determined by spectrophotometry at 600 nm or 620 nm (OD₆₀₀ or OD₆₂₀). One mL fermentation samples were taken at indicated time under sterile conditions and each component was measured by high performance liquid chromatography (HPLC), as described previously (Cao et al., 2014).

RESULTS AND DISCUSSION

Evaluation of Haploid and Diploid Strains Harboring XR and/or XDH Mutations

The previously reported *S. cerevisiae* haploid strain F106-KR with the XR-K270R mutation produced 77.6 g/L ethanol from 220 g/L xylose and had an ethanol yield of 0.42 g/g total sugar in mixed sugar fermentation, which makes it a highly promising industrial strain (Xiong et al., 2013). It was speculated that a redox imbalance caused by different cofactor preferences of XR and XDH leads to increased xylitol accumulation and reduced ethanol formation during fermentation, which could be alleviated by modifying the XR or XDH enzymes via protein engineering (Jeppsson et al., 2006;

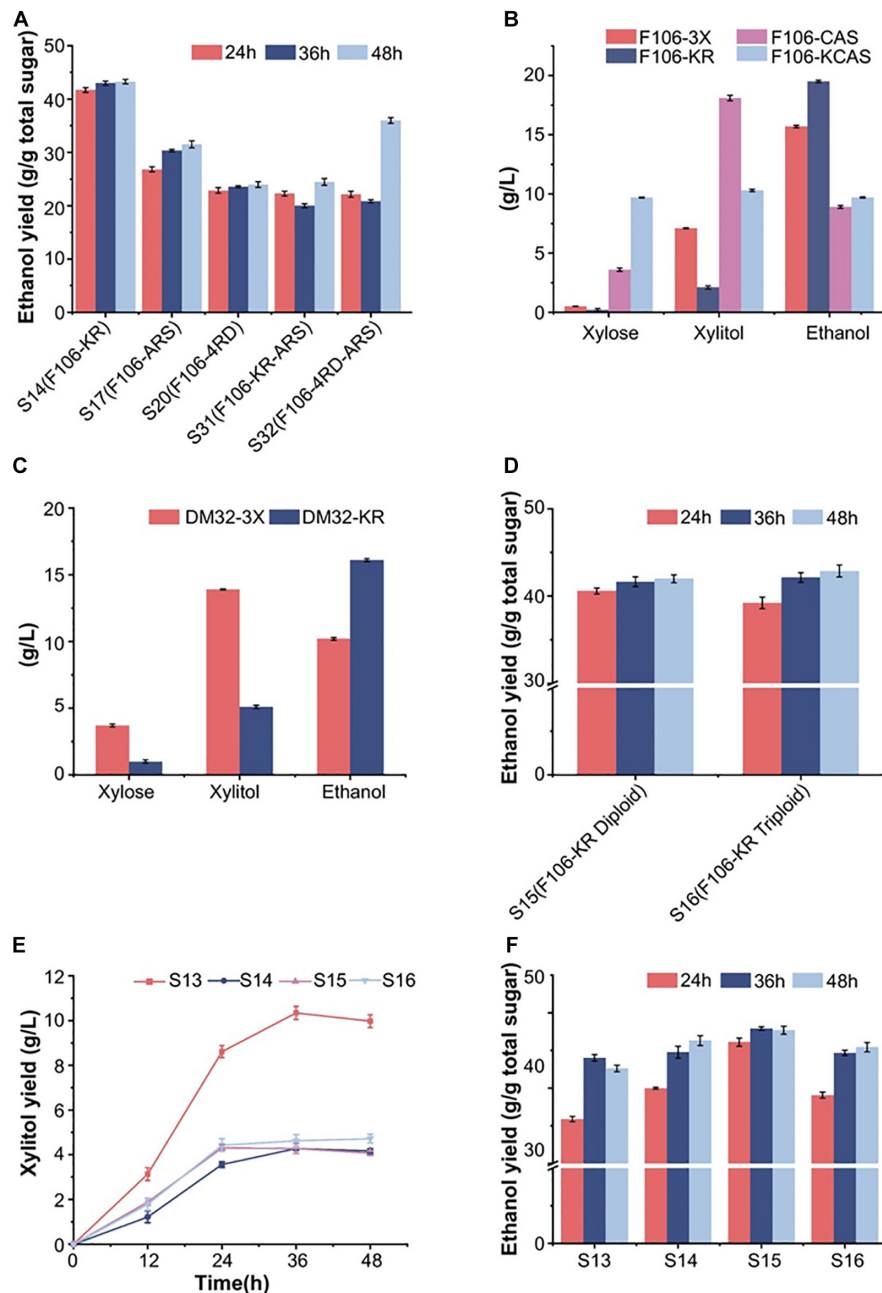


FIGURE 1 | Anaerobic fermentation results of engineered yeast strains in synthetic media (glucose and/or xylose). **(A)** Ethanol production of 5 haploid strains during 48 h in mixed sugar medium (50 g/L glucose and 50 g/L xylose). **(B)** The xylose, xylitol and ethanol production of the haploid F106 carrying different plasmids (3X, KR, CAS, KCAS) after fermentation in pure xylose medium for the indicated time. **(C)** The fermentation results of diploid strains DM-3X and DM-KR for three days in a synthetic xylose medium. **(D)** Ethanol yield of S15 (F106-KR diploid) and S16 (F106-KR triploid) in a mixed sugar medium. Xylitol **(E)** and ethanol **(F)** yield of indicated strains after fermenting for 48 h in simulated corn stover hydrolysate (80 g/L glucose, 40 g/L xylose with 3 g/L acetate). The experimental results were averaged over three parallel experiments with standard deviations.

Watanabe et al., 2007b; Petschacher and Nidetzky, 2008; Matsushika et al., 2009). Indeed, a mutant form of ARSdR XDH with multiple mutations (D207A/I208R/F209S/N211R, or ARS), which resulted in a complete reversal of coenzyme specificity toward NADP⁺, was reported to increase ethanol production with decreased xylitol content (Watanabe et al., 2005, 2007b).

Other *S. cerevisiae* strains harboring the NADH-prefering XR mutations, like *K274R* and *K274R/N276D* (named 4RD) from *Candida tenuis*, also showed increased ethanol yields and decreased xylitol accumulation (Petschacher et al., 2005; Petschacher and Nidetzky, 2008). Hence, we constructed five engineered strains based on strain F106, which were named S14

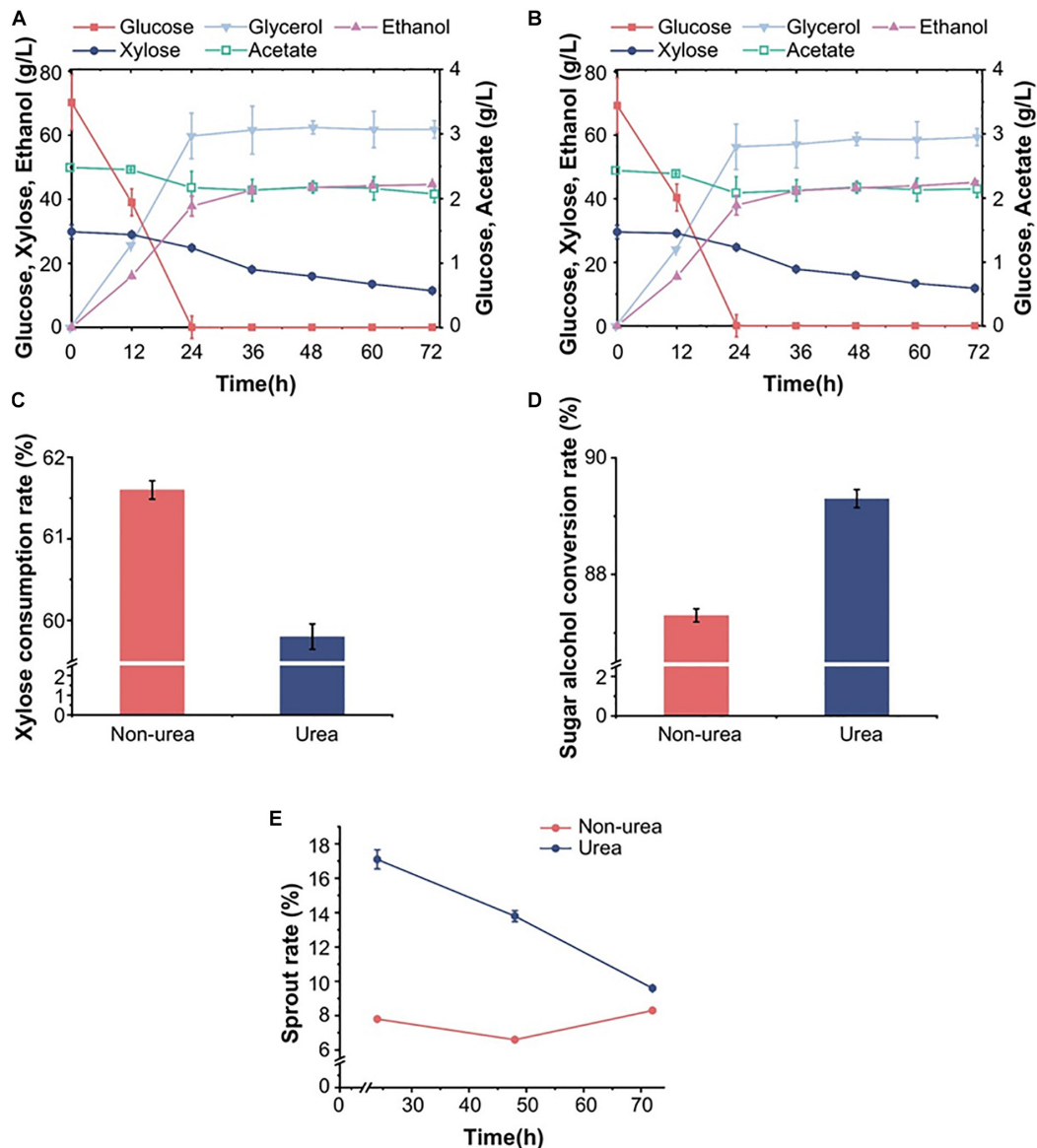
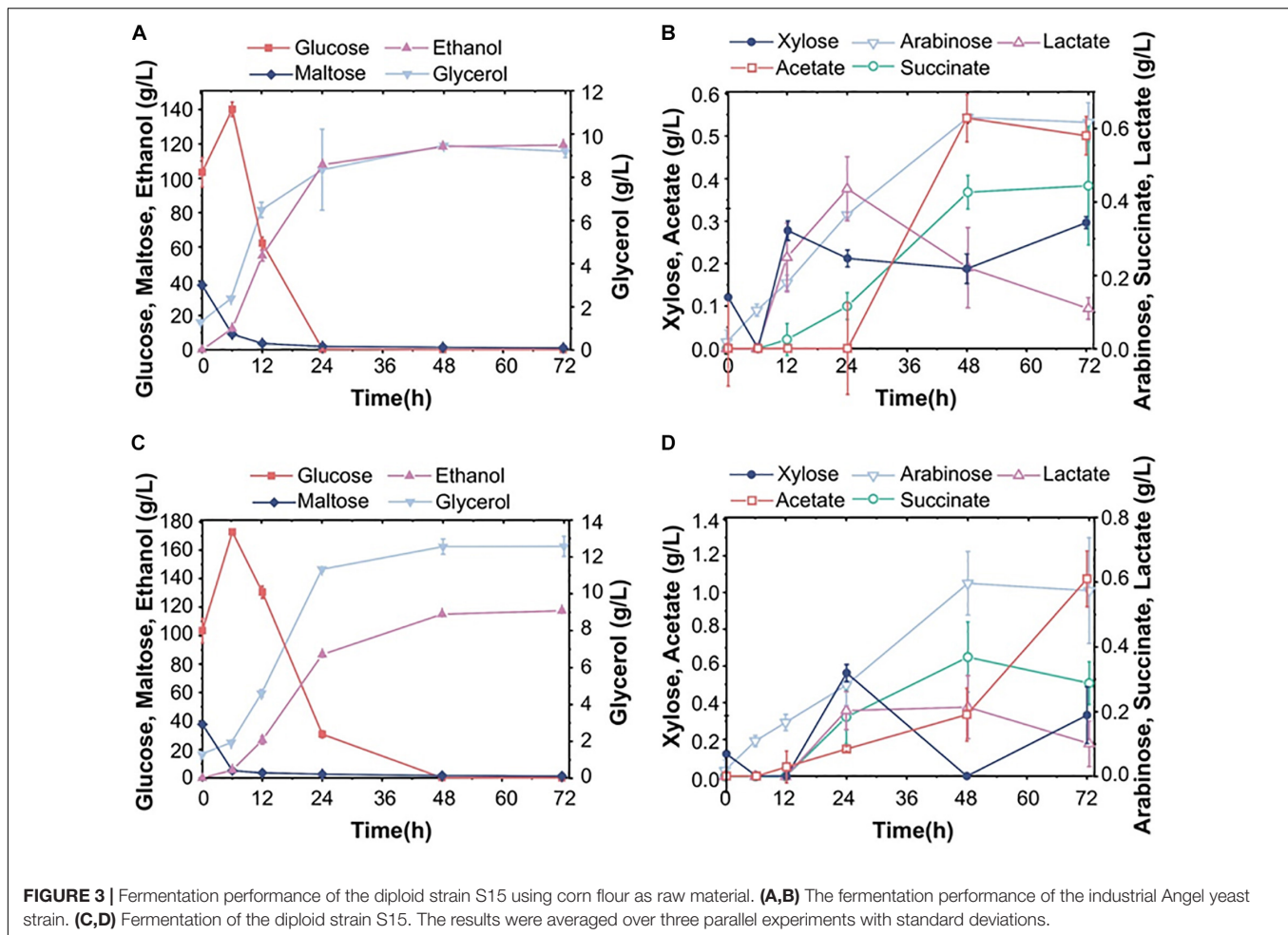


FIGURE 2 | Effects of urea on the fermentation and reproduction ability of diploid strain S15 in corn stover hydrolysates. The fermentation properties of the diploid strain S15 in the hydrolysate (A) with and (B) without urea. Xylose consumption (C) and total sugar-to-alcohol conversion (D) of S15 in the two different hydrolysate-based media. (E) The germination rate of strain S15 under the influence of urea. The results were averaged over three parallel experiments with standard deviations.

(F106-KR, control strain), S17 (F106-ARS), S20 (F106-4RD), S31 (F106-KR-ARS) and S32 (F106-4RD-ARS). After 48 h of fermentation, the ethanol yield of S14 (0.42 g/g) was the highest among the five mutant strains in the mixed sugar medium (50 g/L glucose and 50 g/L xylose) (Figure 1A), indicating that the XR-K270R substitution effectively addressed the redox imbalance to promote ethanol production. In addition, strain S32 with combined ARS and K274R/N276D mutations showed a better ethanol yield over time than other three strains S17, S20 and S31 (Figure 1A). The results showed that the ethanol yield of was different. We speculated that strains with combination of different XR- and XDH-related gene mutations

could alter the redox imbalance and lead to differences in the ethanol production.

We obtained five XR and XDH mutant strains in previous genetic engineering research, including the efficient strain XR-K270R and the ineffective strain XDH-ARS. Here, we included the XDH-related CAS mutant strain in an attempt to minimize the xylitol production. Firstly, we selected F106 strains carrying plasmids YEp-3X (F106-3X), YEp-KR (F106-KR, S14), YEp-CAS (F106-CAS) and YEp-KCAS (F106-KCAS) to assess the effects of these mutations on xylose metabolic efficiency. In a xylose medium, the ethanol yield of S14 was 46% higher, and its xylitol production was 53% lower than those of F106-3X



(Figure 1B). While no strain was able to completely consume xylose, S14 consumed more xylose than F106-3X. These results further indicate that the K270R mutant can minimize the redox imbalance and xylitol accumulation, thereby promoting ethanol production. Based on the confirmed properties of the XR-K270R mutant, we integrated pUC-3XK270R into the diploid strain YC-DM for further evaluation. Compared with DM32-3X, the ethanol yield of DM32-KR was increased by 60%, while the xylitol level was decreased by 63%, indicating that the XR-K270R mutation is more effective in the diploid yeast than in its haploid parent strain (Figures 1B,C). There are two possible explanations for the increased ethanol yield of F106-KR and DM32-KR: (1) Both haploid and diploid strains carrying the XR-K270R mutation alleviated the redox imbalance and reduced the accumulation of xylitol to some extent, resulting in an increase of ethanol production; (2) Diploid strains confer higher ethanol resistance and stronger inhibitor tolerance than haploids, and further exaggerate effects of the K270R mutation, making diploid strains more robust and suitable for industrial ethanol production than haploids. Moreover, we obtained diploid S15 and triploid S16 strains from S14. And our fermentation results show that the ethanol yield of S16 was slightly higher than S15 within 48 h (Figure 1D).

The physiological characteristics of these engineered strains indicate that increased chromosomal copies improve xylose fermentation efficiency.

Fermentation Performance of Different Strains in Simulated Corn Hydrolysates

To investigate the strain tolerance to fermentation inhibitors, we fermented the control strain S13 (F106-3X) and strains S14-16 in simulated corn hydrolysates (80 g/L glucose, 40 g/L xylose and 3 g/L acetate) (Xiong et al., 2011; Xiong et al., 2013). At 48 h, the xylitol yields of S13-16 were 9.97 g/L, 4.16 g/L, 4.06 g/L and 4.72 g/L, respectively (Figure 1E); hence, polyploid strains have significantly lower xylitol production than the haploid, indicating that the XR-K270R mutation successfully restored redox balance in these strains. Furthermore, the xylitol titers were decreased by 59.2% and 52.6%, respectively, in S15 and S16. The ethanol yields of S13-16 were 0.426, 0.463, 0.477 and 0.455 g/g total sugars at 48 h. Among them, the ethanol yields of S14, S15 and S16 were significantly higher than that of S13, and showed an increasing trend among S13-15. To our delight, the ethanol yield of S15 reached 93.9% of the theoretical value within 36 h, which is higher than the haploid S14 (Figure 1F). However, S16 did not

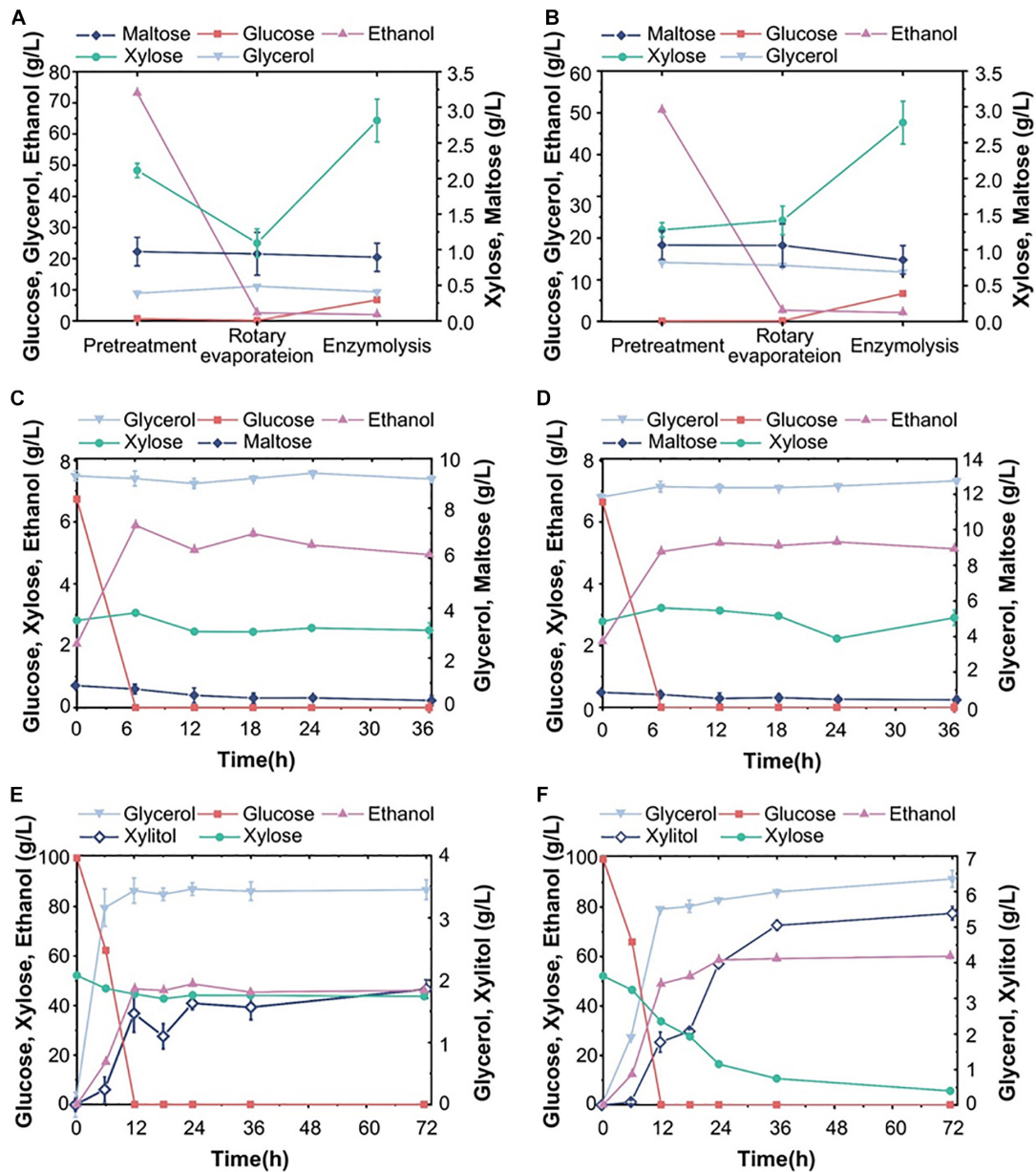


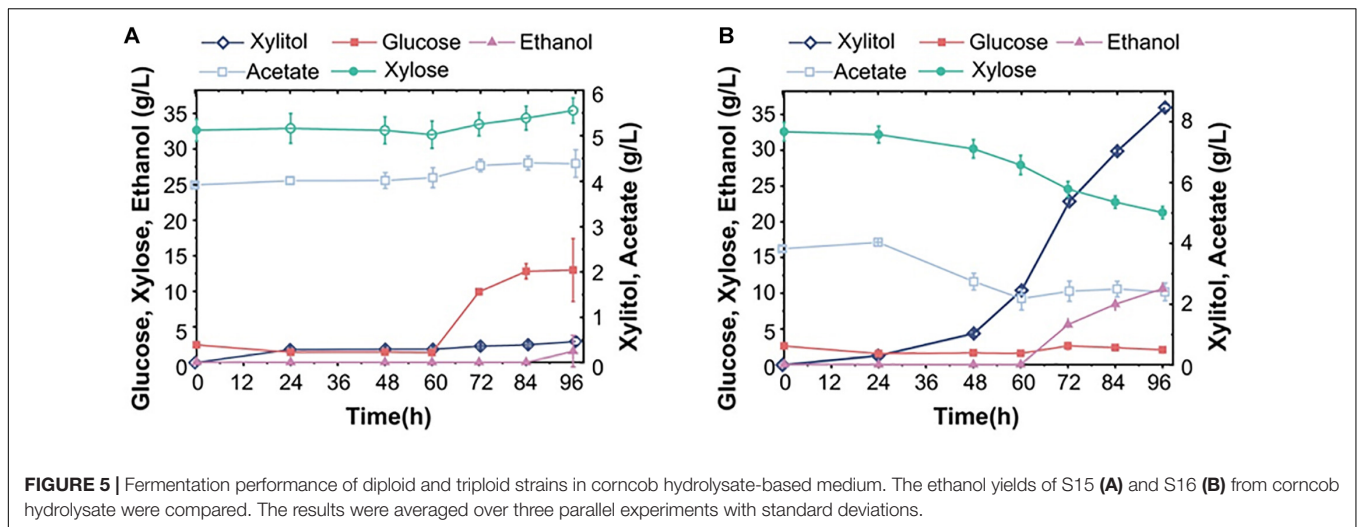
FIGURE 4 | Composition of corn distiller's grains and pure sugar medium. (A,B) The change in the content of each component in the fermentation system after pretreatment, rotary vacuum steam treatment and enzymatic hydrolysis, followed by fermentation with Angel yeast (A) and S15 (B). (C) and (D) show the fermentation properties of Angel yeast and S15, respectively. (E) and (F) show the fermentation performance of Angel yeast and S15, respectively, in a synthetic medium containing 100 g/L glucose and 50 g/L xylose. The experimental results were averaged over three parallel experiments with standard deviations.

show better fermentation performance than S15 in the presence of 3 g/L acetate.

Fermentation Performance of S15 in Corn Hydrolysates With/Without Urea, Corn Flour Hydrolysates and Synthetic Sugars

Generally, yeast strains used in industrial fermentation are diploid, so we focused on the ability of S15 to ferment biomass

hydrolysates. Similar to the fermentation performance of S14-16 in pure mixed sugars and simulated corn stover hydrolysate, S15 had better fermentation ability than S14. In view of the widespread use of diploid strains and corn stover as the raw material in the ethanol industry, we analyzed the fermentation ability of the best performing diploid S15 for 72 h using actual stover hydrolysates, and investigated the effect of urea on its fermentation efficiency. In corn stover hydrolysates with or without urea, S15 had an overall sugar-to-alcohol conversion rate of 89.3 and 87.3%, respectively (Figures 2A–D), suggesting that



S15 achieved a higher ethanol yield in the presence of moderate urea, which was higher than that of the reported SFA1^{OE} strain (Zhu et al., 2020). Moreover, the cell number, the germination rate and the mortality of S15 were quantified by microscopy to assess the effects of urea. The germination rate of S15 with urea showed twofold increase over the culture without urea within 24 h, and it also exhibited an increased germination rate and reduced mortality in the presence of urea from 48 to 72 h (Figure 2E). These results indicate that urea effectively helps ethanol production by promoting yeast cell germination.

In order to evaluate the commercial value of S15, we also fermented it in parallel with the commonly used commercial strain Angel in 30% corn flour hydrolysate (mainly glucose and maltose, mass fraction). As can be seen in Figures 3A,C, the maltose concentration decreased evidently within 12 h, while the glucose content increased briefly, indicating that maltose was preferentially utilized over glucose. The Angel yeast and S15 had ethanol yields of 119.4 and 117.5 g/L, respectively. S15 also accumulated more glycerol and acetate than the control strain within 72 h (Figures 3B,D). After a comprehensive analysis, it was found that the fermentation performance of S15 was slightly lower than that of the industrial strain on corn flour hydrolysates. To overcome this, we improved the utilization rate of corn flour by treating the fermentation broth using different methods (Supplementary Figure 1). After pretreatment, rotary evaporation and enzymolysis, the ethanol level decreased dramatically and xylose increased in corn distiller's grains (Figures 4A,B). Then, Angel yeast and S15 were grown in the processed corn distiller's grains with less carbon sources compared to corn flour, and the two strains had similar low ethanol production (Figures 4C,D). Therefore, we speculated that a large number of by-products were generated after a series of treatments, including acid treatment, which inhibited the fermentation and yeast cell viability. In general, the utilization rate of corn flour and the conversion rate of sugar-to-ethanol were obviously improved through secondary fermentation, which achieved the goal of maximum ethanol production by two successive fermentation stages.

Subsequently, S15 and Angel yeast were fermented in a mixed sugar medium (100 g/L glucose and 50 g/L xylose) for comparative analysis. The results showed that both strains could consume all glucose within 12 h. After 72 h, S15 showed a higher xylose consumption of 46.5 g/L and produced 60.1 g/L ethanol, along with higher concentrations of xylitol and glycerol than that of Angel yeast (Figures 4E,F). These results demonstrated that S15 had a better ability to metabolize xylose and produce ethanol than Angel yeast, but the difference was not obvious in the hydrolysates.

Analysis of Tolerance and Utilization of Corn cob by Strains S15 and S16

After showing that diploid S15 had similar fermentation characteristics with the adapted industrial strains, we further explored whether the triploid S16 could produce more ethanol from corn cob hydrolysates. We tested S15 and S16 in the non-detoxified corn cob fermentation broth using an improved two-stage fermentation strategy at 40°C. S15 and S16 left 13.0 g/L and 2.1 g/L residual glucose while consuming 2.8 g/L and 11.3 g/L xylose within 96 h of SSCF, respectively (Figures 5A,B), showing that S16 converted monosaccharides into ethanol more efficiently than S15. It follows from above that S16 grew better than S15 at high temperature, indicating that S16 has increased temperature tolerance. Moreover, S16 consumed about 1.4 g/L acetate, while S15 produced 0.47 g/L acetate within 96 h (Figures 5A,B). Our results confirmed that S16 could produce more ethanol than S15 largely due to its lower acetate production under the same conditions. As a result, the ethanol yield of S16 was about 10.6 g/L, which was 7 times higher than that of S15.

Taken together, these results show that S16 is superior to S15, an observation consistent with the gradual increase in the performance of S14, S15 and S16 in the pure sugar fermentation medium, which is also in agreement with a recent study (Oomuro et al., 2019). We speculate that as the chromosome copy number increases, the expression of genes involved in high-temperature

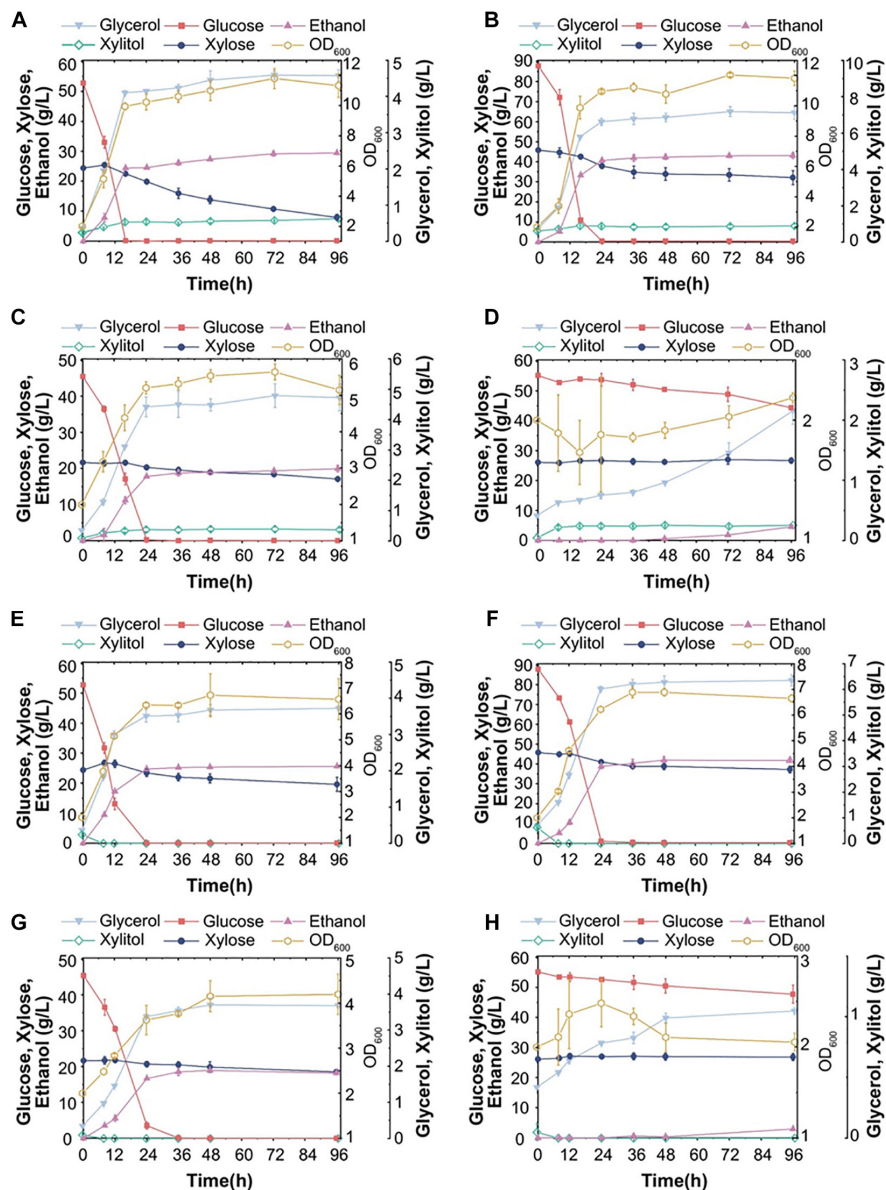


FIGURE 6 | Fermentation ability of S15 and S16 with various corn stover hydrolysates. Fermentation performance of S15 in hydrolysate pretreated with dilute acid (DA) with a substrate concentration of 20% (A) or 30% (B), and in hydrolysates pretreated with dilute alkali (AL) with a substrate concentration of 20% (C) or 30% (D). Fermentation performance of S16 in DA-treated hydrolysates of 20% (E) or 30% (F) substrate, and in AL-treated hydrolysates of 20% (G) or 30% (H) substrate. The results were averaged over three parallel experiments with standard deviations.

tolerance, acetate degradation, xylose utilization and ethanol production are increased, resulting in the enhancement of the fermentation performance in polyploid strains.

Utilization of Acid- or Alkali-Treated Corn Stover Hydrolysates by S15 and S16

Strains S15 and S16 were chosen to study whether the ethanol production in corn stover hydrolysates is positively correlated with the chromosome copy number. We used different evaluated systems with improved pretreatment methods (dilute acid or

alkali treatment) and substrate concentrations (20 or 30%) to assess yeast fermentation performance. **Figures 6A,B** shows that S15 consumed all glucose from DA-treated hydrolysate, at both substrate concentrations of 20% and 30%; however, the corresponding xylose utilization ratios were only 67.7% and 29.9%, while the ethanol yields were 29.4 g/L and 43.2 g/L, respectively. Furthermore, the xylitol production in the hydrolysate with 30% substrate was lower than that with 20% substrate (**Figures 6A,B**). Hence, S15 converted more carbon source into ethanol in corn stover hydrolysates with higher substrate concentration in our experimental setting. In contrast,

in the corn stover hydrolysate treated with AL, S15 consumed all glucose at a substrate concentration of 20%, compared to only 19.5% at a substrate concentration of 30% (Figures 6C,D). Moreover, the yeast cell number was several times higher in AL-treated hydrolysate with 30% substrate than that with 20% substrate, although only small amount of xylose was consumed by S15 in both AL-treated systems (Figures 6C,D). Overall, the ethanol yields from the AL-treated hydrolysates were remarkably lower than from DA-treated hydrolysates, suggesting that corn stover treated with AL contains more inhibitors than that with DA, thus limiting the fermentation capacity of S15.

Under the same experimental conditions, S16 consumed almost all glucose from DA-treated corn stover hydrolysates at both substrate concentrations, but the xylose utilization remained poor and xylitol was almost undetectable (Figures 6E,F). The ethanol production in the hydrolysate with 30% substrate was 41.81 g/L, which was higher than in 20% substrate (Figures 6E,F). The fermentation ability of S16 in AL-treated hydrolysates was lower than DA-treated hydrolysates and comparable to that of S15 (Figures 6G,H). In the AL-treated hydrolysate with 30% substrate, S16 did not consume xylose, and the number of cells remained constant (Figures 6G,H).

In summary, the maximum ethanol productions in four hydrolysates (DA 20%, DA 30%, AL 20% and AL 30%) are 76.2%, 83.3%, 78.1% and 16.3% for S15 (Figures 6A–D), and 87.3%, 85.0%, 73.3% and 10.6% for S16 (Figures 6E–H) of the theoretical value, respectively. Hence, the fermentation performance of S16 appears to be better than that of S15, particularly with DA-treated low substrate concentration.

CONCLUSION

This study constructed the diploid and triploid strains (S15/S16) derived from S14 that harbors a better effective XR-K270R over other mutants with different XR and/or XDH mutation. Diploid and triploid strains were derived from the XR-K270R background, and fermentation results showed that the sugar-ethanol conversion of the diploid reached 93.9% of the theoretical value in simulated corn stover hydrolysates. Furthermore, the triploid displayed better fermentation characteristics than the diploid in hydrolysates of corncob and corn stover with different pretreatment methods (Supplementary Table 4). Compared with other studies, the polyploid strains constructed in this study also have their own advantages with rational mutants and disadvantages (Supplementary Table 5). Our results demonstrate that with the increase of chromosome copy number, the ethanol production was gradually improved, which offers basis for improving cellulosic ethanol production by genetic engineering of yeast.

REFERENCES

Avci, A., Saha, B. C., Kennedy, G. J., and Cotta, M. A. (2013). Dilute sulfuric acid pretreatment of corn stover for enzymatic hydrolysis and efficient ethanol

DATA AVAILABILITY STATEMENT

The original contributions presented in the study are included in the article/Supplementary Material, further inquiries can be directed to the corresponding author/s.

AUTHOR CONTRIBUTIONS

LL did the investigation, formal analysis, and writing – original draft. MH, MJ, WY, ZX, and YK did the supervision. YZ, MK, SA, and ZJ wrote – original draft. WX did the supervision and writing – review and editing. LC did the conceptualization. All authors contributed to the article and approved the submitted version.

FUNDING

This study was funded by grants from the National Natural Science Foundation of China [Grant No. 31570044].

ACKNOWLEDGMENTS

We sincerely thank Dr. Mingyong Xiong for the project design, Mr. Cong Du for experiments conducted at Dalian University of Technology, Ms. Guannan Shen and Mr. Zhao Wang for fermentation at Nanjing University of Science and Technology.

SUPPLEMENTARY MATERIAL

The Supplementary Material for this article can be found online at: <https://www.frontiersin.org/articles/10.3389/fbioe.2021.655272/full#supplementary-material>

Supplementary Figure 1 | Flow chart of the whole acid treatment process from corn flour fermentation broth to corn distiller's grains.

Supplementary Figure 2 | The sugar concentration of corn stover hydrolysates with the treatment of dilute acid (DA) and dilute alkali (AL) at different substrate concentration (20% and 30%).

Supplementary Table 1 | Strains used in this study.

Supplementary Table 2 | Plasmids used in this study.

Supplementary Table 3 | Primers used in this study.

Supplementary Table 4 | Fermentation ability of S15 and S16.

Supplementary Table 5 | Advantages and disadvantages compared with other related articles.

production by recombinant *Escherichia coli* FBR5 without detoxification. *Bioresour. Technol.* 142, 312–319. doi: 10.1016/j.biortech.2013.05.002

Biener, R., Steinkämper, A., and Horn, T. (2012). Calorimetric control of the specific growth rate during fed-batch cultures of *Saccharomyces*

- cerevisiae*. *J. Biotechnol.* 160, 195–201. doi: 10.1016/j.jbiotec.2012.03.006
- Cao, L., Tang, X., Zhang, X., Zhang, J., Tian, X., Wang, J., et al. (2014). Two-stage transcriptional reprogramming in *Saccharomyces cerevisiae* for optimizing ethanol production from xylose. *Metab. Eng.* 24, 150–159. doi: 10.1016/j.ymben.2014.05.001
- Chen, M. T., Lin, S., Shandil, I., Andrews, D., Stadheim, T. A., and Choi, B. K. (2012). Generation of diploid *Pichia pastoris* strains by mating and their application for recombinant protein production. *Microb. Cell Fact.* 11:91. doi: 10.1186/1475-2859-11-91
- Chen, S., Xu, Z., Li, X., Yu, J., Cai, M., and Jin, M. (2018). Integrated bioethanol production from mixtures of corn and corn stover. *Bioresour. Technol.* 258, 18–25. doi: 10.1016/j.biortech.2018.02.125
- Cripwell, R. A., Favaro, L., Viljoen-Bloom, M., and van Zyl, W. H. (2020). Consolidated bioprocessing of raw starch to ethanol by *Saccharomyces cerevisiae*: achievements and challenges. *Biotechnol. Adv.* 42:107579. doi: 10.1016/j.biortechadv.2020.107579
- Du, C., Li, Y., Zong, H., Yuan, T., Yuan, W., and Jiang, Y. (2020). Production of bioethanol and xylitol from non-detoxified corn cob via a two-stage fermentation strategy. *Bioresour. Technol.* 310:123427. doi: 10.1016/j.biortech.2020.123427
- Hu, J., Chandra, R., Arantes, V., Gourlay, K., Susan van Dyk, J., and Saddler, J. N. (2015). The addition of accessory enzymes enhances the hydrolytic performance of cellulase enzymes at high solid loadings. *Bioresour. Technol.* 186, 149–153. doi: 10.1016/j.biortech.2015.03.055
- Huang, C., Zheng, Y., Lin, W., Shi, Y., Huang, G., and Yong, Q. (2020). Removal of fermentation inhibitors from pre-hydrolysis liquor using polystyrene divinylbenzene resin. *Biotechnol. Biofuels* 13:188. doi: 10.1186/s13068-020-01828-3
- Jeppsson, M., Bengtsson, O., Franke, K., Lee, H., Hahn-Hägerdal, B., and Gorwa-Grauslund, M. F. (2006). The expression of a *Pichia stipitis* xylose reductase mutant with higher K(M) for NADPH increases ethanol production from xylose in recombinant *Saccharomyces cerevisiae*. *Biotechnol. Bioeng.* 93, 665–673. doi: 10.1002/bit.20737
- Jo, J. H., Park, Y. C., Jin, Y. S., and Seo, J. H. (2017). Construction of efficient xylose-fermenting *Saccharomyces cerevisiae* through a synthetic isozyme system of xylose reductase from *Scheffersomyces stipitis*. *Bioresour. Technol.* 241, 88–94. doi: 10.1016/j.biortech.2017.05.091
- Kim, S. R., Lee, K. S., Kong, I. I., Lesmana, A., Lee, W. H., Seo, J. H., et al. (2013). Construction of an efficient xylose-fermenting diploid *Saccharomyces cerevisiae* strain through mating of two engineered haploid strains capable of xylose assimilation. *J. Biotechnol.* 164, 105–111. doi: 10.1016/j.jbiotec.2012.12.012
- Kostrzynska, M., Sopher, C. R., and Lee, H. (1998). Mutational analysis of the role of the conserved lysine-270 in the *Pichia stipitis* xylose reductase. *FEMS Microbiol. Lett.* 159, 107–112. doi: 10.1111/j.1574-6968.1998.tb12848.x
- Li, X., Chen, Y., and Nielsen, J. (2019). Harnessing xylose pathways for biofuels production. *Curr. Opin. Biotechnol.* 57, 56–65. doi: 10.1016/j.copbio.2019.01.006
- Mataffo, A., Scognamiglio, P., Dente, A., Strollo, D., Colla, G., Roupael, Y., et al. (2020). Foliar application of an amino acid-enriched urea fertilizer on 'Greco' grapevines at full veraison increases berry yeast-assimilable nitrogen content. *Plants* 9:619. doi: 10.3390/plants9050619
- Matsushika, A., Inoue, H., Watanabe, S., Kodaki, T., Makino, K., and Sawayama, S. (2009). Efficient bioethanol production by a recombinant flocculent *Saccharomyces cerevisiae* strain with a genome-integrated NADP⁺-dependent xylitol dehydrogenase gene. *Appl. Environ. Microbiol.* 75, 3818–3822. doi: 10.1128/aem.02636-08
- Nambu-Nishida, Y., Sakihama, Y., Ishii, J., Hasunuma, T., and Kondo, A. (2018). Selection of yeast *Saccharomyces cerevisiae* promoters available for xylose cultivation and fermentation. *J. Biosci. Bioeng.* 125, 76–86. doi: 10.1016/j.jbiosc.2017.08.001
- Oomuro, M., Motoyama, Y., and Watanabe, T. (2019). Isolation of a lager yeast with an increased copy number of the YCK1 gene and high fermentation performance. *J. Inst. Brew.* 125, 47–52. doi: 10.1002/jib.543
- Petschacher, B., Leitgeb, S., Kavanagh, K. L., Wilson, D. K., and Nidetzky, B. (2005). The coenzyme specificity of *Candida tenuis* xylose reductase (AKR2B5) explored by site-directed mutagenesis and X-ray crystallography. *Biochem. J.* 385(Pt. 1), 75–83. doi: 10.1042/bj20040363
- Petschacher, B., and Nidetzky, B. (2008). Altering the coenzyme preference of xylose reductase to favor utilization of NADH enhances ethanol yield from xylose in a metabolically engineered strain of *Saccharomyces cerevisiae*. *Microb. Cell Fact.* 7:9. doi: 10.1186/1475-2859-7-9
- Sankaran, R., Parra Cruz, R. A., Pakalapati, H., Show, P. L., Ling, T. C., Chen, W. H., et al. (2020). Recent advances in the pretreatment of microalgal and lignocellulosic biomass: a comprehensive review. *Bioresour. Technol.* 298:122476. doi: 10.1016/j.biortech.2019.122476
- Selmecki, A. M., Maruvka, Y. E., Richmond, P. A., Guillet, M., Shores, N., Sorenson, A. L., et al. (2015). Polyploidy can drive rapid adaptation in yeast. *Nature* 519, 349–352. doi: 10.1038/nature14187
- Tani, Y., Tomohiro, Y., Miyata, A., Kurokui, T., and Hayashida, S. (1993). A novel method for breeding polyploid cells by heat-induced endomitotic diploidization in *Saccharomyces cerevisiae*. *Biosci. Biotechnol. Biochem.* 57, 2063–2066. doi: 10.1271/bbb.57.2063
- van Dijk, M., Erdei, B., Galbe, M., Nygård, Y., and Olsson, L. (2019). Strain-dependent variance in short-term adaptation effects of two xylose-fermenting strains of *Saccharomyces cerevisiae*. *Bioresour. Technol.* 292:121922. doi: 10.1016/j.biortech.2019.121922
- Wang, L., Zhang, K., Xu, Y., Zhang, M., and Wang, D. (2018). High-solid pretreatment of corn stover using urea for enzymatic saccharification. *Bioresour. Technol.* 259, 83–90. doi: 10.1016/j.biortech.2018.03.023
- Wang, X., Wang, G., Yu, X., Chen, H., Sun, Y., and Chen, G. (2017). Pretreatment of corn stover by solid acid for d-lactic acid fermentation. *Bioresour. Technol.* 239, 490–495. doi: 10.1016/j.biortech.2017.04.089
- Watanabe, S., Abu Saleh, A., Pack, S. P., Annaluru, N., Kodaki, T., and Makino, K. (2007a). Ethanol production from xylose by recombinant *Saccharomyces cerevisiae* expressing protein-engineered NADH-preferring xylose reductase from *Pichia stipitis*. *Microbiology* 153(Pt. 9), 3044–3054. doi: 10.1099/mic.0.2007/007856-0
- Watanabe, S., Kodaki, T., and Makino, K. (2005). Complete reversal of coenzyme specificity of xylitol dehydrogenase and increase of thermostability by the introduction of structural zinc. *J. Biol. Chem.* 280, 10340–10349. doi: 10.1074/jbc.M409443200
- Watanabe, S., Pack, S. P., Saleh, A. A., Annaluru, N., Kodaki, T., and Makino, K. (2007b). The positive effect of the decreased NADPH-preferring activity of xylose reductase from *Pichia stipitis* on ethanol production using xylose-fermenting recombinant *Saccharomyces cerevisiae*. *Biosci. Biotechnol. Biochem.* 71, 1365–1369. doi: 10.1271/bbb.70104
- Xiao, W., Li, H., Xia, W., Yang, Y., Hu, P., Zhou, S., et al. (2019). Co-expression of cellulase and xylanase genes in *Saccharomyces cerevisiae* toward enhanced bioethanol production from corn stover. *Bioengineered* 10, 513–521. doi: 10.1080/21655979.2019.1682213
- Xiong, M., Chen, G., and Barford, J. (2011). Alteration of xylose reductase coenzyme preference to improve ethanol production by *Saccharomyces cerevisiae* from high xylose concentrations. *Bioresour. Technol.* 102, 9206–9215. doi: 10.1016/j.biortech.2011.06.058
- Xiong, M., Woodruff, A., Tang, X., Tian, X., Zhang, J., and Cao, L. (2013). Comparative study on the mutated xylose reductase to increase ethanol production in xylose-utilizing *Saccharomyces cerevisiae* strains. *J. Taiwan Inst. Chem. Eng.* 44, 605–610. doi: 10.1016/j.jtice.2012.12.016
- Zhu, L., Li, P., Sun, T., Kong, M., Li, X., Ali, S., et al. (2020). Overexpression of *SFA1* in engineered *Saccharomyces cerevisiae* to increase xylose utilization and ethanol production from different lignocellulose hydrolysates. *Bioresour. Technol.* 313:123724. doi: 10.1016/j.biortech.2020.12.3724

Conflict of Interest: The authors declare that the research was conducted in the absence of any commercial or financial relationships that could be construed as a potential conflict of interest.

Copyright © 2021 Liu, Jin, Huang, Zhu, Yuan, Kang, Kong, Ali, Jia, Xu, Xiao and Cao. This is an open-access article distributed under the terms of the Creative Commons Attribution License (CC BY). The use, distribution or reproduction in other forums is permitted, provided the original author(s) and the copyright owner(s) are credited and that the original publication in this journal is cited, in accordance with accepted academic practice. No use, distribution or reproduction is permitted which does not comply with these terms.



Pilot Scale Elimination of Phenolic Cellulase Inhibitors From Alkali Pretreated Wheat Straw for Improved Cellulolytic Digestibility to Fermentable Saccharides

OPEN ACCESS

Ikram ul Haq^{1,2†}, *Ali Nawaz*^{2†}, *Badar Liaqat*², *Yesra Arshad*², *Xingli Fan*¹, *Meitao Sun*¹, *Xin Zhou*³, *Yong Xu*³, *Fatima Akram*² and *Kankan Jiang*^{1*}

Edited by:

Lei Wang,
Jeju National University, South Korea

Reviewed by:

Hongsen Zhang,
Henan Agricultural University, China
Javier Ulises Hernández Beltrán,
Universidad Autónoma de Coahuila,
Mexico

*Correspondence:

Kankan Jiang
jiangkankan@126.com

†These authors share first authorship

Specialty section:

This article was submitted to
Bioprocess Engineering,
a section of the journal
Frontiers in Bioengineering and
Biotechnology

Received: 25 January 2021

Accepted: 18 February 2021

Published: 12 March 2021

Citation:

Haq I, Nawaz A, Liaqat B, Arshad Y, Fan X, Sun M, Zhou X, Xu Y, Akram F and Jiang K (2021) Pilot Scale Elimination of Phenolic Cellulase Inhibitors From Alkali Pretreated Wheat Straw for Improved Cellulolytic Digestibility to Fermentable Saccharides. *Front. Bioeng. Biotechnol.* 9:658159. doi: 10.3389/fbioe.2021.658159

¹ School of Basic Medical Sciences and Forensic Medicine, Hangzhou Medical College, Hangzhou, China, ² Institute of Industrial Biotechnology, Government College University, Lahore, Pakistan, ³ Jiangsu Co-innovation Center of Efficient Processing and Utilization of Forest Resources, College of Chemical Engineering, Nanjing Forestry University, Nanjing, China

Depleting supplies of fossil fuel, regular price hikes of gasoline and environmental deterioration have necessitated the search for economic and eco-benign alternatives of gasoline like lignocellulosic biomass. However, pre-treatment of such biomass results in development of some phenolic compounds which later hinder the depolymerisation of biomass by cellulases and seriously affect the cost effectiveness of the process. Dephenolification of biomass hydrolysate is well cited in literature. However, elimination of phenolic compounds from pretreated solid biomass is not well studied. The present study was aimed to optimize dephenolification of wheat straw using various alkalis i.e., Ca(OH)₂ and NH₃; acids i.e., H₂O₂, H₂SO₄, and H₃PO₄; combinations of NH₃+H₃PO₄ and H₃PO₄+H₂O₂ at pilot scale to increase enzymatic saccharification yield. Among all the pretreatment strategies used, maximum reduction in phenolic content was observed as 66 mg Gallic Acid Equivalent/gram Dry Weight (GAE/g DW), compared to control having 210 mg GAE/g DW using 5% (v/v) combination of NH₃+H₃PO₄. Upon subsequent saccharification of dephenolified substrate, the hydrolysis yield was recorded as 46.88%. Optimized conditions such as using 1%+5% concentration of NH₃+H₃PO₄, for 30 min at 110°C temperature reduced total phenolic content (TPC) to 48 mg GAE/g DW. This reduction in phenolic content helped cellulases to act more proficiently on the substrate and saccharification yield of 55.06% was obtained. The findings will result in less utilization of cellulases to get increased yield of saccharides by hydrolyzing wheat straw, thus, making the process economical. Furthermore, pilot scale investigations of current study will help in upgrading the novel process to industrial scale.

Keywords: green energy, green chemistry, phenols, bioenergy, lignocellulosic biomass, phenolic inhibitors

INTRODUCTION

In the present era, world is facing an inevitable energy crisis due to the depletion of fossil fuel deposits. With ever increasing population, the need to look for alternative energy resources has been a priority for most of the scientists around the world (Ramos et al., 2019). Recent studies indicate that the most promising alternative for non-renewable energy is the use of biofuels. For this purpose, lignocellulosic biomass which is mainly an agricultural waste, is mostly preferred (Novakovic et al., 2020). Lignin, cellulose, and hemicellulose are the main components of lignocellulosic biomass (Hasegawa et al., 2013). Among several agricultural wastes, wheat straw is considered as one of the most promising and abundant agricultural residues in the world (Ondrejovič et al., 2020). According to Celignis analytical located in Ireland, the average yield of wheat straw is 1.3–1.4 kg/kg of wheat grain. Wheat straw being low cost and cheap agricultural by-product, coupled with the high cellulosic proportion (30–50%), makes wheat straw most suitable substrate for the production of bioethanol (Qiu et al., 2018).

The use of wheat straw for bioethanol production involves four basic steps i.e., pretreatment, enzymatic saccharification, fermentation, and down streaming of the product. Pretreatment of the feedstock is the most difficult step in the production of bioethanol using lignocellulosic biomass (Lynd et al., 2008). The complex arrangement of cellulose and hemicellulose hinders the access of enzyme to act on them due to the presence of lignin (Tareen et al., 2020). A variety of methods for pretreatment have been reported which include biological, chemical, mechanical, and thermochemical processes (Xiong et al., 2019).

Despite its primary importance in the process of biofuel formation, the pre-treatment step has certain disadvantages as it may result in the formation of inhibitory compounds (Ahmed et al., 2019). The main inhibitors produced during pretreatment are aliphatic acids such as formic acid, acetic acid, and levulinic acid, derivatives of furan including 5-hydroxymethylfurfural (HMF) and furfural, and various phenolic compounds i.e., phenol, *p*-hydroxybenzoic acid, and vanillin (Qi et al., 2014). These components are toxic or inhibitory to the cellulases and fermenting organisms. Therefore, these compounds must be removed or neutralized before the process of saccharification (Jönsson et al., 2013).

Various biological, physical, and chemical methods have been used for detoxification of lignocellulosic hydrolysate (Horváth et al., 2005). Most employed chemical detoxification methods include acidic and alkaline treatments (Chandel et al., 2011). Among alkalis, sodium hydroxide, aqueous ammonia, and calcium hydroxide are commonly used. Dilute acids including phosphoric acid and sulfuric acid are mostly used acids for detoxification of phenolic content produced during lysis of lignocellulose biomass (Mansour et al., 2016). However, removal of phenolic compounds from pretreated lignocellulosic biomass before enzymatic hydrolysis is rarely reported (Nawaz et al., 2017).

Recently we have demonstrated that the removal of these phenolic compounds can significantly increase the saccharification rate (Haq et al., 2018). However, application of

this process at commercial level needs studies at pilot scale which will provide a better understanding of the process. Therefore, we have evaluated the challenges encountered during the up scaling of a dephenolification and subsequent saccharification of pre-treated wheat straw. In the present study, we have selected a pilot scale detoxification process for maximum saccharification under optimized conditions.

MATERIALS AND METHODS

Chemicals

All chemicals used in the present study were of analytical grade and purchased from authentic suppliers of Sigma and Merck Ltd.

Biomass

Pre-treatment of wheat straw and estimation of lignocellulosic content was carried out according to our previous report by Haq et al. (2018). For pretreatment, 2.5% sodium hydroxide (NaOH) was used for 10 min at a steaming temperature of 200°C in specialized boiler. The mesh size of biomass used was 2 mm. Cellulose and hemicelluloses content of biomass was estimated after Huang et al. (2010) and Lignin content was calculated according to TAPPI standards (TAPPI Standard T236cm-85, 1993). The lignocellulosic content and total phenolic content (TPC) of raw, pretreated and detoxified biomass is presented in **Table 1**.

Cellulases

Thermophilic cellulases were produced by submerged fermentation using *Escherichia coli* BL-21 strain which was genetically modified with plasmid pET 21(b)+ cloned having genes from *Thermotoga petrophila* for endo-1,4-β-glucanase (EC 3.2.1.4), exo-1,4-β-glucanase (EC 3.2.1.91), and β-1,4-glucosidase (EC 3.2.1.21). These thermophilic cellulases were employed for saccharification studies after analyzing their activity against synthetic substrates i.e., Carboxy Methyl Cellulose (CMC) for endoglucanase, pNPC for exoglucanase and pNPG for beta-glucosidase. **Table 2** shows the properties of enzymes used.

Removal of Phenolic Compounds

Pre-treated substrate (1 kg) was treated with 5 L of 5% alkalis i.e., Ca(OH)₂ and NH₃; acids i.e., H₂O₂, H₂SO₄, H₃PO₄; combinations (sequential addition) of NH₃+H₃PO₄ and H₃PO₄+H₂O₂ at different temperatures i.e., 80, 90, 100, 110, 120, 130, 140, and 150°C for incubation periods of 5, 10, 15, 20, 25, 30, 35, and 40 min. A locally manufactured double jacketed, stainless steel vessel with automated temperature, pH, and agitation controls having working volume capacity of 20 L was used for this purpose. Traditional one-factor-at-a-time approach for optimization was followed. Afterward, substrates were rinsed with distilled water thrice. For this purpose, 5 L of water was added in the biomass and stirred at 50 rpm for 10 min, after which the water was removed. The same process was repeated two times for thorough washing. The substrates were then allowed to dry under room temperature before estimating TPC.

TABLE 1 | Lignocellulosic and Phenolic content of raw, pretreated and detoxified wheat straw samples.

Sr. No.	Biomass	Relative Cellulose content (%)	Hemi-cellulose content (%)	Lignin content (%)	Total Phenolic Content (mg GAE/g DW)
1	Wheat straw (raw)	48 ± 0.024	25 ± 0.013	19 ± 0.01	39 ± 0.019
2	Pre-treated Wheat straw	60 ± 0.031	19.3 ± 0.02	13 ± 0.05	210 ± 0.01
3	Detoxified wheat straw	69.5 ± 0.034	15 ± 0.04	5.9 ± 0.02	66 ± 0.03

TABLE 2 | Properties of hyperthermophilic cellulases.

Enzyme	Source	Host organism	Optimum temperature (°C)	Enzyme activity (U/mg)
Endo-1,4-β glucanase	<i>Thermotoga petrophila</i>	<i>E. coli</i> BL-21	90	10
Exo-1,4-β-glucanase	<i>Thermotoga petrophila</i>	<i>E. coli</i> BL-21	90	15
β-1,4-glucosidase	<i>Thermotoga petrophila</i>	<i>E. coli</i> BL-21	90	11525

Detection of Phenolic Content in Biomass

Folin–Ciocalteu (Folin and Ciocalteu, 1927) assay was used for the detection and estimation of TPC in wheat straw samples, before and after the detoxification of biomass. Assay was performed by adding 10 mg sample in a capped test tube with 9 ml distilled water and 1 ml Folin-Ciocalteu reagent. The contents were mixed vigorously and incubated for 5 min before addition of 10 ml 7% Na₂CO₃ solution. Subsequently, test tubes were kept at room temperature for 90 min. The optical density of the sample was measured at 550 nm (John et al., 2014). TPCs present in the biomass were estimated using the standard curve of Gallic acid (Nawaz et al., 2017).

Enzymatic Saccharification

Enzymatic saccharification of detoxified biomass samples was initially carried out at laboratory scale using shake flask. Different parameters for the process were optimized by changing one factor at a time and keeping all the other factors constant. These parameters included temperature (50, 60, 70, 80, and 90°C), pH (5, 6, 7, 8, and 9), reaction time (0.5, 1, 2, 3, 4, and 5 h), and inoculum size (0.5, 1, 1.5, 2, 2.5, and 3%).

After optimizing the conditions at laboratory scale, detoxified wheat straw samples were analyzed for saccharification potential in a locally fabricated double jacketed stainless steel vessel (pilot scale). This vessel was equipped with heater, compressor, agitator, and digital controls for continuous monitoring of temperature and agitation change. Substrate (2.5% w/v) was added in 20 L of phosphate buffer (pH 7) along with 500 U of each of the three cellulase enzyme. The reaction was carried out at 80°C for a period of 3 h. Samples were drawn at regular intervals of 30 min to estimate total reducing sugar and TPC. Saccharification (%) was calculated using the following formula:

$$\% \text{ Saccharification} = \frac{\text{R.S.} \times \text{V} \times \text{F1}}{\text{F2}} \times 100$$

Where:

R.S. = Sugar concentration in hydrolysate estimated as total reducing sugar (mg/ml).

V = Total volume of the reaction mixture (ml).

F1 = Factor used for the conversion of monosaccharide to polysaccharide due to water uptake during hydrolysis (0.9 for hexoses).

F2 = Factor for carbohydrate content of substrate (total carbohydrate, mg/total substrate, mg).

Scanning Electron Microscopy of Biomasses

Samples of wheat straw displaying best saccharification results after detoxification were sent to Center for Advance Studies in Physics (CASP), Government College University Lahore, Pakistan for Scanning Electron Microscopy (SEM). Sample preparation was not required as the samples were polymeric in nature.

Statistical Analysis

The computer statistical software (SPSS 16.0) was used for the statistical analysis of the results. Significant difference among the replicates has been presented as Duncan's multiple range tests in the form of probability (p) values (Duncan, 1995).

RESULTS AND DISCUSSION

Choice of Detoxification Method

Removal of phenolics from pretreated wheat straw using different alkalis [Ca(OH)₂ and NH₃], acids (H₂O₂, H₂SO₄, and H₃PO₄), combination of acids (H₂O₂+H₃PO₄), combination of acid and alkali (H₃PO₄+ NH₃) was assessed. Optimization technique used was traditional one-factor-at-a-time. Subsequently, effect of phenolics removal from pretreated wheat straw on its enzymatic hydrolysis was also chronicled. TPC in control sample was found to be 210 ± 0.02 mg Gallic Acid Equivalent/gram of Dry Weight (GAE/g DW). Among all three acids used, phosphoric acid treated biomass showed maximum reduced phenolic content i.e., 102 ± 0.12 mg GAE/g DW as shown in **Figure 1A**. On the other hand, among alkalis, best results were obtained by aqueous ammonia that reduced TPC to 105 ± 0.04 mg GAE/g DW (**Figure 1B**). Combination of acids resulted in the removal of phenolic compounds to 78 mg GAE/g DW as evident from **Figure 1C**. Among all treatment strategies, combination of acid

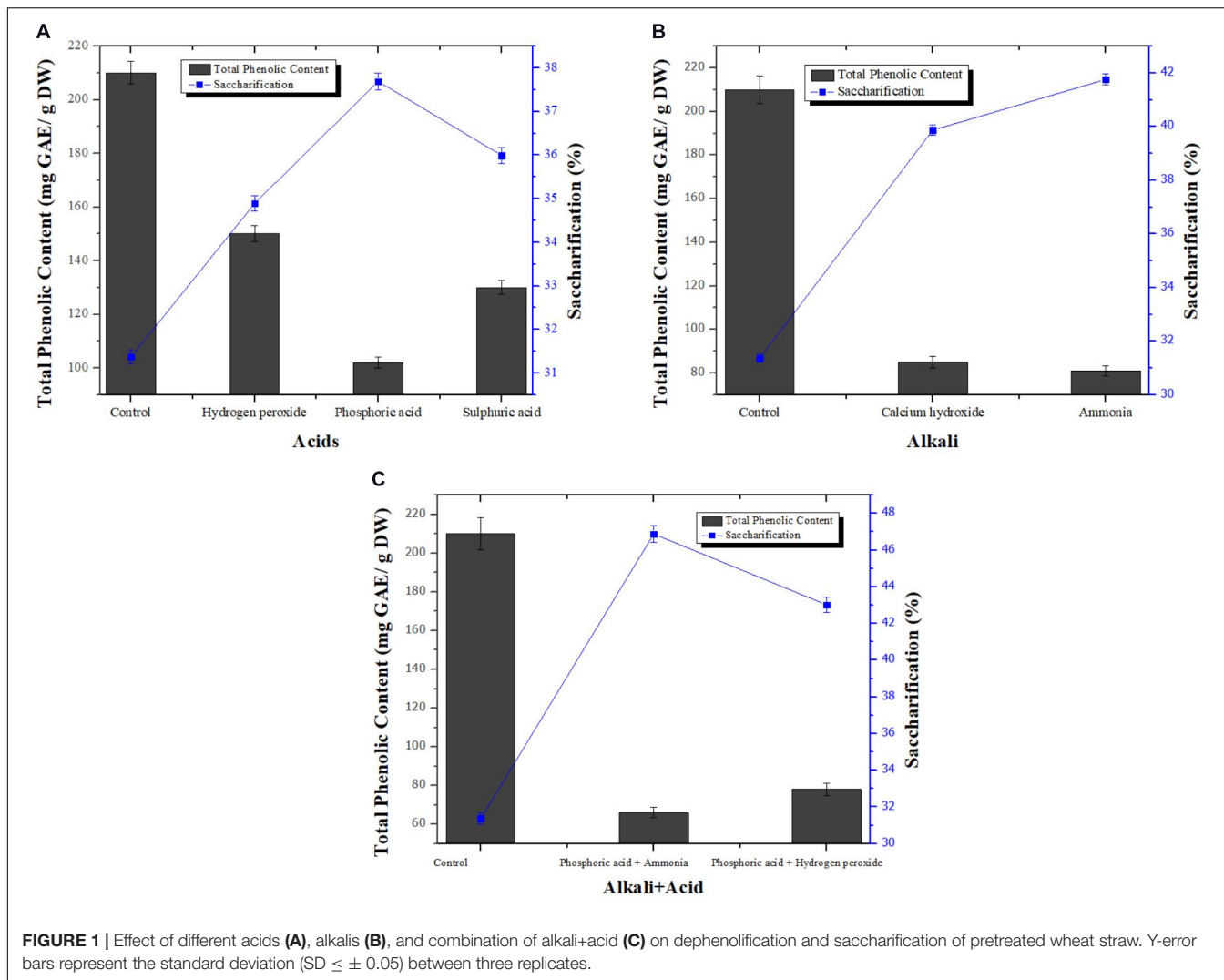


FIGURE 1 | Effect of different acids (A), alkalis (B), and combination of alkali+acid (C) on dephenolification and saccharification of pretreated wheat straw. Y-error bars represent the standard deviation (SD \pm 0.05) between three replicates.

and alkali showed most efficient removal of phenolic content with total reduced phenolic content of 66 ± 0.02 mg GAE/g DW. All the pretreated samples of wheat straw processed for removal of phenolic content showed better saccharification i.e., 39.87 % [$\text{Ca}(\text{OH})_2$ treated sample], 36.01 % (NaOH treated sample), 41.76 % (NH_3 treated sample) 34.89 % (H_2O_2 treated sample), 37.69 % (H_3PO_4 treated sample), 35.98 % (H_2SO_4 treated sample), 43.01 % ($\text{H}_2\text{O}_2 + \text{H}_3\text{PO}_4$ treated sample), and 46.88 % ($\text{H}_3\text{PO}_4 + \text{NH}_3$ treated sample) as compared to control sample (31.37 %) not treated for phenolics removal (Figure 1). Hence, it was considered that phosphoric acid used in combination with aqueous ammonia was the best method for detoxification of biomass. The removal of phenolic compounds is based on the fact that the treatment of biomass with phosphoric acid removes lignin that is present in biomass thus essentially removing phenolic contents. Moreover, cellulosic portion of the biomass remain unaffected by treatment with acid rather it provides more surface area for catalytic action of cellulases (Kim et al., 2011).

Treatment of biomass with ammonia may results in increase in internal surface area of cellulose which in turn decrease

the degree of polymerization. Decrease in crystallinity or polymerization mediates the disruption of lignin content present in biomass that leads to the removal of phenolic inhibitors present in lignin portion along with lignin (Chen et al., 2020). Moreover, high cost of other alkalis hinders their application for detoxification while ammonia is volatile in nature so it is recyclable. Ammonia can be regenerated and reused again in the process of dephenolification (Kim and Holtzapple, 2006). By employing phosphoric acid together with aqueous ammonia, best result in terms of phenolic compounds removal was obtained because efficient fractionation of lignin and hemicellulose to remove phenolic derivatives is hard to achieve using dilute acid or alkali alone. Khobragade et al. (2004) found that removal of phenolic and other inhibitors increases under acidic conditions but detoxification further increased when alkaline conditions were provided along with acidic treatment. Wang et al. (2014) and Qiu et al. (2017) also used ammonia in combination with phosphoric acid for detoxification of wheat straw and rice straw respectively, and obtained results comparable to our findings.

Effect of Incubation Time on Dephenoliphication

Detoxification of pretreated wheat straw using a combination of H_3PO_4 and NH_3 was analyzed for variable time period i.e., 5, 10, 15, 20, 25, 30, 35, and 40 min to determine the optimum time period for maximum removal of TPC. In parallel, saccharification potential was also analyzed for substrate sample treated at various time periods to reduce phenolic content. Increase in incubation time resulted in gradual decrease of phenolic content. Maximum reduction in TPC was observed after 30 min of incubation (66 ± 0.06 mg GAE/g DW). Increase in incubation time beyond 30 min did not further decrease the TPC as shown in **Figure 2**. Similar pattern was noticed for the saccharification studies. Maximum saccharification value of 46.88; $p < 0.05\%$ was recorded using the substrate incubated for 30 min for dephenoliphication (**Figure 2**). Optimization of incubation time for the process is very important as shorter duration of time may not be able to remove sufficient amount of the phenolic compounds and longer time period could possibility lead to the formation of new phenolic compounds due to the fragmentation of soluble aromatic oligomers (Nilvebrant et al., 2003).

Significance of Temperature on Dephenoliphication

Significance of temperature was assessed using different temperature range (80, 90, 100, 110, 120, 130, 140, and $150^\circ C$) for reduction in phenolic content of pretreated wheat straw obtained by combination of aqueous ammonia and phosphoric acid. In addition, saccharification study of dephenoliphied substrates at different temperature was also carried out. TPC was started to decrease with increase of temperature from $80^\circ C$ (130 mg GAE/g DW) and maximum reduction in TPC (50 mg GAE/g DW) was observed at $110^\circ C$. However, further increase in the temperature ensued gradual increase in the TPC which was maximum (103 mg GAE/g DW) at $150^\circ C$.

Analogous tendency was observed for enzymatic hydrolysis of dephenoliphied substrates and maximum saccharification i.e., 48.02% was determined for the substrate having least phenolic content. Substrate samples with increased phenolic content showed decreased saccharification (**Figure 3**). This may be due to the fact that with the increase in temperature, the hemicellulosic content is converted in to furans which can interfere with saccharification. The increase in TPC with time at higher temperature could be due the breakdown of ester bonds in lignin carbohydrate complexes and hence producing more phenolics (Canilha et al., 2008). Nawaz et al. (2017) reported maximum removal of phenolic compounds from pretreated sugarcane bagasse at $75^\circ C$ after 120 min of incubation using $Ca(OH)_2$ with 2.21 folds increase in saccharification. The conditions optimized are mild than used in current study might be due to difference in substrate used. However, no ample data is available on phenolic compounds removal from solid biomass for comparison.

Optimal Concentration of Alkali and Acid Combination

Different concentrations of ammonia [5, 10, 15, 20, 25, and 30 % (v/v)] and phosphoric acid [0.5, 1, 1.5, 2, 2.5, 3, and 3.5% (v/v)] were investigated, in a one constant one variable manner, to find out the best concentrations for the combination in order to achieve maximum removal of phenolics from pretreated wheat straw. All samples treated for phenolics removal were also subjected to saccharification. Among all concentrations used, maximum reduction in phenolic content was observed at 5% (v/v) ammonia i.e., 53.12 mg GAE/g DW and 1% (v/v) phosphoric acid i.e., 48 mg GAE/g DW as evident from **Figures 4A,B**, respectively. Biomass treated at these concentrations for TPC reduction also showed maximum saccharification with a values of 48.37 and 55.06%, respectively. Low dose of acid and base maximally removed the phenolic content. No previous reports are available for utilization of

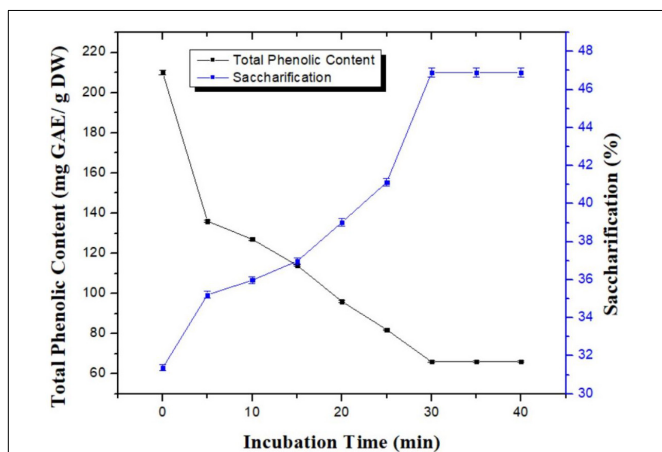


FIGURE 2 | Effect of incubation time on the removal of phenolics from pretreated wheat straw using combination of aqueous ammonia and phosphoric acid. Y-error bars represent the standard deviation ($SD \leq \pm 0.05$) between three replicates.

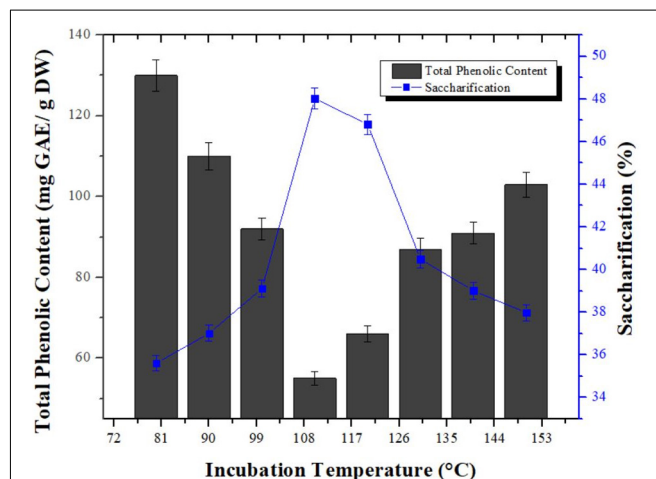


FIGURE 3 | Studies of temperature influence on reduction in phenolic content from pretreated wheat straw. Y-error bars represent the standard deviation ($SD \leq \pm 0.05$) between three replicates.

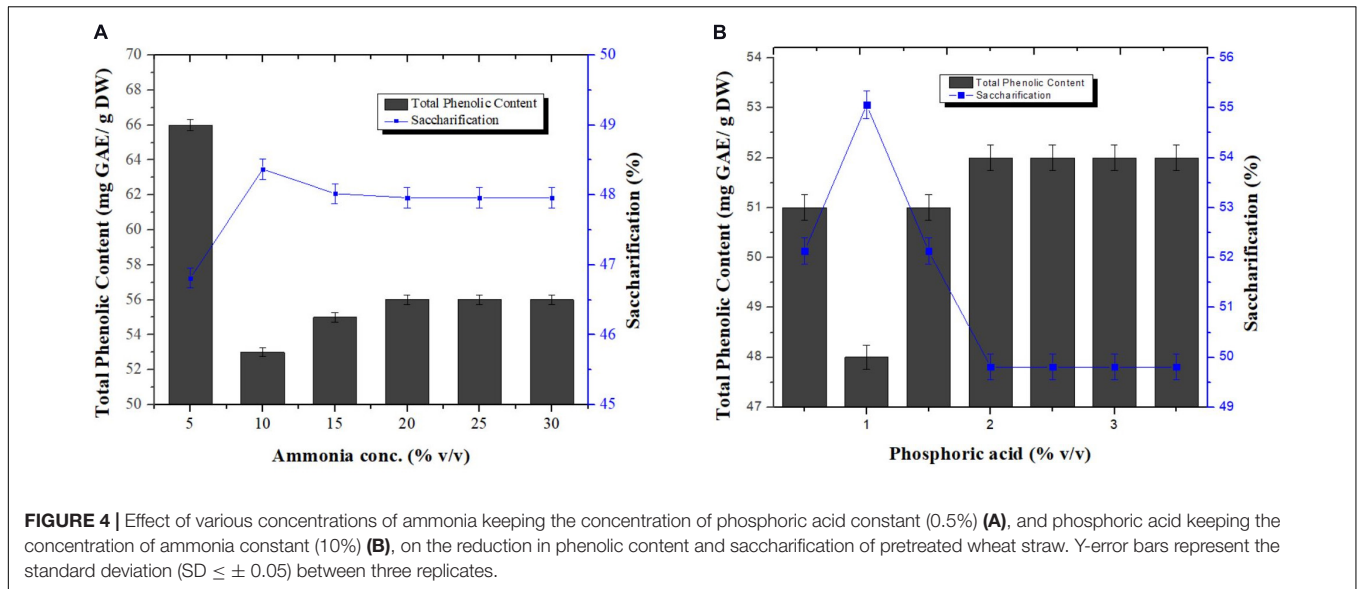


FIGURE 4 | Effect of various concentrations of ammonia keeping the concentration of phosphoric acid constant (0.5%) (A), and phosphoric acid keeping the concentration of ammonia constant (10%) (B), on the reduction in phenolic content and saccharification of pretreated wheat straw. Y-error bars represent the standard deviation ($SD \leq \pm 0.05$) between three replicates.

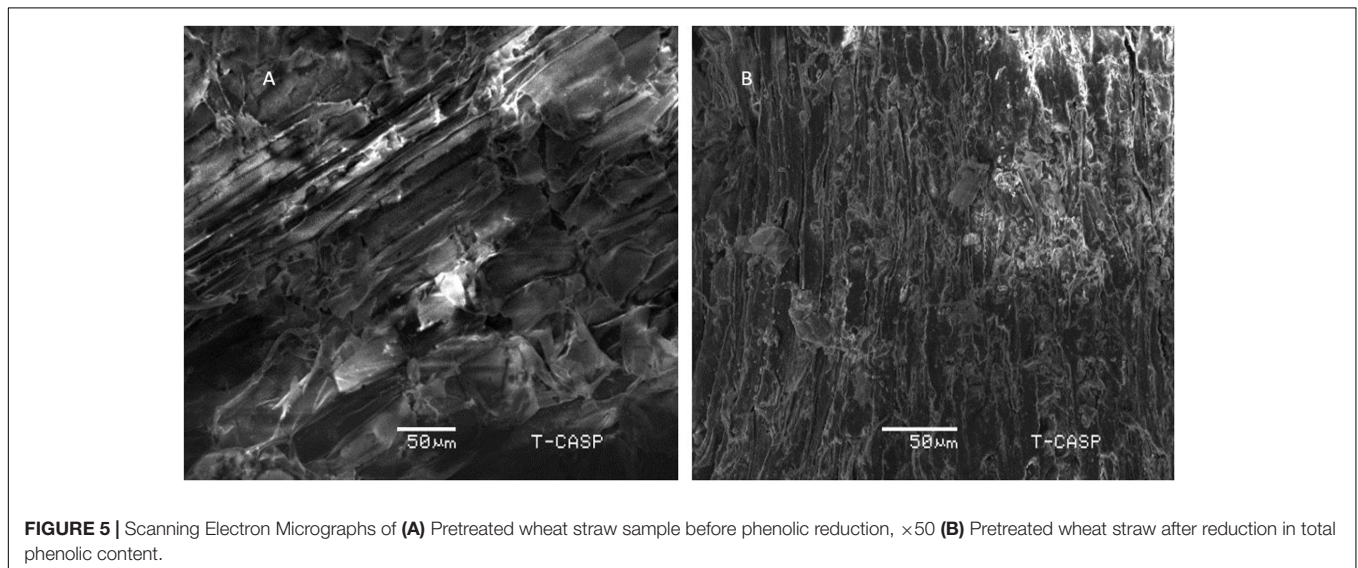


FIGURE 5 | Scanning Electron Micrographs of (A) Pretreated wheat straw sample before phenolic reduction, $\times 50$ (B) Pretreated wheat straw after reduction in total phenolic content.

ammonia and phosphoric acid in combination for removal of phenolic compounds from wheat straw.

Scanning Electron Microscopy of Detoxified Wheat Straw

Scanning electron micrographs of pretreated wheat straw samples, before and after detoxification under optimum conditions are shown in **Figure 5**. Before detoxification, the sample is in compact form, showing crystalline structure. On the other hand, detoxified sample shows loosely bound fibers and less crystallinity. The higher saccharification yield could be attributed to the structural changes in biomass thus making cellulose more assessable. However, evident from the previous study of Rajput et al. (2018), the heat treatment above 180 °C increases its digestibility of wheat straw due to degradation of hemicellulose. Hemicellulose degradation due to heating

biomass at higher temperature (170 °C) has also been reported by Santucci et al. (2015). Since, the detoxification in present study is carried out at 110 °C, much less than 180 °C, it could be inferred that the higher saccharification reported is mainly the result of decreased TPC instead of simultaneous removal of hemicellulose due to detoxification conditions. Although changes in cellulose crystallinity and porosity cannot be ruled out, lignin and phenolic content can be considered here as the main discriminating parameter. However, the exact nature of structural changes is need to be studied in detail.

CONCLUSION

It was concluded from current study that pilot scale removal of TPC from solid biomass has a significant effect on improved

action of cellulases on pretreated wheat straw. Furthermore, treatment strategies and optimization parameters were found to have appreciable impact on removal of phenolic compounds. As the pilot scale studies related to current research are not previously available, there is a strong need to explore different strategies and different biomass for removal of phenolics and their assessment as a potential substrate for proficient conversion to fermentable saccharides enzymatically at industrial scale.

DATA AVAILABILITY STATEMENT

The raw data supporting the conclusions of this article will be made available by the authors, without undue reservation.

REFERENCES

- Ahmed, F., Yan, Z., and Bao, J. (2019). Dry biodegradation of acid pretreated wheat straw for cellulosic ethanol fermentation. *Bioresour. Bioprocess.* 6:24. doi: 10.1186/s40643-019-0260-x
- Canilha, L., Carvalho, W., and Felipe, M. G. (2008). Xylitol production from wheat straw hemicellulosic hydrolysate: hydrolysate detoxification and carbon source used for inoculum preparation. *Braz. J. Microbiol.* 39, 333–336. doi: 10.1590/S1517-83822008000200025
- Chandel, A. K., da Silva, S. S., and Singh, O. V. (2011). Detoxification of lignocellulosic hydrolysates for improved bioethanol production. *Biofuel Prod. Recent Dev. Prospects* 10:225.
- Chen, Z., Ragauskas, A., and Wan, C. (2020). Lignin extraction and upgrading using deep eutectic solvents. *Ind. Crops Prod.* 147:112241. doi: 10.1016/j.indcrop.2020.112241
- Duncan, D. B. (1995). Multiple range and multiple F tests. *Biometrics* 11, 1–42. doi: 10.2307/3001478
- Folin, O., and Ciocalteu, V. (1927). On tyrosine and tryptophane determinations in proteins. *J. Biol. Chem.* 73, 627–650. doi: 10.1016/S0021-9258(18)84277-6
- Haq, I., Arshad, Y., Nawaz, A., Aftab, M., Rehman, A., Mukhtar, H., et al. (2018). Removal of phenolic compounds through overliming for enhanced saccharification of wheat straw. *J. Chem. Technol. Biotechnol.* 93, 3011–3017. doi: 10.1002/jctb.5659
- Hasegawa, I., Khoo, T. H., and Mae, K. (2013). Direct saccharification of lignocellulosic biomass by hydrolysis with formic acid solution. *Green Process. Synth.* 2, 143–149. doi: 10.1515/gps-2012-0090
- Horváth, I. S., Sjöde, A., Alriksson, B., Jönsson, L. J., and Nilvebrant, N. O. (2005). "Critical conditions for improved fermentability during overliming of acid hydrolysates from spruce," in *Proceedings of the Twenty Sixth Symposium on Biotechnology for Fuels and Chemicals*, Vol. 121, (Totowa, NJ: Humana Press), 1031–1044. doi: 10.1007/978-1-59259-991-2_87
- Huang, C., Han, L., Liu, X., and Ma, L. (2010). The rapid estimation of cellulose, hemicellulose, and lignin contents in rice straw by near infrared spectroscopy. *Energy Sources A Recove. Util. Environ. Eff.* 33, 114–120. doi: 10.1080/15567030902937127
- John, B. I., Sulaiman, C. T., George, S., and Reddy, V. R. (2014). Total phenolics and flavonoids in selected medicinal plants from Kerala. *Int. J. Pharm. Pharm. Sci.* 6, 406–408.
- Jönsson, L. J., Alriksson, B., and Nilvebrant, N. (2013). Bioconversion of lignocellulose: inhibitors and detoxification. *Biotechnol. Biofuels* 6:16. doi: 10.1186/1754-6834-6-16
- Khobragade, C. N., Sureshkumara, K., Borkara, P. S., and Sagarb, A. D. (2004). Enzymatic saccharification of cellulosic waste by cellulase system of *Cellulomonas uda* immobilized on tri (4-formyl phenoxy) cyanurate. *Ind. J. Chem. Technol.* 11, 816–819.
- Kim, J. W., Kim, K. S., Lee, J. S., Park, S. M., Cho, H. Y., Park, J. C., et al. (2011). Two-stage pretreatment of rice straw using aqueous ammonia and dilute acid. *Bioresour. Technol.* 102, 8992–8999. doi: 10.1016/j.biortech.2011.06.068

AUTHOR CONTRIBUTIONS

IH, KJ, and YX developed the idea and methodology for the study and helped in manuscript preparation. AN, BL, and YA performed the experiment and prepared the manuscript. XZ, FA, XF, and MS analyzed the results and interpreted them. All the authors proofread the manuscript.

FUNDING

The authors acknowledge the financial support of the Doctoral Scientific Research Foundation of Hangzhou Medical College (0004F1RCYJ1905) and the General Scientific Research Project of Education Department of Zhejiang Province (Y201942775).

- Kim, S., and Holtzapfle, M. T. (2006). Effect of structural features on enzyme digestibility of corn stover. *Bioresour. Technol.* 97, 583–591. doi: 10.1016/j.biortech.2005.03.040
- Lynd, R. L., Laser, M. S., Bransby, D., Dale, B. E., and Davison, B. (2008). How biotech can transform biofuels. *Nat. Biotechnol.* 26, 169–172. doi: 10.1038/nbt0208-169
- Mansour, A. A., Arnaud, T., Lu-Chau, T. A., Fdz-Polanco, M., Moreira, M. T., and Rivero, J. A. (2016). Review of solid state fermentation for lignocellulosic enzyme production: challenges for environmental applications. *Rev. Environ. Sci. Biotechnol.* 15, 31–46. doi: 10.1007/s11157-016-9389-7
- Nawaz, A., Haq, I., and Mukhtar, H. (2017). Removal of phenolic inhibitors from pretreated sugarcane bagasse for enhanced enzymatic recovery of fermentable sugars. *Pak. J. Bot.* 49, 2491–2494.
- Nilvebrant, N. O., Persson, P., Reimann, A., DeSousa, F., Gorton, L., and Jönsson, L. J. (2003). Limits for alkaline detoxification of dilute-acid lignocellulose hydrolysates. *Appl. Biochem. Biotechnol.* 107, 615–628. doi: 10.1385/ABAB:107:1-3:615
- Novakovic, J., Kontogianni, N., Barampouti, E. M., Mai, S., Moustakas, K., Malamis, D., et al. (2020). Towards upscaling the valorization of wheat straw residues: alkaline pretreatment using sodium hydroxide, enzymatic hydrolysis and biogas production. *Environ. Sci. Pollut. Res.* 25, 1–13. doi: 10.1007/s11356-020-08905-y
- Ondrejoví, M., Janíková, V., and Chmelová, D. (2020). Optimization of lime pretreatment for enzymatic saccharification of wheat straw. *J. Microbiol. Biotechnol. Food Sci.* 9, 134–138.
- Qi, F., Kitahara, Y., Wang, Z., Zhao, X., Du, W., and Liu, D. (2014). Novel mutant strains of *Rhodospiridium toruloides* by plasma mutagenesis approach and their tolerance for inhibitors in lignocellulosic hydrolyzate. *J. Chem. Technol. Biotechnol.* 89, 735–742. doi: 10.1002/jctb.4180
- Qiu, J., Ma, L., Shen, F., Yang, G., Zhang, Y., Deng, S., et al. (2017). Pretreating wheat straw by phosphoric acid plus hydrogen peroxide for enzymatic saccharification and ethanol production at high solid loading. *Bioresour. Technol.* 238, 174–181. doi: 10.1016/j.biortech.2017.04.040
- Qiu, J., Tian, D., Shen, F., Hu, J., Zeng, Y., Yang, G., et al. (2018). Bioethanol production from wheat straw by phosphoric acid plus hydrogen peroxide (PHP) pretreatment via simultaneous saccharification and fermentation (SSF) at high solid loadings. *Bioresour. Technol.* 268, 355–362. doi: 10.1016/j.biortech.2018.08.009
- Rajput, A. A., Zeshan, and Visvanathan, C. (2018). Effect of thermal pretreatment on chemical composition, physical structure and biogas production kinetics of wheat straw. *J. Environ. Manage.* 221, 45–52. doi: 10.1016/j.jenvman.2018.05.011
- Ramos, C., García, A. S., Moreno, B., and Díaz, G. (2019). Small-scale renewable power technologies are an alternative to reach a sustainable economic growth: evidence from Spain. *Energy* 167, 13–25. doi: 10.1016/j.energy.2018.10.118
- Santucci, B. S., Maziero, P., and Rabelo, S. C. (2015). Autohydrolysis of hemicelluloses from sugarcane bagasse during hydrothermal pretreatment: a

- kinetic assessment. *Bioenergy Res.* 8, 1778–1787. doi: 10.1007/s12155-015-9632-z
- TAPPI Standard T236cm-85 (1993). Kappa number of pulp. *Tappi J.*
- Tareen, A. K., Punsuvon, V., and Parakulsuksatid, P. (2020). Investigation of alkaline hydrogen peroxide pretreatment to enhance enzymatic hydrolysis and phenolic compounds of oil palm trunk. *3 Biotech* 10:179. doi: 10.1007/s13205-020-02169-6
- Wang, Q., Wang, Z., Shen, F., Hu, J., Sun, F., Lin, L., et al. (2014). Pretreating lignocellulosic biomass by the concentrated phosphoric acid plus hydrogen peroxide (PHP) for enzymatic hydrolysis: evaluating the pretreatment flexibility on feedstocks and particle sizes. *Bioresour. Technol.* 166, 420–428. doi: 10.1016/j.biortech.2014.05.088
- Xiong, S., Martín, C., Eilertsen, L., Wei, M., Myronycheva, O., Larsson, S. H., et al. (2019). Energy-efficient substrate pasteurisation for combined production of shiitake mushroom (*Lentinula edodes*) and bioethanol. *Bioresour. Technol.* 274, 65–72. doi: 10.1016/j.biortech.2018.11.071
- Conflict of Interest:** The authors declare that the research was conducted in the absence of any commercial or financial relationships that could be construed as a potential conflict of interest.
- Copyright © 2021 Haq, Nawaz, Liaqat, Arshad, Fan, Sun, Zhou, Xu, Akram and Jiang. This is an open-access article distributed under the terms of the Creative Commons Attribution License (CC BY). The use, distribution or reproduction in other forums is permitted, provided the original author(s) and the copyright owner(s) are credited and that the original publication in this journal is cited, in accordance with accepted academic practice. No use, distribution or reproduction is permitted which does not comply with these terms.



Changes in the Leaf Physiological Characteristics and Tissue-Specific Distribution of Ginsenosides in *Panax ginseng* During Flowering Stage Under Cold Stress

Tao Zhang, Changbao Chen, Yuqiu Chen, Qinghe Zhang, Qiong Li and Weichen Qi*

Key Laboratory of Chinese Medicine Planting and Development, Changchun University of Chinese Medicine, Changchun, China

OPEN ACCESS

Edited by:

Lei Wang,
Jeju National University, South Korea

Reviewed by:

Zhi Chao,
Southern Medical University, China
Ren Ren,
The University of Texas MD Anderson
Cancer Center, United States

*Correspondence:

Weichen Qi
weichen_qi@163.com

Specialty section:

This article was submitted to
Bioprocess Engineering,
a section of the journal
Frontiers in Bioengineering and
Biotechnology

Received: 03 December 2020

Accepted: 28 January 2021

Published: 17 March 2021

Citation:

Zhang T, Chen C, Chen Y,
Zhang Q, Li Q and Qi W (2021)
Changes in the Leaf Physiological
Characteristics and Tissue-Specific
Distribution of Ginsenosides in *Panax*
ginseng During Flowering Stage
Under Cold Stress.
Front. Bioeng. Biotechnol. 9:637324.
doi: 10.3389/fbioe.2021.637324

Panax ginseng is a valuable traditional herbal medicine material with numerous applications. Ginsenosides are the key bioactive compounds in ginseng. Cold stress can activate stress tolerance mechanisms that regulate biomass and biosynthesis in ginseng tissue. In this study, the effects of short- and long-term cold stress (5°C) on the physiological characteristics, tissue-specific ginsenoside distributions, and ginsenoside synthesis gene expressions of 3-year-old *P. ginseng* during the flowering period were investigated. Short-term cold stress significantly reduced ginseng biomass (root fresh weight and dry weight), and increased malondialdehyde, proline, soluble sugar, and soluble protein concentrations. Superoxide dismutase, peroxidase, and catalase activities also increased significantly under cold stress. With prolongation of the cold stress period, all antioxidant enzyme activity decreased. The protopanaxatriol-type ginsenoside concentrations in the taproots (phloem and xylem) and fibrous roots, as well as the protopanaxadiol-type ginsenoside concentrations in the leaves, increased significantly under short-term cold stress. The key genes (*SE*, *DS-II*, *CYP716A52v2*, and *CYP716A53v2*) involved in the ginsenoside biosynthesis pathway were significantly positively correlated with the ginsenoside accumulation trends. Thus, short-term cold stress can stimulate membrane lipid peroxidation, in turn stimulating the antioxidant enzyme system to alleviate oxidative damage and increasing the expression of key enzyme genes involved in ginsenoside biosynthesis. During agricultural production, protopanaxadiol/protopanaxatriol ratios could be manipulated by low-temperature storage or treatments.

Keywords: *Panax ginseng*, biomass, cold stress, biotechnology, ginsenoside

Abbreviations: CAT, catalase; MDA, malondialdehyde; CYP716A52v2, β -alanine C-28 hydroxylase; DS, dammarenediol synthase; HMGR, 3-hydroxy-3-methylglutaryl-CoA reductase; HPLC, high-performance liquid chromatography; Pro, proline; POD, peroxidase; PPD, protopanaxadiol; PPT, protopanaxatriol; ROS, reactive oxygen species; SOD, superoxide dismutase; SP, soluble protein; SS, soluble sugar; SS1, squalene synthetase; SE, squalene epoxidase.

INTRODUCTION

Panax ginseng C.A. Meyer is a perennial herb and a valuable traditional Chinese medicinal material with a long history of exploitation. Ginsenosides are the key bioactive compounds in ginseng. Modern pharmacological studies have demonstrated that ginsenoside has numerous medicinal applications, such as immunity regulation, anti-stress, anti-fatigue, anti-oxidation, anti-inflammatory, anti-tumor, hypoglycemic, and liver-protective properties (Chao, 2006; Leung and Wong, 2010; Lian-Wen et al., 2011; Liu, 2012). Currently, approximately 180 types of ginsenoside monomers have been isolated from ginseng (Christensen, 2009; Sun et al., 2011; In-Ah et al., 2012; Shi et al., 2013).

Ginsenosides are considered critical biomarkers in ginseng quality evaluation. The 2020 edition of the Chinese Pharmacopoeia defines the appropriate amounts of root ginsenosides: the total Rg1 (C₄₂H₇₂O₁₄) and Re (C₄₈H₈₂O₁₈) content should not be lower than 0.3% and the Rb1 (C₅₄H₉₂O₂₃) content should not be lower than 0.2%. The various ginsenoside aglycones can be divided into oleanane-type pentacyclic triterpene saponins, protopanaxadiol-type saponins (PPD), and protopanaxatriol-type saponins (PPT); both the PPD-type and PPT-type saponins are dammarane-type tetracyclic triterpenoids (Li et al., 2009).

To date, numerous studies have investigated the relationships between ginsenoside composition and biological activity. One study confirmed a close relationship between the biological activity of ginseng and the year of cultivation (Shan et al., 2014). Changes in the proportions of different ginsenosides are a major factor influencing changes in the biological activity of ginseng over time. The PPD/PPT ratio is considered a key factor influencing variations in the biological activity of ginseng (Cho et al., 2017). PPD- and PPT-type ginsenosides have different biological functions, and differences in their composition strongly influence the quality of medicinal materials (Qu et al., 2009).

Cold stress, a major abiotic stress factor, causes plants to adopt strategies that alter their external morphology, and the structure and accumulation of their secondary metabolites (Kim et al., 2013). In addition, a series of physiological and biochemical changes occur in the plant to counteract the potential damage caused by cold stress. Malondialdehyde (MDA) is a critical indicator of the degree of membrane peroxidation. Therefore, MDA concentration can directly reflect the degree of cell membrane damage (Lukatkin et al., 2012). Under stressful environmental conditions, the cell membrane system transmits signals to the plant and the reactive oxygen species (ROS) concentrations in the plant increase significantly. This represents the plants' antioxidant enzyme systems facilitating resistance against adverse environmental factors and maintaining the integrity and stability of the cell membrane. Studies have demonstrated that cold stress can promote the production of antioxidant enzymes such as catalase (CAT), peroxidase (POD), and superoxide dismutase (SOD) in plant tissues, in addition to inducing increases in the accumulation of osmotic regulatory substances, such as proline (Pro), soluble sugar (SS), and soluble protein (SP). Short-term cold stress increases antioxidant enzyme

activity, and increases the synthesis of osmotic regulators; however, under long-term cold stress, antioxidant enzyme activity is inhibited, and the concentrations of osmotic regulators decrease (Lo' Ay and Elkhateeb, 2018; Rezaie et al., 2020).

The biosynthesis of ginsenosides, the primary active compounds in ginseng, is influenced by interactions between genetic and environmental factors. The biosynthetic pathway of ginsenosides is divided into three parts: the main upstream genes include 3-hydroxy-3-methylglutaryl-CoA reductase (HMGR), farnesyl pyrophosphate synthase (FPS), squalene synthetase (SSI), squalene epoxidase (SE), dammareniol synthase (DS), and aromatase (PNT) are the main genes included in the synthesis section; and cytochrome P450 (CYP450) and UDP-glycosyltransferase (UGT) are the main genes downstream of synthesis (Ohyama et al., 2007; Han et al., 2010; Wu et al., 2012; Yang et al., 2018). Studies have demonstrated that temperature could influence the expression of key enzyme genes in the ginsenoside synthesis pathway, and, in turn, the concentrations of ginsenosides (You et al., 2015; Jiang et al., 2016).

In the present study, the physiological indicators of ginseng resistance to abiotic stress were systematically analyzed, including antioxidant enzymes, osmotic regulator molecules, and secondary metabolism (key enzyme gene expression and secondary metabolites). The results of the present study should clarify the potential mechanisms of the physiological and biochemical responses of ginseng to cold stress and facilitate attempts to increase ginsenoside concentrations during ginseng cultivation.

MATERIALS AND METHODS

Plant Materials and Experimental Design

The plant materials used were 3-year-old *P. ginseng* that were purchased from Fusong County, Jilin Province, China, and potted at the end of April 2018. The pots were 16.00 cm tall, with rim diameters of 23.00 cm and base diameters of 13.00 cm. The soil depth was 13.00 cm. Each pot was buried entirely in the soil and the temperature in the pot was maintained at the temperature of the surrounding soil. The soil water content was maintained at 60% of the field water holding capacity. The test soil was microbial substrate soil (44 bags of microbial substrate: 3 bags of vermiculite: 7 bags of perlite). There were three plants per pot, which were regularly watered, weeded, fertilized, and sprayed with pesticides. The flowering stage is a critical period for the growth and development of ginseng, especially for the reproductive organs. Studies have shown that the content of ginsenosides varies greatly during the flowering stage, which has important research significance (Yang et al., 2017). Therefore, in this study, plants in good condition were selected during the flowering stage (June 14–28) for use in the cold stress experiments. The water and light conditions were controlled according to the general requirements under field cultivation, and the day and night lengths were not changed.

A digital artificial climate room was adopted for carrying out the cold stress experiments (5°C). Sampling began on the first day of treatment and was carried out daily. Control (CK)

treatments were set up in the field. During sampling, nine plants were sampled in each group, and the collected ginseng were placed in an ice box and transported to the laboratory. In the laboratory, sediment was washed off with running water, and the surface moisture was absorbed using filter paper. Afterward, the fresh weight was determined and recorded, and the fibrous roots, phloem, xylem, rhizomes, and leaves were separated. An appropriate number of leaves was obtained, placed in a self-sealing bag, and stored in liquid nitrogen at -80°C for later physiological tests. Tissues were ground into fine powder and sieved through a $60\text{-}\mu\text{m}$ mesh sieve for use in the determination of ginsenoside content.

Reagents and Standards

The ginsenoside standards, Ro, Rg1, Re, Rf, Rb1, Rc, Rb2, Rb3, Rd, Rh2, and Rg3, were purchased from the National Institute for the Control of Pharmaceutical and Biological Products (Beijing, China). To satisfy the ultra-performance liquid chromatography analysis requirements, the purity of all standards was greater than 98%. High-performance liquid chromatography (HPLC)-grade acetonitrile and methanol were purchased from Thermo Fisher Scientific (Norcross, GA, United States), and the HPLC water used was Wahaha mineral water (Jilin, China). SOD, POD, CAT, SP, Pro, SS, and MDA assay kits were purchased from the Nanjing Jiancheng Bioengineering Institute (NJBI, Nanjing, China).

Sample and Standard Solution Preparation

A ginseng powder sample (1.0 g) was placed in an Erlenmeyer flask and extracted according to the pharmacopeia method, with slight modification (Kuang et al., 2020). Afterward, 30 mL of methanol was added, and extracted by ultrasonication at 90 Hz for 30 min. The supernatant was then filtered, and the procedure repeated three times. The filtrates were combined and transferred to an evaporating dish and evaporated in a 60°C water bath. The volume was brought to 5 mL in a volumetric flask with a $0.22\text{-}\mu\text{m}$ pinhole filter for HPLC analysis (Guo et al., 2015). Measurements were performed in triplicate.

To establish the calibration curves of the 11 ginsenoside standards (Ro, Rg1, Re, Rf, Rb1, Rc, Rb2, Rb3, Rd, Rh2, and Rg3), stock solutions containing the 11 standards were weighed precisely and dissolved in methanol. Then, the solutions were diluted into a series of standard solutions with gradient concentrations. The solutions were passed through a $0.22\text{-}\mu\text{m}$ membrane and stored in a refrigerator at 4°C .

HPLC Analytical Conditions

The prepared samples were analyzed using an Agilent 1260 HPLC system (Agilent, United States) and separated in an Elite Hypersil ODS2 (250 mm \times 4.6 mm, 5 μm) column. The mobile phase was composed of A (water) and B (acetonitrile). The gradient elution was performed as follows: 0–18.0 min, 19–23% B; 18.1–28.0 min, 23–28% B; 28.1–30.0 min, 28–32% B; 30.1–50.0 min, 32–34% B; and 50.1–70.0 min, 34–80% B. The injection volume was 10 μL , the column temperature was 25°C , UV measurements were obtained at 203 nm, and the flow rate was 1.0 mL/min.

Determination of Osmoregulatory Substances and Malondialdehyde Content

In an ice bath, 0.5-g fresh root tissues were homogenized (by grinding) in 5 mL of phosphate-buffered saline ($0.05\text{ mol}\cdot\text{L}^{-1}$, pH 7.8). The homogenates of the fresh root tissues were assayed with SP, Pro, SS, and MDA kits (NJBI). The absorbance of the reaction solutions was measured at 595, 520, 620, and 530 nm using an enzyme-labeling instrument (SpectraMax 190, Molecular Devices, United States); the values obtained were used to calculate the concentrations of SP, Pro, SS, and MDA, respectively.

Antioxidant Enzyme Extraction and Determination of Enzyme Activity

The method of crude enzyme extract preparation used in the present study was modified from a previously published method (Ba et al., 2013). The samples were ground into homogenates and transferred into centrifuge tubes; afterward, phosphate-buffered saline ($0.05\text{ mol}\cdot\text{L}^{-1}$, pH 7.8) was added up to final volumes of 5 mL. The samples were then centrifuged at 4°C and $10000\text{ rpm}\cdot\text{min}^{-1}$ for 10 min. SOD, POD, and CAT activities were assayed using kits (NJBI) and their activities were expressed as units per milligram of protein.

Extraction of RNA and Gene Expression of Key Enzymes

Total ginseng RNA was extracted using a TaKaRa MiniBEST Universal RNA Extraction Kit (TaKaRa, CA, Japan) and 1.0 μg RNA was used for reverse transcription with a PrimeScriptTM RT Master Mix kit (TaKaRa, CA, Japan) in a 20- μL reaction volume, according to the manufacturer's instructions. The product was stored at -20°C . GAPDH was used as an internal control, and the relative gene expression levels of *HMGR2*, *FPS*, *SSI*, *SE1*, *DS-II*, *PNY1*, *CYP716A52v2*, *CYP716A53v2*, and *CYP716A47* were determined (primer information is listed in **Table 1**). Reverse transcriptase quantitative PCR (RT-qPCR) was performed in 96-well plates in a Stratagene Mx3000P thermocycler (Agilent, Palo Alto, CA, United States) with an SYBR Green-based PCR assay. The final volume for each reaction was 20 μL with the following components: 1 μL diluted cDNA template (1 mg/mL), 10 μL SYBR Green Mix (TaKaRa, DaLian, CA, Japan), 1 μL forward primer (1 mM), 1 μL reverse primer (1 mM), and 7 μL ddH₂O. The reaction was performed under the following conditions: 95°C for 3 min, followed by 40 cycles of denaturation at 95°C for 5 s, annealing at 55°C for 32 s, and extension at 72°C for 20 s. The melting curve was obtained by heating the amplicon from 55 to 95°C with increments of 0.5°C per 5 s. Each RT-qPCR analysis was performed with three biological replicates. The relative gene expression levels were computed using the $2^{-\Delta\Delta\text{Ct}}$ method.

Statistical Analysis

MS Excel 2016 (Microsoft Corp., Redmond, WA, United States) was used to sort the original data, and IBM SPSS Statistics 19.0 (IBM Corp., Armonk, NY, United States) was used for single-factor variance analysis. GraphPad prism 6.0 (GraphPad Software Inc., San Diego, CA, United States) and Origin 9.0

TABLE 1 | Real-time fluorescence quantitative PCR primers.

Gene	Accession No.	Primer sequence 5'-3'	Product length (bp)
<i>GAPDH</i>	KY400031	F: ATGGACCATCAGCAAAGGAC R: GGTAGCACTTTCCCAACAGC	117
<i>HMGGR2</i>	JX648390	F: TCTTCAAAGCCTCTGATGC R: TTTTGGGGATTGGATTGTCA	126
<i>FPS</i>	DQ087959	F: CAAGAAGCATTCCGACAA R: CTCTCCTACAAGGGTGGTGA	116
<i>SS1</i>	AB115496	F: GGACTTGTGGATTAGGGTTG R: ACTGCCTTGGCTGAGTTTTTC	107
<i>SE1</i>	AB122078	F: ATGCTTTGAATATGCGCCATC R: CATGGAGATCGCGTAAAGGTC	102
<i>DS-II</i>	AB265170	F: CAAATGCCACAAGGATATTGTC R: TGCGAAACCACCACCTTACAC	105
<i>PNY1</i>	AB009030	F: GCGGAAGGGAATAAGATGAC R: CTCAGCTCTCCGGACAGC	108
<i>CYP716A47</i>	JN604536	F: TCACCTTGGTTCTCAACTATC R: TCTTCTCAAATCCTCCCAAT	129
<i>CYP716A52v2</i>	JX036032	F: AGGAGCAAATGGAGATAG R: AACCGTTGTAGGTGAAAT	106
<i>CYP716A53v2</i>	JX036031	F: ATCGGACAACGAGGCAGCAC R: GCCAACAGGCCAACTCAA	102

(OriginLab, Northampton, MA, United States) were used for graphic illustration.

RESULTS

Root Fresh and Dry Weight of *Panax ginseng* Under Cold Stress

The effects of cold stress on ginseng root fresh and dry weight at the flowering stage are illustrated in **Figure 1**. During the entire temperature treatment stage, the fresh and dry weights of the roots increased to varying degrees, and the trends in the root dry and fresh weights were similar from June 22 to 28. The root fresh and dry weights in the treatment groups were lower than those in the control group, and they dropped significantly on June 22 and 26 by 15.8 and 23.1%, respectively. Long-term cold stress treatment induced a series of changes in the physiological and metabolic processes of ginseng, which, in turn, inhibited the accumulation of dry and fresh weight in the ginseng roots.

Ginsenoside Concentration Detection and Method Establishment

Eleven ginsenosides were identified based on the retention times of each saponin monomer peak. **Figure 2** presents the HPLC spectrum of the standards (**Figure 2A**) and the main root extract (**Figure 2B**). Linear regression equations were obtained by taking the peak area as the ordinate and the concentration of the reference solution as the abscissa. The 11 compounds exhibited good linear relationships within their respective linear ranges. The results are listed in **Table 2**. The 11 compounds were detected in the main root of the ginseng. The 11 detected constituents had good resolution and could be easily determined. They were also the primary constituents in the assayed samples. The established HPLC quantitative method had good linear ranges and was consistent with the relative requirements.

Change of Ginsenoside Content in Different Ginseng Tissues During the Flowering Stage Under Cold Stress

Change of Rg1 Content

As illustrated in **Figure 3**, the tissue specificity of flowering ginseng was determined by analyzing the concentrations

of Rg1 in each of the tissues in the control group. The order of Rg1 concentration was leaf > fibrous roots > phloem > stem > xylem. The leaf was the primary synthetic site of Rg1, which is consistent with the findings of Kim et al. (2015).

After cold stress treatment, the concentrations of Rg1 in xylem, phloem, stem, and leaf all exhibited increasing trends, followed by decreases. The concentrations of Rg1 in the xylem, phloem, stem, and leaf all increased to varying degrees, and the peaks were observed on June 16, 20, 18, and 18, with concentrations 54.5, 98.7, 58.9, and 29.9% higher than those in the control group, respectively. The xylem Rg1 concentrations were higher than those of the control group throughout the flowering period. The leaf Rg1 concentrations decreased from June 22 to levels below those of the control group, while the fibrous root Rg1 concentrations were suppressed throughout the treatment period following cold stress to levels lower than those in the control group. According to the time taken for a significant difference in the Rg1 content to appear, the order of sensitivity to cold stress was phloem > stem > xylem > leaves > fibrous roots.

Change of Rb1 Content

The tissue-specific distributions of ginsenosides in flowering ginseng were analyzed based on the Rb1 concentrations in each tissue in the control group (**Figure 4**). The order of Rb1 concentrations was leaf > fibrous roots > phloem > stem > xylem, indicating that the leaf is also a primary site of Rb1 biosynthesis during flowering. The concentrations of Rb1 in the fibrous roots and phloem, both after cold stress treatment and in the control group, exhibited gradual upward trends and began to rise rapidly on June 22. Although cold stress seemed to promote the accumulation of phloem Rb1, its effect was not significant. Cold stress promoted the accumulation of Rb1 in the fibrous roots on June 20 and 26 (162.4 and 33.5% higher than that in the control group, respectively).

The concentrations of Rb1 in the treated phloem and stem also seemed to be higher than those in the control group, but there was no significant difference. The concentration in the treated xylem increased rapidly on June 22, and was significantly different from the concentration in the control group; by June 24, the treated xylem Rb1 concentration had increased by 288.8%

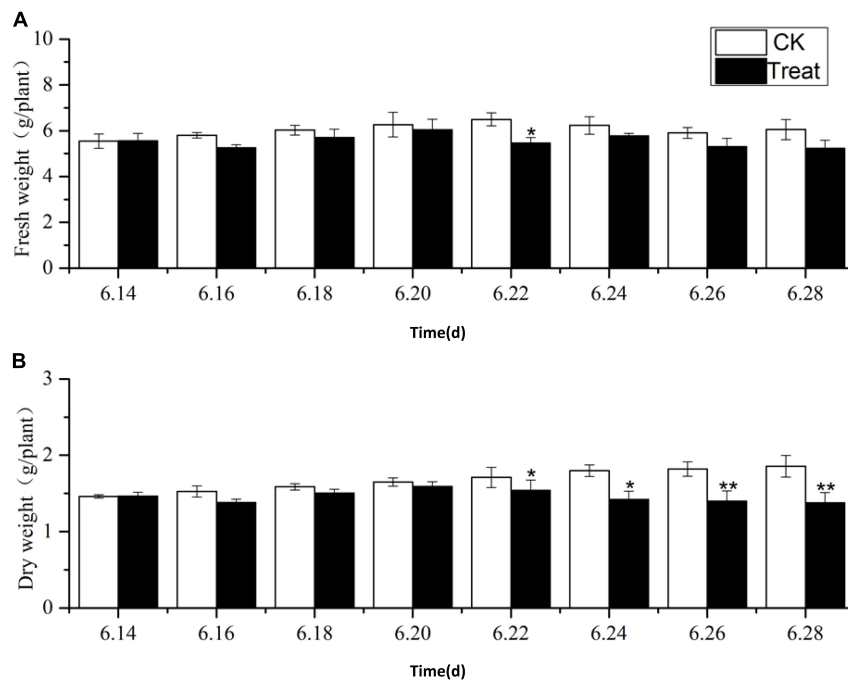


FIGURE 1 | Effects of cold stress on fresh weight and dry weight of ginseng during the flowering stage. The X axis represents the sampling time. **(A)** Represents the change of fresh weight under cold stress. **(B)** Represents the change of dry weight under cold stress. * $p < 0.05$ and ** $p < 0.01$, compared with control group. Vertical bars indicate the mean value \pm standard deviation from three independent experiments. The same below.

compared with the concentration in the control group. The Rb1 concentrations in the treated stem were significantly different from the concentrations in the control group on June 20, representing a 145.5% increase. The Rb1 concentrations in the leaves were higher than those in other tissues, with relatively stable levels. Following cold stress treatment, the leaf Rb1 content decreased, and the decrease became significant on June 26, when it was 37.3% lower than the level in the control group. Rb1 biosynthesis in the xylem, phloem, fibrous roots, and stem were promoted, but Rb1 biosynthesis in the leaves was inhibited. The Rb1 biosynthesis trends under cold stress in different tissues was xylem > fibrous roots > stem > leaf > phloem.

Change of Re Content

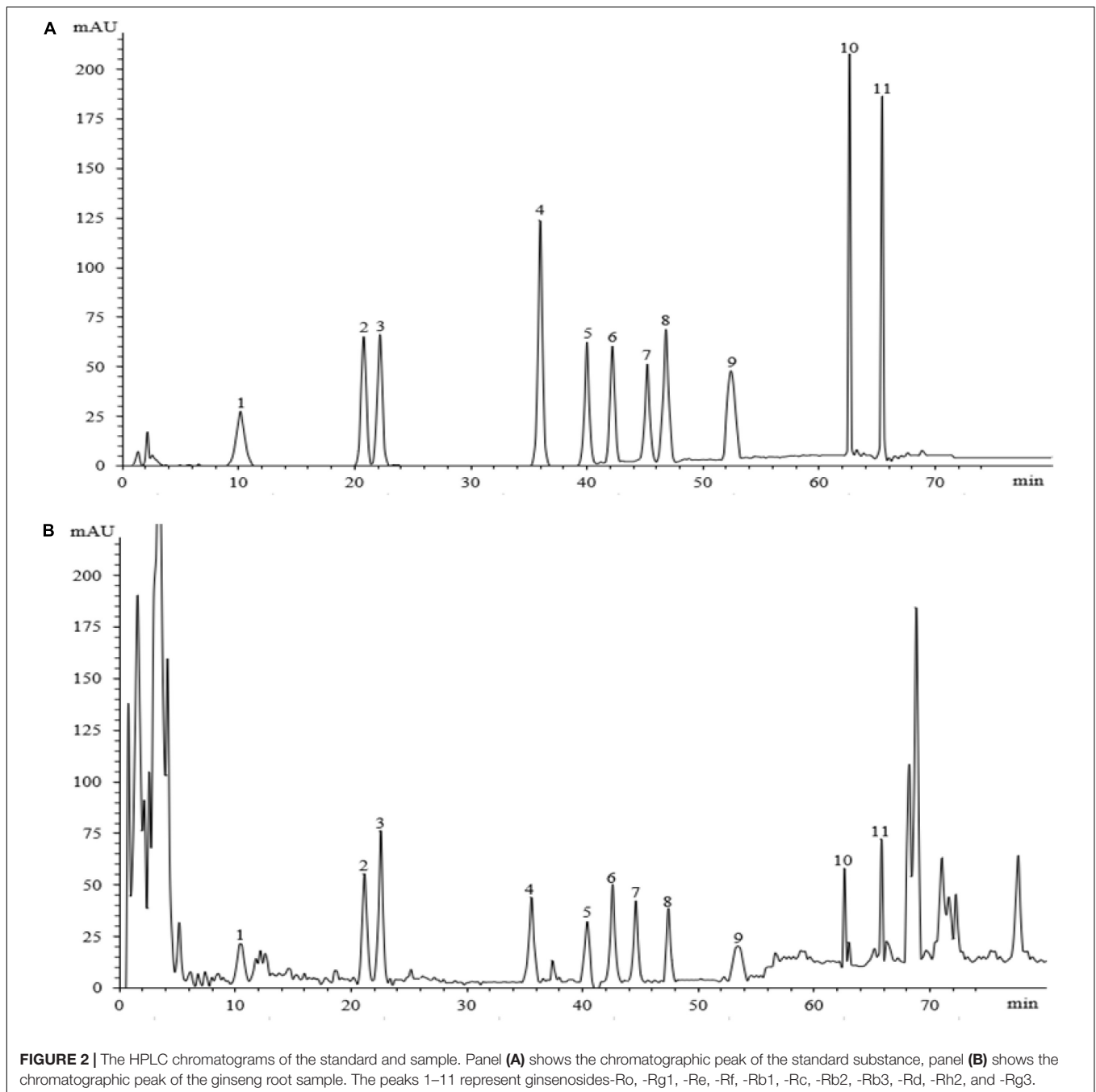
Ginsenoside tissue specificity was determined by analyzing the content of Re in different tissues (Figure 5). The Re concentrations in the tissues were in the order leaf > fibrous roots > phloem > stem > xylem. The Re concentrations in the leaves were 3 to 5-fold higher than those in the fibrous roots, indicating that the leaves were the primary Re biosynthesis sites during flowering. The Re content in the fibrous roots exhibited a gradual upward trend, while the Re content in the xylem, phloem, stem, and leaf remained stable, with no significant changes during flowering. After cold stress treatment, the Re content increased to varying degrees and remained higher than the content in the control group throughout the flowering period. The treated xylem achieved its maximum Re value on June 16, 243.3% higher than the content in the control group, whereas the treated phloem

achieved its maximum value on June 22, which was 170.7% higher than the content in the control group.

The content of Re in the treated fibrous roots and stems reached their highest levels on June 20, 23.2 and 53.9% higher than those in the control group, respectively. The Re content in the leaves under cold stress was lower than that in the control group. On June 24, it was significantly lower than that in the control group, and it fell to the lowest point on June 28, 50.8% lower than the control group. Cold stress promoted the biosynthesis of Re in the xylem, phloem, fibrous roots, and stems, and inhibited the biosynthesis of Re in the leaves. According to the time taken for a significant difference in the Re content to appear, the order of sensitivity to cold stress was xylem > stem > phloem > leaves > fibrous roots.

Change of Total Saponin Content

A comparison of the total saponin content in different ginseng tissues under cold stress treatment revealed that the total saponin content in the control tissues was ordered leaf > fibrous roots > phloem > stem > xylem, and cold stress increased the total saponin content in the xylem, phloem, fibrous roots, and stem (Figure 6). The total saponin content in the xylem was relatively low and did not change significantly across the flowering period. After cold stress treatment, the total saponin content in the xylem first increased and then decreased. It was higher than that in the control group throughout the flowering period, and reached its highest value on June 18, when it displayed a 143.5% increase. Gradual decreasing trends were exhibited by the phloem. The trend following cold treatment was



similar to that in the control group; however, the total saponin content was higher than that in the control group, with significant differences on June 18, 20, and 26.

The total saponin content in the fibrous roots and stems in the control groups exhibited gradual upward trends. After cold stress treatment, the total saponin content increased significantly followed by downward trends. The maximum values for the treated fibrous roots and stems were observed on June 18 (48.89 and 40.1% higher than the control values, respectively). The total saponin content in the control leaves was the highest of all the tissue samples, and there was no significant

change during the flowering period. The concentrations were lower than the control group under cold stress, with the minimum value observed on June 26, 44.3% lower than the control value. These results indicate that cold stress promoted the accumulation of saponins in the xylem and phloem and inhibited the accumulation of total saponins in the leaves. In addition, short-term cold stress promoted the accumulation of saponins in the fibrous roots and stems. The synthesis and accumulation of total saponins in different tissues in response to cold stress followed the order xylem > fibrous roots > leaf > stem > phloem.

TABLE 2 | Linear regression equations, correlation coefficients, and linearity ranges of 11 ginsenosides.

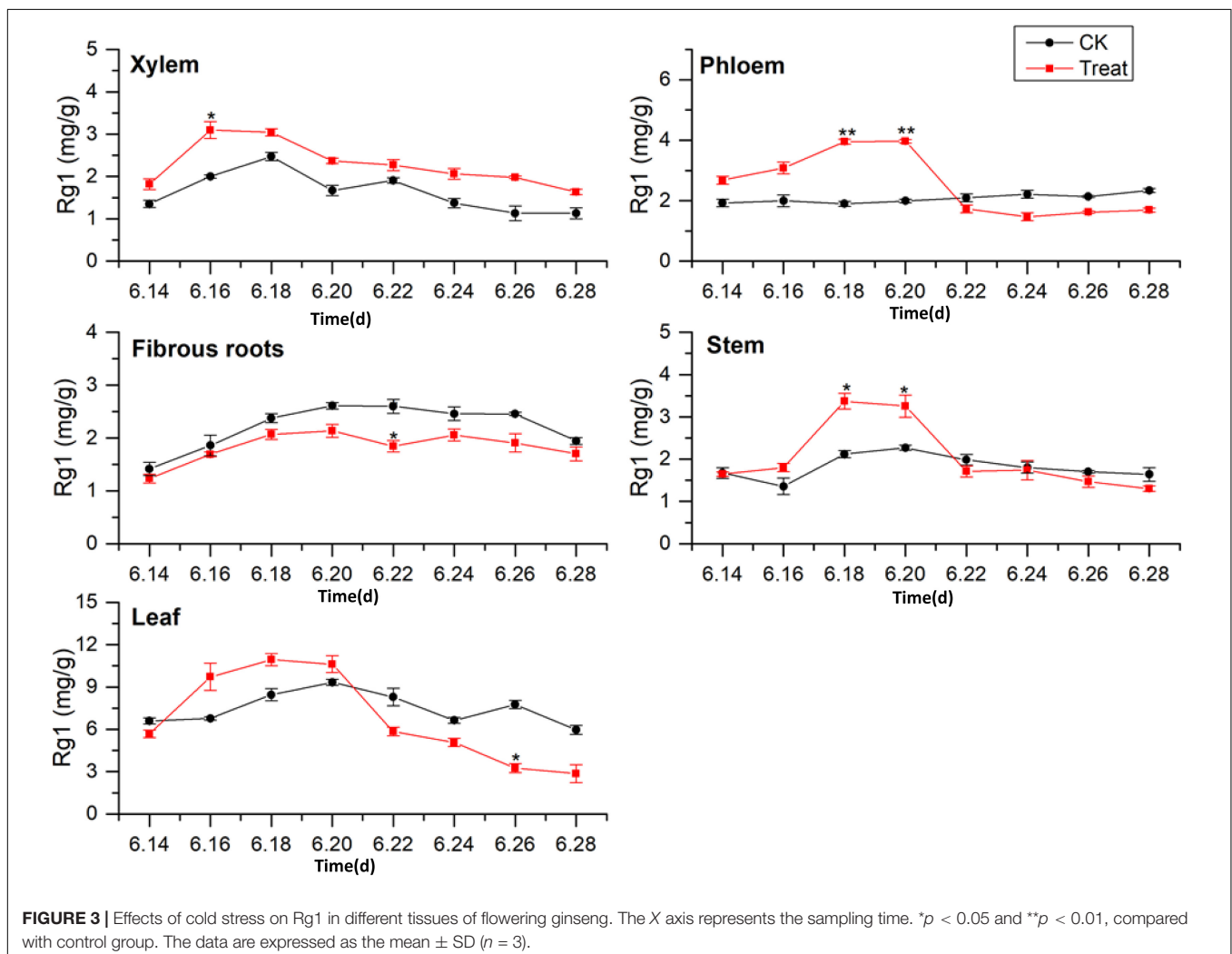
Ginsenosides	Regression Equation	R ²	Linear Range (μg/mL)
Ro	$y = 2796.01x - 40.64132$	0.99969	0.03–0.40
Rg1	$y = 3131.42x - 34.75556$	0.99943	0.01–0.35
Re	$y = 3097.80x - 35.99583$	0.99945	0.04–0.50
Rf	$y = 3614.44x - 32.36528$	0.99912	0.01–0.40
Rb1	$y = 2246.85x - 17.05278$	0.99989	0.01–0.20
Rc	$y = 2528.59x - 19.43056$	0.99985	0.03–0.40
Rb2	$y = 2668.61x - 36.21944$	0.99941	0.01–0.20
Rb3	$y = 3451.35x - 47.50556$	0.99932	0.01–0.20
Rd	$y = 3009.68x - 30.33472$	0.99967	0.02–0.30
Rh2	$y = 3813.16x - 23.14722$	0.99946	0.01–0.10
Rg3	$y = 4742.04x - 45.57500$	0.99955	0.01–0.30

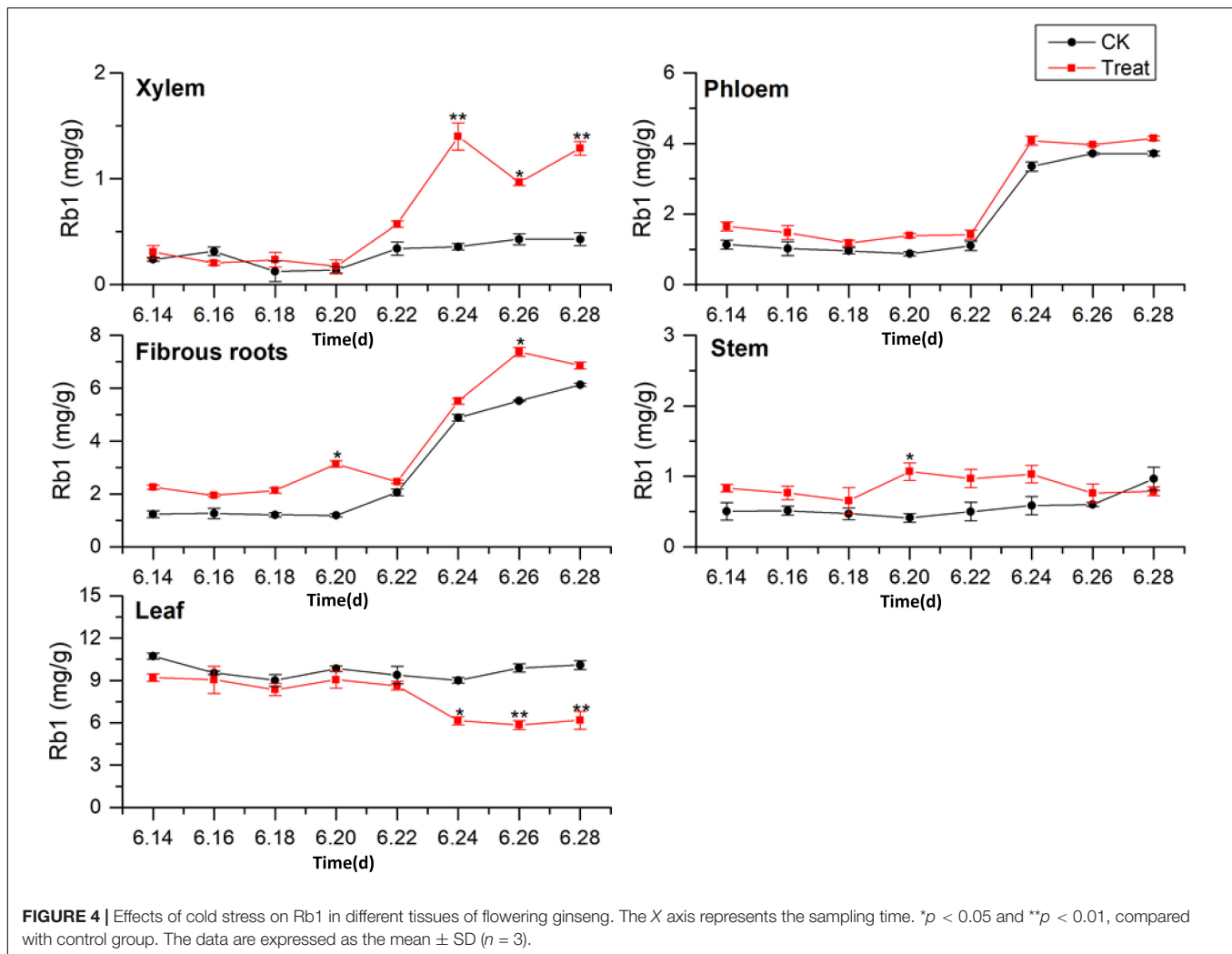
Change of PPD Content

Dammarane-type ginsenosides are divided into PPD- and PPT-type ginsenosides, according to their glycosyl groups. The effects

of cold stress on the accumulation of PPD-type ginsenosides (PPD = Rb1 + Rb2 + Rc + Rd + Rb3 + Rh2 + Rg3) in different ginseng tissues are illustrated in **Figure 7**. The PPD-type ginsenoside concentrations in the control groups followed the order leaf > fibrous roots > phloem > stem > xylem, similar to the total saponin content trends. The PPD ginsenoside content in the xylem was low. Under cold stress, the xylem PPD concentrations accumulated rapidly to the maximum value, which was observed on June 18 and was 123.8% higher than the value in the control group, but the effect was short-lived. The phloem PPD ginsenoside concentrations exhibited declining trends followed by rising trends. After cold stress treatment, the maximum values were observed on June 26, 23.6% higher than the levels in the control group.

The PPD ginsenoside concentrations in the control fibrous roots exhibited gradual increasing trends. After cold stress, the concentrations first increased and then decreased. The maximum values were observed on June 16, displaying a 52.5% increase compared to the levels in the control group. They then decreased to levels below the levels in the control group on June 20. The PPD ginsenoside concentrations in the control stems slowly





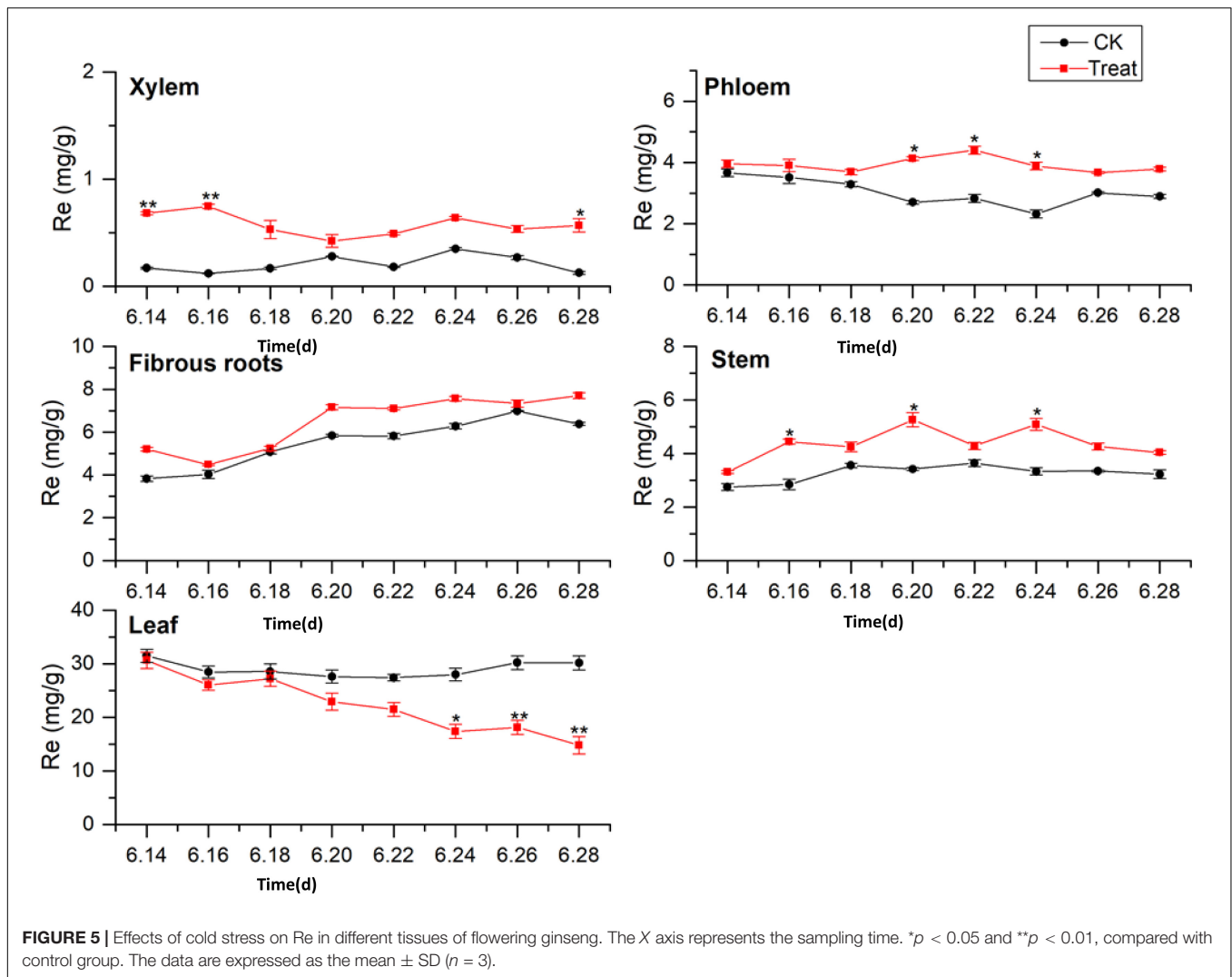
increased, then decreased, and finally rose rapidly. After cold stress treatment, they first increased and then decreased, with the minimum value observed on June 26, 50.6% lower than the level in the control group. The PPD ginsenoside content in the control leaves was the highest of all the tissue samples and remained relatively stable. After cold stress treatment, the content was lower than that in the control group, and reached a minimum on June 26, 33.6% lower than the content in the control group. These results indicate that cold stress promoted the accumulation of PPD ginsenosides in the xylem and phloem and inhibited their accumulation in the leaves, while short-term cold stress promoted PPD ginsenoside accumulation in the fibrous roots and stems. This is the same as the pattern shown by the total saponins responding to the cold treatment. The order of the PPD ginsenoside synthesis and accumulation rates in different tissues in response to cold stress was xylem > fibrous roots > stem > leaf > phloem.

Change of PPT Content

The effects of cold stress on the accumulation of PPT-type ginsenosides (PPT = Re + Rg1 + Rf) in different ginseng

tissues during flowering are illustrated in **Figure 8**. The PPT-type ginsenoside content of the different tissues was ordered leaf > fibrous roots > phloem > stem > xylem, which is similar to the accumulation patterns of the total saponins and PPD-type ginsenosides. The PPT-type ginsenoside content in the xylem was relatively low, first exhibiting a rising trend, followed by a gradual decrease. The PPT ginsenoside content of the treated xylem accumulated rapidly, reaching its the maximum value on June 18, when it displayed an increase of 125.2% compared with the content in the control group. The PPT ginsenoside content in the control phloem exhibited a gradual decreasing trend. After cold stress treatment, the PPT ginsenoside concentrations were similar to those of the control group; however, the variation was greater. The maximum values were observed on June 18 and were a 52.1% higher than the values in the control group.

The PPT ginsenoside concentrations in the fibrous roots exhibited a gradual upward trend. After cold stress treatment, there was accumulation over a relatively short period, with significant differences from the control group. The maximum value was observed on June 18, showing an increase of 37.1% when compared with the value in the control group. The



PPT-type ginsenoside concentration in the control stem did not change significantly during the flowering period. However, it first increased and then decreased following cold stress treatment. It reached its highest on June 22, representing a 59.4% increase when compared with the level in the control group. The levels decreased again on June 24.

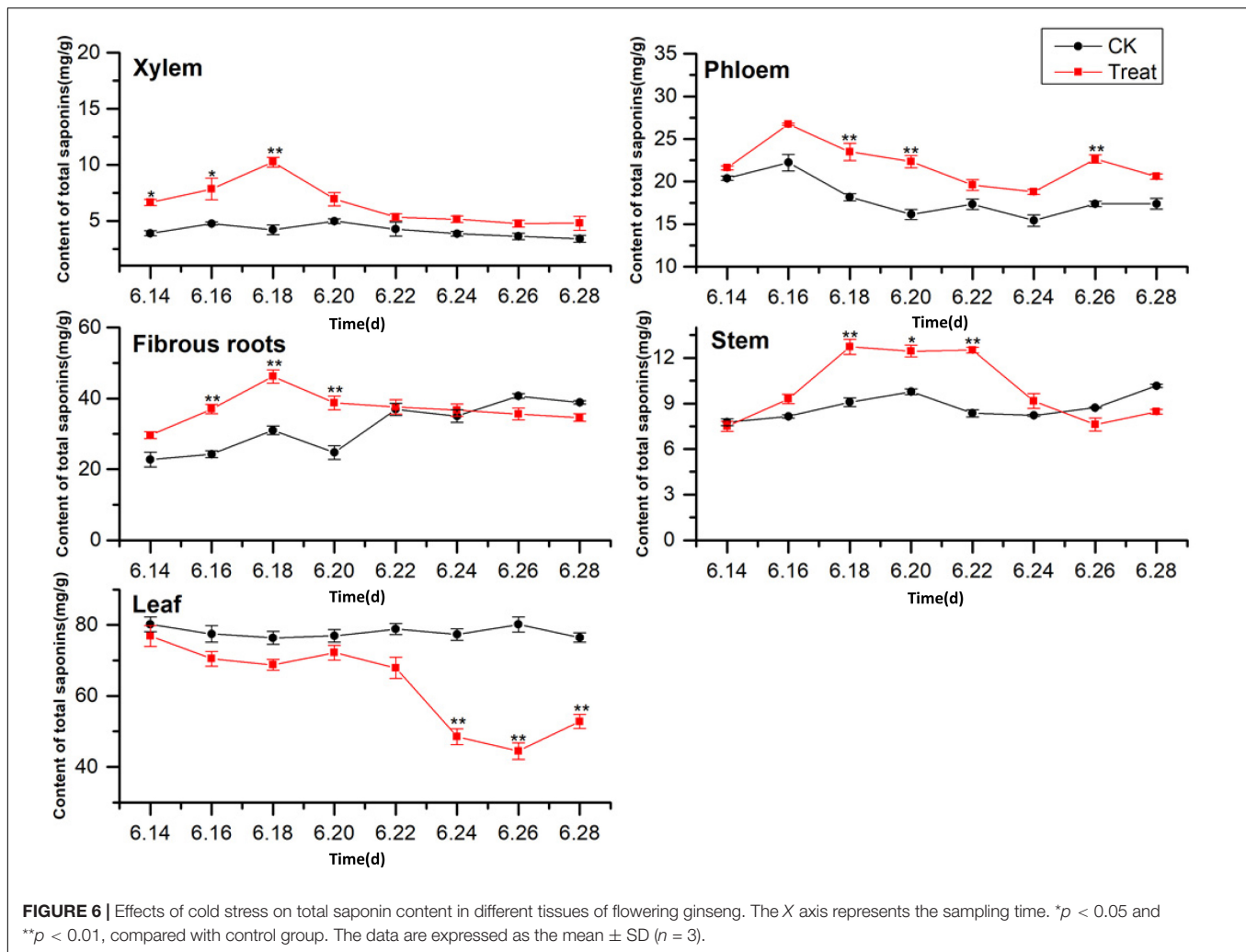
The PPT-type ginsenoside content in the control leaves was the highest of any of the tissue parts, with no significant changes observed during the flowering period. After cold stress treatment, the PPT-type ginsenoside content in the leaves decreased. It was lower than that in the control group throughout the flowering period, and was significantly lower on June 24, decreasing to its minimum value on June 26, 57.9% lower than the control value. These results indicate that low-temperature conditions promoted the accumulation of PPT-type ginsenosides in the xylem and phloem. Short-term low temperatures promoted PPT-type ginsenoside accumulation in the fibrous roots and stems, and low temperatures inhibited PPT-type ginsenoside accumulation in the leaves. The total saponin concentrations and PPD ginsenosides showed similar trends in response to

low temperatures. The synthesis and accumulation of PPT-type ginsenosides in the different tissues followed the order xylem > stem > leaf > phloem > fibrous roots.

Changes in PPD/PPT Values in Different Tissues Under Cold Stress

The PPD/PPT ratios were between 2.00–2.51 and 1.47–1.89 in the fibrous roots and phloem tissues, indicating that the accumulation of PPD-type ginsenoside in the fibrous roots and phloem is faster than that of PPT-type ginsenoside. In the xylem and leaves, the PPD/PPT ratio is slightly less than 1, indicating that the accumulation rates of the two configurations of saponins in the xylem and leaves are similar, while the PPD/PPT ratio in the xylem is between 0.21 and 0.48, indicating that the accumulation of PPT-type ginsenosides in the xylem exceeds that of PPD-type ginsenosides. This indicates that the biosynthesis of ginsenosides has obvious tissue specificity, which is consistent with the results of previous studies (Zhang et al., 2014, 2018).

The PPD/PPT ratio in each of the tissues examined changed following cold stress treatment. The PPD/PPT



ratio order of the treatment groups was fibrous roots > phloem > leaf > xylem > stem, which was slightly different from the order observed in the control groups (Table 3). The PPD/PPT ratio decreased in the xylem, phloem, and fibrous roots, indicating that the proportions of PPT ginsenosides increased in the xylem, phloem, and fibrous roots. Conversely, the PPD/PPT ratio increased in the leaves, indicating that the proportions of PPD ginsenosides increased in the leaves. In addition, the PPD/PPT ratio did not change significantly in the stem, potentially because it is involved in transduction but not in biosynthesis. The results indicate that, following cold stress treatment, the biosynthesis of PPT-type ginsenosides were promoted in the ginseng main roots (xylem and phloem) and fibrous roots, and PPD-type ginsenoside biosynthesis was promoted in the leaves.

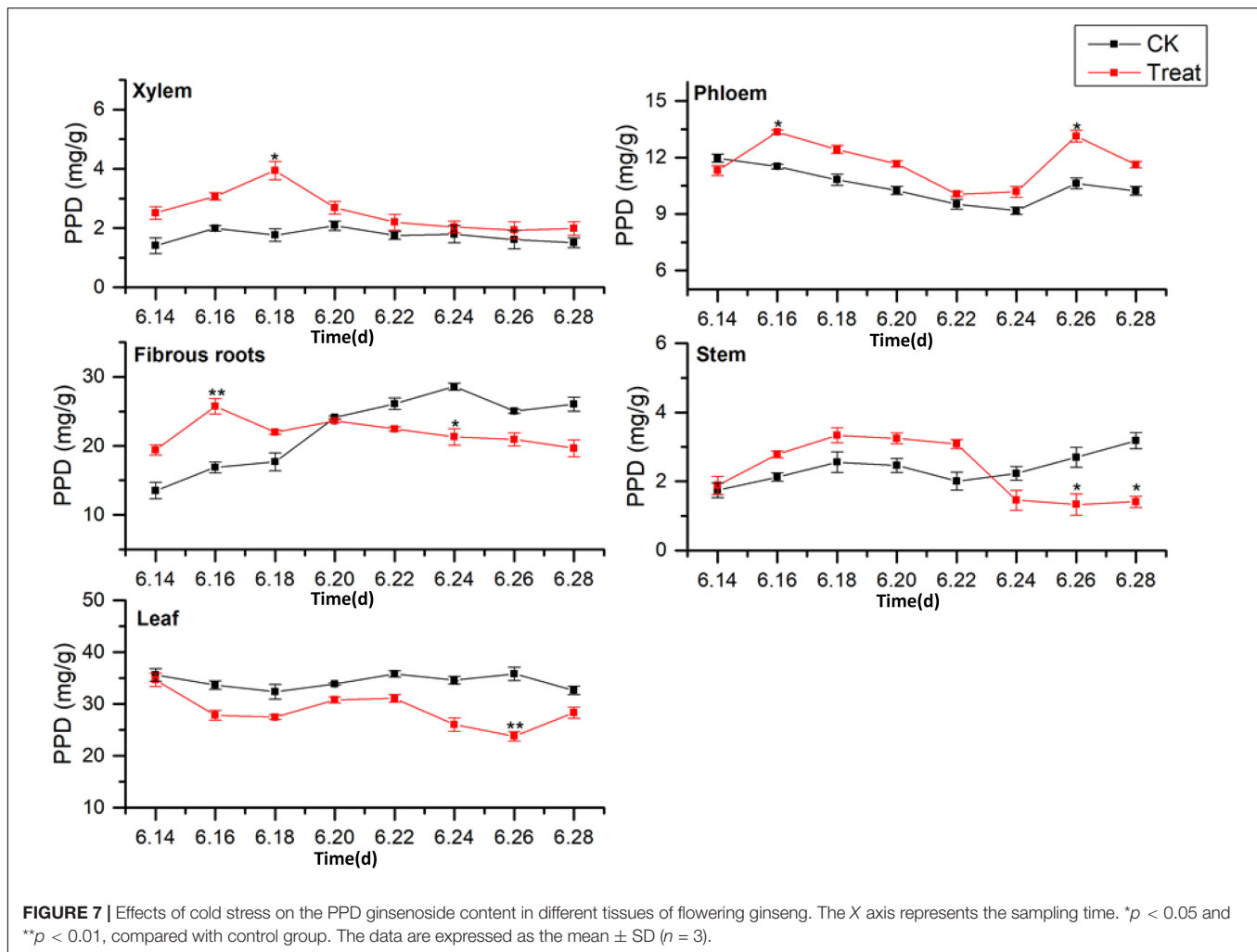
Change of Malondialdehyde and Osmoregulatory Substance Content Under Cold Stress

MDA is the final product of membrane lipid peroxidation, and its content increases when a plant is subjected to oxidative

stress. The concentrations of membranous peroxides and osmoregulatory substances following cold stress are shown in Figure 9. The MDA content increased rapidly and reached a peak on June 16, showing a significant increase of 134.6% compared with the MDA content in the control group ($p < 0.01$). The MDA content was maintained at levels higher than those in the control group throughout the treatment period. The Pro content peaked on June 28, showing a significant increase of 64.1% ($p < 0.05$) when compared to the levels in the control group. The highest SS content was observed on June 18, 39.7% higher than the level in the control group ($p < 0.05$). The effects on MDA, Pro, and SS were relatively obvious, while the effect on SP was less discernible, indicating that different osmotic substances have different functions in low-temperature regulation. There were also differences in the timing of activity.

Change of Antioxidant Enzyme Activity Under Cold Stress

The effects of cold stress on antioxidant enzyme activity in the leaf are illustrated in Figure 10. Under cold stress, antioxidant enzyme activity, including SOD, POD, and CAT



activity, increased initially and then decreased. SOD and POD responded rapidly to cold stress. Their maximum values were observed on June 18 and 16, respectively, and their activities were significantly higher (by 18.1 and 117.2%, respectively) than the levels in the control groups ($p < 0.01$). With the extension of the cold stress treatment period, the SOD and POD activities decreased gradually. The highest CAT activity was observed on June 20; it was significantly higher—41.1%—than the level in the control group ($p < 0.01$). With the prolongation of cold stress treatment, the CAT activity decreased gradually.

Analysis of Key Enzymes Expression Under Cold Stress

The effects of cold stress on the expression of key enzyme genes associated with ginsenoside synthesis in the flowering stage are illustrated in **Figure 11**. *HMRG2*, *FPS*, *SS1*, *DS-II*, *CYP716A53v2*, and *CYP716A47* increased gradually in the control, and first increased and then decreased under low-temperature conditions. After cold stress treatment the *DS-II*, *CYP716A53v2*, and *CYP716A47* expressions reached their highest levels on June 18, and then decreased gradually. The

maximum expression values were 4.8-, 3.9-, and 2.63-fold higher than the levels in the control group. The maximum level of *FPS* expression was recorded on June 20, and was 2.3-fold the level in the control group. The maximum level of *SS1* expression was observed on June 22, and was 1.9-fold the level in the control group. In addition, the maximum level of *HMRG2* expression was observed on June 24, and was 1.5-fold the level in the control group. These results indicate that different genes are expressed at different periods under cold stress treatment, with varying response times. In general, the levels of expression of key enzymes related to ginsenoside biosynthesis increased under short-term cold stress; however, under long-term cold stress, these gene expression levels decreased. Therefore, the secondary metabolic processes in pharmaceutical plants are influenced considerably at the transcriptional level by changes in temperature.

Correlations Between Physiological Stress Indicators and Ginsenoside Content

Total ginsenoside content was significantly correlated with PPT-type ginsenosides and Re ($p < 0.01$), as well as with

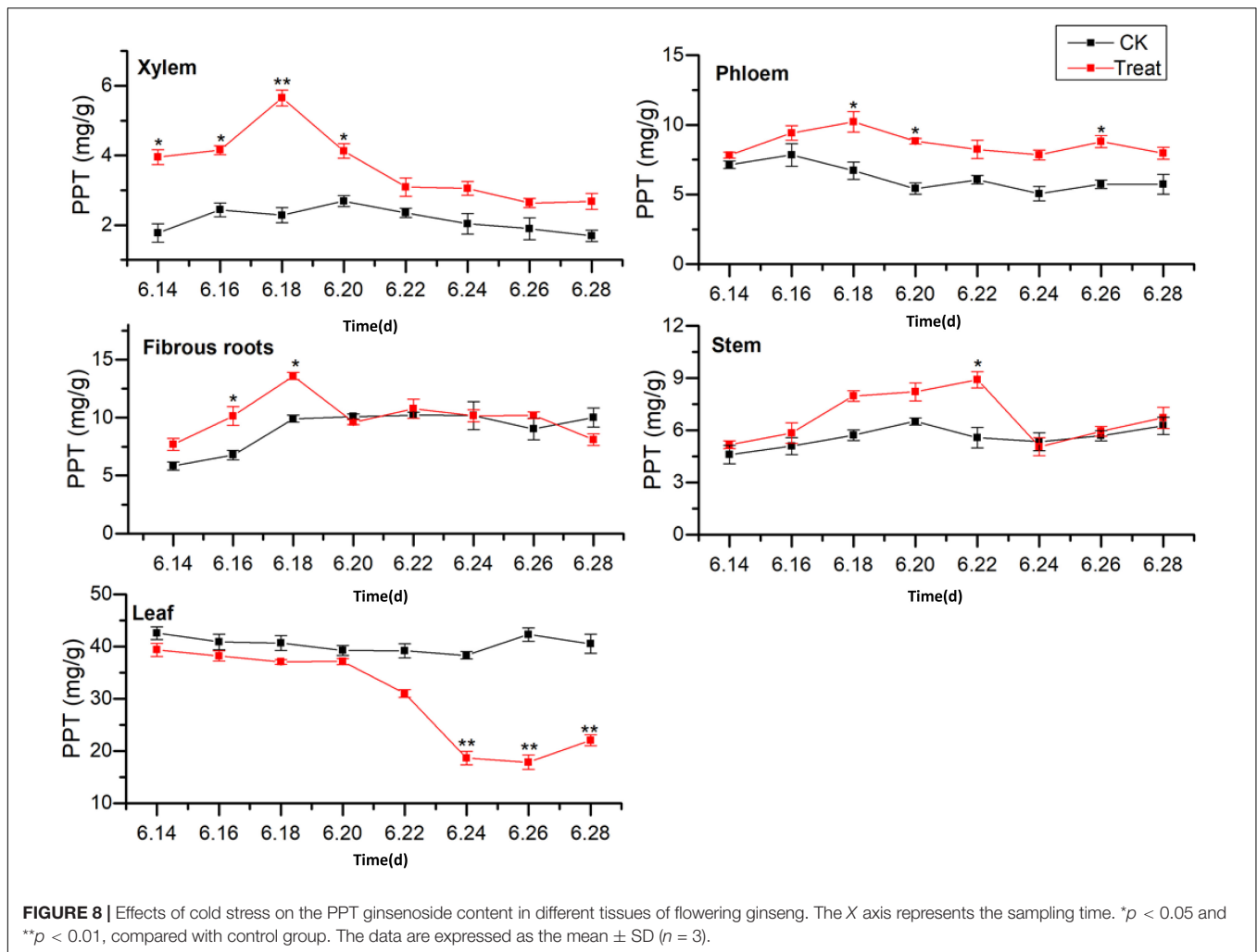
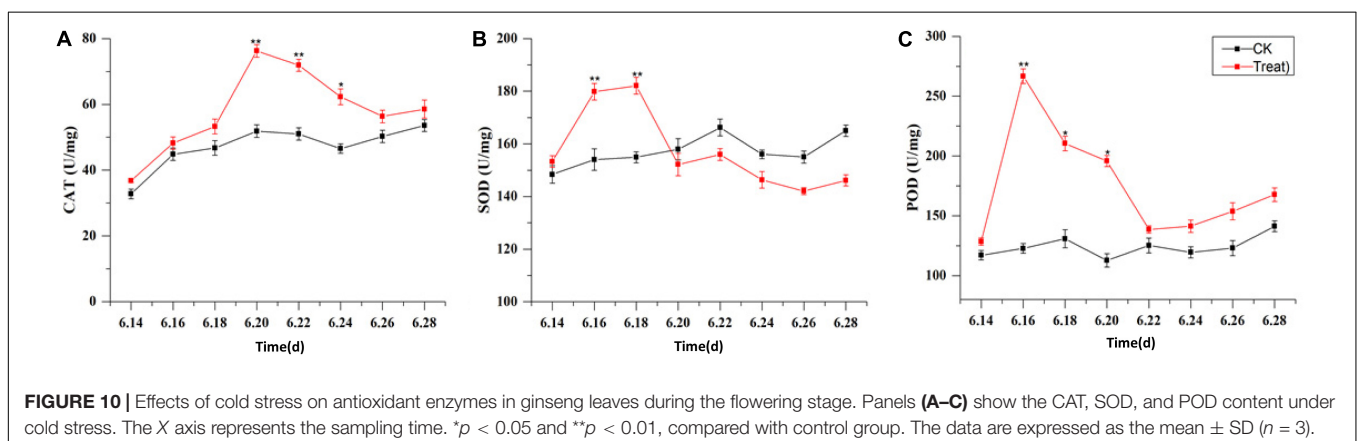
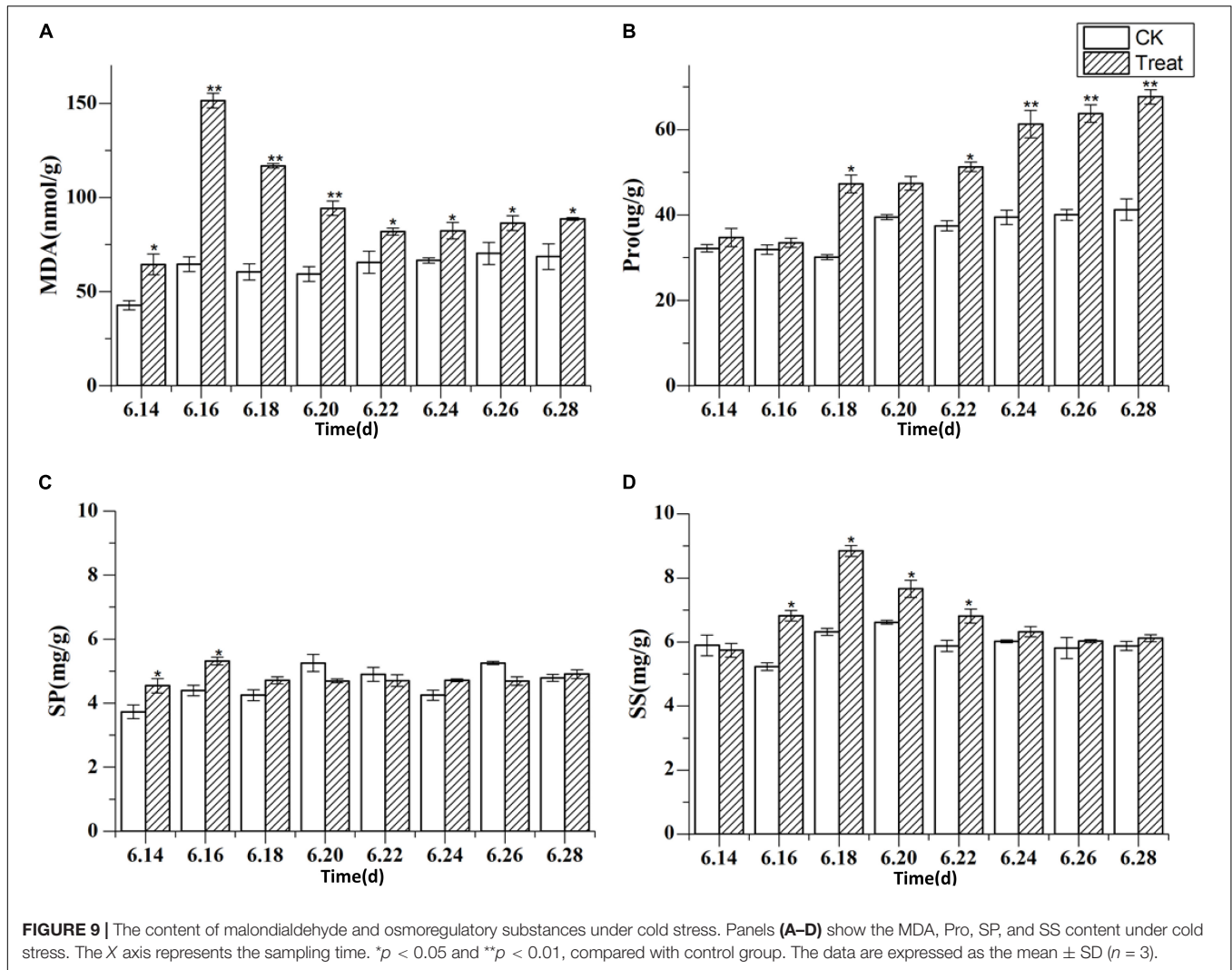


TABLE 3 | PPD/PPT ginsenoside content ratios in different ginseng tissues under cold stress during the flowering stage.

Date	Xylem		Phloem		Fibrous roots		Stem		Leaf	
	CK	Treatment	CK	Treatment	CK	Treatment	CK	Treatment	CK	Treatment
6.14	0.79	0.64	1.67	1.45	2.47	1.84	0.38	0.36	0.84	0.88
6.16	0.82	0.74	1.47	1.42	2.51	1.85	0.42	0.48	0.82	0.73
6.18	0.77	0.70	1.61	1.22	2.00	1.86	0.45	0.42	0.80	0.74
6.20	0.77	0.65	1.89	1.32	2.19	1.77	0.38	0.40	0.86	0.88
6.22	0.74	0.71	1.57	1.22	2.06	1.80	0.36	0.35	0.91	1.00
6.24	0.88	0.67	1.81	1.30	2.20	1.70	0.42	0.29	0.90	1.40
6.26	0.85	0.73	1.85	1.49	2.12	1.72	0.47	0.22	0.85	1.33
6.28	0.89	0.74	1.78	1.46	2.00	1.72	0.51	0.21	0.81	1.29

Rg1 and Rb1 ($p < 0.05$) (Table 4). Rg1 was significantly correlated with SE ($p < 0.01$) and with DS-II, CYP716A52v2, and CYP716A53v2 ($p < 0.05$). In addition, Pro activity was significantly correlated with total ginsenoside, PPT-type ginsenoside, Re, and Rb1 ($p < 0.01$). Other physiological stress indicators were correlated with ginsenoside content; however, the correlations were not significant. In contrast, there were significant correlations between the expression

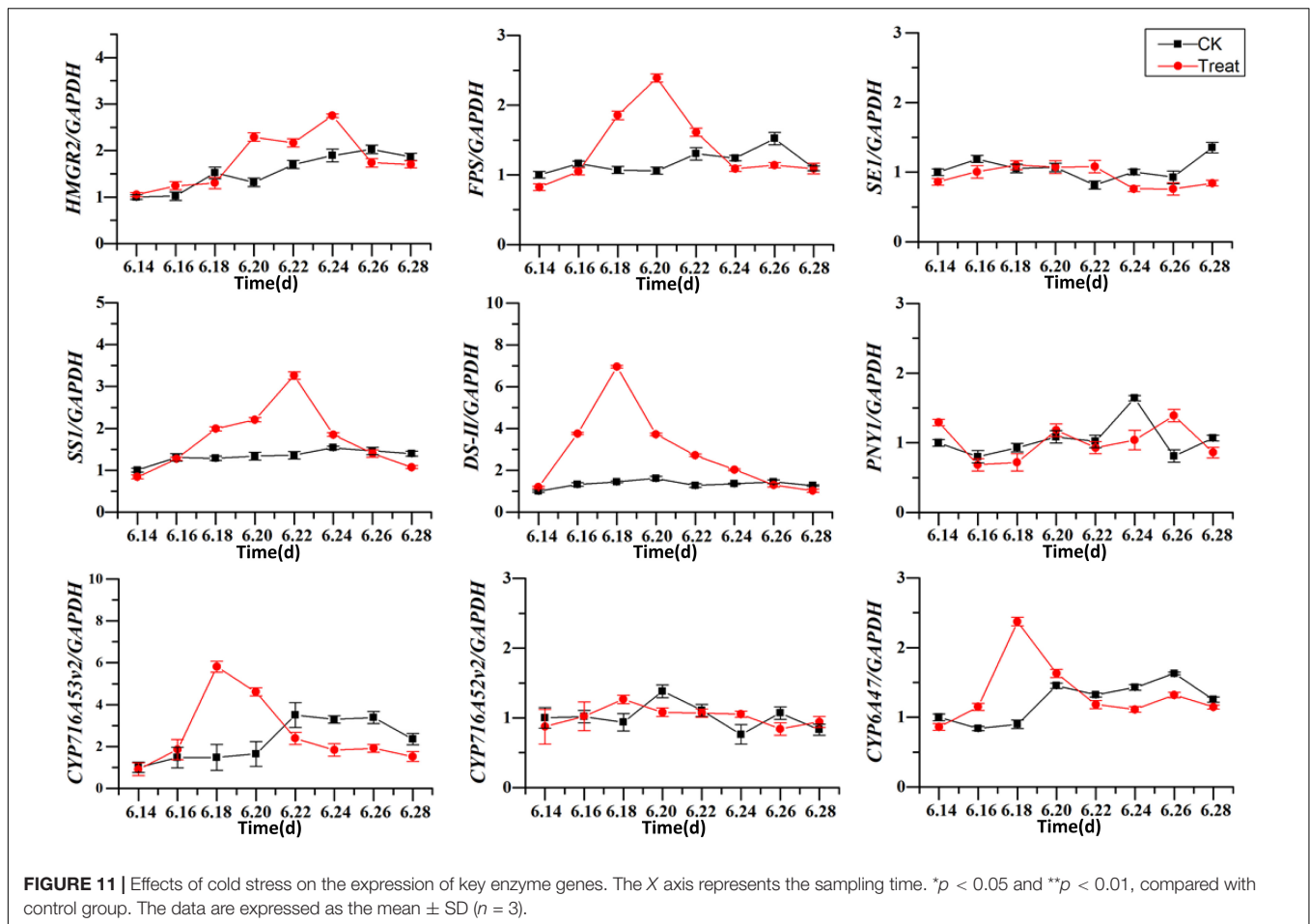
levels of key enzymes in the synthesis pathway, antioxidant enzyme activity, and osmotic regulators. The results potentially indicated that antioxidant enzyme activities, osmoregulatory substances, and key enzyme gene expressions were jointly participated in ginseng resistance to cold stress. In addition, SE, DS-II, CYP716A52v2, CYP716A53v2, and Pro are potential cold stress response-related endogenous signaling molecules in ginseng.



DISCUSSION

The main active components of medicinal plants, such as the perennial herb *P. ginseng*, are secondary metabolites. Ginsenosides are the key bioactive compounds in ginseng and have diverse pharmacological applications. Ginsenoside

concentrations are key criteria for evaluating the quality of ginseng medicinal materials (Kim et al., 2017). Both genetic and environmental factors influence ginsenoside biosynthesis, and appropriate cold stress levels could promote the accumulation of ginsenosides (Zhang et al., 2018). Cold stress is known to affect the growth and metabolism of plants (Jiang et al., 2016).



In this study, short-term cold stress had no obvious effects on the dry or fresh weight of ginseng roots, while long-term cold stress significantly inhibited the accumulation of root dry and fresh weight.

The metabolic systems for scavenging ROS in plants are unbalanced under abiotic stress conditions, leading to the accumulation of ROS, which damages the plant membrane system. SOD, POD, and CAT are key components of the non-enzymatic antioxidant system in plants, and they can convert O_2^- into H_2O (Masood et al., 2006; Mhadhbi et al., 2011; Liu et al., 2016). Cold stress could promote the activities of SOD, POD, and CAT to a certain degree. In the present study, these three enzymes displayed higher activities when exposed to short-term cold stress, to help keep the plant functioning normally. This is consistent with previously published studies (Kaur et al., 2009). These three enzymes had the same response to cold stress, but the rates at which their enzyme activity increased, and the timing of their peak activity, differed. Under cold stress, the synergy of the different enzymes is needed to jointly combat oxidative damage in the plant. However, under long-term cold stress, the activities of the three enzymes were significantly reduced, probably because the ROS content exceeded the capacity of the antioxidant enzyme system of the plant. Thus, the antioxidant enzyme system could not prevent the damage caused by cold stress (Balestrasse et al., 2010).

MDA content is an indicator of the degree of lipid peroxidation in the cell membrane and can directly reflect the degree of cell membrane damage. In the present study, the MDA content increased under cold stress and peaked under short-term cold stress. It indicated that membrane lipid peroxidation increased under cold stress. The response times of the antioxidant enzymes were longer than that of MDA, indicating that plants can transmit signals to the antioxidant enzyme system by accumulating MDA, thereby stimulating the protective functions of the system. Osmoregulation is a critical physiological mechanism that facilitates plant adaptation to environmental stress. By adjusting the concentrations of osmoregulatory substances within the cells, plants can maintain cell turgor pressure and normal physiological processes. In the present study, the Pro, SS, and SP content increased during cold stress; the Pro content increased gradually as the duration of cold stress increased, which is consistent with observations made in a previous study. When *P. ginseng* was subjected to cold stress, the concentrations of osmoregulatory substances in the cells increased to facilitate the maintenance of osmotic balance in the plants (Lo' Ay and Elkhateeb, 2018).

HMGR2, *FPS*, *SS1*, *SE1*, *DS-II*, *PNY1*, *CYP716A52v2*, *CYP716A53v2*, and *CYP716A47* are the key genes that participate in the ginsenoside biosynthesis pathway, and their expression products are the corresponding enzymes. However, their high

TABLE 4 | Correlation analysis among ginsenosides, physiological stress indicators, and secondary metabolism in plants under cold stress.

	Total	PPD	PPT	Rg1	Re	Rb1	HMGR2	FPS	SS1	SE	DS-II	AS	52	53	47	CAT	SOD	POD	Pro	MDA	SS	SP
Total	1	0.34	0.93**	0.77*	0.91**	0.74*	-0.49	0.24	0.52	0.54	0.57	-0.09	0.37	0.49	0.40	-0.35	0.70*	0.26	-0.86**	0.42	0.52	0.04
PPD		1	0.34	-0.21	0.58	0.37	-0.48	-0.57	0.06	-0.07	0.13	0.14	-0.27	-0.29	-0.37	-0.63	0.18	-0.06	-0.52	-0.16	-0.33	-0.14
PPT			1	0.76*	0.94**	0.88**	-0.51	0.13	0.52	0.67	0.56	-0.20	0.37	0.51	0.26	-0.30	0.71*	0.28	-0.95**	0.39	0.47	0.11
Rg1				1	0.55	0.66	-0.12	0.66	0.69	0.81**	0.71*	-0.47	0.77*	0.77*	0.67	0.17	0.78*	0.39	-0.59	0.66	0.86**	0.27
Re					1	0.78*	-0.65	-0.02	0.41	0.49	0.45	-0.07	0.23	0.24	0.19	-0.53	0.64	0.13	-0.93**	0.22	0.32	-0.06
Rb1						1	-0.23	0.10	0.36	0.78*	0.41	-0.13	0.36	0.47	0.13	0.04	0.52	0.10	-0.84**	0.20	0.40	-0.01
HMGR2							1	0.18	-0.47	-0.15	-0.44	0.17	0.16	-0.04	-0.08	0.81**	-0.53	-0.37	0.56	-0.32	-0.04	-0.24
FPS								1	0.38	0.58	0.32	-0.32	0.79*	0.35	0.95**	0.50	0.39	-0.02	0.15	0.34	0.91**	-0.07
SS1									1	0.61	0.99**	-0.80*	0.56	0.70	0.48	-0.19	0.94**	0.79*	-0.49	0.93**	0.60	0.71*
SE										1	0.60	-0.52	0.73*	0.58	0.57	0.32	0.69	0.21	-0.52	0.44	0.79*	0.15
DS-II											1	-0.77*	0.55	0.73	0.41	-0.21	0.94**	0.80*	-0.56	0.93**	0.57	0.71*
AS												1	-0.66	-0.45	-0.35	0.00	-0.75*	-0.60	0.18	-0.72*	-0.51	-0.66
52													1	0.38	0.78*	0.35	0.66	0.08	-0.17	0.43	0.92**	0.05
53														1	0.26	0.23	0.59	0.77*	-0.48	0.84**	0.47	0.70
47															1	0.22	0.54	-0.01	0.01	0.37	0.93	-0.11
CAT																1	-0.29	-0.24	0.45	-0.10	0.30	-0.12
SOD																	1	0.61	-0.65	0.80*	0.69	0.49
POD																		1	-0.38	0.92**	0.12	0.97**
Pro																			1	-0.38	-0.22	-0.22
MDA																				1	0.49	0.85**
SS																					1	0.03
SP																						1

Total: total saponin; HMGR: HMGR2; 52: CYP716A52v2; 53: CYP716A53v2; 47: CYP716A47.

SOD, superoxide dismutase; POD, peroxidase; CAT, catalase; MDA, malondialdehyde; Pro, proline; SS, soluble sugar; SP, soluble protein.

* $p < 0.05$, ** $p < 0.01$.

expression does not always indicate higher enzyme activity (Wang et al., 2012; Yang et al., 2018). In the present study, cold stress influenced the expression of the key genes of enzymes required for ginsenoside biosynthesis. The expression of *HMRG2*, *FPS*, *SSI*, *DS-II*, *CYP716A53v2*, and *CYP716A47* under short-term cold stress was significantly higher than in the control groups; however, under long-term cold stress, gene expression was reduced significantly, which is consistent with the findings of previous studies. This demonstrates that the key enzymes needed for ginsenosides biosynthesis first respond to cold stress at the transcriptional level and this, in turn, influences the biosynthesis and accumulation of ginsenosides.

When plants are exposed to cold stress, they can tolerate changes in the external environment by rapidly synthesizing secondary metabolites as a defense system (Cheng et al., 2018). Ginsenoside content is a key index for evaluating the quality of ginseng medicinal materials. Appropriate cold stress is conducive to the accumulation of ginsenosides. In the present study, ginsenoside content increased under short-term cold stress; however, the increase was inhibited significantly under long-term cold stress. Ginseng leaves are extremely sensitive to cold stress. This seriously inhibits ginsenoside biosynthesis in the leaves, causing the total saponin content in the leaves to drop sharply (Oh et al., 2014; You et al., 2015). The ginsenosides could be transferred to other tissues for storage via the xylem and phloem, since the saponins in the fibrous roots and stems increased by varying degrees under cold stress. This result is the same as that reported by Kim et al. (2014).

Recently, the relationship between active compositions and their bioactivities has attracted the attention of researchers. Previous study suggested that the composition of active ingredients is extremely important for the biological activity of ginseng (Shan et al., 2014). In addition, the PPD/PPT ratio is considered the key factor in determining the different biological activities of ginseng (Cho et al., 2017). PPD- and PPT-type ginsenosides play different roles in certain biological activities, and their compositional differences in ginseng are also a primary factor affecting the quality of the herb (Qu et al., 2009). Only when the PPD/PPT ratio in ginseng samples is within the optimal range can the quality of the ginseng medicinal materials be best reflected and its best medicinal value extracted. In this study, the PPD/PPT ratio in the xylem, phloem, and fibrous roots decreased under cold stress, and the proportion of PPT-type ginsenosides in the xylem, phloem, and fibrous roots increased. In contrast, the PPD/PPT ratio in the leaves increased. It indicates that cold stress promoted the biosynthesis of PPT-type ginsenosides in the main roots (xylem and phloem) and fibrous roots, as well as promoted the biosynthesis of PPD-type ginsenosides in the leaves. These results are consistent with the results of other studies on the accumulation of secondary metabolites in medicinal plants under cold stress (Klára et al., 2012; Dong et al., 2014; Carvajal et al., 2018; Rezaie et al., 2020).

Cold stress can influence secondary metabolic processes. For example, under certain temperatures, ginseng increases the activities of protective enzymes and the amounts of osmoprotective compounds to protect cells from oxidative stress. This enhances the biosynthesis of ginsenosides via the expression of key enzymes in the biosynthetic pathway

and enhances secondary metabolite accumulation, in turn increasing the concentrations of certain ginsenosides. In the present study, the ginsenoside concentrations were significantly positively correlated with *SE* ($p < 0.01$), *DS-II*, *CYP716A52v2*, and *CYP716A53v2* ($p < 0.05$). In addition, the ginsenoside and Pro concentrations were significantly negatively correlated ($p < 0.05$). Antioxidant enzymes can promote or inhibit the expression and activities of key enzymes involved in ginsenoside secondary metabolism and influence the accumulation of ginsenosides. Therefore, *SE*, *DS-II*, *CYP716A52v2*, and *CYP716A53v2* could be the important candidate genes for ginsenoside biosynthesis in response to cold stress, and Pro could be exploited as an endogenous signaling molecule involved in ginseng responses to cold stress.

CONCLUSION

According to the findings of the present study, under cold stress, *P. ginseng* activates its antioxidant enzyme system and accumulates osmoregulatory substances; however, cold stress also reduces the yield of *P. ginseng*. Short-term cold stress could promote the biosynthesis of ginsenosides significantly, and long-term cold stress could inhibit the biosynthesis of ginsenosides. In addition, short-term cold stress promoted PPT-type ginsenoside accumulation in the main roots (phloem and xylem) and fibrous roots, and PPD-type ginsenoside accumulation in the leaves. Furthermore, cold stress led to shifts in the PPD/PPT ratios in different tissues. Therefore, during the cultivation of *P. ginseng*, areas with lower average annual temperatures should be selected to facilitate the establishment of a balance between yield and quality. In industrial production processes, PPD/PPT ratios could be adjusted by low-temperature storage. The results of the present study could facilitate the exploitation of *P. ginseng* as a medicinal resource, through the manipulation of the concentrations of ginsenosides in different tissues, according to specific applications and requirements.

DATA AVAILABILITY STATEMENT

The original contributions presented in the study are included in the article/supplementary material, further inquiries can be directed to the corresponding author/s.

AUTHOR CONTRIBUTIONS

TZ and WQ conceived and designed the experiments. TZ performed most of the experiments, analyzed the data, and completed the first draft. CC, YC, QZ, and QL worked together with TZ to accomplish the experiments. All authors read and approved the manuscript.

FUNDING

This work was financially supported by the Major Science and Technology Project of Jilin Province, China (20200504003YY),

the National Natural Science Foundation of China (82073969), the Natural Science Foundation of Jilin Province (202101ZYTS012), and the Jilin Province Traditional Chinese Medicine Science and Technology Project (2020042).

REFERENCES

- Ba, Q. S., Zhang, G. S., Wang, J. S., Che, H. X., Liu, H. Z., Niu, N., et al. (2013). Relationship between metabolism of reactive oxygen species and chemically induced male sterility in wheat (*Triticum aestivum* L.). *Can. J. Plant Sci.* 93, 675–681. doi: 10.4141/cjps2012-280
- Balestrasse, K. B., Tomaro, M. L., Batlle, A., and Noriega, G. O. (2010). The role of 5-aminolevulinic acid in the response to cold stress in soybean plants. *Phytochemistry* 71, 2038–2045. doi: 10.1016/j.phytochem.2010.07.012
- Carvajal, F., Rosales, R., Palma, F., Manzano, S., Cañizares, J., Jamilena, M., et al. (2018). Transcriptomic changes in *Cucurbita pepo* fruit after cold storage differential response between two cultivars contrasting in chilling sensitivity. *BMC Genom.* 9:125. doi: 10.1186/s12864-018-4500-4509
- Chao, Z. (2006). Pharmacokinetic study of ginsenosides Rb1 and Rg1 in Rat by ELISA using anti-ginsenosides Rb1 and Rg1 monoclonal antibodies. *Am. J. Chin. Med.* 6, 1069–1081. doi: 10.1142/s0192415x06004533
- Cheng, L., Han, M., Yang, L., Yang, L., Sun, Z., and Zhang, T. (2018). Changes in the physiological characteristics and baicalin biosynthesis metabolism of *Scutellaria baicalensis* georgi under drought stress. *Ind. Crops Products* 122, 473–482. doi: 10.1016/j.indcrop.2018.06.030
- Cho, H. T., Kim, J. H., Lee, J. H., and Kim, Y. J. (2017). Effects of Panax ginseng extracts prepared at different steaming times on thermogenesis in rats. *J. Ginseng Res.* 41, 347–352. doi: 10.1016/j.jgr.2016.07.001
- Christensen, L. P. (2009). Ginsenosides chemistry, biosynthesis, analysis, and potential health effects. *Adv. Food Nutr. Res.* 55, 1–99. doi: 10.1016/S1043-4526(08)00401-404
- Dong, C. J., Li, L., Shang, Q. M., Liu, X. Y., and Zhang, Z. G. (2014). Endogenous salicylic acid accumulation is required for chilling tolerance in cucumber (*Cucumis sativus* L.) seedlings. *Planta* 240, 687–700. doi: 10.1007/s00425-014-2115-2111
- Guo, S., Yang, L., Zhang, Y., Yang, L., and Han, M. (2015). Analysis of microwave-assisted extraction of total saponins and ginsenosides in ginseng. *Food Sci.* 36, 1–6. doi: 10.7506/spkx1002-6630-201502001
- Han, J., In, J., Kwon, Y., and Choi, Y. (2010). Regulation of ginsenoside and phytosterol biosynthesis by RNA interferences of squalene epoxidase gene in Panax ginseng. *Phytochemistry* 71, 36–46. doi: 10.1016/j.phytochem.2009.09.031
- In-Ah, L., Hyam, S. R., Se-Eun, J., Myung Joo, H., and Dong-Hyun, K. (2012). Ginsenoside Re ameliorates inflammation by inhibiting the binding of lipopolysaccharide to TLR4 on macrophages. *J. Agric. Food Chem.* 60, 9595–9602. doi: 10.1021/jf301372g
- Jiang, M., Liu, J., Quan, X., Quan, L., and Wu, S. (2016). Different chilling stresses stimulated the accumulation of different types of ginsenosides in Panax ginseng cells. *Acta Physiol. Plant* 210, 1–8. doi: 10.1007/s11738-016-2210-y
- Kaur, S., Gupta, K., Kaur, N., Sandhu, J. S., and Gupta, S. K. (2009). Antioxidative enzymes and sucrose synthase contribute to cold stress tolerance in chickpea. *J. Agronomy Crop Sci.* 195, 393–397. doi: 10.1111/j.1439-037X.2009.00383.x
- Kim, D. S., Song, M., Kim, S. H., Jang, D. S., Kim, J. B., Ha, B. K., et al. (2013). The improvement of ginsenoside accumulation in *Panax ginseng* as a result of gamma-irradiation. *J. Ginseng Res.* 37, 332–340. doi: 10.5142/jgr.2013.37.332
- Kim, J. H., Yi, Y. S., Kim, M. Y., and Cho, J. Y. (2017). Role of ginsenosides, the main active components of *Panax ginseng*, in inflammatory responses and diseases. *J. Ginseng Res.* 41, 435–443. doi: 10.1016/j.jgr.2016.08.004
- Kim, Y., Jeon, J., Jang, M., Oh, J. Y., Kwon, W., Jung, S., et al. (2014). Ginsenoside profiles and related gene expression during foliation in *Panax ginseng* meyer. *J. Ginseng Res.* 38, 66–72. doi: 10.1016/j.jgr.2013.11.001
- Kim, Y., Zhang, D., and Yang, D. (2015). Biosynthesis and biotechnological production of ginsenosides. *Biotechnol. Adv.* 33, 717–735. doi: 10.1016/j.biotechadv.2015.03.001
- Klára, K., Ilja Tom, P. I., Pavel, V., Petre, D., Václav, M., Kristyna, F., et al. (2012). Complex phytohormone responses during the cold acclimation of two wheat cultivars differing in cold tolerance, winter Samanta and spring Sandra. *J. Plant Physiol.* 169, 567–576. doi: 10.1016/j.jplph.2011.12.013
- Kuang, L., Li, C., Cao, S., Li, H., Wang, Z., Wu, S., et al. (2020). *Pharmacopoeia of People's Republic of China*. Beijing: China Medical Science and Technology Press.
- Leung, K. W., and Wong, S. T. (2010). Pharmacology of ginsenosides: a literature review. *Chinese Med.* 5:20. doi: 10.1186/1749-8546-5-20
- Li, Y., Zhang, T., Liu, S., and Chen, C. (2009). Research progress of ginseng chemical composition and pharmacology. *Chinese Trad. Herbal Drugs* 40, 164–166. doi: 10.3321/j.issn:0253-2670.2009.01.049
- Lian-Wen, Q., Chong-Zhi, W., and Chun-Su, Y. (2011). Ginsenosides from American ginseng: chemical and pharmacological diversity. *Phytochemistry* 72, 689–699. doi: 10.1016/j.phytochem.2011.02.012
- Liu, Z., Sun, W., Zhao, Y., and Li, X. (2016). Effects of low nocturnal temperature on photosynthetic characteristics and chloroplast ultrastructure of winter rapeseed. *Russian J. Plant Physiol.* 4, 451–460. doi: 10.1134/s1021443716040099
- Liu, Z. Q. (2012). Chemical insights into ginseng as a resource for natural antioxidants. *Chem. Rev.* 112:3329. doi: 10.1021/cr100174k
- Lo'ay, A. A., and Elkhateeb, A. Y. (2018). Antioxidant enzyme activities and exogenous ascorbic acid treatment of 'Williams' banana during long-term cold storage stress. *Sci. Horticult.* 234, 210–219. doi: 10.1016/j.scienta.2018.02.038
- Lukatkin, A. S., Brazaityte, A., Bobinas, E., and Duchovskis, P. (2012). Chilling injury in chilling-sensitive plants: a review. *Zemdirbyste-agriculture* 99, 111–124. doi: 10.3906/tar-1112-1144
- Masood, A., Shah, N. A., Zeeshan, M., and Abraham, G. (2006). Differential response of antioxidant enzymes to salinity stress in two varieties of Azolla (*Azolla pinnata* and *Azolla filiculoides*). *Environ. Exp. Botany* 58, 216–222. doi: 10.1016/j.envexpbot.2005.08.002
- Mhadhbi, H., Fotopoulos, V., Mylona, P. V., Jebara, M., Elarbi, A. M., and Polidoros, A. N. (2011). Antioxidant gene-enzyme responses in *Medicago truncatula* genotypes with different degree of sensitivity to salinity. *Physiol. Plant* 141, 201–214. doi: 10.1111/j.1399-3054.2010.01433.x
- Oh, J. Y., Kim, Y., Jang, M., Joo, S. C., Kwon, W., Kim, S., et al. (2014). Investigation of ginsenosides in different tissues after elicitor treatment in Panax ginseng. *J. Ginseng Res.* 38, 270–277. doi: 10.1016/j.jgr.2014.04.004
- Ohyama, K., Suzuki, M., Masuda, K., Yoshida, S., and Muranaka, T. (2007). Chemical phenotypes of the hmg1 and hmg2 mutants of *Arabidopsis* demonstrate the in-planta role of HMG-CoA reductase in triterpene biosynthesis. *Chem. Pharmaceut. Bull.* 55, 1518–1521. doi: 10.1248/cpb.55.1518
- Qu, C., Bai, Y., Jin, X., Wang, Y., Zhang, K., You, J., et al. (2009). Study on ginsenosides in different parts and ages of *Panax quinquefolius* L. *Food Chem.* 115, 340–346. doi: 10.1016/j.foodchem.2008.11.079
- Rezaie, R., Mandoulakani, B. A., and Fattahi, M. (2020). Cold stress changes antioxidant defense system, phenylpropanoid contents and expression of genes involved in their biosynthesis in *Ocimum basilicum* L. *Sci. Rep.* 10:5290. doi: 10.1038/s41598-020-62090-z
- Shan, S. M., Luo, J. G., Huang, F., and Kong, L. Y. (2014). Chemical characteristics combined with bioactivity for comprehensive evaluation of *Panax ginseng* C.A.Meyer in different ages and seasons based on HPLC-DAD and chemometric methods. *J. Pharm. Biomed. Anal.* 89, 76–82. doi: 10.1016/j.jpba.2013.10.030
- Shi, Y., Sun, C., Zheng, B., Gao, B., and Sun, A. (2013). Simultaneous determination of ten ginsenosides in American ginseng functional foods and ginseng raw plant materials by liquid chromatography tandem mass spectrometry. *Food Anal. Methods* 6, 112–122. doi: 10.1007/s12161-012-9406-9406
- Sun, B. S., Pan, F. Y., and Sung, C. K. (2011). Repetitious steaming-induced chemical transformations and global quality of black ginseng derived from

ACKNOWLEDGMENTS

We would like to thank Prof. Weichen Qi, Changchun University of Chinese Medicine, for providing financial support for part of this work.

- Panax ginseng by HPLC-ESI-MS/MSbased chemical profiling approach. *Biotechnol. Bioprocess Eng.* 16:956. doi: 10.1007/s12257-011-0079-76
- Wang, J., Gao, W. Y., Zuo, B. M., Zhang, L. M., and Huang, L. Q. (2012). Advances in study of ginsenoside biosynthesis pathway in *Panax ginseng* C. A. Meyer. *Acta Physiol. Plant.* 34, 397–403. doi: 10.1007/s11738-011-0844-843
- Wu, Q., Sun, C., and Chen, S. L. (2012). Identification and expression analysis of a 3-hydroxy-3-methylglutaryl coenzyme a reductase gene from American ginseng. *Plant Omics J. Plant Mol. Biol. Omics* 5, 414–420. doi: 10.3835/plantgenome2012.03.0002
- Yang, J., Hu, Z., Zhang, T., Gu, A., Gong, T., and Zhu, P. (2018). Progress on the studies of the key enzymes of ginsenoside biosynthesis. *Molecules* 23:589. doi: 10.3390/molecules23030589
- Yang, L., Zhang, T., Yang, L., and Han, M. (2017). Effects of ecological factors on ginsenosides synthesis and its key enzyme genes expression. *Chinese Trad. Herbal Drugs* 48, 4296–4304. doi: 10.7501/j.issn.0253-2670.2017.20.026
- You, J., Liu, X., Zhang, B., Xie, Z., Hou, Z., and Yang, Z. (2015). Seasonal changes in soil acidity and related properties in ginseng artificial bed soils under a plastic shade. *J. Ginseng Res.* 39, 81–88. doi: 10.1016/j.jgr.2014.08.002
- Zhang, T., Han, M., Yang, L., Han, Z., and Yang, L. (2018). The effects of environmental factors on ginsenoside biosynthetic enzyme gene expression and saponin abundance. *Molecules* 24:14. doi: 10.3390/molecules24010014
- Zhang, Y. C., Li, G., Jiang, C., Yang, B., Yang, H. J., Xu, H. Y., et al. (2014). Tissue-specific distribution of ginsenosides in different aged ginseng and antioxidant activity of ginseng leaf. *Molecules* 19, 17381–17399. doi: 10.3390/molecules191117381

Conflict of Interest: The authors declare that the research was conducted in the absence of any commercial or financial relationships that could be construed as a potential conflict of interest.

Copyright © 2021 Zhang, Chen, Chen, Zhang, Li and Qi. This is an open-access article distributed under the terms of the Creative Commons Attribution License (CC BY). The use, distribution or reproduction in other forums is permitted, provided the original author(s) and the copyright owner(s) are credited and that the original publication in this journal is cited, in accordance with accepted academic practice. No use, distribution or reproduction is permitted which does not comply with these terms.



MgO Nanoparticles-Incorporated PCL/Gelatin-Derived Coaxial Electrospinning Nanocellulose Membranes for Periodontal Tissue Regeneration

Wenzao Peng^{1,2,3†}, Shuangshuang Ren^{1,2,3†}, Yibo Zhang⁴, Ruyi Fan^{1,2,3}, Yi Zhou^{1,2,3}, Lu Li^{1,2,3}, Xuanwen Xu^{1,2,3} and Yan Xu^{1,2,3*}

¹ Jiangsu Key Laboratory of Oral Diseases, Nanjing Medical University, Nanjing, China, ² Department of Periodontics, Affiliated Hospital of Stomatology, Nanjing Medical University, Nanjing, China, ³ Jiangsu Province Engineering Research Center of Stomatological Translational Medicine, Nanjing, China, ⁴ State Key Laboratory of Pharmaceutical Biotechnology, Department of Sports Medicine and Adult Reconstructive Surgery, Nanjing Drum Tower Hospital, The Affiliated Hospital of Nanjing University Medical School, Nanjing, China

OPEN ACCESS

Edited by:

Caoxing Huang,
Nanjing Forestry University, China

Reviewed by:

Shuangxi Nie,
Guangxi University, China
Zhaobin Guo,
Johns Hopkins University,
United States

*Correspondence:

Yan Xu
yanxu@njmu.edu.cn

† These authors have contributed equally to this work and share first authorship

Specialty section:

This article was submitted to
Bioprocess Engineering,
a section of the journal
Frontiers in Bioengineering and
Biotechnology

Received: 16 February 2021

Accepted: 02 March 2021

Published: 25 March 2021

Citation:

Peng W, Ren S, Zhang Y, Fan R, Zhou Y, Li L, Xu X and Xu Y (2021) MgO Nanoparticles-Incorporated PCL/Gelatin-Derived Coaxial Electrospinning Nanocellulose Membranes for Periodontal Tissue Regeneration. *Front. Bioeng. Biotechnol.* 9:668428. doi: 10.3389/fbioe.2021.668428

Electrospinning technique has attracted considerable attention in fabrication of cellulose nanofibrils or nanocellulose membranes, in which polycaprolactone (PCL) could be used as a promising precursor to prepare various cellulose nanofibril membranes for periodontal tissue regeneration. Conventional bio-membranes and cellulose films used in guided tissue regeneration (GTR) can prevent the downgrowth of epithelial cells, fibroblasts, and connective tissue in the area of tooth root but have limitations related to osteogenic and antimicrobial properties. Cellulose nanofibrils can be used as an ideal drug delivery material to encapsulate and carry some drugs. In this study, magnesium oxide (MgO) nanoparticles-incorporated PCL/gelatin core-shell nanocellulose periodontal membranes were fabricated using coaxial electrospinning technique, which was termed as Coaxial-MgO. The membranes using single-nozzle electrospinning technique, namely Blending-MgO and Blending-Blank, were used as control. The morphology and physicochemical property of these nanocellulose membranes were characterized by scanning electron microscopy (SEM), energy-dispersive spectrum of X-ray (EDS), transmission electron microscopy (TEM), contact angle, and thermogravimetric analysis (TGA). The results showed that the incorporation of MgO nanoparticles barely affected the morphology and mechanical property of nanocellulose membranes. Coaxial-MgO with core-shell fiber structure had better hydrophilic property and sustainable release of magnesium ion (Mg²⁺). CCK-8 cell proliferation and EdU staining demonstrated that Coaxial-MgO membranes showed better human periodontal ligament stem cells (hPDLSCs) proliferation rates compared with the other group due to its gelatin shell with great biocompatibility and hydrophilicity. SEM and immunofluorescence assay results illustrated that the Coaxial-MgO scaffold significantly enhanced hPDLSCs adhesion. *In vitro* osteogenic and antibacterial properties showed that Coaxial-MgO membrane enhanced alkaline phosphatase (ALP)

activity, formation of mineralized nodules, osteogenic-related genes [ALP, collagen type 1 (COL1), runt-related transcription factor 2 (Runx2)], and high antibacterial properties toward *Escherichia coli* (*E. coli*) and *Actinobacillus actinomycetemcomitans* (*A. a*) when compared with controls. Our findings suggested that MgO nanoparticles-incorporated coaxial electrospinning PCL-derived nanocellulose periodontal membranes might have great prospects for periodontal tissue regeneration.

Keywords: nanocellulose membranes, electrospinning, polycaprolactone, MgO nanoparticle, periodontitis

INTRODUCTION

Periodontitis is one of the most ubiquitous chronic oral diseases caused by trauma or various kinds of oral pathogens infection. The major clinical manifestations of periodontitis include the formation of periodontal pockets and alveolar bone resorption, which eventually lead to progressive loss of alveolar bone and teeth (Dentino et al., 2013; Larsson et al., 2016; Liu J. et al., 2019). Consequently, multifunctional membranes with osteogenic and antibacterial properties for periodontal tissue regeneration are highly desirable but also a great challenge to manufacture (Graziani et al., 2017). Among various therapeutic options, the GTR technique (Oortgiesen et al., 2012; Needleman et al., 2019; Stavropoulos et al., 2020), in which membranes are employed as a barrier to prevent the downgrowth of epithelial cells, fibroblasts, and connective tissue in the area of the tooth root, has been widely used in periodontal diseases (Zwahlen et al., 2009; Dentino et al., 2013; Larsson et al., 2016; Liang et al., 2020). The most commonly used membranes in GTR, like Bio-Gide®, have excellent biocompatibility but have limitations in terms of osteogenic and antimicrobial properties. Infection caused by numbers of bacteria may result in unsuccessful treatment. Therefore, considerable attention has been focused on the development of multifunctional membranes for periodontal tissue regeneration (Li et al., 2016; Liang et al., 2020).

To date, a great number of preparation methods have been developed to constitute GTR membranes, among which the electrospinning technique has attracted considerable attention due to its advantage in fabricating nanocellulose membranes simply and versatilely (Szentivanyi et al., 2011; Doostmohammadi et al., 2020). The electrospun membranes possess high specific surface area and porosity, which can mimic the structure and function of the native extracellular matrix (ECM) (Szentivanyi et al., 2011; Kennedy et al., 2017; Meireles et al., 2018). Besides, the diameter and direction of electrospun nanocellulose can also be regulated to enhance attachment, proliferation, migration, and differentiation of biological cells (Lim and Mao, 2009; Lee et al., 2019; Parham et al., 2020). One advantage of electrospinning is its versatility in directly incorporating bioactive agents, including anti-cancer drugs, nanoparticles, growth factors, into the nanocellulose matrix without complicated processes (Xue et al., 2014; Ren et al., 2017). However, a specific disadvantage that should be considered while dealing with the drug delivery system is its high initial release that may cause irreversible damage to the surrounding cells or

tissues (Khalf and Madihally, 2017; De-Paula et al., 2019; Pant et al., 2019). To address this issue, the coaxial electrospun fiber composed of the shell layer and the core layer was introduced to fabricate the bioactive agents-incorporated cellulose membranes (Dayem et al., 2016; Si et al., 2016; Hickey et al., 2017; Ke et al., 2019). The core-shell nanocellulose matrix exhibits a specific advantage whereby the bioactive agents can be restricted to the core layer, alleviating their initial burst release (Lin et al., 2018). In addition, the release rate of bioactive agents can also be controlled by tuning the composition and thickness of the shell, thus avoiding irreversible damage or undesired side effects to surrounding tissues (Li et al., 2013; Khalf and Madihally, 2017). Among the various materials used for coaxial electrospinning, PCL is considered to be a very promising precursor for electrospun cellulose nanofiber due to its good biocompatibility, mechanical properties, and ease of fabrication into fibers. Yet, the synthetic PCL also has some drawbacks, such as limited cell affinity and poor hydrophilicity (Hiep and Lee, 2010; Qian et al., 2019). Gelatin with cell-binding sites and biomolecular signatures is the most widely used natural polymer in tissue engineering, including simulating ECM and promoting cell adhesion due to its low antigenicity, desirable biocompatibility, and biodegradability (Sridhar et al., 2014; Pant et al., 2019). Therefore, hybrid nanofibers with core-shell structure combining PCL and gelatin can be obtained by using coaxial electrospinning and subsequently used as a nanocellulose scaffold in tissue engineering (Ren et al., 2017).

Recently, nanomaterials, such as nanocellulose, nanogel, and nano-membranes, have brought innovation in biomedical application due to their excellent biocompatibility, physicochemical properties and ease of functionalization (Nie et al., 2018a,b; Lu et al., 2020; Wang P. et al., 2020; Zhang et al., 2021). Generally, various extracts and inorganic substances that have ability to scavenge free radicals can inhibit inflammation caused by bacteria (Huang et al., 2018; Dong et al., 2020; Pei et al., 2020; Gu et al., 2021; Zheng et al., 2021), among which MgO nanoparticles have attracted considerable attention in tissue engineering due to their multifold effects on accelerating osteogenic differentiation of biological cells and inhibiting bacterial activity (Khandaker et al., 2013; Ke et al., 2019). Liu et al. (2020) reported that PLA/gelatin periodontal membrane fabricated by electrospinning biodegradable polymers with MgO nanoparticles demonstrated a dose-dependent magnesium ion-induced osteogenic activity of rabbit bone marrow stem cells (rBMSCs). Besides, numerous studies have also demonstrated that MgO nanoparticles have attracted considerable attention in

biomedical applications due to their great antibacterial activities toward various kinds of bacteria (Karthik et al., 2019). Abbas's work demonstrated that MgO nanoparticle solutions had good antimicrobial activity both *in vitro* and *in vivo* with minimal toxicity (Monzavi et al., 2014). Hence, MgO-incorporated coaxial electrospun nanocellulose membrane could be very promising platforms for periodontal tissue regeneration.

In this work, MgO nanoparticles-incorporated PCL/gelatin nanocellulose membranes were fabricated using coaxial electrospinning method, and their morphological and physicochemical features were characterized by TEM, SEM, contact angle, and TGA. Then, comprehensive assessments were carried out to investigate their effect on proliferation, attachment, and osteogenic differentiation of hPDLSCs. Antibacterial properties of as-prepared nanocellulose membranes were evaluated by prohibiting the growth of *Escherichia coli* (*E. coli*) and *Actinobacillus actinomycetemcomitans* (*A. a*). Thus, we speculated that the MgO nanoparticles-incorporated PCL/gelatin nanocellulose membranes fabricated by coaxial electrospinning with excellent osteogenic and antibacterial properties could provide valuable insights into the development of bio-membranes for periodontal regeneration.

MATERIALS AND METHODS

Materials

Polycaprolactone (Mw = 160000) was purchased from Jinan Daigang Biomaterial Co., Ltd, Jinan, China. Gelatin powder (type A) (Mw = 80000) was obtained from Sigma-Aldrich Co., Ltd, China. MgO nanoparticles were purchased from Shanghai Bike New Material Technology Co., Ltd, China. 1,1,1,3,3,3-Hexafluoro-2-propanol (HFIP) was purchased from Aladdin Co., Ltd, China. Cell-Light™ EdU DNA Cell Proliferation Kit was obtained from RiboBio Co., Ltd, China. Cell Counting Kit-8 (CCK-8) was obtained from Dojindo Co., Ltd, Japan.

Characterization

The morphology of MgO nanoparticles was characterized by transmission electron microscopy (JEOL 1200EX). Surface morphology, topography and energy dispersive spectrometer (EDS) analysis of PCL/gelatin nanocellulose membranes were characterized by field-emission SEM (FEI Nova NanoSEM450). The contact angle of PCL/gelatin

nanocellulose membranes was carried out by static water contact angle measurement (Automatic Contact Angle Meter Model SL200B, China). The mechanical property of PCL/gelatin nanocellulose membranes was measured by an electronic universal testing machine (WSM).

Fabrication of PCL/Gelatin Nanocellulose Membranes

Polycaprolactone/gelatin nanocellulose membranes were prepared by the electrospinning method. As for coaxial electrospinning, PCL and gelatin were dissolved in HFIP according to the proportion in **Table 1** to form core solution and shell solution, respectively. The outer and inner tube had a diameter of 1.11 and 0.34 mm, respectively. A constant-volume flow rate of 0.5 ml/h for core solution and 2.5 ml/h for shell solution were accomplished via two syringe pumps. An electrostatic field force was created by applying a current of 20–22 kV voltages, which introduced the formation of nanofibers from the solution. In addition, the distance between the nozzle tip and collector plate was set up to 18 cm. MgO nanoparticles 3% (w/v) were added to the core solution under magnetic stirring at room temperature for 72 h. As a control, the traditional single fiber membrane loaded with the same amount of MgO nanoparticles was also performed (the parameters were shown in **Table 1**).

Mg²⁺ Release Study

Magnesium oxide nanoparticles-incorporated PCL/gelatin nanocellulose membranes were punched into uniform disks with a diameter of 6 mm, which were incubated at 37°C with 5% CO₂ in 48-well plates supplemented with 250 μl PBS buffer (No Calcium, No Magnesium, pH = 7.4). Then, 20 μl PBS buffer was added every 3 days to maintain the total volume, and subsequently, the amount of Mg²⁺ at a predetermined time was quantitatively measured by a Magnesium Assay Kit (Jiancheng, Nanjing).

Cell Experiments

hPDLSCs were individually isolated from healthy premolars extracted for orthodontic treatment from teenagers aged 11–16 years without periodontitis, caries, and cracks and subsequently purified using a limited dilution method (Seo et al., 2004). The cells were identified by detecting the surface markers such as CD73, CD90, CD45, and CD34 (BD, United States) by

TABLE 1 | Parameters for electrospun fibers.

	Solvent	Core		Shell		Voltage (kV)	Time (h)
		Solute (w/v)	Feed speed (ml/h)	Solute (w/v)	Feed speed (ml/h)		
Coaxial-Blank	HFIP	10% PCL	0.5	10% gelatin	2.5	20–22	8
Coaxial-MgO	HFIP	10% PCL + 3% MgO	0.5	10% gelatin	2.5	20–22	8
		Solute (w/v)		Feed speed (ml/h)			
Blending-Blank	HFIP	1.7% PCL + 8.3% gelatin		3		17–19	8
Blending-MgO	HFIP	1.7% PCL + 8.3% gelatin + 0.5% MgO		3		17–19	8

flow cytometry (BD FACSCalibur, United States). Osteogenic differentiation and adipogenic differentiation were respectively introduced to prove the differentiation potential of the cells (Lin et al., 2008; Ng et al., 2016). Cells were cultured at 37°C with 5% CO₂ in the growth medium, α -MEM medium (Gibco, United States) supplemented with 10% fetal bovine serum (Gibco, United States) and 1% penicillin-streptomycin solution (Gibco, United States). The medium was replaced every 3 days.

Cell Proliferation Assay

These sterilized PCL/gelatin nanocellulose membranes with a diameter of 6 mm were cultured with hPDLSCs at a density of 2×10^4 cells at 37°C with 5% CO₂ in 48-well plates. After incubation for 1 day, 3 days, 5 days, and 7 days, the cells were washed with PBS buffer, followed by the addition of 100 μ l α -MEM medium supplemented with 10% Cell Counting Kit-8 and incubated at 37°C for 2 h. The optical density (OD) values at 450 nm was measured by a microplate reader (Spectramax190, MD, United States).

EdU Staining Assay

Electrospun membranes 6 mm in diameter were incubated with hPDLSCs at a density of 2×10^4 cells at 37°C with 5% CO₂ in 48-well plates for 24 h. After that, the cells were washed with PBS three times and fixed with 4% paraformaldehyde for 30 min, stained by Cell-Light™ EdU DNA Cell Proliferation Kit (RiboBio, Guangzhou, China) according to the manufacturer's instructions, and observed under a fluorescence microscope (DMI6000B, Leica, Germany).

Cell Attachment Assay

The sterilized PCL/gelatin nanocellulose membranes were co-cultured with hPDLSCs at a density of 4×10^5 cells at 37°C with 5% CO₂ in 6-well plates for 24 h, followed by washing with PBS buffer for three times to remove the unattached cells and fixing with 4% paraformaldehyde overnight. The cells were stained with rhodamine phalloidin for cytoskeleton and 4', 6-Diamidino-2-phenylindole, dihydrochloride (DAPI) for the nucleus, followed by observation under inverted fluorescence microscope (DMI6000B, Leica, Germany).

ALP Activity and Staining

These four sterilized PCL/gelatin nanocellulose membranes with a diameter of 6 mm were incubated with hPDLSCs at 37°C with 5% CO₂ in 48- and 24-well plates overnight respectively, after which the culture medium was replaced by osteogenic differentiation medium containing growth medium supplemented with 0.1 μ M dexamethasone, 300 μ M ascorbic acid and 10 mM β -glycerophosphate (Sigma, United States). After incubation for 7 days, the cells were harvested, and the ALP activity was measured by Alkaline Phosphatase Assay Kit (Beyotime Biotechnology, China) and stained by BCIP/NBT Alkaline Phosphatase Color Development Kit (Beyotime Biotechnology, China) according to the manufacturer's instructions. The OD values at 520 nm were measured, and the wells were examined under optical microscopy (SMZ1000, Nikon, Japan) and photographed with digital camera (EOS 6D, Japan).

Alizarin Red Staining

These four kinds of sterilized PCL/gelatin nanocellulose membranes with a diameter of 15 mm were incubated with hPDLSCs at a density of 2×10^5 cells at 37°C with 5% CO₂ in 24-well plates overnight. After that, the cells were cultured in osteogenic differentiation medium for 14 days, stained by 2% alizarin red S (ARS, Leagene, China) staining solution for 5 min. After being washed with PBS buffer three times, the plates were observed by optical microscope (SMZ1000, Nikon, Japan). After that, mineralized nodules stained by ARS were desorbed with 10% (w/v) cetylpyridinium chloride (Sigma-Aldrich, China). We measured the absorbance at 562 nm for quantification.

Reverse Transcription-Quantitative Polymerase Chain Reaction (RT-qPCR)

The osteogenic-related genes, including ALP, COL1, and Runx2, were further investigated by RT-qPCR. The hPDLSCs were cultured with different kinds of sterilized PCL/gelatin nanocellulose membranes for 3 days, followed by the isolation of total RNA by the RNAsimple Total Kit (TianGen, China). After that, the cDNA was generated and analyzed by PrimeScript™ RT Master Mix (Perfect Real Time) and TB Green Premix EX Taq II respectively (TaKaRa, Japan), followed by the amplification and detection by LightCycler® 96 (Roche, Mannheim, Germany). The primers are listed in Table 2.

Antibacterial Activity

These sterilized PCL/gelatin nanocellulose membranes with a diameter of 20 mm were incubated with *E. coli* (ATCC-25922) and *A. a* (ATCC-29523) at a density of 1×10^7 CFU for 24 h. After that, the bacterial suspension followed by a series of dilution were swabbed to the surface of LB agar plate and Columbia blood agar respectively and were incubated at 37°C for 24 h. The number of the bacteria colonies were calculated to evaluate the antibacterial activity using a colometer (Interscience Scan1200, France).

Statistical Analysis

The differences between groups were determined by using one-way ANOVA followed by Tukey's *post hoc* analysis. A *p*-value of < 0.05 was considered as statistical significance. Statistical analysis was performed with GraphPad Prism 8.

TABLE 2 | Primer sequences.

Primer name	Forward primer sequence (5'–3')	Reverse primer sequence (5'–3')
ALP	GAGATGTTGTCTGACACTTGTG	AGGCTTCCTCCTTGTGGGT
RUNX2	TGGTACTGTCATGGCGGGTA	TCTCAGATOGTTGAACCTTGCTA
COL1	GAGGGCCAAGACGAAGACATC	CAGATCACGTCATCGCACAAC
Human actin	GTCCCTCACCTCCCAAAAG	GCTGCTCAACACCTCAACCC

RESULTS

Surface Topography of PCL/Gelatin Nanocellulose Membranes

PCL/gelatin nanocellulose membranes were prepared by coaxial or single-nozzle electrospinning technique alone or incorporated with MgO nanoparticles, after which their morphology was characterized. As shown in **Figures 1A,B**, the densely compacted and core-shell structure single fiber for single-nozzle and coaxial electrospinning were observed by TEM images, respectively. The darker (core) and lighter (shell) areas represented the PCL and gelatin region, respectively. After incorporated with MgO nanoparticles, obvious lumps of MgO nanoparticles marked higher in nanocellulose membranes could be observed in both Blending-MgO and Coaxial-MgO (**Figures 1C,D**). The SEM micrographs for four types of PCL/gelatin nanocellulose membranes were shown in **Figures 1E-H**, where it could be seen that the blank nanocellulose membranes without MgO nanoparticles exhibited some web-like fine fibers with a smooth surface and high interconnected porosity. As expected, the

nanocellulose membranes were evenly arranged, and no bead-like structures were observed. EDS (**Figures 1I-M**) was further employed to investigate the elemental composition of our electrospun membranes. In comparison with Blending-Blank and Coaxial-Blank that only contained C and O elements, the magnesium element ratio for Blending-MgO and Coaxial-MgO were 2.27 and 2.46, respectively, indicating the successful incorporation of MgO nanoparticles.

Physicochemical Properties of PCL/Gelatin Nanocellulose Membranes

Mechanical strength of PCL/gelatin nanocellulose membranes were firstly investigated using electronic universal testing machine. As shown in **Figure 2A**, the mean values of tensile strength for Blending-Blank, Coaxial-Blank, Blending-MgO, and Coaxial-MgO were 1.54, 1.61, 1.60, and 1.71 MPA, respectively, and there was no significant difference among these four groups ($p > 0.05$). These results indicated that the incorporation of MgO nanoparticles did not affect the tensile strength of the nanocellulose membranes.

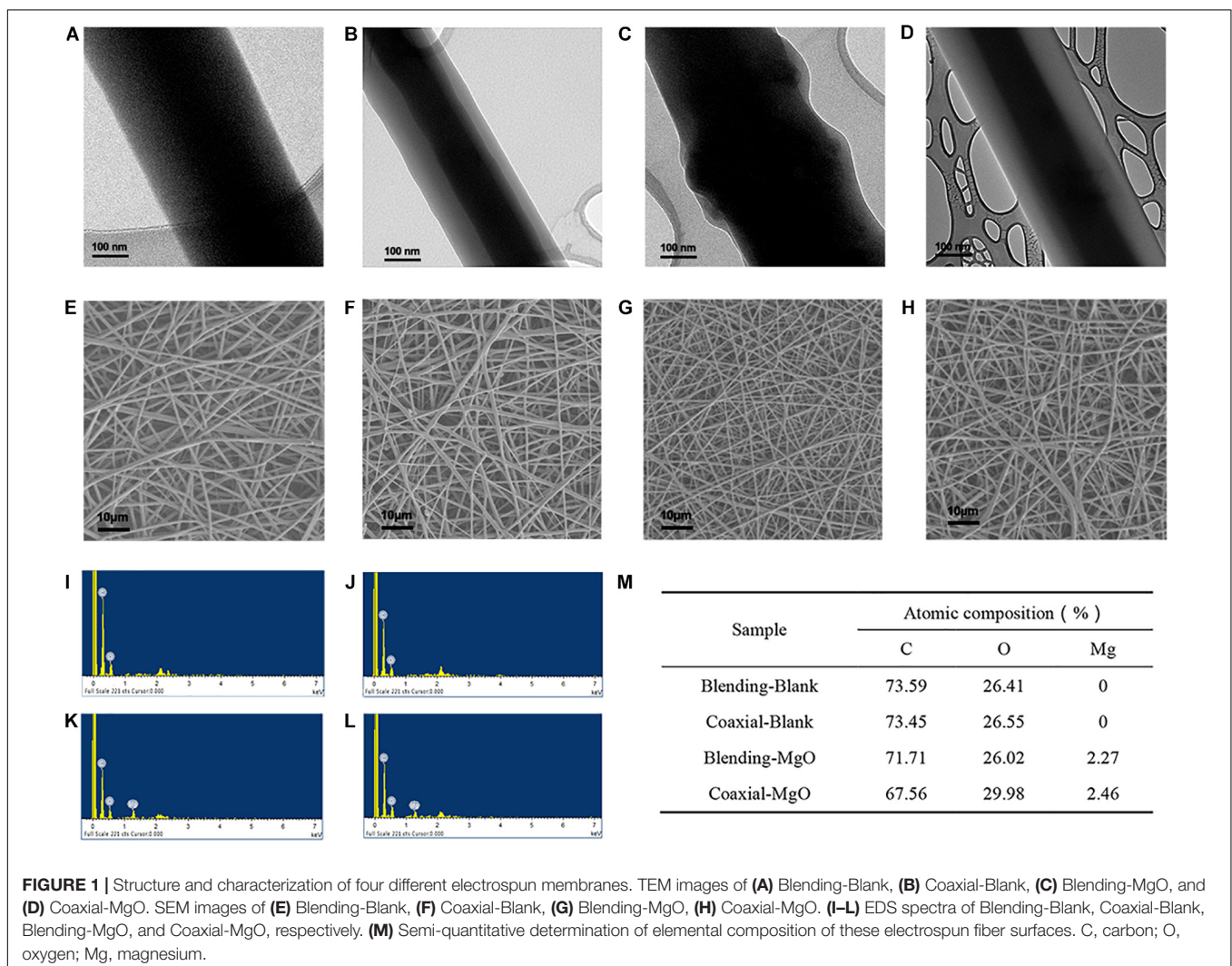
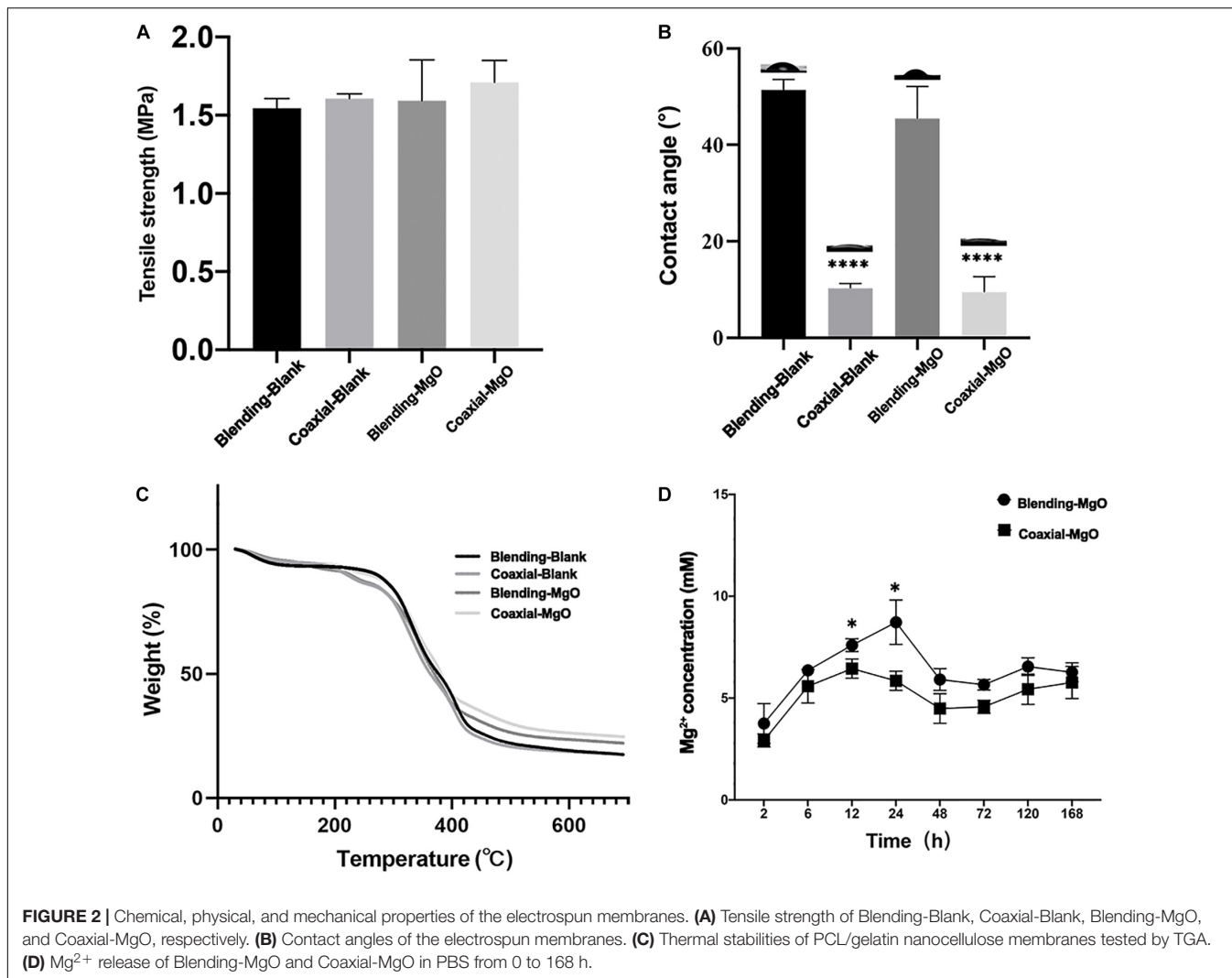


FIGURE 1 | Structure and characterization of four different electrospun membranes. TEM images of **(A)** Blending-Blank, **(B)** Coaxial-Blank, **(C)** Blending-MgO, and **(D)** Coaxial-MgO. SEM images of **(E)** Blending-Blank, **(F)** Coaxial-Blank, **(G)** Blending-MgO, **(H)** Coaxial-MgO. **(I-L)** EDS spectra of Blending-Blank, Coaxial-Blank, Blending-MgO, and Coaxial-MgO, respectively. **(M)** Semi-quantitative determination of elemental composition of these electrospun fiber surfaces. C, carbon; O, oxygen; Mg, magnesium.



It is well known that the hydrophilic property of the scaffold may greatly affect their interaction with biological cells, such as cell adhesion and proliferation. Hence, the surface wettability of the as-prepared PCL/gelatin nanocellulose membranes was evaluated by contact angle. As shown in **Figure 2B**, the average contact angles of coaxial nanocellulose membranes were much smaller than that of single fiber membranes. These results demonstrated that the coaxial structure that was made up of PCL encapsulated in gelatin increased their hydrophilic property, which was conducive to cell adhesion and provided a better physiological environment for cell growth. When MgO nanoparticles were added, a slight decrease from 10.29° (51.4°) to 9.48° (45.5°) was observed for coaxial (single fiber) nanocellulose membrane, indicating that the added MgO nanoparticles could improve the hydrophilic property of the blank PCL/gelatin nanocellulose membranes. Thermal stability of PCL/gelatin nanocellulose membranes was further tested by TGA; the obtained weight loss curves were shown in **Figure 2C**. Our results showed that the initial degradation temperature for coaxial nanocellulose membrane increased

after incorporated MgO nanoparticles but decreased for Blending-MgO and Blending-Blank. This, in turn, suggested that the MgO nanoparticles could enhance the thermal stability of the coaxial nanocellulose membrane. When the temperature was increased to 500°C , the thermal degradation of all the four nanocellulose membranes was relatively stable, and the incorporation of MgO nanoparticles could significantly increase the maximum degradation temperature of nanocellulose membranes.

Furthermore, the accumulated release of Mg^{2+} from the Blending-MgO and Coaxial-MgO nanocellulose membranes in PBS over a period of 168 h was quantified by Magnesium Assay Kit. As shown in **Figure 2D**, a relatively burst initial release of Mg^{2+} within the first 24 h was observed. The results revealed higher quantities of Mg^{2+} , almost beyond 10 mM within 24 h, in group Blending-MgO, which was higher than in group Coaxial-MgO. After that, Mg^{2+} was sustainably released for both Blending-MgO and Coaxial-MgO over 168 h, resulting in a stable Mg^{2+} concentration around 5 mM. Numerous studies have shown that 5–10 mM Mg^{2+}

had a slight cytotoxic effect on cells and could promote cells' osteogenic differentiation (Mangalampalli et al., 2018; Onder et al., 2018). These results indicated that the MgO-incorporated coaxial PCL/gelatin nanocellulose membranes with the sustainable release of Mg^{2+} might be suitable for accelerating osteogenic differentiation of cells.

The Proliferation of hPDLSCs Toward PCL/Gelatin Nanocellulose Membranes

The proliferative capability of hPDLSCs toward PCL/gelatin nanocellulose membranes was further investigated using CCK-8 and EdU assays. As illustrated in **Figures 3A–D**, the cell viability of hPDLSCs exceeds 100% in all groups and exhibited a time-dependent cell proliferation after co-incubation for 1, 3, 5, and 7 days. These results indicated that all the PCL/gelatin nanocellulose membranes were not cytotoxic and had excellent biocompatibility. Surprisingly, the OD values

in Coaxial-MgO group were significantly higher compared to other groups, indicating that the coaxial structure with smart release of Mg^{2+} could promote the proliferation of hPDLSCs. Moreover, EdU staining (**Figure 3E**) also revealed that the proliferation of hPDLSCs after treatment with Coaxial-MgO was the most obvious among the four types of nanocellulose membranes because of its gelatin shell with great biocompatibility and hydrophilicity and suitable Mg^{2+} release.

Attachment of hPDLSCs Toward PCL/Gelatin Nanocellulose Membranes

To further understand how our PCL/gelatin nanocellulose membranes affected the interaction between hPDLSCs and their environment, including cell morphology and cell attachment, SEM was employed. As shown in **Figures 4A–D**, after 24 h of culture, the hPDLSCs randomly spread along the fibers,

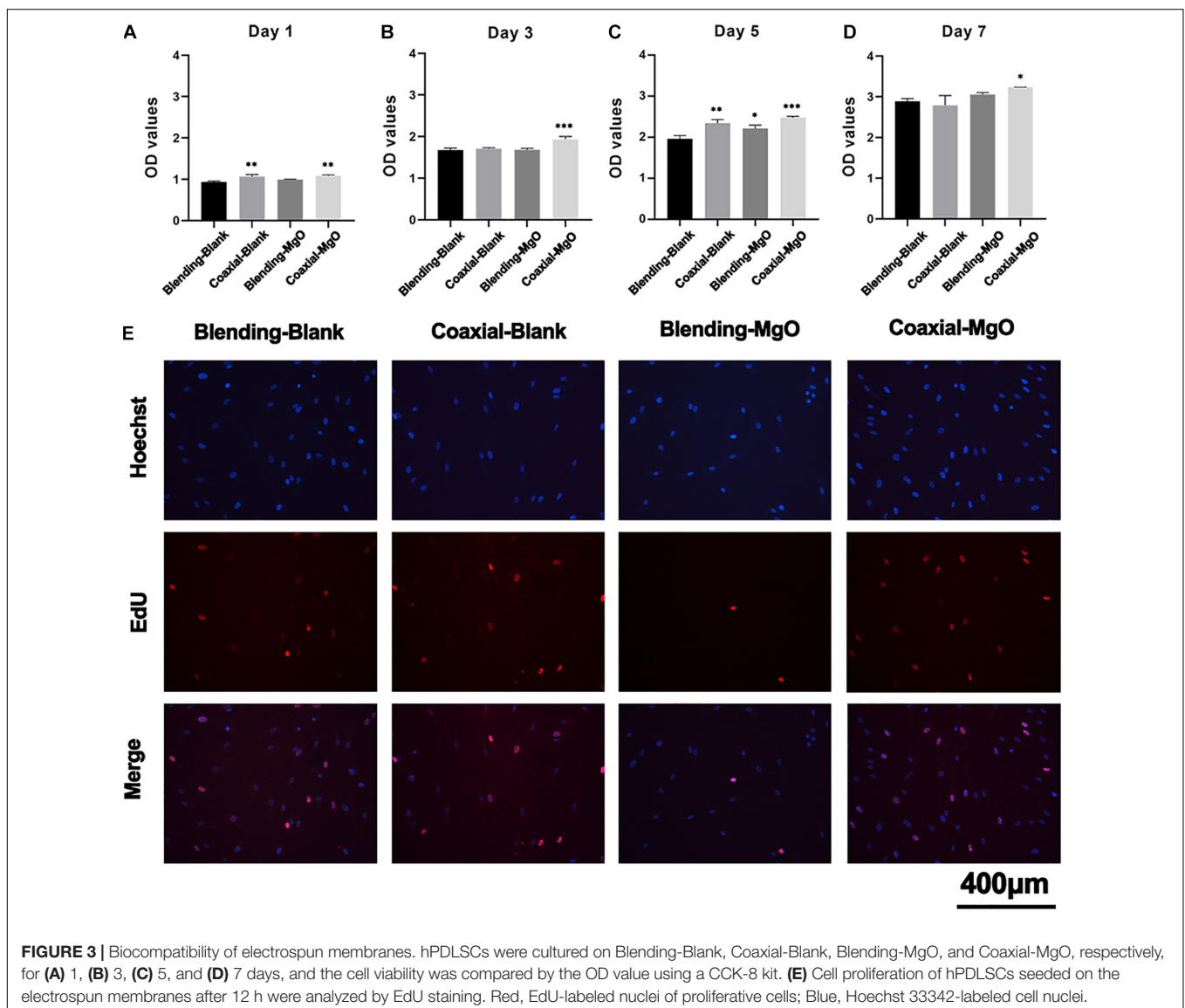
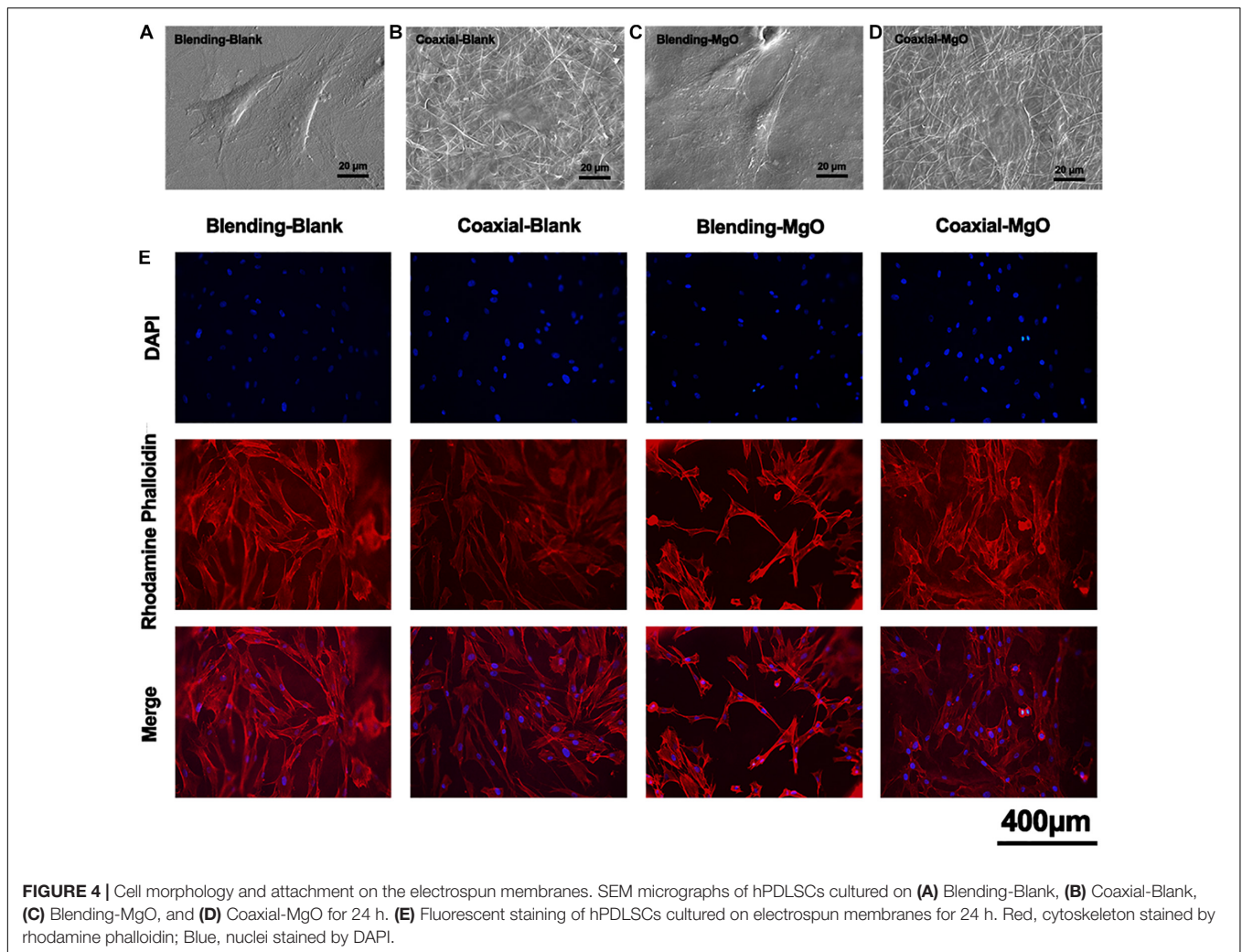


FIGURE 3 | Biocompatibility of electrospun membranes. hPDLSCs were cultured on Blending-Blank, Coaxial-Blank, Blending-MgO, and Coaxial-MgO, respectively, for **(A)** 1, **(B)** 3, **(C)** 5, and **(D)** 7 days, and the cell viability was compared by the OD value using a CCK-8 kit. **(E)** Cell proliferation of hPDLSCs seeded on the electrospun membranes after 12 h were analyzed by EdU staining. Red, EdU-labeled nuclei of proliferative cells; Blue, Hoechst 33342-labeled cell nuclei.



and their filopodia were extended. Specifically, the surfaces of Blending-Blank (Figure 4A) and Blending-MgO (Figure 4C) membranes became smooth due to the disinfection by 75% alcohol, thus exhibiting a convex round shape of hPDLSCs. In contrast, a more flattened morphology for Coaxial-Blank (Figure 4B) and Coaxial-MgO (Figure 4D) was observed. In addition, the cytoskeletal morphology of hPDLSCs was also investigated by the inverted fluorescence microscope (Figure 4E) after 24 h in culture with our electrospinning nanocellulose membranes. The immunofluorescence images demonstrated that the morphology of hPDLSCs was narrow and filamentous, and the cytoskeleton was poorly developed in the Blending-MgO group, while strong F-actin staining and elongated filopodia were observed in Coaxial-MgO. These observations revealed the same tendency with SEM images, which was attributed to the fact that the explosive release of Mg^{2+} from Blending-MgO in a short time might decrease the attachment of hPDLSCs. In addition, the gelatin coating might also enhance the interaction between hPDLSCs and nanocellulose membranes due to the integrin-binding site of the gelatin molecule.

Effects of PCL/Gelatin Nanocellulose Membranes on Osteogenic Differentiation of hPDLSCs

Osteogenic differentiation of hPDLSCs treated with PCL/gelatin nanocellulose membranes were further tested by detecting ALP activity, accumulated mineralized nodules, and expression of osteogenesis-related genes. Based on the ALP staining (Figure 5A), after 7 days of treatment, the expression of ALP showed obvious up-regulation in group Coaxial-MgO compared with other groups. ALP activity level on day 7 demonstrated similar trends, as shown in Figure 5B. These results indicated that Coaxial-MgO nanocellulose membranes could promise a satisfactory effect on the early osteogenic differentiation of hPDLSCs.

The formation of mineralized nodules was investigated by ARS staining. As shown in Figure 5C, after co-culturing with hPDLSCs for 14 days, Coaxial-MgO displayed the most obvious effect on mineralization compared with other groups. After being dissolved in 10% (w/v) cetylpyridinium chloride, the mineralized nodules were quantified by measuring the

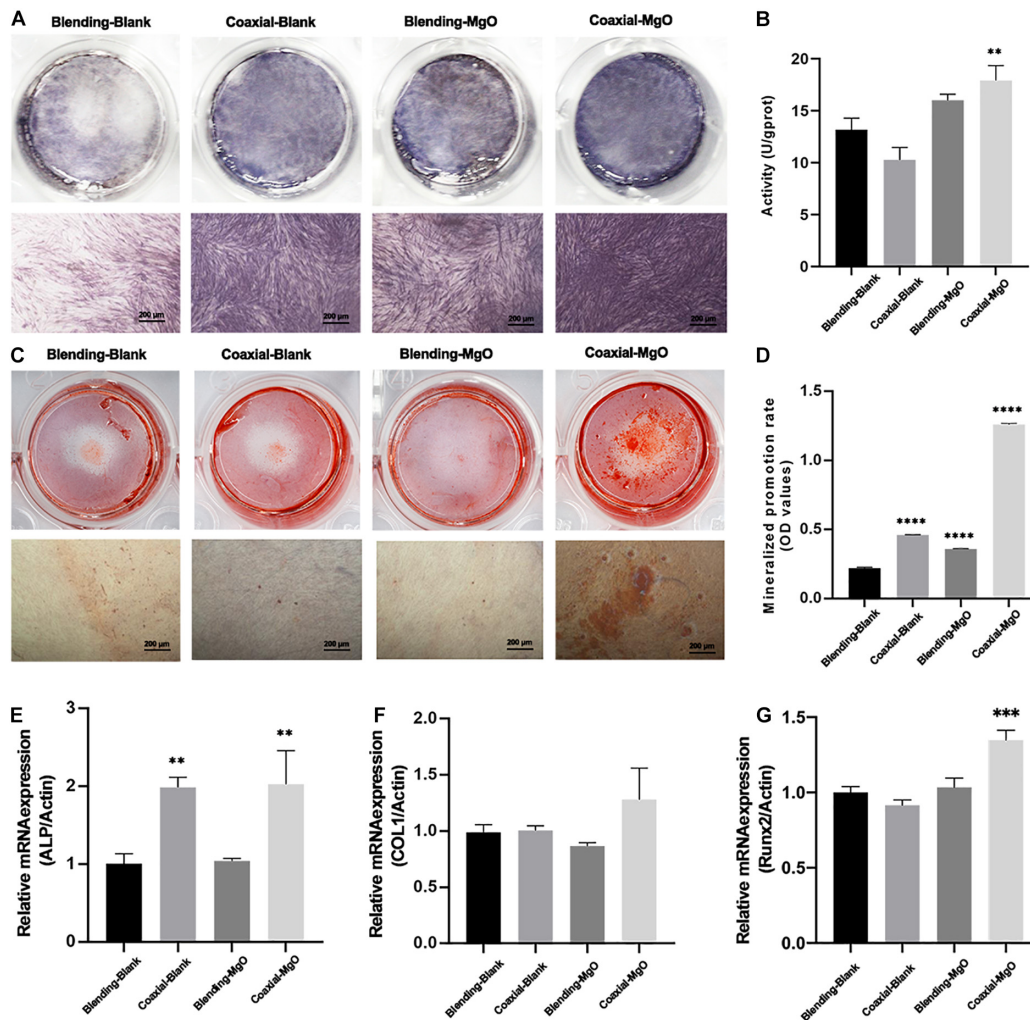


FIGURE 5 | Effects of electrospun membranes on ALP activity and mineralization. **(A)** ALP staining of hPDLSCs after cultured with electrospun membranes for 7 days. **(B)** ALP activity level of hPDLSCs cocultured with electrospun membranes on the 7th day. **(C)** Alizarin red staining of hPDLSCs after seeded on electrospun membranes for 14 days. **(D)** Mineralized promotion rates of cells cultured with each group of the electrospun membranes. RT-qPCR analysis of **(E)** ALP, **(F)** COL1, and **(G)** Runx-2 expression of hPDLSCs after cultured with electrospun membranes for 3 days.

absorbance of ARS deposits at 562 nm, and the results showed the same trend (**Figure 5D**). The effects of PCL/gelatin nanocellulose membranes on osteogenic-related genes, including ALP, COL1, and Runx2, were further investigated by RT-qPCR, as shown in **Figures 5E–G**. After culturing for 3 days, Coaxial-MgO demonstrated the strongest ability in accelerating these mRNA expression levels. For Coaxial-Blank and Coaxial-MgO, the expression of ALP and Runx2 significantly rose, while there was no significant difference for COL1. Taken together, the results unarguably confirmed that Coaxial-MgO had stronger effects on osteogenic differentiation of hPDLSCs.

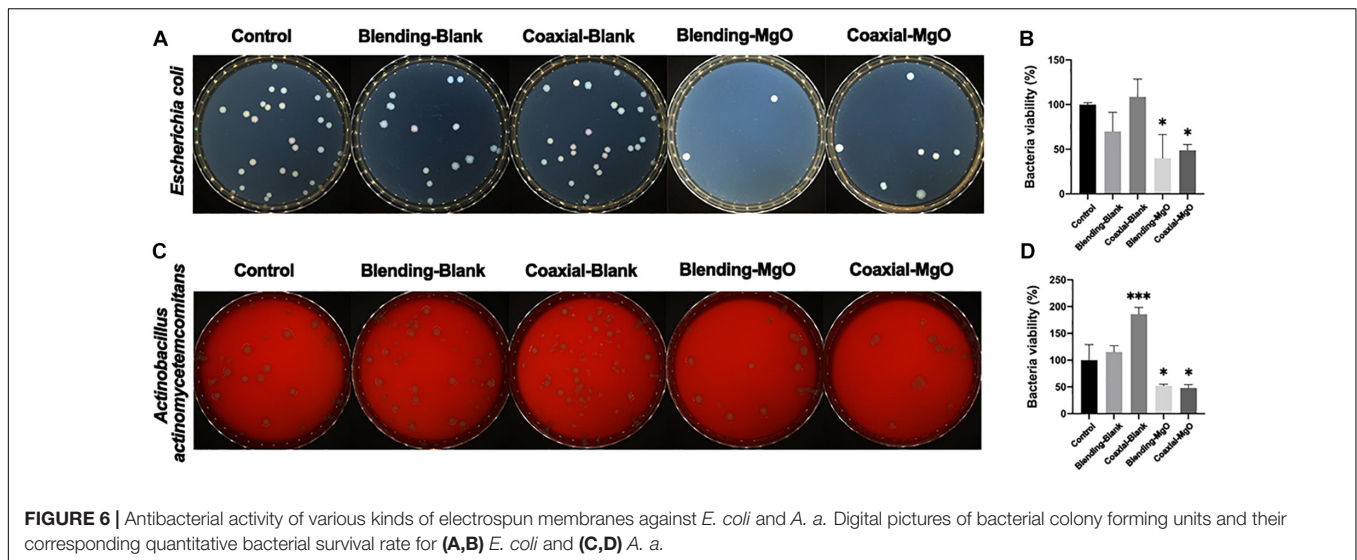
Antimicrobial Activity of PCL/Gelatin Nanocellulose Membranes

In order to understand the antibacterial activities of as-prepared PCL/gelatin nanocellulose membranes, *in vitro* antibacterial

assay was carried out using *E. coli* and *A. a* as model. Colonies of *E. coli* (**Figure 6A**) and *A. a* (**Figure 6C**) significantly decreased when treated with Coaxial-MgO and Blending-MgO, which demonstrated the high antibacterial activities compared with Coaxial-Blank and Blending-Blank. This might be explained by the fact that the added MgO nanoparticles can improve these nanocellulose membranes' antibacterial properties. Quantitative evaluation of bacterial colonies followed the same trends as shown in **Figures 6B,D**.

DISCUSSION

The loss of alveolar bone caused by periodontitis is a common clinical problem (Dentino et al., 2013). While the GTR technique widely uses membrane materials as a barrier in periodontal flap surgery, it still has some limitations,



such as poor osteogenic and antimicrobial properties (Liang et al., 2020). To endow these biodegradable membrane with excellent osteogenic and antimicrobial activities, there are several emerging approaches (Naahidi et al., 2017; Prado-Prone et al., 2020; Shkodenko et al., 2020), among which MgO nanoparticles-incorporated PCL/gelatin nanocellulose membranes fabricated by coaxial electrospinning might be very promising platforms for periodontal tissue regeneration. Our results indicated that Coaxial-MgO had good biocompatibility and affinity to cells due to its gelatin shell, and incorporation of MgO nanoparticles could enhance the mechanical property of membrane. The release of Mg^{2+} is relatively sustainable for Coaxial-MgO, resulting in superior osteogenic and antimicrobial properties compared with Blending-Blank and Coaxial-Blank.

To evaluate the morphology of PCL/gelatin electrospinning nanocellulose membranes, TEM and SEM were analyzed. The results showed that Coaxial-Blank and Coaxial-MgO showed obvious core-shell fiber structure compared with Blending-Blank and Blending-MgO, which was in agreement with previous reports (Wang and Windbergs, 2019). From the TEM images, the MgO nanoparticles were successfully incorporated into the core layer, which was also confirmed by EDS. The distinct core-shell nanocellulose structure with the incorporation of MgO nanoparticles provides the foundation for further cell behavior and antibacterial activity assessment. Moreover, the thermal stability and tensile strength were also affected after the incorporation of MgO nanoparticles. These results were in accordance with Suryavanshi's previous work (Suryavanshi et al., 2017). Nanocellulose membranes fabricated by the coaxial electrospinning method demonstrated relatively superior hydrophilicity compared with that of the single-nozzle electrospinning method, which might be attributed to the success of its gelatin shell. It is well known that Magnesium (Mg^{2+}) has multiple essential roles in biological cells, and Mg^{2+} can regulate various cell behaviors by activating different signal pathways (Leem et al., 2016; Wang et al., 2017; Wang Z. et al., 2020). For example, Mg^{2+} may regulate the adhesion, proliferation, differentiation of human osteoblast via

the TRPM7/PI3K pathway (Zhang et al., 2017). Besides, it has also been reported that Mg^{2+} can promote osteogenic differentiation of human bone marrow stromal cells (hBMSCs) by regulating Wnt, MAPK, and other signal pathways (Hung et al., 2019). Nevertheless, the regulation induced by Mg^{2+} was strictly dose-dependent (Yoshizawa et al., 2014), where the excessive Mg^{2+} could inhibit proliferation or osteogenic differentiation of cells. In our studies, compared with Blending-MgO, a more sustainable release of Mg^{2+} was observed in Coaxial-MgO, thus preventing their initial burst release. The core-shell fiber structure with high hydrophilicity and appropriate release of Mg^{2+} might have an increasingly important role in periodontal tissue engineering.

The GTR membranes are used to prevent epithelial migration into the regenerating area, allowing the slower migrating cells like periodontal ligament cells to occupy the defect site. The interactions between as-prepared nanocellulose membranes and hPDLSCs were investigated. Coaxial-MgO exhibited optimal adhesion and proliferation of hPDLSCs. More cells were attached on Coaxial-MgO's surface, probably because the gelatin shell with great hydrophilicity improved cell adhesion (Liu et al., 2018). Similar positive effects of gelatin on the adhesion and proliferation of cells were also observed in another study (Yue et al., 2015). It has been reported that the excessive Mg^{2+} might be cytotoxic to biological cells (Mangalampalli et al., 2018; Onder et al., 2018). The initial burst release of Mg^{2+} from Blending-MgO might affect the proliferation of hPDLSCs. The effects of nanocellulose membranes on osteogenic differentiation of hPDLSCs were further assessed. There is accumulating evidence that magnesium-based materials were capable of accelerating the osteogenic activity of cells (Liu W. et al., 2019; Huang Y.-z et al., 2020; Li et al., 2020). The expression of ALP activity and formation of mineralized nodules of hPDLSCs treated with Coaxial-MgO were higher than those treated with the other membranes.

Additionally, Coaxial-MgO also significantly improved the expression of osteogenic-related genes, such as ALP and Runx2. Hence, Coaxial-MgO with high hydrophilicity

and sustainable release of Mg^{2+} is beneficial for GTR membranes due to its facilitation in adhesion, proliferation, and osteogenic differentiation of hPDLSCs. The numbers of colonies could be directly visualized from the plate to assess the antibacterial activity. The decrease of colonies in the group Coaxial-MgO was statistically significant, which indicated that the fiber membrane carrying MgO nanoparticles had a certain antibacterial effect. MgO nanoparticles have been confirmed to be effective against pathogenic microorganisms (Nguyen et al., 2018). Generally, the neat nano-cellulose film is absent antimicrobial activity (Huang C. et al., 2020; Xiang et al., 2020; Nie et al., 2021). In this work, both of the prepared films have the antibacterial effect, in which Blending-MgO was more obvious. It is reasonable to speculate that the antibacterial effect might differ due to the preparation method of fiber membranes, which needs to be further studied.

SUMMARY

MgO nanoparticles-incorporated PCL/gelatin nanocellulose membranes were successfully fabricated using the coaxial electrospinning method. The obtained Coaxial-MgO membranes showed improved hydrophilicity and Mg^{2+} release kinetics compared with that of Blending-MgO. Coaxial-MgO also exhibited optimal proliferation, attachment, and osteogenic differentiation of hPDLSCs. In addition, the prepared Coaxial-MgO showed considerable antibacterial activity by prohibiting the growth of *E. coli* and *A. a.* The MgO nanoparticles-incorporated PCL/gelatin nanocellulose membranes fabricated by coaxial electrospinning with excellent osteogenic and antibacterial properties may be used as GTR membranes, which will bring innovation in the field of periodontal regeneration.

REFERENCES

- Dayem, A. A., Choi, H. Y., Yang, G. M., Kim, K., Saha, S. K., Kim, J. H., et al. (2016). The potential of nanoparticles in stem cell differentiation and further therapeutic applications. *Biotechnol. J.* 11, 1550–1560. doi: 10.1002/biot.201600453
- Dentino, A., Lee, S., Mailho, J., and Hefti, A. F. (2013). Principles of periodontology. *Periodontology* 2000 61, 16–53. doi: 10.1111/j.1600-0757.2011.00397.x
- De-Paula, M. M. M., Afewerki, S., Viana, B. C., Webster, T. J., Lobo, A. O., and Marciano, F. R. (2019). Dual effective core-shell electrospun scaffolds: promoting osteoblast maturation and reducing bacteria activity. *Mater. Sci. Eng. C Mater. Biol. Appl.* 103:109778. doi: 10.1016/j.msec.2019.109778
- Dong, H., Zheng, L., Yu, P., Jiang, Q., Wu, Y., Huang, C., et al. (2020). Characterization and application of lignin-carbohydrate complexes from lignocellulosic materials as antioxidants for scavenging in vitro and in vivo reactive oxygen species. *ACS Sustain. Chem. Eng.* 8, 256–266. doi: 10.1021/acssuschemeng.9b05290
- Doostmohammadi, M., Forooutanfar, H., and Ramakrishna, S. (2020). Regenerative medicine and drug delivery: progress via electrospun biomaterials. *Mater. Sci. Eng. C Mater. Biol. Appl.* 109:110521. doi: 10.1016/j.msec.2019.110521
- Graziani, F., Karapetsa, D., Alonso, B., and Herrera, D. (2017). Nonsurgical and surgical treatment of periodontitis- how many options for one disease? *Periodontology* 2000 75, 152–188. doi: 10.1111/prd.12201
- Gu, J., Guo, M., Huang, C., Wang, X., Zhu, Y., Wang, L., et al. (2021). Titanium dioxide nanoparticle affects motor behavior, neurodevelopment and axonal

DATA AVAILABILITY STATEMENT

The original contributions presented in the study are included in the article/**Supplementary Material**, further inquiries can be directed to the corresponding author/s.

AUTHOR CONTRIBUTIONS

YX and SR conceptualized the study. WP performed the experiments. YZha helped to complete part of the experiment. Qing Jiang and WP examined the physicochemical properties of the membranes. RF contributed to the antibacterial evaluation of electrospun nanocellulose membranes. All authors contributed to the article and approved the submitted version.

FUNDING

This study was supported by grants from Priority Academic Program Development of Jiangsu Higher Education Institutions, Grant/Award Number: PAPD, 2018-87; National Natural Science Foundation of China, Grant/Award Number: 81771074; and Key projects of social development of Jiangsu Department of Science and Technology, Grant/Award Number: BE2020707.

SUPPLEMENTARY MATERIAL

The Supplementary Material for this article can be found online at: <https://www.frontiersin.org/articles/10.3389/fbioe.2021.668428/full#supplementary-material>

- growth in zebrafish (*Danio rerio*) larvae. *Sci. Total Environ.* 754:142315. doi: 10.1016/j.scitotenv.2020.142315
- Hickey, D. J., Muthusamy, D., and Webster, T. J. (2017). Electrophoretic deposition of MgO nanoparticles imparts antibacterial properties to poly-L-lactic acid for orthopedic applications. *J. Biomed. Mater. Res. A* 105, 3136–3147. doi: 10.1002/jbm.a.36174
- Hiep, N., and Lee, B. (2010). Electro-spinning of PLGA/PCL blends for tissue engineering and their biocompatibility. *J. Mater. Sci. Mater. Med.* 21, 1969–1978. doi: 10.1007/s10856-010-4048-y
- Huang, C., Dong, H., Zhang, Z., Bian, H., and Yong, Q. (2020). Procuring the nano-scale lignin in prehydrolyzate as ingredient to prepare cellulose nanofibril composite film with multiple functions. *Cellulose* 27, 9355–9370. doi: 10.1007/s10570-020-03427-9
- Huang, C., Tang, S., Zhang, W., Tao, Y., Lai, C., Li, X., et al. (2018). Unveiling the structural properties of lignin-carbohydrate complexes in bamboo residues and its functionality as antioxidants and immunostimulants. *ACS Sustain. Chem. Eng.* 6, 12522–12531. doi: 10.1021/acssuschemeng.8b03262
- Huang, Y.-z., Ji, Y.-r., Kang, Z.-w., Li, F., Ge, S.-f., Yang, D.-P., et al. (2020). Integrating eggshell-derived CaCO₃/MgO nanocomposites and chitosan into a biomimetic scaffold for bone regeneration. *Chem. Eng. J.* 395:125098. doi: 10.1016/j.cej.2020.125098
- Hung, C. C., Chaya, A., Liu, K., Verdelis, K., and Sfeir, C. (2019). The role of magnesium ions in bone regeneration involves the canonical Wnt signaling pathway. *Acta Biomater.* 98, 246–255. doi: 10.1016/j.actbio.2019.06.001
- Karthik, K., Dhanuskodi, S., Gobinath, C., Prabukumar, S., and Sivaramakrishnan, S. (2019). Fabrication of MgO nanostructures and its efficient photocatalytic,

- antibacterial and anticancer performance. *J. Photochem. Photobiol. B* 190, 8–20. doi: 10.1016/j.jphotobiol.2018.11.001
- Ke, D., Tarafder, S., Vahabzadeh, S., and Bose, S. (2019). Effects of MgO, ZnO, SrO, and SiO₂ in tricalcium phosphate scaffolds on in vitro gene expression and in vivo osteogenesis. *Mater. Sci. Eng. C Mater. Biol. Appl.* 96, 10–19.
- Kennedy, K. M., Bhaw-Luximon, A., and Jhurry, D. (2017). Cell-matrix mechanical interaction in electrospun polymeric scaffolds for tissue engineering: implications for scaffold design and performance. *Acta Biomater.* 50, 41–55. doi: 10.1016/j.actbio.2016.12.034
- Khalf, A., and Madhally, S. V. (2017). Recent advances in multiaxial electrospinning for drug delivery. *Eur. J. Pharm. Biopharm.* 112, 1–17. doi: 10.1016/j.ejpb.2016.11.010
- Khandaker, M., Li, Y., and Morris, T. (2013). Micro and nano MgO particles for the improvement of fracture toughness of bone-cement interfaces. *J. Biomech.* 46, 1035–1039. doi: 10.1016/j.jbiomech.2012.12.006
- Larsson, L., Decker, A. M., Nibali, L., Pilipchuk, S. P., Berglundh, T., and Giannobile, W. V. (2016). Regenerative medicine for periodontal and peri-implant diseases. *J. Dent. Res.* 95, 255–266. doi: 10.1177/0022034515618887
- Lee, S., Matsugaki, A., Kasuga, T., and Nakano, T. (2019). Development of bifunctional oriented bioactive glass/poly(lactic acid) composite scaffolds to control osteoblast alignment and proliferation. *J. Biomed. Mater. Res. A* 107, 1031–1041. doi: 10.1002/jbm.a.36619
- Leem, Y. H., Lee, K. S., Kim, J. H., Seok, H. K., Chang, J. S., and Lee, D. H. (2016). Magnesium ions facilitate integrin alpha 2- and alpha 3-mediated proliferation and enhance alkaline phosphatase expression and activity in hBMSCs. *J. Tissue Eng. Regen. Med.* 10, E527–E536. doi: 10.1002/term.1861
- Li, C., Sun, J., Shi, K., Long, J., Li, L., Lai, Y., et al. (2020). Preparation and evaluation of osteogenic nano-MgO/PMMA bone cement for bone healing in a rat critical size calvarial defect. *J. Mater. Chem. B* 8, 4575–4586. doi: 10.1039/d0tb00074d
- Li, L., He, Z. Y., Wei, X. W., and Wei, Y. Q. (2016). Recent advances of biomaterials in biotherapy. *Regen. Biomater.* 3, 99–105. doi: 10.1093/rb/rbw007
- Li, X., Kanjwal, M. A., Lin, L., and Chronakis, I. S. (2013). Electrospun polyvinyl-alcohol nanofibers as oral fast-dissolving delivery system of caffeine and riboflavin. *Colloids Surf. B Biointerfaces* 103, 182–188. doi: 10.1016/j.colsurfb.2012.10.016
- Liang, Y., Luan, X., and Liu, X. (2020). Recent advances in periodontal regeneration: a biomaterial perspective. *Bioact. Mater.* 5, 297–308. doi: 10.1016/j.bioactmat.2020.02.012
- Lim, S. H., and Mao, H. Q. (2009). Electrospun scaffolds for stem cell engineering. *Adv. Drug Deliv. Rev.* 61, 1084–1096. doi: 10.1016/j.addr.2009.07.011
- Lin, N., Micanin, D., Mrozik, K., Gronthos, S., and Bartold, P. (2008). Putative stem cells in regenerating human periodontium. *J. Periodontol. Res.* 43, 514–523. doi: 10.1111/j.1600-0765.2007.01061.x
- Lin, Z., Wu, J., Qiao, W., Zhao, Y., Wong, K. H. M., Chu, P. K., et al. (2018). Precisely controlled delivery of magnesium ions thru sponge-like monodisperse PLGA/nano-MgO-alginate core-shell microsphere device to enable in-situ bone regeneration. *Biomaterials* 174, 1–16. doi: 10.1016/j.biomaterials.2018.05.011
- Liu, J., Ruan, J., Weir, M. D., Ren, K., Schneider, A., Wang, P., et al. (2019). Periodontal bone-ligament-cementum regeneration via scaffolds and stem cells. *Cells* 8:537. doi: 10.3390/cells8060537
- Liu, W., Zou, Z., Zhou, L., Liu, H., Wen, W., Zhou, C., et al. (2019). Synergistic effect of functionalized poly(L-lactide) with surface-modified MgO and chitin whiskers on osteogenesis in vivo and in vitro. *Mater. Sci. Eng. C Mater. Biol. Appl.* 103:109851. doi: 10.1016/j.msec.2019.109851
- Liu, X., He, X., Jin, D., Wu, S., Wang, H., Yin, M., et al. (2020). A biodegradable multifunctional nanocellulose membrane for periodontal tissue regeneration. *Acta Biomater.* 108, 207–222. doi: 10.1016/j.actbio.2020.03.044
- Liu, Z., Tang, M., Zhao, J., Chai, R., and Kang, J. (2018). Looking into the future: toward advanced 3D biomaterials for stem-cell-based regenerative medicine. *Adv. Mater.* 30:e1705388. doi: 10.1002/adma.201705388
- Lu, Y., Tao, P., Zhang, N., and Nie, S. (2020). Preparation and thermal stability evaluation of cellulose nanofibrils from bagasse pulp with differing hemicelluloses contents. *Carbohydr. Polym.* 245:116463. doi: 10.1016/j.carbpol.2020.116463
- Mangalampalli, B., Dumala, N., Perumalla Venkata, R., and Grover, P. (2018). Genotoxicity, biochemical, and biodistribution studies of magnesium oxide nano and microparticles in albino wistar rats after 28-day repeated oral exposure. *Environ. Toxicol.* 33, 396–410. doi: 10.1002/tox.22526
- Meireles, A. B., Correa, D. K., da Silveira, J. V., Millas, A. L., Bittencourt, E., de Brito-Melo, G. E., et al. (2018). Trends in polymeric electrospun fibers and their use as oral biomaterials. *Exp. Biol. Med. (Maywood)* 243, 665–676. doi: 10.1177/1535370218770404
- Monzavi, A., Eshraghi, S., Hashemian, R., and Momen-Heravi, F. (2014). In vitro and ex vivo antimicrobial efficacy of nano-MgO in the elimination of endodontic pathogens. *Clin. Oral Investig.* 19, 349–356. doi: 10.1007/s00784-014-1253-y
- Naahidi, S., Jafari, M., Logan, M., Wang, Y., Yuan, Y., Bae, H., et al. (2017). Biocompatibility of hydrogel-based scaffolds for tissue engineering applications. *Biotechnol. Adv.* 35, 530–544. doi: 10.1016/j.biotechadv.2017.05.006
- Needleman, I., Worthington, H. V., Giedrys-Leeper, E., and Tucker, R. (2019). WITHDRAWN: guided tissue regeneration for periodontal infra-bony defects. *Cochrane Database Syst. Rev.* 5:CD001724. doi: 10.1002/14651858.CD001724.pub3
- Ng, J., Hynes, K., White, G., Sivanathan, K., Vandyke, K., Bartold, P., et al. (2016). Immunomodulatory properties of induced pluripotent stem cell-derived mesenchymal cells. *J. Cell. Biochem.* 117, 2844–2853. doi: 10.1002/jcb.25596
- Nguyen, N.-Y. T., Grelling, N., Wetteland, C. L., Rosario, R., and Liu, H. (2018). Antimicrobial activities and mechanisms of magnesium oxide nanoparticles (nMgO) against pathogenic bacteria, yeasts, and biofilms. *Sci. Rep.* 8:16260. doi: 10.1038/s41598-018-34567-5
- Nie, S., Fu, Q., Lin, X., Zhang, C., Lu, Y., and Wang, S. (2021). Enhanced performance of a cellulose nanofibrils-based triboelectric nanogenerator by tuning the surface polarizability and hydrophobicity. *Chem. Eng. J.* 404:126512. doi: 10.1016/j.cej.2020.126512
- Nie, S., Zhang, C., Zhang, Q., Zhang, K., Zhang, Y., Tao, P., et al. (2018a). Enzymatic and cold alkaline pretreatments of sugarcane bagasse pulp to produce cellulose nanofibrils using a mechanical method. *Ind. Crops Prod.* 124, 435–441. doi: 10.1016/j.indcrop.2018.08.033
- Nie, S., Zhang, K., Lin, X., Zhang, C., Yan, D., Liang, H., et al. (2018b). Enzymatic pretreatment for the improvement of dispersion and film properties of cellulose nanofibrils. *Carbohydr. Polym.* 181, 1136–1142. doi: 10.1016/j.carbpol.2017.11.020
- Onder, S., Calikoglu-Koyuncu, A. C., Kazmanli, K., Urgen, M., Kok, F. N., and Torun-Kose, G. (2018). Magnesium doping on TiN coatings affects mesenchymal stem cell differentiation and proliferation positively in a dose-dependent manner. *Biomed. Mater. Eng.* 29, 427–438. doi: 10.3233/BME-181000
- Oortgiesen, D. A. W., Plachokova, A. S., Geenen, C., Meijer, G. J., Walboomers, X. F., van den Beucken, J. J. P., et al. (2012). Alkaline phosphatase immobilization onto Bio-Gide® and Bio-Oss® for periodontal and bone regeneration. *J. Clin. Periodontol.* 39, 546–555. doi: 10.1111/j.1600-051X.2012.01877.x
- Pant, B., Park, M., and Park, S. J. (2019). Drug delivery applications of core-sheath nanofibers prepared by coaxial electrospinning: a review. *Pharmaceutics* 11:305. doi: 10.3390/pharmaceutics11070305
- Parham, S., Kharazi, A. Z., Bakhsheshi-Rad, H. R., Ghayour, H., Ismail, A. F., Nur, H., et al. (2020). Electrospun nano-fibers for biomedical and tissue engineering applications: a comprehensive review. *Materials (Basel)* 13:2153. doi: 10.3390/ma13092153
- Pei, W., Chen, Z. S., Chan, H. Y. E., Zheng, L., Liang, C., and Huang, C. (2020). Isolation and identification of a novel anti-protein aggregation activity of lignin-carbohydrate complex from *Chionanthus retusus* leaves. *Front. Bioeng. Biotechnol.* 8:573991. doi: 10.3389/fbioe.2020.573991
- Prado-Prone, G., Silva-Bermudez, P., Bazzar, M., Focarete, M. L., Rodil, S. E., Vidal-Gutierrez, X., et al. (2020). Antibacterial composite membranes of polycaprolactone/gelatin loaded with zinc oxide nanoparticles for guided tissue regeneration. *Biomed. Mater.* 15:035006. doi: 10.1088/1748-605X/ab70ef
- Qian, Y., Zhou, X., Zhang, F., Diekwisch, T. G. H., Luan, X., and Yang, J. (2019). Triple PLGA/PCL scaffold modification including silver impregnation, collagen coating, and electrospinning significantly improve biocompatibility, antimicrobial, and osteogenic properties for orofacial tissue regeneration. *ACS Appl. Mater. Interfaces* 11, 37381–37396. doi: 10.1021/acsami.9b07053

- Ren, K., Wang, Y., Sun, T., Yue, W., and Zhang, H. (2017). Electrospun PCL/gelatin composite nanofiber structures for effective guided bone regeneration membranes. *Mater. Sci. Eng. C Mater. Biol. Appl.* 78, 324–332. doi: 10.1016/j.msec.2017.04.084
- Seo, B.-M., Miura, M., Gronthos, S., Mark Bartold, P., Batouli, S., Brahim, J., et al. (2004). Investigation of multipotent postnatal stem cells from human periodontal ligament. *Lancet* 364, 149–155. doi: 10.1016/S0140-6736(04)16627-0
- Shkodenko, L., Kassirov, I., and Koshel, E. (2020). Metal oxide nanoparticles against bacterial biofilms: perspectives and limitations. *Microorganisms* 8:1545. doi: 10.3390/microorganisms8101545
- Si, J., Cui, Z., Wang, Q., Liu, Q., and Liu, C. (2016). Biomimetic composite scaffolds based on mineralization of hydroxyapatite on electrospun poly(ϵ -caprolactone)/nanocellulose fibers. *Carbohydr. Polym.* 143, 270–278. doi: 10.1016/j.carbpol.2016.02.015
- Sridhar, R., Lakshminarayanan, R., Madhaiya, K., Veluchamy, A. B., Lim, K. H. C., Ramakrishna, S., et al. (2014). Electrospun nanoparticles and electrospun nanofibers based on natural materials- applications in tissue regeneration, drug delivery and pharmaceuticals. *Chem. Soc. Rev.* 44:790–814. doi: 10.1039/c4cs00226a
- Stavropoulos, A., Bertl, K., Spineli, L. M., Sculean, A., Cortellini, P., and Tonetti, M. (2020). Medium- and long-term clinical benefits of periodontal regenerative/reconstructive procedures in intrabony defects: systematic review and network meta-analysis of randomized controlled clinical studies. *J. Clin. Periodontol.* 48:410–430. doi: 10.1111/jcpe.13409
- Suryavanshi, A., Khanna, K., Sindhu, K. R., Bellare, J., and Srivastava, R. (2017). Magnesium oxide nanoparticle-loaded polycaprolactone composite electrospun fiber scaffolds for bone-soft tissue engineering applications: in-vitro and in-vivo evaluation. *Biomed. Mater.* 12:055011. doi: 10.1088/1748-605X/aa792b
- Szentivanyi, A., Chakradeo, T., Zernetsch, H., and Glasmacher, B. (2011). Electrospun cellular microenvironments: understanding controlled release and scaffold structure. *Adv. Drug Deliv. Rev.* 63, 209–220. doi: 10.1016/j.addr.2010.12.002
- Wang, J., Ma, X.-Y., Feng, Y.-F., Ma, Z.-S., Ma, T.-C., Zhang, Y., et al. (2017). Magnesium ions promote the biological behaviour of rat calvarial osteoblasts by activating the PI3K/Akt signalling pathway. *Biol. Trace Elem. Res.* 179, 284–293. doi: 10.1007/s12011-017-0948-8
- Wang, J., and Windbergs, M. (2019). Controlled dual drug release by coaxial electrospun fibers – impact of the core fluid on drug encapsulation and release. *Int. J. Pharm.* 556, 363–371. doi: 10.1016/j.ijpharm.2018.12.026
- Wang, P., Yin, B., Dong, H., Zhang, Y., Zhang, Y., Chen, R., et al. (2020). Coupling biocompatible au nanoclusters and cellulose nanofibrils to prepare the antibacterial nanocomposite films. *Front. Bioeng. Biotechnol.* 8:986. doi: 10.3389/fbioe.2020.00986
- Wang, Z., Liu, Q., Liu, C., Tan, W., Tang, M., Zhou, X., et al. (2020). Mg(2+) in beta-TCP/Mg-Zn composite enhances the differentiation of human bone marrow stromal cells into osteoblasts through MAPK-regulated Runx2/Osx. *J. Cell. Physiol.* 235, 5182–5191. doi: 10.1002/jcp.29395
- Xiang, Z., Jin, X., Huang, C., Li, L., Wu, W., Qi, H., et al. (2020). Water cast film formability of sugarcane bagasse xylans favored by side groups. *Cellulose* 27, 7307–7320. doi: 10.1007/s10570-020-03291-7
- Xue, J., He, M., Liu, H., Niu, Y., Crawford, A., Coates, P. D., et al. (2014). Drug loaded homogeneous electrospun PCL/gelatin hybrid nanofiber structures for anti-infective tissue regeneration membranes. *Biomaterials* 35, 9395–9405. doi: 10.1016/j.biomaterials.2014.07.060
- Yoshizawa, S., Brown, A., Barchowsky, A., and Sfeir, C. (2014). Magnesium ion stimulation of bone marrow stromal cells enhances osteogenic activity, simulating the effect of magnesium alloy degradation. *Acta Biomater.* 10, 2834–2842. doi: 10.1016/j.actbio.2014.02.002
- Yue, K., Trujillo-de Santiago, G., Alvarez, M. M., Tamayol, A., Annabi, N., and Khademhosseini, A. (2015). Synthesis, properties, and biomedical applications of gelatin methacryloyl (GelMA) hydrogels. *Biomaterials* 73, 254–271. doi: 10.1016/j.biomaterials.2015.08.045
- Zhang, X., Zu, H., Zhao, D., Yang, K., Tian, S., Yu, X., et al. (2017). Ion channel functional protein kinase TRPM7 regulates Mg ions to promote the osteoinduction of human osteoblast via PI3K pathway: in vitro simulation of the bone-repairing effect of Mg-based alloy implant. *Acta Biomater.* 63, 369–382. doi: 10.1016/j.actbio.2017.08.051
- Zhang, Y., Wang, P., Mao, H., Zhang, Y., Zheng, L., Yu, P., et al. (2021). PEGylated gold nanoparticles promote osteogenic differentiation in in vitro and in vivo systems. *Mater. Des.* 197:109231. doi: 10.1016/j.matdes.2020.109231
- Zheng, L., Yu, P., Zhang, Y., Wang, P., Yan, W., Guo, B., et al. (2021). Evaluating the bio-application of biomacromolecule of lignin-carbohydrate complexes (LCC) from wheat straw in bone metabolism via ROS scavenging. *Int. J. Biol. Macromol.* 176, 13–25. doi: 10.1016/j.ijbiomac.2021.01.103
- Zwahlen, R. A., Cheung, L. K., Zheng, L. W., Chow, R. L., Li, T., Schuknecht, B., et al. (2009). Comparison of two resorbable membrane systems in bone regeneration after removal of wisdom teeth: a randomized-controlled clinical pilot study. *Clin. Oral Implants Res.* 20, 1084–1091. doi: 10.1111/j.1600-0501.2009.01751.x

Conflict of Interest: The authors declare that the research was conducted in the absence of any commercial or financial relationships that could be construed as a potential conflict of interest.

Copyright © 2021 Peng, Ren, Zhang, Fan, Zhou, Li, Xu and Xu. This is an open-access article distributed under the terms of the Creative Commons Attribution License (CC BY). The use, distribution or reproduction in other forums is permitted, provided the original author(s) and the copyright owner(s) are credited and that the original publication in this journal is cited, in accordance with accepted academic practice. No use, distribution or reproduction is permitted which does not comply with these terms.



Cellulose Isolated From Waste Rubber Wood and Its Application in PLA Based Composite Films

Zhiqiang Ou^{1,2}, Qi Zhou^{1,2}, Xin Rao^{1,2}, Haifeng Yang^{1,2}, Chunqing Huo³ and Xueyu Du^{1,2*}

¹ Hainan Provincial Fine Chemical Engineering Research Center, Hainan University, Haikou, China, ² Hainan Provincial Key Laboratory of Fine Chemicals, Hainan University, Haikou, China, ³ School of Materials Science and Engineering, Hainan University, Haikou, China

OPEN ACCESS

Edited by:

Caoxing Huang,
Nanjing Forestry University, China

Reviewed by:

Weijun Yang,
Jiangnan University, China
Javier Ulises Hernández Beltrán,
Universidad Autónoma de Coahuila,
Mexico

*Correspondence:

Xueyu Du
duxueyu@hainanu.edu.cn

Specialty section:

This article was submitted to
Bioprocess Engineering,
a section of the journal
Frontiers in Bioengineering and
Biotechnology

Received: 10 February 2021

Accepted: 10 March 2021

Published: 31 March 2021

Citation:

Ou Z, Zhou Q, Rao X, Yang H,
Huo C and Du X (2021) Cellulose
Isolated From Waste Rubber Wood
and Its Application in PLA Based
Composite Films.
Front. Bioeng. Biotechnol. 9:666399.
doi: 10.3389/fbioe.2021.666399

Waste rubber wood (RW) is the castoff of rubber plantation with abundant reservation but without high-value utilization. In this study, cellulose with high purity has been efficiently isolated from waste RW and further processed into cellulose nanocrystals. By means of acetylation, more hydrophobic cellulose-based products, namely acetylated rubber wood cellulose (Ac-RWC) and acetylated rubber wood cellulose nanocrystals (Ac-RW-CNC) had been attempted as reinforcing fillers for fabricating two series of PLA-based composite films *via* spin coating instead of currently prevailing melt compounding technique. To ensure a uniformed dispersion of fillers in PLA matrix, the addition of reinforcing filler should be equal to or less than 5% based on the film dry weight. Compared with pure PLA film, the Ac-RWC reinforced PLA composite films are more thermally stable, while the Ac-RW-CNC reinforced PLA composite films on the other hand exhibit more enhanced performance in mechanical properties and the degree of crystallinity. The highest tensile strength (55.0 MPa) and Young's modulus (3.9 GPa) were achieved for 5%Ac-RW-CNC/PLA composite film.

Keywords: rubber wood cellulose, cellulose nanocrystals, acetylation, polylactic acid, composite film

INTRODUCTION

Under the requirements of environment protection and sustainable development, large-scale limitation or complete prohibition of disposable plastic products has been implemented by an increasing number of countries and regions (Niu et al., 2018). As promising alternatives of fossil-based plastics, polylactic acid (PLA) along with other well-known biodegradable polymers (e.g., polyvinyl alcohol, polycaprolactone, polyhydroxybutyrate, etc.) have attracted extensive attention in recent years (Chen et al., 2003; Avinc and Khoddami, 2010; Abdulkhani et al., 2014; Niu et al., 2018; Mosnackova et al., 2020). PLA is defined as a linear aliphatic polyester that is mainly manufactured by ring opening polymerization of lactide in industry. Although numerous merits (e.g., non-toxicity, non-irritation, biodegradability, good processability, comparable mechanical properties, etc.) guarantee its critical status both in academia and industry (Abdulkhani et al., 2014; Murariu and Dubois, 2016; Santoro et al., 2016; Tajbakhsh and Hajiali, 2017; Niu et al., 2018), poor thermal stability, high brittleness, and limited gas barrier property are still the limiting factors of PLA in packaging field (Abdulkhani et al., 2014; Liu et al., 2014).

To further remedy the property-limitation mentioned above, blending PLA matrix with natural polymers *via* either melt compounding or solvent casting has been adopted as the feasible pathways

and many efforts have been carried out accordingly (Oksman et al., 2006; Bondeson and Oksman, 2007; Jonoobi et al., 2012). The characteristics of natural polymers (e.g., cellulose, starch, etc.) not only meet the basic requirements of green and sustainable chemistry (e.g., biodegradability, renewability, and cost-effectiveness), but would also endow the ultimate PLA-based bio-composites with improved mechanical properties, thermal stability, and flexibility (Kamal and Khoshkava, 2015; Niu et al., 2018). To date, numerous species of lignocellulosic wastes (e.g., bagasse, cornstalk, coconut husk, etc.) have been attempted for isolation of cellulose (Ditzel et al., 2017; Tuerxun et al., 2019; Wu et al., 2019; Ejaz et al., 2020; Kian et al., 2020; Wang H. et al., 2020) and meanwhile the obtained cellulose could be further processed for high-value utilization.

As a high value-added product disintegrated from cellulose, cellulose nanocrystals (CNCs) possess low density, high crystallinity, and superior stiffness, which are therefore can be employed as a highly promising reinforcement filler for PLA-based films (Ditzel et al., 2017; Tuerxun et al., 2019; Kian et al., 2020). However, the hydrophilic CNCs are theoretically difficult to be uniformly dispersed within the hydrophobic matrix of PLA, for their limited interfacial compatibility (Sullivan et al., 2015; Dong et al., 2017). Proper surface modifications *via* acetylation or silylation are thus motivated to convert hydrophilic hydroxyls of CNC into more hydrophobic functional groups (Kamal and Khoshkava, 2015). In this manner, the partial loss of thermal stability from high crystalline CNC would be timely remedied by the reinforced interfacial interactions between acetylated CNCs and PLA molecular chains.

Rubber tree is one type of important industrial plant resources, which plays a significant role in communication and military industries (Li et al., 2013). Hainan is the largest production base of natural rubber in China and annually a vast amount of rubber wood (RW) wastes from both rubber plantation and rubber processing industry has been generated without efficient utilization. Therefore, rational development of this type of cellulose-rich feedstock not only mitigates the atmospheric pollution caused by conventional incineration of lignocellulosic wastes, but also excavates the intrinsic value of natural polymers present in biomass wastes for conversion of high value-added products (Abdulkhani et al., 2014; Wu et al., 2019; Wang H. et al., 2020).

The aim of the present study is to realize the high value utilization of rubber wood cellulose (RWC) by developing two binary bio-composite film systems composed of acetylated cellulose-based filler and PLA matrix. Moreover, spin coating technique was employed to overcome the drawbacks such as low dispersibility and high energy cost brought about by solvent casting and melt compounding, respectively. Meanwhile, whether the acetylated cellulose-based filler would eventually strengthen interfacial interactions with hydrophobic PLA molecular chains during the process of spin coating will be evaluated. On the basis of comprehensive characterization of various RWC-based products by means of FTIR, XRD, SEM, TEM, and TGA, two sets of PLA-based composite films had been designed, denoted as acetylated rubber wood cellulose reinforced PLA (Ac-RWC/PLA) composite films and acetylated rubber

wood cellulose nanocrystal reinforced PLA (Ac-RW-CNC/PLA) composite films. The performance of different film products had been further evaluated and compared in term of their mechanical properties, surface morphology, thermal stability, crystallization behavior, and light transparency.

MATERIALS AND METHODS

Materials

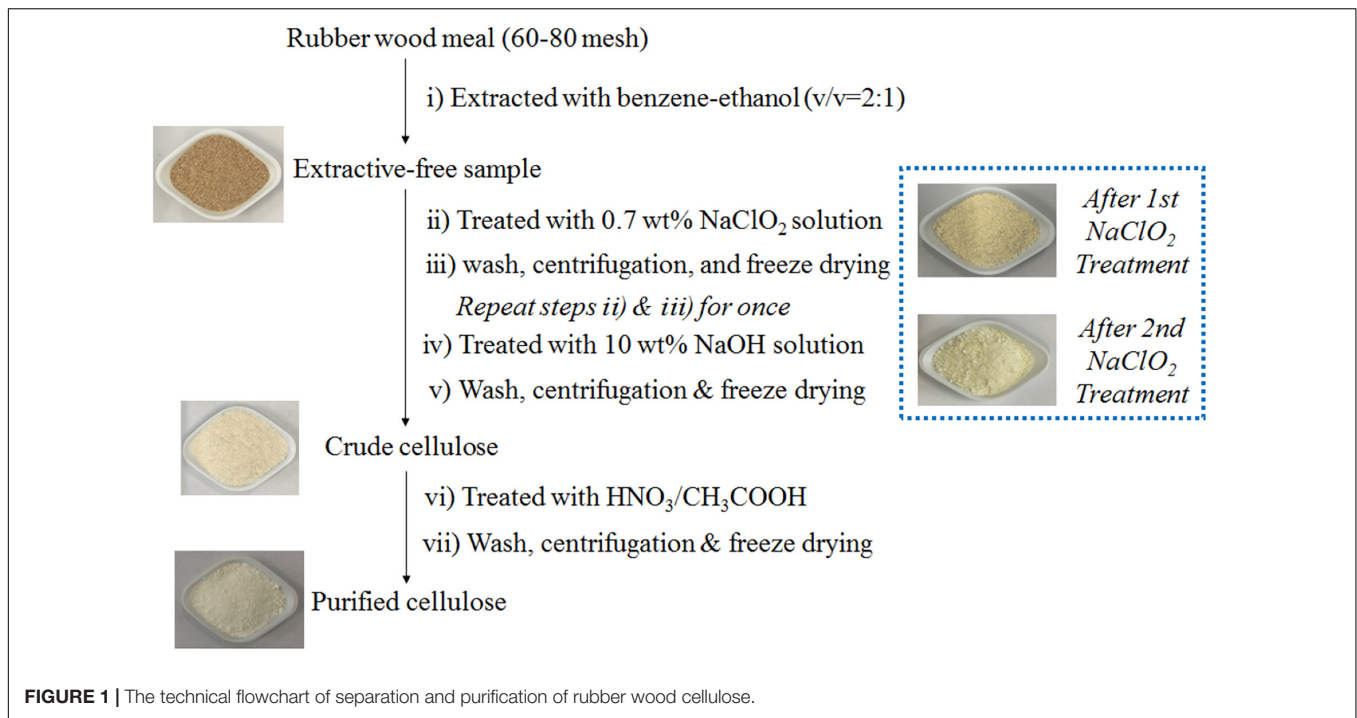
Rubber wood (RW) waste was collected from a local rubber plantation in Hainan, China. Commercial polylactic acid (Ingeo 4032D) with density of 1.24 g/cm³ was provided by Yeqiang Plastic Materials Co., Ltd. (Dongguan, China). Sodium chlorite, sodium hydroxide, and acetic acid were purchased from Aladdin Co., Ltd. Acetic anhydride was supplied from Guangzhou Chemical Reagent Co., Ltd. Benzene, ethanol, and other chemicals were provided by Macklin Co., Ltd. Deionized water was used for all the experiments.

Separation and Purification of Rubber Wood Cellulose

Rubber wood cellulose with high purity was isolated following successive treatments of extractives removal, delignification, and residual lignin removal. The entire technical flowchart was presented in **Figure 1**. In brief, the clean and pre-cut RW chips (around 0.4 cm × 0.8 cm) were disintegrated into the size of 60~80 mesh by using a FZ102 plant mini-mill (Taisite Instrument Ltd., China). Then the milled wood meal was extracted with benzene-ethanol (v/v = 2:1) for 24 h by using a Soxhlet extractor for thorough removal of extractives. Charge given amounts of extractive-free sample and 0.7 wt% sodium chlorite aqueous solution into a flask equipped with a reflux condenser, and mix the suspension under magnetic stirring. The solid-liquid ratio was set as 1:60 and the pH value of the suspension was adjusted to four by addition of 10 wt% acetic acid aqueous solution. The subsequent sodium chlorite (0.7 wt%) treatment proceeded under 85°C for 120 min and the residue was thoroughly washed with deionized water and centrifugated prior to a repeated run of the above sodium chlorite delignification step. After a further extraction step with 10 wt% sodium hydroxide aqueous solution, the crude cellulose was reclaimed by deionized water rinsing, centrifugation, and freeze drying. The ultimate purified cellulose was acquired by means of a core treatment step consisting of 68 wt% nitric acid aqueous solution and 80 wt% acetic acid aqueous solution as well as the following impurity removal and freeze-drying. The related operating parameters are listed as follows: V_{68 wt% HNO₃}:V_{80 wt% HNO₃} is 1:9; sample-mixed acids solution ratio is 1:20; treatment temperature is 120°C; treatment time is 15 min.

Preparation of Rubber Wood Cellulose Nanocrystals

One gram purified RWC and 10 mL 64 wt% sulfuric acid solution were introduced into a 50 mL conical flask sealed with a glass stopper. The acid hydrolysis was carried out at 50°C for 1 h under



magnetic stirring and the reaction was quenched by dilution of excess deionized water. After thorough rinsing under vacuum filtration, the wet cake together with 50 mL deionized water was transferred into a double-layered glass cup that was connected with a recirculating cooler. Once the temperature cooled down to 4°C, the slurry was intermittently treated by a JY98-IIIIL sonicator (Dekelaier Instrument Ltd., China) under the power of 1,200 W. A single cycle of sonication (5 s) includes 1 s of sonication and 4 s of pause, and the accumulated sonication time is 20 min. The rubber wood cellulose nanocrystals (RW-CNC) were then reclaimed by dialysis and freeze drying of the resultant slurry and kept in a desiccator for future use.

Acetylation of RWC and RW-CNC

Pre-submerge 2 g RWC in 50 mL acetic acid at 50°C under magnetic stirring for 30 min. Then charge 10 mL acetic anhydride and 10 μL 98 wt% sulfuric acid into the suspension and keep the reaction under 90°C for 180 min with continuous stirring. When the time was due, quench the reaction with 75% ethanol and collect the precipitate by vacuum filtration. After thorough rinse with deionized water and lyophilization, acetylated RWC (Ac-RWC) was reclaimed and kept in a desiccator for future use. The procedure for preparation of acetylated RW-CNC (Ac-RW-CNC) was similar as the case of acetylation of RWC except a smaller amount (0.5 g) of the starting material.

Chemical Composition Analysis

The contents of extractives, ash, Klason lignin, and acid soluble lignin were determined according to TAPPI standard methods, namely TAPPI T204 cm-97, TAPPI T211 om-07, TAPPI T222 om-06, and TAPPI UM 250. The carbohydrate analysis was

carried out following the standard procedure of TAPPI T222 om-02. Each measurement was performed in duplicate.

Preparation of the Composite Films

Fully dissolve a given amount of Ac-RWC or Ac-RW-CNC in a PLA containing dichloromethane solution and set the obtained solution still for a while to remove residual air bubbles. The composite films were fabricated by using a KW-4A spin coater (Institute of Microelectronics of the Chinese Academy of Sciences, China). Briefly, the solution was dropped slowly onto a clean square polyethylene substrate. The initial spin speed was set as 600 rpm for 6 s, and then followed by 3,000 rpm for 40 s. Detach the substrate and place it horizontally in hood for 48 h to fully evaporate dichloromethane. Peel the film from the substrate and keep it in a plastic bag for future analysis.

Characterization

Fourier Transform Infrared Spectroscopy

The FTIR spectra of five different fiber samples, denoted as RW, RWC, RW-CNC, Ac-RWC, and Ac-RW-CNC were illustrated by applying a Bruker Tensor 27 FTIR spectrometer. Each spectrum was recorded from 4,000 to 500 cm⁻¹ with 32 scans at a resolution of 4 cm⁻¹.

X-ray Diffraction Analysis

Five different fiber samples were analyzed by using a Rigaku Smart Lab X-ray diffractometer equipped with a Ni-filtered CuKα radiation at 30 mA and 40 kV. Each XRD pattern was plotted from 5° to 40° and the scanning rate was 5°/min. The sample crystallinity was estimated according to the method established by Segal et al. (1959).

Determination of Zeta Potential

Zeta potential of RW–CNC dispersed in its sonicated suspension was characterized by using a Zetasizer Nano ZS90 (Malvern Instruments Ltd., United Kingdom). Each measurement was performed in triplicate.

Morphology Characterization

A Phenom ProX scanning electron microscopy (Phenom–World BV, Netherlands) with an accelerating voltage of 5 kV was employed for observing the surface morphology of RW and RWC, while the cross sections of different films were observed by a SU8020 scanning electron microscopy (Hitachi, Japan) at an accelerating voltage of 3 kV. The morphology of RW–CNC was characterized by applying a JEM1200EX transmission electron microscope (JEOL, Japan) and the accelerating voltage was 100 kV. The diameter and length distribution of RW–CNC were determined according to a previously published method (Han et al., 2013).

Thermal Stability

The thermal stability of different test samples were evaluated by a NETZSCH STA 449 F5 thermogravimetric analyzer and the measuring temperature was programed from 30 to 600°C under a heating rate of 10°C/min. The flow rate of nitrogen was set as 40 mL/min.

Mechanical Properties

An Instron 3343 long travel extensometer was applied for measuring the tensile strength and Young's modulus of different films. The test specimens were pre-cut into stripes (50 mm × 10 mm) and five replicates for each measurement were carried out.

Differential Scanning Calorimetry

Thermal behavior of different films was analyzed by applying a differential scanning calorimeter (Q200, TA Instruments Inc., United States). Around 3 mg sample was sealed in an aluminum pan using a sealed empty pan as the reference. In nitrogen atmosphere, the first heating scan was programmed from 20 to 200°C at a heating rate of 10°C/min and held at 200°C for 5 min. Then the temperature was cooled down back to 20°C at the same rate. The second heating scan was carried out afterward from 20 to 200°C at a rate of 10°C/min. The glass transition temperature (T_g) was measured from the thermogram of first heating scan, while other thermal parameters including cold crystallization temperature (T_{cc}), melting temperature (T_m), and enthalpy of cold crystallization (ΔH_{cc}) and melting (ΔH_m) were obtained from the thermographs of second heating scan. Subsequently, the crystallinity of film specimen (X_c) was estimated according to an early documented method (Fischer et al., 1973; Sullivan et al., 2015).

Light Transmittance

An ultraviolet-visible spectrophotometer (UV-3600 Plus, Shimadzu, Japan) was selected for determination of light transmittance of different film specimens. The wavelength range of incident light is from 200 to 800 nm.

RESULTS AND DISCUSSION

Chemical Composition of Rubber Wood and Rubber Wood Cellulose

According to the results of composition analysis, RW can be regarded as an ideal source of cellulose, for its high content of glucan (52.8%) based on the dry weight of the starting material (Table 1). Besides fairly low contents of extractives (1.9%) and ash (1.5%), RW contains moderate amount of lignin (20.8% in total) that is summed up by 18.9% of Klason lignin and 1.9% acid soluble lignin. Xylan and mannan are the only two detected types of hemicellulose, whose contents are 18.0 and 2.2%, respectively. The isolation and purification of RWC is quite efficient, since extractives, ash content, and lignin cannot be detected by using traditional quantification methods. The final yield of purified RWC is 34.7% based on the extractive-free raw materials. Furthermore, the purified RWC is highly rich in glucan (91.3%) with a minor portion of xylan (2.2%) and mannan (2.6%), and these values are close to the results published early (Tuerxun et al., 2019).

FTIR Spectroscopy Analysis of Different Fiber-Based Samples

The FTIR spectra of five different fiber-based samples were demonstrated in Figure 2, the broad adsorption peaks locating around 3,440 cm^{-1} of all samples are originated from O–H stretching vibration of hydroxyls, whose intensity has been evidently weakened in the cases of Ac–RWC and Ac–RW–CNC owing to their reduced numbers of hydroxyl groups. The characteristic adsorption bands at 2,905 cm^{-1} stem from C–H stretching vibrations of methyl and methylene groups (Uma Maheswari et al., 2012). The presence of adsorption peak at 1,739 cm^{-1} is contributed by C = O stretching vibration of original acetyl groups from hemicellulose and carbonyl groups from lignin. However, this band turns out to be diminished, ascribed to the removal of hemicellulose and lignin in RWC. The effective delignification of RWC is also in conformity with the disappearance of aromatic ring skeletal vibration at 1,507 cm^{-1} (Chen et al., 2011; Ditzel et al., 2017). Moisture content present in sample also result in adsorptions around 1,637 cm^{-1} , which is in line with a previous study published elsewhere (Reddy et al., 2018). Compared with RWC and RW–CNC, the extensively strengthened adsorptions at 1,754 cm^{-1} and 1,235 cm^{-1} in their respective acetylated product refer to C = O stretching vibration and C–O–C stretching vibration of acetyl groups. In addition, the increment of –CH₃ from acetyl groups also accounts for the reinforced intensity of C–H bending vibration at 1,370 cm^{-1} . The characteristic adsorption bands of cellulose locating at 1,163, 1,056, and 897 cm^{-1} are observed for all test samples (Pappas et al., 2002; Sun et al., 2004).

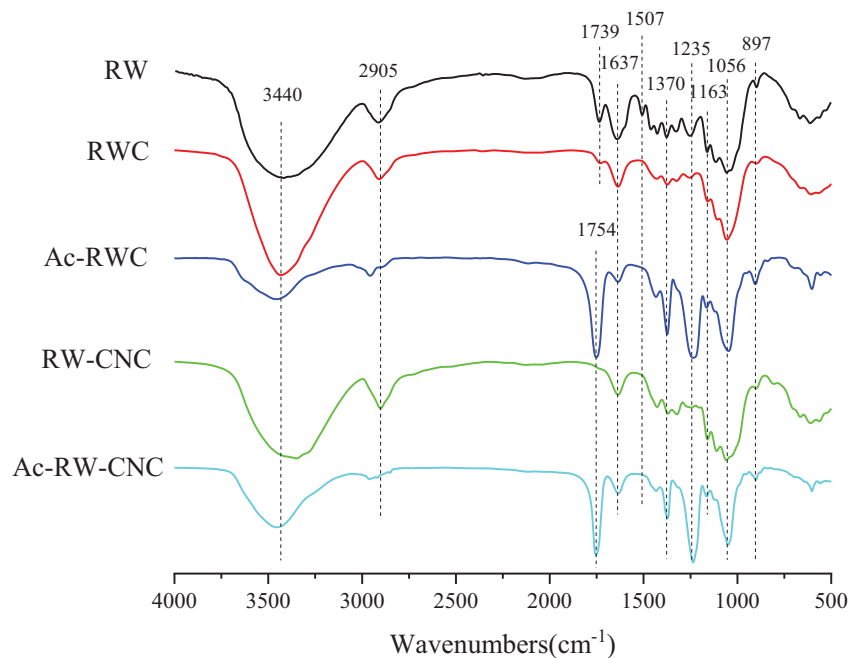
X-ray Diffraction Analysis of Different Fiber-Based Samples

The X-ray diffraction patterns of RW, RWC, and RW–CNC are quite similar, in accordance with the pattern of cellulose I (Figure 3). The signals ranging from 13° to 18° are originated

TABLE 1 | Chemical composition analysis of RW and purified RWC.

Samples	Extractives (%)	Ash content (%)	Klason lignin (%)	Acid soluble lignin (%)	Glucan (%)	Xylan (%)	Mannan (%)
RW	1.9 ± 0.2	1.5 ± 0.1	18.9 ± 0.4	1.9 ± 0.1	52.8 ± 1.2	18.0 ± 0.5	2.2 ± 0.2
RWC	ND ^a	ND ^a	ND ^a	ND ^a	91.3 ± 1.4	2.2 ± 0.1	2.6 ± 0.1

^aND: not detectable.

**FIGURE 2** | FTIR spectra of RW, RWC, Ac-RWC, RW-CNC, and Ac-RW-CNC.

from 101 and 10i planes of cellulose, and the relatively reinforced peak locating around 22° is overlapped by signals of 021 and 002 planes. A solely emerged peak at 34.5° refers to the signal of 040 plane. Although demonstrating analogous X-ray diffraction patterns, these three samples mentioned above still differ in crystallinity. RW, for instance, possesses relatively low crystallinity as 43.0% owing to the existence of moderate amounts of lignin and hemicellulose whose structure are more prone to be amorphous. After effective removal of lignin and majority of hemicellulose, the crystallinity of RWC reaches 65.0%, and this value further climbs up to 74.1% for RW-CNC, since the amorphous domains in RWC had been digested severely during 64 wt% sulfuric acid hydrolysis.

The crystal forms of different fiber samples vary according to their degrees of acetylation. During the early stage of acetylation, the reaction occurred preferentially on the hydroxyl groups within amorphous area, and meanwhile the crystalline region of cellulose remained intact from the attack of acetylation reagents. Therefore, the fiber samples with low substitution degree of acetyl groups still exhibit similar X-ray diffraction pattern as native cellulose. When the reaction continued to proceed, acetylation reagents gradually penetrated into the interior of crystalline sections with an outcome of more interrupted hydrogen bonds that previously played a significant role in maintaining highly

crystalline structure of cellulose. Consequently, more distributed and attenuated diffraction peaks have been observed for highly acetylated fiber samples (e.g., Ac-RWC and Ac-RW-CNC) instead of strong characteristic signals, e.g., diffraction peak for 002 plane (around 22°) of purified cellulose product (**Figure 3**). Based on the findings of a former study, three sharp diffraction peaks from acetylated fiber products, locating at 8.5°, 10.4°, and 13.2° are related to 001 plane, 210 plane, and 310 plane, respectively (He et al., 2008). And a relatively broad peaks around 17.5° are dedicated by 012 plane (He et al., 2008). It is worth mentioning that the higher degree of acetylation results in lower crystallinity of sample.

Morphology Characterization of Different Fiber-Based Samples

As demonstrated in **Figure 4**, the extractive-free RW with coarse surface exhibits more opened structure which was beneficial from mechanical disintegration. The presence of massive pores observed on the surface is attributed to the removal of extractives from the raw material (**Figure 4A**). The surface of RWC turns out to be more smooth and plicated (**Figure 4B**), which is plausible since lignin and majority of hemicellulose have been efficiently removed during the isolation and purification of RWC.

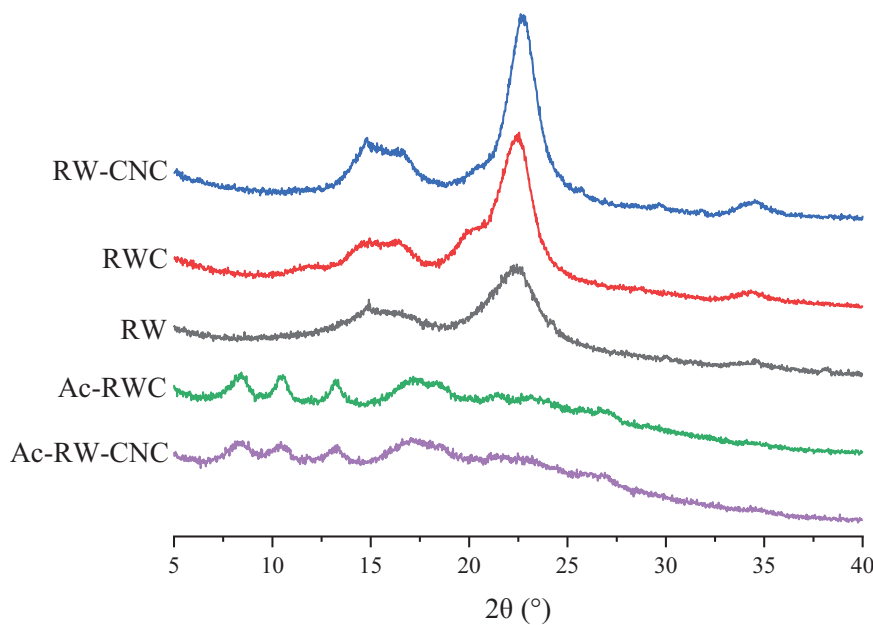


FIGURE 3 | X-ray diffraction patterns of RW, RWC, Ac-RWC, RW-CNC, and Ac-RW-CNC.

RW-CNC was successfully prepared from RWC via 64 wt% sulfuric acid hydrolysis followed by sonication treatment. It is worth noting that RW-CNC aqueous suspension is fairly stable, which is in good agreement with its high zeta potential (-51.8 mV). The sulfonic acid groups introduced during sulfuric acid hydrolysis would endow the surface of RW-CNC with negative charges when present in aqueous media and eventually realize a uniformed dispersion in deionized water (Habibi, 2014). The diameter and length distribution of RW-CNC were obtained, based on the statistical analysis of the entire fibers out of three random selected TEM images. As indicated from the results that the diameters of RW-CNC is mainly in the range of 4–10 nm and the average value is 7.4 ± 2.7 nm (Figure 4C and Supplementary Figure 1A). Furthermore, over 93% of RW-CNCs are scaled in length lower than 400 nm (Supplementary Figure 1B).

Thermal Stability of Different Fiber-Based Samples

Thermogravimetric analysis (TGA) and derivative thermogravimetric analysis (DTG) were conducted to evaluate the thermal stabilities of different fiber-based samples (Figure 5A). The initial stages of weight loss (from 50 to 130°C) for all test samples are explained by the removal of free and bound water from the samples (Wang P. et al., 2020). Later, as for RW, two major decomposition stages are observed (Figure 5B). The first one (from 230 to 320°C) is attributed to the degradation of hemicellulose, since more branched molecular structure renders hemicellulose with more thermally vulnerable in comparison with lignin and cellulose (Shebani et al., 2008). Thermal depolymerization of lignin and cellulose occurred afterward during the second stage ranging from 320 to 410°C and this

section is also covering a relatively narrow decomposition stage of RWC. This experimental finding mentioned above is plausible, since RWC is enriched in cellulose with only a minor portion of hemicellulose. Notably, the maximum decomposition temperature (T_{max}) of RWC (359°C) is slightly higher than that of RW (352°C) due to the higher crystallinity of RWC. It is necessary to point out that RW-CNC is the first specimen to decompose at an onset decomposition temperature (T_{onset}) of 200°C, nearly 100°C lower than that of RWC, though its crystallinity ranks the highest out of all test samples. The possible explanation for this evident drop of T_{onset} can be suggested as follows. Firstly, high crystallinity cannot ensure enhanced thermal stability especially when the sample size belongs to nanoscale, which is in good agreement with our early findings (Wu et al., 2019). Secondly, heat-labile sulfate esters formed on the surface of RW-CNC not only interrupt the linkages of intermolecular hydrogen bonds among RW-CNCs, but also turn out to be more vulnerable during TGA (Tuerxun et al., 2019).

It is worth noting that the thermal stability of RW fibers can be effectively improved by means of acetylation as shown in Figure 5B. The TGA and DTG curves of Ac-RWC and Ac-RW-CNC are fairly consistent, whose primary weight loss takes place from 280 to 430°C with the T_{max} close to 370°C, even higher than that of RWC (359°C). Compared with sulfate esters and hydroxyl groups, acetyl groups are proved to be more favorable for reinforcement of thermal stability (Wan Daud and Djuned, 2015; Leite et al., 2016).

Mechanical Properties of Different Films

The mechanical properties of two sets of different films were determined in terms of tensile strength and Young's modulus. As shown in Figure 6, the addition of Ac-RWC evidently

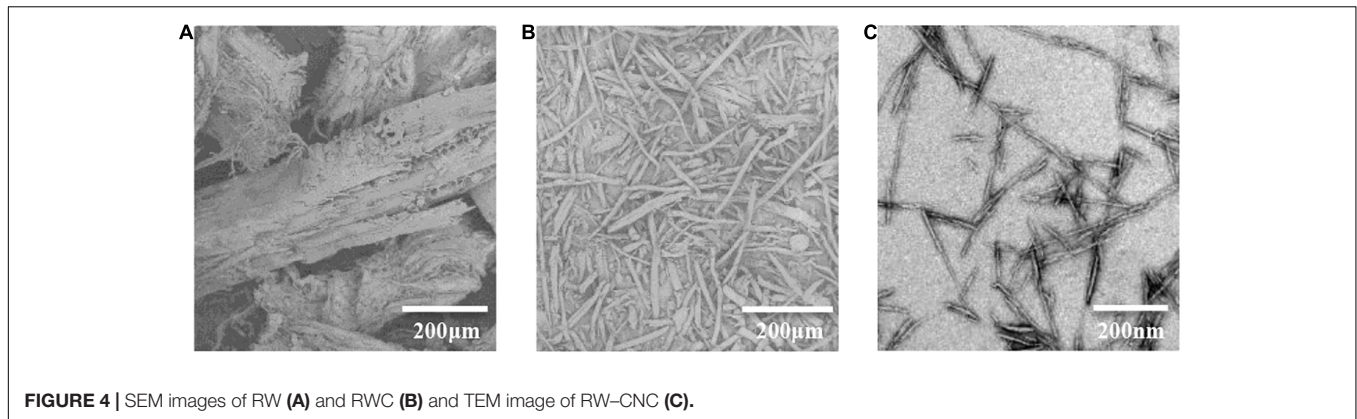


FIGURE 4 | SEM images of RW (A) and RWC (B) and TEM image of RW-CNC (C).

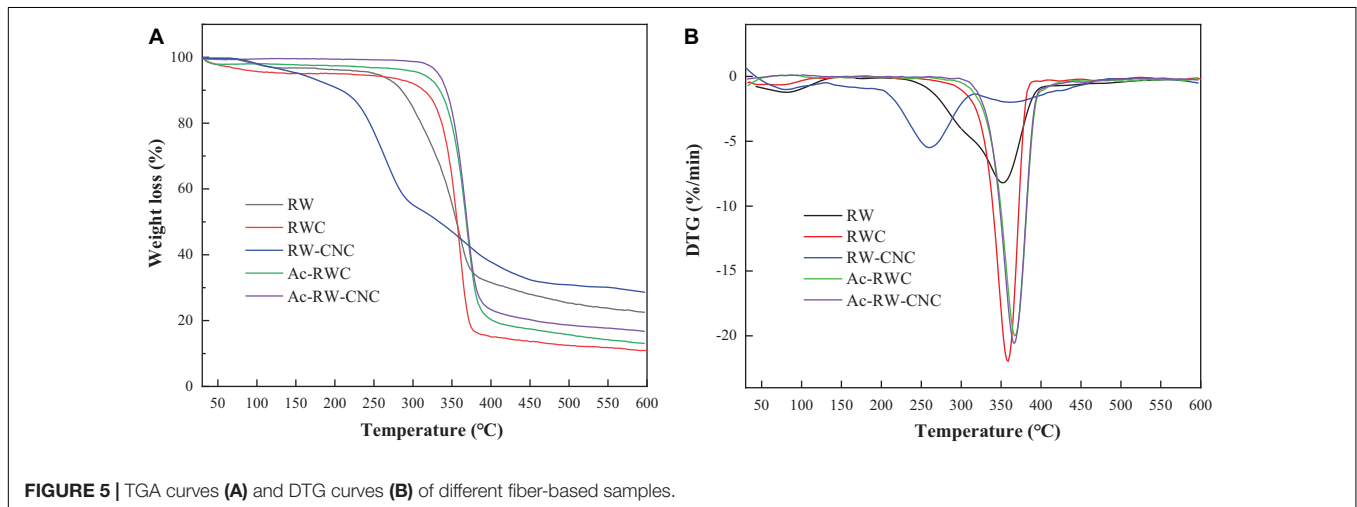


FIGURE 5 | TGA curves (A) and DTG curves (B) of different fiber-based samples.

improves the tensile strength of the composite films, compared with pure PLA film (35.7 MPa). When the addition of Ac-RWC reaches 5%, the value of tensile strength is as high as 48.6 MPa. However, this tendency of increment does not persist and the value starts to drop as the addition of Ac-RWC exceeds 5%. The hydrophobic acetyl groups existing on the surface of Ac-RWC strengthen the compatibility between acetylated fibers and PLA matrix. However, the enhanced interactions between filler and matrix would be effected only if the acetylated products could be uniformly distributed in the matrix. Excess involvement of fillers would inevitably lead to local aggregation and eventually weaken the intermolecular forces (Iwatake et al., 2008; Abdulkhani et al., 2014; Sung et al., 2017; Niu et al., 2018). Similar variation trend is also observed when dealing with the values of Young's modulus. Its maximum value (3,004 MPa) is achieved with 5% addition of Ac-RWC, higher than that of pure PLA film (2,562 MPa).

Although an overall enhancement of mechanical properties has already been obtained for Ac-RWC/PLA composite films, potential means for further improvement can also be attempted by minimizing the filler size (e.g., application of Ac-RW-CNC) for realizing a much more uniformed distribution of filler within PLA matrix. As verified from Figure 7 that, a minor addition of 1% Ac-RW-CNC results in comparable tensile

strength and Young's modulus as those acquired by 5%Ac-RWC/PLA composite film. The tendency of the increments does not cease until the addition of Ac-RW-CNC reaches 5% based on the dry weight of composite film, and the highest values for tensile strength and Young's modulus are 55.0 and 3,942 MPa, respectively. Similarly as mentioned before, excess addition of filler once again brings about decreased values of mechanical properties due to the aggregation of the fillers, which is well reflected from the results obtained for 7%Ac-RW-CNC/PLA.

Morphology of Different Films

Compared with the smooth fracture surface of pure PLA film (Figure 8A), the composite films exhibit different degree of roughness (Figures 8B–I). When the addition of reinforcing filler is low, the well distributed fibers would firmly adhere to matrix chains, namely a better interfacial adhesion had been promoted between fillers and PLA matrix. During the fracture process of the film, pulling out the originally firmly embedded fibers would inevitably stretch the surrounding matrix from the fracture surface owing to the strong interfacial adhesion mentioned above (Figures 8B,F) and this phenomenon is more distinct for lower addition of fillers. Besides, the better mechanical properties of 5%Ac-RWC/PLA and 5%Ac-RW-CNC/PLA composite films are also correlative to their higher amounts of evenly distributed

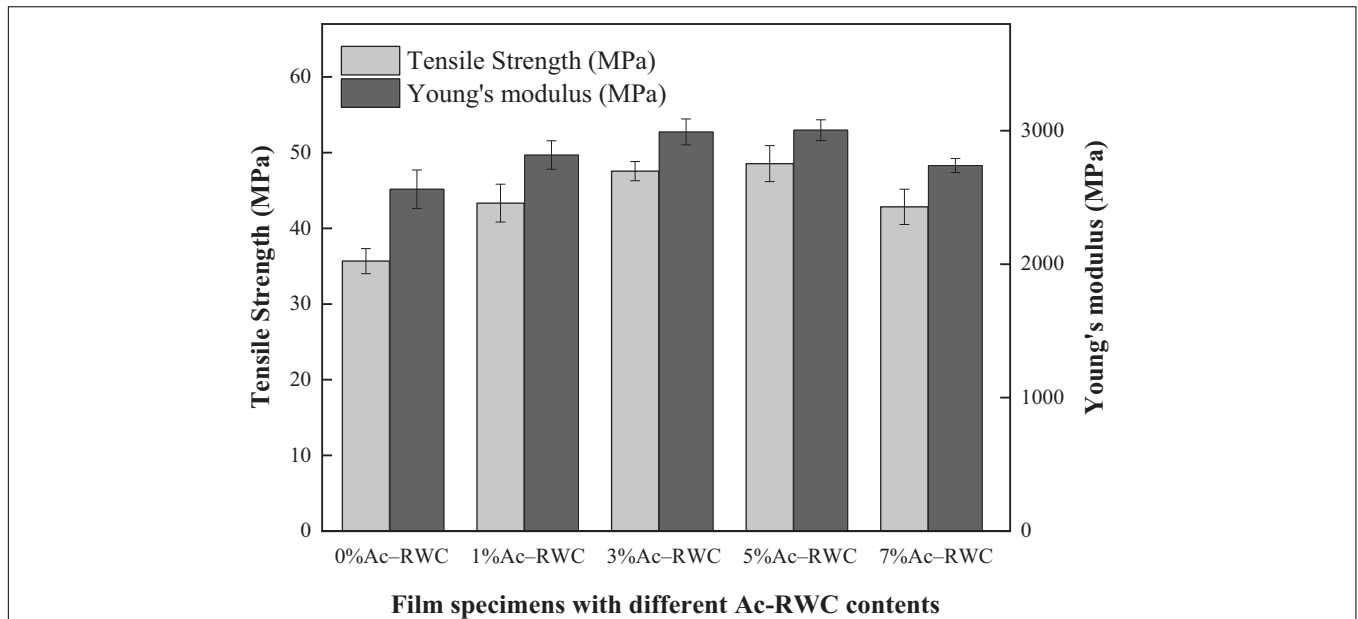


FIGURE 6 | Tensile strength and Young's modulus of Ac-RWC/PLA composite films.

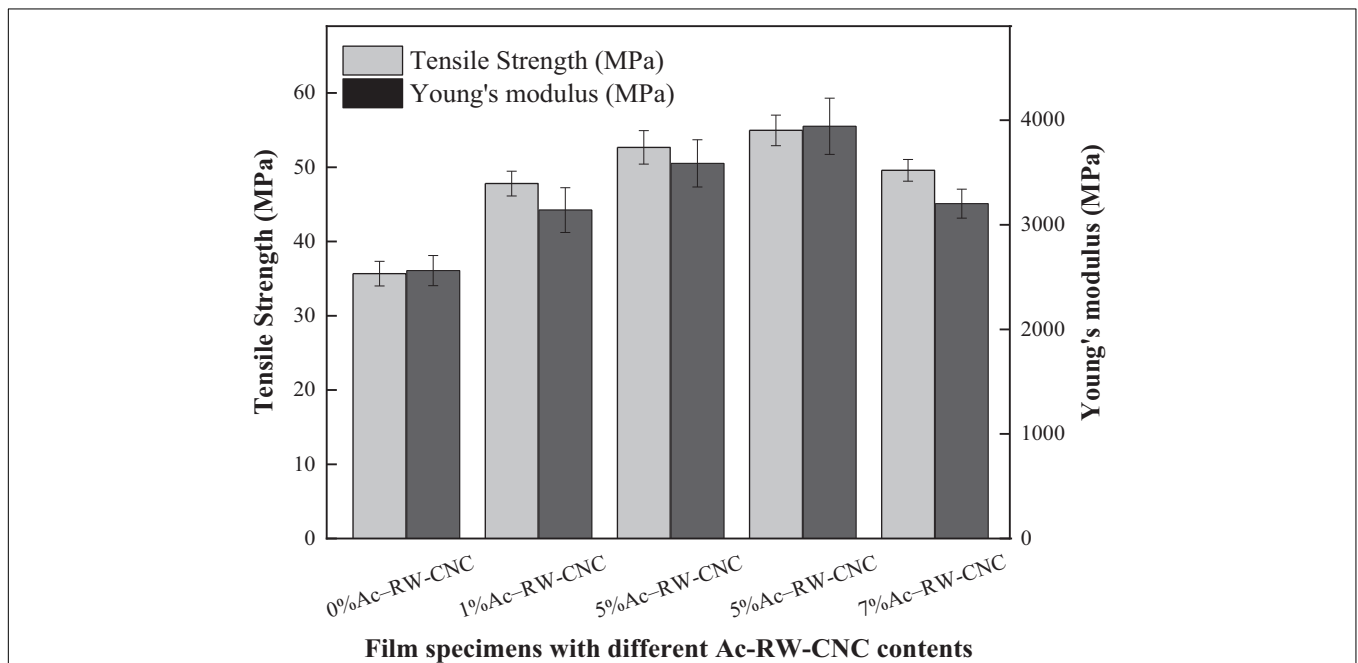


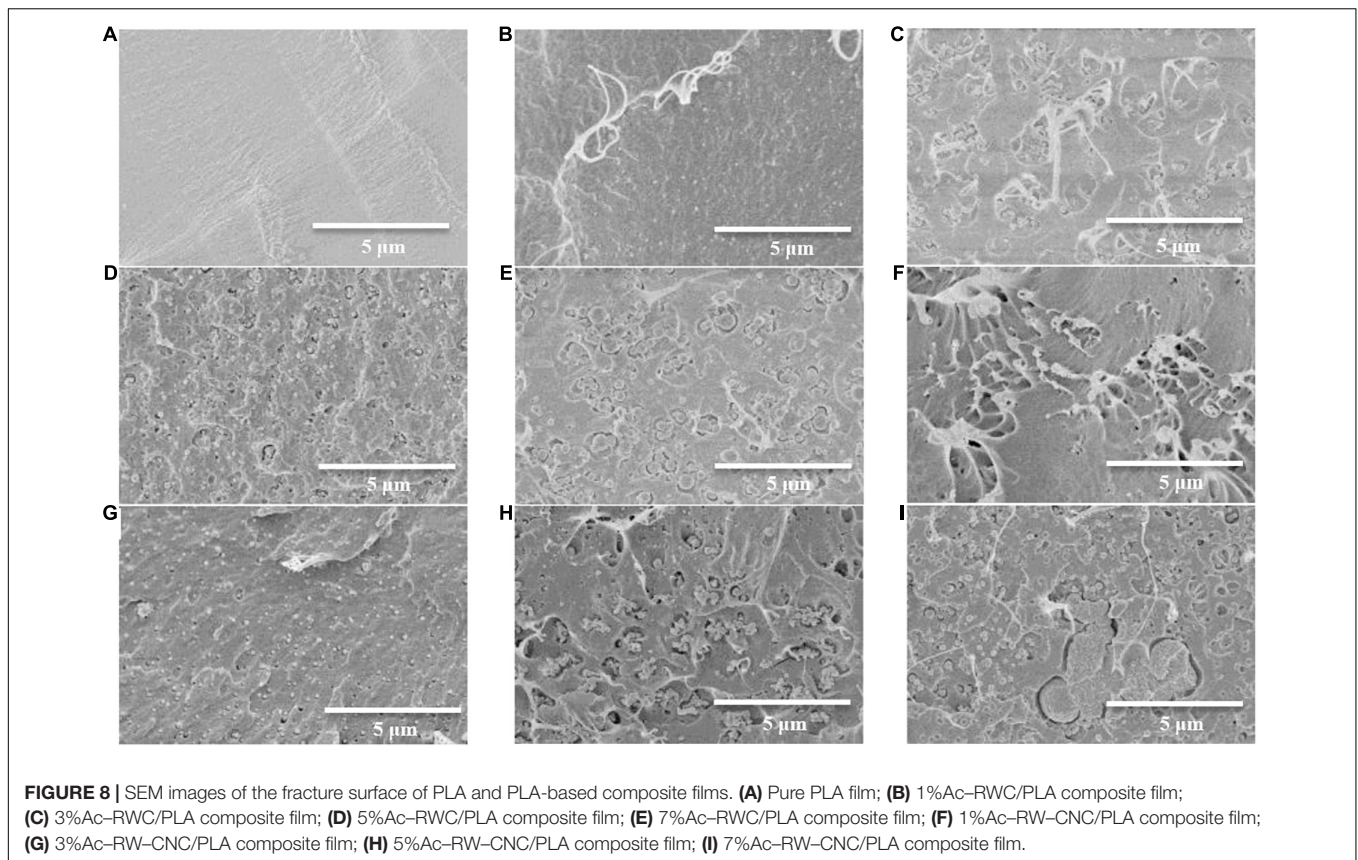
FIGURE 7 | Tensile strength and Young's modulus of Ac-RW-CNC/PLA composite films.

fillers (Figures 8D,H). Once the filler dosage exceeds 7%, the aggregation of the fillers could be clearly observed in Figures 8E,I.

Thermal Stability of Different Films

The TGA and DTG curves of two sets of composite films, designated as Ac-RWC/PLA and Ac-RW-CNC/PLA, were outlined in Supplementary Figures 2, 3. To improve the

compatibility of hydrophilic RWC or RW-CNC in hydrophobic PLA matrix, acetylation had been applied in advance. However, the enhanced interfacial adhesion between filler and matrix has been acquired at a cost of sacrificing filler's high crystallinity due to acetylation. It is widely recognized that the highly crystalline filler can be served as a favorable additive for upgrading the integral thermal stability of the composite films (Xiao et al., 2016). Therefore, the ultimate thermal stability of composite



films benefits both from the strengthened interfacial interactions between acetylated-fillers and matrix, and from the remaining crystallinity of the fillers.

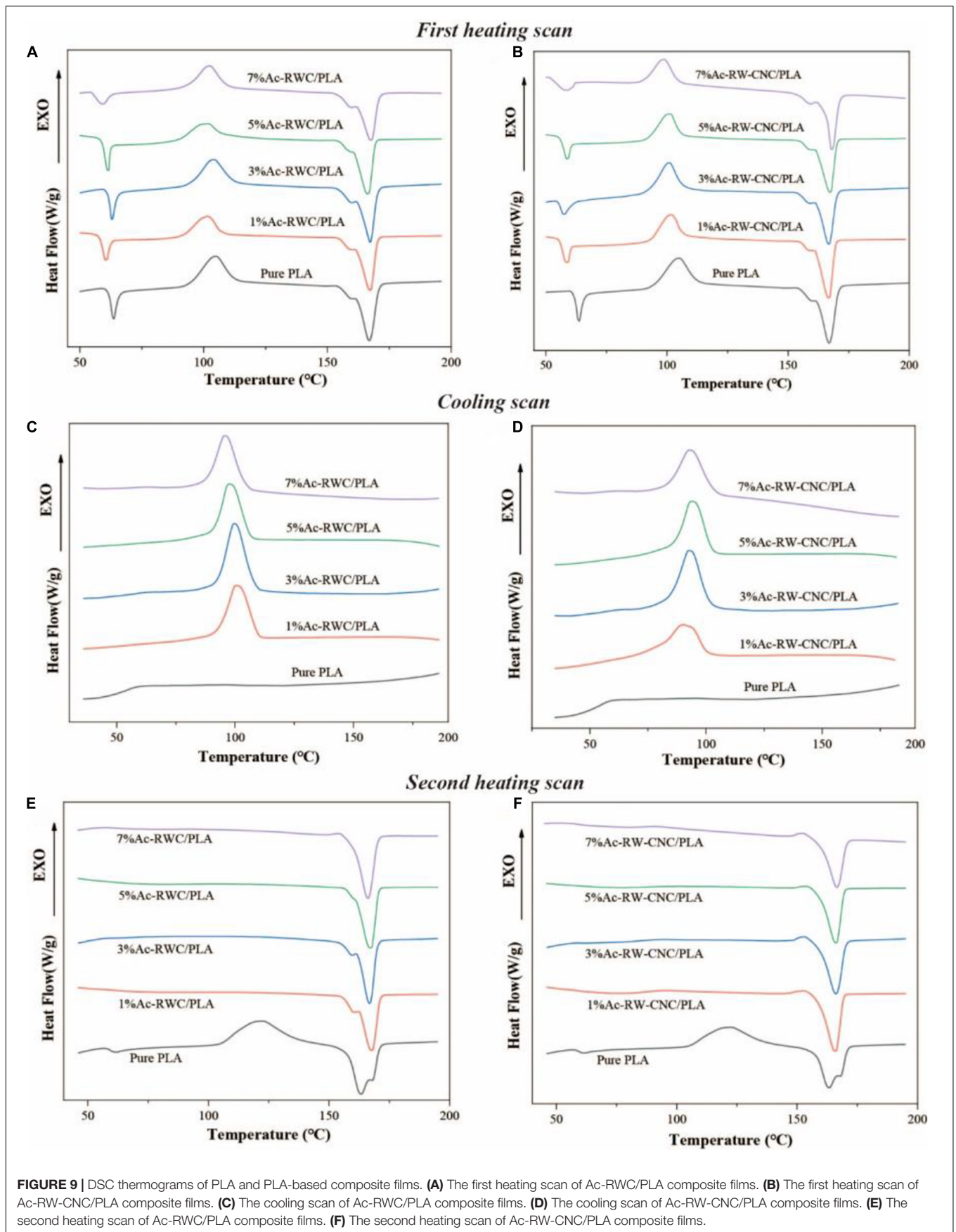
In general, the Ac-RWC reinforced films demonstrate similar thermal decomposition behaviors in comparison with pure PLA film (Lizundia et al., 2016). Although the difference is not evident, a series of Ac-RWC/PLA composite films with filler dosage ranging from 1 to 7% are relatively more thermal stable than pure PLA film (Dong et al., 2017; **Supplementary Figure 2A**). When the filler could be effectively dispersed in PLA matrix, namely the addition of Ac-RWC 5%, the T_{max} value is observed for a continuous shifting to higher temperature (**Supplementary Figure 2B**). A sudden shift to a lower T_{max} occurs, however, when the filler was supplied as 7% based on the dry weight of the film. It could also be explained by the weakened interfacial adhesion arising from the aggregation of fillers. With respect to a set of Ac-RW-CNC/PLA composite films, their thermal stabilities are slightly lower than that of pure PLA film within the temperature difference of roughly 6°C in comparison of individual T_{max} (**Supplementary Figure 3**). Relatively lower thermal stability of Ac-RW-CNC with nano-scaled sample size also accounts for the phenomenon observed above.

Crystallization Behavior of Different Films

Compared with other semi-crystalline polymers, PLA has relatively poor thermal stability. For instance, its glass transition

temperature is only around 60°C (**Figure 9A**). A currently prevailing strategy to overcome this drawback is to increase its crystallinity by introduction of nucleating agents (Ghasemi et al., 2012; Kamal and Khoshkava, 2015), since higher crystallinity of PVA-based composite would positively influence its thermal resistance as well as the mechanical properties. As efficient nucleating agents, several species of nanoparticles (e.g., clay and nanotubes) have been previously documented to vary the crystallinity behavior of semi-crystalline polymers by acting as heterogeneous nucleation sites (Ghasemi et al., 2012). Here, in this study, the possibility of Ac-RWC and Ac-RW-CNC to be served as potential candidates for nucleating agents were attempted and their effects on crystallinity behavior of PLA-based composite films had also been investigated.

The crystallization behavior of all specimens during first heating, cooling, and second heating scans are depicted in **Figure 9** and their corresponding thermal parameters are summarized in **Supplementary Table 1**. The DSC thermographs of first heating scan for all test films are quite similar with each other (**Figures 9A,B**), and the slightly decreased T_g values of composite films accounts for lower influence of fillers on mobility of PLA chains (Sung et al., 2017). During film preparation, rapid evaporation of dichloromethane resulted in sudden cooling of the temperature, which eventually restricted the PLA chains from fully self-adjusted into crystalline structures (Sullivan et al., 2015). Therefore, the exothermic peaks for cold crystallization slightly over 100°C have been observed for all specimens



(Figures 9A,B). Compared with pure PLA film, the crystallization behavior of composite films vary significantly throughout the cooling process by emerging evident exothermic peaks of melt crystallization close to 100°C (Figures 9C,D). This phenomenon directly verifies the capacity of nucleation by Ac-RWC and Ac-RW-CNC in composite films under the selected cooling rate (10°C/min), whereas effective crystal nucleus are hardly to be formed within a homogenous system (pure PLA film). Ascribed to the existence of preformed crystalline structure from an early cooling scan, the phenomenon of cold crystallization does not occur during the second heating scan, the situation, however, is opposite respect to pure PLA film (Figures 9E,F). In addition, the T_{cc} value of PLA film is shifted to higher temperature (around 122°C) in the second heating scan after removal of thermal history.

As shown in **Supplementary Table 1**, the crystallinity of pure PLA film (4.3%) is much lower than that of composite film, even if the addition of reinforcing filler is only 1%. Generally, the crystallinity of Ac-RW-CNC/PLA composite films is higher than that of Ac-RWC/PLA composite films, and the maximum value is up to 47.6% for 3% Ac-RW-CNC/PLA. It is worth mentioning that the double melting peak observed for pure PLA film during second heating (Figures 9E,F) is indicated by either polymorphism or melt recrystallization (Fortunati et al., 2012; Sullivan et al., 2015).

Light Transmittance of Different Films

The light transmittance of PLA and PLA-based composite films has been measured throughout a UV-vis range from 200 to 800 nm (**Supplementary Figure 4**). Theoretically, film transparency is largely depending on the micro-structure of the films (Kim, 2008; Lizundia et al., 2016; Huang et al., 2020). Compared with visible light (400–800 nm), UV light (200–400 nm) is more readily to be absorbed by the test films and the transmittance rate gradually reaches a plateau when the wavelength of incident light exceeds 400 nm. For instance, nearly 93% of visible light could transit pure PLA film and a minor addition (5%) of Ac-RWC or Ac-RW-CNC does not impact the light transmittance to a large extent. 7%Ac-RWC/PLA and 7%Ac-RW-CNC/PLA are the two exceptions, whose light transmittance is dropped to around 85% or even less due to the light scattering and refraction resulted from filler aggregation (Hu and Wang, 2016).

REFERENCES

- Abdulkhani, A., Hosseinzadeh, J., Ashori, A., Dadashi, S., and Takzare, Z. (2014). Preparation and characterization of modified cellulose nanofibers reinforced polylactic acid nanocomposite. *Polym. Test.* 35, 73–79. doi: 10.1016/j.polymertesting.2014.03.002
- Avinc, O., and Khoddami, A. (2010). Overview of poly(lactic acid) (PLA) fiber. *Fibre Chem.* 42, 68–78. doi: 10.1007/s10692-010-9226-7
- Bondeson, D., and Oksman, K. (2007). Dispersion and characteristics of surfactant modified cellulose whiskers nanocomposites.

CONCLUSION

Rubber wood cellulose had been effectively isolated, processed, and surface modified to acetylated cellulose and acetylated cellulose nanocrystals, both of which could be served as promising reinforcing fillers for fabrication of PLA-based composite films owing to their different structural characteristics as well as the improved compatibility with PLA matrix. By means of spin coating technique, the acetylated cellulose reinforced PLA composite films possess higher thermal stability, while the acetylated cellulose nanocrystals reinforced PLA composite films are more superior in mechanical properties and the degree of crystallinity.

DATA AVAILABILITY STATEMENT

The raw data supporting the conclusions of this article will be made available by the authors, without undue reservation.

AUTHOR CONTRIBUTIONS

ZO and XD proposed supporting the conclusions of this article will be made available by the authors, without undue rthe idea. ZO, XR, and QZ performed most of the experiments. HY and CH helped to revise the manuscript. XD supervised the whole work and wrote the manuscript. All authors contributed to the article and approved the submitted version.

FUNDING

This study was financially supported by Hainan Provincial Natural Science Foundation (2019RC154), foundation (2019KF26) of Guangxi Key Laboratory of Clean Pulp and Papermaking and Pollution Control (College of Light Industry and Food Engineering, Guangxi University), and start-up foundation from Hainan University [KYQD(ZR)1717].

SUPPLEMENTARY MATERIAL

The Supplementary Material for this article can be found online at: <https://www.frontiersin.org/articles/10.3389/fbioe.2021.666399/full#supplementary-material>

Compos. Interfaces 14, 617–630. doi: 10.1163/156855407782106519

Chen, C.-C., Chueh, J.-Y., Tseng, H., Huang, H.-M., and Lee, S.-Y. (2003). Preparation and characterization of biodegradable PLA polymeric blends. *Biomaterials* 24, 1167–1173. doi: 10.1016/s0142-9612(02)04666-0

Chen, W., Yu, H., Liu, Y., Chen, P., Zhang, M., and Hai, Y. (2011). Individualization of cellulose nanofibers from wood using high-intensity ultrasonication combined with chemical pretreatments. *Carbohydr. Polym.* 83, 1804–1811. doi: 10.1016/j.carbpol.2010.10.040

- Ditzel, F. I., Prestes, E., Carvalho, B. M., Demiate, I. M., and Pinheiro, L. A. (2017). Nanocrystalline cellulose extracted from pine wood and corncob. *Carbohydr. Polym.* 157, 1577–1585. doi: 10.1016/j.carbpol.2016.11.036
- Dong, F., Yan, M., Jin, C., and Li, S. (2017). Characterization of type-II acetylated cellulose nanocrystals with various degree of substitution and its compatibility in PLA films. *Polymers* 9:346. doi: 10.3390/polym9080346
- Ejaz, U., Muhammad, S., Ali, F. I., Hashmi, I. A., and Sohail, M. (2020). Cellulose extraction from methyltriethylammonium chloride pretreated sugarcane bagasse and its application. *Int. J. Biol. Macromol.* 165, 11–17. doi: 10.1016/j.ijbiomac.2020.09.151
- Fischer, E. W., Sterzel, H. J., and Wegner, G. (1973). Investigation of the structure of solution grown crystals of lactide copolymers by means of chemical reactions. *Kolloid Z. Z. Polym.* 251, 980–990. doi: 10.1007/bf01498927
- Fortunati, E., Armentano, I., Zhou, Q., Puglia, D., Terenzi, A., Berglund, L. A., et al. (2012). Microstructure and nonisothermal cold crystallization of PLA composites based on silver nanoparticles and nanocrystalline cellulose. *Polym. Degrad. Stab.* 97, 2027–2036. doi: 10.1016/j.polymdegradstab.2012.03.027
- Ghasemi, H., Carreau, P. J., and Kamal, M. R. (2012). Isothermal and non-isothermal crystallization behavior of PET nanocomposites. *Polym. Eng. Sci.* 52, 372–384. doi: 10.1002/pen.22092
- Habibi, Y. (2014). Key advances in the chemical modification of nanocelluloses. *Chem. Soc. Rev.* 43, 1519–1542. doi: 10.1039/C3CS60204D
- Han, J., Zhou, C., Wu, Y., Liu, F., and Wu, Q. (2013). Self-assembling behavior of cellulose nanoparticles during freeze-drying: effect of suspension concentration, particle size, crystal structure, and surface charge. *Biomacromolecules* 14, 1529–1540. doi: 10.1021/bm4001734
- He, J., Tang, Y., and Wang, S. (2008). Crystalline structure and thermal property of cellulose acetate. *J. Text. Res.* 29, 12–16.
- Hu, D., and Wang, L. (2016). Physical and antibacterial properties of polyvinyl alcohol films reinforced with quaternized cellulose. *J. Appl. Polym. Sci.* 133, 43552–43560. doi: 10.1002/app.43552
- Huang, C., Dong, H., Zhang, Z., Bian, H., and Yong, Q. (2020). Procuring the nano-scale lignin in prehydrolyzate as ingredient to prepare cellulose nanofibril composite film with multiple functions. *Cellulose* 27, 9355–9370. doi: 10.1007/s10570-020-03427-9
- Iwatake, A., Nogi, M., and Yano, H. (2008). Cellulose nanofiber-reinforced polylactic acid. *Compos. Sci. Technol.* 68, 2103–2106. doi: 10.1016/j.compscitech.2008.03.006
- Jonoobi, M., Mathew, A. P., Abdi, M. M., Makinejad, M. D., and Oksman, K. (2012). A comparison of modified and unmodified cellulose nanofiber reinforced polylactic acid (PLA) prepared by Twin Screw Extrusion. *J. Polym. Environ.* 20, 991–997. doi: 10.1007/s10924-012-0503-9
- Kamal, M. R., and Khoshkava, V. (2015). Effect of cellulose nanocrystals (CNC) on rheological and mechanical properties and crystallization behavior of PLA/CNC nanocomposites. *Carbohydr. Polym.* 123, 105–114. doi: 10.1016/j.carbpol.2015.01.012
- Kian, L. K., Saba, N., Jawaid, M., Alothman, O. Y., and Fouad, H. (2020). Properties and characteristics of nanocrystalline cellulose isolated from olive fiber. *Carbohydr. Polym.* 241:116423. doi: 10.1016/j.carbpol.2020.116423
- Kim, S. W. (2008). Preparation and barrier property of poly(vinyl alcohol)/SiO₂ hybrid coating films. *Korean J. Chem. Eng.* 25, 1195–1200. doi: 10.1007/s11814-008-0197-9
- Leite, L. S. F., Battirolo, L. C., Escobar da Silva, L. C., and Goncalves, M. D. C. (2016). Morphological investigation of cellulose acetate/cellulose nanocrystal composites obtained by melt extrusion. *J. Appl. Polym. Sci.* 133:44201. doi: 10.1002/app.44201
- Li, J., Wang, C., Jiang, J., and Peng, Z. (2013). Current situation, problems and countermeasures of comprehensive development and utilization of *Hevea brasiliensis*. *Chin. J. Trop. Agric.* 33, 71–74.
- Liu, G., Zhang, X., and Wang, D. (2014). Tailoring crystallization: towards high-performance poly(lactic acid). *Adv. Mater.* 26, 6905–6911. doi: 10.1002/adma.201305413
- Lizundia, E., Fortunati, E., Dominici, F., Vilas, J. L., Leon, L. M., Armentano, I., et al. (2016). PLLA-grafted cellulose nanocrystals: Role of the CNC content and grafting on the PLA bionanocomposite film properties. *Carbohydr. Polym.* 142, 105–113. doi: 10.1016/j.carbpol.2016.01.041
- Mosnackova, K., Šišková, A. O., Kleinova, A., Danko, M., and Mosnacek, J. (2020). Properties and degradation of novel fully biodegradable PLA/PHB blends filled with keratin. *Int. J. Mol. Sci.* 21:9678. doi: 10.3390/ijms21249678
- Murariu, M., and Dubois, P. (2016). PLA composites: from production to properties. *Adv. Drug Deliv. Rev.* 107, 17–46. doi: 10.1016/j.addr.2016.04.003
- Niu, X., Liu, Y., Song, Y., Han, J., and Pan, H. (2018). Rosin modified cellulose nanofiber as a reinforcing and co-antimicrobial agents in polylactic acid/chitosan composite film for food packaging. *Carbohydr. Polym.* 183, 102–109. doi: 10.1016/j.carbpol.2017.11.079
- Oksman, K., Mathew, A. P., Bondeson, D., and Kvien, I. (2006). Manufacturing process of cellulose whiskers/polylactic acid nanocomposites. *Compos. Sci. Technol.* 66, 2776–2784. doi: 10.1016/j.compscitech.2006.03.002
- Pappas, C., Tarantilis, P. A., Daliani, I., Mavromoustakos, T., and Polissiou, M. (2002). Comparison of classical and ultrasound-assisted isolation procedures of cellulose from kenaf (*Hibiscus cannabinus* L.) and eucalyptus (*Eucalyptus rodustrus* Sm.). *Ultrason. Sonochem.* 9, 19–23. doi: 10.1016/s1350-4177(01)00095-5
- Reddy, K. O., Maheswari, C. U., Dhlamini, M. S., Mothudi, B. M., Kommula, V. P., Zhang, J., et al. (2018). Extraction and characterization of cellulose single fibers from native african napier grass. *Carbohydr. Polym.* 188, 85–91. doi: 10.1016/j.carbpol.2018.01.110
- Santoro, M., Shah, S. R., Walker, J. L., and Mikos, A. G. (2016). Poly(lactic acid) nanofibrous scaffolds for tissue engineering. *Adv. Drug Deliv. Rev.* 107, 206–212. doi: 10.1016/j.addr.2016.04.019
- Segal, L., Creely, J. J., Martin, A. E. Jr., and Conrad, C. M. (1959). An empirical method for estimating the degree of crystallinity of native cellulose using the X-ray diffractometer. *Text. Res. J.* 29, 786–794. doi: 10.1177/004051755902901003
- Shebani, A. N., van Reenen, A. J., and Meincken, M. (2008). The effect of wood extractives on the thermal stability of different wood species. *Thermochim. Acta* 471, 43–50. doi: 10.1016/j.tca.2008.02.020
- Sullivan, E. M., Moon, R. J., and Kalaitzidou, K. (2015). Processing and characterization of cellulose nanocrystals/polylactic acid nanocomposite films. *Materials* 8, 8106–8116. doi: 10.3390/ma8125447
- Sun, X., Sun, R., Su, Y., and Sun, J. (2004). Comparative study of crude and purified cellulose from wheat straw. *J. Agric. Food Chem.* 52, 839–847. doi: 10.1021/jf0349230
- Sung, S. H., Chang, Y., and Han, J. (2017). Development of polylactic acid nanocomposite films reinforced with cellulose nanocrystals derived from coffee silverskin. *Carbohydr. Polym.* 169, 495–503. doi: 10.1016/j.carbpol.2017.04.037
- Tajbakhsh, S., and Hajiali, F. (2017). A comprehensive study on the fabrication and properties of biocomposites of poly(lactic acid)/ceramics for bone tissue engineering. *Mater. Sci. Eng. C* 70, 897–912. doi: 10.1016/j.msec.2016.09.008
- Tuercun, D., Pulingam, T., Nordin, N. I., Chen, Y. W., Kamaldin, J. B., Julkapli, N. B. M., et al. (2019). Synthesis, characterization and cytotoxicity studies of nanocrystalline cellulose from the production waste of rubber-wood and kenaf-bast fibers. *Eur. Polym. J.* 116, 352–360. doi: 10.1016/j.eurpolymj.2019.04.021
- Uma Maheswari, C., Obi Reddy, K., Muzenda, E., Guduri, B. R., and Varada Rajulu, A. (2012). Extraction and characterization of cellulose microfibrils from agricultural residue – *Cocos nucifera* L. *Biomass Bioenergy* 46, 555–563. doi: 10.1016/j.biombioe.2012.06.039
- Wan Daud, W. R., and Djuned, F. M. (2015). Cellulose acetate from oil palm empty fruit bunch via a one step heterogeneous acetylation. *Carbohydr. Polym.* 132, 252–260. doi: 10.1016/j.carbpol.2015.06.011
- Wang, H., Nie, W., Zhang, H., Jin, H., Bao, Q., Yan, J., et al. (2020). A synthesis of a dust suppressant using the cellulose extracted from maize straw. *Starch* 72:1900187. doi: 10.1002/star.201900187
- Wang, P., Zhang, Y., Jiang, Q., Yin, B., Dong, H., Huang, C., et al. (2020). Coupling biocompatible Au nanoclusters and cellulose nanofibrils to prepare

- the antibacterial nanocomposite films. *Front. Bioeng. Biotechnol.* 8:986. doi: 10.3389/fbioe.2020.00986
- Wu, J., Du, X., Yin, Z., Xu, S., Xu, S., and Zhang, Y. (2019). Preparation and characterization of cellulose nanofibrils from coconut coir fibers and their reinforcements in biodegradable composite films. *Carbohydr. Polym.* 211, 49–56. doi: 10.1016/j.carbpol.2019.01.093
- Xiao, S., Gao, R., Gao, L. K., and Li, J. (2016). Poly(vinyl alcohol) films reinforced with nanofibrillated cellulose (NFC) isolated from corn husk by high intensity ultrasonication. *Carbohydr. Polym.* 136, 1027–1034. doi: 10.1016/j.carbpol.2015.09.115

Conflict of Interest: The authors declare that the research was conducted in the absence of any commercial or financial relationships that could be construed as a potential conflict of interest.

Copyright © 2021 Ou, Zhou, Rao, Yang, Huo and Du. This is an open-access article distributed under the terms of the Creative Commons Attribution License (CC BY). The use, distribution or reproduction in other forums is permitted, provided the original author(s) and the copyright owner(s) are credited and that the original publication in this journal is cited, in accordance with accepted academic practice. No use, distribution or reproduction is permitted which does not comply with these terms.



Using the Major Components (Cellulose, Hemicellulose, and Lignin) of *Phyllostachys praecox* Bamboo Shoot as Dietary Fiber

Jinlai Yang^{1,2,3}, Liangru Wu^{1,2,3*}, Huimin Yang^{1,2,3} and Yanhong Pan^{1,2,3}

¹ China National Bamboo Research Center, Hangzhou, China, ² Key Laboratory of High Efficient Processing of Bamboo of Zhejiang Province, Hangzhou, China, ³ Key Laboratory of Resources and Utilization of Bamboo of State Forestry Administration, Hangzhou, China

OPEN ACCESS

Edited by:

Lei Wang,
Jeju National University, South Korea

Reviewed by:

Jiong Zheng,
Southwest University, China
Thilina U. Jayawardena,
Jeju National University, South Korea
Zhaobin Guo,
Johns Hopkins University,
United States

*Correspondence:

Liangru Wu
bamshoots@163.com

Specialty section:

This article was submitted to
Bioprocess Engineering,
a section of the journal
Frontiers in Bioengineering and
Biotechnology

Received: 19 February 2021

Accepted: 09 March 2021

Published: 31 March 2021

Citation:

Yang J, Wu L, Yang H and Pan Y
(2021) Using the Major Components
(Cellulose, Hemicellulose, and Lignin)
of *Phyllostachys praecox* Bamboo
Shoot as Dietary Fiber.
Front. Bioeng. Biotechnol. 9:669136.
doi: 10.3389/fbioe.2021.669136

Bamboo shoots are a renewable and abundant biomass containing cellulose, hemicellulose, and lignin. Although many studies have explored the applications of each of these components in the preparation of biochemicals and biopolymers, few studies have evaluated the utility of these components as a dietary fiber supplement. In this study, a powder consisting of the main components of bamboo shoots (cellulose, hemicellulose, and lignin) was prepared from fresh *Phyllostachys praecox* shoots and characterized by scanning electron microscopy, infrared spectroscopy, and X-ray diffraction. To evaluate the potential utility of these components as a dietary fiber supplement, we conducted an experiment in which this powder was supplemented in the diet of mice for 7 weeks. The experiment included three diet groups ($n = 10/\text{group}$): a low-fat control diet (LFC), high-fat diet (HFD), and high-fat diet with bamboo shoot powder (HFBSP). Compared with HFD mice, the body weights of LFC and HFBSP mice were lower, indicating that the addition of bamboo shoot powder could reduce the weight gain associated with the HFD. Bamboo shoot powder supplementation could also reduce the levels of triglycerides (TG), blood glucose (GLU), total cholesterol (CHOL), high-density lipoprotein (HDL-C), and low-density lipoprotein (LDL-C) in HFD mice. The fat histology images indicated that obesity was alleviated in HFBSP mice, and the liver histology images indicated that the addition of bamboo shoot powder to the HFD could reduce the risk of fatty liver disease. The addition of bamboo shoot powder to the HFD might also improve the gut microbiota of mice. Thus, the major components of bamboo shoot powder (cellulose, hemicellulose, and lignin) could be used as beneficial natural additives in the food industry.

Keywords: bamboo shoot powder, preparation, dietary fiber, mice, bio-application

INTRODUCTION

Vegetables are important for a balanced and healthy diet (Bvenura and Sivakumar, 2017). However, foods with high calories and fat are also frequently enjoyed in high-income countries (Hunter et al., 2019) because the consumption of healthy vegetables alone is insufficient to meet caloric needs. Bamboo is a useful perennial woody grass in temperate and tropical regions of the world (Huang et al., 2019b; Lin et al., 2019; Zheng Y. et al., 2021); shoots and wood are the two main

products of bamboo. The shoots of bamboo are edible and rich in dietary fiber, protein, amino acids, polysaccharides, polyphenol, and minerals (Singhal et al., 2013; Huang et al., 2018; Dong et al., 2020).

An increasing number of studies have examined bamboo shoots. Cellulose nanocrystals and cellulose nanofibrils can be prepared from bamboo shoots by acid hydrolysis, which can be used in the fields of composite materials, drug delivery, and emulsifiers (Wijaya et al., 2019; Huang et al., 2020; Wang et al., 2020). Water-insoluble bamboo shoot dietary fiber was used as a plant food particle stabilizer to produce stable oil-in-water (O/W) Pickering emulsions (He et al., 2020). A distinctive antifungal protein (20 kDa) was isolated from fresh bamboo shoots (Wang and Ng, 2003). The bioactive constituents of bamboo shoot (*Bambusa balcooa*) extract could cause an imbalance in the oxidative status of thyrocytes, which impairs the action of hormone-synthesizing elements at the cellular and molecular level (Sarkar et al., 2019; Zheng L. et al., 2021). Polysaccharides extracted from bamboo shoots (*Chimonobambusa quadrangularis*) by ultrasonic-assisted extraction (Chen et al., 2019) or accelerated solvent extraction (Chen et al., 2018) show high antioxidant activity. In addition, the compositions in bamboo can be used to prepare the fluorescent composition to image cells and organs in different fields (Huang et al., 2019a; Su et al., 2019; Pei et al., 2020; Chen et al., 2021). A novel fluorescent composition was successfully isolated from winter Moso bamboo shoots and used to image human hepatocellular carcinoma cells (HepG2) (Yang et al., 2019).

A bamboo shoot diet was shown to decrease serum total cholesterol, low-density lipoprotein, and the atherogenic index (Park and Jhon, 2009). Four-week administration of bamboo shoot shell fibers alleviated diabetic syndrome in mice (Zheng et al., 2019). Mice that consumed a diet supplement with bamboo shoot shell (*Leleba oldhami* Nakal) had lower body weight gain (2.84%), total cholesterol (31.53%), triglyceride levels (21.35%), and low-density lipoprotein cholesterol (31.53%) and higher high-density lipoprotein cholesterol (37.6%) (Luo et al., 2017). Mice that consumed a diet supplemented with two bamboo shoot fibers (BSFs) from *D. hamiltonii* and *D. latiflorus* had lower body weight gain, lower levels of fasting glucose and insulin, and lower values of glucose area after 13 weeks, suggesting that BSFs can control insulin resistance and reduce the risk of type 2 diabetes (Li et al., 2018).

Although bamboo shoots are delicious and healthy vegetables, especially when consumed fresh, the freshness of bamboo shoots is difficult to maintain because of lignification (Luo et al., 2012). In addition, the bioavailability of nutrients and other extracts from different biomass depends on a variety of factors, such as compositions, structures and functional groups (Nair and Augustine, 2018; Yu et al., 2020; Tao et al., 2021). In this paper, we prepare a bamboo shoot powder from fresh bamboo shoots (*Phyllostachys violascens*), which contains different compositions of cellulose, hemicellulose, and lignin. The health effects of the powder were assessed by conducting an experiment in which the powder was supplemented in the diet of mice for 7 weeks. Aside from

providing a new edible product of bamboo shoots, the results of our study highlight the potential benefits that the functional components of bamboo shoots could provide as a dietary supplement.

MATERIALS AND METHODS

Materials and Instruments

Fresh bamboo shoots (*Phyllostachys violascens*) were obtained from Jianou, Fujian, China. All animal experiments were conducted with the approval of the Institutional Animal Care and Use Committee (IACUC) of Nanjing Medical University. Female mice were purchased from the Model Animal Research Center of Nanjing University. The lab mice maintenance diet was purchased from Jiangsu Synergetic Pharmaceutical Bioengineering Co., Ltd. (Nanjing, China). Reagents and solvents were purchased from commercial suppliers and used without further purification. The bamboo shoot powder was examined by a SU8010 scanning electron microscope. Infrared (IR) spectra were recorded on a Nicolet 380 FT-IR infrared spectrometer. XRD data were obtained using a Rigaku Ultima IV X-ray diffraction instrument. High-speed double-channel pulping was carried out by a GFM-DFP-200 engine.

Preparation of Bamboo Shoot Powder

Bamboo shoot powder was prepared from fresh Lei bamboo shoots (*Phyllostachys praecox* shoots). The fresh shoots were cut into pieces after removing the peel and washing with water. The shoot pieces (200.0 kg) were crushed to smaller watery particles (<3 mm) through a high-speed double-channel pulping engine (1.0 mm, 0.6 mm), which generated a beating suspension. Finally, a bamboo shoot powder (17.2 kg, <80 mesh) was obtained after the beating suspension was dried by a spray-drying method. The powder had a unique aroma and nutrients; the yield was 8.6%, and the water content was 3.2%.

Mice and Diets

After acclimatization (2 weeks), the mice were fed three types of diets for 7 weeks: a low-fat control diet (LFC), high-fat diet (HFD), and high-fat diet with bamboo shoot powder (HFBSP); the ingredient composition of the experimental diets is shown in **Table 1**. The mice were maintained on a 12 h light/12 h dark cycle at a temperature range of 20–24°C in a humidity-controlled environment.

Serum Lipid Analysis

Samples of blood were obtained from live female mice, and the serum was isolated by clotting and centrifugation. The serum levels of triglycerides (TG), blood glucose (GLU), total cholesterol (CHOL), high-density lipoprotein (HDL-C), and low-density lipoprotein (LDL-C) were determined using a Hitachi 7100 blood automatic biochemical analyzer (Li et al., 2002). Serum levels of CHOL and TG were tested by enzymatic assays. HDL-C levels were measured after precipitation of apolipoprotein B-containing lipoproteins

TABLE 1 | Ingredient composition of the experimental diets.

Ingredients	LFC	HFD	HFBSF
Maintenance diet (g)	100.0	57.6	57.6
Lard oil (g)	–	15.0	15.0
Sucrose (g)	–	20.0	20.0
Casein (g)	–	5.0	5.0
Cholesterol (g)	–	1.2	1.2
Sodium cholate (g)	–	0.2	0.2
Calcium bicarbonate (g)	–	0.6	0.6
Stone powder (g)	–	0.4	0.4
Bamboo shoot powder (g)	–	–	1.0

LFC, low-fat control diet; HFD, high-fat diet; HFBSF, high-fat diet with bamboo shoot powder.

by dextran sulfate/magnesium chloride. LDL-C levels were determined from the Friedewald formula.

Histology and Staining

After dehydration and washing, fat and liver were paraffin-embedded. Each tissue specimen was made into paraffin sections (5 Mm). The sections were stained with hematoxylin-eosin (HE), and the staining images were analyzed on an Olympus microscope.

Gut Microbiota Profiling

Fecal samples were collected from live female mice and stored at -80°C ; DNA was then extracted by the Omega Biotek E.Z.N.A. Stool DNA kit. PCR was used to amplify variable regions (3 and 4, V3-V4) of the 16S rRNA gene with the modified primers 338F (ACTCCTACGGGAGGCAGCAG) and 806R (GGACTACHVGGGTWTCTAAT). The gut microbiota data were collected using previously described methods (Schloss et al., 2009; Segata et al., 2011; Fan et al., 2020).

RESULTS AND DISCUSSION

Bamboo Shoot Powder

The bamboo shoot powder was obtained from fresh Lei bamboo shoots (Figure 1). The powder had a unique aroma, dietary fiber, and abundant nutrients because the fresh shoots were rapidly processed. The main ingredients of the shoot powder were cellulose (12.47%), hemicellulose (12.94%), lignin (20.24%), and protein (21.18%); the total dietary fiber content was 45.65%.

The bamboo shoot powder was also characterized by SEM, IR, and XRD (Figure 2). The bamboo shoot powder was mixed with fibriform material and particulate matter. The fibriform material (Figures 2A-2) had obvious sags and crests, which was similar to the structure of dietary fiber (the main ingredient) in bamboo shoot. Other main ingredients in bamboo shoot were protein; thus, the morphology of the particulate matter (Figures 2A-4) might be related to the ingredient. The bamboo shoot powder showed clear absorption peaks at 3280 (OH), 2929 (CH_2), 1629 ($\text{C}=\text{O}$), 1395 (C-H), 1045 (C-O), and 886 (C-O-C) cm^{-1} (Figure 2B). Generally, the cellulose in bamboo is the crystalline

components with crystallinity degree of 40–60% (Huang et al., 2019b; Lin et al., 2020). In Figure 2C, it is found that there is no crystalline peak in the XRD pattern of bamboo shoot, indicating the obtained substrate contained the amorphous compositions. This can be explained by the fact that the obtained bamboo shoot is the product of bamboo in the early stage (~ 2 months), which cannot endow the cellulose in bamboo shoot to crystallization.

Body Weight

To determine whether bamboo shoot powder suppressed HFD-induced body weight gain, three groups (LFC, HFD, and HFBSF) of mice were separately fed for 7 weeks, and the results are shown in Figure 3.

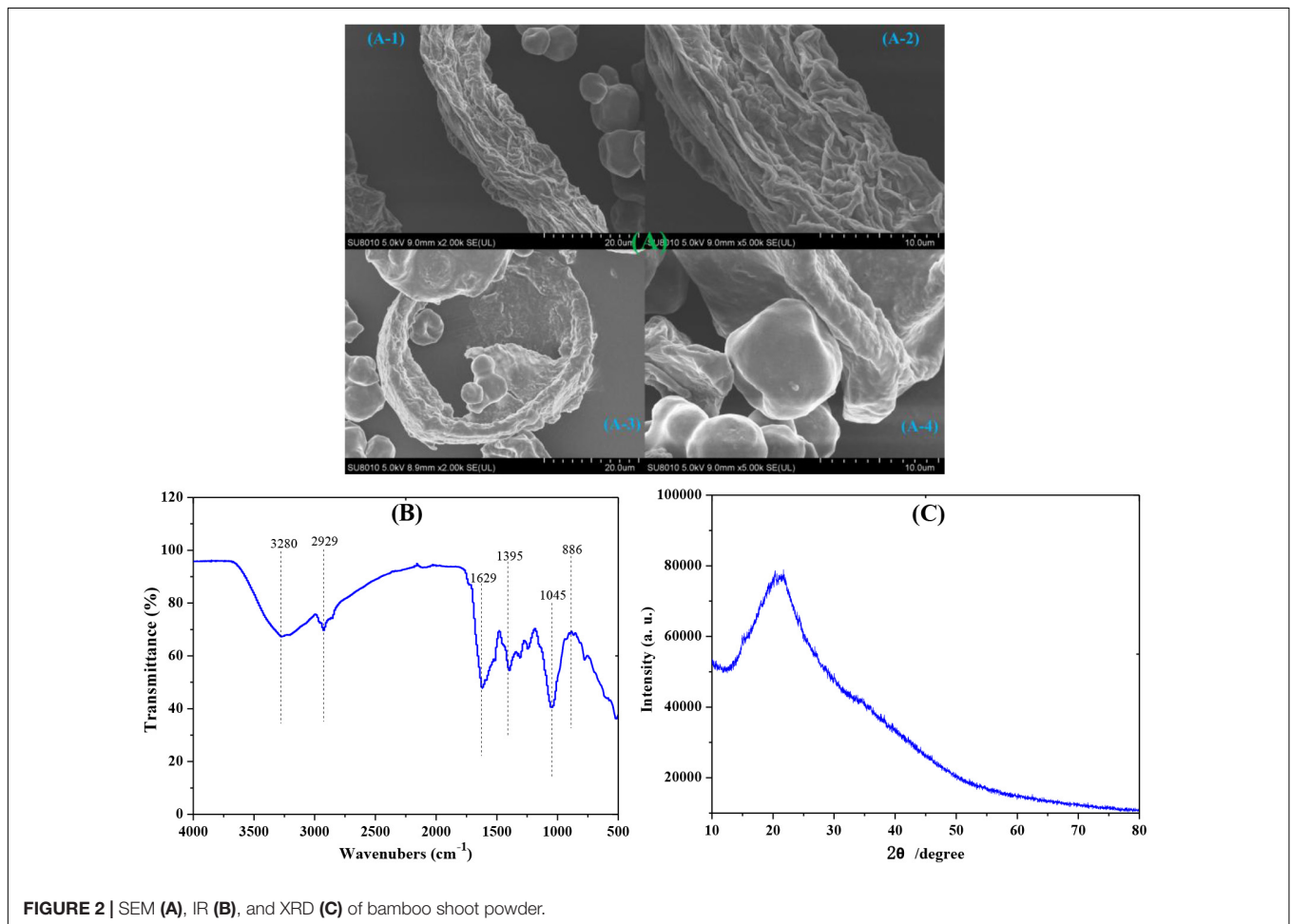
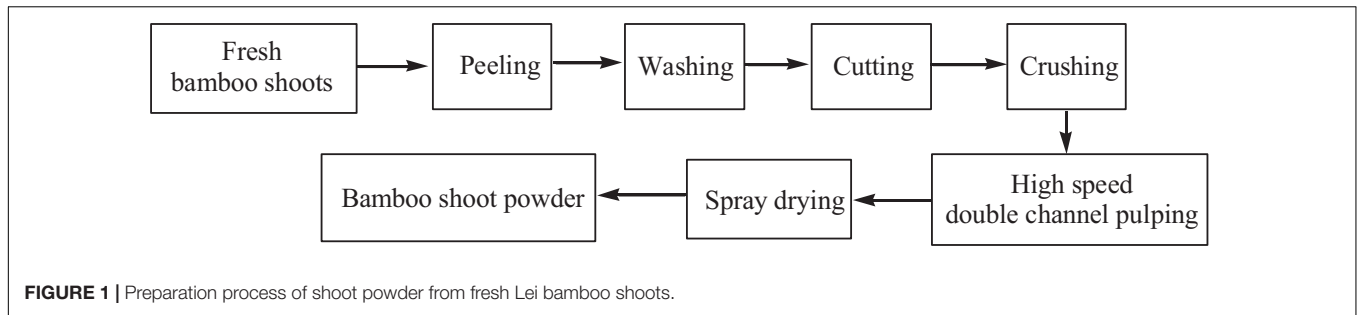
There was no difference in body weight among the three diet groups at the start of the experiment (day 0), and the body weight between the three groups changed little after the mice were fed for 2 weeks. At week three, the body weight of the HFD mice increased compared with the other two groups. After 7 weeks, the body weight of HFBSF mice was close to that of LFC mice, and the body weight of HFBSF and LFC were both significantly lower than the body weight of HFD mice. Thus, the addition of bamboo shoot powder in the diet of mice can mitigate body weight gain associated with a HFD, indicating that the shoot powder provided health benefits to mice.

Biochemical Indicators

To investigate the changes of biochemical indicators in mice during the feeding process, the levels of triglycerides (TG), blood glucose (GLU), total cholesterol (CHOL), high-density lipoprotein (HDL-C), and low-density lipoprotein (LDL-C) were compared among the three groups of mice at the end of the experiment (Figure 4). The levels of all five blood lipid indexes were increased in the HFD group compared with the other two groups. TGs are the main component of body fat, and excessive TGs are a direct cause of obesity and fatty liver disease (Lindkvist et al., 2012). The addition of bamboo shoot powder to the mice's diet could improve the level of TG ($p < 0.05$, vs. HFD group). The GLU level can have a substantial effect on morbidity and mortality; for example, even a slight increase in GLU levels can increase the mortality of patients with COVID-19 (Kesavadev et al., 2021). The GLU level was lower in HFBSF mice than in HFD mice ($p < 0.01$).

Cholesterol CHOL is a key blood lipid index in clinical practice, and high levels of CHOL can lead to diabetes, coronary heart disease, and atherosclerosis (Luo et al., 2019). CHOL levels (3.62 mmol/L, $p < 0.001$) were higher in HFD mice than in LFC mice (2.24 mmol/L). However, the CHOL level of HFBSF mice was low (2.29 mmol/L), which was similar to the CHOL level of LFC mice. Thus, the addition of bamboo shoot powder could decrease the CHOL level when mice consumed a HFD. A high level of LDL-C may lead to atherosclerosis as well as cardiovascular and cerebrovascular diseases, and HFBSF mice had lower LDL-C levels.

Thus, supplementation of fresh Lei bamboo shoot powder reduced the levels of TG, GLU, CHOL, HDL-C, and LDL-C in mice fed a HFD, indicating that the bamboo powder provided health benefits.



Fat and Liver

Significant differences in the pattern and number of mice fat cells were observed among LFC, HFD, and HFBSF mice after they were fed for 7 weeks. Fat histology images with hematoxylin-eosin (HE) staining are shown in **Figure 5**. The fat cells of HFD mice (**Figure 5B**) were larger than those of LFC (**Figure 5A**) and HFBSF mice (**Figure 5C**). This indicated that HFD mice could lead to obesity, and the addition of bamboo shoot powder to the HFD alleviated obesity, which is consistent with the body weight data shown in **Figure 3**.

Liver histology images (HE staining) of hepatocytes are shown in **Figure 6**. The only noticeable (albeit subtle) difference among

the images of the three groups of mice was the presence of a small amount of lipids in the HFD image (**Figure 6B**). This suggests that HFD mice tended to have fatty livers. Given that no significant obesity was observed in HFBSF mice, the addition of bamboo shoot powder to the HFD might reduce the risk of fatty liver disease.

Gut Microbiota

Species with relative abundances greater than 1% are shown in **Figure 7**. The relative abundances of different classes of bacteria significantly differed among LFC, HFD, and HFBSF mice (**Figure 7A**). The abundance of Bacilli was high in HFD mice

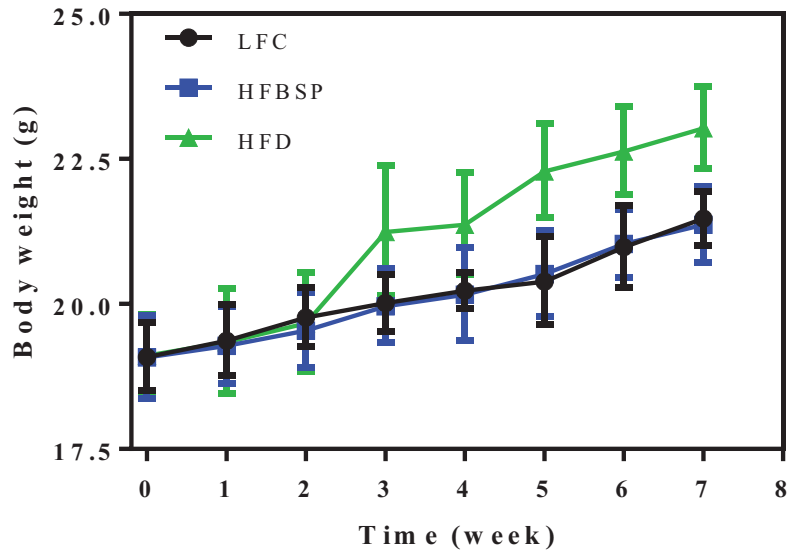


FIGURE 3 | The effect of bamboo shoot powder on the body weight of mice fed a HFD for 7 weeks. Data are means \pm SEM, $n = 10$ /group.

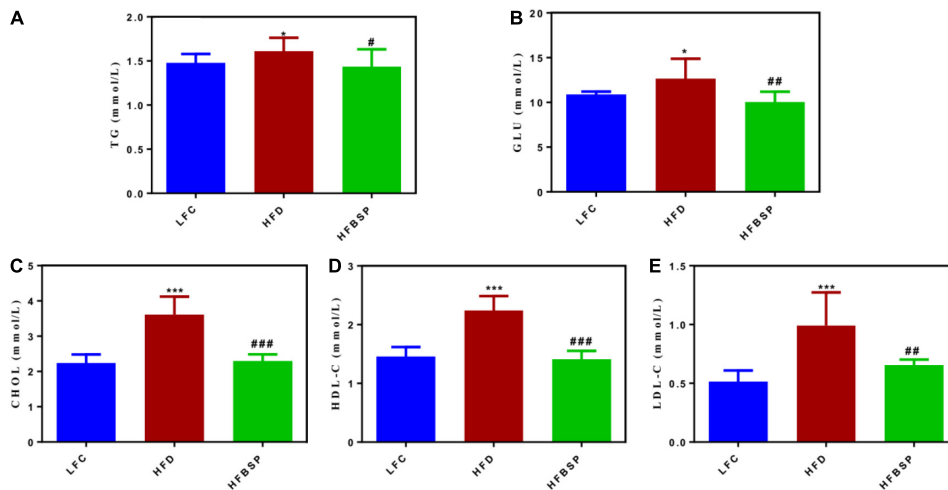


FIGURE 4 | The effect of bamboo shoot powder on the biochemical parameters of TG (A), GLU (B), CHOL (C), HDL-C (D), and LDL-C (E) of mice fed a HFD for 7 weeks. Data are means \pm SEM, $n = 10$ /group. * $p < 0.05$, *** $p < 0.001$, vs. LFC group. # $p < 0.05$, ## $p < 0.01$, ### $p < 0.001$, vs. HFD group.

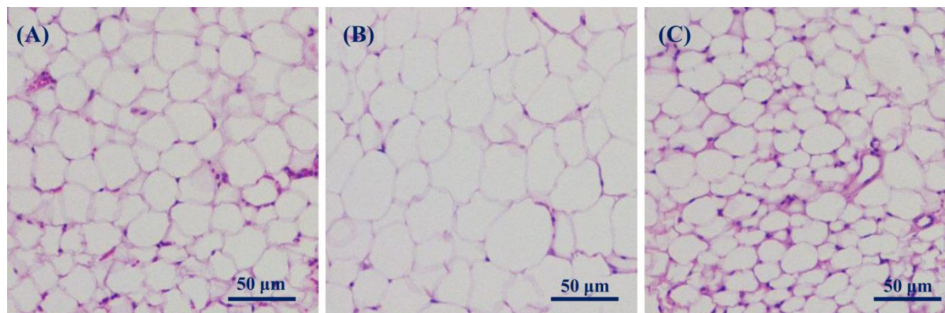


FIGURE 5 | Fat histology images (HE staining). (A) LFC; (B) HFD; and (C) HFBS.

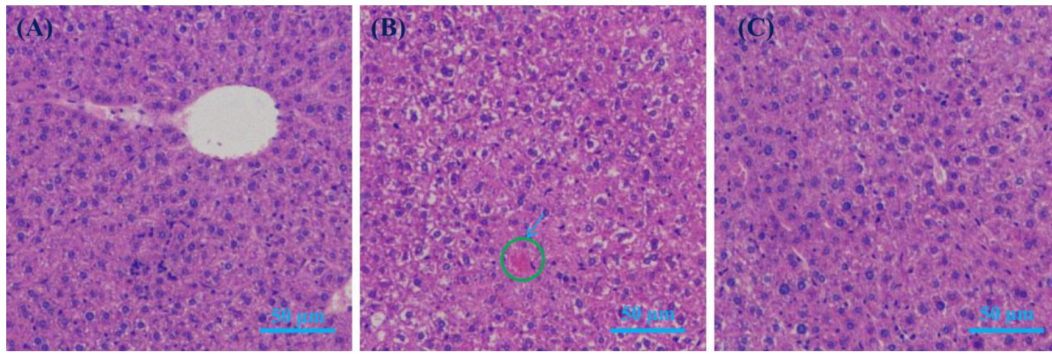


FIGURE 6 | Liver histology images (HE staining). **(A)** LFC; **(B)** HFD; and **(C)** HFBSF.

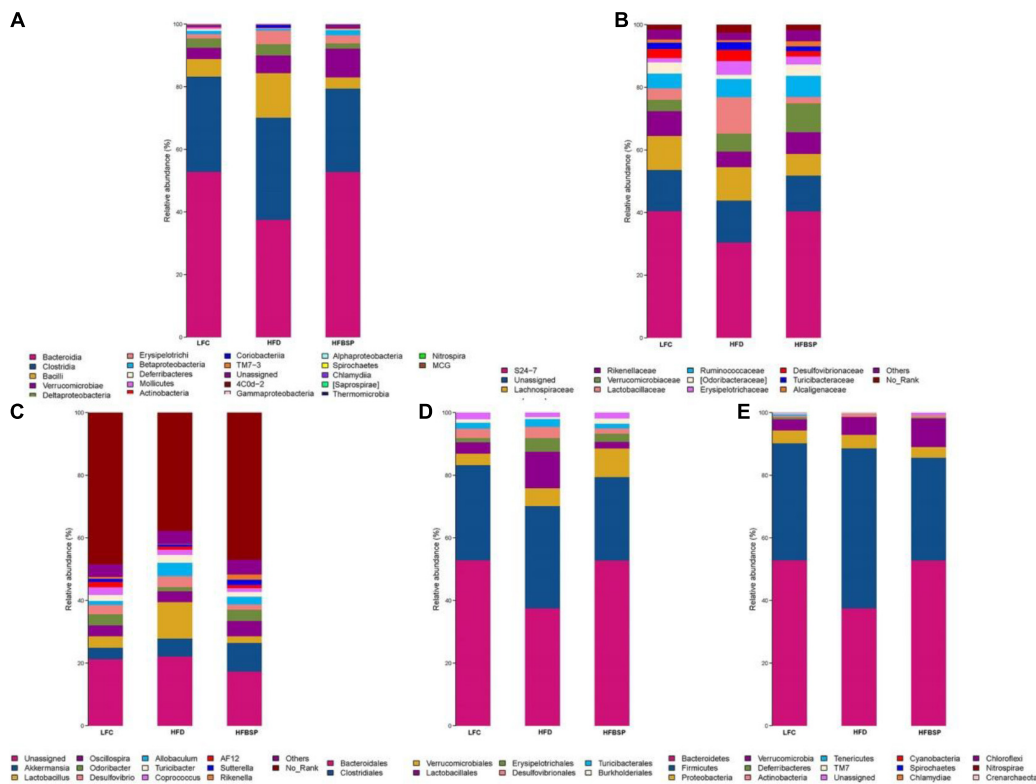


FIGURE 7 | Characterization of the natural gut microbiota of across LFC, HFD, and HFBSF mice ($n = 10/\text{group}$) at the class **(A)**, family **(B)**, genus **(C)**, order **(D)**, and phylum **(E)** level.

but low in HFBSF mice. The abundance of Verrucomicrobiae was higher in HFBSF mice than in LFC and HFD mice. The abundances of different families in each group are shown in **Figure 7B**. The abundance of Lactobacillaceae was significantly higher in HFD mice than in LFC and HFBSF mice, and the abundance of Verrucomicrobiaceae was higher in HFBSF mice than in LFC and HFD mice. **Figure 7C** shows that the abundances of Lactobacillus and Allobaculum were significantly higher in HFD mice than in LFC and HFBSF mice; the abundance of Akkermansia was higher in HFBSF mice than in LFC and HFD mice.

Figure 7D reveals that the abundance of Lactobacillales was significantly higher in HFD mice than in LFC and HFBSF mice, and the abundance of Verrucomicrobiales was higher in HFBSF mice than in LFC and HFD mice. **Figure 7E** displays the relative abundance of intestinal microflora at the phylum level. The abundance of Firmicutes was higher in HFD mice than in LFC and HFBSF mice, but the abundance of Bacteroidetes was relatively low; the abundance of Verrucomicrobia was high in HFBSF mice.

Previous studies have shown that there is a relationship between obesity and intestinal flora composition. The abundance

of *Bacteroides* has often been observed to be low in obese patients. However, *Bacteroides* increased in obese patients during weight loss under a low-fat diet, a finding that is consistent with the body weight data shown in **Figure 3**. *Lactobacillus acidophilus* and *Clostridium difficile* are associated with insulin resistance. *Lactobacillus* is positively correlated with fasting blood glucose and blood HbA1c levels, whereas *C. difficile* is negatively correlated with these indicators. *Bacteroides*, *Akkermansia*, and other bacteria are known to relieve obesity (Precup and Vodnar, 2019). Thus, the addition of bamboo shoot powder to a HFD could improve gut microbiota and alleviate obesity in mice.

CONCLUSION

A bamboo shoot powder was prepared from fresh *Phyllostachys praecox* shoots with a 45.65% dietary fiber content (cellulose, hemicellulose, and lignin). At the end of the 7-week diet experiment, the body weights of HFD mice were higher compared with LFC and HFBSP mice, indicating that this powder could help maintain the weight of HFD mice. The shoot powder supplement could also improve the levels of TG, GLU, CHOL, HDL-C, and LDL-C of HFD mice. In addition, the fat cells of HFD mice were larger than those of LFC and HFBSP mice, which reflected weight gain, and the addition of shoot powder might reduce the fatty liver disease risk of HFD mice. The shoot powder might also improve the gut microbiota profile of HFD mice. Thus, the developed shoot powder could be used as a natural additive that broadens the applications of bamboo shoots in the food industry.

REFERENCES

- Bvenura, C., and Sivakumar, D. (2017). The role of wild fruits and vegetables in delivering a balanced and healthy diet. *Food Res. Int.* 99, 15–30. doi: 10.1016/j.foodres.2017.06.046
- Chen, G., Chen, K., Zhang, R., Chen, X., and Kan, J. (2018). Polysaccharides from bamboo shoots processing by-products: new insight into extraction and characterization. *Food Chem.* 245, 1113–1123. doi: 10.1016/j.foodchem.2017.11.059
- Chen, G., Fang, C., Ran, C. X., Tan, Y., Yu, Q., and Kan, J. (2019). Comparison of different extraction methods for polysaccharides from bamboo shoots (*Chimonobambusa quadrangularis*) processing by-products. *Int. J. Biol. Macromol.* 130, 903–914. doi: 10.1016/j.ijbiomac.2019.03.038
- Chen, J., Yu, Y., Zhu, B., Han, J., Liu, C., Liu, C., et al. (2021). Synthesis of biocompatible and highly fluorescent N-doped silicon quantum dots from wheat straw and ionic liquids for heavy metal detection and cell imaging. *Sci. Total Environ.* 765:142754. doi: 10.1016/j.scitotenv.2020.142754
- Dong, H., Zheng, L., Yu, P., Jiang, Q., Wu, Y., Huang, C., et al. (2020). Characterization and application of lignin-carbohydrate complexes from lignocellulosic materials as antioxidants for scavenging in vitro and in vivo reactive oxygen species. *ACS Sustain. Chem. Eng.* 8, 256–266. doi: 10.1021/acssuschemeng.9b05290
- Fan, Y., Qin, Y., Chen, M., Li, X., Wang, R., Huang, Z., et al. (2020). Prenatal low-dose DEHP exposure induces metabolic adaptation and obesity: role of hepatic thiamine metabolism. *J. Hazard. Mater.* 385:121534. doi: 10.1016/j.jhazmat.2019.121534
- He, K., Li, Q., Li, Y., Li, B., and Liu, S. (2020). Water-insoluble dietary fibers from bamboo shoot used as plant food particles for the stabilization of O/W Pickering emulsion. *Food Chem.* 310:125925. doi: 10.1016/j.foodchem.2019.125925

DATA AVAILABILITY STATEMENT

The raw data supporting the conclusions of this article will be made available by the authors, without undue reservation.

ETHICS STATEMENT

The animal study was reviewed and approved by the Institutional Animal Care and Use Committee (IACUC) of Nanjing Medical University. Written informed consent was obtained from the owners for the participation of their animals in this study.

AUTHOR CONTRIBUTIONS

JY, YP, and HY did the experiments and analyzed experimental data. JY and LW designed the research and wrote the manuscript. All authors contributed to the article and approved the submitted version.

FUNDING

The authors gratefully acknowledge that the project was supported by the Key Research and Development Program of Zhejiang Province (2020C02036), the Special Forestry Industry Research Project of Guizhou Province (2020-28), the Science and Technology Planned Projects of Zhejiang Province (2018F10009), and the National Key Research and Development (R&D) Plan (2016YFD060090305).

- Huang, C., Dong, H., Su, Y., Wu, Y., Narron, R., and Yong, Q. (2019a). Synthesis of carbon quantum dot nanoparticles derived from byproducts in bio-refinery process for cell imaging and in vivo bioimaging. *Nanomaterials* 9:387. doi: 10.3390/nano9030387
- Huang, C., Dong, H., Zhang, Z., Bian, H., and Yong, Q. (2020). Procuring the nano-scale lignin in prehydrolyzate as ingredient to prepare cellulose nanofibril composite film with multiple functions. *Cellulose* 27, 9355–9370. doi: 10.1007/s10570-020-03427-9
- Huang, C., Lin, W., Lai, C., Li, X., Jin, Y., and Yong, Q. (2019b). Coupling the post-extraction process to remove residual lignin and alter the recalcitrant structures for improving the enzymatic digestibility of acid-pretreated bamboo residues. *Bioresour. Technol.* 285:121355. doi: 10.1016/j.biortech.2019.121355
- Huang, C., Tang, S., Zhang, W., Tao, Y., Lai, C., Li, X., et al. (2018). Unveiling the structural properties of lignin-carbohydrate complexes in bamboo residues and its functionality as antioxidants and immunostimulants. *ACS Sustain. Chem. Eng.* 6, 12522–12531. doi: 10.1021/acssuschemeng.8b03262
- Hunter, J. A., Hollands, G. J., Pilling, M., and Marteau, T. M. (2019). Impact of proximity of healthier versus less healthy foods on intake: a lab-based experiment. *Appetite* 133, 147–155. doi: 10.1016/j.appet.2018.10.021
- Kesavadev, J., Misra, A., Saboo, B., Aravind, S. R., Hussain, A., Czupryniak, L., et al. (2021). Blood glucose levels should be considered as a new vital sign indicative of prognosis during hospitalization. *Diabetes Metab. Syndr. Clin. Res. Rev.* 15, 221–227. doi: 10.1016/j.dsx.2020.12.032
- Li, J. J., Jiang, H., Huang, C. X., Fang, C. H., Tang, Q. Z., Xia, H., et al. (2002). Elevated level of plasma C-reactive protein in patients with unstable angina: its relations with coronary stenosis and lipid profile. *Angiology* 53, 265–272. doi: 10.1177/000331970205300303

- Li, X., Fu, B., Guo, J., Ji, K., Xu, Y., Dahab, M. M., et al. (2018). Bamboo shoot fiber improves insulin sensitivity in high-fat diet-fed mice. *J. Funct. Foods* 49, 510–517. doi: 10.1016/j.jff.2018.09.016
- Lin, W., Chen, D., Yong, Q., Huang, C., and Huang, S. (2019). Improving enzymatic hydrolysis of acid-pretreated bamboo residues using amphiphilic surfactant derived from dehydroabietic acid. *Bioresour. Technol.* 293:122055. doi: 10.1016/j.biortech.2019.122055
- Lin, W., Xing, S., Jin, Y., Lu, X., Huang, C., and Yong, Q. (2020). Insight into understanding the performance of deep eutectic solvent pretreatment on improving enzymatic digestibility of bamboo residues. *Bioresour. Technol.* 306:123163. doi: 10.1016/j.biortech.2020.123163
- Lindkvist, B., Appelros, S., Regnér, S., and Manjer, J. (2012). A prospective cohort study on risk of acute pancreatitis related to serum triglycerides, cholesterol and fasting glucose. *Pancreatology* 12, 317–324. doi: 10.1016/j.pan.2012.05.002
- Luo, X., Wang, Q., Zheng, B., Lin, L., Chen, B., Zheng, Y., et al. (2017). Hydration properties and binding capacities of dietary fibers from bamboo shoot shell and its hypolipidemic effects in mice. *Food Chem. Toxicol.* 109, 1003–1009. doi: 10.1016/j.fct.2017.02.029
- Luo, Y., Peng, B., Wei, W., Tian, X., and Wu, Z. (2019). Antioxidant and anti-diabetic activities of polysaccharides from guava leaves. *Molecules* 24:1343. doi: 10.3390/molecules24071343
- Luo, Z., Feng, S., Pang, J., Mao, L., Shou, H., and Xie, J. (2012). Effect of heat treatment on lignification of postharvest bamboo shoots (*Phyllostachys praecox f. prevernalis*). *Food Chem.* 135, 2182–2187. doi: 10.1016/j.foodchem.2012.07.087
- Nair, K. M., and Augustine, L. F. (2018). Food synergies for improving bioavailability of micronutrients from plant foods. *Food Chem.* 238, 180–185. doi: 10.1016/j.foodchem.2016.09.115
- Park, E. J., and Jhon, D. Y. (2009). Effects of bamboo shoot consumption on lipid profiles and bowel function in healthy young women. *Nutrition* 25, 723–728. doi: 10.1016/j.nut.2009.01.007
- Pei, W., Chen, Z. S., Chan, H. Y. E., Zheng, L., Liang, C., and Huang, C. (2020). Isolation and identification of a novel anti-protein aggregation activity of lignin-carbohydrate complex from *Chionanthus retusus* leaves. *Front. Bioeng. Biotechnol.* 8:573991. doi: 10.3389/fbioe.2020.573991
- Precup, G., and Vodnar, D. C. (2019). Gut *Prevotella* as a possible biomarker of diet and its eubiotic versus dysbiotic roles: a comprehensive literature review. *Brit. J. Nutr.* 122, 131–140. doi: 10.1017/S0007114519000680
- Sarkar, D., Chandra, A. K., Chakraborty, A., Ghosh, S., and Ray, I. (2019). Effects of bamboo shoots (*Bambusa balcooa*) on thyroid hormone synthesizing regulatory elements at cellular and molecular levels in thyrocytes. *J. Ethnopharmacol.* 250:112463. doi: 10.1016/j.jep.2019.112463
- Schloss, P. D., Westcott, S. L., Ryabin, T., Hall, J. R., Hartmann, M., Hollister, E. B., et al. (2009). Introducing mothur: open-source, platform-independent, community-supported software for describing and comparing microbial communities. *Appl. Environ. Microbiol.* 75, 7537–7541. doi: 10.1128/AEM.01541-09
- Segata, N., Izard, J., Waldron, L., Gevers, D., Miropolsky, L., Garrett, W. S., et al. (2011). Huttenhower, metagenomic biomarker discovery and explanation. *Genome Biol.* 12:R60. doi: 10.1186/gb-2011-12-6-r60
- Singhal, P., Bal, L. M., Satya, S., Sudhakar, P., and Naik, S. N. (2013). Bamboo shoots: a novel source of nutrition and medicine. *Crit. Rev. Food Sci.* 53, 517–534. doi: 10.1080/10408398.2010.531488
- Su, Y., Dong, H., Li, M., Lai, C., Huang, C., and Yong, Q. (2019). Isolation of the flavonoid from bamboo residues and its application as metal ion sensor in vitro. *Polymers* 11:1377. doi: 10.3390/polym11091377
- Tao, Y., Wang, T., Huang, C., Lai, C., Ling, Z., and Yong, Q. (2021). Effects of seleno-*Sesbania canabina* galactomannan on anti-oxidative and immune function of macrophage. *Carbohydr. Polym.* 261:117833. doi: 10.1016/j.jbiomac.2020.01.281
- Wang, H. X., and Ng, T. B. (2003). Dendrocin, a distinctive antifungal protein from bamboo shoots. *Biochem. Biophys. Res. Commun.* 307, 750–755. doi: 10.1016/S0006-291X(03)01229-4
- Wang, P., Yin, B., Dong, H., Zhang, Y., Zhang, Y., Chen, R., et al. (2020). Coupling biocompatible au nanoclusters and cellulose nanofibrils to prepare the antibacterial nanocomposite films. *Front. Bioeng. Biotechnol.* 18:986. doi: 10.3389/fbioe.2020.00986
- Wijaya, C. J., Ismadji, S., Aparamarta, H. W., and Gunawana, S. (2019). Optimization of cellulose nanocrystals from bamboo shoots using response surface methodology. *Heliyon* 5:e02807. doi: 10.1016/j.heliyon.2019.e02807
- Yang, J., Wu, L., Pan, Y., and Zhong, H. (2019). Extraction, optical properties and bio-imaging of fluorescent composition from Moso bamboo shoots. *J. Renew. Mater.* 7, 1209–1219. doi: 10.32604/jrm.2019.07896
- Yu, P., Zheng, L., Wang, P., Chai, S., Zhang, Y., Shi, T., et al. (2020). Development of a novel polysaccharide-based iron oxide nanoparticle to prevent iron accumulation-related osteoporosis by scavenging reactive oxygen species. *Int. J. Biol. Macromol.* 165, 1634–1645. doi: 10.1016/j.jbiomac.2020.10.016
- Zheng, L., Yu, P., Zhang, Y., Wang, P., Yan, W., Guo, B., et al. (2021). Evaluating the bio-application of biomacromolecule of lignin-carbohydrate complexes (LCC) from wheat straw in bone metabolism via ROS scavenging. *Int. J. Biol. Macromol.* 176, 13–25. doi: 10.1016/j.jbiomac.2021.01.103
- Zheng, Y., Wang, Q., Huang, J., Fang, D., Zhuang, W., Luo, X., et al. (2019). Hypoglycemic effect of dietary fibers from bamboo shoot shell: an in vitro and in vivo study. *Food Chem. Toxicol.* 127, 120–126. doi: 10.1016/j.fct.2019.03.008
- Zheng, Y., Yu, Y., Lin, W., Jin, Y., Yong, Q., and Huang, C. (2021). Enhancing the enzymatic digestibility of bamboo residues by biphasic phenoxymethanol-acid pretreatment. *Bioresour. Technol.* 325:124691. doi: 10.1016/j.biortech.2021.124691

Conflict of Interest: The authors declare that the research was conducted in the absence of any commercial or financial relationships that could be construed as a potential conflict of interest.

Copyright © 2021 Yang, Wu, Yang and Pan. This is an open-access article distributed under the terms of the Creative Commons Attribution License (CC BY). The use, distribution or reproduction in other forums is permitted, provided the original author(s) and the copyright owner(s) are credited and that the original publication in this journal is cited, in accordance with accepted academic practice. No use, distribution or reproduction is permitted which does not comply with these terms.



The *in vitro* and *in vivo* Antioxidant and Immunomodulatory Activity of Incomplete Degradation Products of Hemicellulosic Polysaccharide (Galactomannan) From *Sesbania cannabina*

Yuheng Tao^{1,2}, Ting Wang¹, Chenhuan Lai^{1,2}, Zhe Ling¹, Yanmin Zhou³ and Qiang Yong^{1,2*}

¹ Jiangsu Co-Innovation Center for Efficient Processing and Utilization of Forest Resources, Nanjing Forestry University, Nanjing, China, ² Key Laboratory of Forest Genetics and Biotechnology of Ministry of Education, Nanjing Forestry University, Nanjing, China, ³ College of Animal Science and Technology, Nanjing Agricultural University, Nanjing, China

OPEN ACCESS

Edited by:

Lei Wang,
Jeju National University, South Korea

Reviewed by:

Li Zhang,
Yancheng Institute of Technology,
China
Thilina U. Jayawardena,
Jeju National University, South Korea

*Correspondence:

Qiang Yong
swhx@njfu.com.cn

Specialty section:

This article was submitted to
Bioprocess Engineering,
a section of the journal
Frontiers in Bioengineering and
Biotechnology

Received: 12 March 2021

Accepted: 22 March 2021

Published: 09 April 2021

Citation:

Tao Y, Wang T, Lai C, Ling Z,
Zhou Y and Yong Q (2021) The *in vitro*
and *in vivo* Antioxidant
and Immunomodulatory Activity
of Incomplete Degradation Products
of Hemicellulosic Polysaccharide
(Galactomannan) From *Sesbania*
cannabina.
Front. Bioeng. Biotechnol. 9:679558.
doi: 10.3389/fbioe.2021.679558

As known, the nutritional status affects antioxidant capacity and immunity, ultimately affecting the body's health. Recently, hemicellulosic polysaccharides of galactomannan in different biomass and their degradation products are gaining more attention due to excellent antioxidant enhancement and immunomodulatory activity. Herein, incomplete degradation products of galactomannan (IDPG) were prepared from the enzymatic hydrolysis of *Sesbania cannabina* seeds, followed by the *in vitro* and *in vivo* experiments. Using an H₂O₂-injured RAW264.7 cells model, IDPG was demonstrated to have antioxidant capacity, as indicated by superoxide dismutase (SOD) activity and malondialdehyde (MDA) content. While in the evaluation in laying hens (68-weeks-old), diets were supplemented with 0, 0.01, 0.025, and 0.05% IDPG for 8 weeks, respectively. Our results showed that IDPG can improve antioxidant capacity by increasing antioxidants contents and reducing MDA content. Furthermore, IDPG can increase immunoglobulins and cytokines secretion, thereby enhancing the immunity of laying hens. This result was further demonstrated by *in vitro* experiment, in which IDPG significantly increased the secretion of nitric oxide (NO), tumor necrosis factor- α (TNF- α), interleukin 6 (IL-6), and toll-like receptor 4 (TLR4) in RAW264.7 cells ($P < 0.05$). Overall, IDPG can improve antioxidant function and modulate immunological response, thereby the concept of using IDPG for health may gain a little more credibility.

Keywords: hemicellulosic polysaccharide, incomplete degradation products of galactomannan, antioxidant function, immunomodulatory activity, *Sesbania cannabina*

INTRODUCTION

Hemicellulosic polysaccharides from different biomass have been applied in various fields (Li et al., 2020; Xiang et al., 2020). Recently, numerous *in vitro* experiments about natural polysaccharides from different biomass have confirmed that they can not only enhance immunity but also suppress excessive immune responses caused by various stimuli (Tang et al., 2019). This subset of

polysaccharides includes examples such as arabinogalactans (Tang et al., 2018), galactomannan (Gu et al., 2020), β -glucan (Pan et al., 2020), and so on. Among these examples, polysaccharides with mannose as the main chain, such as yeast cell wall mannan, glucomannan, and galactomannan, have garnered great interest because they are easier to bind several receptors on immune cells to activate immune responses (Hernandez et al., 2011). Toll-like receptor 4 (TLR4), an important receptor in both innate and adaptive immune responses, was identified to have a high affinity for acemannan (Karaca et al., 1995). Moreover, mannose-binding lectins present on macrophages can bind mannan and activate the immunity via a non-self-recognition mechanism (Gamal-Eldeen et al., 2006). These outstanding characteristics constitute the major advantages of polysaccharides with mannose as the main chain different from other types of polysaccharides on immunity function. Besides, mannan or galactomannan has been found to have beneficial antioxidant functionality. For example, galactomannan from *Caesalpinia gilliesii* was found to induce a significant reduction in hepatic malondialdehyde in Wistar albino rats (Abdel-Megeed et al., 2019). Based on these properties, these multifunctional materials can be further applied *in vivo* experimentation as an animal feed additive.

Considering the entire array of components involved in the immune system, it presents as a complex, but precisely interwoven network of biochemical mechanisms (Devasagayam and Sainis, 2002). It is vulnerable to oxidative stress from reactive oxygen, which attacks cellular components produced during the functioning of the immune system and leads immune cells to death (De la Fuente, 2002; Pei et al., 2020; Yu et al., 2020; Gu et al., 2021; Zheng et al., 2021). Therefore, during certain diseased states or aging, there is a need for enhancing the antioxidant capacity while potentiating the immune function. In this concept immunomodulators having antioxidant abilities, especially natural polysaccharides have considerable potential.

The attention was put on the galactomannan from the endosperm of *Sesbania cannabina* seeds, which is widely available in many coastal regions of tropical and subtropical countries of Asia (Hossain et al., 2002). The tolerance of *S. cannabina* to salt and barren companions by growing quickly allows it can grow in poor soil (Cowan et al., 1982). But for too long, the *S. cannabina* seeds have lacked an effective use. A promising use as a plant-based protein source is also no longer valued due to the reduction in nutrient absorption caused by the high viscosity of galactomannan. Hossain et al. (2001) found that the inclusion of *S. aculeate* seeds in the diet of common carp (*Cyprinus carpio*) affects nutrient absorption and utilization. Fortunately, this side effect can be erased by lowering the molecular weight of galactomannan, because an example of partially hydrolyzed guar gum (PHGG) was reported. The supplement of 5% intact guar gum (mainly galactomannan) in the diet of rats decreased food consumption, resulting in a lower increase in body weight gain, as described by Hidehisa et al. (1994). However, the rats fed on 5% PHGG did not show any significant change in the above values relative to the control diet. Based on this successful practice, it is possible to concentrate on the effect of incomplete degradation products of

galactomannan (IDPG) on the antioxidant capacity and immune function of laying hens after eliminating the possible negative effects brought by viscosity.

Generally speaking, the IDPG refer to the degradation products of natural galactomannan with a polymerization degree of more than 2, which do not contain monosaccharides such as mannose and galactose. Herein, an enzymatic degradation process was performed by β -endo-mannanase to obtain IDPG (Tao et al., 2020). Specifically, the hydrolysis effect of mannanase reduced the average molecular weight of galactomannan to one-tenth of the initial value. Next, the anti-oxidative ability of IDPG was evaluated by analyzing the cellular protective effects against H_2O_2 -induced injury in macrophage RAW 264.7 cells. Moreover, the immunomodulatory properties of IDPG were evaluated by analyzing their ability on influencing the secretion of NO and cytokines from macrophage RAW 264.7 cells. Furthermore, a feeding trial involving laying hens was conducted to evaluate how varied IDPG feed addition rates influence antioxidant capacity and immune function. It is our intent for this work to provide new evidence supporting the value in both the preparation and utilization of IDPG for laying hen farming. Moreover, the development of high value-added IDPG to feed additives will increase the economic value of *S. cannabina* seeds.

MATERIALS AND METHODS

Preparation of the IDPG

The IDPG was prepared by enzymatic hydrolysis of galactomannan from *Sesbania cannabina* seeds using β -mannanase. The *Sesbania cannabina* seeds used in this experiment were purchased from a local farm in Yancheng city, Jiangsu Province of China. First, *S. cannabina* seeds were ground (Mini plant shredder F2102, Taisite Instrument Co., Ltd., Tianjin, China) and then suspended in distilled water at a galactomannan concentration of 40 g/L. The suspension was treated with β -mannanase from *Trichoderma reesei* (20 U/g galactomannan, 72 h, 50°C). β -endo-mannanase (EC 3.2.1.78) was obtained from *T. reesei* Rut C-30 using avicel as a substrate. Before adding an enzyme, the pH of the enzyme treatment solution was adjusted to 4.8 with 0.05 M citric acid buffer. After reaction time ceased, enzyme deactivation was applied by boiling the mixture at $\sim 100^\circ\text{C}$ for 10 min. Once boiled, the suspension was centrifuged (10,000 rpm, 10 min) and the obtained supernatants were nanofiltrated (200 Da, ST-Recovery Tech Co., Nanjing, Jiangsu, China) to remove galactose and mannose and henceforth referred to as IDPG solutions. Finally, this solution was spray-dried at 160°C (B-191, BUCHI, Flawil, Switzerland) to obtain solid IDPG. The galactomannan degradation products content in the solid IDPG was 45.96%, which was determined by a sulfuric acid hydrolysis method and high-performance anion-exchange chromatography with pulsed amperometric detection as described by Tao et al. (2020). The weight-average molecular weight of IDPG was finally determined to 1.74~14.12 kDa by high-performance size exclusion chromatography (HPSEC) as described by Tao et al. (2020).

Antioxidant Activity Evaluated by H₂O₂-Induced Injury Cell Model Cell Culture

The cells were cultured in DMEM supplemented with penicillin (100 units/mL), streptomycin (100 units/mL), and 10% (v/v) fetal bovine serum (FBS) at 37°C in a humidified atmosphere with 5% CO₂.

Toxicity Measurements

The toxicity measurements of IDPG on the RAW 264.7 cells were evaluated by cultivating cells with IDPG at different concentrations (25, 50, 100, 200, 400, and 800 µg/mL) for 24 h. Toxicity results were expressed as the cell viability, which was determined by a CCK-8 assay according to the manufacturer's protocols. All toxicity experiments were performed in triplicates.

Injured Cell Model Induced by H₂O₂

RAW 264.7 cells were seeded on a culture of 96-well plates at a density of 1 × 10⁵ cells/mL and cultivated for 24 h. After removing the medium, a new medium containing H₂O₂ (50~3200 µM) was added and incubated for 4 h. The group treated with fresh complete medium without H₂O₂ for 4 h was taken as a control. Assay results were expressed as the cell viability determined by a CCK-8 assay according to the manufacturer's protocols. All experiments were performed in triplicate.

Protective Effects of IDPG Against H₂O₂-Induced Cellular Injury

RAW 264.7 cells were first exposed to IDPG at different concentrations (25, 50, 100, 200, 400, and 800 µg/mL) for 24 h. Then, each treatment was exposed to a medium containing H₂O₂ for another 4 h, while the control group was replaced with a fresh complete medium for 4 h (Wang et al., 2015). Moreover, the H₂O₂ model group was incubated complete medium for 24 h and then treated with a new medium containing H₂O₂ for another 4 h. According to the manufacturer's protocols, results were expressed as the cell viability, as determined by a CCK-8 assay. All these experiments were performed in triplicate.

Determination of SOD Activity and MDA Content

RAW264.7 cells were cultivated with IDPG at different concentrations (25, 50, 100, 200, 400, and 800 µg/mL) for 24 h. Next, the H₂O₂ model group and IDPG groups were exposed to H₂O₂ (2.4 mM) for 4 h, and cells were next dissociated for measurements of the activity of superoxide dismutase (SOD) and lipid peroxidation (MDA). Both the SOD activity and MDA content were evaluated by using kits according to the manufacturer's protocols. SOD activity was analyzed by the hydroxylamine method (Oyanagui, 1984). One unit of SOD is defined as the amount of enzyme per milligram of protein required to produce 50% inhibition of the rate of nitrite production at 37°C. The MDA content was determined by barbiturate thiosulfate assay (Placer et al., 1966) and expressed in nmol/mg protein. The protein concentration was also measured by a BCA protein assay kit according to the manufacturer's protocols. The absorbance was determined by the microplate reader (FilterMax F5, Molecular Devices,

Sunnyvale, CA, United States). All these experiments were also performed in triplicate.

Immunomodulatory Activity Evaluated by RAW264.7 Cells

RAW 264.7 cells (1 × 10⁵ cells/well) were loaded into a 6-well plate and then cultured with different concentrations of IDPG or LPS (1 µg/ml) for another 24 h. After centrifugation of medium, the obtained supernatants were collected and the production of nitric oxide (NO), tumor necrosis factor-α (TNF-α), interleukin 6 (IL-6), and interleukin 1β (IL-1β) were measured by kits according to the manufacturer's protocols. All these experiments were performed in triplicate.

Effect of IDPG on the Antioxidant Capacity and Immune Function of Laying Hens

Animal Care and Experimental Design

The experimental protocols used in this experiment, including animal care and use, were reviewed and approved by the Animal Care and Use Ethics Committee of Nanjing Agricultural University (Nanjing, China). A total of 288 68-weeks-old laying hens (Hy-Line variety brown) were randomly distributed into four dietary treatments consisting of six replicates (cages) with 12 birds per replicate. The four groups were fed a basal diet supplemented with 0 (control group), 0.01, 0.025, and 0.05% IDPG for 8 weeks. The ingredients composition and nutrients content of the basal diet are given in **Table 1**. Kept inside of an environmentally controlled house, the birds were allowed free access to water and mash feed in 3-level

TABLE 1 | Composition and nutrient levels of basal diets (as-fed basis).

Ingredients	Content (%)	Nutrient levels ^b	
Corn	63.50	Apparent metabolizable energy (MJ/kg)	11.16
Soybean meal	18.80	Crude protein (%)	15.37
Fish meal	1.50	Calcium (%)	3.79
Rapeseed meal	2.00	Total phosphorus (%)	0.64
Corn gluten meal	1.20		
Soybean phospholipid	1.00		
Limestone	9.17		
Dicalcium phosphate	1.40		
DL-Methionine	0.10		
Sodium chloride	0.33		
1% Premix ^a	1.00		
Total	100		

^a1% Premix was provided by Huamu Institute of Animal Science and Technology, and provided per kilogram of diet: vitamin A (transretinyl acetate), 1.08 × 10⁴ IU; vitamin D3 (cholecalciferol), 2.7 × 10³ IU; vitamin E (all-rac-α-tocopherol), 27 mg; menadione, 0.84 mg; thiamin, 0.72 mg; riboflavin, 5.4 mg; nicotinamide, 9 mg; calcium pantothenate, 36 mg; pyridoxine·HCl, 2.7 mg; biotin, 0.09 mg; folic acid, 0.24 mg; vitamin B12 (cobalamin), 0.009 mg; Fe (from ferrous sulfate), 100 mg; Cu (from copper sulfate), 8.0 mg; Mn (from manganese sulfate), 100 mg; Zn (from zinc oxide), 60 mg; I (from calcium iodate), 0.9 mg; and Se (from sodium selenite), 0.3 mg.

^bNutrient levels were the calculated values.

cages (120 cm × 60 cm × 50 cm; 0.09 m² per chick) with controlled ventilation and lighting (16L:8D). The laying hens were fed twice per day (6 AM and 3 PM), and the feed was mixed into the trough to ensure its full consumption. According to the feeding situation of the day before, the feeding amount for the proceeding day was appropriately adjusted to ensure that there was no remaining feed in the trough each night. After 2 weeks of preliminary testing, a formal experiment was then initiated and carried out for the next 8 weeks.

Sample Collection

At 76 weeks of age, a total of 24 birds from all treatments were randomly selected (one bird per replicate). Blood samples were collected from wing veins using sterilized needles and syringes. Samples were then centrifuged at 3,000 rpm for 15 min at 4°C to separate the serum. Obtained serum was collected in new tubes and stored at -20°C until further analysis. The randomly selected laying hens were also euthanized by cervical dislocation and necropsied immediately. Their whole gastrointestinal tract was rapidly removed and placed on a chilled stainless-steel tray. The liver was quickly excised and then rapidly frozen in liquid nitrogen. The organ was then stored at -80°C for further analysis. Both the jejunum (from the end of the pancreatic loop to the Meckel's diverticulum) and ileum (from Meckel's diverticulum to the junction of ileocecal) were also separated without the mesentery. Next, the jejunum and ileum were opened longitudinally and the digestive tract was flushed with ice-cold phosphate buffer solution. Subsequently, the jejunal and ileal mucosa were carefully scratched using a sterile glass microscope slide, which was then rapidly frozen in liquid nitrogen and stored at -80°C for further analysis.

Determination of the Serum Parameters

The SOD, glutathione peroxidase (GSH-Px), total antioxidant capacity (T-AOC), and MDA were determined using commercial diagnostic kits (Nanjing Jiancheng Bioengineering Institute, Nanjing, Jiangsu, China) according to the manufacturer's instructions. The SOD activity and MDA concentration were expressed in U/mL serum and mmol/mL of serum, respectively. The ferric-reducing power assay was conducted to determine total antioxidant capacity in serum, and results are expressed in nmol/L of serum (Benzie and Strain, 1996). Therefore, the activity of GSH-Px can be expressed by the reaction speed of GSH-Px catalyzing the reaction of hydrogen peroxide with reduced glutathione (GSH) to produce water and oxidized glutathione (Lawrence and Burk, 1978). GSH-Px activity (U/mL) is defined as the amount of enzyme per milliliter of serum required to decrease the GSH concentration by 1 μmol/L per minute.

The contents of immunoglobulin M (IgM), IgG, TNF-α, IL-6, IL-1β, interferon γ (IFN-γ), and toll-like receptor 4 (TLR4) in serum samples were determined using enzyme-linked immunosorbent assay kits (Nanjing Jiancheng Bioengineering Institute, Nanjing, Jiangsu, China) and expressed as the gram per mL of serum. The operating procedure was carried out according to the manufacturers' instructions.

Determination of the Mucosal and Liver Parameters

Approximately 0.3 g mucosal or liver samples were homogenized (1:9, wt/vol) with ice-cold 0.86% sodium chloride solution using an Ultra-Turrax homogenizer (Tekmar Co., Cincinnati, OH, United States) and centrifuged at 3,000 rpm for 15 min at 4°C. The resultant supernatant was collected and immediately stored at -20°C for subsequent analysis. Secretory IgA (sIgA) content in mucosal samples was determined by enzyme-linked immunosorbent assay using microtiter plates and chicken-specific sIgA quantitation kits (Nanjing Jiancheng Bioengineering Institute, Nanjing, Jiangsu, China). Results are expressed as the μg per mg of protein. The total protein concentration of mucosa and liver was also determined according to the method described by Bradford using bovine serum albumin as the standard protein (Bradford, 1976). The content of IgG, IgM, TNF-α, IL-6, IL-1β, IFN-γ, and TLR4 in the liver and mucosa were measured according to the method described above and expressed as the μg per mg of protein.

Statistical Analysis

Data were analyzed by one-way analysis of variance (ANOVA) using SPSS (2008) statistical software (Ver. 16.0 for windows, SPSS Inc., Chicago, IL, United States). Differences in means among treatment groups were separated using the least significant difference (LSD). *P* values less than 0.05 were considered indicative of statistical significance with 95% confidence.

RESULTS

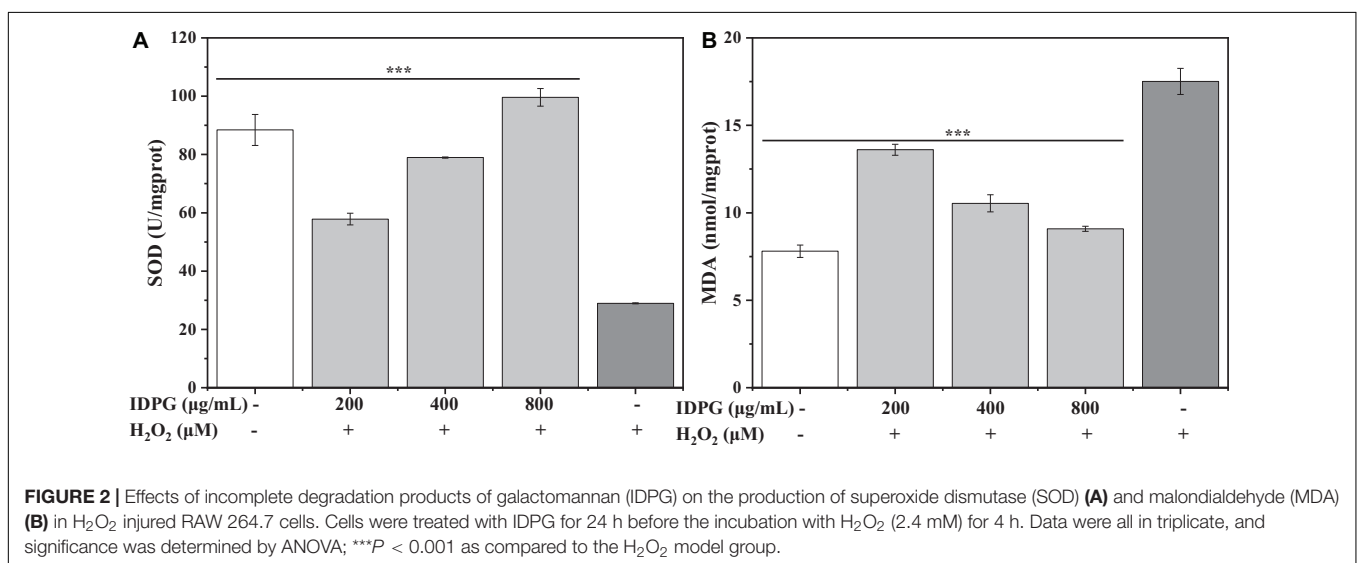
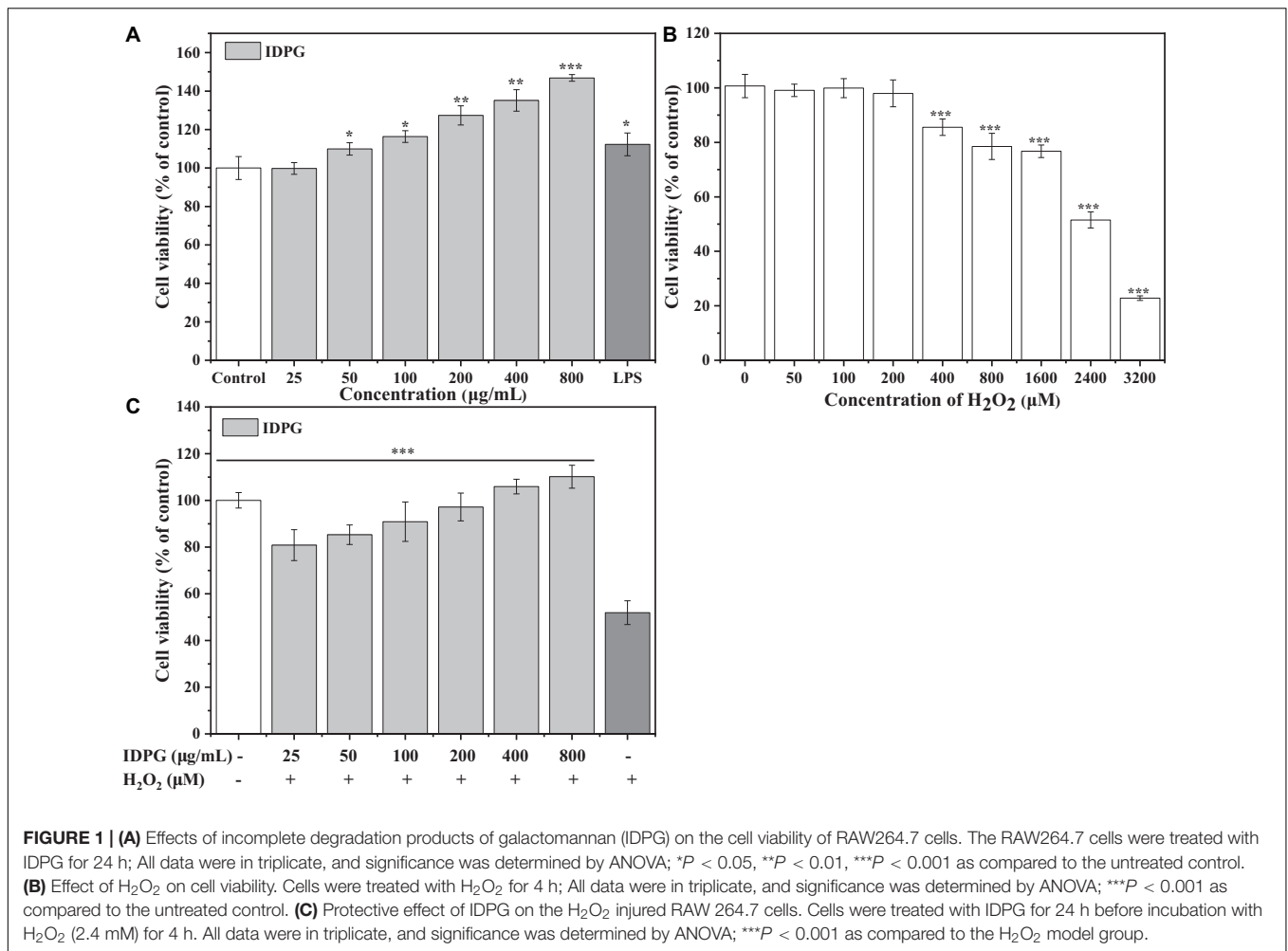
Antioxidant Activity Evaluated by H₂O₂-Induced Injury Cell Model

Effects of IDPG on the Viability of RAW264.7 Cells Treated With or Without H₂O₂

As shown in **Figure 1A**, the IDPG significantly promoted the proliferation of RAW264.7 cells in a concentration-dependent manner (*P* < 0.05). When the concentration of IDPG was 200–800 μg/mL, the relative survival rate of RAW264.7 cells even exceeded the positive control LPS. Regarding H₂O₂, it can cause RAW264.7 cells to lose viability, which was more pronounced at high concentrations (**Figure 1B**). After culturing with 2.4 mM H₂O₂ for 4 h, the survival rate of the cells was 51.51 ± 2.97% of the control group. Therefore, 2.4 mM H₂O₂ was selected to culture the cell for 4 h to investigate the protective effects of IDPG in the system. Compared with the H₂O₂ model group, the cells cultured with IDPG showed a higher survival rate (*P* < 0.05), and it was concentration-dependent (**Figure 1C**).

Effect of IDPG on the Level of MDA and SOD in Cells

As shown in **Figure 2A**, compared with the H₂O₂ model group, the SOD activity in cells cultured with IDPG increased significantly, and the difference was statistically significant (*P* < 0.05). Also, the SOD activity increased with the increase of IDPG concentration. As for MDA, its content is higher in the H₂O₂ model group than (17.51 ± 0.75 U/mg protein) in the control group (7.80 ± 0.35 nmol/mg protein). More importantly,



the MDA content of the IDPG group was significantly lower than that of the H₂O₂ model group ($P < 0.05$), which decreased with the increase of the concentration, as shown in **Figure 2B**.

Effect of IDPG on the Secretion of NO, TNF- α , IL-6, and TLR4 in Cells

As shown in **Figure 3**, compared with the control group, the IDPG significantly increased the secretion of NO, TLR4, TNF- α , and IL-6 ($P < 0.05$) with a concentration-dependent relationship. The promotion effect on NO, TLR4, TNF- α , and IL-6 secretion was more pronounced when the IDPG concentration was 800 $\mu\text{g/mL}$ and exceeded that of the LPS group.

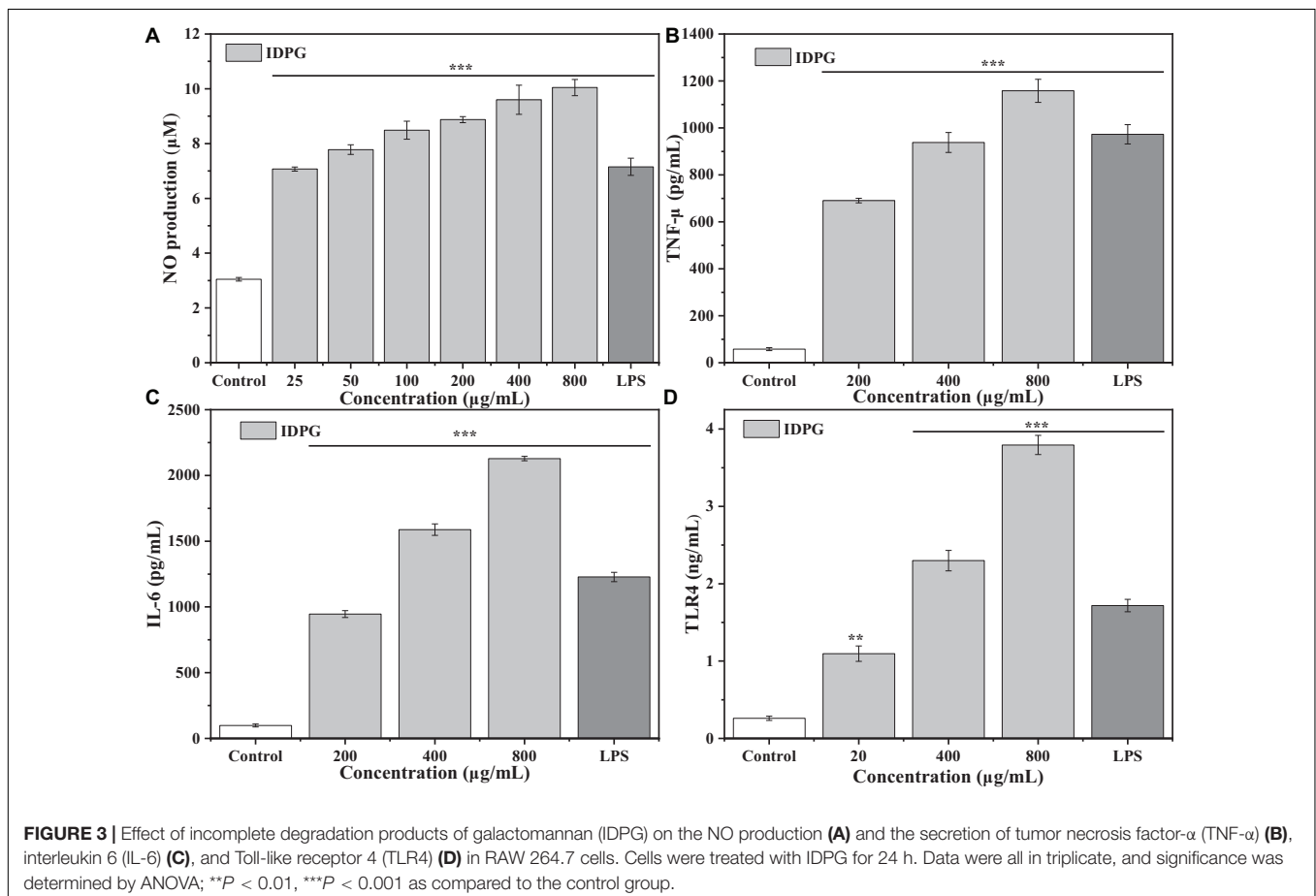
Effect of IDPG on the Antioxidant Function of Laying Hens

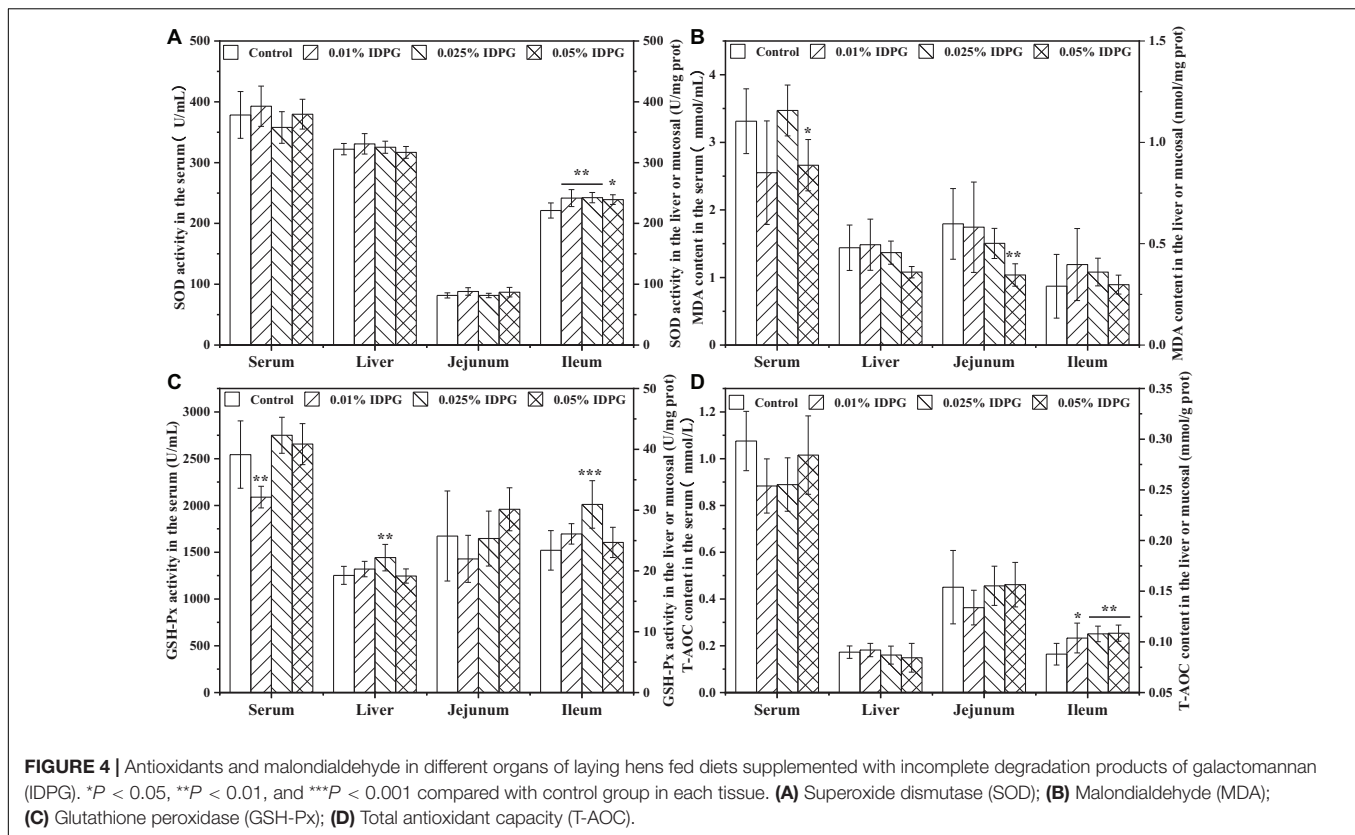
Analysis of the parameters concerning antioxidant capacity in the serum, liver, jejunum, and ileum are shown in **Figure 4**. The addition of IDPG into the diet of laying hens significantly increased SOD activity in the ileum ($P < 0.05$), yet no obvious change occurred on that in the serum, liver, and jejunum. MDA content in the serum and jejunum of the group supplemented with 0.05% IDPG was significantly lower than what was recorded for the control group ($P < 0.05$). However, there was no significant difference in the MDA content of the liver and ileum

between the IDPG-supplemented group and the control group. Concerning the GSH-Px activity and contrary to the previous results of MDA content, GSH-Px activity was significantly increased ($P < 0.05$) in the liver and ileum of the laying hens fed diets supplemented with 0.025% IDPG. However, GSH-Px did not differ among the serum and jejunum with IDPG treatment. Additionally, among the tissues or organs (serum, liver, jejunum, and ileum) selected for testing, only the T-AOC content of ileum increased significantly ($P < 0.05$). Specifically, the T-AOC content in the ileum increased linearly with the increasing concentration of dietary IDPG supplementation (0.01, 0.025, and 0.05%) relative to the control group.

Effect of IDPG on the Immune Function of Laying Hens

Figure 5 displays the contents of immunoglobulins in the serum, jejunum, and ileum of laying hens receiving diets supplemented with and without IDPG. As seen, contents of IgG and IgM in the serum and jejunum were significantly increased by the introduction of IDPG additives in the diet of laying hens ($P < 0.05$). Also, IDPG supplementation increased ($P < 0.05$) the content of secretory IgA (sIgA) in the jejunum. Additionally, in the ileum, laying hens fed diets containing IDPG showed higher





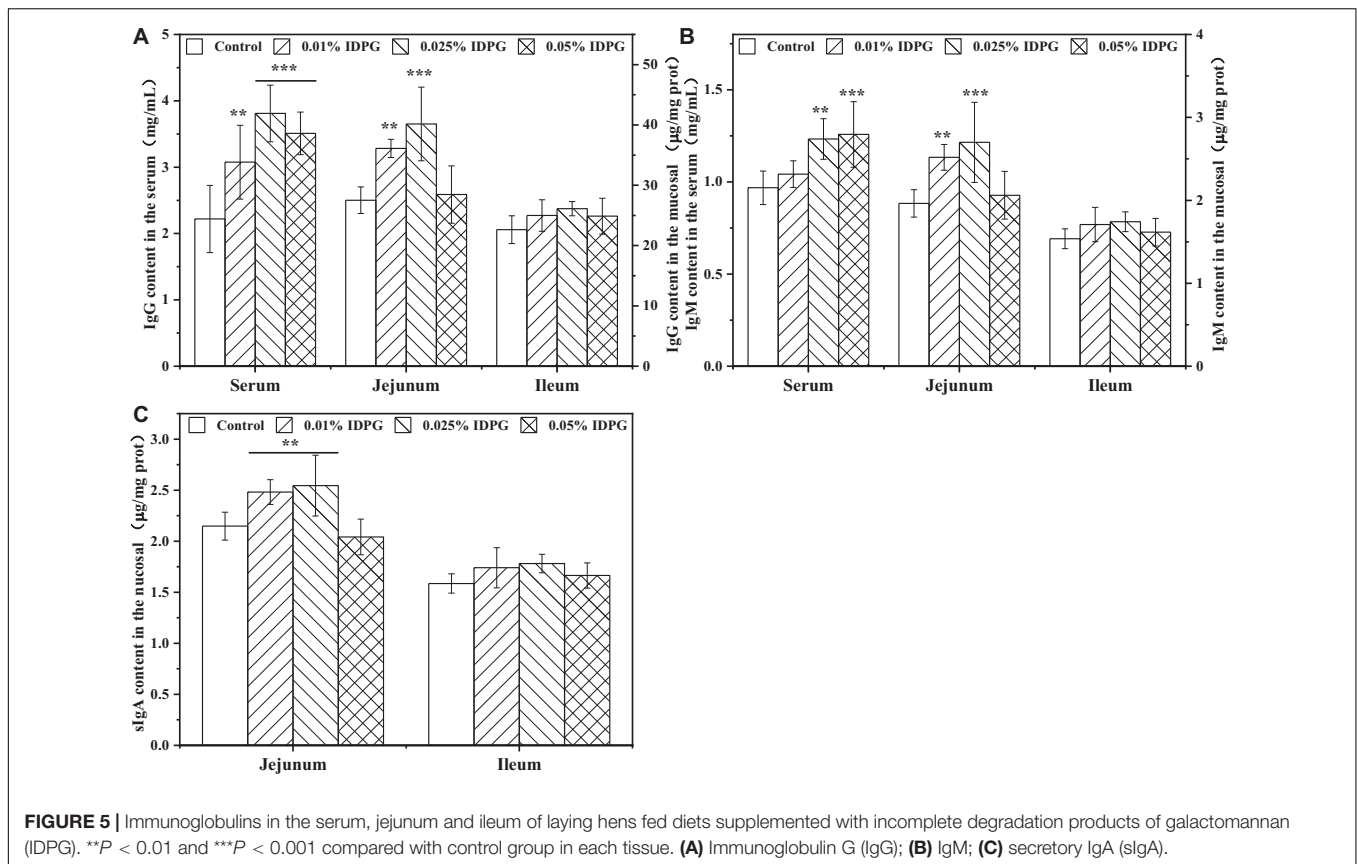
content of IgG, IgM, and sIgA than that fed without IDPG. However, the noted difference was not statistically significant.

Quantification of TNF- α , IL-6, IL-1 β , IFN- γ , and TLR4 in the serum, jejunum, and ileum are displayed in **Figure 6**. Similar to the results of immunoglobulins, dietary IDPG supplementation (0.025% and 0.05%) significantly increased the contents of TNF- α , IL-6, IL-1 β , IFN- γ , and TLR4 ($P < 0.05$) in the serum. As for the jejunum, contents of the quantified cytokines increased with the addition of IDPG (0.01% and 0.025%) into the basal diets. However, contents of TNF- α , IL-6, IL-1 β , IFN- γ , and TLR4 in the ileum did not vary statistically among treatments.

DISCUSSION

Natural polysaccharides and their degradation products have been investigated as antioxidant enhancers and immunomodulators in recent decades. Herein, IDPG was chosen to investigate to understand its positive effects on the antioxidant and immune system of RAW264.7 cells and aged laying hens. Generally, the possible routes by which natural polysaccharides and their degradation products can improve the antioxidant capacity of the body are as follows: (1) activate the antioxidative enzymes such as glutathione peroxidase (GSH-Px) and superoxide dismutase (SOD) through metabolic pathways; and (2) block oxidative chain reactions attributed to lipid peroxide, and eventually inhibit the peroxidation of unsaturated fatty acids on its membrane structure. In the investigation of

the antioxidant system, the free radical theory is an important theory involving free radicals (Hong and Liu, 2004; Dong et al., 2020; Wang et al., 2020). They are a kind of intermediate product formed in the metabolic process of animals. Excessive free radicals in the animal's body will destroy the barrier function of the intestines, cause protein denaturation, block cell division, and affect metabolism and cause diseases. Fortunately, antioxidant active substances can protect the body from the damage of free radicals. Antioxidants in the body can reduce the incidence of diseases. Examples of important antioxidants include SOD and GSH-Px (Dong et al., 2020). The antioxidant enzymes SOD and GSH-Px are considered to be the main elements of the first level of antioxidant defense in a cell because they form a major protective system against oxidative damage. Through *in vitro* experiment, the model of H₂O₂-injured cells was introduced, which is a common model to evaluate the antioxidant capacity of the sample tested (Holmström and Finkel, 2014). In a variety of cellular assays, the IDPG was demonstrated to attenuate H₂O₂-induced oxidative stress injury in macrophages, as shown by the promoted SOD activity and the decreased malondialdehyde (MDA) levels. Wherein, the MDA is a major lipid peroxidation product derived from oxygen radicals attacking polyunsaturated fatty acids in biofilms. The MDA content can reflect the degree of lipid peroxidation and indirectly reflect the extent of cell damage. Consistent with our findings, Germano et al. (2019) found that compared with the uncoated control, the galactomannan-carnauba wax coating increased the SOD activity of guava. Based on these results, the experiments *in vivo* were further



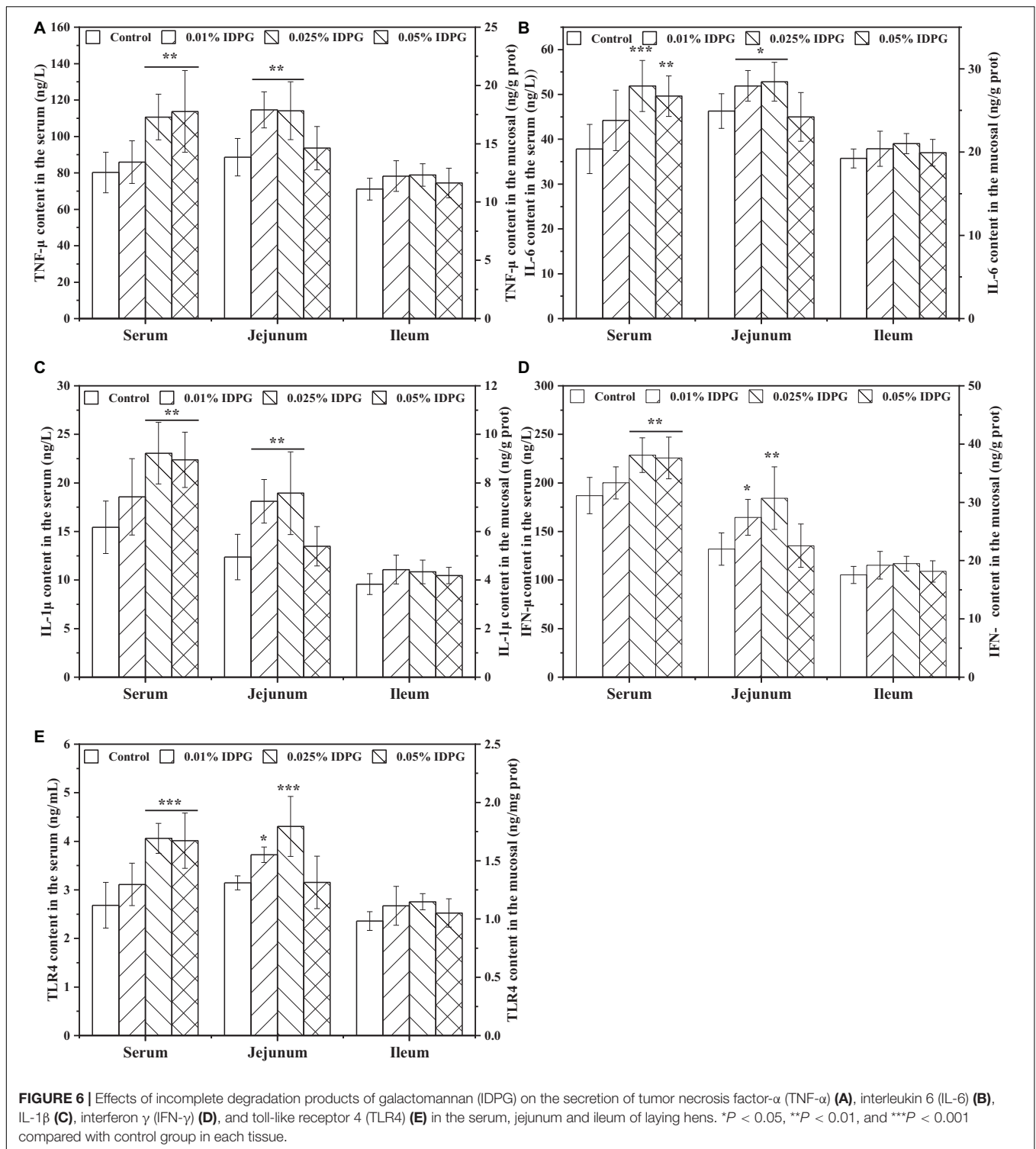
conducted in laying hens to study the effect of IDPG on the antioxidant function.

In the evaluation of the antioxidant capacity of IDPG on laying hens, total antioxidant capacity (T-AOC) and GSH-Px activity were also evaluated except SOD. T-AOC is a helpful representation of the overall level of enzymatic as well as non-enzymatic antioxidants (Surai, 1999). Our results showed that supplementation with IDPG to the basal diet of laying hens increased levels of SOD, GSH-Px, and T-AOC. In agreement with our findings, Bozkurt et al. (2016) found that laying hens fed with yeast cell wall manno-oligosaccharide (MOS) showed a significant improvement in SOD activity in the liver, but not GSH-Px content. However, in the present study, the effect of increasing antioxidants levels differs in the four tissues or organs (serum, liver, jejunum, and ileum), which is more pronounced in the ileum.

In addition to antioxidants, we also tested MDA contents. In this work, 0.05% IDPG dietary supplementation significantly lowered MDA content in the serum and jejunum relative to the control group, while no significant difference was observed in the MDA content of the liver and ileum. Consistent with our findings, Bozkurt et al. (2016) revealed that the usage of yeast cell wall MOS to the diet of laying hens has no significant effect on MDA content in the liver. Another report involving acute alcohol-intoxicated mice found that partially hydrolyzed guar gum had a significant effect on the reduction of MDA content in the serum (Wu et al., 2019). Unfortunately, in the same tissue

or organ, the scavenger roles of these antioxidative enzymes for preventing oxidative damage did not play a significant role in reducing MDA content. For example, the promotion of the level of SOD, GSH-Px, and T-AOC in the ileum response to IDPG supplementation did not result in a reduction in MDA content. A possible reason for this discrepancy could be that IDPG supplementation mainly reduces the formation of free radicals by increasing the content of antioxidants (Captions and Document, 1997). Therefore, more antioxidants mean an overall decrease in free radicals which explains why we did not see the MDA content drop. To conclude, IDPG mainly improved the antioxidant capacity by increasing the antioxidants contents (GSH-Px, SOD, and T-AOC) and secondly by reducing the MDA content. The elevation of the contents of these above-mentioned antioxidants may help in boosting the immune system, based on the cognition that the immune cell functions are strongly influenced by the antioxidant/oxidant balance. Moreover, the immune system cells usually have a high percentage of polyunsaturated fatty acids in their plasma membrane, which are very much susceptible to oxidative attack resulting in highly damaging lipid peroxidation. Therefore, it may be necessary that these cells contain higher concentrations of antioxidants than do other cells (Knight, 2000).

After revealing the ability on enhancing antioxidant function, the ability of IDPG on regulating immune function was next evaluated. The immunoglobulins and cytokines contents were emphatically assessed because immunoglobulins and cytokines play a critical role in humoral immunity and cell-mediated



immunity, respectively, which can closely reflect the effect of any tested materials on the immune system (Ferreira et al., 2015). As an important performer toward humoral immunity, immunoglobulins such as IgA, IgM, and IgG can specifically bind to antigens to resist the invasion of pathogenic bacteria (Su et al., 2013). As shown in **Figure 5**, the inclusion of IDPG

into the basal diet of laying hens significantly increased the content of IgG and IgM in the serum and jejunum. Consistent with the present findings, Yin et al. (2008) reported that the usage of 0.2% galactomanno-oligosaccharide can increase IgG, IgM, and IgA content in the serum of early-weaned piglets. Similarly, Zhou et al. (2019) reported that the addition of 0.1%

MOS, obtained from degraded *Konjac* glucomannan, increased jejunum IgG and IgM contents in broilers after 21 days. Moreover, the sIgA content in the jejunum of laying hens supplemented with IDPG (0.01 or 0.025%) was higher than that of the control birds. As the most secreted immunoglobulin in the body, sIgA is the first effective defense against pathogens that invades mucosa. sIgA can effectively combine with pathogenic microorganisms to form an immune complex and prevent the adhesion of pathogenic microorganisms to mucosal epithelial cells (Fujioka et al., 1998; Robinson et al., 2001). Furthermore, the resultant complex can stimulate goblet cells in intestinal mucosa to secrete a large amount of mucus, thus reducing the contact between pathogenic microorganisms and intestinal mucosa (Rodríguez et al., 2006). Based on the fact that it is almost impossible for serum immunoglobulin to reach the intestine and function, the observed significant increase of sIgA content in the jejunum is important because the increased antibodies can cover the surface of the intestinal mucosa to protect villi from damage (Fujioka et al., 1998). Gómez-Verduzco et al. (2009) observed a similar result in which a significant increase in the mucosal concentration of IgA was observed with 0.05% yeast cell wall MOS supplementation to a broiler diet. It seems that supplemental IDPG could effectively suppress enteric pathogens by promoting the immune system and its responses, as well as improving the integrity of intestinal mucosa. A similar mechanism of benefit was proposed by Spring et al. (2000).

Cytokine, a small molecule polypeptide, is synthesized or secreted by a variety of tissue cells (mainly immune cells). Examples of cytokines include interleukins, interferons, tumor necrosis factors, and more. Cytokines can mediate intercellular interactions while also serving a variety of biological functions, such as cell growth promotion, immune response regulation, participation in inflammatory responses, and inhibition of tumor growth (Bai et al., 2012). In this experiment, we selected TNF- α , IL-6, IL-1 β , IFN- γ , and TLR4 for measurement. The reason why we chose these is that they are reported to be related to galactomannan (Hernandez et al., 2011). Results showed that supplemental IDPG remarkably improved secretion of TNF- α , IL-6, IL-1 β , and IFN- γ in the serum and jejunum. Consistent with our findings, Yin et al. (2008) found that supplementation of 0.2% galactomanno-oligosaccharide into the diet of early-weaned piglets up-regulates serum IL-1 β and IL-6 level. Furthermore, *in vitro* experiments of IDPG also showed its capacity for promoting effective activation of RAW264.7 cells and enhancing the secretion of NO, TNF- α , IL-6, and TLR4 ($P < 0.05$).

Amongst the several cytokines tested, a significant increase in IL-1 β response to IDPG supplementation was notable due to IL-1 β being necessary for inducing a specific adaptive anti-tumor response (Ghiringhelli et al., 2009). More importantly, IDPG-induced secretion of IL-6 and TNF- α may help establish an inflammatory environment that can initiate or maintain the activation of DC that can then activate naive T cells. Meantime, TNF- α may be involved in inducing tumor cells to die (Aymeric et al., 2010; Van Herreweghe et al., 2010). Moreover, the secretion of IFN- γ significantly increased with the addition of IDPG. This finding may be because IFN- γ is the main executive cytokine of T helper lymphocytes (Th1 cells), and mannan

derivatives are conducive to T cell differentiation into Th1 cells (Sheng et al., 2006). The measurement of TLR4 revealed that the usage of IDPG significantly increased the content of TLR4 in the serum and jejunum. It has been reported that TLR4 has a high affinity for acemannan (Karaca et al., 1995), and galactomannan and acemannan share a backbone composed of mannose (differing only in side-chain configuration). Therefore, the noted high-secretion of cytokines in line with the increase in TLR4 content indicates that IDPG may activate TLR4 signaling pathways, triggering the maturation of DCs or other immune cells, all of which elicits an immune response that leads to the stimulated secretion of IgG, IgM, sIgA, TNF- α , IL-6, IL-1 β , and IFN- γ .

CONCLUSION

In the present study, the IDPG was prepared from the *Sesbania cannabina* seeds, and its antioxidant and immunomodulatory activity was evaluated *in vitro* and *in vivo*. Through measuring SOD and MDA, the IDPG showed a stronger protective effect against H₂O₂-induced oxidative damage *in vitro* using macrophage RAW264.7 cell as a model. Moreover, IDPG treatments in basal feeds for laying hens showed higher levels of SOD, GSH-Px, and T-AOC relative to the control group. However, there exist disparities between the extent of beneficial improvements between the four tissues or organs analyzed (serum, liver, jejunum, and ileum). Usage of 0.05% IDPG significantly lowered the MDA content in the serum and jejunum but had no significant effect on the MDA content in the liver and ileum. More importantly, IDPG supplementation to the basal diet of laying hens could promote the secretion of IgG, IgM, sIgA, TNF- α , IL-6, TLR4, IL-1 β , and IFN- γ . This result was consistent with the effect of IDPG on RAW264.7 cells by the evaluation of NO, TNF- α , IL-6, and TLR4. These results indicated that IDPG can be used as an ideal additive to enhance antioxidant and immune function, thereby boosting the health of laying hen. More importantly, the development of *S. cannabina* seeds into feed additives with outstanding antioxidant and immune activity will promote its economic value.

DATA AVAILABILITY STATEMENT

The original contributions presented in the study are included in the article/supplementary material, further inquiries can be directed to the corresponding author/s.

ETHICS STATEMENT

The experimental protocols used in this experiment, including animal care and use, were reviewed and approved by the Animal Care and Use Ethics Committee of Nanjing Agricultural University (Nanjing, China). Written informed consent was obtained from the owners for the participation of their animals in this study.

AUTHOR CONTRIBUTIONS

YT: investigation. TW and CL: supervision. ZL and YZ: writing – original draft. QY: writing – review and editing. All authors contributed to the article and approved the submitted version.

REFERENCES

- Abdel-Megeed, R. M., Hamed, A. R., Matloub, A. A., Kadry, M. O., and Abdel-Hamid, A. H. Z. (2019). Regulation of apoptotic and inflammatory signaling pathways in hepatocellular carcinoma via *Caesalpinia gilliesii* galactomannan. *Mol. Cell. Biochem.* 451, 173–184. doi: 10.1007/s11010-018-3404-y
- Aymeric, L., Apetoh, L., Ghiringhelli, F., Tesniere, A., Martins, I., Kroemer, G., et al. (2010). Tumor cell death and ATP release prime dendritic cells and efficient anticancer immunity. *Cancer Res.* 70, 855–858. doi: 10.1158/0008-5472.can-09-3566
- Bai, Y., Zhang, P., Chen, G., Cao, J., Huang, T., and Chen, K. (2012). Macrophage immunomodulatory activity of extracellular polysaccharide (PEP) of antarctic bacterium *Pseudoalteromonas* sp.S-5. *Int. Immunopharmacol.* 12, 611–617. doi: 10.1016/j.intimp.2012.02.009
- Benzie, I. F. F., and Strain, J. J. (1996). The ferric reducing ability of plasma (FRAP) as a measure of “antioxidant power”: the FRAP assay. *Anal. Biochem.* 239, 70–76. doi: 10.1006/abio.1996.0292
- Bozkurt, M., Tokuşoğlu, Ö., Küçükylmaz, K., Akşit, H., Çatli, A. U., Seyrek, K., et al. (2016). Effects of dietary mannan oligosaccharide and herbal essential oil blend supplementation on performance and oxidative stability of eggs and liver in laying hens. *Ital. J. Anim. Sci.* 11:e41. doi: 10.4081/ijas.2012.e41
- Bradford, M. M. (1976). A rapid and sensitive method for the quantitation of microgram quantities of protein utilizing the principle of protein-dye binding. *Anal. Biochem.* 72, 248–254. doi: 10.1016/0003-2697(76)90527-3
- Captions, A. T., and Document, W. (1997). Effects of adding mannan oligosaccharides on digestibility and metabolism of nutrients, ruminal fermentation parameters, immunity and antioxidant capacity of sheep. *Construction* 96, 284–292. doi: 10.1093/jas/skx040
- Cowan, R. S., Allen, O. N., and Allen, E. K. (1982). *The Leguminosae: A Source Book of Characteristics, Uses, and Nodulation*. Taxon, 31. *city.
- De la Fuente, M. (2002). Effects of antioxidants on immune system ageing. *Eur. J. Clin. Nutr.* 56, S5–S8.
- Devasagayam, T. P. A., and Sainis, K. B. (2002). Immune system and antioxidants, especially those derived from Indian medicinal plants. *Indian J. Exp. Biol.* 40, 639–655.
- Dong, H., Zheng, L., Yu, P., Jiang, Q., Wu, Y., Huang, C., et al. (2020). Characterization and application of lignin-carbohydrate complexes from lignocellulosic materials as antioxidants for scavenging in vitro and in vivo reactive oxygen species. *ACS Sustain. Chem. Eng.* 8, 256–266. doi: 10.1021/acsschemeng.9b05290
- Ferreira, S. S., Passos, C. P., Madureira, P., Vilanova, M., and Coimbra, M. A. (2015). Structure-function relationships of immunostimulatory polysaccharides: a review. *Carbohydr. Polym.* 132, 378–396. doi: 10.1016/j.carbpol.2015.05.079
- Fujioka, H., Emancipator, S. N., Aikawa, M., Huang, D. S., Blatnik, F., Karban, T., et al. (1998). Immunocytochemical colocalization of specific immunoglobulin a with sendai virus protein in infected polarized epithelium. *J. Exp. Med.* 188, 1223–1229. doi: 10.1084/jem.188.7.1223
- Gamal-Eldeen, A. M., Amer, H., and Helmy, W. A. (2006). Cancer chemopreventive and anti-inflammatory activities of chemically modified guar gum. *Chem. Biol. Interact.* 161, 229–240. doi: 10.1016/j.cbi.2006.03.010
- Germano, T. A., Aguiar, R. P., Bastos, M. S. R., Moreira, R. A., Ayala-Zavala, J. F., and de Miranda, M. R. A. (2019). Galactomannan-carnauba wax coating improves the antioxidant status and reduces chilling injury of ‘Paluma’ guava. *Postharvest Biol. Technol.* 149, 9–17. doi: 10.1016/j.postharvbio.2018.11.013
- Ghiringhelli, F., Apetoh, L., Tesniere, A., Aymeric, L., Ma, Y., Ortiz, C., et al. (2009). Activation of the NLRP3 inflammasome in dendritic cells induces IL-1B-dependent adaptive immunity against tumors. *Nat. Med.* 15:1170. doi: 10.1038/nm.2028
- Gómez-Verduzco, G., Cortes-Cuevas, A., Lopez-Coello, C., Vila-González, E., and Nava, G. M. (2009). Dietary supplementation of mannan-oligosaccharide enhances neonatal immune responses in chickens during natural exposure to *Eimeria* spp. *Acta Vet. Scand.* 51:11. doi: 10.1186/1751-0147-51-11
- Gu, J., Guo, M., Huang, C., Wang, X., Zhu, Y., Wang, L., et al. (2021). Titanium dioxide nanoparticle affects motor behavior, neurodevelopment and axonal growth in zebrafish (*Danio rerio*) larvae. *Sci. Total Environ.* 754:142315. doi: 10.1016/j.scitotenv.2020.142315
- Gu, J., Pei, W., Tang, S., Yan, F., Peng, Z., Huang, C., et al. (2020). Procuring biologically active galactomannans from spent coffee ground (SCG) by autohydrolysis and enzymatic hydrolysis. *Int. J. Biol. Macromol.* 149, 572–580. doi: 10.1016/j.ijbiomac.2020.01.281
- Hernandez, J. F., Pombo, M., Aoki, M., Moins-Teisserenc, H., Santander, S. P., Fiorentino, S., et al. (2011). Galactomannan from *caesalpinia spinosa* induces phenotypic and functional maturation of human dendritic cells. *Int. Immunopharmacol.* 11, 652–660. doi: 10.1016/j.intimp.2011.01.006
- Hidehisa, T., Yang, L., Mujo, K., and Takehiko, Y. (1994). Protein and energy utilization of growing rats fed on the diets containing intact or partially hydrolyzed guar gum. *Comp. Biochem. Physiol. Part A Physiol.* 107, 255–260. doi: 10.1016/0300-9629(94)90303-4
- Holmström, K. M., and Finkel, T. (2014). Cellular mechanisms and physiological consequences of redox-dependent signalling. *Nat. Rev. Mol. Cell Biol.* 15, 411–421. doi: 10.1038/nrm3801
- Hong, H., and Liu, G. Q. (2004). Protection against hydrogen peroxide-induced cytotoxicity in PC12 cells by scutellarin. *Life Sci.* 74, 2959–2973. doi: 10.1016/j.lfs.2003.09.074
- Hossain, M. A., Focken, U., and Becker, K. (2001). Galactomannan-rich endosperm of *Sesbania (Sesbania aculeata)* seeds responsible for retardation of growth and feed utilisation in common carp. *Cyprinus carpio* L. *Aquac.* 203, 121–132. doi: 10.1016/s0044-8486(01)00617-2
- Hossain, M. A., Focken, U., and Becker, K. (2002). Nutritional evaluation of dhaincha (*Sesbania aculeata*) seeds as dietary protein source for tilapia *Oreochromis niloticus*. *Aquac. Res.* 33, 653–662. doi: 10.1046/j.1365-2109.2002.00690.x
- Karaca, K., Sharma, J. M., and Nordgren, R. (1995). Nitric oxide production by chicken macrophages activated by acemannan, a complex carbohydrate extracted from aloe vera. *Int. J. Immunopharmacol.* 17, 183–188. doi: 10.1016/0192-0561(94)00102-t
- Knight, J. A. (2000). Review: free radicals, antioxidants, and the immune system. *Ann. Clin. Lab. Sci.* 30, 145–148.
- Lawrence, R. A., and Burk, R. F. (1978). Species, tissue and subcellular distribution of non se-dependent glutathione peroxidase activity. *J. Nutr.* 108, 211–215. doi: 10.1093/jn/108.2.211
- Li, Q., Wang, S., Jin, X., Huang, C., and Xiang, Z. (2020). The application of polysaccharides and their derivatives in pigment, barrier, and functional paper coatings. *Polymers* 12:1837. doi: 10.3390/polym12081837
- Oyanagui, Y. (1984). Reevaluation of assay methods and establishment of kit for superoxide dismutase activity. *Anal. Biochem.* 142, 290–296. doi: 10.1016/0003-2697(84)90467-6
- Pan, W., Hao, S., Zheng, M., Lin, D., Jiang, P., Zhao, J., et al. (2020). Oat-derived β-glucans induced trained immunity through metabolic reprogramming. *Inflammation* 43, 1323–1336. doi: 10.1007/s10753-020-01211-2
- Pei, W., Chen, Z. S., Chan, H. Y. E., Zheng, L., Liang, C., and Huang, C. (2020). Isolation and identification of a novel anti-protein aggregation activity of lignin-carbohydrate complex from *chionanthus retusus* leaves. *Front. Bioeng. Biotechnol.* 8:572991. doi: 10.3389/fbioe.2020.573991
- Placer, Z. A., Cushman, L. L., and Johnson, B. C. (1966). Estimation of product of lipid peroxidation (malonyl dialdehyde) in biochemical systems. *Anal. Biochem.* 16, 359–364. doi: 10.1016/0003-2697(66)90167-9

FUNDING

This work was supported by the National Key R&D Program of China (2016YFD0600803) and Priority Academic Program Development of Jiangsu Higher Education Institutions (PAPD).

- Robinson, J. K., Blanchard, T. G., Levine, A. D., Emancipator, S. N., and Lamm, M. E. (2001). A mucosal IgA-mediated excretory immune system *in vivo*. *J. Immunol.* 166, 3688–3692. doi: 10.4049/jimmunol.166.6.3688
- Rodríguez, A., Rottenberg, M., Tjärnlund, A., and Fernández, C. (2006). Immunoglobulin a and CD8+ T-cell mucosal immune defenses protect against intranasal infection with *Chlamydia pneumoniae*. *Scand. J. Immunol.* 63, 177–183. doi: 10.1111/j.1365-3083.2006.01725.x
- Sheng, K. C., Pouniotis, D. S., Wright, M. D., Tang, C. K., Lazoura, E., Pietersz, G. A., et al. (2006). Mannan derivatives induce phenotypic and functional maturation of mouse dendritic cells. *Immunology* 118, 372–383. doi: 10.1111/j.1365-2567.2006.02384.x
- Spring, P., Wenk, C., Dawson, K. A., and Newman, K. E. (2000). The effects of dietary mannanoligosaccharides on cecal parameters and the concentrations of enteric bacteria in the ceca of *Salmonella*-challenged broiler chicks. *Poult. Sci.* 79, 205–211. doi: 10.1093/ps/79.2.205
- Su, C. A., Xu, X. Y., Liu, D. Y., Wu, M., Zeng, F. Q., Zeng, M. Y., et al. (2013). Isolation and characterization of exopolysaccharide with immunomodulatory activity from fermentation broth of *Morchella conica*. *DARU, J. Pharm. Sci.* 21:5.
- Surai, P. F. (1999). Vitamin E in avian reproduction. *Avian Poult. Biol. Rev.* 10, 1–60. doi: 10.1093/acprof:oso/9780198718666.003.0001
- Tang, C., Ding, R., Sun, J., Liu, J., Kan, J., and Jin, C. (2019). The impacts of natural polysaccharides on intestinal microbiota and immune responses—a review. *Food Funct.* 10, 2290–2312. doi: 10.1039/c8fo01946k
- Tang, S., Jiang, M., Huang, C., Lai, C., Fan, Y., and Yong, Q. (2018). Characterization of arabinogalactans from *larix principis-rupprechtii* and their effects on no production by macrophages. *Carbohydr. Polym.* 200, 408–415. doi: 10.1016/j.carbpol.2018.08.027
- Tao, Y., Yang, L., Lai, C., Huang, C., Li, X., and Yong, Q. (2020). A facile quantitative characterization method of incomplete degradation products of galactomannan by ethanol fractional precipitation. *Carbohydr. Polym.* 250:116951. doi: 10.1016/j.carbpol.2020.116951
- Van Herreweghe, F., Festjens, N., Declercq, W., and Vandebeele, P. (2010). Tumor necrosis factor-mediated cell death: to break or to burst, that's the question. *Cell. Mol. Life Sci.* 67, 1567–1579. doi: 10.1007/s00018-010-0283-0
- Wang, P., Yin, B., Dong, H., Zhang, Y., Zhang, Y., Chen, R., et al. (2020). Coupling biocompatible au nanoclusters and cellulose nanofibrils to prepare the antibacterial nanocomposite films. *Front. Bioeng. Biotechnol.* 18:986.
- Wang, Z. J., Xie, J. H., Kan, L. J., Wang, J. Q., Shen, M. Y., Li, W. J., et al. (2015). Sulfated polysaccharides from *Cyclocarya paliurus* reduce H₂O₂-induced oxidative stress in RAW264.7 cells. *Int. J. Biol. Macromol.* 80, 410–417. doi: 10.1016/j.ijbiomac.2015.06.031
- Wu, C., Liu, J., Tang, Y., Li, Y., Yan, Q., and Jiang, Z. (2019). Hepatoprotective potential of partially hydrolyzed guar gum against acute alcohol-induced liver injury *in vitro* and *in vivo*. *Nutrients* 11, 1–17.
- Xiang, Z., Jin, X., Huang, C., Li, L., Wu, W., Qi, H., et al. (2020). Water cast film formability of sugarcane bagasse xylans favored by side groups. *Cellulose* 27, 7307–7320. doi: 10.1007/s10570-020-03291-7
- Yin, Y. L., Tang, Z. R., Sun, Z. H., Liu, Z. Q., Li, T. J., Huang, R. L., et al. (2008). Effect of galacto-mannan-oligosaccharides or chitosan supplementation on cytoimmunity and humoral immunity in early-weaned piglets. *Asian-Australasian J. Anim. Sci.* 21, 723–731. doi: 10.5713/ajas.2008.70408
- Yu, P., Zheng, L., Wang, P., Chai, S., Zhang, Y., Shi, T., et al. (2020). Development of a novel polysaccharide-based iron oxide nanoparticle to prevent iron accumulation-related osteoporosis by scavenging reactive oxygen species. *Int. J. Biol. Macromol.* 165, 1634–1645. doi: 10.1016/j.ijbiomac.2020.10.016
- Zheng, L., Yu, P., Zhang, Y., Wang, P., Yan, W., Guo, B., et al. (2021). Evaluating the bio-application of biomacromolecule of lignin-carbohydrate complexes (LCC) from wheat straw in bone metabolism via ROS scavenging. *Int. J. Biol. Macromol.* 176, 13–25. doi: 10.1016/j.ijbiomac.2021.01.103
- Zhou, M., Tao, Y., Lai, C., Huang, C., and Zhou, Y. (2019). Effects of mannanoligosaccharide supplementation on the growth performance, immunity, and oxidative status of partridge shank chickens. *Animals* 9:817. doi: 10.3390/ani9100817

Conflict of Interest: The authors declare that the research was conducted in the absence of any commercial or financial relationships that could be construed as a potential conflict of interest.

Copyright © 2021 Tao, Wang, Lai, Ling, Zhou and Yong. This is an open-access article distributed under the terms of the Creative Commons Attribution License (CC BY). The use, distribution or reproduction in other forums is permitted, provided the original author(s) and the copyright owner(s) are credited and that the original publication in this journal is cited, in accordance with accepted academic practice. No use, distribution or reproduction is permitted which does not comply with these terms.



Selective Production of Xylooligosaccharides by Xylan Hydrolysis Using a Novel Recyclable and Separable Furoic Acid

Jianglin Zhao^{1,2}, Xiaotong Zhang^{1,2}, Xin Zhou^{1,2,3*} and Yong Xu^{1,2}

¹ Jiangsu Co-Innovation Center of Efficient Processing and Utilization of Forest Resources, College of Chemical Engineering, Nanjing Forestry University, Nanjing, China, ² Key Laboratory of Forest Genetics and Biotechnology, Ministry of Education, Nanjing Forestry University, Nanjing, China, ³ Jiangsu Province Key Laboratory of Green Biomass-Based Fuels and Chemicals, Nanjing, China

OPEN ACCESS

Edited by:

Xiao-Jun Ji,
Nanjing Tech University, China

Reviewed by:

Noppol – Leksawasdi,
Chiang Mai University, Thailand
JunLi Ren,
South China University of Technology,
China

*Correspondence:

Xin Zhou
xinzhou@njfu.edu.cn

Specialty section:

This article was submitted to
Bioprocess Engineering,
a section of the journal
Frontiers in Bioengineering and
Biotechnology

Received: 29 January 2021

Accepted: 09 March 2021

Published: 09 April 2021

Citation:

Zhao J, Zhang X, Zhou X and
Xu Y (2021) Selective Production
of Xylooligosaccharides by Xylan
Hydrolysis Using a Novel Recyclable
and Separable Furoic Acid.
Front. Bioeng. Biotechnol. 9:660266.
doi: 10.3389/fbioe.2021.660266

Xylooligosaccharides (XOS) have gained considerable attention worldwide as prebiotics due to their immune-strengthening activity and beneficial gut bacteria development and can be produced from xylan-rich resources by acid hydrolysis. The present study proved the organic acid hydrolysis to be beneficial for XOS yield. In this study, a recyclable and separable organic acid, i.e., furoic acid, was used for hydrolyzing xylan to produce XOS, and the response surface methodology design was applied to maximize the XOS yield; the results indicated that the quadratic model terms of the interaction between reaction temperature and hydrolysis time showed the most significant impact on XOS yields ($P < 0.05$). The predicted maximum yield of XOS was 49.0% with 1.2% furoic acid at 167°C for 33 min, being close to the experimental value (49.2%), indicating that the fitted models were in good agreement with the experimental results. Meanwhile, the primary byproducts, including xylose and furfural, were concurrently bio-oxidized into xylonic acid and furoic acid by *Gluconobacter oxydans* and separated by electro dialysis. Subsequently, the furoic acid with low solubility (<3.7%, 25°C) was recovered by natural crystallization. The above results indicate that the use of multi-steps contributes to sustainable XOS production by furoic acid.

Keywords: xylooligosaccharides, xylan, furoic acid, hydrolysis, bio-oxidation, electro dialysis

INTRODUCTION

The emerging health consciousness has concurrently increased the awareness and pivoted the food preferences of consumers to use natural, healthier, and sustainable food resources, such as prebiotics and preventive medicines (Aachary and Prapulla, 2011; Santibáñez et al., 2021). The common prebiotics, defined as a non-digestible food ingredient, consists of oligosaccharides and polysaccharides that are resistant to human digestive enzymes hydrolysis but beneficial to the host by selectively limiting the gut microbiota growth (Gao et al., 2020). Xylooligosaccharides (XOS), the sugar-oligomer prebiotics, composed of β -1,4-linked xylose units, are regarded as potential food ingredients due to their multidimensional physiological properties on human health and livestock, such as lowering cholesterol and risk of colon cancer and improving calcium absorption and intestinal canal function (Samanta et al., 2015). Thus, the XOS market price varies from the

US \$25/kg to \$50/kg; and efficient industrial-based technologies with high XOS production are developing rapidly to fulfill market needs (Jayapal et al., 2013; Mhetras et al., 2019).

Currently, the common technologies for XOS production from xylan hydrolysis are categorized as the acid hydrolysis, the enzymatic hydrolysis, or combination of these two approaches (Carvalho et al., 2013; Hong et al., 2019); and abundant supply of renewable and low-cost lignocellulosic materials guarantee stable production of xylan (Zhao et al., 2020). The potential high market value has driven researchers to develop advanced methods to convert xylan to XOS. The enzymatic hydrolysis requires a relatively prolonged time and unique conditions for enzyme storage, and XOS output is lower (Samanta et al., 2012; Jnawali et al., 2017). In contrast, acid hydrolysis is a practical and conventional industrial technology (Lin et al., 2017). With the action of acid, xylan can be effectively degraded into oligosaccharide and monosaccharide, which can be harvested in the liquid that separated after the acid hydrolysis. Thus, various mineral acids and organic acids were employed to hydrolyze xylan. However, mineral acids (strong acids) as catalyst will lead to the accelerated reaction of xylose into furfural due to the higher activation energy for the dehydration; in addition, the mineral acid application will cause a larger inorganic waste stream and mostly gypsum (Kootstra et al., 2009). Correspondingly, the organic acids exhibit the desirable characteristics, including selective hydrolysis with more oligomeric sugars and lower degradation byproducts (Bian et al., 2014; Cesaro et al., 2020; Guo J. et al., 2020).

Nowadays, various organic acids, such as formic acid, acetic acid, maleic acid, gluconic acid, and oxalic acid, have been introduced to acid-hydrolyze xylan or xylan-rich lignocellulosic materials for XOS production (Guo X. et al., 2020; Han et al., 2020). Lin et al. (2017) developed an oxalic acid hydrolysis strategy for producing XOS using beechwood xylan as feedstock and achieved a yield of 39.31%. Zhang et al. (2017) employed acetic acid to produce XOS with a yield of 45.9%. In addition, Zhou et al. (2019a) found that gluconic acid also performed good ability to decompose sugarcane bagasse-xylan into XOS with a yield of 53.2%. Besides, organic acid byproduct stream could be easily applied in animal feed, fertilizing soil, and co-firing installations (Lin et al., 2017).

Furoic acid (FA) is a heterocyclic carboxylic acid comprising a five-membered aromatic ring and a carboxylic acid group; the dissociation constants of oxalic acid are 3.16 (pKa at 25°C); thus, FA also can release H⁺ at high temperature to depolymerize xylan into the oligosaccharide and monosaccharide. FA has been widely used in food products as preservative and flavoring agent; the solubility of FA was only 37 g/L in 25°C. Dai et al. (2021) reported that FA was an effective catalyst to pretreat the sugarcane bagasse into XOS with a yield of 45.6% and also proved that FA could be recovered easily by cooling and natural crystallization from recovered acid solution. Although FA can result in a high XOS yield using sugarcane bagasse as material, the XOS content was only 11.9 g/L, and the pre-hydrolyzate from acid hydrolysis of sugarcane bagasse contains various byproducts, such as formic acid, acetic acid, phenolic compounds, pectin, and crude proteins (Zheng et al., 2021); it makes direct production of XOS from

biomass not feasible. Thus, in this context, and considering the target of high concentration and purity XOS production, the present work studied its production condition that depends on FA-assisted hydrolysis of alkaline soluble xylan from corncob.

MATERIALS AND METHODS

Preparation of Xylan

Corn cob as feedstock was collected from Dongtai, Jiangsu, China. The dried corncob mainly comprises 34.1% glucan, 30.4% xylan, 18.7% lignin, and 4.2% ash content. The xylan was prepared from the milled corncob in triplicate using 7% sodium hydroxide and then subjected to steam treatment for 45 min at 120°C with a solid to liquid ratio of 1:7. Then the alkali solubilized xylan was first filtered using a zero-filter paper followed by Whatman filter paper 40 and precipitated using 95% ice-cold ethanol (Samanta et al., 2012). The precipitate was further dried in a forced hot air oven at 60°C until constant weight. The xylan was analyzed according to the National Renewable Energy Laboratory's standard method (Sluiter et al., 2008), and the purity and recovery rate of the extracted xylan were 71.6 ± 1.9% and 82.1 ± 1.6%, respectively.

Response Surface Method Design and Optimization

Design-Expert (Version 11.0), a response surface analysis software, was selected to design the experiment; and an appropriate point was selected according to the experimental results (Neto et al., 2020). There were three independent variables in the experiment: reaction temperature (130–170°C), acid concentration (1–3% w/w), and hydrolysis time (10–60 min). The values of these independent variables are listed in **Table 1**. The experiments were run 15 times in triplicate according to the Box–Behnken design matrix. The combination test design principles used three factors: reaction temperature (X_1), retention time (X_2), and FA concentration (X_3).

In a 30-ml steel reactor tube made of 316 stainless, 1.0 g of xylan solids was firstly added, and then 10 ml of 1–3% FA solution was mixed in the tube and stirred uniformly. Subsequently, sealed reactor tube was immersed in oil baths at preset temperatures for varying durations based on the experimental design. Once the hydrolysis reaction was completed, the reactor tube was immediately taken out and cooled to room temperature. The supernatant was collected by centrifuging the mixture at 10,000 × g for 5 min and then subjected for XOS analysis. All experiments were carried out in triplicate. The total XOS content, which contains DP 2–6 oligomers, was calculated as a response variable. Regression analysis of the experimental data and the response surface plots were calculated by using statistical software Design-Expert (Version 11.0). One-way analysis of variance (ANOVA) and Duncan's multiple range test ($P < 0.05$) were carried out to analyze the statistical significance. The relationship between the response variable and independent variables was calculated through the following quadratic polynomial equation.

$$Y = a_0 + \sum a_i X_i + \sum a_{ii} X_i^2 + \sum a_{ij} X_i X_j$$

TABLE 1 | Different combinations of independent variables of software design and experimental results.

Reaction temperature (°C)	Variables		Responses
	FA concentration (% w/w)	Hydrolysis time (min)	XOS yields (%)
130	1	10	2.50
130	1	60	15.6
130	2	35	10.4
130	3	60	37.6
130	3	35	18.6
150	3	10	11.3
150	3	35	44.3
150	2	60	37.7
150	2	35	38.9
150	1	60	43.1
170	2	10	34.5
170	1	35	48.0
170	3	35	14.4
170	2	35	31.2
170	1	60	24.9

XOS, xylooligosaccharides; FA, furoic acid.

where, Y is the yield of XOS (%), a_0 represents a constant term, X (X_i and X_j) represents independent variables, and a_i , a_{ij} , and a_{ij} represent coefficients of linear, quadratic, and interaction parameters, respectively.

The coefficients in the second-order polynomial were calculated based on the experimentally obtained data, and then the predicted optimal conditions for the maximum yield of XOS were obtained. Lastly, an additional experiment with three replications was conducted to verify the validity of the predicted optimum values by the program.

Xylose and Furfural Bioconversion

Gluconobacter oxydans 621H, purchased from the American Type Culture Collection (ATCC), was employed to bio-catalyze xylose and furfural into xylonic acid (XA) and FA. Strain was maintained on sorbitol-agar slant (5.0 g/L of yeast extract, 20 g/L of agar, and 10 g/L of glycerol) at 4°C. *G. oxydans* inoculum was cultivated in 100 g/L sorbitol and 10 g/L yeast extract media in a 1-L Erlenmeyer flask and cultured for 24 h at 220 rpm and 30°C. The cell pellets of *G. oxydans* were then harvested by centrifugation (6,000 × g, 5 min, 4°C). The xylan-hydrolyzate was filtered by a 0.45-μm filter Millipore for sterilization. In a 250-ml Erlenmeyer flask (50 ml of xylan-hydrolyzate, 220 rpm, and 30°C) was loaded 2 g/L *G. oxydans* cells for bio-oxidizing xylose and furfural, and samples were taken at suitable intervals for component analysis (Zhou et al., 2019b).

Furoic Acid Recovery

The bipolar membrane electro dialysis crystallization method was employed for FA recovery. The instrument consisted of four chambers: acid, salt, alkali, and electrode chamber. To increase the electrical conductivity throughout the process, 0.3 mol/L of sodium sulfate was added to the electrode chamber. After

the mixed solution of XOS and FA entered the salt chamber, the FA was collected in the acid chamber through an electric current. However, XOS was still trapped in the salt chamber, and the corresponding alkali compounds were formed in the alkali chamber. Finally, XA, FA, and XOS were separated from the mixed solution by this method.

Analytical Methods

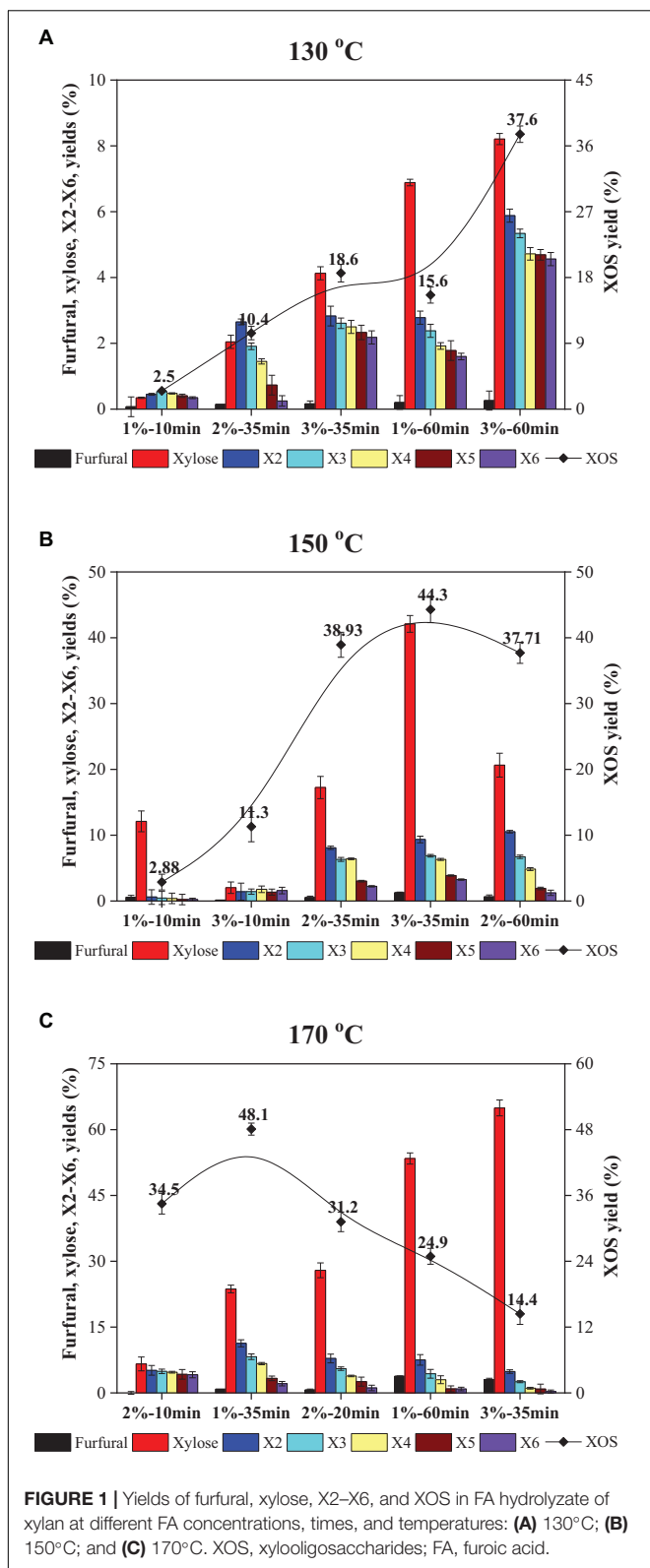
Xylose, xylobiose (X2), xylotriose (X3), xylotetraose (X4), xylopentaose (X5), and xylohexaose (X6) in liquid were simultaneously determined by high-performance anion exchange chromatography (HPAEC) (Dionex ICS-3000, United States) coupled with a CarboPac™ PA200 column (Xu et al., 2013). Furfural and FA were analyzed by a high-performance liquid chromatograph (HPLC) (Agilent 1200, United States) coupled with an Aminex Bio-Rad HPX-87H column (Bio-Rad Laboratories, United States). The yield (%) of furfural, xylose, and XOS was calculated as follows: the content of furfural, xylose yield, and XOS in hydrolyzate is divided by the initial xylan content and multiplied by 100.

RESULTS AND DISCUSSION

Xylooligosaccharides Production by Furoic Acid-Assisted Hydrolysis

Generally, the degradation rate of xylan is positively correlated with the reaction temperature, acid concentration, and hydrolyzed time. The total amount of XOS liberated from xylan during the hydrolysis is a major parameter to determine the effectiveness of these factors. In the present study, the highest acid concentration was 3% because the solubility of FA was below 4%. Previous studies have shown that the hydrolysis of xylan was difficult to be controlled while the acid-assisted hydrolysis temperature was over 170°C, because xylan was easy to be acid hydrolyzed at the case of high temperature, and excessive temperature results in higher activation energy for the dehydration; that is, is easy to accelerate the dehydration of xylose into furfural; therefore, excessive temperature usually leads to large amounts of byproducts (xylose and furfural) being generated (Akpınar et al., 2009; Guo et al., 2019). When hydrolysis temperature was lower than 130°C, xylan is particularly hard to be degraded; lower temperature will lead to a long reaction time, even more than 60 min (Han et al., 2020). According to the preliminary experiment, the acid concentrations of 1–3% and reaction time of 10–60 min at 130–170°C were selected for xylan hydrolysis. In this work, the response surface methodology (RSM) was employed in this work to maximize the XOS yield, and the coefficients of a mathematical model were determined. An experimental design with a total of 15 different runs and the corresponding responses are given in **Table 1**. After the acid hydrolysis, xylose and furfural were determined to compare the effects of different hydrolysis conditions, and the yields are shown in **Figures 1A–C**.

As depicted in **Figure 1A**, the XOS yield at relatively low FA concentration, temperature, and time was low. The XOS



produced by 1% FA after 10 min at 130°C was only 2.5%. That tardy enhancement in XOS yield by extension of hydrolysis time or enhancement of FA concentration at 130°C can also be

seen. When the reaction was conducted at 130°C, the highest yield of XOS was only 37.6%, which should use 3% FA for 60 min, while the XOS yield showed a quick increase from 18.6% (130°C, 3% FA, 35 min) to 44.3% (150°C, 3% FA, 35 min) by improving the reaction temperature, which is depicted in **Figures 1A,B**. A similar observation was also obtained by temperature improvement of 150°C to 170°C; the XOS shows a rapid increase from 11.3% (150°C, 3% FA, 10 min) to 34.5% (170°C, 2% FA, 10 min), as displayed in **Figures 1B,C**.

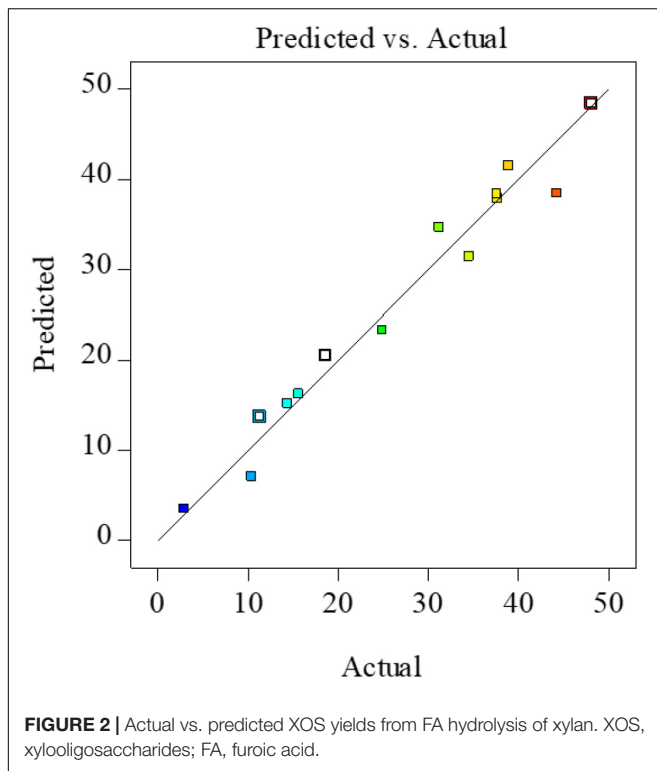
The above results suggested that low temperatures decelerated the xylan hydrolysis, whereas higher temperatures significantly accelerated the degradation of xylan into XOS. This phenomenon was also shown by Lin et al. (2017). Therefore, the temperature range of 150–170°C was considered as the optimum temperature for XOS formation. Additionally, it was observed that XOS yields obtained similar results with 2% FA at 150°C for 35 min (38.9%) and 60 min (37.7%). Prolonged retention time resulted in further degradation of X5 and X6, which means that higher amounts of X2 and X3 would occur. In the case of 1% FA as a catalyst at 170°C, it showed a significant decrease in XOS yields from 48.1% (35 min) to 24.9% (60 min) and a significant increase in xylose yield from 18.1% to 41.4%. Therefore, it was inferred that high reaction temperature and prolonged hydrolysis times would decline the XOS content due to further degradation of XOS to xylose and furfural under these optimum reaction conditions. Generally, the highest XOS yield from organic acid hydrolysis is in the range of 35–50% (Lin et al., 2017; Zhang et al., 2017; Zhou et al., 2019a). Thus, all results indicated that FA was comparable with the reported organic acids (acetic acid, oxalic acid, maleic acid, citric acid, and gluconic acid) and was a practical assist-catalyst.

Fitting Models

All results indicated that the distribution of xylose and X2–X6 was significantly dependent on FA concentration, reaction temperature, and hydrolysis time. Moreover, the XOS decreased with the increasing acid concentration and/or prolonging hydrolysis time at high temperature; meanwhile, it reduced the XOS purity by forming xylose and furfural in the xylan-hydrolyzate. It is worth mentioning that the hydrolysis of xylan took prolonged time in the lower reaction temperature, suggesting the process to be economically unfavorable and that high reaction temperature with short hydrolysis time is much more preferable for oligosaccharide formation with desired DP and lower byproduct yields.

In this study, Design-Expert 11.0 software was employed to establish relationships between the independent and dependent variables. The fit summary report was generated by Design-Expert, which recommended that the quadratic models were suitable for the XOS yields from the experimental responses, which followed the regression equations.

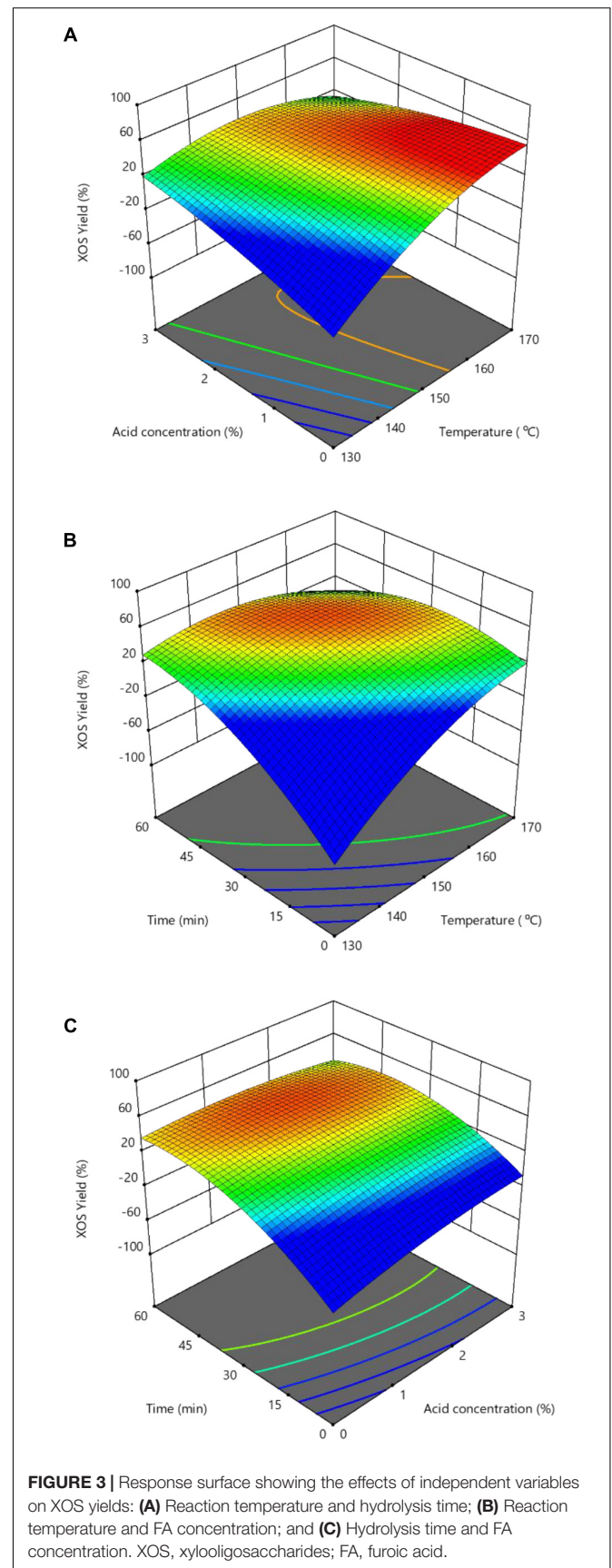
$$Y = -1500.59 + 18.86X_1 + 20.59X_2 + 4.50X_3 - 0.47X_1X_2 - 0.029X_1X_3 + 0.47X_2X_3 - 0.054X_1^2 + 6.11X_2^2 - 0.013X_3^2$$

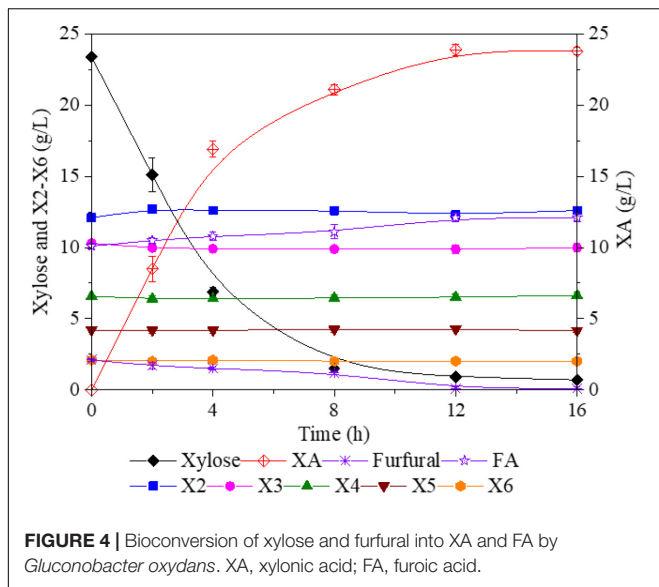


It is well known that the determination coefficient R^2 is defined as the ratio of the explained variation to the total variation and demonstrates the agreement between the observed and predicted results, which used to estimate goodness of fit of the regression equation, and it should be over 0.80 (Nath and Chattopadhyay, 2007). In the present study, R^2 was 0.928, indicating a close relationship between the predicted theoretical values and the experimental results; this similarity could also be verified by the high correlations between the observed and predicted values in **Figure 2**.

Analysis of variance of the model showed the F -value and P -value to be 20.96 and 0.0019, respectively. The F -value of 20.96 and the P -value of less than 0.050 suggest the model to be significant. In this case, the analysis of XOS yields showed the P -values of X_1 , X_3 , X_1X_2 , X_1X_3 , X_1^2 , and X_3^2 to be 0.0021, 0.0031, 0.0024, 0.0020, 0.0038, and 0.0064, respectively, indicating their significant effects on XOS yields. Besides, the P -values of X_1 , X_2 , and X_3 , were 0.0013, 0.0025, and 0.0598, respectively. P -value is used to check the order of significance for independent variables affecting the XOS yield, where smaller P -values mean higher significance (Xue et al., 2016). Thus, according to the P -values, the effect of independent variables on XOS yields in order to sort is as follows: Reaction temperature, hydrolysis time, and FA concentration.

Two-dimensional contour plots and three-dimensional response surface plots were generated from Design-Expert software and depicted in **Figures 3A–C**. These results demonstrated that the reaction temperature effect was more significant on XOS yield than the hydrolysis time and acid concentration. **Figures 3A–C** also illustrate the optimal





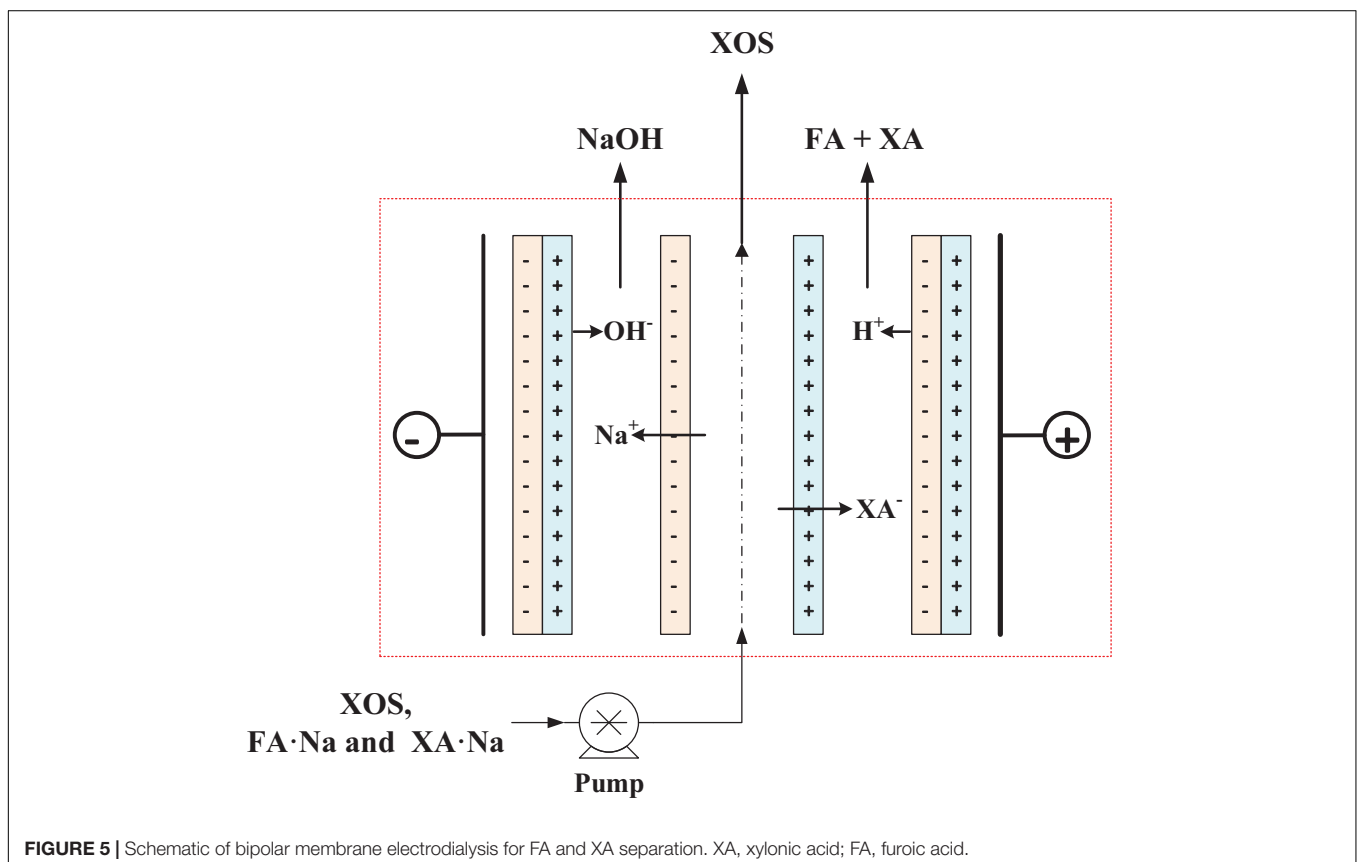
conditions, indicated by the red area. This resulted in the highest XOS yield with a predicted value of approximately 49.0%, which could be achieved at a higher temperature of 167°C with 1.2% FA for 33 min. The experimentally obtained real yield of furfural, xylose, and XOS under the predicted optimized conditions was $1.71 \pm 0.09\%$, $32.3 \pm 2.6\%$, and $49.2 \pm 3.5\%$,

respectively. Further, the real contents of X2–X6 were achieved at 12.10 ± 0.81 , 10.31 ± 0.64 , 6.58 ± 0.42 , 4.01 ± 0.36 , and 2.10 ± 0.28 g/L, respectively; and total XOS was 35.1 ± 2.5 g/L. Apparently, this predicted the XOS yield to be similar to the optimal experimental XOS yield, suggesting the accuracy of the established model to predict the XOS yield.

The mass balance of the two-step process showed that 40% xylan in corncob (contains 30.4% xylan) could be converted into value-added XOS; that is, approximately 125 g XOS could be harvest from 1,000 g of corncob material. The totality of the present results indicated that XOS preparation from corncob with FA-assisted hydrolysis was a profitable option.

Furoic Acid Recovery by a Combination of Bio-Oxidation and Electrodialysis

Xylooligosaccharides, as higher value-added products, therefore, are our prior target. The above results showed that acid hydrolysis at a relatively high temperature could effectively depolymerize xylan into XOS, which suggested that FA was an effective catalyst for XOS production. However, a great deal of xylose and a small quantity of furfural, as main byproducts, were simultaneously generated during the FA hydrolysis process. Under the optimum conditions, 49 g/(100 g xylan) XOS was produced; as well as 32 g/(100 g xylan) xylose and 2 g/(100 g xylan) furfural were accumulated in the xylan-hydrolyzate. In addition, 12 g/L of FA as catalyst was also preserved in the xylan-hydrolyzate. Generally,



commercial XOS products comprise DP 2–6 oligomers with 70–95% purity (Moure et al., 2006; Singh et al., 2018). Thus, both catalyst (FA) and byproducts (xylose and furfural) should be removed to improve purity of XOS. Previously, Zhou et al. (2017) have reported that xylose and furfural could be bio-oxidized into XA and FA by *G. oxydans* with 100% yield. In addition, Cao et al., successfully separated and collected XA from fermented broth by using electro dialysis (Cao and Xu, 2019). These studies suggested that the combination of bioconversion and electro dialysis could effectively remove xylose and recover FA.

After FA hydrolysis, the pH of xylan-hydrolyzate was below 2.5, which would significantly suppress the activity of *G. oxydans*. Thus, the xylan-hydrolyzate was prior adjusted to pH 6.5 with NaOH and then subjected to *G. oxydans* for biotransform xylose and furfural into XA and FA, respectively. During the fermentation, NaOH was also used to maintain pH, which resulted in XA·Na and FA·Na formed in the hydrolyzate. After 12 h of fermentation, 24 g/L of XA with a yield of 97.1% was accumulated in the broth. Besides, 14.1 g/L of FA retained in the solution; of these, 2.1 g/L of FA was from the furfural conversion. These results indicated that xylose and furfural were exclusively and effectively bio-oxidized into XA and FA without further catabolism. Meanwhile, the X2–X6 curves, shown in **Figure 4**, confirmed that XOS could not be utilized by *G. oxydans*, allowing the XOS, FA·Na, and XA·Na to be retained for the downstream separation.

Subsequently, the pH of hydrolyzate after bio-oxidation by *G. oxydans* was first adjusted to 6.5–7.0 for enhancing electro dialysis efficiency; and the mixture of the FA·Na, XA·Na, and XOS was then subjected into salt chamber of electro dialysis for XOS, FA, and NAOH recovery. The schematic of bipolar membrane electro dialysis for FA and XA separation is shown in **Figure 5**. The electro dialysis process was conducted at 50 mA/cm² of current density; and the pH of hydrolyzate in salt chamber was maintained at 6.0–7.0 in the process of electro dialysis (Zhou and Xu, 2019). After approximately 90 min of electro dialysis, 95.1% of FA and 97.6% of XA were recycled, and 98% XOS were retained in the salt chamber solution. Overall, electro dialysis with bipolar membranes is one of the most promising and convenient methods to isolate the ionic salts and recycle sugar compounds (Xu and Huang, 2008; Pan et al., 2017). The solubility of FA was only 37 g/L (25°C) due to the increased acid concentration in the acid chamber during the electro dialysis process. Thus, FA could be recovered easily by natural crystallization in the acid chamber. The recovery of FA not only improved the XOS purity but also reduced the waste stream and the output cost, which can potentially replace the organic acid-assisted XOS production.

REFERENCES

- Aachary, A. A., and Prapulla, S. G. (2011). Xylooligosaccharides (XOS) as an Emerging Prebiotic: Microbial Synthesis, Utilization, Structural Characterization, Bioactive Properties, and Applications. *Compr. Rev. Food Ence Food Safe.* 10, 2–16. doi: 10.1111/j.1541-4337.2010.00135.x
- Akpınar, O., Erdogan, K., and Bostanci, S. (2009). Production of xylooligosaccharides by controlled acid hydrolysis of lignocellulosic

CONCLUSION

In the present study, a recyclable and separable FA was employed to hydrolyze xylan into XOS. The effects of temperature, FA concentration, and hydrolysis time were assessed by RSM design, defining the maximum XOS production point. Finally, 35.1 g/L of XOS at the yield of 49.2% was produced with 1.2% FA at 167°C for 33 min. In conclusion, this study verified the feasibility of XOS production from FA, new organic acid hydrolysis combining recycled techniques. This model offers a practical framework for economical use of resources.

DATA AVAILABILITY STATEMENT

The original contributions presented in the study are included in the article/**Supplementary Material**, further inquiries can be directed to the corresponding author/s.

AUTHOR CONTRIBUTIONS

JZ: methodology, data curation, and formal analysis. XZa: investigation, data curation, and resources. XZo: conceptualization, supervision, validation, and writing—review and editing. YX: project administration and funding acquisition. All authors contributed to the article and approved the submitted version.

FUNDING

This work was supported by the National Key R&D Program of China (2017YFD0601001) and start-up funds for Scientific Research of Nanjing Forestry University (163030127).

ACKNOWLEDGMENTS

We sincerely thank the support of the Advanced Analysis and Testing Center of Nanjing Forestry University.

SUPPLEMENTARY MATERIAL

The Supplementary Material for this article can be found online at: <https://www.frontiersin.org/articles/10.3389/fbioe.2021.660266/full#supplementary-material>

materials. *Carbohydr. Res.* 344, 660–666. doi: 10.1016/j.carres.2009.01.015

Bian, J., Peng, P., Peng, F., Xiao, X., Xu, F., and Sun, R. (2014). Microwave-assisted acid hydrolysis to produce xylooligosaccharides from sugarcane bagasse hemicelluloses. *Food Chem.* 156, 7–13. doi: 10.1016/j.foodchem.2014.01.112

Cao, R., and Xu, Y. (2019). Efficient Preparation of Xylonic Acid from Xylonate Fermentation Broth by Bipolar Membrane Electro dialysis.

- Appl. Biochem. Biotech.* 187, 396–406. doi: 10.1007/s12010-018-2827-y
- Carvalho, A. F. A., Neto, P. D. O., Silva, D. F., and Pastore, G. M. (2013). Xylooligosaccharides from lignocellulosic materials: Chemical structure, health benefits and production by chemical and enzymatic hydrolysis. *Food Res. Int.* 51, 75–85. doi: 10.1016/j.foodres.2012.11.021
- Cesaro, A., Conte, A., Carrère, H., Trably, E., Paillet, F., and Belgiorno, V. (2020). Formic acid pretreatment for enhanced production of bioenergy and biochemicals from organic solid waste. *Biomass Bioener.* 133, 105455. doi: 10.1016/j.biombioe.2019.105455
- Dai, L., Huang, T., Jiang, K., Zhou, X., and Xu, Y. (2021). A novel recyclable furfural acid-assisted pretreatment for sugarcane bagasse biorefinery in co-production of xylooligosaccharides and glucose. *Biotechnol. Biofuels.* 14:35. doi: 10.1186/s13068-021-01884-3
- Gao, J., Azad, M., Han, H., Wan, D., and Li, T. J. (2020). Impact of Prebiotics on Enteric Diseases and Oxidative Stress. *Curr. Pharm. Design.* 26, 2630–2641. doi: 10.2174/1381612826666200211121916
- Guo, J., Cao, R., Huang, K., and Xu, Y. (2020). Comparison of selective acidolysis of xylan and enzymatic hydrolysability of cellulose in various lignocellulosic materials by a novel xyloionic acid catalysis method. *Bioresour. Technol.* 304:122943.
- Guo, J., Huang, K., Zhang, S., and Xu, Y. (2019). Optimization of selective acidolysis pretreatment for the valorization of wheat straw by a combined chemical and enzymatic process. *J. Chem. Technol. Biotechnol.* 95, 694–701. doi: 10.1002/jctb.6251
- Guo, X., Fu, Y., Miao, F., Yu, Q., Liu, N., and Zhang, F. (2020). Efficient separation of functional xylooligosaccharide, cellulose and lignin from poplar via thermal acetic acid/sodium acetate hydrolysis and subsequent kraft pulping. *Ind. Crop. Prod.* 153:112575. doi: 10.1016/j.indcrop.2020.112575
- Han, J., Cao, R., Zhou, X., and Xu, Y. (2020). An integrated biorefinery process for adding values to corncob in co-production of xylooligosaccharides and glucose starting from pretreatment with gluconic acid. *Bioresour. Technol.* 307:123200. doi: 10.1016/j.biortech.2020.123200
- Hong, C., Corbett, D., Venditti, R., Jameel, H., and Park, S. (2019). Xylooligosaccharides as prebiotics from biomass autohydrolyzate. *LWT* 111, 703–710. doi: 10.1016/j.lwt.2019.05.098
- Jayapal, N., Samanta, A. K., Kolte, A. P., Senani, S., Sridhar, M., Suresh, K. P., et al. (2013). Value addition to sugarcane bagasse: Xylan extraction and its process optimization for xylooligosaccharides production. *Ind. Crop. Prod.* 42, 14–24. doi: 10.1016/j.indcrop.2012.05.019
- Jnawali, P., Kumar, V., Tanwar, B., Hirdyani, H., and Gupta, P. (2017). Enzymatic Production of Xylooligosaccharides from Brown Coconut Husk Treated with Sodium Hydroxide. *Waste & Biomass Valorization.* 9:9963
- Kootstra, A. M. J., Beefink, H. H., Scott, E. L., and Sanders, J. P. M. (2009). Comparison of dilute mineral and organic acid pretreatment for enzymatic hydrolysis of wheat straw. *Biochem. Eng. J.* 46, 126–131. doi: 10.1016/j.bej.2009.04.020
- Lin, Q., Li, H., Ren, J., Deng, A., Li, W., Liu, C., et al. (2017). Production of xylooligosaccharides by microwave-induced, organic acid-catalyzed hydrolysis of different xylan-type hemicelluloses: Optimization by response surface methodology. *Carbohydr. Polym.* 157, 214–225. doi: 10.1016/j.carbpol.2016.09.091
- Mhetras, N., Mapre, V., and Gokhale, D. (2019). Xylooligosaccharides (XOS) as Emerging Prebiotics: Its Production from Lignocellulosic Material. *Adv. Microb.* 09, 14–20. doi: 10.4236/aim.2019.91002
- Moure, A., Gullón, P., Domínguez, H., and Parajó, J. C. (2006). Advances in the manufacture, purification and applications of xylo-oligosaccharides as food additives and nutraceuticals. *Proc. Biochem.* 41, 1913–1923. doi: 10.1016/j.procbio.2006.05.011
- Nath, A., and Chattopadhyay, P. K. (2007). Optimization of oven toasting for improving crispness and other quality attributes of ready to eat potato-soy snack using response surface methodology. *J. Food Eng.* 80, 1282–1292. doi: 10.1016/j.jfoodeng.2006.09.023
- Neto, F. S. P. P., Roldán, I. U. M., Galán, J. P. M., Monti, R., de Oliveira, S. C., and Masarin, F. (2020). Model-based optimization of xylooligosaccharides production by hydrothermal pretreatment of Eucalyptus by-product. *Ind. Crop. Prod.* 154, 112707. doi: 10.1016/j.indcrop.2020.112707
- Pan, J., Miao, M., Lin, X., Shen, J., Van der Bruggen, B., and Gao, C. (2017). Production of Aldonic Acids by Bipolar Membrane Electrodialysis. *Ind. Eng. Chem. Res.* 56, 7824–7829. doi: 10.1021/acs.iecr.7b01529
- Samanta, A., Jayapal, N., Jayaram, C., Roy, S., Kolte, A. P., Senani, S., et al. (2015). Xylooligosaccharides as prebiotics from agricultural by-products: Production and applications. *Bioact. Carbohydr. Diet. Fibre.* 5, 62–71. doi: 10.1016/j.bcdf.2014.12.003
- Samanta, A. K., Jayapal, N., Kolte, A. P., Senani, S., Sridhar, M., Suresh, K. P., et al. (2012). Enzymatic production of xylooligosaccharides from alkali solubilized xylan of natural grass (*Sehima nervosum*). *Bioresour. Technol.* 112, 199–205. doi: 10.1016/j.biortech.2012.02.036
- Santibáñez, L., Henríquez, C., Corro-Tejeda, R., Bernal, S., Armijo, B., and Salazar, O. (2021). Xylooligosaccharides from lignocellulosic biomass: A comprehensive review. *Carbohydr. Polym.* 251:117118. doi: 10.1016/j.carbpol.2020.117118
- Singh, R. D., Banerjee, J., Sasmal, S., Muir, J., and Arora, A. (2018). High xylan recovery using two stage alkali pre-treatment process from high lignin biomass and its valorisation to xylooligosaccharides of low degree of polymerisation. *Bioresour. Technol.* 256, 110–117. doi: 10.1016/j.biortech.2018.02.009
- Sluiter, A., Hames, B., Ruiz, R., Scarlata, C., Sluiter, J., Templeton, D., et al. (2008). Determination of structural carbohydrates and lignin in biomass. *Lab. Anal. Proc.* 1617, 1–16.
- Xu, T., and Huang, C. (2008). Electrodialysis-based separation technologies: A critical review. *AIChE J.* 54, 3147–3159. doi: 10.1002/aic.11643
- Xu, Y., Fan, L., Wang, X., Yong, Q., and Yu, S. (2013). Simultaneous separation and quantification of linear xylo- and cello-oligosaccharides mixtures in lignocellulosics processing products on high-performance anion-exchange chromatography coupled with pulsed amperometric detection. *BioResources* 2013, 8.
- Xue, J., Zhao, S., Liang, R., Yin, X., Jiang, S., Su, L., et al. (2016). A biotechnological process efficiently co-produces two high value-added products, glucose and xylooligosaccharides, from sugarcane bagasse. *Bioresour. Technol.* 204, 130–138. doi: 10.1016/j.biortech.2015.12.082
- Zhang, H., Xu, Y., and Yu, S. (2017). Co-production of functional xylooligosaccharides and fermentable sugars from corncob with effective acetic acid prehydrolysis. *Bioresour. Technol.* 234, 343–349. doi: 10.1016/j.biortech.2017.02.094
- Zhao, Z., Huang, C., Wu, D., Chen, Z., Zhu, N., Gui, C., et al. (2020). Utilization of enzymatic hydrolysate from corn stover as a precursor to synthesize an eco-friendly plywood adhesive. *Ind. Crop. Prod.* 152:112501. doi: 10.1016/j.indcrop.2020.112501
- Zheng, Y., Yu, Y., Lin, W., Jin, Y., Yong, Q., and Huang, C. (2021). Enhancing the enzymatic digestibility of bamboo residues by biphasic phenoxethanol-acid pretreatment. *Bioresour. Technol.* 325:124691. doi: 10.1016/j.biortech.2021.124691
- Zhou, X., Han, J., and Xu, Y. (2019a). Electrodialytic bioproduction of xyloionic acid in a bioreactor of supplied-oxygen intensification by using immobilized whole-cell *Gluconobacter oxydans* as biocatalyst. *Bioresour. Technol.* 282, 378–383. doi: 10.1016/j.biortech.2019.03.042
- Zhou, X., Zhou, X., Xu, Y., and Chen, R. R. (2017). *Gluconobacter oxydans* (ATCC 621H) catalyzed oxidation of furfural for detoxification of furfural and bioproduction of furfural. *J. Chem. Technol. Biotechnol.* 92, 1285–1289. doi: 10.1002/jctb.5122
- Zhou, X., Zhao, J., Zhang, X., and Xu, Y. (2019b). An eco-friendly biorefinery strategy for xylooligosaccharides production from sugarcane bagasse using cellulosic derived gluconic acid as efficient catalyst. *Bioresour. Technol.* 289:121755. doi: 10.1016/j.biortech.2019.121755
- Zhou, X., and Xu, Y. (2019). Eco-friendly consolidated process for co-production of xylooligosaccharides and fermentable sugars using self-providing xyloionic acid as key pretreatment catalyst. *Biotechnol. Biofuels* 12:272.

Conflict of Interest: The authors declare that the research was conducted in the absence of any commercial or financial relationships that could be construed as a potential conflict of interest.

Copyright © 2021 Zhao, Zhang, Zhou and Xu. This is an open-access article distributed under the terms of the Creative Commons Attribution License (CC BY). The use, distribution or reproduction in other forums is permitted, provided the original author(s) and the copyright owner(s) are credited and that the original publication in this journal is cited, in accordance with accepted academic practice. No use, distribution or reproduction is permitted which does not comply with these terms.



Valorization of Enzymatic Hydrolysis Residues from Corncob into Lignin-Containing Cellulose Nanofibrils and Lignin Nanoparticles

Rui Xu^{1,2†}, Haishun Du^{3†}, Hui Wang^{1†}, Meng Zhang¹, Meiyan Wu², Chao Liu², Guang Yu², Xinyu Zhang³, Chuanling Si^{1*}, Sun-Eun Choi^{4*} and Bin Li^{2*}

OPEN ACCESS

Edited by:

Xin Zhou,
Nanjing Forestry University, China

Reviewed by:

Bo Pang,
Max Planck Institute of Colloids
and Interfaces, Germany
Jing Shen,
Northeast Forestry University, China

*Correspondence:

Chuanling Si
sichli@tust.edu.cn
Sun-Eun Choi
oregonin@kangwon.ac.kr
Bin Li
libin@qibebt.ac.cn

† These authors have contributed
equally to this work and share first
authorship

Specialty section:

This article was submitted to
Industrial Biotechnology,
a section of the journal
Frontiers in Bioengineering and
Biotechnology

Received: 08 March 2021

Accepted: 15 March 2021

Published: 16 April 2021

Citation:

Xu R, Du H, Wang H, Zhang M,
Wu M, Liu C, Yu G, Zhang X, Si C,
Choi S-E and Li B (2021) Valorization
of Enzymatic Hydrolysis Residues
from Corncob into Lignin-Containing
Cellulose Nanofibrils and Lignin
Nanoparticles.
Front. Bioeng. Biotechnol. 9:677963.
doi: 10.3389/fbioe.2021.677963

¹ Tianjin Key Laboratory of Pulp and Paper, Tianjin University of Science and Technology, Tianjin, China, ² Key Laboratory of Biofuels, Qingdao Institute of Bioenergy and Bioprocess Technology, Chinese Academy of Sciences, Qingdao, China, ³ Department of Chemical Engineering, Auburn University, Auburn, AL, United States, ⁴ Department of Forest Biomaterials Engineering, College of Forest and Environmental Sciences, Kangwon National University, Chuncheon, South Korea

As a kind of biomass waste, enzymatic hydrolysis residues (EHRs) are conventionally burned or just discarded, resulting in environmental pollution and low economic benefits. In this study, EHRs of corncob residues (CCR) were used to produce high lignin-containing cellulose nanofibrils (LCNFs) and lignin nanoparticles (LNPs) through a facile approach. The LCNFs and LNPs with controllable chemical compositions and properties were produced by tuning the enzymolysis time of CCR and the followed homogenization. The morphology, thermal stability, chemical and crystalline structure, and dispersibility of the resultant LCNFs and LNPs were further comprehensively investigated. This work not only promotes the production of lignocellulose-based nanomaterials but also provides a promising utilization pathway for EHRs.

Keywords: lignin-containing cellulose nanofibrils, enzymatic hydrolysis residues, homogenization, corncob, lignin nanoparticles

INTRODUCTION

In recent years, along with the increasing concerns derived from fossil resource dependence and environmental pollution, lignocellulosic biomass has been regarded as an alternative source of biofuels and bio-based products because of its large amount of stock and renewability (Xu et al., 2016; Li et al., 2019, 2020; Lin et al., 2020; Yang et al., 2020; Liu K. et al., 2021; Zheng et al., 2021b). It is worth noting that agricultural residues such as wheat straw, corn stalk, bagasse, and corncob are renewable lignocellulosic biomass yet not properly managed or utilized (Anwar et al., 2019). It has been reported that approximately 900 million tons of agricultural wastes were produced in China each year (Liu et al., 2019; Xu et al., 2019; Chen et al., 2020). However, most of the agricultural wastes are often disposed by burning, which results in low economic benefits and causes severe environmental pollution. Recently, burning of agricultural waste is strictly forbidden to protect the environment and achieve the target carbon neutrality in China. Thus, it is of great importance to valorize these agricultural wastes into valuable products by using sustainable and environmentally friendly processes (Xu et al., 2020).

Recent studies suggested that converting the cellulose and hemicellulose of biomass to monomeric sugars and biofuels could be a great road to meeting the urgent need for renewable

alternative carbon resources (Robertson et al., 2017; Huang et al., 2019; Lin et al., 2019). Among the agricultural wastes, corncob has been widely concerned for its richness in hemicellulose, which is often used to produce xylose, xylitol, xylo-oligosaccharides, or furfural (Si et al., 2009b, 2013b; Zhang et al., 2014; Hu et al., 2016; Liu et al., 2016; Huang et al., 2020b). However, a large amount of corncob residue is produced and it is usually used for burning to generate heat or electricity, cultivation, feed, or just discarded. Yet, corncob residues contain abundant cellulose and lignin, which provide the possibility of creating useful materials from waste biomass, which would enable us to replace artificial and non-renewable resources with renewable resources (Kaneko et al., 2006; Si et al., 2009a, 2013a). Also, enzymatic hydrolysis of corncob residue is commonly used to produce sugar/ethanol (Xie et al., 2018b; Xu et al., 2021). However, the high production cost of enzymatic hydrolysis prevents its large-scale utilization (Lin and Lu, 2021; Liu H. Y. et al., 2021). Thus, apart from optimizing the enzymolysis process parameters, making better use of the solid residues produced after enzymatic hydrolysis could be a feasible method to reduce the total cost, based on the concept of integrated biorefinery.

As a kind of biomass waste, enzymatic hydrolysis residues (EHRs) are conventionally burned for heat and power generation, resulting in low economic benefits. Actually, the EHRs contain a significant amount of lignin, a small amount of cellulose, as well as some extractives and ash, and a trace amount of hemicellulose. As a primary starting material, the EHRs are qualified to produce lignocellulosic nanomaterials (Khan et al., 2018). Moreover, the abundant lignin existing in EHRs would play a good role in some properties such as thermal stability, antioxidation properties, hydrophobicity, and stabilization (Peng et al., 2018; An et al., 2019). By the way, in the actual industrial production, high solid enzymatic hydrolysis residue has more universal application. Thanks to the special structure of EHRs, the fiber is in a scattered and short form with a significant amount of lignin. Usually, fiber with a high content of lignin is difficult to disintegrate down to nanoscale due to the cross-linked barrier properties of lignin.

Lignocellulosic nanomaterials have received much attention at the forefront of bio-based economy in which renewable biomass is used as the raw material for the production of various consumer products (Salas et al., 2014; Song, 2019; Dai et al., 2020a). Recently, cellulose nanomaterials, mainly including cellulose nanocrystals (CNCs) and nanofibers (CNFs), have attracted rapidly growing interest from both academic and industrial researchers due to their superior physiochemical properties (Du et al., 2019; Huang et al., 2020a; Liu et al., 2020; Miao et al., 2020; Wang P. et al., 2020). However, the preparation of cellulose nanomaterials is facing several challenges such as complicated purification and pretreatment process, large amount of chemical and energy consumption, and environmental issues, which limited their large-scale applications (Xie et al., 2018a; Dai et al., 2020b; Wang H. et al., 2020). Fortunately, recent studies showed that lignin-containing cellulose nanomaterials can be obtained directly from raw materials via sustainable and low-cost approaches, and the presence of lignin endows the LCNM with many advantages such as improved thermal stability, UV-blocking performance, and water barrier property

(Nair et al., 2017; Wang et al., 2018; Farooq et al., 2019; Hong et al., 2020). Especially in the last few years, lignin-containing cellulose nanofibrils (LCNFs) have been gradually arousing people's interest. The preparation of LCNFs was confirmed by various approaches from different lignocellulose biomass including unbleached thermomechanical pulp, corn husk, and tobacco stalks, among others (Bian et al., 2017; Hu et al., 2018; Wang et al., 2018; Wen et al., 2019). In addition, lignin nanoparticles (LNPs) have gained significant interest among researchers in recent years, which will play a vital role in promoting lignin valorization (Chauhan, 2020; Dong et al., 2020a). It should be noted that EHRs contain much more lignin compared to unbleached pulp and most of lignocellulosic biomass (Huang et al., 2018), and it is expected that LCNFs with high lignin content or LNPs can be produced from EHRs.

In this work, the preparation of EHRs with different enzymatic hydrolysis times (48, 72, and 108 h, respectively, for comparison) was done in accordance with the previous work of our group (Chi et al., 2019), and subsequently, high-pressure homogenization treatment of the obtained EHR samples was carried out to produce LCNFs or LNPs. The physiochemical properties of the obtained LCNFs and LNPs were further comprehensively investigated. This work will promote the development of lignocellulose-based nanomaterials and provide a promising pathway for the full utilization of agricultural wastes.

MATERIALS AND METHODS

Materials

Corn cob residue (CCR) was purchased from Futaste Co., Ltd. (China), where corncob was used as raw material for the manufacture of xylose and xylitol using dilute acid hydrolysis. All the chemicals (e.g., KOH, H₂SO₄) used in this study were purchased from Sinopharm Chemical Reagent Co. Ltd. and used directly without further purification. Cellulase enzyme was obtained from Qingdao Vland Biotech Inc. The activity of cellulase was 85 FPU mL⁻¹, which was measured by the standard procedure (Ghose, 1987) and the protein content of cellulase was 80 mg-protein per mL, as determined by the standard Bradford method.

Preparation of LCNFs or LNPs

Alkaline Pretreatment of CCR

To improve the enzymatic hydrolysis efficiency of cellulose and effectively utilize the alkali lignin components, the as-received CCR was pretreated with 16 wt.% KOH at 70°C for 90 min following the procedure reported previously (Chi et al., 2019). After alkaline pretreatment, the collected solid was washed with distilled water to neutral pH and stored at 4°C.

Enzymatic Hydrolysis

Enzymatic hydrolysis of the alkaline-pretreated CCR was conducted with a high solid content (20%) under 50°C for different hydrolysis times (48, 72, and 108 h, respectively), and the enzyme dosage for saccharification was 15 FPU/g-cellulose.

Finally, the EHRs were obtained by filtration and washed to neutral pH and stored at 4°C.

High-Pressure Homogenization

The obtained EHR samples were converted to LCNFs or LNPs using a high-pressure homogenizer (GYB49-10s, China). The EHRs treated in different enzymatic hydrolysis times (named EHRs-48 h, EHRs-72 h, and EHRs-108 h, respectively) were homogenized at a concentration of 2 wt.% in deionized water for three times at 30 MPa and then five times at 60 MPa. The obtained products were noted as LCNFs-48 h, LCNFs-72 h, and LNPs-108 h, respectively.

Analytical Method for Composition

The composition of EHRs was determined following the National Renewable Energy Laboratory procedure (NREL). A dried EHR sample (0.30 g) was treated with 3 mL of 72% (w/w) H₂SO₄ at 30°C for 60 min. Then, the acid concentration was diluted to 4% (w/w) by adding deionized water, and the samples were further hydrolyzed at 121°C for 60 min. The residue (Klason lignin) was filtered with deionized water under vacuum and then dried at 105°C to constant weight. The carbohydrate content in the supernatant was quantified by high-performance liquid chromatography system (HPLC, Waters-1525, United States) analysis. The contents of cellulose and hemicellulose of EHR samples were calculated based on the amount of corresponding monomeric sugars (Sluiter et al., 2008).

Morphology Analysis

The microstructure of samples was investigated by an S-4800 field-emission scanning electron microscope (SEM, Hitachi, Japan). After homogenization, the samples of LCNFs and LNPs were freeze dried. The freeze-dried samples were sprinkled on a conductive adhesive tape mounted on a specimen stub and coated with gold by a sputter coater (E-1045, Hitachi, Tokyo, Japan) before observation.

A transmission electron microscope (TEM, Hitachi, H-7650) was also used to investigate the microstructure of samples. LCNF or LNP suspensions with a concentration of 0.03% were deposited on carbon-coated TEM grids. After the drying process, the specimen was stained with 2% uranyl acetate solution for 1.5 h. Then, the excess staining solution was removed, and the samples were dried at ambient before characterization.

Thermogravimetric (TG) Analysis

The thermal stability of the freeze-dried samples was evaluated using a TGA Q600 (TA Instruments, United States) instrument at temperatures ranging from 25 to 550°C. The experiment was carried out under a nitrogen atmosphere at a heating rate of 8°C/min (Yang et al., 2007).

Fourier Transform Infrared Spectroscopy (FTIR)

FTIR spectra of EHR samples were determined using a FTIR spectrometer (Nicolet-6700, America) with a wavenumber region of 4,000–500 cm⁻¹. Freeze-dried samples were diluted with KBr using a KBr tableting process before FTIR analysis.

X-Ray Diffraction (XRD) Analysis

XRD analysis was conducted using an ADVANCE D8 X-ray diffractometer (Bruker Co., Germany) equipped with a Ni-filtered Cu K α radiation operated at 40 kV and 30 mA. Briefly, 0.2 g freeze-dried samples was compressed into a pellet to record patterns from 5° to 60° of diffraction with a scan rate of 4°/min. The crystallinity index (CrI) was calculated according to Segal's method (Segal et al., 1959) with the subtraction of background of glass.

Zeta Potential and Dynamic Light Scattering (DLS)

The zeta potential and DLS analyses of LCNF and LNP suspensions were detected by a microscopic electrophoresis apparatus (Nano Brook 90Plus Zeta, America) and was calculated by the electrophoretic mobility. All the samples were ultrasonically treated for 20 min before analysis, and the solid concentration was around 0.05 wt.%. The measurements were conducted in triplicate for each sample, and the average data was reported.

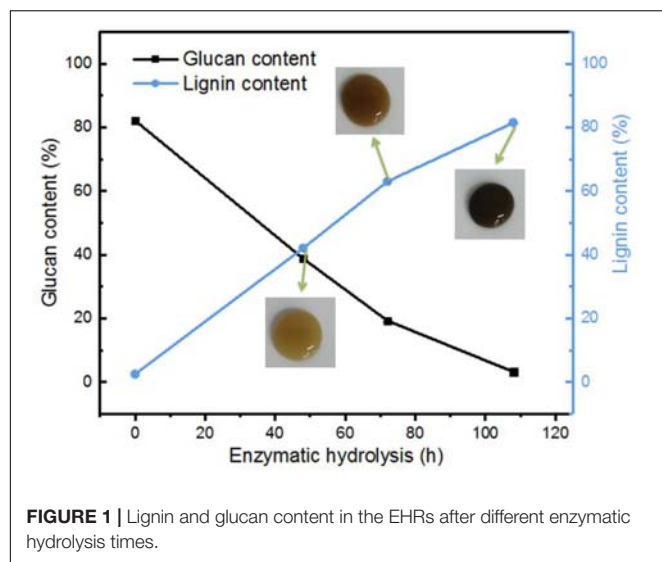
RESULTS AND DISCUSSION

Enzymatic Hydrolysis of CCR

As mentioned in the experiment part, the corncob after dilute acid hydrolysis and the followed alkaline treatment were used as the raw material in this study. As indicated in **Table 1**, the raw material (alkaline pretreated CCR) contains majority of cellulose with a small portion of residual xylan, lignin, and extractives, which could be a great feedstock for the preparation of glucose by enzymatic hydrolysis. **Figure 1** shows the change of lignin and glucan contents in the EHRs with different enzymatic hydrolysis times. It can be clearly seen that with the increase of enzymolysis time, the content of glucan in the EHRs decreased dramatically, while the relative proportion of lignin significantly increased. The insert photos of the collected suspensions of the nanomaterial after homogenization vividly demonstrate the color change, which correlates with the lignin content. **Table 1** gives a detailed description of the changes of each component in the EHRs. We can easily see that the cellulose and lignin account for most of the compositions of the collected EHRs for all the samples. Also, the content of xylan and extractives did not change greatly with enzymolysis time due to the strong specificity of the enzyme. Notably, the glucan content in the EHRs is only around 3.2% after enzymatic hydrolysis for 108 h. Depending on

TABLE 1 | Chemical composition of raw material and EHRs treated at different enzymatic hydrolysis times.

Samples	Extractives content (%)	Glucan content (%)	Xylan content (%)	Lignin content (%)
Raw material	5.3 ± 1.1	82.2 ± 0.9	3.4 ± 0.2	2.5 ± 0.2
EHRs-48 h	8.7 ± 0.8	38.8 ± 0.6	2.6	42.1 ± 0.6
EHRs-72 h	7.1 ± 1.0	19.3 ± 0.5	2.4 ± 0.2	63 ± 0.7
EHRs-108 h	5.9 ± 0.6	3.2 ± 0.9	2.5 ± 0.1	81.5 ± 1



the chemical composition of the collected EHRs after enzymatic hydrolysis, we marked the samples prepared from EHRs-48 h and EHRs-72 h as LCNFs and the sample prepared from EHRs-108 h as LNPs, respectively.

Morphologies of LCNFs and LNPs

Figures 2a,b show the morphology of the raw material (the alkaline-pretreated CCR) before enzymolysis. The cellulose fibers and lignin can be clearly seen, and there are some lignin particles anchored on the surface of cellulose fibers. From **Figures 2c,d**, it can be observed that the LCNFs-48 h was rich in nanofibers, and there were many irregular LNPs adhering on the nanofiber surface. **Figures 2e,f** display the morphology of LCNFs-72 h. According to these two images, the existence of nanofibers and LNPs on the surface of nanofibers could be seen clearly. **Figures 2g,h** show the morphology of LNPs-108 h, only a small number of nanofibers can be seen, and the LNPs show an obvious aggregation state (it is speculated to be the aggregate of LNPs before freeze-drying).

As shown in **Figure 3**, the morphology of LCNFs and LNPs was further examined by TEM analysis and the particle size was evaluated by DLS. From the TEM images, we can see the coexistence of nanofibers and LNPs for the samples of LCNFs-48 h and LCNFs-72 h. It should be noted that the DLS can only be used as a reference for particle distribution, not as a basis for the real particle size. As shown in **Figures 3a,b**, a large number of nanofibers with a clear fiber boundary can be seen and some of the nanofibers are anchored with some LNPs. From **Figures 3d,e**, most of the nanofibers are covered with LNPs, and the fiber boundary can be hardly observed. It can be seen from **Figures 3g,h** that LNPs with a diameter less than 50 nm can be obtained from EHRs-108 h, but it is speculated that there is still a very small amount of cellulose nanofibers embedded among them according to the component analysis results of EHRs-108 h and **Figure 3i**.

In addition, **Figure 3** indicates the measured particle size decreased with the increased lignin content in the samples. This phenomenon can be explained as follows: (1) the measured data

of the sample containing nanocellulose would be larger than the actual, because of the large draw ratio. While, lignin nanoparticles can reduce the interference of draw ratio because of its near spherical shape, which lead to the measurement is closer to the actual. (2) As the lignin content increased in the samples, the possibility of attraction among the nanofibrils decreased, contributing to the separation of nanofibrils. Consequently, the measured data decreased with the increase of lignin content (Ferrer et al., 2012; Dong et al., 2020b; Pei et al., 2020; Zheng et al., 2021a).

Thermal Stability of LCNFs and LNPs

The thermal stability of the as-prepared LCNFs, LNPs, and raw materials was analyzed by TG analysis, and the results are shown in **Figure 4**. As shown in the TG and DTG curves, all samples mainly have two stages of thermal decomposition; one is before 250°C, and the other is between 250 and 400°C. For the raw material, only one weight loss peak was observed at the temperature of 350°C (T_{max}), at which the weight loss rate was around 17.5%/min. In comparison, the DTG of the LCNFs and LNPs illustrated that these samples containing the high lignin content had two weight loss peaks, and one was around 209°C and the other was around 360°C. It can also be observed from these curves that the weight loss rate at T_{max} decreased gradually along with the increase of lignin content. According to the reported literatures, the lignin decomposed slower and in a broad range (between 160 and 900°C), while cellulose decomposition usually occurred in the range of 300–400°C. The reason for the decrease of the weight loss rate at T_{max} is also related to the content of cellulose in the samples. The content of cellulose in raw material was relatively high, resulting in the high degradation rate of cellulose. However, the content of cellulose in LCNFs and LNPs decreased with the prolonging of enzymatic hydrolysis time, causing the weight loss rate decreased at T_{max} . In addition, the comparison of residual carbon produced by lignin was also consistent with the previous results (Wang et al., 2018).

Chemical and Crystalline Structures of LCNFs and LNPs

Figure 5A shows the FT-IR spectra of LCNF and LNP samples. Since no chemical reaction was performed on the lignin or cellulose during the high homogenization, all the spectra were very similar to the characteristic peak of lignin. The typical aromatic ring peaks of lignin fraction at 1,596 and 1,507 cm^{-1} were also evident (Schwanninger et al., 2004). In addition, peaks at 1,125 and 1,329 cm^{-1} were also observed, which were assigned to the condensed guaiacyl units and syringyl units of lignin, respectively (Rana et al., 2009). The peak at 1,735 cm^{-1} (C=O vibration) was observed in EHRs-48 h and EHRs-72 h, indicating the remaining of xylan in short-time EHRs (Sirvio et al., 2016). The characteristic peaks of cellulose were observed at 1,163 and 897 cm^{-1} in LCNFs-48 h and LCNFs-72 h, which was not obvious for LNPs-108 h (Schwanninger et al., 2004).

XRD patterns of the raw material and the LCNF and LNP samples are shown in **Figure 5B**. The raw material displays main characteristic diffraction peaks at 14.6°, 16.5°, 22.6°, and 34.6°, corresponding to the (1–10), (110), (200), and (004) lattice planes, respectively, indicating that the raw materials conform

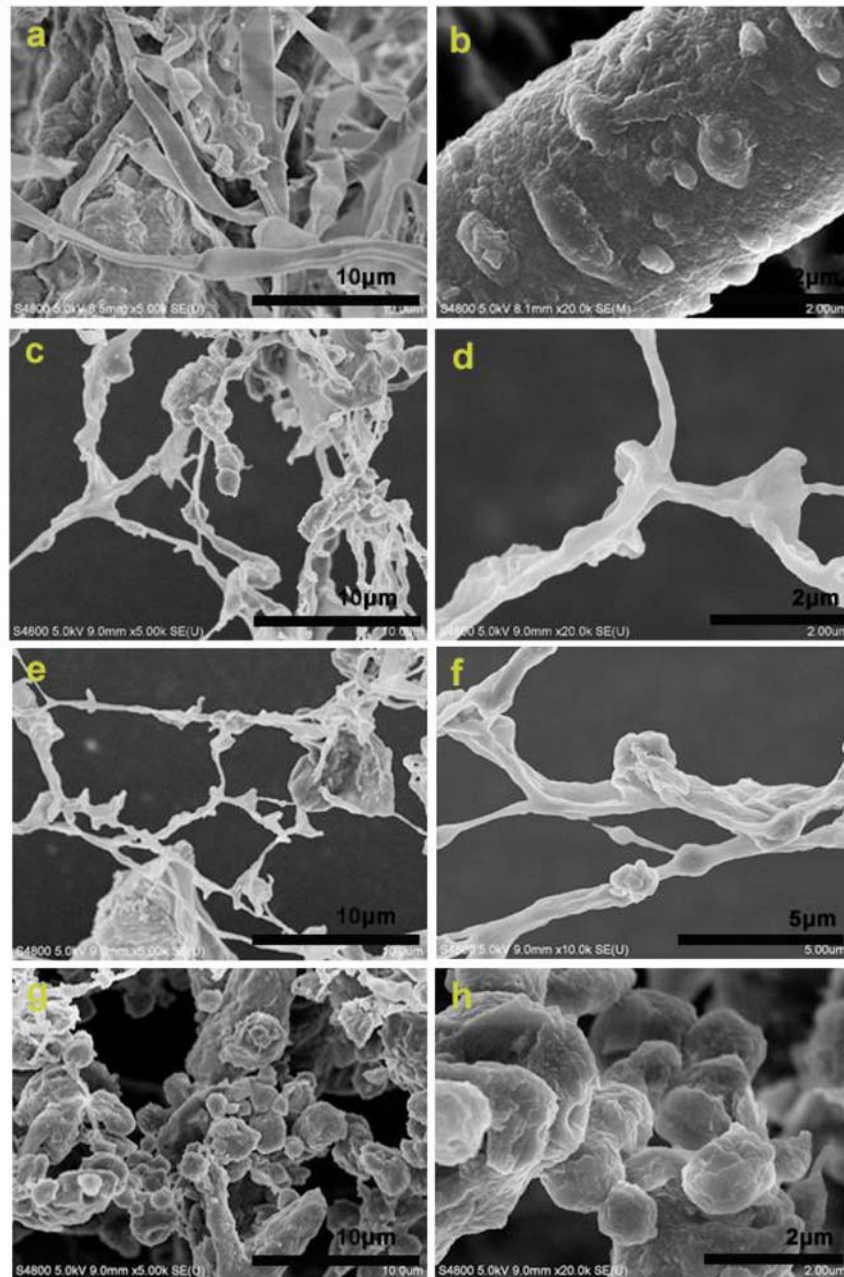


FIGURE 2 | SEM images of the raw material (a,b), LCNFss-48 h (c,d), LCNFs-72 h (e,f), and LNPs-108 h (g,h).

to the cellulose I structure (Sun et al., 2015; Du et al., 2020). On the contrary, the XRD patterns of the LCNFs and LNPs just show a broad amorphous peak, and the highest peak was around 20.5° . This could be ascribed to the removal of cellulose and the amorphous nature of lignin (Peng et al., 2018).

Dispersion Stability

The dispersion stability of LCNF and LNP suspension was evaluated by the zeta potential. It is well documented that the closer the value measured by the zeta potential was to zero,

the easier the dispersion was to agglomerate and settle, and the worse the relative stability is (Herrera et al., 2018). As shown in **Figure 6A**, the zeta-potential value of the dispersion formed by LNPs-108 h was around -52 mV, indicating the best stability. It has been demonstrated that the stability of the solution would increase with the increase of lignin content, for it would improve the fibrillation process (Lahtinen et al., 2014), which increases the surface charge of the material, resulting in repulsion between the fibrils thus allowing an easier separation from each other (Rojo et al., 2015). Moreover, as shown in **Figure 6B**, all the samples

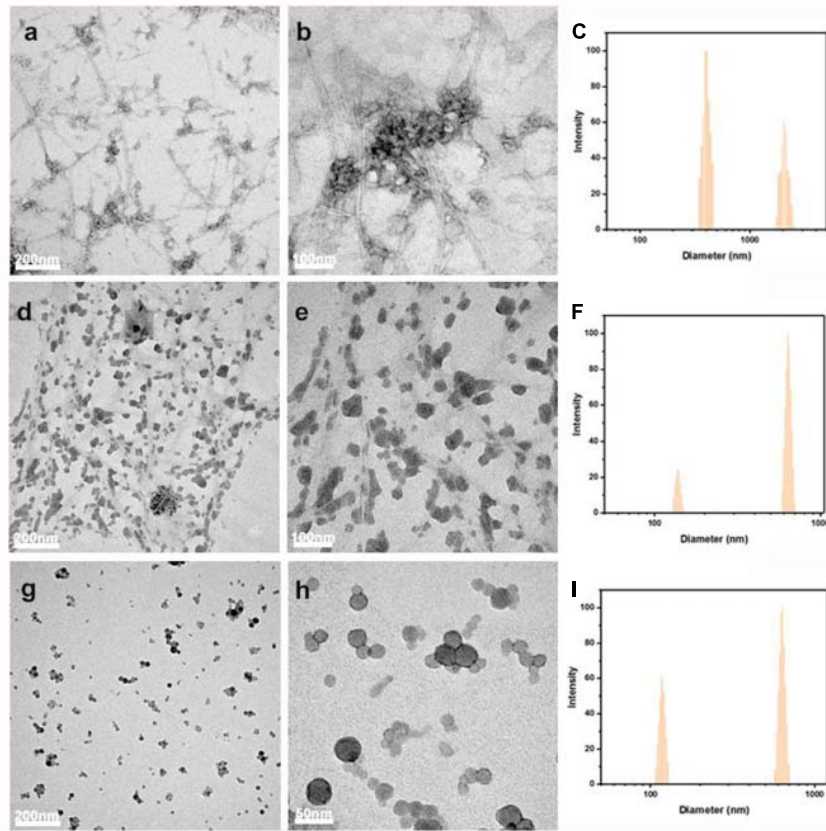


FIGURE 3 | TEM images and the measured size distribution by DLS of LCNFs-48 h (a–c); LCNFs-72 h (d–f); and LNPs-108 h (g–i).

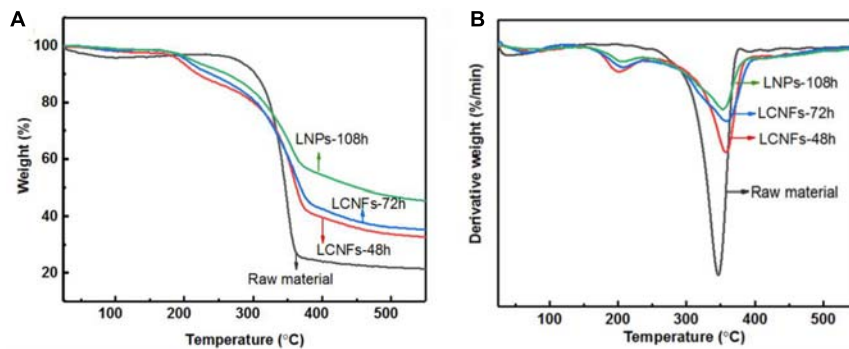


FIGURE 4 | TG (A) and DTG (B) curves of LCNFs-48 h, LCNFs-72 h, LNPs-108 h, and raw material.

exhibit very stable colloidal suspensions in aqueous media for over 1 month, indicating excellent dispersibility.

PROPOSED PROCESS FOR THE FULL UTILIZATION OF CORNCOB

Herein, based on the results obtained in this work and our previous work, we propose the full component utilization of

corn cob to provide a reference for the full utilization of other similar agricultural wastes. Generally, hemicellulose is extracted firstly from corn cob in the industry, which mainly involves acid treatment. On the basis of the research that we had finished (Xie et al., 2018b; Chi et al., 2019), alkali treatment was a convenient way to effectively separate alkali lignin from agricultural lignocellulosic waste and promote the downstream enzymatic hydrolysis for the production of fermentable sugars. The current study demonstrated that the EHRs could be an

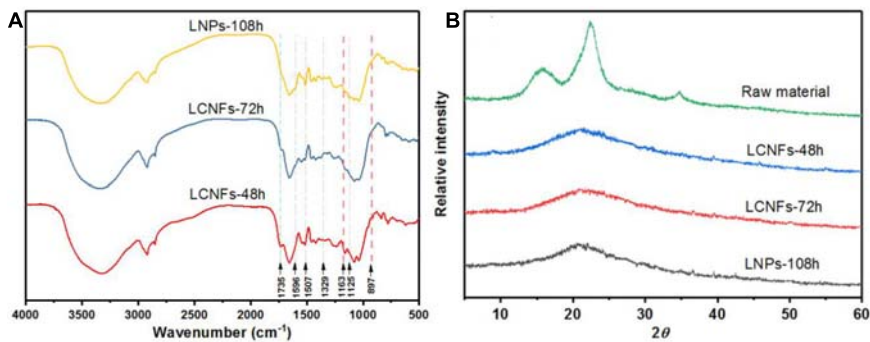


FIGURE 5 | (A) FTIR spectra of the LCNFs-48 h, LCNFs-72 h, and LNPs-108 h. **(B)** X-ray diffraction patterns of raw material and the LCNFs and LNPs samples.

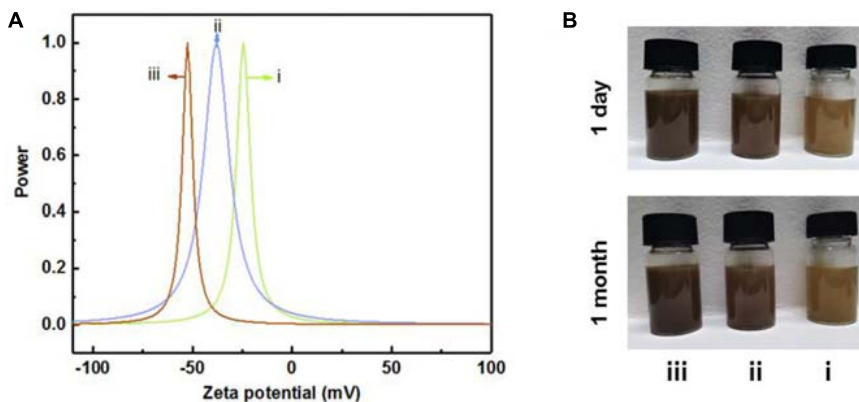


FIGURE 6 | The zeta potential **(A)** and corresponding dispersibility in water **(B)** of LCNFs-48 h (i), LCNFs-72 h (ii), and LNPs-108 h (iii).

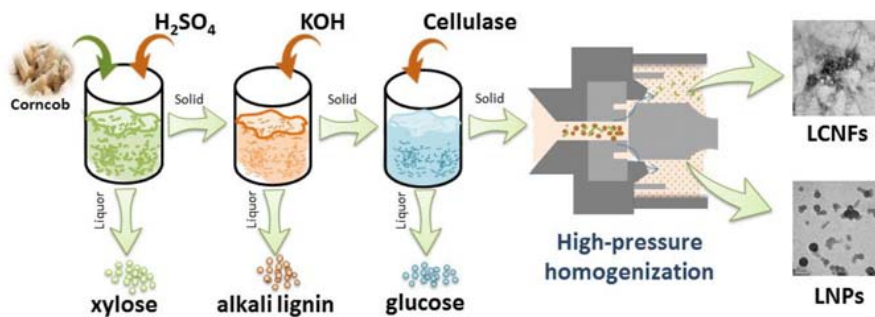


FIGURE 7 | Proposed process for the full utilization of corncob.

attractive material for the preparation of LCNFs or LNPs, which might find applications in diverse fields such as reinforcing nanofillers and Pickering emulsions. In order to show the operation involved in the proposed process more intuitively, **Figure 7** is proposed to facilitate understanding. As shown in the proposed flowchart, the solid residue produced in the previous part is used to produce the desired substance in the next step. Specifically, xylose (originated from hemicellulose) was obtained by acid treatment, alkali lignin was obtained by alkali treatment, monosaccharide (derived from cellulose) was

obtained by enzymatic hydrolysis, and LCNFs with different lignin contents or LNPs could be obtained by homogenization. Thus, the comprehensive utilization of the whole components of corncob can be realized.

CONCLUSION

In summary, high LCNFs and LNPs were successfully prepared from EHRs of corncob residues via high-pressure homogenization. During enzymatic hydrolysis process, with

the increase of enzymolysis time, the lignin content increased and the cellulose content decreased resulting in the EHRs with controllable chemical compositions. It was found that the lignin content had a great influence on the morphology of the obtained nanoparticles after homogenization. The higher the lignin content in the EHRs, the smaller the size and the higher the absolute zeta potential of the obtained nanoparticles observed. This work not only promotes the development of lignocellulose-based nanomaterials but also provides a promising full utilization for the agricultural residue that simultaneously achieves the maximum use of the whole biomass.

DATA AVAILABILITY STATEMENT

The original contributions presented in the study are included in the article/supplementary material, further inquiries can be directed to the corresponding author/s.

REFERENCES

- An, L., Si, C., Wang, G., Sui, W., and Tao, Z. (2019). Enhancing the solubility and antioxidant activity of high-molecular-weight lignin by moderate depolymerization via in situ ethanol/acid catalysis. *Ind. Crops Prod.* 128, 177–185. doi: 10.1016/j.indcrop.2018.11.009
- Anwar, Z., Gulfranz, M., and Irshad, M. (2019). Agro-industrial lignocellulosic biomass a key to unlock the future bio-energy: a brief review. *J. Radiat. Res. Appl. Sci.* 7, 163–173. doi: 10.1016/j.jrras.2014.02.003
- Bian, H., Chen, L., Dai, H., and Zhu, J. Y. (2017). Integrated production of lignin containing cellulose nanocrystals (LCNC) and nanofibrils (LCNF) using an easily recyclable di-carboxylic acid. *Carbohydr. Polym.* 167, 167–176. doi: 10.1016/j.carbpol.2017.03.050
- Chauhan, P. S. (2020). Lignin nanoparticles: eco-friendly and versatile tool for new era. *Bioresour. Technol. Rep.* 9:100374. doi: 10.1016/j.biteb.2019.100374
- Chen, S. L., Wang, G. H., Sui, W. J., Parvez, A. M., Dai, L., and Si, C. L. (2020). Novel lignin-based phenolic nanosphere supported palladium nanoparticles with highly efficient catalytic performance and good reusability. *Ind. Crops Prod.* 145:112164. doi: 10.1016/j.indcrop.2020.112164
- Chi, X., Liu, C., Bi, Y.-H., Yu, G., Zhang, Y., Wang, Z., et al. (2019). A clean and effective potassium hydroxide pretreatment of corncob residue for the enhancement of enzymatic hydrolysis at high solids loading. *RSC Adv.* 9, 11558–11566. doi: 10.1039/c9ra01555h
- Dai, L., Cao, Q. W., Wang, K., Han, S. J., Si, C. L., Liu, D., et al. (2020a). High efficient recovery of L-lactide with lignin-based filler by thermal degradation. *Ind. Crops Prod.* 143:111954. doi: 10.1016/j.indcrop.2019.111954
- Dai, L., Ma, M. S., Xu, J. K., Si, C. L., Wang, X. H., Liu, Z., et al. (2020b). All-lignin-based hydrogel with fast pH-stimuli-responsiveness for mechanical switching and acuation. *Chem. Mater.* 32, 4324–4330. doi: 10.1021/acs.chemmater.0c01198
- Dong, H., Li, M., Jin, Y., Wu, Y., Huang, C., and Yang, J. (2020a). Preparation of graphene-like porous carbons with enhanced thermal conductivities from lignin nano-particles by combining hydrothermal carbonization and pyrolysis. *Front. Energy Res.* 8:148. doi: 10.3389/fenrg.2020.00148
- Dong, H., Zheng, L., Yu, P., Jiang, Q., Wu, Y., Huang, C., et al. (2020b). Characterization and application of lignin-carbohydrate complexes from lignocellulosic materials as antioxidants for scavenging in vitro and in vivo reactive oxygen species. *ACS Sustain. Chem. Eng.* 8, 256–266. doi: 10.1021/acsschemeng.9b05290
- Du, H., Liu, W., Zhang, M., Si, C., Zhang, X., and Li, B. (2019). Cellulose nanocrystals and cellulose nanofibrils based hydrogels for biomedical applications. *Carbohydr. Polym.* 209, 130–144. doi: 10.1016/j.carbpol.2019.01.020
- Du, H., Parit, M., Wu, M., Che, X., Wang, Y., Zhang, M., et al. (2020). Sustainable valorization of paper mill sludge into cellulose nanofibrils and

AUTHOR CONTRIBUTIONS

RX, HD, HW, MZ, MW, CL, GY, and S-EC: investigation. CS, S-EC, and BL: supervision. RX and HD: writing—original draft. XZ, BL, S-EC, and CS: writing—review and editing. All authors contributed to the article and approved the submitted version.

FUNDING

This work was supported by the National Natural Science Foundation of China (No. 31870568) and Shandong Provincial Natural Science Foundation for Distinguished Young Scholar of China (No. ZR2019JQ10) to BL, and the Technology development Program (No. S3030198) funded by the Ministry of SMEs (MSS, South Korea) to S-EC. In addition, HD acknowledges the financial support from the China Scholarship Council (No. 201708120052).

- cellulose nanopaper. *J. Hazard. Mater.* 400:123106. doi: 10.1016/j.jhazmat.2020.123106
- Farooq, M., Zou, T., Riviere, G., Sipponen, M. H., and Osterberg, M. (2019). Strong, ductile, and waterproof cellulose nanofibril composite films with colloidal lignin particles. *Biomacromolecules* 20, 693–704. doi: 10.1021/acs.biomac.8b01364
- Ferrer, A., Quintana, E., Filpponen, I., Solala, I., Vidal, T., Rodriguez, A., et al. (2012). Effect of residual lignin and heteropolysaccharides in nanofibrillar cellulose and nanopaper from wood fibers. *Cellulose* 19, 2179–2193. doi: 10.1007/s10570-012-9788-z
- Ghose, T. K. (1987). Measurement of cellulase activities. *Pure Appl. Chem.* 59, 257–268. doi: 10.1351/pac198759020257
- Herrera, M., Thitiwutthisakul, K., Yang, X., Rujitanaroj, P.-o., Rojas, R., and Berglund, L. (2018). Preparation and evaluation of high-lignin content cellulose nanofibrils from eucalyptus pulp. *Cellulose* 25, 3121–3133. doi: 10.1007/s10570-018-1764-9
- Hong, S., Song, Y., Yuan, Y., Lian, H., and Liimatainen, H. (2020). Production and characterization of lignin containing nanocellulose from luffa through an acidic deep eutectic solvent treatment and systematic fractionation. *Ind. Crops Prod.* 143:111913. doi: 10.1016/j.indcrop.2019.111913
- Hu, L., Du, H., Liu, C., Zhang, Y., Yu, G., Zhang, X., et al. (2018). Comparative evaluation of the efficient conversion of corn husk filament and corn husk powder to valuable materials via a sustainable and clean biorefinery process. *ACS Sustain. Chem. Eng.* 7, 1327–1336. doi: 10.1021/acssuschemeng.8b05017
- Hu, W., Wang, X., Wu, L., Shen, T., Ji, L., Zhao, X., et al. (2016). Apigenin-7-O-beta-D-glucuronide inhibits LPS-induced inflammation through the inactivation of AP-1 and MAPK signaling pathways in RAW 264.7 macrophages and protects mice against endotoxin shock. *Food Funct.* 7, 1002–1013. doi: 10.1039/c5fo01212k
- Huang, C., Dong, H., Zhang, Z., Bian, H., and Yong, Q. (2020a). Procuring the nano-scale lignin in prehydrolyzate as ingredient to prepare cellulose nanofibril composite film with multiple functions. *Cellulose* 27, 9355–9370. doi: 10.1007/s10570-020-03427-9
- Huang, C., Lin, W., Lai, C., Li, X., Jin, Y., and Yong, Q. (2019). Coupling the post-extraction process to remove residual lignin and alter the recalcitrant structures for improving the enzymatic digestibility of acid-pretreated bamboo residues. *Bioresour. Technol.* 285:121355. doi: 10.1016/j.biortech.2019.121355
- Huang, C., Ma, J., Zhang, W., Huang, G., and Yong, Q. (2018). Preparation of lignosulfonates from biorefinery lignins by sulfomethylation and their application as a water reducer for concrete. *Polymers* 10:841. doi: 10.3390/polym10080841
- Huang, C., Zheng, Y., Lin, W., Shi, Y., Huang, G., and Yong, Q. (2020b). Removal of fermentation inhibitors from pre-hydrolysis liquor using polystyrene divinylbenzene resin. *Biotechnol. Biofuels* 13:188. doi: 10.1186/s13068-020-01828-3

- Kaneko, T., Thi, T. H., Shi, D. J., and Akashi, M. (2006). Environmentally degradable, high-performance thermoplastics from phenolic pytomonomers. *Nat. Mater.* 5, 966–970. doi: 10.1038/nmat1778
- Khan, A., Wen, Y., Huq, T., and Ni, Y. (2018). Cellulosic nanomaterials in food and nutraceutical applications: a review. *J. Agric. Food Chem.* 66, 8–19. doi: 10.1021/acs.jafc.7b04204
- Lahtinen, P., Liukkonen, S., Pere, J., Sneck, A., and Kangas, H. (2014). A comparative study of fibrillated fibers from different mechanical and chemical pulps. *BioResources* 9, 2115–2127. doi: 10.15376/biores.9.2.2115-2127
- Li, F. F., Xu, Z. W., Zhang, X. Y., Qin, W., Luo, B., and Xia, Y. (2020). Enhancement of properties of wood plastic composites by modifying lignin. *J. For. Eng.* 5, 45–51. doi: 10.13360/j.issn.2096-1359.201910010
- Li, X., Xu, R., Yang, J., Nie, S., Liu, D., Liu, Y., et al. (2019). Production of 5-hydroxymethylfurfural and levulinic acid from lignocellulosic biomass and catalytic upgradation. *Ind. Crops Prod.* 130, 184–197. doi: 10.1016/j.indcrop.2018.12.082
- Lin, C. Y., and Lu, C. (2021). Development perspectives of promising lignocellulose feedstocks for production of advanced generation biofuels: a review. *J. Renew. Sustain. Energy* 136:110445. doi: 10.1016/j.rser.2020.110445
- Lin, W., Chen, D., Yong, Q., Huang, C., and Huang, S. (2019). Improving enzymatic hydrolysis of acid-pretreated bamboo residues using amphiphilic surfactant derived from dehydroabiatic acid. *Bioresour. Technol.* 293:122055. doi: 10.1016/j.biortech.2019.122055
- Lin, W., Xing, S., Jin, Y., Lu, X., Huang, C., and Yong, Q. (2020). Insight into understanding the performance of deep eutectic solvent pretreatment on improving enzymatic digestibility of bamboo residues. *Bioresour. Technol.* 306:123163. doi: 10.1016/j.biortech.2020.123163
- Liu, C., Li, B., Du, H., Lv, D., Zhang, Y., Yu, G., et al. (2016). Properties of nanocellulose isolated from corn cob residue using sulfuric acid, formic acid, oxidative and mechanical methods. *Carbohydr. Polym.* 151, 716–724. doi: 10.1016/j.carbpol.2016.06.025
- Liu, H. Y., Xu, T., Liu, K., Zhang, M., Liu, W., Li, H., et al. (2021). Lignin-based electrodes for energy storage application. *Ind. Crops Prod.* 165:113425. doi: 10.1016/j.indcrop.2021.113425
- Liu, K., Du, H., Zheng, T., Liu, H., Zhang, M., Zhang, R., et al. (2021). Recent advances in cellulose and its derivatives for oilfield applications. *Carbohydr. Polym.* 259:117740. doi: 10.1016/j.carbpol.2021.117740
- Liu, W., Du, H., Zhang, M., Liu, K., Liu, H., Xie, H., et al. (2020). Bacterial cellulose-based composite scaffolds for biomedical applications: a review. *ACS Sustain. Chem. Eng.* 8, 7536–7562. doi: 10.1021/acsschemeng.0c00125
- Liu, W., Si, C. L., Du, H. S., Zhang, M., and Xie, H. (2019). Advance in preparation of nanocellulose based hydrogels and their biomedical applications. *J. For. Eng.* 4, 11–19. doi: 10.13360/j.issn.2096-1359.2019.05002
- Miao, C., Du, H., Parit, M., Jiang, Z., Tippur, H. V., Zhang, X., et al. (2020). Superior crack initiation and growth characteristics of cellulose nanopapers. *Cellulose* 27, 3181–3195. doi: 10.1007/s10570-020-03015-x
- Nair, S. S., Kuo, P.-Y., Chen, H., and Yan, N. (2017). Investigating the effect of lignin on the mechanical, thermal, and barrier properties of cellulose nanofibril reinforced epoxy composite. *Ind. Crops Prod.* 100, 208–217. doi: 10.1016/j.indcrop.2017.02.032
- Pei, W., Chen, Z. S., Chan, H. Y. E., Zheng, L., Liang, C., and Huang, C. (2020). Isolation and identification of a novel anti-protein aggregation activity of lignin-carbohydrate complex from chionanthus retusus leaves. *Front. Bioeng. Biotechnol.* 8:573991. doi: 10.3389/fbioe.2020.573991
- Peng, Y., Nair, S. S., Chen, H., Yan, N., and Cao, J. (2018). Effects of lignin content on mechanical and thermal properties of polypropylene composites reinforced with micro particles of spray dried cellulose nanofibrils. *ACS Sustain. Chem. Eng.* 6, 11078–11086. doi: 10.1021/acsschemeng.8b02544
- Rana, R., Langenfeld-Heyser, R., Finkeldey, R., and Polle, A. (2009). FTIR spectroscopy, chemical and histochemical characterisation of wood and lignin of five tropical timber wood species of the family of Dipterocarpaceae. *Wood Sci. Technol.* 44, 225–242. doi: 10.1007/s00226-009-0281-2
- Robertson, G. P., Hamilton, S. K., Barham, B. L., Dale, B. E., Izaurralde, R. C., Jackson, R. D., et al. (2017). Cellulosic biofuel contributions to a sustainable energy future: choices and outcomes. *Science* 356:eaal2324. doi: 10.1126/science.aal2324
- Rojo, E., Peresin, M. S., Sampson, W. W., Hoeger, I. C., Vartiainen, J., Laine, J., et al. (2015). Comprehensive elucidation of the effect of residual lignin on the physical, barrier, mechanical and surface properties of nanocellulose films. *Green Chem.* 17, 1853–1866. doi: 10.1039/c4gc02398f
- Salas, C., Nypelö, T., Rodriguez-Abreu, C., Carrillo, C., and Rojas, O. J. (2014). Nanocellulose properties and applications in colloids and interfaces. *Curr. Opin. Colloid Interface Sci.* 19, 383–396. doi: 10.1016/j.cocis.2014.10.003
- Schwanninger, M., Rodrigues, J. C., Pereira, H., and Hinterstoisser, B. (2004). Effects of short-time vibratory ball milling on the shape of FT-IR spectra of wood and cellulose. *Vib. Spectrosc.* 36, 23–40. doi: 10.1016/j.vibspec.2004.02.003
- Segal, L., Conrad, C. M., Creely, J. J., and Martin, A. E. (1959). An empirical method for estimating the degree of crystallinity of native cellulose using the X-ray diffractometer. *Text. Res. J.* 29, 786–794. doi: 10.1177/004051755902901003
- Si, C. L., Jiang, J.-Z., Liu, S.-C., Hu, H.-Y., Ren, X.-D., Yu, G.-J., et al. (2013a). A new lignan glycoside and phenolics from the branch wood of *Populus banksiana* Lambert. *Holzforchung* 67, 357–363. doi: 10.1515/hf-2012-0137
- Si, C. L., Kim, J.-K., Bae, Y.-S., and Li, S.-M. (2009a). Phenolic compounds in the leaves of populus ussuriensis and their antioxidant activities. *Planta Med.* 75, 1165–1167.
- Si, C. L., Shen, T., Jiang, Y. Y., Wu, L., Yu, G. J., Ren, X. D., et al. (2013b). Antioxidant properties and neuroprotective effects of isocampneoside II on hydrogen peroxide-induced oxidative injury in PC12 cells. *Food Chem. Toxicol.* 59, 145–152. doi: 10.1016/j.fct.2013.05.051
- Si, C. L., Wu, L., and Zhu, Z.-Y. (2009b). Phenolic glycosides from *Populus davidiana* bark. *Biochem. Syst. Ecol.* 37, 221–224. doi: 10.1016/j.bse.2009.01.007
- Sirvio, J. A., Visanko, M., and Liimatainen, H. (2016). Acidic deep eutectic solvents as hydrolytic media for cellulose nanocrystal production. *Biomacromolecules* 17, 3025–3032. doi: 10.1021/acs.biomac.6b00910
- Sluiter, A., Hames, B., Ruiz, R., Scarlata, C., Sluiter, J., Templeton, D., et al. (2008). Determination of structural carbohydrates and lignin in biomass. *Lab. Anal. Proc. (LAP)* 1617, 1–16.
- Song, G. Y. (2019). The development of catalytic fractionation and conversions of lignocellulosic biomass under lignin-first strategy. *J. For. Eng.* 4, 1–10. doi: 10.13360/j.issn.2096-1359.2019.05001
- Sun, B., Zhang, M., Hou, Q., Liu, R., Wu, T., Si, C., et al. (2015). Further characterization of cellulose nanocrystal (CNC) preparation from sulfuric acid hydrolysis of cotton fibers. *Cellulose* 23, 439–450. doi: 10.1007/s10570-015-0803-z
- Wang, H., Xie, H., Du, H., Wang, X., Liu, W., Duan, Y., et al. (2020). Highly efficient preparation of functional and thermostable cellulose nanocrystals via H2SO4 intensified acetic acid hydrolysis. *Carbohydr. Polym.* 239:116233. doi: 10.1016/j.carbpol.2020.116233
- Wang, P., Yin, B., Dong, H., Zhang, Y., Zhang, Y., Chen, R., et al. (2020). Coupling biocompatible au nanoclusters and cellulose nanofibrils to prepare the antibacterial nanocomposite films. *Front. Bioeng. Biotechnol.* 8:986. doi: 10.3389/fbioe.2020.00986
- Wang, Q., Du, H., Zhang, F., Zhang, Y., Wu, M., Yu, G., et al. (2018). Flexible cellulose nanopaper with high wet tensile strength, high toughness and tunable ultraviolet blocking ability fabricated from tobacco stalk via a sustainable method. *J. Mater. Chem. A Mater.* 6, 13021–13030. doi: 10.1039/c8ta01986j
- Wen, Y., Yuan, Z., Liu, X., Qu, J., Yang, S., Wang, A., et al. (2019). Preparation and characterization of lignin-containing cellulose nanofibril from poplar high-yield pulp via TEMPO-Mediated Oxidation and Homogenization. *ACS Sustain. Chem. Eng.* 7, 6131–6139. doi: 10.1021/acsschemeng.8b06355
- Xie, H., Du, H., Yang, X., and Si, C. (2018a). Recent strategies in preparation of cellulose nanocrystals and cellulose nanofibrils derived from raw cellulose materials. *Int. J. Polym. Sci.* 2018, 1–25. doi: 10.1155/2018/7923068
- Xie, X., Feng, X., Chi, S., Zhang, Y., Yu, G., Liu, C., et al. (2018b). A sustainable and effective potassium hydroxide pretreatment of wheat straw for the production of fermentable sugars. *Bioresour. Technol. Rep.* 3, 169–176. doi: 10.1016/j.biteb.2018.07.014
- Xu, H., Li, B., and Mu, X. (2016). Review of alkali-based pretreatment to enhance enzymatic saccharification for lignocellulosic biomass conversion. *Ind. Eng. Chem. Res.* 55, 8691–8705. doi: 10.1021/acs.iecr.6b01907
- Xu, J., Liu, B., Wu, L., Hu, J., Hou, H., and Yang, J. (2019). A waste-minimized biorefinery scenario for the hierarchical conversion of agricultural straw into prebiotic xylooligosaccharides, fermentable sugars and lithium-sulfur batteries. *Ind. Crops Prod.* 129, 269–280. doi: 10.1016/j.indcrop.2018.12.002

- Xu, J. Y., Shao, Z. Y., Li, Y., Dai, L., Wang, Z. J., and Si, C. L. (2021). A flow-through reactor for fast fractionation and production of structure-preserved lignin. *Ind. Crops Prod.* 164:113350. doi: 10.1016/j.indcrop.2021.113350
- Xu, R., Si, C., Kong, F., and Li, X. (2020). Synthesis of γ -valerolactone and its application in biomass conversion. *J. For. Eng.* 5, 20–28. doi: 10.13360/j.issn.2096-1359.201904004
- Yang, H., Yan, R., Chen, H., Lee, D. H., and Zheng, C. (2007). Characteristics of hemicellulose, cellulose and lignin pyrolysis. *Fuel* 86, 1781–1788. doi: 10.1016/j.fuel.2006.12.013
- Yang, J., Si, C., Liu, K., Liu, H., Li, X., and Liang, M. (2020). Production of levulinic acid from lignocellulosic biomass and application. *J. For. Eng.* 5, 21–27. doi: 10.13360/j.issn.2096-1359.201905013
- Zhang, Y., Mu, X., Wang, H., Li, B., and Peng, H. (2014). Combined deacetylation and PFI refining pretreatment of corn cob for the improvement of a two-stage enzymatic hydrolysis. *J. Agric. Food Chem.* 62, 4661–4667. doi: 10.1021/jf500189a
- Zheng, L., Yu, P., Zhang, Y., Wang, P., Yan, W., Guo, B., et al. (2021a). Evaluating the bio-application of biomacromolecule of lignin-carbohydrate complexes (LCC) from wheat straw in bone metabolism via ROS scavenging. *Int. J. Biol. Macromol.* 176, 13–25. doi: 10.1016/j.ijbiomac.2021.01.103
- Zheng, Y., Yu, Y., Lin, W., Jin, Y., Yong, Q., and Huang, C. (2021b). Enhancing the enzymatic digestibility of bamboo residues by biphasic phenoxyethanol-acid pretreatment. *Bioresour. Technol.* 325:124691. doi: 10.1016/j.biortech.2021.124691

Conflict of Interest: The authors declare that the research was conducted in the absence of any commercial or financial relationships that could be construed as a potential conflict of interest.

Copyright © 2021 Xu, Du, Wang, Zhang, Wu, Liu, Yu, Zhang, Si, Choi and Li. This is an open-access article distributed under the terms of the Creative Commons Attribution License (CC BY). The use, distribution or reproduction in other forums is permitted, provided the original author(s) and the copyright owner(s) are credited and that the original publication in this journal is cited, in accordance with accepted academic practice. No use, distribution or reproduction is permitted which does not comply with these terms.



A Novel Inulin-Mediated Ethanol Precipitation Method for Separating Endo-Inulinase From Inulinases for Inulooligosaccharides Production From Inulin

Xin Li^{1,2*}, Qiannan Zhang², Wei Wang² and Shang-Tian Yang^{3*}

¹ Jiangsu Co-innovation Center of Efficient Processing and Utilization of Forest Resources, College of Chemical Engineering, Nanjing Forestry University, Nanjing, China, ² Jiangsu Province Key Laboratory of Green Biomass-Based Fuels and Chemicals, Nanjing, China, ³ William G. Lowrie Department of Chemical and Biomolecular Engineering, The Ohio State University, Columbus, OH, United States

OPEN ACCESS

Edited by:

Lei Wang,
Jeju National University, South Korea

Reviewed by:

Jing Yang,
Southwest Forestry University, China
Jinguang Hu,
University of Calgary, Canada

*Correspondence:

Xin Li
xli@njfu.edu.cn
Shang-Tian Yang
yang.15@osu.edu

Specialty section:

This article was submitted to
Industrial Biotechnology,
a section of the journal
Frontiers in Bioengineering and
Biotechnology

Received: 12 March 2021

Accepted: 01 April 2021

Published: 29 April 2021

Citation:

Li X, Zhang Q, Wang W and
Yang S-T (2021) A Novel
Inulin-Mediated Ethanol Precipitation
Method for Separating Endo-Inulinase
From Inulinases
for Inulooligosaccharides Production
From Inulin.
Front. Bioeng. Biotechnol. 9:679720.
doi: 10.3389/fbioe.2021.679720

Inulin is a kind of polysaccharide that can be obtained various biomass. Inulooligosaccharides (IOS), a kind of oligosaccharides that can be obtained from inulin by enzymatic hydrolysis using inulinases, have been regarded as the functional food ingredients. Commercially available inulinases produced by natural *Aspergillus niger* contained both endo- and exo-inulinase activities. For IOS production from inulin, it is desirable to use only endo-inulinase as exo-inulinase would produce mainly the monosaccharide fructose from inulin. In the present study, a simple inulin-mediated ethanol precipitation method was developed to separate endo- and exo-inulinases present in natural inulinases. IOS production from inulin using the enriched endo-inulinase was then optimized in process conditions including pH and temperature, achieving a high yield of ~94%. The resultant IOS products had a degree of polymerization ranging from 2 to 7. The study demonstrated a novel method for obtaining partially purified or enriched endo-inulinase for IOS production from inulin in an efficient process.

Keywords: ethanol gradient precipitation, inulin, inulinase, inulooligosaccharides, biomass

INTRODUCTION

Inulins are polysaccharides derived from biomass, where they function as energy storage within plant biology. The chemical structures of inulin involves a mixture of linear polymers composed of fructose residues which are linked by β -2,1-glycosidic bonds, with a glucose residue through a sucrose-type linkage at the reducing end (Chi et al., 2011). Inulin can be used directly as functional ingredients for food, meaning their inclusion into edible materials imparts a benefit to human health upon consumption, such as function as dietary fiber, relieving constipation, stimulating the growth of *Bifidobacteria* and *Lactobacillus* sp. in the colon, etc (Shoaib et al., 2016; Singh et al., 2016). It is also possible to convert inulin into valuable biologically derived chemicals, such as inulooligosaccharides (IOS), citric acid, butanediol, L-lactic acid, D-lactic acid, and more (Chi et al., 2011; Zheng et al., 2018; Singh et al., 2019).

In the recent years, IOS in particular has gained more attention for their value in functional foods. This increased interest is attributable to IOS' bifidogenic nature and health-benefiting properties. Inulin and oligofructose are "Generally Regarded As Safe (GRAS)", and used as either supplements or macronutrient substitutes (Coussement, 1999). Taking into account IOS' cost, sustainable feedstock and abundance in natural sources, inulin is considered to be a promising substrate for production of IOS (Singh et al., 2016). Inulin can be enzymatically converted to IOS using a controlled hydrolysis process involving endo-inulinase, a conversion that is known to be a single step process (Singh et al., 2016). This means of conversion can be seen as having advantages when considering it from an industrial point of view, primarily due to the reaction conditions and kinetic simplicity of conversion. However, it is most certainly important to highlight the key cost driver in scaling up this conversion process: the preparation of endo-inulinase. natural inulinase is generally composed of endo-inulinase and exo-inulinase activity, as reported in a recent study (Flores et al., 2016). Inulinase-driven hydrolysis of inulin is achieved by the mechanisms of both exo-inulinase (EC 3.2.1.80), which cleaves fructose from the non-reducing end of inulin, and endo-inulinase (EC 3.2.1.7), which breaks the internal linkage of inulin to release intermediate short-chain IOS (Mutanda et al., 2008). Consequently, fructose is the major product with a little IOS in the hydrolyzate after hydrolysis of inulin by natural inulinase.

To obtain high yields of IOS from inulin, an ideal inulinase should lack extracellular exo-inulinase activity to promote more endo-inulinase activity (Singh et al., 2016). Therefore, several approaches have been carried out in recent years to promote endo-inulinase functionality. One reported approach involved chromatographic isolation of endo-inulinase from natural inulinases produced by varying microorganisms (Park et al., 1999; Cho and Yun, 2002; Jin et al., 2005; Naidoo et al., 2015). Unfortunately, the use of column chromatography is an expensive and complex approach which places significant cost burden upon an IOS process (Golunski et al., 2011). A different approach included use of a recombinant endo-inulinase to produce IOS from inulin (He et al., 2014; Xu et al., 2016; Bao et al., 2019; Jiang et al., 2019). Importantly, *Aspergillus niger* and the carbohydrases it produces are recognized as GRAS by the United States Food and Drug Administration (Schuster et al., 2002). However, use of recombinant enzymes is still a subject of practical and ethical debate. This mostly eliminates the aforementioned approach from being economically viable in the short term. Therefore, it remains challenging to obtain endo-inulinase with free exo-inulinase activity without amassing a wealth of additional complications.

In the present study we underwent development of a novel (as well as simple) method to separate endo-inulinase and exo-inulinase activity from natural inulinases derived from *A. niger* (recall that it is GRAS). Our method is based on the differences in how endo-inulinase and exo-inulinase bind linear inulin chains. Endo-inulinase and exo-inulinase bind inulin molecules of different lengths, and also tend to precipitate at different ethanol concentrations. These intrinsic characteristics were manipulated to isolate endo-inulinase exclusively for production

of IOS. Furthermore, the conditions of IOS production by the enriched endo-inulinase were optimized in temperature, inulin concentration, enzyme loading and reaction time. The goal of this work was to demonstrate practical means of using inulinase to produce valuable IOS from sustainably sourced inulin.

MATERIALS AND METHODS

Materials

Natural inulinase from *A. niger* (I6285) was purchased from Sigma-Aldrich (St. Louis, MO, United States). The enzyme solution, once received, was diluted to a final inulinase activity of 12.5 U/mL and stored at 5°C prior to further experimentation. Inulin was purchased from Beneo Orafiti (Tienen, Belgium). Ethanol of analytical purity was purchased from Nanjing Chemical Reagent Co., Ltd. and was used as received without further purification.

Inulin-Mediated Ethanol Gradient Precipitation

Phase I: The initial ethanol solution (40–60%, v/v) was cooled in a water-ice bath for 30 min, and then pH adjusted to 4.6. Next, 20 mL of the chilled and pH-adjusted ethanol solution was mixed with 0.8 g inulin (Beneo Orafiti, Belgium) and the natural inulinase. This mixture was kept at 0°C for 2–4 h. After time, the precipitates (named P40, P45, P50, P55, and P60, respectively) was recovered by centrifugation at 2,000–3,000 g and 0°C for 10 min, which is according to the work of Gu et al. (2020).

Phase II: Following Phase I, the supernatant (ethanol 60%, v/v) was as the initial solution of Phase II. Additional chilled ethanol (at a temperate of –20°C) was dropwise added into the supernatant to reach an ethanol concentration of 65% (v/v). This new mixture was also then kept at 0°C for 2–4 h. A newly precipitated fraction was recovered by centrifugation (same parameters as before) and dubbed P65. This process was repeated in a step-wise fashion to obtain precipitates P70, P75, and P80.

Each recovered precipitate was re-dissolved in sodium acetate buffer (pH 4.6, 100 mM) prior to determine enzyme activity or use in bioconversion. The ethanol gradient precipitation of inulin without the natural inulinase was the same process as above. All experiments were carried out in triplicate.

Determination of Enzyme Activity

Enzyme activity was measured by proxy using the concentration of reducing sugars released from inulin and sucrose. Inulin (Beneo Orafiti, Belgium) was used as the substrate for determination of inulinase activity. Sucrose (Sinopharm, China) was used as substrate for determination of sucrase activity. A reaction mixture containing 50 µL of diluted crude enzyme and 450 µL of 5% (w/v) substrate solution (dissolved in 0.1 M sodium acetate buffer, pH 4.6) was incubated at 60°C for 10 min. A denatured enzyme in inulin or sucrose solution was also used to serve as an experimental control. The amount of reducing sugars liberated from inulin or sucrose was determined using a 3,5-dinitrosalicylic acid (DNS) assay (Xu et al., 2016),

with fructose serving as a standard. Assay response was measured as absorbance at 520 nm. Regarding enzyme activity derived from said assay, one unit of inulinase activity or sucrose activity was defined as the amount of enzyme required that produced 1 μ mol of reducing sugar per minute under the assay conditions used in this study.

Inulooligosaccharides Production by Enzyme Hydrolysis of Inulin

Inulin (Beneo Orafiti, Belgium) was used as the substrate for IOS production. Enzymatic hydrolysis of inulin was carried out under different conditions, including temperature, substrate concentration, enzyme loading, and reaction time. Samples of the hydrolyzates (1 mL) were taken at different intervals and boiled at 100°C for 5 min to denature the enzymes and cease further bioconversion. Following denaturing, all samples were centrifuged at 10,000–12,000 g for 5 min, and the supernatants were analyzed by high-performance anion exchange chromatography quantitatively coupled with pulsed amperometric detection (HPAEC-PAD). The details of this chromatography method are described in the following section.

Analytical Methods

Quantitative analysis of IOS was carried out in accordance with the reported analytical method (Xu et al., 2016), albeit with some modifications. Measurement of resultant IOS concentrations was performed using a HPAEC-PAD with a CarboPac PA200 column (250 mm \times 3 mm, Dionex, Sunnyvale, CA, United States). Water, 200 mM NaOH and 500 mM sodium acetate (NaAc) were used as the mobile phase. A gradient elution strategy was implemented as follows: 60% water, 40% 200 mM NaOH and 0 \rightarrow 12% 500 mM NaAc in 0–5 min; 48% water, 40% 200 mM NaOH and 12% 500 mM NaAc in 5–25 min; 48 \rightarrow 20% water, 40% 200 mM NaOH and 12 \rightarrow 40% 500 mM NaAc in 25–30 min; 20 \rightarrow 0% water, 40 \rightarrow 100% 200 mM NaOH and 40 \rightarrow 0% 500 mM NaAc in 30–33 min; 100% 200 mM NaOH in 33–35 min; 0 \rightarrow 60% water and 100 \rightarrow 40% 200 mM NaOH in 35–50 min. The column temperature was 30°C, and the flow rate was 0.4 mL/min. The method showed that IOS quantitation had a good linear relationship within the 0.1–10 mg/L concentration range. IOS yields were calculated as the ratio of total IOS (g) to the inulin (g). IOS are a group of oligosaccharides, which is formed by β -(2–1) linked fructofuranosyl unit on the end of sucrose molecule, with degree of polymerization (DP) ranging from 2 to 10 (Singh et al., 2016). In the name of simplicity, we arbitrarily defined IOS with chain lengths between 2 and 10 residues. Glucose (G), fructose (F), sucrose (GF), 1-kestose (GF2), 1-nystose (GF3), 1-F-1- β -D-fructofuranosyl nystose (GF4), 1-F-(1- β -D-fructofuranosyl) -2-nystose (GF5) and 1-F-(1- β -D-fructofuranosyl) -3-nystose (GF6) were quantitatively determined by an external standard method, and others were estimated by the ratio of their peak areas to total peak areas of HPAEC.

Gel permeation chromatography (GPC) analysis of inulin was carried out at 35°C with an Agilent 1,260 HPLC equipped with two columns (Ultrasphere-Hydrogel-120 and Ultrasphere-Hydrogel-250). 50 mM potassium dihydrogen phosphate was used as the mobile

phase. Mobile phase flow rate was 0.6 mL/min. The DP value was calculated according to the equation as follows:

$$\text{Average molecular weight (g/mol)} = 162 \times (\text{DP} - 1) + 180$$

Statistical Analysis

Statistical analysis was carried out using Origin 2016 software (OriginLab Corporation, Northampton, MA 01060, United States). The data were assessed using a one-way ANOVA with Tukey's test.

RESULTS AND DISCUSSION

The Inulin-Mediated Ethanol Gradient Precipitation of Natural Inulinase From *Aspergillus niger*

Aspergillus niger is known to produce inulinases with high levels of endo- and exo-inulinase activities (Singh and Gill, 2006). Exo-inulinase removes one fructose from the non-reducing end of inulin, whereas endo-inulinase randomly cleaves the β -2,1-glycosidic bonds in inulin (Qiu et al., 2018). Two different hydrolytic behaviors implied that there are different binding properties existing between inulinases and inulin. To check the idea, ethanol gradient precipitation was applied to explore inulin-binding properties of inulinases. We qualitatively precipitated inulinase by ethanol gradient precipitation both in the presence and absence of inulin at ethanol concentration ranging from 40% (v/v) to 80% (v/v) (**Supplementary Figure S1**). An interesting phenomenon was found that precipitates were obtained at different ethanol concentrations in the presence of inulin while no precipitates were observed when the system had no inulin dissolved within. Comparably, precipitates, showing higher relative inulinase activity (in redissolved form) were also observed at ethanol concentrations of 50% (v/v) and 70% (v/v), respectively. These results demonstrate that inulinases will not precipitate if not in the presence of inulin. This suggests that some sort of association occurs between the enzymes of interest and inulin, which then allows the coordinated enzymes to be precipitated along with the substrate inulin. In addition, results in **Table 1** demonstrate that longer chains of inulin are prone to precipitate at lower ethanol concentrations compared to inulin molecules of shorter length (Xu et al., 2014). Based on all of these findings, we inferred that the two precipitates might be two different inulinases, and one tend to bind the longer chain inulin molecules while the other was likely to bind the shorter chain inulin molecules. Furthermore, ethanol gradient precipitation

TABLE 1 | Estimated molecular weights of inulin precipitates.

	Average molecular weight (g/mol)	Degree of polymerization
Inulin as control	3,260	20
50% (v/v) ethanol	4,730	29
70% (v/v) ethanol	3,730	22

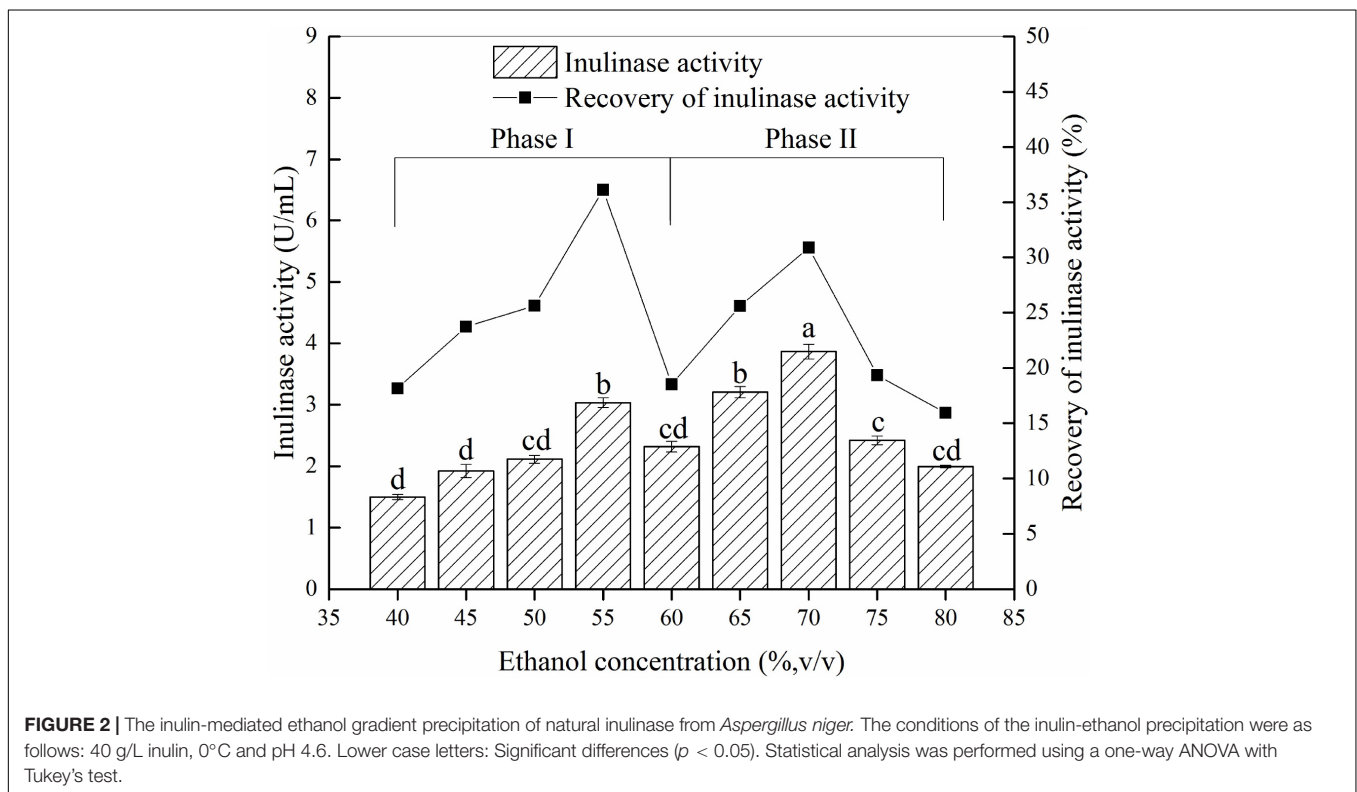
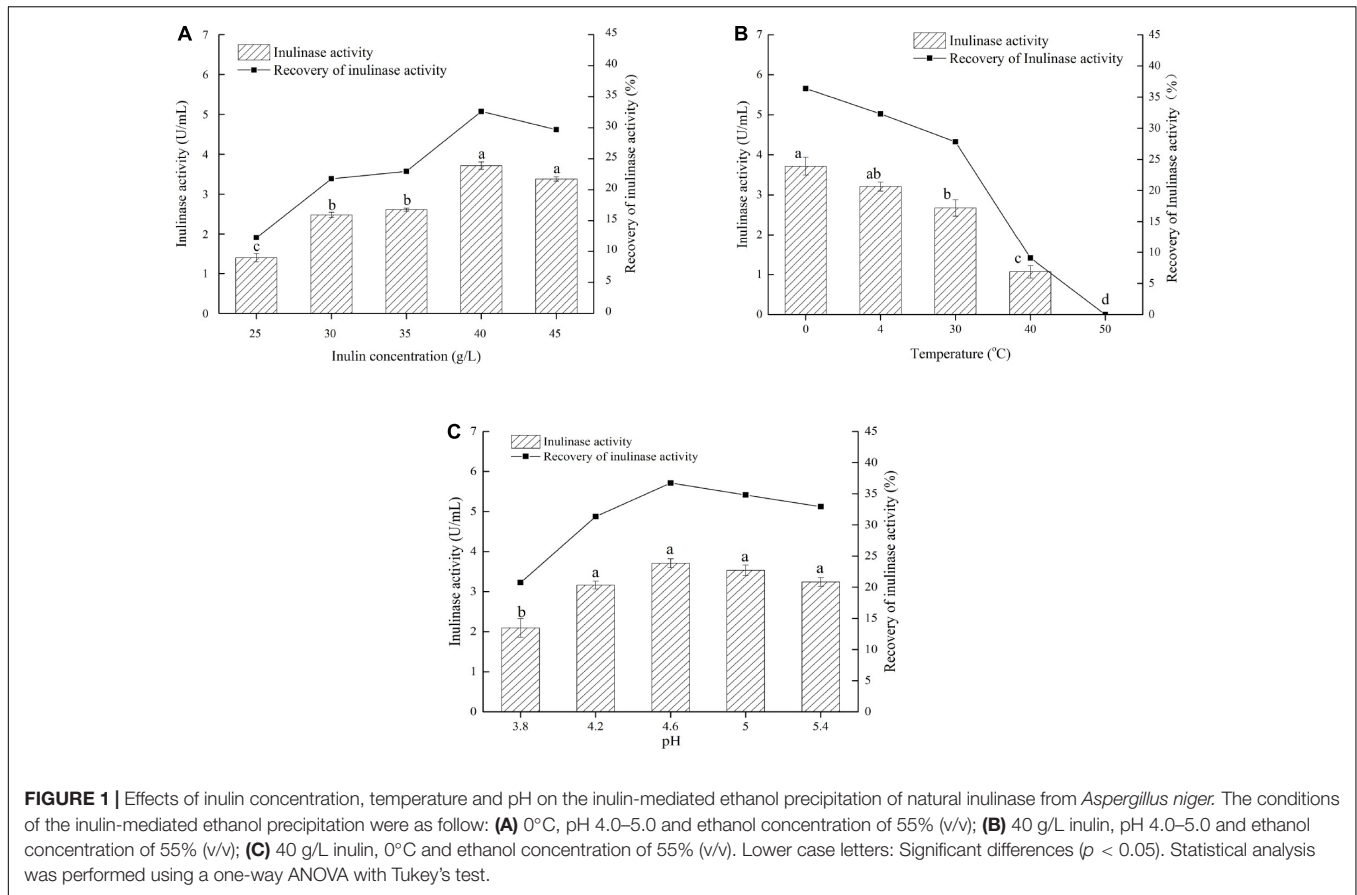


TABLE 2 | The different enzyme activities of precipitates from the inulin-ethanol precipitation of natural inulinase from *Aspergillus niger*.

Precipitate	Inulinase activity (I, U/mL)	Sucrase activity (S, U/mL)	I/S ratio
P55	3.0	1.6	1.9
P70	3.9	0.1	39

might be an effective method to separate endo-inulinase from exo-inulinase present in the natural inulinases.

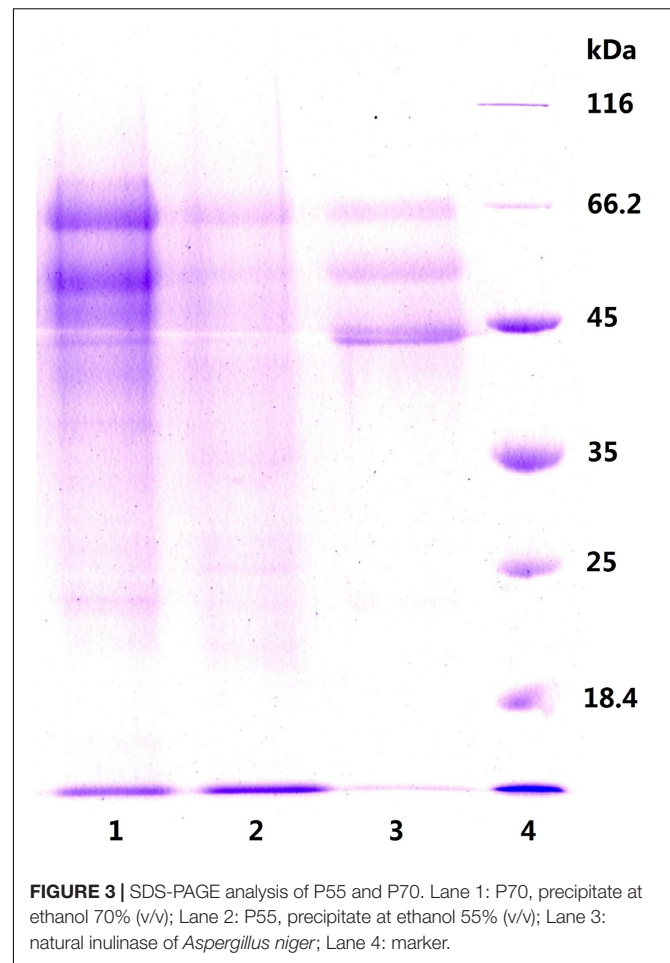
Based on the findings mentioned above, we explored a simple and quick method to separate different inulinases from natural inulinase. In the present work, inulin-mediated ethanol gradient precipitation was carried out to separate different inulinases from natural inulinase. 40 g/L inulin and 0°C were identified as the optimal conditions for inulin-ethanol precipitation (Figures 1A,B). In addition, pH 4.6 was determined to be the optimum pH for the selective isolation (Figure 1C).

Different ethanol concentration demonstrated a significantly effect on precipitation and recovery of inulinase (Figure 2). The results showed that precipitates P55 and P70 [corresponding to the material precipitated at 55% ethanol (Phase I) and 70% ethanol (Phase II), respectively] contained greater inulinase activity (Figure 2), with both recovering about 67% initial inulinase activity. However, because different proteins tend to precipitate at different aqueous ethanol concentrations (van Oss, 1989), we thus inferred that P55 (Phase I) and P70 (Phase II) could be two different inulinases.

To explore this hypothesis, we next carried out another experiment to characterize the precipitates P55 and P70 for both inulinase activity and sucrase activity (Table 2). Generally, a simple identification of endo- and exo-inulinase activity is characterized by the ratio of inulinase (I) activity: sucrase (S) activity (Ettalibi and Baratti, 1987; Kango, 2008). Ettalibi and Baratti (1987) reported that the I/S ratio of endo-inulinase was higher than that of exo-inulinase. Wang et al. (2003) also reported that the I/S ratio of exo-inulinase was lower than 10, while that of endo-inulinase was higher than 10. In our experiment, the drastic difference in I/S ratio between P70 (39) and P55 (1.9) confirmed the different enzymatic composition of P70 and P55, which was expected given that what precipitated at 70% ethanol remained in solution during P55 preparation. Nevertheless, the results suggested that P55 contained mostly exo-inulinase while P70 contained mostly endo-inulinase. According to SDS-PAGE analysis (Figure 3), P70 and P55 consisted of several different protein bands, respectively, indicating that no single protein band could be obtained by the inulin-mediated ethanol gradient precipitation.

Inulin Hydrolysis by Fractionated Inulinases

As discussed earlier, we conjectured that P55 would exhibit strong exo-inulinase activity while P70 should demonstrate high levels of endo-inulinase activity. We tested the hydrolytic behaviors of P55 and P70 by performing enzymatic hydrolysis

**FIGURE 3** | SDS-PAGE analysis of P55 and P70. Lane 1: P70, precipitate at ethanol 70% (v/v); Lane 2: P55, precipitate at ethanol 55% (v/v); Lane 3: natural inulinase of *Aspergillus niger*; Lane 4: marker.

of inulin at the enzyme loading of 10 U/(g inulin) (Figure 4). At 0 h, it can be seen that minute quantities of IOS and fructose were already present in the inulin substrates. As shown in Figure 4A, fructose concentrations significantly increased over time while IOS concentrations gradually decreased. The behavior of P70 was completely different from that of P50, where it can be seen that IOS concentrations continued to increase with hydrolysis times while fructose concentrations remained relatively constant (Figure 4B). In bioconversion using P70, the maximum IOS concentrations and yields were obtained at 15 h (No significant difference between 15 and 24 h), and likely would have further increased given more hydrolysis time (albeit to a likely minor extent). From these observations, it can be seen that inulin was predominantly hydrolyzed into fructose by P55, whereas P70 exclusively acted upon hydrolyzing inulin to IOS. According to their respective inulin hydrolytic mechanisms, endo-inulinases act by producing IOS while exo-inulinases hydrolyze inulin and IOS to form fructose (Chi et al., 2009). Therefore, our results show that the precipitate P55 was dominated by exo-inulinase activity, and the precipitate P70 was dominated by endo-type inulinase activity. These findings further indicate that the inulin-mediated ethanol gradient precipitation method was effective for obtaining

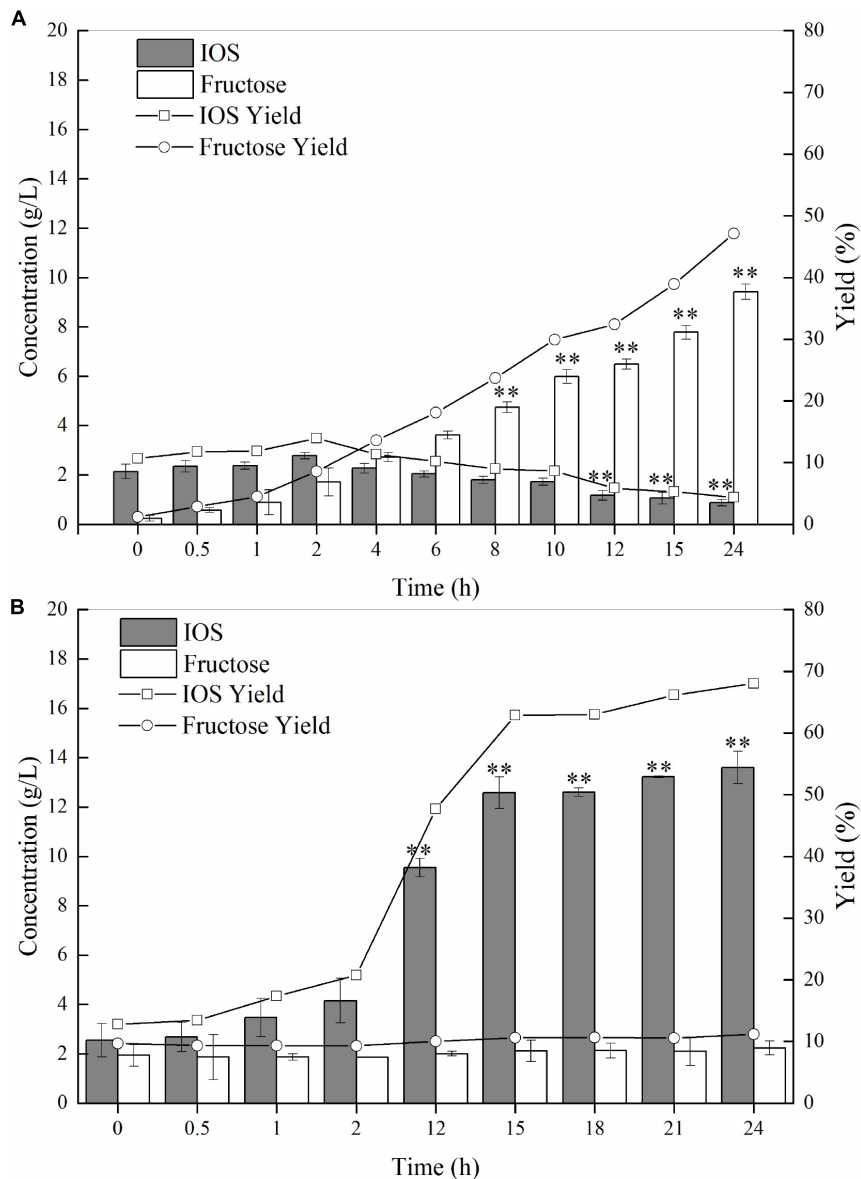


FIGURE 4 | Inulin hydrolysis by P55 (A) and P70 (B). The conditions of 24 h-enzymatic hydrolysis were as follow: 20 g/L inulin, 10 U inulinase activity per gram of inulin, 50°C and pH 4.6. Statistical analysis was performed using a one-way ANOVA with Tukey's test to determine a significant increase or decrease of IOS or fructose compared with those at 2 h ($p < 0.01$). **Indicates a statistical significance.

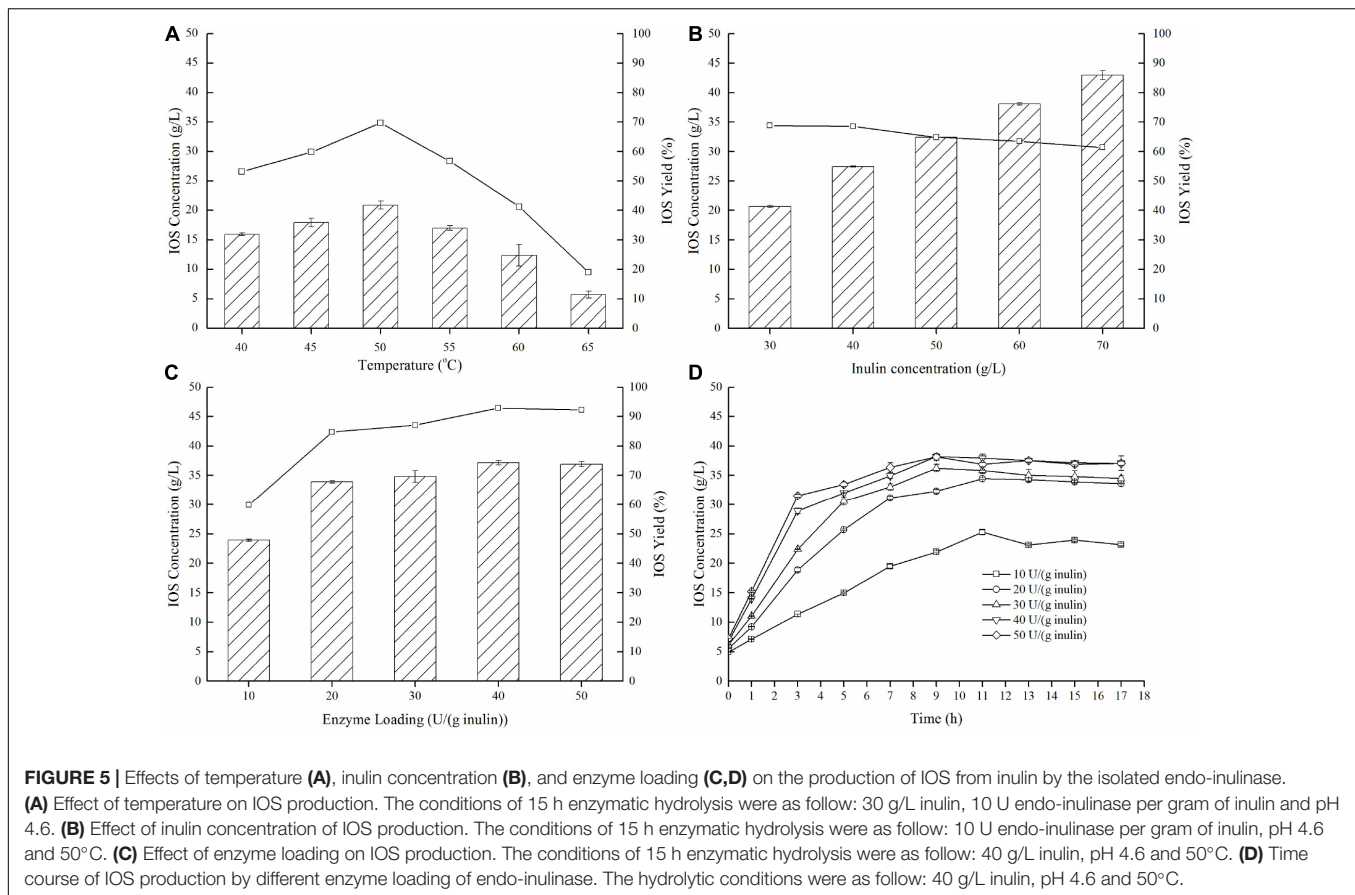
endo-inulinase activity which would be effective in producing IOS at industrial scales.

Optimization of IOS Production by Fractionated Endo-Inulinase

To further demonstrate effective IOS production using the enzyme preparation which was dominant in endo-inulinase activity (P70), enzymatic hydrolysis conditions (temperature, inulin concentration, enzyme loading, and reaction time) were investigated and optimized. As shown in **Figure 5A**, temperatures demonstrate notable influences on both IOS concentrations and

yields, and the optimum temperature for inulin hydrolysis was 50°C. At this temperature, a maximum IOS yield of 69.7% and maximum IOS concentration of 20.9 g/L was achieved. Next, the effect of the inulin concentration was investigated in the range of 30–70 g/L. **Figure 5B** shows that an IOS yield of 68% was obtained at 40 g/L inulin. When the inulin concentration was higher than 40 g/L, the IOS yield decreased gradually. However, the IOS yields were in the range of 60% to 70%. This result suggests that the inulin concentration has a little effect on IOS yield.

Concerning optimal enzyme loading (**Figure 5C**), IOS yields were unsurprisingly larger (80%) when the enzyme loading



was greater than 20 U/(g inulin). It can also be seen that the yield benefits to increasing enzyme loading beyond 20 U/(g inulin) were marginal at best, eliminating any expensive need to dose high levels of enzyme in a real process. Finally, the time course of inulin hydrolysis at different enzyme loadings is shown in **Figure 5D**. For the enzyme loading of 10 U/(g inulin), the maximum IOS concentration (25.3 g/L) was observed at 11 h with an IOS yield of 63.2%. Comparably, the maximum IOS concentrations (over 32 g/L) were observed at 9 h for all of the enzyme loadings between 20 U/(g inulin) and 50 U/(g inulin). This finding indicates that increasing endo-inulinase loading notably enhanced IOS concentrations and shortened required hydrolysis time at constant initial inulin concentrations. It should be pointed out that a higher IOS concentration (38.2 g/L) was observed at 9 h, representing the IOS yield of 95.4% at 40 U/(g inulin). Interestingly, further increasing hydrolytic time resulted in a slight decrease in IOS concentration. This result suggested that the endo-inulinase fraction did bear a slight level of exo-inulinase activity that could not be eliminated despite the fractionation protocol utilized. To minimize this occurrence, the optimal hydrolytic time was identified as 9 h.

Distribution of Hydrolytic Products

To determine distribution of hydrolytic products produced by our endo-inulinase, a separate hydrolysis experiment using fresh

enzyme and inulin was carried out with 40 g/L inulin, enzyme loading of 40 U/(g inulin), at pH 4.6, and 50°C for a total of 9 h. For comparison, a similar experiment was also performed using the natural inulinase. The distributions of reaction products in each hydrolyzate are shown in **Figure 6**. Beginning with **Figure 6A**, the major products produced using the endo-inulinase were oligosaccharides ranging from DP 2 to DP 7, which represented more than 94% of the hydrolyzate. Within this DP range, 85% of hydrolyzate components were between DP 4 and DP 7. The overall distribution of hydrolysis products was as follows: GF3 4.7%, inulotriose (F3) 26.4, GF4 9%, inulotetraose (F4) 19.3, GF5 7, inulopentaose (F5) 13.1, and GF6 5.5%. In contrast, fructose and glucose were the main products from inulin hydrolysis using natural inulinase (**Figure 6B**). Both of them contributed over 87% of hydrolyzate components, and little oligosaccharides were found in the hydrolyzate. This result means natural inulinase hydrolyzed inulin into monosaccharides within a 9-h enzymatic hydrolysis.

It has been reported that endo-inulinases purified from different microorganisms can produce IOS from inulin at yields ranging from 70 to 92% (Singh et al., 2016). In these cases, an endo-inulinase of *Aspergillus ficuum* was purified by column chromatography, and then used to hydrolyze inulin (Jin et al., 2005). In said study, the IOS products mainly consisted of DP 3 and DP 4 oligosaccharides, and the yield of 86%, major products of DP 5 and DP 6, was obtained by the endo-inulinase from

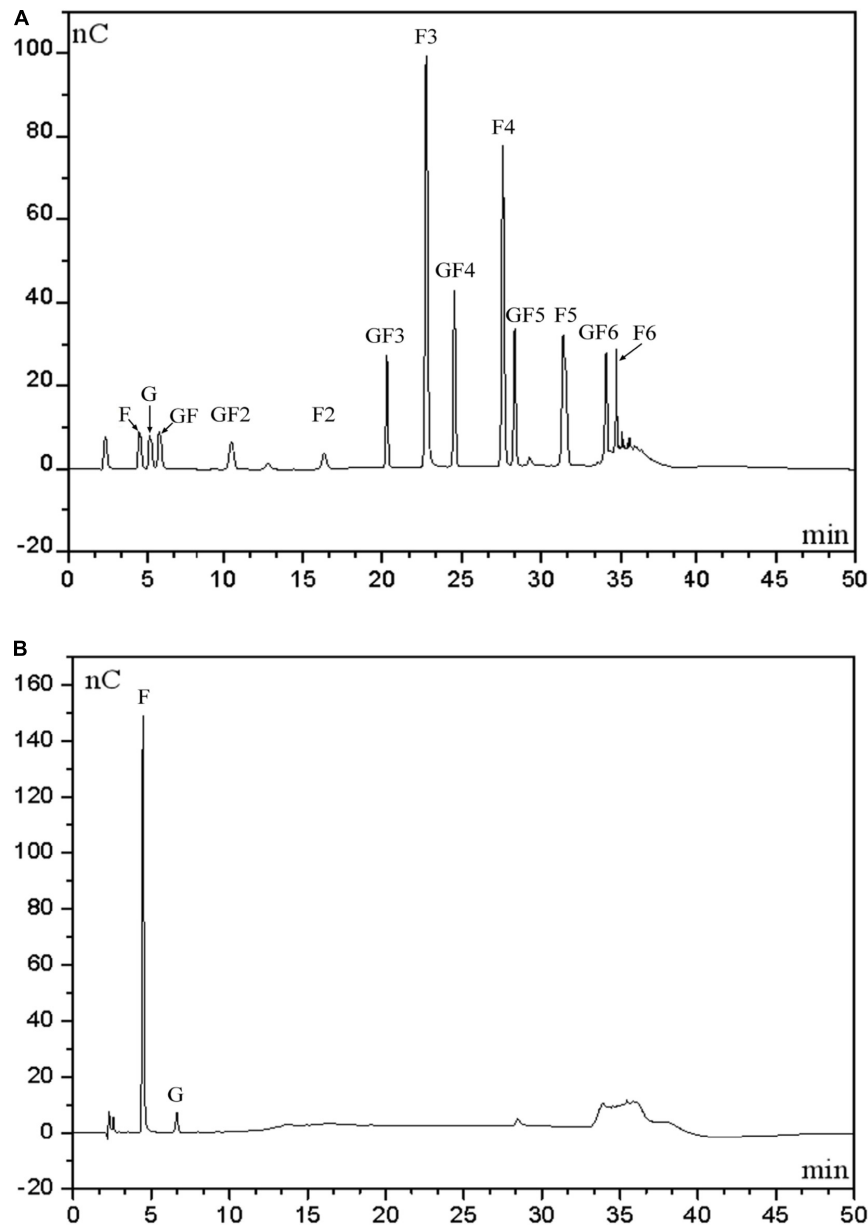


FIGURE 6 | High-performance anion exchange chromatography of inulin hydrolysis products using fractionated endo-inulinase **(A)** and natural inulinase. **(B)** The hydrolysis conditions were: 40 g/L inulin, pH 4.6, enzyme loading 40 U/(g inulin) and 50°C. Abbreviations: glucose, G; sucrose, GF; 1-kestose, GF2; 1-nystose, GF3; 1-F-1- β -D-fructofuranosyl nystose, GF4; 1-F-(1- β -D-fructofuranosyl)-2-nystose, GF5; 1-F-(1- β -D-fructofuranosyl)-3-nystose, GF6; fructose, F; inulobiose, F2; inulotriose, F3; inulotetraose, F4; inulopentaose, F5; inulohexaose, F6.

Xanthomonas sp., which was purified by a DEAE-Sepharose CL 6B chromatography (Park et al., 1999); A dual endo-inulinase system from *Xanthomonas* sp. and *Pseudomonas* sp. was developed for IOS production with a enzyme dosage of 460 U/(g substrate). The IOS yield and DP value of major hydrolytic products after 110-h hydrolysis were 92% and equal or greater than 5, respectively (Cho et al., 2001). Some other attempts were carried out to yield IOS from inulin by recombinant endo-inulinase. Xu et al. (2016) reported DP values ranged from DP 3 to DP 6 produced by the recombinant endo-inulinase from

A. niger DSM 2466 with a IOS yield of 91.3%. He et al. (2014) reported that the recombinant endo-inulinase from *A. niger* CICIM F0620 was applied for IOS production with a IOS yield of 91% and hydrolytic products ranged from DP 2 to DP 5 (He et al., 2014).

A higher IOS yield (~94%) and a reasonable distribution of hydrolyzate ranging from DP 2 to DP 7 were observed in this study. These results proved that separation of endo-inulinase and exo-inulinase activities by the inulin-mediated ethanol gradient precipitation could be an effective alternative method to those

column chromatographic techniques, and achieve a higher IOS yield compared to those by recombinant endo-inulinase.

CONCLUSION

Inulinases produced by natural *A. niger* contained both endo- and exo-inulinase activities. For IOS production from inulin, it is desirable to use only endo-inulinase as exo-inulinase would produce mainly the monosaccharides fructose and glucose from inulin. In the present study, we developed a simple fractionation method using ethanol precipitation to separate endo- and exo-inulinases present in inulinases. The enriched endo-inulinase produced an IOS product containing DP 2 to DP 7 at a high yield of ~94%.

DATA AVAILABILITY STATEMENT

The original contributions presented in the study are included in the article/**Supplementary Material**, further inquiries can be directed to the corresponding author/s.

REFERENCES

- Bao, M., Niu, C., Xu, X., Zheng, F., Liu, C., Wang, J., et al. (2019). Identification, soluble expression, and characterization of a novel endo-inulinase from *Lipomyces starkeyi* NRRL Y-11557. *Int. J. Biol. Macromol.* 137, 537–544. doi: 10.1016/j.ijbiomac.2019.06.096
- Chi, Z., Chi, Z., Zhang, T., Liu, G., and Yue, L. (2009). Inulinase-expressing microorganisms and applications of inulinases. *Appl. Microbiol. Biotechnol.* 82, 211–220. doi: 10.1007/s00253-008-1827-1
- Chi, Z. M., Zhang, T., Cao, T. S., Liu, X. Y., Cui, W., and Zhao, C. H. (2011). Biotechnological potential of inulin for bioprocesses. *Bioresour. Technol.* 102, 4295–4303. doi: 10.1016/j.biortech.2010.12.086
- Cho, Y. J., Sinha, J., Park, J. P., and Yun, J. W. (2001). Production of inuloooligosaccharides from inulin by a dual endoinulinase system. *Enzyme Microb. Technol.* 29, 428–433. doi: 10.1016/s0141-0229(01)00414-8
- Cho, Y. J., and Yun, J. W. (2002). Purification and characterization of an endoinulinase from *Xanthomonas oryzae* No.5. *Process Biochem.* 37, 1325–1331. doi: 10.1016/s0032-9592(02)00018-3
- Coussement, P. A. A. (1999). Inulin and oligofructose: safe intakes and legal status. *J. Nut.* 129, 1412S–1417S.
- Ettalibi, M., and Baratti, J. C. (1987). Purification, properties and comparison of invertase, exoinulinases and endoinulinases of *Aspergillus ficuum*. *Appl. Microbiol. Biotechnol.* 26, 13–20. doi: 10.1007/bf00282143
- Flores, A. C., Morlett, J. A., and Rodríguez, R. (2016). Inulin potential for enzymatic obtaining of prebiotic oligosaccharides. *Crit. Rev. Food Sci. Nutr.* 56, 1893–1902. doi: 10.1080/10408398.2013.807220
- Golunski, S., Astolfi, V., Carniel, N., de Oliveira, D., Luccio, M. D., Mazutti, M. A., et al. (2011). Ethanol precipitation and ultrafiltration of inulinases from *Kluyveromyces marxianus*. *Sep. Purif. Technol.* 78, 261–265. doi: 10.1016/j.seppur.2011.02.019
- Gu, J., Pei, W., Tang, S., Yan, F., Peng, Z., Huang, C., et al. (2020). Procuring biologically active galactomannans from spent coffee ground (SCG) by autohydrolysis and enzymatic hydrolysis. *Int. J. Biol. Macromol.* 149, 572–580. doi: 10.1016/j.ijbiomac.2020.01.281
- He, M., Wu, D., Wu, J., and Chen, J. (2014). Enhanced expression of endoinulinase from *Aspergillus niger* by codon optimization in *Pichia pastoris* and its application in inuloooligosaccharide production. *J. Ind. Microbiol. Biotechnol.* 41, 105–114. doi: 10.1007/s10295-013-1341-z

AUTHOR CONTRIBUTIONS

WW and QZ: investigation and formal analysis. XL: supervision. XL and WW: writing – original draft. S-TY and XL: writing – review and editing. All authors contributed to the article and approved the submitted version.

FUNDING

This work was supported by the Key Research and Development Program of Jiangsu Province (BF2015007) and the National Natural Science Foundation of China (31000278).

SUPPLEMENTARY MATERIAL

The Supplementary Material for this article can be found online at: <https://www.frontiersin.org/articles/10.3389/fbioe.2021.679720/full#supplementary-material>

- Jiang, X., Zhu, Y., Zhang, W., Guang, C., Zhang, T., and Mu, W. (2019). Efficient production of inuloooligosaccharides from inulin by endoinulinase from *Aspergillus arachidicola*. *Carbohydr. Polym.* 208, 70–76. doi: 10.1016/j.carbpol.2018.12.053
- Jin, Z., Wang, J., Jiang, B., and Xu, X. (2005). Production of inuloooligosaccharides by endoinulinases from *Aspergillus ficuum*. *Food Res. Int.* 38, 301–308. doi: 10.1016/j.foodres.2004.04.011
- Kango, N. (2008). Production of inulinase using tap roots of dandelion (*Taraxacum officinale*) by *Aspergillus niger*. *J. Food Eng.* 85, 473–478. doi: 10.1016/j.jfoodeng.2007.08.006
- Mutanda, T., Wilhelmi, B. S., and Whiteley, C. G. (2008). Response surface methodology: synthesis of inuloooligosaccharides with an endoinulinase from *Aspergillus niger*. *Enzyme Microb. Technol.* 43, 362–368. doi: 10.1016/j.enzmictec.2008.06.005
- Naidoo, K., Kumar, A., Sharma, V., Permaul, K., and Singh, S. (2015). Purification and characterization of an endoinulinase from *Xanthomonas campestris* pv. *phaseoli* KM 24 mutant. *Food Technol. Biotechnol.* 53, 146–153.
- Park, J. P., Bae, J. T., You, D. J., Kim, B. W., and Yun, J. W. (1999). Production of inuloooligosaccharides from inulin by a novel endoinulinase from *Xanthomonas* sp. *Biotechnol. Lett.* 21, 1043–1046.
- Qiu, Y., Lei, P., Zhang, Y., Sha, Y., Zhan, Y., Xu, Z., et al. (2018). Recent advances in bio-based multi-products of agricultural Jerusalem artichoke resources. *Biotechnol. Biofuels* 11:151. doi: 10.1186/s13068-018-1152-6
- Schuster, E., Dunn-Coleman, N., Frisvad, J. C., and van Dijck, P. (2002). On the safety of *Aspergillus niger* - a review. *Appl. Microbiol. Biotechnol.* 59, 426–435.
- Shoaib, M., Shehzad, A., Omar, M., Rakha, A., Raza, H., Sharif, H. R., et al. (2016). Inulin: properties, health benefits and food applications. *Carbohydr. Polym.* 147, 444–454. doi: 10.1016/j.carbpol.2016.04.020
- Singh, P., and Gill, P. K. (2006). Production of inulinases: recent advances. *Food Technol. Biotechnol.* 44, 151–162.
- Singh, R. S., Singh, R. P., and Kennedy, J. F. (2016). Recent insights in enzymatic synthesis of fructooligosaccharides from inulin. *Int. J. Biol. Macromol.* 85, 565–572. doi: 10.1016/j.ijbiomac.2016.01.026
- Singh, R. S., Singh, T., and Larroche, C. (2019). Biotechnological applications of inulin-rich feedstocks. *Bioresour. Technol.* 273, 641–653. doi: 10.1016/j.biortech.2018.11.031
- van Oss, C. J. (1989). On the mechanism of the cold ethanol precipitation method of plasma protein fractionation. *J. Protein Chem.* 8, 661–668. doi: 10.1007/bf01025606

- Wang, J., Jin, Z., Jiang, B., and Augustine, A. (2003). Production and separation of exo- and endoinulinase from *Aspergillus ficuum*. *Process Biochem.* 39, 5–11. doi: 10.1016/s0032-9592(02)00264-9
- Xu, J., Yue, R. Q., Liu, J., Ho, H. M., Yi, T., Chen, H. B., et al. (2014). Structural diversity requires individual optimization of ethanol concentration in polysaccharide precipitation. *Int. J. Biol. Macromol.* 67, 205–209. doi: 10.1016/j.ijbiomac.2014.03.036
- Xu, Y., Zheng, Z., Xu, Q., Yong, Q., and Ouyang, J. (2016). Efficient conversion of inulin to inulooligosaccharides through endoinulinase from *Aspergillus niger*. *J. Agric. Food Chem.* 64, 2612–2618. doi: 10.1021/acs.jafc.5b05908
- Zheng, Z., Xu, Q., Liu, P., Zhou, F., and Ouyang, J. (2018). Enhanced inulin saccharification by self-produced inulinase from a newly isolated *Penicillium* sp. and its application in D-lactic acid production. *Appl. Biochem. Biotechnol.* 186, 122–131. doi: 10.1007/s12010-018-2730-6
- Conflict of Interest:** The authors declare that the research was conducted in the absence of any commercial or financial relationships that could be construed as a potential conflict of interest.
- Copyright © 2021 Li, Zhang, Wang and Yang. This is an open-access article distributed under the terms of the Creative Commons Attribution License (CC BY). The use, distribution or reproduction in other forums is permitted, provided the original author(s) and the copyright owner(s) are credited and that the original publication in this journal is cited, in accordance with accepted academic practice. No use, distribution or reproduction is permitted which does not comply with these terms.



A Novel Biosorbent From Hardwood Cellulose Nanofibrils Grafted With Poly(*m*-Aminobenzene Sulfonate) for Adsorption of Cr(VI)

Yong Ho Yu^{1†}, Liangliang An^{1†}, Jin Ho Bae¹, Ji Won Heo¹, Jiansong Chen¹, Hanseob Jeong² and Yong Sik Kim^{1*}

¹ Department of Paper Science and Engineering, College of Forest and Environmental Sciences, Kangwon National University, Chuncheon, South Korea, ² Wood Chemistry Division, National Institute of Forest Science, Seoul, South Korea

OPEN ACCESS

Edited by:

Caoxing Huang,
Nanjing Forestry University, China

Reviewed by:

Bo Pang,
Max Planck Institute of Colloids
and Interfaces, Germany
Xueping Song,
Guangxi University, China

*Correspondence:

Yong Sik Kim
yongsikk@kangwon.ac.kr

[†]These authors have contributed
equally to this work and share first
authorship

Specialty section:

This article was submitted to
Industrial Biotechnology,
a section of the journal
Frontiers in Bioengineering and
Biotechnology

Received: 17 March 2021

Accepted: 06 April 2021

Published: 17 May 2021

Citation:

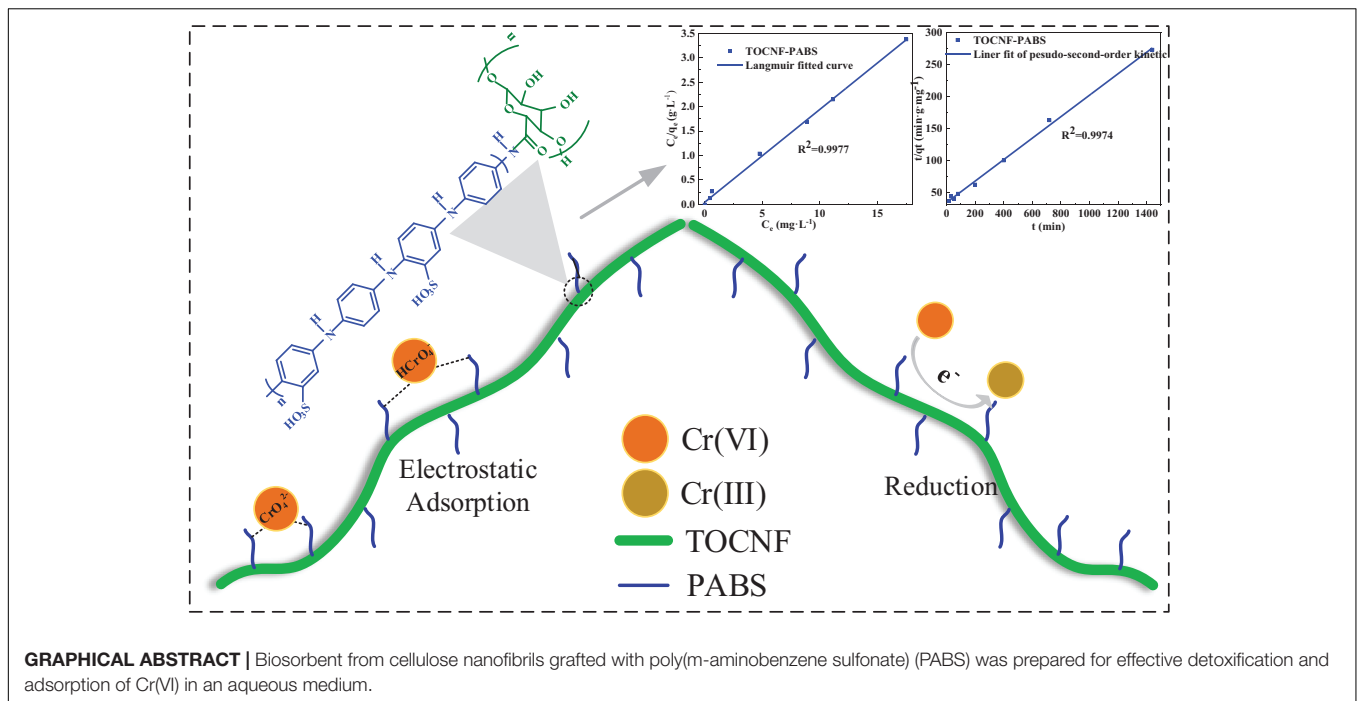
Yu YH, An L, Bae JH, Heo JW,
Chen J, Jeong H and Kim YS (2021)
A Novel Biosorbent From Hardwood
Cellulose Nanofibrils Grafted With
Poly(*m*-Aminobenzene Sulfonate)
for Adsorption of Cr(VI).
Front. Bioeng. Biotechnol. 9:682070.
doi: 10.3389/fbioe.2021.682070

Cellulose from different lignocellulosic biomass can be used to prepare various materials. In this work, the cellulose nanofibrils were produced from hardwood bleached kraft pulp. Then, a novel biosorbent from cellulose nanofibrils grafted with poly(*m*-aminobenzene sulfonate) (PABS) was prepared for effective detoxification and adsorption of Cr(VI) in an aqueous medium. 6,6-tetramethylpiperidine-1-oxyl (TEMPO)-oxidized cellulose nanofibrils (TOCNF) with a high aspect ratio was used as an adsorbent matrix. PABS, an amine-rich conductive polymer, was grafted onto TOCNF via a successive two-step reaction. The analyses of Fourier transform infrared (FT-IR) spectroscopy and X-ray photoelectron spectroscopy (XPS) confirmed the successful grafting reaction between TOCNF and PABS. The biosorbent from TOCNF-bonded PABS with the nitrogen content of 7.0% was synthesized. It exhibited excellent Cr(VI) adsorption capacity at a solution pH below 3, and almost 100% Cr(VI) can be removed. The adsorption of Cr(VI) on the biosorbent was described by a pseudo-second-order model and obeyed the Langmuir model. The Cr(VI) adsorption capacity of the biosorbent from TOCNF-bonded PABS was almost 10 times higher than that of TOCNF. It was interesting to note that part of Cr(VI) ions had been reduced to Cr(III) during the adsorption process. It indicated that the biosorbent from TOCNF grafted with PABS could detoxify and adsorb Cr(VI) synchronously.

Keywords: cellulose nanofibrils, hardwood, detoxification, adsorption, Cr(VI), conductive polymer

INTRODUCTION

Chromium is a common pollutant for surface and groundwater resources, usually produced from industrial processes, such as tanning, textile, electroplating, steel production, and wood preservation (Mishra and Bharagava, 2016). Chromium generally exists with the trivalent Cr(III) and hexavalent Cr(VI) states. Compared to Cr(III), which is less toxic and can be readily removed in the form of insoluble precipitates, Cr(VI) is the most toxic form, being carcinogenic and mutagenic to living organisms (Chen et al., 2015, 2020). Therefore, Cr(VI) must be substantially removed from wastewater before discharge into the aquatic system. Numerous techniques have been developed to remove Cr(VI) from wastewater, including reduction, precipitation, ion exchange, membrane



separation, and adsorption (Jobby et al., 2018). Among these, adsorption is promising and has been widely used due to its easy operation and high efficiency. For example, activated carbon prepared from various matrices has been used as an adsorbent to remove Cr(VI) from an aqueous solution (Wong et al., 2018; Wang P. et al., 2020).

In recent years, biomass-based adsorbents have attracted significant attention as a way to remove Cr(VI) from aqueous solution due to their environmental friendliness, renewability, and biodegradability, such as cellulose (Liang et al., 2020), lignin (Shi et al., 2020), starch (Mohamed and Mahmoud, 2020), and chitosan (Khalil et al., 2020). Cellulose is the most abundant natural polymer on earth and has excellent mechanical and chemical stability properties (An et al., 2019; Liu et al., 2020a; Liu H. et al., 2021; Liu K. et al., 2021). Additionally, cellulose with different sizes and microconformation can be used to produce microcrystalline cellulose, cellulose nanofibrils, and cellulose nanocrystals (Lu et al., 2019; Huang et al., 2020; Liu et al., 2020b; Wang H. et al., 2020; Xu et al., 2021). In particular, cellulose nanofibrils with a high aspect ratio, large surface area, and plentifully available surface hydroxyl groups that can be functionalized to tailor specific properties show great potential as precursors to produce effective adsorbent materials (Zhang et al., 2016; Li et al., 2019; Wang Y. et al., 2020).

Many modifications have been performed for cellulose, including blending and grafting of functional components to increase the active sites of the adsorbent and its uptake capacity for Cr(VI) (Olivera et al., 2016; Jamshaid et al., 2017). The amine group is the most widely explored functional group for enhancing Cr(VI) adsorption owing to its high ability to capture Cr(VI) through electrostatic, reduction/chelating, and hydrogen bonding interactions (Song et al., 2015; Zhang

et al., 2020). The amine-/imine-rich conductive polymers with redox flexibility have shown an interesting fact. They can adsorb negatively charged Cr(VI) onto protonated amine/imine groups and convert the highly toxic Cr(VI) to the much less toxic Cr(III) in an aqueous medium (Ding et al., 2018). Research about adsorbents from cellulose cooperating with conductive polymers for removal of Cr(VI) have arisen, including polypyrrole/cellulose composite (Hosseinkhani et al., 2020), polyaniline/cellulose composite (Liu et al., 2013), polyaniline/cellulose nanocomposite (Hosseini and Mousavi, 2021), and polyaniline-coated cellulose (Qiu et al., 2014). For example, Liu et al. (2012) reported an integrated approach for synchronous Cr(VI) detoxification and adsorption with the polyaniline/cellulose fiber composite. Qiu et al. (2014) reported that polyaniline-coated ethyl cellulose greatly removed Cr(VI). Both amine groups of polyaniline and hydroxyl groups of cellulose participated in the Cr(VI) reduction and adsorption. However, these reports only focused on blending or coating cellulose with conductive polymers. There is little research about bio-adsorbents from cellulose covalently bonded conductive polymers to remove Cr(VI).

In this work, a novel biosorbent from cellulose grafted with a conductive polymer was designed. Poly(*m*-aminobenzene sulfonate) (PABS), a sulfonated polyaniline polymer with unique electroactive properties, thermal stability, and water solubility, was synthesized (Bandyopadhyay et al., 2017). 6,6-Tetramethylpiperidine-1-oxyl (TEMPO)-oxidized cellulose nanofibrils (TOCNF) were prepared as an adsorbent matrix. A novel biosorbent from cellulose nanofibrils grafted with conductive polymer (PABS) was fabricated by a successive two-step reaction. PABS-grafted cellulose nanofibrils were characterized by Fourier transform infrared (FT-IR)

spectroscopy, X-ray photoelectron spectroscopy (XPS), and elemental analysis. The adsorption of Cr(VI) on the biosorbent in an aqueous medium was performed. The effects of adsorbent dosage, pH, and settling time on the removal amount were studied. Adsorption isotherms and adsorption kinetics were investigated.

MATERIALS AND METHODS

Materials

Hardwood bleached kraft pulp (HWBKP) was provided by Moorim P&P Co., Ltd. (South Korea). Aniline (99.5%), ammonium persulfate (APS, 98%), *m*-aminobenzene sulfonic acid (ABS, 99.0%), sodium thiosulfate anhydride (95%), potassium dichromate (99.5%), 1,5-diphenylcarbazide (DPC, $\geq 96\%$), and TEMPO radical (99%) were purchased from Sigma-Aldrich. Acetone (99.5%), dimethylformamide (DMF, 99.5%), oxalyl chloride (98%), hydrogen chloride (35%), ethyl alcohol (99.5%), sulfuric acid (70%), sodium bromide (99%), and sodium hydroxide (98%) were purchased from DaeJung Chemicals & Metals Co., Ltd. (South Korea). Sodium hypochlorite solution (12%) was purchased from YAKURI (Japan). Potassium dichromate (99.5%) was purchased from Kanto Chemical (Japan). These reagents were used without further purification.

Preparation of PABS

Poly(*m*-aminobenzene sulfonate) was prepared according to a methodology from a previous work (Pradeep et al., 2014). First, 0.865 g of ABS was dissolved in 30 ml of 1 mol·L⁻¹ HCl solution. Then the mixture solution was stirred at 0°C for 30 min. Then aniline (90.9 μ l) was added into the mixture and stirred for another 30 min. Finally, 15 ml of 1 mol·L⁻¹ APS solution was added into the mixture and stirred at 0°C for 6 h. After the reaction, the mixture was poured into excess acetone. The precipitated solid was filtrated and washed with acetone to remove the unreacted chemicals. The crude PABS was dissolved in 30 mL of deionized water and filtrated to remove insoluble impurities. The soluble PABS was transferred to a dialysis bag [Cellu-Sep H1, molecular weight cutoff (MWCO): 1,000, United States] for 72 h. After that, the soluble part was freeze-dried to obtain the purified PABS product.

Preparation of TOCNF

First, 20 g of HWBKP was disintegrated at 3,000 rpm in a disintegrator (Lorentzen & Wettre 970154, Sweden). This disintegration was operated three times to disintegrate a total of 60 g of HWBKP. Afterward, the fiber suspension (45 g of dried HWBKP) was oxidized using 157.5 ml of NaClO, catalytic TEMPO (0.72 g), and NaBr (0.45 g), according to a methodology developed by Alves et al. (2020). The TEMPO-oxidized cellulose (TOC) was filtered and washed thoroughly with deionized water. Finally, TOCNF were produced by mechanical treatment of 1% TOC using a grinder (MKVA6-2, Masuko Sangyo, Japan) with stone spacing of 150–200 μ m for passing 15 times. The prepared TOCNF were kept in a refrigerator for future use.

The morphology of TOCNF was analyzed using an ultra-high-resolution field emission transmission electron microscope (FE-TEM)/energy-dispersive X-ray spectroscopy (EDS) (JEM-2100F, JEOL Ltd., Japan) to determine the diameter of TOCNF. Besides, the carboxyl content was determined in duplicate by conductometric titration of the aqueous suspension of TOCNF (acidified to pH 3) with 0.01 mol·L⁻¹ NaOH. An intrinsic viscosity measurement was conducted in the TOCNF suspension by dissolving it in cupriethylenediamine according to the ISO standard 5351:2010. The degree of polymerization (DP) was estimated using the Mark-Houwink equation with parameters $K = 0.42$ and $a = 1$ (Mendoza et al., 2019).

The yield of TOCNF was found to be almost 100% (no phase separation was observed after mechanical treatment). The average diameter of TOCNF was analyzed to be 7.81 nm (Supplementary Figure 1). Besides, the carboxyl content was determined to be 3.38 mmol·g⁻¹, and the DP from the intrinsic viscosity was estimated to be 735.

Preparation of TOCNF Grafted With PABS Copolymer (TOCNF-PABS)

The TOCNF-PABS copolymer was prepared via a two-step reaction, as shown in Supplementary Figure 2. First, an aqueous suspension of TOCNF (0.4 g) was subjected to solvent exchange with DMF by centrifugation at 2,000 rpm three times. Then, TOCNF was dispersed in 50 ml of dried DMF and stirred at 0–5°C for 30 min under N₂ atmosphere. Next, 1 ml of oxalyl chloride was slowly added into the mixture. The mixture was stirred at 0–5°C for 2 h and then at room temperature for another 2 h. After the reaction, the temperature was raised to 70°C and stirred overnight to remove unreacted oxalyl chloride. Finally, the suspension was poured into deionized water. The TOCNF acyl chloride (TOCNF-Cl) was recovered by centrifugation, and DMF was used to wash unreacted chemicals. Finally, the obtained TOCNF-Cl was dispersed in 50 ml of dried DMF with 300 mg of PABS and stirred at 100°C for 24 h under N₂ atmosphere. After the reaction, the mixture was poured into excess deionized water. The precipitate was recovered by centrifugation, and water was used to remove unreacted PABS. TOCNF-PABS was freeze-dried and collected.

Characterization of PABS and Cellulose Samples

The chemical structure analyses of the synthesized PABS and cellulose samples were conducted with an FT-IR spectrophotometer (PerkinElmer Frontier, United States) equipped with an attenuated total reflectance accessory. The spectra were recorded in the wavenumber range of 500–4,000 cm⁻¹ at a resolution of 4.0 cm⁻¹ (An et al., 2020b).

¹H nuclear magnetic resonance (¹H NMR) and gel permeation chromatography (GPC) analyses were performed for a more detailed chemical structure analysis of PABS. ¹H NMR was measured using a 600-MHz Fourier transform nuclear magnetic resonance (FT-NMR) (Bruker Avance Neo 600, Germany). PABS (10 mg) was directly dissolved in 0.5 ml D₂O (99.96%, Sigma-Aldrich) to record the ¹H NMR spectrum. The molecular weight

was analyzed by GPC (Shimadzu 20A, Japan) equipped with PLgel columns (PLgel 5 μm mixed-C and mixed-D and PLgel 3 μm mixed-E). PABS was dissolved in DMF containing 0.1% LiBr to determine its molecular weight (Youe et al., 2018).

The contents of different elements (C, H, N, and S) of the synthesized PABS and cellulose samples were determined using an elemental analyzer (Eurovector EA3000, Italy) with a thermal conductivity detector. The surface element analysis of cellulose samples was measured by XPS (Thermo Scientific, United Kingdom) (An et al., 2020a).

Hexavalent Chromium Adsorption Experiments

A Cr(VI) solution with a concentration of 2.5 $\text{mg}\cdot\text{L}^{-1}$ was prepared from potassium dichromate. Next, 30 ml of the Cr(VI) solution was mixed with TOCNF (10–180 mg) and TOCNF-PABS (10–120 mg) at different pH values (ranging 1–11) in a triangular flask and shaken in a shaker (Serker II, VISION Scientific, South Korea) for different times (0–24 h) at 25°C. After adsorption, filtration was performed by using a polytetrafluoroethylene (PTFE) filter paper (0.45 μm), and the filtrate was collected. The DPC method was used for Cr(VI) determination, according to the methodology from a previous work (Seo et al., 2019). To 20 ml of the filtrate were added 0.1 ml of concentrated nitric acid and 1.2 ml of DPC solution. The residual Cr(VI) of the filtrate was analyzed using ultraviolet-visible (UV-Vis) spectroscopy (X-ma 3000, Human Corporation, South Korea) at 540 nm. An inductively coupled plasma optical emission spectrometer (ICP-OES, Agilent, United States) was used to determine the total Cr [Cr(VI) + Cr(III)] concentration of residual solution after adsorption, and the Cr(III) concentration was obtained by the difference method according to Eq. (1). The adsorbed amount (Q) and the adsorption efficiency (E) of Cr(VI) were calculated according to the Eqs. (2, 3).

$$C_{f3}(\text{mg}\cdot\text{L}^{-1}) = C_{f(3+6)} - C_{f6} \quad (1)$$

$$Q(\text{mg}\cdot\text{g}^{-1}) = (C_i - C_{f6}) \times V/M \quad (2)$$

$$E(\%) = [(C_i - C_{f6}) / C_i] \times 100 \quad (3)$$

where C_{f3} is the Cr(III) concentration of the residual solution after adsorption; $C_{f(3+6)}$ is the total Cr [Cr(VI) + Cr(III)] concentration of the residual solution after adsorption; C_{f6} is the final Cr(VI) concentrations of the solution after adsorption; C_i is the initial Cr(VI) concentration of the solution; V is the volume (L) of the Cr(VI) solution; and M is the weight (g) of the adsorbent.

RESULTS AND DISCUSSION

Characterization of PABS

The chemical structure analysis of PABS copolymer was performed by FT-IR, ^1H NMR, elemental content, and molecular weight. The ^1H NMR and FT-IR spectra were illustrated in **Supplementary Figure 3**. The protons in both aromatic ring and amine were confirmed to be around 7.5–8.0 ppm in ^1H NMR

analysis (Zhao et al., 2004). Furthermore, a series of characteristic PABS peaks can be observed in FT-IR analysis. The bands at 3,200 and 3,056 cm^{-1} were attributed to $-\text{NH}-$ stretching and aromatic C–H stretching, respectively. The absorption peaks at 1,600 and 1,411 cm^{-1} were assigned to the vibrations of aromatic rings plus C–N stretching, and a peak around 1,148 cm^{-1} was assigned to S = O stretching (Rao and Sathyanarayana, 2002; Mu, 2005). Additionally, the peaks at 864, 702, and 583 cm^{-1} were assigned to C–H out-of-plane bending vibrations of benzene rings, S–O stretching, and S–C stretching, respectively (Pradeep et al., 2014). Therefore, the chemical structure of PABS can be confirmed through the results of ^1H NMR and FT-IR analyses.

The molecular weight and element content of PABS were analyzed, as shown in **Supplementary Table 1**. PABS exhibited a weight-average molecular weight of 18,000 $\text{g}\cdot\text{mol}^{-1}$, a number-average molecular weight of 15,900 $\text{g}\cdot\text{mol}^{-1}$, and a polydispersity index of 1.13. In addition, the elemental contents of C, H, N, O, and S of PABS were 40.1, 3.5, 8.2, 36, and 12.2%, respectively. It was found that the contents of N and S were relatively high due to the presence of amine and a sulfonic group of PABS. Overall, it was concluded that PABS was successfully prepared according to chemical structure analysis (^1H NMR and FT-IR), molecular weight distribution, and elemental analysis.

Characterization of TOCNF, TOCNF-Cl, and TOCNF-PABS

(TEMPO)-oxidized cellulose nanofibrils used for the synthesis of TOCNF-PABS was prepared by mechanically treating TEMPO-oxidized HWBKP. TOCNF-PABS was prepared through a two-step synthetic route (**Supplementary Figure 2**). First, the carboxyl group of TOCNF was substituted with an acyl chloride using an excess amount of oxalyl chloride, and then PABS was grafted onto TOCNF, finally to prepare the TOCNF-PABS. **Table 1** shows the yields and elemental analysis results of TOCNF, TOCNF-Cl, and TOCNF-PABS. After the reaction, the yield increased by 26.35%, and the element contents of N (7.0%) and S (3.7%) appeared, indicating that PABS was successfully copolymerized with TOCNF-Cl.

The chemical structure of TOCNF-PABS was analyzed by FT-IR and XPS. **Figure 1** exhibited the FT-IR spectra of TOCNF, TOCNF-Cl, and TOCNF-PABS. The typical band at 1,600 cm^{-1} attributed to $-\text{COONa}$ stretching was observed in TOCNF (Yuan et al., 2019). After reaction with oxalyl chloride, the carboxyl group of TOCNF was converted to acyl chloride, and a new band at 1,722 cm^{-1} attributed to $-\text{COCl}$ stretching

TABLE 1 | Yields and elemental contents of TOCNF, TOCNF-Cl, and TOCNF-PABS.

Sample	Yield (mg)	Elemental content (%)				
		C	H	N	O	S
TOCNF	NA	37.9	6.0	0	56.1	0
TOCNF-Cl	400.3	40.5	5.8	0	53.7	0
TOCNF-PABS	505.4	49.1	6.4	7.0	33.8	3.7

NA, not available.

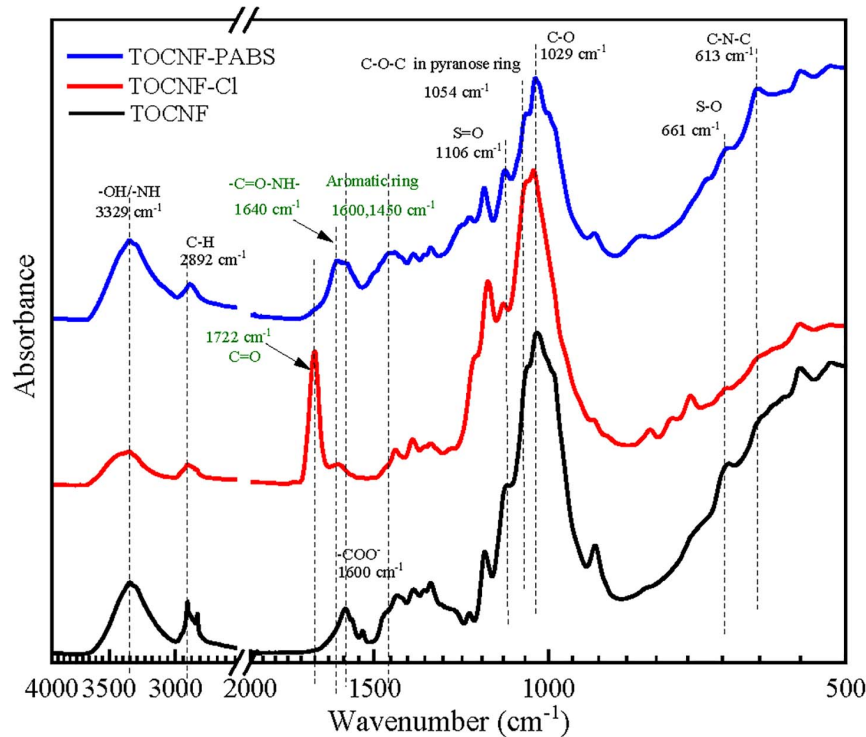


FIGURE 1 | Fourier transform infrared (FT-IR) spectra of TOCNF, TOCNF-Cl, and TOCNF-PABS.

appeared, indicating that the carboxyl group was successfully acyl chlorinated. A clear band shifting from $1,722$ to $1,640$ cm^{-1} was observed in the spectrum of TOCNF-PABS. It is due to $-\text{COCl}$ in TOCNF-Cl reacting with $-\text{NH}_2$ in PABS to form an acylamide ($-\text{C}=\text{O}-\text{NH}-$), which usually resulted in a peak around $1,640$ cm^{-1} (Zhao et al., 2004). It is the primary proof to indicate the successful grafting reaction of PABS onto TOCNF. Additionally, specific functional groups belonging to PABS were identified as follows: the increase in peaks at around $3,329$ cm^{-1} was assigned to $-\text{OH}$ plus $-\text{NH}$ stretching; the peak at $1,600$ and $1,450$ cm^{-1} were assigned to aromatic ring stretching (Mu, 2005); the peak at $1,106$ cm^{-1} was assigned to $\text{S}=\text{O}$ stretching. Additionally, weak peaks at 661 and 613 cm^{-1} assigned to $\text{S}-\text{O}$ stretching and $\text{C}-\text{N}-\text{C}$ stretching, respectively, appeared in the spectrum of TOCNF-PABS (Pradeep et al., 2014).

Figure 2 shows the XPS survey spectra of TOCNF-PABS. As shown in **Figure 2A**, the S_{2p} signal was deconvoluted into two components at 168.1 and 169.9 eV, which correspond to the $\text{S}-\text{O}$ and $\text{S}-\text{C}$ bonding of PABS, respectively (Huang and Xu, 2010). On the other hand, The C_{1s} peak was deconvoluted into four components at 284.8 , 285.8 , 286.3 , and 289.0 eV that account for the $\text{C}-\text{C}$, $\text{C}-\text{S}/\text{C}-\text{N}$, $\text{C}-\text{O}$, and $\text{O}-\text{C}=\text{O}$ bonding, respectively (**Figure 2B**; Liu et al., 2010; Tu et al., 2014). Among these, the $\text{C}-\text{S}/\text{C}-\text{N}$ bonding might have originated from PABS. Similarly, the N_{1s} spectrum also detects two peaks, 399.6 eV belonging to the $-\text{NH}-$ bonding and 401.4 eV for quaternary ammonium bonding (**Figure 2C**; Abdulla et al., 2015). All the XPS results also indicated the successful grafting reaction of PABS onto TOCNF.

Therefore, considering the above chemical structure analyses, it could be concluded that TOCNF-PABS was successfully prepared through a two-step synthetic route.

Cr(VI) Adsorption of TOCNF and TOCNF-PABS

The amount of adsorbent is an important factor as it directly determines the efficiency of TOCNF-PABS for Cr(VI) adsorption. The effect of TOCNF and TOCNF-PABS dosages on Cr(VI) removal is shown in **Figure 3A**. The Cr(VI) adsorption was performed using different adsorbent dosages (10 – 180 mg) at pH 3 for 24 h. As observed, the removal amount increased with the increase of adsorbent dosage, which could be attributed to the increased surface area and presence of more active sites. It was observed that the removal amount increased very rapidly when the amount of TOCNF-PABS was increased from 10 to 60 mg, and the removal amount reached almost 100% for 60 mg. Whereas in the case of TOCNF, even when 160 mg was added, the removal amount was found to be about 40%.

Figure 3B shows the effect of settling time in the range of 0 – $1,440$ min on the removal amount of Cr(VI) for TOCNF (160 mg) and TOCNF-PABS (120 mg). At a settling time ranging from 0 to 400 min, the removal amount of Cr(VI) was rapidly increased to around 80% for TOCNF-PABS, and then, it slowly increased to 100% from 400 to $1,400$ min. However, after reaching 40% in 400 min, there was no significant increase in the removal amount of Cr(VI) for TOCNF. This indicated that adsorption equilibrium was attained for both adsorbents. In comparison,

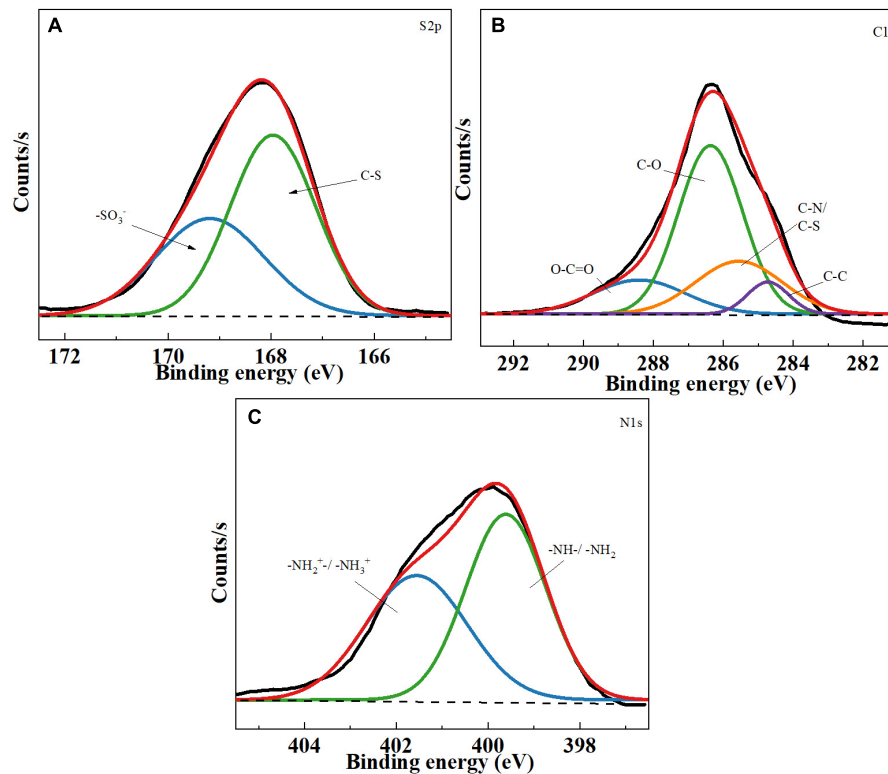


FIGURE 2 | X-ray photoelectron spectroscopy (XPS) spectra of TOCNF-PABS. **(A)** S2p core-level spectra of TOCNF-PABS; **(B)** C1s core-level spectra of TOCNF-PABS; **(C)** N1s core-level spectra of TOCNF-PABS.

even though a relatively small amount of TOCNF-PABS was used, a fast adsorption rate was observed for TOCNF-PABS compared to that for TOCNF.

The pH is one of the most critical factors affecting the adsorption capacity because it can affect the adsorbent's charge density and the adsorbate's present state. Usually, the Cr(VI) removal amount was known to be rapidly increased when pH decreased from 8.0 to 2.0. The effect of pH on the removal amount of Cr(VI) is shown in **Figure 3C**. As observed, the removal amount of Cr(VI) decreased rapidly as the solution pH increased from 3 to 11 when TOCNF-PABS (120 mg) and TOCNF (160 mg) were used. However, the removal amount of Cr(VI) was almost 100% for TOCNF-PABS in the pH range of 1–3, but it decreased from 60% to 40% for TOCNF as the pH increased from 1 to 3. To our knowledge, Cr(VI) ions are known to exist in the form of CrO_4^{2-} species when the pH was higher than 6 and of HCrO_4^- and $\text{Cr}_2\text{O}_7^{2-}$ species when the pH was between 2 and 6 (Zhao et al., 2015; Liang et al., 2020). Meanwhile, in the low pH range of 1–3, amino groups of TOCNF-PABS were extensively protonated to form either $-\text{NH}_3^+$ or $-\text{NH}_2^+$ groups, resulting in strong electrostatic attraction with negatively charged Cr anion species (**Figure 4**). And this caused an increase in Cr(VI) adsorption in the low pH range of 1–3. Likewise, the carboxylic acid group of TOCNF was extensively protonated to

form the COOH_2^+ cation group, which also adsorbed Cr anion species by strong electrostatic attraction. In contrast, when pH increased from 3 to 11, both sulfonic groups of TOCNF-PABS and carboxylic acid of TOCNF were extensively deprotonated to form SO_3^- and COO^- anion groups, respectively, causing strong electrostatic repulsion with negatively charged Cr anion species. So the Cr(VI) removal efficiency fell rapidly. Notably, the Cr(VI) removal efficiency was approximately 100% at pH 3 with TOCNF-PABS, so the adsorption experiments were performed at pH 3.

Additionally, Cr(III) was observed in the residual solution after adsorption. When the pH value was 7, the Cr(VI) removal amount was 57.21%, and the remaining amount of Cr(VI) in solution was 24.66%; then 18.13% Cr(III) was observed in the residual solution. The existence of Cr(III) in the solution indicated that part of Cr(VI) could have been reduced to Cr(III) by TOCNF-PABS during the adsorption process. Some previous works have pointed out that amine groups with high redox potential can reduce Cr(VI) to Cr(III). Part of Cr(III) was released into the aqueous phase owing to the electronic repulsion between the positively charged amine groups and the Cr(III) (Liu et al., 2012, 2013). These results suggested that the biosorbent from TOCNF-bonded PABS could synchronously detoxify and adsorb Cr(VI).

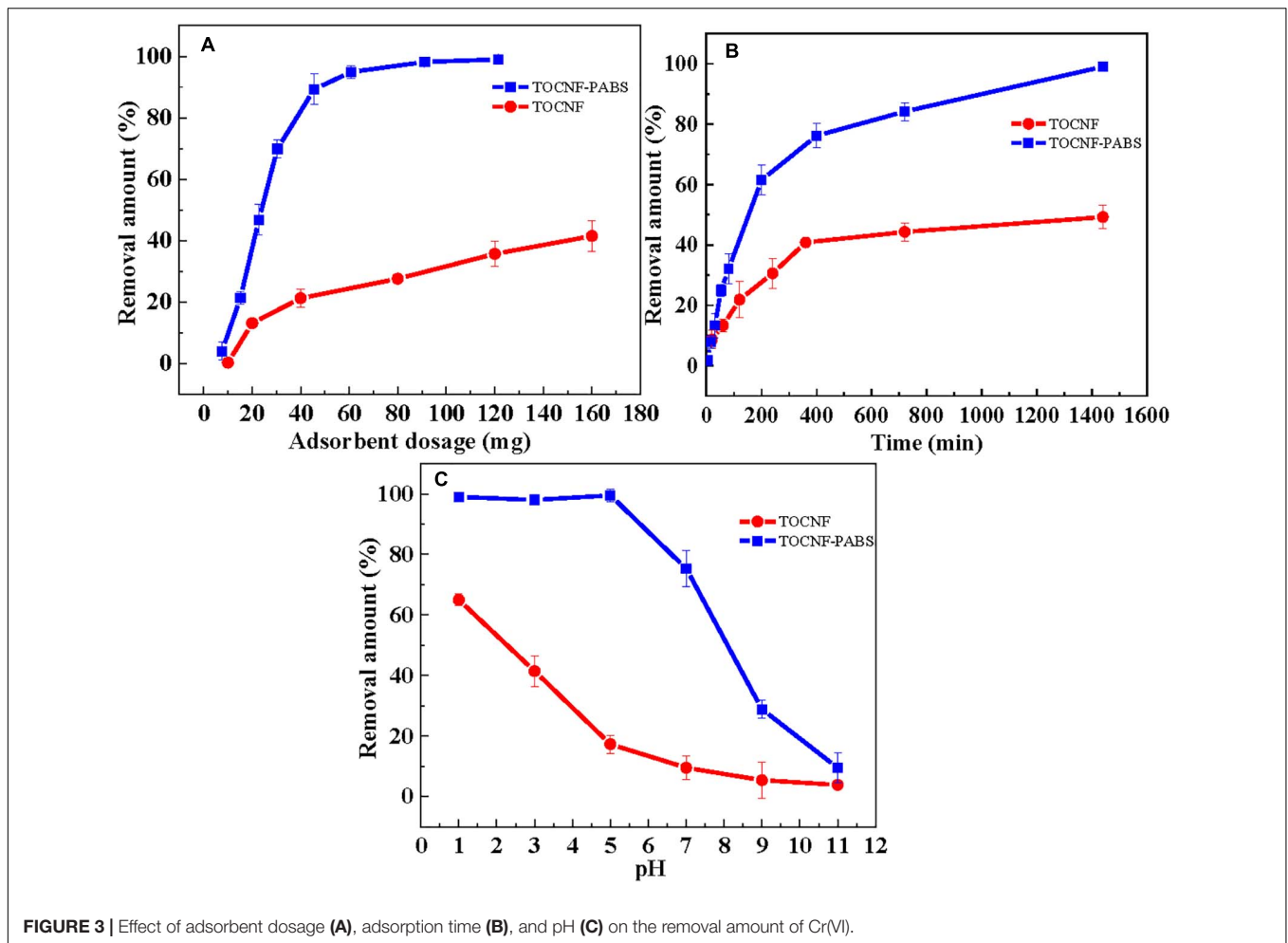


FIGURE 3 | Effect of adsorbent dosage (A), adsorption time (B), and pH (C) on the removal amount of Cr(VI).

TABLE 2 | Characteristic parameters of Langmuir and Freundlich models for the adsorption of Cr(VI) onto TOCNF and TOCNF-PABS.

Samples	Langmuir isotherm			Freundlich isotherm		
	R^2	k_L (L·mg ⁻¹)	q_m (mg·g ⁻¹)	R^2	k_F (mg·g ⁻¹)	n
TOCNF	0.9998	6.349	0.518	0.9427	0.474	39.00
TOCNF-PABS	0.9977	4.317	5.263	0.5423	2.485	3.546

Cr(VI) Adsorption Isotherms and Adsorption Kinetics

To evaluate Cr(VI) adsorption isotherms, different initial Cr(VI) concentration in the range 1–60 mg·L⁻¹ was performed on the adsorption for TOCNF (160 mg) and TOCNF-PABS (120 mg) at pH 3 for 24 h. Langmuir and Freundlich adsorption isotherm models were used to fit the adsorption isotherms (Wang et al., 2018). The linear Langmuir and Freundlich equations are given in Eqs. (4, 5), respectively.

$$\frac{C_e}{q_e} = \frac{C_e}{q_m} + \frac{1}{q_m k_L} \tag{4}$$

$$\ln q_e = \ln k_F + \frac{\ln C_e}{n} \tag{5}$$

where q_e is the equilibrium adsorption capacity (mg·g⁻¹), C_e is the concentration of adsorbate at equilibrium (mg·L⁻¹), q_m is the maximum adsorption capacity (mg·g⁻¹), k_L is the Langmuir constant, and k_F and n are Freundlich constants.

Figures 4A,D showed the effect of the initial concentration of Cr(VI) on the adsorption capacity of TOCNF and TOCNF-PABS, respectively. With the increase of the initial concentration of Cr(VI), the adsorption capacities of both adsorbents were increased and then gradually slowed down from spectra. The maximum adsorption capacities (5.277 mg·g⁻¹ for TOCNF-PABS and 0.518 mg·g⁻¹ for TOCNF) were derived from the experimental data. This result indicated that TOCNF-PABS had better Cr(VI) adsorption capacity than TOCNF. Figures 4B,C,E,F show the results of fitting the experimental data to the Langmuir and Freundlich

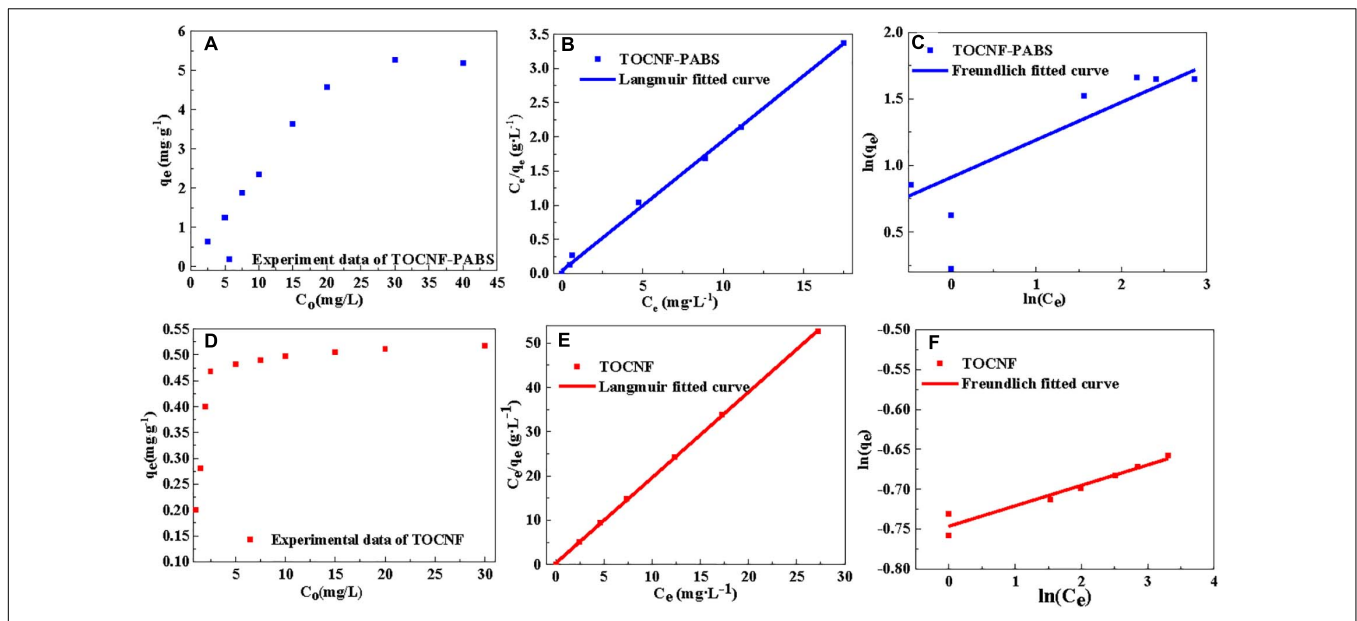


FIGURE 4 | Linear fitting curves of isotherm models (Langmuir and Freundlich models) for the adsorption of Cr(VI) onto TOCNF and TOCNF-PABS. **(A)** Effect of different initial Cr(VI) concentration on the adsorption capacity of TOCNF-PABS; **(B)** Linear fitting curve of Langmuir model for the adsorption of Cr(VI) onto TOCNF-PABS; **(C)** Linear fitting curve of Freundlich model for the adsorption of Cr(VI) onto TOCNF-PABS; **(D)** Effect of different initial Cr(VI) concentration on the adsorption capacity of TOCNF; **(E)** Linear fitting curve of Langmuir model for the adsorption of Cr(VI) onto TOCNF; **(F)** Linear fitting curve of Freundlich model for the adsorption of Cr(VI) onto TOCNF.

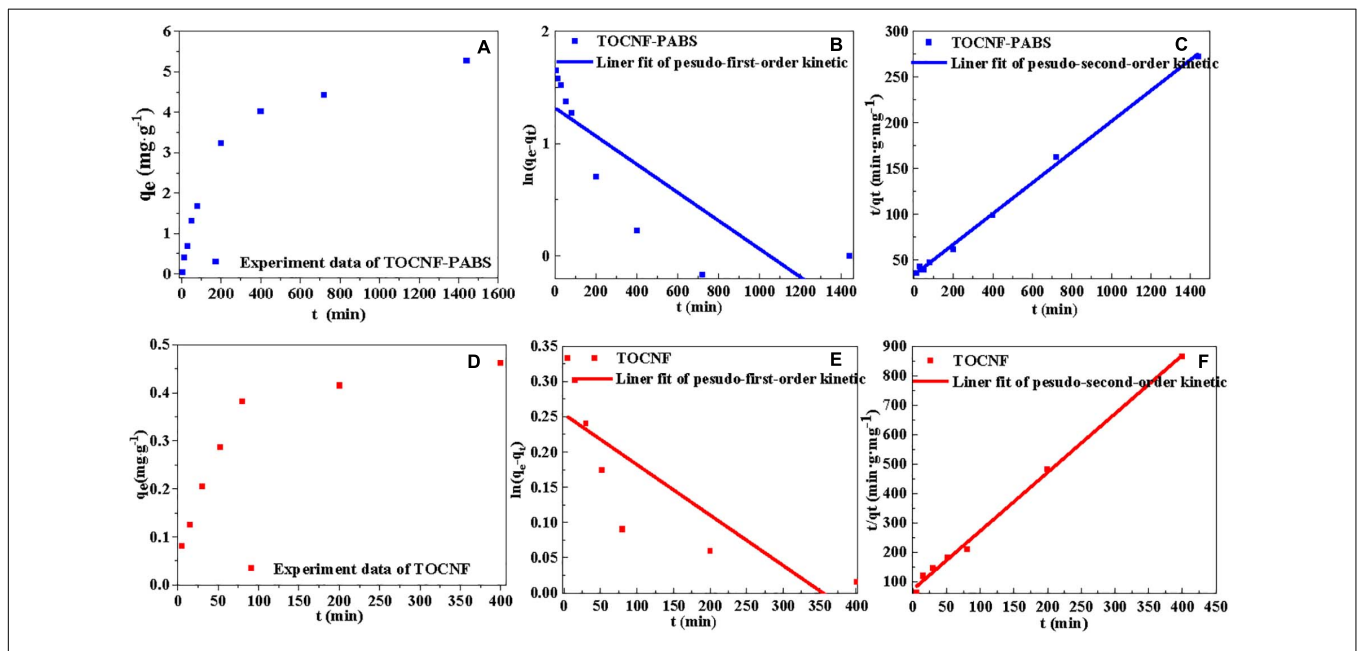


FIGURE 5 | Linear fitting curves of isotherm models (pseudo-first-order and pseudo-second-order kinetic models) for the adsorption of Cr(VI) onto TOCNF and TOCNF-PABS. **(A)** Effect of the adsorption time on the adsorption capacity of TOCNF-PABS; **(B)** Linear fitting curve of pseudo-first-order kinetic model for the adsorption of Cr(VI) onto TOCNF-PABS; **(C)** Linear fitting curve of pseudo-second-order kinetic model for the adsorption of Cr(VI) onto TOCNF-PABS; **(D)** Effect of the adsorption time on the adsorption capacity of TOCNF; **(E)** Linear fitting curve of pseudo-first-order kinetic model for the adsorption of Cr(VI) onto TOCNF; **(F)** Linear fitting curve of pseudo-second-order kinetic model for the adsorption of Cr(VI) onto TOCNF.

isotherm models. The relevant linear equation parameters are listed in **Table 2**. The Langmuir isotherm model fitted well the experimental data for the adsorption of Cr(VI)

on both TOCNF and TOCNF-PABS, as revealed by the high correlation coefficients (R^2), which were 0.9998 and 0.9977, respectively, whereas for the Freundlich isotherm

TABLE 3 | Characteristic parameters of kinetic equations for the adsorption of Cr(VI) onto TOCNF and TOCNF-PABS.

Samples	Pseudo-first-order kinetics			Pseudo-second-order kinetics			
	R^2	K_1 (min^{-1})	$q_{e,cal}$ ($\text{mg}\cdot\text{g}^{-1}$)	R^2	K_2 ($\text{g}\cdot\text{mg}^{-1}\cdot\text{min}^{-1}$)	$q_{e,cal}$ ($\text{mg}\cdot\text{g}^{-1}$)	$q_{e,exp}$ ($\text{mg}\cdot\text{g}^{-1}$)
TOCNF	0.6896	$7.2\cdot 10^{-4}$	1.289	0.9967	$5.4\cdot 10^{-2}$	0.502	0.462
TOCNF-PABS	0.6862	$1.3\cdot 10^{-3}$	3.741	0.9974	$8.4\cdot 10^{-4}$	5.949	5.277

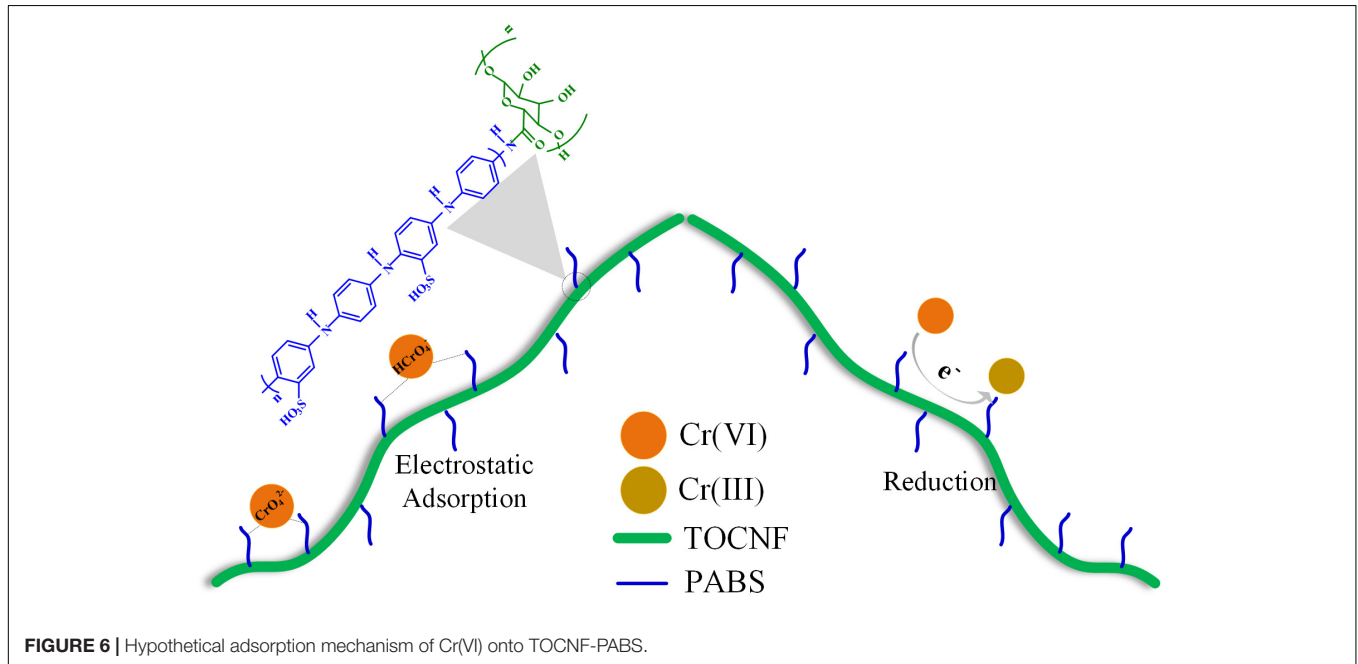


FIGURE 6 | Hypothetical adsorption mechanism of Cr(VI) onto TOCNF-PABS.

model, smaller R^2 values were obtained. The maximum adsorption capacity values of Cr(VI) from the Langmuir isotherm models were $5.263 \text{ mg}\cdot\text{g}^{-1}$ for TOCNF-PABS and $0.518 \text{ mg}\cdot\text{g}^{-1}$ for TOCNF.

The adsorption kinetics were determined based on the effect of the adsorption time on the adsorption capacity. The adsorption was performed using TOCNF (160 mg) and TOCNF-PABS (120 mg) with 30 ml Cr(VI) solution ($30 \text{ mg}\cdot\text{L}^{-1}$) at pH 3 for 0–24 h. The common mathematical models, pseudo-first-order and pseudo-second-order kinetic models, were used to fit the adsorption kinetics data (Wang et al., 2018). The linear pseudo-first-order and pseudo-second-order kinetic equations are given in Eqs. (6, 7), respectively.

$$\ln(q_e - q_t) = \ln q_e - k_1 t \tag{6}$$

$$\frac{t}{q_t} = \frac{1}{k_2 q_e^2} + \frac{t}{q_e} \tag{7}$$

where q_e is the equilibrium adsorption capacity ($\text{mg}\cdot\text{g}^{-1}$), q_t is the adsorption capacity ($\text{mg}\cdot\text{g}^{-1}$) at time t (min), k_1 and k_2 are the kinetics rate constants for pseudo-first-order and pseudo-second-order kinetic models, respectively.

Based on the experimental data obtained from the effect of settling time on the removal amount, the pseudo-first-order and pseudo-second-order kinetic models were used to

fit the data. The results are presented in **Figure 5**. The characteristic kinetic equation parameters are listed in **Table 3**. **Figures 5A,D** show the effect of settling time on the adsorption capacity of TOCNF-PABS and TOCNF, respectively. With the prolonging of the settling time, the adsorption capacity was increased, and the maximum adsorption capacity was reached. As clearly observed from **Table 3**, the values of the correlation coefficient R^2 for the pseudo-second-order kinetic models were slightly higher than those of the pseudo-first-order kinetic models and close to 1. Additionally, the maximum capacity values from the pseudo-second-order kinetic models were close to the adsorption experiment data's values. Therefore, these results indicated that the adsorption of Cr(VI) ions on both TOCNF and TOCNF-PABS followed pseudo-second-order kinetics.

As shown in **Figure 6**, after a two-step reaction, an amine-rich biosorbent was prepared from cellulose nanofibrils and PABS. PABS was dotted on the cellulose chain to form a series of effective adsorption sites. When the solution had a low pH range, Cr(VI) ions existed in the form of negatively charged species, including CrO_4^{2-} , HCrO_4^- , and $\text{Cr}_2\text{O}_7^{2-}$. Meanwhile, the amine groups of TOCNF-PABS were extensively protonated to form either $-\text{NH}_3^+$ or $-\text{NH}_2^+$ groups. It consequently triggered a strong electrostatic attraction between negatively charged Cr anion species and positively charged amine groups. And the electrostatic attraction was the

main adsorption attraction for Cr(VI) onto a TOCNF-PABS in the low pH range of 1–3. Additionally, when Cr(VI) was adsorbed onto the biosorbent surface, the amine groups with high redox potential can reduce Cr(VI) to Cr(III). Part of Cr(III) ions was released into the aqueous phase owing to the electronic repulsion between the positively charged groups and the Cr(III). Therefore, the biosorbent from TOCNF grafted with PABS could detoxify and adsorb Cr(VI) synchronously.

CONCLUSION

A novel biosorbent from hardwood cellulose and a conductive polymer was designed. The high-aspect-ratio cellulose nanofibrils were grafted with PABS via a two-step reaction. FT-IR and XPS analyses confirmed the successful grafting reaction between TOCNF and PABS. And a high nitrogen content (7%) was observed in TOCNF-PABS, which indicated rich amine groups in TOCNF-PABS. The introduction of effective adsorption sites (amine groups) endues TOCNF-PABS with excellent adsorption capacity. The maximum adsorption capacity was $5.263 \text{ mg}\cdot\text{g}^{-1}$ from the Langmuir model, a significant improvement compared to TOCNF with an adsorption capacity of $0.518 \text{ mg}\cdot\text{g}^{-1}$. Additionally, it has been observed that part of Cr(VI) ions was reduced to Cr(III) during the adsorption process. It indicated that the biosorbent from TOCNF grafted with PABS possessed not only effective adsorption capacity but also detoxification ability for Cr(VI) in an aqueous medium.

REFERENCES

- Abdulla, S., Mathew, T. L., and Pullithadathil, B. (2015). Highly sensitive, room temperature gas sensor based on polyaniline-multiwalled carbon nanotubes (PANI/MWCNTs) nanocomposite for trace-level ammonia detection. *Sensor Actuat. B Chem.* 221, 1523–1534. doi: 10.1016/j.snb.2015.08.002
- Alves, L., Ferraz, E., Lourenço, A., Ferreira, P., Rasteiro, M., and Gamelas, J. (2020). Tuning rheology and aggregation behaviour of TEMPO-oxidised cellulose nanofibrils aqueous suspensions by addition of different acids. *Carbohydr. Polym.* 237:116109. doi: 10.1016/j.carbpol.2020.116109
- An, L., Si, C., Bae, J. H., Jeong, H., and Kim, Y. S. (2020a). One-step silanization and amination of lignin and its adsorption of Congo red and Cu (II) ions in aqueous solution. *Int. J. Biol. Macromol.* 159, 222–230. doi: 10.1016/j.ijbiomac.2020.05.072
- An, L., Si, C., Wang, G., Choi, C. S., Yu, Y. H., Bae, J. H., et al. (2020b). Efficient and green approach for the esterification of lignin with oleic acid using surfactant-combined microreactors in water. *BioResources* 15, 89–104. doi: 10.15376/biores.15.1.89-104
- An, L., Si, C., Wang, G., Sui, W., and Tao, Z. (2019). Enhancing the solubility and antioxidant activity of high-molecular-weight lignin by moderate depolymerization via in situ ethanol/acid catalysis. *Ind. Crop Prod.* 128, 177–185. doi: 10.1016/j.indcrop.2018.11.009
- Bandyopadhyay, P., Kuila, T., Balamurugan, J., Nguyen, T. T., Kim, N. H., and Lee, J. H. (2017). Facile synthesis of novel sulfonated polyaniline functionalized graphene using m-aminobenzenesulfonic acid for asymmetric supercapacitor application. *Chem. Eng. J.* 308, 1174–1184. doi: 10.1016/j.cej.2016.10.015
- Chen, S., Wang, G., Sui, W., Parvez, A. M., Dai, L., and Si, C. (2020). Novel lignin-based phenolic nanosphere supported palladium nanoparticles with highly efficient catalytic performance and good reusability. *Ind. Crop Prod.* 145:112164. doi: 10.1016/j.indcrop.2020.112164

DATA AVAILABILITY STATEMENT

The original contributions presented in the study are included in the article/**Supplementary Material**, further inquiries can be directed to the corresponding author/s.

AUTHOR CONTRIBUTIONS

YY, LA, and YK: idea and experimental designing, and writing – original draft. YY, JB, LA, HJ, and YK: investigation. YK: supervision. YY, LA, JB, JH, JC, and YK: writing – reviewing and editing. All authors contributed to the article and approved the submitted version.

FUNDING

This work was supported by Basic Science Research Program through the National Research Foundation of Korea (NRF) funded by the Ministry of Education (No. 2018R1A6A1A0325582).

SUPPLEMENTARY MATERIAL

The Supplementary Material for this article can be found online at: <https://www.frontiersin.org/articles/10.3389/fbioe.2021.682070/full#supplementary-material>

- Chen, T., Zhou, Z., Xu, S., Wang, H., and Lu, W. (2015). Adsorption behavior comparison of trivalent and hexavalent chromium on biochar derived from municipal sludge. *Bioresour. Technol.* 190, 388–394. doi: 10.1016/j.biortech.2015.04.115
- Ding, J., Pu, L., Wang, Y., Wu, B., Yu, A., Zhang, X., et al. (2018). Adsorption and reduction of Cr (VI) together with Cr (III) sequestration by polyaniline confined in pores of polystyrene beads. *Environ. Sci. Technol.* 52, 12602–12611. doi: 10.1021/acs.est.8b02566
- Hosseini, H., and Mousavi, S. M. (2021). Bacterial cellulose/polyaniline nanocomposite aerogels as novel bioadsorbents for removal of hexavalent chromium: experimental and simulation study. *J. Clean. Prod.* 278:123817. doi: 10.1016/j.jclepro.2020.123817
- Hosseinkhani, A., Rad, B. F., and Baghdadi, M. (2020). Efficient removal of hexavalent chromium from electroplating wastewater using polypyrrole coated on cellulose sulfate fibers. *J. Environ. Manag.* 274:111153. doi: 10.1016/j.jenvman.2020.111153
- Huang, C., Dong, H., Zhang, Z., Bian, H., and Yong, Q. (2020). Procuring the nano-scale lignin in prehydrolyzate as ingredient to prepare cellulose nanofibril composite film with multiple functions. *Cellulose* 27, 9355–9370. doi: 10.1007/s10570-020-03427-9
- Huang, J., and Xu, W. (2010). Zwitterionic monomer graft copolymerization onto polyurethane surface through a PEG spacer. *Appl. Surf. Sci.* 256, 3921–3927. doi: 10.1016/j.apsusc.2010.01.051
- Jamshaid, A., Hamid, A., Muhammad, N., Naseer, A., Ghauri, M., Iqbal, J., et al. (2017). Cellulose-based materials for the removal of heavy metals from wastewater—an overview. *ChemBioEng Rev.* 4, 240–256. doi: 10.1002/cben.201700002
- Jobby, R., Jha, P., Yadav, A. K., and Desai, N. (2018). Biosorption and biotransformation of hexavalent chromium [Cr (VI)]: a comprehensive review. *Chemosphere* 207, 255–266. doi: 10.1016/j.chemosphere.2018.05.050
- Khalil, T. E., Elhusseiny, A. F., El-dissouky, A., and Ibrahim, N. M. (2020). Functionalized chitosan nanocomposites for removal of toxic Cr (VI)

- from aqueous solution. *React. Funct. Polym.* 146:104407. doi: 10.1016/j.reactfunctpolym.2019.104407
- Li, X., Xu, R., Yang, J., Nie, S., Liu, D., Liu, Y., et al. (2019). Production of 5-hydroxymethylfurfural and levulinic acid from lignocellulosic biomass and catalytic upgradation. *Ind. Crop. Prod.* 130, 184–197. doi: 10.1016/j.indcrop.2018.12.082
- Liang, X., Liang, B., Wei, J., Zhong, S., Zhang, R., Yin, Y., et al. (2020). A cellulose-based adsorbent with pendant groups of quaternary ammonium and amino for enhanced capture of aqueous Cr (VI). *Int. J. Biol. Macromol.* 148, 802–810. doi: 10.1016/j.ijbiomac.2020.01.184
- Liu, H., Xu, T., Liu, K., Zhang, M., Liu, W., Li, H., et al. (2021). Lignin-based electrodes for energy storage application. *Ind. Crop. Prod.* 165:113425. doi: 10.1016/j.indcrop.2021.113425
- Liu, K., Du, H., Zheng, T., Liu, H., Zhang, M., Xie, H., et al. (2021). Recent advances in cellulose and its derivatives for oilfield applications. *Carbohydr. Polym.* 259:117740. doi: 10.1016/j.carbpol.2021.117740
- Liu, P.-S., Chen, Q., Wu, S.-S., Shen, J., and Lin, S.-C. (2010). Surface modification of cellulose membranes with zwitterionic polymers for resistance to protein adsorption and platelet adhesion. *J. Membr. Sci.* 350, 387–394. doi: 10.1016/j.memsci.2010.01.015
- Liu, W., Du, H., Liu, H., Xie, H., Xu, T., Zhao, X., et al. (2020a). Highly efficient and sustainable preparation of carboxylic and thermostable cellulose nanocrystals via FeCl₃-catalyzed innocuous citric acid hydrolysis. *ACS Sustain. Chem. Eng.* 8, 16691–16700. doi: 10.1021/acssuschemeng.0c06561
- Liu, W., Du, H., Zhang, M., Liu, K., Liu, H., Xie, H., et al. (2020b). Bacterial cellulose-based composite scaffolds for biomedical applications: a review. *ACS Sustain. Chem. Eng.* 8, 7536–7562. doi: 10.1021/acssuschemeng.0c00125
- Liu, X., Qian, X., Shen, J., Zhou, W., and An, X. (2012). An integrated approach for Cr (VI)-detoxification with polyaniline/cellulose fiber composite prepared using hydrogen peroxide as oxidant. *Bioresour. Technol.* 124, 516–519. doi: 10.1016/j.biortech.2012.09.002
- Liu, X., Zhou, W., Qian, X., Shen, J., and An, X. (2013). Polyaniline/cellulose fiber composite prepared using persulfate as oxidant for Cr (VI)-detoxification. *Carbohydr. Polym.* 92, 659–661. doi: 10.1016/j.carbpol.2012.09.083
- Lu, J., Zhu, W., Dai, L., Si, C., and Ni, Y. (2019). Fabrication of thermo- and pH-sensitive cellulose nanofibrils-reinforced hydrogel with biomass nanoparticles. *Carbohydr. Polym.* 215, 289–295. doi: 10.1016/j.carbpol.2019.03.100
- Mendoza, D. J., Browne, C., Raghuvanshi, V. S., Simon, G. P., and Garnier, G. (2019). One-shot TEMPO-periodate oxidation of native cellulose. *Carbohydr. Polym.* 226:115292. doi: 10.1016/j.carbpol.2019.115292
- Mishra, S., and Bharagava, R. N. (2016). Toxic and genotoxic effects of hexavalent chromium in environment and its bioremediation strategies. *J. Environ. Sci. Heal. C* 34, 1–32. doi: 10.1080/10590501.2015.1096883
- Mohamed, A. K., and Mahmoud, M. E. (2020). Nanoscale Pisum sativum pods biochar encapsulated starch hydrogel: a novel nanosorbent for efficient chromium (VI) ions and naproxen drug removal. *Bioresour. Technol.* 308:123263. doi: 10.1016/j.biortech.2020.123263
- Mu, S. (2005). Polyaniline with two types of functional groups: preparation and characteristics. *Macromol. Chem. Phys.* 206, 689–695. doi: 10.1002/macp.200400408
- Olivera, S., Muralidhara, H. B., Venkatesh, K., Guna, V. K., Gopalakrishna, K., and Kumar, Y. (2016). Potential applications of cellulose and chitosan nanoparticles/composites in wastewater treatment: a review. *Carbohydr. Polym.* 153, 600–618. doi: 10.1016/j.carbpol.2016.08.017
- Pradeep, S., Arunraj, L., and Dhatchinamurthy, L. (2014). Synthesis and characterization of poly m-amino benzene sulfonic acid for sensor applications. *J. Nanosci. Nanotechnol.* 2, 390–393.
- Qiu, B., Xu, C., Sun, D., Yi, H., Guo, J., Zhang, X., et al. (2014). Polyaniline coated ethyl cellulose with improved hexavalent chromium removal. *ACS Sustain. Chem. Eng.* 2, 2070–2080. doi: 10.1021/sc5003209
- Rao, P. S., and Sathyanarayana, D. (2002). Effect of the sulfonic acid group on copolymers of aniline and toluidine with m-aminobenzene sulfonic acid. *J. Polym. Sci. Pol. Chem.* 40, 4065–4076. doi: 10.1002/pola.10495
- Seo, J. H., Choi, C. S., Bae, J. H., Jeong, H., Lee, S.-H., and Kim, Y. S. (2019). Preparation of a lignin/Polyaniline composite and its application in Cr (VI) removal from aqueous solutions. *BioResources* 14, 9169–9182. doi: 10.15376/biores.14.4.9169-9182
- Shi, X., Qiao, Y., An, X., Tian, Y., and Zhou, H. (2020). High-capacity adsorption of Cr (VI) by lignin-based composite: Characterization, performance and mechanism. *Int. J. Biol. Macromol.* 159, 839–849. doi: 10.1016/j.ijbiomac.2020.05.130
- Song, W., Gao, B., Zhang, T., Xu, X., Huang, X., Yu, H., et al. (2015). High-capacity adsorption of dissolved hexavalent chromium using amine-functionalized magnetic corn stalk composites. *Bioresour. Technol.* 190, 550–557. doi: 10.1016/j.biortech.2015.01.103
- Tu, Q., Pang, L., Chen, Y., Zhang, Y., Zhang, R., Lu, B., et al. (2014). Effects of surface charges of graphene oxide on neuronal outgrowth and branching. *Analyst* 139, 105–115. doi: 10.1039/c3an01796f
- Wang, H., Xie, H., Du, H., Wang, X., Liu, W., Duan, Y., et al. (2020). Highly efficient preparation of functional and thermostable cellulose nanocrystals via H₂SO₄ intensified acetic acid hydrolysis. *Carbohydr. Polym.* 239:116233. doi: 10.1016/j.carbpol.2020.116233
- Wang, P., Yin, B., Dong, H., Zhang, Y., Zhang, Y., Chen, R., et al. (2020). Coupling biocompatible Au nanoclusters and cellulose nanofibrils to prepare the antibacterial nanocomposite films. *Front. Bioeng. Biotechnol.* 8:986. doi: 10.3389/fbioe.2020.00986
- Wang, X., Jiang, C., Hou, B., Wang, Y., Hao, C., and Wu, J. (2018). Carbon composite lignin-based adsorbents for the adsorption of dyes. *Chemosphere* 206, 587–596. doi: 10.1016/j.chemosphere.2018.04.183
- Wang, Y., Peng, C., Padilla-Ortega, E., Robledo-Cabrera, A., and López-Valdivieso, A. (2020). Cr (VI) adsorption on activated carbon: mechanisms, modeling and limitations in water treatment. *J. Environ. Chem. Eng.* 8:104031. doi: 10.1016/j.jece.2020.104031
- Wong, S., Ngadi, N., Inuwa, I. M., and Hassan, O. (2018). Recent advances in applications of activated carbon from biowaste for wastewater treatment: a short review. *J. Clean. Prod.* 175, 361–375. doi: 10.1016/j.jclepro.2017.12.059
- Xu, R., Du, H., Wang, H., Zhang, M., Wu, M., Liu, C., et al. (2021). Valorization of enzymatic hydrolysis residues from corncob into lignin-containing cellulose nanofibrils and lignin nanoparticles. *Front. Bioeng. Biotechnol.* 9:252. doi: 10.3389/fbioe.2021.677963
- Youe, W.-J., Kim, S. J., Lee, S.-M., Chun, S.-J., Kang, J., and Kim, Y. S. (2018). MnO₂-deposited lignin-based carbon nanofiber mats for application as electrodes in symmetric pseudocapacitors. *Int. J. Biol. Macromol.* 112, 943–950. doi: 10.1016/j.ijbiomac.2018.02.048
- Yuan, H., Guo, X., Xiao, T., Ma, Q., and Wu, Y. (2019). Moisture adsorption in TEMPO-oxidized cellulose nanocrystal film at the nanogram level based on micro-FTIR spectroscopy. *Cellulose* 26, 7175–7183. doi: 10.1007/s10570-019-02593-9
- Zhang, N., Zang, G.-L., Shi, C., Yu, H.-Q., and Sheng, G.-P. (2016). A novel adsorbent TEMPO-mediated oxidized cellulose nanofibrils modified with PEI: preparation, characterization, and application for Cu (II) removal. *J. Hazard Mater.* 316, 11–18. doi: 10.1016/j.jhazmat.2016.05.018
- Zhang, S., Shi, Q., Korfiatis, G., Christodoulatos, C., Wang, H., and Meng, X. (2020). Chromate removal by electrospun PVA/PEI nanofibers: adsorption, reduction, and effects of co-existing ions. *Chem. Eng. J.* 387:124179. doi: 10.1016/j.ccej.2020.124179
- Zhao, B., Hu, H., and Haddon, R. C. (2004). Synthesis and properties of a water-soluble single-walled carbon nanotube-poly (m-aminobenzene sulfonic acid) graft copolymer. *Adv. Funct. Mater.* 14, 71–76. doi: 10.1002/adfm.200304440
- Zhao, J., Zhang, X., He, X., Xiao, M., Zhang, W., and Lu, C. (2015). A super biosorbent from dendrimer poly (amidoamine)-grafted cellulose nanofibril aerogels for effective removal of Cr (VI). *J. Mater. Chem. A* 3, 14703–14711. doi: 10.1039/c5ta03089g

Conflict of Interest: The authors declare that the research was conducted in the absence of any commercial or financial relationships that could be construed as a potential conflict of interest.

Copyright © 2021 Yu, An, Bae, Heo, Chen, Jeong and Kim. This is an open-access article distributed under the terms of the Creative Commons Attribution License (CC BY). The use, distribution or reproduction in other forums is permitted, provided the original author(s) and the copyright owner(s) are credited and that the original publication in this journal is cited, in accordance with accepted academic practice. No use, distribution or reproduction is permitted which does not comply with these terms.



Bio-Based Hydrogels With Ion Exchange Properties Applied to Remove Cu(II), Cr(VI), and As(V) Ions From Water

Julio Sánchez^{1*}, Daniel Dax², Yesid Tapiero¹, Chunlin Xu² and Stefan Willför²

¹ Departamento de Ciencias del Ambiente, Facultad de Química y Biología, Universidad de Santiago de Chile, Santiago, Chile, ² Research Group of Wood and Paper Chemistry, Laboratory of Natural Materials Technology, Åbo Akademi University, Turku, Finland

OPEN ACCESS

Edited by:

Xianzhi Meng,
The University of Tennessee,
Knoxville, United States

Reviewed by:

JunLi Ren,
South China University of Technology,
China
Xueping Song,
Guangxi University, China

*Correspondence:

Julio Sánchez
julio.sanchez@usach.cl

Specialty section:

This article was submitted to
Bioprocess Engineering,
a section of the journal
Frontiers in Bioengineering and
Biotechnology

Received: 20 January 2021

Accepted: 06 April 2021

Published: 20 May 2021

Citation:

Sánchez J, Dax D, Tapiero Y, Xu C
and Willför S (2021) Bio-Based
Hydrogels With Ion Exchange
Properties Applied to Remove Cu(II),
Cr(VI), and As(V) Ions From Water.
Front. Bioeng. Biotechnol. 9:656472.
doi: 10.3389/fbioe.2021.656472

Hydrogels with ion exchange properties were synthesized from compounds derived from wood biopolymer hemicellulose and from commercial vinyl monomers to be tested as active materials for the removal of Cu(II), Cr(VI), and As(V) ions. The hemicellulose O-acetyl galactoglucomanan (GGM) was used as the precursor material, and through a transesterification reaction, GGM was converted into a macromonomer GGM-glycidyl methacrylate (GGM-GMA). Subsequently, the GGM-GMA macromonomer, containing more than one methacrylate group, was used as a crosslinking agent in the synthesis of hydrogels through free-radical polymerization reactions in combination with a 2-acrylamido-2-methyl-1-propanesulfonic acid monomer to produce a cation exchange hydrogel. Also, (3-acrylamidopropyl)trimethylammonium chloride monomer was applied together with the GGM-GMA to form hydrogels that can be used as anion exchange hydrogel. The hydrogels were characterized by Fourier transform-infrared (FT-IR), ¹H-NMR spectroscopy, and thermogravimetric analysis (TGA), as well as derivative thermogravimetry (DTG). The microstructure of the hydrogels was characterized by scanning electron microscopy (SEM) analysis with X-ray microanalysis energy-dispersive spectroscopy (EDS). The results obtained regarding the absorption capacity of the Cu(II), Cr(VI), and As(V) ions were studied as a function of the pH value and the initial concentration of the metal ions in the solutions. Absorption was carried out in consecutive batches, and it was found that the poly(GGM-GMA/AMPSH) hydrogel reached an absorption capacity of 90 mg g⁻¹ for Cu(II). The poly(GGM-GMA/APTACI) hydrogel reached values of 69 and 60 mg g⁻¹ for Cr(VI) and As(V) oxyanions, respectively. Tests with polymer blends (mixtures of anionic and cationic hydrogels) were also carried out to remove Cu(II), Cr(VI), and As(V) ions from multi-ionic solutions, obtaining satisfactory results.

Keywords: arsenic, hemicellulose, hydrogel, metal ions, water treatment

INTRODUCTION

An important material in industry is wood, as it plays a key role in the development of anthropogenic activities at all levels. The main applications of wood include transportation systems, energy, industrial and residential buildings, and works of art, among others. However, as a biomaterial, wood often undergoes decomposition by biotic, chemical, or physical agents. For this reason, different strategies have been designed to extend the useful life of wood through chemical or physical treatments. Water-based chemical treatments are the most commonly used due to their simplicity and because they are economical; of this type, the preservative formulation based on a copper–chromium–arsenic (CCA) mixture stands out (Ohgami et al., 2015). This mixture is generally applied to wood by a vacuum pressure impregnation method. CCA can be classified into three different types: type A (16.4% arsenic, 18.0% copper, and 65.5% chromium), type B (45.1% arsenic, 19.6% copper, and 35.3% chromium), or type C (34.0% arsenic, 18.5% copper, and 47.5% chromium) (Janin et al., 2009a; Coudert et al., 2014; Ohgami et al., 2015). The function of copper is bactericidal and fungicidal, arsenic is an insecticide, and chromium is the binding agent for wood, copper, and arsenic (Zheng et al., 2015; Gezer and Cooper, 2016).

Wood treated with the preservative (CCA) has been shown to last a long time; however, depending on the environmental conditions, release phenomena of arsenic, copper, and chromium can be generated from wood, which can cause serious health problems, as these elements have toxic effects on the cell cycle (Matos et al., 2020). The CCA wood preservative has permitted uses in commercial, industrial, and agricultural activities (Matos et al., 2020), where the components of the preservatives are easily leached, contaminating soil, water, and plants and causing harm to animals and humans. CCA contamination occurs through dermatological absorption, inhalation of wood dust, or contact with contaminated water and soil (Zheng et al., 2015; Safa et al., 2020).

Depending on where wood is used, certain levels of CCA application are required; for example, on land, 4.0 kg m^{-3} of CCA is needed, and for applications at sea, 40.0 kg m^{-3} of CCA is needed (Gezer and Cooper, 2016). A large amount of CCA remains impregnated in wood until the end of its useful life, where it remains a problem as waste (Helsen and Van den Bulck, 2005). When wood treated with the CCA preservative is disposed of in a municipal landfill, where it mixes with common garbage and undergoes decomposition processes, it releases toxic chromium and arsenic ions, contaminating the leachate from waste. There is no waste regulation regarding CCA-treated wood waste in the United States, Canada, or other countries (Janin et al., 2009b). The danger of leachates produced from preservative-treated woods is that exposure to arsenic can generate free radicals and oxidative stress in cells and cause death (Chen and Olsen, 2016). Exposure to chromium is toxic due to its oxidative character (Saha and Orvig, 2010), and prolonged exposure to copper can cause carcinogenic effects (Ohgami et al., 2015). For this reason, the World Health Organization recommends the following maximum concentrations in water: 0.01 mg L^{-1} for

arsenic, 0.05 mg L^{-1} for chromium, and 2.0 mg L^{-1} for copper (Tyagi et al., 2013).

CCA leachates are conventionally treated with chemical methods (oxidizing agents, chelators, and organic and inorganic acids) (Almaroai et al., 2013), chelating polymers (chitin, chitosan, and biomaterials) (Dhillon et al., 2017; Wilson and Tewari, 2018), biodegradation and/or bioleaching with bacteria and fungi (Sierra-Alvarez, 2009), ion exchange processes with resins and coagulation–precipitation techniques (Yan et al., 2020), extraction with hot water and dilute sulfuric acid (Ferrarini et al., 2016), and thermochemical conversion methods (Kramb et al., 2016), among others. The drawbacks of these common treatments are the excessive consumption of reactive material, long reaction times, and generation of toxic sludge. Sahiner et al. designed cryogels and hydrogels based on poly[(3-acrylamidopropyl)trimethylammonium chloride] [poly(APTACl)], which has a high surface porosity capacity, allowing for rapid water absorption, and has a maximum adsorption capacity of approximately 120 mg g^{-1} of As(V) oxyanions. The poly((3-acrylamidopropyl) trimethylammonium chloride) hydrogel can be reused five times in the adsorption of As(V) from aqueous environments. This hydrogel can be rapidly regenerated and does not produce highly hazardous toxic waste in large quantities as occurs in other water treatment processes (Sahiner et al., 2015).

Hydrogels are attractive materials for water treatment because, in some cases, they can be synthesized from biomaterials, and they can also be designed to have adjustable and tuneable properties, including the pH value and ionic strength, for use in an aqueous working medium (Kong et al., 2018). The most important consideration is to identify a raw material that provides a large amount of biocompounds to develop starting materials that can polymerize and produce hydrogels. A promising source is hemicellulose extracted from wood, the second most abundant polysaccharide after cellulose. A hemicellulose hydrogel that is pH-sensitive and partially biodegradable can be prepared by grafting vinyl monomers into a polysaccharide structure, specifically in acetyl bonds. *O*-Acetyl galactoglucomannan (GGM) is a form of hemicellulose and the major type in softwoods and is employed in the production of anionic, cationic, or neutral polysaccharide-based hydrogels. Hydrogels based on the GGM modification can remove heavy metals from aqueous solutions via adsorption. These gels can be reused for up to eight cycles (Farrukh et al., 2018). Likewise, hydrogels derived from cellulose and hemicellulose materials have been reported, which have found applications in the retention of heavy metal ions; for example, Dax et al. (2014) modified GGM by grafting glycidyl methacrylate (GMA) to generate a vinyl macromonomer that can be crosslinked with the monomer [2-(methacryloyloxy)ethyl]trimethylammonium chloride to create a hydrogel with the capacity to remove arsenic and chromium oxyanions at concentrations between 55 and 68 mg g^{-1} at a pH value of 9.0. In another study, the macromonomer GGM-GMA was crosslinked with 2-acrylamido-2-methyl-1-propanesulfonic acid (AMPSH), acrylic acid, and acrylamide to obtain ion exchange hydrogels. These materials were tested for the retention of metallic ions dissolved in

water, such as cadmium, copper, lead, nickel, and zinc; lead was the cation with the greatest strength of interaction and retention in the structure of the hydrogels as compared with the other metallic ions (Elgueta et al., 2016). In all reported cases of the use of GGM crosslinked hydrogels, the removal of metal ions was studied in mono-ion solutions (anionic or cationic), not in mixtures or multi-ion solutions (anionic and cationic).

The aim of this research was to take advantage of the properties of GGM to produce a macromonomer, GGM-GMA, with the ability to generate ion exchange hydrogels to remove Cu(II), Cr(VI), and As(V) ions at various pH levels and concentrations and to study the removal of these ions from CCA multi-ion solutions.

EXPERIMENTAL

Materials

2-acrylamido-2-methyl-1-propanesulfonic acid, AMPSH (99%, Aldrich, Chile), (3-acrylamidopropyl)trimethylammonium chloride, APTACl solution (75% in water, Aldrich, Chile), dimethylsulfoxide (DMSO) (Merck, Chile), acetone (Merck, Chile), GMA (97%, Aldrich, Chile), $(\text{NH}_4)_2\text{S}_2\text{O}_8$ (98%, Aldrich, Chile), 4-(dimethylamino)pyridine (DMAP) (98%, Aldrich, Chile), ethanol (Merck, Chile), sodium hydroxide NaOH (Merck, Chile), nitric acid HNO_3 (65%, Merck, Chile), sodium bisulfite NaHSO_3 (98%, Aldrich, Chile), copper(II) nitrate trihydrate $\text{Cu}(\text{NO}_3)_2 \cdot 3\text{H}_2\text{O}$ (98.9%, Merck, Chile), potassium chromate K_2CrO_4 (99, 9%, Merck, Chile), and sodium arsenate dibasic heptahydrate $\text{Na}_2\text{HAsO}_4 \cdot 7\text{H}_2\text{O}$ (98%, Merck, Chile).

Methods

Synthesis of the (O-Acetyl

Galactoglucomannan–Glycidyl Methacrylate)

Macromonomer

Pressurized hot water-extracted GGM from Norway spruce (*Picea abies*) was provided by The Finnish Forest Research Institute Metla. The extraction conditions were studied and optimized in a previous study (Dax et al., 2014; Elgueta et al., 2016).

The transesterification reaction to obtain macromonomer was performed in a three-necked round-bottom glass flask to introduce the reactive material. The reaction was carried out by mixing O-acetyl-galactoglucomannan (GGM: 10.0 g, 58.1 mmol) with GMA (5.9 g, 41.5 mmol). DMAP (10 mol% GMA) was added as the catalyst, and the reaction medium was DMSO. It was necessary to remove dissolved oxygen from the reagent mixture; therefore, nitrogen gas was injected for 15 min. The transesterification reaction was carried out at a temperature of 50°C for 72 h with constant stirring. At the end of the reaction, acetone was added to the mixture to precipitate the product, followed by a separation process through vacuum filtration. When the precipitated solid was completely dry, it was dissolved in 50 ml of distilled water, and the separation was refined using a dialysis membrane tube (cutoff of 3.5 kDa) for 3 days, with water

exchange every 24 h. Finally, the retentate obtained inside the dialysis tube was lyophilized for 7 days (Dax et al., 2014; Elgueta et al., 2016).

Synthesis of Hydrogels

Synthesis of the hydrogels was carried out through free-radical polymerization using water as the reaction solvent at 60°C for 12 h. Two classes of hydrogels were prepared, one cationic and one anionic. The cationic hydrogel was labeled poly(GGM-GMA/APTACl), and the anionic hydrogel was labeled poly(GGM-GMA/AMPSH). Synthesis of both hydrogels was performed using the same procedure. In a flask, 0.8 g of the macromonomer (GGM-GMA) and 7.20 g of a vinyl monomer (APTACl or AMPSH) were mixed with 32 ml of water, 0.252 g of the radical initiator $(\text{NH}_4)_2\text{S}_2\text{O}_8$, and 0.249 g of the NaHSO_3 oxygen scavenger. After the solid hydrogel was obtained, it was washed with bidistilled water in a flask with constant agitation for 12 h at room temperature. Subsequently, the samples were filtered under vacuum, continuing the lyophilization of the hydrogel until the sample was completely dry.

Characterization

A Bruker Avance 400-MHz spectrometer was used for the ^1H -NMR spectra measurements, with D_2O as the solvent and tetramethylsilane as the internal standard. A Nicolet Magna 550 spectrophotometer was used for the Fourier transform-infrared (FT-IR) measurements of the polymers in the spectral range of 4,000–400 cm^{-1} . Polymer samples were prepared in KBr. A Thermobalance TG209 Iris F1[®] was used for the thermogravimetric analysis (TGA). The analysis was performed under a nitrogen gas atmosphere with a heating rate of 10°C min^{-1} over a temperature range between 30 and 550°C. Scanning electron microscopy (SEM) (20,000 kV JOEL microscopy; JSH 6380 LV model) and an Oxford instruments INCAx-sight instrument were used for SEM–energy-dispersive spectroscopy (EDS) measurements.

Water Uptake

Polymer samples of 0.1 g (m_{dry^0}) were exposed to 100 ml of bidistilled water. The aim was to study the hydrogel–water balance for 24 h at room temperature. The hydrogel was then vacuum filtered, and the weight of the hydrated hydrogel (m_{wetf}) was recorded. The percentage of water uptake is calculated according to the following:

$$\%W = \frac{m_{wetf} - m_{dry^0}}{m_{dry^0}} \times 100\%$$

Removal of Metal Ions

For each metal ion removal experiment, 0.02 g of polymer was placed in 5 ml of a metal ion solution and then stirred at 180 rpm for 1 h at 25°C. The polymer–metal ion solution mixture was then centrifuged at 4,000 rpm for 20 min to separate the solid and liquid phases. Finally, the liquid supernatant was analyzed by atomic absorption spectroscopy (AAS) (Unicam Solaar 5 M series) to determine the metal ion concentration. For the AAS measurements, a flame atomizer with a mixture of 40% acetylene

and 60% oxygen was used. An electrode discharge lamp was used as the radiation source.

To study the retention behavior of Cr(VI) and As(V) oxyanions, a cationic GGM-GMA/APTACl hydrogel was used. Cu(II) retention was studied with the anionic GGM-GMA/AMPSH hydrogel. For the experiment to determine the removal of mono-ion solutions as a function of pH, 100 mg L⁻¹ of Cu(NO₃)₂·3H₂O, 100 mg L⁻¹ of K₂CrO₄, and 100 mg L⁻¹ of Na₂HAsO₄·7H₂O were prepared in separate solutions to study the removal of Cu(II), Cr(VI), and As(V), respectively. The pH values analyzed were 3.0, 6.0, and 9.0 [for Cr(VI) and As(V)], which were adjusted with HNO₃ or NaOH standards. For Cu(II), the pH values analyzed were 2.0, 3.0, and 4.0. To study the retention of metal ions as a function of the metal concentration (50, 100, 200, and 300 mg L⁻¹), Cr(VI) and As(V) were analyzed at pH 9.0, while Cu(II) was analyzed at pH 3.0. In the absorption-desorption studies, solutions of 100 mg L⁻¹ of each metal ion were prepared (feed) at the optimum working pH. First, 0.02 g of the polymer was added to 10.0 ml of an aqueous solution containing the ion of interest. The hydrogel-metal ion solution was kept under constant agitation for 1 h at 180 rpm and 25°C and then centrifuged for 20 min at 4,000 rpm. Subsequently, the supernatant was removed, diluted to 25.0 ml with bidistilled water, and measured by AAS. The hydrogel material was then washed with 1 mol L⁻¹ of NaCl brine to pH 6.7, followed by water washes. Subsequently, the hydrogel added to the same metal solution of the feed, and the process was repeated in three absorption-desorption cycles.

Mixed Bed Column Tests

The mixture of poly(GGM-GMA/APTACl) (0.02 g) and poly(GGM-GMA/AMPSH) (0.02 g) hydrogels was used as ion exchange extracting agents. The hydrogel mixture was then added to 10 ml of each mono-ionic aqueous solution [100 mg L⁻¹ of Cu(II), Cr(VI), and As(V) in separate solutions] and at the optimal pH values. Similarly, the mixture of the ion exchange hydrogels was added to 10 ml of a multi-ionic aqueous solution containing 100 mg L⁻¹ of each metal ion. All the absorption samples were placed in a stirred, thermoregulated bath at 25°C for 1 h, and then, the solution was centrifuged for approximately 20 min at 4,000 rpm. The supernatant was carefully removed with a micropipette and diluted to 25 ml. This procedure was applied in all the experimental tests.

The absorption capacity (*S*) of the hydrogels was evaluated using the following equation:

$$S = \frac{(C_0^{metal} - C_t^{metal}) \times V}{m_{dry}^H}$$

where m_{dry}^H is the mass of the dried hydrogel (mg); C_0^{metal} and C_t^{metal} (mg/L) are the concentrations of the metal ions in the solution before and after sorption by the hydrogels, respectively; and *V* is the volume (L) of the aqueous phase.

RESULTS AND DISCUSSION

Characterization

From the results of the transesterification reaction, a yield of over 47.3% was obtained for the formation of the macromonomer (GGM-GMA) with 4.732 g GGM as the starting material.

Figure 1 shows the signals of the spectrum obtained through ¹H-NMR spectroscopy for the GGM-GMA macromonomer and native GGM. In the spectrum, signal (a) two peaks corresponding to the protons of the double bond –C=C– of the methacrylate group grafted through the transesterification reaction are observed. The peaks between 5.69 and 6.12 ppm correspond to native GGM, but they are small and poorly defined; however, it is observed that in GGM-GMA, they are separate and well-defined peaks. Signal (b) at 2.07 ppm corresponds to the protons of the solvent DMSO (Dax et al., 2014). Signal (c) at 1.85 ppm corresponds to two overlapping and sharp peaks of the methyl group. Signal (d) at 4.70 ppm is attributed to deuterated water, and signal (e) at 4.90 ppm corresponds to the anomeric protons of GGM-GMA. The protons of OC–OCH₃ are observed at 2.86 and 2.64 ppm, and signal (f) between 3.20 and 4.20 ppm corresponds to the protons from H₁ to H₆ of GGM-GMA (Heinze et al., 2006).

Figure 2A shows the FT-IR spectra of GGM as the initial material, where the main characteristic bands are as follows: the signal at 3,408.80 cm⁻¹ is attributed to the –OH stretching vibration, the strong signal at 1,734.39 cm⁻¹ corresponds to the –C–O stretching vibration of the carboxyl group, and finally, the signal that appears at 2,929.70 cm⁻¹ is attributed to CH₂ groups. On the other hand, **Figure 2B** shows the representative signals of the GGM-GMA material, and it is possible to observe differences in the signals of the functional groups compared

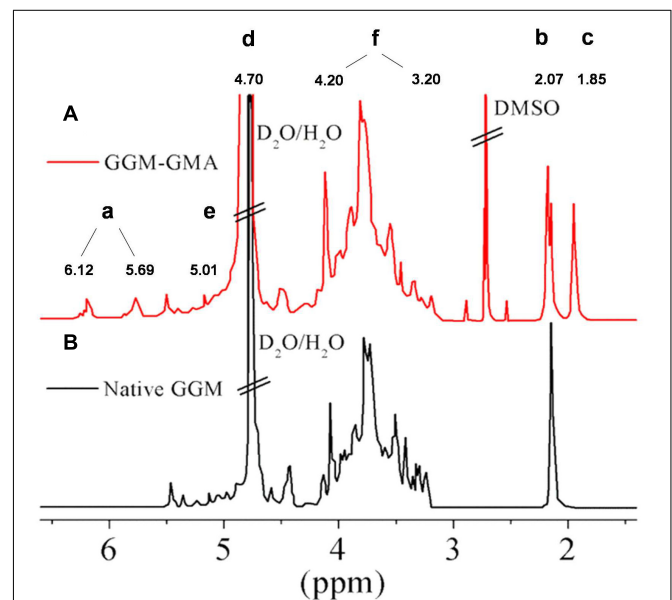
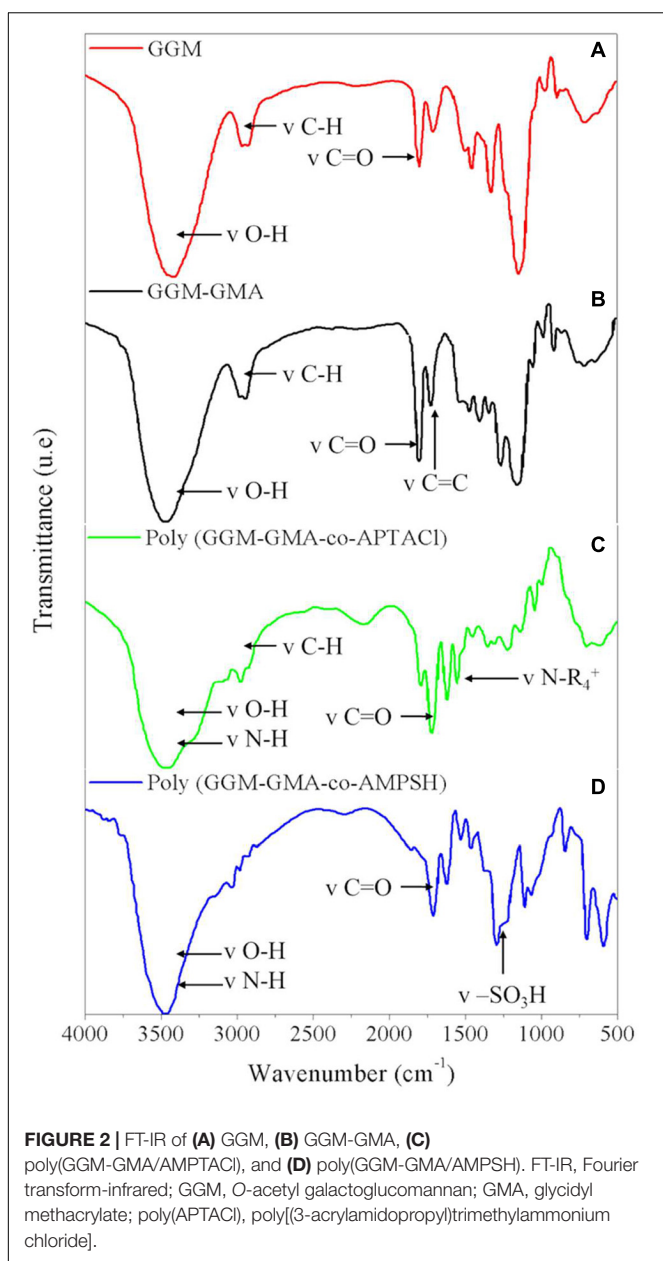


FIGURE 1 | ¹H-NMR spectra of (A) GGM-GMA and (B) native GGM in D₂O. GGM, O-acetyl galactoglucomannan; GMA, glycidyl methacrylate.



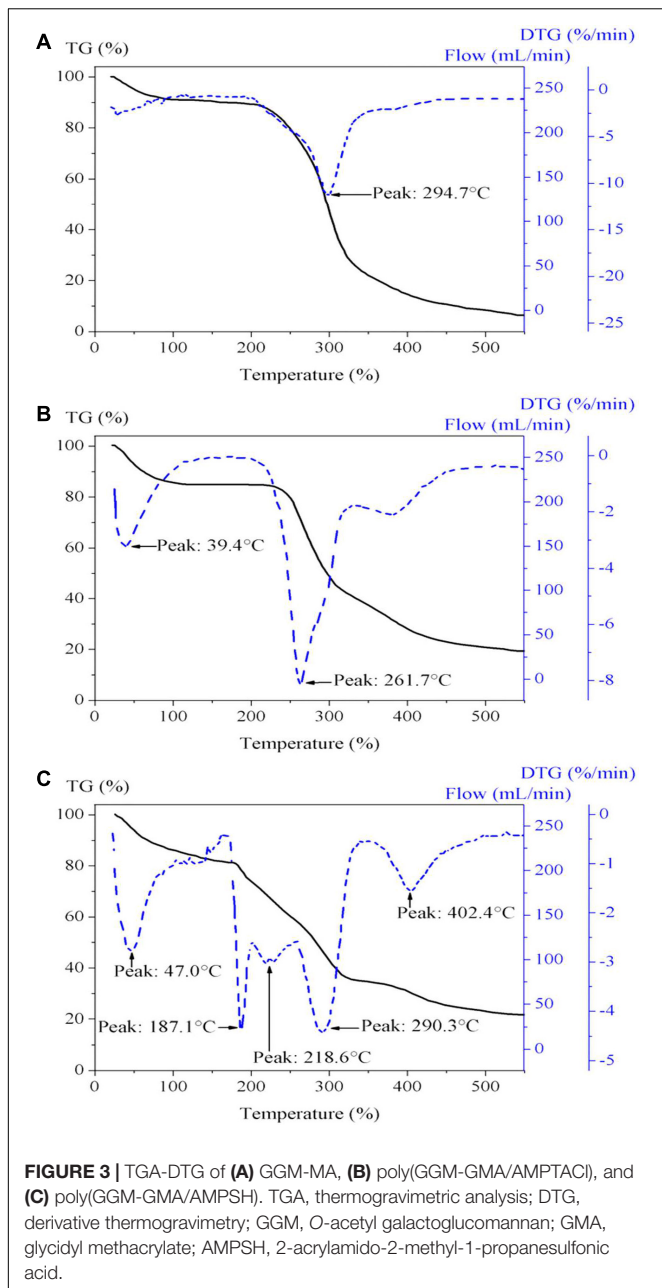
with those of GGM. The main signals of the functional group bands for GGM-GMA are the vibration signal corresponding to the C-C bond at $1,638.56\text{ cm}^{-1}$ (methacrylate group), which is more intense than that at the same value in GGM, and the signal at $1,378\text{ cm}^{-1}$, which indicates acetyl C-CH₃. Other signals of interest for the characterization of the GGM-GMA material include $3,430.34\text{ cm}^{-1}$ (-OH), $2,890.78\text{ cm}^{-1}$ (C-H), $1,167.57\text{ cm}^{-1}$ (C-O-C asymmetric stretching signal), $1,055.65\text{ cm}^{-1}$ (C-O-C, hemicellulose and glycosidic bond signals), 883.97 cm^{-1} (anomeric carbons due to links with the β -glucoside at C-1), and 810.14 cm^{-1} (-CH bending signal of -CH groups). The signals at $1,520$, $1,467$, and $1,420\text{ cm}^{-1}$ associated with lignin are not observed in the FT-IR spectra of GGM-GMA. Signals between 909 and 945 cm^{-1} are not observed

in the spectra; therefore, the presence of the GMA compound without chemical reaction is ruled out.

In the same way, the ion exchange hydrogels show differences in the FT-IR band signals of the functional groups compared with the spectrum obtained for the GGM-GMA precursor material. For analysis of the cationic hydrogel poly(GGM-GMA/APTACl), the FT-IR signals (see **Figure 2C**) display a peak for quaternary ammonium at $1,485.10\text{ cm}^{-1}$; $2,941.87\text{ cm}^{-1}$ represents the vibration of the CH₂ methyl groups; $1,728.14\text{ cm}^{-1}$ corresponds to the ester functional group -C-O (both of the macromonomer and of the vinyl monomer); $3,440.35\text{ cm}^{-1}$ represents hydroxyl and N-H bond groups; and $1,059.28\text{ cm}^{-1}$ corresponds to -C-O-C of the glycosidic bond. On the other hand, when analyzing the anionic hydrogel poly(GGM-GMA/AMPSH), the FT-IR signals (see **Figure 2D**) display the following absorption bands: $3,196\text{ cm}^{-1}$ represents NH, $3,437\text{ cm}^{-1}$ represents (-OH), $1,645.58\text{ cm}^{-1}$ represents (-C-O), $1,036.43\text{ cm}^{-1}$ represents the glycosidic bond of GGM-GMA and to the (-SO) stretch, $1,224\text{ cm}^{-1}$ represents the (-SO₃H group) attributed to the amide and sulfonic groups; and $2,930\text{ cm}^{-1}$ is the vibration of (Csp₃-H). In addition, a band is observed at 619.55 cm^{-1} , which indicates the stretching of the functional group (-SO), and for the secondary amide, there is a signal at $1,558.83\text{ cm}^{-1}$.

TGA-derivative thermogravimetry (DTG) analysis was performed for GGM-GMA and the synthesized ion exchange hydrogels. The thermogram of GGM-GMA is shown in **Figure 3A**, which indicates homogeneous decomposition of this material. In the temperature range between 40 and 220°C , a decrease of 10% in mass is observed, which is due to the release of the absorbed solvent and dehydration of the material. According to this result, it can be seen that the material is hygroscopic and that it absorbs moisture from the environment. GGM-GMA begins to decompose, significantly losing weight, at temperatures from approximately 210°C to approximately 330°C . According to experimental results reported in the literature (Al-Rudainy et al., 2019) on the properties of hemicellulose hydrogels, they indicate that 50% of the decomposition of the macromonomer is due to the decomposition of polysaccharides and branched GGM. From the thermogram of GGM-GMA, according to the DTG curve, 50% of the decomposition of the mass occurs at a temperature of 294.7°C . For GGM-GMA, at the end of the experiment, a residual mass percentage of 7.24% is obtained, which corresponds to the ash from the decomposition of all polysaccharides (Härdelin et al., 2020).

Figure 3B shows the results of the thermogram of the poly(GGM-GMA/APTACl) hydrogel, which presents a heterogeneous decomposition trend. The results show three temperature signals on the DTG curve, indicating the stages of the decomposition of the hydrogel. The first signal is at 39.4°C , which indicates the desorption of solvent and small molecules absorbed in the hydrogel structure and corresponds to 6.5% of the percentage of the loss of mass; the second signal occurs at 261.7°C , with 50% of the decomposition of the mass; and the third signal occurs at 380°C , with 35% of residual mass. The decomposition from 250 to 400°C was increased in the hydrogels containing poly(GGM-GMA/APTACl) compared with GGM due to losses of ammonia gas from the large-scale



oxidative thermal decomposition of the network chains (Sahiner et al., 2015; Atta et al., 2017), which had a greater effect than decarboxylation of GGM.

Figure 3C shows the results of the thermogram for poly(GGM-GMA/AMPSH), which indicates the decomposition temperatures of its components. The curve presents a heterogeneous trend regarding the decomposition of the multiple components that make up the analysis mixture. According to the results of the DTG curve, the following signals can be observed at 47°C (Çavuş et al., 2016): evaporation of solvent molecules occurs, and a 12% loss in mass is recorded; in the temperature range from 100 to 187.1°C, dehydration of the material begins, which apparently absorbs water from the air. In

the temperature range from 187.1 to 218.6°C, the decomposition of carbohydrate-based compounds and the breakdown of the crosslinking of the hydrogel occur. In the temperature range from 218.6 to 290.3°C, the complete decomposition of GGM-GMA and the decomposition of $-\text{SO}_3\text{H}$ groups (namely, SO_2 and SO_3) from the hydrogel occur; in the temperature range from 300 to 500°C, main chain degradation occurs, followed by crosslinking of bridges; and the decomposition temperature range at 180–400°C is attributed to ester bond breakdown in the structure of polymers.

Figure 4A shows an SEM image of the poly(GGM-GMA/APTACl) hydrogel in which an amorphous structure is observed that possesses microcavities similar to those observed in sponges. In addition, the image shows that the material is massive with a large grain size, very similar to the structures of ion exchange resins with a high degree of crosslinking. According to the EDS results (see **Table 1**), it can be seen that the hydrogel has a high percentage of chlorine in the form of a chloride counterion present in the quaternary ammonium group. **Figure 4B** shows the microstructure of poly(GGM-GMA/APTACl) that was previously in a 100 mg L⁻¹ chromate solution at basic pH. It can be seen that the material sample has amorphous particle sizes, and the structure tends to be in the form of thin tapes. On the other hand, the EDS results indicate that 10.94% weight is chromium absorbed (see **Table 1**). **Figure 4C** shows an irregular heterogeneous microstructure with small particle sizes. This structure corresponds to the poly(GGM-GMA/AMPSH) hydrogel. These hydrogel particles are highly porous, and the presence of sulfur, which is part of the sulfonate fixed functional group, can be seen in the EDS analysis results. In general, poly(GGM-GMA/AMPSH) has a different microstructure than poly(GGM-GMA/APTACl).

Figure 4D shows the morphology of poly(GGM-GMA/AMPSH) in a 100 mg L⁻¹ copper(II) solution at acidic pH. The hydrogel sample in contact with copper generated a sponge-like porous structure. According to EDS analysis, 59.63% weight copper absorption was obtained (see **Table 1**).

It is probable that the synthesized hydrogels do not reach adequate mechanical and chemical stability, and they may dissolve and be completely destroyed in the presence of water. It is necessary to ensure that the crosslinking reaction between the GGM-GMA macromonomer and the anionic and cationic monomers is efficient and limits the excess of swelling.

Water Uptake

The ion exchange hydrogels were swollen in deionized water for 24 h. A water absorption percentage of 33.9% was obtained for poly(GGM-GMA/AMPSH), while for poly(GGM-GMA/APTACl), a value of 28.5% was obtained. This small difference could be explained because poly(GGM-GMA/AMPSH) has polar groups such as carbonyl, hydroxyl, and esters and can weakly hydrolyze and acquire negative charges. These negatively charged groups can interact with the negative charge of the sulfonate group exerting intramolecular repulsive forces between the polymer chains of the crosslinked network. On the other hand, the positive charge of the quaternary ammonium groups has the capacity to neutralize to a certain

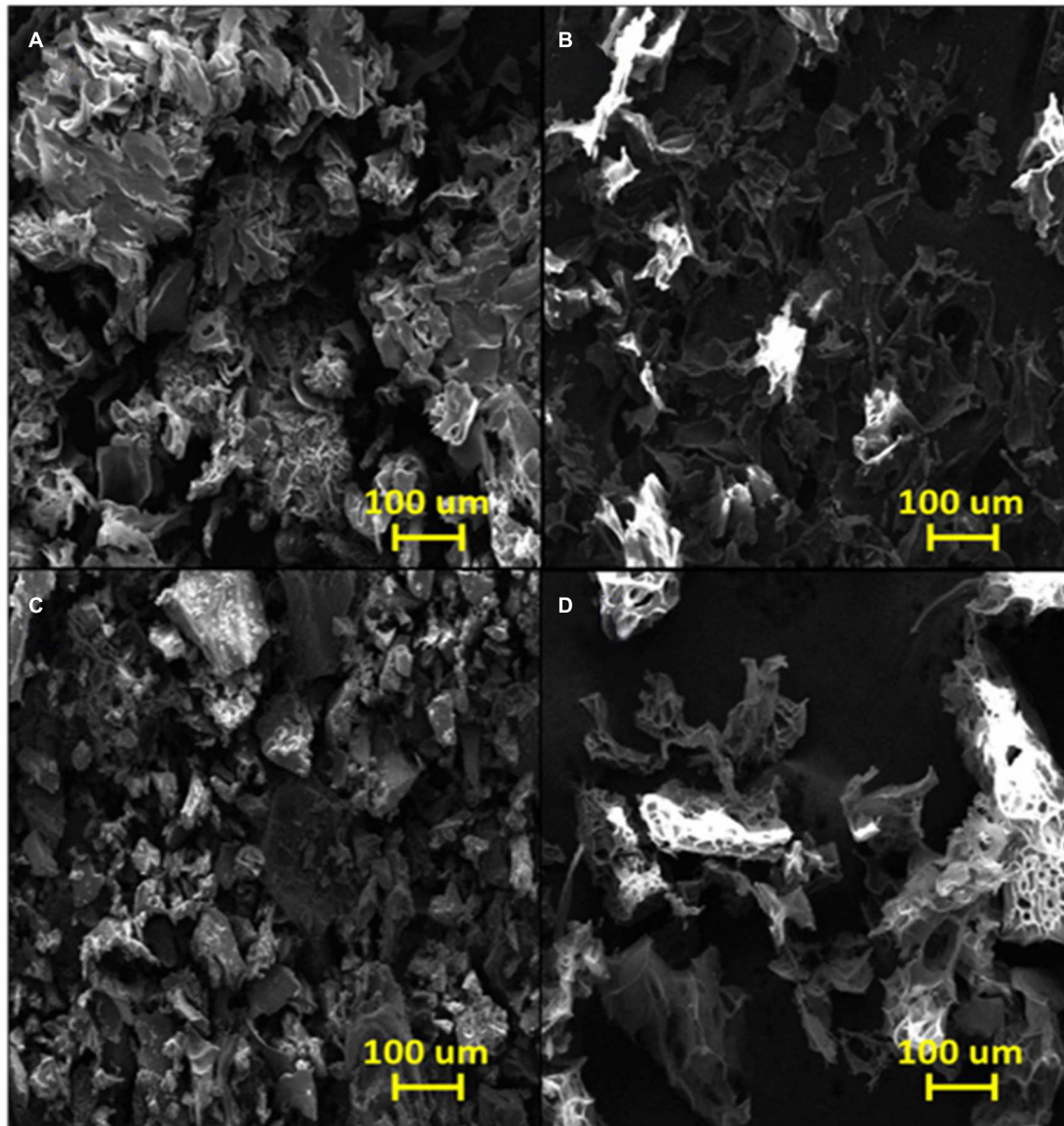


FIGURE 4 | SEM images of (A) poly(GGM-GMA/APTACI), (B) poly(GGM-GMA/APTACI) + Cr(VI), (C) poly(GGM-GMA/AMPSH), and (D) poly(GGM-GMA/AMPSH) + Cu(II). SEM, scanning electron microscopy; GGM, *O*-acetyl galactoglucomannan; GMA, glycidyl methacrylate; APTACI, (3-acrylamidopropyl)trimethylammonium chloride; AMPSH, 2-acrylamido-2-methyl-1-propanesulfonic acid.

extent to the negative charges of the polar groups carbonyl, hydroxyl, and esters of the GGM-GMA, causing the polymeric network not to swell excessively. Therefore, it is stated that poly(GGM-GMA/AMPSH) has a high degree of hydrophilicity. Elgueta et al. also obtained a similar result for a copolymer material of a GGM macromonomer crosslinked with an AMPSH monomer (Elgueta et al., 2016).

Removal of Cu(II)

Copper can generate divalent cations in aqueous solution, and depending on the concentration and pH value, it can change the ionic form or form coordination complexes with water or additional chelating agents. As copper in aqueous solution

generates a stable divalent cation at pH values between 0.0 and 5.0, the poly(GGM-GMA/AMPSH) hydrogel is used because it has sulfonate anionic groups that interact with the positive charge of copper ions. **Figure 5A** shows the absorption capacity of copper ions by the poly(GGM-GMA/AMPSH) hydrogel when in a 100 mg L^{-1} copper(II) solution at pH values of 2.0, 3.0, and 4.0. The copper removal capacity is slightly influenced by pH. The maximum copper absorption was 22.9 mg g^{-1} at pH 4.0. However, the result at pH 3.0 was 21.9 mg g^{-1} , which indicates that the influence of pH is almost null. Copper has the ability to generate various positively charged species [Cu^{2+} , CuNO_3^+ , CuOH^+ , $\text{Cu}_2(\text{OH})_2^{2+}$, and $\text{Cu}_2\text{OH}^{3+}$] capable of interacting more directly with the fixed groups of the hydrogel.

TABLE 1 | EDS analysis of poly(GGM-GMA/APTACI) + Cr(VI), poly(GGM-GMA/APTACI) + As(V), and poly(GGM-GMA/AMPSH) + Cu(II).

Element	Hydrogel					
	Poly(GGM-GMA/APTACI) + Cr(VI)		Poly(GGM-GMA/APTACI) + As(V)		Poly(GGM-GMA/AMPSH) + Cu(II)	
	Weight %	Atomic %	Weight %	Atomic %	Weight %	Atomic %
C	47.94	58.35	51.80	64.34	19.92	48.22
N	7.68	8.01	12.38	13.19	0.77	1.59
O	33.44	30.56	20.74	19.34	5.55	10.09
Cl	–	–	0.55	0.23	–	–
As	–	–	14.52	0.23	–	–
Cr	10.94	3.08	–	–	–	–
S	–	–	–	–	14.13	12.81
Cu	–	–	–	–	59.63	27.29
Total	100.00		100.00		100.00	

EDS, energy-dispersive spectroscopy; GGM, O-acetyl galactoglucomannan; GMA, glycidyl methacrylate; APTACI, (3-acrylamidopropyl) trimethylammonium chloride; AMPSH, 2-acrylamido-2-methyl-1-propanesulfonic acid.

No tests were carried out at pH values higher than 4.0 because divalent copper ions form complex species with different ionic charges or hydroxides that precipitate. At pH 2.0, the sulfonate functional group is moderately ionized, contracted, and packed for electrostatic interactions with copper cations. When the pH value increases, the sulfonate fixed functional groups become ionized, and the material swells because these groups repel due to their ionic charges. The resins that have sulfonate-fixed functional groups have better ion exchange performances at pH 3.0 because it has been shown that at this pH value, more than 85% of the sulfonate is completely ionized and available to perform electrostatic interactions and ion exchange reactions (Urbano and Rivas, 2013).

Figure 5B shows the absorption capacity of copper(II) by poly(GGM-GMA/AMPSH) at different copper concentrations in the feed at pH 3.0. The results indicate the progressive increase of the absorption capacity value when the concentration of the copper ion in the feed is increased. The high absorption capacity toward the divalent copper ion is due to electrostatic interactions between sulfonates and copper(II) cations. In this range of copper(II) concentrations, it was not possible to saturate the polymer. **Figure 5C** shows the results of consecutive batches using the same poly(GGM-GMA/AMPSH) sample at pH 3.0 and 200 mg L⁻¹ of copper(II). After regenerative washing with brine, the divalent copper ion was desorbed from the polymer, and the polymer was ready for absorptive loading of the second cycle. The absorption capacity increased from 42 to 75 mg g⁻¹. It is possible that the high concentration and ionic strength of the regenerating brine caused the hydrogel chains to stretch and relax their intramolecular forces; in this situation, the amount of fixed sulfonate groups could be increased for ion exchange. The absorption capacity increased and stabilized at a constant value between the third and fourth cycles, reaching values between 90 and 96 mg g⁻¹, respectively.

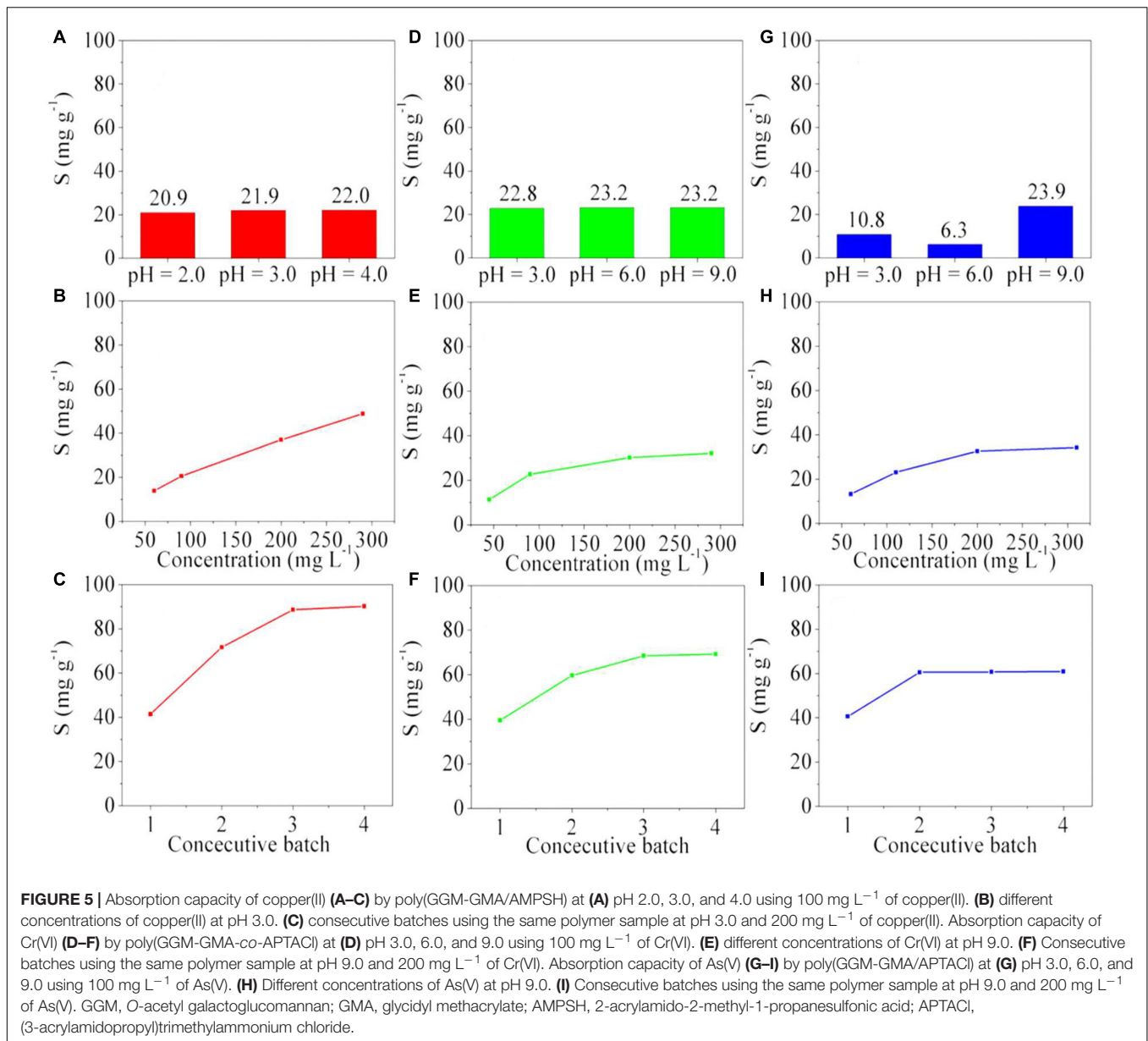
Removal of Cr(VI)

The removal of Cr(VI) oxyanions was evaluated with poly(GGM-GMA/APTACI). **Figure 5D** shows the results of the absorption capacity as a function of pH value using 100 mg L⁻¹ of

Cr(VI). It can be seen that 23.2 mg g⁻¹ absorption was reached at pH values 6.0 and 9.0. In the case of pH 3.0, 22.8 mg g⁻¹ absorption was achieved. These results can be attributed to the fact that the Cr(VI) species are present mostly as Cr₂O₇²⁻ and HCrO₄⁻ oxyanions, depending on pH and concentration. The quaternary ammonium functional groups have high attraction for both bivalent and multivalent anions, and therefore, similar removal capacities can be observed in this pH range. **Figure 5E** shows the absorption capacity of Cr(VI) oxyanions by the poly(GGM-GMA/APTACI) hydrogel as a function of the chromium concentration in the feed at pH 9.0. It can be seen from the results that from 50 to 200 mg L⁻¹ of Cr(VI), an increase occurs in the absorption capacity for this oxyanion. However, between 200 and 300 mg L⁻¹, equilibrium is reached, and the absorption capacity of the poly(GGM-GMA/APTACI) hydrogel stabilizes at 33.3 mg g⁻¹. **Figure 5F** shows the results of the maximum absorption capacity of Cr(VI) oxyanions by the poly(GGM-GMA/APTACI) hydrogel when successive cycles of loading and brine washing are performed. The loading was performed with 200 mg L⁻¹ of Cr(VI) at pH 9.0. The results show an increase of the absorption capacity and the tendency to reach equilibrium in the fourth batch. The maximum absorption value reached is 69.2 mg g⁻¹.

Removal of As(V)

Figure 5G shows the maximum absorption capacity of As(V) by the poly(GGM-GMA/APTACI) hydrogel at different pH values using 100 mg L⁻¹ of arsenic. It can be seen from the results that the absorption capacity of the arsenic oxyanions strongly depends on the pH of the aqueous medium, where the maximum capacity of 23.9 mg g⁻¹ is achieved at pH 9.0. The results obtained occur because at pH 3.0, arsenate is present in aqueous medium as H₃AsO₄ and H₂AsO₄⁻; at pH 6.0, H₂AsO₄⁻ and HAsO₄²⁻; and at pH 9.0, HAsO₄²⁻ and AsO₄³⁻. **Figure 5H** shows the results of the maximum absorption capacity at pH 9.0 of As(V) in the poly(GGM-GMA/APTACI) hydrogel, where the arsenic concentration in the feed is varied in the aqueous phase. These results indicate that an increase of the arsenic concentration produces an increase

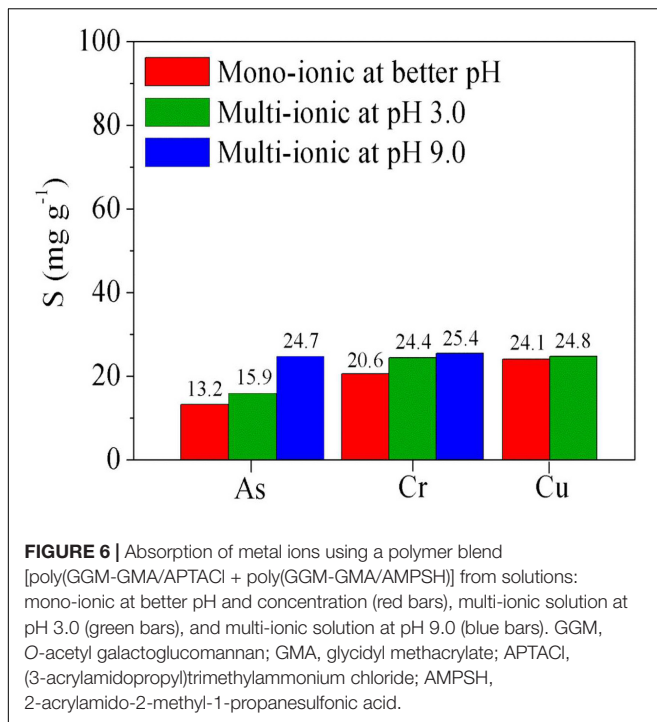


of the absorption capacity of the poly(GGM-GMA/APTACl) hydrogel. However, between 200 and 300 mg L⁻¹, the absorption capacity reaches equilibrium, and the polymer is saturated. The quaternary ammonium functional groups of the hydrogel have a high affinity for divalent anions (HAsO₄²⁻), but the monovalent anion (H₂AsO₄⁻) may compete to occupy these exchange sites and may displace divalent ions. This behavior can also be attributed to the fact that the chains of the hydrogel structure, which are mainly polysaccharides under slightly basic conditions, can be shrunk and packed, where the quaternary ammonium groups can also be balanced with OH⁻ ions. A similar result was obtained in the study of chromium oxyanions under the same pH value. **Figure 5I** shows the results of the absorption capacity of As(V) at pH 9.0 by the poly(GGM-GMA/APTACl) hydrogel when consecutive absorption cycles are carried out. The results

show that the hydrogel material quickly reaches an equilibrium state of 60 mg g⁻¹ after the second test cycle. Since there are two ionic species of arsenic, it is possible that at least one of the two species produces dipolar interactions with the nitrogen of the fixed quaternary ammonium groups and the oxygen of the oxyanion (Rivas et al., 2006).

Removal of Metal Ions Using Polymer Blends and Multi-Ionic Solutions

The experiments described in this section were carried out using polymer blends of poly(GGM-GMA/APTACl) + poly(GGM-GMA/AMPSH) to study their capacity to remove anions and cations from the same solution. **Figure 6** (red bars) shows the results of the absorption of the metal ions from



mono-ionic solutions using the polymer blend at the best removal pH. A high affinity for Cu(II) can be observed due to the multiple interactions that could result from the presence of the poly(GGM-GMA/AMPSH) hydrogel in the blend and its interactions with the ions in the solution. This behavior is similar to that obtained previously with individual hydrogels, indicating the higher removal of Cu(II).

The increase in the Cu(II) metal ion absorption capacity of the hydrogels can be explained by the metal ion binding ability of the formed hydrophilic (carbonyl, esters, hydroxyl, etc.) groups. In addition, copper can generate ionically charged aqueous complexes, which can interact through hydrogen bridges and dipolar interactions with the carbon chain structures of hydrogels. Similarly, Cr(VI) generates a good affinity for the polymer blend hydrogels, leading to efficient removal; however, low absorption of As(V) is achieved. It is possible that the interactions can be improved by altering the energy parameters and contact times between phases. Also the polyanion and polycation interactions do not dramatically decrease metal ion removal capacity. It is an advantage compared with previous results related to the use polycation and polyanion blends to remove metal and metalloid ions. The retention properties of arsenic ions from an aqueous solution by water-soluble cationic (polyquaternary ammonium) and anionic (polyacrylic acid) were investigated. Investigation showed the concerted action of polycations and polyanions on the ability to retain arsenic. The results showed a decrease in the ability of polycation when polyanion is present in the solution. This can be explained by an interaction of the COO⁻ group of the P(AA) with the N⁺(R₃) groups of polycation by charge transfer that should have blocked both functional groups and

the retention of arsenate is negligible (Rivas et al., 2006). In other research, poly(*N*-vinylpyrrolidone) (PVP) and poly(2-acrylamido-2-methylpropanesulfonate sodium) (PAMPS) were prepared and used for the removal of Cu²⁺, Cd²⁺, and Ni²⁺ ions. PAMPS exhibited a high retention capacity for all of the metal ions at both pH values studied. PVP exhibited selectivity for nickel ions. However, the homopolymer mixture containing PAMPS and PVP was inefficient for the retention of the studied metal ions. The electrostatic repulsion between macromolecules PAMPS probably promotes the formation of hydrogen bonds between the carbonyl groups of PVP and secondary amino groups of PAMPS. This favors the steric shielding of charged groups on the PAMPS, the occlusion of a high proportion of these groups in the PAMPS–PVP interpolymer complex, and the decrease of available carbonyl groups to coordinate metal ions (Valle et al., 2015).

In the current research, we found that polyanion and polycation interactions do not dramatically decrease metal ion removal capacity in mono-ionic solutions. It is probably due to the solid–liquid nature of the retention process. The polycation and polyanion interactions can be limited to the surface of the polymer hydrogels, which is different compared with polycation polyanion complex of water-soluble polymers.

Figure 6 (green bars) shows the results of the absorption of metal ions from a multi-ionic solution at pH 3.0 using a polymer blend. In these results, it can be seen that the absorption capacity is slightly improved, likely due to the fast interactions that occur among copper and sulfonic groups of poly(GGM-GMA/AMPSH) and simultaneously the interaction that occurs among chromium and arsenic with quaternary ammonium group of poly(GGM-GMA/APTACI, which stabilizes within the polymer mixture. Here, it is possible to note the similar behaviors of polyanion and polycation interactions, which do not dramatically decrease metal ion removal capacity in multi-ionic solutions.

On the other hand, in multi-ionic solutions, it is highly probable that the presence of the three ions with their respective speciations [Cu(II) (Cu²⁺, CuNO₃⁺, CuOH⁺, and Cu₂OH³⁺), Cr(VI) (HCrO₄⁻, Cr₂O₇²⁻, and CrO₄²⁻ and H₂CrO₄), and As(V) (H₃AsO₄, H₂AsO₄⁻, and HAsO₄²⁻)] generates the same coordination and complexation mechanisms that occur when these ions are applied as wood preservatives. The chromate ions could be reduced by the action of the functional groups of the GGM and hydroxides and then Cr(III), aqueous complexes are formed. These Cr(III) ions interact with the As(V) and with the dissolved copper species [the formation of Cr(III)/As(V) cluster consisting of a Cr dimer bridged by an As(V) oxyanion, Cr(III), and Cu(II) complex with the wood components as well as hydroxide compounds] (Bull, 2001; Nico et al., 2004; Mohajerani et al., 2018).

Figure 6 (blue bars) shows the results of the absorption of Cr(VI) and As(V) from a multi-ionic solution at pH 9.0. It can be seen that the absorption capacity of As(V) increases. This behavior is due to the effect of pH, as well as the fact that the arsenic oxyanions could interact with chromium oxyanions through covalent bonds and interactions of hydrogen bridges, favoring the electrostatic interaction between the quaternary

ammonium groups and the anions. Although the results obtained show a small difference, it is possible to note that there is competition for the quaternary ammonium functional groups between the chromate and arsenate ions. Moreover, these oxy-anions can form chelating bonds with the fixed groups composing the GGM structure.

CONCLUSION

GGM hemicellulose was successfully modified through a transesterification reaction with GMA, generating a macromonomer (GGM-GMA) with the ability to be used as a macro-crosslinker in free-radical polymerization reactions. ¹H-NMR spectroscopy reveals that it is possible to modify the GGM to obtain a GGM-GMA macromonomer. Results showed two peaks corresponding to the protons of the double bond –C=C– of the methacrylate group incorporated through the transesterification reaction.

Hydrogels with anion and cation exchange properties were synthesized successfully. The characterization demonstrated that the hydrogels possessed high hydrophilicity. FT-IR analysis showed that the GGM-GMA macromonomer was polymerized with the AMPSH and AMPTACl monomers, in which the signal corresponding to the alkene double bond disappears and the signals corresponding to the hydroxyl, quaternary ammonium, and sulfonate are intensified. TGA revealed the thermal stability of the hydrogels, and SEM/EDS was used to analyze the porous morphology and composition of the hydrogels.

The cationic hydrogel showed an efficient absorption capacity for Cr(VI) and As(V), and the anionic hydrogel reached

the maximum absorption capacity for Cu(II). The absorption capacities were influenced by pH, concentration, and repeated use. In addition, the absorption of metal ions from multi-ionic solutions using polymer blends showed good results compared with the absorption from mono-ionic solutions. It is also important to observe that polyanion and polycation interactions do not dramatically decrease metal ion removal, and it is possible to design systems focused on the removal of cations and anions simultaneously.

DATA AVAILABILITY STATEMENT

The raw data supporting the conclusions of this article will be made available by the authors, without undue reservation.

AUTHOR CONTRIBUTIONS

JS: synthesis and characterization of hydrogels, metal removal, discussion of experiments, and manuscript writing. DD: contribution in FT-IR and NMR spectroscopy analysis, discussion, and manuscript writing. YT: analysis and discussion of TGA analysis. CX: analysis of SEM micrographs, discussion of GGM, and manuscript writing. SW: analysis and discussion of GGM and manuscript writing. All authors contributed to the article and approved the submitted version.

ACKNOWLEDGMENTS

The authors thank FONDECYT, Project No. 1191336.

REFERENCES

- Almaroai, Y. A., Usman, A. R., Ahmad, M., Kim, K.-R., Vithanage, M., and Sik Ok, Y. (2013). Role of chelating agents on release kinetics of metals and their uptake by maize from chromated copper arsenate-contaminated soil. *Environ. Technol.* 34, 747–755. doi: 10.1080/09593330.2012.715757
- Al-Rudainy, B., Galbe, M., Arcos Hernandez, M., Jannasch, P., and Wallberg, O. (2019). Impact of lignin content on the properties of hemicellulose hydrogels. *Polymers* 11:35. doi: 10.3390/polym11010035
- Atta, A. M., Al-Lohedan, H. A., El-saeed, A. M., Tawfeek, A. M., and Wahby, M. H. (2017). Effect of titanium dioxide nanogel surface charges and particle size on anti-corrosion performances of epoxy coatings. *Int. J. Electrochem. Sci.* 12, 959–974. doi: 10.20964/2017.02.30
- Bull, D. C. (2001). The chemistry of chromated copper arsenate II. Preservative-wood interactions. *Wood Sci. Technol.* 34, 459–466. doi: 10.1007/s002260000066
- Çavuş, S., Yaşar, G., Kaya, Y., Gönder, Z. B., Gürdağ, G., and Vergili, I. (2016). Synthesis and characterization of gel beads based on ethyleneglycol dimethacrylate and 2-acrylamido-2-methyl-1-propane sulfonic acid: removal of Fe (II), Cu (II), Zn (II), and Ni (II) from metal finishing wastewater. *Process Safe. Environ. Protect.* 103, 227–236. doi: 10.1016/j.psep.2016.07.011
- Chen, A. Y.-Y., and Olsen, T. (2016). Chromated copper arsenate-treated wood: a potential source of arsenic exposure and toxicity in dermatology. *Int. J. Womens Dermatol.* 2, 28–30. doi: 10.1016/j.ijwd.2016.01.002
- Coudert, L., Blais, J.-F., Mercier, G., Cooper, P., Janin, A., and Gastonguay, L. (2014). Demonstration of the efficiency and robustness of an acid leaching process to remove metals from various CCA-treated wood samples. *J. Environ. Manag.* 132, 197–206. doi: 10.1016/j.jenvman.2013.11.028
- Dax, D., Chávez, M. S., Xu, C., Willför, S., Mendonça, R. T., and Sánchez, J. (2014). Cationic hemicellulose-based hydrogels for arsenic and chromium removal from aqueous solutions. *Carbohydr. Polym.* 111, 797–805. doi: 10.1016/j.carbpol.2014.05.045
- Dhillon, G. S., Rosine, G. M. L., Kaur, S., Hegde, K., Brar, S. K., Drogui, P., et al. (2017). Novel biomaterials from citric acid fermentation as biosorbents for removal of metals from waste chromated copper arsenate wood leachates. *Int. Biodeterior. Biodegradation* 119, 147–154. doi: 10.1016/j.ibiod.2016.09.014
- Elgueta, E., Sánchez, J., Dax, D., Xu, C., Willför, S., Rivas, B. L., et al. (2016). Functionalized galactoglucomannan-based hydrogels for the removal of metal cations from aqueous solutions. *J. Appl. Polym. Sci.* 133, 44093–44100.
- Farrukh, S., Mustafa, K., Hussain, A., and Ayoub, M. (2018). “Synthesis and applications of carbohydrate-based hydrogels,” in *Cellulose-Based Superabsorbent Hydrogels. Polymers and Polymeric Composites: A Reference Series*, ed. M. Mondal (Cham: Springer).
- Ferrarini, S. F., dos Santos, H. S., Miranda, L. G., Azevedo, C. M. N., Maia, S. M., and Pires, M. (2016). Decontamination of CCA-treated eucalyptus wood waste by acid leaching. *Waste Manag.* 49, 253–262. doi: 10.1016/j.wasman.2016.01.031
- Gezer, E. D., and Cooper, P. A. (2016). Effects of wood species and retention levels on removal of copper, chromium, and arsenic from CCA-treated wood using sodium hypochlorite. *J. Forest. Res.* 27, 433–442. doi: 10.1007/s11676-015-0172-3
- Härdelin, L., Bernin, D., Börjesson, M., Ström, A., and Larsson, A. (2020). Altered thermal and mechanical properties of spruce galactoglucomannan films

- modified with an etherification reaction. *Biomacromolecules* 21, 1832–1840. doi: 10.1021/acs.biomac.9b01730
- Heinze, T., Liebert, T., and Koschella, A. (2006). *Esterification of Polysaccharides*. Berlin: Springer Science & Business Media.
- Helsen, L., and Van den Bulck, E. (2005). Review of disposal technologies for chromated copper arsenate (CCA) treated wood waste, with detailed analyses of thermochemical conversion processes. *Environ. Pollut.* 134, 301–314. doi: 10.1016/j.envpol.2004.07.025
- Janin, A., Blais, J.-F., Mercier, G., and Drogui, P. (2009a). Selective recovery of Cr and Cu in leachate from chromated copper arsenate treated wood using chelating and acidic ion exchange resins. *J. Hazard. Mater.* 169, 1099–1105. doi: 10.1016/j.jhazmat.2009.04.066
- Janin, A., Zaviska, F., Drogui, P., Blais, J.-F., and Mercier, G. (2009b). Selective recovery of metals in leachate from chromated copper arsenate treated wastes using electrochemical technology and chemical precipitation. *Hydrometallurgy* 96, 318–326. doi: 10.1016/j.hydromet.2008.12.002
- Kong, W., Dai, Q., Gao, C., Ren, J., Liu, C., and Sun, R. (2018). “Hemicellulose-based hydrogels and their potential application,” in *Polymer Gels*, eds V. Thakur and M. Thakur (Singapore: Springer), 87–127. doi: 10.1007/978-981-10-6086-1_3
- Kramb, J., Konttinen, J., Backman, R., Salo, K., and Roberts, M. (2016). Elimination of arsenic-containing emissions from gasification of chromated copper arsenate wood. *Fuel* 181, 319–324. doi: 10.1016/j.fuel.2016.04.109
- Matos, R. C., Oliveira, H., Fonseca, H. M., Morais, S., Sharma, B., Santos, C., et al. (2020). Comparative Cr, As and CCA induced Cytostaticity in mice kidney: a contribution to assess CCA toxicity. *Environ. Toxicol. Pharmacol.* 73:103297. doi: 10.1016/j.etap.2019.103297
- Mohajerani, A., Vajna, J., and Ellcock, R. (2018). Chromated copper arsenate timber: a review of products, leachate studies and recycling. *J. Cleaner Product.* 179, 292–307. doi: 10.1016/j.jclepro.2018.01.111
- Nico, P. S., Fendorf, S. E., Lowney, Y. W., Holm, S. E., and Ruby, M. V. (2004). Chemical structure of arsenic and chromium in CCA-treated wood: implications of environmental weathering. *Environ. Sci. Technol.* 38, 5253–5260. doi: 10.1021/es0351342
- Ohgami, N., Yamanoshita, O., Thang, N. D., Yajima, I., Nakano, C., Weting, W., et al. (2015). Carcinogenic risk of chromium, copper and arsenic in CCA-treated wood. *Environ. Pollut.* 206, 456–460. doi: 10.1016/j.envpol.2015.07.041
- Rivas, B. L., Aguirre, M. D. C., and Pereira, E. (2006). Retention properties of arsenate anions of water-soluble polymers by a liquid-phase polymer-based retention technique. *J. Appl. Polym. Sci.* 102, 2677–2684. doi: 10.1002/app.24093
- Safa, M., O’Carroll, D., Mansouri, N., Robinson, B., and Curline, G. (2020). Investigating arsenic impact of ACC treated timbers in compost production (A case study in Christchurch, New Zealand). *Environ. Pollut.* 262:114218. doi: 10.1016/j.envpol.2020.114218
- Saha, B., and Orvig, C. (2010). Biosorbents for hexavalent chromium elimination from industrial and municipal effluents. *Coord. Chem. Rev.* 254, 2959–2972. doi: 10.1016/j.ccr.2010.06.005
- Sahiner, N., Demirci, S., Sahiner, M., Yilmaz, S., and Al-Lohedan, H. (2015). The use of superporous p (3-acrylamidopropyl) trimethyl ammonium chloride cryogels for removal of toxic arsenate anions. *J. Environ. Manag.* 152, 66–74. doi: 10.1016/j.jenvman.2015.01.023
- Sierra-Alvarez, R. (2009). Removal of copper, chromium and arsenic from preservative-treated wood by chemical extraction-fungal bioleaching. *Waste Manag.* 29, 1885–1891. doi: 10.1016/j.wasman.2008.12.015
- Tyagi, S., Sharma, B., Singh, P., and Dobhal, R. (2013). Water quality assessment in terms of water quality index. *Am. J. Water Res.* 1, 34–38. doi: 10.12691/ajwr-1-3-3
- Urbano, B. F., and Rivas, B. L. (2013). Synthesis, characterization, and sorption properties of water-insoluble poly (2-acrylamido-2-methyl-1-propane sulfonic acid)–montmorillonite composite. *Polym. Bull.* 70, 1143–1162. doi: 10.1007/s00289-012-0894-8
- Valle, H., Sánchez, J., and Rivas, B. L. (2015). Poly(N-vinylpyrrolidone-co-2-acrylamido-2-methylpropanesulfonate sodium): synthesis, characterization, and its potential application for the removal of metal ions from aqueous solution. *J. Appl. Polym. Sci.* 132:41272.
- Wilson, L. D., and Tewari, B. B. (2018). Chitosan-based adsorbents: environmental applications for the removal of arsenicals. *Mater. Res. Found.* 34, 133–160. doi: 10.21741/9781945291753-7
- Yan, R., Luo, D., Fu, C., Wang, Y., Zhang, H., Wu, P., et al. (2020). Harmless treatment and selective recovery of acidic Cu (II)-Cr (VI) hybrid wastewater via coupled photo-reduction and ion exchange. *Sep. Purif. Technol.* 234:116130. doi: 10.1016/j.seppur.2019.116130
- Zheng, S., Jiang, W., Rashid, M., Cai, Y., Dionysiou, D. D., and O’Shea, K. E. (2015). Selective reduction of Cr (VI) in chromium, copper and arsenic (CCA) mixed waste streams using UV/TiO₂ photocatalysis. *Molecules* 20, 2622–2635. doi: 10.3390/molecules20022622

Conflict of Interest: The authors declare that the research was conducted in the absence of any commercial or financial relationships that could be construed as a potential conflict of interest.

Copyright © 2021 Sánchez, Dax, Tapiero, Xu and Willför. This is an open-access article distributed under the terms of the Creative Commons Attribution License (CC BY). The use, distribution or reproduction in other forums is permitted, provided the original author(s) and the copyright owner(s) are credited and that the original publication in this journal is cited, in accordance with accepted academic practice. No use, distribution or reproduction is permitted which does not comply with these terms.



Isolating High Antimicrobial Ability Lignin From Bamboo Kraft Lignin by Organosolv Fractionation

Jinyan Yun^{1†}, Liao Wei^{2†}, Wei Li¹, Duqiang Gong¹, Hongyu Qin¹, Xiuqing Feng¹, Guojiang Li¹, Zhe Ling³, Peng Wang^{4*} and Baishuang Yin^{1*}

¹ College of Animal Science and Technology, Jilin Agricultural Science and Technology University, Jilin, China, ² Children's Hospital of Nanjing Medical University, Nanjing, China, ³ Co-innovation Center for Efficient Processing and Utilization of Forest Resources, College of Chemical Engineering, Nanjing Forestry University, Nanjing, China, ⁴ State Key Laboratory of Pharmaceutical Biotechnology, Department of Sports Medicine and Adult Reconstructive Surgery, Nanjing Drum Tower Hospital, The Affiliated Hospital of Nanjing University Medical School, Nanjing, China

OPEN ACCESS

Edited by:

Lei Wang,
Jeju National University, South Korea

Reviewed by:

Shaolong Sun,
South China Agricultural
University, China
Wenhui Geng,
North Carolina State University,
United States
Bailiang Xue,
Shaanxi University of
Technology, China

*Correspondence:

Peng Wang
15850681759@163.com
Baishuang Yin
ybs3421@126.com

[†]These authors have contributed
equally to this work and share first
authorship

Specialty section:

This article was submitted to
Industrial Biotechnology,
a section of the journal
Frontiers in Bioengineering and
Biotechnology

Received: 22 March 2021

Accepted: 13 April 2021

Published: 26 May 2021

Citation:

Yun J, Wei L, Li W, Gong D, Qin H,
Feng X, Li G, Ling Z, Wang P and
Yin B (2021) Isolating High
Antimicrobial Ability Lignin From
Bamboo Kraft Lignin
by Organosolv Fractionation.
Front. Bioeng. Biotechnol. 9:683796.
doi: 10.3389/fbioe.2021.683796

Lignin from different biomasses possess biological antioxidation and antimicrobial activities, which depend on the number of functional groups and the molecular weight of lignin. In this work, organosolv fractionation was carried out to prepare the lignin fraction with a suitable structure to tailor excellent biological activities. Gel permeation chromatography (GPC) analysis showed that decreased molecular weight lignin fractions were obtained by sequentially organosolv fractionation with anhydrous acetone, 50% acetone and 37.5% hexanes. Nuclear magnetic resonance (NMR) results indicated that the lignin fractions with lower molecular weight had fewer substructures and a higher phenolic hydroxyl content, which was positively correlated with their antioxidation ability. Both of the original lignin and fractionated lignins possessed the ability to inhibit the growth of Gram-negative bacteria (*Escherichia coli* and *Salmonella*) and Gram-positive bacteria (*Streptococcus* and *Staphylococcus aureus*) by destroying the cell wall of bacteria *in vitro*, in which the lignin fraction with the lowest molecular weight and highest phenolic hydroxyl content (L3) showed the best performance. Besides, the L3 lignin showed the ability to ameliorate *Escherichia coli*-induced diarrhea damages of mice to improve the formation of intestinal contents *in vivo*. These results imply that a lignin fraction with a tailored structure from bamboo lignin can be used as a novel antimicrobial agent in the biomedical field.

Keywords: lignin, bamboo, organosolv fractionation, antioxidation, antimicrobial property

INTRODUCTION

Lignin is the most abundant naturally phenolic composition in the cell wall of biomass, which is covalently linked with carbohydrates (mainly hemicellulose) to form lignin-carbohydrate complexes (LCC) (Huang et al., 2018; Jiang et al., 2018; Dong et al., 2020a). LCC is regarded as the obstacle for the utilization of biomass to prepare bio-chemicals and bio-polymers, due to the fact that it degrades the polymers (cellulose and hemicellulose) into monosaccharides. Hence, various technologies have been carried out to remove or degrade lignin to break down the firm construction of biomass. During the treatment process, lignin is dissolved in solvent systems, which can be recovered and regenerated for further application to prepare lignin-based adhesives, films,

carriers, fertilizer, et al. (Lateef et al., 2009; Sadeghifar and Ragauskas, 2020; Chen et al., 2021; Wang et al., 2021; Yu et al., 2021). In industry, lignin is mainly derived from black liquor produced in the kraft pulping process in papermaking, which is a by-product of pulp and paper making (Chen J. et al., 2020). Now, most of the black liquor is mainly used for energy supply and alkali recovery of papermaking, resulting in the waste of lignin resources. Therefore, the high-value utilization of kraft lignin (KL) from the pulping process has garnered attention in recent years (Dong et al., 2020b; Torres et al., 2020; Liu et al., 2021; Zhao et al., 2021).

In the cell wall of biomass, lignin is mainly formed by the units of syringyl, guaiacyl, and p-hydroxyphenyl, which are linked by β -O-4 aryl ethers, β - β (resinols), β -5 (phenylcoumarans), β -1 (spirodienones), and 5-5 and 4-O-5 linkages (Chen et al., 2018; Rencoret et al., 2019; Lin et al., 2020). During the cooking stage of pulp, these linkages suffer from degradation, resulting in lignin with a low molecule weight in solvent systems. Although the degradation of β -O-4 endows the obtained lignin with higher contents of phenolic and alcohol hydroxyl groups, the reactivity of lignin still fails to meet the requirement for further application (Tian et al., 2017; Liu et al., 2019). Hence, various technologies should be carried out to improve lignin's reactivity by improving the hydroxyl groups or reducing the molecular weight. Reported technologies mainly include thermal pyrolysis, reduction degradation, oxidation degradation, liquefied degradation, organosolv fractionation, et al. (Schutysen et al., 2018; Torres et al., 2020; Zheng Y. et al., 2021). Thermal pyrolysis has the ability to degrade the molecular weight of lignin, while the approach should be carried out at high temperatures (200–500°C). The reduction and oxidation degradation approach improves the functional groups in lignin, while the resulted lignin always contains different degraded products. Organosolv fractionation is a kind of solvent extraction approach, which is an excellent method to fractionate the lignin into the sample with the desired molecular weight and functional group content (Cui et al., 2014; Jiang et al., 2017; Allegretti et al., 2018).

Due to the existing phenolic and aliphatic hydroxyl groups, carboxyl groups, and methoxy groups in lignin, lignin possesses antibacterial and antioxidant abilities due to carbohydrates from the biomass (Figueiredo et al., 2018; Tao et al., 2021). Hence, lignin has been widely used as an additive in preparing rubber, plastic, foam, elastomer, and other composite materials to improve the strength of the material or endow the materials with the desired property (Bian et al., 2017; Nair et al., 2017; Chen S. L. et al., 2020). In recent years, the biological activities of lignin, such as anti-inflammatory, antioxidation, anticancer, and antimicrobial activities, have been gradually discovered and explored. Anti-oxidation is the main biological activity of lignin, as the hydroxyl groups in lignin endow it with the ability to scavenge the free radicals and reactive oxygen species (ROS) of cells under oxidative stress (Pei et al., 2020; Yu et al., 2020; Gu et al., 2021; Solihat et al., 2021; Zheng L. et al., 2021). The increased level of ROS in the cell can cause many human diseases by changing oxidative stress. For example, Zheng L. et al. (2021) found that lignin in LCC possessed the ability to scavenge the intracellular and endogenous ROS in osteoblast cells

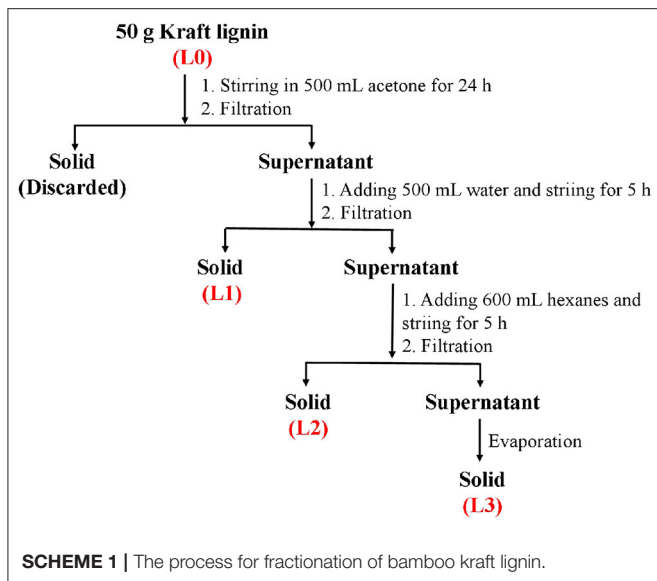
(MC3T3-E1) in an inflammatory environment and then promote osteoblast differentiation. In the work of Pei et al. (2020), they found that lignin and lignin derivatives from different biomasses showed good performance in scavenging free radicals and ROS *in vitro* and *in vivo*, showing an excellent capability to inhibit the aggregation of polyQ protein by reducing the existing ROS in neuronal cells. Generally, the scavenging ability of lignin for ROS is dependent on the quantity of the hydroxyl groups. Hence, seeking lignin fractions with a sufficient amount of hydroxyl groups from kraft lignin is necessary to improve its antioxidation ability. It is well-known that the inhibiting ability of lignin against microorganism growth is related to its antioxidation ability (Yang et al., 2018; Xu et al., 2019). In addition, bacterial diarrhea is a common infectious disease in animal husbandry due to different bacteria, which has brought great losses to economic development. Although antibiotics are effective in preventing the occurrence and development of bacterial infections, their adverse effects will ultimately endanger human health through the food chain (Founou et al., 2016). Therefore, seeking an effective and green extract from different biomasses to treat bacterial infection-induced diarrhea is necessary. Many works showed that lignin from biomass had strong antimicrobial activities for pathogenic bacteria. Most of the evaluations were just carried out at a cell level *in vitro*. Hence, investigating the antimicrobial ability of lignin for pathogenic bacteria *in vivo* is necessary to understand if it can be applied in living animals.

In this work, an industrially feasible organosolv fractionation with different solvents by sequential precipitation was carried out to fractionate kraft lignin into the sample with low molecular weight and high functional groups content, which aimed to improve its antimicrobial activities for bacteria. The chemical structures of obtained lignin were characterized by various technologies. The *in vitro* antioxidant activities of the obtained lignin were evaluated by scavenging capabilities for free radicals. The antimicrobial ability was evaluated by analyzing the inhibition growth for Gram-negative bacteria [*Escherichia coli* (*E. coli*) and *Salmonella*] and Gram-positive bacteria [*Streptococcus* and *Staphylococcus aureus* (*S. aureus*)] *in vitro*. Moreover, the diarrheal mice model induced by *E. coli* were fed with a lignin fraction with the best antioxidant activity to evaluate its antimicrobial ability *in vivo*.

MATERIALS AND METHODS

Materials and Reagents

Five-year-old moso bamboo was acquired from the planting bases in Yibin, China. The moso bamboo was cut into 3–5 cm chips for kraft pulping. The Gram-negative bacteria of *Escherichia coli* (*E. coli*, ATCC-25922), *Salmonella* (ATCC-14028), and Gram-positive bacteria of *Streptococcus* (ATCC-21059) and *Staphylococcus aureus* (*S. aureus*, ATCC-25923) were purchased from China Microbial Culture Preservation Center. Thirty-six Balb/c mice (weight ~20 g), half male and half female, were purchased from the Jitai Animal Products Agency in Chaoyang District. All used chemicals were analytical grade without being purified for use.



Preparing the Kraft Lignin and Fractionation of Kraft Lignin

Kraft pulping with Na_2S and NaOH was carried out to obtain the black liquor from the bamboo at the conditions of 20% sulfidity, 25% effective alkali charge, and a solid-to-liquid ratio of 1:6 at 160°C for 60 min, as per the work of Huang et al. (2017). The dissolved kraft lignin in black liquor was obtained by acid-precipitation. The obtained kraft lignin was washed by distilled water to remove the residual chemicals and air-dried for further use.

Fractionation of kraft lignin was carried out according to **Scheme 1**. Specifically, 50 g of air-dried kraft lignin was dispersed into 500 mL of acetone and stirred at 250 rpm for 24 h. After stirring, the solution was filtrated to obtain the supernatant. Then, 500 mL of distilled water was mixed with the obtained supernatant and stirred at 250 rpm for 5 h. The precipitate (L1) was obtained by filtration. The resulting supernatant was further mixed with 600 mL of hexanes and stirred at 250 rpm for 5 h. After stirring, the solution was filtrated to obtain the precipitate (L2) and supernatant. Then, rotary evaporation was carried out to remove the solvent in the supernatant to obtain the solid (L3). The obtained solids were dried in a vacuum drying oven and weighed to calculate their recovery yields.

Characterization of Fractions From Kraft Lignin

The molecular weight of obtained lignin fractionations was analyzed by a Waters Gel Permeation Chromatography (GPC) instrument, which was equipped with a PL-gel 10 mm mixed-B 7.5 mm i.d. column and an ultraviolet detector. The GPC analysis was carried out using tetrahydrofuran as eluent at a 1 mL/min flow rate.

A Bruker AVANCE 600 MHz nuclear magnetic resonance (NMR) spectrometer equipped with a 5 mm BBO probe was

used to characterize the structures of lignin fractionations. 2D-HSQC NMR analysis was carried out to get the information of linkages and units in lignins. The acquisition parameters were 160 transients from 1,024 data points (53 ms) for the F2 (^1H) dimension and 256 data points (5.14 ms) for the F2 (^{13}C) dimension. Quantitative ^{31}P NMR analysis was carried out to determine the content of the hydroxyl groups and carboxyl groups in lignins. The detailed lignin preparation and acquisition parameters for NMR analysis were carried out according to the work of Pei et al. (2020).

Antioxidant Activity Analysis of Fractions From Kraft Lignin

The *in vitro* antioxidant activity of the lignin fractionations were evaluated by scavenging capabilities on DPPH and $\text{O}_2^{\cdot-}$ radicals. For the DPPH scavenging assay, 3.0 mL of DPPH (0.2 mM) solution (dissolving in anhydrous ethanol) and 3.0 mL of ethanol were added to 3 mL of different concentrations of lignin solution (0.1–1 mg/mL, dissolving in anhydrous ethanol), respectively. After 30 min, the supernates of these mixtures were obtained to measure their absorbance at 517 nm, which were termed as D_{sample} and D_{control} , respectively. In addition, 3.0 mL of ethanol was added to 3 mL of DPPH (0.2 mM) solution, and the absorbance of the mixtures was measured at 517 nm, termed as D_{blank} . The DPPH radical scavenging rate (P) was calculated by the following equation:

$$P(\%) = \frac{1 - (D_{\text{sample}} - D_{\text{control}})}{D_{\text{blank}}} \times 100\%$$

For the $\text{O}_2^{\cdot-}$ scavenging assay, 1.0 mL of lignin solution (0.1–1 mg/mL) was mixed with 4.5 mL of Tris-HCl solution (0.05 mol/L with pH 8.2) in a tube and incubated at 25°C for 20 min. Then, 0.5 mL of pyrogallol solution (45 mmol/L) was added to the tube. After the addition of pyrogallol solution, the absorbance of the mixture was measured at 325 nm every 30 s, termed as O_{sample} . Meanwhile, 0.5 mL of water was used to replace the pyrogallol solution in the system. The supernate from this mixture was obtained to measure its absorbance at 325 nm, which was termed as O_{control} . In addition, 1.0 mL of water ethanol was mixed with 4.5 mL of Tris-HCl solution (0.05 mol/L with pH 8.2) in a tube to measure the absorbance at 325 nm, termed as O_{blank} . $\text{O}_2^{\cdot-}$ radical scavenging rate (R) was calculated by the following equation:

$$R(\%) = \frac{1 - (O_{\text{sample}} - O_{\text{control}})}{O_{\text{blank}}} \times 100\%$$

Antimicrobial Activity Analysis of Fractions From Kraft Lignin

Antimicrobial Activity Analysis by Microdilution Method

The antimicrobial activity of the lignin fractionations was tested against Gram-negative bacteria *E. coli* and *Salmonella* and Gram-positive bacteria of *Streptococcus* and *S. aureus* using the microdilution method. The lignin solution was mixed with the bacteria with a density of 1.0×10^6 CFU/mL and incubated

at 37°C for 12 h. The absorbance value of OD at 620 nm was measured by an enzyme plate analyzer, and the optimal inhibitory effect of lignin on bacteria was evaluated by calculating the reduction of the number of bacteria in the medium.

Antimicrobial Activity Analysis by Agar Media Method

The agar media method was also carried out to further analyze the antimicrobial activity of lignin. Specifically, the bacterial colonies formed on LB-agar plates calculated the inhibition rate of lignin for bacteria. A suspension of 200 colonies in LB agar medium was carried out in triplicate to analyze the antimicrobial activity of lignin with different concentrations (0.4–1.6 mg/mL) against each tested bacteria.

Extracellular Protein Assay

The lignin with the best antimicrobial activity was co-incubated with the tested bacteria for 12 h at a constant temperature of 200 rpm/min at 37°C. The bacterial suspension was centrifuged at 4,000 rpm/min for 10 min to get the supernatant and incubated bacteria. The absorbance value of the supernatant at 595 nm was determined with the BCA protein quantitative kit. Each sample was tested three times in parallel, and the bacterial liquid without extract was used as blank control to calculate the protein concentration of the supernatant. The incubated bacteria were dehydrated with graded ethanol and resuspended by ethyl alcohol for scanning electron microscope (SEM) analysis, which aimed to investigate the changes of the bacterial membrane.

Animal Experiment

Thirty-six Balb/c mice (weight ~20 g), half male and half female, were used to analyze the *in vivo* antimicrobial activity of lignin. The animal experimental protocol was approved by the Animal Ethics Committee of Jilin Agricultural Science and Technology University (No: AWEC2017A01). In order to establish the mice diarrhea model, 200 μ L of *E.coli* (1×10^9 CFU/mL) was injected into the mice by intraperitoneal injection. The lignin solution was irrigated into the mice with a dosage of 2 mg/10 g body weight after diarrhea symptoms appeared in the mice. Seven days after the treatment, the diarrhea status, intestinal inflammation, and colon histological sections of the mice were observed to evaluate the antimicrobial activity of lignin *in vivo*.

Statistical Analysis

All the results were expressed as mean \pm standard deviation. Data were analyzed by one-way analysis of variance (ANOVA) using SPSS (2008) statistical software. Statistical analysis with different asterisks were expressed as * $p < 0.05$, ** $p < 0.01$, *** $p < 0.005$, **** $p < 0.001$.

RESULTS AND DISCUSSION

Recovery Yield and Molecular Weight of Lignin Fractions

In this work, the kraft lignin from bamboo was fractionated into three fractions (L1, L2, and L3) according to the described protocol in **Scheme 1**. The recovery yields of these fractions are shown in **Table 1**. It was shown that anhydrous acetone showed

TABLE 1 | The fractionation yields and molecular weight of lignin fractions.

	Yield (%) ^a	Mw (g/mol)	Mn (g/mol)	PDI (Mw/Mn)
L0	/	5,070	1,432	3.5
L1	22.5	7,260	3,090	2.3
L2	19.6	3,480	1,440	2.4
L3	11.9	1,810	950	1.9

^aBased on the initial L0 weight.

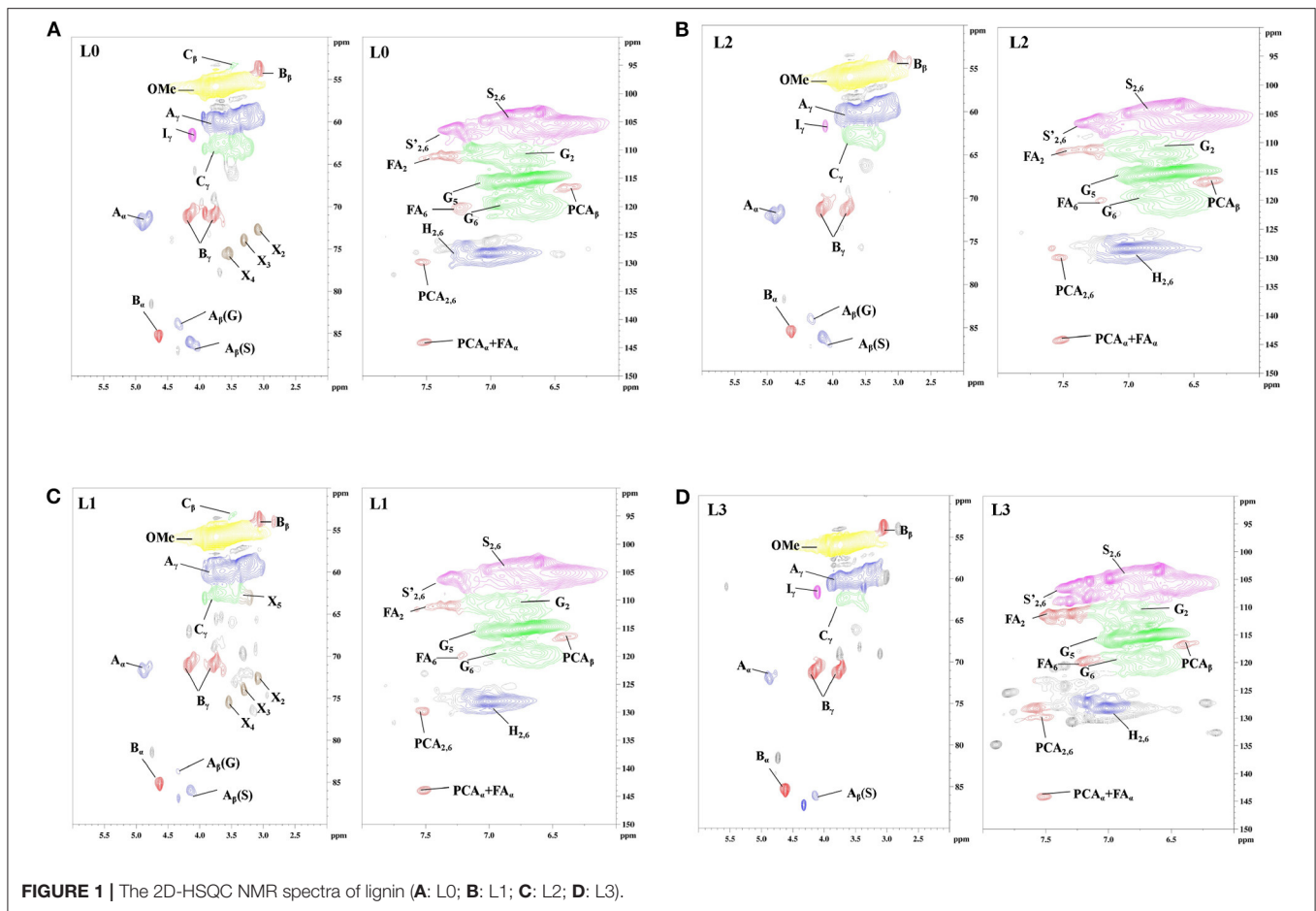
the highest ability to dissolve the lignin with a yield of 22.5%. The lignin fractions obtained from 50% acetone and 37.5% hexane fractionations had yields of 19.6 and 11.9%, respectively. The decreased yield of obtained lignin fractions might be due to the lower polarity of the solvent system, which can dissolve the low molecular weight lignin *via* aromatic π - π interactions (Cui et al., 2014; Jiang et al., 2017).

The molecular weight of different lignin fractions was analyzed and is shown in **Table 1**. It was shown that organosolv fractionation with different solvents had the ability to fractionate the original lignin (L0) into the fractions with different molecular weights. The weight-average (Mw) and number-average (Mn) molecular weight of L0 were 5,070 and 1,432 g/mol, respectively. After sequent fractionation by anhydrous acetone, higher molecular weight lignin (L1) was obtained. While, with sequent fractionation by 50% acetone and 37.5% hexanes, lower molecular weight lignins were obtained with Mw values of 3,480 g/mol (L2) and 1,810 g/mol (L3), respectively. In addition, sequent fractionation dramatically reduced the heterogeneity of original lignin, which decreased the polydispersity index (PDI = Mw/Mn) of L0 from 3.5 to 2.3 and 1.9. This observation was also been found in the work of Cui et al. (2014), who isolated narrow fractions from softwood kraft lignin by fractional precipitation with hexanes and acetone. The higher monodispersity and lower molecular weight of L2 and L3 can endow these fractions with better reactivity and biological activity.

NMR Characterization of Lignin Fractions

In order to understand how the structural changes of lignin linkages of kraft lignin during organosolv fractionation with different solvents, 2D-HSQC NMR spectra of all lignin samples were obtained and are shown in **Figure 1**. The main lignin cross-signals (**Supplementary Table 1**) in the spectra are assigned by aligning the signals in the reported work of Wen et al. (2012), Dong et al. (2020b), and Pei et al. (2020). The main substructures of lignin in the spectra are depicted in **Figure 2**.

In the side-chain regions (δ_C/δ_H 50–90/2.5–6.0) of all lignin's spectra, β -O-4 (A), β - β (B), and β -5 (C) substructures could be clearly observed by their corresponding C-H correlations. Specifically, the C_a - H_a correlations for β -O-4, β - β , and β -5 were shown at δ_C/δ_H 72.1/4.89, 84.9/4.65 and 86.9/5.51, respectively. Two C_β - H_β signals of β -O-4 substructure were observed at δ_C/δ_H 86.1/4.12 and 83.2/4.32, which were attributed to β -O-4 which was linked to the syringyl units (S) and guaiacyl units (G) in lignin. Signals at δ_C/δ_H 71.4/4.20, 3.81 and 53.5/3.39 were attributed the C_β - H_β correlations for β - β and β -5 substructures,



respectively. In the side-chain regions (δ_C/δ_H 160-90/8.0-6.0) of L3 spectra (Figure 1D), the signals for β -O-4 linked to G units were absent, indicating that this substructure might not have survived the organosolv fractionation process in the lignin fraction with the lowest molecular weight. In the aromatic region of all lignin spectra, the syringyl units (S), guaiacyl units (G), and *p*-hydroxyphenyl units (H) in fractionated lignins were also observed through their signals. S units, S units with $C_a = O$ groups (S'), and H units in lignin were identified by their $C_{2,6}$ - $H_{2,6}$ signals at δ_C/δ_H 104.2/6.75, 106.9/7.29, and 128.2/7.01, respectively. The G units showed C-H signals at δ_C/δ_H 111.1/6.75, 116.4/6.73, and 119.9/6.83, which were attributed to the C_2 - H_2 , C_5 - H_5 , and C_6 - H_6 correlations, respectively. In addition, the signals for the ferulate and *p*-coumarate, which are the phenolic compounds possessing antioxidant capacity (Jiang et al., 2018; Zheng L. et al., 2021), were also found in all lignin fractions by identifying their cross-peaks of correlations. Overall, the signals in all spectra indicated that the substructures of the obtained lignin fractions (L1, L2, and L3) did not change during the organosolv fractionation process.

The quantification of the substructures in lignin units were carried out to understand the changes of the interunit linkages of lignin. The amount of lignin substructures were calculated by their intensities in 2D-HSQC spectra and expressed per 100 Ar

(Table 2). It was shown that the amount of β -O-4 substructures in F0, F1, F2, and F3 were 18.8/100 Ar, 13.5/100 Ar, 12.5/100 Ar, and 69.1/100 Ar, respectively. For the β - β and β -5 substructures in F1, F2, and F3, their amount also decreased as their molecular weight went down. These results indicated that sequent fractionation by anhydrous acetone, 50% acetone and 37.5% hexanes, was the approach to obtain lignin fractions with lower substructures along with their decreased molecular weight. In the work of Yang et al. (2018), they also found that the substructures content of different lignin fractions by organosolv fractionation exhibited decreasing trends with their molecular weight gradient.

The functional groups of each lignin fractions were quantitatively analyzed from quantitative ^{31}P NMR analyses and are shown in Table 3. For all the lignin fractions from L0, a decreased order for the contents of aliphatic hydroxyl and increased order for the contents of phenolic hydroxyl were consistent in the sequence of the fractionation process. Specifically, the aliphatic hydroxyl content of F1 was 3.21 mmol/g, which was higher than that of F2 (3.19 mmol/g) and F3 (2.04 mmol/g). The phenolic hydroxyl content of F1, F2, and F3 were in the increased order of 2.78, 2.89, and 3.66 mmol/g. These results were in agreement with the work of Cui et al. (2014) and Brodin et al. (2009), who reported that the amount of functional groups in the lignin fractions obtained by membrane

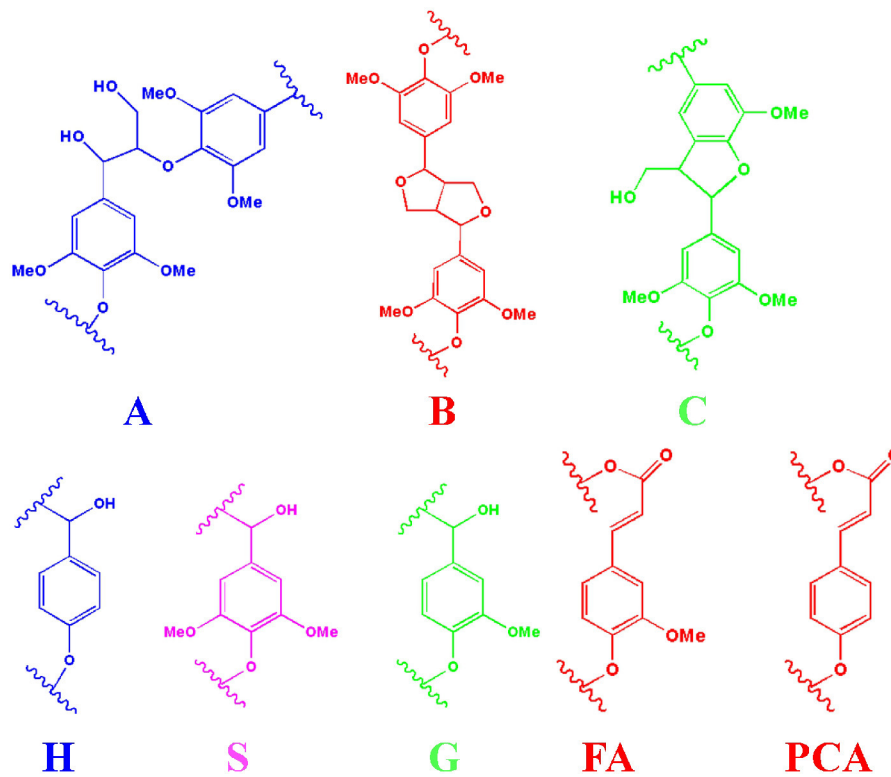


FIGURE 2 | The main substructures of lignin in the spectra (A: β -O-4 substructures; B: resinol substructures; C: phenylcoumaran substructures; H: *p*-hydroxyphenyl units; S: syringyl units; G: guaiacyl units; FA: ferulate; PCA: *p*-coumarate).

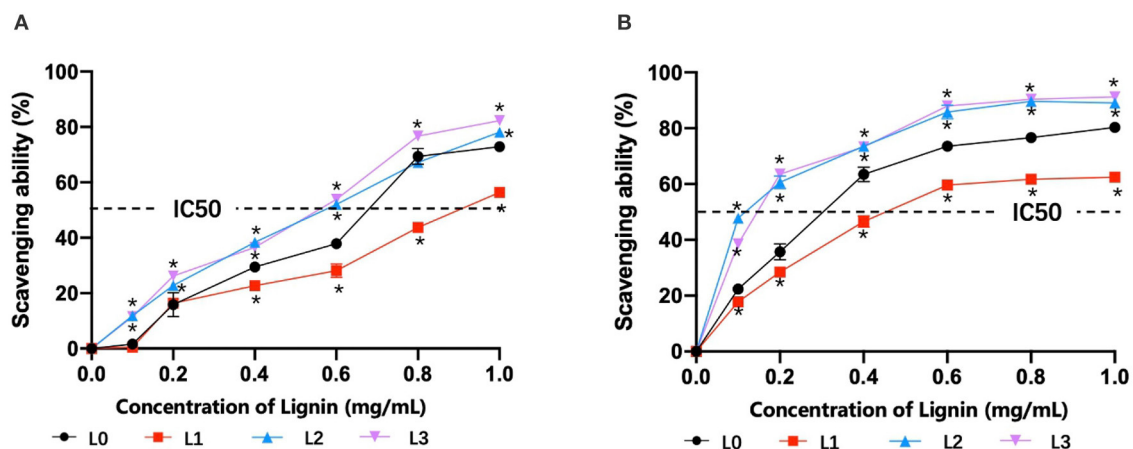


FIGURE 3 | The scavenging abilities of lignin for DPPH radicals (A) and O_2^- radicals (B) (* $p < 0.05$).

filtration and organosolv fractionation were directly related to their molecular weight. In the work of Yang et al. (2018), the antioxidant and antimicrobial capacities of lignin were found to be related to the phenolic hydroxyl group in the lignin structure. Hence, it was speculated that the obtained lignin fraction of L3 with the highest amount of phenolic hydroxyl content might have the best biological activity.

Antioxidant Activity Analysis of Lignin Fractions

To analyze the antioxidant activity of lignin fractions, their scavenging abilities for DPPH and O_2^- radicals were tested and are shown in Figure 3. It showed that the scavenging abilities for DPPH radicals (Figure 3A) and O_2^- radicals (Figure 3B) were increased with the dosage of lignin fractions, in which L3 showed

TABLE 2 | Quantitative amount of substructures in lignin fractions.

	Amount of lignin substructures [100 Ar (C900)] ^a			Percentage of lignin unit (%) ^b		
	β -O-4 (A)	β - β (B)	β -5 (C)	S	G	H
F0	18.8	5.6	0.9	48.8	25.4	25.9
F1	13.5	4.3	0.6	47.4	24.7	27.9
F2	12.5	2.1	0.6	50.8	24.7	23.5
F3	9.1	2.1	0.5	51.0	24.5	24.5

^aThe amounts were calculated based the following formula: $IC900 = 0.5 \times IS_{2,6} + IG_2 + 0.5 \times IH_{2,6}$ $IX\% = IX/IC900 \times 100\%$; where IX is the integral value of a position signal in the lignin sub-linkages (β -O-4, β - β , and β -5) in the 2D spectra region.

^bMolar percentages $S + G + H = 100\%$.

TABLE 3 | The contents of functional groups in lignin fractions (mmol/g).

	Aliphatic hydroxyl	Phenolic hydroxyl		Total phenolic hydroxyl	COOH
		Condensed phenolic OH	Non-condensed phenolic OH		
F0	2.98	1.12	1.59	3.71	0.12
F1	3.21	1.22	1.56	2.78	0.11
F2	3.19	1.23	1.66	2.89	0.12
F3	2.04	1.45	2.21	3.66	0.11

the best performances at higher concentrations. IC₅₀ values, the concentration required for 50% scavenging of the free radical, are generally considered to evaluate the radical scavenging activity of the lignin. From the plotted line in **Figures 3A,B**, it was found that L2 and L3 possessed comparable values for DPPH radicals (0.09 and 0.11 mg/mL) and O₂⁻ radicals (0.56 and 0.57 mg/mL), respectively, which was lower than that of L0 (0.29 mg/mL for DPPH radicals and 0.68 mg/mL for O₂⁻ radicals) and L1 (0.46 mg/mL for DPPH radicals and 0.90 mg/mL for O₂⁻ radicals). These results indicated that L2 and L3 had the best antioxidant activity, which was against with our initial speculation that L3 with the highest phenolic hydroxyl content would possess the best antioxidant ability. The reason for this phenomenon might be explained by the fact that the existing phenolic substances (PCA and FA) in lignin fractions also contribute to its antioxidant ability, in which their amount in L2 and L3 are different (Jiang et al., 2020; Zheng L. et al., 2021).

In vitro Antimicrobial Behavior of Lignin Fractions

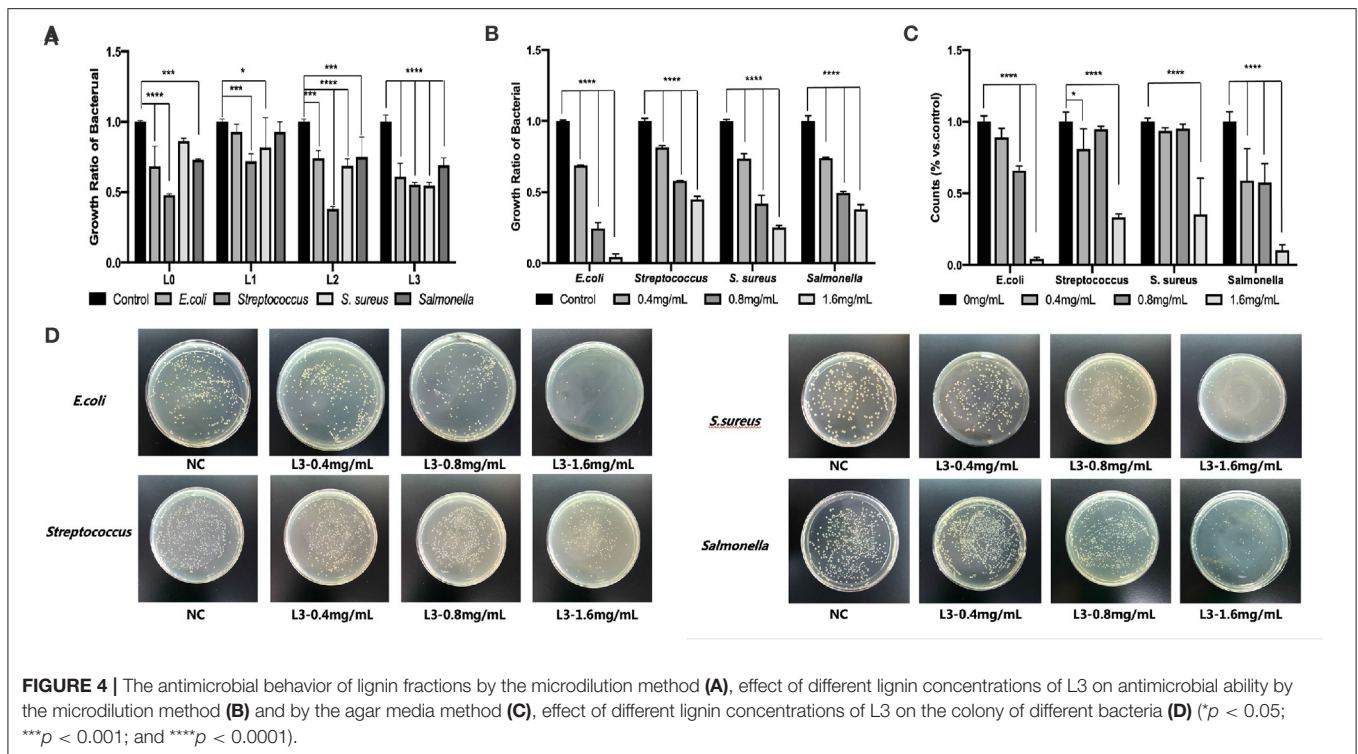
Bacterial diarrhea is a common infectious disease from Gram-negative bacteria and Gram-positive bacteria in animal husbandry, which has brought great losses to economic development. Although antibiotics are effective in preventing the occurrence and development of bacterial infections, their adverse effects will ultimately endanger human health through the food chain (Founou et al., 2016). In order to demonstrate the antimicrobial activity of lignin fractions, *in vitro* assays by the microdilution method were performed using *E.coli*, *Salmonella*, *Streptococcus*, and *S. aureus*, which are common bacteria with strong virulence for diarrhea. **Figure 4A** shows that both the original lignin (L0) and fractionated lignins (L1, L2, and L3) displayed excellent inhibitory effects on all bacteria

by significantly inhibiting their growth, of which L3 had the strongest antimicrobial activity. This might be due to its high content of phenolic hydroxyl groups and lowest molecular weight (Li et al., 2007). Therefore, the antimicrobial properties of lignin L3 were explored in detail in subsequent research.

Figure 4B shows that the L3 lignin significantly decreased the growth and reproduction of *E. coli*, *Salmonella*, *Streptococcus*, and *S. aureus*, which the degree of antimicrobial properties was dependent on the lignin's concentration by the microdilution method. In addition, the L3 lignin showed the best antimicrobial ability for *E. coli*, and a comparable ability for *Salmonella*, *Streptococcus*, and *S. aureus*. For example, an inhibition ratio of 95.61% was found for *E. coli* treated with 1.6 mg/mL of L3, which was higher than that for *Salmonella* (89.60%), *Streptococcus* (66.62%), and *S. aureus* (64.68%). The remarkable inhibitory effect of the L3 lignin on different bacteria in a dose-dependent manner could also be observed from the statistical results (**Figure 4C**) from antimicrobial assays by the agar media method, which were calculated from colony-counting results in **Figure 4D**. Compared to the control group, a debasement of formed bacterial colonies was observed in the groups treated with the L3 lignin with increased concentrations from 0.4 mg/mL to 1.6 mg/mL, indicating the excellent antimicrobial property of the L3 lignin. For example, the colonies of *E. coli*, *Streptococcus*, *S. aureus*, and *Salmonella* were, respectively, decreased from 89, 81, 94, and 59% to 4, 33, 35, and 10% when they were incubated with the L3 lignin with concentrations from 0.4 to 1.6 mg/mL.

Effect of the L3 Lignin on Bacterial Cell Wall

In the work of Medina et al. (2016) and Kaur et al. (2017), they reported that lignin had an inhibitory effect on *Bacillus subtilis*, *E. coli*, *Salmonella*, *Listeria*, *S. aureus*, and *Klebsiella*, which may



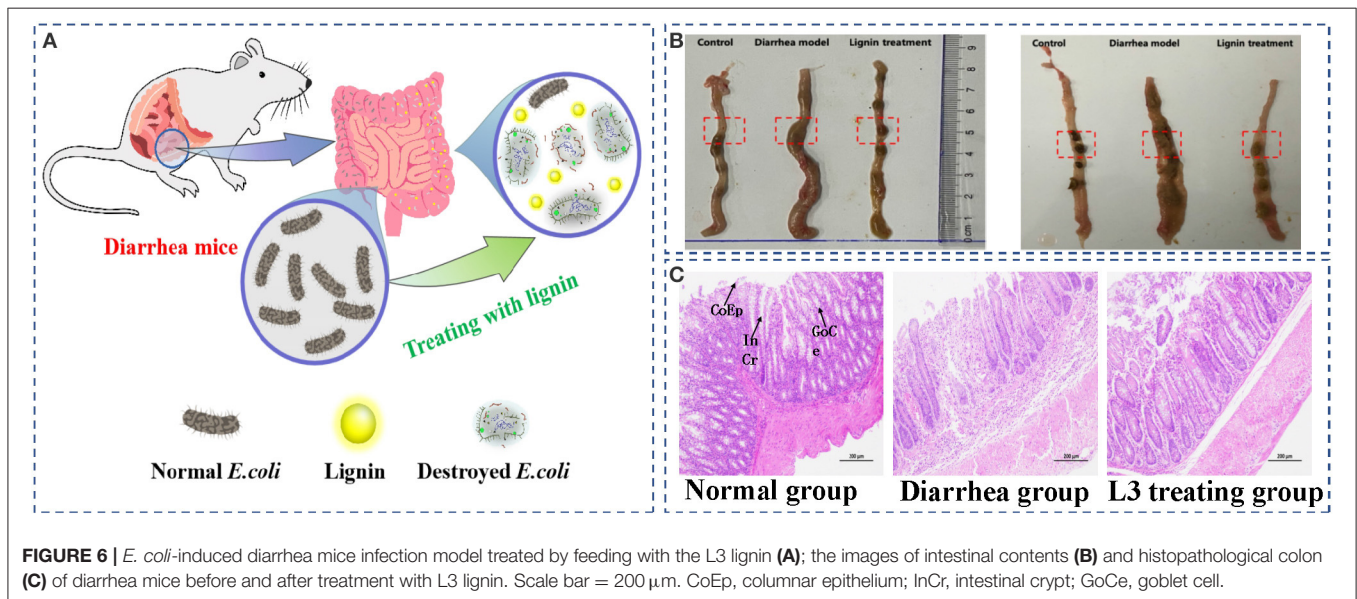
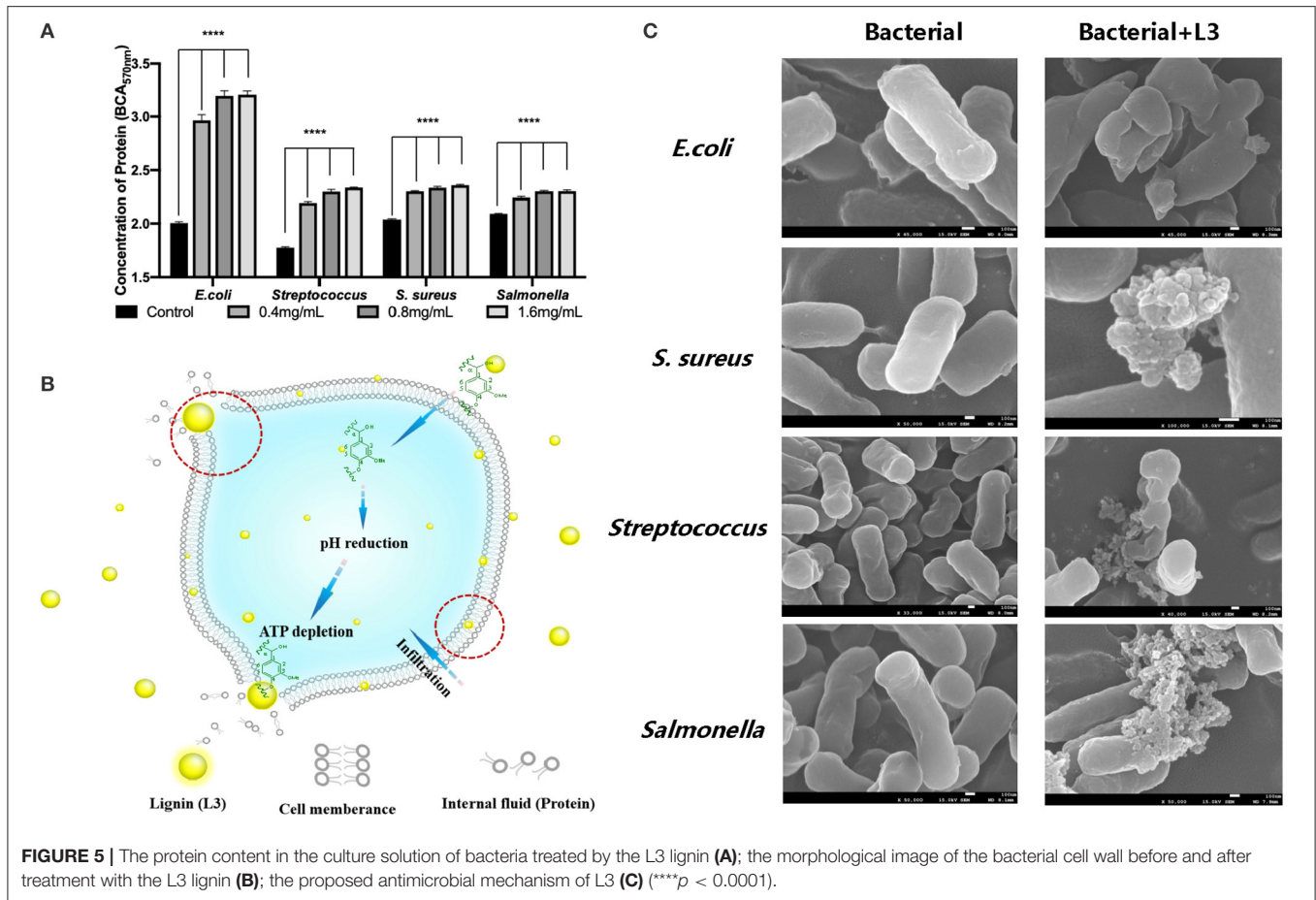
be due to its greater influence on deconstructing the cell wall of bacteria, thus hindering the growth and reproduction of bacteria. In addition, the protein content in the supernatant reflected the damage degree of the bacterial cell wall (Chung and Chen, 2008; Rojas et al., 2018). To understand how L3 affects the cell wall of bacteria, the changes of bacterial cytoderm were investigated by analyzing the released protein content in culture solution.

Figure 5A shows that the protein content of the blank group was maintained at a very low level without significant changes. After treatment with the L3 lignin, the protein content in the culture solution was significantly higher than that in the blank control group, indicating that lignin L3 caused damage to the cytoderm of the bacteria, and the degree of damage was proportional to the increased concentration. Under the action of lignin L3, the protein content in the supernatant increased in a dose-dependent manner, which indicated that the effect of pathogenic damage was strong, especially for *E. coli*. The damages of the different bacteria cell walls were also identified by their morphological changes (Figure 5B). The intact and smooth cell wall could be observed from the morphology images of normal bacterial cells. While, obvious damage resulting in the wizened membranes was formed for the bacteria after being treated with the L3 lignin. The antimicrobial effect of the L3 lignin may be due to the creation of a low pH environment on the cell membrane, which destroyed the proton dynamics of the cell membrane. Polyphenols in lignin have the capacity to damage cell walls by lysis, resulting in effective leakage of the internal fluid, which may be related to the strong antioxidant effects of lignin (Jiang et al., 2020). On the other hand, a large number of reactive oxygen species (ROS) are concentrated on the surface

of lignin. When lignin makes contact with bacteria, ROS may release and induce oxidative stress by changing its normal redox physiological process (Lobo et al., 2010; Yang et al., 2018; Wang et al., 2019; Zheng L. et al., 2021). In this work, with the increase of lignin concentration, the content of soluble protein in the culture medium increased, indicating that the cell membrane of the tested bacteria was damaged and its normal life activities were affected. Hence, the antimicrobial mechanism of L3 was proposed and is shown in Figure 5C.

In vivo Antimicrobial Behavior of the L3 Lignin

To evaluate the *in vivo* antimicrobial behavior of the L3 lignin, an *E. coli*-induced diarrhea mice infection model treated by feeding with the L3 lignin was performed (Figure 6A). The results of the necropsy (Figure 6B) showed that there was colon congestion and swelling in the model group, while the intestinal swelling and hyperemia of the mice treated with lignin were remitted, and inflammation was alleviated. Compared with the control group, the intestinal contents of mice in the diarrhea model group included yellow loose stool and were unformed. However, the diarrhea status of mice in the lignin treatment group was somewhat reduced, indicating that lignin could relieve the *E. coli*-induced diarrhea. Histopathological analyses (Figure 6C) were further carried out to investigate the effects of the L3 lignin on *E. coli*-induced diarrhea. The results of the histological features including crypt shortening, edema, mucosal erosions, and infiltration of inflammatory cells in lamina propria were observed in the diarrhea mice group (Wang et al.,



2019). Unexpectedly, mice with diarrhea treated with the L3 lignin reflected reduced histological changes for pathological inflammation compared with the diarrhea mice group. The results indicated that the L3 lignin exerted obvious protective

effects on bacterial infection-induced intestinal damage in mice. These results showed that the L3 lignin had the ability to ameliorate *E. coli* diarrhea damages, which showed an excellent *in vivo* antimicrobial behavior.

SUMMARY

In this work, the lignin fraction with decreased molecular weight and increased phenolic hydroxyl contents could be successfully prepared from bamboo kraft lignin by sequential organosolv fractionation with anhydrous acetone, 50% acetone and 37.5% hexanes. The antioxidation and antimicrobial properties of the lignin fractions were related to their inherent structural properties. Due to the excellent antioxidation and antimicrobial abilities *in vitro*, the L3 lignin fraction was able to ameliorate *E. coli*-induced diarrhea damages of mice to improve the formation of intestinal contents *in vivo*. All the obtained results indicated that the proposed organosolv fractionation was an excellent way to prepare the high antimicrobial ability lignin from bamboo kraft lignin, which can be further applied in different biomedical fields.

DATA AVAILABILITY STATEMENT

The original contributions presented in the study are included in the article/**Supplementary Material**, further inquiries can be directed to the corresponding authors.

ETHICS STATEMENT

The animal experimental protocol was approved by the Animal Ethics Committee of Jilin Agricultural Science and Technology

REFERENCES

- Allegretti, C., Fontanay, S., Krauke, Y., Luebbert, M., Strini, A., Troquet, J., et al. (2018). Fractionation of soda pulp lignin in aqueous solvent through membrane-assisted ultrafiltration. *ACS Sustain. Chem. Eng.* 6, 9056–9064. doi: 10.1021/acssuschemeng.8b01410
- Bian, H., Chen, L., Dai, H., and Zhu, J. Y. (2017). Integrated production of lignin containing cellulose nanocrystals (LCNC) and nanofibrils (LCNF) using an easily recyclable di-carboxylic acid. *Carbohydr. Polym.* 167, 167–176. doi: 10.1016/j.carbpol.2017.03.050
- Brodin, I., Sjöholm, E., and Gellerstedt, G. (2009). Kraft lignin as feedstock for chemical products: the effects of membrane filtration. *Holzforschung* 63, 290–297. doi: 10.1515/HF.2009.049
- Chen, B. Y., Zhao, B. C., Li, M. F., and Sun, R. C. (2018). Characterization of lignins isolated with alkali from the hydrothermal or dilute-acid pretreated rapeseed straw during bioethanol production. *Int. J. Biol. Macromol.* 106, 885–892. doi: 10.1016/j.ijbiomac.2017.08.090
- Chen, J., Fan, X. L., Zhang, L. D., Chen, X. J., Sun, S. L., and Sun, R. C. (2020). Research progress in lignin-based slow/controlled release fertilizer. *Chem. Sus. Chem.* 13, 4356–4366. doi: 10.1002/cssc.202000455
- Chen, S. L., Wang, G. H., Sui, W. J., Parvez, A. M., Dai, L., and Si, C. L. (2020). Novel lignin-based phenolic nanosphere supported palladium nanoparticles with highly efficient catalytic performance and good reusability. *Ind. Crops. Prod.* 145:112164. doi: 10.1016/j.indcrop.2020.112164
- Chen, X. J., Li, Z. H., Zhang, L. D., Wang, H. R., Qiu, C. Z., Fan, X. L., et al. (2021). Preparation of a novel lignin-based film with high solid content and its physicochemical characteristics. *Ind. Crops Prod.* 164:113396. doi: 10.1016/j.indcrop.2021.113396
- Chung, Y. C., and Chen, C. Y. (2008). Antibacterial characteristics and activity of acid-soluble chitosan. *Bioresour. Technol.* 99, 2806–2814. doi: 10.1016/j.biortech.2007.06.044

University (No: AWEC2017A01). Written informed consent was obtained from the owners for the participation of their animals in this study.

AUTHOR CONTRIBUTIONS

JY and LW undertook the experiments of antimicrobial activity and wrote the manuscript. WLi, DG, HQ, and XF completed the antimicrobial assay of the L3 lignin *in vivo*. ZL did the structural analysis of lignin fractions. GL, PW, and BY proposed the idea and revised the manuscript. All authors contributed to the article and approved the submitted version.

FUNDING

This work was supported by the Science and Technology Development Project of Jilin Province (20190301007NY) and the Doctoral Science Launched Foundation of Jilin Agricultural Science and Technology University (20200003) to JY.

SUPPLEMENTARY MATERIAL

The Supplementary Material for this article can be found online at: <https://www.frontiersin.org/articles/10.3389/fbioe.2021.683796/full#supplementary-material>

- Cui, C., Sun, R., and Argyropoulos, D. S. (2014). Fractional precipitation of softwood kraft lignin: isolation of narrow fractions common to a variety of lignins. *ACS Sustain. Chem. Eng.* 2, 959–968. doi: 10.1021/sc400545d
- Dong, H., Li, M., Jin, Y., Wu, Y., Huang, C., and Yang, J. (2020b). Preparation of graphene-like porous carbons with enhanced thermal conductivities from lignin nano-particles by combining hydrothermal carbonization and pyrolysis. *Front. Energy Res.* 8:148. doi: 10.3389/fenrg.2020.00148
- Dong, H., Zheng, L., Yu, P., Jiang, Q., Wu, Y., Huang, C., et al. (2020a). Characterization and application of lignin-carbohydrate complexes from lignocellulosic materials as antioxidants for scavenging *in vitro* and *in vivo* reactive oxygen species. *ACS Sustain. Chem. Eng.* 8, 256–266. doi: 10.1021/acssuschemeng.9b05290
- Figueiredo, P., Lintinen, K., Hirvonen, J. T., Kostiaainen, M. A., and Santos, H. A. (2018). Properties and chemical modifications of lignin: towards lignin-based nanomaterials for biomedical applications. *Prog. Mater. Sci.* 93, 233–269. doi: 10.1016/j.pmatsci.2017.12.001
- Founou, L. L., Founou, R. C., and Essack, S. Y. (2016). Antibiotic resistance in the food chain: a developing country-perspective. *Front. Microbiol.* 7:1881. doi: 10.3389/fmicb.2016.01881
- Gu, J., Guo, M., Huang, C., Wang, X., Zhu, Y., Wang, L., et al. (2021). Titanium dioxide nanoparticle affects motor behavior, neurodevelopment and axonal growth in zebrafish (*Danio rerio*) larvae. *Sci. Total Environ.* 754:142315. doi: 10.1016/j.scitotenv.2020.142315
- Huang, C., He, J., Narron, R., Wang, Y., and Yong, Q. (2017). Characterization of kraft lignin fractions obtained by sequential ultrafiltration and their potential application as a biobased component in blends with polyethylene. *ACS Sustain. Chem. Eng.* 5, 11770–11779. doi: 10.1021/acssuschemeng.7b03415
- Huang, C., Tang, S., Zhang, W., Tao, Y., Lai, C., Li, X., et al. (2018). Unveiling the structural properties of lignin-carbohydrate complexes in bamboo residues and its functionality as antioxidants and immunostimulants. *ACS Sustain. Chem. Eng.* 6, 12522–12531. doi: 10.1021/acssuschemeng.8b03262

- Jiang, B., Chen, H., Zhao, H., Wu, W., and Jin, Y. (2020). Structural features and antioxidant behavior of lignins successively extracted from ginkgo shells (*Ginkgo biloba* L.). *Int. J. Biol. Macromol.* 163, 694–701. doi: 10.1016/j.ijbiomac.2020.07.027
- Jiang, B., Zhang, Y., Guo, T., Zhao, H., and Jin, Y. (2018). Structural characterization of lignin and lignin-carbohydrate complex (LCC) from ginkgo shells (*Ginkgo biloba* L.) by comprehensive NMR spectroscopy. *Polymers*. 10:736. doi: 10.3390/polym10070736
- Jiang, X., Savithri, D., Du, X., Pawar, S., Jameel, H., Chang, H. M., et al. (2017). Fractionation and characterization of kraft lignin by sequential precipitation with various organic solvents. *ACS Sustain. Chem. Eng.* 5, 835–842. doi: 10.1021/acssuschemeng.6b02174
- Kaur, R., Uppal, S. K., and Sharma, P. (2017). Antioxidant and antibacterial activities of sugarcane bagasse lignin and chemically modified lignins. *Sugar Tech.* 19, 675–680. doi: 10.1007/s12355-017-0513-y
- Lateef, H., Grimes, S., Kewcharoenwong, P., and Feinberg, B. (2009). Separation and recovery of cellulose and lignin using ionic liquids: a process for recovery from paper-based waste. *J. Chem. Technol. Biot.* 84, 1818–1827. doi: 10.1002/jctb.2251
- Li, J., Henriksson, G., and Gellerstedt, G. (2007). Lignin depolymerization/repolymerization and its critical role for delignification of aspen wood by steam explosion. *Bioresour. Technol.* 98, 3061–3068. doi: 10.1016/j.biortech.2006.10.018
- Lin, W., Xing, S., Jin, Y., Lu, X., Huang, C., and Yong, Q. (2020). Insight into understanding the performance of deep eutectic solvent pretreatment on improving enzymatic digestibility of bamboo residues. *Bioresour. Technol.* 306:123163. doi: 10.1016/j.biortech.2020.123163
- Liu, H. Y., Xu, T., Liu, K., Zhang, M., Liu, W., Li, H., et al. (2021). Recent progress in Lignin-based electrodes for energy storage application. *Ind. Crops. Prod.* 164:113390. doi: 10.1016/j.indcrop.2021.113425
- Liu, Z. H., Hao, N., Shinde, S., Pu, Y., Kang, X., Ragauskas, A. J., et al. (2019). Defining lignin nanoparticle properties through tailored lignin reactivity by sequential organosolv fragmentation approach (SOFA). *Green Chem.* 21, 245–260. doi: 10.1039/C8GC03290D
- Lobo, V., Patil, A., Phatak, A., and Chandra, N. (2010). Free radicals, antioxidants and functional foods: impact on human health. *Pharmacogn. Rev.* 4, 118–126. doi: 10.4103/0973-7847.70902
- Medina, J. D. C., Woiciechowski, A. L., Filho, A. Z., Bissoqui, L., Noseda, M. D., de Souza Vandenberghe, L. P., et al. (2016). Biological activities and thermal behavior of lignin from oil palm empty fruit bunches as potential source of chemicals of added value. *Ind. Crops. Products* 94, 630–637. doi: 10.1016/j.indcrop.2016.09.046
- Nair, S. S., Kuo, P. Y., Chen, H., and Yan, N. (2017). Investigating the effect of lignin on the mechanical, thermal, and barrier properties of cellulose nanofibril reinforced epoxy composite. *Ind. Crops. Prod.* 100, 208–217. doi: 10.1016/j.indcrop.2017.02.032
- Pei, W., Chen, Z. S., Chan, H. Y. E., Zheng, L., Liang, C., and Huang, C. (2020). Isolation and identification of a novel anti-protein aggregation activity of lignin-carbohydrate complex from *Chionanthus retusus* leaves. *Front. Bioeng. Biotech.* 8:573991. doi: 10.3389/fbioe.2020.573991
- Rencoret, J., Gutiérrez, A., Castro, E., and José, C. (2019). Structural characteristics of lignin in pruning residues of olive tree (*Olea europaea* L.). *Holzforchung* 73, 25–34. doi: 10.1515/hf-2018-0077
- Rojas, E. R., Billings, G., Odermatt, P. D., Auer, G. K., Zhu, L., Miguel, A., et al. (2018). The outer membrane is an essential load-bearing element in gram-negative bacteria. *Nature* 559, 617–621. doi: 10.1038/s41586-018-0344-3
- Sadeghifar, H., and Ragauskas, A. (2020). Perspective on technical lignin fractionation. *ACS Sustain. Chem. Eng.* 8, 8086–8101. doi: 10.1021/acssuschemeng.0c01348
- Schutyster, W., Renders, A. T., Van den Bosch, S., Koelewijn, S. F., Beckham, G. T., and Sels, B. F. (2018). Chemicals from lignin: an interplay of lignocellulose fractionation, depolymerisation, and upgrading. *Chem. Soc. Rev.* 47, 852–908. doi: 10.1039/C7CS00566K
- Solihat, N. N., Sari, F. P., Falah, F., Ismayati, M., Lubis, M. A. R., Friatiasari, W., et al. (2021). Lignin as an active biomaterial: a review. *J. Sylva Lestari.* 9, 1–22. doi: 10.23960/jsl191-22
- Tao, Y., Wang, T., Lai, C., Ling, Z., Zhou, Y., and Yong, Q. (2021). The *in vitro* and *in vivo* antioxidant and immunomodulatory activity of incomplete degradation products of hemicellulosic polysaccharide (Galactomannan) from *Sesbania cannabina*. *Front. Bioeng. Biotech.* 9:279. doi: 10.3389/fbioe.2021.679558
- Tian, D., Hu, J., Bao, J., Chandra, R. P., Saddler, J. N., and Lu, C. (2017). Lignin valorization: lignin nanoparticles as high-value bio-additive for multifunctional nanocomposites. *Biotechnol. Biofuels* 10, 1–11. doi: 10.1186/s13068-017-0876-z
- Torres, L. A. Z., Woiciechowski, A. L., Tanobe, V. O. D. A., Karp, S. G., and Soccol, C. R. (2020). Lignin as a potential source of high-added value compounds: a review. *J. Clean. Prod.* 263:121499. doi: 10.1016/j.jclepro.2020.121499
- Wang, H. R., Chen, X. J., Zhang, L. D., Li, Z. H., Fan, X. L., and Sun, S. L. (2021). Efficient production of lignin-based slow-release nitrogen fertilizer via microwave heating. *Ind. Crops Prod.* 166, 113481. doi: 10.1016/j.indcrop.2021.113481
- Wang, R., Luo, Y., Lu, Y., Wang, D., Wang, T., Pu, W., et al. (2019). Maggot extracts alleviate inflammation and oxidative stress in acute experimental colitis via the activation of Nrf2. *Oxid. Med. Cell. Longev.* 4703253. doi: 10.1155/2019/4703253
- Wen, J. L., Xue, B. L., Xu, F., and Sun, R. C. (2012). Unveiling the structural heterogeneity of bamboo lignin by in situ HSQC NMR technique. *BioEnergy Res.* 5, 886–903. doi: 10.1007/s12155-012-9203-5
- Xu, Z., Lei, P., Zhai, R., Wen, Z., and Jin, M. (2019). Recent advances in lignin valorization with bacterial cultures: microorganisms, metabolic pathways, and bio-products. *Biotechnol. Biofuels* 12, 1–19. doi: 10.1186/s13068-019-1376-0
- Yang, W., Fortunati, E., Gao, D., Balestra, G. M., Giovanale, G., He, X., et al. (2018). Valorization of acid isolated high yield lignin nanoparticles as innovative antioxidant/antimicrobial organic materials. *ACS Sustain. Chem. Eng.* 6, 3502–3514. doi: 10.1021/acssuschemeng.7b03782
- Yu, P., Zheng, L., Wang, P., Chai, S., Zhang, Y., Shi, T., et al. (2020). Development of a novel polysaccharide-based iron oxide nanoparticle to prevent iron accumulation-related osteoporosis by scavenging reactive oxygen species. *Int. J. Biol. Macromol.* 165, 1634–1645. doi: 10.1016/j.ijbiomac.2020.10.016
- Yu, Y., Ren, Z., Shang, Q., Li, L., Han, J., Tian, Z., et al. (2021). Ionic liquid-induced low temperature graphitization of cellulose-derived biochar for high performance sodium storage. *Surface Coatings Technol.* 127034. doi: 10.1016/j.surfcoat.2021.127034
- Zhao, X., Huang, C., Xiao, D., Wang, P., Luo, X., Liu, W., et al. (2021). Melanin-inspired design: preparing sustainable photothermal materials from lignin for energy generation. *ACS Appl. Mater. Inter.* 13, 7600–7607. doi: 10.1021/acsmi.0c21256
- Zheng, L., Yu, P., Zhang, Y., Wang, P., Yan, W., Guo, B., et al. (2021). Evaluating the bio-application of biomacromolecule of lignin-carbohydrate complexes (LCC) from wheat straw in bone metabolism via ROS scavenging. *Int. J. Biol. Macromol.* 176, 13–25. doi: 10.1016/j.ijbiomac.2021.01.103
- Zheng, Y., Yu, Y., Lin, W., Jin, Y., Yong, Q., and Huang, C. (2021). Enhancing the enzymatic digestibility of bamboo residues by biphasic phenoxethanol-acid pretreatment. *Bioresour. Technol.* 325:124691. doi: 10.1016/j.biortech.2021.124691

Conflict of Interest: The authors declare that the research was conducted in the absence of any commercial or financial relationships that could be construed as a potential conflict of interest.

Copyright © 2021 Yun, Wei, Li, Gong, Qin, Feng, Li, Ling, Wang and Yin. This is an open-access article distributed under the terms of the Creative Commons Attribution License (CC BY). The use, distribution or reproduction in other forums is permitted, provided the original author(s) and the copyright owner(s) are credited and that the original publication in this journal is cited, in accordance with accepted academic practice. No use, distribution or reproduction is permitted which does not comply with these terms.



Preparation of Lignin-Based Magnetic Adsorbent From Kraft Lignin for Adsorbing the Congo Red

Lingyan Fang^{1†}, Hao Wu^{2†}, Yuxuan Shi¹, Yuheng Tao¹ and Qiang Yong^{1*}

¹ Jiangsu Co-Innovation Center for Efficient Processing and Utilization of Forest Resources, College of Chemical Engineering, Nanjing Forestry University, Nanjing, China, ² Department of Biomedical Engineering, School of Biomedical Engineering and Informatics, Nanjing Medical University, Nanjing, China

OPEN ACCESS

Edited by:

Lei Wang,
Ocean University of China, China

Reviewed by:

Wei Liu,
Tianjin University of Science
and Technology, China
Bo Chen,
Suzhou University of Science
and Technology, China
Thilina U. Jayawardena,
Jeju National University, South Korea

*Correspondence:

Qiang Yong
swhx@njfu.com.cn

[†] These authors have contributed
equally to this work and share first
authorship

Specialty section:

This article was submitted to
Bioprocess Engineering,
a section of the journal
Frontiers in Bioengineering and
Biotechnology

Received: 06 April 2021

Accepted: 04 May 2021

Published: 07 June 2021

Citation:

Fang L, Wu H, Shi Y, Tao Y and
Yong Q (2021) Preparation
of Lignin-Based Magnetic Adsorbent
From Kraft Lignin for Adsorbing
the Congo Red.
Front. Bioeng. Biotechnol. 9:691528.
doi: 10.3389/fbioe.2021.691528

The utilization of lignin from different lignocellulosic biomass is the hot topic for the biorefinery of biomass. In this paper, magnetic lignin nanoparticles (MLN) were prepared by kraft lignin from bamboo residue and Fe₃O₄ with different ratios via Mannich reaction. The surface morphology and structure of magnetic lignin were characterized and analyzed by X-ray powder diffraction, Fourier transform infrared spectroscopy, and transmission electron microscopy, which confirmed that the MLN were successfully prepared. The performance of MLN adsorbents was evaluated by adsorbing Congo red solution at different initial concentrations and contact times. The results showed that Fe₃O₄@lignin (1:0.5) had the best adsorption effect on Congo red solution. When the concentration of Congo red reached 0.6 g/L, Fe₃O₄@lignin (1:0.5) had the best adsorption effect on Congo red, reaching 95.5% in only 30 min. As lignin is modified by Fe₃O₄, it can be recovered by magnetic substances after adsorption and has good reuse performance. The results of adsorption kinetics and adsorption isotherm showed that except for the adsorption process of Fe₃O₄@lignin (1:0.5), which is consistent with the chemical adsorption of the multimolecular layer, the adsorption process of other adsorbents is in accordance with the chemical adsorption of the monomolecular layer. In terms of environmental protection and adsorption efficiency, and MLN has become an ideal adsorbent for Congo red dyes due to its simple preparation, superior performance, and convenient recovery.

Keywords: kraft lignin, Mannich reaction, Congo red, magnetic adsorbent, preparation

INTRODUCTION

Due to the impact of environmental issues of dye wastewater from printing and dyeing mill on public health, it has become a global concern (Liu J. et al., 2018). Most of these dyes are soluble in water, complex in composition, and high in organic pollutants (Liu L. et al., 2018). Most of them are difficult to biodegrade and even cause “Triple induction” (carcinogenic, teratogenic, mutagenic) (Konicki et al., 2018; Sham and Notley, 2018). Therefore, the dye wastewater must be properly treated and protected, otherwise it will cause harm to aquatic species and the environment (Ghaedi et al., 2012; Gu et al., 2021). Congo red is a typical biphenyl amine azo dye, which will produce toxic substances in an anaerobic environment and easily accessible to water bodies during industrial

production and use (Zhao et al., 2018). It is one of the representative pollutants in printing and dyeing wastewater. At present, the treatment methods of dye wastewater include radiation method, magnetic separation method, an adsorption method, membrane separation method, and photocatalytic oxidation method (Holkar et al., 2016; Cui et al., 2018; Wang et al., 2018b). Adsorption method is a common method for wastewater treatment because it is efficient, simple, recyclable, produces less secondary pollution, and does not change the structure of pollutants in dye wastewater (Yang et al., 2019).

In recent years, several adsorbents such as activated carbon, zeolite, ion exchange materials, and bentonite have been widely used in dye adsorption. However, due to the problems of difficult recovery, difficulty in regeneration and reuse, high price, and low adsorption efficiency of these adsorbents, if these adsorbents are used for large-scale treatment of dye wastewater adsorption, the cost is relatively expensive (Hassan and Carr, 2018).

As a renewable biomass material, lignin is one of the main components in nature plants, with a wide range of sources (Klapiszewski et al., 2017a; Pei et al., 2020; Zheng et al., 2021). In industry, lignin is mainly separated and extracted from black liquor discharged during the pulping and papermaking process, and can be processed into various functional materials with high value and applied (Kai et al., 2016; Dong et al., 2020a). Lignin contains a large number of functional groups such as benzene ring, hydroxyl group, carbonyl group, carboxyl group, methoxy group, and unsaturated bond (Gall et al., 2017; Dong et al., 2020b). It has the ability of ion exchange and adsorption, which is more advantageous than other adsorbents such as activated carbon, macromolecule resin, and minerals, and has attracted extensive attention (Upton and Kasko, 2016). However, lignin is difficult to separate and recover, and its application is greatly restricted (Humpert et al., 2016). It can be solved by combining with magnetic materials to produce magnetic lignin nano-materials. The magnetic components are mainly nickel, iron, cobalt, iron, and alloy oxides such as γ -Fe₂O₃ and Fe₃O₄. Fe₃O₄ is widely used as the magnetic component of magnetic polymer materials due to its advantages of simple preparation process, stable performance, and low toxicity (Siyasukh et al., 2018; Wang et al., 2018a; Lou et al., 2020, 2021). MLN, such as Fe₃O₄@lignin, can be prepared by Mannich reaction, which is a condensation reaction between amine compounds and aldehydes and containing active hydrogen atoms in lignin (Wang B. et al., 2018). The Mannich reaction usually involves the formation of *N*-hydroxymethyl amines by the reaction of the amine group with the aldehyde group, and condensation of the hydrogen atoms by the substitution of the amine group, namely, the amine methylation reaction (Jiao et al., 2019).

This reaction is particularly useful for the synthesis of β -aminocarbonyl derivatives (Kobayashi et al., 2011). In the Mannich reaction, the crosslinking agent between fatty amine and lignin consists of an aldehyde group, and formaldehyde is currently the most widely used aldehyde (Gao et al., 2020). Because the Mannich reaction is simple, effective, and without by-products, it is widely used in the synthesis of new materials (Guo et al., 2020). Luo et al. (2017) recovered lignin from black liquor, modified the lignin by Mannich reaction with

triethylenetetramine (TETA), and then chelated iron to the aminated lignin to obtain a highly efficient phosphate adsorbent. The magnetic lignin prepared can be simply recovered by using a magnetic substance. Therefore, lignin can be fully utilized, and lignin can be recycled and reused through magnetic properties, thereby improving the economic value of lignin (Calvo-Flores and Dobado, 2010). In the current research, few people load lignin on magnetic nanoparticles of Fe₃O₄ and use the MLN for dye adsorption, which is also the starting point of our work.

In this study, the magnetic Fe₃O₄ with good performance was prepared by co-precipitation method, and then it reacted with ethylsilicate (TEOS) and (3-aminopropyl) triethoxysilane (APTES) to obtain the aminated Fe₃O₄. Then, the aminated Fe₃O₄ was reacted with lignin to obtain a green recyclable MLN adsorbent. The surface morphology and phase composition of magnetic lignin were characterized and analyzed by X-ray powder diffraction (XRD), Fourier transform infrared spectroscopy (FT-IR), transmission electron microscopy (TEM), and apply it to the removal of Congo red. In addition, the adsorption kinetics and adsorption isotherm of MLN for adsorbing the Congo red were also evaluated.

MATERIALS AND METHODS

Materials

Kraft lignin was obtained from black liquor of bamboo residues via acid precipitation. The textile dye Congo red was purchased from China National Pharmaceutical Holding Chemical Reagent Co., Ltd. and was used without further purification. All other chemicals were also used without any other purification.

Preparation of Fe₃O₄

Fe₃O₄ was prepared by the co-precipitation method, based on the principle of $\text{Fe}^{2+} + 2\text{Fe}^{3+} + 8\text{OH}^- = \text{Fe}_3\text{O}_4 + 4\text{H}_2\text{O}$. Specifically, 6.1 g FeCl₃·6H₂O and 4.2 g FeSO₄·7H₂O were dissolved in 100 ml of deionized water, added into a 250-ml three-necked flask. Then the solution was heated to 85°C in an oil bath under an argon atmosphere and mechanically stirred at 300 rpm. When at 70°C, 10 ml ammonia water was added and continued to heat for 1 h at 85°C. After the reaction was finished, the black precipitate was separated from the reaction medium by an external magnetic field and ultrasonically washed three times with deionized water until the pH is neutral, to obtain Fe₃O₄ particles.

Preparation of Fe₃O₄ @lignin Composites

Fe₃O₄ nanoparticles prepared by the aforementioned method were dispersed in 150 ml of ethanol/water (4:1, v/v) solution, and then the mixture was dispersed uniformly in ultrasonic to form magnetic fluid and added into a 250-ml three-necked flask. Then 5 ml of tetraethyl orthosilicate (TEOS) was added, and ammonia water was used to adjust the pH to 9.0. Then the solution was heated to 45°C for 16 h in an oil bath under an argon atmosphere and mechanically stirred at 300 rpm. After 16 h, different proportions of lignin solution (1:0.5, 1:1, 1:2, 1:3), 7 ml formaldehyde, and 10 ml

3-aminopropyltriethoxysilane (APTES) were added to the three-necked flask, then heated to 60°C for 6 h. To prepare the lignin solution, 1.37, 2.74, 5.48, and 8.22 g lignin in black liquor were dissolved in 20 ml ammonia solution, which was proposed based on the amount of Fe₃O₄ to obtain Fe₃O₄@lignin with ratios of 1:0.5, 1:1, 1:2, and 1:3. After the reaction was finished, the mixture was washed with ethanol several times until the pH is neutral. The precipitated solid (MLN) was obtained by frozen drying. The obtained MLN with different ratios of 1:0.5, 1:1, 1:2, and 1:3 for Fe₃O₄ and lignin were termed as Fe₃O₄@lignin (1:0.5), Fe₃O₄@lignin (1:1), Fe₃O₄@lignin (1:2), and Fe₃O₄@lignin (1:3).

Characterization of MLN

The composition of the sample was analyzed by model Rigaku Ultima IV X-ray powder diffraction. The chemical bond structure of the sample was determined using an infrared spectrometer (VERTEX 80V; Bruker, Germany). The internal morphology and structure of the sample was observed by JEM-2100 transmission electron microscope. The magnetic properties of the samples were measured by a Lake Shore 7404 vibrating sample magnetometer.

Determination of Iron Content

Determination of iron content in Fe₃O₄@lignin composite was performed by the phenanthroline method, which is one of the common methods used for the determination of iron content. The key to determining the iron content by the phenanthroline method is to disperse the nano-iron oxide particles under acidic conditions to dissolve them into Fe²⁺/Fe³⁺, and under the action of a reducing agent, all the iron ions in the solution are reduced to Fe²⁺. At this time, the orange-red complex formed in the solution is a complex of phenanthroline and Fe²⁺. According to the literature, the maximum absorption peak of the orange-red complex is obtained at 510 nm. The absorbance of the spot is measured by an ultraviolet-visible spectrophotometer, and the iron content of the sample to be tested can be obtained by comparing the drawn standard curve and the curve equation.

Adsorption Experiment

The effect of magnetic lignin on Congo red concentration adsorption and the effect of magnetic lignin on Congo red adsorption time were determined. Congo red solution was prepared with concentration ranging from 0.01 to 0.8 g/L. Then 20 ml Congo red solution was added into a 50-ml Erlenmeyer flask as well as the addition of 0.05 g magnetic lignin, subsequently reacted at 30°C and 150 rpm for 4 h. The absorption value of supernate was measured at λ_{max} of 496 nm. Further, the adsorption rate and the absorption capacity were calculated.

The effect of magnetic lignin on adsorption time of Congo red was determined. Forty milliliters of 0.6 g/L Congo red solution was added with 0.1 g of magnetic lignin and shaken at 150 rpm for 5 h. The absorbance value of supernate was measured at λ_{max} of 496 nm to determine the concentration of Congo red. Further, the adsorption rate and the absorption capacity were calculated.

In all experiments, the equilibrium adsorption amount q_e (mg/g) was determined by the mass balance of the dye:

$$q_e = \frac{(C_o - C_e) \times V}{m} \quad (1)$$

The initial concentration and adsorption equilibrium concentration of the dyes were C_o (mg/L) and C_e (mg/L), respectively. V (ml) is dye solution's volume and m (g) is adsorbent's amount.

Adsorption Kinetics

To study the control mechanism of the adsorption process, such as mass transfer or chemical reaction, the pseudo-first-order, pseudo-second-order dynamic models and the intraparticle diffusion model given in Eqs. 2–4 were used respectively.

$$\log q_e - q_t = \log q_e - \frac{k_1}{2.303} t \quad (2)$$

$$\frac{t}{q_t} = \frac{1}{q_e^2 k_2} + \frac{t}{q_e} \quad (3)$$

$$q_t = k_i t^{1/2} + C \quad (4)$$

q_t (mg/g) is the adsorption capacity at t (min); q_e (mg/g) is the adsorption capacity when equilibrium is reached, t is the adsorption time, and C is a constant related to the boundary layer thickness; k₁ (min⁻¹) and k₂ (g mg⁻¹ min⁻¹) are pseudo-first-order and pseudo-second-order kinetic adsorption rate constants, respectively, and k_i (mg/g·min^{1/2}) is the intracellular diffusion rate constant. q_e and k₁, k₂, and k_i can be determined from the experimental data by equations.

Adsorption Isotherm

The adsorption equation of the Langmuir model is shown in Eqs. 5 and 6:

$$\frac{C_e}{q_e} = \frac{1}{q_m b} + \frac{C_e}{q_m} \quad (5)$$

$$R_L = \frac{a}{(1 + bC_o)} \quad (6)$$

q_e: Adsorption mass (mg/g) during adsorption equilibrium of Congo red solution

C_e: equilibrium concentration of Congo red solution (mg/L)

q_m: maximum adsorption value of adsorbent (mg/g)

b: Langmuir adsorption constant (L/mg)

Adsorption equation of Freundlich model is shown in Eq. 7:

$$\ln(q_e) = \ln(K_f) + \frac{1}{n} \ln(C_e) \quad (7)$$

q_e: Adsorption mass (mg/g) during adsorption equilibrium of Congo red solution

C_e: equilibrium concentration of Congo red solution (mg/L)

K_f: Freundlich equilibrium constant, roughly indicating the adsorption capacity of the adsorbent (mg/g)

$\frac{1}{n}$: Heterogeneity factor, related to adsorption strength. When 0 < 1/n < 1, the adsorption is advantageous; if

$1/n = 1$, the adsorption is linear, there is no interaction between adsorbates; when $1/n > 1$, the adsorption is negative (Wang et al., 2018b).

RESULTS AND DISCUSSION

Characterization of Adsorbents

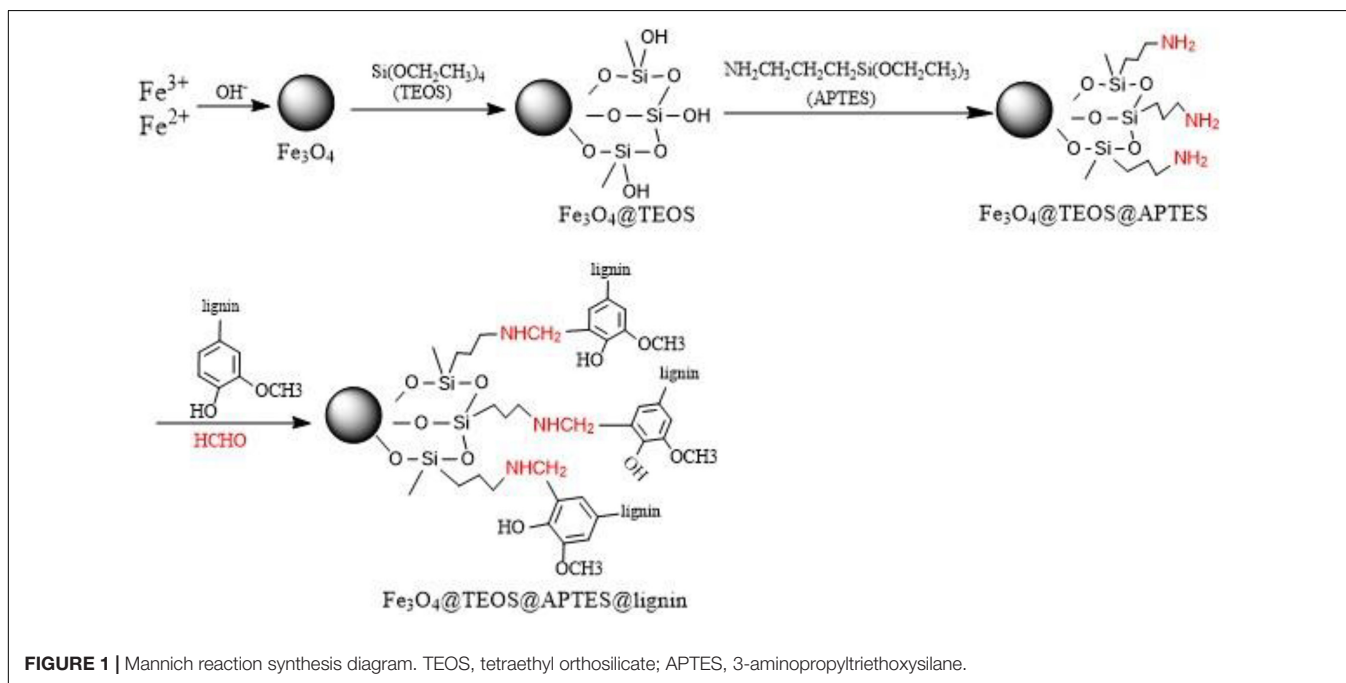
In this paper, through the Mannich reaction, the magnetic Fe_3O_4 reacted with TEOS and APTES in turn, and finally reacted with lignin to obtain MLN. The specific mechanism is shown in **Figure 1**. Characterization analysis was performed on Fe_3O_4 @lignin to understand the structural characteristics of the samples.

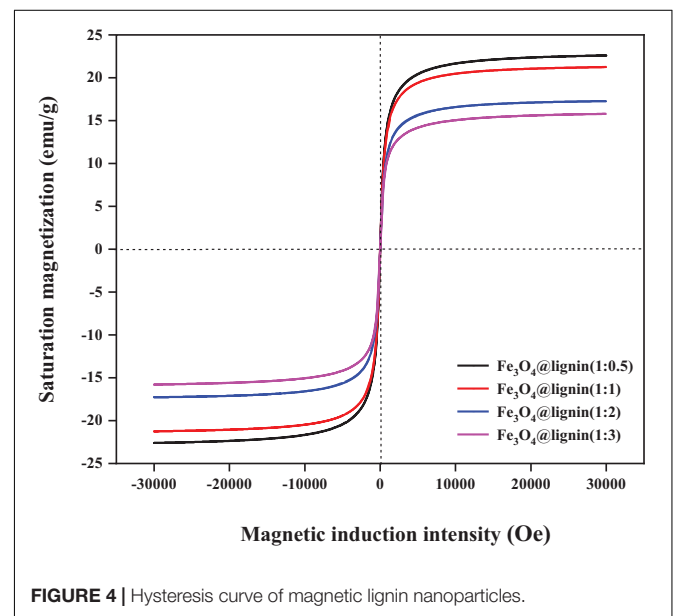
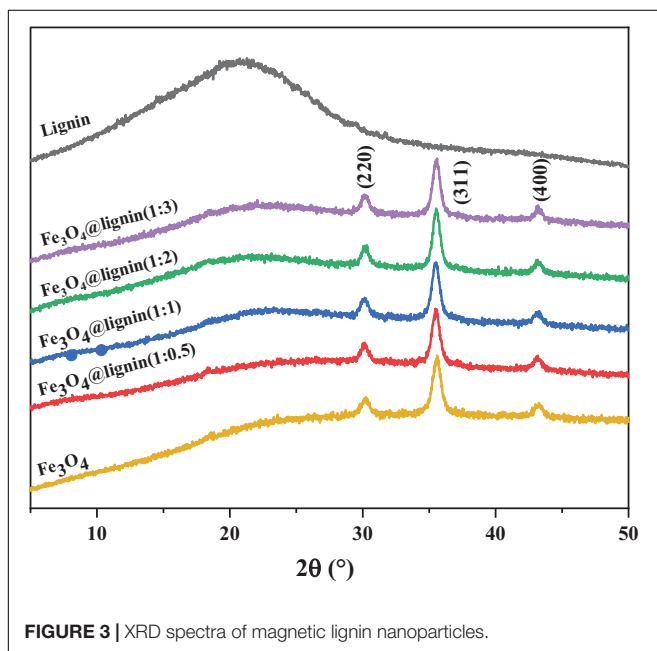
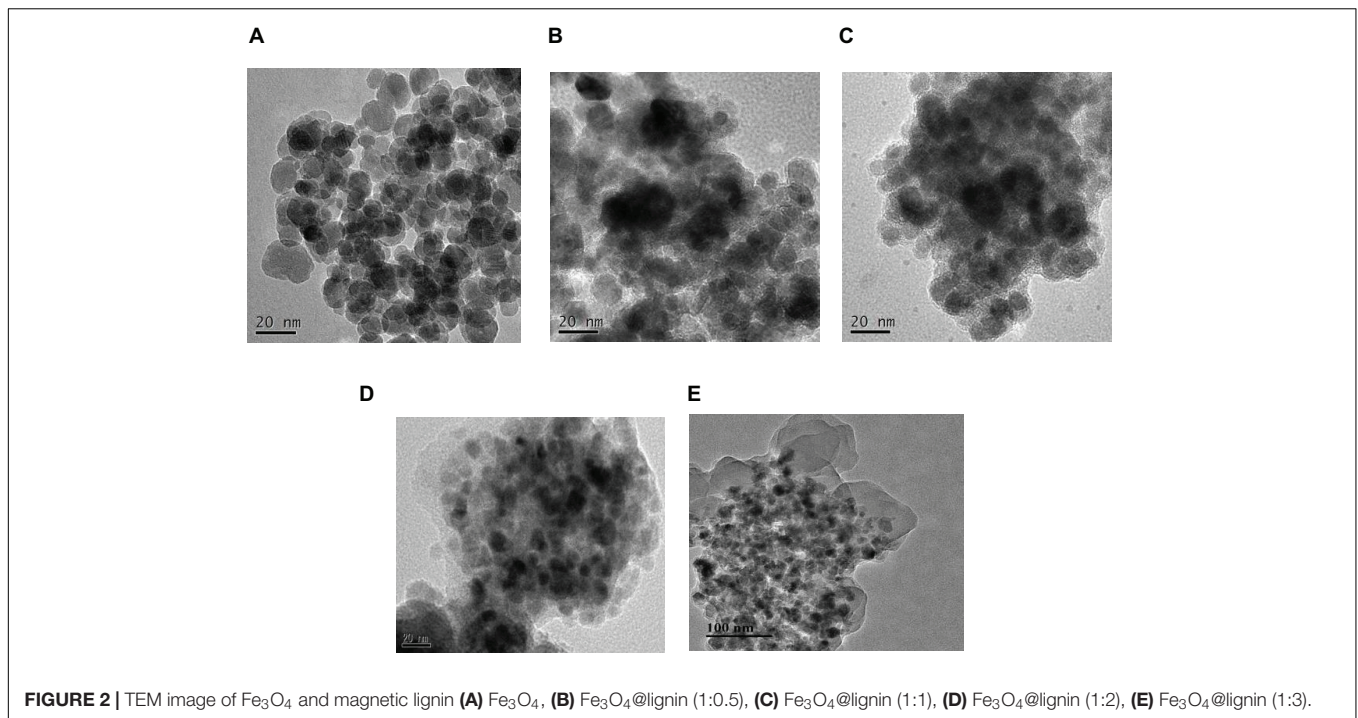
The morphology and particle size distribution of the Fe_3O_4 and Fe_3O_4 @lignin composites were carried out by transmission electron microscope (TEM). It can be seen from **Figure 2** that the average particle size of Fe_3O_4 is about 20 nm, which is spherical. The particles in Fe_3O_4 have a strong agglomeration phenomenon. This is due to the large specific surface area of Fe_3O_4 nanoparticles, the surface energy is in an unstable state, and the intermolecular force, hydrogen bond, static electricity, and other forces make it agglomerate together. When Fe_3O_4 nanoparticles are loaded with lignin, Fe_3O_4 @lignin has an obvious core-shell structure, and lignin is present on the outer layer of Fe_3O_4 . At the same time, the particle agglomeration phenomenon is suppressed to a certain extent and has a good dispersion performance. This may be due to the decrease of the surface energy of the composite magnetic particles after Fe_3O_4 is loaded with lignin and the reduction of the interaction force between the particles, thereby improving the dispersion performance. In addition, the particle size of Fe_3O_4 @lignin is equivalent to that of Fe_3O_4 , indicating that Fe_3O_4 modified APTES and lignin has almost no effect on

the size of magnetic nanoparticles. The magnetite–lignin hybrid materials obtained by Klapiszewski et al. (2017b) also have the same aggregation tendency.

X-ray diffraction (XRD) was used to study the phase and crystal structure of the sample. The XRD patterns of five samples lignin and Fe_3O_4 @lignin composites nanoparticles are shown in **Figure 3**. According to the literatures (An et al., 2017; Wang et al., 2019; Jia et al., 2021) that three diffraction peaks appear on the spectrum of Fe_3O_4 nanoparticles at 30.1° , 35.5° , and 42.9° , which were attributed to the (220), (310), and (401) crystal planes of inverse spinel Fe_3O_4 , respectively. For lignin, only a broad diffraction peak appears around 20° , which is the diffraction peak in the amorphous region of lignin. When lignin is loaded with Fe_3O_4 , the obtained magnetic lignin Fe_3O_4 @lignin composites also show three crystal plane diffraction peaks of inverse spinel Fe_3O_4 , and the position of the diffraction peaks does not shift, indicating that in the process of loading lignin to Fe_3O_4 , it did not change its crystals.

When lignin is loaded on the outer layer of Fe_3O_4 nanoparticles, it will not only directly affect the iron distribution of the particles, but also have a great influence on the magnetic strength of the particles (Mikhaylova et al., 2004). In addition, the magnetic strength of the magnetic adsorbent will directly affect the recovery process of the material. Therefore, the magnetic strength of Fe_3O_4 @lignin was evaluated and shown in **Figure 4**. It can be seen that the hysteresis loops of the four Fe_3O_4 @lignin composites all cross the origin and are symmetrical, which shows that the coercivity of the magnetic lignin is zero. At the same time, no remanence and hysteresis were found in these 4 hysteresis loops, indicating that the prepared magnetic Fe_3O_4 @lignin composites all showed good superparamagnetism. Specifically, the saturation magnetization of Fe_3O_4 @lignin with ratios of 1:0.5, 1:1, 1:2, and 1:3 was 23, 21, 16, and 15 emu g^{-1} , respectively.

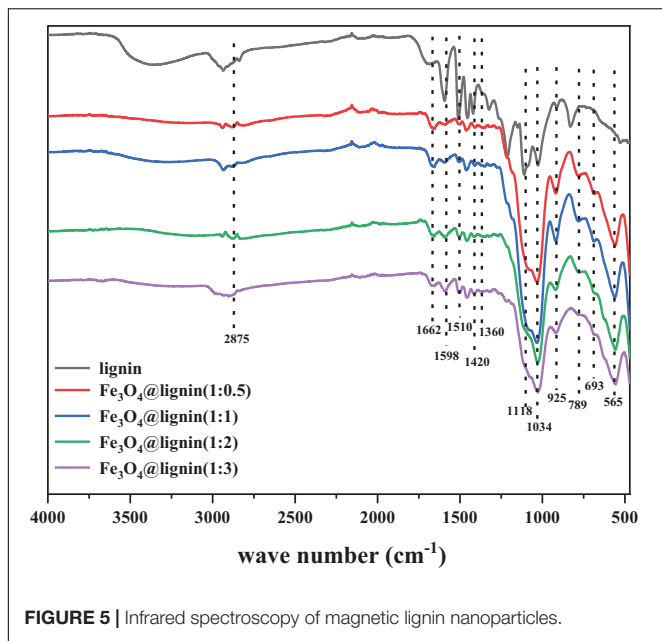




The results indicated that the Fe_3O_4 loaded by a greater amount of lignin could decrease its magnetic strength. The reason for this phenomenon can be explained by the fact that the coating of lignin is a non-magnetic polymer. More coatings will increase the dipole moment of Fe_3O_4 particles and decrease the magnetic content, which will lead to a decrease in magnetic properties (Deatsch and Evans, 2014). In general, the results of the hysteresis curve show that the obtained Fe_3O_4 @lignin composite material

has good magnetic properties and can be easily recovered when used as an adsorbent under an external magnetic field.

Infrared spectroscopy was used to analyze the structure of the prepared Fe_3O_4 @lignin. It can be seen from **Figure 5** that the lignin samples show typical signal peaks of the lignin benzene ring structure at 1,598, 1,510, and 1,420 cm^{-1} (Jiang et al., 2019). In addition, the peak at 1,360 cm^{-1} is attributable to the absorption peaks of lignin syringyl and condensed guaiacyl, and the peak at 1,118 cm^{-1} is attributable to the “S” type lignin absorption peak. The peak at 1,034 cm^{-1} indicates the vibration



of the lignin H unit in the CH plane and the in-plane deformation vibration of the CH coupling bond. These lignin absorption peaks exist in the infrared spectrum of Fe_3O_4 @lignin, indicating that the magnetic lignin obtained by the co-precipitation method will not destroy the original structure of lignin. Fe_3O_4 has a high-intensity absorption peak at 565 cm^{-1} , which is attributed to the stretching vibration peak of Fe–O in Fe_3O_4 nanoparticles. The strong absorption peak was found on the absorption peak of Fe_3O_4 @lignin, but not found in the spectrum of the lignin sample, indicating that the lignin has been successfully loaded on Fe_3O_4 . In addition, the absorption peaks at 693, 925, and $1,662\text{ cm}^{-1}$ in the infrared spectrum of Fe_3O_4 @lignin are attributed to the absorption peaks of bending vibration outside the N–H bond plane, the vibration peaks of the amino curved surface, and N–H stretching vibration peak; these phenomena indicate the successful modification of the amino group, which means that APTES has been successfully modified on Fe_3O_4 (An et al., 2020). Infrared analysis results show that lignin has been loaded on the surface of Fe_3O_4 nanoparticles to form Fe_3O_4 @lignin.

The binding degree of lignin and iron can be determined by measuring the content of iron ions in Fe_3O_4 @lignin. In this work, the iron content of magnetic Fe_3O_4 @lignin is analyzed and shown in **Table 1**. According to **Table 1**, the iron content of the samples Fe_3O_4 @lignin (1:0.5), Fe_3O_4 @lignin (1:1), and Fe_3O_4 @lignin (1:2) gradually increased. For Fe_3O_4 @lignin (1:2), the iron content is the highest, and Fe_3O_4 @lignin (1:3) is decreased. This is because the content of Fe_3O_4 in the prepared raw material is constant, and the maximum grafting number of Fe_3O_4 and lignin is fixed.

Adsorption Performance of Fe_3O_4 @lignin

The concentration of dye solution plays an important role in its absorption and decolorization percentage. The adsorption of

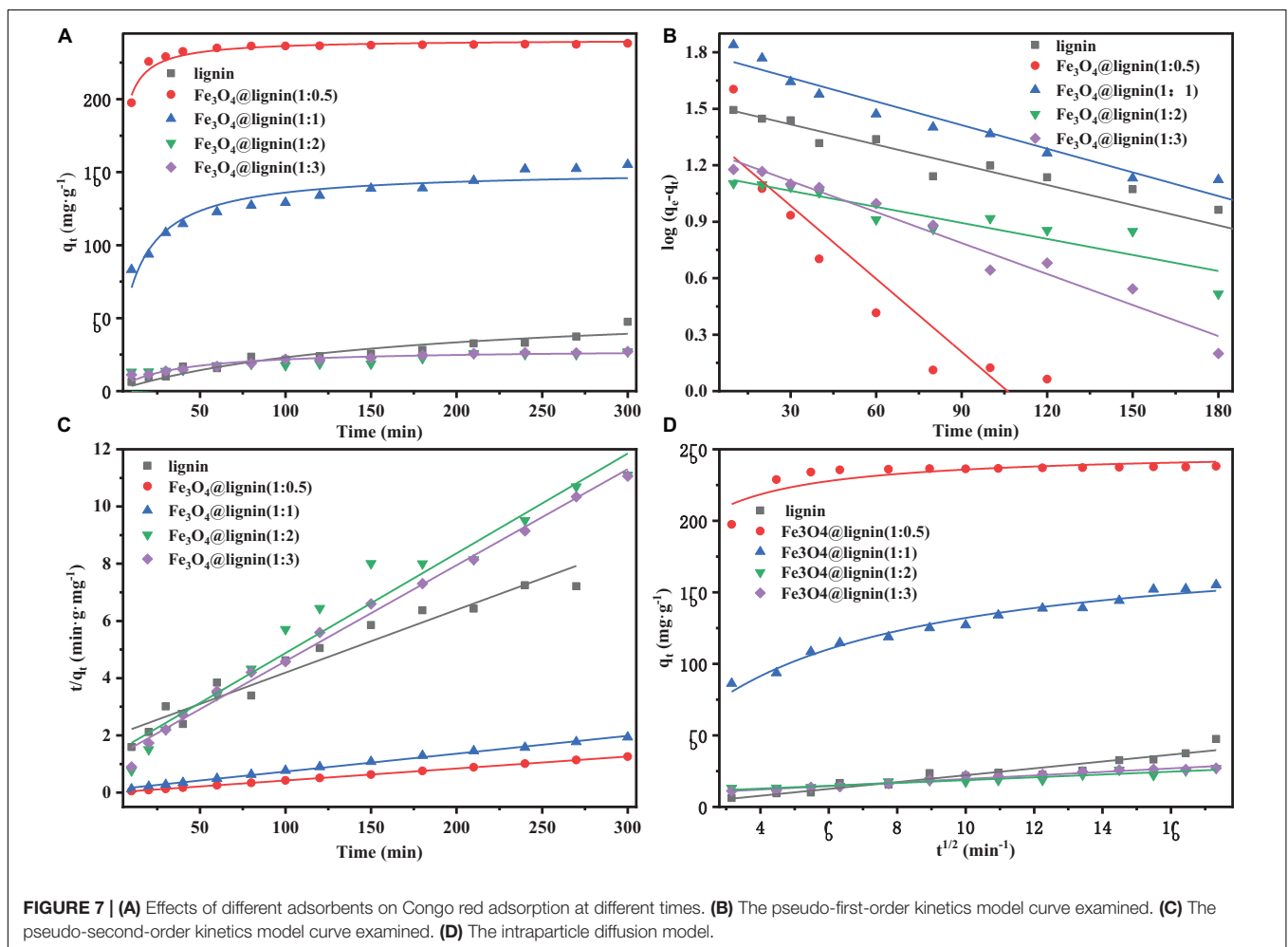
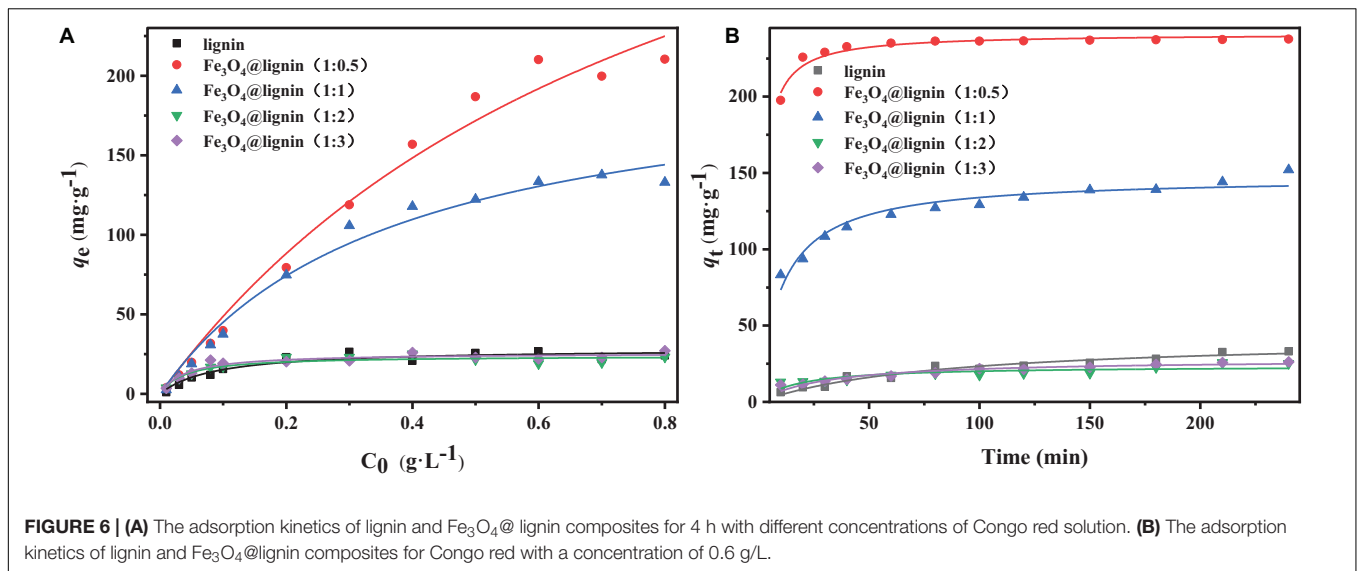
MLN was studied by adsorbing different concentrations of Congo red dye for 4 h and the results are shown in **Figure 6A**. It can be seen that the adsorption amount of Congo red solution of each sample increases first with the increase of the concentration of Congo red solution. After reaching a certain concentration, it remains stable or even decreases. When the concentration was 0.6 g/L, lignin reached the maximum adsorption capacity of Congo red solution, which was 26.77 mg/g . When the concentration was 0.7 g/L, Fe_3O_4 @lignin (1:1) reached the maximum adsorption capacity of Congo red solution, which was 137.69 mg/g . When the concentration is 0.8 g/L, Fe_3O_4 @lignin (1:0.5), Fe_3O_4 @lignin (1:2), and Fe_3O_4 @lignin(1:3) reached the maximum adsorption capacity of Congo red solution, which were 210.40, 23.27, and 27.13 mg/g , respectively. Among these MLN, the Fe_3O_4 @lignin (1:0.5) showed the best adsorption capacity on Congo red and the adsorption effect is stable, which is 7.86 times that of lignin. Compared with other modified lignin or lignin-based adsorbents, the magnetic lignin obtained by cross-linking method in this study showed good adsorption properties to dyes. Wang X. et al. (2018) studied the adsorption performance of carbon composite lignin-based adsorbent for Congo red, and the maximum saturated adsorption capacity was 198.5 mg/g . Jiang et al. (2019) studied the adsorption performance of magnetic lignin adsorbent ($\text{Fe}_3\text{O}_4/\text{C-ACLS}$) for Congo red, and the maximum saturated adsorption capacity was 198.8 mg/g .

The adsorption performance of magnetic lignin for Congo red during different adsorption times has a great significance for its industrial utilization in dye adsorbing. Hence, the lignin and Fe_3O_4 @lignin composites were investigated for adsorption of Congo red at a concentration of 0.6 g/L within 0–300 min, as shown in **Figure 6B**. It can be seen that the adsorption effect of Fe_3O_4 @lignin (1:0.5) on Congo red reaches saturation at 30 min and the adsorption capacity is as high as 229.1 mg/g , and the adsorption effect remains stable after 30 min. For the other MLN, their adsorption capacity also increased steadily with the increase of time and reached the maximum adsorption capacity at 240 min. Specifically, lignin, Fe_3O_4 @lignin (1:1), Fe_3O_4 @lignin (1:2), and Fe_3O_4 @lignin (1:3) reached the maximum adsorption capacity of 33.10, 152.13, 25.22, and 26.23 mg/g , respectively. Wang et al. (2014) studied the ultrasonic-assisted synthesis of aminated lignin by a Mannich reaction as an adsorbent to adsorb Congo red with yield of 95.5% at 48 h. Hence, it can be speculated that the MLN of Fe_3O_4 @lignin (1:0.5) can be regarded as the best adsorber to treat dye wastewater due to its largest adsorption capacity and fastest adsorption rate.

TABLE 1 | Iron content of magnetic lignin nanoparticles.

Sample	Iron concentration (mg/g) ^a
Fe_3O_4 @lignin (1:0.5)	2.71
Fe_3O_4 @lignin (1:1)	3.41
Fe_3O_4 @lignin (1:2)	5.28
Fe_3O_4 @lignin (1:3)	3.97

^aIron concentration (mg/g) is defined as the mass of iron ions (mg) per gram of sample.



Based on the analysis of the initial concentration and adsorption time, it can be found that Fe₃O₄@lignin (1:0.5) is superior than other MLN to adsorb Congo red. Moreover,

the adsorption capacity of 0.6 g/L Congo red solution by Fe₃O₄@lignin (1:0.5) for 30 min is the equilibrium adsorption amount, which is the focus of this study.

TABLE 2 | Kinetic parameters for the adsorption of Congo red dye on lignin and magnetic lignin composites.

Kinetics model	Parameter	Lignin	Fe ₃ O ₄ @lignin			
			1:0.5	1:1	1:2	1:3
Pseudo-first order	q_{eexp} (mg/g)	37.43	237.69	152.44	25.78	26.73
	q_{ecal} (mg/g)	34.52	236.60	136.43	21.14	24.66
	k_1 ($\times 10^{-2}$ /min)	0.10	17.90	6.30	4.10	2.40
	R^2	0.89	0.99	0.68	0.49	0.83
Pseudo-second order	q_{eexp} (mg/g)	37.43	237.69	152.44	25.78	26.73
	q_{tcal} (mg/g)	32.67	261.13	148.27	22.26	28.21
	k_2 ($\times 10^{-2}$ g/mg min ⁻¹)	0.06	0.12	0.07	0.33	0.11
	R^2	0.93	0.98	1.00	0.64	0.99
Intraparticle diffusion model	k_i (mg/g min ^{1/2})	2.45	1.57	4.59	1.04	1.21
	C (mg/g)	1.90	216.00	80.18	8.48	7.50
	R^2	0.94	0.46	0.94	0.94	0.97

Adsorption Kinetics

Adsorption isotherms play an important role in understanding the adsorption mechanism for different adsorbent. In this study, different concentrations of dyes were used to investigate the adsorption mechanism of prepared MLN, which is shown in **Figure 7**.

The pseudo-first-order kinetic equation assumes that the adsorption process is controlled by diffusion. The pseudo-second-order kinetic equation assumes that the adsorption rate is controlled by a chemical adsorption mechanism (Nair et al., 2014). This chemisorption involves electron transfer or electron pairing between the adsorbent molecules and the adsorbates. For the intraparticle diffusion equation, if there is intraparticle diffusion, q_t has a linear relationship with $t^{0.5}$, and if the straight line passes through the origin, the rate control process is only controlled by the internal diffusion. Otherwise, other adsorption mechanisms will be accompanied by internal diffusion process at the same time.

Figure 7B and **Table 2** show the pseudo-first-order curve fitting model and the model parameters, respectively. The R^2 values for each plot are between 0.49 and 0.99. **Figure 7C** and **Table 2** show the pseudo-second-order curve fitting model and model parameters. The R^2 values for each plot are between 0.64 and 0.99, which is higher than the holistic coefficient value (R^2) of the pseudo-first-order kinetic equation. These results showed that the adsorption process of MLN in Congo red is in good agreement with the pseudo-second-order model; the chemical adsorption plays a leading role for MLN comparing with diffusion.

The curves in **Figure 7D** showed that the values between q_t and $t^{0.5}$ signifying intra-particle diffusion model is fitting for the adsorbing, where the value of “C” corresponding to the intercept helped to explain whether the control step is intra-particle diffusion or not. According to the data in **Table 2**, C was a non-zero value which indicated that the relationship between $t^{0.5}$ and q_t is not a straight line passing through the origin, showing that the adsorption rate is controlled by multiple adsorption mechanisms. Two or more steps occur in the process; adsorption process also includes complex mechanism pathways

(Sohni et al., 2018). Jiang et al. (2019) showed that the adsorption rate was generally controlled by three stages. The first stage is the initial stage of the reaction, which is the diffusion stage of the dye in the boundary layer, where the adsorption capacity increases faster. As the reaction continues, the adsorption capacity in the second stage still increases, but the increase rate slows down. The reaction process in this stage is controlled by intraparticle diffusion. In the third stage, the adsorption reaches equilibrium. It can be seen from **Figure 7D** that the adsorption rate of Fe₃O₄@lignin (1:0.5) is faster, and the figure shows the three stages of the adsorption process. While the adsorption rate of the other samples is slower, the figure only shows the second step between the initial rapid external diffusion stage and the equilibrium stage in the adsorption process. The adsorption rate of the second step is relatively stable to each sample, so the second step is chosen to characterize the rate parameters corresponding to diffusion.

The calculated k_i values for each initial concentration are shown in **Table 2**. It can be seen that the R^2 values of the lignin and Fe₃O₄@lignin (1:1) (1:2) (1:3) for the diffusion model were all above 0.9. This indicated that the adsorption process could be followed by an intra-particle diffusion after around 10 min (Liu L. et al., 2018). In contrast, the R^2 value of the adsorption

TABLE 3 | Adsorption isotherm model parameters.

Parameters	Lignin	Fe ₃ O ₄ @lignin			
		1:0.5	1:1	1:2	1:3
Langmuir					
q_m (mg/g)	28.72	470.02	206.29	25.30	27.10
b ($\times 10^{-2}$ L/mg)	1.10	0.11	0.28	2.27	2.33
R^2	0.96	0.98	0.98	0.97	0.93
$R_L = 1/(1+bC_0)$	0.90	0.98	0.97	0.78	0.81
Freundlich					
K_f (L/g)	2.28	0.42	0.74	1.97	1.99
$1/n$	0.41	0.98	0.95	0.44	0.44
R^2	0.80	1.00	0.98	0.89	0.82

curve for Fe₃O₄@lignin (1:0.5) presented a really low R² value of 0.46. This may be due to the adsorption capacity of the adsorbent Fe₃O₄@lignin (1:0.5) for Congo red that is too strong and the high adsorption rate of adsorbent, resulting in the disorder of adsorption curve, which is also consistent with the conclusion of **Figure 7D**. Overall, from the aforementioned results, it can be concluded that the pseudo second-order model is the best model to describe the adsorption kinetics of MLN for adsorbing the Congo red dye.

Adsorption Isotherm

The adsorption isotherm refers to the relationship between the mass of the dye adsorbed on the unit mass of the adsorbent and the concentration of the liquid dye under constant temperature conditions (Masilompane et al., 2018). The equilibrium data were analyzed based on the Langmuir adsorption isotherm and the Freundlich adsorption isotherm. Among them, the Langmuir adsorption isotherm assumes that the adsorbate adsorbs on the monolayer of the surface of the homogeneous adsorbent, and the adsorption activation energy of each molecule adsorbed on its surface is equal. Adsorption migration did not occur after Langmuir adsorption isotherm adsorption. The Freundlich adsorption isotherm describes reversible adsorption not limited to the formation of a single layer; the adsorption is an interaction between heterogeneous multilayer molecules and adsorbates, and the adsorption capacity increased with the increase of the concentration.

From the correlation coefficient (R²) in **Table 3**, it can be seen that Fe₃O₄@lignin (1:0.5) Freundlich isotherm model R² is closer to 1 than the Langmuir isotherm model R². The Freundlich isotherm R² for Fe₃O₄@lignin (1:1) is consistent with the Langmuir model R². Other adsorbents perform better on Langmuir isotherms than Freundlich isotherms, indicating that except for Fe₃O₄@lignin (1:0.5), (1:1), the process of adsorbing Congo red is multilayer adsorption, and the adsorption processes of other adsorbents are all monolayer adsorption. What is more, the value of the separation factor R_L is greater than 0 and less than 1, which results demonstrated that the adsorption process is favorable. This result is consistent with the results of Li et al. (2019) that showed the adsorption of Congo red is more consistent with the Langmuir model, indicating that the adsorption process of Congo red is monolayer adsorption.

The value of theoretical maximum of adsorption capacity (q_m) of the lignin and MLN of Fe₃O₄@lignin (1:0.5), Fe₃O₄@lignin

(1:1), Fe₃O₄@lignin (1:2), and Fe₃O₄@lignin (1:3) derived from the Langmuir model were 28.72, 470.02, 206.29, 25.30, and 27.10 mg/g, respectively, of which lignin, Fe₃O₄@lignin(1:2), and Fe₃O₄@lignin (1:3) were consistent with the corresponding experimental values. The q_m values of Fe₃O₄@lignin (1:0.5) and Fe₃O₄@lignin (1:1) were higher than the experimental data, indicating that these two samples do not conform to the Langmuir model, which is consistent with previous conclusions. According to the Freundlich model, 1/n values of lignin, Fe₃O₄@lignin (1:2), and Fe₃O₄@lignin (1:3) are greater than 0 and less than 1, showing that the adsorption is advantageous. 1/n values of Fe₃O₄@lignin (1:0.5) and Fe₃O₄@lignin (1:1) are close to 1, showing that the adsorption is linear and there is no interaction between adsorbates. The reason for this phenomenon might be due to the high adsorption efficiency of Fe₃O₄@lignin (1:0.5) and Fe₃O₄@lignin (1:1), which leads to inaccurate adsorption model.

CONCLUSION

Studies have shown that MLN is an effective Congo red adsorbent with good adsorption performance, simple preparation, and easy recovery, which is an ideal adsorbent for Congo red dye. For the prepared MLN with different ratios of Fe₃O₄@lignin, Fe₃O₄@lignin (1:0.5) showed the best adsorption performance on Congo red with adsorption rate of 95.5% and adsorbing ability of 229 mg/g. The kinetics and isothermal models show that adsorption process of Fe₃O₄@lignin (1:0.5) belonged to the chemical adsorption of the multimolecular layer, and the adsorption process of other adsorbents is in accordance with the chemical adsorption of the monomolecular layer.

DATA AVAILABILITY STATEMENT

The raw data supporting the conclusions of this article will be made available by the authors, without undue reservation.

AUTHOR CONTRIBUTIONS

LF: investigation. HW and YT: supervision. YS: writing. QY: writing—review and editing. All authors contributed to the article and approved the submitted version.

REFERENCES

- An, L., Si, C., Bae, J. H., Jeong, H., and Kim, Y. S. (2020). One-step silanization and amination of lignin and its adsorption of Congo red and Cu(II) ions in aqueous solution. *Int. J. Biol. Macromol.* 159, 222–230. doi: 10.1016/j.ijbiomac.2020.05.072
- An, X., Cheng, D., Dai, L., Wang, B., Ocampo, H. J., Nasrallah, J., et al. (2017). Synthesis of nano-fibrillated cellulose/magnetite/titanium dioxide (NFC@Fe₃O₄@TNP) nanocomposites and their application in the photocatalytic hydrogen generation. *Appl. Catal. B Environ.* 206, 53–64. doi: 10.1016/j.apcatb.2017.01.021
- Calvo-Flores, F. G., and Dobado, J. A. (2010). Lignin as renewable raw material. *Chem. Sus. Chem.* 3, 1227–1235. doi: 10.1002/cssc.201000157
- Cui, K., Yan, B., Xie, Y., Qian, H., Wang, X., Huang, Q., et al. (2018). Regenerable urchin-like Fe₃O₄@PDA-Ag hollow microspheres as catalyst and adsorbent for enhanced removal of organic dyes. *J. Hazard. Mater.* 350, 66–75. doi: 10.1016/j.jhazmat.2018.02.011
- Deatsch, A. E., and Evans, B. A. (2014). Heating efficiency in magnetic nanoparticle hyperthermia. *J. Magn. Magn. Mater.* 354, 163–172. doi: 10.1016/j.jmmm.2013.11.006
- Dong, H., Li, M., Jin, Y., Wu, Y., Huang, C., and Yang, J. (2020a). Preparation of graphene-like porous carbons with enhanced thermal conductivities from

- lignin nano-particles by combining hydrothermal carbonization and pyrolysis. *Front. Energy Res.* 8:148. doi: 10.3389/fenrg.2020.00148
- Dong, H., Zheng, L., Yu, P., Jiang, Q., Wu, Y., Huang, C., et al. (2020b). Characterization and application of lignin-carbohydrate complexes from lignocellulosic materials as antioxidants for scavenging in vitro and in vivo reactive oxygen species. *ACS Sustain. Chem. Eng.* 8, 256–266. doi: 10.1021/acssuschemeng.9b05290
- Gall, D. L., Ralph, J., Donohue, T. J., and Noguera, D. R. (2017). Biochemical transformation of lignin for deriving valued commodities from lignocellulose. *Curr. Opin. Biotechnol.* 45, 120–126. doi: 10.1016/j.copbio.2017.02.015
- Gao, P., Jiang, H., Chen, W., and Cui, Z. (2020). An intramolecular Mannich type reaction of ortho-amino aromatic azo dye and its detection effect for formaldehyde. *Dye. Pigment.* 179:108376. doi: 10.1016/j.dyepig.2020.108376
- Ghaedi, M., Tavallali, H., Sharifi, M., Kokhdan, S. N., and Asghari, A. (2012). Preparation of low cost activated carbon from *Myrtus communis* and pomegranate and their efficient application for removal of Congo red from aqueous solution. *Spectrochim. Acta Part A Mol. Biomol. Spectrosc.* 86, 107–114. doi: 10.1016/j.saa.2011.10.012
- Gu, J., Guo, M., Huang, C., Wang, X., Zhu, Y., Wang, L., et al. (2021). Titanium dioxide nanoparticle affects motor behavior, neurodevelopment and axonal growth in zebrafish (*Danio rerio*) larvae. *Sci. Total Environ.* 754:142315. doi: 10.1016/j.scitotenv.2020.142315
- Guo, L., Liu, Y., Dou, J., Huang, Q., Lei, Y., Chen, J., et al. (2020). Surface modification of carbon nanotubes with polyethyleneimine through “mussel inspired chemistry” and “mannich reaction” for adsorptive removal of copper ions from aqueous solution. *J. Environ. Chem. Eng.* 8:103721. doi: 10.1016/j.jece.2020.103721
- Hassan, M. M., and Carr, C. M. (2018). A critical review on recent advancements of the removal of reactive dyes from dyehouse effluent by ion-exchange adsorbents. *Chemosphere* 209, 201–219. doi: 10.1016/j.chemosphere.2018.06.043
- Holkar, C. R., Jadhav, A. J., Pinjari, D. V., Mahamuni, N. M., and Pandit, A. B. (2016). A critical review on textile wastewater treatments: possible approaches. *J. Environ. Manage.* 182, 351–366. doi: 10.1016/j.jenvman.2016.07.090
- Humpert, D., Ebrahimi, M., and Czermak, P. (2016). Membrane technology for the recovery of lignin: a review. *Membranes (Basel)* 6, 1–13. doi: 10.3390/membranes6030042
- Jia, C., Xia, T., Ma, Y., He, N., Yu, Z., Lou, Z., et al. (2021). Fe₃O₄/α-Fe decorated porous carbon-based composites with adjustable electromagnetic wave absorption: impedance matching and loading rate. *J. Alloys Compd.* 858:157706. doi: 10.1016/j.jallcom.2020.157706
- Jiang, C., Wang, X., Qin, D., Da, W., Hou, B., Hao, C., et al. (2019). Construction of magnetic lignin-based adsorbent and its adsorption properties for dyes. *J. Hazard. Mater.* 369, 50–61. doi: 10.1016/j.jhazmat.2019.02.021
- Jiao, G. J., Peng, P., Sun, S. L., Geng, Z. C., and She, D. (2019). Amination of biorefinery technical lignin by Mannich reaction for preparing highly efficient nitrogen fertilizer. *Int. J. Biol. Macromol.* 127, 544–554. doi: 10.1016/j.ijbiomac.2019.01.076
- Kai, D., Tan, M. J., Chee, P. L., Chua, Y. K., Yap, Y. L., and Loh, X. J. (2016). ChemInform abstract: towards lignin-based functional materials in a sustainable world. *ChemInform* 47, 611–617. doi: 10.1002/chin.201615279
- Klapiszewski, L., Jamrozik, A., Strzemiescka, B., Matykiewicz, D., Voelkel, A., and Jesionowski, T. (2017a). Activation of magnesium lignosulfonate and kraft lignin: influence on the properties of phenolic resin-based composites for potential applications in abrasive materials. *Int. J. Mol. Sci.* 18:1224. doi: 10.3390/ijms18061224
- Klapiszewski, L., Zdzarta, J., Antecka, K., Synoradzki, K., Siwińska-Stefańska, K., Moszyński, D., et al. (2017b). Magnetite nanoparticles conjugated with lignin: a physicochemical and magnetic study. *Appl. Surf. Sci.* 422, 94–103. doi: 10.1016/j.apsusc.2017.05.255
- Kobayashi, S., Mori, Y., Fossey, J. S., and Salter, M. M. (2011). Catalytic enantioselective formation of C-C bonds by addition to imines and hydrazones: a ten-year update. *Chem. Rev.* 111, 2626–2704. doi: 10.1021/cr100204f
- Konicki, W., Helminiak, A., Arabczyk, W., and Mijowska, E. (2018). Adsorption of cationic dyes onto Fe@graphite core-shell magnetic nanocomposite: Equilibrium, kinetics and thermodynamics. *Chem. Eng. Res. Des.* 129, 259–270. doi: 10.1016/j.cherd.2017.11.004
- Li, J., Li, H., Yuan, Z., Fang, J., Chang, L., Zhang, H., et al. (2019). Role of sulfonation in lignin-based material for adsorption removal of cationic dyes. *Int. J. Biol. Macromol.* 135, 1171–1181. doi: 10.1016/j.ijbiomac.2019.06.024
- Liu, J., Wang, Z., Li, H., Hu, C., Raymer, P., and Huang, Q. (2018). Effect of solid state fermentation of peanut shell on its dye adsorption performance. *Bioresour. Technol.* 249, 307–314. doi: 10.1016/j.biortech.2017.10.010
- Liu, L., Wang, R., Yu, J., Hu, L., Wang, Z., and Fan, Y. (2018). Adsorption of Reactive Blue 19 from aqueous solution by chitin nanofiber-/nanowhiskered hydrogels. *RSC Adv.* 8, 15804–15812. doi: 10.1039/c8ra01563e
- Lou, Z., Li, R., Wang, P., Zhang, Y., Chen, B., Huang, C., et al. (2020). Phenolic foam-derived magnetic carbon foams (MCFs) with tunable electromagnetic wave absorption behavior. *Chem. Eng. J.* 391:123571. doi: 10.1016/j.cej.2019.123571
- Lou, Z., Wang, Q., Zhang, Y., Zhou, X., Li, R., Liu, J., et al. (2021). In-situ formation of low-dimensional, magnetic core-shell nanocrystal for electromagnetic dissipation. *Compos. Part B Eng.* 214:108744. doi: 10.1016/j.compositesb.2021.108744
- Luo, X., Liu, C., Yuan, J., Zhu, X., and Liu, S. (2017). Interfacial solid-phase chemical modification with Mannish reaction and Fe (III) chelation for designing the lignin-based spherical nanoparticle adsorbents for highly efficient removal of low concentration phosphate from water The Supporting Information. *ACS Sustainable Chem. Eng.* 5, 6539–6547.
- Masilompane, T. M., Chaukura, N., Mishra, S. B., and Mishra, A. K. (2018). Chitosan-lignin-titanium nanocomposites for the removal of brilliant black dye from aqueous solution. *Int. J. Biol. Macromol.* 120, 1659–1666. doi: 10.1016/j.ijbiomac.2018.09.129
- Mikhaylova, M., Kim, D. K., Bobrysheva, N. P., Osmolowsky, M., Semenov, V., Tsakalakos, T., et al. (2004). Superparamagnetism of magnetite nanoparticles: dependence on surface modification. *Langmuir* 20, 2472–2477. doi: 10.1021/la035648e
- Nair, V., Panigrahy, A., and Vinu, R. (2014). Development of novel chitosan-lignin composites for adsorption of dyes and metal ions from wastewater. *Chem. Eng. J.* 254, 491–502. doi: 10.1016/j.cej.2014.05.045
- Pei, W., Chen, Z. S., Chan, H. Y. E., Zheng, L., Liang, C., and Huang, C. (2020). Isolation and identification of a novel anti-protein aggregation activity of lignin-carbohydrate complex from chionanthus retusus leaves. *Front. Bioeng. Biotechnol.* 8:573991. doi: 10.3389/fbioe.2020.573991
- Sham, A. Y. W., and Notley, S. M. (2018). Adsorption of organic dyes from aqueous solutions using surfactant exfoliated graphene. *J. Environ. Chem. Eng.* 6, 495–504. doi: 10.1016/j.jece.2017.12.028
- Siyasukh, A., Chimupala, Y., and Tomanon, N. (2018). Preparation of magnetic hierarchical porous carbon spheres with graphitic features for high methyl orange adsorption capacity. *Carbon N. Y.* 134, 207–221. doi: 10.1016/j.carbon.2018.03.093
- Sohni, S., Gul, K., Ahmad, F., Ahmad, I., Khan, A., Khan, N., et al. (2018). Highly efficient removal of acid red-17 and bromophenol blue dyes from industrial wastewater using graphene oxide functionalized magnetic chitosan composite. *Polym. Compos.* 39, 3317–3328. doi: 10.1002/pc.24349
- Upton, B. M., and Kasko, A. M. (2016). Strategies for the conversion of lignin to high-value polymeric materials: review and perspective. *Chem. Rev.* 116, 2275–2306. doi: 10.1021/acs.chemrev.5b00345
- Wang, B., Chen, T. Y., Wang, H. M., Li, H. Y., Liu, C. F., and Wen, J. L. (2018). Amination of biorefinery technical lignins using Mannich reaction synergy with subcritical ethanol depolymerization. *Int. J. Biol. Macromol.* 107, 426–435. doi: 10.1016/j.ijbiomac.2017.09.012
- Wang, G., Liu, Q., Chang, M., Jang, J., Sui, W., Si, C., et al. (2019). Novel Fe₃O₄@lignosulfonate/phenolic core-shell microspheres for highly efficient removal of cationic dyes from aqueous solution. *Ind. Crops Prod.* 127, 110–118. doi: 10.1016/j.indcrop.2018.10.056
- Wang, X., Jiang, C., Hou, B., Wang, Y., Hao, C., and Wu, J. (2018). Carbon composite lignin-based adsorbents for the adsorption of dyes. *Chemosphere* 206, 587–596. doi: 10.1016/j.chemosphere.2018.04.183
- Wang, X., Zhang, Y., Hao, C., Dai, X., Zhou, Z., and Si, N. (2014). Ultrasonic-assisted synthesis of aminated lignin by a Mannich reaction and its decolorizing properties for anionic azo-dyes. *RSC Adv.* 4, 28156–28164. doi: 10.1039/c4ra03133d
- Wang, Y., Wang, X., Ding, Y., Zhou, Z., Hao, C., and Zhou, S. (2018a). Novel sodium lignosulfonate assisted synthesis of well dispersed Fe₃O₄

- microspheres for efficient adsorption of copper (II). *Powder Technol.* 325, 597–605. doi: 10.1016/j.powtec.2017.11.055
- Wang, Y., Zhu, L., Wang, X., Zheng, W., Hao, C., Jiang, C., et al. (2018b). Synthesis of aminated calcium lignosulfonate and its adsorption properties for azo dyes. *J. Ind. Eng. Chem.* 61, 321–330. doi: 10.1016/j.jiec.2017.12.030
- Yang, W., Rallini, M., Natali, M., Kenny, J., Ma, P., Dong, W., et al. (2019). Preparation and properties of adhesives based on phenolic resin containing lignin micro and nanoparticles: a comparative study. *Mater. Des.* 161, 55–63. doi: 10.1016/j.matdes.2018.11.032
- Zhao, G. H., Fang, Y. Y., Dai, W., and Ma, N. (2018). Highly enhanced adsorption of Congo red by functionalized finger-citron-leaf-based porous carbon. *Water Sci. Technol.* 77, 220–228. doi: 10.2166/wst.2017.540
- Zheng, L., Yu, P., Zhang, Y., Wang, P., Yan, W., Guo, B., et al. (2021). Evaluating the bio-application of biomacromolecule of lignin-carbohydrate complexes (LCC) from wheat straw in bone metabolism via ROS scavenging. *Int. J. Biol. Macromol.* 176, 13–25. doi: 10.1016/j.ijbiomac.2021.01.103
- Conflict of Interest:** The authors declare that the research was conducted in the absence of any commercial or financial relationships that could be construed as a potential conflict of interest.
- Copyright © 2021 Fang, Wu, Shi, Tao and Yong. This is an open-access article distributed under the terms of the Creative Commons Attribution License (CC BY). The use, distribution or reproduction in other forums is permitted, provided the original author(s) and the copyright owner(s) are credited and that the original publication in this journal is cited, in accordance with accepted academic practice. No use, distribution or reproduction is permitted which does not comply with these terms.



Application of Ethanol Extracts From *Alnus sibirica* Fisch. ex Turcz in Hair Growth Promotion

Eun Ju Ha^{1†}, Jang-Hyuk Yun^{2†}, Chuanling Si³, Young Soo Bae⁴, Young-Hwan Jeong⁴, Kwang-Hyun Park^{5,6*} and Sun-Eun Choi^{4*}

¹ Department of Cosmetology Science, Nambu University, Gwangju, South Korea, ² College of Veterinary Medicine and Institute of Veterinary Science, Kangwon National University, Chuncheon, South Korea, ³ Tianjin Key Laboratory of Pulp and Paper, Tianjin University of Science and Technology, Tianjin, China, ⁴ Department of Forest Biomaterials Engineering, College of Forest and Environmental Sciences, Kangwon National University, Chuncheon, South Korea, ⁵ Department of Emergency Medical Rescue, Nambu University, Gwangju, South Korea, ⁶ Department of Emergency Medicine, Graduate School of Chonnam National University Gwangju, Gwangju, South Korea

OPEN ACCESS

Edited by:

Caoxing Huang,
Nanjing Forestry University, China

Reviewed by:

Ming-Guo Ma,
Beijing Forestry University, China
Xiao Jiang,
North Carolina State University,
United States
Zhanhua Huang,
Northeast Forestry University, China

*Correspondence:

Sun-Eun Choi
oregonin@kangwon.ac.kr
Kwang-Hyun Park
khpark@nambu.ac.kr

[†] These authors have contributed
equally to this work and share first
authorship

Specialty section:

This article was submitted to
Bioprocess Engineering,
a section of the journal
Frontiers in Bioengineering and
Biotechnology

Received: 27 February 2021

Accepted: 22 April 2021

Published: 08 June 2021

Citation:

Ha EJ, Yun J-H, Si C, Bae YS,
Jeong Y-H, Park K-H and Choi S-E
(2021) Application of Ethanol Extracts
From *Alnus sibirica* Fisch. ex Turcz
in Hair Growth Promotion.
Front. Bioeng. Biotechnol. 9:673314.
doi: 10.3389/fbioe.2021.673314

Alnus sibirica Fisch. ex Turcz (ASFT), belonging to the family of Betulaceae, grows naturally in Asia, Europe, and America. The aims of this study are determining the efficacy of various biomarkers related to hair loss, evaluated by extracting the branch with 60% alcohol, and purely separating diarylheptanoid oregonin, an indicator and active substance, from 60% alcohol extract of the tree. To determine the preventive effects on hair loss, we investigated the anti-oxidative and anti-apoptotic effects on hydrogen peroxide-induced cytotoxicity on human hair dermal papilla cells using 3-(4,5-dimethylthiazol-2-yl)-2,5-diphenyltetrazolium bromide assay and Western blotting analysis for proving of apoptosis-related marker alteration, respectively. Moreover, we examined the ameliorative effects of 60% alcohol extract of the tree and oregonin against changes of oxidative stress-induced cytokine and testosterone-induced dihydrotestosterone production as crucial pathways of the hair loss mechanism. These results suggest that 60% alcohol extract of the tree and oregonin were available as novel natural materials for maintaining hair health in mammals.

Keywords: *Alnus sibirica*, oregonin, constituent, biomass, bio-application, hair growth promoting

INTRODUCTION

Alnus sibirica Fisch. ex Turcz belongs to the family Betulaceae, and more than 17 species of plants of the same genus grow naturally in the Republic of Korea (Lee, 1996). It is a tree resource that grows wild throughout the northern hemisphere such as the Republic of Korea, the United States, Japan, and China (Lee, 1997).

Until now, we isolated diarylheptanoid compounds from plants of the genus *Alnus* and reported various physiological activities such as anti-oxidant activity, anti-inflammatory activity, and anti-atopic activity (Choi et al., 2010). Through these previous studies, we have confirmed

Abbreviations: ASFT, *Alnus sibirica* Fisch. ex Turcz; DHT, dihydrotestosterone; MTT, 3-(4,5-dimethylthiazol-2-yl)-2,5-diphenyltetrazolium bromide; HFDPC, human follicle dermal papilla cells; ELISA, enzyme-linked immunosorbent assay; IGF-I, insulin-like growth factor-I; TGF- β , transforming growth factor-beta; Bax, Bcl-2-associated X protein; Bcl-2, B-cell lymphoma 2; PARP-1, poly ADP-ribose polymerase 1.

the functionality and utility of resources of the genus *Alnus* (Choi et al., 2012). This potent and effective physiological active substance is thought to be oregonin, known as a diarylheptanoid family compound present in high content in plants of the genus *Alnus*. That can be estimated by examining domestic and international research trends focusing on oregonin as an indicator material in the study of chemical system classification of plants of the genus *Alnus* (Lim et al., 2004; Choi, 2013).

A number of studies have been conducted to determine the structure by separating oregonin, a glycoside of diarylheptanoid (Karchesy et al., 1974; Suga et al., 1982; Ohta et al., 1984; Aoki et al., 1990; Choi et al., 2012; Ko et al., 2015; Hu et al., 2018; Huang et al., 2021), by tracking substances that change color to reddish brown when trees of the genus *Alnus* (*Alnus rubra*, *Alnus hirsuta*, and *Alnus japonica*) (Asakawa, 1971; Karchesy et al., 1974) are cut. In addition, many researchers around the world have published a number of research reports using oregonin as an indicator material in the chemical system classification study of the genus *Alnus* (Lee et al., 1992; Guz et al., 2002; Lim et al., 2004; Choi, 2013; Choi et al., 2016).

Diarylheptanoids isolated from plants of the genus *Alnus* prevent oxidation, prevent diarrhea, have anti-cancer effects (Sheth et al., 1973; Kawai et al., 1990; Lee et al., 1998), and inhibit the proliferation and NO production of mouse melanoma cell line B16-F10. In addition, it has a cyclooxygenase-2 inhibitory effect (Lee et al., 2000a), has an effect on dermal inflammation by acting as a 5-lipoxygenase inhibitor, inhibits platelet aggregation, acts as PKC alpha inhibitor, inhibits the enzyme activity involved in prostaglandin biosynthesis, and has antibacterial (Saxena et al., 1995) and liver-protective effects. Recently, it was found that it has anti-atopic efficacy *in vitro* and *in vivo* (Choi et al., 2010). In addition, it was found that oregonin has anti-apoptosis modulation effect by confirming that human dermal papilla cell apoptosis induced by oxidative stress is blocked by oregonin isolated from *A. japonica* branches (Lee et al., 2018). Therefore, many researchers around the world are characteristically paying attention to oregonin among the diarylheptanoid family as the representative compound of the effective substance or indicator substance of the genus *Alnus* (Sin and Ahn, 1991; Yamazaki et al., 1998; Lee et al., 2000b). The *Alnus* plant species is colloquially referred to as *Jeok-Yang* among Chinese traditional doctors and Korean oriental medicine. It is believed that it “clears body heat” and “reduces body heat.” In Chinese and Korean traditional medicine, it has been believed that body heat was closely related with skin diseases (Yang et al., 1999). Accordingly, *Alnus* species has been used in America as a traditional medicine for various skin afflictions (Boericke, 1927). With regard to the application of *Alnus* plants species to various skin diseases in the East and the West, this study attempted to conduct scientific verification on the prevention and treatment of hair loss diseases, which are getting a lot of interest and demand worldwide in recent years.

In addition, the research team is conducting research by utilizing the know-how of extracting and manufacturing polyphenol compounds in high content—in this case, an effective substance derived from arboretum, which has recently been found to have various positive physiological activity effects (Hu et al., 2017; Dong et al., 2020; Pei et al., 2020; Xu et al., 2021). As

a result, by extracting oregonin, a glycoside of diarylheptanoid, from ASFT in high content (Choi, 2019), it has been found to have antioxidant, anti-inflammatory, and anti-allergic effects.

In this study, the efficacy of various biomarkers related to hair loss was evaluated by extracting the ASFT branch with 60% alcohol and singly isolating oregonin, an indicator and active substance, from the 60% alcohol extract of ASFT.

While the market demands related to hair loss, both domestic and in countries abroad, are rapidly increasing recently, it is not easy to discover new natural materials that are safe for the human body with scientific efficacy as collateral.

In this study, the research group confirmed the ability of human dermal papilla cells to inhibit dihydrotestosterone (DHT) production, which is well known as a representative factor in male pattern hair loss. Finally, efficacy experiments were conducted on biomarkers related to oxidative stress-induced apoptosis, namely, Bcl-2, Bax, caspase-3, and PARP.

By carrying out the above-mentioned experimental results, we tried to confirm the possibility of a natural new material related to hair loss with oregonin isolated therefrom.

Thus, we performed the experiments and suggestions of the patho-/pharmaco-physiological evidence of the species and oregonin, typical effective substances of ASFT, reporting its main mechanisms of action, as well as to critically analyze its performance in the fight against oxidative stress-induced hair papilla cell damages and hair loss.

MATERIALS AND METHODS

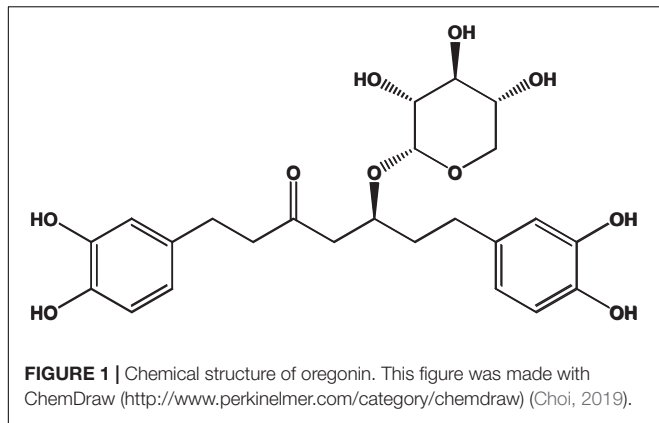
Preparation of ASFT Extract and Isolation

ASFT was collected at 10 kg (branches with barks) from the Special Resource Test Forest (Jinae-ri, Sinbuk-eup, Chuncheon-si, Gangwon-do), Republic of Korea, in September of 2020, certified by Prof. Choi (Wood-Natural Product Functional Materials Lab, College of Forest and Environmental Sciences, Kangwon National University), and a voucher specimen (ASB2020-09) was deposited at the herbarium of the College of Forest and Environmental Sciences, Kangwon National University. The 10-kg ASB was extracted twice with 60% edible ethanol extract at room temperature. The concentration that is removed by the edible ethanol under vacuum afforded to 661 g (6.61%).

Prep-HPLC was used to isolate oregonin from the 60% ethanol extract of ASFT. Silica gel was used as the column, and chloroform/methanol/water (70:30:4) solution was applied as an isocratic condition. These conditions were repeated to obtain a final 100 mg of pure oregonin, which was used in the experiment.

Oregonin

Oregonin, a brown amorphous powder, was purified and characterized following the previous reports (Choi, 2019) (positive LC/MS m/z : 501 $[M + Na]^+$, negative LC/MS m/z : 477 $[M - H]^-$). Definition of the chemical structure of purified oregonin (**Figure 1**) was made with ChemDraw (PerkinElmer, MA, United States).



Cell Culture and Treatment

Human follicle dermal papilla cells (HDFPC) were obtained and cultured in the American Type Culture Collection (VA, United States), following the manufacturer's instruction, in a 37°C humidified incubator supplied with 5% CO₂ and 95% O₂. The cells were seeded and were pretreated for 20 min with various concentrations of drugs and were subsequently incubated with hydrogen peroxide (H₂O₂, Sigma-Aldrich, MO, United States) for the indicated time points.

MTT Assay

Cell viability was calculated by 3-(4,5-dimethylthiazol-2-yl)-2,5-diphenyltetrazolium bromide (MTT) assay with slight modifications (Si et al., 2013b; Hu et al., 2014, 2016). MTT (Sigma-Aldrich, MO, United States) was used as stock solution (×10, 5 mg/ml) with phosphate-buffered saline (PBS, pH 7.2) and filtered. At the end of the indicated treatment time, 10 μl of MTT solution was added to each well. After incubation for 20 min at 37°C, 100 μl of dimethyl sulfoxide was added to each well. After 20 min of incubation, the plate was read by a multiwell plate reader (BMG-biotech, Berlin, GmBh) at 570 nm for absorbance. The percentage of the live cells was calculated using the following formula: viability (%) = [(absorbance of sample)/(absorbance of control) × 100].

Western Blot

Cell lysates were separated with 10 or 12% SDS-PAGE gels and transferred using 20% methanol onto polyvinylidene fluoride (PVDF) membranes (Bio-Rad laboratory, CA, United States). The membranes were blocked for 1 h at room temperature in 3% immunoglobulin-free bovine serum albumin (Invitrogen, CA, United States)-Tris buffered saline (pH 7.4). Primary antibodies to each antigen were administrated with their respective blocking buffers, following the manufacturer's instruction, overnight at 4°C under gentle shaking. Washes were performed with PBS 0.1% Tween-20 (PBST) before the addition of secondary antibody for 1 h at room temperature. Washes were performed with 1 × PBST before imaging on chemoluminescence dye (Bio-Rad Laboratory, CA, United States). Protein detection was performed using Image QuantTM with LAS-500 (GE Healthcare, CA, United States).

ELISA

To measure insulin-like growth factor 1 (IGF-1) (Elh-IGF1, RayBiotech, GA, United States), transforming growth factor-β1 (TGF-β1, Enzo Life Science Inc, NY, United States), and dihydrotestosterone (ALPCO, NH, United States) levels in the cell lysate, enzyme-linked immunosorbent assay was used. All reaction and results were calculated after data were obtained with a microplate reader (BMG Biotech, Berlin, GmBH) at a suggested wavelength according to the manufacturer's instruction.

Statistical Analysis

Student's *t*-test was conducted to assess the effects of the materials on superoxide-induced HDFPCs' damage mechanism. Data are presented as mean ± standard deviation of the mean and as statistical comparisons between each group. Data are representative of three independent experiments. Significance was set at *p* < 0.05.

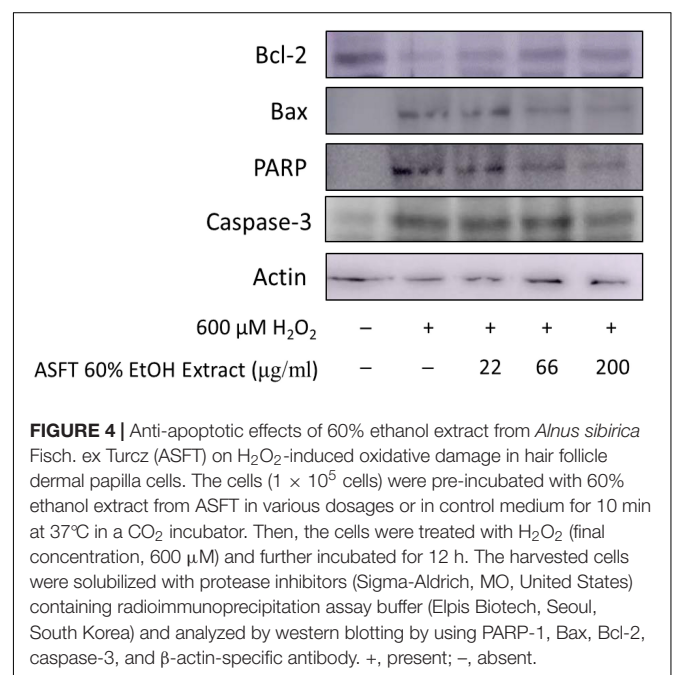
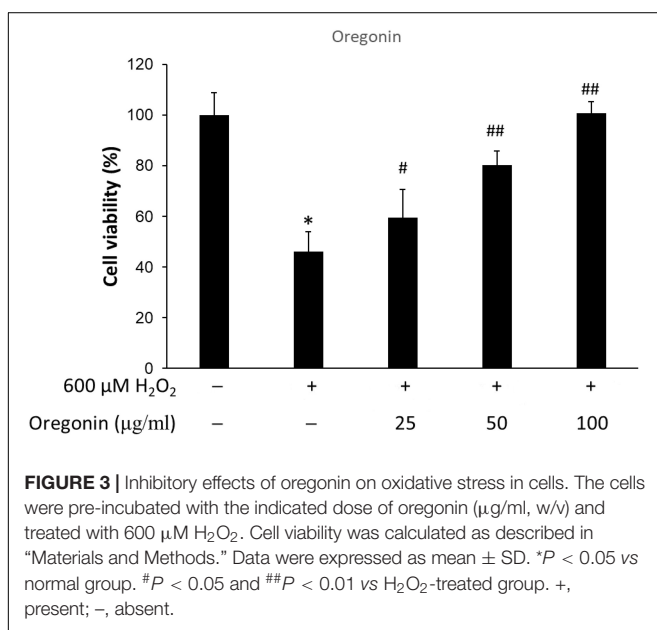
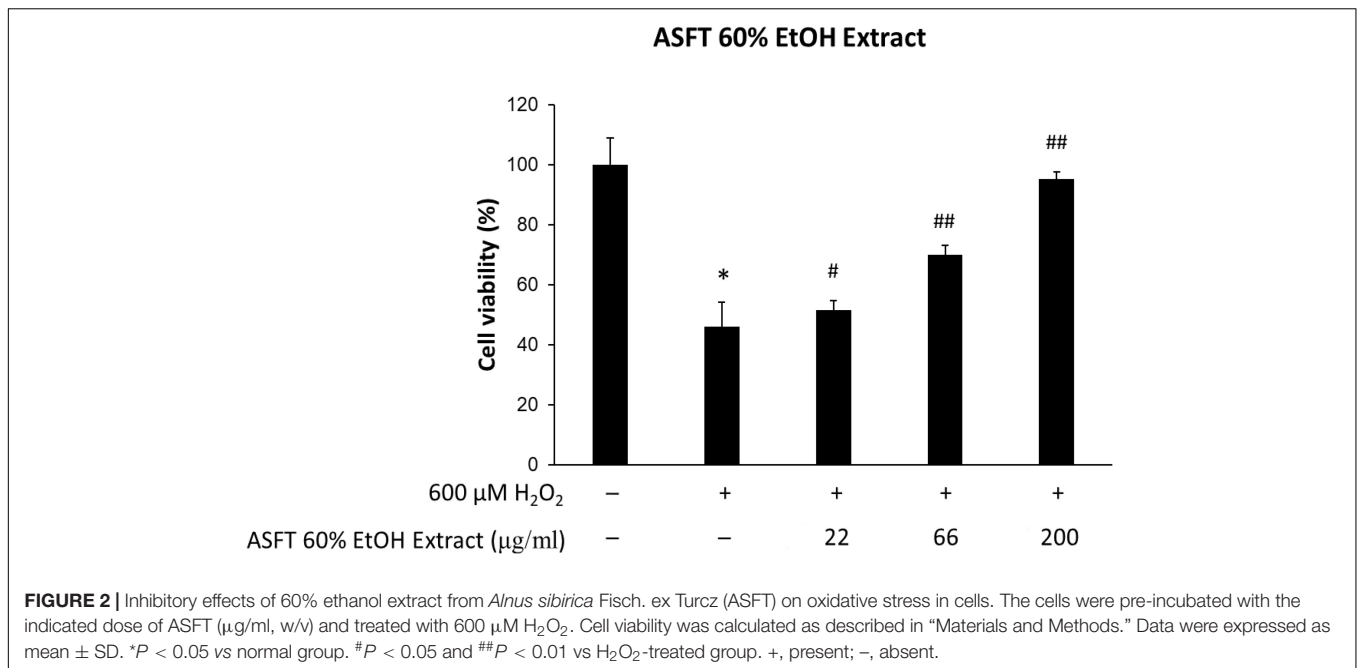
RESULTS

Reduction of Oxidative Stress-Induced Cytotoxicity by Treatment With 60% ASFT EtOH Extracts and Oregonin

The protective effects of 60% EtOH extracts from ASFT and oregonin on oxidative stress-induced HDFPC were evaluated by MTT assay. The results showed that 60% EtOH extracts from ASFT had inhibitory effects on 600 μM H₂O₂-induced cytotoxicity (Figure 2). The viability of HDFPC was reduced by 600 μM H₂O₂ to 50%, and the 60% EtOH extracts from ASFT were gradually increased in viability in a dose-dependent manner. Similarly, oregonin also had ameliorative effects on the same damage model in HDFPC (Figure 3). Isolated oregonin significantly protected against oxidative stress-induced cytotoxicity with a smaller dose than the ethanol extracts.

Protective Mechanisms Against Oxidative Stress-Induced Apoptosis by 60% ASFT EtOH Extracts and Oregonin

In the same manner as described above, we performed experiments wherein 600 μM of H₂O₂ was treated to measure apoptosis in HDFDC. To elucidate the protective mechanisms of 60% EtOH extracts from ASFT and oregonin on oxidative stress-induced HDFPC apoptosis, we analyzed apoptosis marker molecules including Bcl-2 (representative protein molecule involved in inhibition of apoptosis) (Tsujimoto et al., 1985; Cleary et al., 1986) and Bax (Bcl-2-associated X protein, representative apoptosis-inducing protein molecule) (Oltvai et al., 1993; Sedlak et al., 1995), poly ADP-ribosyl polymerase 1 (PARP-1), and caspase-1 (Figures 4, 5). Treatment with H₂O₂ significantly reduced the expression of Bcl-2 molecules, while pretreatment with 60% EtOH extracts from ASFT (Figure 4) and oregonin (Figure 5) markedly elevated the expression of Bcl-2 molecules in a dose-dependent manner. In contrast, treatment with H₂O₂ elevated the expression of Bax, PARP, and caspase-1 protein level. The pretreatment with 60% EtOH extracts from ASFT (Figure 4)



and oregonin (Figure 5) showed reducing properties to these apoptosis signals in a dose-dependent manner.

Efficacy in Increasing IGF-1 Expression

The changes of IGF-1 level on oxidative stress-induced HDFPC damage and the recovery effects of 60% EtOH extracts from ASFT and oregonin are shown in Figures 6, 7, respectively. Treatment with H_2O_2 significantly decreased the IGF-1 level in the intracellular region, whereas 60% EtOH extracts from ASFT (Figure 6) and oregonin (Figure 7) treatment attenuated the

oxidative stress-induced IGF-1 level in a dose-dependent manner compared to H_2O_2 alone.

TGF- β 1 Expression Inhibition Efficacy

The effects of 60% EtOH extracts from ASFT and oregonin on TGF- β 1 expression in the intracellular region were determined (Figures 8, 9, respectively). H_2O_2 treatment significantly increased TGF- β 1 expression compared to the normal controls. However, 60% EtOH extracts from ASFT (Figure 8) and oregonin

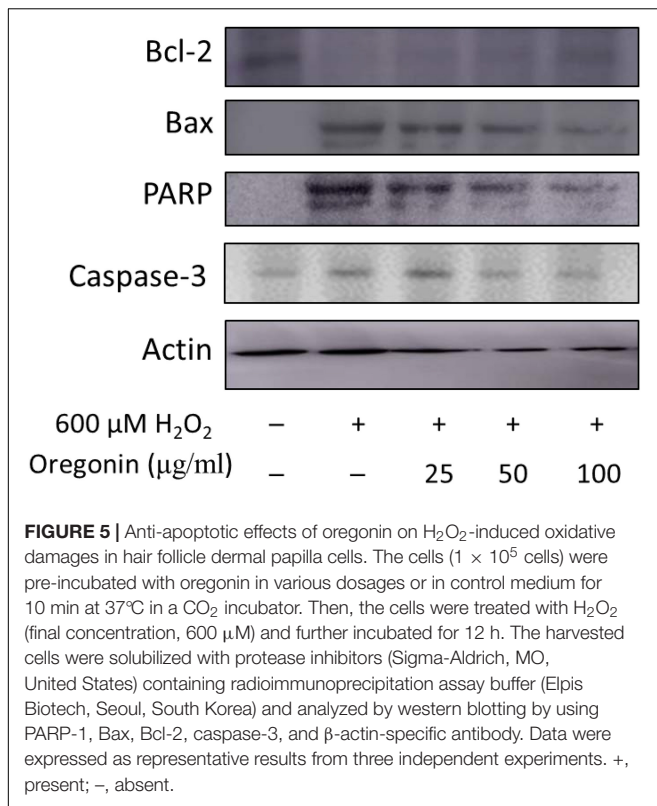


(Figure 9) treatment abrogated these effects in a dose-dependent manner, resulting in a significant reduction in TGF-β1 expression compared to H₂O₂ treatment alone.

Dihydrotestosterone Production Inhibitory Effect

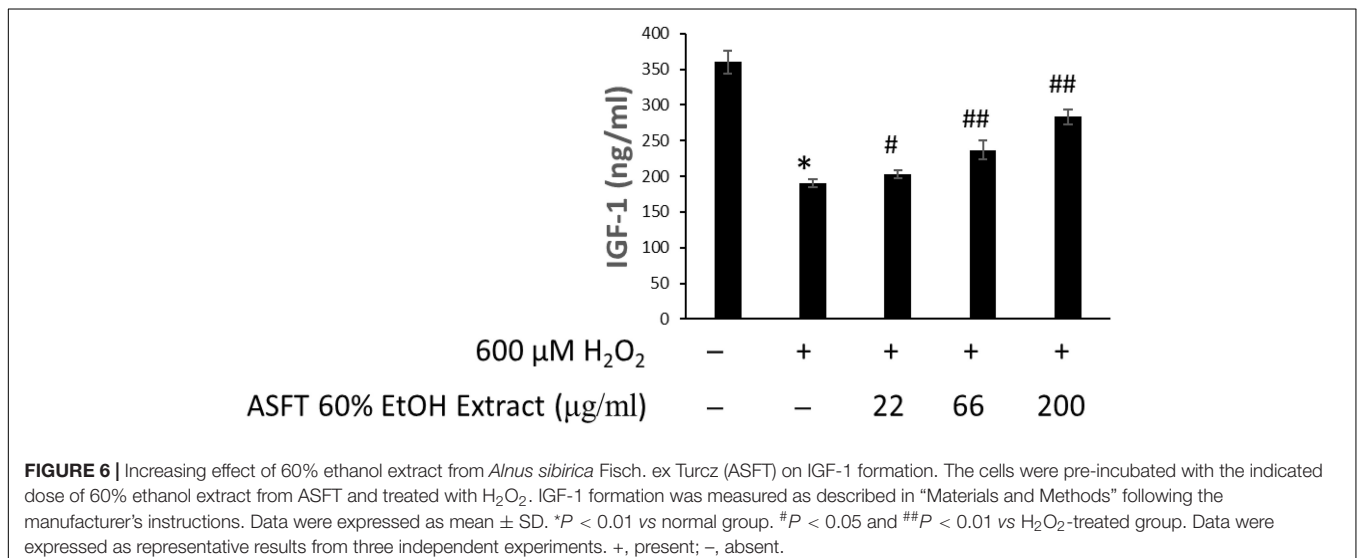
Levels of DHT are shown in Figures 10, 11. The group treated with testosterone, the substrates of 5α-reductase, showed

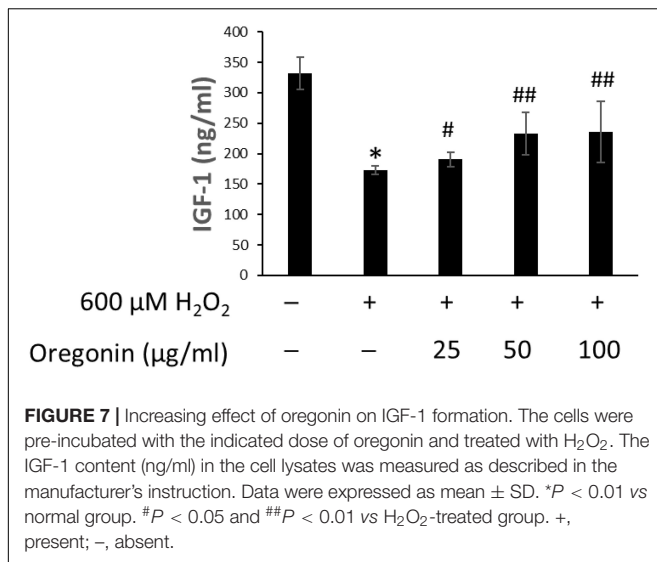
significantly higher levels of DHT than the normal control group. Simultaneous treatment with 60% EtOH extracts from ASFT (Figure 10) and oregonin (Figure 11) to testosterone-treated HDFPC significantly decreased the DHT content compared to testosterone treatment alone. The administration of minoxidil, a well-known inhibitor of 5α-reductase, also significantly reduced DHT production compared to the normal controls. Interestingly, 60% EtOH extracts from ASFT and oregonin showed a similar efficacy in a dose-dependent manner, respectively. These results indicate that 60% EtOH extracts from ASFT and oregonin had an ameliorative effect on DHT-mediated hair loss.

DISCUSSION

Different components in plants are a rich source far from being well utilized (Si et al., 2008b, 2009a; An et al., 2019; Du et al., 2019; Li et al., 2019; Liu et al., 2020a; Liu H. et al., 2021; Liu K. et al., 2021), and chemical constituents from plants demonstrate various significant bioactivities (Si et al., 2008a, 2009b, 2013a; Huang et al., 2018, 2019; Liu et al., 2020b). The present study indicates that 60% EtOH extracts from ASFT or oregonin treatment prevents oxidative stress-induced apoptosis and ameliorated DHT-mediated hair loss signaling (Figure 12) in different dose ranges between each material. The general pattern of male hair loss is determined by genetic causes, and when hair loss begins earlier, the degree of hair loss tends to become more severe. Hair loss symptoms are reported, such as the case that if at least one of the paternal or maternal family members has alopecia, then it is more likely to develop specifically in males in later generations (Olsen, 2001; Yip et al., 2011; Liu et al., 2017; Lu et al., 2019; Kumar et al., 2020).

Oxidative stress is known to induce apoptosis and/or stimulate various cell types within the scalp and hair components; these cell types are keratinocytes, hair follicle cells, papilla cells, and various immune cells. Programmed cell death, commonly referred to as apoptosis, is mediated by various signal cascades including



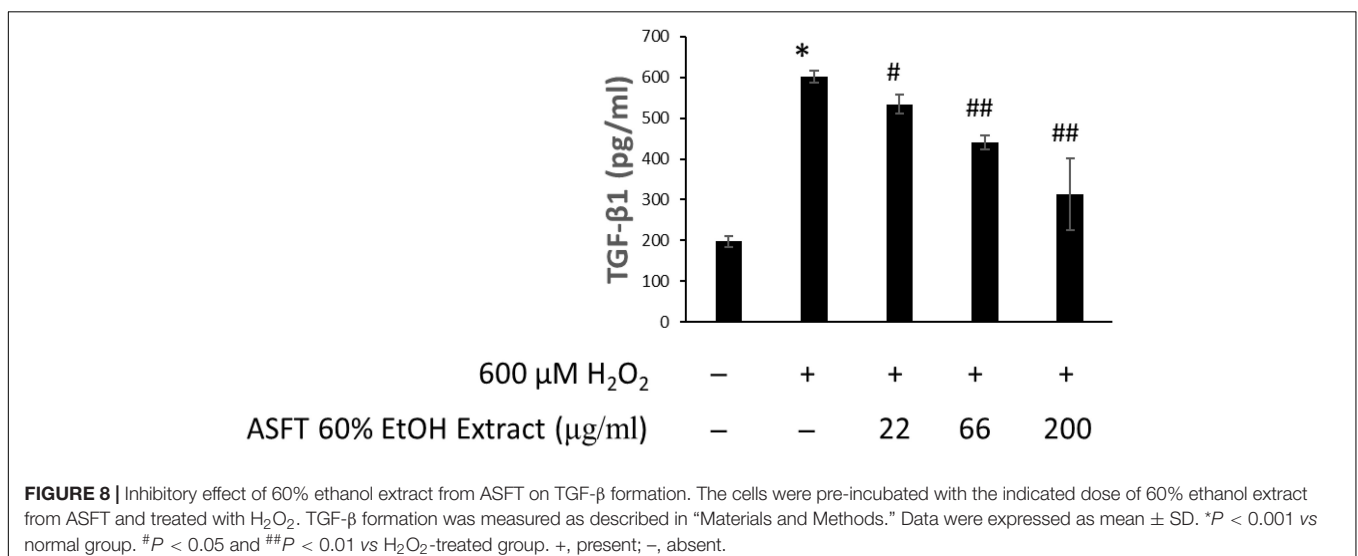


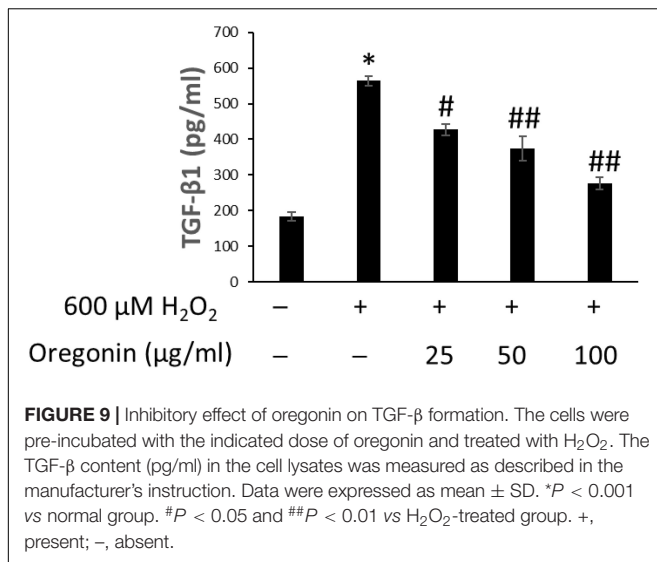
Bax, Bcl-2, PARP-1, and caspase family. PARP-1 is present in the nucleus of cells and uses a large amount of NAD to induce poly-ADP ribosylation of the target protein. Through this, it activates signaling involved in sub-cell death. Activation of PARP-1 has been used as an indicator for the progression of apoptosis (Schultz et al., 2003; Godon et al., 2008). HDFDC treated with 600 μM of H_2O_2 significantly increased the expression of PARP-1 in cells, and this result proves that apoptosis of cells is in progress. An additionally identified biomarker is caspase-3. Caspase-3 is a molecule which is responsible for the final stage of apoptosis of cells and is a protein which is responsible for irreversible cell death through the expression of the above-mentioned various molecules and cell signaling mechanisms. Furthermore, oxidative stress can simulate with hydrogen peroxide, freely translocating to intra-/extra-cellular region. In many experimental trials, it serves as an inducer in normal physiology or malfunctions. As a result, the identification of caspase-3 activation or increased

protein expression has been used as an important final indicator for the progression of apoptosis (Alnemri et al., 1996; Harrington et al., 2008). HDFDC treated with 600 μM of H_2O_2 significantly increased the protein expression of caspase-3 in the cells, and these results could confirm that the apoptosis of cells is actually in progress. In this study, 60% EtOH extracts from ASFT show different dose ranges larger than oregonin in most experiments, but ASFT contains more varied compounds. Thus, we found effective and safe dosages of ASFT and oregonin for these experimental models.

Growth factors in hair growth, e.g., IGF-1, have been reported as important growth factors involved in hair growth and regulation by promoting the growth of epithelial cells in culture, increasing the tissue length of hair follicles, and acting as an important factor promoting hair growth (Itami et al., 1995; Hibino and Nishiyama, 2004). IGF-1 is involved in the increased expression by androgenic hormones and the action of testosterone on the hair, and it is known to play an important role in the mechanism of action that causes androgen-dependent alopecia (Price, 1999; Randall, 2008).

In addition, it has been reported to not only prevent aging, improve dementia, depression, and adult lifestyle diseases but also enhance immunity and improve bone density, prevent skin aging, and induce the transformation of hair from a resting state to a growing state (Rosen et al., 1994). Research results on the increase or decrease in hair loss treatment have also been reported. Furthermore, as the growth of hair has a closer relationship with blood circulation, IGF-1 and EGF have a reported function that contributes to the growth of hair follicles that promote the growth of hair (Hodak et al., 1996; Wells, 1999). As such, increasing the expression of IGF-1 factor, which is an important factor in hair growth, can be expected to be effective in hair growth. Discovering the advantages of developing new materials derived from natural products that minimize the risk of side effects and toxicity of existing synthetic-based compounds is an important factor in developing new technologies. Therefore, we confirmed the

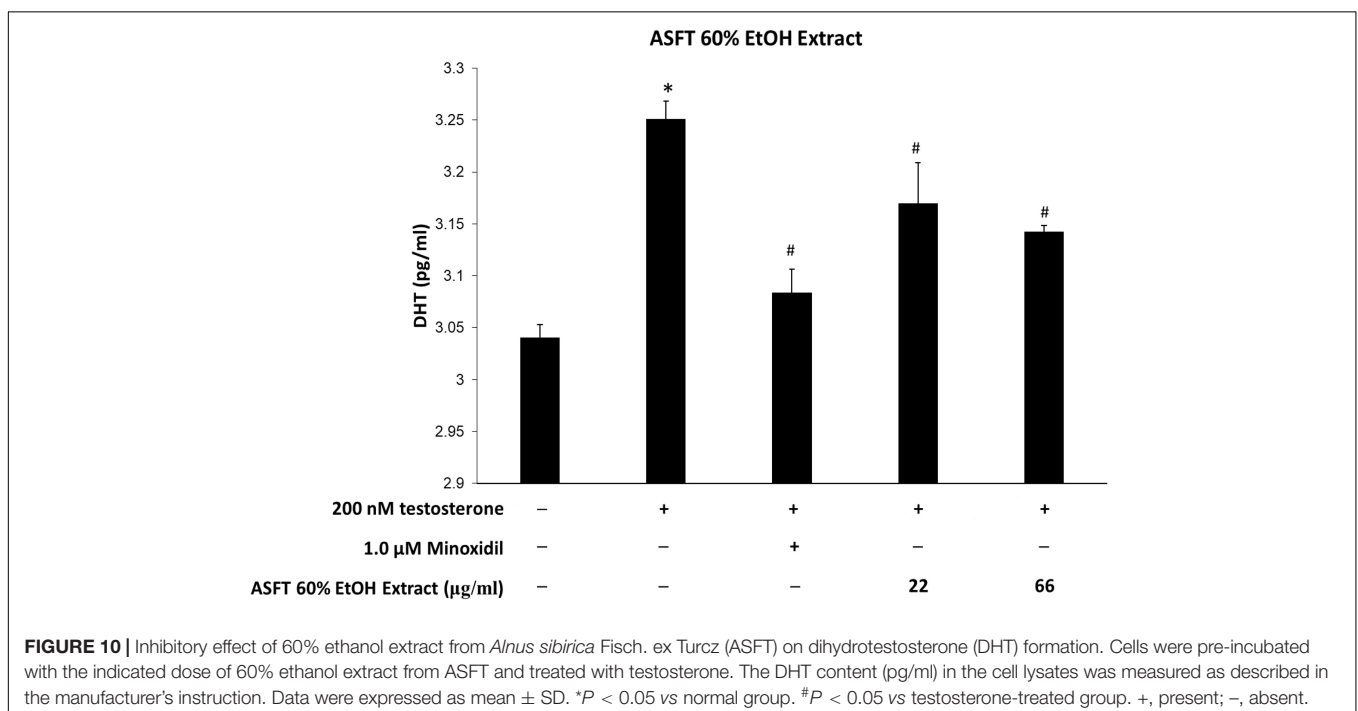


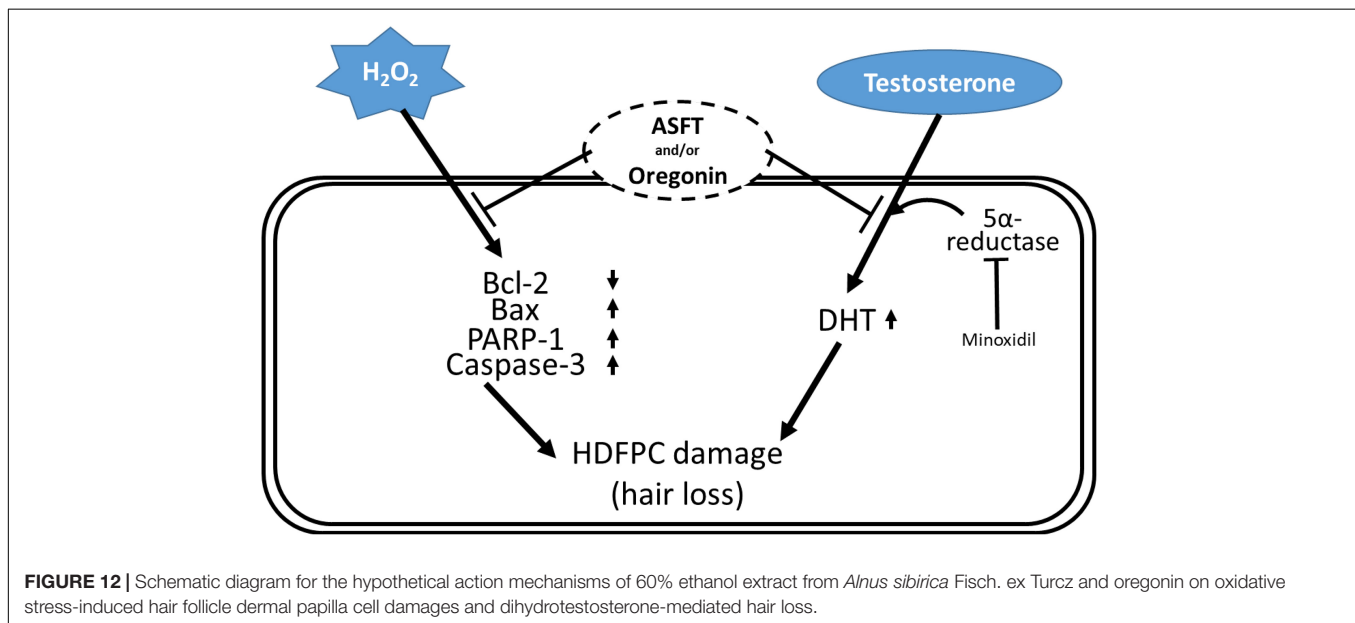
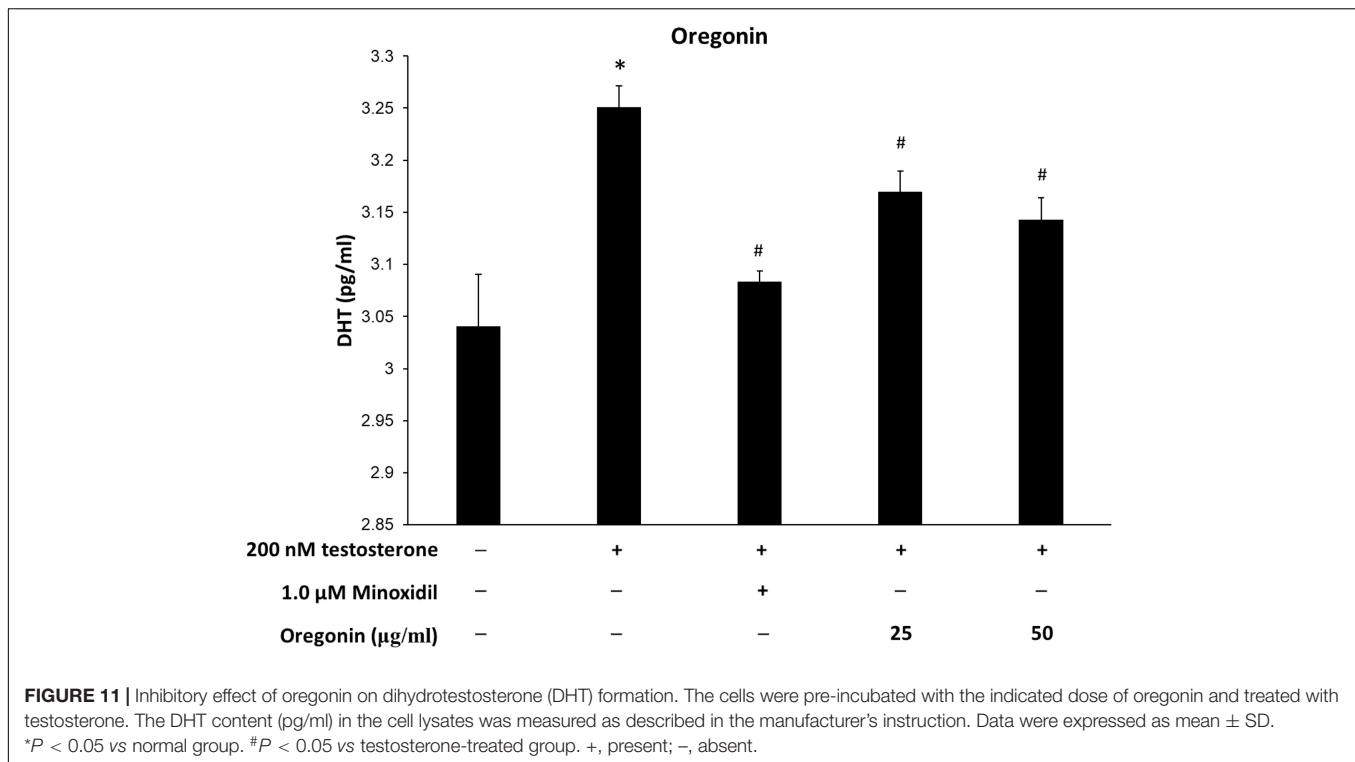


effect of promoting the expression of IGF-1 growth factor in a concentration-dependent manner by treating dermal papilla cells with 60% alcohol extract and oregonin. These results are expected in such a way that both compounds will have a protective effect on hair loss, and the possibility of it being developed as a natural new material for hair health is suggested. Moreover, reactive oxygen species (ROS) formation was increased after the administration of androgens, and TGF- β 1 secretion was increased by the administration of androgen in DP-6 cell line, whereas androgen-induced TGF- β 1 was significantly inhibited by N-acetyl cysteine. In addition, the potential for the treatment of androgen-dependent alopecia has been reported by the induction

of TGF- β 1 by androgens by treatment with antioxidants to block the ROS signaling pathway of hair follicle cells (Olsen et al., 2006). In this study, we explored the 60% EtOH extract from ASFT and oregonin on IGF and TGF- β 1 expression in HFDPC, which is helpful for hair loss. It shows their possibility as an excellent natural new material that can be used in hair loss prevention.

On the other hand, one of the representative factors which cause hair thinning or falling out is testosterone, a male hormone which is changed to dihydrotestosterone (DHT) by 5 α -reductase, and it causes the shrinkage of the dermal papilla on the scalp in people who are not fond of DHT. It is generated, and eventually final hair loss proceeds (Mounsey and Reed, 2009). Male hormones promote the positive function of masculinity and cause seborrheic dandruff to worsen the symptoms of alopecia (Ramos and Miot, 2015). The male hormone, which is the main cause of male pattern hair loss, causes hair loss not due to the amount of male hormone secretion in the hair but due to the influence of 5 α -reductase, an active enzyme acting on male hormones. The changed DHT acts on the hair cells, slowing the atrophy and cell division of the hair follicles and resulting in softening hair and hair loss (Shapiro and Price, 1998). Minoxidil, a treatment for the positive control group used in this experiment, was developed as a vasodilator for the treatment of hypertension in the early 1970s but was used as a hair growth promoter when hirsutism was reported as a side effect (Zappacosta, 1980). The mechanism for the hair growth effect has not been accurately identified, and it has been reported that hair growth is induced by the increased nutritional supply due to vasodilation (Lachgar et al., 1998), but recently the media revealed the mechanism that minoxidil was effective in suppressing male pattern hair loss through





the suppression of DHT production, and accordingly, more aggressive marketing promotions from related pharmaceutical companies are being made. Minoxidil is reported to be most effective only for initial hair loss, in which the hair partially falls out, and for the crown of ongoing hair loss. So only when it is used in the early stages of male pattern hair loss can it prevent the progression of hair loss and contribute to hair growth. It is said that there is no effect on the front of the scalp, which has become bald, and if it is not applied to the scalp steadily

twice a day for 6 to 12 months, it is said that no effect is seen (Kurbel et al., 1999).

In the experiment, minoxidil was applied to the hair loss area; hair growth was promoted not only in men but also in women (Messenger and Rundegren, 2004), but when 5% minoxidil was used, the color of the cilia became darker and thicker, resulting in hirsutism. Therefore, products are manufactured and sold at low concentrations to women in Korea. The side effects include salt and moisture retention, swelling, tachycardia, local peeling,

dermatitis, skin irritation such as soreness, erythema, and peeling at the site of administration (Suchonwanit et al., 2019) or itching, and dryness of the skin due to a small amount of the drug absorbed on the skin. Drops, redness, and contact dermatitis have been reported, and hirsutism can be induced in 0.5–1% (Peluso et al., 1997).

There may be a phenomenon in which the hair loss becomes worse due to the increase of telogen hair shedding due to the temporary effect of minoxidil on the hair cycle (Suchonwanit et al., 2019), Minoxidil's hair growth promotion effect depends on whether or not hair growth is administered, and there is a shortcoming in the period of returning to the state before treatment when it is stopped (Zins, 1988). Due to concerns about these side effects, in recent years, the social demand for the development of new anti-hair loss materials derived from natural products, whose efficacy is scientifically confirmed while being safe for the human body, is high.

The series of the largest characteristic compounds in the *Alnus* species plant is the diarylheptanoid compound (Karchesy et al., 1974; Lee et al., 1992; Guz et al., 2002). Many researchers around the world, including this research team, have found that the representative indicator or effective compound of the *Alnus* species plant is oregonin (Ohta et al., 1984; Aoki et al., 1990; Choi et al., 2012; Ko et al., 2015), which is in the diarylheptanoid series (Asakawa, 1971; Karchesy et al., 1974; Suga et al., 1982; Lim et al., 2004; Choi, 2013). Therefore, in this study, we conducted various experiments related to improving and preventing hair loss by the separation and identification of the diarylheptanoid series, which is an indicator and effective substance from ASFT. Through this research, we believe that the bio-industry has recently conducted a research that suggests significance in the functional material market related to hair loss, which is a large global market, whereas the development of novel materials for prevention of hair loss and/or stimulation of hair growth requires animal experiments or human research for clinical use, but not the cosmetic area because of global ethics. Therefore, each of these materials need further experiments with simulation in human or animals for clinical purposes.

Accordingly, in this study, the result of conducting an experiment on the inhibition of dihydrotestosterone production, which is known as the main cause of male pattern hair loss, with 60% alcohol extract of ASFT and oregonin was shown to be statistically significant when compared with the positive and negative controls. By confirming the DHT reduction effect, 60% alcohol extract of ASFT and oregonin were confirmed to be effective anti-hair loss agents and new materials that promote hair growth for male pattern hair loss.

CONCLUSION

As a product related to “hair loss symptom relief,” which was recently classified as a quasi-drug by the Ministry of Food and

Drug Safety, this was included in the category of functional cosmetics, Therefore, it can be said to be one of great interest in related industries.

In this study, with the aim to discover new materials derived from natural products that can provide an objective basis for scientifically controlling hair loss while having a low risk of side effects, a limitation of existing drugs, it was confirmed that oregonin, isolated from the branches including the bark of ASFT, clearly regulates the death of dermal papilla cells, which is highly related to hair loss, based on strong antioxidant activity. In conclusion, it was confirmed that the anti-hair loss effect can be expected through the inhibition and control of the death of dermal papilla cells caused by oxidative stress based on the effect of powerfully removing oxidative stress from the scalp with ASFT extract and oregonin. In addition, when DHT, a representative causative agent of male pattern hair loss, was compared with the positive control, minoxidil, it was statistically and significantly reduced. It was also confirmed that IGF-1, a representative biomarker for promoting hair growth, was statistically and significantly increased and that TGF- β 1, a representative biomarker for promoting hair loss, was statistically significant.

When the above-mentioned results are combined, it suggests the possibility of the development of a new natural material for hair growth to prevent male pattern alopecia and various hair loss symptoms caused by the death of dermal papilla cells (e.g., alopecia areata, stress-related hair loss, etc.).

DATA AVAILABILITY STATEMENT

The original contributions presented in the study are included in the article/supplementary material, further inquiries can be directed to the corresponding author/s.

AUTHOR CONTRIBUTIONS

EH and J-HY performed the investigation. K-HP and S-EC supervised the study. S-EC and K-HP contributed to writing—original draft. CS, Y-HJ, and YB contributed to writing—review and editing. All authors contributed to the article and approved the submitted version.

FUNDING

This research was supported by the Technology Development Program (S3030198 and S2674466) funded by the Ministry of SMEs and Startups (MSS, South Korea) to S-EC, and this work was also partially supported by a National Research Foundation of Korea grant funded by the Korean government (2015R1A2A2A01007927 to K-HP and NRF-2020R111A3071928 to Y-HJ).

REFERENCES

- Alnemri, E. S., Livingston, D. J., Nicholson, D. W., Salvesen, G., Thornberry, N. A., Wong, W. W., et al. (1996). Human ICE/CED-3 protease nomenclature. *Cell* 87:171. doi: 10.1016/s0092-8674(00)81334-3
- An, L., Si, C., Wang, G., Sui, W., and Tao, Z. (2019). Enhancing the solubility and antioxidant activity of high-molecular-weight lignin by moderate depolymerization via in situ ethanol/acid catalysis. *Ind. Crops Prod.* 128, 177–185. doi: 10.1016/j.indcrop.2018.11.009
- Aoki, T., Ohta, S., and Suga, T. (1990). Triterpenoids, diarylheptanoids and their glycosides in the flowers of *Alnus* species. *Phytochemistry* 23, 3611–3614. doi: 10.1016/0031-9422(90)85286-o
- Asakawa, Y. (1971). Chemical constituents of *Alnus sieboldiana* (Betulaceae) II. The isolation and structure of flavonoids and stilbenes. *Bull. Chem. Soc. Jpn.* 44, 2761–2766. doi: 10.1246/bcsj.44.2761
- Boericke, W. (1927). *Pocket Manual of Homeopathic Materia Medica with Repertory*, 9th Edn. Santa Rosa, CA: Boericke & Tafel, Inc, 24.
- Choi, H. N., Joung, S. W., Jin, H. Y., and Choi, S. E. (2016). Oregonin from the barks and xylenes of Chinese *Alnus* species. *J. Chem. Pharm. Res.* 8, 295–298.
- Choi, S. E. (2013). Chemotaxonomic significance of oregonin in *Alnus* species. *Asian J. Chem.* 25, 6989–6990. doi: 10.14233/ajchem.2013.15090
- Choi, S. E. (2019). Extraction method and physiological activity of high content oregonin derived from plant of *Alnus sibirica* Fisch. ex Turcz. *Korean J. Pharmacogn.* 50, 165–174.
- Choi, S. E., Jeong, M. S., Kang, M. J., Lee, D. I., Joo, S. S., Lee, C. S., et al. (2010). Effect of topical application and intraperitoneal injection of oregonin on atopic dermatitis in NC/Nga mice. *Exp. Dermatol.* 19, 37–43. doi: 10.1111/j.1600-0625.2009.00961.x
- Choi, S. E., Park, K. H., Kim, M. H., Song, J. H., Jin, H. Y., and Lee, M. W. (2012). Diarylheptanoids from the bark of *Alnus pendula* Matsumura. *Nat. Prod. Sci.* 18, 106–110.
- Cleary, M. L., Smith, S. D., and Sklar, J. (1986). Cloning and structural analysis of cDNAs for bcl-2 and a hybrid bcl-2/immunoglobulin transcript resulting from the t(14;18) translocation. *Cell* 47, 19–28. doi: 10.1016/0092-8674(86)90362-4
- Dong, H., Zheng, L., Yu, P., Jiang, Q., Wu, Y., Huang, C., et al. (2020). Characterization and application of lignin-carbohydrate complexes from lignocellulosic materials as antioxidants for scavenging in vitro and in vivo reactive oxygen species. *ACS Sustain. Chem. Eng.* 8, 256–266. doi: 10.1021/acscchemeng.9b05290
- Du, H., Liu, W., Zhang, M., Si, C., Zhang, X., and Li, B. (2019). Cellulose nanocrystals and cellulose nanofibrils based hydrogels for biomedical applications. *Carbohydr. Polym.* 209, 130–144. doi: 10.1016/j.carbpol.2019.01.020
- Godon, C., Cordelières, F. P., Biard, D., Giocanti, N., Mégnin-Chanet, F., Hall, J., et al. (2008). PARP inhibition versus PARP-1 silencing: different outcomes in terms of single-strand break repair and radiation susceptibility. *Nucleic Acids Res.* 36, 4454–4464. doi: 10.1093/nar/gkn403
- Guz, N. R., Lorenz, P., and Metraux, J. P. (2002). Oregonin from the bark of European *Alnus* species. *Biochem. Syst. Ecol.* 30, 471–474. doi: 10.1016/s0305-1978(01)00084-9
- Harrington, H. A., Ho, K. L., Ghosh, S., and Tung, K. C. (2008). Construction and analysis of a modular model of caspase activation in apoptosis. *Theor. Biol. Med. Model.* 5:26. doi: 10.1186/1742-4682-5-26
- Hibino, T., and Nishiyama, T. (2004). Role of TGF-beta2 in the human hair cycle. *J. Dermatol. Sci.* 35, 9–18. doi: 10.1016/j.jdermsci.2003.12.003
- Hodak, E., Gottlieb, A. B., Anzilotti, M., and Krueger, J. G. (1996). The insulin-like growth factor 1 receptor is expressed by epithelial cells with proliferative potential in human epidermis and skin appendages: correlation of increased expression with epidermal hyperplasia. *J. Invest. Dermatol.* 106, 564–570. doi: 10.1111/1523-1747.ep12344044
- Hu, L., Du, H., Liu, C., Zhang, Y., Yu, G., Zhang, X., et al. (2018). Comparative evaluation of the efficient conversion of corn husk filament and corn husk powder to valuable materials via a sustainable and clean biorefinery process. *ACS Sustain. Chem. Eng.* 7, 1327–1336. doi: 10.1021/acscchemeng.8b05017
- Hu, L., Wang, K., Li, G., Zhang, R., Luo, Y., Si, C., and Wang, J. (2017). Isolation and structural elucidation of heartwood extractives of *Juglans sigillata*. *Holzforschung* 71, 785–791. doi: 10.1515/hf-2017-0036
- Hu, W. C., Wang, G. C., Li, P. X., Wang, Y. N., Si, C. L., He, J., et al. (2014). Neuroprotective effects of macranthoin G from *Eucommia ulmoides* against hydrogen peroxide-induced apoptosis in PC12 cells via inhibiting NF-kappa B activation. *Chem. Biol. Interact.* 224, 108–116. doi: 10.1016/j.cbi.2014.10.011
- Hu, W. C., Wang, X. F., Wu, L., Shen, T., Ji, L. L., Zhao, X. H., et al. (2016). Apigenin-7-O-beta-D-glucuronide inhibits LPS-induced inflammation through the inactivation of AP-1 and MAPK signaling pathways in RAW 264.7 macrophages and protects mice against endotoxin shock. *Food Funct.* 7, 1002–1013. doi: 10.1039/c5fo01212k
- Huang, C., Tang, S., Zhang, W., Tao, Y., Lai, C., Li, X., et al. (2018). Unveiling the structural properties of lignin-carbohydrate complexes in bamboo residues and its functionality as antioxidants and immunostimulants. *ACS Sustain. Chem. Eng.* 6, 12522–12531. doi: 10.1021/acscchemeng.8b03262
- Huang, C., Tao, Y., Li, M., Zhang, W., Fan, Y., and Yong, Q. (2019). Synthesis and characterization of an antioxidative galactomannan-iron(III) complex from *Sesbania* seed. *Polymers* 11:28. doi: 10.3390/polym11010028
- Huang, L.-Z., Ma, M.-G., Ji, X.-X., Choi, S.-E., and Si, C. (2021). Recent developments and applications of hemicellulose from wheat straw: a review. *Front. Bioeng. Biotechnol.* 9:690773. doi: 10.3389/fbioe.2021.690773
- Itami, S., Kurata, S., and Takayasu, S. (1995). Androgen induction of follicular epithelial cell growth is mediated via insulin-like growth factor-I from dermal papilla cells. *Biochem. Biophys. Res. Commun.* 212, 988–994. doi: 10.1006/bbrc.1995.2067
- Karchesy, J. J., Laver, M. L., Barofsky, D. F., and Barofsky, E. (1974). Structure of oregonin, a natural diarylheptanoid xyloside. *J. Chem. Soc. Chem. Commun.* 16, 649–650. doi: 10.1039/c39740000649
- Kawai, N., Ando, Y. U., Ando, Y. O., and Nishibe, Y. (1990). Extraction of antimutagenic tannins from *Alnus firma* plant. *Pat. Jpn. Kokai Tokyo Koho O2* 117:685.
- Ko, E. K., Choi, H. N., Jin, H. Y., and Choi, S. E. (2015). Oregonin from the stems and leaves of Korean *Alnus* species (Betulaceae). *J. Chem. Pharm. Res.* 7, 234–238.
- Kumar, A., Sharma, G., Naushad, M., Al-Muhtaseb, A. H., Garcia-Penas, A., Mola, G. T., et al. (2020). Bio-inspired and biomaterials-based hybrid photocatalysts for environmental detoxification: a review. *Chem. Eng. J.* 382:122937. doi: 10.1016/j.cej.2019.122937
- Kurbel, S., Kurbel, B., and Zanić-Matanić, D. (1999). Minoxidil and male-pattern alopecia: a potential role for a local regulator of sebum secretion with vasoconstrictive effects? *Med. Hypotheses* 53, 402–406. doi: 10.1054/mehy.1998.0793
- Lachgar, S., Charveron, M., Gall, Y., and Bonafe, J. (1998). Minoxidil upregulates the expression of vascular endothelial growth factor in human hair dermal papilla cells. *Br. J. Dermatol.* 138, 407–411. doi: 10.1046/j.1365-2133.1998.02115.x
- Lee, D. I., Chang, J. K., Lee, M. W., and Hong, S. G. (1998). Effects of oregonin, diarylheptanoid derivative from plant on antitumor. *Chung Ang J. Pharm. Sci.* 12, 67–72.
- Lee, G. H., Park, K. H., and Choi, S. E. (2018). Modulative effect of human hair dermal papilla cell apoptosis by oregonin from the braches of *Alnus japonica*. *Korean J. Plant Res.* 31, 322–329.
- Lee, M. W., Kim, J. H., Jeong, D. W., Ahn, K. H., Toh, S. H., and Surh, Y. J. (2000a). Cyclooxygenase-2 inhibitory effect of diarylheptanoids from the barks of *Alnus hirsuta* var. *sibirica*. *Biol. Pharm. Bull.* 23, 517–518.
- Lee, M. W., Kim, N. Y., Park, M. S., Ahn, K. H., Toh, S. H., Hahn, D. R., et al. (2000b). Diarylheptanoids with in vitro inducible nitric oxide synthesis inhibitory activity from *Alnus hirsuta*. *Planta Med.* 66, 551–553. doi: 10.1055/s-2000-8606
- Lee, M. W., Tanaka, T., Nonakr, G. I., and Nishioka, I. (1992). Dimeric ellagitannins from *Alnus japonica*. *Phytochemistry* 31, 2835–2839. doi: 10.1016/0031-9422(92)83642-c
- Lee, W. C. (1996). *Lineamenta Florae Koreae*. Seoul: Academy Publishing, 154.
- Lee, Y. N. (1997). *Flora of Korea*. Seoul: Kyohak Publishing, 64.
- Li, X. Y., Xu, R., Yang, J. X., Nie, S. X., Liu, D., Liu, Y., et al. (2019). Production of 5-hydroxymethylfurfural and levulinic acid from lignocellulosic biomass and catalytic upgradation. *Ind. Crop. Prod.* 130, 184–197. doi: 10.1016/j.indcrop.2018.12.082

- Lim, H. W., Kim, M. K., Kim, H. J., Shim, J. G., Kim, G. H., Choi, H. K., et al. (2004). Quantitative determination of diarylheptanoid compounds from Korean *Alnus*. *Korean J. Pharmacogn.* 35, 384–387.
- Liu, C., Wang, G., Sui, W., An, L., and Si, C. (2017). Preparation and characterization of chitosan by a novel deacetylation approach using glycerol as green reaction solvent. *ACS Sustain. Chem. Eng.* 5, 4690–4698. doi: 10.1021/acsschemeng.7b00050
- Liu, H., Xu, T., Liu, K., Zhang, M., Liu, W., Li, H., et al. (2021). Lignin based electrodes for energy storage application. *Ind. Crops Prod.* 165:113425. doi: 10.1016/j.indcrop.2021.113425
- Liu, K., Du, H., Zheng, T., Liu, H., Zhang, M., Zhang, R., et al. (2021). Recent advances in cellulose and its derivatives for oilfield applications. *Carbohydr. Polym.* 259:117740. doi: 10.1016/j.carbpol.2021.117740
- Liu, W., Du, H., Liu, H., Xie, H., Xu, T., Zhao, X., et al. (2020a). Highly efficient and sustainable preparation of carboxylic and thermostable cellulose nanocrystals via fecl3-catalyzed innocuous citric acid hydrolysis. *ACS Sustain. Chem. Eng.* 8, 16691–16700. doi: 10.1021/acsschemeng.0c06561
- Liu, W., Du, H. S., Zhang, M. M., Liu, K., Liu, H. Y., Xie, H. X., et al. (2020b). Bacterial cellulose based composite scaffolds for biomedical applications: a review. *ACS Sustain. Chem. Eng.* 8, 7536–7562. doi: 10.1021/acsschemeng.0c00125
- Lu, J., Zhu, W., Dai, L., Si, C., and Ni, Y. (2019). Fabrication of thermo- and pH-sensitive cellulose nanofibrils-reinforced hydrogel with biomass nanoparticles. *Carbohydr. Polym.* 219, 289–295. doi: 10.1016/j.carbpol.2019.03.100
- Messenger, A. G., and Rundegren, J. (2004). Minoxidil: mechanisms of action on hair growth. *Br. J. Dermatol.* 150, 186–194. doi: 10.1111/j.1365-2133.2004.05785.x
- Mounsey, A. L., and Reed, S. W. (2009). Diagnosing and treating hair loss. *Am. Fam. Physician* 80, 356–362.
- Ohta, S., Aoki, T., Hirata, T., and Suga, T. (1984). The structures of four diarylheptanoid glycosides from the female flowers of *Alnus serrulatoidea*. *J. Chem. Soc. Perkin Trans. 1* 8, 1635–1642. doi: 10.1039/p1984001635
- Olsen, E. A. (2001). Female pattern hair loss. *J. Am. Acad. Dermatol.* 45, 171–186. doi: 10.1007/978-3-540-46911-7-10
- Olsen, E. A., Hordinsky, M., Whiting, D., Stough, D., Hobbs, S., Ellis, M. L., et al. (2006). The importance of dual 5 α -reductase inhibition in the treatment of male pattern hair loss: results of a randomized placebo-controlled study of dutasteride versus finasteride. *J. Am. Acad. Dermatol.* 55, 1014–1023. doi: 10.1016/j.jaad.2006.05.007
- Oltvai, Z. N., Milliman, C. L., and Korsmeyer, S. J. (1993). Bcl-2 heterodimerizes in vivo with a conserved homolog, Bax, that accelerates programmed cell death. *Cell* 74, 609–619. doi: 10.1016/0092-8674(93)90509-o
- Pei, W., Chen, Z. S., Chan, H. Y. E., Zheng, L., Liang, C., and Huang, C. (2020). Isolation and identification of a novel anti-protein aggregation activity of lignin-carbohydrate complex from *Chionanthus retusus* leaves. *Front. Biotechnol.* 8:573991. doi: 10.3389/fbioe.2020.573991
- Peluso, A. M., Misciali, C., Vincenzi, C., and Tosti, A. (1997). Diffuse hypertrichosis during treatment with 5% topical minoxidil. *Br. J. Dermatol.* 136, 118–120. doi: 10.1046/j.1365-2133.1997.d01-1156.x
- Price, V. H. (1999). Treatment of hair loss. *N. Engl. J. Med.* 341, 964–973. doi: 10.1056/nejm199909233411307
- Ramos, P. M., and Miot, H. A. (2015). Female pattern hair loss: a clinical and pathophysiological review. *An. Bras. Dermatol.* 90, 529–543. doi: 10.1590/abd1806-4841.20153370
- Randall, V. A. (2008). Androgens and hair growth. *Dermatol. Ther.* 21, 314–328. doi: 10.1111/j.1529-8019.2008.00214.x
- Rosen, C. J., Holick, M. F., and Millard, P. S. (1994). Premature graying of hair is a risk marker for osteopenia. *J. Clin. Endocrinol. Metab.* 79, 854–857. doi: 10.1210/jcem.79.3.8077373
- Saxena, G., Farmer, S., Hancock, R. E. W., and Towers, G. H. N. (1995). Antimicrobial compounds from *Alnus rubra*. *Int. J. Pharmacogn.* 33, 33–36. doi: 10.3109/13880209509088144
- Schultz, N., Lopez, E., Saleh-Gohari, N., and Helleday, T. (2003). Poly(ADP-ribose) polymerase (PARP-1) has a controlling role in homologous recombination. *Nucleic Acids Res.* 31, 4959–4964. doi: 10.1093/nar/kgk703
- Sedlak, T. W., Oltvai, Z. N., Yang, E., Wang, K., Boise, L. H., Thompson, C. B., et al. (1995). Multiple Bcl-2 family members demonstrate selective dimerizations with Bax. *Proc. Natl. Acad. Sci. U.S.A.* 92, 7834–7838. doi: 10.1073/pnas.92.17.7834
- Shapiro, J., and Price, V. H. (1998). Hair regrowth: therapeutic agents. *Dermatol. Clin.* 16, 341–356. doi: 10.1016/s0733-8635(05)70017-6
- Sheth, K., Bianchi, E., Wiedhopf, R., and Cole, J. R. (1973). Antitumor agents from *Alnus oregona* (Betulaceae). *J. Pharm. Sci.* 62, 139–140. doi: 10.1002/jps.2600620129
- Si, C. L., Deng, X. J., Liu, Z., Kim, J. K., and Bae, Y. S. (2008a). Studies on the phenylethanoid glycosides with anti-complement activity from *Paulownia tomentosa* var. *tomentosa* wood. *J. Asian Nat. Prod. Res.* 10, 1003–1008. doi: 10.1080/10286020802242364
- Si, C. L., Jiang, J. Z., Liu, S. C., Hu, H. Y., Ren, X. D., Yu, G. J., et al. (2013a). A new lignan glycoside and phenolics from the branch wood of *Pinus banksiana* Lambert. *Holzforchung* 67, 357–363. doi: 10.1515/hf-2012-0137
- Si, C. L., Kim, J. K., Bae, Y. S., and Li, S. M. (2009a). Phenolic compounds in the leaves of *Populus ussuriensis* and their antioxidant activities. *Planta Med.* 75, 1165–1167. doi: 10.1055/s-0029-1185476
- Si, C. L., Liu, Z., Kim, J. K., and Bae, Y. S. (2008b). Structure elucidation of phenylethanoid glycosides from *Paulownia tomentosa* Steud. var. *tomentosa* wood. *Holzforchung* 62, 197–200. doi: 10.1515/HF.2008.047
- Si, C. L., Shen, T., Jiang, Y. Y., Wu, L., Yu, G. J., Ren, X. D., et al. (2013b). Antioxidant properties and neuroprotective effects of isocampneoside II on hydrogen peroxide-induced oxidative injury in PC12 cells. *Food Chem. Toxicol.* 59, 145–152. doi: 10.1016/j.fct.2013.05.051
- Si, C. L., Wu, L., and Zhu, Z. Y. (2009b). Phenolic glycosides from *Populus davidiana* bark. *Biochem. Syst. Ecol.* 37, 221–224. doi: 10.1016/j.bse.2009.01.007
- Sin, S. J., and Ahn, W. Y. (1991). Some triterpenoids in bark of Korean water alder, *Alnus hirsuta Ruprecht*. *J. Korean For. Energy* 11, 36–44.
- Suchonwanit, P., Thammarucha, S., and Leerunyakul, K. (2019). Minoxidil and its use in hair disorders: a review. *Drug Des. Devel. Ther.* 9, 2777–2786. doi: 10.2147/dddt.s214907
- Suga, T., Ohta, S., Hirata, T., and Aoki, T. (1982). The absolute configuration of diarylheptanoid xyloside, oregonin, isolated from the female flowers of *Alnus serrulatoidea*. *Chem. Lett.* 11, 895–898. doi: 10.1246/cl.1982.895
- Tsujimoto, Y., Cossman, J., Jaffe, E., and Croce, C. M. (1985). Involvement of the bcl-2 gene in human follicular lymphoma. *Science* 228, 1440–1443. doi: 10.1126/science.3874430
- Wells, A. (1999). EGF receptor. *Int. J. Biochem. Cell Biol.* 31, 637–643. doi: 10.1016/S1357-2725(99)00015-1
- Xu, R., Du, H., Wang, H., Zhang, M., Wu, M., Liu, C., et al. (2021). Valorization of enzymatic hydrolysis residues from corncob into lignin-containing cellulose nanofibrils and lignin nanoparticles. *Front. Bioeng. Biotech.* 9:677963. doi: 10.3389/fbioe.2021.677963
- Yamazaki, R., Aiyama, R., Matsuzaki, T., Hashimoto, S., and Yokokura, T. (1998). Anti-inflammatory effect of YPE-01, a novel diarylheptanoid derivative, on dermal inflammation in mice. *Inflamm. Res.* 47, 182–186. doi: 10.1007/s001110050315
- Yang, C. H., Park, S. D., and Kong, N. M. (1999). Western medicine and oriental medicine study about the meaning of atopic dermatitis. *J. Jeahan Orient. Med. Acad.* 4, 416–427.
- Yip, L., Rufaut, N., and Sinclair, R. (2011). Role of genetics and sex steroid hormones in male androgenetic alopecia and female pattern hair loss: an update of what we now know. *Australas. J. Dermatol.* 52, 81–88. doi: 10.1111/j.1440-0960.2011.00745.x
- Zappacosta, A. R. (1980). Reversal of baldness in patient receiving minoxidil for hypertension. *N. Engl. J. Med.* 303, 1480–1481. doi: 10.1056/nejm198012183032516
- Zins, G. R. (1988). The history of the development of minoxidil. *Clin. Dermatol.* 6, 132–147. doi: 10.1016/0738-081x(88)90078-8

Conflict of Interest: The authors declare that the research was conducted in the absence of any commercial or financial relationships that could be construed as a potential conflict of interest.

Copyright © 2021 Ha, Yun, Si, Bae, Jeong, Park and Choi. This is an open-access article distributed under the terms of the Creative Commons Attribution License (CC BY). The use, distribution or reproduction in other forums is permitted, provided the original author(s) and the copyright owner(s) are credited and that the original publication in this journal is cited, in accordance with accepted academic practice. No use, distribution or reproduction is permitted which does not comply with these terms.



OPEN ACCESS

Edited by:

Xianzhi Meng,
The University of Tennessee,
United States

Reviewed by:

Guoyou Li,
Chengdu Institute of Biology, Chinese
Academy of Sciences, China
Chaoran Song,
Sungkyunkwan University,
South Korea

***Correspondence:**

Weicheng Hu
hu_weicheng@163.com
Yufeng Cao
17851567661@163.com
Lingyun Lv
lly810524@sina.com

† These authors have contributed
equally to this work and share first
authorship

Specialty section:

This article was submitted to
Industrial Biotechnology,
a section of the journal
Frontiers in Bioengineering and
Biotechnology

Received: 28 April 2021

Accepted: 19 May 2021

Published: 17 June 2021

Citation:

Yang X, Zhou J, He Y, Lv L, Cao Y
and Hu W (2021)
20-Hydroxy-3-Oxolupan-28-Oic Acid,
a Minor Component From *Mahonia
bealei* (Fort.) Carr. Leaves Alleviates
Lipopolysaccharide-Induced
Inflammatory in Murine Macrophages.
Front. Bioeng. Biotechnol. 9:701876.
doi: 10.3389/fbioe.2021.701876

20-Hydroxy-3-Oxolupan-28-Oic Acid, a Minor Component From *Mahonia bealei* (Fort.) Carr. Leaves Alleviates Lipopolysaccharide-Induced Inflammatory in Murine Macrophages

Xiaojun Yang^{1†}, Jing Zhou^{1,2†}, Yang He^{1,2}, Lingyun Lv^{3*}, Yufeng Cao^{2*} and Weicheng Hu^{2*}

¹ College of Food Science and Pharmacology, Xinjiang Agricultural University, Ürümqi, China, ² Jiangsu Collaborative Innovation Center of Regional Modern Agriculture and Environmental Protection, School of Life Sciences, Huaiyin Normal University, Huai'an, China, ³ Department of Otorhinolaryngology-Head and Neck Surgery, The Affiliated Huaian No.1 People's Hospital of Nanjing Medical University, Huai'an, China

20-Hydroxyl-3-oxolupan-28-oic acid (HOA), a minor component from *Mahonia bealei* (Fort.) Carr. leaves, has been found to attenuate inflammatory responses. However, the underlying molecular mechanism is still unclear. In this study, we performed a comprehensive transcriptional study to investigate genetic changes. We used RNA sequencing technology to analyse the transcriptional changes in RAW 264.7 cells in a control group, lipopolysaccharide (LPS)-induced group, and HOA-treated group. We identified 1,313 and 388 differentially expressed genes (DEGs) in the control/LPS group and LPS/HOA group, respectively. Gene Ontology (GO) classification revealed that the DEGs were mainly enriched in a series of inflammatory and immune-related processes. The results of Kyoto Encyclopedia of Genes and Genomes (KEGG) pathway analyses showed that the DEGs were mainly enriched in inflammatory-related pathways such as the nuclear factor-kappa B (NF- κ B) signaling pathway, cytokine-cytokine receptor interaction, chemokine signaling pathway, mitogen-activated protein kinase (MAPK) pathway, and Janus kinase-signal transducer and activator of transcription proteins (JAK-STAT) signaling pathway. The results of qPCR validation revealed that dynamic changes in immune-related mRNAs such as Saa3, Bcl2l1, Mapkapk2, Ccl9, Sdc4, Ddx3x, Socs3, Prdx5, Tlr4, Lif, IL15, Tnfaip3, Tet2, Tgf- β 1, and Ccl20, which were significantly upregulated in the LPS group and downregulated in the HOA group. Taken together, these results suggest that HOA may be used as a source of anti-inflammatory agents as well as a dietary complement for health promotion.

Keywords: 20-hydroxy-3-oxolupan-28-oic acid, anti-inflammatory, NF- κ B, transcriptome analyses, *Mahonia bealei*

INTRODUCTION

Inflammation, as a defense system, is an extremely important process that protects the body from bacterial, viral, and fungal infections (Guinane and Cotter, 2013). The moderate inflammatory response can remove foreign body antigens, necrotic tissue, and injury factors, and an appropriate number of inflammatory factors can participate in the regeneration of damaged tissues, which are conducive to wound repair and healing (Pappas et al., 2013). However, excessive inflammatory reactions can destroy normal tissues and cells, and induce various inflammatory diseases such as atherosclerosis, cardiovascular disease, sepsis, diabetes, and arthritis (Pan et al., 2010; Du et al., 2019). The spread of inflammation can further induce an acute systemic inflammatory response. Macrophages play a crucial role in the occurrence, maintenance, and elimination of inflammation. When stimulated, macrophages produce a variety of cytokines and inflammatory-related enzymes, such as interleukin-1 (IL-1 β), interleukin-6 (IL-6), tumor necrosis factor- α (TNF- α), and nitric oxide (NO) (Hu et al., 2016a; Li et al., 2016, 2019). Inhibiting the excessive production of these inflammatory mediators may play a beneficial role in inflammatory diseases.

With the development of second-generation sequencing technology, transcriptomics has entered a period of rapid development. RNA sequencing (RNA-seq) technology can comprehensively and deeply record the sequences of mRNA, small RNA, and non-coding RNA (ncRNA). Compared to the traditional hybrid sequencing method, RNA-seq can reveal the exact location of the transcriptional boundary and achieve single-base resolution (Levy and Myers, 2016). It can also describe the multi-functional elements such as exons, introns, and transcriptional initiation sites in the genome, and display the sequence changes in the transcriptional region (Kukurba and Montgomery, 2015). In addition, new transcripts and splice sites can be found, and gene expression and differential expression analyses of transcripts under different conditions can be quantified. Finally, the functions of non-coding regions, such as microRNA, non-coding long RNA, and RNA editing, can be discussed (Wang et al., 2016). The application of this technology can provide more rapid and accurate biological transcription data in humans. RNA-seq has been used to study the transcriptomes of *Arabidopsis thaliana*, mice, and humans (Zhang et al., 2019).

Mahonia, a flowering evergreen tree of the family Berberidaceae has been reported to show a variety of biological activities, including anti-bacterial, antioxidant, anti-proliferation, and anti-inflammatory effects (Hu et al., 2011). In previous work, we isolated a lupane-type triterpene, 20-hydroxy-3-oxolupan-28-oic acid (HOA), from the dichloromethane fraction of *Mahonia bealei* (Fort.) Carr leaves, which has an obvious anti-inflammatory effect in RAW 264.7 cells (Hu et al., 2016b; Cao et al., 2019). However, the precise mechanism of its action is still unclear. In this study, RNA-seq was used to detect genomic changes induced by HOA in lipopolysaccharide (LPS)-stimulated RAW 264.7 cells. The sequencing results lay a foundation for further studies of the anti-inflammatory mechanism of HOA.

MATERIALS AND METHODS

Materials

Experiments were performed with the RAW 264.7 cell line, obtained from the American Type Culture Collection (Rockville, MD, United States). TRIzol reagent used to separate RNA was purchased from Ambion (Austin, TX, United States). The fetal bovine serum (FBS) was from Corning (Medford, MA, United States). The RPMI1640 medium was from Gibco BRL (Life Technologies, China). Penicillin-streptomycin solution (10,000 unit/10,000 μ g/mL) was purchased from Invitrogen-Gibco (Carlsbad, CA, United States). SYBR real-time PCR kit was obtained from Bio-Rad (Hercules, CA, United States).

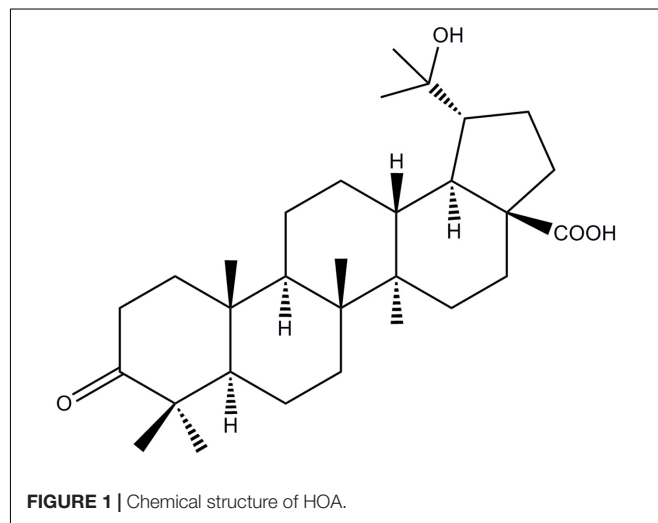
Extraction and Isolation

The HOA used in the experiment was separated from the leaves of *M. bealei* (Figure 1). Briefly, the active fraction was prepared as our previous literature under the active-guide isolation way (Hu et al., 2016b). Forty-gram of CH₂Cl₂ fraction was then subjected to a silica gel with a gradient solvent system of hexane/CH₂Cl₂ (5:1:1:2) affording 11 fractions based on TLC analysis. Fra 8 was further purified by preparative HPLC to afford HOA (21.0 mg) and the purity of HOA was about 97% determined by high performance liquid chromatography (HPLC).

RAW 264.7 Cells Culture and HOA Treatment for RNA-Seq Experiment

RAW 264.7 cells were maintained in RPMI 1640 medium supplemented with 10% FBS and 1% antibiotics (v/v) at 37°C in 5% CO₂ atmosphere. For the RNA-Seq and RT-qPCR validation experiments, cells were pre-treated with 40 μ g/mL HOA for 30 min and then incubated with LPS (1 μ g/mL) for 6 h. Total RNA was extracted using TRIzol reagent according to the manufacturer's protocol.

The quantitative and qualitative analysis of RNA was carried out with 1% agarose gel, and the degradation and pollution of



RNA were monitored. The purity of RNA was determined by the Nano-Drop One (Thermo Fisher Scientific, Waltham, MA, United States). RNA concentration was measured using Nano and the integrity was assessed using the RNA Nano 6000 Assay Kit of the Bioanalyzer 2100 system (Agilent Technologies, Santa Clara, CA, United States).

RNA-Seq Library Construction and Sequencing

Approximately 1 μ g of RNA per sample was used for the RNA sample preparations. Sequencing libraries were generated using NEBNext[®] Ultra[™] RNA Library Prep Kit for Illumina[®] (NEB, United States) following manufacturer's recommendations and index codes were added to attribute sequences to each sample. In simple terms, RNA fragments are reversely transcribed and amplified into double-stranded cDNA, which is then connected to a NEBNext adapter with a hairpin ring structure. PCR products were purified by magnetic bead method and library quality was evaluated on Agilent Bioanalyzer 2100 system. Sequencing were performed on Illumina HiSeq[™]4000.

RNA-Seq Data Analysis

In order to ensure the quality of the data for the following analysis, the raw data of nine samples were firstly processed through in-house perl scripts. In this step, clean data were obtained by removing reads containing adapter, reads containing ploy-N and low quality reads from raw data. At the same time, Q20, Q30, and GC content the clean data were calculated. All the downstream analyses were based on the clean data with high quality.

Differentially Expressed Genes (DEGs)

The differential expression of C/LPS and LPS/HOA genes was analyzed by DESeqR package (1.18.0). DESeq provides a model for detecting negative binomial distribution to determine the expression of differentially expressed genes between each two groups.

The *p*-value of the result was assigned to each gene, carramine and Hochberg were used to control the error detection rate. The differential expression genes were screened under the conditions of fold change (FC) ≥ 2 and FDR < 0.05 .

GO and KEGG Pathway Enrichment Analysis of Differentially Expressed Genes

The DEGs were referred to the DAVID¹ v6.7 for gene ontology (GO) and pathway analysis. GO terms with corrected *p*-value less than 0.05 were considered significantly enriched by DEGs. Pathway enrichment was determined using the Kyoto Encyclopedia of Genes and Genomes (KEGG) Pathway annotation. Pathways were considered enriched with *p* < 0.05 .

¹<http://david.abcc.ncifcrf.gov/home.jsp>

Reverse-Transcribed and Quantitative PCR (RT-qPCR)

To validate the RNA sequencing data, 15 differential expression genes in the Control group, LPS-induced group and HOA pre-treated group were selected for RT-qPCR analysis. cDNA was synthesized as described previously (Shen et al., 2017). A 20 μ L PCR reaction mixture was prepared using a SYBR Green PCR Kit (Bio-Rad, Foster City, CA, United States) with four micrograms of cDNA as a template. After mixing, the PCR reaction was performed using CFX-96[™] Real-Time instrument (Bio-Rad, Foster City, CA, United States). The GAPDH gene was used as a house keeping gene to normalize the expression level of the test gene, and the relative gene expression level was analyzed using the $2^{-\Delta\Delta CT}$ method. All of the primers were synthesized by Sangon Biotech (Shanghai, China) and were listed in **Table 1**. All of the samples were analyzed in triplicate.

Data Analysis

Data were presented as the mean \pm standard deviation (SD). The significance was analyzed between the two groups using Student's *t*-test and multigroup comparisons were compared using one-way analysis of variance (ANOVA). *P*-values of less than 0.05 were considered significant.

RESULTS

mRNA Data Generation and Gene Comparison

The HiSeq[™] 4000 was used for sequencing. We obtained 27,805,302 (98.297%), 26,990,712 (98.76%), and 29,943,562 (98.67%) clean reads in the control, LPS, and HOA groups, respectively (**Table 2**). The proportions of Q30 in the three samples were more than 92%. Therefore, the quality of clean reads obtained was high, and the results met the analysis requirements for subsequent experiments. The gene comparison showed that the rates of clean reads from the control, LPS, and HOA groups relative to the reference genome were 90.77, 92.66, and 93.61%, respectively, indicating that the utilization rate of sequencing data was high.

Response of Differentially Expressed Genes (DEGs) to LPS Induction and HOA Pre-treatment

The differential expression multiple between different samples was determined by the amount of gene expression. Using Log₂ fold change ≥ 2 and FDR < 0.05 as criteria, a total of 1,313 DEGs were identified in the Control/LPS group, including 606 upregulated genes and 707 downregulated genes (**Figure 1**). In addition, 388 DEGs were identified in the HOA/LPS group, including 201 downregulated genes and 187 upregulated genes (**Figure 2**). DEGs identified in the biological replicates clustered together (**Figure 3**), indicating good reproducibility of treatments.

TABLE 1 | Primer sequences of real-time qPCR assay.

Gene name	Forward primer (5'-3')	Reverse primer (5'-3')
Saa3	TGCCATCATTCTTTGCATCTTGA	CCGTGAACCTCTGAACAGCCTG
Bcl2l1	ATGTCTCAGAGCAACCGGGAGCT	TCACTTCCGACTGAAGAGTGAGCC
Mapkapk2	GGGCACCATGCTGTGGGGCTC	CGAGACACTCCATGACAATCAGC
Ccl9	AACAGAGACAAAAGAAGTCCAGAG	CTTGCTGATAAAAGATGATGCC
Sdc4	GGGCAAGAAACCCATCTACAAA	CTCCAC TCCTCTCCCAATAAGT
Ddx3x	CTCCGATTCTCGGTACTCT	GACTTCCCTCTTGAATCACC
Socs3	CACAGCAAGTTTCCCGCGGCC	GTGCACCAGCTTGAGTACACA
Prdx5	TGGCAGAGCTGTTCAAGGGCAAGAA	TCAGCCAGGAGCCGAACTTGCCCTTC
TLR4	TCAGCAAAGTCCCTGATGACATTCC	AGAGGTGGTGAAGCCATGCCA
Lif	GCTATGTGCGCCTAACATGAC	CGCTCAGGTATGCGACCAT
IL15	GCTCTTACCTGGGCATTAAGTAATGAA	CGCATGCAGTCAGGACGTGTTGATG
Tnfrsf3	AACCAATGGTGATGGAACTG	GTTGTCCCATTCGTCATTCC
TET2	TGTTGTTGTCAGGGTGAGAATC	TCTTGCTTCTGGCAAACCTTACA
TGF-β1	CTCCCGTGCTTCTAGTGC	GCCTTAGTTTGACAGGATCTG
CCl20	CGACTGTTGCCTCTCGTACA	AGGAGGTTACAGCCCTTTT

GO Enrichment Analyses of DEGs

The DEGs in the control/LPS and HOA/LPS groups were analyzed for GO functional enrichment (Figure 4). Each group of DEGs was annotated into three GO classifications: molecular function, cell components, and biological processes. In the biological process classification, the DEGs in the control/LPS group were mainly enriched in the inflammatory response, the immune system process, response to viruses, and the cellular response to interferon (IFN)-β. In the molecular function classification, the genes related to cytokine activity, protein binding, and chemokine activity significantly changed. In the cellular component classification, membrane, cytoplasm, and extracellular space changed significantly. After RAW 264.7 macrophages were pre-treated with HOA, the DEGs of the biological process classification in the LPS/HOA group were highly enriched in chemotaxis, response to laminar shear stress, positive regulation of GTPase activity and immune response. In the molecular function, the genes related to oxidoreductase,

cytokine, and interleukin-1 receptor activity were significantly changed. In the cellular component classification, the external side of the plasma membrane, intrinsic components of the plasma membrane and extracellular space were significantly changed. These processes are involved in the inflammatory and immunomodulatory function of RAW 264.7 macrophages and provide a direction for the identification of DEGS in the future.

KEGG Pathway Enrichment Analyses of DEGs

Kyoto Encyclopedia of Genes and Genomes pathway analyses of the DEGs in control/LPS and LPS/HOA groups were performed using OmicShare. The DEGs of the two groups were mapped to the KEGG pathway database, and all pathways clustered into six categories: environmental information processing, human diseases, metabolic, organismal systems, cellular process, and genetic information processing. Environmental information

TABLE 2 | Data quality and reference sequence alignment analysis results.

Summary	Control	LPS	HOA
N	50415	73089	84576
	0.14%	0.27%	0.27%
Adapters	326343	180454	178983
	0.67%	0.58%	0.57%
Low quality	149190	78390	84079
	0.34%	0.29%	0.27%
Clean	27805302	26990712	29943562
	98.30%	98.76%	98.67%
Clean base	8.34G	8.10G	8.98G
GC (%)	52%	51.04%	51.52%
Q30 (%)	94.12%	92.81%	92.73%
Genome map rate of clean reads	90.77%	92.66%	93.61%
Unique match in genome mapped reads	85%	86.99%	87.77%
Multiple match in genome mapped reads	5.77%	5.67%	5.81%

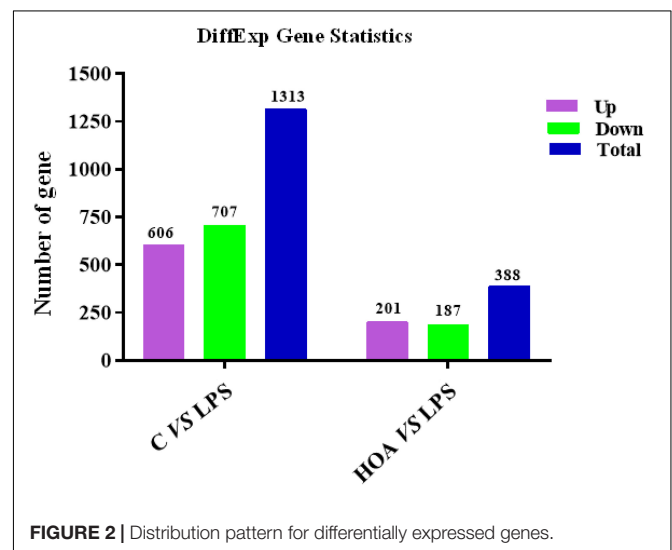
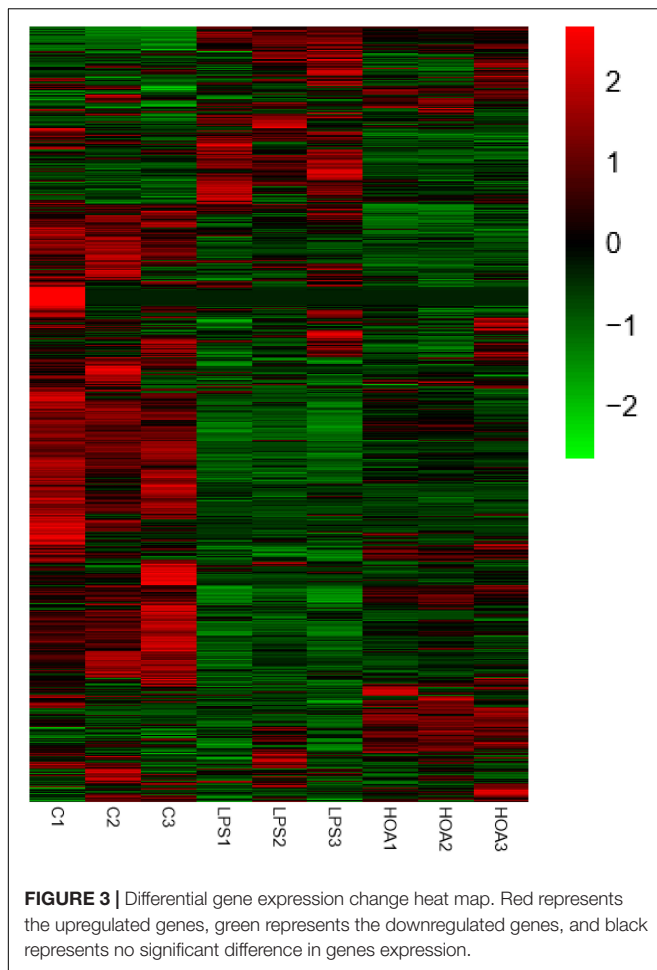


FIGURE 2 | Distribution pattern for differentially expressed genes.



processing mainly includes signal transduction, signal molecules and interaction, and membrane transport (Figure 5). A scatter plot was used to show the results of KEGG enrichment analyses. The top 20 signaling pathways enriched in the control/LPS group were biological processes related to inflammation, including the nuclear factor-kappa B (NF- κ B) signaling pathway, TNF signaling pathway, toll-like receptor signaling pathway, chemokine signaling pathway, and NOD-like receptor signaling pathway (Figure 6A). In the LPS/HOA group, a total of 17 signaling pathways were enriched, in which NF- κ B signaling pathway, cytokine-cytokine receptor interaction, Rap1 signaling pathway, chemokine signaling pathway, and the Janus kinase-signal transducer and activator of transcription proteins (JAK-STAT) signaling pathway were significantly enriched (Figure 6B).

Differential Gene Annotation Into Immune-Related Metabolic Pathways

The DEGs of the control/LPS group and LPS/HOA group were analyzed using KEGG. The results showed that when RAW 264.7 cells were pre-treated with HOA for 30 min, the number of DEGs involved in the metabolic pathway of RAW 264.7 macrophages induced by LPS decreased significantly (Table 3). There were 939 and 151 DEGs involved in the pathway of

the control/LPS group and LPS/HOA group, respectively. The number of annotated metabolic pathways in the HOA-treated group was significantly reduced, and there were 54 and 17 annotated metabolic pathways, respectively. By comparing the same inflammatory-related pathway between the two groups, the number of DEGs in the LPS/HOA group decreased in the same inflammatory immune-related pathway.

Differential Expression Level Analyses

Combined with the GO and KEGG enrichment results, 15 immune-related DEGs were selected for heat mapping (Figure 7). The results of thermography showed that immune-related genes such as Saa3, Bcl2l1, Mapkapk2, Ccl9, Sdc4, Ddx3x, Socs3, Prdx5, TLR4, Lif, IL15, Tnfaip3, TET2, TGF- β 1, and CCL20 were significantly upregulated after LPS stimulation, but were downregulated in the HOA pre-treatment group.

Verification of the RNA-Seq Data

To verify the accuracy of transcriptional sequencing data, we selected 15 DEGs associated with inflammation and immunity, including Saa3, Bcl2l1, Mapkapk2, Ccl9, Sdc4, Ddx3x, Socs3, Prdx5, TLR4, Lif, IL15, Tnfaip3, TET2, TGF- β 1, and CCL20. RT-qPCR showed that the expression of these DEGs was increased (Figure 8), with similar trends as the RNA-seq samples, indicating that the sequencing results were reliable.

DISCUSSION

Lupane triterpenes have diverse pharmacological activities such as anti-inflammatory, anti-oxidation, anti-virus, anti-malaria, and immune regulatory effects (Sultana et al., 2003; Saleem, 2009). In addition, they also showed high anti-cancer activities including pancreatic cancer cells, breast cancer cells, melanoma, and prostate cancer cells (Hata et al., 2003; Saleem et al., 2009). Lupeol significantly decreases the expression of RAS protein in the human pancreatic cancer cell line ASPC-1, regulates the protein expression of protein kinase C, phosphatidylinositol 3'-kinase (PI3K)/Akt and mitogen-activated protein kinases (MAPKs), and significantly decreases the activation of the NF- κ B signaling pathway (Murtaza et al., 2009). In a previous study, four triterpene acetates and four triterpene cinnamates isolated from the kernel fat of the shea tree effectively inhibited the 12-O-tetradecanoylphorbol-12-acetate-induced inflammation in mice. Lupeol cinnamate had the highest anti-inflammatory activity, including an obvious anti-inflammatory effect on carrageenan-induced paw swelling in rats (Akihisa et al., 2010).

To further prove the anti-inflammatory effects of HOA in macrophages, we also studied its effects on NO production in peritoneal macrophages induced by LPS. It inhibited the production of NO, was induced by LPS in a dose-dependent manner, and had no effect on cell activity, which further proves its anti-inflammatory activity (Cao et al., 2019).

The pathogenesis of inflammation is a complex process involving coordinated gene regulation. To understand the effects of HOA pre-treatment on the occurrence and development of inflammation in RAW 264.7 cells induced by LPS, RNA-seq was

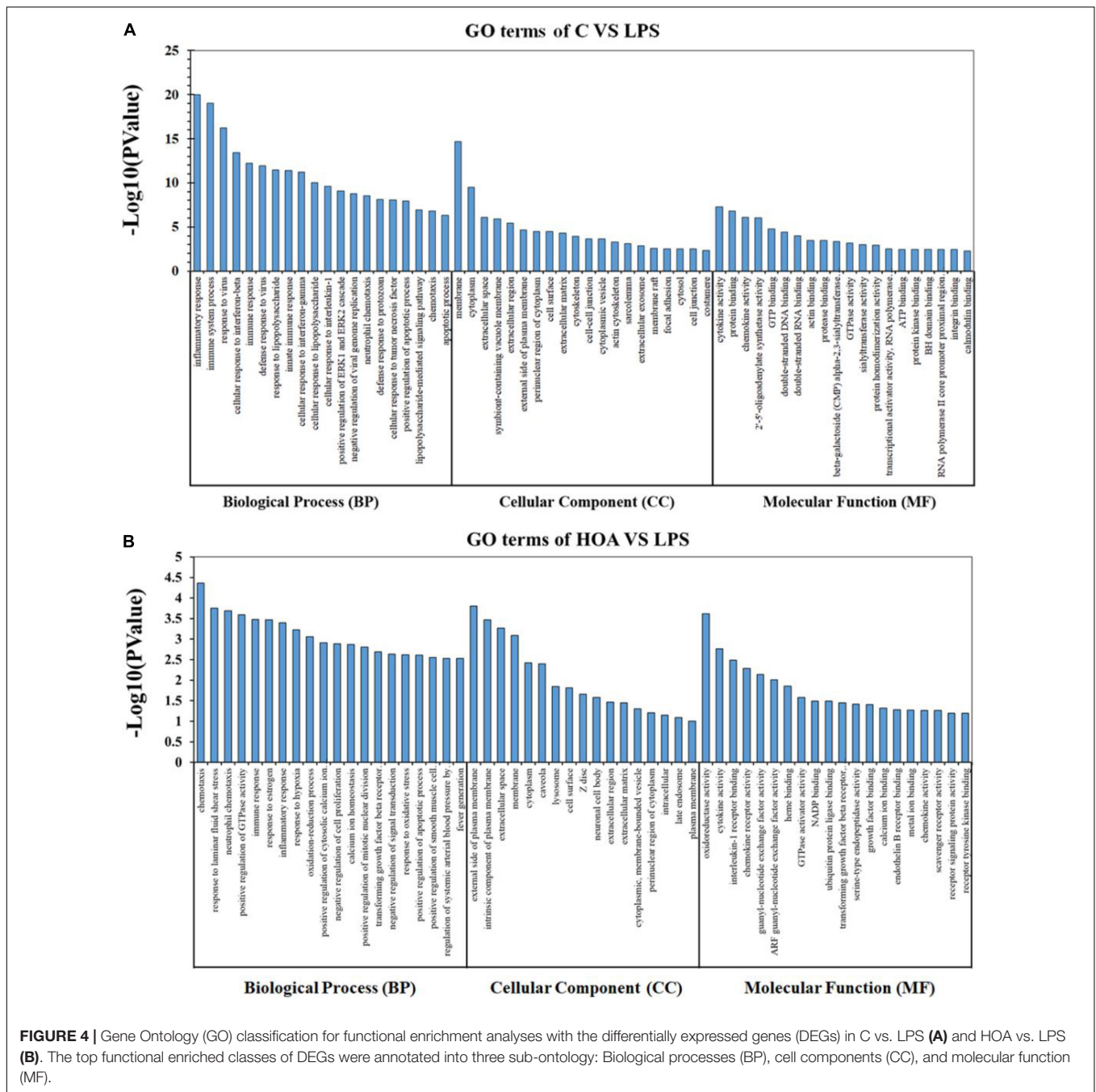


FIGURE 4 | Gene Ontology (GO) classification for functional enrichment analyses with the differentially expressed genes (DEGs) in C vs. LPS **(A)** and HOA vs. LPS **(B)**. The top functional enriched classes of DEGs were annotated into three sub-ontology: Biological processes (BP), cell components (CC), and molecular function (MF).

performed on normal cells, LPS-induced cells, and cells treated with HOA and LPS. There were significant differences in gene expression among the groups. HOA pre-treatment significantly inhibited the transcription of genes in RAW 264.7 cells induced by LPS compared to the LPS group (**Figure 3**), indicating that HOA pre-treatment might inhibit the activation and expression of related genes *in vitro*.

GO enrichment analyses indicated that DEGs in the control/LPS group were mainly enriched in the inflammatory response, immune system process, response to virus, and changes in IFN- β in cells (**Figure 4A**). This is consistent with

the mechanism of action of LPS on macrophages (Mosser and Edwards, 2008). LPS stimulation activates macrophages to produce corresponding inflammatory and immune responses, and studies have shown that TLR4 endocytosis occurs in a dynamin-dependent manner after LPS stimulation, which induces IFN- β production. IFNs are proteins with immune activity, which can activate and regulate immune cells (Medzhitov, 2007). IFN interacts with specific receptors to activate STAT complexes. In the LPS/HOA group, the biological functions of DEGs mainly included chemotaxis, laminar shear stress response, and positive regulation of

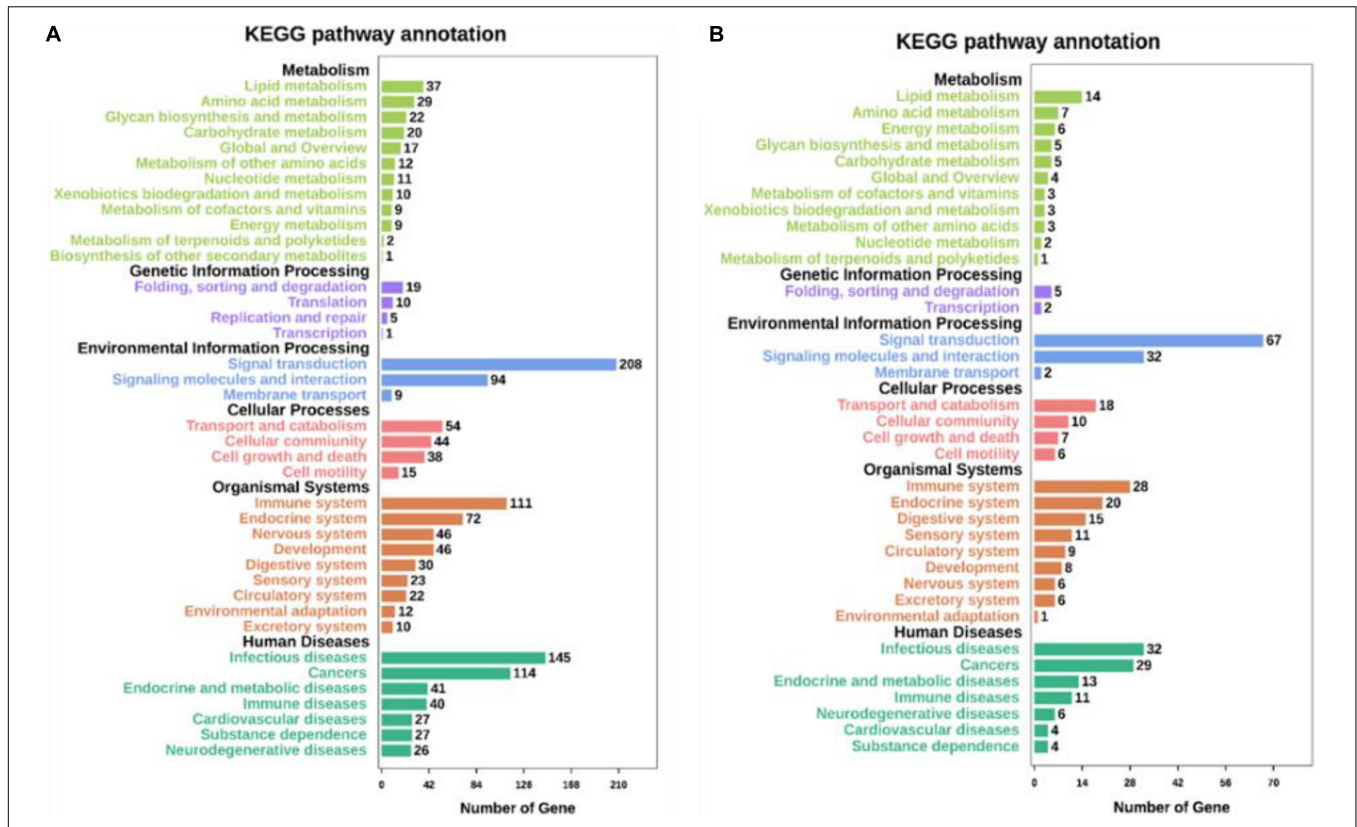


FIGURE 5 | Kyoto Encyclopedia of Genes and Genomes (KEGG) pathways annotation and classification of DEGs in C vs. LPS (A) and LPS vs. HOA (B).

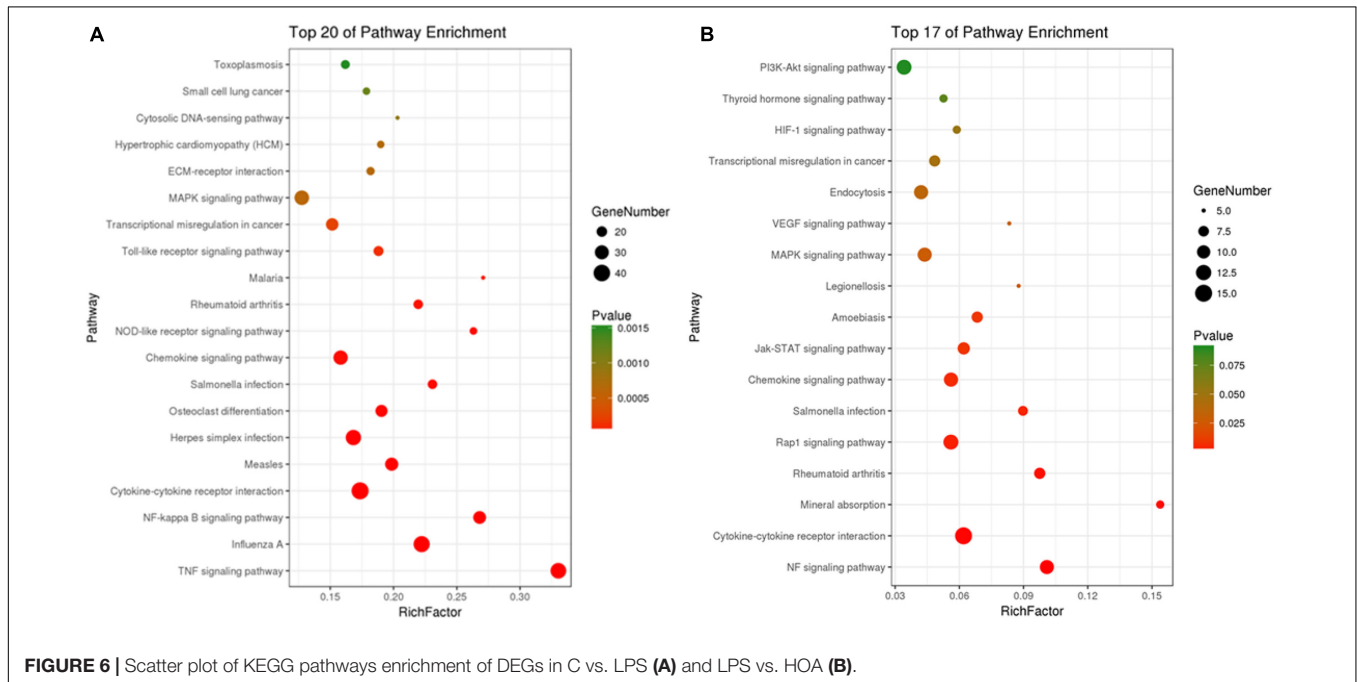


FIGURE 6 | Scatter plot of KEGG pathways enrichment of DEGs in C vs. LPS (A) and LPS vs. HOA (B).

GTPase activity (Figure 4B). Inflammatory chemokines can modulate leukocytes (such as monocytes and neutrophils) from blood circulation to infection or tissue damage. In

vascular endothelial cells, low levels of shear stress promote the secretion of endothelin, and endothelin-1 stimulates the release of other humoral inflammatory factors, cytokines, and

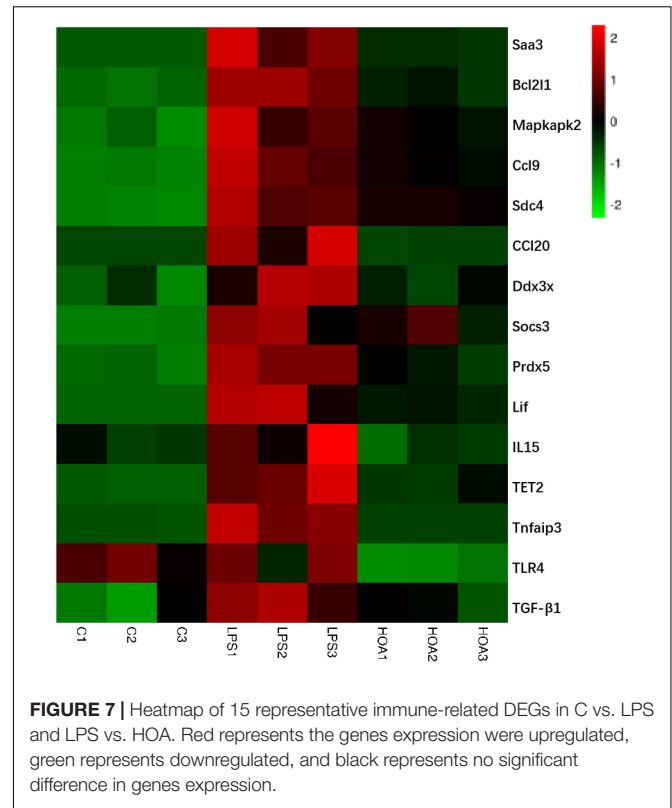
TABLE 3 | Top 10 of KEGG pathways of C vs. LPS and HOA vs. LPS.

KEGG pathways of C vs. LPS	
Pathway	Count
TNF signaling pathway	36 (2.79%)
Influenza A	38 (2.95%)
NF-kappa B signaling pathway	26 (2.02%)
Cytokine-cytokine receptor interaction	42 (3.25%)
Chemokine signaling pathway	31 (2.40%)
Toll-like receptor signaling pathway	19 (1.47%)
Transcriptional misregulation in cancer	25 (1.94%)
MAPK signaling pathway	32 (2.48%)
PI3K-Akt signaling pathway	37 (2.86%)
Jak-STAT signaling pathway	19 (1.47%)

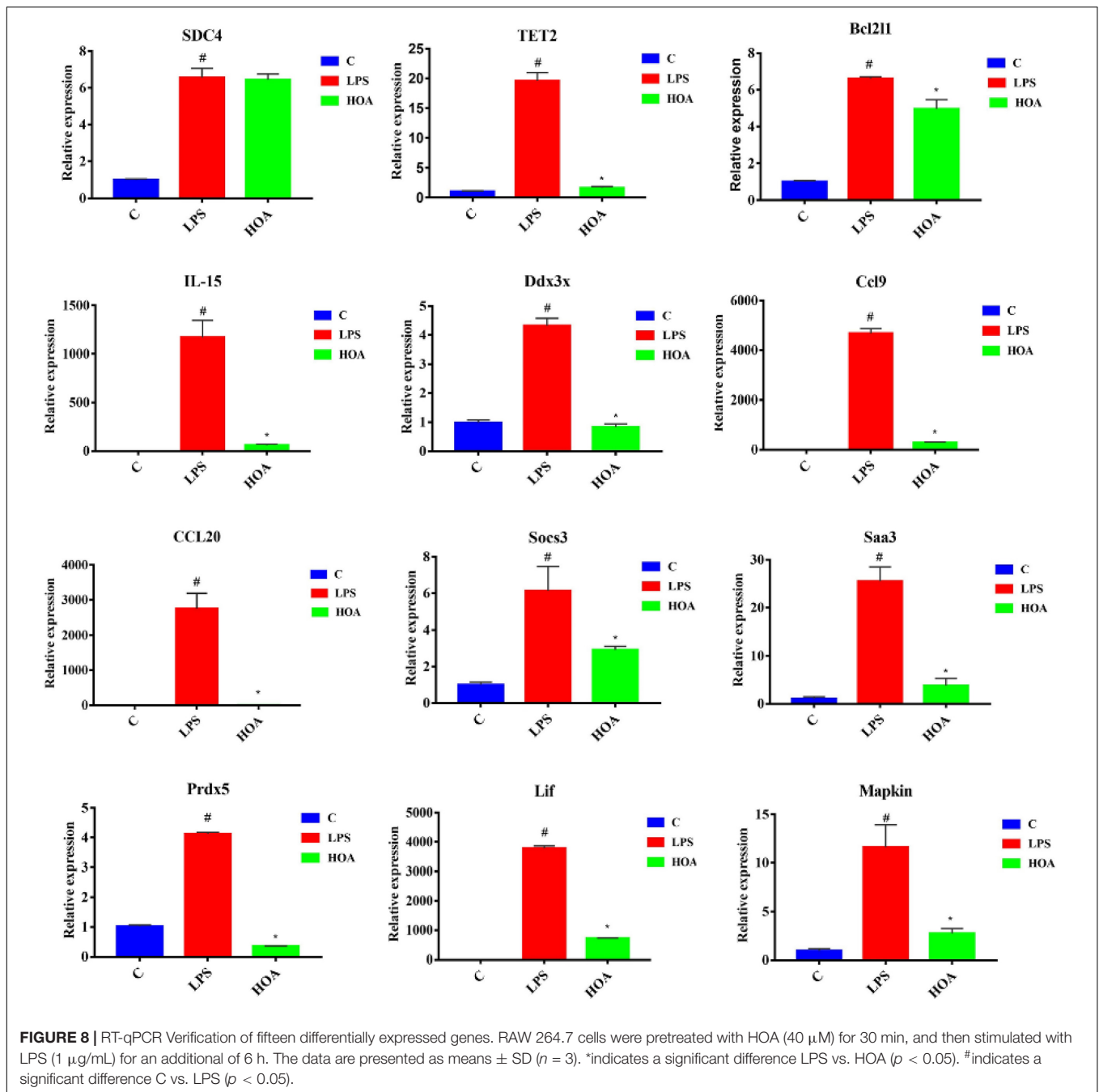
KEGG pathways of LPS vs. HOA	
Pathway	Count (of 151)
TNF signaling pathway	11 (1.89%)
Cytokine-cytokine receptor interaction	12 (3.95%)
Rheumatoid arthritis	13 (2.11%)
Rap1 signaling pathway	14 (3.16%)
Chemokine signaling pathway	15 (2.89%)
Jak-STAT signaling pathway	16 (2.37%)
MAPK signaling pathway	17 (2.89%)
VEGF signaling pathway	18 (1.32%)
Endocytosis	19 (2.89%)
Transcriptional misregulation in cancer	20 (2.11%)

leukocyte-releasing factors such as TNF- α and IL-6 (Pinho-Ribeiro et al., 2016). Therefore, the significant enrichment of genes in shear stress may inhibit LPS-induced inflammatory factor production in RAW 264.7 macrophages. Cytokines and inflammatory mediators produced by various stimuli can change the cytoskeleton of vascular endothelial cells (ECs), shrink ECs, and increase their permeability because cytokines and inflammatory mediators can activate GTPase through their corresponding receptors (Krishnamurti et al., 2002). These results suggest that GTPase may play an important role in vascular endothelial barrier dysfunction.

Kyoto Encyclopedia of Genes and Genomes pathway enrichment analyses showed that five inflammation-related pathways were screened from both the control/LPS group and LPS/HOA group at the same time, including the NF- κ B signaling pathway, cytokine-cytokine receptor interaction, chemokine signaling pathway, the MAPK pathway, and the JAK-STAT signaling pathway (Figure 6). NF- κ B is an important regulatory factor of proinflammatory gene expression. Local cells recognize pathogen-associated molecular patterns and release cytokines, which trigger an inflammatory cascade. Cytokines activate NF- κ B and promote the localization and activation of macrophages in the infected site (Baker et al., 2010). Activated macrophages produce bacteriostatic molecules, release chemokines and cytokines, and promote macrophage activation and recruitment to damaged tissues. Bacteriostatic molecules work with aggregated white blood cells to kill pathogens and remove infected and dead cells. The NF- κ B signaling pathway



plays a key role in the development of inflammation-related metabolic diseases in the adipose tissue, central nervous system, and liver (Tornatore et al., 2012). Proinflammatory chemokines are produced by cells and have many biological functions, such as directional migration of leukocytes, inflammatory response, immune response, development and differentiation, and stimulation or inhibition of angiogenesis (Newton et al., 2016). The most important concern is the role of chemokines in inflammatory responses. It gathers white blood cells to the site of infection or injury and participates in leukocyte adhesion, migration, and chemotaxis. Chemokines prevent these cells from rolling and exudate through endothelial cells by inducing the expression of integrin in target leukocytes. Many chemokines have additional housekeeping functions in initiating an adaptive immune response and immune surveillance, and can activate JAK-STAT, MAPK, and protein kinase B pathways, thus regulating the inflammatory response. The JAK-STAT signaling pathway is used by many cytokines, and interferon and plays an important role in the development and function of innate and adaptive immunity (Crocker et al., 2008). The JAK-STAT pathway acts as a central fulcrum in cell growth, differentiation, proliferation, and immunomodulation. Various growth factors, protein tyrosine kinases, and cytokines communicate through the JAK-STAT pathway to regulate gene transcription. In the pathogenesis of inflammatory diseases, many cytokines use JAK and STATs to transmit intracellular signals. In addition, MAPK signaling pathways are involved in intracellular inflammatory signaling cascades and are closely



related to proinflammatory cytokines and NF- κ B transcription activation (Zhou et al., 2016; Long et al., 2018). The MAPK signaling pathways are involved in a series of biological processes from inflammation, proliferation, differentiation, transformation, and apoptosis. These results suggest that LPS might stimulate macrophage activation through a variety of signaling pathways. Cytokine-cytokine interactions play an important role in immune and inflammatory responses. Interactions among proinflammatory cytokines (IL-1 β , IL-6, IL-8, and TNF- α) play a synergistic role in cytokine production and cytokine activity. Anti-inflammatory cytokines such as

IL-1Ra, IL-4, IL-10, and TGF- β 1 play an antagonistic role in proinflammatory cytokines (Minciullo et al., 2016). Cytokine balance consists of two parts. The first is the balance in the cytokine system, such as IL-1 increasing the synthesis and secretion of IL-1RA, which may be upregulated by blocking the IL-1 receptor to weaken the harmful effects of IL-1. The other is the balance between different cytokine systems, such as TGF- β 1 inhibiting the activities of IL-1 and TNF- α (Rubio-Perez and Morillas-Ruiz, 2012). In the LPS/HOA group, the number of inflammatory immune-related signaling pathways enriched by DEGs in the experimental group pre-treated with

HOA decreased. Furthermore, the number of genes enriched in the same signaling pathway decreased, indicating that HOA pre-treatment of RAW 264.7 cells might inhibit LPS-induced activation of inflammatory-related signaling pathways in RAW 264.7 macrophages as well as the expression of some inflammatory-related genes (Table 3). To demonstrate that the DEGs obtained by transcriptome sequencing were more reliable, we selected 15 DEGs associated with inflammatory immunity using RT-qPCR to verify the sequencing results (Figure 8). The RNA-seq results showed consistent trends, demonstrating that RNA-seq sequencing data are reliable.

CONCLUSION

We identified 15 significantly enriched GO terms and five typical pathways, suggesting that HOA may inhibit the inflammatory response induced by LPS in RAW 264.7 cells through a variety of targets and pathways. Additional studies are currently underway to prepare larger quantities of HOA and investigate its overall *in vivo* anti-inflammatory effect.

REFERENCES

- Akihisa, T., Kojima, N., Kikuchi, T., Yasukawa, K., Tokuda, H., Masters, E. T., et al. (2010). Anti-inflammatory and chemopreventive effects of triterpene cinnamates and acetates from shea fat. *J. Oleo Sci.* 59, 273–280. doi: 10.5650/jos.59.273
- Baker, R. G., Hayden, M. S., and Ghosh, S. (2010). NF- κ B, inflammation, and metabolic disease. *Cell Metab.* 13, 11–22. doi: 10.1016/j.cmet.2010.12.008
- Cao, Y., Li, F., Luo, Y., Zhang, L., Lu, S., Xing, R., et al. (2019). 20-Hydroxy-3-oxolupan-28-oic acid attenuates inflammatory responses by regulating PI3K⁻¹Akt and MAPKs signaling pathways in LPS-stimulated RAW264.7 macrophages. *Molecules* 24:386. doi: 10.3390/molecules24030386
- Crocker, B. A., Kiu, H., and Nicholson, S. E. (2008). SOCS regulation of the JAK/STAT signalling pathway. *Cell Dev. Biol.* 19, 414–422. doi: 10.1016/j.semdb.2008.07.010
- Du, H., Liu, W., Zhang, M., Si, C., Zhang, X., and Li, B. (2019). Cellulose nanocrystals and cellulose nanofibrils based hydrogels for biomedical applications. *Carbohydr. Polym.* 209, 130–144. doi: 10.1016/j.carbpol.2019.01.020
- Guinane, C. M., and Cotter, P. D. (2013). Role of the gut microbiota in health and chronic gastrointestinal disease: understanding a hidden metabolic organ. *Therap. Adv. Gastroenterol.* 6, 295–308. doi: 10.1177/1756283X13482996
- Hata, K., Hori, K., and Takahashi, S. (2003). Role of p38 MAPK in lupeol-induced B16 F2F mouse melanoma cell differentiation. *J. Biochem.* 134, 441–445. doi: 10.1093/jb/mvg162
- Hu, W., Wang, X., Wu, L., Shen, T., Ji, L., Zhao, X., et al. (2016a). Apigenin-7-O- β -D-glucuronide inhibits LPS-induced inflammation through the inactivation of AP-1 and MAPK signaling pathways in RAW 264.7 macrophages and protects mice against endotoxin shock. *Food Funct.* 7, 1002–1013. doi: 10.1039/C5FO01212K
- Hu, W., Wu, L., Qiang, Q., Ji, L., Wang, X., Luo, H., et al. (2016b). The dichloromethane fraction from *Mahonia bealei* (Fort.) Carr. leaves exerts an anti-inflammatory effect both *in vitro* and *in vivo*. *J. Ethnopharmacol.* 188, 134–143. doi: 10.1016/j.jep.2016.05.013
- Hu, W., Yu, L., and Wang, M. H. (2011). Antioxidant and antiproliferative properties of water extract from *Mahonia bealei* (Fort.) Carr. leaves. *Food Chem. Toxicol.* 49, 799–806. doi: 10.1016/j.fct.2010.12.001
- Krishnamurti, C., Peat, R. A., Cutting, M. A., and Rothwell, S. W. (2002). Platelet adhesion to dengue-2 virus-infected endothelial cells. *Am. J. Trop. Med. Hyg.* 66, 435–441. doi: 10.1016/S0001-706X(02)00003-7

DATA AVAILABILITY STATEMENT

The original contributions presented in the study are included in the article/Supplementary Material, further inquiries can be directed to the corresponding author/s.

AUTHOR CONTRIBUTIONS

XY, JZ, YH, and YC: investigation. WH, LL, and YC: supervision and writing—review and editing. WH and YC: writing—original draft. All authors contributed to the article and approved the submitted version.

FUNDING

This research was funded by the National Natural Science Foundation of China (31600281) and Natural Science Foundation of Jiangsu Province (BK20171269).

- Kukurba, K. R., and Montgomery, S. B. (2015). RNA sequencing and analysis. *Cold Spring Harb. Protoc.* 2015, 951–969. doi: 10.1101/pdb.top084970
- Levy, S. E., and Myers, R. M. (2016). Advancements in next-generation sequencing. *Annu. Rev. Genom. Hum. Genet.* 17, 95–115. doi: 10.1146/annurev-genom-083115-022413
- Li, F., Cao, Y., Luo, Y., Liu, T., Yan, G., and Chen, L. (2019). Two new triterpenoid saponins derived from the leaves of *Panax ginseng* and their anti-inflammatory activity. *J. Ginseng Res.* 43, 600–605. doi: 10.1016/j.jgr.2018.09.004
- Li, X., Shen, J., Jiang, Y., Shen, T., You, L., Sun, X., et al. (2016). Anti-inflammatory effects of chloranthalactone B in LPS-stimulated RAW264.7 cells. *Int. J. Mol. Sci.* 17:1938. doi: 10.3390/ijms17111938
- Long, T., Liu, Z., Shang, J., Zhou, X., Yu, S., Tian, H., et al. (2018). *Polygonatum sibiricum* polysaccharides play anti-cancer effect through TLR4-MAPK/NF- κ B signaling pathways. *Int. J. Biol. Macromol.* 111, 813–821. doi: 10.1016/j.ijbiomac.2018.01.070
- Medzhitov, R. (2007). Recognition of microorganisms and activation of the immune response. *Nature* 449, 819–826. doi: 10.1038/nature06246
- Minciullo, P. L., Catalano, A., Mandraffino, G., Casciaro, M., Crucitti, A., Maltese, G., et al. (2016). Inflammaging and anti-inflammaging: The role of cytokines in extreme longevity. *Arch. Immunol. Ther. Exp.* 64, 111–126. doi: 10.1007/s00005-015-0377-3
- Mosser, D. M., and Edwards, J. P. (2008). Exploring the full spectrum of macrophage activation. *Nat. Rev. Immunol.* 8, 958–969. doi: 10.1038/nri2448
- Murtaza, I., Saleem, M., Adhami, V. M., Hafeez, B. B., and Mukhtar, H. (2009). Suppression of cFLIP by lupeol, a dietary triterpene, is sufficient to overcome resistance to TRAIL-mediated apoptosis in chemoresistant human pancreatic cancer cells. *Cancer Res.* 69, 1156–1165. doi: 10.1158/0008-5472.CAN-08-2917
- Newton, A. H., Cardani, A., and Braciale, T. J. (2016). The host immune response in respiratory virus infection: balancing virus clearance and immunopathology. *Semin. Immunopathol.* 38, 471–482. doi: 10.1007/s00281-016-0558-0
- Pan, M. H., Lai, C. S., and Ho, C. T. (2010). Anti-inflammatory activity of natural dietary flavonoids. *Food Funct.* 1, 15–31. doi: 10.1039/c0fo00103a
- Pappas, K., Papaioannou, A. I., Kostikas, K., and Tzanakis, N. (2013). The role of macrophages in obstructive airways disease: chronic obstructive pulmonary disease and asthma. *Cytokine* 64, 613–625. doi: 10.1016/j.cyto.2013.09.010
- Pinho-Ribeiro, F. A., Zarpelon, A. C., Mizokami, S. S., Borghi, S. M., Bordignon, J., Silva, R. L., et al. (2016). The citrus flavonone naringenin reduces lipopolysaccharide-induced inflammatory pain and leukocyte recruitment by inhibiting NF- κ B activation. *J. Nutr. Biochem.* 33, 8–14. doi: 10.1016/j.jnutbio.2016.03.013

- Rubio-Perez, J. M., and Morillas-Ruiz, J. M. (2012). A review: inflammatory process in Alzheimer's disease, role of cytokines. *Sci. World J.* 2012, 756357–756357. doi: 10.1100/2012/756357
- Saleem, M. (2009). Lupeol, a novel anti-inflammatory and anti-cancer dietary triterpene. *Cancer Lett.* 285, 109–115. doi: 10.1016/j.canlet.2009.04.033
- Saleem, M., Murtaza, I., Tarapore, R. S., Suh, Y., Adhami, V. M., Johnson, J. J., et al. (2009). Lupeol inhibits proliferation of human prostate cancer cells by targeting beta-catenin signaling. *Carcinogenesis* 30, 808–817. doi: 10.1093/carcin/bgp044
- Shen, T., Wang, G., You, L., Zhang, L., Ren, H., Hu, W., et al. (2017). Polysaccharide from wheat bran induces cytokine expression via the toll-like receptor 4-mediated p38 MAPK signaling pathway and prevents cyclophosphamide-induced immunosuppression in mice. *Food Nutr. Res.* 61:1344523. doi: 10.1080/16546628.2017.1344523
- Sultana, S., Saleem, M., Sharma, S., and Khan, N. (2003). Lupeol, a triterpene, prevents free radical mediated macromolecular damage and alleviates benzoyl peroxide induced biochemical alterations in murine skin. *Ind. J. Exp. Biol.* 41, 827–831.
- Tornatore, L., Thotakura, A. K., Bennett, J., Moretti, M., and Franzoso, G. (2012). The nuclear factor kappa B signaling pathway: integrating metabolism with inflammation. *Trends Cell Biol.* 22, 557–566. doi: 10.1016/j.tcb.2012.08.001
- Wang, Y., Xue, S., Liu, X., Liu, H., Hu, T., Qiu, X., et al. (2016). Analyses of Long Non-Coding RNA and mRNA profiling using RNA sequencing during the pre-implantation phases in pig endometrium. *Sci. Rep.* 6, 20238–20238. doi: 10.1038/srep20238
- Zhang, J., Li, W., Yuan, Q., Zhou, J., Zhang, J., Cao, Y., et al. (2019). Transcriptome analyses of the anti-proliferative effects of 20(S)-ginsenoside Rh2 on HepG2 cells. *Front. Pharmacol.* 10:1331. doi: 10.3389/fphar.2019.01331
- Zhou, X., Naguro, I., Ichijo, H., and Watanabe, K. (2016). Mitogen-activated protein kinases as key players in osmotic stress signaling. *Biochim. Biophys. Acta Gen.* 1860, 2037–2052. doi: 10.1016/j.bbagen.2016.05.032

Conflict of Interest: The authors declare that the research was conducted in the absence of any commercial or financial relationships that could be construed as a potential conflict of interest.

Copyright © 2021 Yang, Zhou, He, Lv, Cao and Hu. This is an open-access article distributed under the terms of the Creative Commons Attribution License (CC BY). The use, distribution or reproduction in other forums is permitted, provided the original author(s) and the copyright owner(s) are credited and that the original publication in this journal is cited, in accordance with accepted academic practice. No use, distribution or reproduction is permitted which does not comply with these terms.



Recent Developments and Applications of Hemicellulose From Wheat Straw: A Review

Ling-Zhi Huang¹, Ming-Guo Ma^{1*}, Xing-Xiang Ji^{2*}, Sun-Eun Choi^{3*} and Chuanling Si^{4*}

¹ Beijing Key Laboratory of Lignocellulosic Chemistry, Research Center of Biomass Clean Utilization, Engineering Research Center of Forestry Biomass Materials and Bioenergy, College of Materials Science and Technology, Beijing Forestry University, Beijing, China, ² State Key Laboratory of Biobased Material and Green Papermaking, Qilu University of Technology (Shandong Academy of Sciences), Jinan, China, ³ Department of Forest Biomaterials Engineering, College of Forest and Environmental Sciences, Kangwon National University, Chuncheon, South Korea, ⁴ Tianjin Key Laboratory of Pulp and Paper, Tianjin University of Science and Technology, Tianjin, China

OPEN ACCESS

Edited by:

Xianzhi Meng,
The University of Tennessee,
Knoxville, United States

Reviewed by:

Yang Tian,
Capital Normal University, China
Jiefang Zhu,
Uppsala University, Sweden

*Correspondence:

Ming-Guo Ma
mg_ma@bjfu.edu.cn
Xing-Xiang Ji
jxx@qlu.edu.cn
Sun-Eun Choi
oregonin@kangwon.ac.kr
Chuanling Si
sichli@tust.edu.cn

Specialty section:

This article was submitted to
Bioprocess Engineering,
a section of the journal
Frontiers in Bioengineering and
Biotechnology

Received: 04 April 2021

Accepted: 05 May 2021

Published: 22 June 2021

Citation:

Huang L-Z, Ma M-G, Ji X-X,
Choi S-E and Si C (2021) Recent
Developments and Applications
of Hemicellulose From Wheat Straw:
A Review.
Front. Bioeng. Biotechnol. 9:690773.
doi: 10.3389/fbioe.2021.690773

Hemicellulose is an important component of plant cell walls, which is mainly used in biofuels and bioproducts. The hemicellulose extracted from different plant sources and plant locations has different microstructure and molecule. Wheat straw is an important biomass raw material for the extraction of hemicellulose. The aims of this review are to summary the recent developments and various applications of hemicellulose from wheat straw. The microstructure and molecule of hemicellulose extracted by different methods are comparably discussed. The hemicellulose-based derivatives and composites are also reviewed. Special attention was paid to the applications of hemicellulose such as biofuel production, packaging field, and adsorbent. The problems and developing direction were given based on our knowledge. We expect that this review will put forward to the development and high-value applications of hemicellulose from wheat straw.

Keywords: hemicellulose, wheat straw, structure, development, applications

INTRODUCTION

Hemicellulose can be defined as cell wall polysaccharides, which binds strongly to cellulose microfibrils by hydrogen bonds and Van der Waals force (Carvalho et al., 2008; Liu et al., 2020; Liu K. et al., 2021). In general, hemicellulose consisted of a heterogeneous group of plant-derived polysaccharides including D-xylose, D-mannose, D-galactose, L-arabinose, D-galactose, and 4-O-methyl-D-glucuronic acid. Hemicellulose is used to produce alcohol by fermentation and sorbitol by reduction (Girio et al., 2010), which has important applications in food, toothpaste, cosmetics, explosive manufacturing, and papermaking (Falco et al., 2013; Zhao et al., 2014). Pentose of hemicellulose is also used to produce feed yeast, furoic acid, xylose, and xylitol (Yoon et al., 2006; Du et al., 2019; Liu X. et al., 2019). More importantly, xylooligosaccharides, as one of the degradation products of hemicellulose, are widely used in functional food and pharmaceutical fields due to their unique physical and chemical properties and physiological functions (Bian et al., 2014).

The hemicellulose is extracted from different plant sources and plant locations which has different structure and molecule (Peng et al., 2012; Fu et al., 2017). For example, the hemicelluloses from different biomass species such as hardwood, softwood, and gramineous plants have different chemical structures. The hemicelluloses in the secondary wall of hardwood cells are mainly glucuronoxylan or 4-O-methyl-glucuronoxylan with some acetyl groups; meanwhile the

hemicelluloses of softwood cells are mainly galactose glucose mannan or *O*-ethyl-galactose glucose mannan (Kapu and Trajano, 2014). The structures of hemicellulose are different with different parts of the same raw material. Moreover, different raw materials and different extraction methods lead to different types and contents of side chains in the as-obtained hemicelluloses (Buranov and Mazza, 2010; Ma et al., 2012; Sun et al., 2014). Wheat straw is an important biomass raw material for the extraction of hemicellulose (Sun et al., 2005a). Recently, more attentions have been focused on the hemicellulose from wheat straw (Zhong et al., 2015).

This current review aims to describe the recent developments and various applications of hemicellulose from wheat straw, introduce the structures and molecules of hemicellulose extracted by different methods, provide the applications as biofuel production, packaging materials, and adsorbent via some typical examples about the hemicellulose-based derivatives and composites, and suggest the problems and develops direction of hemicellulose from wheat straw. We expect that this review will put forward to the development and high-value applications of hemicellulose from wheat straw.

THE EXTRACTION AND STRUCTURE OF HEMICELLULOSE FROM WHEAT STRAW

Acid Hydrolysis Technology

Hemicellulose is the second largest component of lignocellulosic biomass. Development of efficient and low-cost extraction methods of hemicellulose is important to realize the practical applications of biomass. Dilute acid hydrolysis technology is widely used to hydrolyze hemicellulose with high conversion rate, further fermenting to produce fuel ethanol (Jiang et al., 2015). Hemicellulose can also be hydrolyzed directly to produce functional foods such as oligosaccharides and chemicals such as furfural (Luo et al., 2019). As early as 1986, in the Gonzalez's work, a kinetic model was suggested about the hydrolysis of wheat straw hemicellulose with sulfuric acid at 34 and 90°C (Gonzalez et al., 1986). It yielded complete solubilization of hemicellulose to xylose and arabinose without significant amounts of furfural at 90°C. Authors provided a two-consecutive reaction mechanism on the kinetic model of the acid-catalyzed hydrolysis to explain the different behavior of the concentration of the two main sugars. In 2006, Canilha et al. (2006) estimated the effects of temperature and acid loading on the yield of monomeric xylose recovery from wheat straw hemicellulose. It achieved a xylitol production of 30.8 g L⁻¹ after 54 h of fermentation, resulting in a productivity of 0.57 g L⁻¹ h⁻¹ and bioconversion yield of 0.88 g g⁻¹. Authors also obtained the maximum specific rates of 0.19 g g⁻¹ h⁻¹ for xylose consumption and 0.15 g g⁻¹ h⁻¹ for xylitol production. Then, Sun's group applied the different acid solutions of acetic acid/H₂O, acetic acid/H₂O, and formic acid/acetic acid/H₂O for the treatment of the dewaxed wheat straw using 0.1% HCl as a catalyst at 85°C for 4 h, yielding 14.2–76.5% of the original hemicelluloses (Xu et al., 2006). It was found that xylose as a major constituent, glucose and arabinose

in noticeable amounts, uronic acids (principally 4-*O*-methyl-D-glucuronic acid) in a small amount, and galactose, mannose, and rhamnose as minor components. They indicated that organic acids treatment induced the more linear and partially acetylated hemicelluloses with lower molecular weights ranging between 8,480 and 18,940 g mol⁻¹. After that, they acetylated wheat straw hemicellulose with acetic anhydride using iodine as a catalyst in 1-butyl-3-methylimidazolium chloride [(C₄mim)Cl] ionic liquid (Ren et al., 2007). It esterified 83% hydroxyl groups in native hemicellulose and achieved acetylated hemicellulose with yield from 70.5 to 90.8% and degree of substitution between 0.49 and 1.53 by changing the experimental parameters. The dilute sulfuric acid was also used as a catalyst for the extraction of hemicellulose with 85.5% of the total sugar from rapeseed straw at 152.6°C for 21 min (Jeong et al., 2010). The hemicellulose-derived carbohydrates were obtained from wheat straw using dilute HCl or FeCl₃ solutions at 120°C by Marcotullio et al. (2011). It approached the recovery of 100% of xylose and arabinose. Authors found the partial precipitation of FeCl₃ dilute solutions to iron oxides and consequent formation of HCl, facilitating the hydrolysis of hemicellulose. Obviously, acid was reported as catalyst for the extraction of hemicellulose. A solid acid SO₄²⁻/Fe₂O₃ catalyst with both Lewis and Brønsted acidity was applied for the selective hydrolysis of hemicellulose from wheat straw (Zhong et al., 2015). It obtained a maximum hemicellulose hydrolysis yield of 63.5% from wheat straw at 141.97°C for 4.1 h with the ratio of wheat straw to catalyst (w/w) of 1.95:1. The catalyst was reported to be recycled six times with high activity remaining. The acidic dioxane/water solution and dimethyl sulfoxide was also reported to extract the original hemicellulose with high yield/purity from ball-milled wheat straw (Sun et al., 2005a). The toxicity of acidic dioxane don't meet the principles of green chemistry. It obtained the arabinoxylans as the major polysaccharides, substituted by R-L-arabino furanose, 4-*O*-methylglucuronic acid, acetyl group, and xylose at *O*-3 and/or *O*-2 of xylans. Recently, the acid hydrolysis of hemicellulose containing about 30% xylan was also reported for the preparation of xylo-oligosaccharides (Wang et al., 2019). Authors found that sulfuric acid as the hydrolysis catalyst influenced the yield of xylo-oligosaccharides. The acid hydrolysis technology is a traditional process for the hydrolyze hemicellulose. However, some problems need to be solved in the near future such as the chemical reactivity, active site, and proton affinity.

Supercritical CO₂ Technology

CO₂ has the advantages of non-toxic, low cost, and non-flammable (Middleton et al., 2015; Li M. G. et al., 2020). Supercritical CO₂ can be used for the precipitation of hemicellulose due to its special physical and chemical properties at critical temperature of 31.8°C and pressure at 7.4 MPa. For example, supercritical CO₂ as an antisolvent was applied to precipitate hemicellulose from the mixture of dimethyl sulfoxide and water by Haimer et al. (2010). The antisolvent CO₂ was added to hemicellulose solution by single-phase transfer in supercritical state, inducing the precipitation of hemicellulose under supersaturated condition. A high-pressure CO₂ was also

used as catalyst for the selective hydrolysis of wheat straw hemicellulose on the hydrothermal production of hemicellulose-derived sugars (Relvas et al., 2015). It yielded 79.6 g of xylo-oligosaccharide per 100 g of the initial xylan content, compared with that of water (70.8 g). Authors suggested a high dissolution of wheat straw hemicellulose due to the *in situ* formation of carbonic acid by the addition of CO₂ to water-based processes. More recently, high-pressure CO₂-H₂O was also reported to treat wheat straw to selectively hydrolyze hemicellulose with low concentration of acetic acid at 180°C for 1 h due to the *in situ* formation of carbonic acid and acetic acid (Yang H. P. et al., 2020). It obtained the removal ratio of 82.3% for hemicellulose. Authors suggested the high-pressure CO₂-H₂O as effective method in removing and hydrolyzing the hemicellulose of wheat straw. Hydrothermal CO₂-assisted pretreatment was carried out for selective degradation of hemicellulose in wheat straw to produce pentose and enhancement the efficiency of enzymatic hydrolysis for glucose production (Wang et al., 2021). It achieved the improved efficiency of enzymatic hydrolysis and 90.0% of degraded hemicellulose at 200°C for 10 min. More than 72.7% of glucose was observed after enzymatic hydrolysis, compared with that of the untreated sample (30.2%). The hydrothermal CO₂-assisted pretreatment was developed as an effective approach for pretreatment of biomass. In general, supercritical CO₂-assisted pretreatment is a promising route for the extraction of hemicellulose. However, it has the disadvantages of high pressure, high cost, expensive equipment, and destroy chemical structure of hemicellulose more or less. It is necessary to balance the advantages and disadvantages of supercritical CO₂-assisted pretreatment for the extraction of hemicellulose.

Hydrothermal Treatment Technology

Hydrothermal treatment is to create a high temperature of 100–1,000°C and high pressure of 1–100 MPa reaction environment using water as reaction medium in a special closed vessel. In 2008, Thomsen et al. (2008) reported hydrothermal treatment of wheat straw at pilot plant scale (120–150 kg h⁻¹) using a three-step reactor system aiming at high hemicellulose recovery, high cellulose digestibility, and low lignin hydrolysis. It obtained the high hemicellulose recovery (83%) at the water addition (600 kg h⁻¹) at 170–180°C, meanwhile it resulted in low hemicellulose recovery (33%) and high glucose yield in the enzymatic hydrolysis with no water addition xylose degradation. The hydrolysis technology of hemicellulose was studied in corncob (Thomsen et al., 2008). It obtained the gradually increasing D-xylose and L-arabinose concentration with the growing time of repeated use of corncob hydrolyzate. Authors achieved the concentrations of D-xylose of 196.7 g·L⁻¹ and L-arabinose of 22.0 g·L⁻¹ after the fifth repetition. More recently, the combination of hydrothermal treatments and alkalis was also used to extract hemicellulose from de-starched corn fiber (Kaur et al., 2020). It obtained maximum yield of 47% soluble (w/w) via thermochemical treatment in the liquid fraction. It observed the compositions of extracted soluble in arabinoxylan, monosaccharides, ferulic acid, and oligosaccharides. The main difference of hydrothermal treatments lied in temperature and pressure, inducing different reaction environment and favoring the extraction of biomass.

The basic mechanism of thermodynamics and kinetics of hydrothermal treatment is complex and needs to be investigated in the near future.

Alkali Treatment Method

Besides acid hydrolysis technology, alkali method is widely used for the extraction of hemicellulose, making the cellulose swelling, breaking the bonds between hemicellulose and lignin, and dissolving the hemicellulose from the cell wall. All the type and concentration of alkali, extraction time and temperature are found to affect the yield of hemicellulose. As early as the year of 1951, Adams and Castagne (1951) did pioneering work on the alkali treatment on biomass. They first reported the various hemicellulose fractions extracted from wheat straw holocellulose with cold and hot water, and potassium hydroxide recovered by precipitation with alcohol. In their work, it found a high uronic acid and methoxyl content in the soluble fractions and a high pentosan content in the less soluble fractions. All the D-xylose, L-arabinose, D-glucose, and D-galactose were obtained. It also achieved the acid-resistant uronic acid complex of D-xylose and a monomethoxyl galacturonic acid. After that, there are many reports on the alkali treatment for hemicellulose extraction. For example, Jin et al. (2009) dissolved hemicellulose from mild ball-milled cell wall of lignified barley straw and maize stems using alkali treatments. It obtained the dissolution of the original hemicellulose of 94.6% from barley straw and of 96.4% from maize stems. Authors found the different components using different alkali solutions. The high concentration of alkali improved the isolation of hemicellulose. Sun et al. (2011) extracted the 87% of original hemicellulose from the sequential treatments of barley straw using alkali treatments. It obtained the acidic arabinoxylans as the major polysaccharides, substituted by α -L-arabinofuranose, 4-O-methyl-glucuronic acid, acetyl group, and xylose at O-3 and/or O-2 of xylan. The cold alkaline extraction and subsequent separation by precipitation with ethanol was also developed to selective extract the hemicellulose from wheat straw (Garcia et al., 2013). It achieved the 56.1% of all hemicellulose using cold alkaline at 40°C for 90 min and recovered 39.4% of all hemicellulose by precipitation with ethanol in the raw material. The autohydrolysis and aqueous ammonia extraction of wheat straw was reported at 170–200°C by Sipponen et al. (2014). It obtained the oligomeric arabinoxylans at 66% xylan recovery yield. Authors found the autohydrolysis severity as a crucial parameter affecting properties of hemicellulose and lignin. Recently, Ragab et al. (2018) extracted hemicellulose from Egyptian agriculture wastes rice straw and husk by 4% sodium hydroxide at 90°C, purifying by 5% hydrogen peroxide, and sulfating using two catalysts of *N,N*-dicyclohexylcarbodiimide and 4-dimethylaminopyridine. The sulfated hemicellulose has the highest degree of sulfation with low total carbohydrate content, showing the promising biological activities such as anticoagulation activity at 31.25 μ g mL⁻¹ and fibrinolytic activity lysis more than 80% at 2,000 μ g mL⁻¹. During the process of alkaline treatment, it ionized the anions of OH compounds in aqueous solution, accepted protons, and provided electron donors. There are many types of

organic and inorganic bases, ringing infinite opportunity for the hemicellulose extraction.

Combination of Various Methods

Combination of various methods such as ultrasonic-assisted method, basic hydrogen peroxide method, mixed organic solvent extraction method, steam pretreatment method, microwave-assisted method, and mechanical-assisted method, maybe induce unexpected results for the extraction of biomass. Various separation and purification for wheat straw, and their advantages and disadvantages, are summarized in **Table 1**. In 2002, Sun et al. (2002) comparatively studied the effect of ultrasound on the yield and physiochemical properties of hemicellulose from wheat straw using 0.5 M NaOH in 60% aqueous methanol. Cavitation effect is produced by instantaneous high-temperature and high-pressure during ultrasound process, providing microenvironment for the extraction of biomass. It obtained an increasing yield of hemicellulose from 2.9 to 9.2% of the original hemicellulose for 5–35 min. The hemicellulose showed a slightly low molecular weight and slightly more linear, compared with that without ultrasonic-assisted irradiation, confirming a noticeable effect of ultrasonic irradiation. Then, 27.1–28.1% of the original hemicellulose was also extracted by the ultrasound irradiated and alkali pre-treated wheat straw with 2% H₂O₂-0.2% tetraacetylenediamine at pH 11.8 and 48°C for 12 h (Sun and Tomkinson, 2003). It obtained Xylose as a predominant sugar comprising 72.0–73.1% of the total sugars. The bleaching activator tetraacetylenediamine was found to form peracetic acid with hydroperoxide anion in aqueous alkali and improve the brightness of the solubilized hemicelluloses. In the existence of H₂O₂, it is easy to decompose into hydroxyl radical and superoxide anion radical, causing the oxidation of lignin structure, breaking the chemical bonds between lignin molecular units, and separating hemicellulose. Seven residual hemicelluloses were extracted from wheat straw pretreated with various organic solvents using 1.8% H₂O₂-0.18% cyanamide at 50°C and pH 10.0 for 4 h (Sun et al., 2005b). It obtained heteropolysaccharides containing xylose, glucose, arabinose, galactose, mannose, rhamnose, and 4-*O*-methyl- α -D-glucopyranosyluronic acid for the hemicellulose. It achieved the predominant monosaccharide of xylose composed mainly of L-arabino-(4-*O*-methyl-D-glucurono)-D-xylan. Cengiz et al. (2010) extracted the hemicellulose from opium poppy and cotton stalks in water at varying NaOH and H₂O₂. It obtained a yield of 0.8% using 2.0% H₂O₂ and 3.2% of the hemicellulose in the opium poppy stalks. An alkaline peroxide solution was also used to extract the hemicellulose from wheat straw, producing biodegradable hemicellulose-based films with improved water resistance and water vapor barrier properties in glycerol using citric acid as a crosslinking agent (Azeredo et al., 2015). It found the effect of the citric acid on the tensile properties of film ascribing to a flexible crosslinking.

Steam Explosion Pretreatment

Steam explosion pretreatment mainly uses high-temperature and high-pressure steam to treat biomass raw materials, which realizes the separation of components due to the explosion

effect. All the time, temperature, pressure, and size of raw material have an effect on the extraction of biomass during the steam explosion process. The steam pretreatment in an alkaline environment was used to pretreat the wheat and barley straw to access high-molecular-mass hemicellulose prior to ethanol production (Persson et al., 2009). It obtained 30% of the arabinoxylan with high-molecular-mass in barley straw and more than 40% of the arabinoxylan could be extracted with high-molecular-mass in wheat straw. The steam explosion was also reported to recover hemicellulose hydrolyzates from wheat straw at 200°C for 5 min, producing microbial oil by the oleaginous fungus *Microsphaeropsis* sp. (Peng and Chen, 2012). It obtained 3.8 g L⁻¹ of reducing sugar and 22.3 g L⁻¹ of total soluble sugars with a 10-fold excess (w/w) of water at 40°C to wash the wheat straw. Recently, Mihiretu et al. (2019) applied steam explosion pre-treatment to extract xylan-rich biopolymers from alkali-impregnated lignocelluloses and investigated simultaneously increasing the enzymatic digestibility of cellulose. It achieved the maximum xylan yields of 51% for sugarcane trash at 204°C for 10 min. The steam explosion pre-treatment was suggested as viable biorefinery approach to co-produce xylan biopolymers and bioethanol. Based on our knowledge, steam explosion pretreatment is a promising strategy for the industrial production.

N,N-Dimethylformamide–Lithium Chloride System

The *N,N*-dimethylformamide and lithium chloride system was usually applied to dissolve the cellulose. Besides, this system was also developed to treat hemicellulose (Farhat et al., 2017). Sun's group did many works on the lauroylation of hemicellulose in a *N,N*-dimethylformamide and lithium chloride system. In 2000, 10% KOH/0.5% Na₂B₄O₇·10 H₂O was used to extract hemicellulose from delignified rye straw, performing esterification of the hemicelluloses with various acyl chlorides in a *N,N*-dimethylformamide and lithium chloride system using 4-(dimethylamino)pyridine catalyst and triethylamine as a neutralizer (Sun et al., 2000). It stearoylated >90% of the free hydroxyl groups in native hemicelluloses at 75°C for 40 min. Only a minimal degradation of the macromolecular hemicellulose was observed during rapid reactions at 48–75°C for 20–40 min. Then, they reported lauroylation of wheat straw hemicelluloses with lauroyl chloride and degrees of substitution ranging from 0.46 to 1.54 in *N,N*-dimethylformamide–lithium chloride using 4-dimethylaminopyridine as a catalyst (Peng et al., 2008). It observed the lauroylation preferably at the C-3 hydroxyl group of b-D-Xylp units in the hemicelluloses, and the increased thermal stability of the hydrophobic polymers by esterification. They also applied microwave-assisted method for the esterification of wheat straw hemicelluloses using *N*-bromosuccinimide as a catalyst in *N,N*-dimethylformamide–lithium chloride medium with acetyl chloride, propionyl chloride, n-octanoyl chloride, lauroyl chloride, palmitoyl chloride, stearoyl chloride, and oleoyl chloride (Xu et al., 2008). Microwave-assisted extraction is to heat biomass by electromagnetic radiation, heating the water molecules in a very

TABLE 1 | Summary of the separation and purification of hemicellulose from wheat straw.

Separation and purification methods	Advantages	Limitations and disadvantages
Acid hydrolysis technology	Effectively hydrolyze hemicellulose	Requires higher temperature and pressure
Hydrothermal treatment technology	Small structure damage; high sugar yield	High temperature
Alkali treatment method	Lower reaction temperature and pressure	Lignin dissolves more; the conversion of alkali into irrecoverable salts
Steam explosion pretreatment	Uses less chemicals; does not excessively dilute the sugar produced in the hydrolyzate; does not require excessive energy consumption	High pressure resistance of production equipment; high energy consumption
Supercritical CO ₂ technology	Non-toxic; low cost; non-flammable	High pressure; high lost; expensive equipment; destroy chemical structure of hemicellulose
Membrane separation technology	Simple to operate; the separation effect is significant	--
Graded ethanol precipitation	The simplest and most commonly used method	--

short time, converting the microwave field energy into heat energy, and promoting the extraction of the main components of the biomass. It observed the esterification preferentially at the C-3 and C-2 positions. It found a partial degradation of the polymer and a slight decrease in thermal stability of the hemicellulosic derivatives by microwave irradiation. The microwave irradiation was also used for the lauroylation of wheat straw hemicellulose in the *N,N*-dimethylformamide/lithium chloride system at 78°C for 1–8 min (Ren et al., 2008). It observed the lauroylation at the C-3 position of the xylose unit in hemicelluloses. Authors indicated the high thermal stability of lauroylated polymers with high degree of substitution. Recently, the microwave-assisted hydrothermal pretreatment and subsequent alkali post-treatment was performed to isolate water- and alkali-soluble hemicellulose from hybrid pennisetum (Sun et al., 2019), which was mainly composed of β -(1→4)-linked xylans. It obtained 92.8% of the enzymatic digestibility of the cellulose-rich substrate, which was 3.4 times higher than that of raw material (27.4%). Yuan et al. (2019) also investigated microwave-assisted hydrothermal extraction of non-structural carbohydrates and hemicelluloses from tobacco biomass. It achieved the maximum yields for the leaf of 118.57 mg g⁻¹ and stem of 120.33 mg g⁻¹ biomass, producing the hemicelluloses yield of 105.15 mg g⁻¹ at 200°C, and obtaining heterogeneous compositional type including xylan, glucuronoxylan, and xylanglucan. Obviously, combination of various methods displayed widely applications and distinct advantages over the traditional system for the extraction of biomass.

Membrane Separation Technology

Membrane separation technologies such as microfiltration, ultrafiltration, nanofiltration, and reverse osmosis, have been widely used in polymer separation in recent years. Both ultrafiltration and nanofiltration are applied in the separation and purification of hemicellulose, which can be used to concentrate the extract and remove some low molecular weight lignin and inorganic salts. Thuvander and Jönsson (2019) used ultrafiltration to concentrate arabinoxylan isolated from wheat bran. It obtained the flux of the untreated solution of 51 L m⁻¹ for 2 h, the flux after prefiltration of the solution with diatomaceous earth of 62 L m⁻¹ for 2 h, and the flux of 230 L m⁻¹ for 2 h

after 5 h of air sparging during ultrafiltration. It achieved the retention of hemicellulose of 96% during ultrafiltration with a ceramic membrane and 93% with the prefiltered, air-sparged solution due to the size reduction of the hemicelluloses. Al-Rudainy et al. (2020) reported the recovery of hemicellulose by ultrafiltration from lab-scale to on-site pilot trials. It kept a stable average flux of 88 L m⁻¹ for 2 h and the non-changing retention of products using an alkaline cleaning step (pH 11) for 1 h. Thuvander et al. (2018) used air sparging to increase the flux during ultrafiltration of alkali-extracted wheat bran hemicelluloses. Air sparging reduced the energy demand per m³ permeate produced during dead-end batch ultrafiltration at 80°C and 1 m/s from 0.96 kWh/m³ to 0.51 kWh/m³. They also developed air sparging of alkaline-extracted wheat bran hemicellulose prior to ultrafiltration to increase the flux (Thuvander and Jonsson, 2020). It obtained the increased average flux during ultrafiltration of 151 L m⁻¹ for 2 h and during diafiltration of 130 L m⁻¹ for 2 h by air sparging. The cost of purifying the hemicellulose was reduced from 1375 €/ton hemicellulose to 1122 €/ton by sparging the solution with air prior to membrane filtration.

Besides the extraction of hemicellulose from wheat straw, there are some reports on the extraction and purification of hemicellulose from other biomass. For example, sugarcane is one of the main raw materials for sugar production. In general, about 50% of the fiber of bagasse left after sugar extraction can be used for papermaking. The extraction of hemicellulose was developed by a pH pre-corrected hot water pretreatment to reduce adsorbable organichalogen formation in chlorine dioxide bleaching of bagasse pulp (Yao et al., 2017). It found the differences in the structure of the bagasse hemicelluloses and the solid residual hemicelluloses. De Oliveira Santos et al. (2018) pretreated three diverse sugarcane hybrids with dilute sulfuric acid to evaluate the role of hemicellulose removal on the efficiency of enzymatic conversion of glucan. It found the selective removal of hemicellulose with the enhanced efficiency of glucan enzymatic hydrolysis up to 63% conversion and enhanced enzymatic glucan conversions to 92–100% by post-delignification of acid-pretreatment. The purification of hemicellulose was also reported from sugarcane bagasse alkaline hydrolyzate using an aromatic-selective adsorption resin (You et al., 2019). Resin

treatment had a minute effect on the molecular weight, structure, and property of hemicellulose, but could significantly improve its separation and purification. Both the chemical and structural differences were investigated in hemicellulose isolated from the sugarcane stem using chemical techniques (Yang H. Q. et al., 2020). It obtained the sugarcane hemicellulose backbone of xylose residues connected via β -1,4 glycosidic linkages, substituted with arabinose, acetyl, and glucuronic acid side chains. Manaf et al. (2018) investigated the potential usage of soluble products of oil palm frond bagasse upon dilute-acid hydrolysis. It recovered 18.4 g xylose and 8.9 g glucose per 100 g oil palm frond from 4% (v/v) HNO_3 at 130°C for 20 min. Authors found structural changes of the oil palm frond upon acid hydrolysis, obtaining the maximum yield of 0.35 g xylitol per g of sugars using the oil palm frond hydrolyzate.

Corn straw is an important production resource for industrial and agricultural production. As a kind of feed, corn straw is rich in nutrients and available chemical components, which can be used as raw materials for animal feed. Egues et al. (2012) performed the potential of autohydrolysis and alkaline extraction processes from corn stalks for high purity hemicellulose extraction. It obtained the maximum yield of 54% of the raw material lignin-free autohydrolysis hemicellulose with the presence of sulfur as predominant contaminant in alkaline extraction. Zhang et al. (2018) studied the effect of the organizational difference of corn stalk of leaf, bark, and pith on hemicellulose extraction and biotransformation efficiency. Authors found the corn pith as more conducive to the subsequent hemicellulose extraction and enzymatic hydrolysis to produce xylo-oligosaccharides. It obtained the highest purity of xylan of 84.89% from pith, the lowest color value of 1.43×10^5 , and the highest hemicellulose recovery ratio of 91.03%. It achieved the enzymatic hydrolysis ratio of 40% by pith, 30% by leaf, and 20% by bark. The molecular structure of xylooligosaccharides was investigated from corn cob in a continuous flow type hydrothermal reactor (Arai et al., 2019). It found high yields and high solubility of the CX due to the acetylation and ferulic acid modification of pentose residues. He et al. (2020) analyzed the composition and structure of the different parts of corn stalk and provided models of alkali-soluble hemicellulose transportation from corn stalk. It obtained physical mass transfer-dominated process for the dissolution processes of hemicellulose from the three parts.

Graded Ethanol Precipitation

The graded ethanol precipitation is a simple method for hemicellulose purification, in which the separated hemicellulose solution is precipitated in different concentrations of ethanol to obtain hemicellulose with different physical and chemical properties. The graded ethanol precipitation was used for the corn stalk hemicellulose from yellow liquor of active oxygen cooking (Shi et al., 2013). It observed only 5.31% hemicellulose with high molecular weight of $24,824 \text{ g mol}^{-1}$ in the liquor and the degraded hemicellulose with low molecular weight of $2,020\text{--}4,574 \text{ g mol}^{-1}$ during the cooking process. The hydrothermal-ethanol method was used for hemicellulose separation by the addition of 3% NaOH and 3% H_2O_2 (Li

J. B. et al., 2020). It occurred the lignin degradation and crosslinking/polymerization in parallel both the hydrothermal treatment and ethanol extraction. The hemicellulose pyrolysis mechanism was investigated based on the functional group evolution in xylan chars between 200 and 600°C by two-dimensional correlation infrared spectroscopy (Yang H. P. et al., 2020). It observed the depolymerization and ring-opening reactions of xylan at 200°C, the decarbonylation reaction at 300–450°C, and the increased dehydrogenation and polycondensation reaction of xylan at 450–600°C.

THE APPLICATIONS OF HEMICELLULOSES FROM WHEAT STRAW

The Xylitol and Biofuel Production of Hemicellulose

Biofuel generally refers to solid, liquid or gaseous fuels extracted from biomass, replacing gasoline and diesel made from petroleum, which is an important direction of renewable energy development and utilization. Biofuels include mainly bioethanol, biodiesel, and aviation biofuels produced from biomass resources (Liu H. Y. et al., 2021). There is no doubt about wheat straw hemicellulose for the biofuel production. As early as 1982, Detroy et al. (1982) reported bioconversion of wheat straw cellulose/hemicellulose to ethanol by *Saccharomyces uvarum* and *Pachysolen tannophilus*. It obtained the yield of cellulosic pulp of 70–82% at 170°C for 30–60 min at a water-to-solids ratio of 7:1. However, it achieved the ethanol efficiencies of only 40–60% due to the inhibition by substances introduced by thermal and alkali treatment of the straws. *Pachysolen tannophilus* strain NRRL 2460 is found to be capable of producing ethanol from both glucose and xylose. In 2001, Nigam evaluated the ethanol production from wheat straw hemicellulose acid hydrolyzate by boiling and over-liming with $\text{Ca}(\text{OH})_2$ using an adapted and parent strain of *Pichia stipitis*. NRRL Y-7124 (Nigam, 2001). It achieved 2.4 folds of ethanol yield and 5.7 folds of productivity, compared to neutralized hydrolyzate. It obtained the maximum yield of $0.41 \text{ g}_p \text{ g}_s^{-1}$, equivalent to 80.4% theoretical conversion efficiency. The acetic acid, furfurals, and lignin were inhibitory to microbial growth and ethanol production, resulted a reduction in ethanol yield and productivity.

Koti et al. (2016) reported the enhanced bioethanol production from wheat straw hemicellulose by mutant strains of pentose fermenting organisms *Pichia stipitis* and *Candida shehatae*. It obtained the enhanced ethanol production of $12.15 \pm 0.57 \text{ g L}^{-1}$ and yield of $0.450 \pm 0.009 \text{ g g}^{-1}$, compared with that of the wild strains ($8.28 \pm 0.54 \text{ g L}^{-1}$ and yield $0.380 \pm 0.006 \text{ g g}^{-1}$). In their work, the excellent points are about the stable of mutant strains for 19 cycles in hemicellulosic hydrolyzates of wheat straw, and the combination of chemical mutagenesis and UV induced mutants. Tsegaye et al. (2019) investigated microwave-assisted NaOH pretreatment of wheat straw using central composite design under varying operating variables of pretreatment time, temperature, and

NaOH concentration. It preserved 38.34% of hemicellulose and 74.15% of cellulose in the solid residue and solubilized 69.49% of lignin. It released 718 mg g⁻¹ of reducing sugar after hydrolysis pretreated wheat straw by *Bacillus* sp. *BMP01* and obtained ethanol yield of 68.2% after 96 h of fermentation due to the combination of microwave-assisted NaOH pretreatment coupled with microbial hydrolysis and C5 and C6 fermenting microbes. Then, they optimized organosolv pretreatment parameters for lignin removal and polysaccharide release using response surface methodology by microbial hydrolysis for biofuel production (Tsegaye et al., 2020). It solubilized 73.17% of lignin and 46.62% hemicellulose, and released 74.09% of cellulose at 75.4°C for about 30 min. The enhanced sugar and ethanol yields were due to the combination of organosolv pretreatment and *Bacillus* sp. *BMP01* hydrolysis of rice straw. The subcritical water pretreatment and high solid hydrolysis were used to improve the conversion efficiency of bioethanol from wheat straw (Chen et al., 2021), as shown in **Figure 1**. It carried out the yields of hydrolysis of 77.85–89.59% and fermentation of 93.34–96.18%. It observed the improved ethanol concentration of 37.00 g L⁻¹. Authors indicated the subcritical water pretreatment combined with high solid hydrolysis as an effective solution for bioethanol conversion.

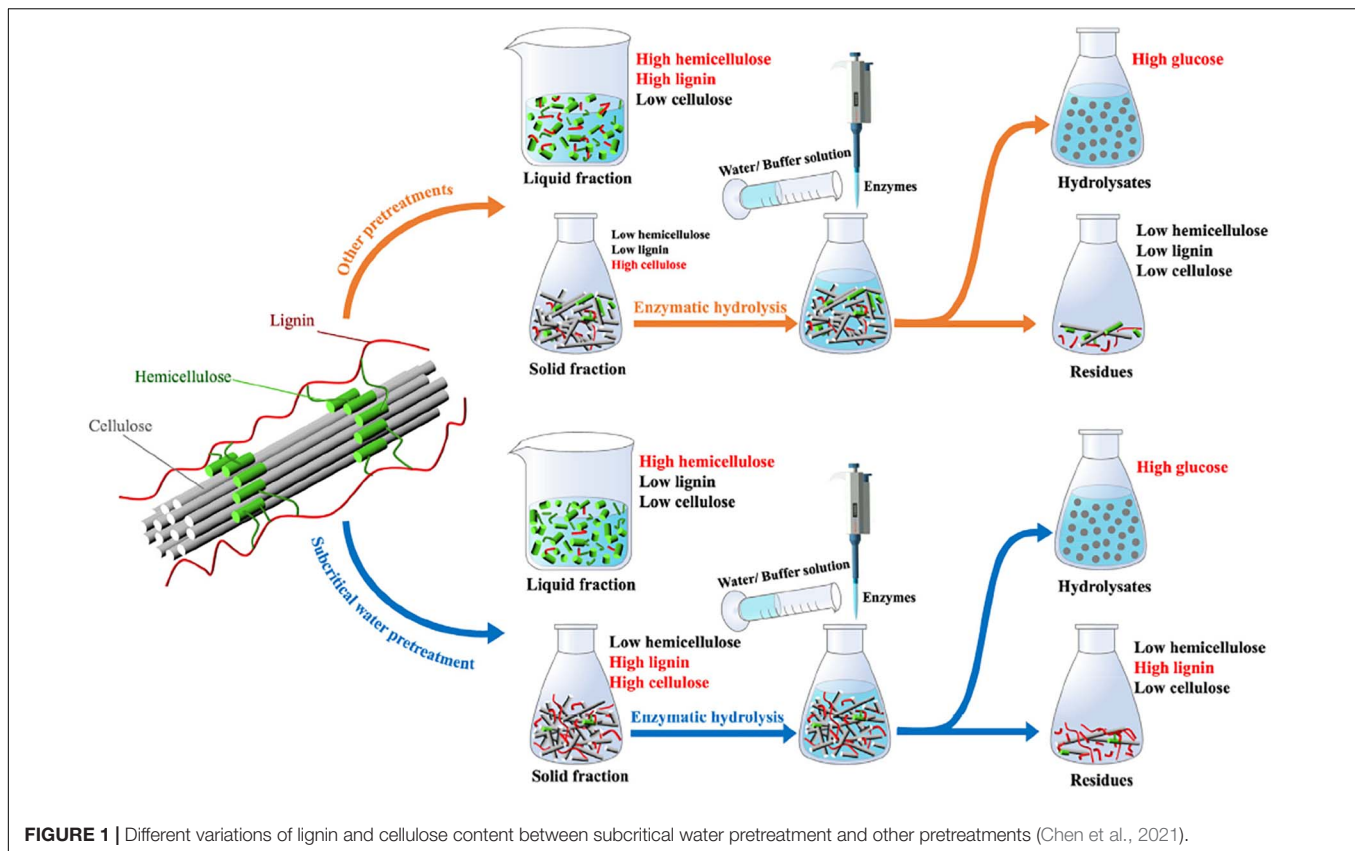
Besides wheat straw hemicellulose, the hemicellulose from other biomass was also applied for ethanol production. Tabañag et al. (2018) reported ethanol production from hemicellulose by a consortium of different genetically modified *Saccharomyces cerevisiae*. It observed the improved hydrolytic activities of the hemicellulase mixtures by displaying the hemicellulase on the yeast surface as whole-cell biocatalysts. The resulting consortium of hemicellulase mixtures was found to grow and produce ethanol from different xylan substrates. Scordia et al. (2012) evaluated the production of ethanol by *Scheffersomyces (Pichia) stipitis* CBS6054 from sugars contained in the giant reed (*Arundo donax* L.) hemicellulosic hydrolyzate. Authors found the improved fermentability of the giant reed hemicellulose hydrolyzate due to the increasing initial pH from 5.0 to 6.5. It obtained 8.20 g L⁻¹ of ethanol at pH 6.0 after 48 h with an ethanol yield of 0.33 (g/g) and a productivity of 0.17 g L⁻¹ h⁻¹. Mihiretu et al. (2017) investigated the viability of microwave-induced pressurized hot water conditions for co-production of xylan-based biopolymers and bioethanol from aspen wood sawdust and sugarcane trash. It obtained maximum xylan extraction yields of 66% for aspen wood and 50% for sugarcane trash. Authors found the xylan extracts predominantly in non-monomeric form. Batog et al. (2020) reported bioethanol production from biomass of selected sorghum varieties cultivated as main and second crop. It recommended the *Sucrosorgo* 506 variety for the production of bioethanol both in main and second crop cultivation. Sharma et al. (2019) reported the ethanol production from rice straw with 1% NaOH by autoclaving at 121°C for 30 min at 10% solid loading. It obtained 2 and 4 g L⁻¹ ethanol with fermentation efficiency 55–66% fermented by *S. cerevisiae* LN for 24 h.

There are a few reports on the other biofuel production of hemicellulose. Hydrotropic reagent sodium xylene sulfonate was used to treat wheat straw for biobutanol production (Qi et al., 2019). It obtained butanol production with 12.41 g

L⁻¹ ABE produced by *C. acetobutylicum* using hexoses and pentoses in the enzymatic hydrolyzates. Roberto et al. (1996) evaluated the effect of inoculum level on xylitol production by *Candida guilliermondii* in a rice straw hemicellulose hydrolyzate. It reached the maximum xylitol yield of 0.71 g g⁻¹ and volumetric productivity of 0.56 g L⁻¹ h⁻¹ with an inoculum level of 0.9 g L⁻¹. It obtained the xylitol from rice straw hemicellulose hydrolyzate by the yeast *C. guilliermondii* with efficiency values as high as 77% of the theoretical maximum. Terrone et al. (2018) investigated the xylanase production by *Penicillium chrysogenum* F-15 strain using biomass as substrate. It observed the low enzymatic activity on commercial xylan of xylanase, compared with that on hemicellulose from agroindustry biomass. In the review article, Luo et al. (2019) summarized an overview of the production of furfural directly from hemicellulose in lignocellulosic biomass with special emphasis on achieving the effective utilization of hemicellulose, including the selective dissolution of hemicellulose from lignocellulosic biomass and the selective formation of furfural from hemicellulose derivatives. They considered solvents and catalysts as two main factors in this valorization process of hemicellulose. Gao et al. (2020) investigated the pyrolysis behavior of xylan-based hemicellulose in a fixed bed reactor. It found the increase xylan conversion and yield of bio-oil at high temperature due to the violent decomposition of xylan. Shi et al. (2021) relieved the inhibition of high concentration of alkali on xylose production from hydrolysis of hemicellulose in PIE. It observed the decreased polymerization degree of the hemicellulose by 73.4%, promoting the subsequent enzymatic hydrolysis process. Authors obtained the xylose yield followed by enzymatic hydrolysis of 57.15 g L⁻¹, which was 145.38% more than that of enzymatic hydrolysis alone.

The Application of Hemicellulose-Materials in Packaging Field

Packaging materials refer to the materials used to meet the requirements of product packaging, including metal, plastic, paper, natural fiber, chemical fiber, and composite materials. Hemicellulose was expected to be used packaging field due to their hydrophilic nature, biodegradable, and low-cost. In the review paper by Farhat et al. (2017), they ascribed the processing and applications of water-resistant hemicellulose-based films and composites. They summarized the most useful pathways to change the hydrophilic character of hemicelluloses to hydrophobic and discussed several applications of these materials. The biodegradable films were formed by using wheat straw hemicelluloses as a matrix with cellulose nanocrystals and citric acid (Pereira et al., 2017). It obtained the improved tensile strength and modulus, water resistance and water vapor barrier with the addition of cellulose nanocrystals, and the plasticizing and crosslinking effects by citric acid due to a crosslinking extension by glycerol. Authors suggested the films with enhanced modulus, elongation, water resistance, and barrier to water vapor for wrapping or coating a variety of foods. In the work by Ma et al. (2018), the potential of an acid hydro-tropic process was evaluated at low temperatures for on-farm valorization



of wheat straw by producing ligocellulosic nanofibrils, lignin nanoparticles, and furfural. It obtained wheat straw films with excellent mechanical properties and specific tensile strength over 120 kN.m kg^{-1} . The addition of inorganic and/or inorganic materials into hemicellulose matrix is important to improve its properties. Recently, Rao et al. (2019) fabricated the hemicellulose films with enhanced mechanical properties by graphene oxide for bio-medicine, packaging materials, and humidity sensing. It obtained a high tensile strength of 43.83 MPa due to that addition of graphene oxide and high sensitivity to humidity. The storage modulus of the hybrid films had an order of magnitude change in value at different humidities. Lucenius et al. (2019) researched the hemicellulose-cellulose nanofibrils films for the packaging and medical applications to understand the interactions between the components at nano/microscale affect macroscopic mechanical properties of toughness and strength. It reported the decreased aggregates of cellulose nanofibrils and the enhanced strength of dry films due to the adsorbed polysaccharides and a moderate reduction in friction between cellulose surfaces. It obtained the improved mechanical properties of composites due to high affinity for cellulose and moderate hydration in wet conditions.

The extraction step and treatment methods played an important role in the properties of films. Jin et al. (2019) investigated the factors affecting the film-forming properties of the originally isolated xylan-hemicelluloses and promoting their material properties from the extraction step. It improved tensile

strength of films up to 52% using sodium hypochlorite solution as the delignification agents. Authors predicted better mechanical properties due to hemicellulose with higher molecular weight, more linear structure, and lower lignin content. Hu et al. (2019) fabricated polysaccharide composite film from wheat straw hemicellulose and methylcellulose for packaging. It obtained films with compact layer structure and the maximum tensile strengths using 75 wt% methylcellulose. Mugwagwa and Chimphango (2020) obtained the enhanced hemicellulose acetylation, filler compatibility, and film hydrophobicity by optimizing alkali-catalyzed organosolv treatment conditions for wheat straw before hemicellulose extraction. It obtained water contact angle of 68.1° for the films. The acetylated nanocellulose reinforced films had high tensile strength of 10.59 MPa and Young modulus of 590.15 MPa.

The multifunctional films could open the new applications of wheat straw. Li J. et al. (2019) proposed an approach to directly and completely convert natural wheat straw into multifunctional films with high mechanical strength by introducing an entanglement network of additional cellulose to enhance the strength of the regenerated straw in the ionic liquid 1-allyl-3-methylimidazolium chloride (AmimCl). It observed the spinnability and film-forming properties based on an increase in the capillary break-up time. It obtained a tensile strength of 62 MPa, a superhigh haze of 97%, preventing 97% UVA (320–400 nm), and almost 100% UVB (280–320 nm) for the films. The high-strength, high-haze, and UV-shielding

all-biomass films have great potential in low-cost, biodegradable, and environmentally friendly packaging. More recently, Zhao et al. (2020) reviewed research progress in development of hemicellulose film with regard to application in the field of food packaging due to its combination of such advantages as abundance, biodegradability, and renewability. They presented the mechanical, barrier properties, and hydrophobicity for food packing materials by various physical and chemical modification approaches. Dixit and Yadav (2020) comparative studied the polystyrene/chemically modified wheat straw composite in improving surface morphology using solution casting method for packaging application. It observed the changes in crystalline structure, hydrophobicity, water vapor migration rate, and thermal and mechanical stabilities of bio-composites. There existed some impurities such as residual lignin in the surface of native wheat straw, irregular shape after applying the HCl and H₂SO₄ pre-treatments, and a cylindrical shape with filaments, cells, and pores after NaOH pre-treatment (Figure 2). Authors demonstrated the alkali-treated wheat straw to synthesize a biodegradable composite film for various industrial packaging application.

In general, development of transparent thin packaging materials with low-cost, non-toxic, high buffering strength, good retraction rate, puncture resistant, and tear resistance are important for their industrial applications. The wheat straw hemicellulose composite films may be a promising candidate for this purpose. The increased enhanced mechanical properties and packaging properties still need to be improved in the next work.

The Application of Hemicellulose-Materials as Adsorbent

Batzias et al. (2009) investigated the simulation of batch and column kinetics of methylene blue and red basic 22 adsorption on mild acid hydrolyzed wheat straw as a low-cost adsorbent for wastewater dye removal. It achieved the enhanced adsorption properties of the original material by the mild acid hydrolysis, attributing to the removal of the hemicelluloses during sulfuric acid treatment, resulting in the open pores of lignocellulosic matrix's structure and the increasing of the BET surface area. The hydrophobic hemicelluloses with the degree of substitution from 0.09 to 0.35 were prepared by the benzylation of wheat straw hemicelluloses under the presence of catalyst in an ethanol/water system (Ren et al., 2012). It observed the increased thermal stability and the hydrophobicity after the modification of hemicelluloses due to the introduction of benzyl groups. The pH-responsive hydrogels based on hemicellulose of wheat straw were prepared as a carrier for controlled drug delivery (Sun et al., 2013). It followed the swelling kinetics of the hydrogels for a Fickian diffusion process. The biodegradability of the hemicellulose-based hydrogels was affected by hemicellulose content and the crosslinking density. Both the hydrogel and the intrinsic character of the drug controlled the drug release. A stimuli-responsive porous hydrogels were synthesized from wheat straw hemicellulose using CaCO₃ as the porogen for the removal of methylene blue (Sun et al., 2013, 2015a). The porous hydrogels showed the sensitivity to pH and salt, exhibiting rapid shrinking in NaCl aqueous solutions. Authors demonstrated

the adsorption data fitted to the pseudo-first-order, pseudo-second-order, and intra-particle diffusion kinetics models for the adsorption process. The xylen/poly(acrylic acid) magnetic nanocomposite hydrogel adsorbent with semi-interpenetrating network structure was prepared from wheat straw xylan and Fe₃O₄ nanoparticles for methylene blue removal (Sun et al., 2015b). It observed a macroporous structure with interconnected porous channels. It observed the removal percentage above 90%, the adsorption isotherm of the Langmuir model, and the pseudo-second-order kinetic model of the adsorption process.

The glow discharge electrolysis plasma was used to prepare the temperature/pH dual sensitivity reed hemicellulose-based hydrogels with high deswelling ratio (Zhang et al., 2015). It found the phase transition temperatures of all approximately 33°C and the deswelling dynamics of the first model. A superabsorbent hemicelluloses-g-AA/bentonite/polyvinyl alcohol hydrogel with the enhanced swelling properties was fabricated by using waste hemicelluloses lye and polyvinyl alcohol (Liu et al., 2019). A dialdehyde hemicellulose-based chitosan-Fe₃O₄ composite aerogel with magnetism was synthesized to remove the Congo red, extracted from straw with NaIO₄ (Guan et al., 2020). The hydrogels were prepared by the Schiff's base reaction, processed to obtain aerogels by vacuum freeze-drying technique. The addition of Fe₃O₄ was reported to improve the thermal stability, mechanical properties, and adsorption property of the aerogels. It obtained the maximum compress strength of aerogel of 0.37 MPa, and the maximum absorption capacity of Congo red dye of 137.74 mg g⁻¹. Nascimento and Neto (2021) reported hydrothermal pretreatment steam explosion in the production of an adsorbent material. It observed the adsorption of the monocomponent Cu²⁺ and Cd²⁺ at room temperature due to the increase of biomass crystallinity and porosity. It found the kinetic pseudo-second-order model and the Langmuir model isotherm for the adsorption process with a maximum adsorption capacity of Cu²⁺ of 18.86 mg g⁻¹ and Cd²⁺ of 17.9 mg g⁻¹. da Silva et al. (2020) investigated the methylene blue adsorption by ryegrass straw as adsorbent materials. It obtained the biochar with a well-developed porous structure. It found the kinetic studies, the pseudo-first-order, pseudo-second-order, and Avrami models for the adsorption process. It obtained the maximum adsorption capacity to the milled straw of 28.7 mg g⁻¹ and treated straw of 67.19 mg g⁻¹ by the Sips model. Authors achieved the high efficiency in the removal of the methylene blue dye higher than 99% using the treated straw.

The Other Applications of Hemicellulose-Materials

Ghaffar et al. (2015) reported bioengineering for utilization and bioconversion of straw biomass into bio-products of bioethanol, biogas, and bio-composites. They paid attention to the applications and limitations of biological pre-treatment in combination with mild chemical and or physical pre-treatments. Wheat straw-polypropylene composites were formed by mixing compression molding to evaluate the susceptibility to mold fungi colonization (He et al., 2016). It found the degraded hemicellulose, followed by lignin, and then cellulose via fungi.

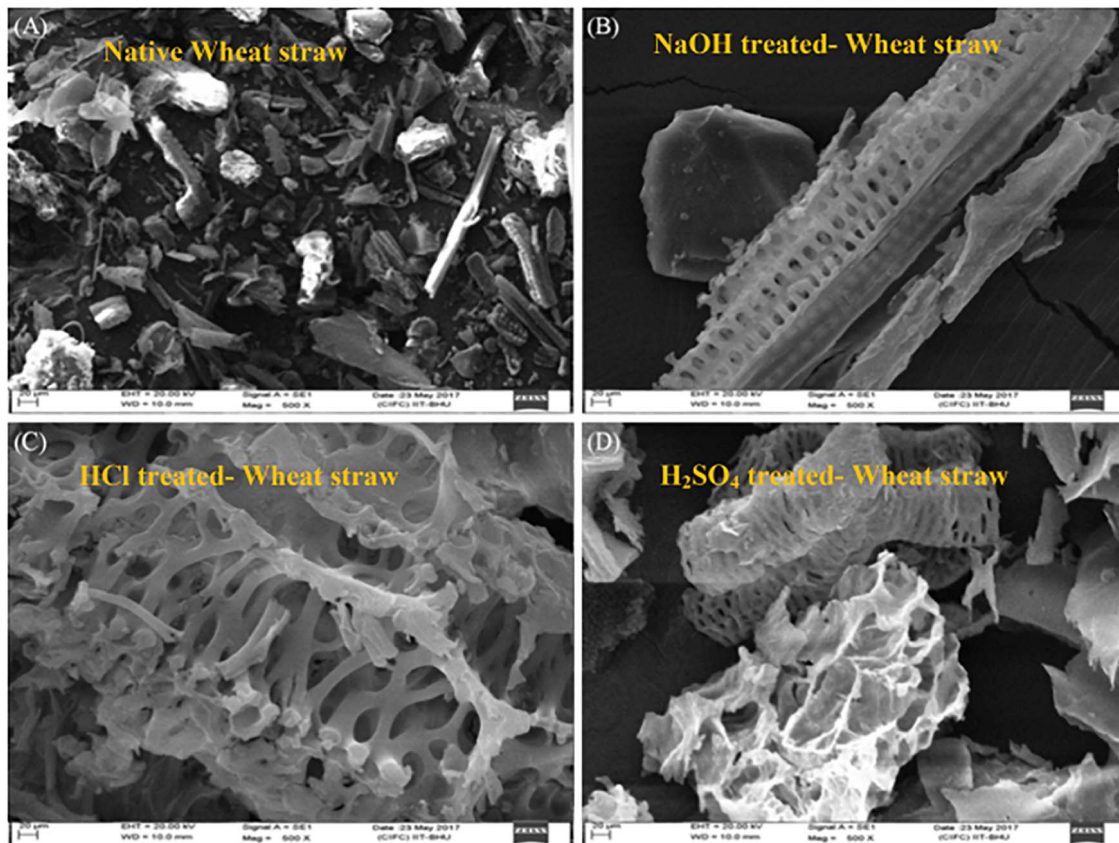


FIGURE 2 | Scanning electron microscopy micrographs of native wheat straw and all pre-treated wheat straw biomass: **(A)** native wheat straw, **(B)** NaOH-treated wheat straw, **(C)** HCl-treated wheat straw, **(D)** H₂SO₄-treated wheat straw (Dixit and Yadav, 2020).

The color change was relative to carbonyl index and the process of degradation in wheat straw. Tian et al. (2018) reported the pretreatment and bioconversion of lignocellulosic biomass from wheat straw materials. They summarized the application fields, main pretreatment processing methods, and bioproducts of bioethanol, biohydrogen, and bio-composites of wheat straw. The hemicellulose was subjected to a chemical modification by ring-opening graft polymerization of ϵ -caprolactone to improve its processability for the bioplastic industry (Farhat et al., 2018). It synthesized hemicellulose-graft-poly-(ϵ -caprolactone) copolymers with a biodegradation of 95.3–99.7% using 1,5,7-triazabicyclodecene as an organic catalyst. It observed the enhanced mechanical and the hydrophobic properties by poly-(ϵ -caprolactone) grafting onto hemicellulose. Castillo et al. (2020) investigated the effects and mineral/reagent interactions of hemicelluloses monosaccharides of D-xylose, D-mannose, and D-glucose on the flotation behavior of molybdenite. Authors indicated the strong depressing effects of D-mannose and D-glucose due to more carbon atoms and hydroxyl groups in their structure, providing more chances to interact with the metallic sites existing on molybdenite surfaces. It found the increase depressing effect of the monosaccharides with pH by the increase of the concentration of basic sites on molybdenite surfaces and by ionization of the hydroxyl groups of

monosaccharide molecules. It observed the reduced depressing effect of the monosaccharides by the addition of kerosene.

CONCLUSION

In summary, there are many reports on the extractions and applications of hemicellulose from wheat straw. Rapid progress had paid on the developments of wheat straw hemicellulose. The extraction methods played an important role in the structures and molecules of hemicellulose. The different extraction methods of hemicellulose were compared and analyzed in this article. The structures and molecules of the hemicellulose obtained by different extraction methods were different. The wheat straw hemicellulose-based derivatives and composites have widely applications as biofuel production, packaging materials, and adsorbent. Hemicellulose can be converted into biofuel production by hydrolysis reaction. Hemicellulose can be used for packaging materials due to its advantages of hydrophilicity, biodegradability, and low cost. Based on our knowledge, there are some problems need to be solved: (1) Further exploring the structure-properties relationship and mechanism of hemicellulose and its derivatives; (2) Developing the new methods such as fluorescent labeling

technology to study the distribution of hemicellulose in the cell wall of different raw materials and the dissolution of hemicellulose in the process of separation and extraction, so as to build a more efficient hemicellulose separation system; (3) Finding a low-cost purification process for hemicellulose and realizing industrial production, and further combining various separation and purification technologies to realize the hierarchical purification of hemicellulose; (4) Paying more attention to the separation and purification of hemicelluloses with different structures to obtain hemicelluloses with different biological and physiological activities; (5) Developing new ways of hemicellulose functionalization, optimizing the existing chemical modification system, and further studying the homogeneous derivatization of hemicellulose in various fully soluble systems and exploring its reaction mechanism; (6) Designing the structure and function of hemicellulose derivatives by molecular modification, and exploring the structure, physicochemical properties, and potential applications (especially in biomedicine and pharmaceutical chemistry) of hemicellulose derivatives to provide theoretical basis for their promotion and applications; (7) Constructing new hemicellulose functional materials at the molecular level and synthesizing the nano-hemicellulose such as hemicellulose nanoparticles and hemicellulose nanomaterials. The nano-hemicellulose was currently used in a variety of biomedical, food or food packaging, energy and environmental applications due to their enhanced bioavailability, biocompatibility, bioactivity, and lower toxicity to healthy cells and the environment; (8) Finding an effective way to increase the strength and hydrophilicity of hemicellulose membrane; (9) Exploring the

biomedical properties of hemicellulose and its derivatives, such as cytotoxicity, metabolic degradation characteristics, environmental response of different parts of the body, drug and gene binding properties, etc. In essence, hemicellulose is closely attached to the surface of cellulose by hydrogen bond and van der Waals force and connects lignin by ferulic acid. The research on hemicellulose favored the applications of cellulose and lignin in the biomass. Therefore, the developments of hemicellulose not only open its new applications, but accelerate the approaches of utilization for industrial hemicellulose.

AUTHOR CONTRIBUTIONS

L-ZH and M-GM: investigation and writing—original draft. X-XJ, S-EC, and CS: supervision. M-GM, X-XJ, S-EC, and CS: writing—review and editing. All authors contributed to the article and approved the submitted version.

FUNDING

Financial supported from the National Key R&D Program of China (2019YFC1905901) is gratefully acknowledged and this work was also partially supported by the Technology Development Program (S3030198) funded by the Ministry of SMEs (MSS, South Korea) and this work was also partially supported by R&D program for Forest Science Technology (2019151D10-2023-0301) provided by Korea Forest Service (Korea Forestry Promotion Institute) to S-EC.

REFERENCES

- Adams, G. A., and Castagne, A. E. (1951). Hemicelluloses of wheat straw. *Can. J. Chem.* 29, 109–122. doi: 10.1139/v51-015
- Al-Rudainy, B., Galbe, M., and Wallberg, O. (2020). From lab-scale to on-site pilot trials for the recovery of hemicellulose by ultrafiltration: experimental and theoretical evaluations. *Sep. Purif. Technol.* 250:117187. doi: 10.1016/j.seppur.2020.117187
- Arai, T., Biely, P., Uhlirlikova, I., Sato, N., Makishima, S., Mizuno, M., et al. (2019). Structural characterization of hemicellulose released from corn cob in continuous flow type hydrothermal reactor. *J. Biosci. Bioeng.* 127, 222–230. doi: 10.1016/j.jbiosc.2018.07.016
- Azeredo, H. M. C., Kontou-Vrettou, C., Moates, G. K., Wellner, N., Cross, K., Pereira, P. H. F., et al. (2015). Wheat straw hemicellulose films as affected by citric acid. *Food Hydrocoll.* 50, 1–6. doi: 10.1016/j.foodhyd.2015.04.005
- Batog, J., Frankowski, J., Wawro, A., and Lacka, A. (2020). Bioethanol production from biomass of selected sorghum varieties cultivated as main and second crop. *Energies* 13:6291. doi: 10.3390/en13236291
- Batzias, F., Sidiras, D., Schroeder, E., and Weber, C. (2009). Simulation of dye adsorption on hydrolyzed wheat straw in batch and fixed-bed systems. *Chem. Eng. J.* 148, 459–472. doi: 10.1016/j.cej.2008.09.025
- Bian, J., Peng, P., Peng, F., Xiao, X., Xu, F., and Sun, R. C. (2014). Microwave-assisted acid hydrolysis to produce xylooligosaccharides from sugarcane bagasse hemicelluloses. *Food Chem.* 156, 7–13. doi: 10.1016/j.foodchem.2014.01.112
- Buranov, A. U., and Mazza, G. (2010). Extraction and characterization of hemicelluloses from flax shives by different methods. *Carbohydr. Polym.* 79, 17–25. doi: 10.1016/j.carbpol.2009.06.014
- Canilha, L., Carvalho, W., and Almeida e Silva, J. B. (2006). Xylitol bioproduction from wheat straw: hemicellulose hydrolysis and hydrolyzate fermentation. *J. Sci. Food Agric.* 86, 1371–1376. doi: 10.1002/jsfa.2524
- Carvalho, F., Duarte, L. C., and Girio, F. M. (2008). Hemicellulose biorefineries: a review on biomass pretreatments. *J. Sci. Ind. Res. India* 67, 849–864.
- Castillo, I., Gutierrez, L., Hernandez, V., Diaz, E., and Ramirez, A. (2020). Hemicelluloses monosaccharides and their effect on molybdenite flotation. *Powder Technol.* 373, 758–764. doi: 10.1016/j.powtec.2020.07.032
- Cengiz, M., Dincturk, O. D., and Sahin, H. T. (2010). Fractional extraction and structural characterization of opium poppy and cotton stalks hemicelluloses. *Pharmacogn. Mag.* 6, 315–319. doi: 10.4103/0973-1296.71798
- Chen, J., Wang, X., Zhang, B., Yang, Y., Song, Y., Zhang, F., et al. (2021). Integrating enzymatic hydrolysis into subcritical water pretreatment optimization for bioethanol production from wheat straw. *Sci. Total Environ.* 770:145321. doi: 10.1016/j.scitotenv.2021.145321
- da Silva, E. O., dos Santos, V. D., de Araujo, E. B., Guterres, F. P., Zottis, R., Flores, W. H., et al. (2020). Removal of methylene blue from aqueous solution by ryegrass straw. *Int. J. Environ. Sci. Technol.* 17, 3723–3740. doi: 10.1007/s13762-020-02718-9
- De Oliveira Santos, V. T., Siqueira, G., Ferreira Milagres, A. M., and Ferraz, A. (2018). Role of hemicellulose removal during dilute acid pretreatment on the cellulose accessibility and enzymatic hydrolysis of compositionally diverse sugarcane hybrids. *Ind. Crops Prod.* 111, 722–730. doi: 10.1016/j.indcrop.2017.11.053
- Detroy, R. W., Cunningham, R. L., Bothast, R. J., Bagby, M. O., and Herman, A. (1982). Bioconversion of wheat straw cellulose/hemicellulose to ethanol by *Saccharomyces uvarum* and *Pachysolen tannophilus*. *Biotechnol. Bioeng.* 24, 1105–1113. doi: 10.1002/bit.260240507

- Dixit, S., and Yadav, V. L. (2020). Comparative study of polystyrene/chemically modified wheat straw composite for green packaging application. *Polym. Bull.* 77, 1307–1326. doi: 10.1007/s00289-019-02804-0
- Du, H., Liu, W., Zhang, M., Si, C., Zhang, X., and Li, B. (2019). Cellulose nanocrystals and cellulose nanofibrils based hydrogels for biomedical applications. *Carbohydr. Polym.* 209, 130–144. doi: 10.1016/j.carbpol.2019.01.020
- Egues, I., Sanchez, C., Mondragon, I., and Labidi, J. (2012). Effect of alkaline and autohydrolysis processes on the purity of obtained hemicelluloses from corn stalks. *Bioresour. Technol.* 103, 239–248. doi: 10.1016/j.biortech.2011.09.139
- Falco, C., Sieben, J. M., Brun, N., Sevilla, M., van der Maelen, T., Morallon, E., et al. (2013). Hydrothermal carbons from hemicellulose-derived aqueous hydrolysis products as electrode materials for supercapacitors. *Chemosuschem* 6, 374–382. doi: 10.1002/cssc.201200817
- Farhat, W., Venditti, R. A., Hubbe, M., Taha, M., Becquart, F., and Ayoub, A. (2017). A review of water-resistant hemicellulose-based materials: processing and applications. *Chemosuschem* 10, 305–323. doi: 10.1002/cssc.201601047
- Farhat, W., Venditti, R., Ayoub, A., Prochazka, F., Fernandez-de-Alba, C., Mignard, N., et al. (2018). Towards thermoplastic hemicellulose: chemistry and characteristics of poly-(epsilon-caprolactone) grafting onto hemicellulose backbones. *Mater. Des.* 153, 298–307. doi: 10.1016/j.matdes.2018.05.013
- Fu, L. H., Liu, S., Li, S. L., Li, Y. Y., and Ma, M. G. (2017). Isolation and characterization of hemicelluloses by hydrothermal method with ethanol from *Populus tomentosa* Carr. *Paper Biomater.* 2, 1–11.
- Gao, Z. X., Li, N., Wang, Y. Q., Niu, W. S., and Yi, W. M. (2020). Pyrolysis behavior of xylan-based hemicellulose in a fixed bed reactor. *J. Anal. Appl. Pyrolysis* 146:104772. doi: 10.1016/j.jaap.2020.104772
- Garcia, J. C., Diaz, M. J., Garcia, M. T., Ferial, M. J., Gomez, D. M., and Lopez, F. (2013). Search for optimum conditions of wheat straw hemicelluloses cold alkaline extraction process. *Biochem. Eng. J.* 71, 127–133. doi: 10.1016/j.bej.2012.12.008
- Ghaffar, S. H., Fan, M., and McVicar, B. (2015). Bioengineering for utilisation and bioconversion of straw biomass into bio-products. *Ind. Crops Prod.* 77, 262–274. doi: 10.1016/j.indcrop.2015.08.060
- Girio, F., Fonseca, C., Carvalho, F., Duarte, L. C., Marques, S., and Bogel-Lukasik, R. (2010). Hemicelluloses for fuel ethanol: a review. *Bioresour. Technol.* 101, 4775–4800. doi: 10.1016/j.biortech.2010.01.088
- Gonzalez, G., Lopez-Santin, J., Caminal, G., and Sola, C. (1986). Dilute acid hydrolysis of wheat straw hemicellulose at moderate temperature: a simplified kinetic model. *Biotechnol. Bioeng.* 28, 288–293. doi: 10.1002/bit.260280219
- Guan, Y., Rao, J., Wu, Y. L., Gao, H., Liu, S. Q., Chen, G. G., et al. (2020). Hemicelluloses-based magnetic aerogel as an efficient adsorbent for Congo red. *Int. J. Biol. Macromol.* 155, 369–375. doi: 10.1016/j.ijbiomac.2020.03.231
- Haimer, E., Wendland, M., Potthast, A., Henniges, U., Rosenau, T., and Liebner, F. (2010). Controlled precipitation and purification of hemicellulose from DMSO and DMSO/water mixtures by carbon dioxide as anti-solvent. *J. Supercrit. Fluids* 53, 121–130. doi: 10.1016/j.supflu.2010.02.009
- He, C., Yao, X., Xue, J., Xiong, J., and Zhao, L. (2016). Influences of mold fungi colonization on wheat straw-polypropylene composites. *For. Prod. J.* 66, 472–479. doi: 10.13073/FPJ-D-15-00004
- He, L., Yang, S. B., Chen, D., Peng, L. C., Liu, Y. X., Guan, Q. Q., et al. (2020). Hemicellulose transportation from different tissues of corn stalk to alkaline hydrogen peroxide solution. *Cellulose* 27, 4255–4269. doi: 10.1007/s10570-020-03088-8
- Hu, G. C., Fu, S. Y., Chu, F. Q., and Wu, G. Y. (2019). Fabrication of an all-polysaccharide composite film from hemicellulose and methylcellulose. *Bioresources* 14, 6716–6726. doi: 10.15376/biores.14.3.6716-6726
- Jeong, T. S., Um, B. H., Kim, J. S., and Oh, K. K. (2010). Optimizing dilute-acid pretreatment of rapeseed straw for extraction of hemicellulose. *Appl. Biochem. Biotechnol.* 161, 22–33. doi: 10.1007/s12010-009-8898-z
- Jiang, L. Q., Zheng, A. Q., Zhao, Z. L., He, F., Li, H. B., and Liu, W. G. (2015). Obtaining fermentable sugars by dilute acid hydrolysis of hemicellulose and fast pyrolysis of cellulose. *Bioresour. Technol.* 182, 364–367. doi: 10.1016/j.biortech.2015.01.032
- Jin, A. X., Ren, J. L., Peng, F., Xu, F., Zhou, G. Y., Sun, R. C., et al. (2009). Comparative characterization of degraded and non-degradative hemicelluloses from barley straw and maize stems: composition, structure, and thermal properties. *Carbohydr. Polym.* 78, 609–619. doi: 10.1016/j.carbpol.2009.05.024
- Jin, A. X., Ren, J. L., Peng, F., Xu, F., Zhou, G. Y., Sun, R. C., et al. (2019). Promoting the material properties of xylan-type hemicelluloses from the extraction step. *Carbohydr. Polym.* 215, 235–245. doi: 10.1016/j.carbpol.2019.03.092
- Kapu, N. S., and Trajano, H. L. (2014). Review of hemicellulose hydrolysis in softwoods and bamboo. *Biofuels Bioprod. Bior.* 8, 857–870. doi: 10.1002/bbb.1517
- Kaur, D., Singla, G., Singh, U., and Krishania, M. J. (2020). Efficient process engineering for extraction of hemicellulose from corn fiber and its characterization. *Carbohydr. Polym. Technol. Appl.* 1:100011. doi: 10.1016/j.carpta.2020.100011
- Koti, S., Govumoni, S. P., Gentela, J., and Rao, L. V. (2016). Enhanced bioethanol production from wheat straw hemicellulose by mutant strains of pentose fermenting organisms *Pichia stipitis* and *Candida shehatae*. *Springerplus* 5:1545. doi: 10.1186/s40064-016-3222-1
- Li, J. B., Feng, P., Xiu, H. J., Zhang, M. Y., Li, J. Y., Du, M., et al. (2020). Wheat straw components fractionation, with efficient delignification, by hydrothermal treatment followed by facilitated ethanol extraction. *Bioresour. Technol.* 316:123882. doi: 10.1016/j.biortech.2020.123882
- Li, J. Y., Zhang, X. C., Zhang, J. M., Mi, Q. Y., Jia, F. W., Wu, J., et al. (2019). Direct and complete utilization of agricultural straw to fabricate all-biomass films with high-strength, high-haze and UV-shielding properties. *Carbohydr. Polym.* 223:115057. doi: 10.1016/j.carbpol.2019.115057
- Li, M. G., Yang, X. M., Lu, T. L., and Zhou, L. P. (2020). Selective hydrolysis of hemicellulose component of wheat straw in high-pressure CO₂ and water with low concentration of acetic acid. *J. Chem. Technol. Biot.* 95, 2237–2242. doi: 10.1002/jctb.6411
- Li, X., Xu, R., Yang, J., Nie, S., Liu, D., Liu, Y., et al. (2019). Production of 5-hydroxymethylfurfural and levulinic acid from lignocellulosic biomass and catalytic upgradation. *Ind. Crops Prod.* 130, 184–197. doi: 10.1016/j.indcrop.2018.12.082
- Liu, H. Y., Xu, T., Liu, K., Zhang, M., Liu, W., Li, H., et al. (2021). Lignin-based electrodes for energy storage application. *Ind. Crops Prod.* 165:113425. doi: 10.1016/j.indcrop.2021.113425
- Liu, K., Du, H., Zheng, T., Liu, H., Zhang, M., Zhang, R., et al. (2021). Recent advances in cellulose and its derivatives for oilfield applications. *Carbohydr. Polym.* 259:117740. doi: 10.1016/j.carbpol.2021.117740
- Liu, W., Du, H., Zhang, M., Liu, K., Liu, H., Xie, H., et al. (2020). Bacterial cellulose-based composite scaffolds for biomedical applications: a review. *ACS Sustain. Chem. Eng.* 8, 7536–7562. doi: 10.1021/acssuschemeng.0c00125
- Liu, X. W., Luan, S., and Li, W. (2019). Utilization of waste hemicelluloses lye for superabsorbent hydrogel synthesis. *Int. J. Biol. Macromol.* 132, 954–962. doi: 10.1016/j.ijbiomac.2019.04.041
- Lucenius, J., Valle-Delgado, J. J., Parikka, K., and Osterberg, M. (2019). Understanding hemicellulose-cellulose interactions in cellulose nanofibril-based composites. *J. Colloid. Interf. Sci.* 555, 104–114. doi: 10.1016/j.jcis.2019.07.053
- Luo, Y. P., Li, Z., Li, X. L., Liu, X. F., Fan, J. J., Clark, J. H., et al. (2019). The production of furfural directly from hemicellulose in lignocellulosic biomass: a review. *Catal. Today* 319, 14–24. doi: 10.1016/j.cattod.2018.06.042
- Ma, M. G., Jia, N., Zhu, J. F., Li, S. M., Peng, F., and Sun, R. C. (2012). Isolation and characterization of hemicelluloses extracted by hydrothermal pretreatment. *Bioresour. Technol.* 114, 677–683. doi: 10.1016/j.biortech.2012.03.048
- Ma, Q. L., Zhu, J. J., Gleisner, R., Yang, R. D., and Zhu, J. Y. (2018). Valorization of wheat straw using a recyclable hydrotrope at low temperatures (<= 90 degrees C). *ACS Sustain. Chem. Eng.* 6, 14480–14489. doi: 10.1021/acssuschemeng.8b03135
- Manaf, S. F. A., Jahim, J. M., Harun, S., and Luthfi, A. A. I. (2018). Fractionation of oil palm fronds (OPF) hemicellulose using dilute nitric acid for fermentative production of xylitol. *Ind. Crops Prod.* 115, 6–15. doi: 10.1016/j.indcrop.2018.01.067
- Marcotullio, G., Krisanti, E., Giuntoli, J., and de Jong, W. (2011). Selective production of hemicellulose-derived carbohydrates from wheat straw using dilute HCl or FeCl₃ solutions under mild conditions. X-ray and thermogravimetric analysis of the solid residues. *Bioresour. Technol.* 102, 5917–5923. doi: 10.1016/j.biortech.2011.02.092
- Middleton, R. S., Carey, J. W., Currier, R. P., Hyman, J. D., Kang, Q. J., Karra, S., et al. (2015). Shale gas and non-aqueous fracturing fluids: opportunities and

- challenges for supercritical CO₂. *Appl. Energy* 147, 500–509. doi: 10.1016/j.apenergy.2015.03.023
- Mihiretu, G. T., Brodin, M., Chimphango, A. F., Oyaas, K., Hoff, B. H., and Gorgens, J. F. (2017). Single-step microwave-assisted hot water extraction of hemicelluloses from selected lignocellulosic materials - a biorefinery approach. *Bioresour. Technol.* 241, 669–680. doi: 10.1016/j.biortech.2017.05.159
- Mihiretu, G. T., Chimphango, A. F., and Gorgens, J. F. (2019). Steam explosion pre-treatment of alkali-impregnated lignocelluloses for hemicelluloses extraction and improved digestibility. *Bioresour. Technol.* 294:122121. doi: 10.1016/j.biortech.2019.122121
- Mugwagwa, L. R., and Chimphango, A. F. A. (2020). Optimising wheat straw alkali-organosolv pre-treatment to enhance hemicellulose modification and compatibility with reinforcing fillers. *Int. J. Biol. Macromol.* 143, 862–872. doi: 10.1016/j.ijbiomac.2019.09.147
- Nascimento, P. F. P., and Neto, E. L. B. (2021). Steam explosion: hydrothermal pretreatment in the production of an adsorbent material using coconut husk. *BioEnergy Res.* 14, 153–162. doi: 10.1007/s12155-020-10159-y
- Nigam, J. N. (2001). Ethanol production from wheat straw hemicellulose hydrolysate by *Pichia stipitis*. *J. Biotechnol.* 87, 17–27. doi: 10.1016/S0168-1656(00)00385-0
- Peng, F., Peng, P., Xu, F., and Sun, R. C. (2012). Fractional purification and bioconversion of hemicelluloses. *Biotechnol. Adv.* 30, 879–903. doi: 10.1016/j.biotechadv.2012.01.018
- Peng, F., Ren, J. L., Peng, B., Xu, F., Sun, R. C., and Sun, J. X. (2008). Rapid homogeneous lauroylation of wheat straw hemicelluloses under mild conditions. *Carbohydr. Res.* 343, 2956–2962. doi: 10.1016/j.carres.2008.08.023
- Peng, X., and Chen, H. (2012). Hemicellulose sugar recovery from steam-exploded wheat straw for microbial oil production. *Process Biochem.* 47, 209–215. doi: 10.1016/j.procbio.2011.10.035
- Pereira, P. H. F., Waldron, K. W., Wilson, D. R., Cunha, A. P., de Brito, E. S., Rodrigues, T. H. S., et al. (2017). Wheat straw hemicelluloses added with cellulose nanocrystals and citric acid. effect on film physical properties. *Carbohydr. Polym.* 164, 317–324. doi: 10.1016/j.carbpol.2017.02.019
- Persson, T., Ren, J. L., Joellson, E., and Jonsson, A. S. (2009). Fractionation of wheat and barley straw to access high-molecular-mass hemicelluloses prior to ethanol production. *Bioresour. Technol.* 100, 3906–3913. doi: 10.1016/j.biortech.2009.02.063
- Qi, G. X., Xiong, L., Li, H. L., Huang, Q. L., Luo, M. T., Tian, L. L., et al. (2019). Hydrotropic pretreatment on wheat straw for efficient biobutanol production. *Biomass Bioenergy.* 122, 76–83. doi: 10.1016/j.biombioe.2019.01.039
- Ragab, T., Amer, H., Mossa, A. T., Emam, M., Hasaballah, A. A., and Helmy, W. A. J. B. (2018). Anticoagulation, fibrinolytic and the cytotoxic activities of sulfated hemicellulose extracted from rice straw and husk. *Biocatal. Agric. Biotechnol.* 15, 86–91. doi: 10.1016/j.cbab.2018.05.010
- Rao, J., Gao, H., Guan, Y., Li, W. Q., and Liu, Q. (2019). Fabrication of hemicelluloses films with enhanced mechanical properties by graphene oxide for humidity sensing. *Carbohydr. Polym.* 208, 513–520. doi: 10.1016/j.carbpol.2018.12.099
- Relvas, F. M., Morais, A. R. C., and Bogel-Lukasik, R. (2015). Selective hydrolysis of wheat straw hemicellulose using high-pressure CO₂ as catalyst. *RSC Adv.* 5, 73935–73944. doi: 10.1039/C5RA14632A
- Ren, J. L., Peng, X. W., Zhong, L. X., Peng, F., and Sun, R. C. (2012). Novel hydrophobic hemicelluloses: synthesis and characteristic. *Carbohydr. Polym.* 89, 152–157. doi: 10.1016/j.carbpol.2012.02.064
- Ren, J. L., Sun, R. C., Liu, C. F., Cao, Z. N., and Luo, W. (2007). Acetylation of wheat straw hemicelluloses in ionic liquid using iodine as a catalyst. *Carbohydr. Polym.* 70, 406–414. doi: 10.1016/j.carbpol.2007.04.022
- Ren, J. L., Xu, F., Sun, R. C., Peng, B., and Sun, J. X. (2008). Studies of the lauroylation of wheat straw hemicelluloses under heating. *J. Agric. Food Chem.* 56, 1251–1258. doi: 10.1021/jf072983q
- Roberto, I. C., Sato, S., and de Mancilha, I. M. (1996). Effect of inoculum level of xylitol production from rice straw hemicellulose hydrolysate by *Candida guilliermondii*. *J. Ind. Microbiol.* 16, 348–350. doi: 10.1007/BF01570113
- Scordia, D., Cosentino, S. L., Lee, J. W., and Jeffries, T. W. (2012). Bioconversion of giant reed (*Arundo donax* L.) hemicellulose hydrolysate to ethanol by *Scheffersomyces stipitis* CBS6054. *Biomass Bioenergy* 39, 296–305. doi: 10.1016/j.biombioe.2012.01.023
- Sharma, S., Nandal, P., and Arora, A. (2019). Ethanol production from NaOH pretreated rice straw: a cost effective option to manage rice crop residue. *Waste Biomass Valorization* 10, 3427–3434. doi: 10.1007/s12649-018-0360-4
- Shi, J. B., Yang, Q. L., Lin, L., and Peng, L. C. (2013). Fractionation and characterization of physicochemical and structural features of corn stalk hemicelluloses from yellow liquor of active oxygen cooking. *Ind. Crops Prod.* 44, 542–548. doi: 10.1016/j.indcrop.2012.09.026
- Shi, Y. F., Du, X. H., Jin, M. T., Wu, S., Wang, L., Qiao, N., et al. (2021). A two-step process for pre-hydrolysis of hemicellulose in pulp-impregnated effluent with high alkali concentration to improve xylose production. *J. Hazard. Mater.* 402:123573. doi: 10.1016/j.jhazmat.2020.123573
- Sipponen, M. H., Pihlajaniemi, V., Sipponen, S., Pastinen, O., and Laakso, S. (2014). Autohydrolysis and aqueous ammonia extraction of wheat straw: effect of treatment severity on yield and structure of hemicellulose and lignin. *RSC Adv.* 4, 23177–23184. doi: 10.1039/C4RA03236E
- Sun, D., Wang, H. M., Wang, B., Wen, J. L., Li, M. F., and Sun, R. C. (2019). Comparative study of hemicelluloses from Hybrid Pennisetum via a green and clean integrated process. *Carbohydr. Polym.* 205, 135–142. doi: 10.1016/j.carbpol.2018.10.027
- Sun, R. C., and Tomkinson, J. (2003). Characterization of hemicelluloses isolated with tetraacetylenediamine activated peroxide from ultrasound irradiated and alkali pre-treated wheat straw. *Eur. Polym. J.* 39, 751–759. doi: 10.1016/S0014-3057(02)00274-4
- Sun, R. C., Fang, J. M., Tomkinson, J., and Chemistry, F. (2000). Characterization and esterification of hemicelluloses from rye straw. *J. Agric. Food Chem.* 48, 1247–1252. doi: 10.1021/jf990570m
- Sun, R. C., Sun, X. F., and Ma, X. H. (2002). Effect of ultrasound on the structural and physicochemical properties of organosolv soluble hemicelluloses from wheat straw. *Ultrason. Sonochem.* 9, 95–101. doi: 10.1016/S1350-4177(01)00102-X
- Sun, S. L., Wen, J. L., Ma, M. G., Song, X. L., and Sun, R. C. (2014). Integrated biorefinery based on hydrothermal and alkaline treatments: investigation of sorghum hemicelluloses. *Carbohydr. Polym.* 111, 663–669. doi: 10.1016/j.carbpol.2014.04.099
- Sun, X. F., Gan, Z., Jing, Z. X., Wang, H. H., Wang, D., and Jin, Y. A. (2015a). Adsorption of methylene blue on hemicellulose-based stimuli-responsive porous hydrogel. *J. Appl. Polym. Sci.* 132:41606. doi: 10.1002/app.41606
- Sun, X. F., Jing, Z. X., Fowler, P., Wu, Y. G., and Rajaratnam, M. (2011). Structural characterization and isolation of lignin and hemicelluloses from barley straw. *Ind. Crop Prod.* 33, 588–598. doi: 10.1016/j.indcrop.2010.12.005
- Sun, X. F., Liu, B. C., Jing, Z. X., and Wang, H. H. (2015b). Preparation and adsorption property of xylan/poly(acrylic acid) magnetic nanocomposite hydrogel adsorbent. *Carbohydr. Polym.* 118, 16–23. doi: 10.1016/j.carbpol.2014.11.013
- Sun, X. F., Sun, R. C., Fowler, P., and Baird, M. S. (2005a). Extraction and characterization of original lignin and hemicelluloses from wheat straw. *J. Agric. Food Chem.* 53, 860–870. doi: 10.1021/jf040456q
- Sun, X. F., Wang, H. H., Jing, Z. X., and Mohanathas, R. (2013). Hemicellulose-based pH-sensitive and biodegradable hydrogel for controlled drug delivery. *Carbohydr. Polym.* 92, 1357–1366. doi: 10.1016/j.carbpol.2012.10.032
- Sun, X. F., Xu, F., Zhao, H., Sun, R. C., Fowler, P., and Baird, M. S. (2005b). Physicochemical characterisation of residual hemicelluloses isolated with cyanamide-activated hydrogen peroxide from organosolv pre-treated wheat straw. *Bioresour. Technol.* 96, 1342–1349. doi: 10.1016/j.biortech.2004.11.018
- Tabaňag, I. D. F., Chu, I. M., Wei, Y. H., and Tsai, S. L. (2018). Ethanol production from hemicellulose by a consortium of different genetically-modified *saccharomyces cerevisiae*. *J. Taiwan Inst. Chem. Eng.* 89, 15–25. doi: 10.1016/j.jtice.2018.04.029
- Terrone, C. C., de Freitas, C., Fanchini Terrasan, C. R., de Almeida, A. F., and Carmona, E. C. (2018). Agroindustrial biomass for xylanase production by *Penicillium chrysogenum*: purification, biochemical properties and hydrolysis of hemicelluloses. *Electron. J. Biotechnol.* 33, 39–45. doi: 10.1016/j.ejbt.2018.04.001
- Thomsen, M. H., Thygesen, A., and Thomsen, A. B. (2008). Hydrothermal treatment of wheat straw at pilot plant scale using a three-step reactor system aiming at high hemicellulose recovery, high cellulose digestibility and low lignin hydrolysis. *Bioresour. Technol.* 99, 4221–4228. doi: 10.1016/j.biortech.2007.08.054

- Thuvander, J., and Jönsson, A. S. (2019). Influence of air and nitrogen sparging on flux during ultrafiltration of hemicelluloses extracted from wheat bran. *Sep. Purif. Technol.* 212, 84–88. doi: 10.1016/j.seppur.2018.11.010
- Thuvander, J., and Jonsson, A. S. (2020). Techno-economic impact of air sparging prior to purification of alkaline extracted wheat bran hemicelluloses by membrane filtration. *Sep. Purif. Technol.* 253:117498. doi: 10.1016/j.seppur.2020.117498
- Thuvander, J., Arkell, A., and Jonsson, A. S. (2018). Reduction of energy demand by use of air sparging during ultrafiltration of alkali-extracted wheat bran hemicelluloses. *Chem. Eng. Res. Des.* 138, 43–50. doi: 10.1016/j.cherd.2018.08.001
- Tian, S. Q., Zhao, R. Y., and Chen, Z. C. (2018). Review of the pretreatment and bioconversion of lignocellulosic biomass from wheat straw materials. *Sustainable Energy Rev.* 91, 483–489. doi: 10.1016/j.rser.2018.03.113
- Tsegaye, B., Balomajumder, C., and Roy, P. (2019). Optimization of microwave and NaOH pretreatments of wheat straw for enhancing biofuel yield. *Energy Convers. Manag.* 186, 82–92. doi: 10.1016/j.enconman.2019.02.049
- Tsegaye, B., Balomajumder, C., and Roy, P. (2020). Organosolv pretreatments of rice straw followed by microbial hydrolysis for efficient biofuel production. *Renewable Energy* 148, 923–934. doi: 10.1016/j.renene.2019.10.176
- Wang, R. Z., Yue, J. F., Jiang, J. C., Li, J., Zhao, J. P., Xia, H. H., et al. (2021). Hydrothermal CO₂-assisted pretreatment of wheat straw for hemicellulose degradation followed with enzymatic hydrolysis for glucose production. *Waste Biomass Valorization* 12, 1483–1492. doi: 10.1007/s12649-020-01103-4
- Wang, T., Li, C., Song, M., and Grain, R. F. J. (2019). Xylo-oligosaccharides preparation through acid hydrolysis of hemicelluloses isolated from press-lye. *Grain Oil Sci. Technol.* 2, 21–25. doi: 10.1016/j.gaost.2019.07.001
- Xu, F., Jiang, J. X., Sun, R. C., She, D., Peng, B., Sun, J. X., et al. (2008). Rapid esterification of wheat straw hemicelluloses induced by microwave irradiation. *Carbohydr. Polym.* 73, 612–620. doi: 10.1016/j.carbpol.2008.01.002
- Xu, F., Liu, C. F., Geng, Z. C., Sun, J. X., Sun, R. C., Hei, B. H., et al. (2006). Characterisation of degraded organosolv hemicelluloses from wheat straw. *Polym. Degrad. Stabil.* 91, 1880–1886. doi: 10.1016/j.polymdegradstab.2005.11.002
- Yang, H. P., Li, S. J., Liu, B., Chen, Y. Q., Xiao, J. J., Dong, Z. G., et al. (2020). Hemicellulose pyrolysis mechanism based on functional group evolutions by two-dimensional perturbation correlation infrared spectroscopy. *Fuel* 267:117302. doi: 10.1016/j.fuel.2020.117302
- Yang, H. Q., Yi, N., Zhao, S., Qaseem, M. F., Zheng, B., Li, H. L., et al. (2020). Characterization of hemicelluloses in sugarcane (*Saccharum* spp. hybrids) culm during xylogenesis. *Int. J. Biol. Macromol.* 165, 1119–1128. doi: 10.1016/j.ijbiomac.2020.09.242
- Yao, S. Q., Nie, S. X., Zhu, H. X., Wang, S. F., Song, X. P., and Qin, C. R. (2017). Extraction of hemicellulose by hot water to reduce adsorbable organic halogen formation in chlorine dioxide bleaching of bagasse pulp. *Ind. Crop Prod.* 96, 178–185. doi: 10.1016/j.indcrop.2016.11.046
- Yoon, K. Y., Woodams, E. E., and Hang, Y. D. (2006). Enzymatic production of pentoses from the hemicellulose fraction of corn residues. *LWT Food Sci. Technol.* 39, 388–392. doi: 10.1016/j.lwt.2005.02.005
- You, X., Wang, X., Liang, C., Liu, X. L., and Wang, S. F. (2019). Purification of hemicellulose from sugarcane bagasse alkaline hydrolysate using an aromatic-selective adsorption resin. *Carbohydr. Polym.* 225:115216. doi: 10.1016/j.carbpol.2019.115216
- Yuan, Y., Zou, P., Zhou, J. H., Geng, Y. T., Fan, J. J., Clark, J., et al. (2019). Microwave-assisted hydrothermal extraction of non-structural carbohydrates and hemicelluloses from tobacco biomass. *Carbohydr. Polym.* 223:11543. doi: 10.1016/j.carbpol.2019.115043
- Zhang, J., Wang, Y. H., Qu, Y. S., Wei, Q. Y., and Li, H. Q. (2018). Effect of the organizational difference of corn stalk on hemicellulose extraction and enzymatic hydrolysis. *Ind. Crops Prod.* 112, 698–704. doi: 10.1016/j.indcrop.2018.01.007
- Zhang, W., Zhu, S., Bai, Y., Xi, N., Wang, S., Bian, Y., et al. (2015). Glow discharge electrolysis plasma initiated preparation of temperature/pH dual sensitivity reed hemicellulose-based hydrogels. *Carbohydr. Polym.* 122, 11–17. doi: 10.1016/j.carbpol.2015.01.007
- Zhao, W., Glavas, L., Odelius, K., Edlund, U., and Albertsson, A. C. (2014). Facile and green approach towards electrically conductive hemicellulose hydrogels with tunable conductivity and swelling behavior. *Chem. Mater.* 26, 4265–4273. doi: 10.1021/cm501852w
- Zhao, Y. L., Sun, H., Yang, B., and Weng, Y. X. (2020). Hemicellulose-based film: potential green films for food packaging. *Polymers* 12:1775. doi: 10.3390/polym12081775
- Zhong, C., Wang, C., Huang, F., Wang, F., Jia, H., Zhou, H., et al. (2015). Selective hydrolysis of hemicellulose from wheat straw by a nanoscale solid acid catalyst. *Carbohydr. Polym.* 131, 384–391. doi: 10.1016/j.carbpol.2015.05.070

Conflict of Interest: The authors declare that the research was conducted in the absence of any commercial or financial relationships that could be construed as a potential conflict of interest.

Copyright © 2021 Huang, Ma, Ji, Choi and Si. This is an open-access article distributed under the terms of the Creative Commons Attribution License (CC BY). The use, distribution or reproduction in other forums is permitted, provided the original author(s) and the copyright owner(s) are credited and that the original publication in this journal is cited, in accordance with accepted academic practice. No use, distribution or reproduction is permitted which does not comply with these terms.



Multifunctional Lignin-Based Composite Materials for Emerging Applications

Chang Ma^{1,2}, Tae-Hee Kim³, Kun Liu⁴, Ming-Guo Ma^{1*}, Sun-Eun Choi^{3*} and Chuanling Si^{4*}

¹ Research Center of Biomass Clean Utilization, Engineering Research Center of Forestry Biomass Materials and Bioenergy, Beijing Key Laboratory of Lignocellulosic Chemistry, College of Materials Science and Technology, Beijing Forestry University, Beijing, China, ² Material Science and Engineering College, Northeast Forestry University, Harbin, China, ³ Department of Forest Biomaterials Engineering, College of Forest and Environmental Sciences, Kangwon National University, Chuncheon-si, South Korea, ⁴ Tianjin Key Laboratory of Pulp and Paper, Tianjin University of Science and Technology, Tianjin, China

OPEN ACCESS

Edited by:

Xin Zhou,
Nanjing Forestry University, China

Reviewed by:

Bailiang Xue,
Shaanxi University of Technology,
China
Wei Xia,
Uppsala University, Sweden

*Correspondence:

Ming-Guo Ma
mg_ma@bjfu.edu.cn
Sun-Eun Choi
oregonin@kangwon.ac.kr
Chuanling Si
sichli@tust.edu.cn

Specialty section:

This article was submitted to
Bioprocess Engineering,
a section of the journal
Frontiers in Bioengineering and
Biotechnology

Received: 13 May 2021

Accepted: 25 May 2021

Published: 02 July 2021

Citation:

Ma C, Kim T-H, Liu K, Ma M-G,
Choi S-E and Si C (2021)
Multifunctional Lignin-Based
Composite Materials for Emerging
Applications.
Front. Bioeng. Biotechnol. 9:708976.
doi: 10.3389/fbioe.2021.708976

Lignin exhibited numerous advantages such as plentiful functional groups, good biocompatibility, low toxicity, and high carbon content, which can be transformed into composites and carbon materials. Lignin-based materials are usually environmentally friendly and low cost, and are widely used in energy storage, environment, electronic devices, and other fields. In this review article, the pretreatment separation methods like hydrothermal process are illustrated briefly, and the properties and categories of technical lignin are introduced. Then, the latest progress of lignin-based composites and lignin-derived carbon materials is summarized. Finally, the current challenges and future developments were suggested based on our knowledge. It is expected that this review paper favored the applications of composites and lignin-derived carbon materials in the future.

Keywords: lignin, composites, carbon, synthesis, applications

INTRODUCTION

Cellulose, lignin, and hemicellulose are the main chemical components of plant fiber raw materials (Li S.X. et al., 2019; Yang et al., 2019; Liu W. et al., 2020; Liu H. et al., 2021; Liu K. et al., 2021; Liu W. et al., 2021; Wang et al., 2021). Among these three components of lignocellulose, lignin is the only amorphous aromatic polymer (Figure 1A; Deuss et al., 2015; Xu J. et al., 2020; Ma et al., 2021b). Previously, the production of Kraft lignin and soda lignin was mainly used as a dye to provide a heat source for the burning section of the alkali recovery in the pulp and paper industry (Li et al., 2016; Xu et al., 2021). Given that lignin is a rich natural resource, increasing attention is paid to the research, development, and utilization of lignin in today's increasingly scarce resources (Upton and Kasko, 2016; Li X. et al., 2019; Li et al., 2021). The structure of lignin is relatively complex than other biomass; therefore, it has a broad research prospect to develop appropriate methods for separation and refinery of lignin, conduct detailed research, and then unitize it to prepare materials rationally (Ragauskas et al., 2014; Chen et al., 2016; Meng L.Y. et al., 2019; Chen et al., 2020b; Ma et al., 2020).

Lignin is composed of three kinds of structural units such as syringyl unit (S), guaiacol unit (G), and p-hydroxyphenyl unit (H) (Figure 1B; Decostanzi et al., 2019; Chen et al., 2020c; Shi and Ma, 2019; Liu K. et al., 2021). In the previous literatures, the lignin of softwoods is mainly G-type units; meanwhile, hardwoods are mainly G-type and S-type units. There are more abundant types of lignin in gramineous plants, including G, S, and H-type units. They are connected by ether bonds

(about 60–70%) and carbon–carbon bonds (about 30–40%). Among them, all the alkyl-aryl ether bonds (β -O-4 and α -O-4), the β - β' linkages, and the β -5 linkages are predominant between above three structural units (Figure 1C; Zheng et al., 2021). The structure composition and interunit linkages of lignin are also closely related to the external factors such as the growing environment of plants. Therefore, the different structural units, different linkage, and the complex relationship between lignin and glycan in the cell wall endow lignin one of the most complex natural polymers in nature. Lignin molecules contained a variety of active functional groups both on the benzene ring and the side chain, including aliphatic hydroxyl (Al-OH), phenolic hydroxyl (Ph-OH), carboxyl (-COOH), carbonyl (-C = O), and methoxy groups (-OCH₃), determining the chemical properties and reactivity of lignin. The chemical properties of lignin allow it and its derivatives to be used as materials for value-high. Furthermore, considering the high carbon content of lignin, it is also an ideal carbon material precursor (Shi and Ma, 2019). Lignin-derived carbon materials are widely used in various fields like energy storage, adsorbent, and catalyst carriers (Suhas et al., 2007; Saha et al., 2014).

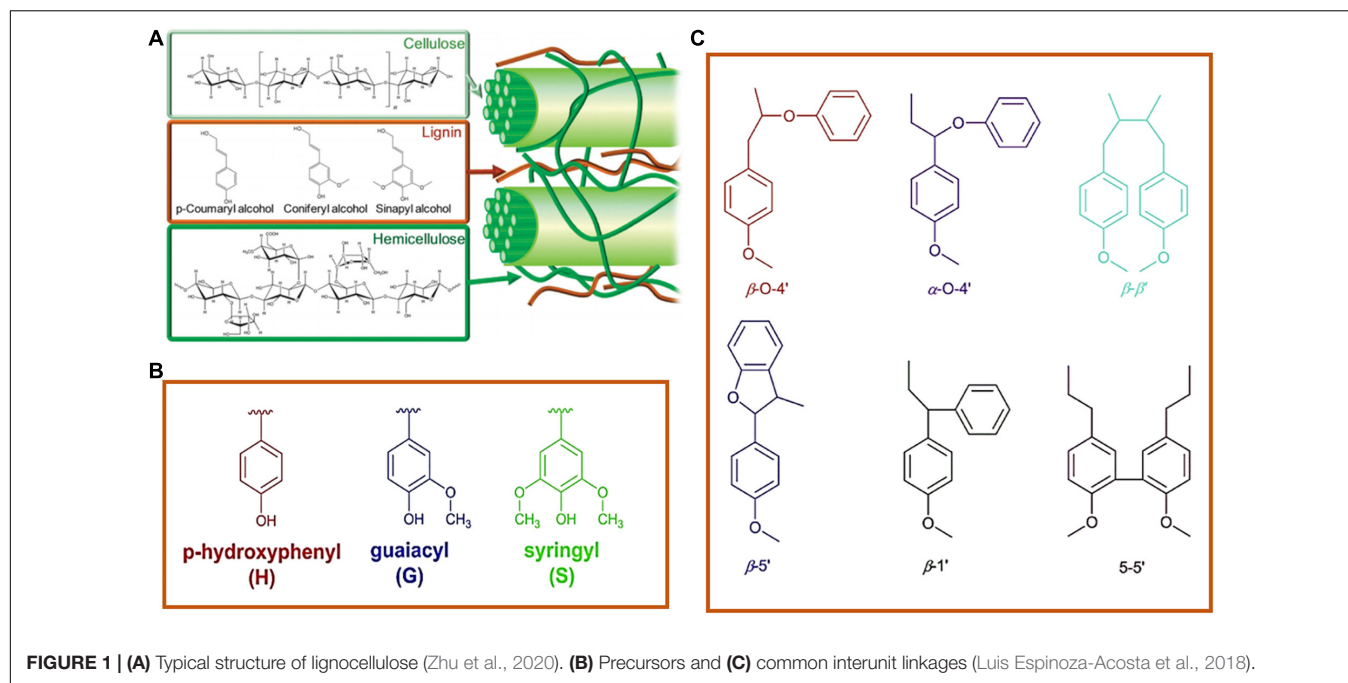
In this review article, we focus on the current achievements of lignin-based materials. The categories of lignin were introduced briefly. Then, the lignin-based materials like lignin-based hydrogels, flocculants, and resin adhesive, and lignin-plastic composites are summarized. In addition, the lignin-derived carbon materials such as activation carbon, carbon fibers, and carbon dots are discussed in detail. Finally, the existed problems and future trends of lignin-derived materials are proposed as well. It is expected that the lignin-based materials are promising applications in various fields.

THE SEPARATION METHODS AND COMPOSITIONS OF LIGNIN

Lignocellulose is one of the most abundant biomass resources, mainly composed of 40–50% cellulose, 20–30% hemicellulose, and 25–35% lignin (Lievenon et al., 2016). According to statistics, about five thousand million tons of lignin has been produced globally every year (Chio et al., 2019; Meng Y. et al., 2019). Chemical structures of lignin varied among different plants species, such as softwoods, hardwoods, and grasses (Boerjan et al., 2003). Lignin does not stand for a single substance, but for a group of substance that have common properties in plants (Garcia Calvo-Flores and Dobado, 2010). The separation of lignin, based on the raw materials, can be divided into three types of separation from plant raw materials, separation from pulp, and separation from pulp waste liquid. Based on the separation principle, the first one is to remove the cellulose and hemicellulose by dissolution, leaving the insoluble residue of lignin. Meanwhile, the second is to dissolve the lignin, leave the insoluble residue of cellulose and hemicellulose, and recover lignin from the solution (Zhao and Abu-Omar, 2021). Bjorkman proposed a classic method for separating lignin by extraction after ball milling as early as 1953, resulting in the production of milled wood lignin. The milled wood

lignin is closed to natural lignin, but in view of the yield is low, so it is often used to study the structure of lignin (Wang et al., 2009). Therefore, it is always a challenge to find a clean and efficient process to separate and recover lignin components with high yield and high structural integrity. Now, the research on biomass refining became a hot direction, which is to separate and extract lignin from biomass feedstock by pretreatment to make it easier for subsequent conversion and further applications. Numerous efforts have been devoted to find the potential pretreatment methods, and various methods have been explored, such as physical, chemical, physicochemical, and biological methods (Hochegger et al., 2019). For example, hydrothermal pretreatment is an environmental-friendly method for biomass separation. Sun et al. (2014) developed an integrated strategy including hydrothermal pretreatment and alkaline post-treatment, studied the changes of linkages during process, and obtained the highest yield of lignin up to 79.3%. These findings are beneficial to understand depolymerization and maximize the potential utilizations of lignin. In addition, there have been noticeable advances using novel solvents like ionic liquids, which are called “green solvents.” Since no toxic chemicals are formed and almost 100% can be recycled, it is considered that the ionic liquid pretreatment is a green solvent. Sun et al. (2019) applied a microwave-assisted ionic liquid approach to decrease the resistance of biomass in biorefinery and led to a high yield of lignin and efficient extraction of biomass. Deep eutectic solvent (DES) pretreatment is another new blooming green strategy for reducing biomass recalcitrance. Shen et al. (2019) employed biomass-derived DES including biomass-derived chemicals to deconstruct the structure of *Eucalyptus* for lignin valorization. Ma et al. (2021a) used microwave-assisted DES pretreatment to improve the lignin extractability and valorization of poplars. After DES pretreatment, the enzymatic saccharification ratios were significantly increased, indicating that this microwave-assisted DES method could reduce the biomass recalcitrance and promote the lignin valorization. There have been series of review papers that summarize lignin extracted methods (Azadi et al., 2013; Chio et al., 2019). Herein, we mainly discuss the common industrial lignin.

In the paper industry, the four main methods of separating technical lignin (or pulping) are the Kraft pulping, sulfite pulping, soda pulping, and organosolv pulping processes. The obtained lignin types are Kraft lignin, lignosulfonate, soda lignin, and organosolv lignin, respectively (El Mansouri and Salvado, 2006). Due to the different processing methods, these four technical lignins have different structures, compositions, and properties. Kraft lignin is the residue of sulfate pulping in paper production, which is precipitated by adjusting the pH value of black liquor (Huang et al., 2017). The structure of Kraft lignin is highly modified and soluble in alkaline solution and organic solvents with high polarity (Chakar and Ragauskas, 2004). Lignosulfonate is sulfonated lignin, which is removed from the wood raw materials by sulfite pulping. Lignosulfonate is soluble in acidic solution, alkaline solution, and organic solvents with high polarity. Even though they contain sulfur, these two kinds of lignin have different characteristics, and the molecular weight of lignosulfonate is



higher (Visital and Kraslawski, 2011). Soda lignin (or Alkaline lignin) is generally free of sulfur, which has a relatively lower molecular weight (Woermeyer et al., 2011). Organic solvents lignin is collected by organosolv pulping process, which has the characteristics of high purity, high homogeneity, and low molecular weight (Li and Takkellapati, 2018; Yu and Kim, 2020). However, the process includes the necessary solvent recovery steps, increasing the cost (Zhao and Abu-Omar, 2021).

THE FABRICATION AND PROPERTIES OF LIGNIN-BASED MATERIALS

Owing to its good biocompatibility, ecological friendliness, and low toxicity, lignin is widely explored for high-value materials instead of burning (Si, 2019; Huang et al., 2020; Liu R. et al., 2020). The aromatic properties also make it possible to replace phenol to prepare phenolic resin adhesives (Pang et al., 2020; Pei et al., 2020). Herein, the synthesis and properties of lignin-based materials with various applications are described.

Lignin-Based Hydrogels

Hydrogel is a kind of hydrophilic three-dimensional network gel, which can swell and hold large amounts of water. Forest biomass materials such as cellulose and hemicellulose are widely used in the preparation of hydrogels (Liu et al., 2017; Du et al., 2019; Li et al., 2020). Moreover, lignin is in its infancy as strength modifier, adhesive agents, or other functional fillers in hydrogels for lignin fractionation, wearable electronics, UV shielding, and biomaterials (Thakur and Thakur, 2015). Dai et al. (2019) fabricated a lignin-contained cellulose hydrogel for lignin fractionation. In this hydrogel,

alkaline lignin was employed to play as a functional cross-linker to simultaneously improve the mechanical performances and realize specific absorbed or filtered. This lignin-cellulose hydrogel showed a reliable way to integrate lignin materials and lignin fractionation. Han et al. (2021) developed a polyvinyl alcohol (PVA) hydrogel with lignin-silver hybrid nanoparticles, which exhibited exceptional compressibility. As a strength modifier of hydrogel, lignin-silver hybrid nanoparticles provided strong hydrogen bonds and facilitated the electron transfer. Considering these outstanding traits of this PVA/lignin-silver hybrid nanoparticle hydrogel, this hydrogel could be used as a pressure-sensitive sensor to monitor signals. After demethylation, the phenolic hydroxyl groups of lignin have been released, which not only made the lignin with adhesion property but also improved the reducibility. Qian et al. (2021) took full advantage of this to reduce graphene oxide and develop a catechol lignin/reduced graphene oxide/sodium alginate/polyacrylamide double network hydrogel with integrated conductive, adhesive, and UV-blocking performance. The obtained hydrogel exhibited great potential in flexible electronic skin. Gao et al. (2021) designed a nanosilver immobilized glycine decorated lignin hydrogel as a catalyst, which showed outstanding catalytic performance of p-nitrophenol reduction. Amino modified lignin hydrogel networks played a role for catalyst carrier with abundant anchoring sites to disperse and stabilize the silver nanoparticles. After 10 cycles, the obtained catalyst can still maintain a catalytic efficiency of 98%, and there is no obvious collapse of the structure as well as the leaching of nanosilver can be ignored.

For the biomedical field, Zhang et al. (2020) assembled a biomimetic lignin/poly(ionic liquids) composite hydrogel by supramolecular interactions for the application of wound dressing. The resultant hydrogel exhibited satisfying

mechanical strength, self-healing properties, bactericidal activity, and anti-oxidant activity. Lignin as reinforcement and antioxidant improved the mechanical enhancement and antioxidant activity of the hydrogel. Besides, lignin-based hydrogels have been used for the controlled release of drug (Witzler et al., 2018). Borisenkov et al. (2016) synthesized a hemicellulose and lignin composite hydrogel for drug delivery. Pectin was embedded in the hydrogel to form hydrophilic supramolecular complexes, which was employed to deliver β -glucuronidase and estrogens.

In addition, due to the changes of solubility, lignin can be used as pH-sensitive ingredient to form pH-responsive hydrogel in shape memory and controlled release (Figueiredo et al., 2017; Jin et al., 2018). Dai L. et al. (2020) prepared an all-lignin-based pH-stimuli-responsive hydrogel for the actuator. Herein, the kraft lignin was crosslinked with poly(ethylene glycol) diglycidyl ether to build this lignin hydrogel. As shown in **Figure 2A**, the lignin-based hydrogel bended spontaneously as the pH changes. Therefore, a mimetic behavior to hook up a wire has been achieved by adjusting pH (**Figure 2B**). These studies demonstrated that the use of lignin in hydrogel can contribute to areas such as electronics manufacturing, wearable devices, drug delivery, and actuators.

Lignin-Phenol-Formaldehyde Resin Adhesive

From the perspective of the structural characteristics of lignin, it is also a high-value approach to prepare lignin-phenol-formaldehyde resin adhesive. Pang et al. (2017) studied the relationships between structure and property of two technical lignins in synthesis and performance of lignin-phenol-formaldehyde resin adhesive. They were obtained from acidic and alkaline organosolv pulping of bamboo. After purification, they were both characterized thoroughly, and the structural features were compared. The results showed that the long-chain hydrocarbon derivatives presented in lignin would affect the synthesis of lignin-phenol-formaldehyde resin.

Depolymerization, activation, phenolate, and demethylation are the common pre-treatment processes to release the phenolic hydroxyl group of lignin (Naseem et al., 2016; Wang et al., 2018; An et al., 2019; Gan and Pan, 2019). For example, Ma et al. (2018) investigated a catalytic oxidative depolymerization process for increasing the content of phenolic hydroxy groups of Kraft lignin. Hydrogen peroxide and copper sulfate were used as catalysts in this process. After reaction, the phenolic hydroxyl content increased from 1.55 to 2.66 mmol g⁻¹, and both the molecular weight and polydispersity decreased. The resultant lignin was used to synthesize lignin-phenol-formaldehyde resin with 50% substitution rate, whose various indexes all achieved the national standards. Base-catalyzed depolymerization of softwood Kraft lignin was used to release the phenolic hydroxyl of lignin to substitute phenol in resins (Solt et al., 2018). Modified renewable lignin-based phenols could replace phenol even at a high degree of substitution of 70%. As shown in **Figure 3**, Li et al. (2018) employed NaOH/urea aqueous solution to depolymerize the alkali lignin to prepare low molecular weight lignin derivatives, so as to further prepare lignin-phenol-formaldehyde resin. After depolymerization treatment process, phenyl-propane trimers were mainly obtained, and the phenolic hydroxyl group content increased from 0.07 to 0.12 mmol g⁻¹. The resultant depolymerized alkali lignin-phenol-formaldehyde resin displayed fast curing rate, low formaldehyde emission, and high bonding strength. Microbes such as the brown-rot, white-rot, and soft-rot fungi were also investigated for the demethylation of Kraft lignin (Venkatesagowda and Dekker, 2020). Demethylation by the action of enzymes removed the *O*-methyl/methoxy of lignin and produced the demethylated Kraft lignin enriched in vicinal-hydroxyl groups, which has potential in lignin-phenol-formaldehyde resin. These studies demonstrated that the depolymerized lignin derivatives can replace phenol in the preparation of phenolic resin.

Lignin-Based Flocculants

Lignin can be employed to treat wastewater. However, most of them suffered from poor solubility, chemical inactivity, and

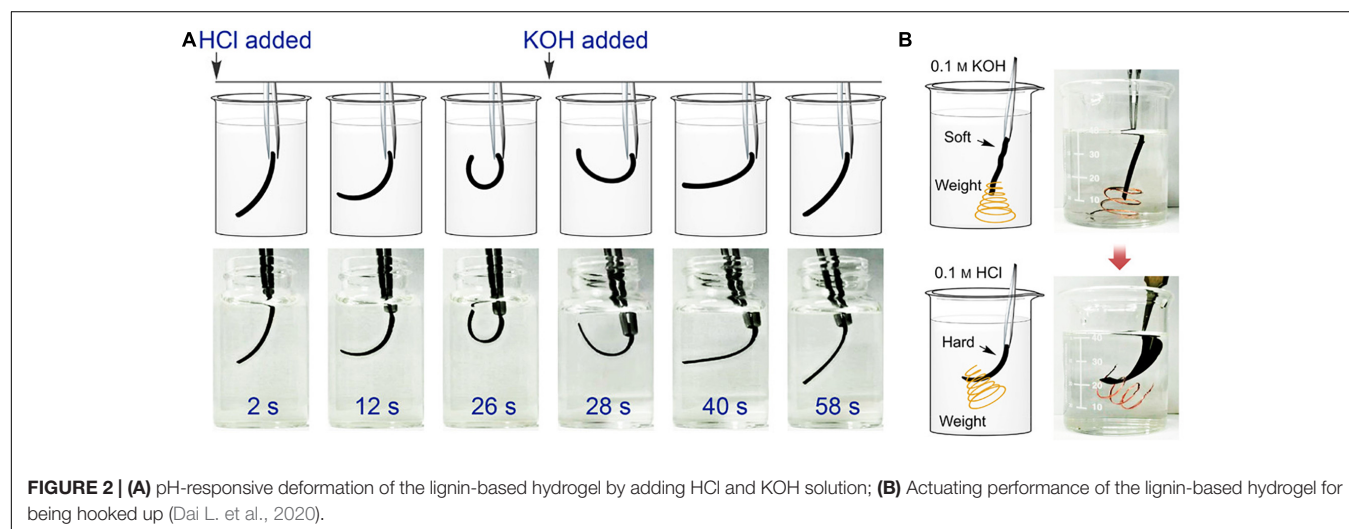
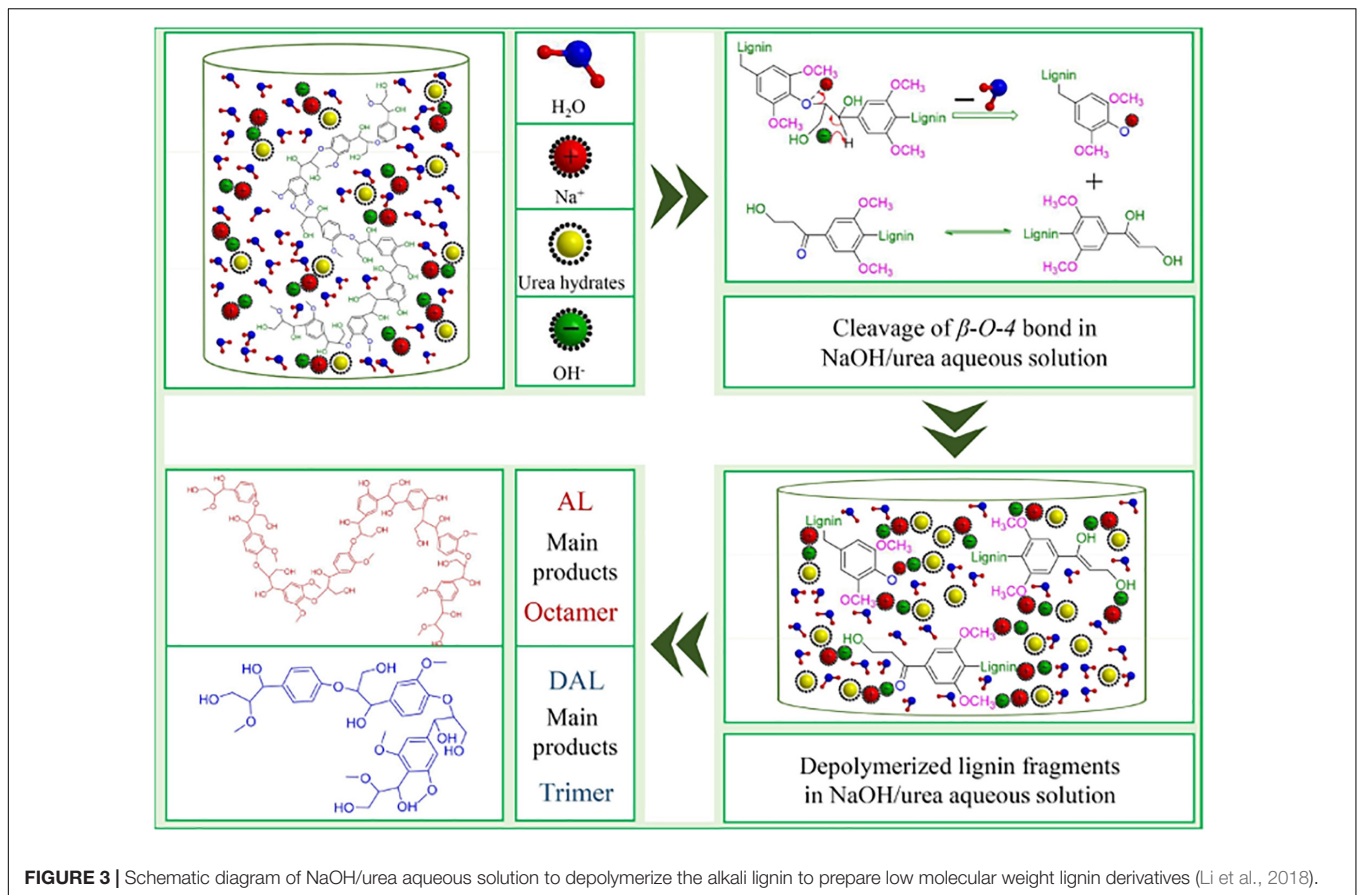


FIGURE 2 | (A) pH-responsive deformation of the lignin-based hydrogel by adding HCl and KOH solution; **(B)** Actuating performance of the lignin-based hydrogel for being hooked up (Dai L. et al., 2020).



low molecular weight. Therefore, various chemical modification methods have been utilized to lignin to improve the flocculation performance (Wang et al., 2020b). Guo et al. (2018) developed an environmentally friendly lignin-based flocculant with improved flocculation by grafting the cationic acrylamide and dimethyl diallyl ammonium chloride monomers onto the alkaline lignin. The flocculation performance of the obtained lignin-based flocculant was low affected by pH. Moreover, the addition of Ca^{2+} and Mg^{2+} could significantly enhance the flocculation performance. Chen et al. (2020a) employed enzymatic hydrolysis lignin as raw materials, using polyacrylamide and methylacryloyloxyethyltrimethyl ammonium chloride as graft agent to synthesize a lignin-based cationic flocculant (L-CPA). The resultant L-CPA could self-assemble into octopus-like nanospheres, which endowed the high flocculation efficiency under the pH condition of 5–9. A small flocculant could be used to flocculate kaolin suspension. Such cheap, environmentally friendly, and technically feasible lignin-based flocculant exhibited a broad prospect in wastewater treatment process. Wang et al. (2020a) designed a lignin-based flocculant by mild copolymerization of lignosulfonate and [2-(methacryloyloxy) ethyl] trimethylammonium chloride solution. By changing the reaction conditions, two classes of flocculant were obtained, which were suitable for simulated dye wastewater (removal rate up to 95%), kaolin (turbidity removal rate up to 99.2%), and *Escherichia coli* suspensions (bacterial

removal rate up to 97.5%), respectively. Anionic lignin-based flocculant was also prepared (Aldajani et al., 2021). Aldajani et al. (2021) prepared a hydrolyzed anionically modified lignin-acrylamide flocculant and investigated the different properties of polymer on the suspension's attributes such as zeta potential, relative turbidity, flocs strength, and recoverability. Through the combination of many of its functional groups, namely, amide, carboxyl, and hydroxyl, it is observed that this lignin-based flocculant had a deeper adsorption on alumina particles than other polymers. These studies exhibited that the production and application of high-efficiency lignin-based flocculants are of great significance for resource conservation, low carbon footprint, and wastewater reuse.

Lignin-Plastic Composites

In past decades, billions of tons of non-biodegradable plastics have been produced, which is a significant source of pollution. As an abundant natural polymer, lignin could be integrated into plastics to fabricate high-value biodegradable materials with economic competitiveness (Sen et al., 2015; Kazzaz et al., 2019). Therefore, the preparation of composite materials by mixing lignin with various plastics had attracted attention. For example, Cerro et al. (2021) produced a poly(lactic acid) (PLA)/lignin nanoparticle composite containing cinnamaldehyde (Ci) for packaging and biomedical applications, which exhibited a better UV-light barrier property and biodegradable performance.

Herein, lignin nanoparticles are used as fillers to enhance the mechanical strength of polymer composites. The toxicity of PLA/lignin composites has been studied as well, and the results showed normal blood parameters after a single dose of composites. Xiong et al. (2020) produced a composite by blending poly(butylene adipate-co-terephthalate) (PBAT) and Eucalypt hydrothermal lignin (**Figure 4A**). Two strategies were followed to improve the performance of composites, including methylated lignin replaced neat lignin as filler, and twin-screw extrusion was used as preparation method. The obtained PBAT/lignin composite materials exhibited a price advantage, in which the cost was significantly reduced by 36%.

Three-dimensional (3D) printing is a method of shape rendering. The ideal materials for 3D printing need to have good extrudability. The unique structures of lignin such as ether groups, β -O-4' linkages, and oxygenated aromatic bonds endow it suitable to incorporate into conventional plastic materials to build hybrid materials by 3D printing with more environmentally friendly and better printability (Nguyen et al., 2018b). A study reported that organosolv hardwood lignin was mixed with nylon as 3D printing ink, and the lignin was found to improve the printability by reducing the melt viscosity and enhance the stiffness and tensile strength of the structure (Nguyen et al., 2018a). The proposed mechanism was lignin domains forming hydrogen bonds with the plastic matrix. This study came up with a new strategy of using biomass lignin as a feedstock for valuable 3D printing materials. Sutton et al. (2018) reported renewable, modified lignin-containing photopolymer resins for 3D printing by stereolithography. Compared to conventional photoactive resins, the lignin-containing resins displayed satisfied ductility, in which the lignin content can reach up to 15%. High print quality and visual clarity were obtained as shown in **Figure 4B** of the photographs of formulations with different lignin content. These studies showed that lignin is cheap and eco-friendly as a feedstock for plastic composites.

LIGNIN-DERIVED CARBON MATERIALS

Carbon materials were extensively applied in numerous fields such as energy storage and conversion, environmental applications, and catalyst (Dong et al., 2020). Generally, carbon materials are derived from petroleum-based chemicals by carbonization treatment, which is non-renewable, non-cyclable, and less environmentally friendly (Shi and Ma, 2019). Lignins are ideal raw materials as carbon precursors due to the low cost and high carbon content. It is of great significance to protect the environment, save resources, and develop the economy harmoniously.

Lignin-Derived Activated Carbons

Due to the high cost of producing activated carbon from coal, the production of activated carbon from lignocellulosic feedstock has attracted much attention (Jiao et al., 2021). A series of chemical activators like KOH and K_2CO_3 was adopted. For example, He et al. (2021) chose lignin-based pitch from black liquor as carbon precursor and KOH as chemical activator to synthesize porous activated carbon materials. The activation temperature on the lignin-derived active carbon was also explored. It was found that the maximum specific surface area and total pore volume reached the values of $3652 \text{ m}^2 \text{ g}^{-1}$ and $2.35 \text{ cm}^3 \text{ g}^{-1}$ under the activation temperature of 850°C . In addition, the ability of the lignin-derived activated carbon to absorb gaseous benzene has also been studied, and the adsorption performance exhibited that the carbon could be a good candidate for absorbing. As shown in **Figure 5**, Xu Q. Q. et al. (2020) employed sodium lignosulfonate (SLS) and ionic liquid ([Amim]Cl) to produce a new polymeric ionic liquid [Amim]LS and NaCl. The mixture was used as a precursor to prepare N-doped porous carbon material *via* direct carbonization without other activations. Herein, NaCl played the role of temple and activation agent. The obtained lignin-based porous carbon achieved a nitrogen content of 4.68%. Under the carbonization temperature of 700°C , a good energy density of

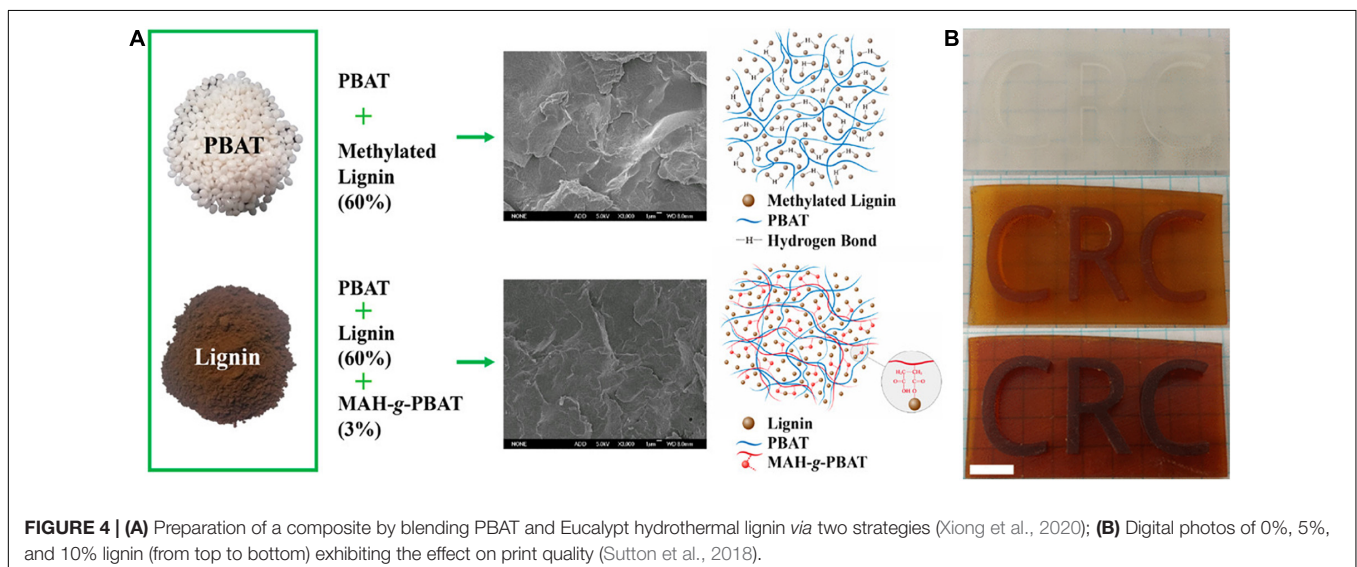




FIGURE 5 | Schematic diagram of [Amim]LS precursors for N-doped porous carbon material fabrication (Xu Q. Q. et al., 2020).

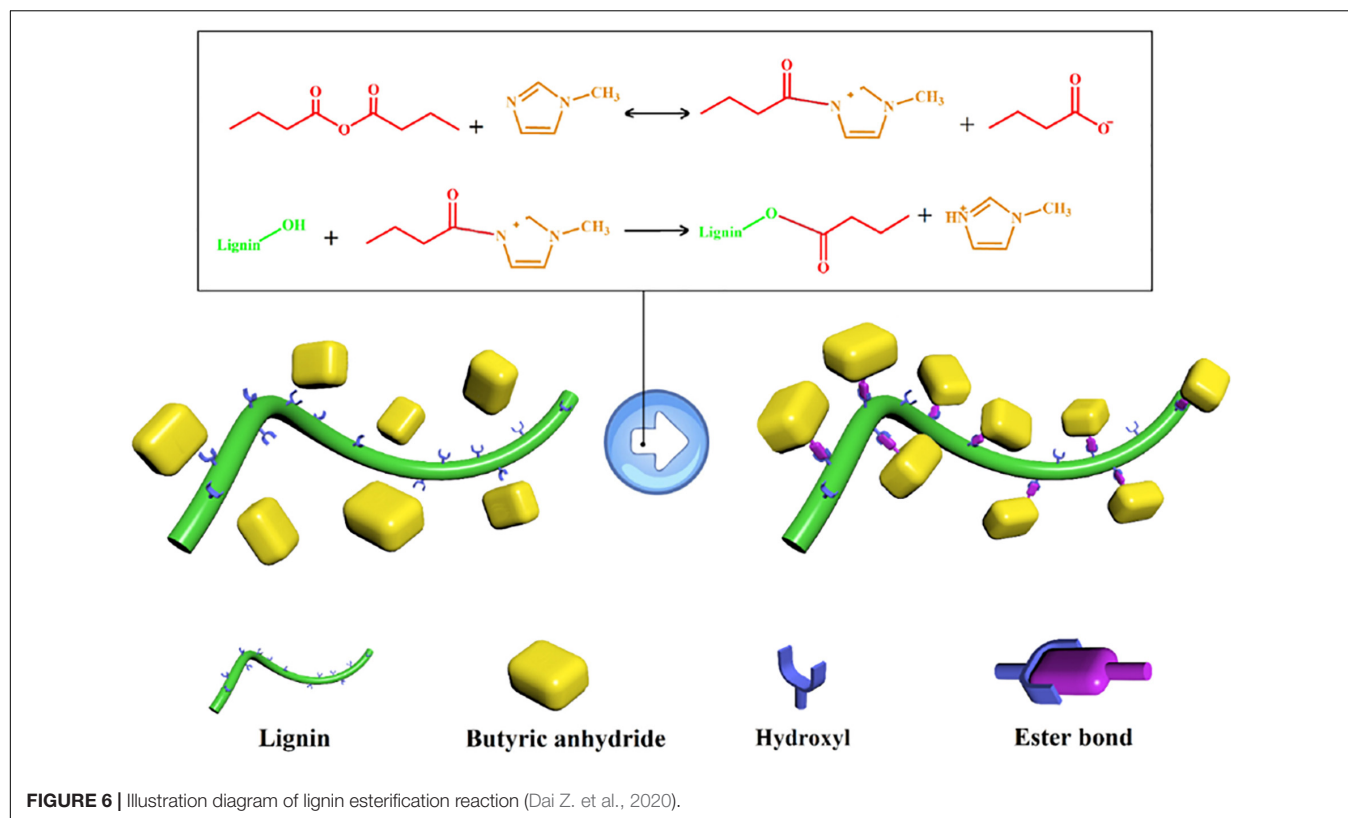
7.99 Wh kg⁻¹ at the power density of 25 W kg⁻¹ and cycling stability of 90.3% after 20000 cycles are shown. There are also some studies on the lignin-derived carbon with hierarchical porous architectures (Zhang et al., 2015a,b). Xi et al. (2021) obtained lignin-derived porous carbons with microstructural characteristics, high graphitization, high specific surface area, and hierarchical porosity for fabrication composites to alleviate the expansion and pulverization phenomena of lithium-ion batteries. Such lignin-derived porous carbons facilitated dispersing/coating of SnO₂ and increased the reversible specific capacity from 64 to 620 mAh g⁻¹. Wan et al. (2021) converted lignin to carbon materials with 3D hierarchical porous structures. After phosphoric acid plus hydrogen peroxide (PHP) oxidation pretreatment and KOH activation, the carbonized lignin reached a high surface area of 3094 m² g⁻¹ and pore volume of 1.72 cm³ g⁻¹. The electrochemical measure results showed that the lignin-based carbon achieved a specific capacitance of 352.9 F g⁻¹ at 0.5 A g⁻¹, indicating an outstanding rate performance of this carbon electrode.

Lignin-Derived Carbon Fibers

Lignin can be used as a cheap precursor in the preparation of carbon fibers instead of petroleum-based polymers by electrospinning technique and carbonization (Garcia-Mateos et al., 2019). Lignin-based carbon fibers with different functions can be obtained by adjusting the parameters of electrospinning, the template selected, and the materials loaded. For example, Ma et al. (2021c) prepared carbon nanofibers using lignin and polyvinylpyrrolidone as carbon precursor by electrospinning, peroxidation, carbonization, and pickling processes. Zinc nitrate hexahydrate was added and pyrolyzed to produce zinc oxide, which was used as a template to produce abundant micropores, resulting in the high specific surface area of 1363 m² g⁻¹. In view of the high specific surface area and

abundant N/O groups, these lignin-derived carbon fibers with a specific capacitance of 289 F g⁻¹ were seen as potential candidates for supercapacitor electrodes. Furthermore, the assembled symmetrical supercapacitor displayed outstanding cycling stability. Liu and Ma (2020) employed lignin as a renewable carbon source with polyacrylonitrile (PAN) and urea to prepare N-doped carbon nanofibers and then coated with polyaniline (PANI) for energy storage. The obtained lignin-based carbon fiber electrode displayed exceptional properties, including large specific surface areas of 483.1 m² g⁻¹, uniform pore size distribution of 9.1 nm, and specific capacitance up to 199.5 F g⁻¹ at 1 A g⁻¹. Eighty-two percent of the initial capacitance was maintained after 1000 charge/discharge at 4 A g⁻¹. Dai Z. et al. (2020) developed a N,O co-doped carbon nanofibers (E-CNFs) from waste lignin and PAN by facile esterification and electrospinning method. The lignin esterification reaction was displayed in **Figure 6**, and the resultant esterified lignin had a low glass transition temperature for higher heteroatom content and better wettability of carbon nanofibers. E-CNF electrode exhibited a high capacitance of 320 F g⁻¹ at a current density of 1 A g⁻¹. An outstanding energy density of 17.92 Wh kg⁻¹ at the power density of 800 W kg⁻¹ was achieved by E-CNF symmetric supercapacitors.

In addition to energy storage, lignin-derived carbon fibers have been used in the field of catalysis as well. Lignin-based Pt supported carbon fiber electrocatalysts were prepared for alcohol electro-oxidation (Garcia-Mateos et al., 2017). Lignin/ethanol/phosphoric acid/platinum acetylacetonate solutions were chosen as precursors for electrospinning. After thermostabilization and carbonization at 900°C, carbon fibers with porous structure and Pt particle loading were obtained. Among them, the addition of phosphorus improved the oxidation resistance, avoided the oxidation of the lignin-based carbon fibers in the preparation process, and led to the



generation of microporous architectures, which were beneficial to enhance the catalyst performance in the electro-oxidation of methanol and ethanol.

Lignin-Derived Carbon Dots

Carbon dot is a novel type of carbon nanomaterial, which was found in 2004 (Xu et al., 2004; Kang et al., 2020). Zhang et al. (2019) prepared carbon quantum dots with bright green fluorescence by a simple one-pot route. Alkali lignin was employed as a precursor. Chao et al. (2021) employed lignin-derived carbon dots as photothermal thermogenesis materials to enhance wood-derived evaporation system. Herein, the lignin-derived carbon dots were obtained by hydrothermal method. An evaporation performance of 1.18 kg m^{-2} and efficiency up to 79.5% were achieved. Yang et al. (2020) developed a green approach to prepare sulfur-doped carbon dots by hydrothermal treatment of lignin. The obtained lignin-derived carbon dots possessed sulfur-containing groups, exhibiting good fluorescence with a quantum yield up to 13.5% and outstanding stability in acidic environments with a wide pH range of 0–5.0. Therefore, this lignin-derived carbon dots were successfully used in detection of Sudan I in acidic conditions.

CONCLUSION AND PERSPECTIVES

With the intensive investigation of lignin-based materials, the great development potential has been revealed in various

fields. More and more efforts should be devoted on lignin-based materials and lignin-derived carbon materials. Further perspectives in lignin-based materials and lignin-derived carbon materials are proposed as follows.

- (1) The low reactivity, solubility, and compatibility with conventional polymers of technical lignin enhance the difficulty of lignin to be a candidate to fabricate materials. Through chemical modification and careful design, these problems are partially or fully worked out, which expands the application of lignin in composite materials.
- (2) Lignin does not stand for a single substance, but for a group of substances that have common properties in plants. Lignin is heterogeneous in nature, and it usually has heterogeneous molecular weights, different functional groups, and different proportions of structural units. It is not conducive to repeatability, uniformity, and scalability of lignin-based materials. The obtained uniform lignin product *via* fractionation process may be one of the solutions for this problem.
- (3) For lignin-derived activated carbon materials, chemical activators such as KOH and H_3PO_4 are often used to increase the specific surface area and the number of pores. However, most of these chemical activators are highly corrosive to the instrument and not recoverable. Therefore, it is vital to adopt green activators or design physical approaches for preparation of lignin-derived activated carbon.

- (4) The morphologies of lignin-derived carbon materials are always disordered and uncontrollable. It is necessary to design hierarchical porous architectures according to different applications.
- (5) For lignin composite materials, more advanced technologies and strategies should be developed, like 3D printing and screen process. In addition, other applications of lignin-derived materials should also be designed, such as nanogenerators, thermal management, biomedical field, and so on.

AUTHOR CONTRIBUTIONS

CM, KL, and M-GM: investigation. T-HK, S-EC, and CS: supervision. CM and M-GM: writing – original draft. M-GM,

T-HK, KL, S-EC, and CS: writing – review and editing. All authors contributed to the article and approved the submitted version.

FUNDING

This research was supported by the cultivating excellent doctoral dissertation of forestry engineering (LYGCVB202011) and the Technology Development Program (S3030198) funded by the Ministry of SMEs and Startups (MSS, South Korea), and this work was also partially supported by R&D Program for Forest Science Technology (2019151D10-2023-0301) provided by Korea Forest Service (Korea Forestry Promotion Institute) to S-EC.

REFERENCES

- Aldajani, M., Alipoormazandarani, N., Kong, F., and Fatehi, P. (2021). Acid hydrolysis of kraft lignin-acrylamide polymer to improve its flocculation affinity. *Sep. Purif. Technol.* 258:117964. doi: 10.1016/j.seppur.2020.117964
- An, L., Si, C., Wang, G., Sui, W., and Tao, Z. (2019). Enhancing the solubility and antioxidant activity of high-molecular-weight lignin by moderate depolymerization via in situ ethanol/acid catalysis. *Ind. Crops Prod.* 128, 177–185. doi: 10.1016/j.indcrop.2018.11.009
- Azadi, P., Inderwildi, O. R., Farnood, R., and King, D. A. (2013). Liquid fuels, hydrogen and chemicals from lignin: a critical review. *Renew. Sustain. Energy Rev.* 21, 506–523. doi: 10.1016/j.rser.2012.12.022
- Boerjan, W., Ralph, J., and Baucher, M. (2003). Lignin biosynthesis. *Annu. Rev. Plant Biol.* 54, 519–546. doi: 10.1146/annurev.arplant.54.031902.134938
- Borisenkov, M. F., Karmanov, A. P., Kocheva, L. S., Markov, P. A., Istomina, E. I., Bakutova, L. A., et al. (2016). Adsorption of beta-glucuronidase and estrogens on pectin/lignin hydrogel particles. *Int. J. Polym. Mater. Polym. Biomater.* 65, 433–441. doi: 10.1080/00914037.2015.1129955
- Cerro, D., Bustos, G., Villegas, C., Buendia, N., Truffa, G., Godoy, M. P., et al. (2021). Effect of supercritical incorporation of cinnamaldehyde on physical-chemical properties, disintegration and toxicity studies of PLA/lignin nanocomposites. *Int. J. Biol. Macromol.* 167, 255–266. doi: 10.1016/j.ijbiomac.2020.11.140
- Chakar, F. S., and Ragauskas, A. J. (2004). Review of current and future softwood kraft lignin process chemistry. *Ind. Crops Prod.* 20, 131–141. doi: 10.1016/j.indcrop.2004.04.016
- Chao, W. X., Li, Y. D., Sun, X. H., Cao, G. L., Wang, C. Y., and Ho, S. H. (2021). Enhanced wood-derived photothermal evaporation system by in-situ incorporated lignin carbon quantum dots. *Chem. Eng. J.* 405:126703. doi: 10.1016/j.cej.2020.126703
- Chen, N., Liu, W. F., Huang, J. H., and Qiu, X. Q. (2020a). Preparation of octopus-like lignin-grafted cationic polyacrylamide flocculant and its application for water flocculation. *Int. J. Biol. Macromol.* 146, 9–17. doi: 10.1016/j.ijbiomac.2019.12.245
- Chen, S., Wang, G., Sui, W., Parvez, A. M., Dai, L., and Si, C. (2020b). Novel lignin-based phenolic nanosphere supported palladium nanoparticles with highly efficient catalytic performance and good reusability. *Ind. Crop Prod.* 145:112164. doi: 10.1016/j.indcrop.2020.112164
- Chen, S., Wang, G., Sui, W., Parvez, A. M., and Si, C. (2020c). Synthesis of lignin-functionalized phenolic nanosphere supported Ag nanoparticles with excellent dispersion stability and catalytic performance. *Green Chem.* 22, 2879–2888. doi: 10.1039/c9gc04311j
- Chen, X., Yang, Q., Si, C. L., Wang, Z., Huo, D., Hong, Y., et al. (2016). Recovery of oligosaccharides from prehydrolysis liquors of poplar by microfiltration/ultrafiltration membranes and anion exchange resin. *ACS Sustain. Chem. Eng.* 4, 937–943. doi: 10.1021/acssuschemeng.5b01029
- Chio, C., Sain, M., and Qin, W. (2019). Lignin utilization: a review of lignin depolymerization from various aspects. *Renew. Sustain. Energy Rev.* 107, 232–249. doi: 10.1016/j.rser.2019.03.008
- Dai, L., Ma, M. S., Xu, J. K., Si, C. L., Wang, X. H., Liu, Z., et al. (2020). All-lignin-based hydrogel with fast pH-stimuli responsiveness for mechanical switching and actuation. *Chem. Mater.* 32, 4324–4330. doi: 10.1021/acs.chemmater.0c01198
- Dai, L., Zhu, W., Lu, J., Kong, F., Si, C. L., and Ni, Y. (2019). A lignin-containing cellulose hydrogel for lignin fractionation. *Green Chem.* 21, 5222–5230. doi: 10.1039/c9gc01975h
- Dai, Z., Ren, P. G., He, W. W., Hou, X., Ren, F., Zhang, Q., et al. (2020). Boosting the electrochemical performance of nitrogen-oxygen co-doped carbon nanofibers based supercapacitors through esterification of lignin precursor. *Renew. Energy* 162, 613–623. doi: 10.1016/j.renene.2020.07.152
- Decostanzi, M., Auvergne, R., Boutevin, B., and Caillol, S. (2019). Biobased phenol and furan derivative coupling for the synthesis of functional monomers. *Green Chem.* 21, 724–747. doi: 10.1039/c8gc03541e
- Deuss, P. J., Scott, M., Tran, F., Westwood, N. J., de Vries, J. G., and Barta, K. (2015). Aromatic monomers by in situ conversion of reactive intermediates in the acid-catalyzed depolymerization of lignin. *J. Am. Chem. Soc.* 137, 7456–7467. doi: 10.1021/jacs.5b03693
- Dong, H. L., Li, M., Jin, Y. C., Wu, Y., Huang, C. X., and Yang, J. L. (2020). Preparation of graphene-like porous carbons with enhanced thermal conductivities from lignin nano-particles by combining hydrothermal carbonization and pyrolysis. *Front. Energy Res.* 8:148. doi: 10.3389/fenrg.2020.00148
- Du, H., Liu, W., Zhang, M., Si, C., Zhang, X., and Li, B. (2019). Cellulose nanocrystals and cellulose nanofibrils based hydrogels for biomedical applications. *Carbohydr. Polym.* 209, 130–144. doi: 10.1016/j.carbpol.2019.01.020
- El Mansouri, N. E., and Salvado, J. (2006). Structural characterization of technical lignins for the production of adhesives: application to lignosulfonate, kraft, soda-anthraquinone, organosolv and ethanol process lignins. *Ind. Crops Prod.* 24, 8–16. doi: 10.1016/j.indcrop.2005.10.002
- Figueiredo, P., Ferro, C., Kemell, M., Liu, Z., Kiriazis, A., Lintinen, K., et al. (2017). Functionalization of carboxylated lignin nanoparticles for targeted and pH-responsive delivery of anticancer drugs. *Nanomedicine* 12, 2581–2596. doi: 10.2217/nnm-2017-0219
- Gan, L. H., and Pan, X. J. (2019). Phenol-enhanced depolymerization and activation of kraft lignin in alkaline medium. *Ind. Eng. Chem. Res.* 58, 7794–7800. doi: 10.1021/acs.iecr.9b01147
- Gao, C., Xiao, L. P., Zhou, J. H., Wang, H. S., Zhai, S. R., and An, Q. D. (2021). Immobilization of nanosilver onto glycine modified lignin hydrogel composites for highly efficient p-nitrophenol hydrogenation. *Chem. Eng. J.* 403:126370. doi: 10.1016/j.cej.2020.126370
- Garcia Calvo-Flores, F., and Dobado, J. A. (2010). Lignin as renewable raw material. *Chemsuschem* 3, 1227–1235. doi: 10.1002/cssc.201000157

- Garcia-Mateos, F. J., Cordero-Lanzac, T., Berenguer, R., Morallon, E., Cazorla-Amoros, D., Rodriguez-Mirasol, J., et al. (2017). Lignin-derived Pt supported carbon (submicron) fiber electrocatalysts for alcohol electro-oxidation. *Appl. Catal. B Environ.* 211, 18–30. doi: 10.1016/j.apcatb.2017.04.008
- Garcia-Mateos, F. J., Ruiz-Rosas, R., Rosas, J. M., Rodriguez-Mirasol, J., and Cordero, T. (2019). Controlling the composition, morphology, porosity, and surface chemistry of lignin-based electrospun carbon materials. *Front. Mater.* 6:114. doi: 10.3389/fmats.2019.00114
- Guo, K., Gao, B., Yue, Q., Xu, X., Li, R., and Shen, X. (2018). Characterization and performance of a novel lignin-based flocculant for the treatment of dye wastewater. *Int. Biodeterior. Biodegradation* 133, 99–107. doi: 10.1016/j.ibiod.2018.06.015
- Han, X., Lv, Z., Ran, F., Dai, L., Li, C., and Si, C. L. (2021). Green and stable piezoresistive pressure sensor based on lignin-silver hybrid nanoparticles/polyvinyl alcohol hydrogel. *Int. J. Biol. Macromol.* 176, 78–86. doi: 10.1016/j.ijbiomac.2021.02.055
- He, S., Shi, G. B., Xiao, H., Sun, G. X., Shi, Y. J., Chen, G. Y., et al. (2021). Self S-doping activated carbon derived from lignin-based pitch for removal of gaseous benzene. *Chem. Eng. J.* 410:128286. doi: 10.1016/j.cej.2020.12.8286
- Hochegger, M., Trimmel, G., Cottyn-Boitte, B., Cezard, L., Majira, A., Schober, S., et al. (2019). Influence of base-catalyzed organosolv fractionation of larch wood sawdust on fraction yields and lignin properties. *Catalysts* 9:20. doi: 10.3390/catal9120996
- Huang, C. X., Dong, H. L., Zhang, Z. P., Bian, H. Y., and Yong, Q. (2020). Procuring the nano-scale lignin in prehydrolyzate as ingredient to prepare cellulose nanofibril composite film with multiple functions. *Cellulose* 27, 9355–9370. doi: 10.1007/s10570-020-03427-9
- Huang, C. X., He, J., Narron, R., Wang, Y. H., and Yong, Q. (2017). Characterization of kraft lignin fractions obtained by sequential ultrafiltration and their potential application as a biobased component in blends with polyethylene. *ACS Sustain. Chem. Eng.* 5, 11770–11779. doi: 10.1021/acssuschemeng.7b03415
- Jiao, G.-J., Ma, J., Li, Y., Jin, D., Guo, Y., Zhou, J., et al. (2021). Enhanced adsorption activity for phosphate removal by functional lignin-derived carbon-based adsorbent: optimization, performance and evaluation. *Sci. Total Environ.* 761:143217. doi: 10.1016/j.scitotenv.2020.14.3217
- Jin, C., Song, W., Liu, T., Xin, J., Hiscox, W. C., Zhang, J., et al. (2018). Temperature and pH responsive hydrogels using methacrylated lignosulfonate cross-linker: synthesis, characterization, and properties. *ACS Sustain. Chem. Eng.* 6, 1763–1771. doi: 10.1021/acssuschemeng.7b03158
- Kang, C., Huang, Y., Yang, H., Yan, X. F., and Chen, Z. P. (2020). A review of carbon dots produced from biomass wastes. *Nanomaterials* 10:2316. doi: 10.3390/nano10112316
- Kazzaz, A. E., Feizi, Z. H., and Fatehi, P. (2019). Grafting strategies for hydroxy groups of lignin for producing materials. *Green Chem.* 21, 5714–5752. doi: 10.1039/c9gc02598g
- Li, J. J., Zhang, J. Z., Zhang, S. F., Gao, Q., Li, J. Z., and Zhang, W. (2018). Alkali lignin depolymerization under eco-friendly and cost-effective NaOH/urea aqueous solution for fast curing bio-based phenolic resin. *Ind. Crops Prod.* 120, 25–33. doi: 10.1016/j.indcrop.2018.04.027
- Li, N., Hu, Y. J., Bian, J., Li, M. F., Hao, X., Peng, F., et al. (2020). Enhanced mechanical performance of xylan-based composite hydrogel via chain extension and semi-interpenetrating networks. *Cellulose* 27, 4407–4416. doi: 10.1007/s10570-020-03080-2
- Li, S. X., Li, M. F., Bian, J., Wu, X. F., Peng, F., and Ma, M. G. (2019). Preparation of organic acid lignin submicrometer particle as a natural broad-spectrum photo-protection agent. *Int. J. Biol. Macromol.* 132, 836–843. doi: 10.1016/j.ijbiomac.2019.03.177
- Li, T., and Takkellapati, S. (2018). The current and emerging sources of technical lignins and their applications. *Biofuel. Bioprod. Biorefin.* 12, 756–787. doi: 10.1002/bbb.1913
- Li, X., Xu, R., Yang, J., Nie, S., Liu, D., Liu, Y., et al. (2019). Production of 5-hydroxymethylfurfural and levulinic acid from lignocellulosic biomass and catalytic upgradation. *Ind. Crops Prod.* 130, 184–197. doi: 10.1016/j.indcrop.2018.12.082
- Li, Y. J., Li, F., Yang, Y., Ge, B. C., and Meng, F. Z. (2021). Research and application progress of lignin-based composite membrane. *J. Polym. Eng.* 41, 245–258. doi: 10.1515/polyeng-2020-0268
- Li, Y., Wu, M., Wang, B., Wu, Y., Ma, M. G., and Zhang, X. (2016). Synthesis of magnetic lignin-based hollow microspheres: a highly adsorptive and reusable adsorbent derived from renewable resources. *ACS Sustain. Chem. Eng.* 4, 5523–5532. doi: 10.1021/acssuschemeng.6b01244
- Lievonen, M., Valle-Delgado, J. J., Mattinen, M. L., Hult, E. L., Lintinen, K., Kostianinen, M. A., et al. (2016). A simple process for lignin nanoparticle preparation. *Green Chem.* 18, 1416–1422. doi: 10.1039/c5gc01436k
- Liu, H., Xu, T., Liu, K., Zhang, M., Liu, W., Li, H., et al. (2021). Lignin-based electrodes for energy storage application. *Ind. Crops Prod.* 165:113425. doi: 10.1016/j.indcrop.2021.113425
- Liu, K., Du, H., Zheng, T., Liu, H., Zhang, M., Zhang, R., et al. (2021). Recent advances in cellulose and its derivatives for oilfield applications. *Carbohydr. Polym.* 259:117740. doi: 10.1016/j.carbpol.2021.117740
- Liu, R., Dai, L., Xu, C., Wang, K., Zheng, C., and Si, C. (2020). Lignin-based micro- and nanomaterials and their composites in biomedical applications. *ChemSusChem* 13, 4266–4283. doi: 10.1002/cssc.202000783
- Liu, S., and Ma, M. G. (2020). Lignin-derived nitrogen-doped polyacrylonitrile/polyaniline carbon nanofibers by electrospun method for energy storage. *Ionics* 26, 4651–4660. doi: 10.1007/s11581-020-03603-8
- Liu, W., Du, H., Zhang, M., Liu, K., Liu, H., Xie, H., et al. (2020). Bacterial cellulose-based composite scaffolds for biomedical applications: a review. *ACS Sustain. Chem. Eng.* 8, 7536–7562. doi: 10.1021/acssuschemeng.0c00125
- Liu, W., Du, H., Liu, K., Liu, H., Xie, H., Si, C., et al. (2021). Sustainable preparation of cellulose nanofibrils via choline chloride-citric acid deep eutectic solvent pretreatment combined with high-pressure homogenization. *Carbohydr. Polym.* 267:118220. doi: 10.1016/j.carbpol.2021.118220
- Liu, Y. J., Cao, W. T., Ma, M. G., and Wan, P. B. (2017). Ultrasensitive wearable soft strain sensors of conductive, self-healing, and elastic hydrogels with synergistic “soft and hard” hybrid networks. *ACS Appl. Mater. Interfaces* 9, 25559–25570. doi: 10.1021/acsmi.7b07639
- Luis Espinoza-Acosta, J., Torres-Chavez, P. I., Olmedo-Martinez, J. L., Vega-Rios, A., Flores-Gallardo, S., and Armando Zaragoza-Contreras, E. (2018). Lignin in storage and renewable energy applications: a review. *J. Energy Chem.* 27, 1422–1438. doi: 10.1016/j.jechem.2018.02.015
- Ma, C., Yuan, Q., Du, H., Ma, M. G., Si, C., and Wan, P. (2020). Multiresponsive MXene (Ti₃C₂T_x)-decorated textiles for wearable thermal management and human motion monitoring. *ACS Appl. Mater. Interfaces*, 12, 34226–34234. doi: 10.1021/acsmi.0c10750
- Ma, C. Y., Gao, X., Peng, X. P., Gao, Y. F., Liu, J., Wen, J. L., et al. (2021a). Microwave-assisted deep eutectic solvents (DES) pretreatment of control and transgenic poplars for boosting the lignin valorization and cellulose bioconversion. *Ind. Crops Prod.* 164:113415. doi: 10.1016/j.indcrop.2021.113415
- Ma, C., Mei, X., Fan, Y., and Zhang, Z. (2018). Oxidative depolymerization of kraft lignin and its application in the synthesis of lignin-phenol-formaldehyde resin. *Bioresources* 13, 1223–1234. doi: 10.15376/biores.13.1.1223-1234
- Ma, C., Ma, M. G., Si, C., Ji, X. X., and Wang, P. (2021b). Flexible MXene-based composites for wearable devices. *Adv. Funct. Mater.* 2009524. doi: 10.1002/adfm.202009524
- Ma, C., Wu, L. Q., Dirican, M., Cheng, H., Li, J. J., Song, Y., et al. (2021c). ZnO-assisted synthesis of lignin-based ultra-fine microporous carbon nanofibers for supercapacitors. *J. Colloid Interface Sci.* 586, 412–422. doi: 10.1016/j.jcis.2020.10.105
- Meng, L. Y., Ma, M. G., and Ji, X. X. (2019). Preparation of lignin-based carbon materials and its application as a sorbent. *Materials* 12:1111. doi: 10.3390/ma12071111
- Meng, Y., Lu, J., Cheng, Y., Li, Q., and Wang, H. (2019). Lignin-based hydrogels: a review of preparation, properties, and application. *Int. J. Biol. Macromol.* 135, 1006–1019. doi: 10.1016/j.ijbiomac.2019.05.198
- Naseem, A., Tabasum, S., Zia, K. M., Zuber, M., Ali, M., and Noreen, A. (2016). Lignin-derivatives based polymers, blends and composites: a review. *Int. J. Biol. Macromol.* 93, 296–313. doi: 10.1016/j.ijbiomac.2016.08.030
- Nguyen, N. A., Barnes, S. H., Bowland, C. C., Meek, K. M., Littrell, K. C., Keum, J. K., et al. (2018a). A path for lignin valorization via additive manufacturing of

- high-performance sustainable composites with enhanced 3D printability. *Sci. Adv.* 4:eaat4967. doi: 10.1126/sciadv.aat4967
- Nguyen, N. A., Bowland, C. C., and Naskar, A. K. (2018b). General method to improve 3D-printability and inter-layer adhesion in lignin-based composites. *Appl. Mater. Today* 12, 138–152. doi: 10.1016/j.apmt.2018.03.009
- Pang, B., Cao, X. F., Sun, S. N., Wang, X. L., Wen, J. L., Lam, S. S., et al. (2020). The direct transformation of bioethanol fermentation residues for production of high-quality resins. *Green Chem.* 22, 439–447. doi: 10.1039/c9gc03568k
- Pang, B., Yang, S., Fang, W., Yuan, T. Q., Argyropoulos, D. S., and Sun, R. C. (2017). Structure-property relationships for technical lignins for the production of lignin-phenol-formaldehyde resins. *Ind. Crops Prod.* 108, 316–326. doi: 10.1016/j.indcrop.2017.07.009
- Pei, W. H., Shang, W. Q., Liang, C., Jiang, X., Huang, C. X., and Yong, Q. (2020). Using lignin as the precursor to synthesize Fe₃O₄@lignin composite for preparing electromagnetic wave absorbing lignin-phenol-formaldehyde adhesive. *Ind. Crops Prod.* 154:112634. doi: 10.1016/j.indcrop.2020.11.2638
- Qian, Y., Zhou, Y., Lu, M., Guo, X., Yang, D., Lou, H., et al. (2021). Direct construction of catechol lignin for engineering long-acting conductive, adhesive, and UV-blocking hydrogel bioelectronics. *Small Methods* 5:2001311. doi: 10.1002/smt.202001311
- Ragauskas, A. J., Beckham, G. T., Biddy, M. J., Chandra, R., Chen, F., Davis, M. F., et al. (2014). Lignin valorization: improving lignin processing in the biorefinery. *Science* 344:1246843. doi: 10.1126/science.1246843
- Saha, D., Li, Y., Bi, Z., Chen, J., Keum, J. K., Hensley, D. K., et al. (2014). Studies on supercapacitor electrode material from activated lignin-derived mesoporous carbon. *Langmuir* 30, 900–910. doi: 10.1021/la404112m
- Sen, S., Patil, S., and Argyropoulos, D. S. (2015). Thermal properties of lignin in copolymers, blends, and composites: a review. *Green Chem.* 17, 4862–4887. doi: 10.1039/c5gc01066g
- Shen, X. J., Wen, J. L., Mei, Q. Q., Chen, X., Sun, D., Yuan, T. Q., et al. (2019). Facile fractionation of lignocelluloses by biomass-derived deep eutectic solvent (DES) pretreatment for cellulose enzymatic hydrolysis and lignin valorization. *Green Chem.* 21, 275–283. doi: 10.1039/c8gc03064b
- Shi, Z. J., and Ma, M. G. (2019). Synthesis, structure, and applications of lignin-based carbon materials: a review. *Sci. Adv. Mater.* 11, 18–32. doi: 10.1166/sam.2019.3382
- Si, C. (2019). The Development of lignocellulosic biomass in medicinal applications. *Curr. Med. Chem.* 26, 2408–2409. doi: 10.2174/092986732614190724160641
- Solt, P., Rossiger, B., Konnerth, J., and van Herwijnen, H. W. G. (2018). Lignin phenol formaldehyde resoles using base-catalysed depolymerized kraft lignin. *Polymers* 10:1162. doi: 10.3390/polym10101162
- Suhas, Carrott, P. J. M., and Carrott, M. M. L. R. (2007). Lignin- from natural adsorbent to activated carbon: a review. *Bioresour. Technol.* 98, 2301–2312. doi: 10.1016/j.biortech.2006.08.008
- Sun, S. L., Wen, J. L., Ma, M. G., and Sun, R. C. (2014). Structural elucidation of sorghum lignins from an integrated biorefinery process based on hydrothermal and alkaline treatments. *J. Agric. Food Chem.* 62, 8120–8128. doi: 10.1021/jf501669r
- Sun, Y. C., Liu, X. N., Wang, T. T., Xue, B. L., and Sun, R. C. (2019). Green process for extraction of lignin by the microwave-assisted ionic liquid approach: toward biomass biorefinery and lignin characterization. *ACS Sustain. Chem. Eng.* 7, 13062–13072. doi: 10.1021/acsschemeng.9b02166
- Sutton, J. T., Rajan, K., Harper, D. P., and Chmely, S. C. (2018). Lignin-containing photoactive resins for 3D printing by stereolithography. *ACS Appl. Mater. Interfaces* 10, 36456–36463. doi: 10.1021/acsmi.8b13031
- Thakur, V. K., and Thakur, M. K. (2015). Recent advances in green hydrogels from lignin: a review. *Int. J. Biol. Macromol.* 72, 834–847. doi: 10.1016/j.ijbiomac.2014.09.044
- Upton, B. M., and Kasko, A. M. (2016). Strategies for the conversion of lignin to high-value polymeric materials: review and perspective. *Chem. Rev.* 116, 2275–2306. doi: 10.1021/acs.chemrev.5b00345
- Venkatesagowda, B., and Dekker, R. F. H. (2020). Enzymatic demethylation of Kraft lignin for lignin-based phenol-formaldehyde resin applications. *Biomass Convers. Biorefin.* 10, 203–225. doi: 10.1007/s13399-019-00407-3
- Vishtal, A., and Kraslawski, A. (2011). Challenges in industrial applications of technical lignins. *Bioresources* 6, 3547–3568.
- Wan, X., Shen, F., Hu, J., Huang, M., Zhao, L., Zeng, Y., et al. (2021). 3-D hierarchical porous carbon from oxidized lignin by one-step activation for high-performance supercapacitor. *Int. J. Biol. Macromol.* 180, 51–60. doi: 10.1016/j.ijbiomac.2021.03.048
- Wang, B., Wang, H. M., Sun, D., Yuan, T. Q., Song, G. Y., Shi, Q., et al. (2020a). Chemosynthesis, characterization and application of lignin-based flocculants with tunable performance prepared by short-wavelength ultraviolet initiation. *Ind. Crops Prod.* 157:112897. doi: 10.1016/j.indcrop.2020.11.2897
- Wang, B., Wang, S. F., Lam, S. S., Sonne, C., Yuan, T. Q., Song, G. Y., et al. (2020b). A review on production of lignin-based flocculants: sustainable feedstock and low carbon footprint applications. *Renew. Sustain. Energy Rev.* 134:110384. doi: 10.1016/j.rser.2020.110384
- Wang, G., Liu, X., Zhang, J., Sui, W., Jang, J., and Si, C. L. (2018). One-pot lignin depolymerization and activation by solid acid catalytic phenolation for lightweight phenolic foam preparation. *Ind. Crops Prod.* 124, 216–225. doi: 10.1016/j.indcrop.2018.07.080
- Wang, H., Du, H., Liu, K., Liu, H., Xu, T., Zhang, S., et al. (2021). Sustainable preparation of bifunctional cellulose nanocrystals via mixed H₂SO₄/formic acid hydrolysis. *Carbohydr. Polym.* 266:118107. doi: 10.1016/j.carbpol.2021.118107
- Wang, S. R., Wang, K. G., Liu, Q., Gu, Y. L., Luo, Z. Y., Cen, K. F., et al. (2009). Comparison of the pyrolysis behavior of lignins from different tree species. *Biotechnol. Adv.* 27, 562–567. doi: 10.1016/j.biotechadv.2009.04.010
- Witzler, M., Alzageem, A., Bergs, M., El Khaldi-Hansen, B., Klein, S. E., Hielscher, D., et al. (2018). Lignin-derived biomaterials for drug release and tissue engineering. *Molecules* 23:1885. doi: 10.3390/molecules23081885
- Woermeyer, K., Ingram, T., Saake, B., Brunner, G., and Smirnova, I. (2011). Comparison of different pretreatment methods for lignocellulosic materials. Part II: influence of pretreatment on the properties of rye straw lignin. *Bioresour. Technol.* 102, 4157–4164. doi: 10.1016/j.biortech.2010.11.063
- Xi, Y. B., Yang, D. J., Lou, H. M., Gong, Y. Y., Yi, C. H., Lyu, G. J., et al. (2021). Designing the effective microstructure of lignin-based porous carbon substrate to inhibit the capacity decline for SnO₂ anode. *Ind. Crops Prod.* 161:113179. doi: 10.1016/j.indcrop.2020.11.3179
- Xiong, S. J., Bo, P., Zhou, S. J., Li, M. K., Yang, S., Wang, Y. Y., et al. (2020). Economically competitive biodegradable PBAT/lignin composites: effect of lignin methylation and compatibilizer. *ACS Sustain. Chem. Eng.* 8, 5338–5346. doi: 10.1021/acsschemeng.0c00789
- Xu, J., Li, C., Dai, L., Xu, C., Zhong, Y., Yu, F., et al. (2020). Biomass fractionation and lignin fractionation towards lignin valorization. *ChemSusChem* 13, 4284–4295. doi: 10.1002/cssc.202001491
- Xu, J., Shao, Z., Li, Y., Dai, L., Wang, Z., and Si, C. (2021). A flow-through reactor for fast fractionation and production of structure-preserved lignin. *Ind. Crops Prod.* 164:113350. doi: 10.1016/j.indcrop.2021.11.3350
- Xu, Q. Q., Wang, X., Cheng, J., Zhang, L., He, F., and Xie, H. B. (2020). Self-template/activation nitrogen-doped porous carbon materials derived from lignosulfonate-based ionic liquids for high performance supercapacitors. *RSC Adv.* 10, 36504–36513. doi: 10.1039/d0ra06821g
- Xu, X. Y., Ray, R., Gu, Y. L., Ploehn, H. J., Gearheart, L., Raker, K., et al. (2004). Electrophoretic analysis and purification of fluorescent single-walled carbon nanotube fragments. *J. Am. Chem. Soc.* 126, 12736–12737. doi: 10.1021/ja040082h
- Yang, X., Xie, H., Du, H., Zhang, X., Zou, Z., Zou, Y., et al. (2019). Facile extraction of the thermally stable and dispersible cellulose nanocrystals with high yield via a green and recyclable FeCl₃-catalyzed deep eutectic solvent system. *ACS Sustain. Chem. Eng.* 7, 7200–7208. doi: 10.1021/acsschemeng.9b00209
- Yang, X. X., Guo, Y. Z., Liang, S., Hou, S. Y., Chu, T. T., Ma, J. L., et al. (2020). Preparation of sulfur-doped carbon quantum dots from lignin as a sensor to detect Sudan I in an acidic environment. *J. Mater. Chem. B* 8, 10788–10796. doi: 10.1039/d0tb00125b
- Yu, O., and Kim, K. H. (2020). Lignin to materials: a focused review on recent novel lignin applications. *Appl. Sci.* 10:4626. doi: 10.3390/app10134626
- Zhang, B. H., Liu, Y. J., Ren, M. Q., Li, W. T., Zhang, X., Vajtai, R., et al. (2019). Sustainable synthesis of bright green fluorescent nitrogen-doped carbon quantum dots from alkali lignin. *ChemSuschem* 12, 4202–4210. doi: 10.1002/cssc.201901693

- Zhang, W., Yin, J., Lin, Z., Lin, H., Lu, H., Wang, Y., et al. (2015a). Facile preparation of 3D hierarchical porous carbon from lignin for the anode material in lithium ion battery with high rate performance. *Electrochim. Acta* 176, 1136–1142. doi: 10.1016/j.electacta.2015.08.001
- Zhang, W., Zhao, M., Liu, R., Wang, X., and Lin, H. (2015b). Hierarchical porous carbon derived from lignin for high performance supercapacitor. *Colloids Surf. A Physicochem. Eng. Asp.* 484, 518–527. doi: 10.1016/j.colsurfa.2015.08.030
- Zhang, Y. W., Yuan, B., Zhang, Y. Q., Cao, Q. P., Yang, C., Li, Y., et al. (2020). Biomimetic lignin/poly(ionic liquids) composite hydrogel dressing with excellent mechanical strength, self-healing properties, and reusability. *Chem. Eng. J.* 400:125984. doi: 10.1016/j.cej.2020.125984
- Zhao, S., and Abu-Omar, M. M. (2021). Materials based on technical bulk lignin. *ACS Sustain. Chem. Eng.* 9, 1477–1493. doi: 10.1021/acssuschemeng.0c08882
- Zheng, L., Yu, P., Zhang, Y., Wang, P., Yan, W., Guo, B., et al. (2021). Evaluating the bio-application of biomacromolecule of lignin-carbohydrate complexes (LCC) from wheat straw in bone metabolism via ROS scavenging. *Int. J. Biol. Macromol.* 176, 13–25. doi: 10.1016/j.ijbiomac.2021.01.103
- Zhu, J. D., Yan, C. Y., Zhang, X., Yang, C., Jiang, M. J., and Zhang, X. W. (2020). A sustainable platform of lignin: from bioresources to materials and their applications in rechargeable batteries and supercapacitors. *Prog. Energy Combust. Sci.* 76:100788. doi: 10.1016/j.pecs.2019.100788

Conflict of Interest: The authors declare that the research was conducted in the absence of any commercial or financial relationships that could be construed as a potential conflict of interest.

Copyright © 2021 Ma, Kim, Liu, Ma, Choi and Si. This is an open-access article distributed under the terms of the Creative Commons Attribution License (CC BY). The use, distribution or reproduction in other forums is permitted, provided the original author(s) and the copyright owner(s) are credited and that the original publication in this journal is cited, in accordance with accepted academic practice. No use, distribution or reproduction is permitted which does not comply with these terms.



Genetic Diversity, Chemical Components, and Property of Biomass *Paris polyphylla* var. *yunnanensis*

Nong Zhou^{1*}, Lingfeng Xu¹, Sun-Min Park², Ming-Guo Ma^{1,3*}, Sun-Eun Choi^{2*} and Chuanling Si^{4*}

OPEN ACCESS

Edited by:

Xin Zhou,
Nanjing Forestry University, China

Reviewed by:

Xiaoju Wang,
Åbo Akademi University, Finland
Wen Zeng,
Chongqing University, China

*Correspondence:

Nong Zhou
erhaizn@126.com
Ming-Guo Ma
mg_ma@bjfu.edu.cn
Sun-Eun Choi
oregonin@kangwon.ac.kr
Chuanling Si
sichli@tust.edu.cn

Specialty section:

This article was submitted to
Bioprocess Engineering,
a section of the journal
Frontiers in Bioengineering and
Biotechnology

Received: 24 May 2021

Accepted: 22 June 2021

Published: 22 July 2021

Citation:

Zhou N, Xu L, Park S-M, Ma M-G,
Choi S-E and Si C (2021) Genetic
Diversity, Chemical Components,
and Property of Biomass *Paris
polyphylla* var. *yunnanensis*.
Front. Bioeng. Biotechnol. 9:713860.
doi: 10.3389/fbioe.2021.713860

¹ Chongqing Engineering Laboratory of Green Planting and Deep Processing of Famous-Region Drug in the Three Gorges Reservoir Region, College of Biology and Food Engineering, Chongqing Three Gorges University, Chongqing, China, ² Department of Forest Biomaterials Engineering, College of Forest and Environmental Sciences, Kangwon National University, Chuncheon, South Korea, ³ Beijing Key Laboratory of Lignocellulosic Chemistry, Research Center of Biomass Clean Utilization, Engineering Research Center of Forestry Biomass Materials and Bioenergy, College of Materials Science and Technology, Beijing Forestry University, Beijing, China, ⁴ Tianjin Key Laboratory of Pulp and Paper, Tianjin University of Science and Technology, Tianjin, China

Paris polyphylla var. *yunnanensis* is a kind of biomass resource, which has important medicinal and economical values with a huge market. This review article aims to summarize the recent development of biomass *P. polyphylla* var. *yunnanensis*. The genetic diversity and chemical components of biomass *P. polyphylla* var. *yunnanensis* were reviewed based on the literature. Both the genetic diversity and genetic structure of biomass *P. polyphylla* var. *yunnanensis* were compared by using molecular marker technologies. All the extraction processes, harvest time, and drying methods on the chemical components were summarized in detail. The differences of arbuscular mycorrhizal fungi on the infection rate, diosgenin content, microorganisms, enzyme activities, rhizospheric environment, and endogenous hormones were discussed. This review article is beneficial for the applications of biomass *P. polyphylla* var. *yunnanensis* as a biomass resource in the biomedical field.

Keywords: *Paris polyphylla* var. *yunnanensis*, development, genetic diversity, molecular markers, chemical components

INTRODUCTION

Paris polyphylla is a perennial herb and has various properties including clearing away heat, detoxification, detumescence, pain relief, and calming convulsion, which is widely used in the furuncle, carbuncle, sore throat, snakebite, tumbling pain, and convulsion fields. It was reported that *P. polyphylla* is mainly distributed in the tropics of Europe and Asia (Liang and Victor, 2000). In China, it is mainly distributed in Sichuan Province, Guizhou Province, Yunnan Province, Guangxi Province, Guangdong Province, Jiangxi Province, Fujian Province, etc. *P. polyphylla* var.

yunnanensis is located in Yunnan Province, Guizhou Province, Sichuan Province, and Chongqing city (Liu et al., 2015). *P. polyphylla* var. *yunnanensis* mainly contains chemical constituents of steroidal saponins, β -ecdysone, polysaccharide, flavone glycoside, and amino acids, which have important medicinal and economical values. Research shows that *P. polyphylla* var. *yunnanensis* has antibacterial and antitussive effects. In addition, the saponins of *P. polyphylla* var. *yunnanensis* have anticancer, analgesic, and sedative properties. The Chinese Pharmacopoeia (2015 edition) collected *P. polyphylla* var. *yunnanensis* as an important medicinal plant in 81 kinds of Chinese patent medicines, such as “Yunnan Baiyao,” “Gongxuening Capsule,” and so on (National Pharmacopoeia Commission, 2015).

With the rapid development of the Chinese traditional medicine industry, the demand for *P. polyphylla* var. *yunnanensis* as a raw material increased greatly. The wild *P. polyphylla* var. *yunnanensis* does not meet the requirements. More importantly, it takes 8–10 years from planting to harvesting and utilization of *P. polyphylla* var. *yunnanensis*. The price of *P. polyphylla* var. *yunnanensis* increased dramatically, resulting in the scarcity of the species. It was reported that more than 1,000 tons of *P. polyphylla* var. *yunnanensis* was utilized every year and about 80% of the wild *P. polyphylla* var. *yunnanensis* distributed in China has been utilized. Currently, wild resources cannot meet the demand of the market. The scarcity of *P. polyphylla* var. *yunnanensis* resources may become a bottleneck, restricting the sustainable development of the related pharmaceutical industry. Therefore, the development of artificial planting is an important choice to solve the shortage of *P. polyphylla* var. *yunnanensis* resources (Cunningham et al., 2018). In addition, the current research is about the total saponins of *P. polyphylla* var. *yunnanensis*. The basic research of *P. polyphylla* var. *yunnanensis* needs to be further explored in detail. It is necessary to separate and purify the active monomer components and study their activity to develop more valuable new drugs (Chen et al., 2016; Yang et al., 2019, 2021; Chen et al., 2020a; Ma et al., 2020; Wang et al., 2021). In the previous article, Negi et al. (2014) reviewed the developmental prospects of chemistry and biology of *P. polyphylla*. After that, Cunningham et al. (2018) assessed the scale of *P. polyphylla* trade, reviewing evidence about the impacts of wild harvest on *P. polyphylla* populations and the role of cultivation as an alternative to wild harvest. More recently, Pei et al. (2020) reviewed medicinal records of ethnic minorities for *P. polyphylla* in China and indicated the applications of authentic evaluation techniques of ethnobotanical medicinal plant of genus *P. polyphylla*.

The purpose of this review article is to introduce the development and problem of *P. polyphylla* var. *yunnanensis* based on previous research. The article analyzed the genetic diversity and structure of wild populations and cultivated populations of *P. polyphylla* var. *yunnanensis* and compared the different molecular markers methods. Then, the effects of fungi on the properties of *P. polyphylla* var. *yunnanensis* were also reviewed. Finally, the problems and suggestions were given on the *P. polyphylla* var. *yunnanensis* based on our present knowledge. It was expected that this review article favored the applications of *P. polyphylla* var. *yunnanensis* in the natural medicine field.

More research should be focused on the artificial planting, genetic diversity, structure, properties, and applications of *P. polyphylla* var. *yunnanensis*.

THE POPULATION GENETICS OF *Paris polyphylla* var. *yunnanensis*

In the literature, *P. polyphylla* var. *yunnanensis* was first recorded in Shennong's Herbal Classic of Materia Medica under the name of “Zaoxiu.” After that, it was recorded in famous books, such as “Supplementary Records of Famous Physicians,” “Tang Materia Medica,” “Rihuazi Materia Medica,” and so on, containing the contents of the morphology, growth environment, and properties of *P. polyphylla* var. *yunnanensis*.

There are many reports on the genetic diversity and genetic structure of *P. polyphylla* and its related species inside and outside the region (He et al., 2007; Yang et al., 2015; Zhao X.P. et al., 2020). A random amplified polymorphic DNA (RAPD) molecular marker was developed by Wiliam and Welsh in 1990 to detect DNA polymorphism by PCR. This research indicated the important applications of *P. polyphylla*. For example, Zhang et al. (2004) reported the genetic diversity of *P. polyphylla* var. *yunnanensis* from Yunnan, Guangxi, and Vietnam using RAPD molecular marker.

Simple sequence repeats (SSRs) molecular marker is a DNA molecular marker technology based on PCR. In He et al. (2007), the genetic diversity and genetic structure of cultivated and wild *P. polyphylla* were reported based on inter-simple sequence repeat (ISSR) molecular marker. It showed that the genetic diversity (polymorphism) of the cultivated population was higher than that of the wild population (0.153 vs. 0.151). The result indicated that the artificial planting was a realistic strategy for solving the shortage of *P. polyphylla* var. *yunnanensis* resource. In addition, the genetic diversity (polymorphism) of 62 individuals of *P. polyphylla* var. *yunnanensis* from Yunnan Province was explored based on SSRs molecular marker (Song et al., 2015). They developed 10 pairs of primers to provide a primer basis for the SSR marker of *P. polyphylla* var. *yunnanensis*. In Chen et al. (2017), the genetic diversity of 115 samples from 5 populations in Yunnan was analyzed based on simple sequence repeats (SSR) molecular marker. The results showed that the expected heterozygosity was 0.774 at the species level and 0.655 at the population level, respectively, indicating the high genetic diversity of *P. polyphylla* var. *yunnanensis*.

Amplified fragment length polymorphism (AFLP) molecular marker was a method for detecting DNA polymorphism developed by Vos et al. (1995) in Netherlands in 1995, which is a combination of RFLP and PCR. Li et al. (2018) used AFLP molecular marker to analyze the genetic diversity of *P. polyphylla* var. *yunnanensis* from 15 populations in Yunnan Province. Research group investigated the genetic diversity (polymorphism) and genetic structure of *P. polyphylla* var. *yunnanensis*, 15 wild populations, and 17 cultivated populations, based on AFLP molecular marker and cpDNA fragments (Huang Y. et al., 2019; Hu et al., 2014, 2016). According to the analysis of molecular variance (AMOVA), only 1.35% of genetic variation existed between wild and cultivated populations,

indicating that there was no obvious genetic differentiation between wild and cultivated populations, due to the relatively short history of the domestication of cultivated populations. The chloroplast gene, cpDNA fragment (trnL TRNF), was used to analyze the phylogeography of wild *P. polyphylla* var. *yunnanensis* (Zhao J.J. et al., 2020). The genetic structure of 17 cultivated populations showed mixed provenances in the cultivation base, leading to unstable quality. The cpDNA fragment (trnL TRNF) is a rapid, economic, and effective strategy to analyze the phylogeography of *P. polyphylla* var. *yunnanensis*.

A variety of molecular marker technologies have been developed rapidly, which were widely used in plant genetic research (Chen et al., 2020b; Liu H. et al., 2021a,b; Liu K. et al., 2021; Liu et al., 2021). Molecular marker technologies is used in the applications of the breeding and production of animals and plants, which mainly focus on gene mapping, assisted breeding, disease treatment, etc. The development of molecular marker technology is a hot topic in the field of molecular biology (An et al., 2019; Du et al., 2019, 2021; Li et al., 2019; Xu J. et al., 2021). With the rapid development of molecular biology theory, molecular marker technology will be developed with fast analysis speed, low cost, and more information (Ma et al., 2021a,b; Xu et al., 2020; Xu R. et al., 2021).

Yang et al. (2016) reported the bacterial strain, py1294(T), isolated from a root of *P. polyphylla* var. *yunnanensis* by using a polyphasic approach to clarify its taxonomic position. They indicated that the strain py1294(T) formed a well-supported clade with *Oceanobacillus damuensis* PT-20(T) (97.9% sequence similarity) within the genus *Oceanobacillus*. It obtained the DNA-DNA relatedness value of 29.7% between strain py1294(T) and *O. damuensis* PT-20(T). Jia et al. (2016) isolated two actinobacteria, designated strains NEAU-JM1(T) and NEAU-CL2(T), from volcanic sediment and the rhizosphere soil of *P. polyphylla*. They established the taxonomic positions of these strains and concluded these two species of the genus *Catellatospora*.

As early as Xuan et al. (2010) isolated fungal endophyte from *P. polyphylla* Smith var. *yunnanensis* and identified its antibacterial ability. Authors obtained 18 fungal endophytes, parasitizing the famous Chinese medicinal plant *P. polyphylla* Smith var. *yunnanensis*, and evaluating the effect of endophytes on the growth of human pathogenic microbes *in vitro* using disk diffusion assay. Then, Zhou et al. (2012) investigated the effects of fungal elicitors on the secondary metabolite steroidal saponin in *P. polyphylla* var. *yunnanensis*. There was selectivity between arbuscular mycorrhizal fungal and *P. polyphylla* var. *yunnanensis*, and *Glomus intraradice* was the most appropriate strain for inoculation of *P. polyphylla* var. *yunnanensis*. Recently, Wang Y. et al. (2020) investigated the effects of altitude on the community composition of endophytic fungal communities and the differentiation of endophytic microorganisms among different niches in *P. polyphylla*. The author also indicated that the structural variability in the rhizosphere fungal community was significantly lower than that in the endophytic communities, confirming the presence of niche differentiation among members of the endophytic microbial community.

There is a connection between the genetic and the fungal sections; however, there are few reports on this topic. Therefore,

more rapid attention should be paid on the connection between the genetic and the fungal sections of *P. polyphylla* var. *yunnanensis* in the near future.

THE CHEMICAL COMPONENTS OF *Paris polyphylla* var. *yunnanensis*

The polysaccharides have a variety of pharmacological and biological functions, such as antioxidant, antitumor, antiviral, immune regulation, and anti-inflammatory (Si et al., 2008a,b, 2009, 2013; Dai et al., 2020a,b). *P. polyphylla* var. *yunnanensis*, as an important plant polysaccharide, has attracted more attention in recent years (Jing et al., 2017; Shen et al., 2018). *P. polyphylla* has been reported to contain a variety of chemical components including daucosterol, polyphyllin D, beta-ecdysterone, Paris saponins I, II, V, VI, VII, H, dioscin, oligosaccharides, heptasaccharide, octasaccharide, triglofoenolide A, protogracillin, Paris yunnanosides G-J, padelaoside B, and pinnatasterone, which have biological properties, such as anticancerous, antitumor, cytotoxic, anthelmintic, antimicrobial, antiangiogenic, immunostimulating, contractile, and hemostatic (Negi et al., 2014; Liu et al., 2020a,b; Wang H. et al., 2020). There are many reports on the extraction and applications of polysaccharides, *P. polyphylla* var. *yunnanensis* (Huang et al., 2007; Chan et al., 2011; Wu et al., 2012; Qin et al., 2016).

As early as Zhou et al. (2003) investigated the heptasaccharide and octasaccharide isolated from *P. polyphylla* var. *yunnanensis* and their plant growth-regulatory activity. In Shen et al. (2014) reported the optimization of the extraction process and antioxidant activity of polysaccharides from the leaves of *P. polyphylla*. The monosaccharide components of *P. polyphylla* var. *yunnanensis* were obtained using the hydrolysis method at 110°C temperature for 6 h in 2 mol·L⁻¹ trifluoroacetic acid (Wang et al., 2019). The recoveries of five monosaccharide components were 92.38–99.98%. The polysaccharides of *P. polyphylla* var. *yunnanensis* were mainly composed of glucose, mannose, galactose, rhamnose, and arabinose, whose molar ratio in wild species was 219.22:28.23:1.83:1.44:1.00.

Research group extracted the polysaccharide of *P. polyphylla* var. *yunnanensis* through three different extraction processes, such as reflux extraction, hot water extraction, and ultrasonic-assisted extraction (Zhou et al., 2014). It was found that the *P. polyphylla* var. *yunnanensis* extracted by ultrasonic-assisted extraction method had the highest polysaccharide content of 24.32 mg g⁻¹. We also found the change content of diosgenin significantly in *P. polyphylla* var. *yunnanensis* at different harvest times (Zhou et al., 2010). It has been observed that the content was increased gradually from April to June, the highest content was from May to June, and the content was decreased sharply from June to July. The influence of the drying method on the diosgenin of *P. polyphylla* var. *yunnanensis* was also explored (Zhou et al., 2015b). It was found that the color changed from white to light brown and powdery using the drying at 35°C, natural shade drying, and sun-drying had good color, while the color changed from brown to dark brown and horny by those of other drying methods. Different drying methods had different effects on the diosgenin of *P. polyphylla* var. *yunnanensis*.

As early as Lee et al. (2005) investigated the effects of polyphyllin D, a steroidal saponin in *P. polyphylla*, on growth inhibition of human breast cancer cells and in xenograft. Then, Yan et al. (2009) confirmed anticancer activity of steroid saponins of *P. polyphylla* var. *yunnanensis* by both *in vitro* and *in vivo*. After that, Wang et al. (2010) investigated the anthelmintic activity of crude extracts and pure compounds from the rhizomes of *P. polyphylla*. In addition, steroidal saponins from the rhizome of *P. polyphylla* and their cytotoxic activities were also researched using two new furostanol saponins and one new spirostanol saponin isolated from the rhizome of *P. polyphylla* var. *yunnanensis*, together with 18 known steroidal saponins (Zhao et al., 2009; Hu et al., 2017, 2018). There was a report on the steroidal saponins with antimicrobial activity from stems and leaves of *P. polyphylla* var. *yunnanensis* (Qin et al., 2012). The effects of nine different drying methods on the content of total saponins in rhizomes of *P. polyphylla* var. *yunnanensis* and the differences in antioxidant activity were also studied (Zhang et al., 2016). The total saponin content of different drying methods was significantly different in rhizomes of *P. polyphylla* var. *yunnanensis*.

Four saponins were investigated in *P. polyphylla* var. *yunnanensis* with different growth years (Zhang et al., 2011). It was found that the content of saponins of *P. polyphylla* var. *yunnanensis* in 3-year-old herbs was lower than those in 4-year-old and 5-year-old herbs. The contents of nine steroidal saponins were reported in rhizomes and fibrous roots of *P. polyphylla* var. *yunnanensis* (Gu et al., 2020a). The quite different content of steroidal saponins in 32 samples of *P. polyphylla* var. *yunnanensis* was obtained from different areas. Most of them could detect nine kinds of steroidal saponins in rhizomes. The *P. polyphylla* var. *yunnanensis* had rich contents of saponins I and II and relatively low contents of saponins VI and dioscin. The effects of ultrasonic extraction and hot water extraction on the extraction of nucleoside from *P. polyphylla* var. *yunnanensis* were analyzed using rhizome as experimental materials and the total extraction amount of six nucleosides (cytidine, uridine, guanosine, thymidine, adenosine, and deoxyadenosine) as the index was analyzed, in which the extraction amount was determined by high-performance liquid chromatography (HPLC) (Yang et al., 2017). The results showed that the total extraction amount of six nucleosides from rhizomes of *P. polyphylla* var. *yunnanensis* by ultrasonic extraction was higher than that of the hot water extraction method. The total extraction amount of cytidine, uridine, guanosine, thymidine, adenosine, and deoxyadenosine from rhizomes of *P. polyphylla* var. *yunnanensis* was 1.422 mg g⁻¹, which was higher than the theoretical value of 1.343 mg g⁻¹.

The amino acids of *P. polyphylla* var. *yunnanensis* were investigated in 27 samples of *P. polyphylla* var. *yunnanensis* collected from Yunnan Province, Guizhou Province, and Sichuan Province (Gu et al., 2020b). The good linear relationship of 15 amino acids in fibrous roots of *P. polyphylla* var. *yunnanensis* was observed, among which the highest contents of aspartic acid and glutamic acid were found in all producing areas. The transplanting *P. polyphylla* var. *yunnanensis* had high contents of amino acids in fibrous roots compared with that of the wild *P. polyphylla* var. *yunnanensis*. The contents of

inorganic elements were investigated in both Yunnan Province and Guizhou Province (Yang et al., 2018). The good linear relationship of 14 inorganic elements and the average recovery rate of 90.81–109.73% was found. There are obvious differences among the mass fraction and composition structure ratio of 14 inorganic elements in *P. polyphylla* var. *yunnanensis* medicinal material from different places.

Based on the previous reports, it was found that the extraction processes, harvest time, drying methods, growth years, extraction methods, and other factors had an impact on the chemical components of *P. polyphylla* var. *yunnanensis*. More research should be developed on the chemical components of *P. polyphylla* var. *yunnanensis* in detail.

THE EFFECTS OF FUNGI ON THE CONTENT AND PROPERTIES OF *Paris Polyphylla* var. *Yunnanensis*

In the literature, the fungi were reported to play an important role in the contents and properties of *P. polyphylla* var. *yunnanensis* (Li et al., 2008; Huang et al., 2009; Liu et al., 2017). The effects of 28 arbuscular mycorrhizal fungi on the infection rate and diosgenin content of *P. polyphylla* var. *yunnanensis* were explored in sterilized soil (Wang et al., 2018). The results indicated that there was a good symbiotic relationship between *P. polyphylla* var. *yunnanensis* and arbuscular mycorrhizal fungi, and the significant increase in infection rate. More importantly, it was found that there was no significant difference between the diosgenin contents of *P. polyphylla* var. *yunnanensis* and the control group; however, it was observed a significant increase in diosgenin content of 41.40 mg g⁻¹ after treatment with Svi fungi. The effects of inoculation periods on growth and steroidal saponin content of *P. polyphylla* var. *yunnanensis* seedlings infected by arbuscular mycorrhizal fungi were investigated (Huang Y.P. et al., 2019). The strong infection rate of arbuscular mycorrhizal fungi in different inoculation periods, the increased protective enzyme activity, photosynthetic pigment, and soluble sugar content were found. The inoculation time had a certain influence on the growth and development of *P. polyphylla* var. *yunnanensis* seedlings infected by arbuscular mycorrhizal fungi and the saponins content of *P. polyphylla* var. *yunnanensis*. The effects of arbuscular mycorrhizal fungi on the number of microorganisms and enzyme activities in rhizosphere soil of *P. polyphylla* var. *yunnanensis* were investigated (Ou et al., 2016). One can observe that there was a certain degree of mutual selectivity between *P. polyphylla* var. *yunnanensis* and arbuscular mycorrhizal fungi. After the induction of arbuscular mycorrhizal fungi, the different arbuscular mycorrhizal fungus had different effects on the number of microorganisms, microbial biomass carbon, and soil enzyme activities in rhizosphere soil of *P. polyphylla* var. *yunnanensis*.

Research group (Zhou et al., 2020) studied the effect of arbuscular mycorrhizal fungi treatments of different combinations on the rhizospheric environment of *P. polyphylla* var. *yunnanensis*. The inoculation of arbuscular mycorrhizal fungi could regulate the spore densities and the colonizations

of *P. polyphylla* var. *yunnanensis* rhizosphere arbuscular mycorrhizal to improve the root activity. Effects of arbuscular mycorrhizal fungi on endogenous hormones in *P. polyphylla* var. *yunnanensis* were reported (Zhou et al., 2017). It was found that the inoculation of exogenous arbuscular mycorrhizal fungi could improve the mycorrhizal infection rate and seedling rate of *P. polyphylla* var. *yunnanensis* seedlings. The arbuscular mycorrhizal fungi had different rules on the changes in the rhizome and fibrous root of *P. polyphylla* var. *yunnanensis* seedlings. Fifty strains of endophytic fungus were isolated from phloem, xylem, and seed of rhizome of *P. polyphylla* var. *yunnanensis* collected from Yunnan Province (Zhou et al., 2004). The most endophytic fungi was isolated from the phloem of the rhizome. In addition, steroids in the fermentation cultures of 32 strains of endophytic fungus was detected, and the yield of steroids in the fermentation cultures of five strains of endophytic fungus exceeded 50 mg L⁻¹.

Zhang et al. (2019) reported the arbuscular mycorrhizal fungi suitable for the growth and development of *P. polyphylla* var. *yunnanensis* seedlings screened with mycorrhizal viability, rhizome biomass, and active components as indexes. It was found that the 28 arbuscular mycorrhizal fungi inoculated with *P. polyphylla* var. *yunnanensis* formed a symbiotic system, and could improve the mycorrhizal viability of *P. polyphylla* var. *yunnanensis* seedlings. Research group found that exogenous arbuscular mycorrhizal fungi could regulate the spore density, infection rate, and infection intensity of arbuscular mycorrhizal fungi in roots of *P. polyphylla* var. *yunnanensis*, and enhance the activities of succinate dehydrogenase and alkaline phosphatase of hyphae in roots of *P. polyphylla* var. *yunnanensis* (Zhou et al., 2015a). After treated with arbuscular mycorrhizal fungal elicitors, the different effects of different arbuscular mycorrhizal fungus on different steroidal saponins in rhizomes of *P. polyphylla* var. *yunnanensis* was observed. The application of arbuscular mycorrhizal fungi could improve the medicinal quality of *P. polyphylla* var. *yunnanensis*.

Indeed, the mechanism at the molecular level is also needed to be further studied in detail, which is important for the applications of *P. polyphylla* var. *yunnanensis*. In addition, the utilization of biotechnological processes should be developed for the production of *P. polyphylla* var. *yunnanensis* under controlled conditions.

CONCLUSION AND PERSPECTIVES

There are many reports on the genetic diversity, genetic structure, and chemical components of *P. polyphylla* var. *yunnanensis*. The fungi also affected the contents and properties of *P. polyphylla*

var. *yunnanensis*; however, there are few review articles on the *P. polyphylla* var. *yunnanensis*. This review article provided the recent development about the genetic diversity and structure of *P. polyphylla* var. *yunnanensis* based on the literature. More attention should be paid to the genetic diversity and genetic structure, which favored the replacement of the wild population by the cultivated population. In addition, the differences between wild population and cultivated population should be investigated in detail, which is important for the applications of *P. polyphylla* var. *yunnanensis*. Especially, the effect of areas on the quality and chemical components of *P. polyphylla* var. *yunnanensis* should be explored. Furthermore, more methods should be developed on the extraction and purity of the chemical components of *P. polyphylla* var. *yunnanensis*. The mechanism between chemical components and biological activities should be discussed by more experimental results. Furthermore, the utilization of fungi on the properties of *P. polyphylla* var. *yunnanensis* should be developed in detail. More biomedical properties should be investigated. It is well-known that *P. polyphylla* var. *yunnanensis* is an important biomass resource in the natural medicine field (Liu H. et al., 2021a,b). Therefore, the mechanism between chemical components and properties should be researched in depth. We expected that this review article is beneficial to expand the applications of *P. polyphylla* var. *yunnanensis* in the biomedical field.

AUTHOR CONTRIBUTIONS

NZ, LX, and M-GM: investigation. S-MP, S-EC, and CS: supervision. NZ and M-GM: writing – original draft. M-GM, S-MP, LX, S-EC, and CS: writing – review and editing. All authors contributed to the article and approved the submitted version.

FUNDING

This research was supported by the National Natural Science Foundation of China (No. 81260622), Chongqing Science and Technology Commission (cstc2018jcyjAX026), the “Beyond Research Innovation & Development for Good Enterprises+” Project, supported by the Ministry of Education (MOE), the Technology Development Program (S3030198) funded by the Ministry of SMEs and Startups (MSS, South Korea), and this work was also partially supported by 2020’ Jeollanam-do (“Industry-University-Institute collaboration agricultural industrial complex R&D supporting program” operated by Jeonnam Technopark) to S-EC.

REFERENCES

- An, L., Si, C., Wang, G., Sui, W., and Tao, Z. (2019). Enhancing the solubility and antioxidant activity of high-molecular-weight lignin by moderate depolymerization via in situ ethanol/acid catalysis. *Ind. Crops Prod.* 128, 177–185. doi: 10.1016/j.indcrop.2018.11.009
- Chan, J. Y. W., Koon, J. C. M., Liu, X. Z., Detmar, M., Yu, B. A., Kong, S. K., et al. (2011). Polyphyllin D, a steroidal saponin from *Paris polyphylla*, inhibits endothelial cell functions in vitro and angiogenesis in *Zebrafish* embryos in vivo. *J. Ethnopharmacol.* 137, 64–69. doi: 10.1016/j.jep.2011.04.021
- Chen, S., Wang, G., Sui, W., Parvez, A. M., Dai, L., and Si, C. (2020a). Novel lignin-based phenolic nanosphere supported palladium nanoparticles with highly efficient catalytic performance and good reusability. *Ind. Crop Prod.* 145:112164. doi: 10.1016/j.indcrop.2020.11.2164
- Chen, S., Wang, G., Sui, W., Parvez, A. M., and Si, C. (2020b). Synthesis of lignin-functionalized phenolic nanosphere supported Ag nanoparticles with excellent

- dispersion stability and catalytic performance. *Green Chem.* 22, 2879–2888. doi: 10.1039/c9gc04311j
- Chen, X., Yang, Q., Si, C. L., Wang, Z., Huo, D., Hong, Y., et al. (2016). Recovery of oligosaccharides from prehydrolysis liquors of poplar by microfiltration/ultrafiltration membranes and anion exchange resin. *ACS Sustain. Chem. Eng.* 4, 937–943. doi: 10.1021/acssuschemeng.5b01029
- Chen, Z. S. Z., Tian, B., and Cai, C. T. (2017). Genetic diversity of *Paris polyphylla* var. *yunnanensis* based on SSR molecular markers. *Chin. Herb. Med.* 48, 1834–1838.
- Cunningham, A. B., Brinckmann, J. A., Bi, Y. F., Pei, S. J., Schippmann, U., and Luo, P. (2018). Paris in the spring: a review of the trade, conservation and opportunities in the shift from wild harvest to cultivation of *Paris polyphylla* (Trilliaceae). *J. Ethnopharmacol.* 222, 208–216. doi: 10.1016/j.jep.2018.04.048
- Dai, L., Cao, Q., Wang, K., Han, S., Si, C., Liu, D., et al. (2020a). High efficient recovery of L-lactide with lignin-based filler by thermal degradation. *Ind. Crop Prod.* 143:111954. doi: 10.1016/j.indcrop.2019.111954
- Dai, L., Ma, M., Xu, J., Si, C., Wang, X., Liu, Z., et al. (2020b). All-lignin-based hydrogel with fast pH-stimuli responsiveness for mechanical switching and actuation. *Chem. Mater.* 32, 4324–4330. doi: 10.1021/acs.chemmater.0c01198
- Du, H., Liu, W., Zhang, M., Si, C., Zhang, X., and Li, B. (2019). Cellulose nanocrystals and cellulose nanofibrils based hydrogels for biomedical applications. *Carbohydr. Polym.* 209, 130–144. doi: 10.1016/j.carbpol.2019.01.020
- Du, H., Parit, M., Liu, K., Zhang, M., Jiang, Z., Huang, T.-S., et al. (2021). Engineering cellulose nanopaper with water resistant, antibacterial, and improved barrier properties by impregnation of chitosan and the followed halogenation. *Carbohydr. Polym.* 270:118372. doi: 10.1016/j.carbpol.2021.118372
- Gu, W. C., Guo, D. Q., Yang, M., Huang, X. L., Li, H. L., and Zhou, N. (2020a). Determination of 9 steroidal saponins in rhizome and fibrous roots of wild and cultivated *Paris polyphylla* var. *yunnanensis* by UPLC. *Trad. Chin. Drug Res. Clin. Pharmacol.* 31, 838–847.
- Gu, W. C., Zhao, S. X., Yang, M., Huang, X. L., Li, H. L., and Zhou, N. (2020b). Simultaneous determination of amino acids in *Paris polyphylla* var. *yunnanensis* fibril from different habitats by UPLC. *Nat. Product Res. Dev.* 32, 1562–1575.
- He, J., Wang, H., Li, D. Z., and Chen, S. F. (2007). Genetic diversity of *Paris polyphylla* var. *yunnanensis*, a traditional Chinese medicinal herb, detected by ISSR markers. *Planta Med.* 73, 1316–1321. doi: 10.1055/s-2007-981617
- Hu, L., Du, H., Liu, C., Zhang, Y., Yu, G., Zhang, X., et al. (2018). Comparative evaluation of the efficient conversion of corn husk filament and corn husk powder to valuable materials via a sustainable and clean biorefinery process. *ACS Sustain. Chem. Eng.* 7, 1327–1336. doi: 10.1021/acssuschemeng.8b05017
- Hu, L., Wang, K., Li, G., Zhang, R., Luo, Y., Si, C., et al. (2017). Isolation and structural elucidation of heartwood extractives of *Juglans sigillata*. *Holzforchung* 71, 785–791. doi: 10.1515/hf-2017-0036
- Hu, W. C., Wang, G. C., Li, P. X., Wang, Y. N., Si, C. L., He, J., et al. (2014). Neuroprotective effects of macranthoin G from *Eucommia ulmoides* against hydrogen peroxide-induced apoptosis in PC12 cells via inhibiting NFκB activation. *Chem. Biol. Interact.* 224, 108–116. doi: 10.1016/j.cbi.2014.10.011
- Hu, W. C., Wang, X. F., Wu, L., Shen, T., Ji, L. L., Zhao, X. H., et al. (2016). Apigenin-7-O-beta-D-glucuronide inhibits LPS-induced inflammation through the inactivation of AP-1 and MAPK signaling pathways in RAW 264.7 macrophages and protects mice against endotoxin shock. *Food Funct.* 7, 1002–1013. doi: 10.1039/c5fo01212k
- Huang, Y., Cui, L. J., Zhan, W. H., Dou, Y. H., Wang, Y. L., Wang, Q., et al. (2007). Separation and identification of steroidal compounds with cytotoxic activity against human gastric cancer cell lines in vitro from the rhizomes of *Paris polyphylla* var. *chinensis*. *Chem. Nat. Comp.* 43, 672–677. doi: 10.1007/s10600-007-0225-8
- Huang, Y., Zhou, N., Yang, M., Shen, Y. X., and Zhang, D. Q. (2019). A comparative study of the population genetics of wild and cultivated populations of *Paris polyphylla* var. *yunnanensis* based on amplified fragment length polymorphism markers. *Ecol. Evol.* 9, 10707–10722. doi: 10.1002/ece3.5589
- Huang, Y. P., Zhang, J., Yang, M., Ding, B., Guo, D. Q., Pan, X. J., et al. (2019). Effects of different inoculation periods on seedling growth and steroidal saponin content of *Paris polyphylla* var. *yunnanensis*. *Chin. Trad. Herb. Drugs* 50, 4438–4448.
- Huang, Y. F., Zhao, J. L., Zhou, L. G., Wang, M. A., Wang, J. G., Li, X. L., et al. (2009). Antimicrobial compounds from the endophytic Fungus *Fusarium* sp Ppf4 isolated from the medicinal plant *Paris polyphylla* var. *yunnanensis*. *Nat. Product Commun.* 4, 1455–1458. doi: 10.1177/1934578X09000401102
- Jia, F. Y., Guo, S. Y., Shen, Y., Gao, M. Y., Liu, C. X., Zhou, S. Y., et al. (2016). *Catellatospora vulcania* sp nov and *Catellatospora paridis* sp nov., two novel actinobacteria isolated from volcanic sediment and the rhizosphere of *Paris polyphylla*. *Antonie Van Leeuwenhoek Intern. J. Gen. Mol. Microbiol.* 109, 43–50. doi: 10.1007/s10482-015-0608-y
- Jing, S. S., Wang, Y., Li, X., Man, S. L., and Gao, W. Y. (2017). Chemical constituents and antitumor activity from *Paris polyphylla* Smith var. *yunnanensis*. *Nat. Product Res.* 31, 660–666. doi: 10.1080/14786419.2016.1219861
- Lee, M. S., Yuet-Wa, J. C., Kong, S. K., Yu, B., Eng-Choon, V. O., Nai-Ching, H. W., et al. (2005). Effects of polyphyllin D, a steroidal saponin in *Paris polyphylla*, in growth inhibition of human breast cancer cells and in xenograft. *Cancer Biol. Ther.* 4, 1248–1254. doi: 10.4161/cbt.4.11.2136
- Li, J., Zhao, J. L., Xu, L. J., Zhou, L. G., Li, X. L., and Wang, J. G. (2008). Endophytic fungi from rhizomes of *Paris polyphylla* var. *yunnanensis*. *World J. Microbiol. Biotechnol.* 24, 733–737. doi: 10.1007/s11274-007-9531-3
- Li, Y. B., Wang, L., and He, Z. J. (2018). AFLP analysis of genetic diversity of *Paris polyphylla*. *Botan. Res.* 7, 45–53. doi: 10.12677/br.2018.71007
- Li, X., Xu, R., Yang, J., Nie, S., Liu, D., Liu, Y., et al. (2019). Production of 5-hydroxymethylfurfural and levulinic acid from lignocellulosic biomass and catalytic upgradation. *Ind. Crops Prod.* 130, 184–197. doi: 10.1016/j.indcrop.2018.12.082
- Liang, S., and Victor, G. S. (2000). “Paris L,” in *Flora of China*, eds Z. Y. Wu and P. H. Raven (Beijing: China Sciences Press), 88–95.
- Liu, H., Xu, T., Liu, K., Zhang, M., Liu, W., Li, H., et al. (2021a). Lignin-based electrodes for energy storage application. *Ind. Crops Prod.* 165:113425. doi: 10.1016/j.indcrop.2021.113425
- Liu, H., Du, H., Zheng, T., Liu, K., Ji, X., and Xu, T. (2021b). Cellulose based composite foams and aerogels for advanced energy storage devices. *Chem. Eng. J.* 426:130817. doi: 10.1016/j.cej.2021.130817
- Liu, K., Du, H., Zheng, T., Liu, H., Zhang, M., Zhang, R., et al. (2021). Recent advances in cellulose and its derivatives for oilfield applications. *Carbohydr. Polym.* 259:117740. doi: 10.1016/j.carbpol.2021.117740
- Liu, T., Greenslade, A., and Yang, S. C. (2017). Levels of rhizome endophytic fungi fluctuate in *Paris polyphylla* var. *yunnanensis* as plants age. *Plant Diver.* 39, 60–64. doi: 10.1016/j.pld.2016.11.006
- Liu, W., Du, H., Liu, H., Xie, H., Xu, T., Zhao, X., et al. (2020a). Highly efficient and sustainable preparation of carboxylic and thermostable cellulose nanocrystals via FeCl₃-catalyzed innocuous citric acid hydrolysis. *ACS Sustain. Chem. Eng.* 8, 16691–16700. doi: 10.1021/acssuschemeng.0c06561
- Liu, W., Du, H., Liu, K., Liu, H., Xie, H., Si, C., et al. (2021). Sustainable preparation of cellulose nanofibrils via choline chloride-citric acid deep eutectic solvent pretreatment combined with high-pressure homogenization. *Carbohydr. Polym.* 267:118220. doi: 10.1016/j.carbpol.2021.118220
- Liu, W., Du, H., Zhang, M., Liu, K., Liu, H., Xie, H., et al. (2020b). Bacterial cellulose based composite scaffolds for biomedical applications: a review. *ACS Sustain. Chem. Eng.* 8, 7536–7562. doi: 10.1021/acssuschemeng.0c00125
- Liu, X. D., Wang, Z. H., and Xu, Y. Q. (2015). Research progress of Chinese herbal medicine *Paris*. *Guid. J. TCM* 21, 90–93.
- Ma, C., Ma, M. G., Si, C., Ji, X. X., and Wang, P. (2021a). Flexible mxene-based composites for wearable devices. *Adv. Funct. Mater.* 1:2009524. doi: 10.1002/adfm.202009524
- Ma, C., Kim, T.-H., Liu, K., Ma, M.-G., Choi, S.-E., and Si, C. (2021b). Multifunctional lignin-based composite materials for emerging applications. *Front. Bioeng. Biotechnol.* 9:708976. doi: 10.3389/fbioe.2021.708976
- Ma, C., Yuan, Q., Du, H., Ma, M. G., Si, C., and Wan, P. (2020). Multiresponsive MXene (Ti₃C₂T_x)-decorated textiles for wearable thermal management and human motion monitoring. *ACS Appl. Mater. Interfaces* 12, 34226–34234. doi: 10.1021/acsmi.0c10750
- National Pharmacopoeia Commission (2015). *Pharmacopoeia of PR China*, 2015 Edn, Vol. I. Beijing: China Pharmaceutical Science and Technology Press, 260.
- Negi, J. S., Bisht, V. K., Bhandari, A. K., Bhatt, V. P., Singh, P., and Singh, N. (2014). *Paris polyphylla*: chemical and biological prospectives. *Anti Cancer Agents Med. Chem.* 14, 833–839. doi: 10.2174/187152061466611010140

- Ou, H., Guo, D. Q., Lin, J. J., Yan, Z. Y., Teng, Z., Wang, G. Z., et al. (2016). Effects of different AM fungi on quantity and enzyme activity of Hizoosphere soil microorganism of *Paris polyphylla* var. *Yunnanensis*. *J. Chin. Med. Mater.* 39, 948–955.
- Pei, Y. F., Zhang, Q. Z., and Wang, Y. Z. (2020). Application of authentication evaluation techniques of Ethnobotanical medicinal plant genus Paris: a review. *Crit. Rev. Analyt. Chem.* 50, 405–423. doi: 10.1080/10408347.2019.1642734
- Qin, X. J., Sun, D. J., Ni, W., Chen, C. X., Hua, Y., He, L., et al. (2012). Steroidal saponins with antimicrobial activity from stems and leaves of *Paris polyphylla* var. *yunnanensis*. *Steroids* 77, 1242–1248. doi: 10.1016/j.steroids.2012.07.007
- Qin, X. J., Yu, M. Y., Ni, W., Yan, H., Chen, C. X., Cheng, Y. C., et al. (2016). Steroidal saponins from stems and leaves of *Paris polyphylla* var. *yunnanensis*. *Phytochemistry* 121, 20–29. doi: 10.1016/j.phytochem.2015.10.008
- Shen, S., Xu, Z., Feng, S. L., Wang, H. D., Liu, J., Zhou, L. J., et al. (2018). Structural elucidation and antiaging activity of polysaccharide from *Paris polyphylla* leaves. *Intern. J. Biol. Macromol.* 107, 1613–1619. doi: 10.1016/j.ijbiomac.2017.10.026
- Shen, S. A., Chen, D. J., Li, X., Li, T., Yuan, M., Zhou, Y. H., et al. (2014). Optimization of extraction process and antioxidant activity of polysaccharides from leaves of *Paris polyphylla*. *Carbohydr. Polym.* 104, 80–86. doi: 10.1016/j.carbpol.2014.01.006
- Si, C. L., Deng, X. J., Liu, Z., Kim, J. K., and Bae, Y. S. (2008a). Studies on the phenylethanoid glycosides with anti-complement activity from *Paulownia tomentosa* var. *tomentosa* wood. *J. Asian Nat. Products Res.* 10, 1003–1008.
- Si, C. L., Liu, Z., Kim, J. K., and Bae, Y. S. (2008b). Structure elucidation of phenylethanoid glycosides from *Paulownia tomentosa* Steud. var. *tomentosa* wood. *Holzforchung* 62, 197–200. doi: 10.1515/hf.2008.047
- Si, C. L., Jiang, J. Z., Liu, S. C., Hu, H. Y., Ren, X. D., Yu, G. J., et al. (2013). A new lignan glycoside and phenolics from the branch wood of *Pinus banksiana* Lambert. *Holzforchung* 67, 357–363. doi: 10.1515/hf-2012-0137
- Si, C. L., Wu, L., and Zhu, Z. Y. (2009). Phenolic glycosides from *Populus davidiana* bark. *Biochem. Syst. Ecol.* 37, 221–224. doi: 10.1016/j.bse.2009.01.007
- Song, Y., Li, M. F., and Xu, J. (2015). Polymorphic microsatellite markers in the traditional Chinese medicinal plant *Paris polyphylla* var. *yunnanensis*. *Genet. Mol. Res.* 14, 9939–9942. doi: 10.4238/2015.august.19.29
- Vos, P., Hogers, R., Bleeker, M., Reijmans, M., van de Lee, T., Hornes, M., et al. (1995). AFLP: a new technique for DNA fingerprinting. *Nucleic Acids Res.* 23, 4407–4414.
- Wang, G. X., Han, J., Zhao, L. W., Jiang, D. X., Liu, Y. T., and Liu, X. L. (2010). Anthelmintic activity of steroidal saponins from *Paris polyphylla*. *Phytomedicine* 17, 1102–1105. doi: 10.1016/j.phymed.2010.04.012
- Wang, H., Du, H., Liu, K., Liu, H., Xu, T., Zhang, S., et al. (2021). Sustainable preparation of bifunctional cellulose nanocrystals via mixed H₂SO₄/formic acid hydrolysis. *Carbohydr. Polym.* 266:118107. doi: 10.1016/j.carbpol.2021.118107
- Wang, H., Xie, H., Du, H., Wang, X., Liu, W., Duan, Y., et al. (2020). Highly efficient preparation of functional and thermostable cellulose nanocrystals via H₂SO₄ intensified acetic acid hydrolysis. *Carbohydr. Polym.* 239:116233. doi: 10.1016/j.carbpol.2020.116233
- Wang, Q., Yang, M., Guo, D. Q., Tang, D. H., Mu, M. J., Huang, Y., et al. (2019). Determination of monosaccharide composition of polysaccharides from wild and transplanted *Paris polyphylla* var. *yunnanensis* by HPLC with PMP pre-column derivatization. *Chin. Drug Res. Clin. Pharmacol.* 30, 1503–1509.
- Wang, Q., Zhang, H. J., Yang, M., Zhang, H., Zhou, N., and Li, Y. (2018). Effects of 28 species of AM fungi on diosgenin contents in *Paris polyphylla* var. *yunnanensis*. *J. Dali Univer.* 3, 22–25.
- Wang, Y., Wang, H. P., Cheng, H. Y., Chang, F., Wan, Y., and She, X. P. (2020). Niche differentiation in the Rhizosphere and Endosphere fungal microbiome of wild *Paris polyphylla* Sm. *PeerJ* 8:e8510. doi: 10.7717/peerj.8510
- Wu, X., Wang, L., Wang, H., Dai, Y., Ye, W. C., and Li, Y. L. (2012). Steroidal saponins from *Paris polyphylla* var. *yunnanensis*. *Phytochemistry* 81, 133–143. doi: 10.1016/j.phytochem.2012.05.034
- Xu, J., Li, C., Dai, L., Xu, C., Zhong, Y., Yu, F., et al. (2020). Biomass fractionation and lignin fractionation towards lignin valorization. *ChemSusChem* 13, 4284–4295. doi: 10.1002/cssc.202001491
- Xu, J., Shao, Z., Li, Y., Dai, L., Wang, Z., and Si, C. (2021). A flow-through reactor for fast fractionation and production of structure-preserved lignin. *Ind. Crops Prod.* 164:113350. doi: 10.1016/j.indcrop.2021.113350
- Xu, R., Du, H., Liu, C., Liu, H., Wu, M., Zhang, X., et al. (2021). An efficient and magnetic adsorbent prepared in a dry process with enzymatic hydrolysis residues for wastewater treatment. *J. Clean. Prod.* 313:127834. doi: 10.1016/j.jclepro.2021.127834
- Xuan, Q., Bao, F. K., Pan, H. M., and Liu, A. H. (2010). Isolating fungal endophyte from *Paris polyphylla* Smith var. *yunnanensis* and identifying their antibacterial ability. *Afri. J. Microbiol. Res.* 4, 1001–1004.
- Yan, L. L., Zhang, Y. J., Gao, W. Y., Man, S. L., and Wang, Y. (2009). In vitro and in vivo anticancer activity of steroid saponins of *Paris polyphylla* var. *yunnanensis*. *Exper. Oncol.* 31, 27–32.
- Yang, L. L., Tang, S. K., Chu, X., Jiang, Z., Xu, L. H., and Zhi, X. Y. (2016). *Oceanobacillus endoradicis* sp nov., an endophytic bacterial species isolated from the root of *Paris polyphylla* Smith var. *yunnanensis*. *Antonie Van Leeuwenhoek Intern. J. Gen. Mol. Microbiol.* 109, 957–964. doi: 10.1007/s10482-016-0695-4
- Yang, M., Guo, D. Q., Shen, Y. X., Pan, X. J., Zhang, J., Zhang, J., et al. (2017). Optimization of extraction of nucleosides from *Paris polyphylla* var. *yunnanensis* by orthogonal test. *J. S. Agric.* 48, 876–882.
- Yang, M., Wang, R., Zhou, N., Tang, S. F., and Shen, Y. X. (2018). Analysis of 14 elements in *Paris polyphylla* in Yunnan and Guizhou. *Heilongjiang Anim. Sci. Vet. Med.* 8, 200–205.
- Yang, X., Xie, H., Du, H., Zhang, X., Zou, Z., Zou, Y., et al. (2019). Facile extraction of thermally stable and dispersible cellulose nanocrystals with high yield via a green and recyclable FeCl₃-catalyzed deep eutectic solvent system. *ACS Sustain. Chem. Eng.* 7, 7200–7208. doi: 10.1021/acssuschemeng.9b00209
- Yang, X., Xie, H., Zou, Y., Huang, Y., Jiang, L.-W., Wang, X., et al. (2021). Cost-effective and efficient plum-pudding-like Fe_xNi_{1-x}S₂/C composite electrocatalysts for oxygen evolution reaction. *Renew. Energ.* 168:416e423. doi: 10.1016/j.renene.2020.12.072
- Yang, Y., Yang, S. C., Zhao, J., Udikeri, S., and Liu, T. (2015). Microbial diversity in *Paris polyphylla* var. *yunnanensis* rhizomes of varying ages. *Genet. Mol. Res.* 14, 17612–17621. doi: 10.4238/2015.december.21.34
- Zhang, H., Du, H. H., Guo, D. Q., Yang, M., Wang, M. J., and Zhou, N. (2019). Effects of inoculation with different AM fungi on functional gene expression in seedlings of *Paris polyphylla* var. *Yunnanensis*. *Nat. Product Res. Dev.* 31, 318–324.
- Zhang, J., Ding, B., Zhang, H., Qi, J. S., Shen, Y. X., Zhou, N., et al. (2016). Effects of different drying methods on total saponin content and antioxidant capacity of *Paris polyphylla* var. *Yunnanensis*. *Chin. J. Inform. Trad. Chin. Med.* 23, 95–97.
- Zhang, J. Y., Yu, H., and Zhang, S. G. (2004). RAPD analysis of genetic diversity of *Paris polyphylla*. *Biodiversity* 12, 517–522.
- Zhang, Y., Lü, S. S., Zhou, N., Ma, Y. X., Gao, K. J., and Wu, S. W. (2011). Comparison of 4 kinds of chonglou saponins contents in *Paris polyphylla* of different growing years. *China Pharm.* 22, 4081–4083.
- Zhao, J. J., Huang, Y., Zhang, D. Q., and Zhou, N. (2020). Phylogeography of *Paris polyphylla* var. *yunnanensis* based on chloroplast gene trnL-trnF sequences. *China J. Chin. Mater. Med.* 46, 1094–1101.
- Zhao, X. P., Zou, G. F., Zhao, J., Hu, L. Y., Lan, Y. F., and He, J. L. (2020). Genetic relationships and diversity among populations of *Paris polyphylla* assessed using SCoT and SRAP markers. *Physiol. Mol. Biol. Plants* 26, 1281–1293. doi: 10.1007/s12298-020-00808-z
- Zhao, Y., Kang, L. P., Liu, Y. X., Liang, Y. G., Tan, D. W., Yu, Z. Y., et al. (2009). Steroidal saponins from the rhizome of *Paris polyphylla* and their cytotoxic activities. *Planta Med.* 75, 356–363. doi: 10.1055/s-0028-1088380
- Zhou, L. A., Yang, C. Z., Li, J. Q., Wang, S. L., and Wu, J. Y. (2003). Heptasaccharide and octasaccharide isolated from *Paris polyphylla* and their plant growth-regulatory activity. *Plant Sci.* 165, 571–575. doi: 10.1016/s0168-9452(03)00216-4
- Zhou, L. G., Cao, X. D., Yang, C. Z., Wu, X. H., and Zhang, L. Q. (2004). Endophytic fungi of *Paris polyphylla* var. *yunnanensis* and analysis of their steroids. *Nat. Product Res. Dev.* 16, 120–198.
- Zhou, N., Ding, B., Feng, Y., Qi, W. H., Zhang, H., Guo, D. Q., et al. (2015a). Effects of mycorrhizal colonization and medicine quality of *Paris polyphylla* var. *yunnanensis* inoculated with different foreign AM fungi species. *China J. Chin. Mater. Med.* 40, 3158–3167.
- Zhou, N., Zhang, H. Q., Ding, B., Guo, D. Q., Zhang, D. Q., Zeng, Y., et al. (2015b). Effects of different drying methods on the content of diosgenin

- in *Paris polyphylla* var. *yunnanensis*. *Lishizhen Med. Mater. Med. Res.* 26, 361–362.
- Zhou, N., Guo, D. Q., Wang, K. T., Zhang, D. Q., Peng, G. H., and Zhang, C. Q. (2014). Comparative study on different extraction methods of polysaccharide from *Paris polyphylla* var. *yunnanensis*. *Sci. Technol. Food Industry* 35, 326–329.
- Zhou, N., Guo, J. F., Yang, L. Y., Xu, P., and Jiang, B. (2010). Determination of diosgenin in *Paris polyphylla* var. *yunnanensis* at different collecting time by HPLC. *Chin. J. Exper. Trad. Med. Formul.* 16, 54–56.
- Zhou, N., Zhang, D. Q., Sun, Q., Jiang, B., and Huang, Z. C. (2012). Effects of fungal elicitors on the secondary metabolite steroidal saponin in *Paris polyphylla* var. *yunnanensis*. *Acta Pharm. Sinica* 47, 1237–1242.
- Zhou, N., Zhang, J., Pan, X. J., Du, H. H., Guo, D. Q., Ding, B., et al. (2017). Effect of arbuscular mycorrhizal fungi on endogenous hormones in *Paris polyphylla* var. *yunnanensis*. *Chin. Trad. Herb. Drugs* 48, 4970–4978.
- Zhou, Y., Yang, M., Guo, D. Q., Pan, X. J., Ding, B., Zhang, J., et al. (2020). Effects on the Rhizosphere soil environment and the medicine quality of *Paris polyphylla* var. *yunnanensis* inoculated by different exogenous AM fungi combination. *Chin. J. Exper. Trad. Med. Formul.* 26, 96–109.

Conflict of Interest: The authors declare that the research was conducted in the absence of any commercial or financial relationships that could be construed as a potential conflict of interest.

Copyright © 2021 Zhou, Xu, Park, Ma, Choi and Si. This is an open-access article distributed under the terms of the Creative Commons Attribution License (CC BY). The use, distribution or reproduction in other forums is permitted, provided the original author(s) and the copyright owner(s) are credited and that the original publication in this journal is cited, in accordance with accepted academic practice. No use, distribution or reproduction is permitted which does not comply with these terms.



Improved Production of Xylanase in *Pichia pastoris* and Its Application in Xylose Production From Xylan

Ting Miao¹, Abdul Basit^{1,2*}, Junquan Liu¹, Fengzhen Zheng¹, Kashif Rahim³, Huiqiang Lou¹ and Wei Jiang^{1*}

¹State Key Laboratory of Agro-Biotechnology, College of Biological Sciences, China Agricultural University, Beijing, China,

²Department of Microbiology and Molecular Genetics, Faculty of Life Sciences, University of Okara, Okara, Pakistan, ³Department of Microbiology, Cholistan University of Veterinary and Animal Sciences (CUVAS), Bahawalpur, Pakistan

OPEN ACCESS

Edited by:

Caoxing Huang,
Nanjing Forestry University, China

Reviewed by:

Arabinda Ghosh,
Gauhati University, India
Kankan Jiang,
Hangzhou Medical College, China
Zhaojiang Wang,
Qilu University of Technology, China

*Correspondence:

Abdul Basit
abdul_9090@yahoo.com
Wei Jiang
jiangwei01@cau.edu.cn

Specialty section:

This article was submitted to
Industrial Biotechnology,
a section of the journal
Frontiers in Bioengineering and
Biotechnology

Received: 03 April 2021

Accepted: 16 August 2021

Published: 27 August 2021

Citation:

Miao T, Basit A, Liu J, Zheng F,
Rahim K, Lou H and Jiang W (2021)
Improved Production of Xylanase in
Pichia pastoris and Its Application in
Xylose Production From Xylan.
Front. Bioeng. Biotechnol. 9:690702.
doi: 10.3389/fbioe.2021.690702

Xylanases with high specific activity has been focused with great interest as a useful enzyme in biomass utilization. The production of recombinant GH11 xylanase (MYCTH_56237) from *Myceliophthora thermophila* has been improved through N-terminal signal peptide engineering in *P. pastoris*. The production of newly recombinant xylanase (termed Mtxyn11C) was improved from 442.53 to 490.7 U/mL, through a replacement of α -factor signal peptide with the native xylanase signal peptide segment (MVSVKAVLLLGAAGTTLA) in *P. pastoris*. Scaling up of Mtxyn11C production in a 7.5 L fermentor was improved to the maximal production rate of 2503 U/mL. In this study, the degradation efficiency of Mtxyn11C was further examined. Analysis of the hydrolytic mode of action towards the birchwood xylan (BWV) revealed that Mtxyn11C was clearly more effective than commercial xylanase and degrades xylan into xylooligosaccharides (xylobiose, xylotriose, xylotetraose). More importantly, Mtxyn11C in combination with a single multifunctional xylanolytic enzyme, improved the hydrolysis of BWV into single xylose by 40%. Altogether, this study provided strategies for improved production of xylanase together with rapid conversion of xylose from BWV, which provides sustainable, cost-effective and environmental friendly approaches to produce xylose/XOSs for biomass energy or biofuels production.

Keywords: *Myceliophthora thermophila*, *Pichia pastoris*, xylanase, improved production, hydrolytic activity, xylan, xylose

INTRODUCTION

Xylanases an integral group of hemicelluloses and offers an opportunity of best interest area for researchers on account of their insightful investigation and prospective of industrial applications, especially in the degradation of biomass into fermentable sugars (Basit et al., 2018a). On account of the heterogeneity and complexity, the complete degradation of xylan necessitates multiple enzymes (particularly endoxylanases and β -xylosidase) in association with accessory enzymes to interplay in the process, which liberates xylooligosaccharides (XOS) (Gaurav et al., 2017). XOS have been extensively applied in a variety of industrial processes, particularly in chemical industries and biofuel production (Samanta et al., 2012).

Albeit, the enzymatic hydrolysis demonstrates better results and low process energy requirements, however, the high cost of commercial enzymes and probably enzymes with low activity, creates a bottleneck for complete degradation of hemicelluloses. Therefore, more potent and efficient enzymes

with high activity need to be developed for more economical purposes. Several approaches have been adopted to minimize the expenses of hydrolysis process such as improving enzyme activity and enzyme production (Lin et al., 2017; Zhou et al., 2015; Wang et al., 2012). The genetic engineering paved the way for the mass scale production of xylanases (Uday et al., 2016). Recent developments in recombinant protein engineering also helped in expressing xylanases in heterologous hosts (*Pichia pastoris*) for mass production.

P. pastoris has been substantiated as a more successful system for recombinant proteins, due to the high cell densities and therefore yield high volumetric products (Ahmad et al., 2014). Moreover, *P. pastoris* secretes less native proteins and enable the purification of recombinant protein in supernatant easier, through directing signal peptide. To intensify heterologous protein expression in *P. pastoris*, different procedures have been established, including the optimization of the secretory signal peptide sequence (Zheng et al., 2018). Protein expression levels have been improved with greater success prospects through regulation of the several factors such as recruitment of natural pro-peptides and gene dosage (Aw et al., 2018). Secretory signal peptides have been assessed to improve the protein expression level in *P. pastoris*, particularly, the secretion/releasing efficiency and optimization of the signal peptide codons of the α -factor. Multiple revealed studies indicate the impacts of secretory signal peptides on the yield expression. Bovine-casein (signal peptide) resulted in lower yield for the secretion of the xylanase *xynB* instead of the α -mating factor (α -MF) peptide from *S. cerevisiae* (He et al., 2012). Similarly, for the expression of bovine pancreatic trypsin inhibitor (BPTI) displayed no effective impact while using the α -MF, however, using human serum albumin (HSA) signal peptide sequence demonstrated an effective secretion into the medium (Yang et al., 2008).

In our previous study, the gene encoding GH11 xylanase MYCTH_56237 from *M. thermophila* was expressed in *P. pastoris* and achieved a high specific xylanase activity of 1533.71 U/mg (Basit et al., 2018b). However, the xylanase secretions into the culture medium was inadequate. Therefore, the present study was aimed to improve the xylanase production through the engineering of N-terminal peptide in *P. pastoris*. As expected an increased production of the xylanase in (both shake flasks and 7.5 L fermentor) was achieved by substituting of the secretory α -MF with the native signal peptide. In this study, the degradation efficiency of newly improved xylanase was clearly more effective and produced xylobiose, xylotriose and xylohexose from birchwood-xylan (BWV). This study also elucidated the improved conversion of xylan into xylose by 40%, when integrated with the multifunctional xylanolytic enzyme (Basit et al., 2019).

MATERIALS AND METHODS

Reagents

Restriction enzymes and ligases were purchased from New England Biolabs (NEB). Substrates 4-nitrophenyl β -D-xylopyranoside

(pNPX), 4-nitrophenyl β -D-glucopyranoside (pNPG), 4-nitrophenyl β -D-cellobioside (pNPC), and commercial xylanase from Sigma-Aldrich (United States). Birchwood-xylan (BWV), commercial β -xylosidase (EC 3.2.1.37, *Bacillus pumilus*), and standard xylooligosaccharides (X₂, xylobiose; X₃, xylotriose; X₄, xylohexose; X₅, xylopentaose) were from Megazyme (Ireland). XOSs (a mixture of X₂, X₃, X₄ and X₅) were provided by Aladdin (X140487), China. X₂, X₃, X₄ and X₅ were further identified on HPLC analysis.

Cultivation media [Yeast extract peptone dextrose (YPD) and buffered minimal glycerol medium (BMGY)], and gene expression medium for *P. pastoris* [buffered minimal methanol medium (BMMY)] were prepared according to the manual in the *Pichia* Expression Kit (Invitrogen). Other chemicals used were analytical grade unless otherwise stated.

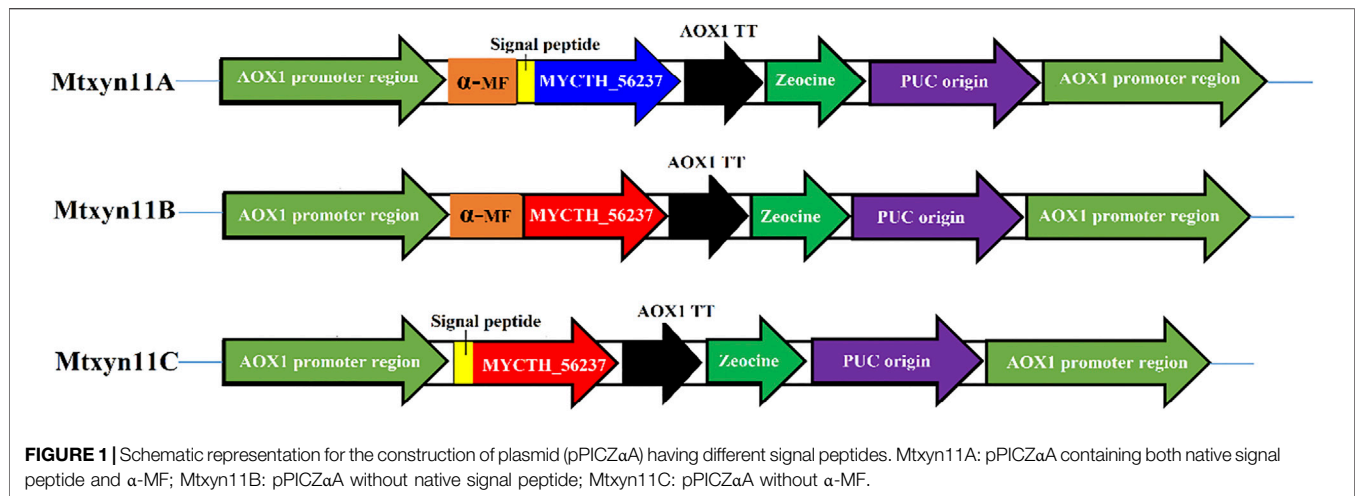
Construction of Recombinant Plasmids and Strains

The full-length of xylanase gene MYCTH_56237 was amplified from pMD19-T simple vector harboring the MYCTH_56237 using specific primers (**Supplementary Table S1**). The amplified PCR product was purified from gel using the Gel Extraction Kit (Thermo Fisher Scientific, Waltham, MA, United States) and ligated to expression plasmid pPICZaA, pre-digested with *Eco*RI and *Xba*I. The resultant recombinant plasmid was transformed into *E. coli* strain DH5 α , as further confirmed by PCR and DNA sequencing. The expression plasmid pPICZaA encoding α -factor signal peptide and MYCTH_56237 were designed to facilitate the construction of variants as described by Zheng et al. (2018).

Enzyme activity of MYCTH_56237 was improved through replacement of α -factor in *P. pastoris* with different signal peptide sequences. The peptide signals of MYCTH_56237 secreted 18 amino acids (MVSVKAVLLGGAAGTTLA) was predicted based on SignalP (<http://www.cbs.dtu.dk/services/SignalP/>). The native signal peptide segment of MYCTH_56237 positioned between the C-terminus of the α -MF and the N-terminus of pPICZaA termed Mtxyn11A, and pPICZaA without native signal peptide of MYCTH_56237 termed Mtxyn11B. Similarly, the pPICZaA with native signal peptide segment of MYCTH_56237 (without α -MF) termed Mtxyn11C (**Figure 1**). The expression plasmids Mtxyn11A, Mtxyn11B and Mtxyn11C were constructed with corresponding primers (Mtxyn11A-F/ Mtxyn11A-R, Mtxyn11B-F/ Mtxyn11B-R and Mtxyn11C-F/ Mtxyn11C-R) by one step PCR according to the Phanta Max Super-Fidelity DNA Polymerase (primers are listed in the **Supplementary Table S1**). The recombinant strains Mtxyn11A, Mtxyn11B and Mtxyn11C were obtained by transformation of the corresponding plasmids into *P. pastoris*. Transformants were grown on YPD agar plates containing 100 μ g/mL Zeocin (Invitrogen, United States) and further confirmed by colony PCR with AOX-F/AOX-R primers and DNA sequencing should be inserted in editable format from the equation editor.

Protein Expression and SDS-PAGE Analysis

The *P. pastoris* colonies were cultured in BMGY medium (5 mL tubes) at 28°C, 200 rpm until the OD₆₀₀ of the culture reached to



4–6. The culture was then resuspended in BMMY medium (50 mL) containing YNB (1.34%) and biotin (4.0 μg/mL). Pure methanol was added to the culture to a final concentration of 1% every 24 h to maintain induction (Basit et al., 2018b). The induction process was done in triplicate.

The culture supernatants were pooled and analyzed by Tricine-SDS-PAGE (sodium dodecyl sulfate-polyacrylamide gel electrophoresis) followed by the purification through Ni-affinity column (Bio-Beads™, Sweden) equilibrated with 1 × phosphate buffer (PB, 10 mM imidazole) (Basit et al., 2018b). Protein concentration was determined through the Bradford method by using bovine serum albumin as standard (Bio-Rad protein assay kit, Bio-Rad Laboratories, Inc.).

Xylanase Activity Assay

Xylanase activity of the recombinant strains Mtxyn11A, Mtxyn11B, and Mtxyn11C was assayed by 3,5-dinitrosalicylic acid (DNS) method (Miller, 1959). The reaction system contained 1% BWX (w/v) in sodium phosphate buffer (pH 6.0) with appropriate diluted enzyme. The reaction system was then incubated at 50°C for 10 min, and terminated by the addition of 50 μL of NaOH (1 M). DNS reagent (150 μL) was added to the reaction mixture, boiled for 5 min, and then cooled at room temperature. Xylanase activity assay were performed in triplicate. One unit (U) of xylanase activity was defined as the amount of enzyme that released 1 μmol reducing sugar from the substrate (equivalent to xylose) per min under assay conditions.

The enzyme activity of the recombinant xylanase was compared with commercial xylanase from *Trichoderma longibrachiatum* (X2629, Sigma-Aldrich), under the assay conditions as described above. Optimum temperature and pH for commercial xylanase activity were sustained as per provided information.

Expression of Xylanase in a Bioreactor

Fed-batch fermentation of xylanase was performed in a 7.5 L fermentor (Shanghai Boxing Bio-engineering Equipment Co., Ltd.) with 4 L basal salts medium (BSM) (glycerol (40 g/L), KOH (4.13 g/L), MgSO₄ · 7H₂O (14.9 g/L), H₃ PO₄ (26.7 mL/

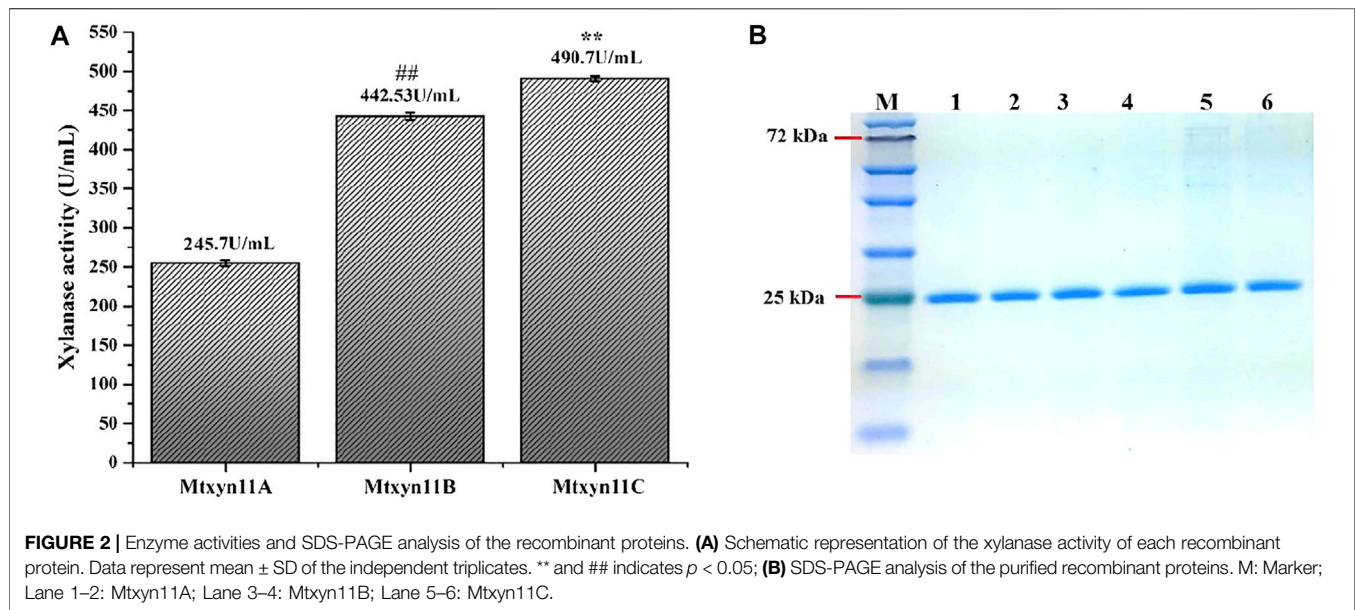
L), CaSO₄ · 7H₂O (14.9 g/L), K₂ SO₄ (18.2 g/L). BSM was supplemented containing 17.3 mL PTM1 solution. Fermentation of MYCTH_56237 and MYCTH_49824 was applied based on the *Pichia* Fermentation Process Guidelines (Invitrogen). The temperature and pH were maintained at 29°C and 5.0, respectively. Growth phase of the yeast cells were continued until the glycerol utilization from the feeding medium, which was indicated by the dissolved oxygen (DO) spike. When the glycerol was fully utilized from the feeding medium containing glycerol, 12 mL/L PTM1 solution was fed to fermenter according to a pre-adjusted DO level (10%). When the DO level reached higher than 60%, the glycerol feeding was stopped and pure methanol containing 12 mL/L PTM1 solution was pumped to induce the targeted gene expression, with the DO being set to 10–20%. Culture samples were collected at different time intervals to determine the OD₆₀₀ and xylanase activity.

Hydrolytic Activity of Xylanase

Hydrolytic activity of recombinant xylanase was estimated based on the hydrolysis of substrate BWX. For this purpose, reactions mixture containing 900 μL of 1% BWX (w/v) with 100 μL of appropriate diluted enzyme, in sodium phosphate buffer (pH 6.0) was prepared. The reaction mixture was then incubated at 50°C for 12 h and reducing sugars released from substrates were determined by DNS method (as above). The degradation rate (percent of total BWX) was calculated according to the following equation:

$$\text{Degradation rate (\%)} = \left(\frac{\text{The reducing sugars obtained by enzymatic hydrolysis (mg)}}{\text{Amount of BWX used (mg)}} \right) \times 100\% \quad (1)$$

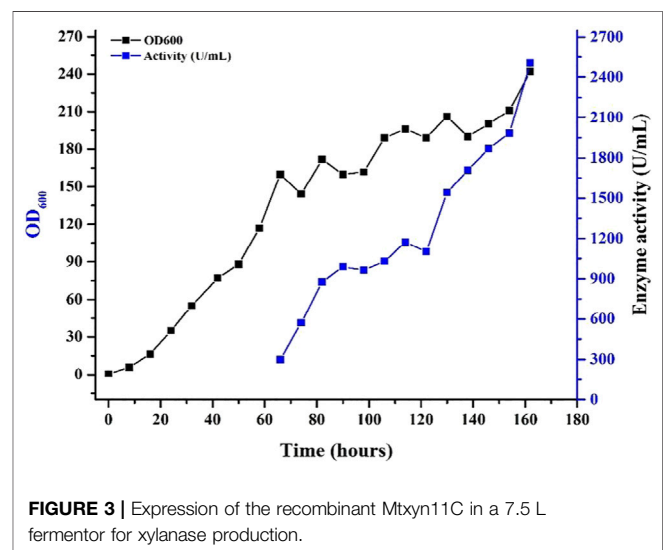
Hydrolysis products were analyzed by LC-20A HPLC (Shimadzu, Japan) with xylose and XOSs (X₅, X₄, X₃, X₂) as standards. HPLC system was equipped with a ROA-Organic Acid H⁺ (8%) column (Phenomenex) and a RIDL10A refractive index detector. The HPLC column was sustained at 50°C with H₂SO₄ (5 mM) as the mobile phase at a flow rate of 0.6 mL/min.



RESULTS AND DISCUSSION

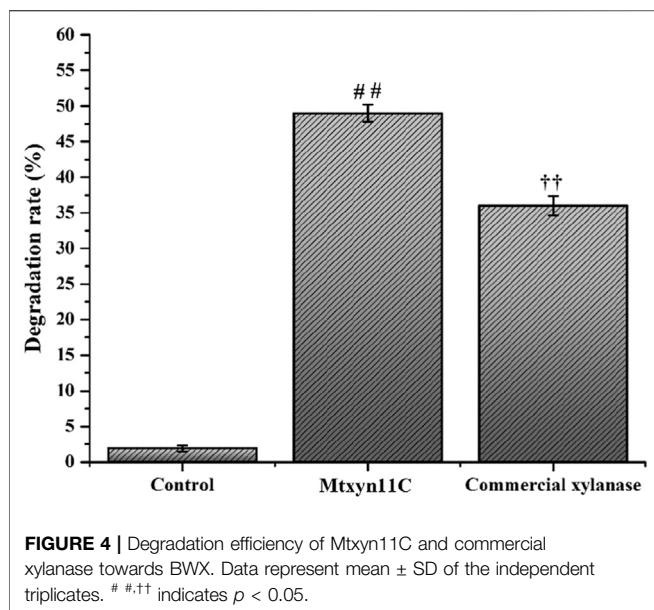
Improved Production of Xylanase

In this study, we employed the secretion machinery system of *P. pastoris* and promising results were noted. Because of the secretion of few proteins, heterologous protein expression in secretory manner in *P. pastoris* is thought to be the foremost step in purification. The process was noted with key factors that played a tangible role in the secretion system. Therefore, xylanase activity of previously expressed MYCTH_56237 was further improved through adopting a commonly used strategy of replacement of α -factor in *P. pastoris* with signal peptide sequences. For this purpose, different expression plasmids Mtxyn11A (with native signal peptide of MYCTH_56237), Mtxyn11B (without native signal peptide of MYCTH_56237) and Mtxyn11C (without the sequence of α -MF) were constructed for the expression in *P. pastoris* (Figure 1). The expression plasmids were successfully cloned in the *P. pastoris* and positive transformants of recombinant strains Mtxyn11A, Mtxyn11B and Mtxyn11C were obtained on YPD agar plates containing Zeocin (100 μ g/mL) and further regulated by an AOX1 promoter (induced by methanol). After 120 h of cultivation in BMMY medium, significantly observed was the parameter of a single peptide involved in the secretion. The xylanase activity of the recombinant strain Mtxyn11C (with native signal peptide) was significantly 1.2-folds higher than that of Mtxyn11B (without native signal peptide), followed by Mtxyn11C (Figure 2A). The SDS-PAGE analysis of the recombinant proteins (Mtxyn11A, Mtxyn11B and Mtxyn11C) indicated the estimated molecular weights of about 26 kDa, almost near to the range of calculated weights of MYCTH_56237 (Figure 2B). The single peptide is found to guide protein trafficking through the secretory pathway. The most common signal peptides which are integrated in plasmid of *P. pastoris* include *S. cerevisiae* α -MF, which have been used



efficiently for the secretion of various heterologous proteins in *P. pastoris* (Kommoju et al., 2007). Protein secretion in yeast follows a pathway from endoplasmic reticulum to Golgi and then tracks to extracellular space. An important step in this process is site-specific breakage of the signal peptide from pre-protein (Lee et al., 2003). Subsequently, the sequences of signal peptide were evaluated to improved protein expression levels in *P. pastoris*, with a special focus on secretion efficiency of the α -factor signal peptide (Huang et al., 2014). The variations in research findings have been reported indicating conflicts in results. Reportedly these conflicting results have been reported in some studies conducted by different researchers (Ghosalkar et al., 2008).

The present study also showed that replacement of α -MF secretion signal with native signal sequence of xylanase, led to an enormously higher yield of xylanase in the culture supernatant in



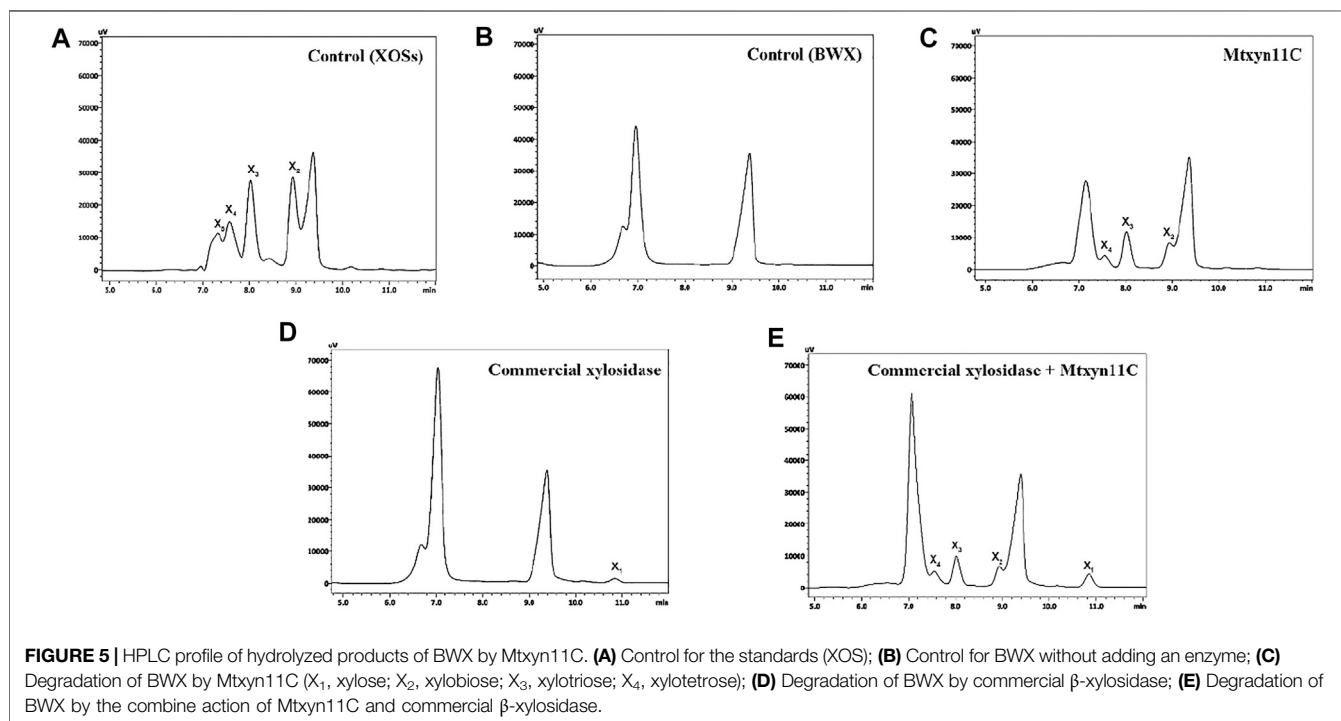
shake flasks and in 7.5 L fermentor as well. Fed-batch fermentation of the (improved activity of xylanase) Mtxyn11C was employed in 7.5 L fermentor. The recombinant strain (*Mtxyn11C*) was inoculated to the medium and glycerol was supplemented after 24 h. The rate of dissolved oxygen (DO) was raised up to 50% after the termination of glycerol feeding. Methanol was then pumped into the medium to induce the xylanase production with a stepwise increasing rate. Xylanase activity in the culture supernatant was not detected until the

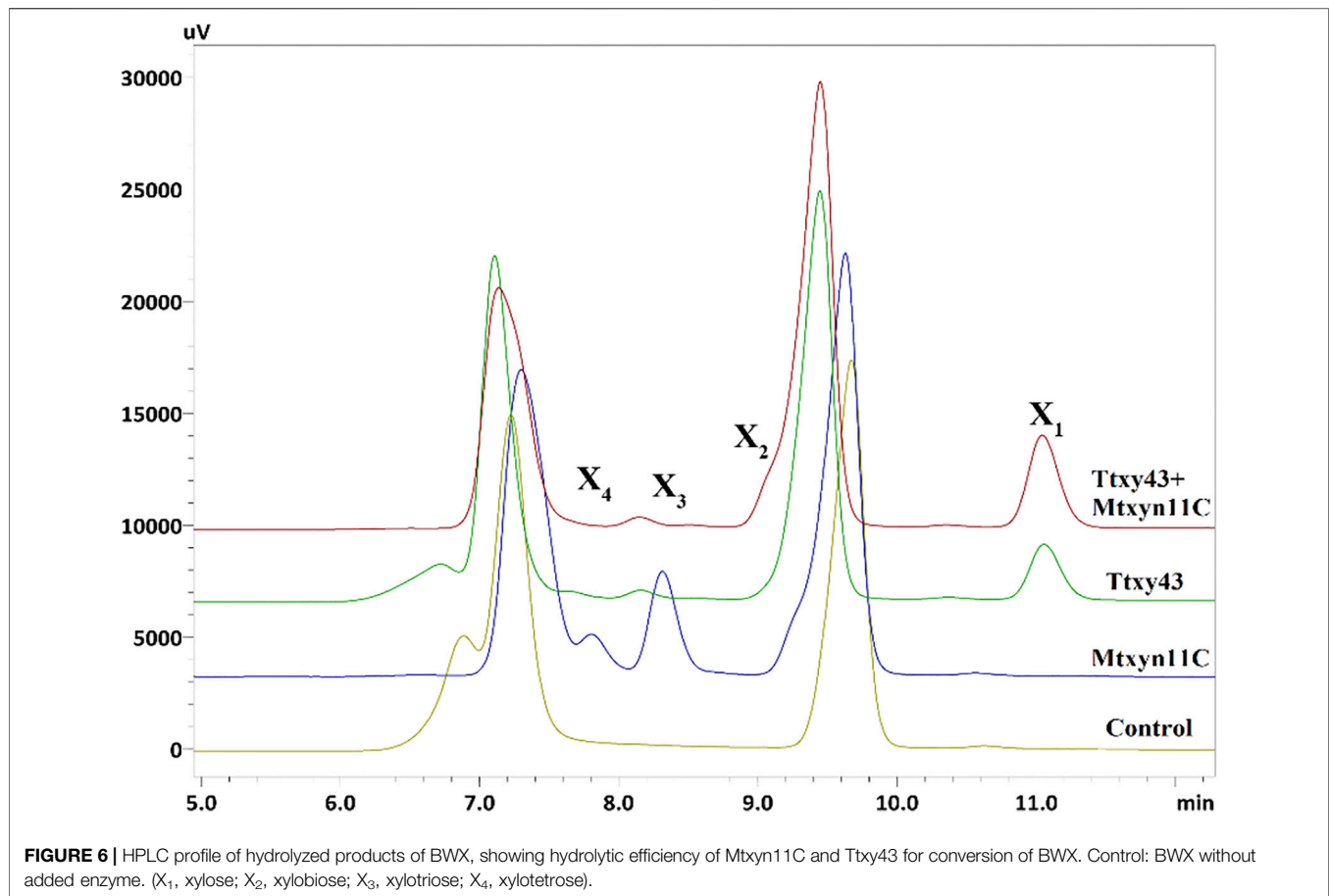
initiation of methanol feeding. Followed by the methanol feeding for 83 h, the maximum xylanase activity in the supernatant was 2503 U/mL (**Figure 3**). Xylanase activity of Mtxyn11C was successfully improved from 2,010.4 to 2503 U/mL, which is significantly higher than the native MYCTH_56237 (Basit et al., 2018b).

Hydrolytic Activity of Mtxyn11C and Applications

Production of xylooligosaccharides is great research interest due to its importance in various industrial sectors, in biofuel production and formation of the other valuable biomolecules. Therefore, the hydrolytic mode of action was estimated by inoculating Mtxyn11C (2 U) with 1% BWX, in sodium phosphate buffer (pH 6.0) at 50°C. The maximum degradation rate of Mtxyn11C was observed towards BWX and reached to 49% in 6 h (**Figure 4**). Moreover, HPLC analyses were performed and it was observed that a significant amount of xylobiose (X_2), xylotriose (X_3) and xylotetrose (X_4), among the hydrolysis product (**Figures 5A–C**) was present. In comparison, the degradation efficiency of Mtxyn11C against the commercial endoxylanase (2 U) from *Trichoderma longibrachiatum* (according to conditions provided by the manufacturer's) and Mtxyn11C was observed more effective than commercial endoxylanase (**Figure 4**).

Furthermore, the complete degradation of lignocellulosic biomass entails the specific degrading enzymes acting synergistically and considered as the rate-limiting step in biofuels production. Therefore, in this study, degradation efficiency of Mtxyn11C was evaluated with that of





synergistically acting commercial β -xylosidase. The degradation efficiency of Mtxyn11C was further examined with that of synergistically acting commercial β -xylosidase (1.6 U/20 mg) using BWX as substrate (in pH 6.0 buffer at 50°C for 1 h), using identical reaction conditions. Consequently, Mtxyn11C liberated a notable amount of xylose, with a trace amount of XOSs (X₂, X₃, X₄). The amount of xylose produced in result of both enzymes synergism was higher than that of commercial β -xylosidase (Figures 5D,E). Mtxyn11C was obviously more effective for BWX degradation and liberated a notable amount of xylose, with a trace amount of XOSs (X₂, X₃, X₄). The oligosaccharides (X₂, X₃, X₄) are used in dietary supplements and used as byproducts in various chemical industries (Chapla et al., 2012; Rastall, 2010).

The synergic study of Mtxyn11C was performed against a multifunctional xylanolytic enzyme from *M. thermophila* (termed Ttxy43). Ttxy43 showed multi-enzyme activities of endoxylanase (105.42 U/mg), β -xylosidase (80.8 U/mg) and α -L-arabinofuranosidase (15.81 U/mg). The catalytic mode of action of Ttxy43 towards BWX revealed that xylanase firstly degrades xylan to XOSs (X₂, X₃, X₄) as intermediates, which were then rapidly hydrolyzed into single xylose by β -xylosidase [14]. In order to improve further the xylose production, 2 U of Mtxyn11C and Ttxy43 was incubated

with 1% BWX in sodium phosphate buffer (pH 6.0) at 50°C for 1 h. Consequently, the xylose production was successfully improved by 40% in short duration of 30 min (Figure 6). This improved conversion of xylan into xylose along with the production of X₂, X₃ and X₄, is a highly desirable property with the potential to reduce cost and energy required for the production of pure xylose. Therefore, these findings elucidate an effective integrated degradation mechanism which provides innovative approaches for biomass energy or biofuels production.

CONCLUSION

In this study, the xylanase activity from previously identified from the *M. thermophila* was further increased through construction of engineering strains of *P. pastoris* by substituting of the secretory α -MF with the native signal peptide. The xylanase activity was significantly enhanced by 1.2-folds compared with the native one. The hydrolytic activity of Mtxyn11C towards the BWX was further revealed the production of xylobiose, xylotriose and xylotetrose from BWX. This study also elucidated the improved conversion of xylan into xylose (by 40%) when integrated with the multifunctional xylanolytic enzyme.

Altogether, these findings illustrate innovative strategies for biomass energy or biofuels production.

DATA AVAILABILITY STATEMENT

The raw data supporting the conclusion of this article will be made available by the authors, without undue reservation.

AUTHOR CONTRIBUTIONS

Conceptualization, TM and AB; methodology, TM and AB; Fermentation, JL and FZ; writing—original draft preparation, AB; writing—review and editing, KR and WJ; supervision, HL and WJ. All authors have read and agreed to the published version of the manuscript.

REFERENCES

- Ahmad, M., Hirz, M., Pichler, H., and Schwab, H. (2014). Protein Expression in *Pichia pastoris*: Recent Achievements and Perspectives for Heterologous Protein Production. *Appl. Microbiol. Biotechnol.* 98 (12), 5301–5317. doi:10.1007/s00253-014-5732-5
- Aw, R., McKay, P. F., Shattock, R. J., and Polizzi, K. M. (2018). A Systematic Analysis of the Expression of the Anti-HIV VRC01 Antibody in *Pichia pastoris* through Signal Peptide Optimization. *Protein Expr. Purif.* 149, 43–50. doi:10.1016/j.pep.2018.03.013
- Basit, A., Liu, J., Miao, T., Zheng, F., Rahim, K., Lou, H., et al. (2018b). Characterization of Two Endo- β -1, 4-Xylanases from *Myceliophthora thermophila* and Their Saccharification Efficiencies, Synergistic with Commercial Cellulase. *Front. Microbiol.* 9, 233. doi:10.3389/fmicb.2018.00233
- Basit, A., Liu, J., Rahim, K., Jiang, W., and Lou, H. (2018a). Thermophilic Xylanases: from Bench to Bottle. *Crit. Rev. Biotechnol.* 38 (7), 989–1002. doi:10.1080/07388551.2018.1425662
- Basit, A., Miao, T., Liu, J., Wen, J., Song, L., Zheng, F., et al. (2019). Highly Efficient Degradation of Xylan into Xylose by a Single Enzyme. *ACS Sust. Chem. Eng.* 7 (13), 11360–11368. doi:10.1021/acssuschemeng.9b00929
- Chapla, D., Pandit, P., and Shah, A. (2012). Production of Xylooligosaccharides from Corn Cob Xylan by Fungal Xylanase and Their Utilization by Probiotics. *Bioresour. Tech.* 115, 215–221. doi:10.1016/j.biortech.2011.10.083
- Gaurav, N., Sivasankari, S., Kiran, G., Ninawe, A., and Selvin, J. (2017). Utilization of Bioresources for Sustainable Biofuels: a Review. *Renew. Sust. Energ. Rev.* 73, 205–214. doi:10.1016/j.rser.2017.01.070
- Ghosalkar, A., Sahai, V., and Srivastava, A. (2008). Secretory Expression of Interferon-Alpha 2b in Recombinant *Pichia pastoris* Using Three Different Secretion Signals. *Protein Expr. Purif.* 60 (2), 103–109. doi:10.1016/j.pep.2008.02.006
- He, Z., Huang, Y., Qin, Y., Liu, Z., Mo, D., Cong, P., et al. (2012). Comparison of Alpha-Factor Preprosequence and a Classical Mammalian Signal Peptide for Secretion of Recombinant Xylanase xynB from Yeast *Pichia pastoris*. *J. Microbiol. Biotechnol.* 22 (4), 479–483. doi:10.4014/jmb.1109.09031
- Huang, J., Xia, J., Yang, Z., Guan, F., Cui, D., Guan, G., et al. (2014). Improved Production of a Recombinant *Rhizomucor miehei* Lipase Expressed in *Pichia pastoris* and its Application for Conversion of Microalgae Oil to Biodiesel. *Biotechnol. Biofuels* 7, 111. doi:10.1186/1754-6834-7-111
- Kommoju, P. R., Macheroux, P., and Ghisla, S. (2007). Molecular Cloning, Expression and Purification of L-Amino Acid Oxidase from the Malayan Pit viper *Calloselasma rhodostoma*. *Protein Expr. Purif.* 52, 89–95. doi:10.1016/j.pep.2006.09.016
- Lee, R. C., Hrmova, M., Burton, R. A., Lahnstein, J., and Fincher, G. B. (2003). Bifunctional Family 3 Glycoside Hydrolases from Barley with α -L-Arabinofuranosidase and β -D-Xylosidase Activity. *J. Biol. Chem.* 278 (7), 5377–5387. doi:10.1074/jbc.m210627200
- Lin, C., Shen, Z., and Qin, W. (2017). Characterization of Xylanase and Cellulase Produced by a Newly Isolated *Aspergillus fumigatus* N2 and its Efficient

FUNDING

This research was funded by National Natural Science Foundation of China (Key Program 31570067 and 31630005), and Opening Project of the State Key Laboratory of Microbial Resources.

ACKNOWLEDGMENTS

We acknowledge all authors and our prestigious institute for their valuable contribution and support in this study.

SUPPLEMENTARY MATERIAL

The Supplementary Material for this article can be found online at: <https://www.frontiersin.org/articles/10.3389/fbioe.2021.690702/full#supplementary-material>

- Saccharification of Barley Straw. *Appl. Biochem. Biotechnol.* 182 (2), 559–569. doi:10.1007/s12010-016-2344-9
- Miller, G. L. (1959). Use of Dinitrosalicylic Acid Reagent for Determination of Reducing Sugar. *Anal. Chem.* 31 (3), 426–428. doi:10.1021/ac60147a030
- Rastall, R. A. (2010). Functional Oligosaccharides: Application and Manufacture. *Annu. Rev. Food Sci. Technol.* 1, 305–339. doi:10.1146/annurev.food.080708.100746
- Samanta, A. K., Jayapal, N., Kolte, A. P., Senani, S., Sridhar, M., Suresh, K. P., et al. (2012). Enzymatic Production of Xylooligosaccharides from Alkali Solubilized Xylan of Natural Grass (*Sehima Nervosum*). *Bioresour. Tech.* 112, 199–205. doi:10.1016/j.biortech.2012.02.036
- Uday, U. S. P., Choudhury, P., Bandyopadhyay, T. K., and Bhunia, B. (2016). Classification, Mode of Action and Production Strategy of Xylanase and its Application for Biofuel Production from Water Hyacinth. *Int. J. Biol. Macromolecules* 82, 1041–1054. doi:10.1016/j.ijbiomac.2015.10.086
- Wang, J., Wang, D., Wang, B., Mei, Z.-h., Liu, J., and Yu, H.-w. (2012). Enhanced Activity of *Rhizomucor miehei* Lipase by Directed Evolution with Simultaneous Evolution of the Propeptide. *Appl. Microbiol. Biotechnol.* 96 (2), 443–450. doi:10.1007/s00253-012-4049-5
- Yang, L., Dong, W., He, J., Ren, X., and Yan, W. (2008). Expression and Purification of Natural N-Terminal Recombinant Bovine Pancreatic Trypsin Inhibitor from *Pichia pastoris*. *Biol. Pharm. Bull.* 31 (9), 1680–1685. doi:10.1248/bpb.31.1680
- Zheng, F., Liu, J., Basit, A., Miao, T., and Jiang, W. (2018). Insight to Improve α -L-Arabinofuranosidase Productivity in *Pichia pastoris* and its Application on Corn Stover Degradation. *Front. Microbiol.* 9, 3016. doi:10.3389/fmicb.2018.03016
- Zhou, W.-J., Yang, J.-K., Mao, L., and Miao, L.-H. (2015). Codon Optimization, Promoter and Expression System Selection that Achieved High-Level Production of *Yarrowia lipolytica* Lipase in *Pichia pastoris*. *Enzyme Microb. Tech.* 71, 66–72. doi:10.1016/j.enzmictec.2014.10.007

Conflict of Interest: The authors declare that the research was conducted in the absence of any commercial or financial relationships that could be construed as a potential conflict of interest.

Publisher's Note: All claims expressed in this article are solely those of the authors and do not necessarily represent those of their affiliated organizations, or those of the publisher, the editors and the reviewers. Any product that may be evaluated in this article, or claim that may be made by its manufacturer, is not guaranteed or endorsed by the publisher.

Copyright © 2021 Miao, Basit, Liu, Zheng, Rahim, Lou and Jiang. This is an open-access article distributed under the terms of the Creative Commons Attribution License (CC BY). The use, distribution or reproduction in other forums is permitted, provided the original author(s) and the copyright owner(s) are credited and that the original publication in this journal is cited, in accordance with accepted academic practice. No use, distribution or reproduction is permitted which does not comply with these terms.



Transcriptomic and Metabolomic Differences Between Two *Saposhnikovia divaricata* (Turcz.) Schischk Phenotypes With Single- and Double-Headed Roots

Tao Zhang, Yuqiu Chen, Qinghe Zhang, Peng Yu, Qiong Li, Weichen Qi* and Changbao Chen*

OPEN ACCESS

Key Laboratory of Chinese Medicine Planting and Development, Changchun University of Chinese Medicine, Changchun, China

Edited by:

Lei Wang,
Ocean University of China, China

Reviewed by:

Yidan Li,
Jilin Academy of Agricultural
Sciences, China
Ting Wang,
Nagoya University, Japan

*Correspondence:

Weichen Qi
weichen_qi@163.com
Changbao Chen
ccb2021@126.com

Specialty section:

This article was submitted to
Bioprocess Engineering,
a section of the journal
Frontiers in Bioengineering and
Biotechnology

Received: 25 August 2021

Accepted: 12 October 2021

Published: 28 October 2021

Citation:

Zhang T, Chen Y, Zhang Q, Yu P, Li Q,
Qi W and Chen C (2021)
Transcriptomic and Metabolomic
Differences Between Two
Saposhnikovia divaricata (Turcz.)
Schischk Phenotypes With Single- and
Double-Headed Roots.
Front. Bioeng. Biotechnol. 9:764093.
doi: 10.3389/fbioe.2021.764093

Saposhnikovia divaricata is derived from the dried roots of *Saposhnikovia divaricata* (Turcz.) Schischk and used as a Chinese herbal medicine for treating respiratory, immune, and nervous system diseases. The continuously increasing market demand for traditional Chinese medicine requires the commercial cultivation of *Saposhnikovia divaricata* using standardized methods and high yielding genotypes, such as double-headed root plants, for achieving consistent quality and a reliable supply. In this study, we aimed to identify the quantitative differences in chromone, a precursor of flavonoid biosynthesis, between plants with single- and double-headed roots using high-performance liquid chromatography and further explore the two phenotypes at the transcriptomic and metabolomic levels. Our results showed that the chromone content was significantly higher in plants with double-headed roots than in those with single-headed roots. Transcriptomic analysis revealed six significantly differentially expressed genes between the two phenotypes, including five key genes in the flavonoid biosynthesis pathway (*4-coumarate-CoA ligase*, *chalcone synthase 1*, *vinorine synthase*, *chalcone-flavonone isomerase 1*, and *flavanone 3 beta-hydroxylase*) and one key gene in the abscisic acid biosynthetic pathway (*zeaxanthin epoxidase*). Moreover, metabolomic analysis showed that the 126 differentially expressed metabolites were mainly enriched in the biosynthesis of secondary metabolites and phytohormones. Overall, our results suggest that plants with double-headed roots have higher medicinal value than those with single-headed roots, probably due to differences in various biosynthetic pathways. These data might help select the genotypes with superior yield and therapeutic properties.

Keywords: *Saposhnikovia divaricata*, transcriptome, metabolite, biotechnology, chromone

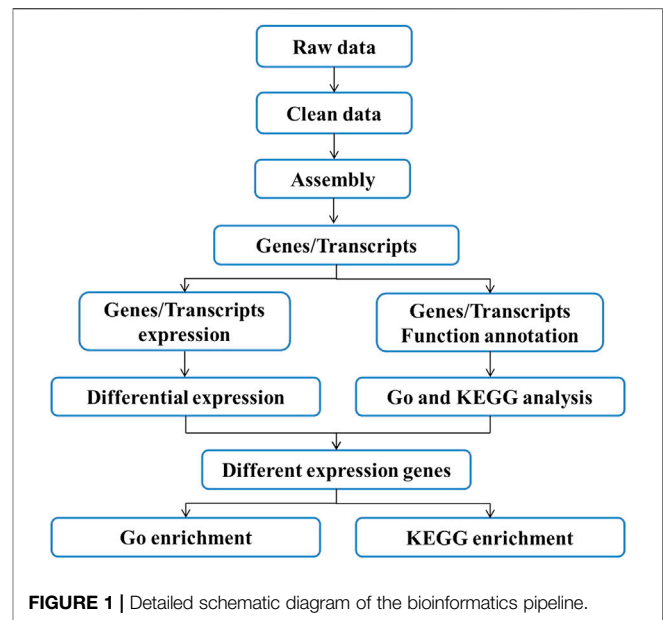
Abbreviations: ABA, Abscisic acid; DEGs, Differentially expressed genes; DEMs, Differentially expressed metabolites; *GAPDH*, Glyceraldehyde-3-phosphate dehydrogenase; GO, Gene Ontology; KEGG, Kyoto Encyclopedia of Genes and Genomes; LC-MS, Liquid Chromatography Mass-Spectroscopy; QC, Quality control.

INTRODUCTION

Saposhnikovia divaricata, also known as Fangfeng, is derived from the dried roots of *Saposhnikovia divaricata* (Turcz.). Schischk and used as a Chinese herbal material owing to its antipyretic, analgesic, antioxidant, antiproliferative, and anti-inflammatory properties (Khan et al., 2011; Okuyama et al., 2019). The chemical composition of *S. divaricata* is complex and includes more than 100 compounds, such as chromone, which is a precursor of flavonoid biosynthesis, coumarin, and volatile oil. Previous studies have shown that the root has the highest medicinal value during the vegetative stage (Liu et al., 2020), which is significantly reduced in the reproductive stage (Li et al., 2017). Therefore, it is necessary to determine the medicinal substances of *S. divaricata* and elucidate the underlying formation mechanism (Liu and Zhang, 2007).

Transcriptomics is the study of gene expression at the RNA level under specific physiological conditions and helps identify the differentially expressed genes (DEGs) (Armstrong and Que, 2012; Hamilton and Buell, 2012; Ramaswami et al., 2013) and understand the molecular basis of phenotypic differences (Forrest and Carninci, 2009; Rodríguez-García et al., 2017). Transcriptomics has been used for gene mining, function prediction, and metabolic pathway analysis of various medicinal plants, including *Panax ginseng* (Hongzhe et al., 2015; Li et al., 2013; Liu et al., 2016; Zhang et al., 2021), *Panax quinquefolius* (Wu et al., 2013; Zou et al., 2015), *Scutellaria baicalensis* (Cheng et al., 2018), *Salvia miltiorrhiza* (Gao et al., 2014), and *Bupleurum chinense* (Sui et al., 2011). Transcription factors initiate and regulate gene expression by recognizing and binding to cis-acting elements in the promoter region of genes. Studies have shown that WRKY, bHLH, and bZIP transcription factors play important roles in defense responses against various abiotic stresses (Madhuni and Ralf, 2014), in plant growth, stress resistance, and signal transduction (Liu et al., 2015), and in plant development and physiological metabolic processes (Zhang et al., 2011), respectively. Therefore, genome-wide transcriptomics, together with transcription factor analysis, allows us to understand plant responses via transcriptional changes and elucidate the molecular mechanisms underlying the biosynthesis of secondary metabolites in medicinal plants.

Metabolomics is the comprehensive qualitative and quantitative characterization of all endogenous small molecule metabolites in biological systems. It has been widely applied to study metabolites in medicinal plants due to its high sensitivity, resolution, accuracy, and wide dynamic range. Phytohormones are signal molecules that are naturally present in plants in extremely low concentrations, influencing plant growth and development (Hong and Xu, 2013). Of these, brassinolide, salicylic acid, and jasmonic acid are involved in plant-pathogen interactions (Jameson et al., 2016); cytokinin (CTK) is a derivative of adenine and, together with indolyl acetic acid, induces plant cell division, inhibits leaf senescence, and defends against abiotic stress (Werner and Schmulling 2009); zeatin nucleoside, which is the main form of CTK transported in the xylem, controls the differentiation of plant flower buds; and



abscisic acid (ABA) regulates plant and environmental signals (Zhang et al., 2010). Plant endogenous hormones play an important role in the process of plant growth and development, which may be the cause of the double-headed roots of *S. divaricata*.

The market demand for traditional Chinese medicine continues to grow worldwide. Thus, the commercial cultivation of *S. divaricata* using standardized methods is required for achieving consistent quality and a reliable supply. The conventional cultivation of *S. divaricata* includes plants with single-headed roots (one aerial part); however, we found that those with double-headed roots (two aerial parts) have a higher yield potential. In this study, we aimed to identify the differences in the chromone content between plants with single- and double-headed roots using high-performance liquid chromatography and further explore the two phenotypes via transcriptomic and metabolomic analyses. Our study provides an important theoretical basis for the quality research of *S. divaricata* medicinal materials.

MATERIALS AND METHODS

Plant Material

The *S. divaricata* roots of Umbelliferae plants were selected as the test materials. Samples of *S. divaricata* were collected from its cultivation base in Baicheng City, Jilin Province (E122.51, N45.37) at the end of September 2020. Single and double-headed root plants were still grown under the well-cultivated conditions. Those were dug out from the soil, all root tissues from every 3 individual plants were mixed as one biological replicate to be stored in liquid nitrogen. Three biological replicates were respectively collected from the treatment and control groups for transcriptome sequencing. Six biological replicates were respectively collected from the treatment and control groups

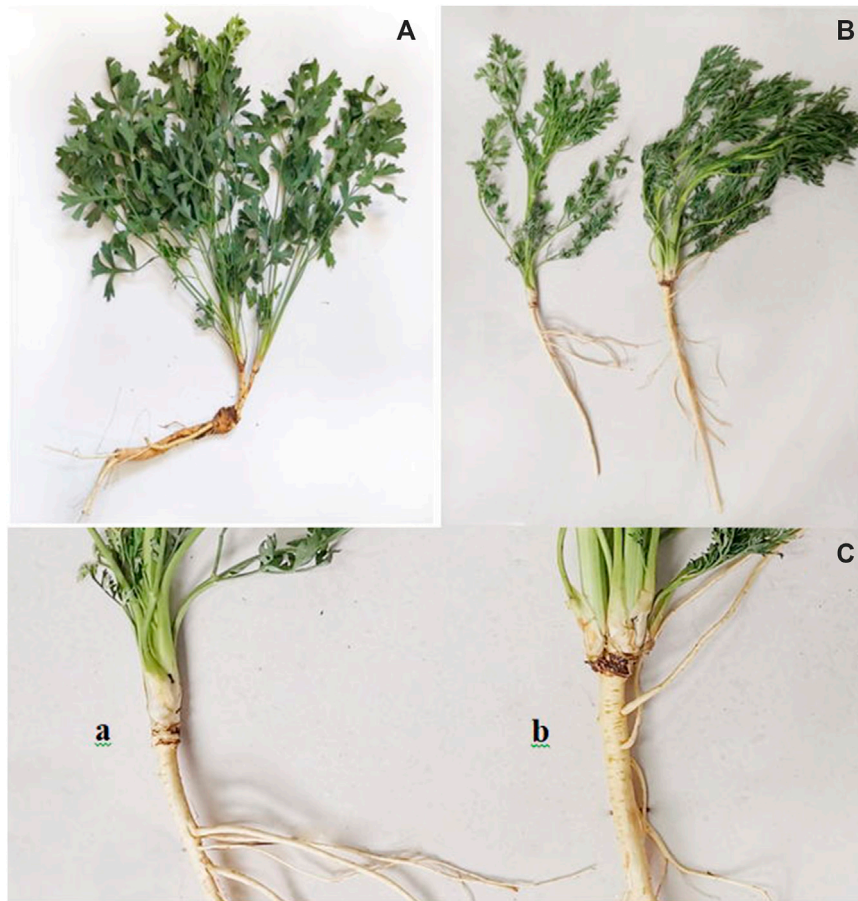


FIGURE 2 | The sample of SD. Note: **(A)** is double-headed root SD; **(B)** is the whole plant of single-headed root and double-headed root; In **(C)**, a is a single-headed root, and b is a double-headed root.

for metabolomic sequencing. The remaining samples were dried at 45°C to a constant weight, mixed and crushed, for determining ginsenoside content. The differences between plants with single- and double-headed roots are shown in **Figure 1**.

Determination of the Chromone Content

After drying the samples, these were ground into a powder. The ground powder was filtered through a 60-mesh sieve and then weighed in three replicates, each weighing 1.0 g. Chromogen ketones were extracted ultrasonically (extraction conditions: ultrasonic frequency, 40 kHz; extraction temperature, 30°C; extraction time, 30 min; liquid ratio, 1:15), extracted three times with methanol, filtered in a funnel, and then the filtered liquids were combined. After the filtrate was evaporated in an evaporating dish and transferred to a 5 ml volumetric flask, the volume was adjusted to 5 ml and the solution was filtered using a 0.22 μm filter. High-performance liquid chromatography was performed using an Agilent 1,200 series high-performance liquid chromatography system (Agilent, Palo Alto, CA, United States), equipped with an autosampler and a

UV detector with a C18 column (4.6 mm × 250 mm, 5 μm; Agilent). Gradient elution was performed using solvent A (100% methanol) and solvent B (100% water) at 30°C, according to the following gradient program: 0–20 min, 30% A; 20–25 min, 45% A; 25–50 min, 60% A; 50–55 min, 90% A; and 55–60 min, 100% A. The flow rate was maintained at 1.0 ml/min, the sample injection volume was 10 μl, and UV absorption was measured at 254 nm. Quantitative analysis was performed using the one-point curve method using an external standard of authentic chromones (prim-*O*-glucosylcimifugin, 4'-*O*-β-*D*-glucosyl-5-*O*-methylvisamminol, cimifugin, and sec-*O*-glucosylhamaudol) and the following equations:

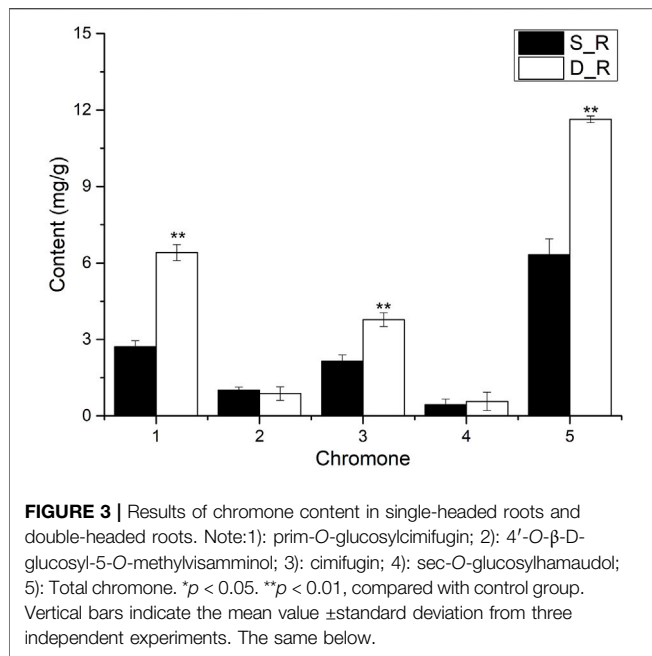
$$y = 5013.2x - 4988.3 \quad (r^2 = 0.9983)$$

$$y = 7810.9x - 5120.6 \quad (r^2 = 0.9990)$$

$$y = 6177.9x - 3435.5 \quad (r^2 = 0.9997)$$

$$y = 2867.9x - 2658.2 \quad (r^2 = 0.9992)$$

For prim-*O*-glucosylcimifugin, 4'-*O*-β-*D*-glucosyl-5-*O*-methylvisamminol, cimifugin, and sec-*O*-glucosylhamaudol, respectively.



RNA Sequencing

The total RNA was extracted according to the instruction manual of TRIzol reagent (Invitrogen, Waltham, MA, United States). Bioanalyzer 2100 and RNA 1000 Nano LabChip Kit (Agilent) were used to analyze the total RNA quantity and purity. Poly(A) RNA was purified from the total RNA using magnetic beads linked to poly-T oligonucleotides. Next, at a temperature of 95°C, divalent cations were used to fragment the mRNA into small pieces. The RNA-Seq sample preparation kit (Illumina, San Diego, CA, United States) was used to reverse transcribe the cleaved RNA fragments to create the final cDNA library. The average insert size of the double-ended library was 300 ± 50 bp. Paired-end sequencing was performed by LC Sciences (Houston, TX, United States) using an IlluminaHiSeq 4,000 sequencer.

De Novo Assembly, Unigene Annotation, and Functional Classification

The workflow of the bioinformatics analysis is shown in **Figure 2**. Cutadapt and Perl scripts were used to delete the reads containing adapter contamination, low-quality bases, and undetermined bases (Martin, 2011). FastQC (<http://www.bioinformatics.babraham.ac.uk/projects/fastqc/>) was used to verify sequence quality and calculate the Q20, Q30, and GC content of clean data. All downstream analyses were based on high-quality, clean data. The *de novo* assembly of the transcriptome data was performed using Trinity 2.4.0. The transcripts were grouped into clusters according to the shared sequence content, and the transcript with the largest expansion in each cluster was selected as the unigene (Grabherr et al., 2011). All assembled unigenes were linked to the non-redundant protein database (<http://www.ncbi.nlm.nih.gov/>), Gene Ontology (GO; <http://www.geneontology.org/>),

SwissProt for comparison (<http://www.expasy.ch/sprot/>), Kyoto Encyclopedia of Genes and Genomes (KEGG; <http://www.genome.jp/kegg/>), and eggNOG (<http://eggnogdb.embl.de/>). A DIAMOND threshold E value of <0.00001 was used (Buchfink et al., 2015).

Identification of the DEGs

Salmon (<https://combine-lab.github.io/salmon/>) was used to determine the expression level of unigenes by calculating the transcripts per million (Patro et al., 2017). The “edgeR” package in R was used to select the DEGs at *p* < 0.05 when the log₂ (multiple change) > 1 or log₂ (multiple change) < -1 (Robinson et al., 2010).

Metabolite Extraction and Liquid Chromatography Mass-Spectroscopy

The collected samples were thawed on ice, and 120 μl of pre-chilled 50% methanol buffer was used to extract the metabolites from 20 μl of each sample. The metabolite mixture was vortexed for 1 min, incubated at 20°C–25°C for 10 min, and stored at -20°C overnight. The mixture was centrifuged at 4,000 × *g* for 20 min, and the supernatant was transferred to a 96-well plate. The samples were stored at -80°C before the LC-MS analysis. Mixed quality control (QC) samples were prepared by combining 10 μl of each extraction mixture.

LC-MS Analysis

All test samples were analyzed using a TripleTOF 5,600 Plus high-resolution tandem mass spectrometer (SCIEX, Warrington, United Kingdom) in the positive and negative ion modes, and an ultra-high-performance liquid chromatography system equipped with Acquity ultra-high-performance liquid T3 columns (SCIEX) for separation (100 mm × 2.1 mm, 1.8 μm; Waters, Milford, MA, United States). The mobile phase consisted of solvent A (water, 0.1% formic acid) and solvent B (acetonitrile, 0.1% formic acid). The gradient elution conditions were as follows: flow rate, 0.4 ml/min; 5% solvent B, for 0–0.5 min; 5%–100% solvent B for 0.5–7 min; 100% solvent B for 7–8 min; 100%–5% solvent B for 8–8.1 min; and 5% solvent B for 8.1–10 min. The column temperature was maintained at 35°C. The TripleTOF 5,600 Plus system was used to detect the metabolites eluted from the column. The curtain gas pressure was set to 30 psi, and the pressure of the ion source gas 1 and 2 was set to 60 psi. The temperature of the interface heater was set to 650°C. For the positive and negative ion modes, the ion spray float voltage values used were 5 and -4.5 kV, respectively. MS data were collected in IDA mode. The time of flight mass range used was 60–1,200 Da. Survey scans were collected every 150 ms, and up to 12 production scans were collected if the threshold of 100 counts exceeded the 1+ charge state. The total cycle time was set to 0.56 s. The four-time periods of each scan were summed at a pulse frequency of 11 kHz by monitoring using a 40 GHz multi-channel thermal conductivity detector with four anodes/channel detection. Dynamic exclusion was set to 4 s. During the entire collection period, every 20 samples, the system was calibrated for mass accuracy, and every ten samples, one QC sample was analyzed to evaluate the stability of the LC-MS.

TABLE 1 | The RNA-seq data for these 6 samples.

Sample	Raw reads	Raw bases (G)	Valid eads	Valid bases (G)	Valid %	Q20%	Q30%	GC %
D_R_1	41,486,368	6.22	40,820,710	5.72	98.40	98.18	93.77	43.69
D_R_2	52,422,016	7.86	51,496,090	7.21	98.23	98.21	93.91	43.59
D_R_3	47,555,580	7.13	46,691,176	6.54	98.18	98.29	94.12	43.92
S_R_1	47,065,328	7.06	46,114,706	6.46	97.98	98.18	93.86	43.83
S_R_2	48,422,758	7.26	47,510,030	6.65	98.12	98.22	93.97	43.79
S_R_3	48,893,016	7.33	48,060,970	6.73	98.30	98.27	94.05	43.71

TABLE 2 | Summary of assembly results of *SD*.

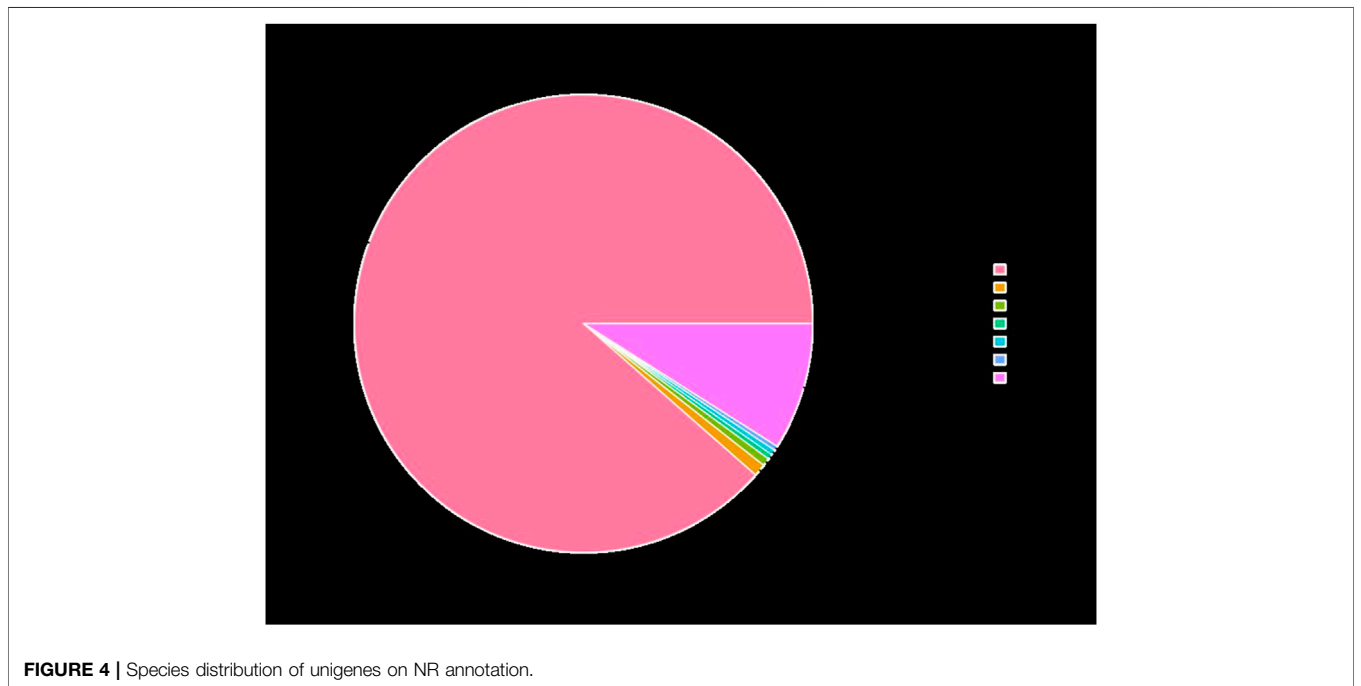
Index	All	GC%	Min length	Median length	Max length	Total assembled bases	N50
Transcript	103,139	40.10	201	755	15,586	108,266,339	1,599
Gene	44,258	40.18	201	610.00	15,586	43,027,640	1,617

TABLE 3 | Summary of function annotation of *SD*.

DB	Num	Ratio (%)
All	44,258	100.00
GO	23,417	52.91
KEGG	18,487	41.77
Pfam	20,999	47.45
SwissProt	19,125	43.21
eggNOG	25,735	58.15
NR	28,726	64.91

Metabolomic Data Processing

XCMS was used to preprocess the obtained LC-MS data. The original data file was converted to the mzXML format and then processed using the “XCMS,” “CAMERA,” and “metal” packages in R. Each ion was identified based on comprehensive information about the retention time and m/z. The intensity of each peak was determined, and a three-dimensional matrix containing any specified peak index (retention time-m/z pair), the sample name (observation result), and ion intensity information (variable)



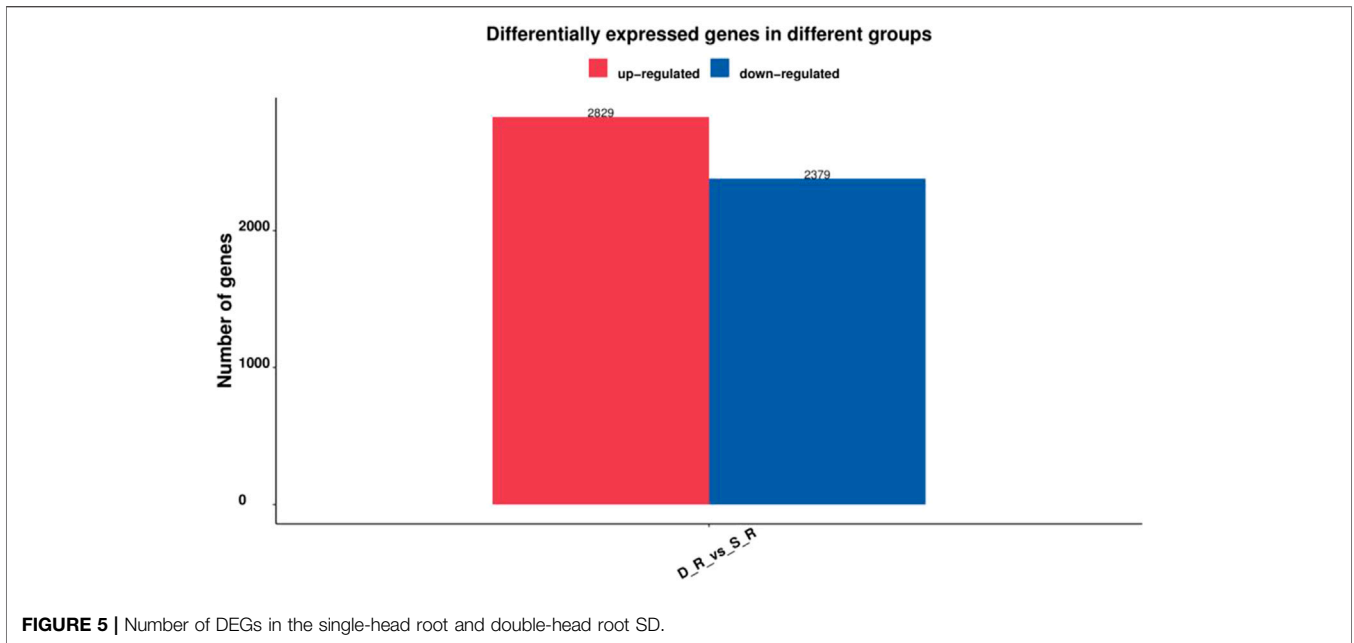


FIGURE 5 | Number of DEGs in the single-head root and double-head root SD.

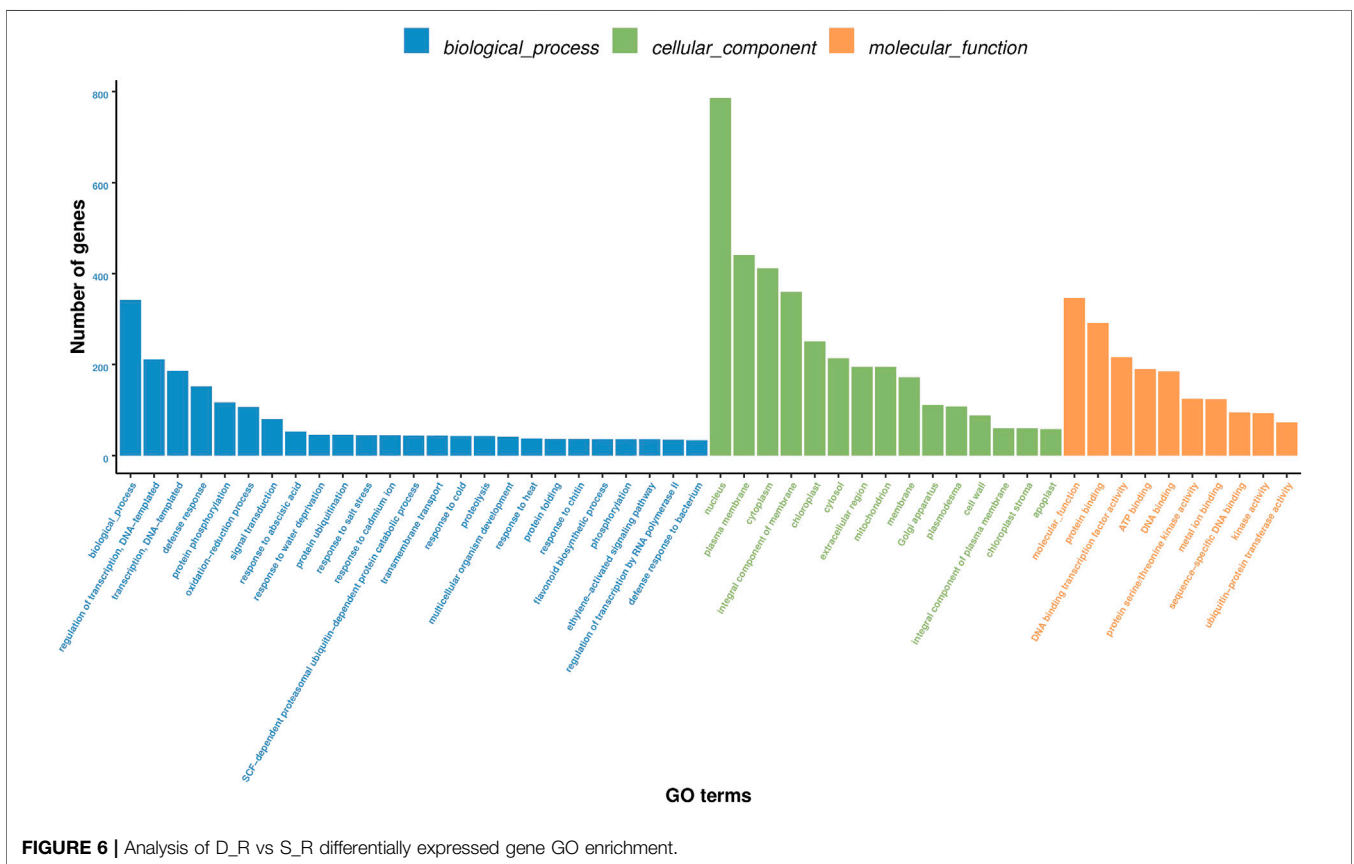
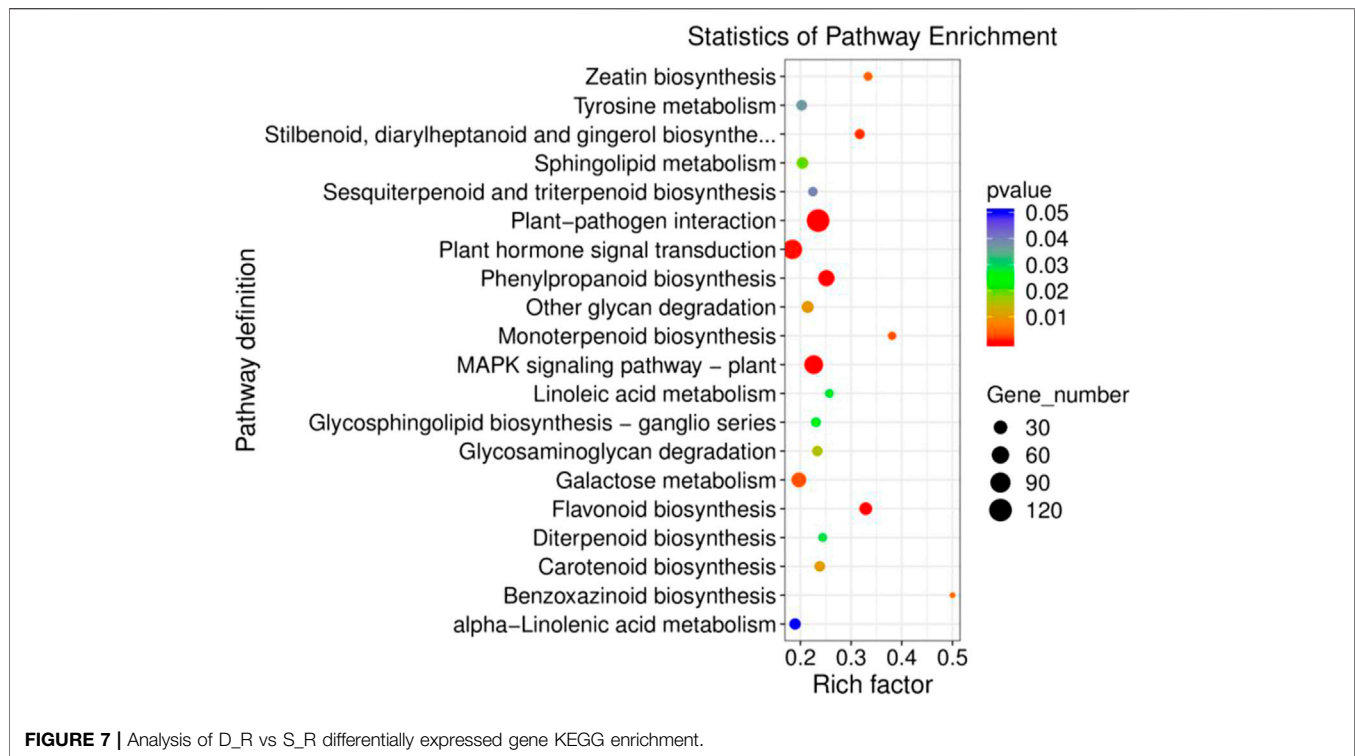


FIGURE 6 | Analysis of D_R vs S_R differentially expressed gene GO enrichment.

was generated. Then, the information was matched with internal and public databases. KEGG and the human metabolome database were used to annotate the metabolites by matching their molecular weight data (m/z) within the 10-

ppm threshold. The “metal” R package was used to further process the peak intensity data. The features detected in <50% of the QC samples or 80% of the test samples were deleted, and the k-nearest neighbor algorithm was used to extrapolate the



values of the missing peaks to further improve data quality. Principal component analysis was performed to use the processed data set to detect any outliers and batch effects. QC data about the injection sequence were fit to QC-based local regressions to minimize the signal intensity drift over time. In addition, the relative standard deviations of the metabolic characteristics were calculated for all QC samples, and those with standard deviations >30% were eliminated. Before performing QC-robust spline batch correction, the data were normalized using a probability quotient normalization algorithm. Student's t-test was used to determine the significant differences, and then the Benjamini-Hochberg procedure was used to adjust for multiple tests. Furthermore, the “metal” R package was used to perform a supervised partial least squares discriminant analysis using a variable importance cutoff value of 1.0 to identify the differentially expressed metabolites (DEMs) between the two phenotypes.

Quantitative Reverse Transcription-PCR

The instructions of the TaKaRa MiniBEST Universal RNA Extraction Kit were followed for total RNA extraction (TaKaRa, Kusatsu, Shiga, Japan), and the PrimeScript™ RT Master Mix Kit (TaKaRa) was used for reverse transcription. RT-qPCR was performed on a 96-well plate using an Agilent Technologies Stratagene Mx3000P thermal cycler and a SYBR Green-based PCR kit. Each reaction involved 1 µl of cDNA template (1 mg/ml), 10 µl of SYBR Green Mix (TaKaRa), 1 µl of forward primer (1 mM), 1 µl of reverse primer (1 mM), and 7 µl of ddH₂O. The thermal conditions were as follows: 95°C for 3 min, followed by 40 cycles at 95°C for 5 s, 55°C for 32 s, and 72°C

for 20 s. The melting curve was obtained by gradually increasing the temperature from 55°C to 95°C at a heating rate of 0.1°C/s. RT-qPCR analysis was performed using three biological replicates. *GAPDH* (glyceraldehyde-3-phosphate dehydrogenase) was used as a housekeeping gene to estimate the relative gene expression using the $2^{-\Delta\Delta C_t}$ method. The primer sequences used in this study are shown in **Supplementary Table S1**.

Statistical Analysis

The original data were compiled using the MS Excel 2016 software (Microsoft, Redmond, WA, United States), and SPSS 19.0 was used for data analysis (IBM, Armonk, NY, United States). GraphPad Prism 6.0 (GraphPad Software, San Diego, CA, United States) and Origin 9.0 (OriginLab, Northampton, MA, United States) were used to create the graphic illustrations.

RESULTS

Chromone Content

The chromone content in the single- and double-headed roots is shown in **Figure 3**. The prim-*O*-glucosylcimifugin, cimifugin, and total chromone contents in the double-headed roots were significantly higher ($p < 0.01$) than those in the single-headed roots, with 2.36, 1.76, and 1.84-fold differences, respectively. On the basis of the detection indicators stipulated in the 2020 edition of the Chinese Pharmacopoeia, the measurement indicators were enriched (Commission, 2020). The measurement results showed

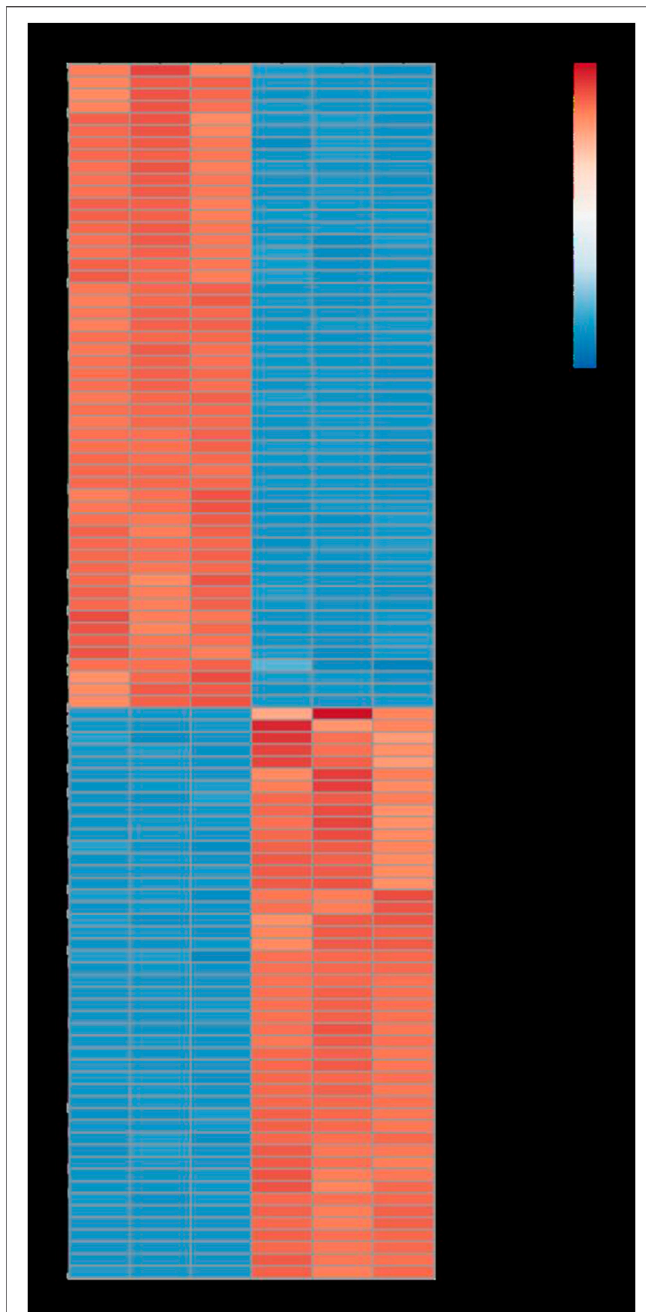


FIGURE 8 | Heatmap analysis describing the differentially expressed genes. Red, up-regulated genes. Blue, down-regulated genes.

that the double-headed roots were superior to the single-headed roots in terms of the effective ingredients. Prim-*O*-glucosylcimifugin is colling and relieves pain, which are good pharmacological effects; therefore, it can be used as the first choice medicine in clinical practice.

Transcriptomic Data Analysis

Six cDNA libraries from each phenotype generated 285,845,066 raw reads. After removing the adapters and filtering out the low-

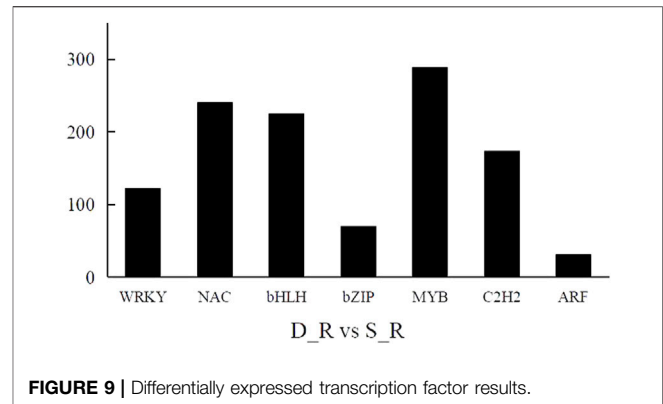


FIGURE 9 | Differentially expressed transcription factor results.

TABLE 4 | Candidate genes differentially expressed in single-head root and double-head root SD.

Name	Gene ID	Gene expression (log ₂ ratio)	up/down
4CLL9	TRINITY_DN17215_c0_g5	-1.30	down
4CLL7	TRINITY_DN15920_c0_g4	-1.53	down
CHI3	TRINITY_DN13271_c0_g7	-1.42	down
4CL	TRINITY_DN12193_c0_g5	1.06	up
CHS2	TRINITY_DN12770_c0_g2	1.20	up
ZEP	TRINITY_DN6974_c0_g1	4.15	up

quality sequences, 280,693,682 clean reads were obtained from the six libraries (Table 1). After *de novo* assembly, mapping to contigs, and redundancy removal, 44,258 unigenes were obtained with an N50 length of 1,599 nucleotides (Table 2, Supplementary Figure S1). Therefore, the quality of the experimental data obtained via sequencing was high, meeting the conditions for the subsequent experimental analysis. Of the 44,258 unique sequences, 90.67% showed homology to known genes of existing models (88.51% to *Daucus carota*, 0.87% to *Quercus suber*, 0.57% to *Vitis vinifera*, 0.36% to *Actinidia chinensis*, and 0.36% to *Helianthus annuus*; Table 3 and Figure 4). Salmon was used to determine the expression levels of the unigenes. A total of 5,208 DEGs were screened in the D_R vs. S_R comparison group, of which 2,829 were upregulated and 2,379 were downregulated. The number of upregulated genes was higher than that of downregulated genes, indicating that the DEGs upregulated in the double-headed roots can be used as important candidate genes to identify the quality differences between both phenotypes (Figure 5).

Furthermore, GO function enrichment analysis revealed that the DEGs were enriched in biological processes (i.e., biological process, regulation of transcription, DNA-templated transcription, DNA-templated defense response, and protein phosphorylation), cellular components (i.e., nucleus, plasma membrane, cytoplasm, integral components of membrane, and chloroplast), and molecular functions (i.e., molecular function, protein binding, DNA binding transcription factor activity, ATP binding, and DNA binding) (Figure 6). To further determine the internal cause of the difference in quality observed between the

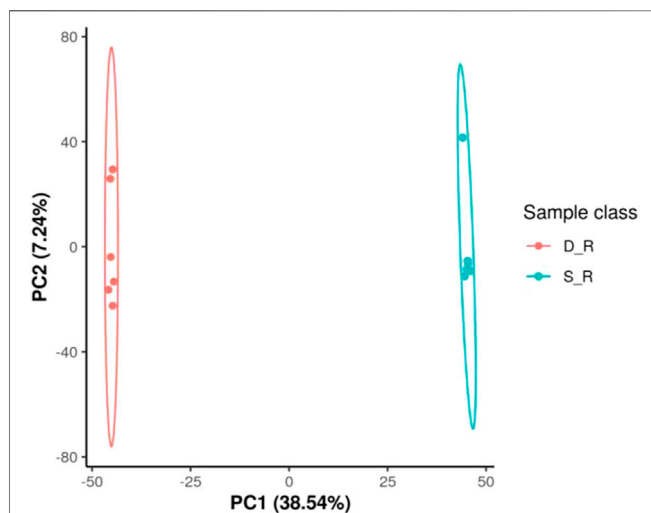
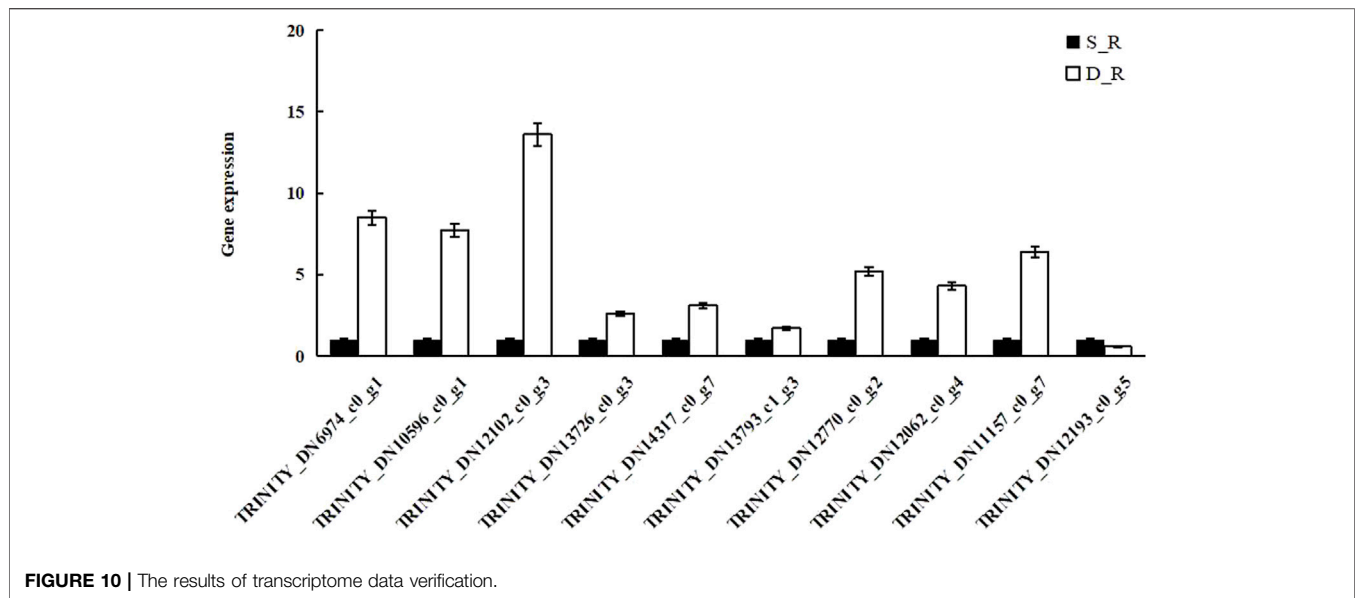


FIGURE 11 | Root metabolome variation among samples as determined by principal component analysis (PCA). a Positive electrospray ionization (ESI) mode, b negative ESI mode; PC1 represents the first principal component; PC2 represents the second principal component. D_R, double-head root; S_R, single-head root; QC, quality control (a mixture of experimental samples prepared in equal amounts). The data shown are the means of six biological replicates.

single- and double-headed roots (that is, the metabolic pathways associated with the quality of the medicinal material), we mapped the DEGs to the KEGG database. KEGG pathway analysis showed that the DEGs were highly associated with several pathways, including plant-pathogen interaction, plant hormone signal transduction, MAPK signaling pathway-plant, phenylpropanoid biosynthesis, and galactose metabolism (Figure 7). The DEGs were enriched in plant hormone signal transduction pathways, indicating that hormones may be essential for the quality of the medicinal materials. In addition,

many genes are involved in the MAPK signaling pathway and phenylpropanoid biosynthesis-related pathways. Chromone is the most important active ingredient in *S. divaricata* and the basic framework for flavonoid synthesis. Therefore, this research focused on the synthesis pathways of plant hormones and flavonoids. Cluster analysis demonstrated that the number of upregulated genes was significantly higher than that of downregulated genes Figure 8. The test results indicated that the higher number of upregulated genes in double-headed roots may be related to the accumulation of active ingredients. This experimental result was mutually corroborated by the previous differential gene expression analysis.

A transcription factor is a protein with a special structure that regulates gene expression. Transcription factors initiate and regulate gene expression by recognizing and binding to cis-acting elements in the promoter region of genes. We also performed a statistical analysis of the differential transcription factors in the D_R vs. S_R comparison group and screened 4,166 differential transcription factors. These factors mainly belonged to the MYB (290 genes), bHLH (278 genes), NAC (241 genes), ERF (186 genes), C2H2 (174 genes), WRKY (123 genes), and bZIP (71 genes) families, as shown in Figure 9. This shows that the transcription factors of these families play an important role in the formation of double-headed root medicinal materials.

Furthermore, through the functional analysis of the differential genes and further screening, we obtained six key differential genes related to the synthesis of flavonoids and plant hormones, including five key genes in the flavonoid synthesis pathway (*4-coumarate-CoA ligase*, *chalcone synthase 1*, *vinorine synthase*, *chalcone-flavonone isomerase 1*, and *flavanone 3 beta-hydroxylase*) and one key gene in the ABA biosynthetic pathway (*zeaxanthin epoxidase*) (Table 4). Therefore, the above six genes can be used as key candidate genes to study the quality differences of double-headed root medicinal materials.

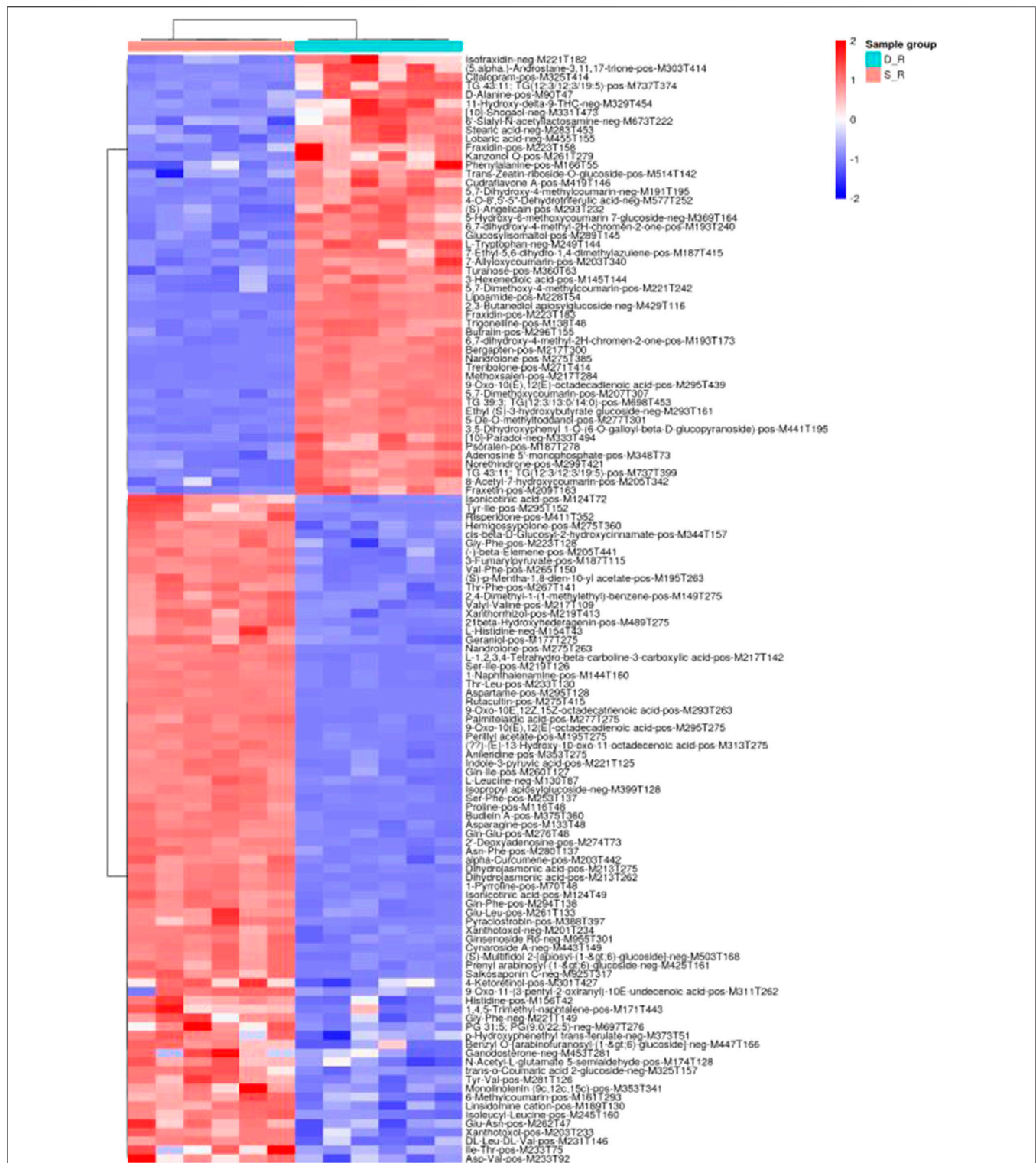
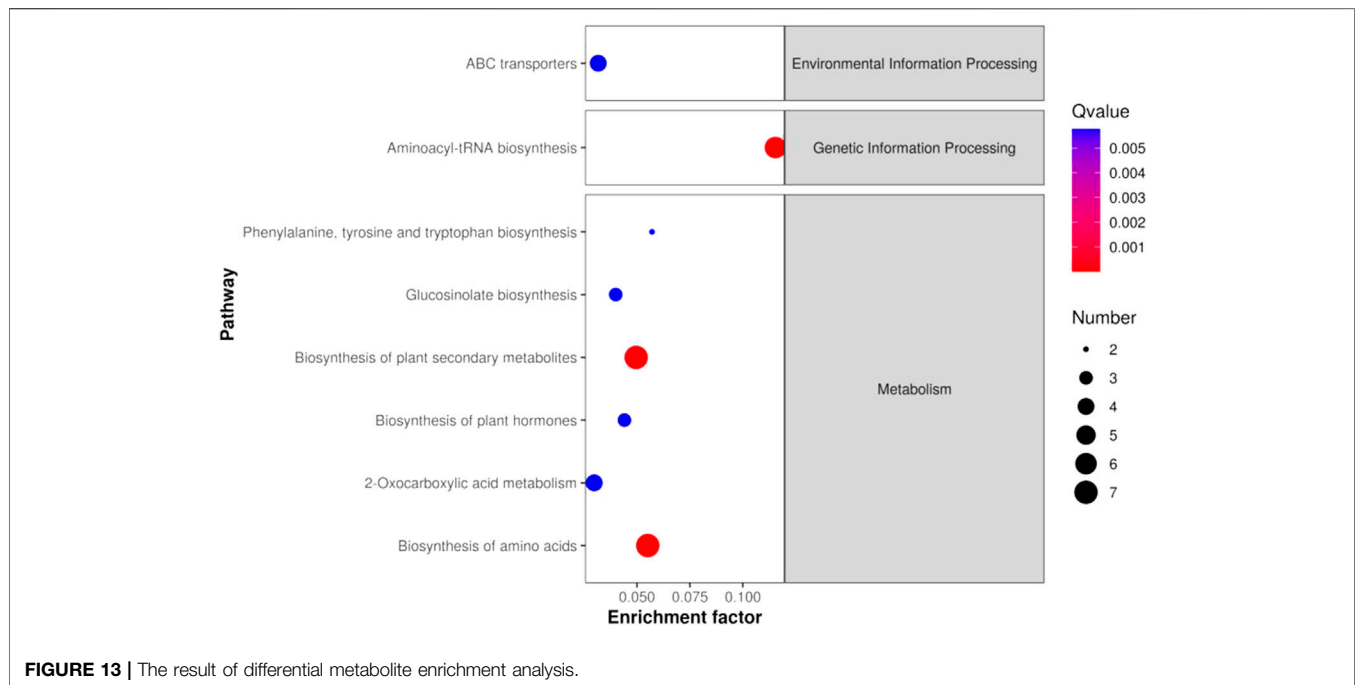


FIGURE 12 | Results of hierarchical clustering analysis of altered metabolite pools in the single-headed roots and double-headed roots ($p < 0.01$). Heatmap color indicate the abundance of each metabolite in the single-headed roots and double-headed roots.



Validation of the Transcriptome Data

To verify the reliability of the transcriptome data, qRT-PCR was performed for ten randomly selected DEGs. qRT-PCR was used to compare and analyze the expression of these genes between samples and the results were consistent with the transcriptome analysis results for all the targets, except for TRINITY_DN12193_c0_g5. These results are summarized in **Figure 10** and support our assertion that the transcriptome sequencing data were reliable.

Metabolomic Data and Analysis

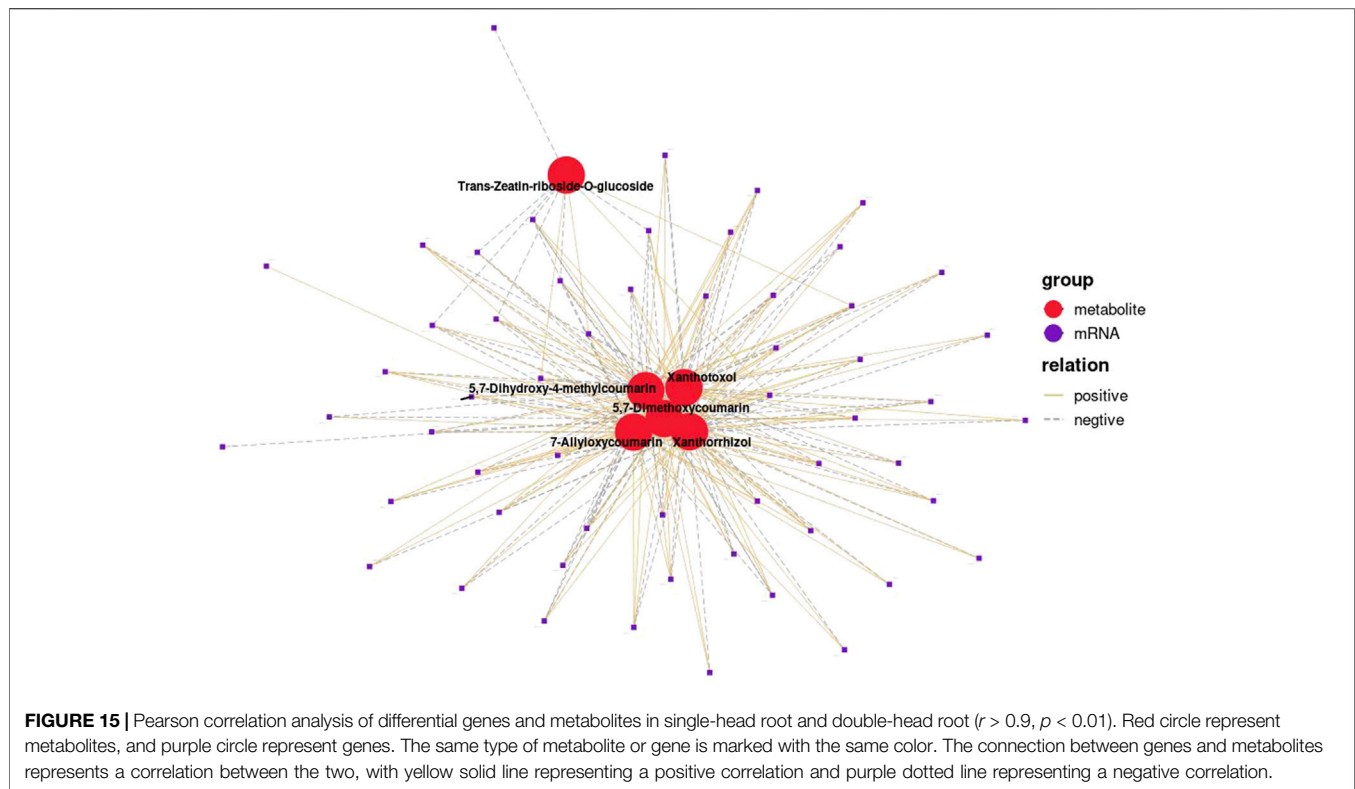
The analysis of the metabolomic data revealed 126 DEMs (30 organic acids and derivatives, 30 lipids and lipid-like molecules, 20 phenylpropanoids and polyketides, 11 organoheterocyclic compounds, eight organic oxygen compounds, six benzenoids, two nucleosides, nucleotides, and analogs, one alkaloid and derivatives, one hydrocarbon, one organooxygen compound, and 16 other compounds; **Supplementary Table S2**). According to principal component analysis for the positive electrospray ionization (ESI) mode, the first PC (PC1) and the second PC (PC2) explained 38.54 and 7.24% of the total measured metabolite variation, respectively, in the direction of the treatments. Similar results were obtained for the negative ESI mode (**Figure 11**). Using heat map analysis, we observed that the abundance of primary metabolites was significantly different between phenotypes (**Figure 12**). The major metabolites in the double-headed root phenotype were phenylpropanoids, polyketides, lipids, lipid-like molecules, organic acids, and derivatives. Moreover, the cudraflavone A and coumarin contents were 6.38 and 3.27-fold higher, respectively, in the double-headed roots than in the single-headed roots. KEGG analysis of the DEMs revealed that they were mainly enriched in phenylalanine, tyrosine, tryptophan, and glucosinolate

biosynthesis, in the biosynthesis of plant secondary metabolites and plant hormones, 2-oxocarboxylic acid metabolism, and in the biosynthesis of amino acids (**Figure 13**).

Correlation analysis between the DEGs and the DEMs showed that the genes associated with flavonoid synthesis, such as *flavanone isomerase* (EC 5.5.1.6), *chalcone synthase* (EC 2.3.1.74), and *vinorine synthase* (EC 2.3.1.133), were upregulated, whereas *flavanone 3 beta-hydroxylase* (EC 1.14.11.9) was downregulated in the double-headed root phenotype (**Figure 14**). A network diagram of the relevant genes and metabolites was constructed to analyze the correlation between the DEGs and DEMs in the two phenotypes (**Figure 15**). The results showed that the changes in 5,7-Dimethoxycoumarin, 5,7-Dimethoxy-4-methylcoumarin, 5,7-Dihydroxy-4-methylcoumarin, 7-Allyloxycoumarin, and *trans*-zeatin-riboside-O-glucoside were correlated with several genes.

DISCUSSION

Here, we assessed the morphology of *S. divaricata* with single- and double-headed roots, and tested samples for four kinds of medicinal ingredients. Simultaneously, we used transcriptomic and metabolomic analyses to identify the differences between the two phenotypes. We found that plants with double-headed roots had a superior yield potential and efficiency in accumulating organic matter. Moreover, the contents of prim-O-glucosylcimifugin, cimifugin, and total chromone in the double-headed root phenotype were significantly higher than those in the single-headed root phenotype. Flavonoids are a major class of secondary metabolites (Pourcel et al., 2007; Takao et al., 2021), and the chromone content is considered



phenotype, with a 4.15-fold difference compared to the single-headed root phenotype ($p < 0.01$), leading to changes in ABA accumulation, and then transmitting the signal to flavonoids. In the synthetic pathway, the differential accumulation of the secondary metabolites of Fangfeng eventually leads to differences in the quality of medicinal materials (Zhang et al., 2010). These six genes can be used as important candidate genes to reveal the differences in the quality of the single- and double-headed root *S. divaricata* medicinal materials.

Metabolomics analysis helps identify the changes in metabolites (Hall et al., 2002), which are the final products of cell regulation processes and are regarded as responses to genetic and environmental cues (Fiehn, 2002). Therefore, metabolomic analysis enables the investigation of the relationship between biological processes and phenotypes. Furthermore, some intuitive changes can also be observed at the metabolic level (Zhang et al., 2017). Previous studies have examined the metabolic responses of different plant species, such as *Fagopyrum esculentum* (Kim et al., 2013) and *Camellia sinensis* (Yang JM. et al., 2017), and have suggested that they affect flavonoid biosynthesis. Therefore, here, we conducted a metabolomic analysis of samples based on transcriptomic sequencing. Here, we identified 126 DEMs between the two phenotypes, of which cudraflavone A and coumarin showed the biggest differences (6.38-fold and 3.27-fold, respectively). Moreover, the DEMs were mainly enriched in the biosynthesis of secondary metabolites and phytohormones. Thus, metabolomics might help elucidate the internal mechanism leading to the medicinal property differences between plants with single- and double-headed roots.

We used the transcriptome and metabolome data to identify the genes related to flavonoid biosynthesis and explain any differences between the single- and double-headed root phenotypes. Plants with double-headed roots probably have superior medicinal value than those with single-headed roots. Six DEGs were identified, including five key genes in the flavonoid synthesis pathway and one in the ABA synthesis pathway. Correlation analysis revealed that most of the DEGs were significantly related to chromone and coumarin metabolites. Moreover, *trans-zeatin-riboside-O-glucoside*, an intermediate metabolite in ABA synthesis, was also correlated with the DEGs. Thus, the accumulation of active ingredients in double-headed root plants is closely related to hormone synthesis, which is affected by flavonoid synthesis. ABA regulation in *S. divaricata* might also affect its medicinal properties.

CONCLUSION

Our study showed significant differences in the quality of medicinal materials between single- and double-headed roots. The prim-*O*-glucosylcimifugin, cimifugin, and total chromone contents in double-headed roots were significantly higher than those in the single-headed roots. Using metabolome and transcriptome analyses, we identified six DEGs and 126 DEMs between the single- and double-headed root phenotypes, indicating that flavonoids and ABA synthesis pathways may play an important role in the synthesis of the active ingredients of *S. divaricata*. Furthermore, the six genes can be

used as important candidate genes for analyzing the quality differences in wind-breaking medicinal materials. In general, our research provides important information on the quality differences of the *S. divaricata* medicinal materials. The double-headed root phenotype can be used as a candidate phenotype for clinical drugs, providing theoretical support for selecting and breeding *S. divaricata* medicinal materials.

DATA AVAILABILITY STATEMENT

The original contributions presented in the study are included in the article/**Supplementary Material**, further inquiries can be directed to the corresponding authors.

AUTHOR CONTRIBUTIONS

TZ, WQ, and CC conceived and designed the experiments. TZ performed most of the experiments, analyzed the data, and completed the first draft. YC, QZ, PY, and QL worked together with TZ to perform the experiments. All authors read and approved the manuscript.

REFERENCES

- Armstrong, F., and Que, L. (2012). Current Opinion in Chemical Biology. *Curr. Opin. Chem. Biol.* 16 (1-2), 1–2. doi:10.1016/j.cbpa.2012.03.011
- Buchfink, B., Xie, C., and Huson, D. H. (2015). Fast and Sensitive Protein Alignment Using DIAMOND. *Nat. Methods* 12 (1), 59–60. doi:10.1038/nmeth.3176
- Cheng, L., Han, M., Yang, L.-m., Li, Y., Sun, Z., and Zhang, T. (2018). Changes in the Physiological Characteristics and Baicalin Biosynthesis Metabolism of *Scutellaria Baicalensis* Georgi under Drought Stress. *Ind. Crops Prod.* 122 (122), 473–482. doi:10.1016/j.indcrop.2018.06.030
- Commission, C. P. (2020). *Pharmacopoeia of the People's Republic of China*. China: The Medicine Science and Technology Press of China.
- Fiehn, O. (2002). Metabolomics - the Link between Genotypes and Phenotypes. *Plant Mol. Biol.* 48, 155–171. doi:10.1007/978-94-010-0448-0_11
- Forrest, A. R. R., and Carninci, P. (2009). Whole Genome Transcriptome Analysis. *Rna Biol.* 6 (2), 107–112. doi:10.4161/rna.6.2.7931
- Gao, W., Sun, H. X., Xiao, H., Cui, G., Hillwig, M. L., Jackson, A., et al. (2014). Combining Metabolomics and Transcriptomics to Characterize Tanshinone Biosynthesis in *Salvia Miltiorrhiza*. *Bmc Genomics* 15 (1), 73–14. doi:10.1186/1471-2164-15-73
- Grabherr, M. G., Haas, B. J., Yassour, M., Levin, J. Z., Thompson, D. A., Amit, I., et al. (2011). Full-length Transcriptome Assembly from RNA-Seq Data without a Reference Genome. *Nat. Biotechnol.* 29 (7), 644–652. doi:10.1038/nbt.1883
- Hall, R., Beale, M., Fiehn, O., Hardy, N., Sumner, L., and Bino, R. (2002). Plant Metabolomics. *Plant Cell* 14, 1437–1440. doi:10.1105/tpc.140720
- Hamilton, J. P., and Robin Buell, C. (2012). Advances in Plant Genome Sequencing. *Plant J.* 70 (1), 177–190. doi:10.1111/j.1365-313x.2012.04894.x
- Hong, J. H., Seah, S. W., and Xu, J. (2013). The Root of ABA Action in Environmental Stress Response. *Plant Cell Rep* 32 (7), 971–983. doi:10.1007/s00299-013-1439-9
- Hongzhe, C., Mohammed, N., Hao, X., Jingjia, H., Kunlu, W., Xianghui, C., et al. (2015). Transcriptome Analysis of Methyl Jasmonate-Elicited *Panax ginseng* Adventitious Roots to Discover Putative Ginsenoside Biosynthesis and Transport Genes. *Int. J. Mol. Sci.* 16 (2), 3035–3057. doi:10.3390/ijms16023035

FUNDING

This work was financially supported by the National Key Research and Development Plan of China (2019YFC1710704), the Natural Science Foundation of Jilin Province (YDZJ202101ZYTS012), and the fifth batch of Jilin Province young scientific and technological talent support project (QT202117).

ACKNOWLEDGMENTS

We would like to thank WQ and CC, Changchun University of Chinese Medicine, for providing financial support for part of this work.

SUPPLEMENTARY MATERIAL

The Supplementary Material for this article can be found online at: <https://www.frontiersin.org/articles/10.3389/fbioe.2021.764093/full#supplementary-material>

Supplementary Figure 1 | The length distribution and GC content.

- Jameson, P. E., Dhandapani, P., Novak, O., and Song, J. (2016). Cytokinins and Expression of SWEET, SUT, CWINV and AAP Genes Increase as Pea Seeds Germinate. *Int. J. Mol. Sci.* 17 (12), 1–13. doi:10.3390/ijms17122013
- Khan, S., Shin, E. M., Choi, R. J., Jung, Y. H., Kim, J., Tosun, A., et al. (2011). Suppression of LPS-Induced Inflammatory and NF-Kb Responses by Anomalin in RAW 264.7 Macrophages. *J. Cel. Biochem.* 112 (8), 2179–2188. doi:10.1002/jcb.23137
- Kim, Y. B., Park, S.-Y., Thwe, A. A., Seo, J. M., Suzuki, T., Kim, S.-J., et al. (2013). Metabolomic Analysis and Differential Expression of Anthocyanin Biosynthetic Genes in White- and Red-Flowered Buckwheat Cultivars (*Fagopyrum Esculentum*). *J. Agric. Food Chem.* 61 (44), 10525–10533. doi:10.1021/jf402258f
- Kuang, L., Li, C., Cao, S., Li, H., Wang, Z., Wu, S., et al. (2020). *Pharmacopoeia of People's Republic of China*. Beijing: China Medical Science and Technology Press.
- Li, C., Zhu, Y., Guo, X., Sun, C., Luo, H., Song, J., et al. (2013). Transcriptome Analysis Reveals Ginsenosides Biosynthetic Genes, microRNAs and Simple Sequence Repeats in *Panax ginseng* C. Meyer. *Bmc Genomics* 14 (1), 245. doi:10.1186/1471-2164-14-245
- Li, Y., Wang, X., Li, Z., Zhang, J., Meng, H., Lv, Q., et al. (2017). Separation and Identification of Chemical Constituents of *Saposhnikovia Divaricata*. *Chin. J. Exp. Formulas* 23 (15), 60–64. doi:10.1016/j.jchro.2010.09.027
- Liu, L., Zhang, N., Jin, H., and Ma, S. (2020). Comparative Study on Chromones in Wild Bolted and Unbolted *Saposhnikovia Divaricata*. *Chin. Pharm. J.* 55 (08), 637–642. doi:10.11669/cpj.2020.08.012
- Liu, S., Wang, S., Liu, M., Yang, F., Zhang, H., Liu, S., et al. (2016). De Novo sequencing and Analysis of the Transcriptome of *Panax Ginseng* in the Leaf-Expansion Period. *Mol. Med. Rep.* 14 (2), 1404–1412. doi:10.3892/mmr.2016.5376
- Liu, S., and Zhang, L. (2007). Quality Analysis of Different Medicinal Parts of Cultivated *Saposhnikovia Divaricata*. *Ginseng Res.* (1), 8–11.
- Liu, Y. M., Zhang, L., Zhou, J. Y., and Cao, M. J. (2015). Research Progress of the bHLH Transcription Factors Involved in Genic Male Sterility in Plants. *Yi Chuan* 37 (12), 1194–1203. doi:10.16288/j.ycz.15-229
- Lv, X., Chen, S., and Wang, Y. (2019). Advances in Understanding the Physiological and Molecular Responses of Sugar Beet to Salt Stress. *Front. Plant Sci.* 10, 1431. doi:10.3389/fpls.2019.01431

- Madhuni, B., and Ralf, O. (2014). WRKY Transcription Factors: Jack of many Trades in Plants. *Plant Signal. Behav.* 9 (2), e27700. doi:10.4161/psb.27700
- Martin, M. (2011). Cutadapt Removes Adapter Sequences from High-Throughput Sequencing Reads. *Embnet J.* 17 (1), 1–3. doi:10.14806/ej.17.1.200
- Okuyama, E., Hasegawa, T., Matsushita, T., Fujimoto, H., Ishibashi, M., and Yamazaki, M. (2019). Analgesic Components of *Saposhnikovia* Root (*Saposhnikovia Divaricata*). *Chem. Pharm. Bull. (Tokyo)* 49 (2), 154–160. doi:10.1248/cpb.49.154
- Patro, R., Duggal, G., Love, M. I., Irizarry, R. A., and Kingsford, C. (2017). Salmon Provides Fast and Bias-Aware Quantification of Transcript Expression. *Nat. Methods* 14 (4), 417–419. doi:10.1038/nmeth.4197
- Pourcel, L., Routaboul, J., Cheynier, V., Lepiniec, L., and Debeaujon, I. (2007). Flavonoid Oxidation in Plants: from Biochemical Properties to Physiological Functions. *Trends Plant Sci.* 12 (1), 29–36. doi:10.1016/j.tplants.2006.11.006
- Ramaswami, G., Zhang, R., Piskol, R., Keegan, L. P., Deng, P., O'Connell, M. A., et al. (2013). Identifying RNA Editing Sites Using RNA Sequencing Data Alone. *Nat. Methods* 10 (2), 128–132. doi:10.1038/nmeth.2330
- Robinson, M. D., McCarthy, D. J., and Smyth, G. K. (2010). edgeR: a Bioconductor Package for Differential Expression Analysis of Digital Gene Expression Data. *Bioinformatics* 26 (1), 139–140. doi:10.1093/bioinformatics/btp616
- Rodriguez-Garcia, A., Sola-Landa, A., and Barreiro, C. (2017). RNA-Seq-Based Comparative Transcriptomics: RNA Preparation and Bioinformatics. *Methods Mol. Biol.* 1645, 59–72. doi:10.1007/978-1-4939-7183-1_5
- Sui, C., Zhang, J., Wei, J., Chen, S., Li, Y., Xu, J., et al. (2011). Transcriptome Analysis of *Bupleurum Chinense* Focusing on Genes Involved in the Biosynthesis of Saikosaponins. *Bmc Genomics* 12 (1), 539. doi:10.1186/1471-2164-12-539
- Takao, K., Takemura, Y., Nagai, J., Kamauchi, H., Hoshi, K., Mabashi, R., et al. (2021). Synthesis and Biological Evaluation of 3-styrylchromone Derivatives as Selective Monoamine Oxidase B Inhibitors. *Bioorg. Med. Chem.* 42, 116255. doi:10.1016/j.bmc.2021.116255
- Werner, T., and Schülling, T. (2009). Cytokinin Action in Plant Development. *Curr. Opin. Plant Biol.* 12, 527–538. doi:10.1016/j.pbi.2009.07.002
- Wu, D., Austin, R. S., Zhou, S., and Brown, D. (2013). The Root Transcriptome for North American Ginseng Assembled and Profiled across Seasonal Development. *Bmc Genomics* 14 (1), 564. doi:10.1186/1471-2164-14-564
- Xue, B., Li, W., Li, L., and Xiao, Y. (2000). Study on the Pharmacological Activity of the Chromone Glycosides of *Saposhnikovia Divaricata*. *China J. Chin. Materia Med.* 25 (5), 41–45. doi:10.3321/j.issn:1001-5302.2000.05.016
- Yang, D.-s., Zhang, J., Li, M.-x., and Shi, L.-x. (2017a). Metabolomics Analysis Reveals the Salt-Tolerant Mechanism in Glycine Soja. *J. Plant Growth Regul.* 36 (2), 460–471. doi:10.1007/s00344-016-9654-6
- Yang, J. M., Jiang, H., Dai, H. L., Wang, Z. W., Jia, G. Z., and Meng, X. C. (2017b). Feeble Antipyretic, Analgesic, and Anti-inflammatory Activities Were Found with Regular Dose 4'-O- β -D-Glucosyl-5-O-Methylvisamminol, One of the Conventional Marker Compounds for Quality Evaluation of *Radix Saposhnikovia*. *Pharmacogn. Mag.* 13 (49), 168–174. doi:10.4103/0973-1296.197637
- Zhang, H., Han, W., De Smet, I., Talboys, P., Loya, R., Hassan, A., et al. (2010). ABA Promotes Quiescence of the Quiescent centre and Suppresses Stem Cell Differentiation in the Arabidopsis Primary Root Meristem. *Plant J.* 64 (5), 764–774. doi:10.1111/j.1365-313x.2010.04367.x
- Zhang, J. Y., Shen-Chun, Q. U., Guo, Z. R., Xiao-Li, D. U., Bei-Bei, D. U., and Zhang, Z. (2011). Biology Function of bZIP Transcription Factors in Plants. *Acta Botanica Boreali-Occidentalia Sinica* 5 (31), 1066–1075.
- Zhang, Q., Liu, M., and Ruan, J. (2017). Metabolomics Analysis Reveals the Metabolic and Functional Roles of Flavonoids in Light-Sensitive tea Leaves. *BMC Plant Biol.* 17 (1), 64. doi:10.1186/s12870-017-1012-8
- Zhang, T., Gao, Y., Han, M., and Yang, L. (2021). Changes in the Physiological Characteristics of *Panax Ginseng* Embryogenic Calli and Molecular Mechanism of Ginsenoside Biosynthesis under Cold Stress. *Planta* 253 (79), 1–23. doi:10.1007/s00425-020-03535-7
- Zou, L.-q., Kuang, X.-j., and Sun, C. (2015). Advances in Transcriptomic Studies and Ginsenoside Biosynthesis of American Ginseng. *Chin. Herbal Medicines* 7 (2), 116–122. doi:10.1016/s1674-6384(15)60028-4

Conflict of Interest: The authors declare that the research was conducted in the absence of any commercial or financial relationships that could be construed as a potential conflict of interest.

Publisher's Note: All claims expressed in this article are solely those of the authors and do not necessarily represent those of their affiliated organizations, or those of the publisher, the editors and the reviewers. Any product that may be evaluated in this article, or claim that may be made by its manufacturer, is not guaranteed or endorsed by the publisher.

Copyright © 2021 Zhang, Chen, Zhang, Yu, Li, Qi and Chen. This is an open-access article distributed under the terms of the Creative Commons Attribution License (CC BY). The use, distribution or reproduction in other forums is permitted, provided the original author(s) and the copyright owner(s) are credited and that the original publication in this journal is cited, in accordance with accepted academic practice. No use, distribution or reproduction is permitted which does not comply with these terms.



Improvement of Nicotine Removal and Ethanol Fermentability From Tobacco Stalk by Integration of Dilute Sulfuric Acid Presoak and Instant Catapult Steam Explosion Pretreatment

Hongsen Zhang¹, Chenqing Fu¹, Tianbao Ren², Hui Xie¹, Guotao Mao¹, Zhimin Wang³, Fengqin Wang^{1*} and Andong Song^{1*}

¹Key Laboratory of Enzyme Engineering of Agricultural Microbiology, College of Life Science, Ministry of Agriculture, Henan Agricultural University, Zhengzhou, China, ²College of Tobacco, Henan Agricultural University, Zhengzhou, China, ³College of Science, Henan Agricultural University, Zhengzhou, China

OPEN ACCESS

Edited by:

Xin Zhou,
Nanjing Forestry University, China

Reviewed by:

Chen Huang,
Chinese Academy of Forestry, China
Ali Nawaz,
Government College University,
Pakistan

*Correspondence:

Andong Song
song1666@126.com
Fengqin Wang
w_fengqin@163.com

Specialty section:

This article was submitted to
Bioprocess Engineering,
a section of the journal
Frontiers in Bioengineering and
Biotechnology

Received: 24 August 2021

Accepted: 14 September 2021

Published: 29 October 2021

Citation:

Zhang H, Fu C, Ren T, Xie H, Mao G, Wang Z, Wang F and Song A (2021) Improvement of Nicotine Removal and Ethanol Fermentability From Tobacco Stalk by Integration of Dilute Sulfuric Acid Presoak and Instant Catapult Steam Explosion Pretreatment. *Front. Bioeng. Biotechnol.* 9:763549. doi: 10.3389/fbioe.2021.763549

The nicotine from tobacco stalk showed obvious inhibitory effect on the activity of cellulase and fermentability of microorganisms, which seriously hinders the utilization of tobacco stalk. Dilute sulfuric acid presoak of tobacco stalk was used to enhance the performance of instant catapult steam explosion (ICSE) for tobacco stalk pretreatment. The presoak was beneficial to break the recalcitrant structure of tobacco stalk, reduce nicotine content to relieve the inhibition on the activity of cellulase and metabolism of microorganisms, and promote the performance of enzymatic hydrolysis and ethanol fermentation. The optimized 0.8% sulfuric acid (w/w) presoak-integrated ICSE pretreatment resulted in 85.54% nicotine removal from tobacco stalk; meanwhile, the total sugar concentration from enzymatic hydrolysis of pretreated tobacco stalk increased from 33.40 to 53.81 g/L (the ratio of dry tobacco stalk to water was 1:8, w/w), ethanol concentration increased 103.36% from 5.95 to 12.10 g/L in flask, compared with separate ICSE pretreatment. Finally, the ethanol concentration achieved the highest 23.53 g/L in a 5-L fermenter with the ethanol yield from the glucose of tobacco stalk hydrolysate achieving 71.40% by increasing the solid loading of the tobacco stalk in the enzymatic hydrolysis process (the ratio of dry tobacco stalk to water was 1:4, w/w). These results achieved the expected purpose of efficient utilization of discarded tobacco stalk.

Keywords: tobacco stalk, nicotine, dilute sulfuric acid presoak, instant catapult steam explosion (ICSE), enzymatic hydrolysis, ethanol fermentation

INTRODUCTION

With the vigorous development of the world economy, the environment pollution and nonrenewable resources consumption have become a severe challenge to the human society; more and more attention has been focused on new renewable and environment-friendly energy; and relevant research has become a mainstream of scientific community (Herbert and Krishnan, 2016). As a clean and renewable energy, bioethanol showed many significant advantages such as being green and

environment-friendly, having low manufacturing cost, having wide availability, and so on (Zhou et al., 2019). In the foreseeable future, it is expected to gradually replace the diminishing fossil fuels, such as oil, coal, and natural gas (Morales et al., 2015).

The planting area and annual output of tobacco in China ranked first in the world in recent years (Qin et al., 2018). Tobacco stalk as the main waste of the tobacco industry had resulted in a series of environmental problems (Wang et al., 2019). The resource utilization of tobacco stalk has become an urgent problem to be solved. As a kind of lignocellulosic biomass, tobacco stalk could be used to produce many valuable bio-based products, such as bioethanol by biorefinery. Tobacco stalk was mainly composed of cellulose, hemicellulose, and lignin, and their content in tobacco stalk was approximately 45, 15, and 20%, respectively (Su et al., 2016). In addition, tobacco stalk also contains nicotine, solanesol, pectin, protein, amino acid, organic acids, sugar, and other compounds (Akpınar et al., 2010; Huang et al., 2019). Nicotine is the main alkaloid of tobacco, which accounts for over 95% of the total alkaloid content of tobacco (Henry et al., 2019). Meanwhile, nicotine is both an addictive and a toxic substance, which can inhibit the activity of biological enzymes and the growth of microorganisms, and finally can go against tobacco stalk efficient utilization (Swanson et al., 1994; Zhong et al., 2010; Falco and Bevins, 2015). Therefore, removal of nicotine is as important as the breaking of the compact structure for the bioconversion of tobacco stalk. Pretreatment of tobacco stalk was the precondition for the conversion of cellulose and hemicellulose of tobacco stalk into fermentable sugar. The pretreatment methods of lignocellulose at present mainly includes physical, chemical, biological methods, or a mixture of these methods (Cai et al., 2016; Sun et al., 2020; Zhang et al., 2020). Instant catapult steam explosion (ICSE) has become an efficient, economic, and environmental pretreatment technology, depending on its short pretreatment time, low energy consumption, and zero pollution to the environment (Wang et al., 2020; Xie et al., 2020).

The mechanism of ICSE is to break the compact physical structure by the energy from high pressure release to barometric pressure and high temperature cool down, not more than 100°C, instantly (Yu et al., 2012). The cellulose, hemicellulose, and lignin were all hydrolyzed partly and separated in this ICSE process, which benefits the subsequent cellulosic ethanol fermentation. However, a separate ICSE pretreatment could not reduce nicotine to a satisfactory concentration, and this pretreatment method had to be improved. As an alkaloid, nicotine easily combines with acid to form salt, which is more easily dissolved in water and excluded from tobacco stalk (Henry et al., 2019). In addition, acid can change the surface chemical and cellulose crystalline structure of the tobacco stalk (Liang et al., 2021). The integrated dilute acid presoak and ICSE technology was used for tobacco stalk pretreatment in this study, where the compact crystal structure of the tobacco stalk was broken and more than 80% of the nicotine removed, which could improve the enzymatic hydrolysis of the tobacco stalk and fermentability of bioethanol. This study provides a kind of lignocellulosic ethanol production process from tobacco stalk with a potential

for industrial applications, and also a theoretical basis for the diversified utilization of tobacco stalk to produce more bio-based products.

MATERIALS AND METHODS

Feedstocks

Tobacco stalk was harvested from a tobacco test field at the Henan Agricultural University (Xuchang campus) in the fall of 2018. After collection, the biomass was milled coarsely using a hammer crusher and screened through a mesh with the circle diameter of 10 mm. The milled tobacco stalk was washed to remove field dirt, stones, and metals, and then dried to constant weight at 105°C in an air oven. The composition of the tobacco stalk after pre-handling treatment contained 41.64% cellulose, 14.96% hemicellulose, 15.74% lignin, and 7.43% ash determined by the method described in the NREL protocols (Sluiter et al., 2008). The nicotine content of the tobacco stalk was 0.83% (w/w), which was measured by HPLC (Dash and Wong, 1996).

Enzyme

Commercial cellulase was purchased from Hunan Youtell Biochemical Co., Yueyang, Hunan, China. The filter paper activity was 214 FPU/g cellulase, according to the National Renewable Energy Laboratory (NREL) protocol LAP-006 (Adney and Baker, 1996).

Strains and Mediums

Issatchenkia orientalis HN-1 was isolated from decayed tobacco stalk at our lab and stored at Key Laboratory of Enzyme Engineering of Agricultural Microbiology.

Saccharomyces cerevisiae 1308 was obtained from Henan Tianguan Group Co., Ltd., Nanyang city, Henan province, China.

Strain activation medium: 30 g of glucose, 10 g of yeast extract, 20 g of peptone, 20 g of agar in 1 L deionized water.

Seed medium: 30 g of glucose, 10 g of yeast extract, 20 g of peptone in 1 L deionized water.

Fermentation medium for ethanol production (synthetic medium): 50 g of glucose (or tobacco stalk hydrolysate), 3 g of yeast extract, 5 g of peptone, 0.2 g of urea, 0.1 g of (NH₄)₂HPO₄ in 1 L deionized water, pH 5.5.

Fermentation medium for ethanol production (tobacco stalk hydrolysate): 3 g of yeast extract, 5 g of peptone, 0.2 g of urea, 0.1 g of (NH₄)₂HPO₄ in 1 L tobacco stalk hydrolysate, pH 5.5.

All the medium of *I. orientalis* HN-1 and *S. cerevisiae* 1308 were the same in this study.

Activation and Large Scale of Strain

The culture solution of *I. orientalis* HN-1 (or *S. cerevisiae* 1308) was maintained at -80°C in a freezer in 2-ml stock vials containing 30% (v/v) glycerol solution. 100 µL of liquid from one stock vial was inoculated onto a plate with activation medium by spread plate method and cultured at 38°C for 48 h. A whole colony of *I. orientalis* HN-1 growing on slant medium was inoculated into a 250-ml flask containing 50 ml seed medium for seed culture at 38°C, 180 rpm for 12 h. A whole colony of *S.*

cerevisiae 1308 growing on a slant medium was inoculated into a 250-ml flask containing 50 ml seed medium for seed culture at 30°C, 150 rpm for 16 h.

The Effect of Nicotine on Activity of Cellulase

The carboxymethyl cellulase (CMC) activity of cellulase was measured by the DNS method (Eveleigh et al., 2009). The filter paper activity of cellulase was measured by the National Renewable Energy Laboratory (NREL) protocol LAP-006 (Adney and Baker, 1996). 0.1, 0.2, 0.3, and 0.5% (w/w) nicotine were added into the enzymatic reaction system.

Dilute Sulfuric Acid Presoak

The tobacco stalk was presoaked into a series of dilute sulfuric acid solution concentrations (0.2–1.0%, w/w, on dry tobacco stalk weight) at a ratio of the solid (the dry materials) to the liquid (the sulfuric acid solution) of 1:10 (w/w) for 12 h at room temperature. The presoak slurry was filtered using double gauze; the solid residue was collected and dried, until the moisture was maintained at 60°C.

Instant Catapult Steam Explosion Pretreatment

The ICSE method was used for pretreating the tobacco stalk feedstock in this study (Yu et al., 2012). 100 g fresh dry tobacco stalk (or presoaked dry tobacco stalk) was fed into a pretreatment reactor directly, and the pretreatment was operated at 2.0 MPa for 2.5 min (the optimized condition obtained from previous studies). The pretreated tobacco stalk after ICSE contained approximately 40% water of dry solid matter (w/w).

Washing of the Pretreated Material

The pretreated material was washed by tenfold volume of water at 60°C for 1 h, and then the solid residue was collected by Buchner funnel filtration. After this operation was repeated, the solid residue was dried at 75°C in an oven until constant weight, then sealed in plastic bags and stored at room temperature until use.

Enzymatic Hydrolysis

The pretreated tobacco stalk solution at a ratio of the solid (the dry materials) to the liquid (the deionized water) of 1:8 or 1:4 (w/w) was hydrolyzed at 50°C, 150 rpm, pH 4.8 for 48 h at the cellulase dosage of 15 FPU/g DM (dry materials). The hydrolysate slurry was centrifuged to remove the solids, then autoclaved, and filtered by filter paper before use.

Ethanol Fermentation

The seed broth of *I. orientalis* HN-1 was inoculated into a 300-ml flask containing 240 ml fermentation medium with 10% (v/v) inoculation ratio at 38°C, stationary culture for 72 h. The seed broth of *S. cerevisiae* 1308 was inoculated into a 300-ml flask containing 240 ml fermentation medium with 10% (v/v) inoculation ratio at 30°C, stationary culture for 72 h. All flask

cultures were carried out in triplicate. For the fermenter culture, the seed broth of *I. orientalis* HN-1 was inoculated into a 5-L fermenter containing 3 L fermentation medium with 10% (v/v) inoculation ratio at 38°C, pH 5.5, 100 rpm for 72 h.

Analysis Methods

Samples were periodically taken, centrifuged, and filtrated through 0.22- μ m filters before analysis. Glucose, xylose, and ethanol were measured by HPLC (LC-20 AD, refractive index detector RID-10A, Shimadzu, Kyoto, Japan) with Aminex HPX-87H column (Bio-Rad, Hercules, United States) at 65°C using the mobile phase of 5 mM H₂SO₄ at the flow rate of 0.6 ml/min. The sample size was 10 μ L (Zhao et al., 2020). The concentration of nicotine was determined by HPLC (Thermo UltiMate 3000, UVVis detector, Thermo, Waltham, United States) with Inertsil ODS-3 C18 column (Shimadzu, Kyoto, Japan) at 35°C using the mobile phase of methanol–citrate phosphate buffer (15:85 v/v, pH 2.4 adjusted by addition of perchloric acid) at the flow rate of 0.7 ml/min. The column effluent was monitored at 260 nm with a UV-Vis spectrophotometric detector (Dash and Wong, 1996).

Calculation of Ethanol Yield

Ethanol yield based on glucose of tobacco stalk hydrolysate was calculated by the following formula:

$$\text{Ethanol yield (\%)} = \frac{[C_1] - [C_0]}{0.511 \times [\text{Glucose}]} \times 100\%$$

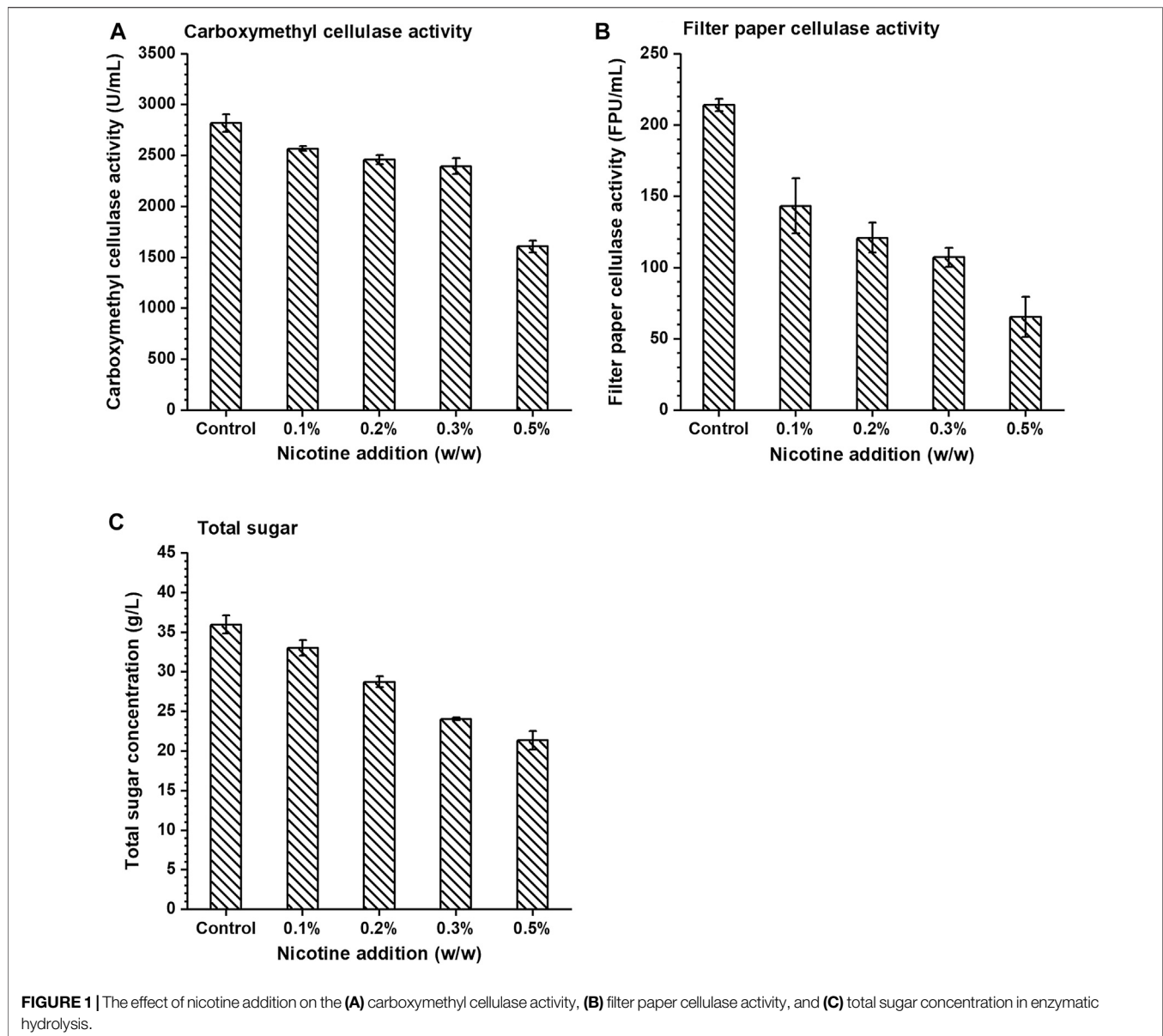
where $[C_1]$ is the final ethanol concentration (g/L) of the fermentation broth at the end of fermentation; $[C_0]$ is the initial ethanol concentration (g/L) of the fermentation broth at the start of fermentation; $[\text{Glucose}]$ is the initial glucose concentration (g/L) of the fermentation broth at the start of fermentation; 0.511 is the conversion factor for glucose to ethanol based on the stoichiometric biochemistry of yeast.

RESULTS AND DISCUSSION

The Effect of Nicotine on Activity of Cellulase and Ethanol Productivity of Yeasts

Tobacco stalk as a bulk lignocellulosic biomass would have an important impact on biorefinery if it could be used for biochemical production efficiently. Previous research indicated that the tobacco stalk was more difficult to be used in biochemical production than common crop stalks (such as corn stover, wheat stalk, and so on) because of its high nicotine content. Nicotine from tobacco stalk has been shown to obviously inhibit the activity of glutathione reductase, aldehyde dehydrogenase, lactate dehydrogenase, and lipase (Gan and Zhuang, 2002; Erat et al., 2007; Trigo and Foll, 2016; Yalcin et al., 2018). However, the effect of nicotine on cellulase has been rarely reported.

Three substrates (sodium carboxymethylcellulose, filter paper, and corn stover) were used to study the effects of nicotine on the activity of cellulase which was always used in biomass hydrolysis



processes. In this study, cellulase activity was characterized by CMC activity and filter paper cellulase activity (FPA), and the results showed that the activity of cellulase decreased gradually with the increase of nicotine concentration (Figure 1). In the control group, CMC activity and FPA were 2820.99 U/ml and 214.12 FPU/ml, respectively, under zero nicotine addition. When nicotine addition reached 0.1% (w/v), CMC activity and FPA were 2567.90 U/ml and 143.29 FPU/ml, respectively, which decreased by 8.97 and 33.08% compared with the control group, respectively. The enzyme activity decreased more significantly with more nicotine addition, and when the addition was 0.5% (w/v), the CMC activity and FPA decreased by 42.99 and 69.44% compared with the control group, respectively. The results demonstrated that nicotine inhibited the activity of cellulase significantly.

Based on the above results, the effect of nicotine on enzymatic hydrolysis of pretreated corn stover (the ratio of dry corn stover to water was 1:10, w/w) by ICSE (2.0 MPa, 2.5 min) was subsequently verified. With the increase of nicotine concentration in the enzymatic hydrolysis system of corn stover, the concentration of total sugar (glucose, xylose, cellobiose, and arabinose, similarly hereinafter) showed a significant decrease compared with the control group (Figure 1C). The total sugar concentration in the hydrolysate reached the highest 35.99 g/L in the control group and gradually decreased in the range of 0.1–0.5% (w/v). When the nicotine concentration was 0.5% (w/v), the total sugar concentration reached the lowest 21.38 g/L which decreased by 40.59% compared with the control group. The trend demonstrated that nicotine had a significant inhibitory effect on the enzymatic hydrolysis of corn stover.

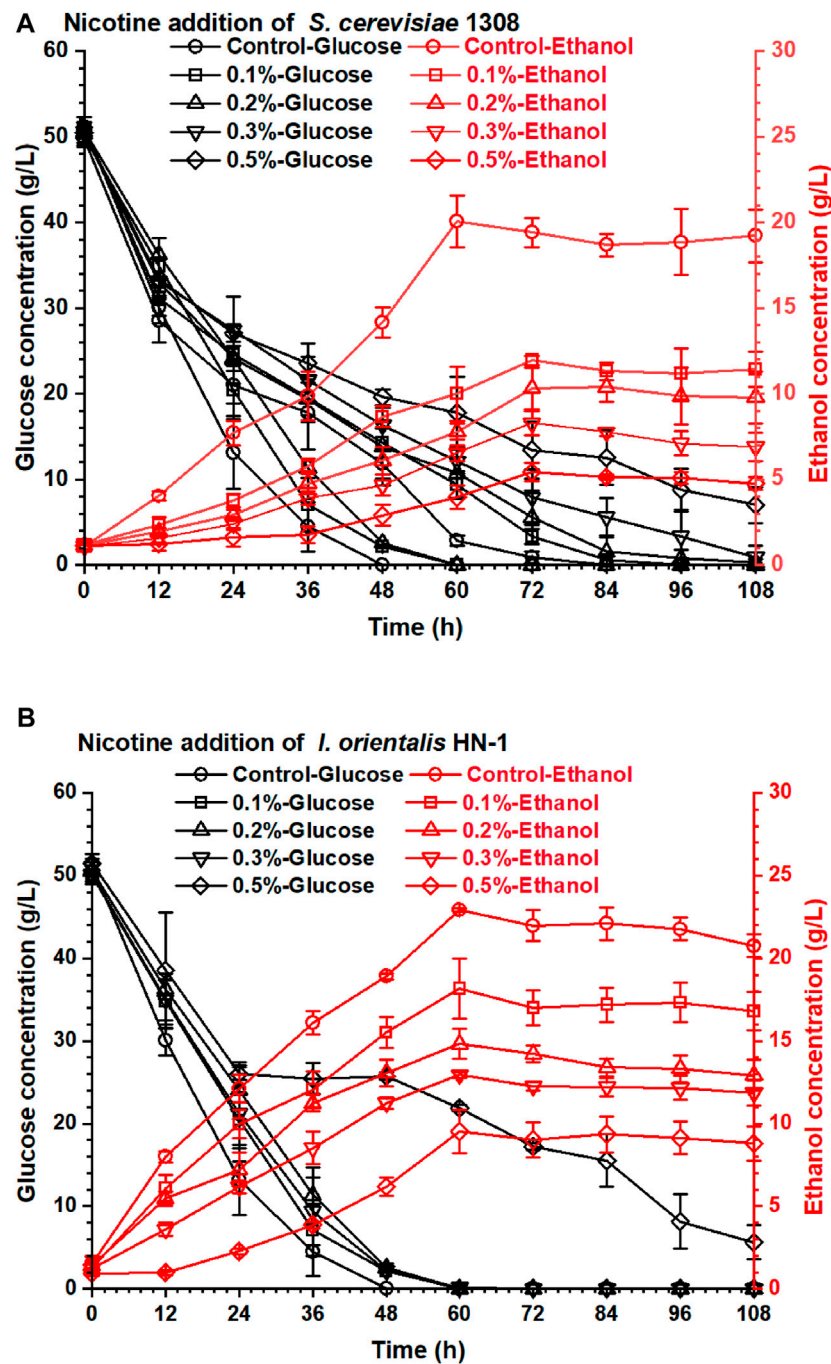


FIGURE 2 | The effect of nicotine addition on the ethanol fermentability of yeasts: **(A)** *S. cerevisiae* 1308; **(B)** *I. orientalis* HN-1.

The nicotine not only inhibited the enzymatic activity of the cellulose system but also inhibited the fermentability of ethanol producer strains. *S. cerevisiae* 1308 is an excellent industrial ethanol producer which was obtained from the largest producer of fuel ethanol in China, but its fermentability decreased obviously under the nicotine stress (Figure 2A). Yeast (*I. orientalis* HN-1) isolated from decayed tobacco stalk showed excellent nicotine tolerance and was used in this research.

The obtained highest ethanol concentration from *I. orientalis* HN-1 (22.94 g/L) in 60 h was similar to that from *S. cerevisiae* 1308 (20.05 g/L) under the control group (no nicotine addition in the fermentation medium). But when nicotine addition achieved just 0.1% (w/v), the ethanol concentration of *I. orientalis* HN-1 (18.17 g/L) decreased by 20.70%, and the ethanol concentration of *S. cerevisiae* 1308 (11.95 g/L) was even more inhibited, with 40.40% reduction compared with the control group. The results

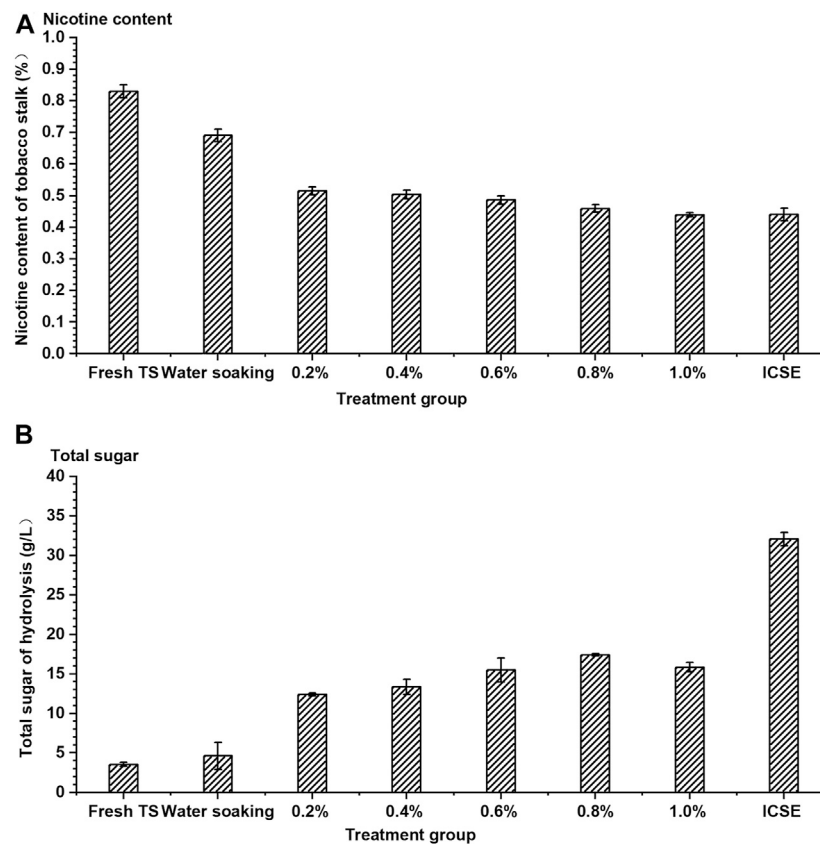


FIGURE 3 | The (A) nicotine content of tobacco stalk and (B) total sugar after hydrolysis by different single pretreatment methods. TS means tobacco stalk; 0.2–1.0% means concentration of dilute sulfuric acid solution (0.2–1.0%, w/w, on dry tobacco stalk weight) at a ratio of the solid (the dry materials) to the liquid (the sulfuric acid solution) of 1:10 (w/w) for 12 h at room temperature. ICSE means instant catapult steam explosion pretreatment, 2.0 MPa, 2.5 min.

shown in **Figure 2** indicate that nicotine had a serious impact on ethanol concentrations of both strains, especially on *S. cerevisiae* 1308. Therefore, the removal of nicotine from the tobacco stalk is essential in order to produce ethanol from discarded tobacco stalk. In addition, it is worth noting that *I. orientalis* HN-1 which was isolated from decayed tobacco stalk had a stronger nicotine tolerance than *S. cerevisiae* 1308 obviously, this laid a good foundation for subsequent high concentrations of ethanol production from tobacco stalk.

The Effect of Separate Pretreatment Methods on Removal of Nicotine and Enzymatic Hydrolysis of Tobacco Stalk

The existence of nicotine had seriously hindered the effective utilization of tobacco stalk, which might be the reason that tobacco stalks were rarely used to produce a bio-based chemical in previous studies. Therefore, efficient nicotine removal was particularly important for the development process of tobacco stalk utilization. A separate dilute sulfuric acid soaking pretreatment and a separate ICSE pretreatment were carried out in this experiment firstly. The nicotine removal rate and enzymatic saccharification efficiency of pretreated tobacco stalk

were investigated and demonstrated in **Figure 3**. Dilute sulfuric acid solution could break the compact structure of tobacco stalk slightly; meanwhile, the nicotine from tobacco stalk as an alkaloid could combine with sulfuric acid easily. The nicotine content of pretreated tobacco stalk decreased gradually with increase in sulfuric acid adding dosage. The nicotine content achieved was the lowest at 0.44% (w/w) when the sulfuric acid adding dosage was 1.0% (w/v), and the nicotine removal rate was 46.99%. The nicotine always existed inside the tobacco stalk and was difficult to remove by water soaking. Yet, when 83.13% of the nicotine was retained in the tobacco stalk after water soaking, only 53.01% of nicotine was retained by water soaking after steam explosion pretreatment. This could be attributed to ICSE pretreatment that could break the internal structure of the tobacco stalk deeply, leading to more nicotine release into water that could be removed from pretreated tobacco stalk. The dilute sulfuric acid soaking could increase the nicotine removal rate significantly compared to water soaking; however, the nicotine removal rate was increased with the sulfuric acid concentration increasing inconspicuously. When the sulfuric acid concentration increased from 0.2 to 1.0% in the soaking process, the removal rates of nicotine were all similar to those of ICSE.

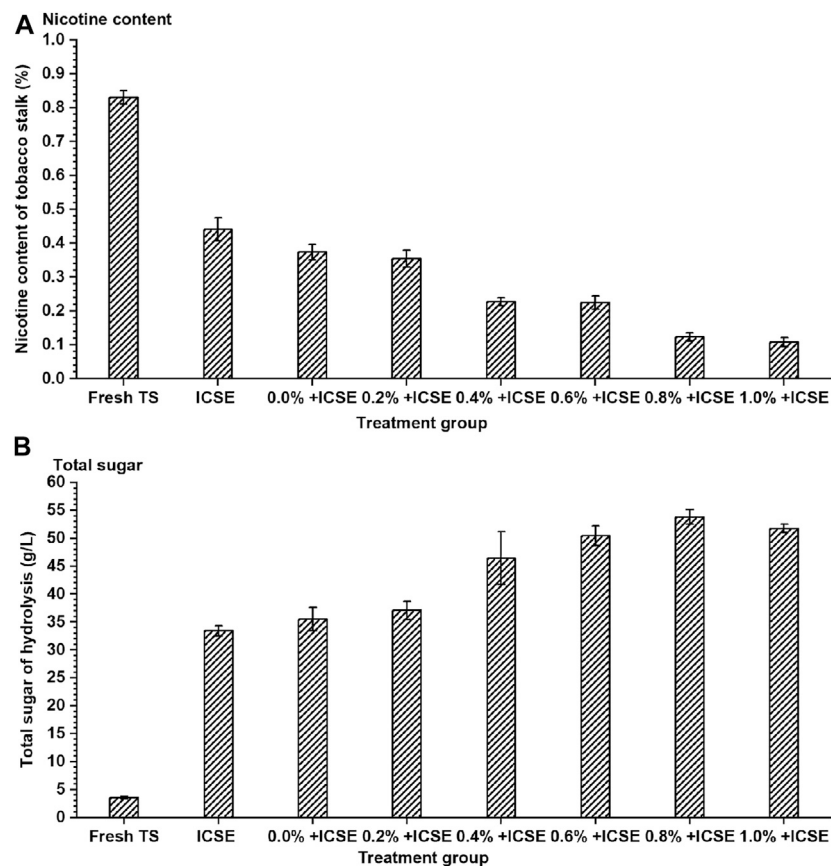


FIGURE 4 | The (A) nicotine content of tobacco stalk and (B) total sugar after hydrolysis by different integrated pretreatment methods. TS means tobacco stalk; ICSE means instant catapult steam explosion pretreatment, 2.0 MPa, 2.5 min; 0.0%+ ICSE 1.0%+ICSE means concentration of dilute sulfuric acid (0.0–1.0%, w/w, on dry tobacco stalk weight) in the presoak progress of integrated pretreatment.

The removal rate of nicotine was an important indicator in this study, but the concentration of total sugar from enzymatic hydrolysis could not be ignored. Although dilute sulfuric acid soaking was effective with removal of nicotine, its contribution to the efficiency of enzymatic hydrolysis was limited compared with ICSE. The total sugar concentration from enzymatic hydrolysis (the ratio of dry pretreated tobacco stalk to water was 1:8, w/w) of the separate dilute sulfuric acid soaking pretreatment was 12.41–17.41 g/L and increased 252.56–394.60% compared with fresh tobacco stalk when sulfuric acid adding dosage was from 0.2 to 1.0% (w/v), but the highest total sugar concentration was approximately half that of ICSE. The total sugar concentration of ICSE was 32.05 g/L, but it still did not achieve satisfactory results because of a certain concentration of nicotine being present in the enzymatic hydrolysis system.

Optimization of Integrated Pretreatment Condition for Tobacco Stalk

Separate sulfuric acid pretreatment or steam explosion pretreatment for tobacco stalk showed unsatisfying enzymatic hydrolysis efficiency and nicotine removal rate, and the integrated pretreatment carried out achieved better

performance (Figure 4). The nicotine content further significantly decreased from 0.37 to 0.11% (w/w) with sulfuric acid addition of presoak increasing from 0.0 to 1.0% in the integrated pretreatment (Figure 4A). Meanwhile, the total sugar concentration achieved the highest 53.81 g/L when sulfuric acid addition of presoak was 0.8% (w/w), which increased 74.58% compared with separate ICSE. When sulfuric acid addition of presoak increased continuously more than 0.8% (w/w), the total sugar concentration reduced a little and achieved 51.76 g/L at sulfuric acid dosage 1.0% of presoak (Figure 4B). High sulfuric acid addition of presoak might have enhanced the pretreatment strength too much to convert the sugar into inhibitors.

Therefore, the compositions of pretreated tobacco stalk materials by integrated pretreatment and separate ICSE were measured (Figure 5). The results demonstrated that the hemicellulose and lignin content of pretreated tobacco stalk were both decreased which lead to the increase of cellulose content after both separate ICSE and integrated pretreatment compared with fresh tobacco stalk. But the cellulose and hemicellulose content decreased with the increase of sulfuric acid addition of presoak from 0.2 to 1.0% (w/v) in the integrated pretreatment, and this indicated that high-titer

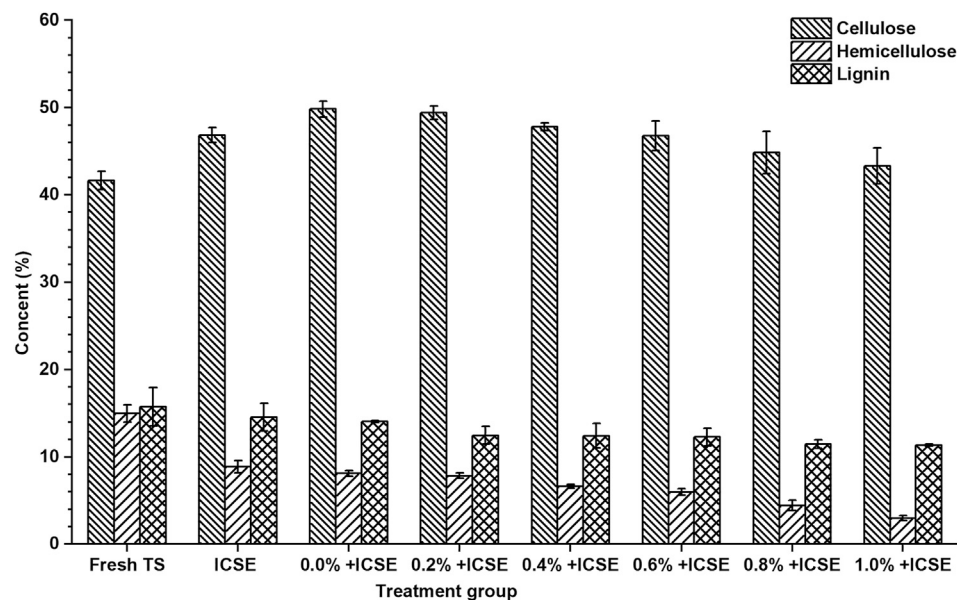


FIGURE 5 | The cellulose, hemicellulose, and lignin content of pretreated tobacco stalk by different pretreatment methods.

sulfuric acid enhances the hydrolysis of hemicellulose and cellulose, and the presence of free monosaccharides was more likely to produce inhibitors in the intense pretreatment process. Consider both the total sugar concentration and nicotine removal rate comprehensively, 0.8% (w/w) sulfuric acid dosage of presoak was used in subsequent ethanol fermentation.

Ethanol Fermentation of Pretreated Tobacco Stalk

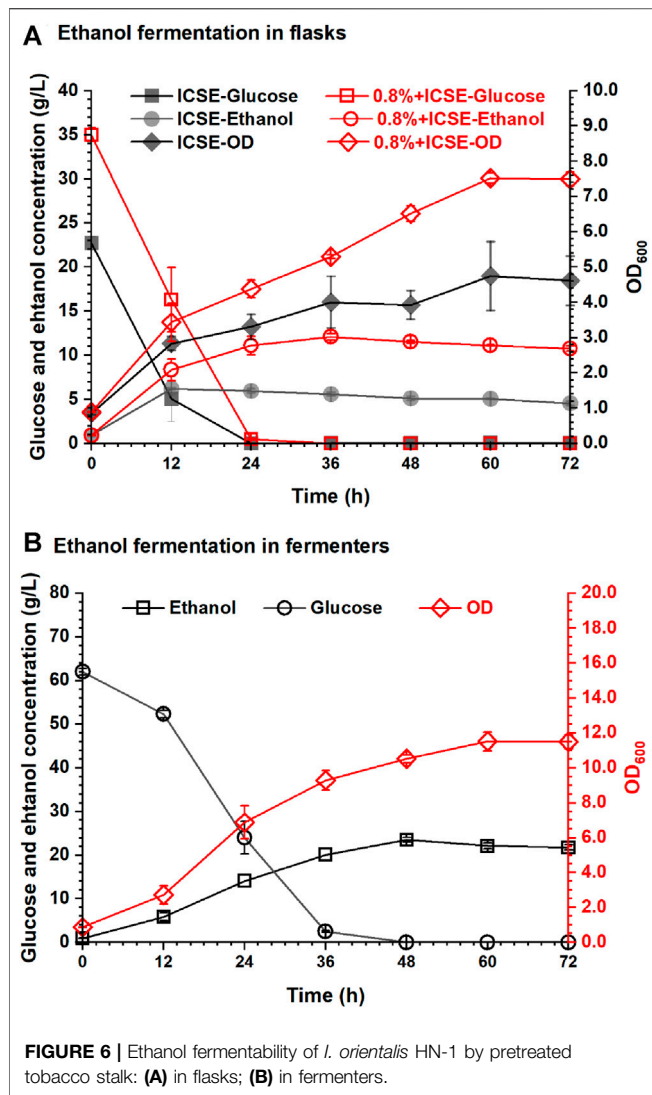
The ethanol fermentation by using tobacco stalk after integrated pretreatment with 0.8% (w/w) sulfuric acid presoak was carried out in this experiment, and the results are shown in **Figure 6**. The glucose concentration of tobacco stalk hydrolysate (the ratio of dry tobacco stalk to water was 1:8, w/w) through integrated pretreatment was 38.73 g/L, and the nicotine content was only 0.02% (w/v). Such a low concentration of nicotine would hardly affect the efficiency of enzymatic hydrolysis and *I. orientalis* HN-1. The ethanol concentration reached 12.10 g/L in 36 h, which increased 103.36% compared with 5.95 g/L of separate ICSE, the ethanol productivity was 0.31 g/L/h and the ethanol yield was 62.57%.

Based on the excellent nicotine removal performance of the integrated pretreatment, high solid loading of tobacco stalk could be implemented during enzymatic hydrolysis. A higher concentration of glucose could be obtained to produce higher concentration of ethanol. The glucose concentration of high solid loading tobacco stalk hydrolysate (the ratio of dry tobacco stalk to water was 1:4) through integrative pretreatment was 69.53 g/L, and the nicotine content was 0.05% (w/v). For better mixing and more precise control of pH, the next ethanol fermentation was carried out in the 5-L fermenter, and the results are shown in **Figure 6B**. With the increase in solid loading of tobacco stalk, the

initial glucose concentration achieved was 62.00 g/L, and the growth of *I. orientalis* HN-1, consumption of glucose, and production of ethanol were affected to some extent in the first 12 h compared with the results shown in **Figure 6A**. But, the final ethanol concentration and yield for glucose of tobacco stalk hydrolysate were both increased and were 23.53 g/L and 71.40%, respectively, in 48 h.

Discussion

In recent years, more attention has been paid to the effective utilization of tobacco residual. A combined hydrothermal (100°C, 20 min) and alkaline (2% CaO, w/v) pretreatment was used for bioethanol production from tobacco stalk, and the highest 5.43 g/L reducing sugar and 1.58 g/L ethanol were obtained in the fermentation process (Sophanodorn et al., 2020). Alkali pretreatment and acid pretreatment were used for ethanol production from tobacco stalk, and the highest 4.17 g/L ethanol was obtained under 2% NaOH pretreatment for 60 min (Guo et al., 2019). Yuan et al. compared ethanol fermentability of two different pretreatments (alkaline and acid-catalyzed steam pretreatments) for resource utilization of tobacco stalk, and the final ethanol concentration of alkaline pretreatment (14.2 g/L) was slightly higher than that of acid-catalyzed steam pretreatment (13.8 g/L) (Yuan et al., 2019). The integrated dilute sulfuric acid presoak and ICSE pretreatment technology were used in this study, which could enhance the degradation of hemicellulose in tobacco stalk and the removal of nicotine, and then weaken the inhibition of nicotine on the activity of cellulase in enzymatic saccharification process and fermentability of yeast strains. In this study, the highest ethanol concentration was 23.53 g/L, which was at a relatively high level compared with the current researches on the resource utilization of tobacco stalk.



In addition, it is worth noting that the important role of nicotine in ethanol fermentation by using tobacco stalk was studied in this work. Even though the low concentration of nicotine showed significant inhibition of cellulase and microorganisms, the ethanol concentration increased significantly after a large proportion of nicotine was removed in this integrated sulfuric acid presoak and ICSE pretreatment process. The reasons for insufficient ethanol yield (71.40%) might be because, although the nicotine in the tobacco stalk was almost removed out, there was still a variety of harmful substances (such as tar, benzopyrene, and so on) that could still inhibit the microorganisms. Although *I. orientalis* HN-1 showed strong tolerance to nicotine, the tolerance to other harmful substances remained to be studied. On the other hand, high-intensity pretreatment could produce a large number of common inhibitors (such as furfural, HMF, phenolic aldehyde, and so on), which could also inhibit the growth and ethanol fermentability of *I. orientalis* HN-1. In the future, some weak acids (such as organic

acids) could be used for presoak to reduce the intensity in order to reduce the production of inhibitors. Dai et al. used furoic acid to assist hydrolysis of sugarcane bagasse, and a satisfactory result was obtained with a low concentration of inhibitors (Dai et al., 2021). In addition, many kinds of byproducts such as acetic acid and glycerol were generated inductively from *I. orientalis* HN-1 under the stress of inhibitors. These factors would lead to a reduction of ethanol yield. In order to achieve higher ethanol yield, the ethanol production strain should be strengthened in the future.

CONCLUSION

A lignocellulosic ethanol production from residual tobacco stalk by integrating sulfuric acid presoak and ICSE pretreatment was investigated in this study. The optimum concentration of sulfuric acid for presoak of tobacco stalk was obtained. Neither single dilute acid soaking nor single ICSE could achieve a satisfactory nicotine removal rate, but the integrated pretreatment methods could remove almost all the nicotine of tobacco stalk. Effective removal of nicotine is essential to ensure that a high glucose concentration is achieved in the enzymatic hydrolysis process, and finally, a satisfactory ethanol concentration and yield were achieved by *I. orientalis* HN-1 in the fermenter. This environment-friendly technology provided a promising option for tobacco stalk resource utilization for ethanol production. Tobacco residual could be an important alternative feedstock for future industrial ethanol production.

DATA AVAILABILITY STATEMENT

The original contributions presented in the study are included in the article/Supplementary Material, and further inquiries can be directed to the corresponding authors.

AUTHOR CONTRIBUTIONS

HZ: data curation, writing—review and editing. CF: experimental operation, data analysis. TR: resources. HX: investigation. GM: experimental guidance. ZW: methodology. FW: supervision, validation. AS: project administration, funding acquisition.

FUNDING

This work was supported by the Zhongyuan Thousand Talents Project (204200510018), the National Natural Science Foundation of China (21908044), the Key Scientific Research Project of Universities of Henan Province (20A180012), and the Program for Science and Technology Innovation Talents in Universities of Henan Province (18HASTIT038).

REFERENCES

- Adney, B., and Baker, J. (1996). Measurement of Cellulase Activities. *Lab. Anal. procedure* 6, 1–11.
- Akpinar, O., Erdogan, K., Bakir, U., and Yilmaz, L. (2010). Comparison of Acid and Enzymatic Hydrolysis of Tobacco Stalk Xylan for Preparation of Xylooligosaccharides. *LWT - Food Sci. Technol.* 43, 119–125. doi:10.1016/j.lwt.2009.06.025
- Cai, J., Li, B., Chen, C., Wang, J., Zhao, M., and Zhang, K. (2016). Hydrothermal Carbonization of Tobacco Stalk for Fuel Application. *Bioresour. Technol.* 220, 305–311. doi:10.1016/j.biortech.2016.08.098
- Dai, L., Huang, T., Jiang, K., Zhou, X., and Xu, Y. (2021). A Novel Recyclable Furoic Acid-Assisted Pretreatment for Sugarcane Bagasse Biorefinery in Co-production of Xylooligosaccharides and Glucose. *Biotechnol. Biofuels.* 14, 35. doi:10.1186/s13068-021-01884-3
- Dash, A. K., and Wong, S.-T. (1996). Liquid Chromatographic Method for the Determination of Nicotine in Pharmaceutical Formulations. *J. Chromatogr. A* 749, 81–85. doi:10.1016/0021-9673(96)00369-X
- Erat, M., Ciftci, M., Gumustekin, K., and Gul, M. (2007). Effects of Nicotine and Vitamin E on Glutathione Reductase Activity in Some Rat Tissues *In Vivo* and *In Vitro*. *Eur. J. Pharmacol.* 554, 92–97. doi:10.1016/j.ejphar.2006.10.008
- Eveleigh, D. E., Mandels, M., Andreotti, R., and Roche, C. (2009). Measurement of Saccharifying Cellulase. *Biotechnol. Biofuels.* 2, 21. doi:10.1186/1754-6834-2-21
- Falco, A. M., and Bevins, R. A. (2015). Individual Differences in the Behavioral Effects of Nicotine: A Review of the Preclinical Animal Literature. *Pharmacol. Biochem. Behav.* 138, 80–90. doi:10.1016/j.pbb.2015.09.017
- Gan, Z., and Zhuang, Q. (2002). Investigation of the Effect of Nicotine on the Activity of Lactate Dehydrogenase. *Chin. J. Anal. Chem.* 30, 385–387. doi:10.1016/S0956-5663(01)00270-6
- Guo, G.-N., Cai, B., Li, R., Pan, X., Wei, M., and Zhang, C. (2019). Enhancement of Saccharification and Ethanol Conversion from Tobacco Stalks by Chemical Pretreatment. *Biomass Conv. Bioref.* 11, 1085–1092. doi:10.1007/s13399-019-00478-2
- Henry, J. B., Vann, M. C., and Lewis, R. S. (2019). Agronomic Practices Affecting Nicotine Concentration in Flue-Cured Tobacco: A Review. *Agron. J.* 111, 3067–3075. doi:10.2134/agronj2019.04.0268
- Herbert, G. M. J., and Krishnan, A. U. (2016). Quantifying Environmental Performance of Biomass Energy. *Renew. Sustain. Energ. Rev.* 59, 292–308. doi:10.1016/j.rser.2015.12.254
- Huang, C., Sun, R., Chang, H., Yong, Q., Jameel, H., and Phillips, R. (2019). Production of Dissolving Grade Pulp from Tobacco Stalk through SO₂-Ethanol-Water Fractionation, Alkaline Extraction, and Bleaching Processes. *BioResources* 14, 5544–5558.
- Liang, M., Yang, T., Zhang, G., Zhang, K., Wang, L., Li, R., et al. (2021). Effects of Hydrochloric Acid Washing on the Structure and Pyrolysis Characteristics of Tobacco Stalk. *Biomass Conv. Bioref.* doi:10.1007/s13399-021-01616-5
- Morales, M., Quintero, J., Conejeros, R., and Aroca, G. (2015). Life Cycle Assessment of Lignocellulosic Bioethanol: Environmental Impacts and Energy Balance. *Renew. Sustain. Energ. Rev.* 42, 1349–1361. doi:10.1016/j.rser.2014.10.097
- Qin, Z., Sun, M., Luo, X., Zhang, H., Xie, J., Chen, H., et al. (2018). Life-cycle Assessment of Tobacco Stalk Utilization. *Bioresour. Technol.* 265, 119–127. doi:10.1016/j.biortech.2018.05.110
- Sluiter, A., Hames, B., Ruiz, R., Scarlata, C., Sluiter, J., Templeton, D., et al. (2008). Determination of Structural Carbohydrates and Lignin in Biomass. *Lab. Anal. procedure* 1617, 1–16.
- Sophanodorn, K., Unpaprom, Y., Whangchai, K., Homdoun, N., Dussadee, N., and Ramaraj, R. (2020). Environmental Management and Valorization of Cultivated Tobacco Stalks by Combined Pretreatment for Potential Bioethanol Production. *Biomass Conv. Bioref.* doi:10.1007/s13399-020-00992-8
- Su, Y., Xian, H., Shi, S., Zhang, C., Manik, S. M. N., Mao, J., et al. (2016). Biodegradation of Lignin and Nicotine with white Rot Fungi for the Delignification and Detoxification of Tobacco Stalk. *BMC Biotechnol.* 16, 81. doi:10.1186/s12896-016-0311-8
- Sun, D., Sun, S.-C., Wang, B., Sun, S.-F., Shi, Q., Zheng, L., et al. (2020). Effect of Various Pretreatments on Improving Cellulose Enzymatic Digestibility of Tobacco Stalk and the Structural Features of Co-produced Hemicelluloses. *Bioresour. Technol.* 297, 122471. doi:10.1016/j.biortech.2019.122471
- Swanson, J. A., Lee, J. W., and Hopp, J. W. (1994). Caffeine and Nicotine: A Review of Their Joint Use and Possible Interactive Effects in Tobacco Withdrawal. *Addict. Behaviors* 19, 229–256. doi:10.1016/0306-4603(94)90027-2
- Trigo, J. M., and Foll, B. L. (2016). Inhibition of Monoacylglycerol Lipase (MAGL) Enhances Cue-Induced Reinstatement of Nicotine-Seeking Behavior in Mice. *Psychopharmacology* 233, 1815–1822. doi:10.1007/s00213-015-4117-5
- Wang, F., Dong, H., Hassanpour, M., Zhang, K., Xie, H., Zhang, H., et al. (2020). Glycerol-assisted One-step Instant Catapult Steam Explosion Enhances Enzymatic Digestibility of Corn stover. *Ind. Crops Prod.* 157, 112907. doi:10.1016/j.indcrop.2020.112907
- Wang, Q., Xu, F.-Z., An, L.-L., Xiang, H.-Y., Zhang, W.-H., Liu, G.-S., et al. (2019). Molecular Characterization of a New Recombinant brassica Yellow Virus Infecting Tobacco in China. *Virus Genes* 55, 253–256. doi:10.1007/s11262-019-01636-4
- Xie, H., Li, Z., Wang, Z., Mao, G., Zhang, H., Wang, F., et al. (2020). Instant Catapult Steam Explosion: A Rapid Technique for Detoxification of Aflatoxin-Contaminated Biomass for Sustainable Utilization as Animal Feed. *J. Clean. Prod.* 255, 120010. doi:10.1016/j.jclepro.2020.120010
- Yalcin, E. B., Tong, M., Gallucci, G., and de la Monte, S. M. (2018). Effects of Tobacco Nicotine-Derived Nitrosamine Ketone (NNK) Exposures on Brain Alcohol Metabolizing Enzyme Activities. *Drug Metab. Lett.* 12, 117–124. doi:10.2174/1872312812666180611115418
- Yu, Z., Zhang, B., Yu, F., Xu, G., and Song, A. (2012). A Real Explosion: The Requirement of Steam Explosion Pretreatment. *Bioresour. Technol.* 121, 335–341. doi:10.1016/j.biortech.2012.06.055
- Yuan, Z., Wei, W., Wen, Y., and Wang, R. (2019). Comparison of Alkaline and Acid-Catalyzed Steam Pretreatments for Ethanol Production from Tobacco Stalk. *Ind. Crops Prod.* 142, 111864. doi:10.1016/j.indcrop.2019.111864
- Zhang, H., Wang, L., Dai, Z., Zhang, R., Chen, C., and Liu, G. (2020). Effect of Organic Loading, Feed-To-Inoculum Ratio, and Pretreatment on the Anaerobic Digestion of Tobacco Stalks. *Bioresour. Technol.* 298, 122474. doi:10.1016/j.biortech.2019.122474
- Zhao, J., Zhang, X., Lei, W., Ji, X., Zhou, X., and Xu, Y. (2020). Mannonic Acid and Bio-Ethanol Production from Konjac Using a Two-step Bioprocess with *Candida Shehatae* and *Gluconobacter Oxydans*. *J. Renew. Mater.* 8, 79–88. doi:10.32604/jrm.2020.08761
- Zhong, W., Zhu, C., Shu, M., Sun, K., Zhao, L., Wang, C., et al. (2010). Degradation of Nicotine in Tobacco Waste Extract by Newly Isolated *Pseudomonas* Sp. ZUTSKD. *Bioresour. Technol.* 101, 6935–6941. doi:10.1016/j.biortech.2010.03.142
- Zhou, X., Hua, X., Huang, L., and Xu, Y. (2019). Bio-Utilization of Cheese Manufacturing Wastes (Cheese Whey Powder) for Bioethanol and Specific Product (Galactonic Acid) Production via a Two-step Bioprocess. *Bioresour. Technol.* 272, 70–76. doi:10.1016/j.biortech.2018.10.001

Conflict of Interest: The authors declare that the research was conducted in the absence of any commercial or financial relationships that could be construed as a potential conflict of interest.

Publisher's Note: All claims expressed in this article are solely those of the authors and do not necessarily represent those of their affiliated organizations, or those of the publisher, the editors, and the reviewers. Any product that may be evaluated in this article, or claim that may be made by its manufacturer, is not guaranteed or endorsed by the publisher.

Copyright © 2021 Zhang, Fu, Ren, Xie, Mao, Wang, Wang and Song. This is an open-access article distributed under the terms of the Creative Commons Attribution License (CC BY). The use, distribution or reproduction in other forums is permitted, provided the original author(s) and the copyright owner(s) are credited and that the original publication in this journal is cited, in accordance with accepted academic practice. No use, distribution or reproduction is permitted which does not comply with these terms.



Synthesis of pH-Sensitive and Self-Fluorescent Polymeric Micelles Derived From Rosin and Vegetable Oils *via* ATRP

Juan Yu^{1,2}, Chaoqun Xu¹, Chuanwei Lu^{1,2}, Qian Liu³, Jifu Wang^{2*} and Fuxiang Chu^{1,2*}

¹Key Laboratory of Forestry Genetics and Biotechnology, Jiangsu Province Key Laboratory of Green Biomass-based Fuels and Chemicals, Ministry of Education, Jiangsu Co-Innovation Center of Efficient Processing and Utilization of Forest Resources, College of Chemical Engineering, Nanjing Forestry University, Nanjing, China, ²National Engineering Laboratory of Biomass Chemical Utilization, Key and Laboratory of Forest Chemical Engineering, SFA, Key Laboratory of Biomass Energy and Material, Institute of Chemical Industry of Forest Products, CAF, Nanjing, China, ³Research Center for Nanophotonic and Nanoelectronic Materials, School of Materials Science and Engineering, Suzhou University of Science and Technology, Suzhou, China

OPEN ACCESS

Edited by:

Lei Wang,
Ocean University of China, China

Reviewed by:

Enmin Zong,
Taizhou University, China
Xin Wang,
Nanjing Tech University, China

*Correspondence:

Jifu Wang
wjf118@126.com
Fuxiang Chu
chufuxiang@caf.ac.cn

Specialty section:

This article was submitted to
Bioprocess Engineering,
a section of the journal
Frontiers in Bioengineering and
Biotechnology

Received: 05 August 2021

Accepted: 20 September 2021

Published: 02 November 2021

Citation:

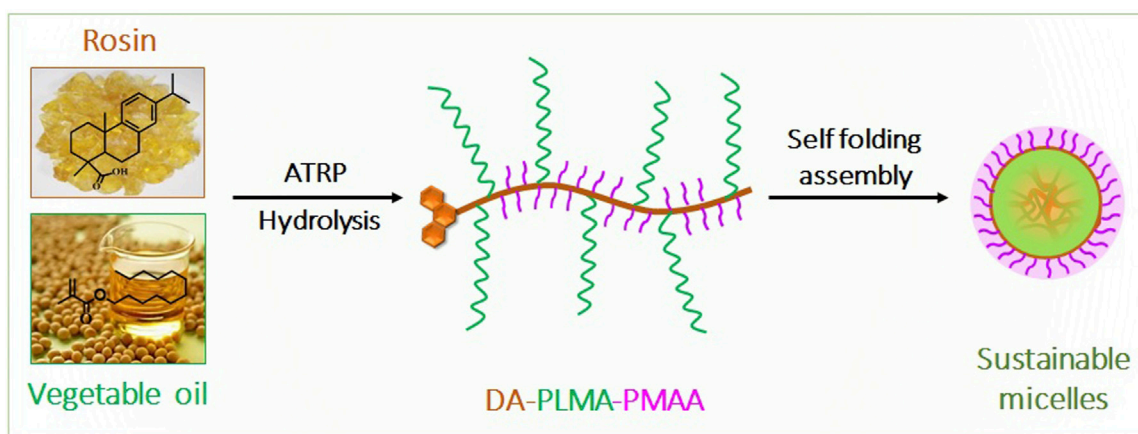
Yu J, Xu C, Lu C, Liu Q, Wang J and
Chu F (2021) Synthesis of pH-Sensitive
and Self-Fluorescent Polymeric
Micelles Derived From Rosin and
Vegetable Oils *via* ATRP.
Front. Bioeng. Biotechnol. 9:753808.
doi: 10.3389/fbioe.2021.753808

Preparation and application of sustainable polymers derived from renewable resources are of great significance. The aim of this study is to synthesize a kind of sustainable polymeric micelles from rosin and vegetable oils *via* atom transfer radical polymerization (ATRP) and to investigate the doxorubicin delivery properties of these micelles. Dehydroabietic acid-based poly lauryl methacrylate (DA-PLMA) with narrow PDI of 1.13 was prepared in a well-controlled process using rosin as an ATRP initiator. Thereafter, carboxylic groups were introduced to form poly methacrylic acid (PMAA) moieties in DA-PLMA polymer *via* acid hydrolysis. The resulted DA-PLMA-PMAA could self-assemble in water to form pH-dependent polymeric micelles with a diameter of ~65 nm and PDI as low as 0.105. Owing to the existence of rosin, DA-PLMA-PMAA micelles also showed self-fluorescence properties. In addition, Dox-loaded micelles were prepared in aqueous solution with the drug-loading capacity as high as 16.0% and showed sustained-release characteristics. These results demonstrate great promise for designing polymeric micellar from rosin and vegetable oils.

Keywords: pH-sensitive, self-fluorescence, polymeric micelles, rosin, vegetable oils, ATRP, doxorubicin

INTRODUCTION

The application of renewable raw materials (included natural polymers and chemicals) can take advantage of the synthetic potential of nature and avoid or minimize CO₂ emission, which is of great significance for carbon emissions and carbon neutralization (Meier et al., 2007; Thyavihalli Girijappa et al., 2019). Renewable natural polymers such as cellulose, hemicellulose, starch, chitin, lignin, and natural rubber have been widely explored in chemical industry for the partial replacement of fossil fuel-based polymeric materials (Biermann et al., 2011; Zhang et al., 2017; Wang J. et al., 2020; Sun et al., 2020). However, natural rosin, a kind of important natural chemicals, which can be easily obtained from pine resins and some other related plants, has been modified to be various kinds of fine chemicals and monomers to replace petrochemicals in industry (Cai et al., 2021). These rosin-based monomers could be polymerized *via* controlled radical polymerization resulting in a class of well-defined rosin-derived polymers. Owing to the good thermal properties, excellent hydrophobicity,



SCHEME 1 | Schematic illustration of synthesis of DA-PLMA-PMAA sustainable micelles from rosin and vegetable oil.

biocompatibility, and UV absorption properties, these renewable rosin-derived polymers could be potential candidates for thermoplastic elastomers. Recently, rosin was transferred to an atom transfer radical polymerization (ATRP) initiator which provides an alternative avenue for the designation of rosin-based polymers (with rosin content less than 10 wt%) to achieve the improvement in thermal, UV-blocking, and mechanical performance (Yu et al., 2021).

Polymeric micelles formed by self-assembly of amphiphilic block copolymers have been widely applied as excellent carriers for hydrophobic drugs because they have high drug-loading capacity, sustained release manner (owing to their hydrophobic core), and the stabilization ability in aqueous solution (owing to their hydrophilic shell) (Tyrrell et al., 2010; Tang et al., 2011; Bastakoti et al., 2013; Sun et al., 2018). Therefore, a number of amphiphilic block copolymers have been synthesized and reported to form a hydrophilic shell of micelles in aqueous solution. Regarding amphiphilic block copolymers for polymeric micelles, PEG is the most widely used hydrophilic block; the commonly reported hydrophobic blocks are poly (propylene oxide) (PPO), poly (ϵ -caprolactone) (PCL) and poly (lactide) (PLA), and poly lauryl methacrylate (PLMA) (Tyrrell et al., 2010; Tang et al., 2011; Hattori et al., 2017). There are various method choices for the synthesis of amphiphilic block copolymers, including free radical polymerization (Debele et al., 2017), ring-opening polymerization (Dai et al., 2011), reversible addition-fragmentation chain transfer (RAFT) (Wang C. et al., 2020), and ATRP (Oh et al., 2007).

However, most of the reported polymeric micelles were prepared from fossil fuel-based polymers. Research works focusing on polymeric micelles from renewable resource were rarely reported. Hespel et al. (2012) reported the synthesis of pH-sensitive micelles from renewable linseed oil *via* ATRP. The amphiphilic copolymers from linseed oils were prepared by ATRP of tert-butyl acrylate (tBA) from a linseed oil initiator and subsequent acidolysis of the PtBA block into poly(acrylic acid) (PAA). Compared to amphiphilic block copolymers, the

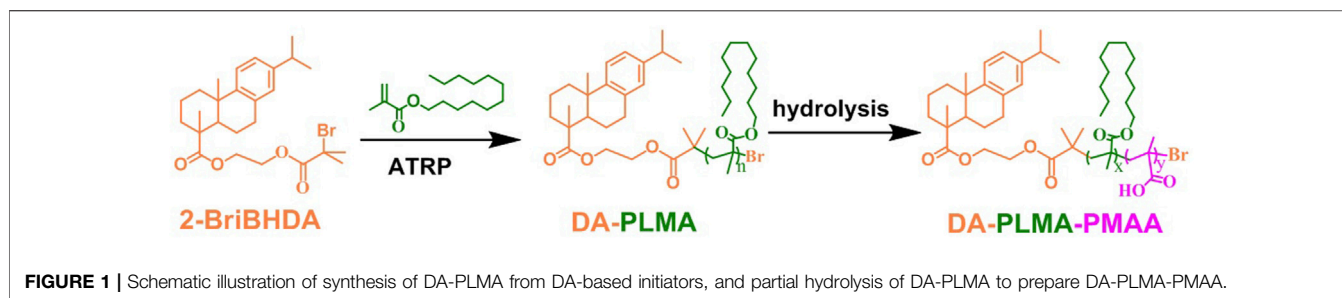
preparation of amphiphilic random copolymers is much easier. In addition, it is reported that amphiphilic copolymers obtained by copolymerizing a hydrophilic poly(ethylene glycol) (PEG) monomer and a hydrophobic lauryl monomer with a random monomer sequence could produce uniform micelles in water, and the micelle's size was determined by the composition (Hattori et al., 2017). These results promote the fabrication of polymeric micelles derived from renewable vegetable oil resources.

The objective of this study was to develop polymeric micelles based on rosin and vegetable oils as a drug carrier and to reveal the role of rosin in polymeric micelles. As shown in **Scheme 1**, a rosin-based initiator (2-BriBEDA) and lauryl methacrylate (LMA, derived from vegetable oil) were used as raw materials. Hydrophobic dehydroabietic acid-based poly (lauryl methacrylate) (DA-PLMA) was prepared *via* ATRP using 2-BriBEDA as an initiator. After acid hydrolysis, poly methacrylic acid (PMAA) moieties were introduced in PLMA blocks, resulting in an amphiphilic random copolymer (DA-PLMA-PMAA). The self-assembly of DA-PLMA-PMAA into polymeric micelles was verified and characterized. Hydrophobic drug doxorubicin (Dox) was encapsulated into the resulted micelles. This novel type of biomass-based polymeric micelles exhibit pH-sensitivity, self-fluorescent, high drug-loading level capacity, and aqueous stability, making it an extremely promising nanoplatform for the drug carrier field.

EXPERIMENTAL

Materials

A rosin-based ATRP initiator (2-BriBEDA) was prepared using dehydroabietic acid (DA, main content of rosin) as a raw material according to our previous study (Yu et al., 2021). *N,N,N',N'',N'''*-pentamethyldiethylenetriamine (PMDETA, 99%, Aladdin Industrial Inc.), lauryl methacrylate (LMA, 96%, Aldrich), and CuBr (99.999%, Aldrich) were used as received. Doxorubicin hydrochloride (Dox HCl) was purchased from Beijing Huafeng United Technology Company. Tetrahydrofuran (THF, AR



reagents), dichloromethane (DCM, AR reagents), methanol (AR reagents), and petroleum ether (AR reagents) were purchased from Nanjing Reagent Chemical Co. Ltd. Anisole was dried over 4A molecular sieves and then distilled before use.

Characterization

An FT-IR analysis of rosin-based polymers before and after acid hydrolysis was performed using a Nicolet iS10 FT-IR spectrometer by an attenuated total reflectance method.

A ^1H NMR analysis of rosin-based polymers before and after acid hydrolysis was carried out on a Bruker DMX 300 NMR spectrometer, and CDCl_3 or DMSO-d_6 was used as the solvent.

Gel permeation chromatography (GPC) was performed at 40°C to measure molecular weight and molecular weight distribution of rosin-based polymers. All samples were filtered over a microfilter with a pore size of $0.22\ \mu\text{m}$ (Nylon, Millex-HN 13 mm Syringes Filters, Millipore). A Malvern Viscotek 3580 System, a Viscotek GPC2502 refractive detector, and a GPC1007 pump were involved. An HPLC-grade THF was used as the eluent, and the flow rate was 1 ml/min. Monodispersed polystyrene (PS) was used as the standard to generate the calibration curve.

A UV-visible spectrophotometer (UV/vis) analysis was performed by recording the solution of rosin-based polymers before and after acid hydrolysis in THF on a Shimadzu UV-1800, Shimadzu Scientific Instruments Incorporated in a double-beam mode, whereas pure THF was used as a reference of the copolymer solution while the wavelength is between 200 and 400 nm.

Fluorescence (FL) spectra were used to characterize the fluorescence properties, which were measured on a HITACHI F-4500 spectrofluorometer with the band widths of 10 nm for excitation and 2.5 nm for emission, where the excitation wavelength (λ_{ex}) was 360 nm. The samples were dissolved in THF with a concentration of 2 mg/ml.

Surface tension of the micelle's solution was measured by using the Wilhelmy plate technique at 25°C . The tensiometer was calibrated against water before measurements. The platinum plate was always cleaned and heated to red color with an alcohol lamp.

Transmission electron microscope (TEM) images were obtained by a JEOL JEM-2011 instrument operated at 100 kV. For TEM studies, a drop of micellar solution was deposited on an electron microscopy copper grid coated with a carbon film, and the water was evaporated at room temperature.

The sizes, size distributions, and zeta-potentials of prepared micelles were determined using a Zetasizer Nano-ZS Instrument (ZEM4228, Malvern Instruments, United Kingdom). Each sample was equilibrated at 25°C for 1 min before measurement, and five sets of time-averaged measurements were taken. A 633 nm He-Ne laser was the light source.

Synthesis of DA-PLMA via ATRP

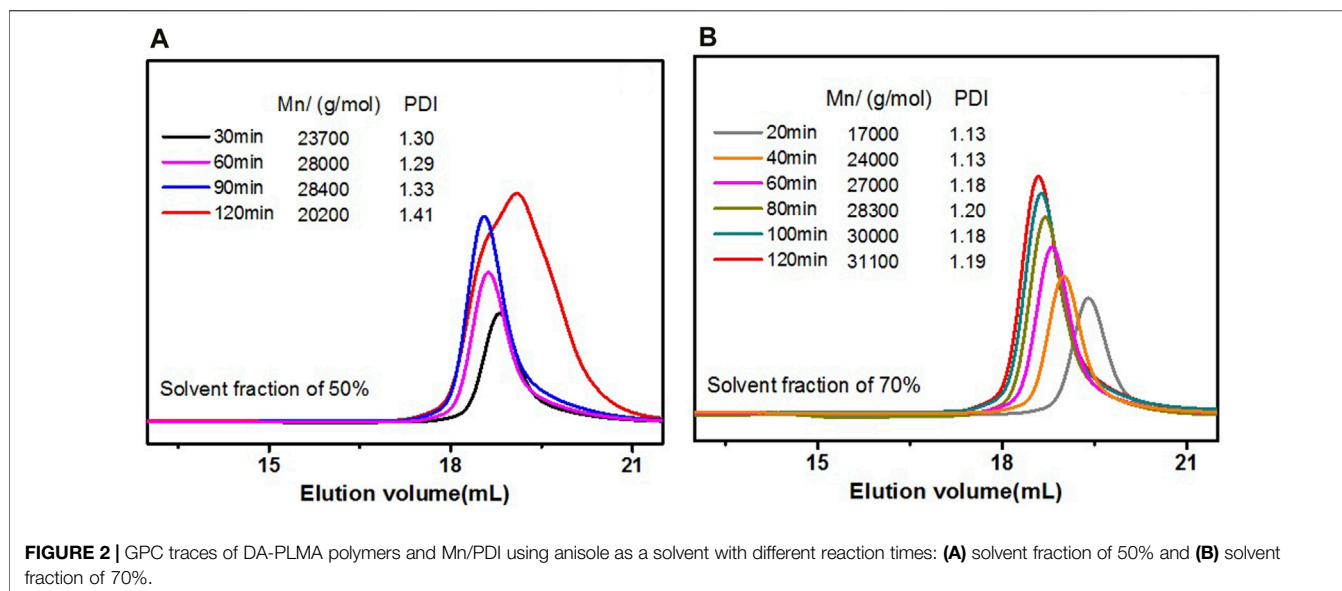
2-BriBHDA was used as the initiator to initiate the polymerization of vegetable oil-based monomer lauryl methacrylate (LMA) via ATRP. As shown in **Figure 1**, for a typical polymerization procedure, a mixture of LMA (2.57 g, 1.01×10^{-2} mol), PMDETA (9.13 mg, 5.07×10^{-5} mol), 2-BriBHDA (25 mg, 5.07×10^{-5} mol), and anisole (3 ml) was charged into a round-bottom flask and degassed by three freeze-pump-thaw cycles. Thereafter, the mixture was transferred into a Schlenk flask that contained Cu(I)Br (7.5 mg, 5.07×10^{-5} mol) under nitrogen and soon placed in an oil bath set at 100°C . Periodically, samples were withdrawn from the Schlenk flask via a syringe under nitrogen to determine the monomer conversion, molecular weight, and polydispersity of the resulted polymer. The polymerization was stopped by pouring the reaction mixture with THF. After passing through an alkaline alumina column, the product was precipitated into methanol, collected, and dried under vacuum until constant weight.

Preparation of DA-PLMA-PMAA by Acid Hydrolysis of DA-PLMA

1.5 ml of concentrated sulfuric acid was added to a Teflon centrifugal tube containing 100 mg DA-PLMA copolymer; subsequently, the reaction mixture was stirred in 45°C water bath for 12 h. DA-PLMA-PMAA were obtained by filtration and washed with a plenty of water/methanol mixture prior to being lyophilized (Semen, 1969).

Micelle Formation

Briefly, the DA-PLMA-PMAA copolymer (10 mg) was dissolved in 2 ml THF to give 5 mg/ml solutions, followed by the dropwise addition into distilled water with vigorous stirring until the concentration reached to 0.1 mg/ml. The mixture was left to stand at room temperature for 24 h and was filtered over a microfilter with a pore size of $0.45\ \mu\text{m}$ prior to the subsequent measurement. The polymeric micelle with concentration of 1 mg/ml was prepared in a similar way.



Preparation of Dox-Loaded Micelles and *In Vitro* Drug Release

Dox-loaded micelles were prepared by an incubation method according to our previous study (Nan et al., 2014). The micelle solution (prepared above) was mixed with Dox solution of various predetermined concentrations at room temperature. Subsequently, in order to allow the DOX/micelle mixture to reach an equilibrium state, the mixed solution was incubated at 37°C for 12 h. To determine the entrapment efficiency (EE) and drug-loading efficiency (LE), the drug-loaded micelle solution was centrifuged, and the amount of free Dox in the solution was analyzed by using a UV-vis spectrometer at 495 nm, using a standard calibration curve experimentally obtained with DOX/water solution. The drug-loading capacity (LC) and drug-loading efficiency (LE) were calculated according to the following formulas:

$$LE(\%) = \text{Weight of DOX Loaded in micelles} / \text{Weight of feeding DOX} * 100\%, \quad (1)$$

$$LC(\%) = \text{Weight of DOX Loaded in micelles} / \text{Weight of micelles} * 100\%. \quad (2)$$

The centrifuged DOX/micelle mixture was dispersed in water and then loaded into a dialysis bag (molecular weight cut-off: 14 kDa) and dialyzed against PBS (pH = 7.4) in a beaker at 37°C for *in vitro* drug release. At selective time intervals, 3 ml of solution was withdrawn from the release medium and replaced with 3 ml fresh PBS. The DOX content in the samples was analyzed using the UV-vis spectrophotometer at 495 nm.

RESULTS AND DISCUSSION

Synthesis of DA-PLMA *via* ATRP

Given that the polydispersion index (PDI) of the polymer has a key effect on the PDI of polymeric micelles, the ATRP

polymerization condition of DA-PLMA was optimized first to obtain narrow PDI for the polymers. As shown that PMDETA/CuBr is the best catalyst system for the rosin-based ATRP initiator (Yu et al., 2021), the influence of solvents was emphasized in this study. It is reported that for the polymerization of PLMA, the PDI of PLMA obtained in anisole was a little narrower than those obtained in the other investigated solvents (DMF, acetonitrile, benzene, or toluene) (Çaylı and Meier, 2008). Therefore, anisole was chosen as the solvent in this condition. Two different solvent fractions were employed, respectively, with the same feeding ratio $\{[LMA]/[I]/[Cu(I)]/PMDETA = 200/1/1/1\}$ as solvent fraction could affect ATRP equilibrium constants (K_{ATRP}) (Wang et al., 2012). Commonly, the lower K_{ATRP} may lead to a better controlled polymerization. The results of Mn as well as PDI were monitored by GPC. As shown in **Figure 2A**, the GPC traces of DA-PLMA were symmetrical and monomodal peaks at first 60 min, but became wider after 60 min with a decrease of Mn and increase of PDI. The final products obtained at 120 min had a Mn of 20,200 g/mol and PDI of 1.41, which means that the ATRP polymerization of LMA was not controlled well in this condition. However, when the solvent fraction increased to 70%, all the GPC traces at different reaction times (from 20 to 120 min) showed symmetrical and monomodal peaks, Mn values changed linearly with the reaction time, and all the PDI values were not more than 1.2, confirming the controlled character of polymerization (**Figure 2B**). It should be noted that the reaction medium is initially a mixture of solvent/monomer, but it gradually changed to solvent/monomer/polymer as the polymerization proceeds. The polymer fraction increased with increasing reaction time, and so was the viscosity of the reaction medium, especially in the reaction with lower solvent fraction. The reason why higher solvent fraction leads to a better control of polymerization in this study is probably because the viscosity of the reaction medium was not increased so much that affects the

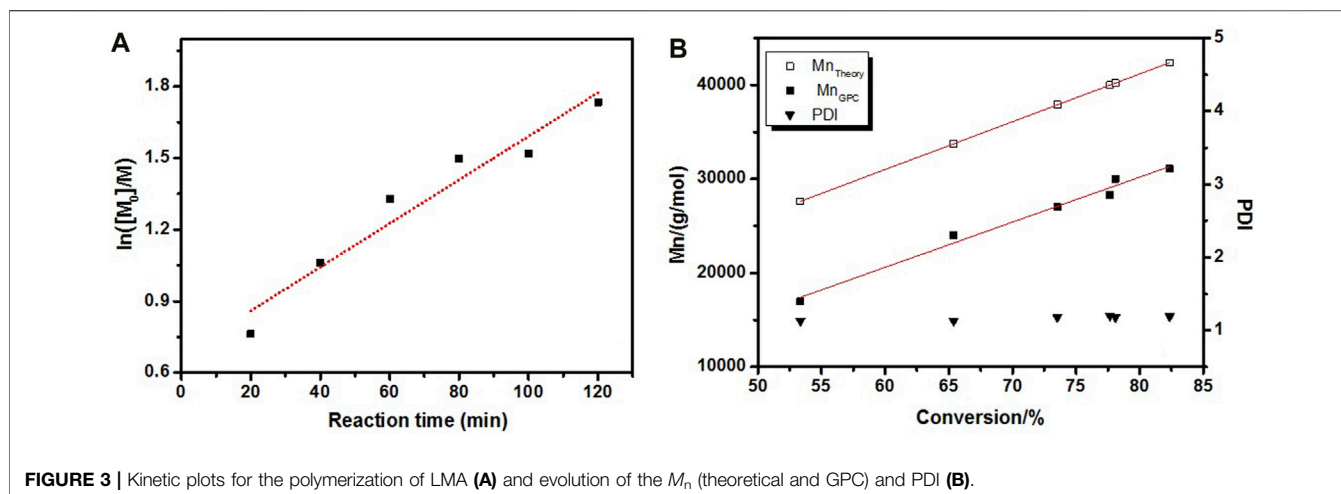


FIGURE 3 | Kinetic plots for the polymerization of LMA (A) and evolution of the M_n (theoretical and GPC) and PDI (B).

polymerization. Thus, anisole (volume 70%) was used as the solvent in most cases.

The controlled and living nature of polymerizations were verified through kinetic experiment which was monitored by analyzing the reaction mixture with ^1H NMR spectroscopy and GPC. The monomer conversion was calculated *via* the ^1H NMR spectrum of the reaction mixture according to Eq. 3 and GPC given M_n and PDI of resulted polymer. The semilogarithmic plot of monomer conversion vs. reaction time is shown in Figure 3A. The linear dependence of $\ln([M]_0/[M])$ on time suggested that the polymerization is a well-controlled process. The M_n s obtained by GPC is shown in Figure 3B, and the molecular weight of copolymers increased with conversion. Meanwhile, the PDI remained less than 1.2 over the whole reaction, meaning a good control of the final copolymer composition (Hespel et al., 2012). In addition, the number average molecular weights of the copolymers determined by GPC were not in fair agreement with the theoretical values calculated by ^1H NMR (Figure 3B). The lower molecular weights determined by GPC could be explained by a notion that molecular weights determined by GPC using PS standards correspond to PS-equivalent molecular weights (Netopil'ik and Kratochvíl, 2003). Therefore, it is the hydrodynamic volume disparity between PS and PLMA that leads to the discrepancy between theoretical and experimental M_n s.

$$\text{LMA conversion (\%)} = (1 - 18/A_{1.31} * A_{5.54}) * 100\%, \quad (3)$$

where $A_{1.31}$ is the ^1H NMR integration area (~ 1.31 ppm) of methylene protons in the lauryl of LMA, $A_{5.54}$ is the ^1H NMR integration area (~ 5.54 ppm) of unsaturated protons in LMA, and 18 is the number of protons of methylene protons in the lauryl of LMA.

Chemical Structure of DA-PLMA and DA-PLMA-PMAA

Amphiphilic copolymers with both hydrophobic segments and hydrophilic segments could autonomously self-assemble to be

micelles or vesicles in water *via* hydrophobic effects (Hattori et al., 2017). Therefore, DA-PLMA-PMAA was obtained by acid hydrolysis of the hydrophobic polymer DA-PLMA. During acid hydrolysis, hydrophobic lauryl was removed while the hydrophilic carboxyl group was introduced at the same time. ATR-FT-IR, ^1H NMR, the UV/vis analysis, and GPC were employed to characterize the chemical structure of DA-PLMA before and after hydrolysis.

The ATR-FT-IR analysis (Figure 4A) of DA-PLMA showed the appearance of C=O signal peak at 1730 cm^{-1} as well as the peak of C-O-C at $1,240\text{ cm}^{-1}$ which ascribed to ester group in PLMA parts. The absorption peaks at around 720 cm^{-1} and 750 cm^{-1} correspond to the $-\text{CH}_2$ group in the side lauryl chain of PLMA and the main chain of PLMA, respectively, while the appearance of absorption peaks at around $3,100\text{ cm}^{-1}$ (O-H), $2,600\text{ cm}^{-1}$ (O-H), and $1,700\text{ cm}^{-1}$ (C=O) in the spectra of hydrolysis polymer (DA-PLMA-PMAA) indicated the formation of carboxylic groups after hydrolysis; however, the peak at $1,730\text{ cm}^{-1}$ and 720 cm^{-1} still exist meant that the partial hydrolysis of DA-PLMA and the hydrophobic lauryl side chain was also retained in the resulted DA-PLMA-PMAA. The ^1H NMR analysis (Figure 4B) showed the appearance of peak at 12.2 ppm corresponding to the protons of O-H moiety in carboxylic groups which verifies the successful introduction of carboxylic groups by acid hydrolysis. The $-\text{OCH}_2$ protons of PLMA (3.9 ppm) and $-\text{CH}_2$ protons (~ 1.31 ppm) in lauryl side chains of LMA still present in the ^1H NMR spectrum of DA-PLMA-PMAA, further confirming the partial hydrolysis of DA-PLMA. The absence of the protons of rosin (usually around 6.8–7.3 ppm) probably caused the entanglement of lauryl long side chains of PLMA around the rosin-based initiator, which could be seen by zooming in the ^1H NMR spectrum (Yu et al., 2021).

As rosin and its derivatives have an absorption in the UV region (200–400 nm), the UV/vis analysis was further employed to confirm the existence of rosin in DA-PLMA and DA-PLMA-PMAA. As shown in Figure 5A, the rosin-based initiator (2-BriBHDA, 0.33 mg/ml) had a UV absorption peak around 250–280 nm. The obvious absorption around 250–280 nm was

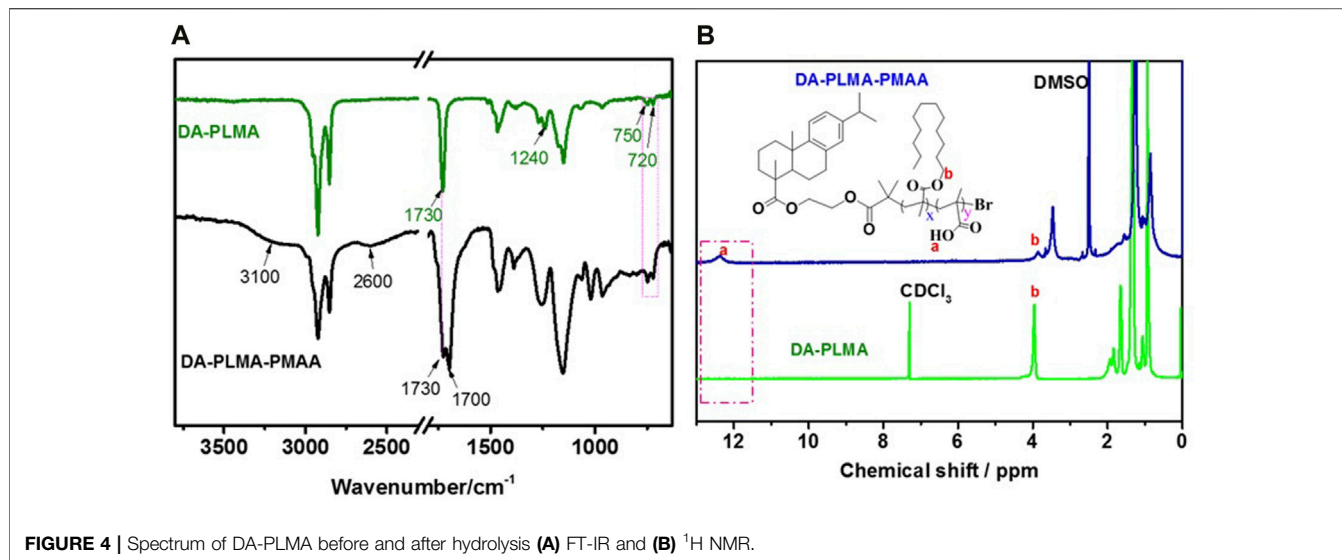


FIGURE 4 | Spectrum of DA-PLMA before and after hydrolysis **(A)** FT-IR and **(B)** ^1H NMR.

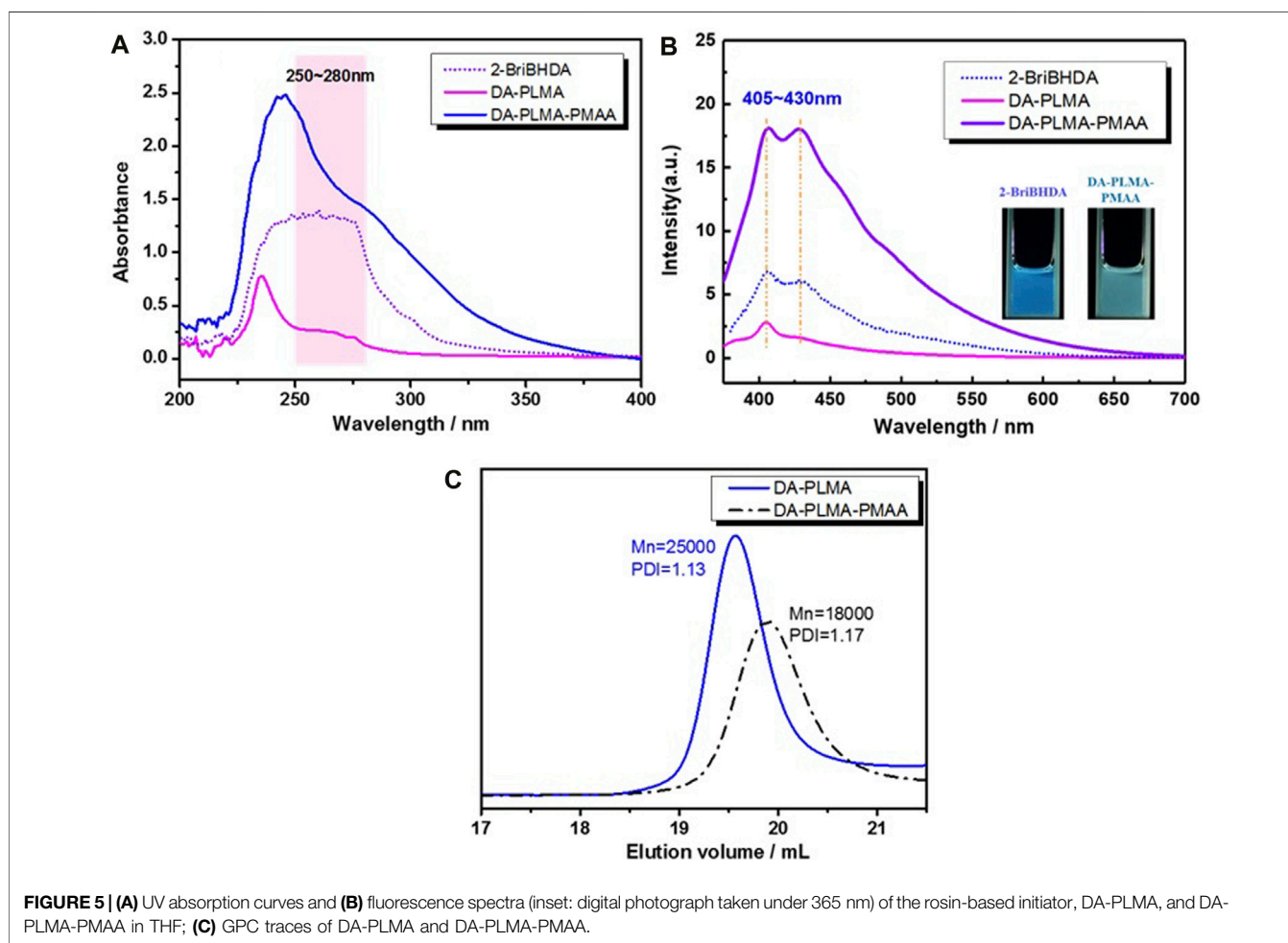
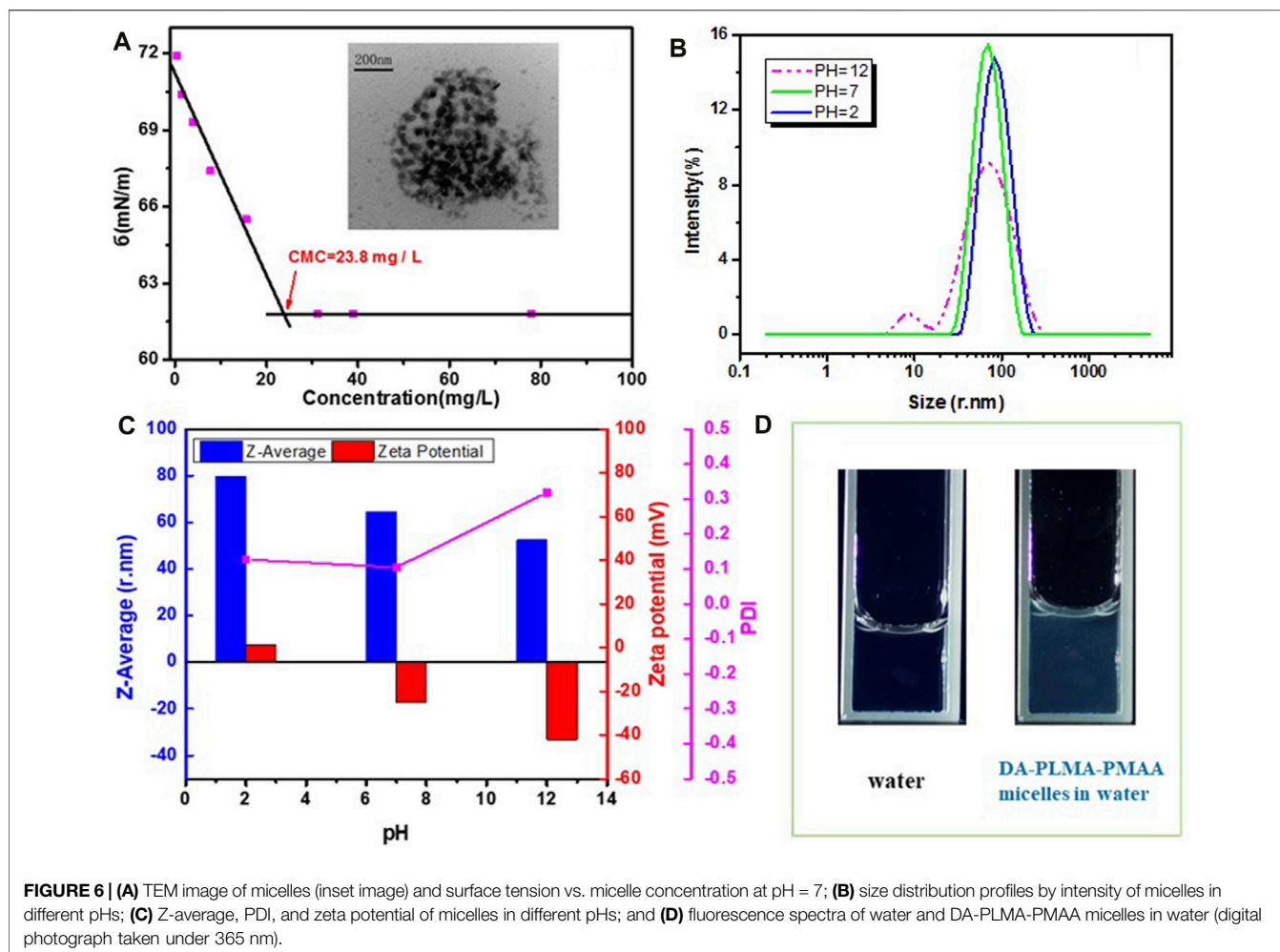


FIGURE 5 | **(A)** UV absorption curves and **(B)** fluorescence spectra (inset: digital photograph taken under 365 nm) of the rosin-based initiator, DA-PLMA, and DA-PLMA-PMAA in THF; **(C)** GPC traces of DA-PLMA and DA-PLMA-PMAA.



clearly presented in the UV spectrum of DA-PLMA (2 mg/ml). After acid hydrolysis, UV absorption intensity around 250–280 nm increased significantly for DA-PLMA-PMAA (2 mg/ml). This is caused by the fact that the DA molar concentration increased after partial hydrolysis of DA-PLMA under the same mass concentration. As shown in **Figure 5B** (inset), the rosin-based ATRP initiator 2-BriBHDA (10 mg/ml) displayed the fluorescence in THF when excited at 365 nm, so was DA-PLMA-PMAA (1 mg/ml). Therefore, the fluorescent emission spectra of 2-BriBHDA, DA-PLMA (4 mg/ml), and DA-PLMA-PMAA (1 mg/ml) in THF ($\lambda_{\text{ex}} = 365 \text{ nm}$) were recorded to verify the role of rosin in regard to the fluorescence property (**Figure 5B**). 2-BriBHDA has a λ_{em} of 405–430 nm in its fluorescent emission spectrum. As expected, the peaks around 405–430 nm were also presented in fluorescence spectra of DA-PLMA and DA-PLMA-PMAA, indicating that the fluorescence property was ascribed to the existence of rosin. The peak intensity of 405–430 nm was decreased for DA-PLMA but increased significantly for DA-PLMA-PMAA, which was consistent with that of the UV/vis analysis. Overall, the results from both the UV/vis and fluorescent analysis confirm the existence of DA before and after acid

hydrolysis, and DA-PLMA-PMAA showed the self-fluorescence property which has promising application in the drug delivery field. It was normal that the Mn of DA-PLMA-PMAA (18,000 mol/g) was lower than that of DA-PLMA (25,000 mol/g) after hydrolysis. However, after hydrolysis, the PDI of DA-PLMA-PMAA (after hydrolysis) was still as low as 1.17 (**Figure 5B**), which meant the partial hydrolysis process was reliable for the following preparation of micelles.

DA-PLMA-PMAA Micelles With pH Sensitivity and Self-Fluorescence

After acid hydrolysis of DA-PLMA copolymer, the resulting products contain both hydrophilic poly methacrylic acid and hydrophobic poly lauryl methacrylate which were commonly known to self-assemble to form micelle structures in aqueous solution. Indeed, the THF solution of DA-PLMA-PMAA was added into deionized water at room temperature, and the mixture was stirred for 24 h for the evaporation of THF. The morphology of micelles was observed using transmission electron microscopy (TEM). **Figure 6A** (inset) showed the TEM image of DA-PLMA-PMAA in deionized water (pH = 7) with concentration of

0.1 mg/ml, from which the spherical micelles with the diameter of ~40 nm were clearly seen. The hydrodynamic diameter (Z-average) of micelles obtained from DLS was ~65 nm, and the PDI of micelles was as low as 0.105, which was much lower than that of sustainable micelles derived from chitosan or lignin (Zhou et al., 2019; Pornpitchanarong et al., 2020) and polymeric micelles prepared by Reversible Addition–Fragmentation Transfer (RAFT) polymerization (Wang C. et al., 2020). This probably ascribes to the relatively low PDI (1.17) of the DA-PLMA-PMAA copolymer. In addition, the zeta potential was –17.3 mV, and the negative surface could facilitate drug loading and the delivery process (Yang et al., 2017).

Surface tension measurements were adopted to determine the critical micellar concentration, which is an important parameter to characterize the stability of polymeric micelles (Patist et al., 2000; Calvo et al., 2009). As shown in **Figure 6A**, the surface tension came to be a constant when the surface is saturated at a surface tension value of ~61.8 mN/m in pH = 7. The critical micellar concentration (CMC) read from the point of intersection between the two linear lines in **Figure 6A** was 22.5 mg/L, which was in appropriate concentration, allowing their use in body fluids (Wei et al., 2007). In addition, the CMC of DA-PLMA-PMAA micelles was much lower than that of common surfactant sodium lauryl sulfate (CMC was 2.5 g/L), suggesting that DA-PLMA-PMAA micelles could be stable enough to serve as a drug carrier for drug delivery.

pH sensitivity is approved to be one of the most efficient stimuli for drug delivery. In order to investigate the pH influence on the formation of DA-PLMA-PMAA micelles, the size, size distribution, and zeta potential of the micelles in different pH were analyzed by DLS. As shown in **Figures 6B,C**, the hydrodynamic diameter (Z-average) was decreased with the increase of pH; inversely, PDI increased with the increase of pHs. Particularly, in acidic solutions (pH = 2 and 5), the Z-average value was ~80 nm, while in basic solutions (pH = 10 and 12), the Z-average value decreased to ~50 nm. This is mainly caused by conformational change of PMAA parts in acidic and basic solutions. It is well known that PMAA chains could be protonated and presenting expanding conformation in the acidic condition; however, in the basic condition, PMAA chains adopt a compact conformation due to the deprotonation of PMAA parts (Xiong et al., 2011; Yuan et al., 2012; Nan et al., 2014). Besides, due to the protonation of PMAA parts at low pH, there were many positive charges in solution, resulting in a positive zeta potential value (7.53 mV, pH = 2; 0.25 mV, pH = 5). With increasing pH, carboxylic groups (–COOH) in PAA could be highly ionized, resulting in a negative zeta potential value of the micelles solution (–33.2 mV, pH = 10; –33.1 mV, pH = 12). The change of the Z-average value and the zeta potential value of micelles solution vs. pH confirmed the pH-dependent properties of micelles. As described above, DA-PLMA-PMAA showed an obvious self-fluorescence property under the excitation of 365 nm. The fluorescence property of DA-PLMA-PMAA micelles in water was also investigated, and the bright fluorescence was observed under a UV lamp (365 nm) (**Figure 6D**). It is well known that fluorescent property is highly desirable for both *in vitro* and *in vivo* applications of

drug-loading micelles because it allows for easy tracking of the nanocarriers using microscopy (Chen et al., 2015). Therefore, the resulted micelles with good fluorescence property would find promising application in the field of drug delivery.

DOX Loading and *In Vitro* Release Studies of DA-PLMA-PMAA Micelles

It is well known that micelles with large size could facilitate the drug release rate; however, particles with size over 200 nm are easily cleared by the reticuloendothelial system (RES) *in vivo* (Maeda and Matsumura, 2011). Therefore, the size of DA-PLMA-PMAA was optimized to be the Z-average value of ~85 nm for the drug-loading experiment. Thereafter, hydrophobic doxorubicin (Dox), a popular model anticancer drug, was chosen as a model drug for fundamental studies of drug loading and releasing properties of DA-PLMA-PMAA micelles. The size and PDI for Dox-loaded micelles were increased to ~95 nm and 0.084 (**Figure 7A**), indicating that Dox was successfully loaded into micelles. The UV-vis spectrum of Dox, free micelles, and Dox-loaded micelles in **Figure 7A** (inset) showed the presence of Dox characteristic absorption peak at ~495 nm for Dox and Dox-loaded micelles samples. This further confirmed a successful entrapment of Dox into the micelles.

The drug-loading capacity and drug-loading efficiency of DOX were analyzed by the UV-vis spectrophotometer at 495 nm, and the results are summarized in **Figure 7B**. The drug-loading capacity (LC) of DOX increased from 8.9 wt% to 16.0 wt%, corresponding to different feeding Dox concentrations at pH = 7.0, while the drug-loading efficiencies (LEs) decreased from 17.35 to 7.80%. Commonly, physical entrapment of drugs in polymeric micelles is driven by the hydrophobic interactions as well as the electrostatic interaction between drugs and the polymer micelles. The LC of DA-PLMA-PMAA micelles was superior to that of most reported Dox-loaded polymeric micelles prepared by ATRP or other polymerization methods (**Table 1**). It is probably the similarity of aromatic chemical structures between DA and Dox that contributes to the good LC property of these micelles. As reported by Cuong et al. (2012), the aromatic folic acid could improve the LC of PEG–PCL polymeric nanocarrier from 5.5 to 10.9%. Overall, the results indicated the feasibility of DA-PLMA-PMAA micelles as drug carriers.

To mimic the physiological blood environment, the *in vitro* release profiles of Dox-loaded polymeric micelles were examined *in vitro* at 37°C via a dialysis method using PBS buffers at pH 7.4 (**Figure 7C**). The results showed an initial burst release of Dox (within 12 h), followed by a sustained and slow release over a prolonged time (until 120 h). Around 24% of Dox was released within first 12 h, which could be attributed to the diffusion of Dox located close to the surface of the micelles. However, the amount of Dox released after 120 h was only 30.6%, indicating that DA-PLMA-PMAA micelles were relatively stable under physiological conditions. This can reduce the loss of drug during circulation in the blood stream (pH 7.4), which was highly desirable for drug carriers.

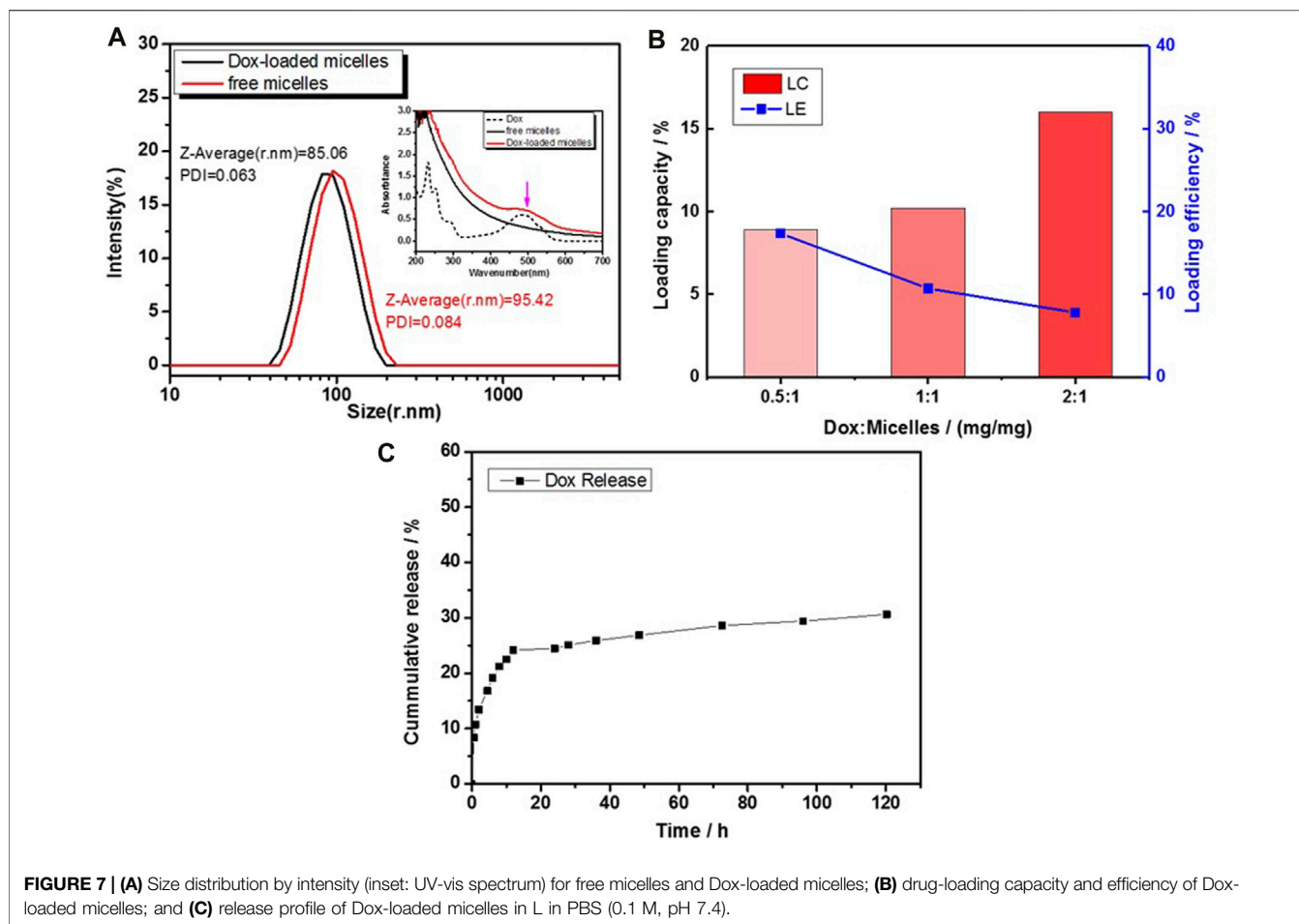


FIGURE 7 | (A) Size distribution by intensity (inset: UV-vis spectrum) for free micelles and Dox-loaded micelles; **(B)** drug-loading capacity and efficiency of Dox-loaded micelles; and **(C)** release profile of Dox-loaded micelles in L in PBS (0.1 M, pH 7.4).

TABLE 1 | Drug-loading capacity (LC) of reported polymeric micelles.

Entry	Polymer micelles	Polymerization method	Functional	LC (wt%)	Reference
1	PEG-b-PEYM	ATRP	pH-sensitive	2.6	Tang et al. (2011)
2	POEOMA nano-hydrogels	ATRP	—	5.4–16.4	Oh et al. (2007)
3	mPEG-PCL-PDMA/mPEG-PCL-PVBA-Dox	RAFT	pH-sensitive	8.1–10.1	Wang et al. (2020a)
4	Folate-decorated star-shaped PEG-PCL	Free-radical polymerization	—	4.6–13.0	Cuong et al. (2012)
5	P(MPC-co-PCL)	Free-radical polymerization	—	6.7–12.6	Zhao et al. (2016)
6	mPEG-b-P(HPMA-g-a-TOS-g-His)	Free-radical polymerization	pH-sensitive	9.6	Debele et al. (2017)
7	mPEG-PAsp(MEA) -PAsp(DIP)	Ring-opening polymerization	Reduction and pH sensitivity	10.5	Dai et al. (2011)
8	H40-BPLP-PEG-OCH ₃ /cRGD	Commercial PEG	Self-fluorescent and pH-sensitive	15.7	Chen et al. (2015)
9	LHRH-PEG-PHIS-Dox	Commercial PEG	pH-sensitive	28	Yang et al. (2015)
10	DA-PLMA-PMAA	ATRP	Self-fluorescent and pH-sensitive	8.9–16.0	This study

SUMMARY

In summary, a facile strategy of preparation multifunctional polymeric micelles was successfully demonstrated. Sustainable dehydroabiatic acid-based poly lauryl methacrylate (DA-PLMA) with narrow PDI of 1.13 was prepared first *via* ATRP of hydrophobic lauryl methacrylate using rosin as an initiator. After simple acid hydrolysis, hydrophilic poly

methacrylic acid (PMAA) moieties were formed, resulting in an amphiphilic polymer (DA-PLMA-PMAA) which spontaneously self-assembled into pH-sensitive micelles in aqueous solutions. The spherical micelles had an average diameter of ~65 nm and PDI as low as 0.105, and showed self-fluorescence properties since they contained rosin segments. The Dox-loading capacity was as high as 16.0 wt%, indicating that DA-PLMA-PMAA had a good

drug-loading ability. The *in vitro* drug release study revealed that DA-PLMA-PMAA micelles were relatively stable under physiological conditions showing sustained-release characteristic. This study not only supported the DA-PLMA-PMAA micelles as a promising efficient drug delivery carrier but also provided a facile approach to utilize renewable rosin and vegetable oils.

DATA AVAILABILITY STATEMENT

The original contributions presented in the study are included in the article/**Supplementary Material**; further inquiries can be directed to the corresponding authors.

AUTHOR CONTRIBUTIONS

JY: conceived and designed the experiments, performed experiments, analyzed the data, and contributed to original draft; CX and CL: performed experiments and analyzed the data; QL: analyzed the data; JW and FC: contributed to writing—review and editing.

REFERENCES

- Bastakoti, B. P., Wu, K. C.-W., Inoue, M., Yusa, S.-i., Nakashima, K., and Yamauchi, Y. (2013). Multifunctional Core-Shell-Corona-Type Polymeric Micelles for Anticancer Drug-Delivery and Imaging. *Chem. Eur. J.* 19 (15), 4812–4817. doi:10.1002/chem.201203958
- Biermann, U., Bornscheuer, U., Meier, M. A. R., Metzger, J. O., and Schäfer, H. J. (2011). “Oils and Fats as Renewable Raw Materials in Chemistry,” *Angew. Chem. Int. Ed.* 50, 3854–3871. doi:10.1002/anie.201002767
- Cai, X., Lin, Y., Li, Y., Chen, X., Wang, Z., Zhao, X., et al. (2021). BioAIEgens Derived from Rosin: How Does Molecular Motion Affect Their Photophysical Processes in Solid State. *Nat. Commun.* 12 (1), 1–9. doi:10.1038/s41467-021-22061-y
- Calvo, E., Bravo, R., Amigo, A., and Gracia-Fadrique, J. (2009). Dynamic Surface Tension, Critical Micelle Concentration, and Activity Coefficients of Aqueous Solutions of Nonyl Phenol Ethoxylates. *Fluid Phase Equilibria* 282 (1), 14–19. doi:10.1016/j.fluid.2009.04.016
- Çaylı, G., and Meier, M. A. R. (2008). Polymers from Renewable Resources: Bulk ATRP of Fatty Alcohol-Derived Methacrylates. *Eur. J. Lipid Sci. Technol.* 110 (9), 853–859. doi:10.1002/ejlt.200800028
- Chen, G., Wang, L., Cordie, T., Vokoun, C., Eliceiri, K. W., and Gong, S. (2015). Multi-functional Self-Fluorescent Unimolecular Micelles for Tumor-Targeted Drug Delivery and Bioimaging. *Biomaterials* 47, 41–50. doi:10.1016/j.biomaterials.2015.01.006
- Cuong, N.-V., Li, Y.-L., and Hsieh, M.-F. (2012). Targeted Delivery of Doxorubicin to Human Breast Cancers by Folate-Decorated star-shaped PEG-PCL Micelle. *J. Mater. Chem.* 22 (3), 1006–1020. doi:10.1039/C1JM13588K
- Dai, J., Lin, S., Cheng, D., Zou, S., and Shuai, X. (2011). Interlayer-Crosslinked Micelle with Partially Hydrated Core Showing Reduction and pH Dual Sensitivity for Pinpointed Intracellular Drug Release. *Angew. Chem. Int. Ed.* 50 (40), 9404–9408. doi:10.1002/anie.201103806
- Debele, T. A., Lee, K.-Y., Hsu, N.-Y., Chiang, Y.-T., Yu, L.-Y., Shen, Y.-A., et al. (2017). A pH Sensitive Polymeric Micelle for Co-delivery of Doxorubicin and α -TOS for colon Cancer Therapy. *J. Mater. Chem. B* 5 (29), 5870–5880. doi:10.1039/c7tb01031a
- Hattori, G., Hirai, Y., Sawamoto, M., and Terashima, T. (2017). Self-assembly of PEG/dodecyl-graft Amphiphilic Copolymers in Water: Consequences of the

FUNDING

This work was supported by the National Natural Science Foundation of China (grant number: 31901275), the Youth Science and Technology Innovation Fund of Nanjing Forestry University (grant number: CX2017006), the project funded by the National First-class Disciplines (PNFD), the project funded by the Priority Academic Program Development of Jiangsu Higher Education Institutions (PAPD), and the Overseas Research and Study Program of Jiangsu Universities.

ACKNOWLEDGMENTS

We would like to express our gratitude to the advanced analysis and testing center of Nanjing Forestry University for the assistance in this study.

SUPPLEMENTARY MATERIAL

The Supplementary Material for this article can be found online at: <https://www.frontiersin.org/articles/10.3389/fbioe.2021.753808/full#supplementary-material>

- Monomer Sequence and Chain Flexibility on Uniform Micelles. *Polym. Chem.* 8 (46), 7248–7259. doi:10.1039/C7PY01719G
- Hespele, L., Kaifas, E., Lecamp, L., Picton, L., Morandi, G., and Burel, F. (2012). Synthesis of pH-Sensitive Micelles from Linseed Oil Using Atom Transfer Radical Polymerisation (ATRP). *Polymer* 53 (20), 4344–4352. doi:10.1016/j.polymer.2012.07.041
- Maeda, H., and Matsumura, Y. (2011). EPR Effect Based Drug Design and Clinical Outlook for Enhanced Cancer Chemotherapy. *Adv. Drug Deliv. Rev.* 63 (3). doi:10.1016/j.addr.2010.05.001
- Meier, M. A. R., Metzger, J. O., and Schubert, U. S. (2007). Plant Oil Renewable Resources as green Alternatives in Polymer Science. *Chem. Soc. Rev.* 36 (11), 1788–1802. doi:10.1039/B703294C
- Nan, J., Chen, Y., Li, R., Wang, J., Liu, M., Wang, C., et al. (2014). Polymeric Hydrogel Nanocapsules: a Thermo and pH Dual-Responsive Carrier for Sustained Drug Release. *Nano-micro Lett.* 6 (3), 200–208. doi:10.1007/BF03353784
- Netopil'k, M., and Kratochvíl, P. (2003). Polystyrene-equivalent Molecular Weight versus True Molecular Weight in Size-Exclusion Chromatography. *Polymer* 44 (12), 3431–3436. doi:10.1016/S0032-3861(03)00258-1
- Oh, J. K., Siegwart, D. J., Lee, H.-i., Sherwood, G., Peteanu, L., Hollinger, J. O., et al. (2007). Biodegradable Nanogels Prepared by Atom Transfer Radical Polymerization as Potential Drug Delivery Carriers: Synthesis, Biodegradation, *In Vitro* Release, and Bioconjugation. *J. Am. Chem. Soc.* 129 (18), 5939–5945. doi:10.1021/ja069150l
- Patist, A., Bhagwat, S. S., Penfield, K. W., Aikens, P., and Shah, D. O. (2000). On the Measurement of Critical Micelle Concentrations of Pure and Technical-Grade Nonionic Surfactants. *J. Surfact Deterg* 3 (1), 53–58. doi:10.1007/s11743-000-0113-4
- Pornpitchanarong, C., Rojanarata, T., Opanasopit, P., Ngawhirunpat, T., and Patrojanasophon, P. (2020). Catechol-modified Chitosan/hyaluronic Acid Nanoparticles as a New Avenue for Local Delivery of Doxorubicin to Oral Cancer Cells. *Colloids Surf. B: Biointerfaces* 196, 111279. doi:10.1016/j.colsurfb.2020.111279
- Semen, J., and Lando, J. B. (1969). The Acid Hydrolysis of Isotactic and Syndiotactic Poly(methyl Methacrylate). *Macromolecules* 2 (6), 570–575. doi:10.1021/ma60012a003

- Sun, H., Zhang, Y., and Zhong, Z. (2018). Reduction-sensitive Polymeric Nanomedicines: An Emerging Multifunctional Platform for Targeted Cancer Therapy. *Adv. Drug Deliv. Rev.* 132, 16–32. doi:10.1016/j.addr.2018.05.007
- Sun, Y., Ma, Z., Xu, X., Liu, X., Liu, L., Huang, G., et al. (2020). Grafting Lignin with Bioderived Polyacrylates for Low-Cost, Ductile, and Fully Biobased Poly(lactic Acid) Composites. *ACS Sustain. Chem. Eng.* 8 (5), 2267–2276. doi:10.1021/acssuschemeng.9b06593
- Tang, R., Ji, W., Panus, D., Palumbo, R. N., and Wang, C. (2011). Block Copolymer Micelles with Acid-Labile Ortho Ester Side-Chains: Synthesis, Characterization, and Enhanced Drug Delivery to Human Glioma Cells. *J. Controlled Release* 151 (1), 18–27. doi:10.1016/j.jconrel.2010.12.005
- Thyaviahalli Girijappa, Y. G., Mavinkere Rangappa, S., Parameswaranpillai, J., and Siengchin, S. (2019). Natural Fibers as Sustainable and Renewable Resource for Development of Eco-Friendly Composites: a Comprehensive Review. *Front. Mater.* 6, 226. doi:10.3389/fmats.2019.00226
- Tyrrell, Z. L., Shen, Y., and Radosz, M. (2010). Fabrication of Micellar Nanoparticles for Drug Delivery through the Self-Assembly of Block Copolymers. *Prog. Polym. Sci.* 35 (9), 1128–1143. doi:10.1016/j.progpolymsci.2010.06.003
- Wang, C., Qi, P., Lu, Y., Liu, L., Zhang, Y., Sheng, Q., et al. (2020a). Bicomponent Polymeric Micelles for pH-Controlled Delivery of Doxorubicin. *Drug Deliv.* 27 (1), 344–357. doi:10.1080/10717544.2020.1726526
- Wang, J., Zhang, D., and Chu, F. (2020b). Wood-Derived Functional Polymeric Materials. *Adv. Mater.* 33 (28), 2001135. doi:10.1002/adma.202001135
- Wang, Y., Kwak, Y., Buback, J., Buback, M., and Matyjaszewski, K. (2012). Determination of ATRP Equilibrium Constants under Polymerization Conditions. *ACS Macro Lett.* 1 (12), 1367–1370. doi:10.1021/mz3005378
- Wei, H., Zhang, X., Cheng, C., Cheng, S.-X., and Zhuo, R.-X. (2007). Self-assembled, Thermosensitive Micelles of a star Block Copolymer Based on PMMA and PNIPAAm for Controlled Drug Delivery. *Biomaterials* 28 (1), 99–107. doi:10.1016/j.biomaterials.2006.08.030
- Xiong, Z., Peng, B., Han, X., Peng, C., Liu, H., and Hu, Y. (2011). Dual-stimuli Responsive Behaviors of Diblock Polyampholyte PDMAEMA-B-PAA in Aqueous Solution. *J. Colloid Interf. Sci.* 356 (2), 557–565. doi:10.1016/j.jcis.2011.01.067
- Yang, S., Tang, Z., Zhang, D., Deng, M., and Chen, X. (2017). pH and Redox Dual-Sensitive Polysaccharide Nanoparticles for the Efficient Delivery of Doxorubicin. *Biomater. Sci.* 5 (10), 2169–2178. doi:10.1039/c7bm00632b
- Yang, T., Li, F., Zhang, H., Fan, L., Qiao, Y., Tan, G., et al. (2015). Multifunctional pH-Sensitive Micelles for Tumor-specific Uptake and Cellular Delivery. *Polym. Chem.* 6 (8), 1373–1382. doi:10.1039/C4PY01403K
- Yu, J., Xu, C., Song, X., Lu, C., Wang, C., Wang, J., et al. (2021). Synthesis and Properties of Rosin Grafted Polymers Via "grafting from" ATRP: The Role of Rosin-Based Initiator. *Ind. Crops Prod.* 168, 113610. doi:10.1016/j.indcrop.2021.113610
- Yuan, W., Zhang, J., Zou, H., Shen, T., and Ren, J. (2012). Amphiphilic Ethyl Cellulose brush Polymers with Mono and Dual Side Chains: Facile Synthesis, Self-Assembly, and Tunable Temperature-pH Responsivities. *Polymer* 53 (4), 956–966. doi:10.1016/j.polymer.2012.01.003
- Zhang, C., Garrison, T. F., Madbouly, S. A., and Kessler, M. R. (2017). Recent Advances in Vegetable Oil-Based Polymers and Their Composites. *Prog. Polym. Sci.* 71, 91–143. doi:10.1016/j.progpolymsci.2016.12.009
- Zhao, Y., He, G., Guo, W., Bao, L., Yi, M., Gong, Y., et al. (2016). Self-assembled Micelles Prepared from Amphiphilic Copolymers Bearing Cell Outer Membrane Phosphorylcholine Zwitterions for a Potential Anti-phagocytic Clearance Carrier. *Polym. Chem.* 7 (36), 5698–5708. doi:10.1039/C6PY00845C
- Zhou, Y., Han, Y., Li, G., Yang, S., Xiong, F., and Chu, F. (2019). Preparation of Targeted Lignin-Based Hollow Nanoparticles for the Delivery of Doxorubicin. *Nanomaterials* 9 (2), 188. doi:10.3390/nano9020188

Conflict of Interest: The authors declare that the research was conducted in the absence of any commercial or financial relationships that could be construed as a potential conflict of interest.

Publisher's Note: All claims expressed in this article are solely those of the authors and do not necessarily represent those of their affiliated organizations, or those of the publisher, the editors, and the reviewers. Any product that may be evaluated in this article, or claim that may be made by its manufacturer, is not guaranteed or endorsed by the publisher.

Copyright © 2021 Yu, Xu, Lu, Liu, Wang and Chu. This is an open-access article distributed under the terms of the Creative Commons Attribution License (CC BY). The use, distribution or reproduction in other forums is permitted, provided the original author(s) and the copyright owner(s) are credited and that the original publication in this journal is cited, in accordance with accepted academic practice. No use, distribution or reproduction is permitted which does not comply with these terms.



Structural Characterization of Sulfated Polysaccharide Isolated From Red Algae (*Gelidium crinale*) and Antioxidant and Anti-Inflammatory Effects in Macrophage Cells

Yu Pei^{1,2}, Shengtao Yang^{1,2}, Zhenbang Xiao^{1,2}, Chunxia Zhou^{1,2*}, Pengzhi Hong^{1,2*} and Zhong-Ji Qian^{1,2*}

OPEN ACCESS

Edited by:

Lei Wang,
Ocean University of China, China

Reviewed by:

Venkatesan Jayachandran,
Yenepoya University, India
Thi Hong Minh Nguyen,
University of Science and Technology
of Hanoi (USTH), Vietnam
Bomi Ryu,
Jeju National University, South Korea

*Correspondence:

Chunxia Zhou
chunxia.zhou@163.com
Pengzhi Hong
hongpengzhigdou@163.com
Zhong-Ji Qian
zjqian@gdou.edu.cn
zjqian78@163.com

Specialty section:

This article was submitted to
Bioprocess Engineering,
a section of the journal
Frontiers in Bioengineering and
Biotechnology

Received: 14 October 2021

Accepted: 20 October 2021

Published: 18 November 2021

Citation:

Pei Y, Yang S, Xiao Z, Zhou C, Hong P
and Qian Z-J (2021) Structural
Characterization of Sulfated
Polysaccharide Isolated From Red
Algae (*Gelidium crinale*) and
Antioxidant and Anti-Inflammatory
Effects in Macrophage Cells.
Front. Bioeng. Biotechnol. 9:794818.
doi: 10.3389/fbioe.2021.794818

¹College of Food Science and Technology, School of Chemistry and Environment, Shenzhen Institute of Guangdong Ocean University, Zhanjiang, China, ²Southern Marine Science and Engineering Guangdong Laboratory, Zhanjiang, China

Gelidium crinale, the red algae belonging to Geliales *Gelidium*, is a traditional edible and industrial alga in China. A sulfated polysaccharide (GNP) is successfully separated from *Gelidium crinale* by acid extraction and two-step column chromatography. Chemical analysis showed that the molecular weight of GNP was 25.8 kDa and the monosaccharide composition had the highest galactose content and confirmed the presence and content (16.5%) of sulfate by Fourier transform infrared spectroscopy (FT-IR) spectrometry as well as barium chloride-gelatin methods. In addition, the effect of GNP on lipopolysaccharide (LPS)-induced oxidative stress and inflammation in macrophages was also evaluated. The research results showed that GNP had fairly strong scavenging activities on 2,2'-azino-bis(3-ethylbenzothiazoline-6-sulfonic acid) (ABTS) radical, hydroxyl radical, and 1,1-diphenyl-2-picrylhydrazyl (DPPH) radical and had Fe²⁺-chelating ability in a dose-dependent manner. At the same time, it significantly inhibits the expression of inducible nitric oxide synthase (iNOS) and cyclooxygenase-2 (COX-2) and the production of pro-inflammatory cytokines in RAW 264.7 cells induced by LPS through blocking the mitogen-activated protein kinase (MAPK)/nuclear factor kappa beta (NF-κB) signaling pathway. These results indicate that GNP may be a latent component anti-inflammation in pharmaceutical and functional food industries.

Keywords: *Gelidium crinale*, sulfated polysaccharide, structural characterization, anti-oxidation, anti-inflammation

INTRODUCTION

Seaweeds are a natural source which not only contain a variety of essential nutrients but also meet the needs of therapeutic, pharmaceutical, and nutritional fields. Generally speaking, they are divided into three groups, namely, brown algae (*Phaeophyceae*), green algae (*Chlorophyceae*), and red algae (*Rhodophyceae*). According to reports, it has a variety of important biologically active compounds, such as lipids, polysaccharides, polyphenols, anthraquinones, steroids, flavonoids, alkaloids, triterpenoids, and cardiac glycosides (Cao et al., 2020). Among them, red algae had been widely used in multiple applications like agriculture, food, biomedical, and cosmetics. The red algal polysaccharides usually consist of carrageenan cellulose, starch, xylan, and porphyrin.

Gelidium species, the red algae, have been traditionally used in the phycocolloid industry for agar-agar production. It has been widely used in many countries. Among them, *Gelidium amansii* (GA) is a kind of widely widespread edible red algae and harvested in the Asian countries, including China, Korea, Japan, Thailand, and Singapore (Kang et al., 2016). Several studies have reported that GA has multiple biological activities, such as enhancing immune activities, preventing obesity caused by diet, anti-inflammatory effects, and improving lipid metabolism, among others (Wang et al., 2013; Liu et al., 2017; Yang et al., 2017). *Gelidium crinale* (GC), also known as Ma Mao (Shandong Province), Gou Mao Cai (Guangdong Province), and Yan Yi (Zhejiang Province), is a traditional edible marine economic red alga of *Gelidium* in China. Compared with GA by GC, it is clear that the morphology and size of algae are different, but the biological activity of components has not been studied. Therefore, the research is to extract sulfated polysaccharides from GC and evaluate their structure characterization and anti-inflammatory effects, as well as provide an experimental basis for the high-value utilization of GC.

Sulfated polysaccharides represent an important class of glycans. These polysaccharides are often endowed with high bioactivity related to their sulfate functional groups, which can interact with many positively charged biological macromolecules. In recent years, sulfated polysaccharides isolated from seaweeds (red algae and brown algae) have attracted more and more attention. Moreover, the sulfated polysaccharides in algae have anti-inflammatory, antioxidant, and other pharmacological activities (de Sousa Oliveira Vanderlei et al., 2011; Li et al., 2017; Lima de Castro et al., 2018) and can be used in nutrition and healthcare, pharmaceutical, and cosmetic industries. Moreover, inflammation is an important biological process for protecting the human body from diverse hazardous stimuli, such as infection, injury, and irritation (Kim et al., 2018). The characteristic of inflammation is that leukocytes migrate from blood to tissues and circulate in the tissues through proliferation, which relates to a range of adhesion processes between resident leukocytes and vascular endothelia. Chronic inflammation and prolonged inflammation may be harmful and can lead to many diseases, including neurodegenerative diseases, fever, atherosclerosis, and even cancer (Ryu et al., 2017). Lipopolysaccharides, found in the outer membranes of Gram-negative bacteria, can activate a series of signaling pathways related to inflammation, such as NF- κ B and MAPK pathways (Guha and Mackman, 2001). The activation of NF- κ B promotes the expression of genes related to inflammation, including iNOS, COX-2, and pro-inflammatory cytokines (interleukin 6 (IL-6), interleukin-1 β (IL-1 β), and tumor necrosis factor- α (TNF- α)) (Baeuerle and Baichwal, 1997). In addition, the production of inflammation is also related to oxidative stress, and excessive reactive oxygen species (ROS) in cells can be considered as one of the causes of oxidative stress. The ROS molecule has high activity and plays a significant role in cell function. It can induce cells to secrete inflammatory factors and lead to inflammation. Overexpression of ROS can cause inflammation and promote the expression of inflammatory

factors. Nitric oxide (NO) is also involved in the oxidation reaction caused by ROS, which promotes inflammatory response. Moreover, ROS can act as a second messenger of intracellular signal transduction and regulate iNOS, COX-2, and the expression of pro-inflammatory cytokines through MAPK/NF- κ B activation; thus, inhibiting the level of ROS may be an anti-inflammatory method (Cobourne-Duval et al., 2016). Therefore, proper adjustment of the expression of inflammatory factors may reduce the adverse reactions of inflammation, thereby preventing the occurrence of inflammation-related diseases (Hou et al., 2020).

In the study, we first reported sulfated polysaccharides (GNP) isolated from *Gelidium crinale* (Naozhou Island Sea, Zhanjiang City). The structure of the polysaccharides was investigated through chemical analysis, Fourier transformation infrared spectroscopy (FT-IR), high-performance liquid chromatography (HPLC), and gel permeation chromatography system (GPC). The antioxidant activity of the obtained polysaccharides (including ABTS radical scavenging capacity, ferrous ion (Fe²⁺) chelating capacity, DPPH radical scavenging capacity, and hydroxyl radical scavenging capacity) was determined. In addition, the anti-inflammatory effects *in vitro* were evaluated, and the signal pathway was discussed in RAW 264.7 macrophages cell.

MATERIALS AND METHODS

Materials and Chemicals

Fresh *Gelidium crinale* were collected from about 1-m depth of Naozhou Island Sea, Zhanjiang City, Guangdong Province, in summer 2020. Algae were identified through the morphological characters of the herbarium and the appraisal scheme of the Prof. Zhang C (Guangdong Ocean University).

The standards (fucose, galactose, glucuronic acid, rhamnose, arabinose, ribose, xylose, glucose, and aminogalactose) were provided by Sigma-Aldrich (Sigma Chemicals, St. Louis, MO, USA). The bicinchoninic acid (BCA) assay kit and all cell culture chemicals were provided by Thermo Fisher Scientific, Inc. (Waltham, MA, USA). LPS, 2,7-dichlorodihydrofluorescein diacetate (DCFH-DA), 3-(4,5-dimethylthiazol-2-yl)-2,5-diphenyltetrazolium bromide (MTT), and dimethyl sulfoxide (DMSO) were purchased from Sigma-Aldrich (St. Louis, MO, USA). Mouse polyclonal antibodies, including p65 (sc-8008), p-p65 (sc-136548), I κ B α (sc-1643), p-I κ B α (sc-8404), p-JNK (sc-6254), JNK (sc-7345), p-p38 (sc-166182), and p-ERK (sc-81492); rabbit polyclonal antibodies (p38, (sc-535); ERK (sc-94)); and secondary antibodies, such as goat anti-rabbit IgG-HRP (sc-2004), and goat anti-mouse IgG-HRP (sc-2005) were provided by Santa Cruz Biotechnology (Santa Cruz, CA, USA).

Preparation of Sulfated Polysaccharide from *Gelidium Crinale*

Sulfated polysaccharide was extracted using the method of Sun et al. (2018). *Gelidium crinale* (500 g) was extracted twice with 90% ethanol (W/V = 1:8) to remove pigments, lipids, and other

impurities, and it was dried at 45°C and extracted with 0.1 M HCl (W/V = 1:8) for 8 h; the extraction solution was then neutralized. After centrifugation, the supernatant was condensed to one-fourth volume by a rotary evaporator at 50°C and was sedimented with 80% ethanol at 4°C overnight. The precipitate was taken after centrifugation, then redissolved with distilled water; the protein in the solution was removed with Sevag reagent, and the solution was concentrated and dialyzed.

In the second step of extraction, the solution was filtered through the Sepharose CL-6B column (2.5 × 60 cm), and the elution phase was 0.1 mol/l NaCl. Finally, the fractions were gathered and then freeze-dried to obtain the *Gelidium crinale* polysaccharide designated as native GNP.

Chemical Composition Determination

The total sugar content was determined according to the phenol-sulfuric acid method (Nair and Vaidyanathan, 1964). The content of reducing sugar was determined by the 3,5-dinitrosalicylic acid (DNS) method. The sulfate content was determined by the barium chloride-gelatin method (Dodgson and Price, 1962).

Monosaccharide Composition Determination

PMP (1-phenyl-3-methyl-5-pyrazolone) pre-column derivatization combined with HPLC was used to determine the monosaccharide composition of GNP. Firstly, GNP (10 mg) was hydrolyzed by trifluoroacetic acid solution for 4 h at 110°C and cooled to ambient temperature. Then, methanol (1 ml) was added and dried with nitrogen three to four times. One milliliter of NaOH (0.3 mol/l) solution was added to fully dissolve the residue, which is a polysaccharide hydrolysate, and derivatized after a certain dilution. Four hundred microliters of mixed monosaccharide standard solution or polysaccharide hydrolysate was taken respectively in a 5-ml test tube with a stopper, in which 400 µl of PMP methanol solution was added to mix and reacted in a 70°C water bath for 2 h. It was then cooled to room temperature, HCl was added to adjust the pH to 7, and the solution volume was diluted to 1 ml with water. Chloroform was added, let to stand as well as the organic solution to be discarded, and then extracted twice. The water phase was analyzed by HPLC after using a 0.45-µm microporous filter. Then, the mixture was further passed through an HPLC instrument equipped with a UV detector at 30°C column temperature and an Agilent Eclipse XDB-C18 column (250 × 4.6 mm, 5 µm) for detection. The mobile phase is phosphate buffer (pH = 6.6) and acetonitrile (Cao et al., 2019).

Relative Molecular Weight Determination

The molecular weight was determined by the GPC system, which has a Waters 515 refractive index detector and a Shodex SBOHPAK-806-803 chromatographic column, and the column temperature is 40°C. The sample (500 µl) was injected, and the flow rate was set to 1 ml/min. The mobile phase was ultrapure water (0.02% sodium azide, pH = 6). The time and logarithm of molecular weight were used as the abscissa and ordinate, respectively (Cui et al., 2019). The Jiangshen workstation

(produced by Dalian Jiangshen Chromatography Software Co., Ltd.) for data processing to obtain the weight average molecular weight (Mw), number average molecular weight (Mn), and molecular weight distribution Mw/Mn.

Fourier Transform Infrared Spectroscopy Analysis

Potassium bromide was first ground with an agate mortar, then passed through a mesh screen with an aperture of 0.147 mm and dried under an infrared light for 4 h. Potassium bromide was pressed into a translucent sheet as a blank, and the sample was mixed with potassium bromide to make a pressed sheet, and the scanning was performed in the range of 4,000–400 cm⁻¹ (Jia et al., 2015).

In vitro Antioxidant Activities

ABTS Radical Scavenging Capacity Assay

The ABTS radical scavenging capacity was measured according to the method of Wang et al. (2021). Potassium persulfate at 2.45 mM and ABTS at 7 mM were mixed in equal volumes and kept protected from light for 16 h at room temperature to prepare ABTS radicals. ABTS free radicals were diluted in phosphate-buffered saline (PBS) to an absorbance of 0.70 ± 0.02 at 734 nm. Then, 2.5 ml of ABTS radical and 0.5 ml of different concentrations of GNP were mixed and reacted for 25 min at room temperature. Last, the absorbance of the mixture was measured at 734 nm and calculated according to the following formula, where Ai is the absorbance of GNP mixed with the reaction solution; A0 is the absorbance of the mixture solution without sample; and Aj is the absorbance of GNP.

$$\text{ABTS radical scavenging capacity (\%)} = \frac{(A_0 - A_i + A_j)}{A_0} \times 100\%$$

Ferrous Ion (Fe²⁺) Chelating Capacity Assay

The ferrous ion chelating potency was measured according to the method of Sun et al. (2018). One milliliter of GNP with different concentrations was mixed with 0.2 ml of ferrozine (5 mM) and 0.1 ml of ferrous chloride (2 mM) and let to stand at room temperature for 15 min. Last, the absorbance of the mixture was measured at 562 nm and calculated according to the following formula.

$$\text{Ferrous ion chelating rate (\%)} = \frac{(A_0 - A_i + A_j)}{A_0} \times 100\%$$

DPPH Radical Scavenging Capacity Assay

The DPPH radical scavenging capacity was measured according to the method of Jia et al. (2015). In short, 4 ml of DPPH (0.5 mmol/l) and 2 ml different concentrations of GNP were mixed and let to stand for 30 min. Last, the absorbance of the mixture was measured at 517 nm and calculated according to the following formula.

$$\text{DPPH radical scavenging capacity (\%)} = \frac{(A_0 - A_i + A_j)}{A_0} \times 100\%$$

Hydroxyl Radical Scavenging Capacity Assay

The hydroxyl radical scavenging ability was measured according to the method of Wang et al. (2021). In short, 2 ml of different concentrations of GNP, 2 ml H₂O₂ (9 mM), and 2 ml FeSO₄ (9 mM) were mixed and reacted at 25°C for 10 min. Then, 2 ml salicylic acid (9 mmol/l) was added and reacted for 30 min. Last, the absorbance of the mixture was measured at 540 nm and calculated according to the following formula.

$$\text{Hydroxyl radical scavenging capacity (\%)} = \frac{(A_0 - A_i + A_j)}{A_0} \times 100\%$$

Cell Cultures and Cell Viability Assay

RAW 264.7 cells were provided by Fudan IBS Cell Resource Center. Cells were plated in DMEM and contained 10% fetal bovine serum (FBS) and 1% penicillin–streptomycin in 5% CO₂ at 37°C. RAW 264.7 cells were seeded into a 96-well plate and incubated at 37°C for 24 h, and then GNP (1, 10, 50, 100, 200, 500, and 1,000 µg/ml) was added to the wells. Then, 100 µl (0.5 mg/ml) MTT was added to each well and left for 4 h. After cultivation, the supernatants were removed and the dark blue crystals were dissolved with dimethyl sulfoxide. Also, the absorbance of the mixture was measured at 540 nm with a microplate reader (Wang et al., 2021).

NO Production

The amount of NO released was measured by the Griess method. Briefly, RAW 264.7 cells were seeded into a 96-well plate at a concentration of 5 × 10³ cells/ml, and then cells were treated with GNP and LPS for 24 h. Fifty microliters of supernatant was collected and mixed with the NO detection kit. The absorbance was determined at 540 nm (Jia et al., 2020).

Productions of Intracellular ROS Assess

RAW 264.7 cells were seeded into a 96-well plate, then cells were treated with GNP and LPS for 24 h, and then DCF (10 µM) was added into each well. After 30 min of incubation in the dark, the cells were washed with PBS. Subsequently, Hoechst 33342 (5 µg/ml) was added and incubated for 10 min. The fluorescence values of Hoechst 33342 and DCF were measured with a microplate reader. The excitation and emission wavelengths for DCF are 485 and 530 nm, respectively; those for Hoechst 33342 were 500 and 460 nm, respectively (Yu et al., 2016).

ELISA Analysis of Cytokines

RAW 264.7 cells were treated with GNP and LPS for 24 h. According to the manufacturer's instructions, the ELISA kit was used to measure the concentrations of TNF-α and IL-6 in the supernatant (Xiao et al., 2020).

Western Blot

RAW 264.7 cells were seeded into a six-well plate at a concentration of 5 × 10⁶ cells/ml and cultured for 24 h. The old medium was aspirated and discarded and then treated with GNP for 2 h, then LPS was added for a 24-h incubation. The

protein content was determined with the BCA protein quantification kit and separated by electrophoresis. Then, it was shifted to NC membranes. The membrane is sealed with 5% skimmed milk for 2 h and incubated with primary antibody (dilution ratio 1: 500) at 4°C. The secondary antibody (dilution ratio of 1: 2,000) was incubated for 2 h and then washed with TBST three times. Protein expression levels were detected by using enhanced chemiluminescence substrates (Yang et al., 2020).

Statistical Analysis

All results represent the average of three independent experiments. GraphPad Prism 8 (GraphPad Prism Software Inc., La Jolla, CA, USA) and ImageJ (Version 1.46r, NIH, Bethesda, MD, USA) were used for data analyses, and statistical analyses between different groups were performed by t-tests or one-way ANOVA. *p* < 0.05 was judged to be statistically significant and was highlighted with asterisks.

RESULTS AND DISCUSSION

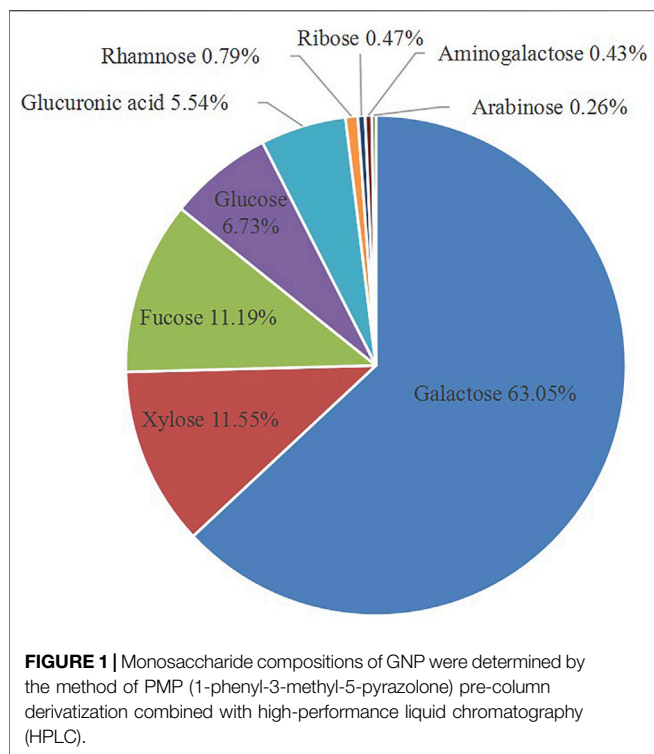
Chemical Composition and Monosaccharide Composition of GNP

Acid extraction is a commonly used method for extracting polysaccharides, which shows a relatively high sulfate content and improves the biological activity. The acid extraction of GNP was processed with treatment of 0.1 M HCl. The total yield of GNP by several times of acid extraction process was about 3.2% on the basis of lyophilized dry weight. Then, the impurities were removed and the total sugar content was determined, and the content was increased to 75.78% (date not show). In addition, as shown in **Table 1**, the reducing sugar content was 8.42%, and the sulfate group content was 16.50%. PMP pre-column derivatization and HPLC analysis of the monosaccharide composition of GNP were performed. As shown in **Figure 1**, the GNP was mainly composed of galactose (65.05%), xylose (11.55%), fucose (11.19%), glucose (6.73%), glucuronic acid (5.54%), rhamnose (0.79%), ribose (0.47%), amino galactose (0.43%), and arabinose (0.26%). Among them, galactose has the highest content, followed by fucose and xylose. Galactose accounts for more than half of all monosaccharides. Cui et al. (2019) used the GC-MS analysis method to analyze the monosaccharide composition of sulfated polysaccharide from the red seaweed *Gelidium pacificum*. Research indicated that the main monosaccharide composition of GPOP-1 was

TABLE 1 | The chemical properties and molecular weight of GNP.

Parameters	GNP
Chemical properties	
Reducing sugar content	8.42%
Sulfate content	16.50%
Molecular weight	
Weight-average molecular weight (Mw)	25.77 kDa
Number-average molecular weight (Mn)	13.39 kDa
Polydispersity (Mw/Mn)	1.92

Relative molecular weight of GNP.



galactose (59.7%), xylose (7.1%), and galacturonic acid (19.76%); it was determined that the sulfate group content was 8.80%. Moreover, Yang et al. (2019) analyzed the monosaccharide composition of polysaccharide from the red algae GA, and the results showed that the main monosaccharide composition of GHE was galactose (86.0%), fucose (8.3%), and xylose (1.1%). GNP obviously accords with the characteristics of the *Gelidium amansii* polysaccharide. Moreover, the sulfuric acid group content of GNP is relatively high. Many studies have proved that the higher the sulfate content, the better the biological activity of polysaccharides (Hou et al., 2020).

As shown in **Table 1**, the molecular weight of GNP was analyzed using the GPC method to obtain several molecular weights, such as weight average molecular weight (Mw), number average molecular weight (Mn), and polydispersity (Mw/Mn). Research indicated that the Mn and Mw of GNP were 13.39 and 25.77 kDa, respectively, and the Mw/Mn was 1.92. Jia et al. (2015) indicated that the smaller molecular weight of the polysaccharide isolated and purified from *R. minima* root had a higher cancer-destroying activity. Furthermore, Sun et al. (2018) extracted polysaccharides from *Laminaria japonica* and found that polysaccharides with smaller molecular weight had a higher antioxidant activity. Meanwhile, Dou et al. (2019) discovered that the lower molecular weight blackberry polysaccharide had a stronger bile acid-binding ability and was more easily used by intestinal bacteria.

Bioactivities of GNP are related to its structure, including sulfate group content and relative molecular weight. Studies

have shown that polysaccharides with smaller relative molecular weight and higher sulfate content had better biological activity (Hou et al., 2020; Mou et al., 2018). It is shown in **Table 2** that the molecular weight of red algae polysaccharides ranges from tens to hundreds of kDa, and the sulfate group content is generally about 10%. However, GNP has a higher content of sulfate groups and a smaller molecular weight.

FT-IR Spectral Analysis

It is shown in **Figure 2** that there is an absorption peak at $3,400\text{ cm}^{-1}$, which is closely related to the O–H bond stretching of polysaccharides, indicating that there are power intramolecular or intermolecular interactions between polysaccharide chains (Wang et al., 2021). The weak band at about $2,930\text{ cm}^{-1}$ is closely related to the C–H tensile vibration (Jiao et al., 2018). The absorption band in the range of $1,600\text{--}1,650\text{ cm}^{-1}$ is caused by C=O asymmetric stretching vibration, which proves that the polysaccharide contains uronic acid, which is an acidic polysaccharide (Shu et al., 2018). There is a stretching vibration of S=O at $1,200\text{--}1,250\text{ cm}^{-1}$, and S=O is the characteristic group of the sulfate group (Sanjeeva et al., 2018). The strong absorption band at approximately $1,000\text{--}1,200\text{ cm}^{-1}$ is closely related to the existence of C–O–H and C–O–C stretching vibrations, which are pyranose rings (Zhu et al., 2021). In addition, the characteristic absorption at 896 cm^{-1} indicates the presence of β configuration in polysaccharides (Bi et al., 2018). Therefore, these characteristics demonstrated that GNP is a sulfated polysaccharide.

In vitro Antioxidant Activities







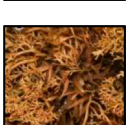
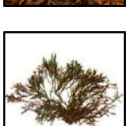


The antioxidant activities of GNP estimated through four experiments are shown in **Figures 3A–D**. GNP exhibits extremely antioxidant activities in a concentration-dependent manner. The ABTS radical scavenging capacity, Fe^{2+} chelating ability, and DPPH radical scavenging capacity were 89.10%, 76.81%, and 56.11%, respectively, when the consistency of GNP was 8 mg/ml. The hydroxyl free radical scavenging ability was 50.43%, with the consistency of GNP of 12 mg/ml. The IC_{50} of its ABTS free radical scavenging ability, Fe^{2+} chelating ability, hydroxyl free radical scavenging ability, and DPPH free radical scavenging ability were 2.22, 2.69, 13.56, and 7.41 mg/ml, respectively. Many studies have reported that sulfated polysaccharides are good protective agents for antioxidant enzymes in cells. Thus, the sulfate content and molecular weight of sulfated polysaccharides will have a certain impact on the antioxidant activity (Andrew and Jayaraman, 2021). Sun et al. (2018) indicated that *Laminaria japonica* polysaccharides with a higher content of sulfuric acid groups and a smaller molecular weight have a strong ability to scavenge free radicals. Rozi et al. (2019) extracted polysaccharide from *Fritillaria pallidiflora* and believed that its hydroxyl radical scavenging activity was higher due to its lower molecular weight. Hence, GNP can be used as potential radical scavengers.

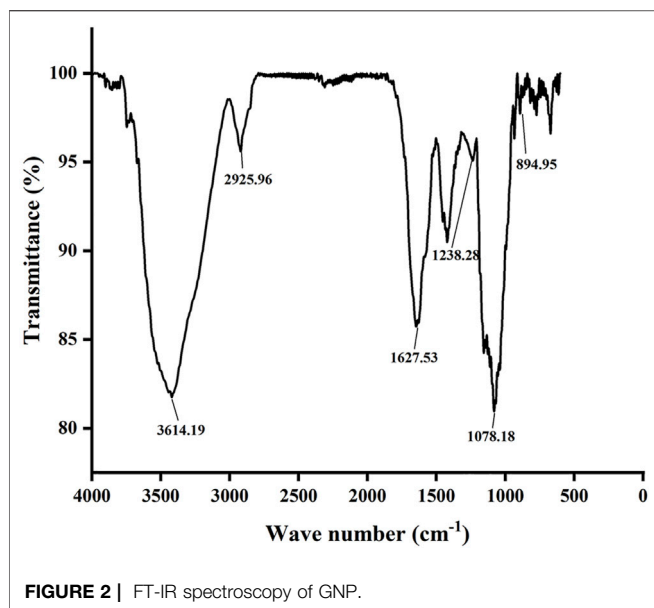
Cell Viability Assay

In order to avoid the unnatural death of RAW 264.7 cells induced by GNP, the effect of GNP on the viability of RAW 264.7 cells was

detected by MTT analysis (Du et al., 2018). It is shown in **Figure 4** that compared with the blank group without GNP, the cell survival rate of the experimental group with GNP (1, 10, 50,

TABLE 2 | Comparison of the sulfuric acid content and molecular weight of different types of red algae.

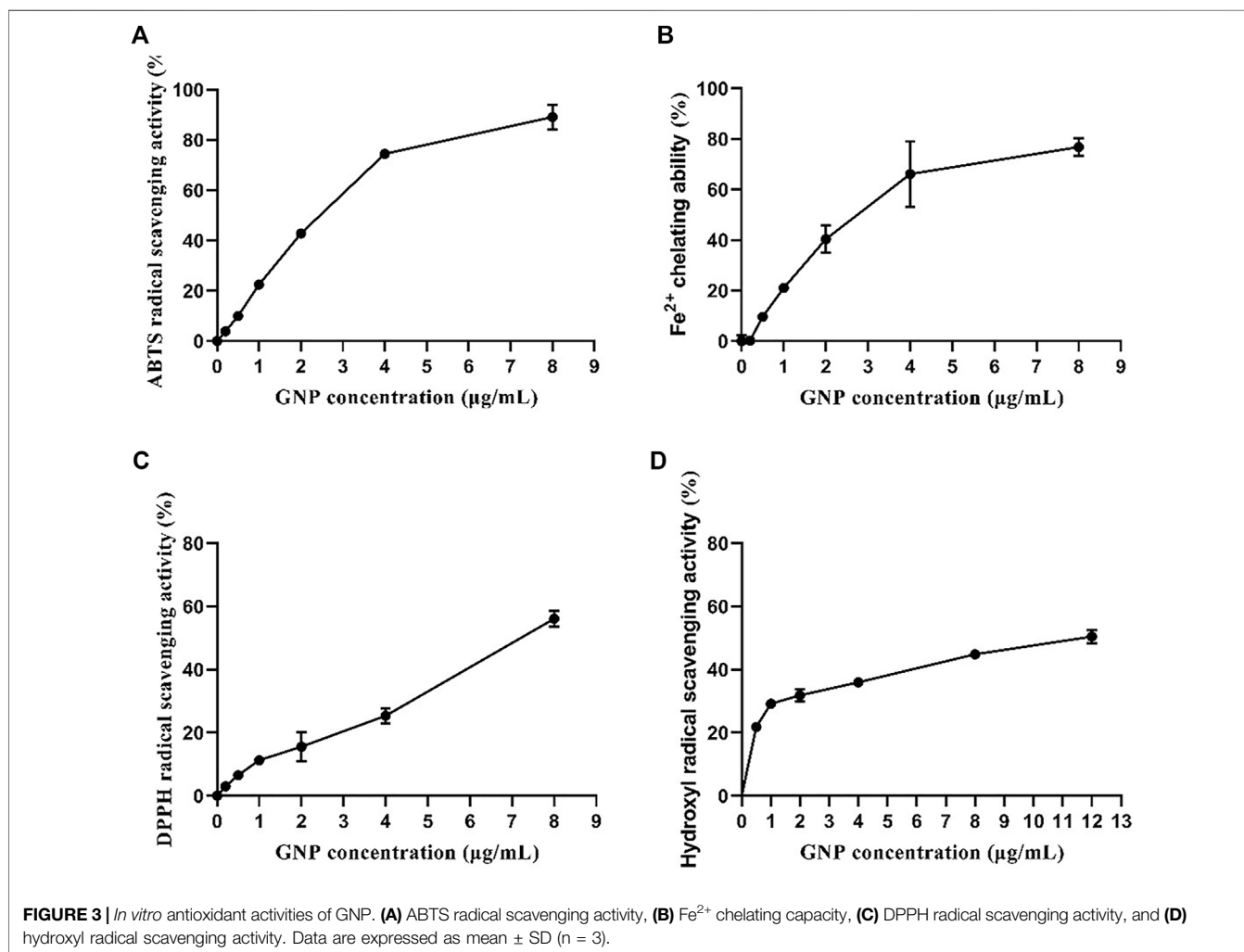
Raw material name	Sulfate content (%)	Molecular weight (kDa)	Physical map	References
<i>Gracilaria caudata</i>	—	250		Barros et al. (2013)
<i>Gracilaria birdiae</i>	6.4	—		Maciel et al. (2008)
<i>Gloiopeltis tenax</i>	8.2	—		Lim and Ryu, (2009)
<i>Solieria filiformis</i>	—	28		Chaves et al. (2018)
<i>Gloiopeltis furcata</i>	24.8	20.6		Hu et al. (2012)
<i>Gracilaria intermedia</i>	6.6	—		Lima de Castro et al. (2018)
<i>Gracilaria corticata</i>	—	43		Seedevi et al. (2017)
<i>Gelidium pacificum</i> Okamura	8.8	28.81		Cui et al. (2019)
<i>Gelidium amansii</i>	3.72–4.02	31.62–75.86		Yu et al. (2021)
<i>Gelidium crinale</i>	16.50	25.77		No reports

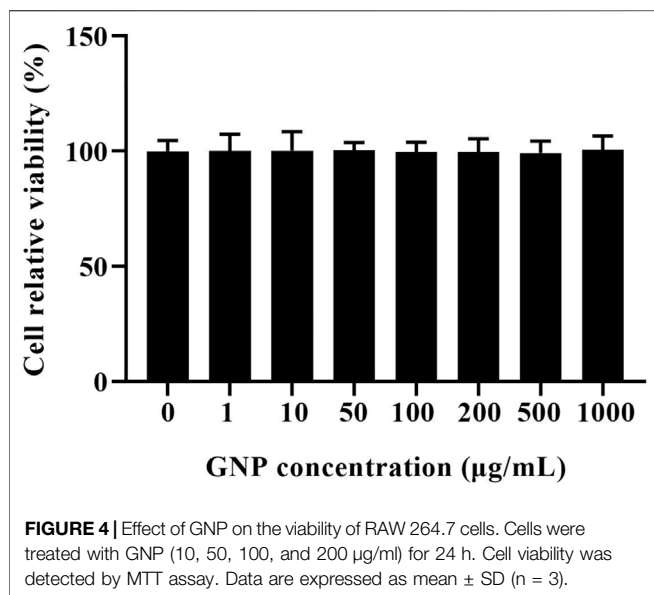


100, 200, 500, and 1,000 $\mu\text{g/ml}$) did not change significantly. It shows that the GNP has no poison effect on RAW 264.7 cells, and GNP at this concentration can be selected for subsequent experiments.

Effects of GNP on NO, ROS, and Inflammatory Cytokine Production

Macrophages are a type of immune cells that participate in the inflammatory responses. However, uncontrolled inflammation would lead to tissue damage and further diseases. Inflammation can lead to the secretion of inflammatory mediators (Rahmati et al., 2016; Hou et al., 2020). It is shown in **Figures 5A–D** that the levels of NO and ROS in RAW 264.7 cells treated with 1 $\mu\text{g/ml}$ LPS for 24 h significantly increased. However, GNP can reduce the levels of NO and ROS in cells stimulated by LPS, indicating that GNP can relieve LPS-induced inflammation. Wang et al. (2020) reported that SNPS inhibited LPS-induced TNF- α and IL-6 protein and mRNA expression levels in RAW 264.7 cells. Moreover, Le et al. (2020) showed that MESP inhibits the



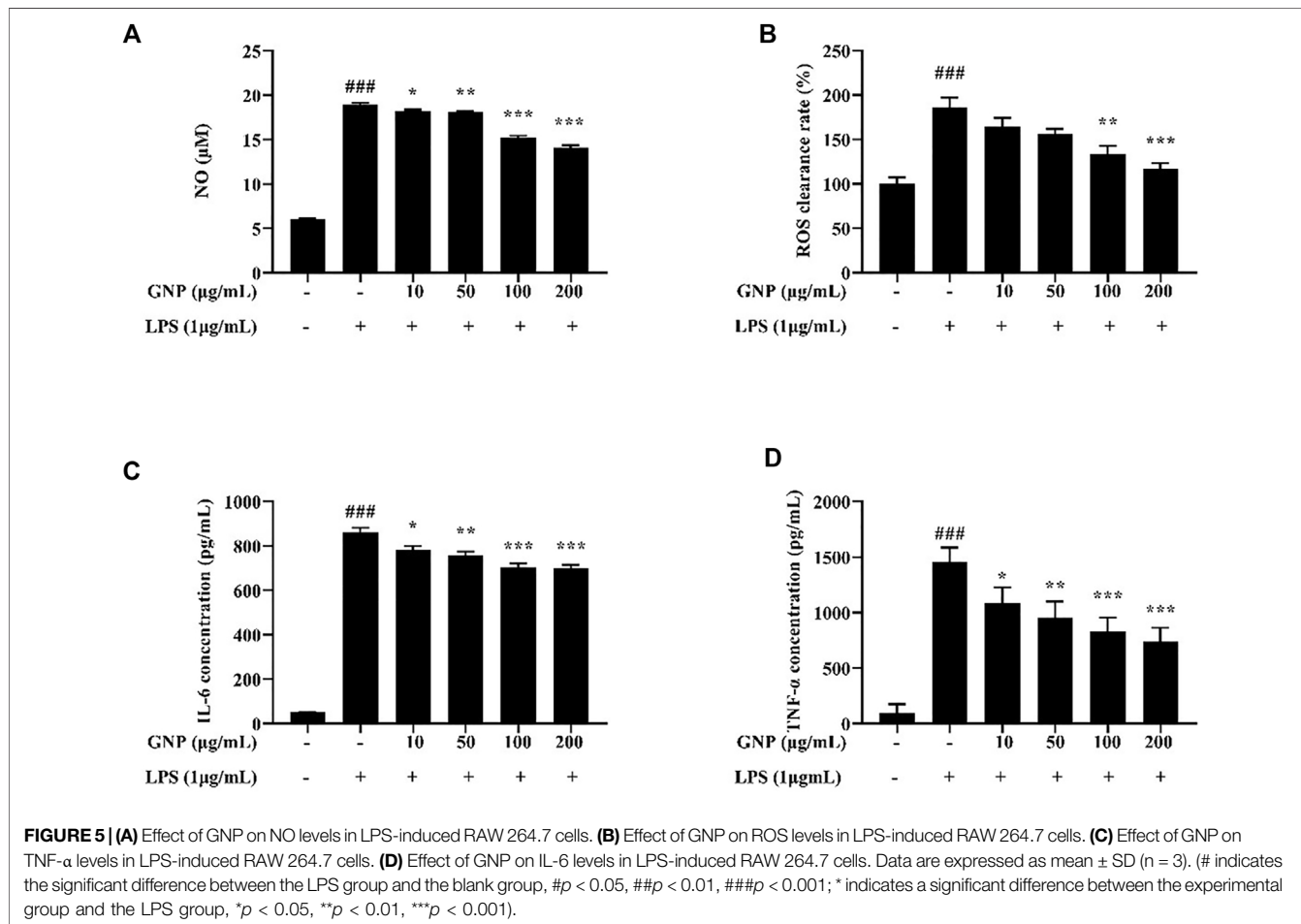


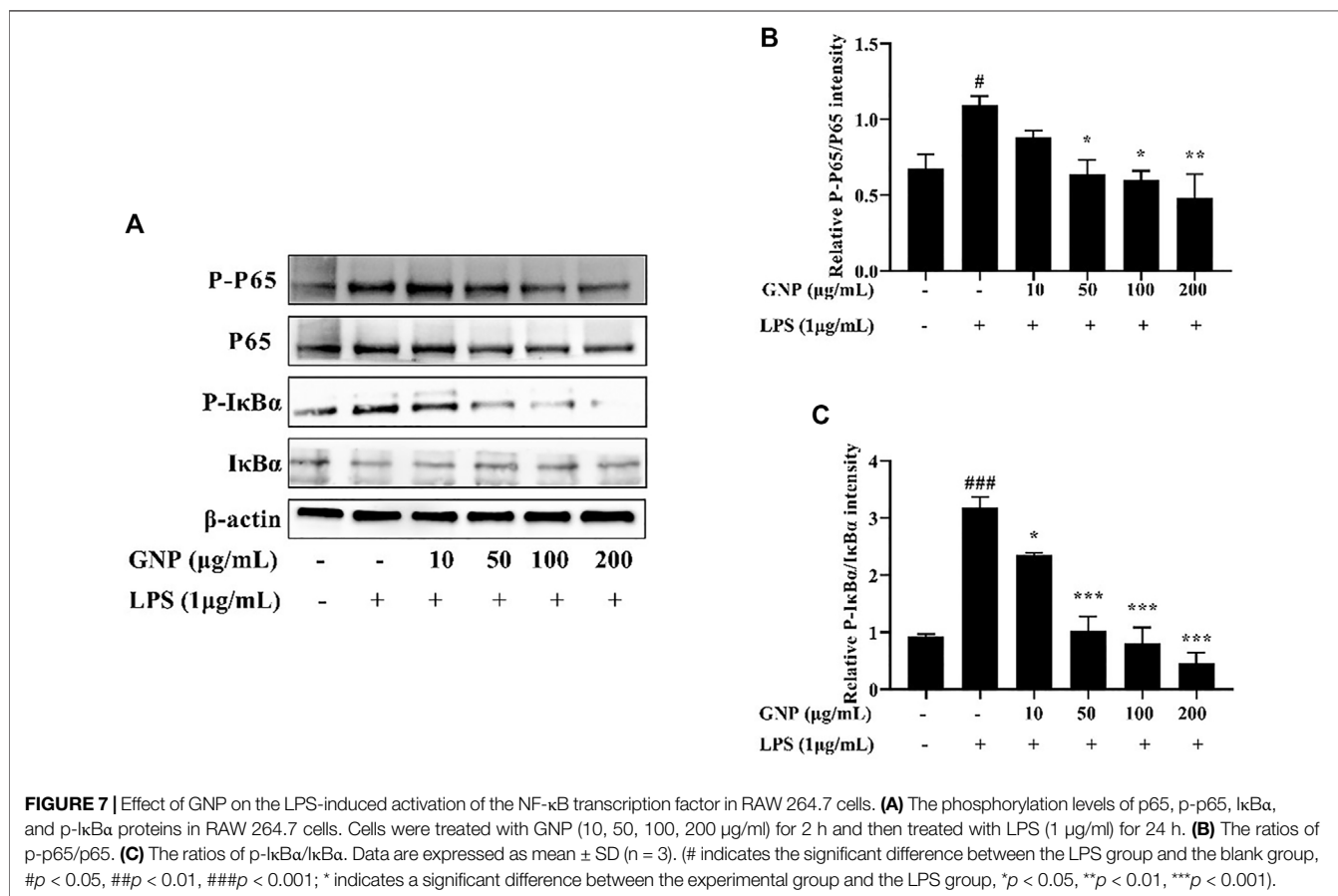
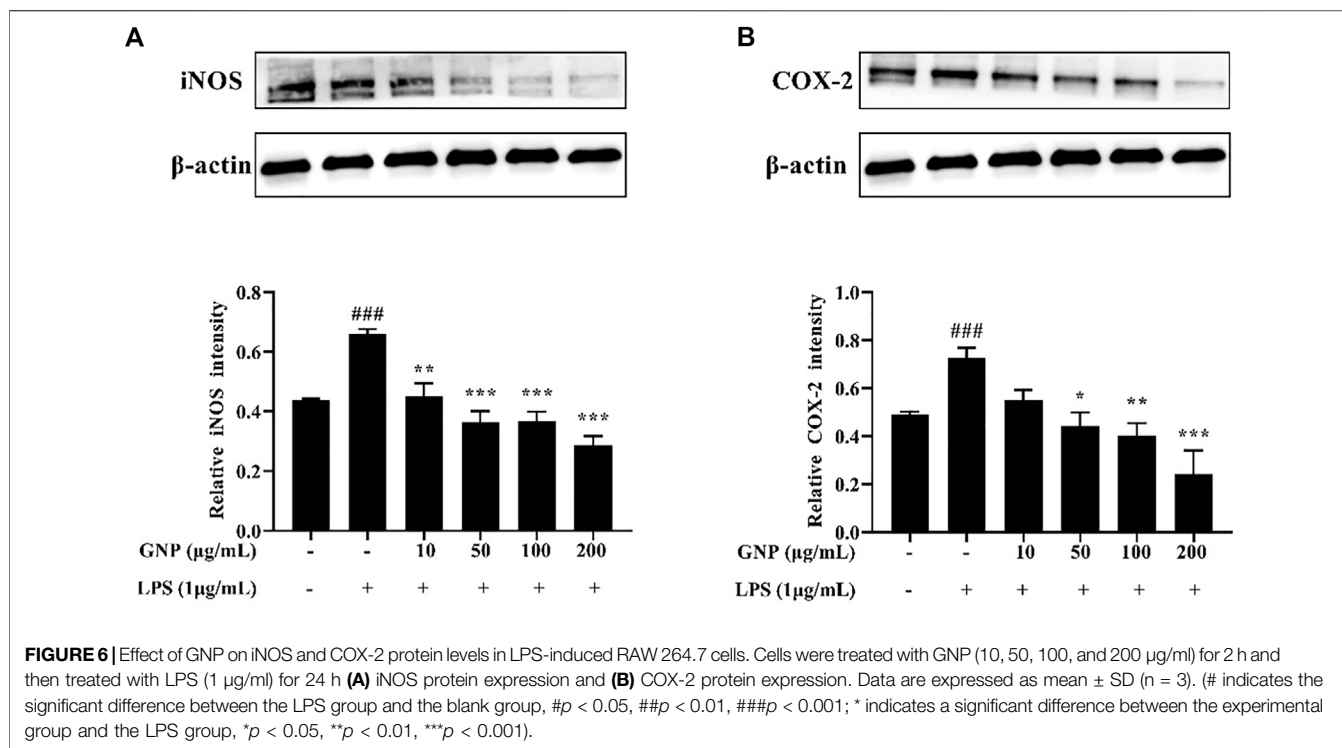
levels of NO, TNF-α, IL-1β, IL-6, and IL-10 to reduce LPS-induced inflammatory response in macrophages. Meanwhile, Wang et al. (2021) found that CGP-BG inhibited the protein

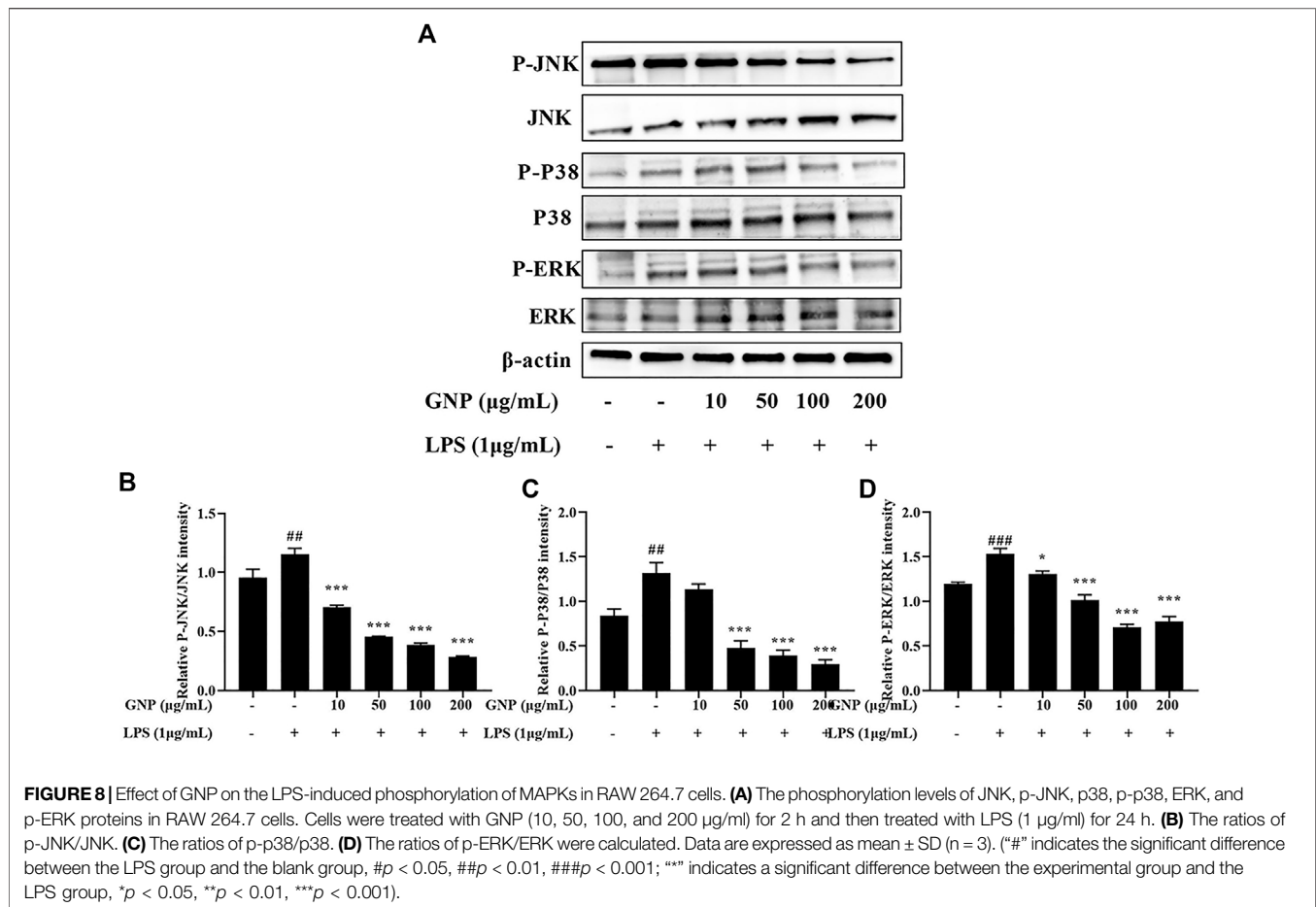
levels of NO, IL-1β, IL-6, and TNF-α by LPS induction. Therefore, it can be explained that GNP has anti-inflammation activity by inhibiting inflammatory mediators.

Effects of GNP on iNOS and COX-2 Protein Expression

iNOS can induce the production of NO and is an indicator to identify whether inflammation occurs; COX-2 is also involved in inflammation. They all catalyze the production of a large number of pro-inflammatory mediators. Therefore, inhibiting its activity can effectively reduce the degree of inflammation (Du et al., 2018; Zhu et al., 2018; Hou et al., 2020). Sanjeeva et al. (2018) reported that sulfated polysaccharide from *Sargassum horneri* dose-dependently inhibited the expression of COX-2 and iNOS. Meanwhile, Wu et al. (2016) reported that sulfated polysaccharide from the brown alga *Sargassum cristaefolium* can inhibit the expression of iNOS. It is shown in **Figures 6A,B** that the protein levels of COX-2 and iNOS in cells increased significantly after LPS treatment in cells, but their protein levels decreased after GNP treatment. GNP can inhibit the expression of iNOS and COX-2 in cells induced by LPS. It can be seen that GNP can inhibit the expression of iNOS and COX-2 in cells to play an anti-inflammatory effect.







The Effect of GNP on the NF- κ B Signaling Pathway

NF- κ B participates in the transactivation of various genes related to the regulation of immune and inflammatory responses. It is the most important transcription factor and consists of homodimers or heterodimers of Rel proteins (Du et al., 2015). In normal cells, it binds to I κ B and locates in the cytoplasm, thereby inhibiting its entry into the nucleus. Then, phosphorylation of I κ B causes NF- κ B to be activated to enter the nucleus, thereby starting to produce various mediators (Levy-Ontman et al., 2011; Wu et al., 2016). As shown in Figures 7A–C, the gray levels of the bands were analyzed in each group. After LPS treatment, the protein expression levels of p-p65 and p-I κ B α in RAW 264.7 cells increased significantly, while after GNP treatment, their protein expression decreased. This indicates that GNP can block NF- κ B from entering the nucleus by inhibiting the phosphorylation of p65 and I κ B α .

The Effect of GNP on the MAPK Signaling Pathway

Mitogen-activated protein kinase (MAPK), including extracellular signal-regulated kinase (ERK), c-Jun NH2-terminal kinase (JNK), and P38 participate in the mediation of

cell growth, apoptosis, and proliferation (Arthur et al., 2013). MAPK is the upstream signaling molecule of NF- κ B, and it also participates in the inflammatory response and regulates the expression of related genes (Paunovic and Harnett, 2013; Jia et al., 2020). This study evaluated the expression of ERK, JNK, and p38 by Western blotting. It is shown in Figures 8A–D that the protein expression levels of p-p38, p-JNK, and p-ERK in RAW 264.7 cells were increased after LPS induction. However, after GNP treatment, their protein levels decreased. This indicates that GNP can block the MAPK signaling pathway by restraining the phosphorylation of P38, JNK, and ERK.

From the structure–activity relationship, the GNP from *Gelidium crinale* has rich potential sulfate content (16.5%), galactose content (63.05%), and smaller molecular weight (25.8 kDa) compared with other red algae (*Gloiopeltis furcata*, *Gracilaria intermedia*, *Gelidium pacificum* Okamura, and *Gelidium amansii*, Table 2). In red algae, sulfate content, monosaccharide composition, and relative molecular weight are important factors for the activity level and intensity. Sulfate content might affect the binding of polysaccharides with the cell wall receptor, thereby affecting the production of NO, but the specific reason for it still unknown (Hou et al., 2020). A lot of research has shown that the lower molecular weight makes the spatial conformation of the polysaccharides easy to be

combined with macrophage cells, especially polysaccharides with molecular weight of 10–200 kDa, which are the most active (Zhang et al., 2016; Ji et al., 2018). In addition, glucose, galactose, and mannose combine with other monosaccharides to produce polysaccharides with high activity, which are also important structure–activity groups in active polysaccharides (Zhang et al., 2016). Our results show that the structure and monosaccharide compositions of GNP are similar to other studies, which is completely consistent with the properties of red algal polysaccharides. Therefore, GNP from *Gelidium crinale* can be used as a good potential active material for pharmaceuticals.

CONCLUSION

In conclusion, a sulfated polysaccharide was successfully extracted from the red seaweed *Gelidium crinale*, which has a smaller molecular weight and a higher sulfate group. It has antioxidant effects and inhibits the activation of NF- κ B and MAPK signaling in RAW 264.7 cells induced by LPS. GNP can effectively downregulate the production of inflammatory factors, which has strong anti-inflammatory properties. Our results provide experimental data for the further effective development and utilization of GNP and *Gelidium crinale*.

REFERENCES

- Andrew, M., and Jayaraman, G. (2021). Marine Sulfated Polysaccharides as Potential Antiviral Drug Candidates to Treat Corona Virus Disease (COVID-19). *Carbohydr. Res.* 505, 108326. doi:10.1016/j.carres.2021.108326
- Arthur, J. S. C., Ley, S. C., and Ley, S. C. (2013). Mitogen-activated Protein Kinases in Innate Immunity. *Nat. Rev. Immunol.* 13, 679–692. doi:10.1038/nri3495
- Bauerle, P. A., and Baichwal, V. R. (1997). NF- κ B as a Frequent Target for Immunosuppressive and Anti-inflammatory Molecules**This Article Was Accepted for Publication on 27 September 1996. *Adv. Immunol.* 65, 111–137. doi:10.1016/S0065-2776(08)60742-7
- Barros, F. C. N., da Silva, D. C., Sombra, V. G., Maciel, J. S., Feitosa, J. P. A., Freitas, A. L. P., et al. (2013). Structural Characterization of Polysaccharide Obtained from Red Seaweed *Gracilaria Caudata* (J Agardh). *Carbohydr. Polym.* 92, 598–603. doi:10.1016/j.carbpol.2012.09.009
- Bi, S., Jing, Y., Zhou, Q., Hu, X., Zhu, J., Guo, Z., et al. (2018). Structural Elucidation and Immunostimulatory Activity of a New Polysaccharide from *Cordyceps Militaris*. *Food Funct.* 9, 279–293. doi:10.1039/c7fo01147d
- Cao, H., Ma, S., Guo, H., Cui, X., Wang, S., Zhong, X., et al. (2019). Comparative Study on the Monosaccharide Compositions, Antioxidant and Hypoglycemic Activities *In Vitro* of Intracellular and Extracellular Polysaccharides of Liquid Fermented *Coprinus Comatus*. *Int. J. Biol. Macromolecules* 139, 543–549. doi:10.1016/j.ijbiomac.2019.08.017
- Cao, L., Lee, S. G., Lim, K. T., and Kim, H.-R. (2020). Potential Anti-aging Substances Derived from Seaweeds. *Mar. Drugs* 18, 564. doi:10.3390/md18110564
- Chaves, R. P., Silva, S. R. d., Nascimento Neto, L. G., Carneiro, R. F., Silva, A. L. C. d., Sampaio, A. H., et al. (2018). Structural Characterization of Two Isolectins from the marine Red Alga *Solieria Filiformis* (Kützting) P.W. Gabrielson and Their Anticancer Effect on MCF-7 Breast Cancer Cells. *Int. J. Biol. Macromolecules* 107, 1320–1329. doi:10.1016/j.ijbiomac.2017.09.116
- Cobourne-Duval, M. K., Taka, E., Mendonca, P., Bauer, D., and Soliman, K. F. A. (2016). The Antioxidant Effects of Thymoquinone in Activated BV-2 Murine

DATA AVAILABILITY STATEMENT

The original contributions presented in the study are included in the article/Supplementary Material; further inquiries can be directed to the corresponding authors.

AUTHOR CONTRIBUTIONS

YP performed the experiment and wrote the manuscript; Z-JQ and CZ conceived the research and revised the manuscripts; SY and ZX analyzed the data; and PH contributed materials and analysis tools. All authors have read and agreed to the published version of the manuscript.

FUNDING

The research was funded by the 2020 Shenzhen International Scientific and Technological Cooperation R&D Project (GJHZ2019082311601682) and the Natural Science Foundation of Guangdong Province (2020A1515011075). The study was supported by the Development Project about Marine Economy Demonstration of Zhanjiang City (XM-202008-01B1) and Southern Marine Science and Engineering Guangdong Laboratory (Zhanjiang, ZJW-2019-07).

Microglial Cells. *Neurochem. Res.* 41, 3227–3238. doi:10.1007/s11064-016-2047-1

- Cui, M., Wu, J., Wang, S., Shu, H., Zhang, M., Liu, K., et al. (2019). Characterization and Anti-inflammatory Effects of Sulfated Polysaccharide from the Red Seaweed *Gelidium Pacificum Okamura*. *Int. J. Biol. Macromolecules* 129, 377–385. doi:10.1016/j.ijbiomac.2019.02.043
- de Sousa Oliveira Vanderlei, E., de Araújo, I. W. F., Quinderé, A. L. G., Fontes, B. P., Eloy, Y. R. G., Rodrigues, J. A. G., et al. (2011). The Involvement of the HO-1 Pathway in the Anti-inflammatory Action of a Sulfated Polysaccharide Isolated from the Red Seaweed *Gracilaria Birdiae*. *Inflamm. Res.* 60, 1121–1130. doi:10.1007/s00011-011-0376-8
- Dodgson, K., and Price, R. (1962). A Note on the Determination of the Ester Sulphate Content of Sulphated Polysaccharides. *Biochem. J.* 84, 106–110. doi:10.1042/bj0840106
- Dou, Z., Chen, C., and Fu, X. (2019). Digestive Property and Bioactivity of Blackberry Polysaccharides with Different Molecular Weights. *J. Agric. Food Chem.* 67, 12428–12440. doi:10.1021/acs.jafc.9b03505
- Du, B., Lin, C., Bian, Z., and Xu, B. (2015). An Insight into Anti-inflammatory Effects of Fungal Beta-Glucans. *Trends Food Sci. Tech.* 41, 49–59. doi:10.1016/j.tifs.2014.09.002
- Du, J., Li, J., Zhu, J., Huang, C., Bi, S., Song, L., et al. (2018). Structural Characterization and Immunomodulatory Activity of a Novel Polysaccharide from *Ficus Carica*. *Food Funct.* 9, 3930–3943. doi:10.1039/c8fo00603b
- Guha, M., and Mackman, N. (2001). LPS Induction of Gene Expression in Human Monocytes. *Cell Signal.* 13, 85–94. doi:10.1016/S0898-6568(00)00149-2
- Hou, C., Chen, L., Yang, L., and Ji, X. (2020). An Insight into Anti-inflammatory Effects of Natural Polysaccharides. *Int. J. Biol. Macromolecules* 153, 248–255. doi:10.1016/j.ijbiomac.2020.02.315
- Hu, Y., Yu, G., Zhao, X., Wang, Y., Sun, X., Jiao, G., et al. (2012). Structural Characterization of Natural Ideal 6-O-Sulfated Agarose from Red Alga *Gloiopeltis Furcata*. *Carbohydr. Polym.* 89, 883–889. doi:10.1016/j.carbpol.2012.04.026
- Ji, X., Peng, Q., and Wang, M. (2018). Anti-colon-cancer Effects of Polysaccharides: A Mini-Review of the Mechanisms. *Int. J. Biol. Macromolecules* 114, 1127–1133. doi:10.1016/j.ijbiomac.2018.03.186

- Jia, X., Zhang, C., Bao, J., Wang, K., Tu, Y., Wan, J.-B., et al. (2020). Flavonoids from *Rhynchosia Minima* Root Exerts Anti-inflammatory Activity in Lipopolysaccharide-Stimulated RAW 264.7 Cells via MAPK/NF- κ B Signaling Pathway. *Inflammopharmacol* 28, 289–297. doi:10.1007/s10787-019-00632-2
- Jia, X., Zhang, C., Qiu, J., Wang, L., Bao, J., Wang, K., et al. (2015). Purification, Structural Characterization and Anticancer Activity of the Novel Polysaccharides from *Rhynchosia Minima* Root. *Carbohydr. Polym.* 132, 67–71. doi:10.1016/j.carbpol.2015.05.059
- Jiao, Y., Kuang, H., Hu, J., and Chen, Q. (2018). Structural Characterization and Anti-hypoxia Activities of Polysaccharides from the Sporocarp, Fermentation Broth and Cultured Mycelium of *Agaricus Bitorquis* (Qué.) Sacc. Chaidam in Mice. *J. Funct. Foods* 51, 75–85. doi:10.1016/j.jff.2018.10.017
- Kang, M.-C., Kang, N., Kim, S.-Y., Lima, I. S., Ko, S.-C., Kim, Y.-T., et al. (2016). Popular Edible Seaweed, *Gelidium Amansii* Prevents against Diet-Induced Obesity. *Food Chem. Toxicol.* 90, 181–187. doi:10.1016/j.fct.2016.02.014
- Kim, J., Kim, H., Choi, H., Jo, A., Kang, H., Yun, H., et al. (2018). Anti-inflammatory Effects of a *Stauntonia Hexaphylla* Fruit Extract in Lipopolysaccharide-Activated RAW-264.7 Macrophages and Rats by Carrageenan-Induced Hind Paw Swelling. *Nutrients* 10, 110. doi:10.3390/nu10010110
- Le, B., Pham, T. N. A., and Yang, S. H. (2020). Prebiotic Potential and Anti-inflammatory Activity of Soluble Polysaccharides Obtained from Soybean Residue. *Foods* 9, 1808. doi:10.3390/foods9121808
- Levy-Ontman, O., Huleihel, M., Hamias, R., Wolak, T., and Paran, E. (2017). An Anti-inflammatory Effect of Red Microalga Polysaccharides in Coronary Artery Endothelial Cells. *Atherosclerosis* 264, 11–18. doi:10.1016/j.atherosclerosis.2017.07.017
- Li, S., Li, J., Zhi, Z., Wei, C., Wang, W., Ding, T., et al. (2017). Macromolecular Properties and Hypolipidemic Effects of Four Sulfated Polysaccharides from Sea Cucumbers. *Carbohydr. Polym.* 173, 330–337. doi:10.1016/j.carbpol.2017.05.063
- Lim, B.-L., and Ryu, I.-H. (2009). Purification, Structural Characterization, and Antioxidant Activity of Antioxidant Substance from the Red Seaweed *Gloiopeltis Tenax*. *Gloiopeltis tenax Journal Med. Food* 12, 442–451. doi:10.1089/jmf.2007.0688
- Lima de Castro, J. P., Costa, L. E. C., Pinheiro, M. P., Francisco, T. d. S., Vasconcelos, P. H. M. d., Funari, L. M., et al. (2018). Polysaccharides of Red Alga *Gracilaria Intermedia*: Structure, Antioxidant Activity and Rheological Behavior. *Polimeros* 28, 178–186. doi:10.1590/0104-1428.013116
- Liu, H.-C., Chang, C.-J., Yang, T.-H., and Chiang, M.-T. (2017). Long-term Feeding of Red Algae (*Gelidium Amansii*) Ameliorates Glucose and Lipid Metabolism in a High Fructose Diet-Impaired Glucose Tolerance Rat Model. *J. Food Drug Anal.* 25, 543–549. doi:10.1016/j.jfda.2016.06.005
- Maciél, J., Chaves, L., Souza, B., Teixeira, D., Freitas, A., Feitosa, J., et al. (2008). Structural Characterization of Cold Extracted Fraction of Soluble Sulfated Polysaccharide from Red Seaweed *Gracilaria Birdiae*. *Carbohydr. Polym.* 71, 559–565. doi:10.1016/j.carbpol.2007.06.026
- Mou, J., Li, Q., Qi, X., and Yang, J. (2018). Structural Comparison, Antioxidant and Anti-inflammatory Properties of Fucosylated Chondroitin Sulfate of Three Edible Sea Cucumbers. *Carbohydr. Polym.* 185, 41–47. doi:10.1016/j.carbpol.2018.01.017
- Nair, P. M., and Vaidyanathan, C. S. (1964). A Colorimetric Method for Determination of Pyrocatechol and Related Substances. *Anal. Biochem.* 7, 315–321. doi:10.1016/0003-2697(64)90136-8
- Paunovic, V., and Harnett, M. M. (2013). Mitogen-activated Protein Kinases as Therapeutic Targets for Rheumatoid Arthritis. *Drugs* 73, 101–115. doi:10.1007/s40265-013-0014-6
- Rahmati, M., Mobasheri, A., and Mozafari, M. (2016). Inflammatory Mediators in Osteoarthritis: A Critical Review of the State-Of-The-Art, Current Prospects, and Future Challenges. *Bone* 85, 81–90. doi:10.1016/j.bone.2016.01.019
- Rozi, P., Abuduwaili, A., Mutailifu, P., Gao, Y., Rakhmanberdieva, R., Aisa, H. A., et al. (2019). Sequential Extraction, Characterization and Antioxidant Activity of Polysaccharides from *Fritillaria Pallidiflora* Schrenk. *Int. J. Biol. Macromolecules* 131, 97–106. doi:10.1016/j.ijbiomac.2019.03.029
- Ryu, H. W., Lee, S. U., Lee, S., Song, H.-H., Son, T. H., Kim, Y.-U., et al. (2017). 3-Methoxy-catalposide Inhibits Inflammatory Effects in Lipopolysaccharide-Stimulated RAW264.7 Macrophages. *Cytokine* 91, 57–64. doi:10.1016/j.cyto.2016.12.006
- Sanjeeva, K. K. A., Fernando, I. P. S., Kim, S.-Y., Kim, H.-S., Ahn, G., Jee, Y., et al. (2018). *In Vitro* and *In Vivo* Anti-inflammatory Activities of High Molecular Weight Sulfated Polysaccharide; Containing Fucose Separated from *Sargassum Horneri*: Short Communication. *Int. J. Biol. Macromolecules* 107, 803–807. doi:10.1016/j.ijbiomac.2017.09.050
- Seedevi, P., Moovendhan, M., Viramani, S., and Shanmugam, A. (2017). Bioactive Potential and Structural Characterization of Sulfated Polysaccharide from Seaweed (*Gracilaria Corticata*). *Carbohydr. Polym.* 155, 516–524. doi:10.1016/j.carbpol.2016.09.011
- Shu, Z., Yang, Y., Xing, N., Wang, Y., Wang, Q., and Kuang, H. (2018). Structural Characterization and Immunomodulatory Activity of a Pectic Polysaccharide (CALB-4) from *Fructus Aurantii*. *Int. J. Biol. Macromolecules* 116, 831–839. doi:10.1016/j.ijbiomac.2018.01.165
- Sun, Y., Hou, S., Song, S., Zhang, B., Ai, C., Chen, X., et al. (2018). Impact of Acidic, Water and Alkaline Extraction on Structural Features, Antioxidant Activities of *Laminaria Japonica* Polysaccharides. *Int. J. Biol. Macromolecules* 112, 985–995. doi:10.1016/j.ijbiomac.2018.02.066
- Wang, J. A., Huang, L., Ren, Q., Wang, Y., Zhou, L., Fu, Y., et al. (2020/2020). Polysaccharides of *Scrophularia Ningpoensis* Hemsl.: Extraction, Antioxidant, and Anti-inflammatory Evaluation. *Evidence-Based Complement. Altern. Med.* 2020, 1–13. doi:10.1155/2020/8899762
- Wang, M.-L., Hou, Y.-Y., Chiu, Y.-S., and Chen, Y.-H. (2013). Immunomodulatory Activities of *Gelidium Amansii* Gel Extracts on Murine RAW 264.7 Macrophages. *J. Food Drug Anal.* 21, 397–403. doi:10.1016/j.jfda.2013.09.002
- Wang, Z., Liu, X., Bao, Y., Wang, X., Zhai, J., Zhan, X., et al. (2021). Characterization and Anti-inflammation of a Polysaccharide Produced by *Chaetomium globosum* CGMCC 6882 on LPS-Induced RAW 264.7 Cells. *Carbohydr. Polym.* 251, 117129. doi:10.1016/j.carbpol.2020.117129
- Wu, G.-J., Shiu, S.-M., Hsieh, M.-C., and Tsai, G.-J. (2016). Anti-inflammatory Activity of a Sulfated Polysaccharide from the Brown Alga *Sargassum Cristaeifolium*. *Food Hydrocolloids* 53, 16–23. doi:10.1016/j.foodhyd.2015.01.019
- Xiao, Z., Yang, S., Chen, J., Li, C., Zhou, C., Hong, P., et al. (2020). Trehalose against UVB-Induced Skin Photoaging by Suppressing MMP Expression and Enhancing Procollagen I Synthesis in HaCaT Cells. *J. Funct. Foods* 74, 104198. doi:10.1016/j.jff.2020.104198
- Yang, S., Chen, M.-F., Ryu, B., Chen, J., Xiao, Z., Hong, P., et al. (2020). The Protective Effect of the Polysaccharide Precursor, D-Isofloridoside, from *Laurencia Undulata* on Alcohol-Induced Hepatotoxicity in HepG2 Cells. *Molecules* 25, 1024. doi:10.3390/molecules25051024
- Yang, T.-H., Yao, H.-T., and Chiang, M.-T. (2017). Red Algae (*Gelidium Amansii*) Hot-Water Extract Ameliorates Lipid Metabolism in Hamsters Fed a High-Fat Diet. *J. Food Drug Anal.* 25, 931–938. doi:10.1016/j.jfda.2016.12.008
- Yang, T. H., Chiu, C. Y., Lu, T. J., Liu, S. H., and Chiang, M. T. (2019). The Anti-obesity Effect of Polysaccharide-Rich Red Algae (*Gelidium Amansii*) Hot-Water Extracts in High-Fat Diet-Induced Obese Hamsters. *Mar. Drugs* 17, 532. doi:10.3390/md17090532
- Yu, G., Zhang, Q., Wang, Y., Yang, Q., Yu, H., Li, H., et al. (2021). Sulfated Polysaccharides from Red Seaweed *Gelidium Amansii*: Structural Characteristics, Anti-oxidant and Anti-glycation Properties, and Development of Bioactive Films. *Food Hydrocolloids* 119, 106820. doi:10.1016/j.foodhyd.2021.106820
- Yu, J., Liu, S., Wu, B., Shen, Z., Cherr, G. N., Zhang, X.-X., et al. (2016). Comparison of Cytotoxicity and Inhibition of Membrane ABC Transporters Induced by MWCNTs with Different Length and Functional Groups. *Environ. Sci. Technol.* 50, 3985–3994. doi:10.1021/acs.est.5b05772
- Zhang, X., Qi, C., Guo, Y., Zhou, W., and Zhang, Y. (2016). Toll-like Receptor 4-related Immunostimulatory Polysaccharides: Primary Structure, Activity Relationships, and Possible Interaction Models. *Carbohydr. Polym.* 149, 186–206. doi:10.1016/j.carbpol.2016.04.097

- Zhu, F., Du, B., and Xu, B. (2018). Anti-inflammatory Effects of Phytochemicals from Fruits, Vegetables, and Food Legumes: A Review. *Crit. Rev. Food Sci. Nutr.* 58, 1260–1270. doi:10.1080/10408398.2016.1251390
- Zhu, M., Huang, R., Wen, P., Song, Y., He, B., Tan, J., et al. (2021). Structural Characterization and Immunological Activity of Pectin Polysaccharide from Kiwano (*Cucumis Metuliferus*) Peels. *Carbohydr. Polym.* 254, 117371. doi:10.1016/j.carbpol.2020.117371

Conflict of Interest: The authors declare that the research was conducted in the absence of any commercial or financial relationships that could be construed as a potential conflict of interest.

Publisher's Note: All claims expressed in this article are solely those of the authors and do not necessarily represent those of their affiliated organizations, or those of the publisher, the editors, and the reviewers. Any product that may be evaluated in this article, or claim that may be made by its manufacturer, is not guaranteed or endorsed by the publisher.

Copyright © 2021 Pei, Yang, Xiao, Zhou, Hong and Qian. This is an open-access article distributed under the terms of the Creative Commons Attribution License (CC BY). The use, distribution or reproduction in other forums is permitted, provided the original author(s) and the copyright owner(s) are credited and that the original publication in this journal is cited, in accordance with accepted academic practice. No use, distribution or reproduction is permitted which does not comply with these terms.



The Effect of Ball Milling Time on the Isolation of Lignin in the Cell Wall of Different Biomass

Guangrong Yang^{1,2†}, Xueying An^{3†} and Shilong Yang^{4*}

¹College of Furniture and Industrial Design, Nanjing Forestry University, Nanjing, China, ²School of Landscape Architecture, Jiangsu Vocational College of Agriculture and Forestry, Jurong, China, ³State Key Laboratory of Pharmaceutical Biotechnology, Department of Sports Medicine and Adult Reconstructive Surgery, Nanjing Drum Tower Hospital, The Affiliated Hospital of Nanjing University Medical School, Nanjing, China, ⁴Advanced Analysis and Testing Center, Nanjing Forestry University, Nanjing, China

OPEN ACCESS

Edited by:

Lei Wang,
Ocean University of China, China

Reviewed by:

Chuan-Ling Si,
Tianjin University of Science and
Technology, China
Zhiwen Wang,
University of Groningen, Netherlands

*Correspondence:

Shilong Yang
yshl6072@163.com

[†]These authors have contributed
equally to this work and share first
authorship

Specialty section:

This article was submitted to
Bioprocess Engineering,
a section of the journal
Frontiers in Bioengineering and
Biotechnology

Received: 02 November 2021

Accepted: 15 November 2021

Published: 14 December 2021

Citation:

Yang G, An X and Yang S (2021) The
Effect of Ball Milling Time on the
Isolation of Lignin in the Cell Wall of
Different Biomass.
Front. Bioeng. Biotechnol. 9:807625.
doi: 10.3389/fbioe.2021.807625

Ball milling technology is the classical technology to isolate representative lignin in the cell wall of biomass for further investigation. In this work, different ball milling times were carried out on hardwood (poplar sawdust), softwood (larch sawdust), and gramineous material (bamboo residues) to understand the optimum condition to isolate the representative milled wood lignin (MWL) in these different biomass species. Results showed that prolonging ball milling time from 3 to 7 h obviously increased the isolation yields of MWL in bamboo residues (from 39.2% to 53.9%) and poplar sawdust (from 15.5% to 35.6%), while only a slight increase was found for the MWL yield of larch sawdust (from 23.4% to 25.8%). Importantly, the lignin substructure of β -O-4 in the MWL samples from different biomasses can be a little degraded with the increasing ball milling time, resulting in the prepared MWL with lower molecular weight and higher content of hydroxyl groups. Based on the isolation yield and structure features, milling time with 3 and 7 h were sufficient to isolate the representative lignin (with yield over 30%) in the cell wall of bamboo residues and poplar sawdust, respectively, while more than 7 h should be carried out to isolate the representative lignin in larch sawdust.

Keywords: biomass, milled wood lignin, β -O-4, molecular weight, functional group

INTRODUCTION

As the depletion of fossil energy and its derived environment issues, a sustainable alternative program is sought urgently. Lignocellulosic biomass is regarded as a clean and renewable resource and shows potential to replace petrochemicals to produce biochemicals, biopolymers, biofuels, etc. (Himmel et al., 2007; Pei et al., 2020; Lin et al., 2021; Zhao et al., 2021a). Hence, developing lignocellulosic biomass to produce green energy and biomaterials is the main concern of scientists in this century. All of lignocellulosic biomass is composed of the cellulose, hemicellulose, and lignin with different proportions (Hu et al., 2021; Zhang et al., 2021; Zhao et al., 2021b). Currently, the application of cellulose and hemicellulose have been much investigated and converted into energy chemicals in industry (Huang et al., 2016a; Chen et al., 2018; Lai et al., 2019; Luo et al., 2021). However, lignin, the major phenolic polymers in biomass, remains underutilized in biorefining, which is required to explore the potential applications in theory (Liu et al., 2021a; Liu et al., 2021b; Huang et al., 2022). Actually, many works have shown that lignin possesses the potential to be further converted into different chemicals and materials, such as phenolic resins, dispersants, binders,

carbon fibers, and active substance (Ragauskas et al., 2006; Yang et al., 2007; Jiang et al., 2017a; Zheng et al., 2021a). In addition, lignin is composed of cross-linked phenylpropanoid units, including *p*-hydroxyphenyl (H), guaiacyl (G), and syringyl (S). In the network of lignin biomacromolecule, both of these units are linked by inter-unit linkages of carbon-carbon (β - β , β -5, β -1, and 5-5') and ether bonds (β -O-4', *a*-O-4', and 5-O-4') (Martín-Sampedro et al., 2019). Therefore, due to the highly variable complex structure of lignin, how to effectively separate lignin from lignocellulosic biomass is the key to efficient utilization of lignin (Yuan et al., 2013).

Now, a variety of extraction methods has been reported to isolate the lignin in biomass. Generally, the extraction methods can be divided according to the used solvent, such as alkaline lignin, lignosulfonate, organic solvent lignin, milled wood lignin (MWL), Klason lignin, and cellulolytic enzyme lignin (Lange et al., 2013; Huang et al., 2017b; Huang et al., 2018; Yun et al., 2021). Different types of lignin show different characterizations of lignin. Even though these methods have been proposed, there are still some issues. For example, the structures of lignin can be severely degraded during alkaline extraction process (alkaline lignin and organic solvent lignin) and condensed during acid hydrolysis process (Klason lignin) (Yuan et al., 2010; Sun et al., 2013; Jiang et al., 2020). For cellulolytic enzyme lignin, a lot of enzymes should be used to degrade the carbohydrate that linked to lignin, and the obtained lignin sample still possesses a high amount of carbohydrate (Guerra et al., 2006). Currently, MWL is considered as the most comprehensive method of keeping native-like lignin structure from biomass (Zhang et al., 2010). The MWL separation method was proposed by Bjorkman in 1956, which uses the solvent of dioxane/water to extract the sufficient milled lignocellulosic biomass (Bjorkman, 1956). It has been reported that the structure of MWL has only minor changes occurring during the extraction process of lignin, which is very fit with the lignin structure in the original biomass. However, the extraction method of MWL also has unexpected problems in practical application of yields of lignin, which is dependent on the ball milling time (Wang et al., 2019; Wang R. et al., 2021). Therefore, this method is only widely used in theoretical research, contributed to provide more accurate theoretical foundations for industrialized applications of lignin. Technologically, ball milling should be carried out to isolate MWL from biomass. However, due to the diversified and complex cell structure of biomass, different ball milling time should be carried out to isolate the representative MWL from different biomass.

Technologically, many advanced technologies have been investigated to characterize the structure of lignin, such as gel permeation chromatography (GPC), Fourier transform infrared spectroscopy (FTIR), nuclear magnetic resonance technology (NMR), etc. (Huang et al., 2017a; Xu et al., 2011; Zhang et al., 2010; Martín-Sampedro et al., 2019). NMR is a state-of-the-art analytical technique that can be applied to analyze the structural features of the lignin samples from different biomasses (Liao et al., 2020). The NMR technology is considered to be non-destructive technology for lignin during analysis process, which is able to detect different nuclei of the different linkages in lignin. Meanwhile, NMR is a structure-sensitive analysis technology,

which can get the structural information of lignin in solution phase and solid phase (Liao et al., 2020; Halleraker and Barth., 2020; Zhao et al., 2021a). Hence, the application of NMR technology to analyze the structure of lignin can provide detailed and comprehensive information about them (Luykx et al., 2008). Specifically, the ^1H NMR spectroscopy can get the hydrogen (proton) signal information of lignin, which can be subdivided into different structural regions (Azhar et al., 2007). The quantitative methods of ^{13}C NMR spectroscopy can measure the carbon signals at different categories of C structures in lignin (Capanema et al., 2004). Meanwhile, 2D heteronuclear single quantum coherence (HSQC) NMR technology has also been developed to get the quantitative information of lignin structures, including lignin aliphatic and aromatic areas (Ibrahim et al., 2012; Tang et al., 2021). In addition, ^{31}P NMR spectroscopy has also been widely used to quantify the functional groups (hydroxyl and the carboxyl groups) of lignin (Hussin et al., 2014). Overall, with the scientific research of this century focused on the comprehensive utilization of lignin, the NMR is considered to be an important lignin structure analysis technology.

Even the influence of ball milling on the efficiency of MWL isolation and structure has been substantially studied. There is no comparative work showing how the structure of MWL samples from different biomass species changes by ball milling at the same milling time. In this work, different ball milling times of 3–7 h were carried out for different biomass of bamboo residues, poplar sawdust, and larch sawdust. This is aimed to provide an appropriate protocol to obtain the representative MWL for further application. To understand the effect of ball milling time on the structure of prepared MWL samples, the chemical composition, molecular weight, lignin substructure, and content of functional groups were analyzed by high-performance liquid chromatography (HPLC), gel permeation chromatography (GPC), 2D-HSQC nuclear magnetic resonance (NMR), and quantitative ^{31}P NMR, respectively.

MATERIALS AND METHODS

Materials

The moso bamboo residues, poplar sawdust, and larch sawdust were collected from the furniture process factory in Fujian, China. Before the analysis of the major components in all sawdust, they were ground into particles with the size of 2–5 mm and then extracted by benzene/ethanol (2:1, v/v) for 16 h to remove the solvent extractives. The major components of the bamboo residues, poplar sawdust, and larch sawdust were 43.5%, 46.6%, and 41.8% of glucan, 19.5%, 19.8%, and 21.7% of xylan, and 35.4%, 28.3%, and 29.4% of lignin, respectively.

Isolation and purification of lignin from different biomasses

The lignins in the biomass of bamboo residues, poplar sawdust, and larch sawdust were isolated according to the standard method proposed by Bjorkman (1956). Specifically, 10 g of

wood sawdust particle was loaded in a 100-ml ZrO_2 bowl with 25 ZrO_2 balls ($\Phi A = 1$ cm). Then the particle was milled by the planetary ball milling under a rotation speed of 600 rpm for a total effective time of 3, 5, and 7 h. During milling process, a milling time of 10 min and a pause time of 15 min were carried out for the planetary ball milling instrument. After milling, all ball-milled meals were collected to extract the lignin using a mixture of 1,4-dioxane and water (96:4, v/v) with a liquid-to-solid ratio of 20:1 for 24 h. The extraction process was repeated three times with a fresh mixture of 1,4-dioxane and water. After three times of extraction, all filtrates were mixed and evaporated by vacuum rotary evaporation at 45°C to get the crude lignin solid, which was termed as milled wood lignin (MWL). To purify the crude MWL, the solid was dissolved in a mixture of acetic acid and water (90:10, v/v) with a liquid-to-solid ratio of 20:1 (ml:g). Then the dissolved lignin in the mixtures was precipitated by adding distilled water. The precipitated MWL was washed with water several times and freeze dried to get the solid. The dried MWL solid was dissolved in a mixture of dichloroethane and ethanol (2:1, v/v) with a liquid-to-solid ratio of 10:1 and then precipitated by adding ether (10 ml/ml of dichloroethane/ethanol). The precipitated MWL was sequentially washed by ether and petroleum and then air dried to obtain the purified MWL.

Component analysis of biomasses and prepared lignins

The major components of three sawdust and the purified MWL preparations were measured according to the standard procedure proposed by the National Renewable Energy Laboratory (NREL) (Sluiter et al., 2011). Specifically, 30 mg of extractive-free sawdust particles (20–40 mesh) or MWL powder was hydrolyzed by 0.3 ml of 72% H_2SO_4 at 25°C for 1 h. The hydrolyzed substrate by 72% H_2SO_4 was diluted to 4% H_2SO_4 with distilled water and auto-hydrolyzed at 121°C for 1 h. The sugar contents in the acid-hydrolyzate were analyzed by high-performance liquid chromatography (HPLC, Agilent 1,260), which is equipped with HPX-87H column and refractive index (RI) detector. The acid-soluble lignin in the acid-hydrolyzate was determined by the ultraviolet spectrophotometer at 205 nm. The acid-insoluble lignin was determined by weighting the residual solid (oven dried) in the acid-hydrolyzate. The lignin content in three sawdust and the purified MWL preparations was referred to the total amount of acid-soluble lignin and acid-insoluble lignin.

Molecular weight analysis of prepared lignins

The molecular weight determination for the prepared lignins was carried out by gel permeation chromatography (GPC). In order to improve the dissolving capacity of lignin in the tetrahydrofuran for GPC analysis, all MWL samples were acetylated according to the work of Pan (2008). For analysis, 2 mg of acetylated lignin was dissolved in 2 ml of tetrahydrofuran and ejected into the GPC system, which is equipped with a PL-gel 10 mm mixed-B 7.5 mm i.d. column and an ultraviolet detector. The analysis was

performed at ambient temperature using tetrahydrofuran as the eluent (1 ml/min). Monodisperse polystyrene was used as the standard to calibrate the molecular weight of lignin in the GPC system.

2D-HSQC nuclear magnetic resonance analysis of prepared lignins

To get the information of the substructure of lignins from different biomasses under various milling times, 2D-HSQC NMR analysis was carried out using a Bruker AVANCE 600 MHz NMR spectrometer equipped with a 5-mm BBO probe. For analysis, 100 mg of oven-dried lignin was dissolved in 400 μ l of DMSO- d_6 and then transferred into an NMR tube. The acquisition data points for F2 (1H) dimension and F2 (13C) dimension were 1,024 (53 ms) and 256 data points (5.14 ms), respectively. The total delay time and scan times were 1.5 s and 160 for the acquisition process, respectively. The 2D-HSQC NMR spectra were processed using the TopSpin software (4.0.5 version).

Functional groups analysis of prepared lignins

Quantitative ^{31}P NMR was carried out to analyze the functional groups using the NMR spectrometer (the same as 2D-HSQC NMR analysis). For analysis, 0.04 g of oven dried lignin and 0.5 ml of anhydrous pyridine/ $CDCl_3$ mixture (1.6:1, v/v) were introduced into the NMR tube to dissolve the lignin. Then 0.2 ml of internal standard solution (endo-N-hydroxy-5-norbornene-2,3-dicarboximide, 9.23 g/L), 0.05 ml of relaxation reagent solution (chromium (III) acetylacetonate, 5.6 g/L) and 0.1 ml of phosphitylating reagent solution (2-chloro-4,4,5,5-tetramethyl-1,2,3-dioxaphospholane) were sequentially added into the NMR tube for analysis. The acquisition parameters for ^{31}P NMR analysis were according to the standard protocol in NMR spectrometer.

RESULTS AND DISCUSSION

Effect of different milling times on the isolation yield and chemical composition of lignin from different biomass

As the balling milling is the first step to isolate the MWL sample as the native-like lignin in wood and different pretreated wood, it is important to understand how the milling time affects the isolation yield and structural changes of lignin in different woods. In this work, ball milling with 3, 5, and 7 h were performed on the different biomass (bamboo residues, poplar sawdust, and larch sawdust) to isolate the native-like lignin, which is aimed to provide an appropriate protocol to obtain the representative lignin for further application. In **Table 1**, it can be seen that the isolation yields of each MWL sample from different biomass were linearly increased with the milling time from 3 to 7 h. These results were in accordance with the work of

TABLE 1 | The isolation yield and composition content of prepared milled wood lignin (MWL) samples from different biomass with different milling times.

Biomass	Milling time (h)	Isolation yield of MWL (%)	Composition content of MWL (%)				
			Xylan	Arabinan	Glucan	Mannan	Lignin
Bamboo residues	3	39.2	4.9	1.1	0.8	/	91.5
	5	45.7	4.9	0.8	0.6	/	92.8
	7	53.9	3.6	0.8	0.6	/	94.6
Poplar sawdust	3	15.5	5.8	0.9	0.2	/	90.5
	5	24.3	6.5	0.7	0.5	/	92.4
	7	35.6	5.6	0.6	0.3	/	92.8
Larch sawdust	3	23.4	/	/	2.8	6.8	90.1
	5	24.8	/	/	1.1	5.6	92.1
	7	25.8	/	/	1.0	5.4	92.9

Capanema et al. (2015), who reported that the MWL yields of birch and maple could be enhanced from 8% to 28% and from 12% to 30% with an increased milling time from 2.5 to 10 h, respectively, while it should be pointed out that there are some differences in the isolation yields of MWL (based on the Klason lignin in biomass) from bamboo residues, poplar sawdust, larch sawdust, which were in the range of 39.2%–53.9%, 15.5%–35.6%, and 23.4%–25.8%, respectively. It is reported that MWL preparation isolated from biomass with a yield over 30% can be regarded as the representative lignin in cell wall (Huang et al., 2016a). Hence, the results showed that milling times with 3 and 7 h were sufficient to isolate the representative lignin in the cell wall of bamboo residues and poplar sawdust, respectively, while, more than 7 h should be carried out to isolate the representative lignin in larch sawdust. This might be due to the more tough cell structure of larch than that of bamboo and poplar.

For the isolated lignin from the cell wall of biomass, the residual carbohydrate in the MWL preparation can affect its dissolving capacity in the DMSO- d_6 for further analysis by NMR technology. Hence, the composition content of all prepared MWL samples were analyzed and shown in **Table 1**. From **Table 1**, it can be seen that both MWL preparations from bamboo residues, poplar sawdust, and larch sawdust contained carbohydrates of 5.0%–6.8%, 6.5%–7.7%, and 6.4%–9.6%, respectively. For the existing carbohydrates in MWL preparations, xylan was the major carbohydrate in MWL preparations from bamboo residues and poplar sawdust, while mannan was the major carbohydrate in MWL preparations from larch sawdust, which was due to their different biomass species. In this work, all the

MWL preparations were obtained from the crude lignin, and after tedious purification procedures, there are still some carbohydrates in the MWL preparations. This can be explained by the hemicellulose, which is covalently linked to lignin by phenyl glycoside linkages (PhGlc), benzyl ethers (BE), and -esters (Est), which is termed as lignin-carbohydrate complexes (LCC) (Zheng et al., 2021b; Gu et al., 2021). Technically, the existing LCC in the cell wall of biomass can be degraded during the milling process, while it is hard to remove during the purification process by various solvents, which can be the reason why the prepared MWL samples from different biomass cannot reach to a purity of 100% (Henriksson, 2017). Overall, the obtained MWL preparations from bamboo residues, poplar sawdust, and larch sawdust contained over 90% of lignin.

Molecular weight analysis of prepared milled wood lignin samples

To verify how the milling time affects the prepared MWL samples in bamboo residues, poplar sawdust, and larch sawdust by different milling times, the weight average molecular weight (M_w) and number average molecular weight (M_n) were analyzed and are shown in **Table 2**. It can be seen that the M_w values of the prepared MWL sample bamboo residues, poplar sawdust, and larch sawdust decreased from 8,577 to 5,324, 6,509 to, and 16,296 to 13,345 g/mol, respectively, when the milling increased from 3 to 7 h. These results indicated that the increased milling time can decrease the molecular weight of prepared MWL from biomass. In the work of Guerra et al. (2006) and Wang R.

TABLE 2 | The molecular weight of prepared MWL samples from biomass at different milling times.

Biomass	Milling time (h)	Molecular weight (g/mol)		Polydispersity index (PDI)
		Weight average (M_w)	Number average (M_n)	
Bamboo residues	3	8,577	4,754	1.80
	5	5,411	3,456	1.57
	7	5,324	2,816	1.89
Poplar sawdust	3	6,509	3,430	1.90
	5	6,337	3,214	1.97
	7	4,330	2,436	1.78
Larch sawdust	3	16,296	7,230	2.25
	5	14,105	4,888	2.89
	7	13,345	4,848	2.75

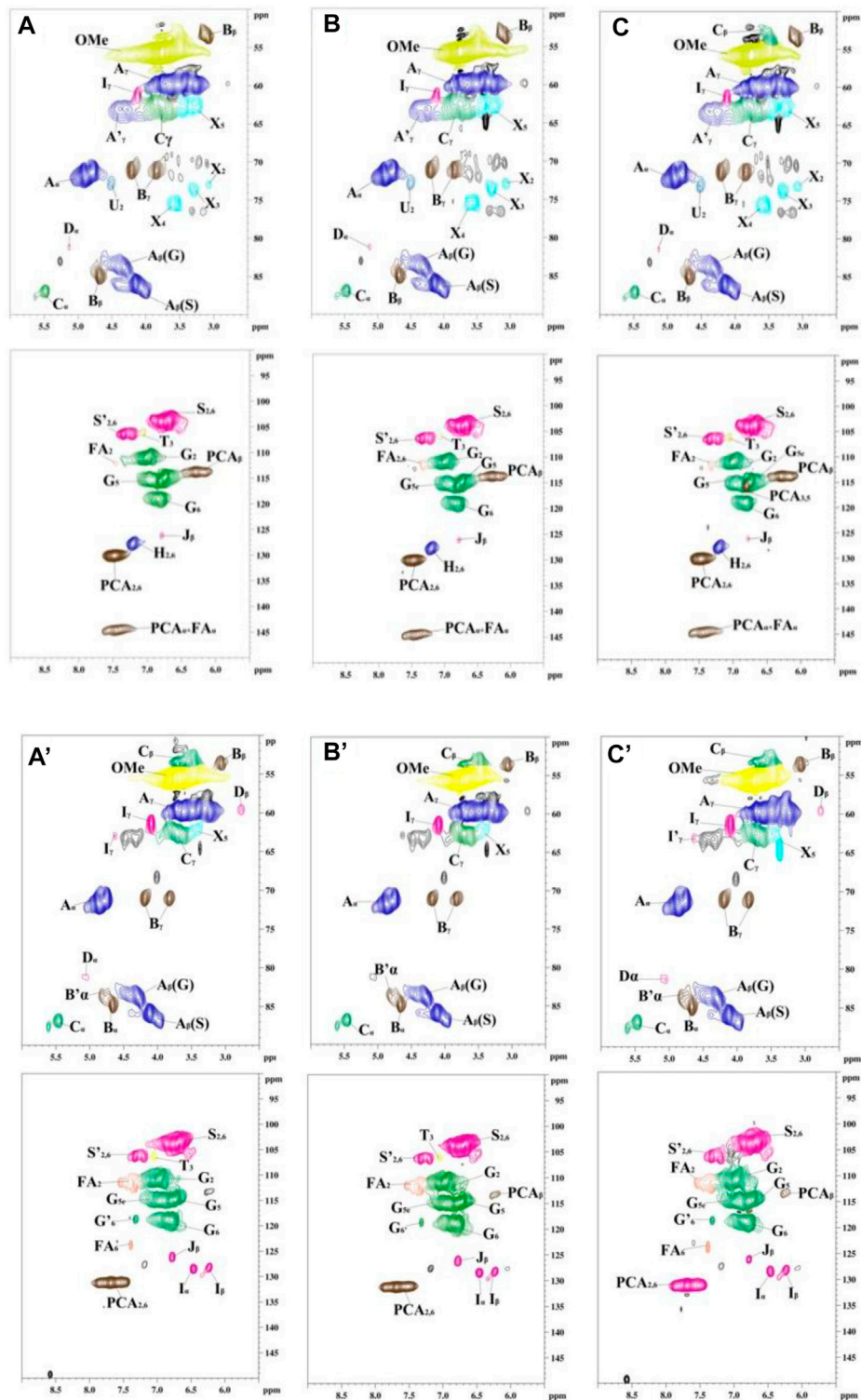


FIGURE 1 | The 2D-HSQC nuclear magnetic resonance (NMR) spectra of all prepared milled wood lignin (MWL) samples from different biomass by different milling times [(**A–C**) are the MWL from bamboo residues with 3-, 5-, and 7-h milling time, respectively; (**A'–C'**) are the MWL from poplar sawdust with 3-, 5-, and 7-h milling time, respectively; (**A''–C''**) are the MWL from larch sawdust with 3-, 5-, and 7-h milling time, respectively].

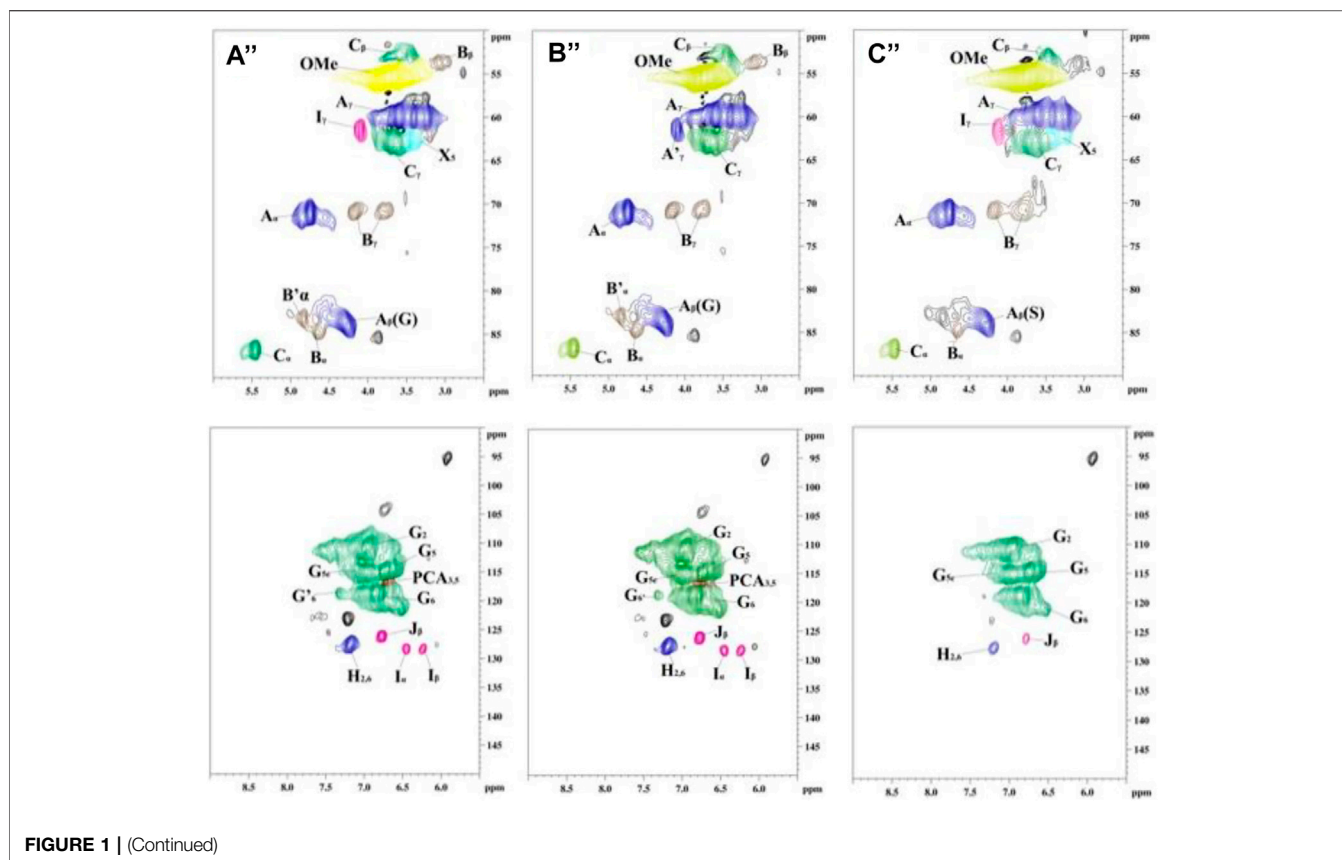


FIGURE 1 | (Continued)

et al. (2021), it was also reported that the intensive milling time can show the performance by decreasing the molecular weight of lignin in the cell wall of different biomass. In addition, **Table 2** shows that both of the prepared MWL samples from different milling times possessed PDI values lower than 3, indicating that the isolated MWL samples possessed a relative homogeneity (Kim et al., 2011; Huang et al., 2016b).

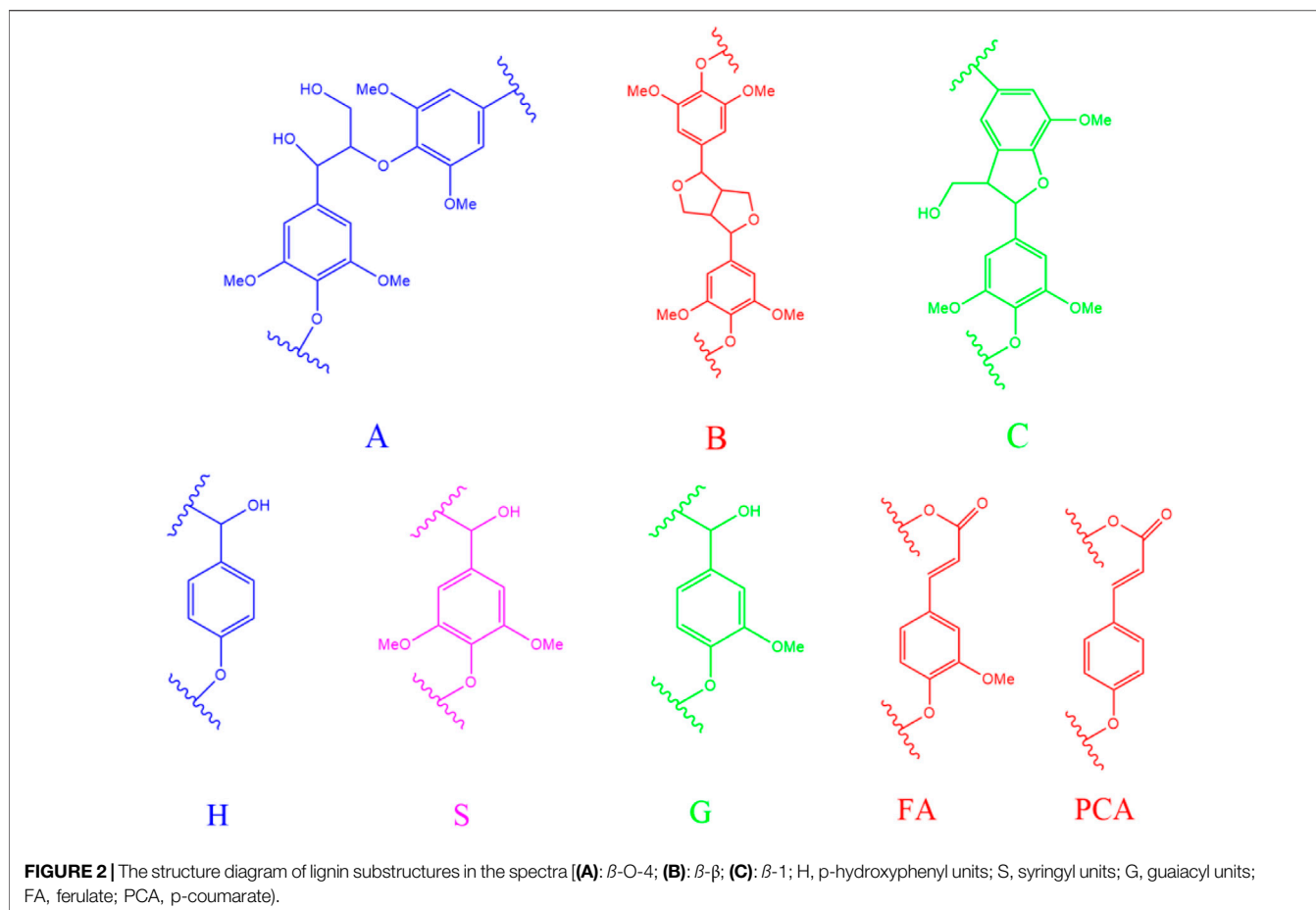
Effect of different milling times on the structure of prepared milled wood lignin samples

To indepthly elucidate the structure features of MWL samples in bamboo residues, poplar sawdust, and larch sawdust by different milling times, 2D-HSQC NMR analysis was carried out by dissolving lignin in DMSO- d_6 . The obtained NMR spectra of all MWL samples and the main structure diagram of lignin substructures in the spectra are shown in **Figures 1** and **2**, respectively.

In the side-chain (δ_C/δ_H 90–50/6.0–2.5) spectra, the substructures of β -O-4 (A), β - β (B), and β -5 (C) in all MWL samples can be clearly observed by identifying their corresponding C–H correlation signals (Jiang et al., 2017b; Huang et al., 2020; Wang R. et al., 2021; Wang Z. et al., 2021). In addition, the lignin units of syringyl units (S), guaiacyl units (G), or p-hydroxyphenyl units (H) can also be

observed in the aromatic region (δ_C/δ_H 135–100/8.5–5.5) spectra of MWL samples with some differences (Dong et al., 2020; Wang R. et al., 2021). Specifically, the S, G, and H units can be found in the MWL spectra of bamboo residues, while only S/G units and G/H units existed in the MWL spectra of poplar sawdust and larch sawdust, respectively. Overall, the results indicated that increasing the ball milling time with different times did not show the performance in changing the phenylpropane structure of lignin units in all MWL samples, which is in accordance with the work of Huang et al. (2011).

It should be pointed out that only the overview of the presented lignin substructures in MWL samples can be obtained in **Figure 1**, which cannot provide the quantitative changes in each substructure. Hence, the amount of lignin substructures in MWL samples from different biomass were semiquantitatively calculated according to their signal clusters in 2D-HSQC spectra. The results were expressed based on 100 aromatic rings (100Ar) and are shown in **Table 3**. **Table 3** shows that a decreased trend was observed for the amount of β -O-4 in MWL samples of different biomass treated by increased ball milling time. Specifically, the amount β -O-4 in MWL of bamboo residues, poplar sawdust, and larch sawdust were decreased from 68.2/100Ar to 60.1/100Ar, from 58.7/100Ar to 55.5/100Ar, and from 66.0/100Ar to 59.4/100Ar, respectively, when the ball milling time was prolonged from 3 to 7 h. In the work of Wang R. et al. (2021), they also found that the increased



ball milling time indeed showed a performance in degrading the β -O-4 in the isolated lignin from different biomass, resulting in a decreased amount, while the amount of β - β in MWL samples were increased when prolonging the ball milling time, indicating it is more recalcitrant than β -O-4 to be degraded during ball milling process. From **Table 3**, it can be obviously found that the β -O-4 was the major linkage in all MWL samples, which is in agreement with the report of Kishimoto et al. (2006) that the

frequency of β -O-4 linkage accounts for 40%–65% in the lignin bi macromolecule.

Generally, the value of S/G ratio is the key index to evaluate which kind of lignin can be easily isolated during ball milling process (Wen et al., 2015; Jiang et al., 2017a). **Table 3** shows that there was no significant difference in the S/G ratio for the MWL samples from different milling time for the bamboo residues (~1.0) and poplar sawdust (~0.8), while MWL samples from

TABLE 3 | The amount of lignin substructures and S/G ratio of prepared MWL samples from biomass at different milling times.

Biomass	Milling time (h)	Amount of lignin substructures (100Ar)			S/G ratio ^a
		β -O-4 (A)	β - β (B)	β -5 (C)	
Bamboo residues	3	68.2	12.7	4.1	1.0
	5	61.3	15.6	4.8	1.1
	7	60.1	16.2	4.1	1.1
Poplar sawdust	3	58.7	10.7	5.9	0.8
	5	56.4	14.7	8.3	0.8
	7	55.5	25.1	5.4	0.7
Larch sawdust	3	66.0	15.2	7.5	/
	5	60.9	16.6	6.6	/
	7	59.4	16.2	4.2	/

Note. a: $S/G = (I_{S2,6}/I_{G2})$

TABLE 4 | The contents of functional groups in MWL samples from different biomass (mmol/g).

	Milling time (h)	Aliphatic hydroxyl	Phenolic hydroxyl		Total phenolic hydroxyl	COOH
			Condensed phenolic OH	Noncondensed phenolic OH		
Bamboo residues	3	1.8	1.6	1.5	3.1	0.3
	5	2.1	1.6	2.4	4.0	0.3
	7	2.2	1.8	2.4	4.2	0.5
Poplar sawdust	3	1.8	1.6	2.1	3.7	0.5
	5	2.6	1.5	2.6	4.1	0.6
	7	2.9	1.6	2.6	4.2	0.5
Larch sawdust	3	1.9	1.8	1.8	3.6	0.4
	5	1.9	1.9	2.1	4.0	0.4
	7	2.2	1.9	2.2	4.1	0.5

bamboo residues possessed a higher S/G ratio than that of poplar sawdust, indicating that the S-type lignin in poplar sawdust is more recalcitrant to be isolated. In the work of Capanema et al. (2015), they found that the obtained lignin from hardwood with a greater content of S-type unit shows a tendency to endow lignin with a higher amount of β -O-4 linkage. Hence, it can be speculated that the higher value of S/G ratio in MWL samples from bamboo residues might be the reason why they had the highest amount of β -O-4 than that of MWL samples from poplar sawdust. Based on the aforementioned results, it can be seen that increasing ball milling time indeed degraded the β -O-4 in the obtained MWL sample, while it showed little effect on the ratio of lignin unit type in the MWL biomacromolecule.

Effect of different milling time on the functional group of prepared milled wood lignin samples

Generally, the degradation of substructures (β -O-4, β - β , β -1, et al.) of lignin inevitably affected the content of the functional group of the prepared lignin (Shao et al., 2020). Hence, quantitative ^{31}P NMR technology was performed to analyze the changes in the functional group (aliphatic hydroxyl and phenolic hydroxyl) of the prepared MWL samples in bamboo residues, poplar sawdust, and larch sawdust by different milling times. From **Table 4**, it can be seen that prolonging the milling time resulted in the prepared MWL samples with the increased contents of aliphatic hydroxyl and phenolic hydroxyl groups. The reason for these results can be explained by the increased degradation degree of β -O-4, which can result in the lignin with enhanced amount of hydroxyl groups. In addition, it is found that increasing the ball milling time from 5 to 7 h did not seriously affect the contents of aliphatic hydroxyl and total phenolic hydroxyl groups in all MWL samples. These results were similar to the work of Wang R. et al. (2021) wherein increasing ball milling time showed a small effect on the structure of lignin during isolation process. It should be pointed out that there was no significant difference in the contents of functional groups in MWL samples from different biomasses treating by the same ball milling time.

CONCLUSION

In this work, ball milling with different times (3, 5, and 7 h) using ZrO_2 bowl with ZrO_2 balls ($\Phi = 1$ cm) at 600 rpm was carried out to isolate the MWL samples in poplar sawdust, larch sawdust, and bamboo residues. It is found that milling time with 3 and 7 h was sufficient to isolate the representative lignin with yields over 30% for bamboo residues and poplar sawdust, respectively, while more than 7 h should be carried out to isolate the representative lignin in larch sawdust. During the ball milling process with prolonged time, the prepared MWL possessed a smaller substructure of β -O-4, lower molecular weight, and higher content of hydroxyl groups, which was due to the occurred degradation. To prepare the representative MWL in different biomass, not only the ball milling time should be considered; it also should be focused on the degradation degree of the substructure of lignin.

DATA AVAILABILITY STATEMENT

The original contributions presented in the study are included in the article/Supplementary Material. Further inquiries can be directed to the corresponding author.

AUTHOR CONTRIBUTIONS

GY isolated the lignin and wrote the manuscript. XA performed the structural analysis of MWL samples by NMR technology. SY proposed the idea and revised the manuscript.

FUNDING

This work was supported by the Natural Science Research of Jiangsu Higher Education Institutions of China (19KJB220005), the Innovation Fund for Young Scholars of Nanjing Forestry University (CX2017004).

REFERENCES

- Azhar, S. S., Suhardy, D., Kasim, F. H., and Nazry Saleh, M. (2007). Isolation and Characterization of Pulp from Sugarcane Bagasse and rice Straw. *J. Nucl. Relat. Tech.* 4, 109–113. doi:10.1016/j.bej.2007.06.005
- Bjorkman, A. (1956). Studies on Finely Divided wood. Part I. Extraction of Lignin with Neutral Solvents. *Sven. Papperstidning*. 59, 477–485.
- Capanema, E. A., Balakshin, M. Y., and Kadla, J. F. (2004). A Comprehensive Approach for Quantitative Lignin Characterization by NMR Spectroscopy. *J. Agric. Food Chem.* 52, 1850–1860. doi:10.1021/jf035282b
- Capanema, E., Balakshin, M., Katahira, R., Chang, H.-m., and Jameel, H. (2015). How Well Do MWL and CEL Preparations Represent the Whole Hardwood Lignin? *J. Wood Chem. Tech.* 35 (1), 17–26. doi:10.1080/02773813.2014.892993
- Chen, X., Li, H., Sun, S., Cao, X., and Sun, R. (2018). Co-production of Oligosaccharides and Fermentable Sugar from Wheat Straw by Hydrothermal Pretreatment Combined with Alkaline Ethanol Extraction. *Ind. Crops Prod.* 111, 78–85. doi:10.1016/j.indcrop.2017.10.014
- Dong, H., Zheng, L., Yu, P., Jiang, Q., Wu, Y., Huang, C., et al. (2020). Characterization and Application of Lignin-Carbohydrate Complexes from Lignocellulosic Materials as Antioxidants for Scavenging *In Vitro* and *In Vivo* Reactive Oxygen Species. *ACS Sust. Chem. Eng.* 8 (1), 256–266. doi:10.1021/acsschemeng.9b05290
- Gu, J., Guo, M., Zheng, L., Yin, X., Zhou, L., Fan, D., et al. (2021). Protective Effects of Lignin-Carbohydrate Complexes from Wheat Stalk against Bisphenol a Neurotoxicity in Zebrafish via Oxidative Stress. *Antioxidants* 10 (10), 1640. doi:10.3390/antiox10101640
- Guerra, A., Filpponen, I., Lucia, L. A., Saquing, C., Baumberger, S., and Argyropoulos, D. S. (2006). Toward a Better Understanding of the Lignin Isolation Process from wood. *J. Agric. Food Chem.* 54, 5939–5947. doi:10.1021/jf060722v
- Halleraker, H. V., and Barth, T. (2020). Quantitative NMR Analysis of the Aqueous Phase from Hydrothermal Liquefaction of Lignin. *J. Anal. Appl. Pyrolysis* 151, 104919. doi:10.1016/j.jaap.2020.104919
- Henriksson, G. (2017). What Are the Biological Functions of Lignin and its Complexation with Carbohydrates? *Nord Pulp Papres J.* 32 (4), 527–541. doi:10.3183/NPPRJ-2017-32-04-p527-541
- Himmel, M. E., Ding, S.-Y., Johnson, D. K., Adney, W. S., Nimlos, M. R., Brady, J. W., et al. (2007). Biomass Recalcitrance: Engineering Plants and Enzymes for Biofuels Production. *Science* 315, 804–807. doi:10.1126/science.1137016
- Hu, Y. Y., Yan, B. W., Chen, Z. S., Wang, L., Tang, W., and Huang, C. X. (2021). Recent Technologies for the Extraction and Separation of Polyphenols in Different Plants: A Review. *J. Renew. Mater.* doi:10.32604/jrm.2022.018811
- Huang, C., Dong, H., Zhang, Z., Bian, H., and Yong, Q. (2020). Procuring the Nano-Scale Lignin in Prehydrolyzate as Ingredient to Prepare Cellulose Nanofibril Composite Film with Multiple Functions. *Cellulose* 27 (16), 9355–9370. doi:10.1007/s10570-020-03427-9
- Huang, C., He, J., Du, L., Min, D., and Yong, Q. (2016a). Structural Characterization of the Lignins from the green and Yellow Bamboo of Bamboo Culm (*Phyllostachys Pubescens*). *J. Wood Chem. Tech.* 36 (3), 157–172. doi:10.1080/02773813.2015.1104544
- Huang, C., He, J., Narron, R., Wang, Y., and Yong, Q. (2017b). Characterization of Kraft Lignin Fractions Obtained by Sequential Ultrafiltration and Their Potential Application as a Biobased Component in Blends with Polyethylene. *ACS Sust. Chem. Eng.* 5, 11770–11779. doi:10.1021/acsschemeng.7b03415
- Huang, C., Jeuck, B., Du, J., Yong, Q., Chang, H.-m., Jameel, H., et al. (2016b). Novel Process for the Coproduction of Xylo-Oligosaccharides, Fermentable Sugars, and Lignosulfonates from Hardwood. *Bioresour. Tech.* 219, 600–607. doi:10.1016/j.biortech.2016.08.051
- Huang, C., Jiang, X., Shen, X., Hu, J., Tang, W., Wu, X., et al. (2022). Lignin-enzyme Interaction: A Roadblock for Efficient Enzymatic Hydrolysis of Lignocellulosics. *Renew. Sust. Energ. Rev.* 154, 111822. doi:10.1016/j.rser.2021.111822
- Huang, C., Lai, C., Wu, X., Huang, Y., He, J., Huang, C., et al. (2017a). An Integrated Process to Produce Bio-Ethanol and Xylooligosaccharides Rich in Xylobiose and Xylotriose from High Ash Content Waste Wheat Straw. *Bioresour. Tech.* 241, 228–235. doi:10.1016/j.biortech.2017.05.109
- Huang, C., Ma, J., Zhang, W., Huang, G., and Yong, Q. (2018). Preparation of Lignosulfonates from Biorefinery Lignins by Sulfomethylation and Their Application as a Water Reducer for concrete. *Polymers* 10 (8), 841. doi:10.3390/polym10080841
- Huang, F., Singh, P. M., and Ragauskas, A. J. (2011). Characterization of Milled wood Lignin (MWL) in Loblolly pine Stem wood, Residue, and Bark. *J. Agric. Food Chem.* 59 (24), 12910–12916. doi:10.1021/jf202701b
- Hussin, M. H., Rahim, A. A., Mohamad Ibrahim, M. N., Yemloul, M., Perrin, D., and Brosse, N. (2014). Investigation on the Structure and Antioxidant Properties of Modified Lignin Obtained by Different Combinative Processes of Oil palm Fronds (OPF) Biomass. *Ind. Crops Prod.* 52, 544–551. doi:10.1016/j.indcrop.2013.11.026
- Ibrahim, M. N. M., Rosli, W. D. W., and Chuah, S. B. (2012). Monitoring Quality of Soda Black Liquor of Oil palm Empty Fruit bunch Fibers in Terms of Storage Time and Temperature. *J. Teknol.* 42, 21–28. doi:10.11113/jt.v42.744
- Jiang, B., Cao, T., Gu, F., Wu, W., and Jin, Y. (2017a). Comparison of the Structural Characteristics of Cellulolytic Enzyme Lignin Preparations Isolated from Wheat Straw Stem and Leaf. *ACS Sust. Chem. Eng.* 5 (1), 342–349. doi:10.1021/acsschemeng.6b01710
- Jiang, X., Abbati de Assis, C., Kollman, M., Sun, R., Jameel, H., Chang, H.-m., et al. (2020). Lignin Fractionation from Laboratory to Commercialization: Chemistry, Scalability and Techno-Economic Analysis. *Green. Chem.* 22 (21), 7448–7459. doi:10.1039/d0gc02960b
- Jiang, X., Savithri, D., Du, X., Pawar, S., Jameel, H., Chang, H.-m., et al. (2017b). Fractionation and Characterization of Kraft Lignin by Sequential Precipitation with Various Organic Solvents. *ACS Sust. Chem. Eng.* 5, 835–842. doi:10.1021/acsschemeng.6b02174
- Kim, J.-Y., Shin, E.-J., Eom, I.-Y., Won, K., Kim, Y. H., Choi, D., et al. (2011). Structural Features of Lignin Macromolecules Extracted with Ionic Liquid from poplar wood. *Bioresour. Tech.* 102 (19), 9020–9025. doi:10.1016/j.biortech.2011.07.081
- Kishimoto, T., Uraki, Y., and Ubukata, M. (2006). Chemical Synthesis of β -O-4 Type Artificial Lignin. *Org. Biomol. Chem.* 4, 1343–1347. doi:10.1039/B518005H
- Lai, C., Jia, Y., Wang, J., Wang, R., Zhang, Q., Chen, L., et al. (2019). Co-production of Xylooligosaccharides and Fermentable Sugars from poplar through Acetic Acid Pretreatment Followed by Poly (Ethylene Glycol) Ether Assisted Alkali Treatment. *Bioresour. Tech.* 288, 121569. doi:10.1016/j.biortech.2019.12.1569
- Lange, H., Decina, S., and Crestini, C. (2013). Oxidative Upgrade of Lignin - Recent Routes Reviewed. *Eur. Polym. J.* 49, 1151–1173. doi:10.1016/j.eurpolymj.2013.03.002
- Liao, J. J., Latif, N. H. A., Trache, D., Brosse, N., and Hussin, M. H. (2020). Current Advancement on the Isolation, Characterization and Application of Lignin. *Int. J. Biol. Macromolecules* 162, 985–1024. doi:10.1016/j.ijbiomac.2020.06.168
- Lin, W., Yang, J., Zheng, Y., Huang, C., and Yong, Q. (2021). Understanding the Effects of Different Residual Lignin Fractions in Acid-Pretreated Bamboo Residues on its Enzymatic Digestibility. *Biotechnol. Biofuels.* 14 (1), 143. doi:10.1186/s13068-021-01994-y
- Liu, H., Xu, T., Liu, K., Zhang, M., Liu, W., Li, H., et al. (2021b). Lignin-based Electrodes for Energy Storage Application. *Ind. Crops Prod.* 165, 113425. doi:10.1016/j.indcrop.2021.113425
- Liu, K., Du, H., Zheng, T., Liu, W., Zhang, M., Liu, H., et al. (2021a). Lignin-containing Cellulose Nanomaterials: Preparation and Applications. *Green. Chem.* doi:10.1039/D1GC02841C
- Luo, Y., Li, Y., Cao, L., Zhu, J., Deng, B., Hou, Y., et al. (2021). High Efficiency and Clean Separation of eucalyptus Components by Glycolic Acid Pretreatment. *Bioresour. Tech.* 341, 125757. doi:10.1016/j.biortech.2021.125757
- Luykx, D. M. A. M., Peters, R. J. B., Van Ruth, S. M., and Bouwmeester, H. (2008). A Review of Analytical Methods for the Identification and Characterization of Nano Delivery Systems in Food. *J. Agric. Food Chem.* 56, 8231–8247. doi:10.1021/jf8013926
- Martin-Sampedro, R., Santos, J. I., Fillat, Ú., Wicklein, B., Eugenio, M. E., and Ibarra, D. (2019). Characterization of Lignins from *Populus alba* L. Generated as By-Products in Different Transformation Processes: Kraft Pulping, Organosolv and Acid Hydrolysis. *Int. J. Biol. Macromolecules* 126, 18–29. doi:10.1016/j.ijbiomac.2018.12.158
- Pan, X. -J. (2008). Role of Functional Groups in Lignin Inhibition of Enzymatic Hydrolysis of Cellulose to Glucose. *J. Biobased Mater. Bio.* 2 (1), 25–32. doi:10.1166/jbmb.2008.005

- Pei, W., Shang, W., Liangjiang, C. X., Jiang, X., Huang, C., and Yong, Q. (2020). Using Lignin as the Precursor to Synthesize Fe₃O₄@lignin Composite for Preparing Electromagnetic Wave Absorbing Lignin-Phenol-Formaldehyde Adhesive. *Ind. Crops Prod.* 154, 112638. doi:10.1016/j.indcrop.2020.112638
- Ragauskas, A. J., Williams, C. K., Davison, B. H., Britovsek, G., Cairney, J., Eckert, C. A., et al. (2006). The Path Forward for Biofuels and Biomaterials. *Science* 311, 484–489. doi:10.1126/science.1114736
- Shao, Z., Fu, Y., Wang, P., Zhang, Y., Qin, M., Li, X., et al. (2020). Modification of the aspen Lignin Structure during Integrated Fractionation Process of Autohydrolysis and Formic Acid Delignification. *Int. J. Biol. Macromolecules* 165, 1727–1737. doi:10.1016/j.ijbiomac.2020.10.026
- Sluiter, A., Hames, B., Ruiz, R., Scarlata, C., Sluiter, J., and Templeton, D. (2011). Determination of Structural Carbohydrates and Lignin in Biomass. National renewable energy laboratory Anal.Procedure, Technical Report NREL/TP-510-42618.
- Sun, Y.-C., Xu, J.-K., Xu, F., and Sun, R.-C. (2013). Efficient Separation and Physico-Chemical Characterization of Lignin from eucalyptus Using Ionic Liquid-Organic Solvent and Alkaline Ethanol Solvent. *Ind. Crops Prod.* 47, 277–285. doi:10.1016/j.indcrop.2013.03.025
- Tang, W., Wu, X., Huang, C., Ling, Z., Lai, C., and Yong, Q. (2021). Revealing the Influence of Metallic Chlorides Pretreatment on Chemical Structures of Lignin and Enzymatic Hydrolysis of Waste Wheat Straw. *Bioresour. Tech.* 342, 125983. doi:10.1016/j.biortech.2021.125983
- Wang, R., Zheng, L., Xu, Q., Xu, L., Wang, D., Li, J., et al. (2021). Unveiling the Structural Properties of Water-Soluble Lignin from Gramineous Biomass by Autohydrolysis and its Functionality as a Bioactivator (Anti-inflammatory and Antioxidative). *Int. J. Biol. Macromolecules* 191, 1087–1095. doi:10.1016/j.ijbiomac.2021.09.124
- Wang, Y., Liu, W., Zhang, L., and Hou, Q. (2019). Characterization and Comparison of Lignin Derived from Corn cob Residues to Better Understand its Potential Applications. *Int. J. Biol. Macromolecules* 134, 20–27. doi:10.1016/j.ijbiomac.2019.05.013
- Wang, Z., Zhu, X., and Deuss, P. J. (2021). The Effect of ball Milling on Birch, pine, Reed, walnut Shell Enzymatic Hydrolysis Recalcitrance and the Structure of the Isolated Residual Enzyme Lignin. *Ind. Crops Prod.* 167, 113493. doi:10.1016/j.indcrop.2021.113493
- Wen, J.-L., Sun, S.-L., Yuan, T.-Q., and Sun, R.-C. (2015). Structural Elucidation of Whole Lignin from eucalyptus Based on Preswelling and Enzymatic Hydrolysis. *Green. Chem.* 17 (3), 1589–1596. doi:10.1039/c4gc01889c
- Xu, Q. H., Wang, Y. P., Qin, M. H., Fu, Y. J., Li, Z. Q., Zhang, F. S., et al. (2011). Fiber Surface Characterization of Old Newsprint Pulp Deinked by Combining Hemicellulase with Laccase-Mediator System. *Bioresour. Tech.* 102, 6536–6540. doi:10.1016/j.biortech.2011.03.051
- Yang, D., Qiu, X., Zhou, M., and Lou, H. (2007). Properties of Sodium Lignosulfonate as Dispersant of Coal Water Slurry. *Energ. Convers. Manage.* 48, 2433–2438. doi:10.1039/b915105b10.1016/j.enconman.2007.04.007
- Yuan, T.-Q., Xu, F., and Sun, R.-C. (2013). Role of Lignin in a Biorefinery: Separation Characterization and Valorization. *J. Chem. Technol. Biotechnol.* 88, 346–352. doi:10.1002/jctb.3996
- Yuan, Z., Cheng, S., Leitch, M., and Xu, C. (2010). Hydrolytic Degradation of Alkaline Lignin in Hot-Compressed Water and Ethanol. *Bioresour. Tech.* 101 (23), 9308–9313. doi:10.1016/j.biortech.2010.06.140
- Yun, J., Wei, L., Li, W., Gong, D., Qin, H., Feng, X., et al. (2021). Isolating High Antimicrobial Ability Lignin from Bamboo Kraft Lignin by Organosolv Fractionation. *Front. Bioeng. Biotechnol.* 9, 683796. doi:10.3389/fbioe.2021.683796
- Zhang, A., Lu, F., Liu, C., and Sun, R.-C. (2010). Isolation and Characterization of Lignins from eucalyptus Tereticornis (12ABL). *J. Agric. Food Chem.* 58, 11287–11293. doi:10.1021/jf103354x
- Zhang, Q., Cheng, L., Ma, X., Zhou, X., and Xu, Y. (2021). Revalorization of sunflower Stalk Pith as Feedstock for the Coproduction of Pectin and Glucose Using a Two-step Dilute Acid Pretreatment Process. *Biotechnol. Biofuels* 14 (1), 194. doi:10.1186/s13068-021-02045-2
- Zhao, J., Zhang, X., Zhou, X., and Xu, Y. (2021a). Selective Production of Xylooligosaccharides by Xylan Hydrolysis Using a Novel Recyclable and Separable Furoic Acid. *Front. Bioeng. Biotechnol.* 9, 660266. doi:10.3389/fbioe.2021.660266
- Zhao, X., Meng, X., Ragauskas, A. J., Lai, C., Ling, Z., Huang, C., et al. (2021b). Unlocking the Secret of Lignin-Enzyme Interactions: Recent Advances in Developing State-Of-The-Art Analytical Techniques. *Biotechnol. Adv.* 107830. doi:10.1016/j.biotechadv.2021.107830
- Zheng, L., Lu, G., Pei, W., Yan, W., Li, Y., Zhang, L., et al. (2021a). Understanding the Relationship between the Structural Properties of Lignin and Their Biological Activities. *Int. J. Biol. Macromolecules* 190, 291–300. doi:10.1016/j.ijbiomac.2021.08.168
- Zheng, L., Yu, P., Zhang, Y., Wang, P., Yan, W., Guo, B., et al. (2021b). Evaluating the Bio-Application of Biomacromolecule of Lignin-Carbohydrate Complexes (LCC) from Wheat Straw in Bone Metabolism via ROS Scavenging. *Int. J. Biol. Macromolecules* 176, 13–25. doi:10.1016/j.ijbiomac.2021.01.103

Conflict of Interest: The authors declare that the research was conducted in the absence of any commercial or financial relationships that could be construed as a potential conflict of interest.

Publisher's Note: All claims expressed in this article are solely those of the authors and do not necessarily represent those of their affiliated organizations, or those of the publisher, the editors, and the reviewers. Any product that may be evaluated in this article, or claim that may be made by its manufacturer, is not guaranteed or endorsed by the publisher.

Copyright © 2021 Yang, An and Yang. This is an open-access article distributed under the terms of the Creative Commons Attribution License (CC BY). The use, distribution or reproduction in other forums is permitted, provided the original author(s) and the copyright owner(s) are credited and that the original publication in this journal is cited, in accordance with accepted academic practice. No use, distribution or reproduction is permitted which does not comply with these terms.



Thermostable Cellulases / Xylanases From Thermophilic and Hyperthermophilic Microorganisms: Current Perspective

Samaila Boyi Ajeje¹, Yun Hu^{1*}, Guojie Song¹, Sunday Bulus Peter¹, Richmond Godwin Afful¹, Fubao Sun¹, Mohammad Ali Asadollahi², Hamid Amiri², Ali Abdulkhani³ and Haiyan Sun^{4*}

¹Key Laboratory of Industrial Biotechnology, Ministry of Education, School of Biotechnology, Jiangnan University, Wuxi, China, ²Department of Biotechnology, Faculty of Biological Science and Technology, University of Isfahan, Isfahan, Iran, ³Department of Wood and Paper Science and Technology, Faculty of Natural Resources, University of Tehran, Karaj, Iran, ⁴Institute of Tropical Bioscience and Biotechnology, Chinese Academy of Tropical Agricultural Sciences, Haikou, China

OPEN ACCESS

Edited by:

Caoxing Huang,
Nanjing Forestry University, China

Reviewed by:

Guodong Liu,
Shandong University, China
Wensheng Qin,
Lakehead University, Canada

*Correspondence:

Yun Hu
huyun@jiangnan.edu.cn
Haiyan Sun
sunhaiyan@itbb.org.cn

Specialty section:

This article was submitted to
Industrial Biotechnology,
a section of the journal
Frontiers in Bioengineering and
Biotechnology

Received: 13 October 2021

Accepted: 02 November 2021

Published: 15 December 2021

Citation:

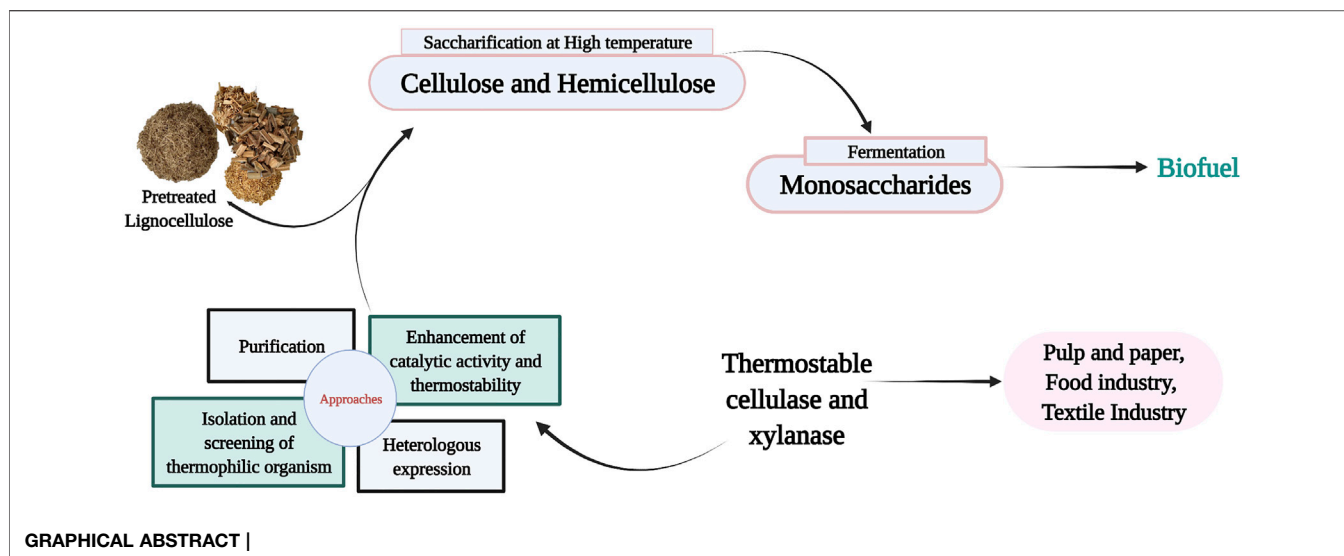
Ajeje SB, Hu Y, Song G, Peter SB,
Afful RG, Sun F, Asadollahi MA,
Amiri H, Abdulkhani A and Sun H
(2021) Thermostable Cellulases /
Xylanases From Thermophilic and
Hyperthermophilic Microorganisms:
Current Perspective.
Front. Bioeng. Biotechnol. 9:794304.
doi: 10.3389/fbioe.2021.794304

The bioconversion of lignocellulose into monosaccharides is critical for ensuring the continual manufacturing of biofuels and value-added bioproducts. Enzymatic degradation, which has a high yield, low energy consumption, and enhanced selectivity, could be the most efficient and environmentally friendly technique for converting complex lignocellulose polymers to fermentable monosaccharides, and it is expected to make cellulases and xylanases the most demanded industrial enzymes. The widespread nature of thermophilic microorganisms allows them to proliferate on a variety of substrates and release substantial quantities of cellulases and xylanases, which makes them a great source of thermostable enzymes. The most significant breakthrough of lignocellulolytic enzymes lies in lignocellulose-deconstruction by enzymatic depolymerization of holocellulose into simple monosaccharides. However, commercially valuable thermostable cellulases and xylanases are challenging to produce in high enough quantities. Thus, the present review aims at giving an overview of the most recent thermostable cellulases and xylanases isolated from thermophilic and hyperthermophilic microbes. The emphasis is on recent advancements in manufacturing these enzymes in other mesophilic host and enhancement of catalytic activity as well as thermostability of thermophilic cellulases and xylanases, using genetic engineering as a promising and efficient technology for its economic production. Additionally, the biotechnological applications of thermostable cellulases and xylanases of thermophiles were also discussed.

Keywords: thermostable cellulase, thermostable xylanase, thermophilic microorganism, thermostability, lignocellulose, genetic engineering, enzyme hydrolysis

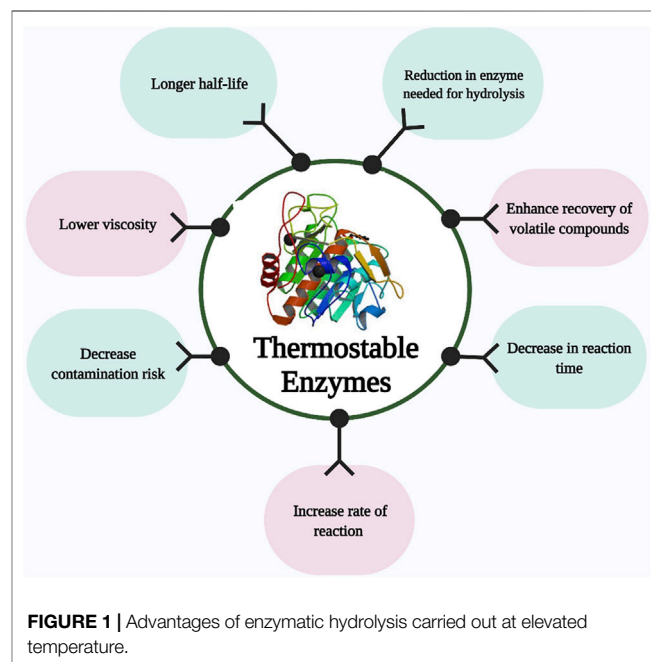
INTRODUCTION

Enzymes are natural catalysts capable of accelerating highly efficient chemical reactions. However, the inability of these catalyst to withstand harsh industrial conditions have limit their application in various industries. After a sharp increase in biofuel-related research studies during 2004–2008, the enzymatic hydrolysis of cellulose and hemicellulose content of lignocellulose has been identified as one of the main challenging steps of the lignocellulose bioconversion, an important part of circular



bioeconomy. Moving from mesophilic to thermophilic enzymes is a vital approach to address the technical and economical drawbacks of typical enzymatic hydrolysis gaining attention in recent years (Arora et al., 2015; Boyce and Walsh, 2018; Fusco et al., 2018b; Singh N. et al., 2021). Lignocellulosic biomass, as an inexpensive and abundant substrate, can be used for the manufacturing of second-generation biofuels as well as a variety of valuable chemicals through biorefinery platforms (Benedetti et al., 2019; Ho et al., 2019). Bioethanol produced from lignocellulosic biomass is an important source of renewable transport fuel since it can reduce greenhouse gas emissions, decrease fossil fuel dependency, improve energy security, and decrease food prices without compromising food production (Majidian et al., 2018; Tian et al., 2018; Patel et al., 2019; Solarte-Toro et al., 2019; Lee and Park, 2020). However, lignocellulosic biomass needs to be degraded prior to use by microorganisms because most of microorganisms cannot use it directly. There is numerous chemical, physical, and enzymatic processes for the degradation of lignocellulosic biomass (Nwamba et al., 2021a). Enzymatic methods offer many advantages over chemical and physical pretreatments as they are environmental friendly, and do not need harmful chemicals such as acids or bases as among all known processes, the enzyme-based hydrolysis of lignocellulose feedstock using cellulase and xylanase is best because of its enhanced specificity, toxic substance is not produced, and no substrate loss (Mohsin et al., 2019). Cellulase and xylanase are the main enzymes required for the hydrolysis of lignocellulosic biomass (Mukasekuru et al., 2020; Ariaenejad et al., 2021). However, the enzymatic process has been hampered by the cost of enzymes (Pihlajaniemi et al., 2021). Despite decades of research on reducing the cost of enzymatic hydrolysis, its contribution to the economics of bioethanol production process, i.e., 0.68–1.47 \$ per gallon of produced ethanol, is still too high to be feasible (Klein-Marcuschamer et al., 2012). Regardless of the tremendous research progress recorded in this research field, a more recent

study shows the average cost of bioethanol production from lignocellulosic biomass ranges from \$1.91 to \$3.48 per gallon ethanol (Saini et al., 2020). It has been emphasized by different researchers like Stephanopoulos (Gregory, 2007) that it is very important to decrease the cost of enzyme down to 3–4 cents per gallon of ethanol before commercializing the lignocellulosic bioethanol. Increased enzyme activity at high temperature in the trade-off between activity and stability has been suggested as a possible approach to reduce the enzyme dosage and consequently the cost contribution of enzymes. It has been suggested that these limitations could be overcome by using highly thermostable enzymes from thermophilic and



hyperthermophilic microbes (Viikari et al., 2007; Yeoman et al., 2010). Furthermore, saccharification carried out at an elevated temperature is very advantageous as shown in **Figure 1**. Concerning configurations of processes and processes with high specificities, thermostable enzymes have more stability, significantly reducing the quantity of enzymes needed for hydrolysis and decrease in reaction time (Yang et al., 2018; Karnaouri et al., 2019). At elevated temperatures, a decrease in viscosity enhances the diffusion rate of the substrate for effective enzymatic degradation (Bhalla et al., 2013). Thermostable enzymes increase the rate of reaction, enzymes tend to have a longer half-life, decrease contamination risk when compared to enzymes from mesophiles. In addition, they enhance the solubility of the feedstock, recoveries of volatile compounds, and also enzymatic efficiency is enhanced in industrial processes (Arora et al., 2015; Yadav et al., 2018). Before enzymatic degradation, lignocellulosic biomass usually undergoes acidic or alkaline pretreatment followed by neutralization. Thermo-acidophilic and thermo-alkalophilic enzymes could prevent the need for this neutralization step (Bhalla et al., 2013).

A deep understanding of thermophilic microorganisms is required to develop processes for commercializing thermostable or thermotolerant enzymes, especially cellulases and xylanases. In prokaryotes, thermophilic microorganisms include photosynthetic bacteria, blue-green algae, spore-forming bacteria (*Bacillus* and *Clostridium*), actinomycetes, bacteria that oxidize and reduce sulfur, bacteria that oxidize and produce methane, and Gram-negative aerobes (Bala and Singh, 2019a). The genera *Bacillus*, *Thermus*, and *Clostridium* contain microorganisms that can grow between the temperatures of 55°C and 70°C. While the temperature ranges for the growth of hyperthermophiles are between 65°C and 110°C, they are mainly archaea and bacteria, but because of their limited membrane adaptation at elevated temperatures and unfavorable growth and development conditions, eukaryotes are rarely found in this group (Boyce and Walsh, 2018; Straub et al., 2018; Bala and Singh, 2019b; Bala and Singh, 2019a). There are more than seven species, two genera, and order of bacteria belong to the hyperthermophiles. However, most of them are archaea since they excellently adapt to extreme temperatures in the environment (Bala and Singh, 2019a). Fungi are the only group in eukaryotes with the unique capability of thriving in high temperatures and are of special interest due to their potential to synthesize a remarkable range of heat-stable enzymes (Prasad, 2019). Thermophilic fungi can proliferate in many different natural environments, such as habitats and soil where the decay of dead plant materials occurs, compost piles, nests of birds, and municipal waste. Hundred years ago, *Mucor pusillus* was isolated from bread as the first thermophilic fungus. A thermophilic fungus known as *Thermomyces lanuginosus* has been discovered on potatoes inoculated with garden soil after several years (Bala and Singh, 2019a; Prasad, 2019).

Almost all known enzymes, e.g., proteases, lipases, amylases, cellulases, xylanases, and cell-associated enzymes (trehalase, invertase, and glycosidase), are obtainable from thermophilic and thermotolerant microorganisms (Bala and

Singh, 2017). In contrast to mesophilic enzymes, enzymes secreted from thermophilic microorganisms are very active and extremely stable in the presence of alcoholic substances, detergents and organic solvents, thereby negating the usage of expensive industrial catalytic agents which are useful in different industries (Arora et al., 2015; Bala and Singh, 2019a; Prasad, 2019). A lack of information on thermostabilized enzymes with high specific activities is limited in the literature, while limited information is available on how to improve their production and thermostability from thermophilic organisms. Thus, the present review aims at giving an overview of the most recent thermostable cellulases and xylanases isolated from thermophilic and hyperthermophilic microbes and from metagenomes with emphasis placed on trends recently used to manufacture these enzymes in mesophilic host in large quantity and enhancement of specific activity as well as thermostability of thermophilic cellulases and xylanases, while also highlighting their biotechnological applications.

CELLULASE AND XYLANASE OF THERMOPHILES

Cellulase of Thermophiles

Cellulose hydrolysis is mainly carried out by β -endoglucanase (EC 3.2.1.4) as the polymer is cleaved to produce short oligosaccharides followed by the simultaneous action of 1,4 β -cellobiohydrolase (EC 3.2.1.91) and β -glucosidase (EC 3.2.1.21), which hydrolyzes it to glucose (Prasad et al., 2018). Cellulases have broad commercial applications because they convert lignocellulosic biomass into simple monosaccharides via enzymatic degradation, which can then be used to manufacture several valuable products in the industry (Patel et al., 2019). Furthermore, cellulase can be used for many other applications, including waste management, pigment extraction, and bioactive molecules extraction from plant materials (Ghosh et al., 2020). Thermostable cellulase is of great interest in the depolymerization of complex lignocellulose polymers. Chemically pretreated biomass can be hydrolyzed by this group of cellulolytic enzymes from thermophilic organisms (Azadian et al., 2017). These enzymes can be secreted as free enzymes or consolidated into complexes of multienzymes known as cellulosome, which can efficiently release sugar when directly applied to a cellulosic substrate (Thomas et al., 2014a; Singh N. et al., 2021).

Characteristics and Properties of Thermostable Cellulase From Thermophilic Bacteria

A lesser amount of attention is paid to cellulases of bacterial origin since the fungi are known to secrete this catalyst more efficiently. The production of cellulase is known to occur both in aerobic and anaerobic bacteria. There are striking similarities and differences between bacteria that can grow aerobically and anaerobically concerning their cellulase enzyme systems, cell mass yields, and yields of lignocellulose polymer hydrolysis (Kuhad et al., 2016).

TABLE 1 | Thermostable cellulases from various thermophilic microorganism and their characteristics.

Microorganism	Enzyme	Optimum pH	Optimum temperature	Specific activity	Thermostability/half-life	References
Geobacillus sp. T1	Cellulase	6.5	70°C	ND	Stable for 1 h at 60°C	Assareh et al. (2012)
Thermotoga naphthophila RKU-10 ^T	endo-1,4-β-glucanase	6	90°C	1664 U mg ⁻¹	Half-life of 180 min at 95°C	Akram and Haq, (2020)
Dictyoglomus turgidum	β-glucosidase	5.4	80°C	160 U mg ⁻¹	After incubation at 70°C for 2 h, it retained 70% of its activity	Fusco et al. (2018a)
Dictyoglomus thermophilum	endo-1,4-β-glucanase	5.0	50–85°C	7.47 ± 0.06 U/mg	It retained 80% of its relative activity after incubation at 50°C for 135 days	Shi et al. (2013)
Sulfolobus shibatae	endo-1,4-β-glucanase	3–5	95–100°C	ND	Retained 98, 90, and 84% of its activity at 75°C, 80°C, and 85°C, respectively after 120 min	Boyce and Walsh, (2018)
Bacillus licheniformis A5	Cellulase	6.0	50°C	ND	Retained 82% of its activity after 120 min at 80°C	Yang et al. (2021)
Aspergillus heteromorphus	Cellulase	4.5	60°C	ND	Retained 60.0% of its activity after 1 h at 90°C	Singh et al. (2009)
Sporothrix carnis	Cellulase	5.0	80°C	ND	Retained 75% of its activity after 300 min at 80°C	Olajuyigbe and Ogunyewo, (2016)
Paecilomyces thermophila	β-glucosidase	6.0	65°C	ND		Yan et al. (2012)
Putranjiva roxburghii (PRGH1)	β-glucosidase	5.0	65°C	ND	75°C for 60 min	Kar et al. (2017)
Thermoascus aurantiacus	β-glucosidase	5.0	70°C	23.3 U/mg	It maintained 70% of its relative activity after incubation at 60°C for 1 h	Hong et al. (2007)
Geobacillus sp. HTA426	Cellulase	7.0	60°C	ND	Stable at 50–70°C for 300 min	Potprommanee et al. (2017)
Talaromyces emersonii	β-glucosidase		71.5°C	482.8 U/mg	Half-life of 62 min at 65°C	Murray et al. (2004)
Talaromyces emersonii	Cellobiohydrolase	5.0	68°C	ND	Half-life of 68 min at 80°C	Grassick et al. (2004)
Talaromyces emersonii CBS394.64	endo-1,4-β-glucanase	4.5	90°C	ND	Highly thermostable at 70°C	Wang et al. (2014)

Many thermophilic bacteria have produced thermostable cellulolytic enzymes. These include *Bacillus*, *Geobacillus*, *Caldibacillus*, *Acidothermus*, *Caldocellum*, and *Clostridium* (Ghosh et al., 2020). The Hyperthermophilic anaerobe *Caldicellulosiruptor bescii*, isolated from a Kamchatka hot spring, contained highly active cellulases. This bacterium depolymerized cellulose substrate without treatment with chemical, and this was because it produced a multi-modular and multi-functional enzyme known as CelA that was superior to commercially available cellulases (Singh N. et al., 2021). Recently, cellulolytic enzymes of *C. bescii* were used to build a “designer cellulosome” that showed stability and activity at 75°C (Kahn et al., 2019). A hyperthermophilic bacterium *Dictyoglomus turgidum* has a gene (Dtur_0,462) that encodes β-glucosidase was expressed in *E. coli*. This enzyme has a maximum activity at a temperature of 80°C and pH 5.4. This β-glucosidase is extremely stable over a pH range of 5–8, and it retains 70% of its relative activity after 2 h at 70°C. It proved to be suitable for the industrial production of bioethanol, because the enzyme showed high glucose and ethanol tolerance (Fusco et al., 2018a). A cellulolytic gene from *Thermotoga naphthophila* RKU-10^T was isolated and expressed in *E. coli*. The purified TnCel12B shows maximum relative activity at pH 6.0 and temperature of 90°C. After incubation at 85°C, it maintained 100% activity after 8 h with excellent stability over a broad temperature range (50–85°C) and pH range (5.0–9.0) (Akram and Haq, 2020). A gene from

hyperthermophilic archaea *Sulfolobus shibatae* that encodes endo-1,4-β-D-glucanase was cloned and overexpressed in *E. coli*. The recombinant enzyme has relative optimum activity at 95–100°C. The enzyme showed excellent resistance to high temperatures and 100% relative activity was detected after 60 min at 75°C, 80°C, and 85°C; 98, 90, and 84% of original relative activity were observed after 120 min at 75°C, 80°C, and 85°C, respectively (Boyce and Walsh, 2018). Likewise, there have also been some discoveries of new thermostable cellulases from archaea. Oil reservoir metagenome cellulase F1 proved to contain two cellulase modules, likely derived from two different archaeal cellulases. Compared to commercially available enzymes, the fusion enzyme proved to be more thermostable and active (Lewin et al., 2017). A summary of the thermostability of cellulase from thermophilic and hyperthermophilic bacteria is shown in **Table 1**.

Characteristics and Properties of Thermostable Cellulase From Thermophilic Fungi

A variety of applications require thermostable enzymes; which thermophilic fungi provide. These thermostable enzymes, which are found in their habitat, have recently received significant attention, especially in biomass degradation (Thapa et al., 2020). Many thermophilic fungi have been identified to be able to produce highly thermostable cellulase, including *Sporotrichum* sp. (Ishihara et al., 1999), *Thermoascus*

aurantiacus (Gomes et al., 2000), *Talaromyces emersonii* (Murray et al., 2001), and *Syncephalastrum racemosum* (Wonganu et al., 2008). They exhibit maximum activity at 70°C, 80°C, 75°C, and 70°C, respectively. Purified cellulases secreted by these eukaryotic microorganisms have undergone structurally and functionally characterization (Patel et al., 2019). A gene TeEgl5A that encodes a highly thermostable β -endoglucanase was isolated from a thermophilic fungi *Talaromyces emersonii* CBS394.64 and it was overexpressed in *Pichia pastoris*. After purification, the recombinant β -endoglucanase shows optimal relative activity at a temperature of 90°C and pH of 4.5. It has very high stability at 70°C and over a wide pH range of 1.0–10.0, and it is very resistant to the majority of metal ions, proteases, and sodium dodecyl sulfate. TeEgl5A possesses a wide range of substrate specificity and shows increased activity against polymers that contain β -1,4-glycosidic bonds and β -1,3-glycosidic bonds (Wang et al., 2014). *Thermoascus aurantiacus* possess the ability to secrete a highly thermostable cellulase for biomass deconstruction (Mohsin et al., 2019). The best cellulase producer among fungi was thought to be *Trichoderma* sp. but it can be susceptible to product inhibition (Akram et al., 2018).

Both novel thermostable β -glucosidases from filamentous fungi were expressed in *Trichoderma reesei*. They both have an optimum temperature at 60°C and pH 5.0 both enzymes were highly thermostable. Enzymes from CEL3a and CEL3b were incubated at pH 5.0; and 60°C they retained 98 and 88% of their relative activity after 6 h of incubation (Colabardini et al., 2016). The cellulase activity of *Sporotrichum thermophile* (Coutts and Smith, 1976) and *Talaromyces emersonii* (Folan and Coughlan, 1978) is almost the same as the cellulase activity of a mesophilic fungi *Trichoderma reesei*. Compared to the relative cellulase activity of *Trichoderma viridae*, some thermophilic fungi *C. thermophile*, *S. thermophile*, and *T. aurantiacus* were identified to produce cellulase that is twice or thrice greater in activity (Akram et al., 2018). There have been more significant temperature stable proteins in thermophilic bacteria and hyperthermophilic archaea than in thermophilic fungi (Patel et al., 2019). A summary of the thermostability of cellulase from thermophilic fungi is shown in **Table 1**.

Xylanase of Thermophiles

Plants and algae contain hemicellulose, a complex polymeric carbohydrate found in their cell walls. About 33% of the world's green organic carbon is made up of hemicellulose, which is composed primarily of xylan (Bhardwaj et al., 2019; Yang H. et al., 2020; Nwamba et al., 2021b; Shen et al., 2021; Sun et al., 2021). Hemicellulose is hydrolyzed by a variety of enzymes due to its heterogeneous structural composition (Zhuo et al., 2018). Specifically, endo-mannanases are responsible for cleaving of β -1,4 D-manno-pyranosyl bonds a linear and branched oligosaccharide is produced within the main chain (Nwamba et al., 2021b). Different types of microorganisms produce xylanases including thermophilic/thermotolerant fungi, yeast, and thermophilic/extreme thermophilic bacteria.

Characteristics and Properties of Thermostable Xylanases From Thermophilic and Hyperthermophilic Bacteria

Thermophilic and hyperthermophilic bacteria such as *Bacillus licheniformis* (Raj et al., 2018) *Rhodothermus marinus* (Karlsson et al., 2004), *Caldicoprobacter algeriensis* (Mhiri et al., 2020), *Thermococcus zilligii*, *Sulfolobus solfataricus*, and *Pyrodictium abyssi* have been extensively studied to produce highly thermostable xylanase. The majority of the xylanase produced from these thermophiles were identified to be members of families 10 and 11 of glycoside hydrolases (GH) (Ghosh et al., 2020). *Geobacillus* sp. Strain WSUCF1 has drawn attention lately because it produces highly thermotolerant xylanase with an exceptional thermostability with half-lives of 18 days at 60°C and 12 days at 70°C (Bhalla et al., 2015). In another study, a gene that encodes GH10 endo-xylanase was isolated from *Geobacillus* sp. WSUCF1 and overexpressed in *E. coli*. After purifying the endo-xylanase it was tested against birchwood and showed maximum relative activity at a temperature of 70°C and pH 6.5. It was discovered to be highly thermostable at 60°C retaining 50% and also at 50°C retaining 82% of its original activity after 60 h (Bhalla et al., 2014). Similarly, a gene for xylanase xynBCA encoding a polypeptide of 439 residues (XynBCA) was isolated from *Caldicoprobacter algeriensis* and overexpressed heterologously in *E. coli* BL21 (DE3). The purified thermostable xylanase was optimally active at pH 6.5 and 80°C. It exhibited excellent thermostability with a half-life of 20 min at 80°C (Mhiri et al., 2020). A xylanase from *B. licheniformis* had optimum relative activity at pH 9.0 and 60°C and maintained 80% of its relative activity when incubated for 1 h at a 60°C (Raj et al., 2018). Some thermostable xylanases have also been reported from thermohalophiles, thermoacidophiles, and thermoalkaliphiles. For example, thermostable xylanase from thermoacidophilic *Alicyclobacillus* sp. was overexpressed heterologously in *E. coli* and was reported to have a broad pH range (3.8–9.4) and retained 90% of its relative activity when incubated for 1h at 60°C (Bai et al., 2010). Thermostable xylanase from halophilic bacterium, *Thermoanaerobacterium saccharolyticum* NTOU1, has a very high resistance to high salt concentration (when incubated in 2 M NaCl for 24 h it maintained 71% of its relative activity). Also, 50% of the relative activity of this xylanase was maintained when incubated at 65°C for 0.91 h (Hung et al., 2011). Similarly, thermo-alkalophilic xylanase was cloned from *Enterobacter* sp. MTCC 5112 and maintained 90% of its relative activity when incubated at pH 9.0 and 80°C for 0.66 h. It also maintained 85 and 64% of its relative activity at 60°C and 70°C after 18 h, respectively (Khandeparkar and Bhosle, 2006). **Table 2** demonstrates a summary of thermostable xylanases from thermophilic and hyperthermophilic bacteria.

Characteristics and Properties of Thermostable Xylanases From Thermophilic Fungi

Different thermophilic fungi such as *Thielavia terrestris* (García-Huante et al., 2017), *Rhizomucor pusillus* (Hüttner et al., 2018), and *Corynascus thermophiles* (van den Brink et al., 2013) have been reported as very good sources of thermostable xylanase. It

TABLE 2 | Thermostable xylanases from various thermophilic microorganism.

Microorganism	Enzyme	Optimum pH	Optimum temperature	Specific activity	Thermostability/half-life	References
Caldicoprobacter algeriensis	xynBCA	6.5	80°C	117 U/mg	20 min at 80°C	Mhiri et al. (2020)
Streptomyces griseorubens LH-3	Endo-xylanase	5.0	60°C	767.2 U/mg	Retained 60% of its activity at 50°C for 1 h	Wu et al. (2018)
Chaetomium sp. CQ31	Xylanase	6.5	85°C	2489 U/mg	It maintained over 90% of its relative activity at 60°C for half an hour	Yu et al. (2021)
Thermotoga maritima, TmxB	Endo-β-1,4-xylanase	5.0	100°C	ND		Yang et al. (2020b)
Thermotoga neapolitana	hemicellulolytic	6.0	90°C	ND		Benedetti et al. (2019)
Dictyoglomus turgidum	Endomannase	5.4	70°C	ND	It retained 50% of its relative activity when incubated for 2 h at 70°C	Fusco et al. (2018b)
Dictyoglomus turgidum	β-xylosidase	5.0	98°C	ND	retained over 90% of its relative activity within this range of temperature 80°C–95°C	Tong et al. (2021)
Dictyoglomus turgidum	β-xylosidase	5.0	75°C	6.79 U/mg	retaining 88% activity at 65°C for 60 min	Li et al. (2020b)
Acinetobacter Johnsonii	Xylanase	6.0	55°C	ND	retained 80% relative activity after 60 min at 65°C	Xue et al. (2019)
Thermoascus aurantiacus M-2	Xylanase	5.0	75°C	ND	Highly Stable for 2 h from 30°C to 80°C temperature range	Ping et al. (2018)

was recently shown that *Thielavia terrestris* Co3Bag1 produces a highly thermostable xylanase with a molecular weight of 82 kDa. This enzyme has maximum relative activity at pH 5.5 and 85°C. After incubation at 65°C, it has a half-life of 23.1 days (García-Huante et al., 2017). It was found that *R. pusillus* isolated from maize silage could produce 824 (U/g) of xylanase that is highly stable at 75°C (Robledo et al., 2016). Genes encoding putative xylan degrading enzymes were identified in the thermophilic fungus *R. pusillus* (Hüttner et al., 2018). A thermophilic xylanase (XynC01) was identified in the thermophilic fungus *Achaetomium* sp. Xz-8 and overexpressed in *P. pastoris*. It exhibited maximum relative activity at pH 5.5 and 75°C with very good stability over a broad range of pH (pH 4.0–10.0) and at temperatures of 55°C and lower. This thermostable xylanase exhibits excellent tolerance to metal ions and chemical reagents. Combining this xylanase with commercial β-glucanase enhanced its performance (38.50%). These properties make it suitable for industrial applications particularly in breweries (Zhao et al., 2013). Another thermostable xylanase (Xyn11A) was obtained from *Corynascus thermophilus* and it expressed in *P. pastoris*. This thermostable xylanase has maximum relative activity at pH 7.4 and 70°C. When incubated at 50°C and 60°C for 60 min, Xyn11A maintained more than 90% of its relative activity. Xyn11A shows great stability over a wide pH range (2.0–11.0). Its relative activity was not inhibited by metal ions, making it suitable candidate for industrial applications (Yang and Zhang, 2017). In another study, a gene encoding a highly thermostable xylanase in *Paecilomyces thermophile* was overexpressed in *P. pastoris*. XynA shows maximum activity at 75°C and is highly stable when exposed to 80°C for 30 min. XynA produces xylobiose and xylotriose as its main products after hydrolyzing birchwood xylan, beechwood xylan and xylooligosaccharides (Fan et al., 2012). The thermostable fungus, *Thermoascus aurantiacus* M-2 produced xylanase with relative molecular mass of approximately 31.0 kDa showing optimal relative activity at 75°C and pH 5.0. It was active

over a wide range of pH (pH 2.0–10.0) and it showed excellent stability over a wide temperature range (30°C–80°C) for 120 min. The xylanase relative activity was enhanced by Mn²⁺ and Ag⁺ to 120.0 and 119.6%, respectively (Ping et al., 2018). **Table 2** demonstrates a summary of thermostable xylanases from thermophilic fungi.

Bioprospecting Novel Thermostable and Hyper-Thermostable Cellulase and Xylanase From Metagenomes

Increasing interest has been shown in finding thermostable cellulases and xylanases which lie in huge unculturable microbial diversity found in extreme habitats (Zhong et al., 2021). Metagenomics are widely used as very powerful techniques to identify, isolate, and characterized novel thermostable enzymes with efficient catalytic activities from extreme environment which includes various environment that are usually characterized by extreme temperature like hot springs, deserts, compost, hydrocarbon reservoirs, hydrothermal vents, e. t.c. (Zarafeta et al., 2016; Madhavan et al., 2017b; Hebal et al., 2021). The ability of a microbes to survive in these extreme habitat makes their protein to be highly thermostable. Mining of novel biocatalyst through metagenomics can be carried out using functional-based screening of the expression libraries in which metagenomics expression libraries are constructed and screened for target enzyme activity. It can also be carried out through sequenced-based gene searches which rely on known conserved sequences, where target genes are amplified from metagenomic DNA using conserved sequences as primers and subsequently cloned into the appropriate expression systems (Li et al., 2009). The first attempt at discovering novel enzymes using a functional metagenomic approach was made by (Healy et al., 1995) from “zoolibraries” by cloning cellulases with temperature (60–65°C) and pH optima (6–7) Since then, metagenomics approaches have been used to screen and isolate thermostable cellulase from

different ecological niches. A novel β -glucosidase like gene was cloned using function-based screening of metagenomic library from uncultured soil microorganism (Jiang et al., 2009). Similarly, a novel cellulase cocktail was screened and isolated from the camel rumen metagenome. This cellulase cocktail shows enhanced activity at high temperatures above 50°C when compared to the activity of the individual cellulase (Maleki et al., 2020). Another thermostable cellulase was also isolated and expressed from buffalo rumen metagenomic library, which was optimally active at temperature of 50°C and pH 5.0 (Pabbathi et al., 2021).

A novel xylanase was isolated from chicken cecum metagenome, which was highly active at high concentration of salt. It has high potential of application in chicken feed (Al-Darkazali et al., 2017). Furthermore, it was proposed that the primary composition of poultry feed is a high ratio of non-starch polysaccharides that include xylans and arabinoxylans, so the microorganisms capable of degrading these polysaccharides should be abundant in chicken intestine. A novel alkali-stable and thermostable GH11 endoxylanase encoding gene (Mxyl) was retrieved by functional screening of a compost soil metagenome. The recombinant xylanase (1,077 bp) shows optimum activity at 80°C and pH 9.0 (Verma et al., 2013). In another study, a xylanase gene was isolated and expressed in *B. Megaterium* from metagenomic DNA of cow dung. The recombinant xylanase was found to be optimally active at pH 7 and 75°C (Sun et al., 2015).

EXPRESSION OF THERMOSTABLE CELLULASE AND XYLANASE

To conquer the current bottleneck of the synthesis of thermostable lignocellulolytic enzymes in large quantities, we must first figure out how to get them at a cost-effective price. Enzymes are routinely over-expressed with the help of recombinant DNA technology (Juturu and Wu, 2014). In nature, cellulases and xylanase are secreted by broad species of microorganisms. One of the best ways of obtaining new thermoenzymes is through the screening and isolation of cellulase and xylanase-producing microorganisms from nature (Parveen et al., 2019). Saprophytic microorganisms are typically responsible for secreting cellulases and xylanases from dead decaying organic matters. Several plant pathogens also secrete cellulases and xylanase (Wang L. et al., 2020). Microbes producing xylanase and cellulase are typically isolated from soil samples obtained from forest and nature preserves, hot springs, compost, sewage, animal manure, and bovine rumens. These enzymes are excreted outside the cell and have high quality, making cellulases and xylanases from fungi beneficial for industry (Cai et al., 2018; Joseph et al., 2019; Bhatia et al., 2021).

In Bacteria

Recombinant protein expression has been used to increase productivity in a shorter duration and also reduce production costs. Homologous and heterologous expressions of cellulase and xylanase in bacteria, yeasts, filamentous fungi, and plants have been reported for increasing thermostable enzyme production

(Juturu and Wu, 2012). The most regularly used bacteria used for the expression of recombinant proteins are *E. coli* and *Bacillus* (Juturu and Wu, 2014). Several factors contribute to the success of this host as a platform for recombinant expression of the protein, including rapid growth on cheap media, simplicity of the transformation procedure, and ease of isolation and purification of expressed proteins. However, the absence of repetitive codons and the need for specific post-translation modifications such as the formation of disulfide bond and glycosylation limit the ability to efficiently express xylanase heterologous in *E. coli* (Juturu and Wu, 2012). Most xylanases require N-glycosylation, whereas *E. coli* can only achieve simple O-glycosylation. However, an exception was observed in a glycosylated -xylosidase gene isolated from a thermophilic fungus, *P. thermophila*, and overexpressed in *E. coli*, yielding a titer of up to 98.0 U/ml (Juturu and Wu, 2012). Similarly, a gene that encodes a GH10 endo-xylanase was cloned from *Geobacillus* sp. WSUCF1 and heterologously expressed in *E. coli*. This recombinant protein showed a very high specific activity (461.0 U/mg), very high hydrolytic activity (92%), and a very high thermostability. Potential applications of this enzyme include pulp bleaching and biofuel production (Damm et al., 2016). This means glycosylation did not play a very vital role in keeping the activity of these enzymes. The expression of Endo-xylanase in *Lactobacillus* and *B. subtilis* is usually higher compared to *E. coli* because they are Gram-positive and they perform N-glycosylation (Upreti et al., 2003). The advantages of using *B. subtilis* heterologous expression of recombinant protein include lack of pathogenicity and endotoxins, no appreciable codon usage bias, and inexpensive protein purification methods (Wang et al., 2019). *Streptomyces lividans* is also a Gram-positive bacteria found in the soil, that has been utilized for the synthesis of the recombinant enzyme. It can also be used for the synthesis of secondary metabolites (Binnie et al., 1997). The ability of *Streptomyces* to secrete high concentration of recombinant protein and the ease for bacterial transformation makes it a suitable host for enzyme expression. Furthermore, it has a proven track record for expressing enzymes that have been used for the synthesis of pharmaceutical drugs (Anné et al., 2012; Kang and Kim, 2021).

Zymomonas mobilis is an ethanol-tolerant bacterium that ferments a wide variety of monosaccharides and produces bioethanol in significant quantities (Kurumbang et al., 2019). It possesses some unique properties that make it an excellent candidate to be considered as a substitute for yeast in the manufacturing of bioethanol (Li et al., 2019). Utilizing this bacterium as an expression platform for recombinant protein shows about 12–30 times higher protein expression when compared to *E. coli* (Kurumbang et al., 2019). Other advantages include: relatively simple gene transformation techniques, and the ability to express recombinant protein both intracellularly and extracellularly. Expression plasmids can be kept either as autonomous replication DNAs or integrated into the host genome (Ray and Behera, 2017).

In Yeast

Saccharomyces cerevisiae was the first yeast that was implemented for recombinant protein production in 1981 (Hitzeman et al., 1981). *Saccharomyces cerevisiae*, *Pichia*

pastoris, *Hansenula polymorpha*, *Kluyveromyces lactis*, and *Yarrowia lipolytica* are the most common yeasts utilized for recombinant protein production. Their potential in food production is attributed to the non-production of toxins (Nøhr et al., 2003; Liu et al., 2012).

S. cerevisiae is a well-characterized eukaryotic microorganism that has been utilized for the synthesis of thermostable recombinant protein (Baptista et al., 2021). A larger number of cellulase and xylanase from thermophilic microorganisms have been efficiently expressed in *Saccharomyces cerevisiae* (Li J. et al., 2020).

K. lactis has so many advantages as a platform for the expression of a recombinant protein, which include easy genetic manipulation, application of both integrative and episomal expression vectors, it is known to produce a protein that is very useful in the food and dairy industry (Spohner et al., 2016). A thermostable endoglucanase was cloned from *Aspergillus fumigatus* DBINU-1 and it was heterologously expressed in *K. lactis* this recombinant enzyme has optimal activity at pH 5.0 and 60°C (Rungrattanakasin et al., 2018). Similarly, an alkali-thermostable xylanase was cloned from *Bacillus pumilus* and it was expressed in *K. lactis* this shows very good stability at pH 12.0 retaining 74% of its activity after incubation for 2 h it is suitable for application in pulp and paper industry (Thomas et al., 2014b).

P. pastoris is a methylotrophic organism and it was first used as a platform for heterologous expression in 1985 (Cregg et al., 1985). It is presently considered one of the most efficient systems for producing and expressing recombinant proteins (Potvin et al., 2012). *P. pastoris* can produce structurally and functionally stable recombinant proteins, particularly when the recombinant protein is derived from eukaryotic sources. It is capable of performing post-translational modifications, forming disulfide bonds, and folding proteins properly, and is a proliferator of essential proteases (Çalik et al., 2015). Its promising characteristics are leading to a range of interesting studies covering several aspects of improving the efficiency of the bioprocess, from strain engineering to bioprocess engineering (García-Ortega et al., 2019). A study was carried out recently on thermostable endoglucanase that was cloned from *Sclerotinia sclerotiorum* and it was expressed in *P. pastoris* this recombinant enzyme was relatively stable at high temperature and it shows maximum activity at pH 7.0 and 60°C when compared to the native enzyme which have an optimum activity at pH 5.0 and 50°C (Chahed et al., 2018). Another study was carried out on high level expression of highly thermostable xylanase cloned from *Chaetomium* sp. CQ31 and overexpressed in *P. pastoris*. This novel recombinant xylanase exhibit high specific activity against oat-spelt xylan (2, 489 U/mg), beechwood xylan (1522 U/mg), birchwood xylan (1067 U/mg), and arabinoxylan (1208 U/mg), with an optimum activity at pH 6.5 and 85°C. This xylanase have a great potential of application in the brewery industry (Yu et al., 2021).

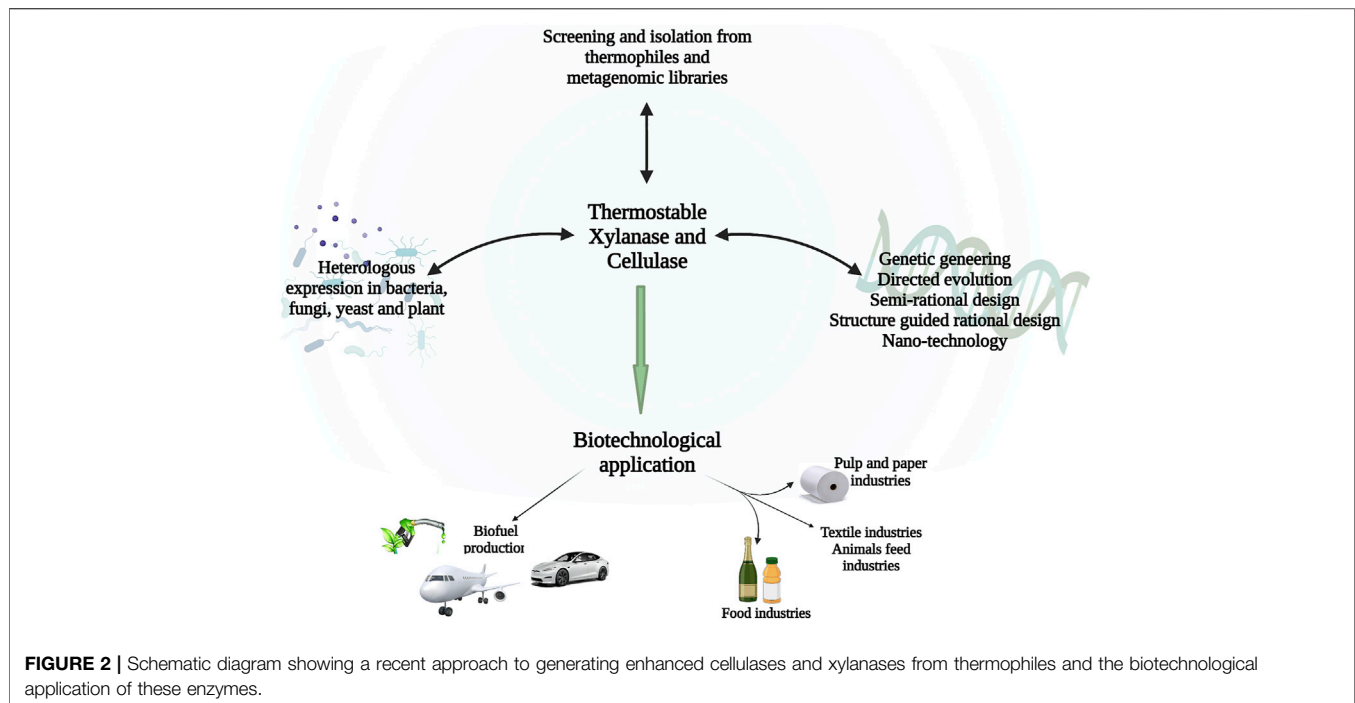
In Filamentous Fungi

Many filamentous fungi are excellent producers of extracellular protein, and their ability to secrete a wide array of proteins and to facilitate the post-translational modification of proteins makes

them more advantageous than bacteria for heterologous metabolite production (Khare et al., 2020). It has been reported that *A. niger* can produce 25–30 g/L of glucoamylase, and *Trichoderma species* can produce 100 g/L of extracellular proteins, proving the importance of protein production and secretion for these organisms. Recombinant DNA technology offers an easy way to express heterologous cellulases and xylanases in fungi due to their high protein secretion ability (Ward, 2012). Gene fusion strategies, overexpression of chaperones, or selecting host strains deficient in protease may be used to attain higher titer of recombinant proteins from filamentous fungi (Juturu and Wu, 2014). Cellobiohydrolase gene was cloned from *Trichoderma virens* cDNA and expressed in *A. niger*. This thermostable enzyme attained optimum activity at pH of 4.0 and 60°C. This partially purified enzyme shows a very high inhibition constant (K_i) compared to other fungal cellobiohydrolases (Wahab et al., 2019). Similarly, a highly thermostable xylanase B gene was cloned from hyperthermophilic bacteria *Thermotoga maritima* and it was heterologously expressed in *A. niger*. This thermostable xylanase exhibit optimum activity at very high temperature >90°C (Zhang et al., 2008).

In Plant

Cloning of thermophilic enzymes in mesophilic species or production of the enzymes directly in plants is a possible method of thermophilic enzyme expression. Transgenic plants could be used to synthesize enzymes for the conversion of complex lignocellulosic polymers (Zhang et al., 2012). As a result of the expression of recombinant proteins in plants, enzyme production costs can be reduced, improving plant autohydrolysis and a very small quantity of exogenous enzyme loading will be needed during lignocellulosic biomass degradation (Phitsuwan et al., 2013). It is more expensive to produce enzymes in submerged fermentation reactions than it is to produce them in plants, as plants are easier to handle and can produce large volumes and high yields of protein (Wilson, 2009). Many studies have been done on the heterologous expression of thermophilic enzymes in plant biomass. A highly thermophilic endoglucanase gene (SSO1354) was cloned from *Sulfolobus solfataricus* and was functionally expressed in tobacco plant (*Nicotiana tabacum*). The recombinant enzyme (SSO1354) shows similar activity when compared to the wild type. The enzyme remains inactive at normal growth conditions, but it exhibited biological activity at elevated temperatures. There have been no adverse effects noticed during the development and growth of plants, and in ionic liquids used for pre-treatment of biomass, its heat-induced activation remains active (Klose et al., 2012). Heterologous expression of thermostable cellulytic and xylanolytic enzymes has been successfully carried out in plants which were very active under harsh conditions, which give way to combined pretreatment and enzymatic hydrolysis which is an effectual process of deconstruction of lignocellulose biomass into fermentable sugars. Similarly, another study was carried out on another hyper thermostable endoglucanase (E1) gene cloned from *Acidothermus cellulolyticus* and it was expressed in rice plant (*Oryza sativa*) under the optimized condition of Gt1



promoter. Interestingly, the enzyme produced in seeds shows similar properties to the endoglucanase in the native host (Zhang et al., 2012). Another endoglucanase gene has been cloned from *Acidothermus cellulolyticus* and heterologously expressed in different types of plants such as maize (Brunecky et al., 2011), rice (Oraby et al., 2007), potatoes (Dai et al., 2000), tobacco (Ziegelhoffer et al., 2009) and they have been considered as a good alternative for the production of biofuel in the nearest future.

STRATEGIES TO ENHANCE THERMOSTABILITY AND SPECIFIC ACTIVITY OF CELLULASE AND XYLANASE OF THERMOPHILES

The applicability of thermostable cellulase and xylanase mainly depends on their productivity, thermostability, specific activity, a wide range of pH, and broad specificity of substrate (Behera and Ray, 2016). As shown in **Figure 2**. To increase the large-scale application of thermostable enzymes, different approaches have been utilized to enhance the thermostability of cellulase and xylanase from thermophiles and these include genetic modifications, expression regulation, and enzyme immobilization. (Boonyapakron et al., 2017; Zhang et al., 2017). The sequence alignment of the amino acid, crystallographic, and mutagenesis studies indicate that several minor modifications contribute to the enhanced temperature stability of xylanases. There is hydrogen bonds and ion pairs, as well as disulfide network formation, specifically in the N- to C-terminals and α -helix, of thermophiles and thermophilic glycoside hydrolases, and aromatic residues which, as a result,

lead to the formation of 'sticky patches' on the surface of the protein (Ghosh et al., 2020).

Genetic Engineering Directed Evolution

Directed evolution is a way of mimicking natural evolution in the lab, in an accelerated fashion, and it can be used in the modification of proteins at will, to endow them with more desirable properties (Gargiulo and Soumillion, 2021). The application of directed evolution by random mutation has become a leading research field in protein engineering, particularly when there is insufficient information about crystal structures of the targeted proteins. Biocatalysts with greater power and efficiency can be generated through directed evolution, which is a widely used strategy in protein engineering (Goldsmith and Tawfik, 2012; Xu et al., 2016; Madhavan et al., 2017a). Direct evolution was utilized to enhance the thermostability and pH stability of *endo*- β -1,4-glucanase III which was active at 50°C for 30 min and pH range of 4.4–8. It was obtained from *T. reesei* QM9414 (Nakazawa et al., 2009). Another study was conducted recently on the enhancement of the temperature tolerance of the GH11 family using directed evolution, the variant Xyn376 showed excellent thermostability, it has a half-life at 70°C for 410 min, which is 820-fold greater after comparing it with the wild-type enzyme (Xing et al., 2021). Similarly, the specific activity of *Bacillus stearothermophilus* xylanase A (BaxA) was increased by 3.5-fold (9.38 Umg⁻¹) using directed evolution (Xu et al., 2016). The cellulase activity of a recombinant enzyme from *Thermotoga neapolitana* was enhanced using Random mutagenesis, the best mutants obtained when compared to the wild type shows 2.7-, 5- and 4.8- fold increase in activity against

CMC, RAC and Avicel respectively (Basit et al., 2019). The use of mutations is an accepted method to improve recombinant proteins at a genetic level, although screening hundreds or thousands of mutants is tedious (Stephens et al., 2014).

Semi-Rational Design

Bioinformatics analysis is used to provide conserved regions of thermostable enzymes or active sites for mutation through semi-rational design (Wang et al., 2018; Wang H. et al., 2020). A semi-rational design was done to alter the activity of a chitinase PpChi1 cloned from *Paenibacillus pasadenensis* CS0611. This mutant S244C-I319C/T259P with proline substitution and disulfide bond introduction exhibits increased specific activity at elevated temperatures as well as a 26.3-fold increase in half-life value at 50°C. It also shows an increase in half-inactivation temperature with a 7.9°C when compared to the wild type protein (Xu et al., 2020). A single point mutation was introduced into *Penicillium canescens* xylanase PcXylA, resulting in a 2.5-fold higher half-life at 50–60°C (Denisenko et al., 2017). In recent years, site-directed mutagenesis and directed evolution have attracted much attention. With the use of these genetic modifications, the best mutant xylanase FC06T was obtained, which has a higher maximum temperature (shift from 77°C to 87°C) and a very high catalytic efficiency (up to 90%) (Zhang et al., 2010).

Structure-Guided Rational Design

In contrast to random mutagenesis, rational design requires *in silico* simulation and substantial crystal structure information (De Simone et al., 2015). By generating purpose-specific sequences with protein structure data, SCHEMA minimizes structure disruption in chimeric proteins when they are recombined (Heinzelman et al., 2013). A study was carried out on two cellulases, each from *Bacillus* and *Geobacillus*, to show the mechanism of their thermostability by comparing the enzymes from the two bacteria. Biofuels and animal feed industries may find these cellulases useful because of their unique thermostability. It was discovered that the cellulase from *Bacillus* BsCel5A is less thermostable compared to the cellulase from thermophilic *Geobacillus* sp. 70PC53. Therefore, these two cellulases are ideal for studying the mechanisms that enable them to remain active at elevated temperatures (Chang et al., 2016). A new recombinant enzyme with excellent enhanced activity could be synthesized by combining crystal structure determinations and structure-guided SCHEMA recombination. (Patel et al., 2019). Disulfide bonds in enzymes play a very important role in their biotechnological application. Replacement of some amino acids that are not consistent with catalytic activity can inherently affect the enzyme structure by strongly affecting the rate of irreversible protein inactivation (Mrudula Vasudevan et al., 2019). The introduction of disulfide bridge Q1C-Q24C at the N-terminal region of GH11 xylanase that was obtained from *Thermomyces lanuginosus* has led to the enhancement of melting temperature by 10°C (Wang et al., 2012). Between the N-terminal and -helix of Xyn2 and the β -sheet core two disulfide bonds were also introduced, which led to enhanced resistance to alkali and acid (Tang et al., 2017). Xyn12.2 was isolated from the termite gut

symbiont metagenome its k_{cat} and catalytic activity was improved by an increase in disulfide bonds, and its thermostability and alkali stability also improved (Boonyapakron et al., 2017). Chemical covalent modification of enzymes can effectively improve and facilitate catalysis. This rational design, guided by the structures of tiny particles incorporated into selected retro covalently modified enzyme BtGH84 cloned from *Bacteroides thetaiotaomicron*, resulted in a 35-fold increase in relative enzyme activity (Darby et al., 2017).

Immobilization on Nano-Structures

Nanotechnology has given rise to new opportunities in different biotechnological field, particularly in enzymes field which have been used in the enhancement of enzyme catalytic activity, thermostability, reusability and many other characteristics through enzyme immobilization (Rai et al., 2019; Gkantzou et al., 2021). The movement of enzymes at elevated temperature is limited by immobilization, which leads to enhanced stability of the enzyme. Furthermore, thermostable enzyme offers greater reaction rate, lower diffusional limitations and enhanced yields (Lee and Au-Duong, 2018). The separation of enzymes is made easier with magnetic nanoparticles, which allows them to be reused, and they also reduce processing costs (Ingle et al., 2017). Recently a research was carried out on β -glucosidase obtained from *Thermotoga maritima* (Tm- β -Glu) and it was functionally immobilized on magnetic nanoparticles (MNPs) with chitin (Ch), this research shows that the novel thermostable chitin-binding domain had the highest binding capacity and Galacto-oligosaccharide synthesis when it was compared with native production of enzyme. In addition, magnetic separation technology have been successfully used in recycling the immobilized β -glucosidase for repetitive batch-wise Galacto-oligosaccharide without significant reduction or loss of enzyme activity (Alnadari et al., 2020). Similarly, another investigation was carried out on thermostable β -glucosidase (Tpebg13) of *Thermotoga petrophila* it was immobilized on macro-porous resin modified with polyethyleneimine and glutaraldehyde. The thermostability, pH stability and glucose tolerance were greatly enhanced, so also the relative activity of this enzyme was found to be 21% higher than that of free enzyme at 85°C (Shi et al., 2018). The thermal stability of free and immobilized β -galactosidase on amino- and cyanuric chloride-modified silica NPs were tested, and the investigation shows that immobilized enzymes retained 72% while the free enzyme only retained 35% of its initial activity after incubation at 60°C for 12 h (Banjanac et al., 2016).

BIOTECHNOLOGICAL APPLICATION OF THERMOSTABLE CELLULASES AND XYLANASES

Biofuel Production

A global crude oil problem hit in the 1970s, which prompted many industries to focus on using cellulases and xylanases in producing biofuel. Bioethanol, bio-butanol, acetoin, and 2,3-

butanediol are produced by degrading cellulose and hemicellulose by cellulase and xylanase (Gusakov, 2013). As of today, ethanol production is not only needed because of oil crisis reasons, but it also reduces greenhouse gas emissions drastically (Bala and Singh, 2019b). This makes bioethanol the most common and widely used renewable fuel today (Pereira et al., 2016). Bioethanol derived from lignocellulose is environmentally friendly, and this process involves pretreatment, enzymatic degradation of polysaccharides into fermentable monosaccharides, and then fermentation of these sugars to bioethanol (Akram et al., 2018). Enzymatic saccharification of biomass is considered a vital step that contributes so much to the overall production cost, and this process can be enhanced by using thermostable enzymes produced from thermophilic microorganisms (Kuhad et al., 2016). Thermostability is a vital and desirable property needed to speed up the saccharification process of biomass (Candido et al., 2019). Within consolidated bioprocesses (CBP), genetically engineered microorganisms can perform enzyme production, enzymatic hydrolysis, and fermentation simultaneously (Antonov et al., 2017). Cellulolytic organisms can either be genetically modified to produce ethanol (CBP-I), or ethanol-producing organisms can be genetically modified to produce cellulases (CBP-II) (Houfani et al., 2020). Most consolidated bioprocesses (CBP) prefers thermophilic microorganisms over mesophilic microorganisms because thermophiles produce a catalyst that can facilitate the conversion of biomass to biofuel at elevated temperatures (Jiang et al., 2017). According to a study, *Trichoderma* has low β -glucosidase activity, which makes cellulose hydrolysis inefficient (Mohanram et al., 2013). Some thermophilic fungi, for example, *Sporotrichum thermophile* (Kaur et al., 2004), *Thermoascus aurantiacus* (Bala and Singh, 2017), *Scytalidium thermophilum*, and *Thielavia terrestris* can be used to replace it because they effectively degrade lignocellulosic biomass through the production of secretory enzymes (Berka et al., 2011). Therefore, these microorganisms have been proposed as an excellent candidate for the degradation of lignocellulosic polymers to simple fermentable monosaccharides that can be used in bio-ethanol industries (Berka et al., 2011). Molecular biology and metabolic engineering have enabled the introduction of strong promoters and regulatory elements to improve the expression of cellulase and xylanase (Beier et al., 2020). *T. reesei* cellulose yield and its activity level increased exponentially after overexpression of gene *Cbh2*, with a maximum yield of 119.49 IU L⁻¹ h⁻¹ (Li et al., 2017). A versatile cellulase system was constructed with a combination of genetic manipulations for the enzymatic saccharification of complex polymers and the production of powerful cellulase inducers (Gao et al., 2017).

Biobutanol production by reviving the old process using acetone-butanol-ethanol (ABE) fermentation has been suggested to address some important weak points of bioethanol, especially based on higher energy density of butanol and its compatibility with current fueling and engine infrastructures. Despite the great potential of butanol as a liquid

fuel, its production process faced with important economic drawbacks. In this regard, efficient utilization of lignocellulosic wastes has been suggested based on the significant contribution of the carbon source in the economics of biobutanol production (Amiri et al., 2014). The typical process of biobutanol production from lignocellulose consists of 1) pretreatment, 2) enzymatic hydrolysis of cellulose, and 3) ABE fermentation of hydrolysate by solvent producing *Clostridia* Especially *Clostridium acetobutylicum* or *C. beijerinckii* to acetone, butanol, ethanol, acetic acid, and butyric acid (Amiri and Karimi, 2018). In this process, between 120 and 250 g total ABE is produced from each kg lignocellulose, utilizing about 1 g cellulase per each Gram produced butanol (Tao et al., 2014). Recently, utilization of hemicellulose content of lignocellulose for biobutanol production has been suggested based on the ability of solvent producing *Clostridia* in efficient utilization of hemicellulose derived pentoses (Mirfakhar et al., 2020). In this regard, a number of studies were devoted to thermostable xylanases for biobutanol production (Xin and He, 2013). characterized cellulase-free and thermo-alkali-stable xylanase by isolated anaerobic bacterium (*Kluyvera* sp. Strain OM3) and utilized it for biobutanol production leading to 1.2 g/L butanol from hemicellulose content of palm oil fiber.

Pulp and Paper Industry

Xylanase and cellulase that have resistance to high pH and are very stable at elevated temperatures have tremendous potential for application in pulp and paper industries (Cui et al., 2015). Cellulase and xylanase have been reported to improve the dissolved pulp concentration, purity, brightness, and permeability of fiber surfaces, improving paper strength and improving the diffusion of bleaching chemicals (Yang et al., 2019). An experiment with cellulases showed a significant energy reduction (20–40%) in the refinement phase and improved hand-sheet strength (Yang et al., 2019). Highly thermostable endo-xylanase that has maximum activity at a temperature of 60°C and pH of 5.0 was synthesized from *Streptomyces griseorubens* LH-3 this Purified xylanase was utilized in the process of bio bleaching eucalyptus Kraft pulp, and results showed an increase in brightness by 14.5% and decreased kappa numbers by 24.5%. Because it possessed all of these industrially suitable attributes, it could be used in pulp and paper manufacturing as a bio bleaching agent (Wu et al., 2018). Similarly, the bio bleaching effect on rice straw pulp was evaluated using the Thermo-alkali-stable xylanase produced from *Bacillus tequilensis* strain UD-3 isolated from a hot spring. Xylanase. This xylanase shows optimum activity at a temperature of 50°C and pH8.0. There was a remarkable reduction in the various compound such as reducing sugars (50%), phenolic (29.19%), hydrophobic (33.20%), and lignin compounds (35.86 and 40.48%) during the Xyl + Zn treatment of pulp samples when compared to the activity of just xylanase (Patel and Dudhagara, 2020). A study was carried out on enzyme cocktail containing 9.9 IU/g of cellulase and 3811 IU/g of xylanase obtained from *Trichoderma longibrachiatum* MDU 6 for deinking of different types of papers. And it was discovered that it effectively removes ink

from old newspapers and significantly remove chromophores, phenolics and hydrophobic compounds (Chutani and Sharma, 2016).

Food Industries

Cellulases from fungi and bacteria have the potential for application in food production (Singh A. et al., 2021). The juice industry uses cellulases in conjunction with other enzymes to increase productivity and yield, improve extraction methods, clarify and stabilize juices (Chakraborty et al., 2016). They can further lower the viscosity of nectar and puree made from fruits such as apricot, mango, pomegranate, pear, and peach, and they can be used to extract flavonoids from flower nectars and seeds (Uzuner and Cekmecelioglu, 2019). As part of the wine production process, cellulase is combined with other enzymes to improve the yield and quality of the wine. Enhancement maceration, better color development, clarification, and finally improved wine consistency and quality are the main benefits of these enzymes. β -glucosidases can be used through modifications of glycosylated precursors to improve wine aroma (Chakraborty et al., 2016). In addition to higher yields, less heat damage, and shorter processing times, cellulase-mediated extraction is much more preferable to conventional methods. Phenolic compounds can be extracted from grape pomace using cellulase. They are also used to enhance the aroma and taste of citrus fruits as well as reduced their bitterness. Combining β -Glucosidases with pectinase can alter the structure, taste, and aroma of vegetables and fruits (Toushik et al., 2017). Olive oil has so many health benefits; in addition to being a good source of monounsaturated fat, it is also associated with reduced risks of stroke and heart disease, it contains fatty acids, vitamin E, and it also contains some phenolic elements and antioxidants, cellulase can be efficiently utilized when combined with other enzymes to extract olive oil (Bisht et al., 2015).

In bread making, xylanases are used with other enzymes because they have the potential benefit of enhancing the volume of the bread and contributing to its improved quality and they allow faster baking times and increase yields (Tekkol et al., 2017). Wheat flour is treated with xylanase to break down hemicellulose, increasing the binding of water to the flour, allowing it to become softer and more elastic (Dahiya and Singh, 2019). The taste, texture, and palatability of biscuits can also be enhanced using xylanase (Rosmine et al., 2017). In the brewing industry, xylanases are used to hydrolyze the barley cellular wall; using xylanases reduces the viscosity of beer and the cloudy appearance of the beer (Yu et al., 2021).

Textile Industries

Thermostable cellulase and xylanase are widely used in the textile industries for stone washing of Jeans, Biopolishing of cotton and other fabrics that contains cellulose (Anish et al., 2007; Escuder-Rodríguez et al., 2018). Biopolishing is typically done after desizing, an enzymatic process that involves temperatures over 70°C. Hence, cellulases and xylanases operating at such elevated temperatures could be useful for combining the two enzymatic processes (Bala and Singh, 2017). Cellulase and xylanase are also used in detergent

industries they are incorporated with other catalytic agents into detergents; all of these enzymes help to break down the chemical bonds present in dirt, which are more effective at higher temperatures (Rigoldi et al., 2018). Thus, they are highly stable at extreme temperatures 60°C and pH ranges 9.0 to 11.0, and detergent resistant. Numerous thermostable cellulase and xylanase that are detergent tolerant have been studied (Frock and Kelly, 2012; Bagewadi et al., 2016).

Animal Feed Industries

Thermostable cellulases and xylanases are used in animal feed industry because of their ability to enhance digestibility and quality of animal feed (Bedford, 2018; Costa et al., 2019). A study was carried out on xylanase 50,316 produced from *Pseudomonas fluorescens*, it have the ability to hydrolyze the glycosidic linkages of the xylan found in animals feed (Van Dorn et al., 2018). Similar, a study was conducted on thermostable xylanase as dietary supplement and its effect on the viscosity of digesta as well as live performances of broiler chicks was also evaluated. This enzyme proved to be effective in improving bird performance as well as the dietary in poultry up to 21 days (Barasch and Grimes, 2021). A thermostable carbohydrases AC1 which contains β -1,4-glucanase, endo-cellulase and cellobiohydrolases activities was expressed in corn for easy inclusion in animals feed, it was used to feed 5 weeks old pigs and the study show no adverse effect on the performance metrics of the pig and the digestibility of this feed was greatly improved (Lessard et al., 2021).

CONCLUSION AND FUTURE PERSPECTIVES

To turn the vision of environmentally friendly lignocellulosic ethanol technology into a reality, there is a significant role in developing thermostable cellulases and xylanases. Many researchers have isolated and characterized thermostable cellulases and xylanases from thermophilic and hyperthermophilic microbes from different environments. So far, metagenomic libraries have been an excellent source of novel thermostable enzymes. Any industrial enzyme that can react rapidly at high temperatures is most desirable as it reduces the need for enzyme and lowers the rate of microbial contamination, which in turn shortens the time needed for the conversion of lignocellulosic polymers into biofuel and valuable products. Some of the few strategies that have been employed for *in vitro* production of thermostable enzymes with improved catalytic characteristics for application in various industries includes; utilization of mesophilic host for heterologous expression of these proteins, strain enhancement, genetic and metabolic engineering. In order to understand and improve the catalytic activity, thermostability, synergism with other enzymes, and evolutionary relationships of cellulases and xylanases it is very important to biochemically characterized these enzymes systemically. Presently, directed evolution, semi-rational design, structure-guided rational design, nanotechnology and metagenomics library are the most alluring approaches for the synthesis of novel cellulase and xylanase. The

genomes of several hyperthermophilic microbes are now available, which could lead to new insights into thermostable cellulases and xylanases. Currently the advancement in metabolic and genetic engineering, molecular microbiology, and structural biochemistry, have helped in synthesis of thermostable cellulases and xylanase. The use of thermostable cellulases and xylanase to transform lignocellulosic biomass into value-added green products can be applied in many sectors, but yet there are many approaches to be explored and developed. Additionally, advancements in bioinformatics will lead to a better understanding and selection of biocatalysts with enhanced properties.

AUTHOR CONTRIBUTIONS

SA: Conceptualization, Writing- original draft YH: Conceptualization, and visualization GS: visualization SP:

REFERENCES

- Akram, F., and Haq, I. U. (2020). Overexpression and Characterization of TnCel12B, a Hyperthermophilic GH12 Endo-1,4- β -Glucanase Cloned from Thermotoga Naphthophila RKU-10T. *Anal. Biochem.* 599, 113741. doi:10.1016/j.ab.2020.113741
- Akram, F., Haq, I. u., Imran, W., and Mukhtar, H. (2018). Insight Perspectives of Thermostable Endoglucanases for Bioethanol Production: A Review. *Renew. Energy* 122, 225–238. doi:10.1016/j.renene.2018.01.095
- Al-Darkazali, H., Meevootisom, V., Isarangkul, D., and Wiyakrutta, S. (2017). Gene Expression and Molecular Characterization of a Xylanase from Chicken Cecum Metagenome. *Int. J. Microbiol.* 2017, 4018398. doi:10.1155/2017/4018398
- Alnadari, F., Xue, Y., Zhou, L., Hamed, Y. S., Taha, M., and Foda, M. F. (2020). Immobilization of β -Glucosidase from Thermotoga Maritima on Chitin-Functionalized Magnetic Nanoparticle via a Novel Thermostable Chitin-Binding Domain. *Sci. Rep.* 10, 1663. doi:10.1038/s41598-019-57165-5
- Amiri, H., and Karimi, K. (2018). Pretreatment and Hydrolysis of Lignocellulosic Wastes for Butanol Production: Challenges and Perspectives. *Bioresour. Technol.* 270, 702–721. doi:10.1016/j.biortech.2018.08.117
- Amiri, H., Karimi, K., and Zilouei, H. (2014). Organosolv Pretreatment of rice Straw for Efficient Acetone, Butanol, and Ethanol Production. *Bioresour. Technol.* 152, 450–456. doi:10.1016/j.biortech.2013.11.038
- Anish, R., Rahman, M. S., and Rao, M. (2007). Application of Cellulases from an Alkalothermophilic Thermomonospora Sp. In Biopolishing of Denims. *Biotechnol. Bioeng.* 96, 48–56. doi:10.1002/bit.21175
- Anné, J., Maldonado, B., Van Impe, J., Van Mellaert, L., and Bernaerts, K. (2012). Recombinant Protein Production and Streptomycetes. *J. Biotechnol.* 158, 159–167. doi:10.1016/j.jbiotec.2011.06.028
- Antonov, E., Schlembach, I., Regestein, L., Rosenbaum, M. A., and Büchs, J. (2017). Process Relevant Screening of Cellulolytic Organisms for Consolidated Bioprocessing. *Biotechnol. Biofuels* 10, 106. doi:10.1186/s13068-017-0790-4
- Ariaeenejad, S., Kavousi, K., Mamaghani, A. S. A., Motahar, S. F. S., Nedaei, H., and Salekdeh, G. H. (2021). In-silico Discovery of Bifunctional Enzymes with Enhanced Lignocellulose Hydrolysis from Microbiota Big Data. *Int. J. Biol. Macromol.* 177, 211–220. doi:10.1016/j.ijbiomac.2021.02.014
- Arora, R., Behera, S., and Kumar, S. (2015). Bioprospecting Thermophilic/thermotolerant Microbes for Production of Lignocellulosic Ethanol: A Future Perspective. *Renew. Sustain. Energy Rev.* 51, 699–717. doi:10.1016/j.rser.2015.06.050
- Assareh, R., Shahbani Zahiri, H., Akbari Noghahi, K., Aminzadeh, S., and Bakhshi khaniki, G. (2012). Characterization of the Newly Isolated Geobacillus Sp. T1, the Efficient Cellulase-Producer on Untreated Barley and Wheat Straws. *Bioresour. Technol.* 120, 99–105. doi:10.1016/j.biortech.2012.06.027
- Azadian, F., Badoei-dalfard, A., Namaki-Shoushtari, A., Karami, Z., and Hassanshahian, M. (2017). Production and Characterization of an Acido-Thermophilic, Organic Solvent Stable Cellulase from Bacillus Sonorensis

Software RA: Software FS: Supervision and funding Acquisition MA: Writing-review and editing HA: Writing-review and editing AA: Writing-review and editing HS: Writing-review and editing.

FUNDING

This work was funded by the National Key Research and Development Program of China (2019YFE0114600) and the National Science Foundation of China (21776114; 52106245; 22,108,096).

ACKNOWLEDGMENTS

The authors also give thanks to the 111 Project (No. 111-2-06).

- HSC7 by Conversion of Lignocellulosic Wastes. *J. Genet. Eng. Biotechnol.* 15, 187–196. doi:10.1016/j.jgeb.2016.12.005
- Bagewadi, Z. K., Mulla, S. I., and Ninnekar, H. Z. (2016). Purification and Characterization of Endo β -1,4-d-glucanase from Trichoderma harzianum Strain HZN11 and its Application in Production of Bioethanol from Sweet Sorghum Bagasse. *Biotech.* 6, 101. doi:10.1007/s13205-016-0421-y
- Bai, Y., Wang, J., Zhang, Z., Yang, P., Shi, P., Luo, H., et al. (2010). A New Xylanase from Thermoacidophilic Alicyclobacillus Sp. A4 with Broad-Range pH Activity and pH Stability. *J. Ind. Microbiol. Biotechnol.* 37, 187–194. doi:10.1007/s10295-009-0662-4
- Bala, A., and Singh, B. (2019a). Cellulolytic and Xylanolytic Enzymes of Thermophiles for the Production of Renewable Biofuels. *Renew. Energy* 136, 1231–1244. doi:10.1016/j.renene.2018.09.100
- Bala, A., and Singh, B. (2017). Concomitant Production of Cellulase and Xylanase by Thermophilic Mould Sporotrichum Thermophile in Solid State Fermentation and Their Applicability in Bread Making. *World J. Microbiol. Biotechnol.* 33, 109. doi:10.1007/s11274-017-2278-6
- Bala, A., and Singh, B. (2019b). Development of an Environmental-Benign Process for Efficient Pretreatment and Saccharification of Saccharum Biomasses for Bioethanol Production. *Renew. Energy* 130, 12–24. doi:10.1016/j.renene.2018.06.033
- Banjanac, K., Carević, M., Čorović, M., Milivojević, A., Prlainović, N., Marinković, A., et al. (2016). Novel β -galactosidase Nanobiocatalyst Systems for Application in the Synthesis of Bioactive Galactosides. *RSC Adv.* 6, 97216–97225. doi:10.1039/C6RA20409K
- Baptista, S. L., Costa, C. E., Cunha, J. T., Soares, P. O., and Domingues, L. (2021). Metabolic Engineering of *Saccharomyces cerevisiae* for the Production of Top Value Chemicals from Biorefinery Carbohydrates. *Biotechnol. Adv.* 47, 107697. doi:10.1016/j.biotechadv.2021.107697
- Barasch, I. B., and Grimes, J. L. (2021). The Effect of a Heat-Stable Xylanase on Digesta Viscosity, Apparent Metabolizable Energy and Growth Performance of Broiler Chicks Fed a Wheat-Based Diet. *Poult. Sci.* 100, 101275. doi:10.1016/j.psj.2021.101275
- Basit, A., Tajwar, R., Sadaf, S., Zhang, Y., and Akhtar, M. W. (2019). Improvement in Activity of Cellulase Cel12A of Thermotoga Neapolitana by Error Prone PCR. *J. Biotechnol.* 306, 118–124. doi:10.1016/j.jbiotec.2019.09.011
- Bedford, M. R. (2018). The Evolution and Application of Enzymes in the Animal Feed Industry: the Role of Data Interpretation. *Br. Poult. Sci.* 59, 486–493. doi:10.1080/00071668.2018.1484074
- Behera, S. S., and Ray, R. C. (2016). Solid State Fermentation for Production of Microbial Cellulases: Recent Advances and Improvement Strategies. *Int. J. Biol. Macromol.* 86, 656–669. doi:10.1016/j.ijbiomac.2015.10.090
- Beier, S., Hinterdobler, W., Bazafkan, H., Schillinger, L., and Schmol, M. (2020). CLR1 and CLR2 Are Light Dependent Regulators of Xylanase and Pectinase Genes in Trichoderma Reesei. *Fungal Genet. Biol.* 136, 103315. doi:10.1016/j.fgb.2019.103315

- Benedetti, M., Vecchi, V., Betterle, N., Natali, A., Bassi, R., and Dall'Osto, L. (2019). Design of a Highly Thermostable Hemicellulose-Degrading Blend from Thermotoga Neapolitana for the Treatment of Lignocellulosic Biomass. *J. Biotechnol.* 296, 42–52. doi:10.1016/j.jbiotec.2019.03.005
- Berka, R. M., Grigoriev, I. V., Otilar, R., Salamov, A., Grimwood, J., Reid, I., et al. (2011). Comparative Genomic Analysis of the Thermophilic Biomass-Degrading Fungi Myceliophthora Thermophila and Thielavia Terrestris. *Nat. Biotechnol.* 29, 922–927. doi:10.1038/nbt.1976
- Bhalla, A., Bansal, N., Kumar, S., Bischoff, K. M., and Sani, R. K. (2013). Improved Lignocellulose Conversion to Biofuels with Thermophilic Bacteria and Thermostable Enzymes. *Bioresour. Technol.* 128, 751–759. doi:10.1016/j.biortech.2012.10.145
- Bhalla, A., Bischoff, K. M., and Sani, R. K. (2015). Highly Thermostable Xylanase Production from A Thermophilic Geobacillus Sp. Strain WSUCF1 Utilizing Lignocellulosic Biomass. *Front. Bioeng. Biotechnol.* 3, 84. doi:10.3389/fbioe.2015.00084
- Bhalla, A., Bischoff, K. M., Uppugundla, N., Balan, V., and Sani, R. K. (2014). Novel Thermostable Endo-Xylanase Cloned and Expressed from Bacterium Geobacillus Sp. WSUCF1. *Bioresour. Technol.* 165, 314–318. doi:10.1016/j.biortech.2014.03.112
- Bhardwaj, N., Kumar, B., and Verma, P. (2019). A Detailed Overview of Xylanases: an Emerging Biomolecule for Current and Future Prospective. *Bioresour. Bioprocess* 6, 40. doi:10.1186/s40643-019-0276-2
- Bhatia, R. K., Ullah, S., Hoque, M. Z., Ahmad, I., Yang, Y.-H., Bhatt, A. K., et al. (2021). Psychrophiles: A Source of Cold-Adapted Enzymes for Energy Efficient Biotechnological Industrial Processes. *J. Environ. Chem. Eng.* 9, 104607. doi:10.1016/j.jece.2020.104607
- Binnie, C., Douglas Cossar, J., and Stewart, D. I. H. (1997). Heterologous Biopharmaceutical Protein Expression in Streptomyces. *Trends Biotechnol.* 15, 315–320. doi:10.1016/S0167-7799(97)01062-7
- Bisht, T. S., Sharma, S. K., Sati, R. C., Rao, V. K., Yadav, V. K., Dixit, A. K., et al. (2015). Improvement of Efficiency of Oil Extraction from Wild Apricot Kernels by Using Enzymes. *J. Food Sci. Technol.* 52, 1543–1551. doi:10.1007/s13197-013-1155-z
- Boonyapakron, K., Jaruwat, A., Liwnaree, B., Nimchua, T., Champreda, V., and Chitnumsub, P. (2017). Structure-based Protein Engineering for Thermostable and Alkaliphilic Enhancement of Endo- β -1,4-Xylanase for Applications in Pulp Bleaching. *J. Biotechnol.* 259, 95–102. doi:10.1016/j.jbiotec.2017.07.035
- Boyce, A., and Walsh, G. (2018). Expression and Characterisation of a Thermophilic Endo-1,4- β -Glucanase from Sulfolobus Shibatae of Potential Industrial Application. *Mol. Biol. Rep.* 45, 2201–2211. doi:10.1007/s11033-018-4381-7
- Brunecky, R., Selig, M. J., Vinzant, T. B., Himmel, M. E., Lee, D., Blaylock, M. J., et al. (2011). In Planta Expression of A. Cellulolyticus Cel5A Endocellulase Reduces Cell wall Recalcitrance in Tobacco and maize. *Biotechnol. Biofuels* 4, 1. doi:10.1186/1754-6834-4-1
- Cai, Z.-W., Ge, H.-H., Yi, Z.-W., Zeng, R.-Y., and Zhang, G.-Y. (2018). Characterization of a Novel Psychrophilic and Halophilic β -1, 3-xylanase from Deep-Sea Bacterium, Flammeovirga pacifica Strain WPAGA1. *Int. J. Biol. Macromol.* 118, 2176–2184. doi:10.1016/j.ijbiomac.2018.07.090
- Çalık, P., Ata, Ö., Güneş, H., Massahi, A., Boy, E., Keskin, A., et al. (2015). Recombinant Protein Production in Pichia pastoris under Glyceraldehyde-3-Phosphate Dehydrogenase Promoter: From Carbon Source Metabolism to Bioreactor Operation Parameters. *Biochem. Eng. J.* 95, 20–36. doi:10.1016/j.bej.2014.12.003
- Candido, R. G., Mori, N. R., and Gonçalves, A. R. (2019). Sugarcane Straw as Feedstock for 2G Ethanol: Evaluation of Pretreatments and Enzymatic Hydrolysis. *Ind. Crops Prod.* 142, 111845. doi:10.1016/j.indcrop.2019.111845
- Chahed, H., Boumaiza, M., Ezzine, A., and Marzouki, M. N. (2018). Heterologous Expression and Biochemical Characterization of a Novel Thermostable Sclerotinia sclerotiorum GH45 Endoglucanase in Pichia pastoris. *Int. J. Biol. Macromol.* 106, 629–635. doi:10.1016/j.ijbiomac.2017.08.062
- Chakraborty, S., Gupta, R., Jain, K. K., Hemansi, S., and Kuhad, R. C. (2016). “Chapter 17-Cellulases: Application in Wine and Brewery Industry,” in *New and Future Developments in Microbial Biotechnology and Bioengineering* (Amsterdam: Elsevier), 193–200. doi:10.1016/B978-0-444-63507-5.00017-4
- Chang, C.-J., Lee, C.-C., Chan, Y.-T., Trudeau, D. L., Wu, M.-H., Tsai, C.-H., et al. (2016). Exploring the Mechanism Responsible for Cellulase Thermostability by Structure-Guided Recombination. *PLoS One* 11, e0147485. doi:10.1371/journal.pone.0147485
- Chutani, P., and Sharma, K. K. (2016). Concomitant Production of Xylanases and Cellulases from Trichoderma Longibrachiatum MDU-6 Selected for the Deinking of Paper Waste. *Bioproc. Biosyst. Eng.* 39, 747–758. doi:10.1007/s00449-016-1555-3
- Colabardini, A. C., Valkonen, M., Huuskonen, A., Siika-aho, M., Koivula, A., Goldman, G. H., et al. (2016). Expression of Two Novel β -Glucosidases from Chaetomium Atrobrunneum in Trichoderma Reesei and Characterization of the Heterologous Protein Products. *Mol. Biotechnol.* 58, 821–831. doi:10.1007/s12033-016-9981-7
- Costa, A. C., da Cavalheiro, G. F., Vieira, E. R., de, Q., Gandra, J. R., Goes, R. H., et al. (2019). Catalytic Properties of Xylanases Produced by Trichoderma Piluliferum and Trichoderma Viride and Their Application as Additives in Bovine Feeding. *Biocatal. Agric. Biotechnol.* 19, 101161. doi:10.1016/j.cbac.2019.101161
- Coutts, A. D., and Smith, R. E. (1976). Factors Influencing the Production of Cellulases by Sporotrichum Thermophile. *Appl. Environ. Microbiol.* 31, 819–825. doi:10.1128/aem.31.6.819-825.1976
- Cregg, J. M., Barringer, K. J., Hessler, A. Y., and Madden, K. R. (1985). Pichia pastoris as a Host System for Transformations. *Mol. Cell. Biol.* 5, 3376–3385. doi:10.1128/mcb.5.12.3376-3385.1985
- Cui, L., Meddeb-Mouelhi, F., Laframboise, F., and Beaugard, M. (2015). Effect of Commercial Cellulases and Refining on Kraft Pulp Properties: Correlations between Treatment Impacts and Enzymatic Activity Components. *Carbohydr. Polym.* 115, 193–199. doi:10.1016/j.carbpol.2014.08.076
- Dahiya, S., and Singh, B. (2019). “Microbial Xylanases in Bread Making,” in *Reference Module in Food Science* (Oxford: Academic Press), 140–149. doi:10.1016/B978-0-08-100596-5.21644-2
- Dai, Z., Hooker, B. S., Anderson, D. B., and Thomas, S. R. (2000). Improved Plant-Based Production of E1 Endoglucanase Using Potato: Expression Optimization and Tissue Targeting. *Mol. Breed.* 6, 277–285. doi:10.1023/A:1009653011948
- Damm, T., Commandeur, U., Fischer, R., Usadel, B., and Klose, H. (2016). Improving the Utilization of Lignocellulosic Biomass by Polysaccharide Modification. *Process. Biochem.* 51, 288–296. doi:10.1016/j.procbio.2015.12.003
- Darby, J. F., Atobe, M., Firth, J. D., Bond, P., Davies, G. J., O'Brien, P., et al. (2017). Increase of Enzyme Activity through Specific Covalent Modification with Fragments. *Chem. Sci.* 8, 7772–7779. doi:10.1039/C7SC01966A
- De Simone, G., Monti, S. M., Alterio, V., Buonanno, M., De Luca, V., Rossi, M., et al. (2015). Crystal Structure of the Most Catalytically Effective Carbonic Anhydrase Enzyme Known, SazCA from the Thermophilic Bacterium Sulfurihydrogenibium Azorense. *Bioorg. Med. Chem. Lett.* 25, 2002–2006. doi:10.1016/j.bmcl.2015.02.068
- Denisenko, Y. A., Gusakov, A. V., Rozhkova, A. M., Osipov, D. O., Zorov, I. N., Matys, V. Y., et al. (2017). Site-directed Mutagenesis of GH10 Xylanase A from Penicillium canescens for Determining Factors Affecting the Enzyme Thermostability. *Int. J. Biol. Macromol.* 104, 665–671. doi:10.1016/j.ijbiomac.2017.06.079
- Escuder-Rodríguez, J.-J., DeCastro, M.-E., Cerdán, M.-E., Rodríguez-Belmonte, E., Becerra, M., and González-Siso, M.-I. (2018). Cellulases from Thermophiles Found by Metagenomics. *Microorganisms* 6, 66. doi:10.3390/microorganisms6030066
- Fan, G., Katrolia, P., Jia, H., Yang, S., Yan, Q., and Jiang, Z. (2012). High-level Expression of a Xylanase Gene from the Thermophilic Fungus Paecilomyces Thermophila in Pichia pastoris. *Biotechnol. Lett.* 34, 2043–2048. doi:10.1007/s10529-012-0995-3
- Folan, M. A., and Coughlan, M. P. (1978). The Cellulase Complex in the Culture Filtrate of the Thermophilic Fungus, Talaromyces emersonii. *Int. J. Biochem.* 9, 717–722. doi:10.1016/0020-711X(78)90038-1
- Frock, A. D., and Kelly, R. M. (2012). Extreme Thermophiles: Moving beyond Single-Enzyme Biocatalysis. *Curr. Opin. Chem. Eng.* 1, 363–372. doi:10.1016/j.coche.2012.07.003
- Fusco, F. A., Fiorentino, G., Pedone, E., Contursi, P., Bartolucci, S., and Limauro, D. (2018a). Biochemical Characterization of a Novel Thermostable β -glucosidase

- from *Dictyoglomus Turgidum*. *Int. J. Biol. Macromol* 113, 783–791. doi:10.1016/j.ijbiomac.2018.03.018
- Fusco, F. A., Ronca, R., Fiorentino, G., Pedone, E., Contursi, P., Bartolucci, S., et al. (2018b). Biochemical Characterization of a Thermostable Endomannanase/endoglucanase from *Dictyoglomus Turgidum*. *Extremophiles* 22, 131–140. doi:10.1007/s00792-017-0983-6
- Gao, J., Wang, E., Ren, W., Liu, X., Chen, Y., Shi, Y., et al. (2017). Effects of Simulated Climate Change on Soil Microbial Biomass and Enzyme Activities in Young Chinese Fir (*Cunninghamia Lanceolata*) in Subtropical China. *Acta Ecol. Sin* 37, 272–278. doi:10.1016/j.chnaes.2017.02.007
- García-Huante, Y., Cayetano-Cruz, M., Santiago-Hernández, A., Cano-Ramírez, C., Marsch-Moreno, R., Campos, J. E., et al. (2017). The Thermophilic Biomass-Degrading Fungus *Thielavia Terrestris* Co3Bag1 Produces a Hyperthermophilic and Thermostable β -1,4-xylanase with Exo- and Endo-Activity. *Extremophiles* 21, 175–186. doi:10.1007/s00792-016-0893-z
- García-Ortega, X., Cámara, E., Ferrer, P., Albiol, J., Montesinos-Seguí, J. L., and Valero, F. (2019). Rational Development of Bioprocess Engineering Strategies for Recombinant Protein Production in *Pichia pastoris* (Komagataella Phaffii) Using the Methanol-free GAP Promoter. Where Do We Stand? *N. Biotechnol.* 53, 24–34. doi:10.1016/j.nbt.2019.06.002
- Gargiulo, S., and Soumillion, P. (2021). Directed Evolution for Enzyme Development in Biocatalysis. *Curr. Opin. Chem. Biol.* 61, 107–113. doi:10.1016/j.cbpa.2020.11.006
- Ghosh, S., Lepcha, K., Basak, A., and Mahanty, A. K. (2020). *Chapter 16- Thermophiles and Thermophilic Hydrolases*. Sharma (Academic Press), 219–236. doi:10.1016/B978-0-12-818322-9.00016-2
- Gkantzou, E., Chatzikonstantinou, A. V., Fotiadou, R., Giannakopoulou, A., Patila, M., and Stamatis, H. (2021). Trends in the Development of Innovative Nanobiocatalysts and Their Application in Biocatalytic Transformations. *Biotechnol. Adv.* 1, 107738. doi:10.1016/j.biotechadv.2021.107738
- Goldsmith, M., and Tawfik, D. S. (2012). Directed Enzyme Evolution: beyond the Low-Hanging Fruit. *Curr. Opin. Struct. Biol.* 22, 406–412. doi:10.1016/j.sbi.2012.03.010
- Gomes, I., Gomes, J., Gomes, D. J., and Steiner, W. (2000). Simultaneous Production of High Activities of Thermostable Endoglucanase and β -glucosidase by the Wild Thermophilic Fungus *Thermoascus Aurantiacus*. *Appl. Microbiol. Biotechnol.* 53, 461–468. doi:10.1007/s002530051642
- Grassick, A., Murray, P. G., Thompson, R., Collins, C. M., Byrnes, L., Berrane, G., et al. (2004). Three-dimensional Structure of a Thermostable Native Cellobiohydrolase, CBH IB, and Molecular Characterization of the Cel7 Gene from the Filamentous Fungus *Talaromyces emersonii*. *Eur. J. Biochem.* 271, 4495–4506. doi:10.1111/j.1432-1033.2004.04409.x
- Gregory, S. (2007). Challenges in Engineering Microbes for Biofuels Production. *Science (80-.)* 315, 801–804. doi:10.1126/science.1139612
- Gusakov, A. (2013). Cellulases and Hemicellulases in the 21st century Race for Cellulosic Ethanol. *Biofuels* 4, 567–569. doi:10.4155/bfs.13.55
- Healy, F. G., Ray, R. M., Aldrich, H. C., Wilkie, A. C., Ingram, L. O., and Shanmugam, K. T. (1995). Direct Isolation of Functional Genes Encoding Cellulases From the Microbial Consortia in a Thermophilic, Anaerobic Digester Maintained on Lignocellulose. *Appl. Microbiol. Biotechnol.* 43, 667–674. doi:10.1007/BF00164771
- Hebal, H., Boucherba, N., Binay, B., and Turunen, O. (2021). Activity and Stability of Hyperthermostable Cellulases and Xylanases in Ionic Liquids. *Biocatal. Biotransformation* 39, 242–259. doi:10.1080/10242422.2021.1882430
- Heinzelman, P., Romero, P. A., and Arnold, F. H. (2013). “Chapter Sixteen - Efficient Sampling of SCHEMA Chimera Families to Identify Useful Sequence Elements,” in *Methods in Protein Design* (Academic Press), 351–368. doi:10.1016/B978-0-12-394292-0.00016-3
- Hitzeman, R. A., Hagie, F. E., Levine, H. L., Goeddel, D. V., Ammerer, G., and Hall, B. D. (1981). Expression of a Human Gene for Interferon in Yeast. *Nature* 293, 717–722. doi:10.1038/293717a0
- Ho, M. C., Ong, V. Z., and Wu, T. Y. (2019). Potential Use of Alkaline Hydrogen Peroxide in Lignocellulosic Biomass Pretreatment and Valorization – A Review. *Renew. Sustain. Energ. Rev.* 112, 75–86. doi:10.1016/j.rser.2019.04.082
- Hong, J., Tamaki, H., and Kumagai, H. (2007). Cloning and Functional Expression of Thermostable β -glucosidase Gene from *Thermoascus Aurantiacus*. *Appl. Microbiol. Biotechnol.* 73, 1331–1339. doi:10.1007/s00253-006-0618-9
- Houfani, A. A., Anders, N., Spiess, A. C., Baldrian, P., and Benallaoua, S. (2020). Insights from Enzymatic Degradation of Cellulose and Hemicellulose to Fermentable Sugars– a Review. *Biomass and Bioenergy* 134, 105481. doi:10.1016/j.biombioe.2020.105481
- Hung, K.-S., Liu, S.-M., Tzou, W.-S., Lin, F.-P., Pan, C.-L., Fang, T.-Y., et al. (2011). Characterization of a Novel GH10 Thermostable, Halophilic Xylanase from the marine Bacterium *Thermoanaerobacterium Saccharolyticum* NTOU1. *Process. Biochem.* 46, 1257–1263. doi:10.1016/j.procbio.2011.02.009
- Hüttner, S., Granchi, Z., Nguyen, T. T., van Pelt, S., Larsbrink, J., Thanh, V. N., et al. (2018). Genome Sequence of *Rhizomucor Pusillus* FCH 5.7, a Thermophilic Zygomycete Involved in Plant Biomass Degradation Harboring Putative GH9 Endoglucanases. *Biotechnol. Rep.* 20, e00279. doi:10.1016/j.btre.2018.e00279
- Ingle, A. P., Rathod, J., Pandit, R., da Silva, S. S., and Rai, M. (2017). Comparative Evaluation of Free and Immobilized Cellulase for Enzymatic Hydrolysis of Lignocellulosic Biomass for Sustainable Bioethanol Production. *Cellulose* 24, 5529–5540. doi:10.1007/s10570-017-1517-1
- Ishihara, M., Tawata, S., and Toyama, S. (1999). Disintegration of Uncooked rice by Carboxymethyl Cellulase from *Sporotrichum* Sp. HG-I. *J. Biosci. Bioeng.* 87, 249–251. doi:10.1016/S1389-1723(99)89023-9
- Jiang, C., Ma, G., Li, S., Hu, T., Che, Z., Shen, P., et al. (2009). Characterization of a Novel β -glucosidase-like Activity from a Soil Metagenome. *J. Microbiol.* 47, 542. doi:10.1007/s12275-009-0024-y
- Jiang, Y., Xin, F., Lu, J., Dong, W., Zhang, W., Zhang, M., et al. (2017). State of the Art Review of Biofuels Production from Lignocellulose by Thermophilic Bacteria. *Bioresour. Technol.* 245, 1498–1506. doi:10.1016/j.biortech.2017.05.142
- Joseph, B., Kumar, V., and Ramteke, P. W. (2019). *Chapter 47-Psychrophilic Enzymes: Potential Biocatalysts for Food Processing*. Academic Press, 817–825. doi:10.1016/B978-0-12-813280-7.00047-5
- Juturu, V., and Wu, J. C. (2014). Microbial Cellulases: Engineering, Production and Applications. *Renew. Sustain. Energ. Rev.* 33, 188–203. doi:10.1016/j.rser.2014.01.077
- Juturu, V., and Wu, J. C. (2012). Microbial Xylanases: Engineering, Production and Industrial Applications. *Biotechnol. Adv.* 30, 1219–1227. doi:10.1016/j.biotechadv.2011.11.006
- Kahn, A., Morais, S., Galanopoulou, A. P., Chung, D., Sarai, N. S., Hengge, N., et al. (2019). Creation of a Functional Hyperthermostable Designer Cellulosome. *Biotechnol. Biofuels* 12, 44. doi:10.1186/s13068-019-1386-y
- Kang, H.-S., and Kim, E.-S. (2021). Recent Advances in Heterologous Expression of Natural Product Biosynthetic Gene Clusters in Streptomyces Hosts. *Curr. Opin. Biotechnol.* 69, 118–127. doi:10.1016/j.copbio.2020.12.016
- Kar, B., Verma, P., den Haan, R., and Sharma, A. K. (2017). Characterization of a Recombinant Thermostable β -glucosidase from *Putranjiva Roxburghii* Expressed in *Saccharomyces cerevisiae* and its Use for Efficient Biomass Conversion. *Process. Biochem.* 63, 66–75. doi:10.1016/j.procbio.2017.08.005
- Karlsson, E. N., Hachem, M. A., Ramchuran, S., Costa, H., Holst, O., Svenningsen, F., et al. (2004). The Modular Xylanase Xyn10A from *Rhodothermus Marinus* Is Cell-Attached, and its C-Terminal Domain Has Several Putative Homologues Among Cell-Attached Proteins within the Phylum Bacteroidetes. *FEMS Microbiol. Lett.* 241, 233–242. doi:10.1016/j.femsle.2004.10.026
- Karnaouri, A., Antonopoulou, I., Zerva, A., Dimarogona, M., Topakas, E., Rova, U., et al. (2019). Thermophilic Enzyme Systems for Efficient Conversion of Lignocellulose to Valuable Products: Structural Insights and Future Perspectives for Esterases and Oxidative Catalysts. *Bioresour. Technol.* 279, 362–372. doi:10.1016/j.biortech.2019.01.062
- Kaur, G., Kumar, S., and Satyanarayana, T. (2004). Production, Characterization and Application of a Thermostable Polyalacturonase of a Thermophilic Mould *Sporotrichum Thermophile* Anpinis. *Bioresour. Technol.* 94, 239–243. doi:10.1016/j.biortech.2003.05.003
- Khandeparkar, R., and Bhosle, N. B. (2006). Purification and Characterization of Thermoalkalophilic Xylanase Isolated from the Enterobacter Sp. MTCC 5112. *Res. Microbiol.* 157, 315–325. doi:10.1016/j.resmic.2005.12.001
- Khare, N., Bhagat, P., Verma, S. K., Yadav, S., Alpheus, A. E., Saxena, S., et al. (2020). *Chapter 1-Filamentous Fungi: An Ideal Host for Heterologous*

- Protein Expression*. Gehlot (Elsevier), 1–9. doi:10.1016/B978-0-12-821008-6.00001-3
- Klein-Marcuschamer, D., Oleskowicz-Popiel, P., Simmons, B. A., and Blanch, H. W. (2012). The Challenge of Enzyme Cost in the Production of Lignocellulosic Biofuels. *Biotechnol. Bioeng.* 109, 1083–1087. doi:10.1002/bit.24370
- Klose, H., Röder, J., Girfoglio, M., Fischer, R., and Commandeur, U. (2012). Hyperthermophilic Endoglucanase for in Planta Lignocellulose Conversion. *Biotechnol. Biofuels* 5, 63. doi:10.1186/1754-6834-5-63
- Kuhad, R. C., Deswal, D., Sharma, S., Bhattacharya, A., Jain, K. K., Kaur, A., et al. (2016). Revisiting Cellulase Production and Redefining Current Strategies Based on Major Challenges. *Renew. Sustain. Energ. Rev.* 55, 249–272. doi:10.1016/j.rser.2015.10.132
- Kurumbang, N. P., Vera, J. M., Hebert, A. S., Coon, J. J., and Landick, R. (2019). Heterologous Glycosyl Hydrolase Expression and Cellular Reprogramming Resembling Sucrose-Induction Enable *Zymomonas Mobilis* Growth on Cellobiose. *bioRxiv* 1, 854646. doi:10.1101/854646
- Lee, C.-K., and Au-Duong, A.-N. (2018). Enzyme Immobilization on Nanoparticles: Recent Applications. *Emerg. Areas Bioeng.* 1, 67–80. doi:10.1002/9783527803293.ch4
- Lee, J., and Park, K. Y. (2020). Impact of Hydrothermal Pretreatment on Anaerobic Digestion Efficiency for Lignocellulosic Biomass: Influence of Pretreatment Temperature on the Formation of Biomass-Degrading Byproducts. *Chemosphere* 256, 127116. doi:10.1016/j.chemosphere.2020.127116
- Lessard, P. A., Li, X., Broomhead, J. N., Parker, M. H., Bailey, C., and Raab, R. M. (2021). Properties of Corn-Expressed Carbohydrase AC1 in Swine Diets and its Effects on Apparent Ileal Digestibility, Performance, Hematology, and Serum Chemistry. *Heliyon* 7, e07696. doi:10.1016/j.heliyon.2021.e07696
- Lewin, A., Zhou, J., Pham, V. T. T., Haugen, T., Zeiny, M., El, O., et al. (2017). Novel Archaeal Thermostable Cellulases from an Oil Reservoir Metagenome. *AMB Express* 7, 183. doi:10.1186/s13568-017-0485-z
- Li, J., Zhang, M.-M., Wan, C., Den Haan, R., Bai, F.-W., and Zhao, X.-Q. (2020a). Improved Cellulase Production in Recombinant *Saccharomyces cerevisiae* by Disrupting the Cell wall Protein-Encoding Gene CWP2. *J. Biosci. Bioeng.* 129, 165–171. doi:10.1016/j.jbiosc.2019.08.012
- Li, L.-L., McCorkle, S. R., Monchy, S., Taghavi, S., and van der Lelie, D. (2009). Bioprospecting Metagenomes: Glycosyl Hydrolases for Converting Biomass. *Biotechnol. Biofuels* 2, 10. doi:10.1186/1754-6834-2-10
- Li, Q., Jiang, Y., Tong, X., Pei, J., Xiao, W., Wang, Z., et al. (2020b). Cloning and Characterization of the β -xylosidase from *Dictyoglomus Turgidum* for High Efficient Biotransformation of 10-Deacetyl-7-Xylosyltaxol. *Bioorg. Chem.* 94, 103357. doi:10.1016/j.bioorg.2019.103357
- Li, Y., Zhai, R., Jiang, X., Chen, X., Yuan, X., Liu, Z., et al. (2019). Boosting Ethanol Productivity of *Zymomonas Mobilis* 8b in Enzymatic Hydrolysate of Dilute Acid and Ammonia Pretreated Corn Stover through Medium Optimization, High Cell Density Fermentation and Cell Recycling. *Front. Microbiol.* 10, 2316. doi:10.3389/fmicb.2019.02316
- Li, Y., Zhang, X., Xiong, L., Mehmood, M. A., Zhao, X., and Bai, F. (2017). On-site Cellulase Production and Efficient Saccharification of Corn stover Employing Cbh2 Overexpressing *Trichoderma Reesei* with Novel Induction System. *Bioresour. Technol.* 238, 643–649. doi:10.1016/j.biortech.2017.04.084
- Liu, Z., Tyo, K. E. J., Martinez, J. L., Petranovic, D., and Nielsen, J. (2012). Different Expression Systems for Production of Recombinant Proteins in *Saccharomyces cerevisiae*. *Biotechnol. Bioeng.* 109, 1259–1268. doi:10.1002/bit.24409
- Madhavan, A., Sindhu, R., Binod, P., Sukumaran, R. K., and Pandey, A. (2017a). Strategies for Design of Improved Biocatalysts for Industrial Applications. *Bioresour. Technol.* 245, 1304–1313. doi:10.1016/j.biortech.2017.05.031
- Madhavan, A., Sindhu, R., Parameswaran, B., Sukumaran, R. K., and Pandey, A. (2017b). Metagenome Analysis: a Powerful Tool for Enzyme Bioprospecting. *Appl. Biochem. Biotechnol.* 183, 636–651. doi:10.1007/s12010-017-2568-3
- Majidian, P., Tabatabaei, M., Zeinolabedini, M., Naghsbandi, M. P., and Chisti, Y. (2018). Metabolic Engineering of Microorganisms for Biofuel Production. *Renew. Sustain. Energ. Rev.* 82, 3863–3885. doi:10.1016/j.rser.2017.10.085
- Maleki, M., Shahraki, M. F., Kavousi, K., Ariaeenejad, S., and Hosseini Salekdeh, G. (2020). A Novel Thermostable Cellulase Cocktail Enhances Lignocellulosic Bioconversion and Biorefining in a Broad Range of pH. *Int. J. Biol. Macromol.* 154, 349–360. doi:10.1016/j.jbiomac.2020.03.100
- Mhiri, S., Bouanane-Darenfed, A., Jemli, S., Neifar, S., Ameri, R., Mezghani, M., et al. (2020). A Thermophilic and Thermostable Xylanase from *Caldicoprobacter Algeriensis*: Recombinant Expression, Characterization and Application in Paper Biobleaching. *Int. J. Biol. Macromol.* 164, 808–817. doi:10.1016/j.jbiomac.2020.07.162
- Mirfakhhar, M., Asadollahi, M. A., Amiri, H., and Karimi, K. (2020). Co-fermentation of Hemicellulosic Hydrolysates and Starch from Sweet Sorghum by *Clostridium Acetobutylicum*: A Synergistic Effect for Butanol Production. *Ind. Crops Prod.* 151, 112459. doi:10.1016/j.indcrop.2020.112459
- Mohanram, S., Amat, D., Choudhary, J., Arora, A., and Nain, L. (2013). Novel Perspectives for Evolving Enzyme Cocktails for Lignocellulose Hydrolysis in Biorefineries. *Sustain. Chem. Process.* 1, 15. doi:10.1186/2043-7129-1-15
- Mohsin, I., Poudel, N., Li, D.-C., and Papageorgiou, A. C. (2019). Crystal Structure of a GH3 β -Glucosidase from the Thermophilic Fungus *Chaetomium Thermophilum*. *Int. J. Mol. Sci.* 20, 5962. doi:10.3390/ijms20235962
- Mrudula Vasudevan, U., Jaiswal, A. K., Krishna, S., and Pandey, A. (2019). Thermostable Phytase in Feed and Fuel Industries. *Bioresour. Technol.* 278, 400–407. doi:10.1016/j.biortech.2019.01.065
- Mukasekuru, M. R., Kaneza, P., Sun, H., Sun, F. F., He, J., and Zheng, P. (2020). Fed-batch High-Solids Enzymatic Saccharification of Lignocellulosic Substrates with a Combination of Additives and Accessory Enzymes. *Ind. Crops Prod.* 146, 112156. doi:10.1016/j.indcrop.2020.112156
- Murray, P., Aro, N., Collins, C., Grassick, A., Penttilä, M., Saloheimo, M., et al. (2004). Expression in *Trichoderma Reesei* and Characterisation of a Thermostable Family 3 β -glucosidase from the Moderately Thermophilic Fungus *Talaromyces emersonii*. *Protein Expr. Purif.* 38, 248–257. doi:10.1016/j.pep.2004.08.006
- Murray, P. G., Grassick, A., Laffey, C. D., Cuffe, M. M., Higgins, T., Savage, A. V., et al. (2001). Isolation and Characterization of a Thermostable Endo- β -Glucanase Active on 1,3-1,4- β -D-Glucans from the Aerobic Fungus *Talaromyces Emersonii* CBS 814.70. *Enzyme Microb. Technol.* 29, 90–98. doi:10.1016/S0141-0229(01)00354-4
- Nakazawa, H., Okada, K., Onodera, T., Ogasawara, W., Okada, H., and Morikawa, Y. (2009). Directed Evolution of Endoglucanase III (Cel12A) from *Trichoderma Reesei*. *Appl. Microbiol. Biotechnol.* 83, 649–657. doi:10.1007/s00253-009-1901-3
- Nøhr, J., Kristiansen, K., and Krogsdam, A.-M. (2003). “Protein Expression in Yeasts BT - Protein Misfolding and Disease: Principles and Protocols,” in *Methods in Molecular Biology* (Totowa, NJ: Humana Press), 111–125. doi:10.1385/1-59259-394-1:111
- Nwamba, M. C., Song, G., Sun, F., Mukasekuru, M. R., Ren, H., Zhang, Q., et al. (2021a). Efficiency Enhancement of a New Cellulase Cocktail at Low Enzyme Loading for High Solid Digestion of Alkali Catalyzed Atmospheric Glycerol Organosolvent Pre-treated Sugarcane Bagasse. *Bioresour. Technol.* 338, 125505. doi:10.1016/j.biortech.2021.125505
- Nwamba, M. C., Sun, F., Mukasekuru, M. R., Song, G., Harindintwali, J. D., Boyi, S. A., et al. (2021b). Trends and Hassles in the Microbial Production of Lactic Acid from Lignocellulosic Biomass. *Environ. Technol. Innov.* 21, 101337. doi:10.1016/j.eti.2020.101337
- Olajuyigbe, F. M., and Ogunyewo, O. A. (2016). Enhanced Production and Physicochemical Properties of Thermostable Crude Cellulase from *Sporothrix Carnis* Grown on Corn Cob. *Biocatal. Agric. Biotechnol.* 7, 110–117. doi:10.1016/j.bcab.2016.05.012
- Oraby, H., Venkatesh, B., Dale, B., Ahmad, R., Ransom, C., Oehmke, J., et al. (2007). Enhanced Conversion of Plant Biomass into Glucose Using Transgenic rice-produced Endoglucanase for Cellulosic Ethanol. *Transgenic Res.* 16, 739–749. doi:10.1007/s11248-006-9064-9
- Pabbathi, N. P. P., Velidandi, A., Gandam, P. K., Koringa, P., Parcha, S. R., and Baadhe, R. R. (2021). Novel buffalo Rumen Metagenome Derived Acidic Cellulase Cel-3.1 Cloning, Characterization, and its Application in Saccharifying rice Straw and Corncob Biomass. *Int. J. Biol. Macromol.* 170, 239–250. doi:10.1016/j.jbiomac.2020.12.041
- Parveen, T., Kamran, M., and Fatmi, M. Q. (2019). Structural and Dynamical Thermostability of Psychrophilic Enzyme at Various Temperatures: Molecular Dynamics Simulations of Tryptophan Synthase. *Arch. Biochem. Biophys.* 663, 297–305. doi:10.1016/j.abb.2019.01.022

- Patel, A. K., Singhanian, R. R., Sim, S. J., and Pandey, A. (2019). Thermostable Cellulases: Current Status and Perspectives. *Bioresour. Technol.* 279, 385–392. doi:10.1016/j.biortech.2019.01.049
- Patel, K., and Dudhagara, P. (2020). Optimization of Xylanase Production by *Bacillus Tequilensis* Strain UD-3 Using Economical Agricultural Substrate and its Application in rice Straw Pulp Bleaching. *Biocatal. Agric. Biotechnol.* 30, 101846. doi:10.1016/j.bcab.2020.101846
- Pereira, S. C., Maehara, L., Machado, C. M. M., and Farinas, C. S. (2016). Physical–chemical–morphological Characterization of the Whole Sugarcane Lignocellulosic Biomass Used for 2G Ethanol Production by Spectroscopy and Microscopy Techniques. *Renew. Energ.* 87, 607–617. doi:10.1016/j.renene.2015.10.054
- Phitsuwon, P., Sakka, K., and Ratanakhanokchai, K. (2013). Improvement of Lignocellulosic Biomass in Planta: A Review of Feedstocks, Biomass Recalcitrance, and Strategic Manipulation of Ideal Plants Designed for Ethanol Production and Processability. *Biomass and Bioenergy* 58, 390–405. doi:10.1016/j.biombioe.2013.08.027
- Pihlajaniemi, V., Kallioinen, A., Sipponen, M. H., and Nyyssölä, A. (2021). Modeling and Optimization of Polyethylene Glycol (PEG) Addition for Cost-Efficient Enzymatic Hydrolysis of Lignocellulose. *Biochem. Eng. J.* 167, 107894. doi:10.1016/j.bej.2020.107894
- Ping, L., Wang, M., Yuan, X., Cui, F., Huang, D., Sun, W., et al. (2018). Production and Characterization of a Novel Acidophilic and Thermostable Xylanase from *Thermoascus Aurantiacus*. *Int. J. Biol. Macromol.* 109, 1270–1279. doi:10.1016/j.ijbiomac.2017.11.130
- Potprommanee, L., Wang, X.-Q., Han, Y.-J., Nyobe, D., Peng, Y.-P., Huang, Q., et al. (2017). Characterization of a Thermophilic Cellulase from *Geobacillus* Sp. HTA426, an Efficient Cellulase-Producer on Alkali Pretreated of Lignocellulosic Biomass. *PLoS One* 12, e0175004. doi:10.1371/journal.pone.0175004
- Potvin, G., Ahmad, A., and Zhang, Z. (2012). Bioprocess Engineering Aspects of Heterologous Protein Production in *Pichia pastoris*: A Review. *Biochem. Eng. J.* 64, 91–105. doi:10.1016/j.bej.2010.07.017
- Prasad, G. S. (2019). “Pharmaceutical Applications of Thermophilic Fungi BT - Fungi in Extreme Environments: Ecological Role and Biotechnological Significance,” in *Fungi in Extreme Environments: Ecological Role and Biotechnological Significance* (Cham: Springer International Publishing), 269–289. doi:10.1007/978-3-030-19030-9_14
- Prasad, R. K., Chatterjee, S., Sharma, S., Mazumder, P. B., Vairale, M. G., and Raju, P. S. (2018). “Insect Gut Bacteria and Their Potential Application in Degradation of Lignocellulosic Biomass: A Review BT - Bioremediation: Applications for Environmental Protection and Management,” in *Bioremediation: Applications for Environmental Protection and Management*. Editors S. J. Varjani, A. K. Agarwal, E. Gnansounou, and B. Gurusathan (Singapore: Springer), 277–299. doi:10.1007/978-981-10-7485-1_14
- Rai, M., Ingle, A. P., Pandit, R., Paralikar, P., Biswas, J. K., and da Silva, S. S. (2019). Emerging Role of Nanobiocatalysts in Hydrolysis of Lignocellulosic Biomass Leading to Sustainable Bioethanol Production. *Catal. Rev.* 61, 1–26. doi:10.1080/01614940.2018.1479503
- Raj, A., Kumar, S., Singh, S. K., and Prakash, J. (2018). Production and Purification of Xylanase from Alkaliphilic *Bacillus Licheniformis* and its Pretreatment of eucalyptus Kraft Pulp. *Biocatal. Agric. Biotechnol.* 15, 199–209. doi:10.1016/j.bcab.2018.06.018
- Ray, R. C., and Behera, S. S. (2017). “Chapter 3-Solid State Fermentation for Production of Microbial Cellulases,” in *Biotechnology of Microbial Enzymes* (Academic Press), 43–79. doi:10.1016/B978-0-12-803725-6.00003-0
- Rigoldi, F., Donini, S., Redaelli, A., Parisini, E., and Gautieri, A. (2018). Review: Engineering of Thermostable Enzymes for Industrial Applications. *APL Bioeng.* 2, 11501. doi:10.1063/1.4997367
- Robledo, A., Aguilar, C. N., Belmares-Cerda, R. E., Flores-Gallegos, A. C., Contreras-Esquivel, J. C., Montañez, J. C., et al. (2016). Production of Thermostable Xylanase by Thermophilic Fungal Strains Isolated from maize Silage. *Cyta - J. Food* 14, 302–308. doi:10.1080/19476337.2015.1105298
- Rosmine, E., Sainjan, N. C., Silvester, R., Alikkunju, A., and Varghese, S. A. (2017). Statistical Optimisation of Xylanase Production by Estuarine *Streptomyces* Sp. And its Application in Clarification of Fruit Juice. *J. Genet. Eng. Biotechnol.* 15, 393–401. doi:10.1016/j.jgeb.2017.06.001
- Rungtattanakasin, B., Premjet, S., Thanonkeo, S., Klanrit, P., and Thanonkeo, P. (2018). Cloning and Expression of an Endoglucanase Gene from the Thermotolerant Fungus *Aspergillus fumigatus* DBiNU-1 in *Kluyveromyces Lactis*. *Braz. J. Microbiol.* 49, 647–655. doi:10.1016/j.bjm.2017.10.001
- Saini, S., Chandel, A. K., and Sharma, K. K. (2020). Past Practices and Current Trends in the Recovery and Purification of First Generation Ethanol: A Learning Curve for Lignocellulosic Ethanol. *J. Clean. Prod.* 268, 122357. doi:10.1016/j.jclepro.2020.122357
- Shen, F., Ling, H., Ge, W., Yang, Y., Wang, X., Ren, J., et al. (2021). Self-assembly Behavior and Conformation of Amphiphilic Hemicellulose-Graft-Fatty Acid Micelles. *Carbohydr. Polym.* 261, 117886. doi:10.1016/j.carbpol.2021.117886
- Shi, R., Li, Z., Ye, Q., Xu, J., and Liu, Y. (2013). Heterologous Expression and Characterization of a Novel Thermo-Halotolerant Endoglucanase Cel5H from *Dictyoglomus Thermophilum*. *Bioresour. Technol.* 142, 338–344. doi:10.1016/j.biortech.2013.05.037
- Shi, X., Zhao, L., Pei, J., Ge, L., Wan, P., Wang, Z., et al. (2018). Highly Enhancing the Characteristics of Immobilized Thermostable β -glucosidase by Zn²⁺. *Process. Biochem.* 66, 89–96. doi:10.1016/j.procbio.2018.01.004
- Singh, A., Bajar, S., Devi, A., and Pant, D. (2021a). An Overview on the Recent Developments in Fungal Cellulase Production and Their Industrial Applications. *Bioresour. Technol. Rep.* 14, 100652. doi:10.1016/j.biteb.2021.100652
- Singh, N., Mathur, A. S., Gupta, R. P., Barrow, C. J., Tuli, D. K., and Puri, M. (2021b). Enzyme Systems of Thermophilic Anaerobic Bacteria for Lignocellulosic Biomass Conversion. *Int. J. Biol. Macromol.* 168, 572–590. doi:10.1016/j.ijbiomac.2020.12.004
- Singh, R., Kumar, R., Bishnoi, K., and Bishnoi, N. R. (2009). Optimization of Synergistic Parameters for Thermostable Cellulase Activity of *Aspergillus heteromorphus* Using Response Surface Methodology. *Biochem. Eng. J.* 48, 28–35. doi:10.1016/j.bej.2009.08.001
- Solarte-Toro, J. C., Romero-García, J. M., Martínez-Patiño, J. C., Ruiz-Ramos, E., Castro-Galiano, E., and Cardona-Alzate, C. A. (2019). Acid Pretreatment of Lignocellulosic Biomass for Energy Vectors Production: A Review Focused on Operational Conditions and Techno-Economic Assessment for Bioethanol Production. *Renew. Sustain. Energ. Rev.* 107, 587–601. doi:10.1016/j.rser.2019.02.024
- Spohner, S. C., Schaum, V., Quitmann, H., and Czermak, P. (2016). *Kluyveromyces Lactis*: An Emerging Tool in Biotechnology. *J. Biotechnol.* 222, 104–116. doi:10.1016/j.jbiotec.2016.02.023
- Stephens, D. E., Khan, F. I., Singh, P., Bisetty, K., Singh, S., and Permaul, K. (2014). Creation of Thermostable and Alkaline Stable Xylanase Variants by DNA Shuffling. *J. Biotechnol.* 187, 139–146. doi:10.1016/j.jbiotec.2014.07.446
- Straub, C. T., Counts, J. A., Nguyen, D. M. N., Wu, C.-H., Zeldes, B. M., Crosby, J. R., et al. (2018). Biotechnology of Extremely Thermophilic Archaea. *FEMS Microbiol. Rev.* 42, 543–578. doi:10.1093/femsre/fuy012
- Sun, M., Zheng, H., Meng, L., Sun, J., Song, H., Bao, Y., et al. (2015). Direct Cloning, Expression of a Thermostable Xylanase Gene from the Metagenomic DNA of Cow Dung Compost and Enzymatic Production of Xylooligosaccharides from Corn cob. *Biotechnol. Lett.* 37, 1877–1886. doi:10.1007/s10529-015-1857-6
- Sun, S.-F., Yang, H.-Y., Yang, J., Wang, D.-W., and Shi, Z.-J. (2021). Integrated Treatment of Perennial Ryegrass: Structural Characterization of Hemicelluloses and Improvement of Enzymatic Hydrolysis of Cellulose. *Carbohydr. Polym.* 254, 117257. doi:10.1016/j.carbpol.2020.117257
- Tang, F., Chen, D., Yu, B., Luo, Y., Zheng, P., Mao, X., et al. (2017). Improving the Thermostability of *Trichoderma Reesei* Xylanase 2 by Introducing Disulfide Bonds. *Electron. J. Biotechnol.* 26, 52–59. doi:10.1016/j.ejbt.2017.01.001
- Tao, L., Tan, E. C. D., McCormick, R., Zhang, M., Aden, A., He, X., et al. (2014). Techno-economic Analysis and Life-Cycle Assessment of Cellulosic Isobutanol and Comparison with Cellulosic Ethanol and N-Butanol. *Biofuels, Bioprod. Biorefining* 8, 30–48. doi:10.1002/bbb.1431
- Tekkkol, G. E., Sargin, S., Karaçanci, S., Pembeci, C., Mandaci, S., Akgun, I. H., et al. (2017). Production of GH11 Xylanase for Bakery Industry by Solid State Fermentation. *J. Biotechnol.* 256 (S55), 1. doi:10.1016/j.jbiotec.2017.06.985
- Thapa, S., Mishra, J., Arora, N., Mishra, P., Li, H., O’Hair, J., et al. (2020). Microbial Cellulolytic Enzymes: Diversity and Biotechnology with Reference to

- Lignocellulosic Biomass Degradation. *Rev. Environ. Sci. Bio/technology* 19, 621–648. doi:10.1007/s11157-020-09536-y
- Thomas, L., Joseph, A., and Gottumukkala, L. D. (2014a). Xylanase and Cellulase Systems of *Clostridium* sp.: An Insight on Molecular Approaches for Strain Improvement. *Bioresour. Technol.* 158, 343–350. doi:10.1016/j.biortech.2014.01.140
- Thomas, L., Ushasree, M. V., and Pandey, A. (2014b). An Alkali-Thermostable Xylanase from *Bacillus Pumilus* Functionally Expressed in *Kluyveromyces Lactis* and Evaluation of its Deinking Efficiency. *Bioresour. Technol.* 165, 309–313. doi:10.1016/j.biortech.2014.03.037
- Tian, S.-Q., Zhao, R.-Y., and Chen, Z.-C. (2018). Review of the Pretreatment and Bioconversion of Lignocellulosic Biomass from Wheat Straw Materials. *Renew. Sustain. Energ. Rev.* 91, 483–489. doi:10.1016/j.rser.2018.03.113
- Tong, X., Qi, Z., Zheng, D., Pei, J., Li, Q., and Zhao, L. (2021). High-level Expression of a Novel Multifunctional GH3 Family β -xylosidase/ α -arabinosidase/ β -glucosidase from *Dictyoglomus Turgidum* in *Escherichia coli*. *Bioorg. Chem.* 111, 104906. doi:10.1016/j.bioorg.2021.104906
- Toushik, S. H., Lee, K.-T., Lee, J.-S., and Kim, K.-S. (2017). Functional Applications of Lignocellulolytic Enzymes in the Fruit and Vegetable Processing Industries. *J. Food Sci.* 82, 585–593. doi:10.1111/1750-3841.13636
- Upreti, R. K., Kumar, M., and Shankar, V. (2003). Bacterial Glycoproteins: Functions, Biosynthesis and Applications. *Proteomics* 3, 363–379. doi:10.1002/pmic.200390052
- Uzuner, S., and Cekmecelioglu, D. (2019). “Chapter 3-Enzymes in the Beverage Industry,” in *Enzymes in Food Biotechnology* (Academic Press), 29–43. doi:10.1016/B978-0-12-813280-7.00003-7
- van den Brink, J., van Muiswinkel, G. C. J., Theelen, B., Hinz, S. W. A., and de Vries, R. P. (2013). Efficient Plant Biomass Degradation by Thermophilic Fungus *Myceliophthora Heterothallica*. *Appl. Environ. Microbiol.* 79, 1316–1324. doi:10.1128/AEM.02865-12
- Van Dorn, R., Shanahan, D., and Ciofalo, V. (2018). Safety Evaluation of Xylanase 50316 Enzyme Preparation (Also Known as VR007), Expressed in *Pseudomonas Fluorescens*, Intended for Use in Animal Feed. *Regul. Toxicol. Pharmacol.* 97, 48–56. doi:10.1016/j.yrtph.2018.05.016
- Verma, D., Kawarabayasi, Y., Miyazaki, K., and Satyanarayana, T. (2013). Cloning, Expression and Characteristics of a Novel Alkalistable and Thermostable Xylanase Encoding Gene (Mxyl) Retrieved from Compost-Soil Metagenome. *PLoS One* 8, e52459. doi:10.1371/journal.pone.0052459
- Viikari, L., Alapuranen, M., Puranen, T., Vehmaanperä, J., and Siika-aho, M. (2007). “Thermostable Enzymes in Lignocellulose Hydrolysis BT - Biofuels,” in *Advances in Biochemical Engineering/Biotechnology*. Editor L. Olsson (Berlin, Heidelberg: Springer), 121–145. doi:10.1007/10_2007_065
- Wahab, A. F. F. A., Karim, A. N. A., Ling, J. G., Hasan, N. S., Yong, H. Y., Bharudin, I., et al. (2019). Functional Characterisation of Cellobiohydrolase I (Cbh1) from *Trichoderma Virens* UKM1 Expressed in *Aspergillus niger*. *Protein Expr. Purif.* 154, 52–61. doi:10.1016/j.pep.2018.09.014
- Wang, H., Lin, X., Li, S., Lin, J., Xie, C., Liu, D., et al. (2020a). Rational Molecular Design for Improving Digestive Enzyme Resistance of Beta-Glucosidase from *Trichoderma Viride* Based on Inhibition of Bound State Formation. *Enzyme Microb. Technol.* 133, 109465. doi:10.1016/j.enzmictec.2019.109465
- Wang, K., Luo, H., Bai, Y., Shi, P., Huang, H., Xue, X., et al. (2014). A Thermophilic Endo-1,4- β -Glucanase from *Talaromyces emersonii* CBS394.64 with Broad Substrate Specificity and Great Application Potentials. *Appl. Microbiol. Biotechnol.* 98, 7051–7060. doi:10.1007/s00253-014-5680-0
- Wang, L., Mou, Y., Guan, B., Hu, Y., Zhang, Y., Zeng, J., et al. (2020b). Genome Sequence of the Psychrophilic Cryobacterium Sp. LW097 and Characterization of its Four Novel Cold-Adapted β -galactosidases. *Int. J. Biol. Macromol.* 163, 2068–2083. doi:10.1016/j.ijbiomac.2020.09.100
- Wang, X.-C., You, S.-P., Zhang, J.-X., Dai, Y.-M., Zhang, C.-Y., Qi, W., et al. (2018). Rational Design of a Thermophilic β -mannanase from *Bacillus Subtilis* TJ-102 to Improve its Thermostability. *Enzyme Microb. Technol.* 118, 50–56. doi:10.1016/j.enzmictec.2018.07.005
- Wang, X., Nie, Y., and Xu, Y. (2019). Industrially Produced Pullulanases with Thermostability: Discovery, Engineering, and Heterologous Expression. *Bioresour. Technol.* 278, 360–371. doi:10.1016/j.biortech.2019.01.098
- Wang, Y., Fu, Z., Huang, H., Zhang, H., Yao, B., Xiong, H., et al. (2012). Improved thermal Performance of *Thermomyces Lanuginosus* GH11 Xylanase by Engineering of an N-Terminal Disulfide Bridge. *Bioresour. Technol.* 112, 275–279. doi:10.1016/j.biortech.2012.02.092
- Ward, O. P. (2012). Production of Recombinant Proteins by Filamentous Fungi. *Biotechnol. Adv.* 30, 1119–1139. doi:10.1016/j.biotechadv.2011.09.012
- Wilson, D. B. (2009). Cellulases and Biofuels. *Curr. Opin. Biotechnol.* 20, 295–299. doi:10.1016/j.copbio.2009.05.007
- Wonganu, B., Pootanakit, K., Boonyapakron, K., Champreda, V., Tanapongpipat, S., and Eurwilaichitr, L. (2008). Cloning, Expression and Characterization of a Thermotolerant Endoglucanase from *Syncephalastrum Racemosum* (BCC18080) in *Pichia pastoris*. *Protein Expr. Purif.* 58, 78–86. doi:10.1016/j.pep.2007.10.022
- Wu, H., Cheng, X., Zhu, Y., Zeng, W., Chen, G., and Liang, Z. (2018). Purification and Characterization of a Cellulase-free, Thermostable Endo-Xylanase from *Streptomyces Griseorubens* LH-3 and its Use in Biobleaching on eucalyptus Kraft Pulp. *J. Biosci. Bioeng.* 125, 46–51. doi:10.1016/j.jbiosc.2017.08.006
- Xin, F., and He, J. (2013). Characterization of a Thermostable Xylanase from a Newly Isolated *Kluyvera* Species and its Application for Biobutanol Production. *Bioresour. Technol.* 135, 309–315. doi:10.1016/j.biortech.2012.10.002
- Xing, H., Zou, G., Liu, C., Chai, S., Yan, X., Li, X., et al. (2021). Improving the Thermostability of a GH11 Xylanase by Directed Evolution and Rational Design Guided by B-Factor Analysis. *Enzyme Microb. Technol.* 143, 109720. doi:10.1016/j.enzmictec.2020.109720
- Xu, P., Ni, Z.-F., Zong, M.-H., Ou, X.-Y., Yang, J.-G., and Lou, W.-Y. (2020). Improving the Thermostability and Activity of *Paenibacillus Pasadenensis* Chitinase through Semi-rational Design. *Int. J. Biol. Macromol.* 150, 9–15. doi:10.1016/j.ijbiomac.2020.02.033
- Xu, X., Liu, M., Huo, W., and Dai, X. (2016). Obtaining a Mutant of *Bacillus Amyloliquefaciens* Xylanase A with Improved Catalytic Activity by Directed Evolution. *Enzyme Microb. Technol.* 86, 59–66. doi:10.1016/j.enzmictec.2016.02.001
- Xue, D., Zeng, X., Lin, D., and Yao, S. (2019). Thermostable Ethanol Tolerant Xylanase from a Cold-Adapted marine Species *Acinetobacter Johnsonii*. *Chinese J. Chem. Eng.* 27, 1166–1170. doi:10.1016/j.cjche.2018.06.019
- Yadav, P., Maharjan, J., Korpole, S., Prasad, G. S., Sahni, G., Bhattarai, T., et al. (2018). Production, Purification, and Characterization of Thermostable Alkaline Xylanase from *Anoxybacillus Kamchatkensis* NASTPD13. *Front. Bioeng. Biotechnol.* 6, 65. doi:10.3389/fbioe.2018.00065
- Yan, Q., Hua, C., Yang, S., Li, Y., and Jiang, Z. (2012). High Level Expression of Extracellular Secretion of a β -glucosidase Gene (PtBglu3) from *Paecilomyces Thermophila* in *Pichia pastoris*. *Protein Expr. Purif.* 84, 64–72. doi:10.1016/j.pep.2012.04.016
- Yang, G., Yang, D., Wang, X., and Cao, W. (2021). A Novel Thermostable Cellulase-Producing *Bacillus Licheniformis* A5 Acts Synergistically with *Bacillus Subtilis* B2 to Improve Degradation of Chinese Distillers’ Grains. *Bioresour. Technol.* 325, 124729. doi:10.1016/j.biortech.2021.124729
- Yang, H., Yi, N., Zhao, S., Qaseem, M. F., Zheng, B., Li, H., et al. (2020a). Characterization of Hemicelluloses in Sugarcane (*Saccharum* Spp. Hybrids) Culm during Xylogenesis. *Int. J. Biol. Macromol.* 165, 1119–1128. doi:10.1016/j.ijbiomac.2020.09.242
- Yang, H., Zhang, Y., Li, X., Bai, Y., Xia, W., Ma, R., et al. (2018). Impact of Disulfide Bonds on the Folding and Refolding Capability of a Novel Thermostable GH45 Cellulase. *Appl. Microbiol. Biotechnol.* 102, 9183–9192. doi:10.1007/s00253-018-9256-2
- Yang, J., Ma, T., Shang-guan, F., and Han, Z. (2020b). Improving the Catalytic Activity of Thermostable Xylanase from *Thermotoga Maritima* via Mutagenesis of Non-catalytic Residues at Glycone Subsites. *Enzyme Microb. Technol.* 139, 109579. doi:10.1016/j.enzmictec.2020.109579
- Yang, S., Yang, B., Duan, C., Fuller, D. A., Wang, X., Chowdhury, S. P., et al. (2019). Applications of Enzymatic Technologies to the Production of High-Quality Dissolving Pulp: A Review. *Bioresour. Technol.* 281, 440–448. doi:10.1016/j.biortech.2019.02.132
- Yang, Z., and Zhang, Z. (2017). Codon-optimized Expression and Characterization of a pH Stable Fungal Xylanase in *Pichia pastoris*. *Process. Biochem.* 53, 80–87. doi:10.1016/j.procbio.2016.11.022
- Yeoman, C. J., Han, Y., Dodd, D., Schroeder, C. M., Mackie, R. I., and Cann, I. K. O. B. T.-A. (2010). “Chapter 1-Thermostable Enzymes as Biocatalysts in the Biofuel Industry,” in *Advances in Applied Microbiology* (Academic Press), 1–55. doi:10.1016/S0065-2164(10)70001-0

- Yu, J., Liu, X., Guan, L., Jiang, Z., Yan, Q., and Yang, S. (2021). High-level Expression and Enzymatic Properties of a Novel Thermostable Xylanase with High Arabinoxylan Degradation Ability from *Chaetomium* Sp. Suitable for Beer Mashing. *Int. J. Biol. Macromol.* 168, 223–232. doi:10.1016/j.ijbiomac.2020.12.040
- Zarafeta, D., Kissas, D., Sayer, C., Gudbergsdottir, S. R., Ladoukakis, E., Isupov, M. N., et al. (2016). Discovery and Characterization of a Thermostable and Highly Halotolerant GH5 Cellulase from an Icelandic Hot Spring Isolate. *PLoS One* 11, e0146454. doi:10.1371/journal.pone.0146454
- Zhang, J., Pan, J., Guan, G., Li, Y., Xue, W., Tang, G., et al. (2008). Expression and High-Yield Production of Extremely Thermostable Bacterial xylanaseB in *Aspergillus niger*. *Enzyme Microb. Technol.* 43, 513–516. doi:10.1016/j.enzmictec.2008.07.010
- Zhang, Q., Zhang, W., Lin, C., Xu, X., and Shen, Z. (2012). Expression of an *Acidothermus Cellulolyticus* Endoglucanase in Transgenic rice Seeds. *Protein Expr. Purif.* 82, 279–283. doi:10.1016/j.pep.2012.01.011
- Zhang, X., Li, Y., Zhao, X., and Bai, F. (2017). Constitutive Cellulase Production from Glucose Using the Recombinant *Trichoderma Reesei* Strain Overexpressing an Artificial Transcription Activator. *Bioresour. Technol.* 223, 317–322. doi:10.1016/j.biortech.2016.10.083
- Zhang, Z.-G., Yi, Z.-L., Pei, X.-Q., and Wu, Z.-L. (2010). Improving the Thermostability of *Geobacillus Stearothermophilus* Xylanase XT6 by Directed Evolution and Site-Directed Mutagenesis. *Bioresour. Technol.* 101, 9272–9278. doi:10.1016/j.biortech.2010.07.060
- Zhao, L., Meng, K., Shi, P., Bai, Y., Luo, H., Huang, H., et al. (2013). A Novel Thermophilic Xylanase from *Achaetomium* Sp. Xz-8 with High Catalytic Efficiency and Application Potentials in the Brewing and Other Industries. *Process. Biochem.* 48, 1879–1885. doi:10.1016/j.procbio.2013.08.020
- Zhong, C., Chen, C., Wang, L., and Ning, K. (2021). Integrating Pan-Genome with Metagenome for Microbial Community Profiling. *Comput. Struct. Biotechnol. J.* 19, 1458–1466. doi:10.1016/j.csbj.2021.02.021
- Zhuo, R., Yu, H., Qin, X., Ni, H., Jiang, Z., Ma, F., et al. (2018). Heterologous Expression and Characterization of a Xylanase and Xylosidase from white Rot Fungi and Their Application in Synergistic Hydrolysis of Lignocellulose. *Chemosphere* 212, 24–33. doi:10.1016/j.chemosphere.2018.08.062
- Ziegelhoffer, T., Raasch, J. A., and Austin-Phillips, S. (2009). Expression of *Acidothermus Cellulolyticus* E1 Endo- β -1,4-Glucanase Catalytic Domain in Transplastomic Tobacco. *Plant Biotechnol. J.* 7, 527–536. doi:10.1111/j.1467-7652.2009.00421.x

Conflict of Interest: The authors declare that the research was conducted in the absence of any commercial or financial relationships that could be construed as a potential conflict of interest.

Publisher's Note: All claims expressed in this article are solely those of the authors and do not necessarily represent those of their affiliated organizations, or those of the publisher, the editors and the reviewers. Any product that may be evaluated in this article, or claim that may be made by its manufacturer, is not guaranteed or endorsed by the publisher.

Copyright © 2021 Ajeje, Hu, Song, Peter, Afful, Sun, Asadollahi, Amiri, Abdulkhani and Sun. This is an open-access article distributed under the terms of the Creative Commons Attribution License (CC BY). The use, distribution or reproduction in other forums is permitted, provided the original author(s) and the copyright owner(s) are credited and that the original publication in this journal is cited, in accordance with accepted academic practice. No use, distribution or reproduction is permitted which does not comply with these terms.



Improved Release of Monosaccharides and Ferulic Acid Using Enzyme Blends From *Aspergillus Niger* and *Eupenicillium Parvum*

Zhenghui Liu¹, Enze Shi¹, Feng Ma¹, Xin Zhou² and Kankan Jiang^{1*}

¹School of Basic Medical Sciences and Forensic Medicine, Hangzhou Medical College, Hangzhou, China, ²Jiangsu Co-innovation Center of Efficient Processing and Utilization of Forest Resources, College of Chemical Engineering, Nanjing Forestry University, Nanjing, China

OPEN ACCESS

Edited by:

Helen Treichel,
Universidade Federal da Fronteira Sul,
Brazil

Reviewed by:

Anne S. Meyer,
Technical University of Denmark,
Denmark
Héctor A. Ruiz,
Universidad Autónoma de Coahuila,
Mexico

*Correspondence:

Kankan Jiang
jiangkankan@126.com

Specialty section:

This article was submitted to
Bioprocess Engineering,
a section of the journal
Frontiers in Bioengineering and
Biotechnology

Received: 13 November 2021

Accepted: 17 December 2021

Published: 27 January 2022

Citation:

Liu Z, Shi E, Ma F, Zhou X and Jiang K
(2022) Improved Release of
Monosaccharides and Ferulic Acid
Using Enzyme Blends From *Aspergillus
Niger* and *Eupenicillium Parvum*.
Front. Bioeng. Biotechnol. 9:814246.
doi: 10.3389/fbioe.2021.814246

Supplementing commercial xylanase and cellulase with selected debranching enzymes only resulted in slight enhancement of the enzymatic hydrolysis of wheat bran autohydrolysis residues (WBAR) which was obtained at 160°C over a 30-min period of autohydrolysis, while a blend of enzymes from *Aspergillus niger* and *Eupenicillium parvum* achieved synergistic efficacy in this context. Using an equal mixture blend of these enzymes at a 0.5% (w/w) enzyme loading dosage with the addition of ferulic acid esterase (1 U/g substrate), the obtained hydrolysis yields were desirable, including 84.98% of glucose, 84.74% of xylose, 80.24% of arabinose, and 80.86% of ferulic acid. Following further separation using an HP-20 resin, the final ferulic acid recovery levels were as high as 62.5% of the esterified ferulic acid present within the initial WBAR input. Together, these data suggest that a combination of autohydrolysis and enzymatic hydrolysis using crude enzyme blends can efficiently achieve wheat bran enzymatic saccharification and associated ferulic acid release.

Keywords: wheat bran autohydrolysis residue, enzymatic hydrolysis, monosaccharide, ferulic acid, enzyme blend

INTRODUCTION

Wheat bran, which accounts for 25% of the weight of wheat grains, is a byproduct of the wheat production process. Approximately 150 million tons of wheat bran are generated globally each year, and this bran is most commonly utilized as a feed for livestock (Si et al., 2020). However, bran-based feeds are of low commercial value, leading to efforts in the wheat industry to convert this byproduct into a higher value commodity. Wheat bran is composed primarily of arabinoxylan (38–55% of dry mass), cellulose (16–30%), and esterified ferulic acid (~1%). Ferulic acid (FA) offers value as an antimicrobial compound with antioxidant properties, and it can additionally serve as a preservative for food products (Li et al., 2021; Hu et al., 2022). Moreover, it can be converted into vanillin for use as a flavoring agent in the food and perfume industries (Ferri et al., 2020). Wheat bran thus represents an ideal low-cost, abundant, organic source of natural FA production and a valuable source for other biochemical compounds of potential commercial value.

Most studies to date have primarily focused on preparing and processing wheat bran-derived xylooligosaccharides (Mathew et al., 2017; Wu et al., 2017; Bhattacharya et al., 2020; Sonkar et al.,

2021) or arabinoxylan (Aguedo et al., 2014; Sánchez-Bastardo et al., 2017; Kaur et al., 2021). Other researchers have sought to improve wheat bran utilization efficiency by developing approaches to generating fermentable sugars as products of wheat bran decomposition, providing an efficient source for the precursors necessary for bioethanol preparation. Enzymatic saccharification can maintain the production of these fermentable sugars without favoring the concomitant production of inhibitory compounds (Huang et al., 2022). However, achieving complete enzyme-mediated hydrolysis of raw wheat bran remains challenging owing to the complexity and heterogeneity of arabinoxylan. Wheat bran arabinoxylan exhibits a high degree of substitution, with a β -1,4-linked xylopyranose backbone linked to α -L-arabinofuranose units that can either be unsubstituted or exhibit xylose C(O)-2 and/or C(O)-3 substitutions (Gullón et al., 2014). Moreover, these molecules can exhibit α -1,2-linked glucuronic, acetyl, D-galactopyranosyl or methyl-glucuronic acid residue substituents, and ferulic acid can be esterified to arabinose units at the O-5 position (Mathew and Abraham, 2004; Ma et al., 2012; Peng et al., 2012). Additionally, ferulic acid can form dehydromers that can facilitate arabinoxylan polymer cross-linking (Mandalari et al., 2005). Owing to these complexities, highly efficient enzymatic cocktails are essential to fully unlock the commercial and biological potential of wheat bran polysaccharides. On the other hand, in prior studies, the underlying utility of wheat bran-derived ferulic acid generated in the context of enzymatic hydrolysis has largely been overlooked, highlighting an untapped resource that has the potential to be enriched from prepared enzymatic hydrolysates.

To alter the chemical and microscopic structural properties of wheat bran and to increase its amenability to subsequent enzymatic hydrolysis, bran initially undergoes pretreatment processing. Prior studies focused on bioethanol production have utilized H_2SO_4 , H_3PO_4 , or other acids to liberate sugars from wheat bran (Palmarola-Adrados et al., 2005; Cripwell et al., 2015; Nair et al., 2015). While this resulted in acceptable rates of sugar recovery, such harsh acidic pretreatment ultimately results in the degradation of a portion of the sugar molecules. In contrast, hydrothermal autohydrolysis-based pretreatment efforts are cost-effective, straightforward, and do not incur significant environmental harm (Batalha et al., 2015; Khalili and Amiri, 2020; Wang et al., 2021). Mild heat-based autohydrolysis treatment can facilitate partial arabinoxylan depolymerization and debranching, breaking down complex hemicellulose molecular networks within wheat bran. However, the full degradation of wheat bran substrates necessitates the use of a complex enzymatic mixture including both cellulolytic and hemicellulolytic enzymes. Owing to enzymatic synergy such that the products of a given reaction can serve as substrates for a different enzyme, crude enzyme extract blends with extensive enzyme activities can enhance lignocellulose hydrolytic efficiency (Saini et al., 2016). For example, α -L-arabinofuranosidases are unable to liberate L-arabinofuranosyl residue (Araf) that are esterified with phenolic acids (Biely et al., 2016). Therefore, the prior action of ferulic acid esterase (FAE) to liberate *trans*-ferulic acid from 5-O-feruloylated Araf is essential for the subsequent action of α -L-arabinofuranosidases. Besides,

WB xylan backbone is highly substituted with arabinofuranosyl substituents singly attached to C(O)-2/C(O)-3, or doubly linked to C(O)-2,3 of the xylose residues (Sørensen et al., 2007a; Sakamoto et al., 2011). These arabinose substitutions partly impede the action of endo-xylanase by causing steric hindrance for accessing the β -1,4-bonds in xylan, resulting in the limited release of xylobiose, xylotriose and other short-chain xylooligosaccharides from partially shaved xylan backbone (Sørensen et al., 2005; Sørensen et al., 2007a). In other words, the depolymerization of xylan backbone by endo-xylanase is depended on the removal of the arabinofuranosyl residues from arabinoxylan by arabinofuranosidases catalysis, and this depolymerization also makes β -xylosidase perform better on the catalysis release of xylose from produced xylobiose, xylotriose, and short-chain xylooligosaccharides (Sørensen et al., 2005; Sørensen et al., 2007b). As such, wheat bran autohydrolysis residue (WBAR) derived from the pretreatment of de-starched wheat bran using hot water was subjected to further enzymatic hydrolysis in order to facilitate monosaccharide and FA recovery through synergistic enzymatic activity using a blend of crude enzymatic extracts derived from *Aspergillus niger* and *Eupenicillium parvum*. This strategy offers potential value as a reliable approach to biomass hydrolysis for the preparation of fermentable sugars and natural FA. Many different fungal strains such as those belonging to *Aspergillus*, *Trichoderma* as well as *Penicillium*, and their combinations have been used to prepare synergistic cellulase blends either by co-culture or by mixing of broths in the past. However, as far as our knowledge is concerned, there are fewer reports on the synergistic crude enzyme preparations from *Eupenicillium* and *Aspergillus*.

MATERIALS AND METHODS

Materials

Wheat bran was obtained from Nanyang, Henan Province, China, and was treated with papain and amylase (Imperial Jade Biotechnology Co., Ltd., Ningxia, China) based on a modified version of the protocol developed by Rose and Inglett to yield de-starched WB (DSWB) (Rose and Inglett, 2010). One hundred grams of wheat bran were treated with 0.3% amylase enzyme solution at 65°C for 30 min, and then incubated at 55°C for 30 min after addition of 0.3% (w/v) papain enzyme, followed by heat deactivation at 99°C for 20 min and extensive washing with distilled water to remove starch. Commercial cellulase, β -glucosidase, and xylanase were obtained from Sigma Aldrich (MO, USA). Arabinofuranosidase (AF) and acetyl xylan esterase (AXE) were from Megazyme (Bray, Ireland). FA esterase (FAE) derived from *Myceliophthora thermophila* (ATCC 42464) that had been recombinantly expressed in *Pichia pastoris* strain X33 was provided as a kind gift by Prof. Ding of Nanjing Forestry University, who also provided the hemicellulolytic enzyme-producing *E. parvum* 4-14 strain. *E. parvum* 4-14 was isolated from soil (Nanjing, China) and deposited in the China Center for Type Culture Collection (CCTCC) (Long et al., 2016). All other chemicals used herein were of analytical grade

and were from Sinopharm Chemical Reagent Co., Ltd. (Shanghai, China). *A. niger* TRIIM 3.00944 was from Tianjin Institute of Industrial Microorganism in China.

Solid-State Fermentation

Crude enzymatic preparations were prepared *via* SSF from *A. niger* and *E. parvum* strains grown in modified Mandel's medium in which wheat bran served as a carbon source as per the methods described previously by Long et al. (Long et al., 2016). In a 250 ml Erlenmeyer flask, for every 1.5 g of delignified wheat straw (1–2 mm), 1.5 g of DSWB was mixed with 5 ml of 10 × Mandel's medium without any other carbon source, followed by sterilization at 121°C for 20 min. A fungal block derived from a PDA slant was then inoculated into a 250 ml Erlenmeyer flask containing 50 ml of liquid medium, followed by culture for 7 days at 37°C with constant agitation (200 rpm). Then, 2 ml of the prepared fungal culture was used to inoculate the Erlenmeyer flask containing SSF medium prepared above, followed by fermentation for 10 days at 37°C with 70% humidity. Following the completion of this fermentation step, flasks were mixed well with 25 ml of sterilized H₂O supplemented with 0.1% (v/v) Tween-80, shaken (120 rpm) for 2 h at 28°C, and centrifuged for 10 min at 7,000 × g. Supernatants were then transferred to fresh tubes for enzymatic analyses. Tetracycline was added to crude enzyme preparations (0.05%, w/v), followed by storage at 4°C.

WBAR Preparation

A stainless steel batch reactor (model YRG2-10 × 1.25 L, ZhengJie Technology and Development Co., Ltd., Nanjing, China) was utilized for autohydrolysis. Briefly, DSWB (50 g) was added to the reactor and mixed with ultrapure water (500 ml) followed by immersion in an oil bath. Autohydrolysis was then conducted for 30 min at 160°C, not including periods for heating and cooling. Following the completion of autohydrolysis, reactors were immersed in cool water to lower the reaction system temperature to the ambient temperature. Solid residues were then washed repeatedly using tap water, collected on a filtration cloth, and dried under vacuum for 24 h at 40°C. Samples were then sealed in zipper-locked bags prior to subsequent composition analyses and enzymatic hydrolysis.

WBAR Hydrolysis Using Commercial Enzymes or Crude Enzyme Blends

WBAR was used as a substrate for enzymatic hydrolysis performed in 50 ml conical flasks at a substrate loading of 5% (w/v, 5 ml total volume) at 50°C using 50 mM sodium citrate buffer (pH 5.0). Flasks were constantly agitated (150 rpm) for 72 h, with added enzymes including 15 CBU β-glucosidase (Novozyme 188, 269 CBU/g), 15 FPU cellulase (Sigma C2730, 117 FPU/g), and 200 U xylanase (Sigma X2629, 7700 U/g) per gram of dry biomass. Tetracycline (0.05%, w/v) was added to prevent bacterial contamination. Reactions were terminated *via* transferring the flasks into boiling water for 10 min and then clarifying hydrolysates *via* centrifugation. Supernatant glucose, xylose, and arabinose levels were assessed *via* HPLC. Analyses

were repeated in duplicate. Glucose and xylose yields were determined with the following equations:

$$\text{Glucose yield (\%)} = \frac{100\% \times (0.9 \times \text{glucose released following enzymatic hydrolysis})}{\text{amount of cellulose in WBAR}} \quad (1)$$

$$\text{Xylose yield (\%)} = \frac{100\% \times (0.88 \times \text{xylose released following enzymatic hydrolysis})}{\text{amount of xylan in WBAR}} \quad (2)$$

The conversion factor for dehydration on polymerization to cellulose was 162/180 (0.9) for glucose; to xylan and arabinan, it was 132/150 (0.88) for xylose and arabinose, respectively.

In experiments in which debranching enzymes were added, experimental protocols were as above with the addition of 1 U of AF (Megazyme, E-ABFAN), AXE (Megazyme, E-AXEAO), and FAE complemented with 15 FPU of cellulase, 15 CBU of β-glucosidase, and 200 U of xylanase. FA oxidation was prevented *via* the addition of sodium hydrogen sulfite (100 mg/L). Glucose and xylose yields were calculated as above, while arabinose, FA, and acetic acid yields were calculated with the following equations:

$$\text{Arabinose yield (\%)} = \frac{100\% \times (0.88 \times \text{arabinose released following enzymatic hydrolysis})}{\text{amount of arabinan in WBAR}} \quad (3)$$

$$\text{Ferulic acid yield (\%)} = \frac{100\% \times (\text{ferulic acid released following enzymatic hydrolysis})}{\text{amount of esterified ferulic acid in WBAR}} \quad (4)$$

$$\text{Acetic acid yield (\%)} = \frac{100\% \times (\text{acetic acid released following enzymatic hydrolysis})}{\text{amount of acetic acid in WBAR}} \quad (5)$$

WBAR enzymatic hydrolysis using crude blends of enzymes derived from *E. parvum* and *A. niger* was conducted as above at a range of experimentally appropriate enzyme doses. Monosaccharide and FA hydrolysis yields were calculated using **Equations 1–4**.

Carbohydrate, Ferulic Acid, and Acetic Acid Analyses

A two-step sulfuric acid-based hydrolysis approach was used to measure xylan, cellulose, arabinan, and other structural carbohydrates derived from WBAR (Sluiter et al., 2005). An HPLC approach was utilized to measure levels of glucose, xylose, and arabinose in the acid hydrolysate samples by using an Agilent 1,100 (USA) instrument with a Bio-Rad Aminex HPX-87H column (300 mm × 7.8 mm; USA) and a refractive index detector. This analytical column was used at a constant 55°C temperature with a mobile phase composed of H₂SO₄ (5 mM) and a constant 0.6 ml/min flow rate. The conversion factor for dehydration on polymerization to cellulose was 162/180 (0.9) for glucose; to xylan and arabinan, it was 132/150 (0.88) for xylose and arabinose. All analyses were conducted in triplicate.

Levels of acetic acid and monosaccharides present within enzymatic hydrolysates were measured *via* HPLC as above. Esterified FA levels in WBAR were measured following NaOH saponification as in a prior report (Jiang et al., 2016). Levels of free FA were assessed *via* HPLC (Agilent Technologies 1,260 Infinity) with a ZORBAX Eclipse Plus C18 column (4.6 × 100 mm,

TABLE 1 | The content of different components in de-starched wheat bran and wheat bran autohydrolysis residue.

	DSWB ^a (%)	WBAR ^b (%)
Arabinan	22.2	13.1
Xylan	29.2	25.2
Mannan	0.6	0.3
Galactan	1.4	0.7
Cellulose	19.1	35.1
Glucuronic acid	5.0	2.6
Esterified ferulic acid	1.0	0.8
Acetic acid	0.5	0.3
Acid insoluble constituents	11.7	13.5

^aDSWB, de-starched wheat bran.

^bWBAR, wheat bran autohydrolysis residue.

Agilent, CA, USA) at 30°C with a mobile phase composed of acetic acid (0.1%)-methanol (65:35) and a 0.8 ml/min flow rate. An external standard-based method was utilized for final quantitative analyses at 320 nm. Levels of FA in enzymatic hydrolysates were directly assessed *via* HPLC as above. All analyses were conducted in triplicate.

Crude Enzyme Activity Analyses

Crude enzyme activity levels were assessed at 50°C in 50 mM sodium phosphate buffer (pH 5.0). Endoglucanase (CMCase) and xylanase activities were assayed in 2.5 ml reaction mixtures containing 100 µL crude enzymatic extract and carboxymethyl cellulose (CMC-Na) or beechwood xylan (Sigma, St. Louis, MO) at the final concentration of 1% or 0.2% (w/v) respectively. Reaction mixtures were incubated at 50°C for 30 min for CMCase or 10 min for xylanase, and the released reducing sugar was quantified by the Somogyi-Nelson method using glucose or xylose standard curves. Enzymatic activity on filter paper was determined in a similar method that was used to determine endoglucanase activity, by taking 30 mg of Whatman No. 1 filter paper in 2.5 ml of 50 mM sodium citrate buffer (pH 5.0) as the substrate. The activities of β-xylosidase, β-glucosidase, arabinofuranosidase, and glucuronidase were assessed in 1 ml reaction mixtures containing 900 µL of 50 mM sodium citrate buffer (pH 5.0), 50 µL enzyme solution, and respective 50 µL of 50 mM *p*-nitrophenyl β-D-xyloside, *p*-nitrophenyl β-D-glucoside, *p*-nitrophenyl α-L-arabinoside, or *p*-nitrophenyl β-D-glucuronide (Sigma, St. Louis, MO) as the substrates. After incubating at 50°C for 30 min, the reaction was stopped by adding 4 ml of glycine buffer (0.4 M, pH 10.8), and the liberated *p*-nitrophenol was measured at 405 nm. One unit (U) of enzyme activity was defined as the amount of enzyme required to liberate 1 µmol *p*-nitrophenol from the corresponding substrates per millilitre per minute under the assay conditions. The AXE activity was determined spectrophotometrically at 50°C by measuring the increasing in A₃₅₄ nm during the initial 1 min of the assay resulting from the release of 4-methylumbelliferone from 4-methylumbelliferyl acetate. Reaction mixtures consisted of 1,390 µL 50 mM sodium citrate buffer (pH 5.0), 100 µL of 10 mM 4-methylumbelliferyl acetate and 10 µL crude enzyme. One unit of enzyme activity (U) was defined as the quantity of enzyme

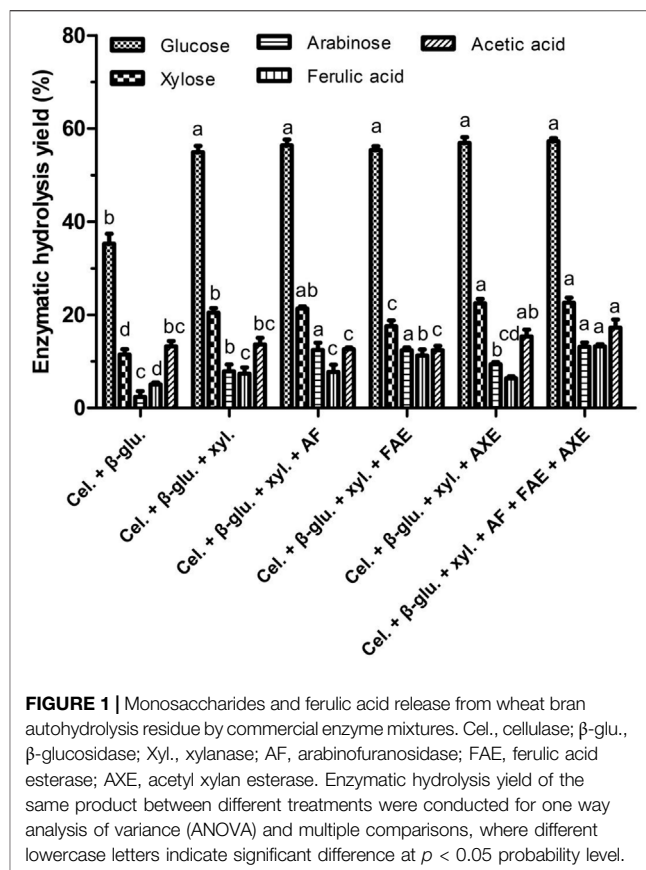


FIGURE 1 | Monosaccharides and ferulic acid release from wheat bran autohydrolysis residue by commercial enzyme mixtures. Cel., cellulase; β-glu., β-glucosidase; Xyl., xylanase; AF, arabinofuranosidase; FAE, ferulic acid esterase; AXE, acetyl xylan esterase. Enzymatic hydrolysis yield of the same product between different treatments were conducted for one way analysis of variance (ANOVA) and multiple comparisons, where different lowercase letters indicate significant difference at $p < 0.05$ probability level.

required to release 1 µmol of 4-methylumbelliferone per minute. FAE activity was assessed based upon the rate of methyl-ferulate (MFA) conversion into FA. Briefly, 100 µL of crude enzyme was mixed with 900 µL of 50 mM sodium citrate buffer (pH 5.0) containing 5.0 mM MFA. After incubating at 50°C for 30 min, the reaction was terminated at 99°C for 10 min. The released free FA was analysed using HPLC. One unit (U) of FAE activity was defined as the amount of enzyme liberating 1 µmol of free FA per min under the standard assay conditions. Benzyl alcohol release from benzyl-D-glucuronate was measured *via* HPLC to assess glucuronoyl esterase activity levels, which was similar to the determination of FAE activity. All assays were conducted in triplicate and the results were averaged together for final report.

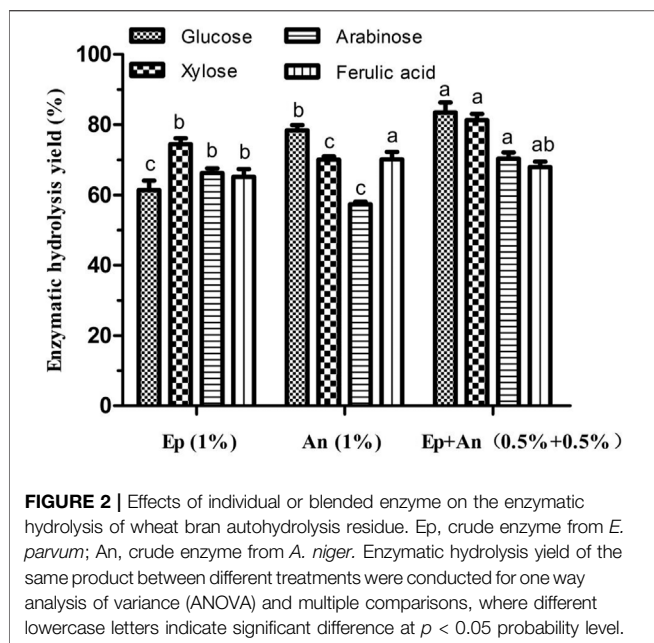
Date Analysis

One way analysis of variance (ANOVA) was conducted by SPSS software (Version 19.0) at $p < 0.05$ probability level. Multiple comparisons were conducted by Duncan method.

RESULTS AND DISCUSSION

Wheat Bran Sample Composition

DSWB used in the present study was primarily composed of cellulose, xylan, and arabinan, accounting for 19.1, 29.2, and 22.2% of the total weight, respectively, demonstrating the high levels of carbohydrates therein (Table 1). Esterified FA and acetic



acid levels in DSWB were 1.0 and 0.5%, respectively. The high FA and polysaccharide levels within this wheat bran input underscore the promise of DSWB as a source of fermentable monosaccharides and natural FA. Following autohydrolysis treatment (30 min at 160°C), marked arabinan depolymerization had occurred such that it accounted for just 13.1% of WBAR. Moreover, xylan content declined from 29.2 to 25.2%, indicating that arabinan and xylan exhibit different levels of autohydrolysis sensitivity. These findings are consistent with prior studies (Silva-Fernandes et al., 2015). Other component levels were also reduced following autohydrolysis with the exception of cellulose, the levels of which rose from 19.1 to 35.1%, suggesting that autohydrolysis did not significantly promote cellulose dissolution (Jiang et al., 2018; Tang et al., 2021). Additionally, it was found that there were also some acid insoluble constituents in both DSWB and WBAR, respectively accounting for 11.7 and 13.5%. These acid insoluble constituents might include lignin and ashes, etc.

The Impact of Commercial Enzymatic Preparations on the Release of FA and Monosaccharides From WBAR

Next, the impacts of the debranching enzymes FAE, AXE, and AF on the release of FA, monosaccharide, and acetic acid release from WBAR were assessed. As illustrated in Figure 1, the addition of both cellulase and β -glucosidase led to a glucose yield of 35.27% and xylose yield of 11.47% as the commercial cellulase also showed some xylanase activities. The addition of xylanase to cellulase and β -glucosidase resulted in respective increases in glucose and xylose yields by 55.68 and 78.47%, although overall xylose yield remained relatively low (20.47%). Adding AF to this enzymatic mixture increased arabinose yield by 57.92% to a relatively low final yield of

TABLE 2 | Activity profiles of the crude enzymes from solid state fermentation by *E. parvum* and *A. oryzae*. The activities of crude enzyme extracts from *E. parvum* and *A. niger* were conducted for one way analysis of variance (ANOVA) and multiple comparisons, where different lowercase letters indicate significant difference at $p < 0.05$ probability level.

	Enzyme produced by <i>E. parvum</i> (U/mL)	Enzyme produced by <i>A. niger</i> (U/mL)
Filter paper activity	0.1 \pm 0.01b	0.2 \pm 0.01a
CMC-Na ^a activity	15.7 \pm 0.7b	46.3 \pm 0.7a
β -glucosidase	0.7 \pm 0.04b	3.8 \pm 0.02a
Xylanase	53.4 \pm 1.2a	43.9 \pm 1.6b
β -xylosidase	5.8 \pm 0.7a	4.7 \pm 0.3a
Acetyl xylan esterase	2.8 \pm 0.02b	3.0 \pm 0.01a
Arabinofuranosidase	76.8 \pm 1.4a	38.3 \pm 1.7b
Ferulic acid esterase	0.2 \pm 0.01b	0.7 \pm 0.1a
Glucuronoyl esterase	0.5 \pm 0.02a	0.3 \pm 0.02b
Glucuronidase	0.1 \pm 0.01a	0.02 \pm 0.01b

^aCMC-Na, sodium carboxymethyl cellulose.

12.46%, while FAE addition improved FA yield by 52.17% to a final yield of 11.23%. Adding AXE to the enzymatic mixture did not significantly increase acetic acid yield. Finally, the combined addition of AF, FAE, and AXE as accessory enzymes resulted in respective xylose, arabinose, FA, and acetic acid yields of 22.58, 13.12, 13.25, and 17.22%. The heterogeneous makeup of wheat bran-derived arabinoxylan thus makes it difficult for these combinations of debranching enzymes to effectively degrade, with hydrolysis likely being restricted by steric hindrance or an absence of other enzymes including glucuronidase, β -xylosidase, glucuronoyl esterase, etc, which can catalyze the hydrolysis of certain atypical bond types including glucuronide linkages, glycosidic bonds, glucuronoyl esters, etc (Biely et al., 2016). A range of enzymes with different activity profiles is essential to enhance monosaccharide and FA release from wheat bran.

Assessment of the Synergistic Hydrolytic Activity of Crude Enzymes Derived From Two Fungal Species

As shown in Figure 2, the enzymatic yields of glucose, xylose, arabinose and ferulic acid were respectively 61.38, 74.39, 66.23 and 65.17% when using the crude enzyme of 1% (w/w) from *E. parvum*, while that were respectively 78.35, 70.02, 57.37 and 70.12% when using the same enzyme dose from *A. niger*. However, 83.46% of glucose, 81.28% of xylose, 70.34% of arabinose and 67.89% of ferulic acid were respectively yielded when using an equal-parts mixture of 0.5% (w/w) of each crude enzyme extract. Therefore, generally, an enzymatic blend derived from *A. niger* and *E. parvum*, which consisted of an equal-parts mixture of 0.5% (w/w) of each crude enzyme extract, achieved greater hydrolysis efficiency than did either enzyme crude individually at an equivalent dose (1%, w/w). Relative to an equivalent dose of *E. parvum*-derived enzymes, the enzymatic blend yielded glucose, xylose, and arabinose levels that were 35.97, 9.26, and 6.21% higher, respectively, with FA yield showing no significant difference. Similarly, relative to *A.*

niger-derived enzyme yields, the enzymatic blend yielded glucose, xylose, and arabinose levels that were 6.52, 16.08, and 22.61% higher, while FA yield showed no significant difference either. **Table 2** compiles the cellulolytic and hemicellulolytic activity profiles for these crude enzyme preparations from *A. niger* and *E. parvum*. *E. parvum* enzyme extracts exhibited higher levels of hemicellulase activity (including xylanase and arabinofuranosidase), whereas *A. niger* enzyme extracts exhibited more robust cellulase activity (including filter paper, CMC-Na, and β -glucosidase activity). The activities of xylanase and arabinofuranosidase from *E. parvum* respectively reached 53.4 U/mL and 76.8 U/mL, while that from *A. niger* were only 43.9 U/mL and 38.3 U/mL, respectively. On the other hand, the activities of filter paper, CMC-Na, and β -glucosidase from *E. parvum* reached 0.1 U/mL, 15.7 U/mL and 0.7 U/mL, whereas that from *A. niger* were significantly higher (0.2 U/mL, 46.3 U/mL and 3.8 U/mL, respectively). Both of these fungal enzyme preparations exhibited other accessory hydrolase activities for other side groups, including acetyl xylan esterase, FA esterase, and glucuronoyl esterase activity levels. The synergistically enhanced enzymatic yields of xylose and arabinose might be partly due to different glycoside hydrolase (GH) families which the related enzyme components were classified in the crude enzymes from *A. niger* and *E. parvum*. Such enhanced enzymatic hydrolysis appears to be attributable to the complementary activities of enzymes with different action modes and substrate specificities derived from these two fungi. Cooperative interactions between two or more hydrolytic components such that the product of one enzymatic reaction can serve as a substrate for another, produce combined total effects that are more than the sum of the effects of the components individually (E.M. Visser, et al., 2013; Saini et al., 2016). For example, α -L-arabinofuranosidases can be divided into GH 43 and GH 51. GH 51 shows enzyme activity on Xylp (D-xylopyranosyl residue) monosubstituted by Araf at either position 2 or 3, while GH 43 is specific for doubly arabinosylated Xylp from which they selectively liberate only the α -1,3-linked Araf, leaving the α -1,2-linked Araf on the main chain (Sørensen et al., 2006; Sørensen et al., 2007b). As WB xylan is highly substituted with α -L-arabinofuranosyl residues singly attached to C(O)-2/C(O)-3, or doubly linked to both C(O)-2,3 of the xylose residues, the mutual action of these two groups of α -L-arabinofuranosidases can facilitate the synergistic debranching of all the α -L-arabinofuranosyls from xylan backbone and the complete enzymatic degradation of arabinoxylan into monosaccharides by the subsequent synergy action of endo-xylanase and β -xylosidase (Sørensen et al., 2006; Sørensen et al., 2007b). On the other hand, all the different groups of FA esterases can liberate *trans*-ferulic acid from 5-O-feruloylated Araf (Biely et al., 2016). Furthermore, generally, *trans*-ferulic acid is terminally positioned on arabinofuranosyl in the short heterogeneous side chains or on the arabinofuranosyl moiety, and mainly exists in the form of 5-O-feruloylated Araf (Saulnier et al., 1995; Agger et al., 2010). These might cause no significant synergistic enhancement of enzymatic ferulic acid yield using the enzyme blends as shown in **Figure 2**. Therefore, the crude enzymatic blend may thus be better suited to overall

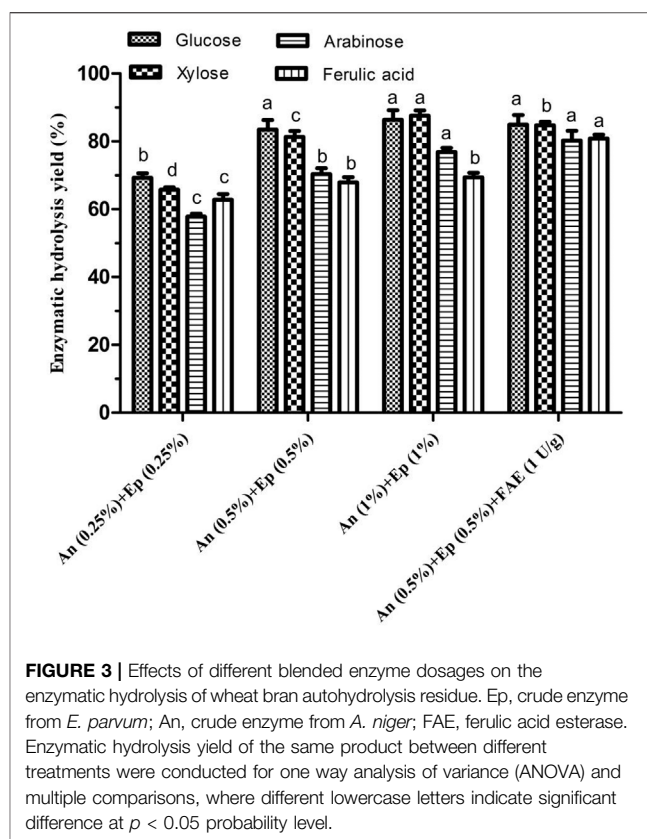
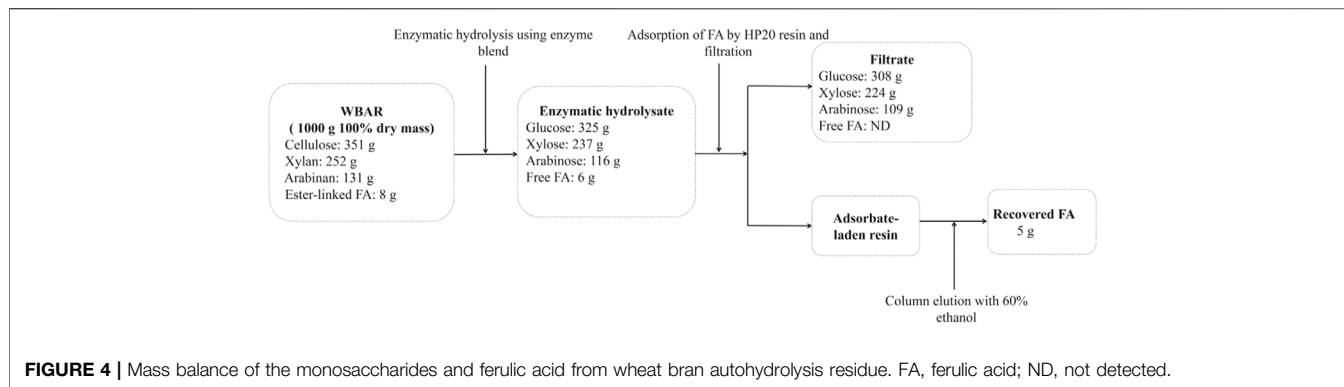


FIGURE 3 | Effects of different blended enzyme dosages on the enzymatic hydrolysis of wheat bran autohydrolysis residue. Ep, crude enzyme from *E. parvum*; An, crude enzyme from *A. niger*; FAE, ferulic acid esterase. Enzymatic hydrolysis yield of the same product between different treatments were conducted for one way analysis of variance (ANOVA) and multiple comparisons, where different lowercase letters indicate significant difference at $p < 0.05$ probability level.

improvements in hydrolytic efficiency at a given enzyme dosage with concomitant reductions in costs.

The Effects of Different Enzyme Blends Dosages on Hydrolytic Efficiency

The effects of different *A. niger* and *E. parvum* enzyme blends (0.25–1%, w/w) on WBAR enzymatic hydrolysis were next assessed. Glucose, arabinose, xylose, and FA yields rose with increasing enzyme dosage (**Figure 3**). The yields of glucose, xylose, arabinose, and FA were respectively 69.26, 65.79, 57.82 and 62.78% with an addition of 0.25% enzyme dose. An enzyme dose of 0.5% was associated with glucose yield of 83.46%, xylose yield of 81.28%, arabinose yield of 70.34% and FA yield of 67.89%, achieving respective 20.50, 23.54, 21.65, and 8.14% improvements in glucose, xylose, arabinose, and FA yields relative to a 0.25% dose. However, these yields were respectively 86.37, 87.58, 76.89 and 69.37% when using 1% enzyme dose, with xylose and arabinose only respectively increased by 7.75 and 9.31%, yet glucose and FA yields displaying no significant difference relative to 0.5% dose. This suggested that the 0.5% dose was close to the saturation point. Besides, when additional FAE (1 U/g substrate) was added to this enzymatic mixture, FA and arabinose yields significantly rose by 19.10 and 14.07%, respectively. Arabinoxylan is heterogeneous and exhibits extensive covalent cross-linking between arabinofuranosyl and feruloyl residues. FAE was able to disrupt these linkages, thereby releasing arabinose and FA. Final respective glucose, xylose, arabinose,



and FA yields were 84.98, 84.74, 80.24, and 80.86% of input. Reisinger et al. (Reisinger et al., 2013) previously reported glucose, xylose, and arabinose yields of 68, 55, and 48%, respectively, relative to raw wheat bran following hydrothermal treatment (30 min at 160°C) and enzymatic treatment with a mixture of 2% cellulase and 0.52% xylanase (w/w). Jiang et al. (Jiang and Guo, 2016) were only able to achieve respective glucose, xylose, and arabinose yields of 6, 12, and 1.5% when processing wheat bran *via* steam explosion (1.0 Mpa, 120 s) despite the application of high xylanase and cellulase doses (3% each, w/w). As such, these findings suggest that the enzymatic blend used in the present study can achieve hydrolytic outcomes superior to those in prior studies relying on commercial enzymes.

Overall Mass Balance

The overall composition of and mass balance for 1,000 g of dried WBAR over the course of the enzymatic hydrolysis process is outlined in Figure 4. Enzymatic hydrolysis was conducted at 50°C for 72 h using an enzymatic blend (0.5% derived from *A. niger* and 0.5% derived from *E. parvum* with an addition of 1 U/g FAE). This hydrolytic processing step yielded 325 g glucose, 237 g xylose, 116 g arabinose, and 6 g FA. Following the use of an HP-20 resin column for further FA enrichment, the final FA yield was 5 g, corresponding to 62.5% of the esterified FA present within the initial WBAR input. Levels of glucose, xylose, and arabinose in the resultant filtrate were 308 g, 224 g, and 109 g, respectively, corresponding to 79.0, 78.2, and 73.2% of the levels present within the initial WBAR input, with no FA remaining detectable within this filtrate. As such, FA can be reliably enriched from enzymatic hydrolysates through resin-based adsorption and subsequent ethanol elution.

CONCLUSION

Herein, an enzyme blend derived from *A. niger* and *E. parvum* was used to achieve the enzymatic hydrolysis of wheat bran autohydrolysis residue, thereby achieving ferulic acid and

monosaccharide co-production with high efficiency. Final ferulic acid recovery rates were as high as 62.5% of the levels of esterified ferulic acid present within the starting WBAR input, with limited monosaccharide loss following additional HP-20 resin-mediated separation. Together, these results suggest that wheat bran offers value as a biomass source that can be leveraged to prepare ferulic acid and to facilitate efficient enzymatic saccharification following autohydrolysis pretreatment.

DATA AVAILABILITY STATEMENT

The raw data supporting the conclusions of this article will be made available by the authors, without undue reservation.

AUTHOR CONTRIBUTIONS

ZL: Methodology, Formal analysis, Investigation. ES: Investigation, Validation, Resources. FM: Investigation, Data curation. XZ: Formal analysis. KJ: Funding acquisition, Writing - original draft, Supervision, Conceptualization, Writing - review and editing. All authors have read and agreed to the published version of the manuscript.

FUNDING

The works were supported by Scientific Research Fund of Zhejiang Provincial Education Department (Y202146043), and the National Financial Support of Undergraduate Training Program for Innovation (202113023019).

ACKNOWLEDGMENTS

We sincerely thank for the support of the Advanced Analysis and Testing Center of Nanjing Forestry University.

REFERENCES

- Agger, J., Viksø-Nielsen, A., and Meyer, A. S. (2010). Enzymatic Xylose Release from Pretreated Corn Bran Arabinoxylan: Differential Effects of Deacetylation and Deferuloylation on Insoluble and Soluble Substrate Fractions. *J. Agric. Food Chem.* 58, 6141–6148. doi:10.1021/jf100633f
- Aguedo, M., Fougny, C., Dermience, M., and Richel, A. (2014). Extraction by Three Processes of Arabinoxylans from Wheat Bran and Characterization of the Fractions Obtained. *Carbohydr. Polym.* 105, 317–324. doi:10.1016/j.carbpol.2014.01.096
- Batalha, L. A. R., Han, Q., Jameel, H., Chang, H.-m., Colodette, J. L., and Borges Gomes, F. J. (2015). Production of Fermentable Sugars from Sugarcane Bagasse by Enzymatic Hydrolysis after Autohydrolysis and Mechanical Refining. *Bioresour. Technol.* 180, 97–105. doi:10.1016/j.biortech.2014.12.060
- Bhattacharya, A., Ruthes, A., Vilaplana, F., Karlsson, E. N., Adlercreutz, P., and Stålbrand, H. (2020). Enzyme Synergy for the Production of Arabinoxyloligosaccharides from Highly Substituted Arabinoxylan and Evaluation of Their Prebiotic Potential. *Lwt* 131, 109762. doi:10.1016/j.lwt.2020.109762
- Biely, P., Singh, S., and Puchart, V. (2016). Towards Enzymatic Breakdown of Complex Plant Xylan Structures: State of the Art. *Biotechnol. Adv.* 34, 1260–1274. doi:10.1016/j.biotechadv.2016.09.001
- Cripwell, R., Favaro, L., Rose, S. H., Basaglia, M., Cagnin, L., Casella, S., et al. (2015). Utilisation of Wheat Bran as a Substrate for Bioethanol Production Using Recombinant Cellulases and Amyolytic Yeast. *Appl. Energ.* 160, 610–617. doi:10.1016/j.apenergy.2015.09.062
- Ferri, M., Happel, A., Zanaroli, G., Bertolini, M., Chiesa, S., Commisso, M., et al. (2020). Advances in Combined Enzymatic Extraction of Ferulic Acid from Wheat Bran. *New Biotechnol.* 56, 38–45. doi:10.1016/j.nbt.2019.10.010
- Gullón, B., Gullón, P., Tavaría, F., Pintado, M., Gomes, A. M., Alonso, J. L., et al. (2014). Structural Features and Assessment of Prebiotic Activity of Refined Arabinoxyloligosaccharides from Wheat Bran. *J. Funct. Food.* 6, 438–449. doi:10.1016/j.jff.2013.11.010
- Hu, Y., Yan, B., Stephen Chen, Z., Wang, L., Tang, W., and Huang, C. (2022). Recent Technologies for the Extraction and Separation of Polyphenols in Different Plants: A Review. *J. Renew. Mater.* 10, 1–20. doi:10.32604/jrm.2022.018811
- Huang, C., Jiang, X., Shen, X., Hu, J., Tang, W., Wu, X., et al. (2022). Lignin-enzyme Interaction: A Roadblock for Efficient Enzymatic Hydrolysis of Lignocelluloses. *Renew. Sustain. Energ. Rev.* 154, 111822. doi:10.1016/j.rser.2021.111822
- Jiang, K., Li, L., Long, L., and Ding, S. (2016). Comparison of Alkali Treatments for Efficient Release of *p*-Coumaric Acid and Enzymatic Saccharification of Sorghum Pith. *Bioresour. Technol.* 207, 1–10. doi:10.1016/j.biortech.2016.01.116
- Jiang, K., Li, L., Long, L., and Ding, S. (2018). Comprehensive Evaluation of Combining Hydrothermal Pretreatment (Autohydrolysis) with Enzymatic Hydrolysis for Efficient Release of Monosaccharides and Ferulic Acid from Corn Bran. *Ind. Crops Prod.* 113, 348–357. doi:10.1016/j.indcrop.2018.01.047
- Jiang, S.-T., and Guo, N. (2016). The Steam Explosion Pretreatment and Enzymatic Hydrolysis of Wheat Bran. *Energy Sourc. A: Recovery, Utilization, Environ. Effects.* 38, 295–299. doi:10.1080/15567036.2012.744118
- Kaur, A., Singh, B., Yadav, M. P., Bhinder, S., and Singh, N. (2021). Isolation of Arabinoxylan and Cellulose-Rich Arabinoxylan from Wheat Bran of Different Varieties and Their Functionalities. *Food Hydrocolloids.* 112, 106287. doi:10.1016/j.foodhyd.2020.106287
- Khalili, F., and Amiri, H. (2020). Integrated Processes for Production of Cellulosic and Hemicellulosic Biobutanol from Sweet Sorghum Bagasse Using Autohydrolysis. *Ind. Crops Prod.* 145, 111918. doi:10.1016/j.indcrop.2019.111918
- Li, D., Rui, Y.-x., Guo, S.-d., Luan, F., Liu, R., and Zeng, N. (2021). Ferulic Acid: A Review of its Pharmacology, Pharmacokinetics and Derivatives. *Life Sci.* 284, 119921. doi:10.1016/j.lfs.2021.119921
- Long, L., Ding, D., Han, Z., Zhao, H., Lin, Q., and Ding, S. (2016). Thermotolerant Hemicellulolytic and Cellulolytic Enzymes from *Eupenicillium parvum* 4-14 Display High Efficiency upon Release of Ferulic Acid from Wheat Bran. *J. Appl. Microbiol.* 121, 422–434. doi:10.1111/jam.13177
- Ma, M.-G., Jia, N., Zhu, J.-F., Li, S.-M., Peng, F., and Sun, R.-C. (2012). Isolation and Characterization of Hemicelluloses Extracted by Hydrothermal Pretreatment. *Bioresour. Technol.* 114, 677–683. doi:10.1016/j.biortech.2012.03.0410.1016/j.biortech.2012.03.048
- Mandalari, G., Faulds, C. B., Sancho, A. I., Saija, A., Bisignano, G., LoCurto, R., et al. (2005). Fractionation and Characterisation of Arabinoxylans from Brewers' Spent Grain and Wheat Bran. *J. Cereal Sci.* 42, 205–212. doi:10.1016/j.jcs.2005.03.001
- Mathew, S., and Abraham, T. E. (2004). Ferulic Acid: an Antioxidant Found Naturally in Plant Cell walls and Feruloyl Esterases Involved in its Release and Their Applications. *Crit. Rev. Biotechnol.* 24, 59–83. doi:10.1080/07388550490491467
- Mathew, S., Karlsson, E. N., and Adlercreutz, P. (2017). Extraction of Soluble Arabinoxylan from Enzymatically Pretreated Wheat Bran and Production of Short Xylo-Oligosaccharides and Arabinoxyloligosaccharides from Arabinoxylan by Glycoside Hydrolase Family 10 and 11 Endoxylanases. *J. Biotechnol.* 260, 53–61. doi:10.1016/j.jbiotec.2017.09.006
- Murlidhar Sonkar, R., Savata Gade, P., Bokade, V., Mudliar, S. N., and Bhatt, P. (2021). Ozone Assisted Autohydrolysis of Wheat Bran Enhances Xylooligosaccharide Production with Low Generation of Inhibitor Compounds: A Comparative Study. *Bioresour. Technol.* 338, 125559. doi:10.1016/j.biortech.2021.125559
- Nair, R. B., Lundin, M., Brandberg, T., Lennartsson, P. R., and Taherzadeh, M. J. (2015). Dilute Phosphoric Acid Pretreatment of Wheat Bran for Enzymatic Hydrolysis and Subsequent Ethanol Production by Edible Fungi *Neurospora Intermedia*. *Ind. Crops Prod.* 69, 314–323. doi:10.1016/j.indcrop.2015.02.038
- Palmarola-Adrados, B., Chotéborská, P., Galbe, M., and Zacchi, G. (2005). Ethanol Production from Non-starch Carbohydrates of Wheat Bran. *Bioresour. Technol.* 96, 843–850. doi:10.1016/j.biortech.2004.07.004
- Peng, F., Peng, P., Xu, F., and Sun, R.-C. (2012). Fractional Purification and Bioconversion of Hemicelluloses. *Biotechnol. Adv.* 30, 879–903. doi:10.1016/j.biotechadv.2012.01.018
- Reisinger, M., Tirpanalan, Ö., Prückler, M., Huber, F., Kneifel, W., and Novalin, S. (2013). Wheat Bran Biorefinery - A Detailed Investigation on Hydrothermal and Enzymatic Treatment. *Bioresour. Technol.* 144, 179–185. doi:10.1016/j.biortech.2013.06.088
- Rose, D. J., and Inglett, G. E. (2010). Production of Feruloylated Arabinoxyloligosaccharides from maize (*Zea mays*) Bran by Microwave-Assisted Autohydrolysis. *Food Chem.* 119, 1613–1618. doi:10.1016/j.foodchem.2009.09.053
- Saini, J. K., Singhania, R. R., Satlewal, A., Saini, R., Gupta, R., Tuli, D., et al. (2016). Improvement of Wheat Straw Hydrolysis by Cellulolytic Blends of Two *Penicillium* Spp. *Renew. Energ.* 98, 43–50. doi:10.1016/j.renene.2016.01.025
- Sakamoto, T., Ogura, A., Inui, M., Tokuda, S., Hosokawa, S., Ihara, H., et al. (2011). Identification of a GH62 α -l-arabinofuranosidase Specific for Arabinoxylan Produced by *Penicillium chrysogenum*. *Appl. Microbiol. Biotechnol. Appl. Microbiol. Biot.* 90, 137–146. doi:10.1007/s00253-010-2988-2
- Sánchez-Bastardo, N., Romero, A., and Alonso, E. (2017). Extraction of Arabinoxylans from Wheat Bran Using Hydrothermal Processes Assisted by Heterogeneous Catalysts. *Carbohydr. Polym.* 160, 143–152. doi:10.1016/j.carbpol.2016.12.035
- Saulnier, L., Vigouroux, J., and Thibault, J.-F. (1995). Isolation and Partial Characterization of Feruloylated Oligosaccharides from maize Bran. *Carbohydr. Res.* 272, 241–253. doi:10.1016/0008-6215(95)00053-V
- Si, D., Shang, T., Liu, X., Zheng, Z., Hu, Q., Hu, C., et al. (2020). Production and Characterization of Functional Wheat Bran Hydrolysate Rich in Reducing Sugars, Xylooligosaccharides and Phenolic Acids. *Biotechnol. Rep.* 27, e00511. doi:10.1016/j.btre.2020.e00511
- Silva-Fernandes, T., Duarte, L. C., Carvalho, F., Loureiro-Dias, M. C., Fonseca, C., and Girio, F. (2015). Hydrothermal Pretreatment of Several Lignocellulosic Mixtures Containing Wheat Straw and Two Hardwood Residues Available in Southern Europe. *Bioresour. Technol.* 183, 213–220. doi:10.1016/j.biortech.2015.01.059
- Sluiter, A., Hames, B., Ruiz, R., Scarlata, C., Sluiter, J., Templeton, D., et al. (2005). *Determination of Structural Carbohydrates and Lignin in Biomass*. Denver, Colorado: Laboratory Analytical Procedure, the National Renewable Energy Laboratory Biomass Analysis Technology (NREL BAT) Team.
- Sørensen, H. R., Jørgensen, C. T., Hansen, C. H., Jørgensen, C. I., Pedersen, S., and Meyer, A. S. (2006). A Novel GH43 α -l-arabinofuranosidase from *Humicola Insolens*: Mode of Action and Synergy with GH51 α -l-arabinofuranosidases on

- Wheat Arabinoxylan. *Appl. Microbiol. Biotechnol.* 73, 850–861. doi:10.1007/s00253-006-0543-y
- Sørensen, H. R., Pedersen, S., Jørgensen, C. T., and Meyer, A. S. (2007a). Enzymatic Hydrolysis of Wheat Arabinoxylan by a Recombinant "Minimal" Enzyme Cocktail Containing β -Xylosidase and Novel Endo-1,4- β -Xylanase and α -L-Arabinofuranosidase Activities. *Biotechnol. Prog.* 23, 100–107. doi:10.1021/bp0601701
- Sørensen, H. R., Pedersen, S., and Meyer, A. S. (2007b). Synergistic Enzyme Mechanisms and Effects of Sequential Enzyme Additions on Degradation of Water Insoluble Wheat Arabinoxylan. *Enzyme Microb. Techn.* 40, 908–918. doi:10.1016/j.enzmictec.2006.07.026
- Sørensen, H. R., Pedersen, S., Viksø-Nielsen, A., and Meyer, A. S. (2005). Efficiencies of Designed Enzyme Combinations in Releasing Arabinose and Xylose from Wheat Arabinoxylan in an Industrial Ethanol Fermentation Residue. *Enzyme Microb. Techn.* 36, 773–784. doi:10.1016/j.enzmictec.2005.01.007
- Tang, W., Wu, X., Huang, C., Ling, Z., Lai, C., and Yong, Q. (2021). Revealing Migration Discipline of Lignin during Producing Fermentable Sugars from Wheat Straw through Autohydrolysis. *Ind. Crops Prod.* 171, 113849. doi:10.1016/j.indcrop.2021.113849
- Visser, E. M., Falkoski, D. L., de Almeida, M. N., Maitan-Alfenas, G. P., and Guimarães, V. M. (2013). Production and Application of an Enzyme Blend from *Chrysosporthe Cubensis* and *Penicillium pinophilum* with Potential for Hydrolysis of Sugarcane Bagasse. *Bioresour. Techn.* 144, 587–594. doi:10.1016/j.biortech.2013.07.015
- Wang, Z.-K., Huang, C., Zhong, J.-L., Wang, Y., Tang, L., Li, B., et al. (2021). Valorization of Chinese hickory Shell as Novel Sources for the Efficient Production of Xylooligosaccharides. *Biotechnol. Biofuels.* 14, 226. doi:10.1186/s13068-021-02076-9
- Wu, H., Li, H., Xue, Y., Luo, G., Gan, L., Liu, J., et al. (2017). High Efficiency Co-production of Ferulic Acid and Xylooligosaccharides from Wheat Bran by Recombinant Xylanase and Feruloyl Esterase. *Biochem. Eng. J.* 120, 41–48. doi:10.1016/j.bej.2017.01.001

Conflict of Interest: The authors declare that the research was conducted in the absence of any commercial or financial relationships that could be construed as a potential conflict of interest.

Publisher's Note: All claims expressed in this article are solely those of the authors and do not necessarily represent those of their affiliated organizations, or those of the publisher, the editors and the reviewers. Any product that may be evaluated in this article, or claim that may be made by its manufacturer, is not guaranteed or endorsed by the publisher.

Copyright © 2022 Liu, Shi, Ma, Zhou and Jiang. This is an open-access article distributed under the terms of the Creative Commons Attribution License (CC BY). The use, distribution or reproduction in other forums is permitted, provided the original author(s) and the copyright owner(s) are credited and that the original publication in this journal is cited, in accordance with accepted academic practice. No use, distribution or reproduction is permitted which does not comply with these terms.



Metabolic and Evolutionary Engineering of Diploid Yeast for the Production of First- and Second-Generation Ethanol

Yang Sun¹, Meilin Kong², Xiaowei Li², Qi Li², Qian Xue², Junyan Hou², Zefang Jia², Zhipeng Lei¹, Wei Xiao², Shuobo Shi^{3*} and Limin Cao^{2*}

¹Key Laboratory of Straw Comprehensive Utilization and Black Soil Conservation, Ministry of Education, College of Life Science, Jilin Agricultural University, Changchun, China, ²College of Life Sciences, Capital Normal University, Beijing, China, ³Beijing Advanced Innovation Center for Soft Matter Science and Engineering, College of Life Science and Technology, Beijing University of Chemical Technology, Beijing, China

OPEN ACCESS

Edited by:

Xin Zhou,
Nanjing Forestry University, China

Reviewed by:

Bintao Cui,
RMIT University, Australia
Xiuping He,
Institute of Microbiology (CAS), China

*Correspondence:

Shuobo Shi
shishuobo@buct.edu.cn
Limin Cao
caolimin@cnu.edu.cn

Specialty section:

This article was submitted to
Industrial Biotechnology,
a section of the journal
Frontiers in Bioengineering and
Biotechnology

Received: 15 December 2021

Accepted: 31 December 2021

Published: 28 January 2022

Citation:

Sun Y, Kong M, Li X, Li Q, Xue Q, Hou J, Jia Z, Lei Z, Xiao W, Shi S and Cao L (2022) Metabolic and Evolutionary Engineering of Diploid Yeast for the Production of First- and Second-Generation Ethanol. *Front. Bioeng. Biotechnol.* 9:835928. doi: 10.3389/fbioe.2021.835928

Despite a growing preference for second-generation (2G) ethanol in industries, its application is severely restricted owing to a major obstacle of developing a suitable yeast strain for fermentation using feedstock biomasses. In this study, a yeast strain, *Saccharomyces cerevisiae* A31Z, for 2G bioethanol production was developed from an industrial strain, Angel, using metabolic engineering by the incorporation of gene clusters involved in the xylose metabolism combined with adaptive evolution for evolving its anti-inhibitory properties. This strain outcompeted its ancestors in xylose utilization and subsequent ethanol production and manifested higher tolerance against common inhibitors from lignocellulosic hydrolysates, and also it lowered the production of glycerol by-product. Furthermore, A31Z outperformed in ethanol production using industrial hydrolysate from dried distillers grains with solubles and whole corn. Overall, this study provided a promising path for improving 2G bioethanol production in industries using *S. cerevisiae*.

Keywords: *Saccharomyces cerevisiae*, 1G and 2G ethanol, xylose, evolutionary engineering, lignocellulosic hydrolysates

INTRODUCTION

Second-generation (2G) ethanol produced from lignocellulosic biomasses has received growing attention and has been considered as a promising replacement for petroleum fuel due to its eco-friendly features (Antunes et al., 2019); and lignocellulosic wastes are recognized as the most feasible feedstock used for the 2G ethanol production owing to their low costs, renewability, and availability (Fatma et al., 2018). In the process of feedstock utilization, lignocellulosic biomasses were initially subjected to break the rigid structure of lignin, hemicelluloses, and cellulose, followed by hydrolyzation with enzymes or chemicals. Different mono-sugars could be released from the hydrolysate, such as glucose, xylose, and arabinose, which would be converted into ethanol and other bioproducts by microbes. The brewer's yeast *Saccharomyces cerevisiae* is one of the most widely used cell factories. However, *S. cerevisiae* cannot assimilate xylose naturally, resulting in incomplete usage of sugars in lignocellulosic hydrolysates. This is one of the problems for inefficient production of 2G ethanol. Recently, various strategies have been attempted to develop a modified yeast strain so that it can maximize the ethanol production using xylose as the substrate (Zhang et al., 2019).

The metabolism of xylose in yeast has been extensively studied (Li X. et al., 2019). Generally, nice enzymes, including XR, XDH, Xks1p, Tal1p, Pyk1p, Rki1p, Rpe1p, Tkl1p, and MGT05196, play a key role in xylose utilization in yeasts. Xylose reductase (XR or Xyl1), encoded by the XR gene, was used to convert xylose into xylitol, which was then transformed into xylulose using xylitol dehydrogenase (XDH, Xyl2). Subsequently, xylulose was phosphorylated to form xylulose-5-phosphate by xylulokinase (XK, Xks1) in the pentose phosphate pathway (PPP) (Li X. et al., 2019). The implementation of this three-enzyme pathway (XR, XDH, and XK) enabled the cell growth and production of ethanol from xylose. On the other hand, xylose could be also converted into xylulose directly by xylose isomerase (XI). The transaldolase Tal1, responsible for the regulation of the balance of metabolites in the pentose phosphate pathway, and the pyruvate kinase Pyk1, involved in the conversion of phosphoenolpyruvate and ADP to pyruvate and ATP in glycolysis, are usually considered rate-limiting enzymes in the non-oxidative pentose phosphate and glycolysis pathways, respectively. Variations in the expression of these two enzymes would result in the fluctuation of ethanol metabolism notably (Zhang et al., 2019). Upregulation of the gene *PYK1* promoted the pyruvate metabolic flow to the ethanol production (Gruning et al., 2011; Cao et al., 2014; Gruning et al., 2014; Xu et al., 2016). Finally, the transporter Mgt05196, responsible for the uptake of xylose in the absence of glucose inhibition, was crucial for simultaneously catabolizing glucose and xylose in yeast (Wang et al., 2015). Currently, the most efficient xylose-fermenting yeast strains could use both glucose and xylose as substrates from lignocellulosic feedstocks and could generate ethanol yields of 0.46–0.47 g/g (Zhang et al., 2019). Most yeasts developed so far for 2G ethanol production are haploids due to their ease with genetic manipulations. Nevertheless, diploid yeasts or polyploids have shown to be more resistant to harsh environmental conditions in industries, whereas the expertise from haploid yeasts facilitated paving a practical path for constructing the diploid yeast strain for bioethanol production in this study.

Owing to the recalcitrant structure of lignocellulose biomass, pretreatments are needed prior to the hydrolysis to facilitate the following sugar conversion by microbes (Baruah et al., 2018; Chandel et al., 2018; Abo et al., 2019; Rempel et al., 2019). Various strategies have been adopted, which are typically categorized into four types: physical, chemical, physicochemical, and biological approaches (Baruah et al., 2018). Chemical and enzymic degradation have gained much interest in recent years due to their high hydrolytic biomasses and low costs (Wang et al., 2017; Tian et al., 2018). Subsequently, polysaccharides produced in these ways could readily be transformed into monosaccharides with high efficiency and specificity, especially by using enzymes (Wu et al., 2019). The hydrolysates from lignocellulosic feedstocks such as corn stover (CS), corn cob (CC), or the specific four pairs of *Miscanthus* were widely used for bioethanol production (Alam et al., 2019; Watanabe et al., 2019; Wu et al., 2019). However, various inhibitory substances, including acetate, furans, and phenolic compounds, produced during the hydrolytic process severely suppressed the growth of yeasts, leading to the poor performance of subsequent

fermentation (Klinke et al., 2004; Koppram and Olsson, 2014; Gutierrez-Macias and Nacheva, 2015). To address these problems, various studies revealed that yeast cells could develop high tolerance against the inhibitory effects of lignocellulosic hydrolysates by adapting them in a medium containing external acetate, which led to a pronounced improvement of the xylose utilization and therefore ethanol production (Li H. et al., 2019; Kwak et al., 2019; Zhang et al., 2019). Deparis et al. (2017) developed yeasts with high resistance to the inhibitors by repetitive batch cultivation of the strains in lignocellulosic hydrolysate. *In situ* detoxification of fural was confirmed to be one of the underlying mechanisms for tolerance to phenolic compounds in yeasts (Deparis et al., 2017). In addition, the enzymes Pad1 and Fdc1, responsible for aromatic acid conversion, were shown to be involved in the removal of fural from hydrolysates of lignin (Scanes et al., 1998).

In this study, based on our previous study in haploid yeasts (Zhang et al., 2019), this work constructed several diploid ethanol-producing yeasts that can use xylose by incorporation of various metabolic gene clusters into the genome of two industrial diploid yeasts as well as direct adaption. The best diploid producer A21Z showed higher fermentation efficiency compared to its ancestors. Then it was further optimized by adaptation of A21Z in medium containing 15% of industrial hydrolysate from wheat straw, evolving into strain A31Z which displayed a superior xylose utilization and tolerance against inhibitors from hydrolysates of lignocelluloses compared to its ancestors. Our study showed that metabolic engineering combined with adaptive evolution was suitable for improving yeast resistance to inhibitory conditions and enhancing the xylose utilization for ethanol production in industries.

MATERIALS AND METHODS

Construction of Yeast Strains

All DNA manipulations were carried out in *Escherichia coli* strain DH5 α as described (Sambrock and Russel, 2001). *S. cerevisiae* diploid strains, Angel and Henderson, used in this study were obtained from Angel Yeast Co., Ltd. Plasmid pUC-TTRR (Xiong et al., 2011) containing the non-oxidative phosphate pathway with four gene transcription units *PDC1p-TKL1-TKL1t/PGK1p-TAL1-TAL1t/TPI1p-RKII-RKII1t/ADH1p-RPE1-RPE1t* and pUC-fps1-nat (Zhang et al., 2018) containing xylose utilization pathway with three gene transcription units *ADH1p-XYL1-ADH1t/PGK1p-XYL2-PGK1t/PGK1p-XKS1-PGK1t* were used for genetic engineering in diploid Angel and Henderson, respectively, resulting in strain ABN and BBN, separately. Genes (*TAL1*, *TKL1*, *RKII*, and *RPE1*) in the non-oxidative phosphate pathway for plasmid pUC-TTRR were integrated into the non-functional sites *HOG1* and *HOG2*. This pUC-fps1-nat was used to integrate the three genes of *XYL1*, *XYL2*, and *XKS1* into the yeast chromosome site *FPS1*. Repeated batch cultivation of yeast strain ABN was performed for independent evolution using a previously reported method (Zhang et al., 2019). Serial transfer was done by alternating cultivation in YP

with 20 g/L xylose and 3 g/L to 12 g/L acetate. At periodic intervals (5 days), the fastest growing colonies were selected for independent evolution to propagate the improved fitness colonies. After one and half year, the evolved strain A1 was obtained from the wild-type strain ABN. Then the new evolved strain A2 was further obtained from the aforementioned strain A1. Thus, strains A1 and A2 were obtained after a 3-year evolutionary process. The strain A21Z was obtained by integrating the expression cassette 1z-e7 (*XYL1(K270R)-XYL2-TALI-PYK1-MGT05196-PYK1-MGT05196*) (Zhang et al., 2019) into the strain A2. And the strain A22Z was obtained by integrating another copy of the 1z-e7 into A21Z. Then the strain A31Z was obtained by adapting growth of A21Z in 15% wheat straw stover hydrolysate using a previously reported method (Zhang et al., 2019). *S. cerevisiae* strains used in this study are listed in **Supplementary Table S1**. The transformation of yeast strains in this study was done following the standard LiAc/SS carrier DNA/PEG method (Gietz and Schiestl, 2007).

Medium

The strains cultured in YPD (20 g/L tryptone, 10 g/L yeast extract, and 20 g/L glucose) at 200 rpm for 24 h were collected, centrifuged, and washed, which were then inoculated into a 500-ml shaker flask (initial OD₆₀₀ of 1) containing fresh fermentation medium. The YP medium contained 50 g/L glucose, 50 g/L xylose, and 3 g/L acetate at pH 5.5 for the comparative fermentation for Angel, Henderson, ABN, and BBN. The YP medium of mimic Dried distillers grains with solubles (DDGS) hydrolysate contained 100 g/L glucose and 50 g/L xylose at pH 5.5 for fermentation performance analysis of A31Z. The evolutionary engineering of strains were conducted in YP + acetate + xylose domestication medium (YPAX) with 10 g/L yeast extract, 20 g/L tryptone, 20 g/L xylose, and 8 g/L of acetate.

Enzymatic Hydrolysis of Lignocellulosic Biomasses

The biomass powders (0.300 g) of *Miscanthus*, maize, and wheat straw, were, respectively, incubated with 0.012 g mixed cellulases (cellulases at 10.60 FPU g⁻¹ biomass and xylanase at 6.72 U g⁻¹ biomass from Imperial Jade Bio-technology Co., Ltd) containing 0.8% Tween-80 at 5% solid loading, and shaken under 150 rpm for 48 h at 50°C. The samples were centrifuged at 3,000 g for 5 min, and the supernatants were then collected to conduct hexose and pentose assay. The sugar yields (% dry matter) released from enzymatic hydrolysis of *Miscanthus*, maize, and wheat straw with different solid-to-liquid ratio fermentation was described in **Supplementary Table S2**. The cell wall composition (% dry matter) from enzymatic hydrolysis of *Miscanthus*, maize, and wheat straw is described in **Supplementary Table S3**.

Fermentation From Hydrolysis of Corn Starch and Dried Distillers Grains With Soluble

To obtain hydrolysis of corn starch, starch samples with 30% solids were mixed with the enzyme liquozyme at a loading of 0.064% under 85°C with a pH at 5.7 for 4 h. Then the

saccharification was performed by the addition of 0.1% starch hydrolyzing enzyme and 0.6% Novozymes Celluclast® at pH 4.8 for 0.5 h. The fermentation was carried out under 30°C at pH 4.6 and 150 rpm for 72 h. The initial value of OD₆₀₀ nm for the fermentation was set up as 1.0. The residual corn starch was recovered with 1% H₂SO₄ under 95°C for 90 min upon finishing based on the situ dilute acid pretreatment. Then the sample was subjected to evaporation to remove the remaining ethanol at 0.09 mpa under 85°C for 30 min. After this, water was added to the sample up to its initial volume accompanied with the adjustment of the pH at between 4.8 and 5.0. Subsequently, 0.6% cellulases and 1.5% xylanase were added and incubated at 50°C, 250 rpm for 24 h. Finally, the hydrolysis was adjusted to pH 4.6 and adopted as the medium for fermentation from DDGS.

Simultaneous Saccharification and Co-fermentation of Whole Corn

The corn stover was pretreated using dilute sulfuric acid (1% v/v) at 160°C for 10 min with a solid loading at 10% (w/v). Then the hemicelluloses released from the corn stover were incubated under 50°C for 48 h at 250 rpm mixed with 40 mg cellulases per gram glucan (containing cellulases and xylanase with a ratio at 9:1). Meanwhile, the corn flour underwent liquefaction using the liquozyme at 0.064% under 85°C for 4 h.

The schematic process of SSCF is illustrated in **Supplementary Figure S1**. The co-fermentation was performed under 30°C for 72 h containing 12% corn flour and 12% corn stover hydrolysis, and 0.1% diastase with an initial OD₆₀₀ of 1.0.

Analytical Methods

The measurements of OD₆₀₀ nm and cell dry weights (CDW) were recorded according to the previous description (Cao et al., 2014). Glucose, xylose, xylitol, ethanol, and acetic acid were analyzed by HPLC using its related column and detector run with 5 mM H₂SO₄ as the mobile phase at a flow rate of 0.4 ml/min (Cao et al., 2014). The pentose and hexose of soluble sugars were, respectively, detected as described previously (Wu et al., 2019).

Calculation of Ethanol Production

The following formula was adopted for the calculation of ethanol production:

$$\text{Ethanol yield} = \frac{\text{Ethanol concentration at the end of fermentation}}{\text{Total sugars concentration at 0h}}$$

RESULTS

Fermentation Performance of Original Yeast Strains, Angel, and Henderson

Due to the better performance of diploid yeast strains in cell viability, genetic stability, and stress endurance than those of haploid strain in the fermentation process (Kim et al., 2013), two

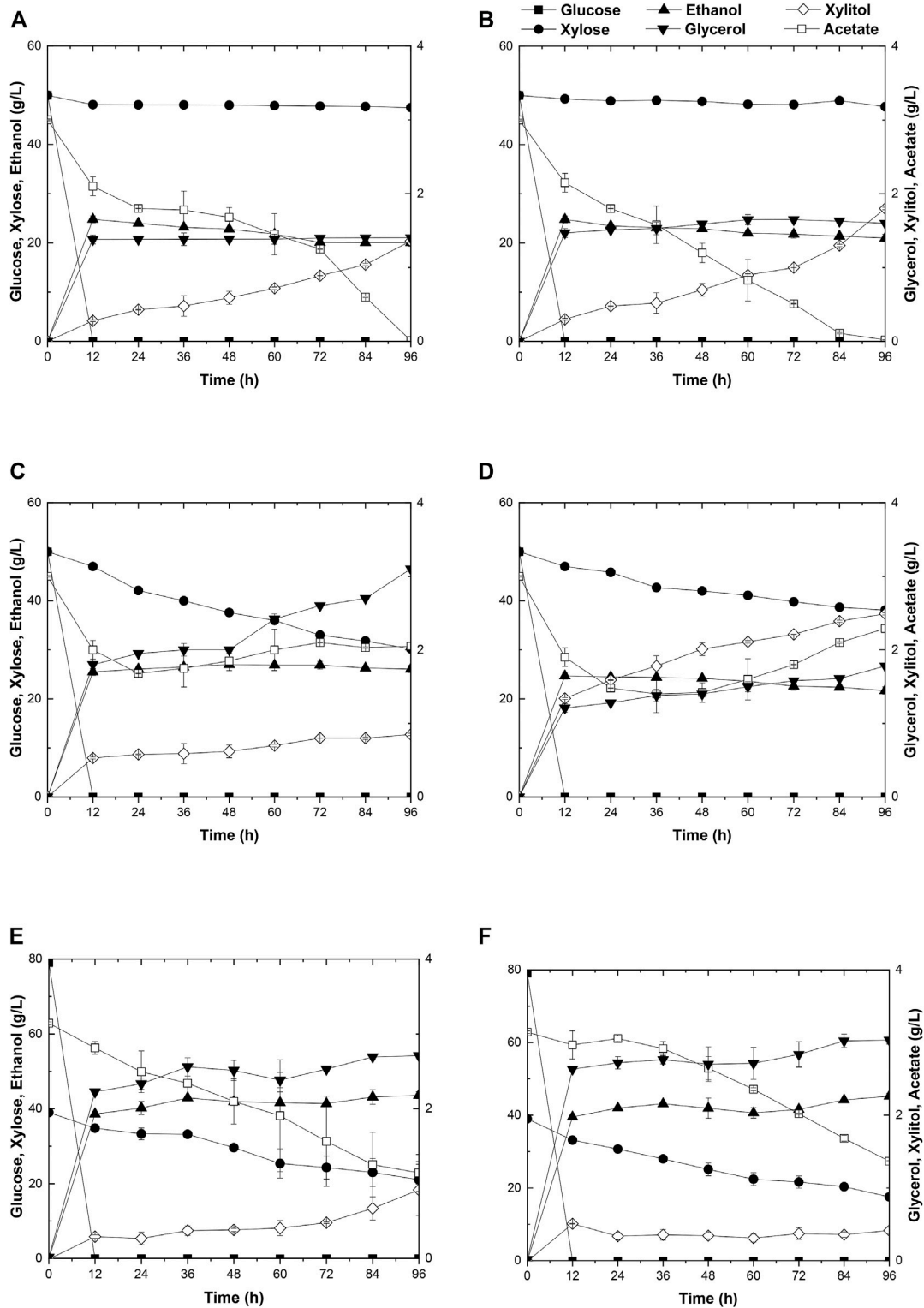


FIGURE 1 | Time-dependent ethanol fermentation of yeast strains in this study. Fermentation profile of yeast Angel (**A**) and yeast Henderson (**B**) in mixed sugar medium of 50 g/L glucose and 50 g/L xylose containing 3 g/L acetate. Fermentation of ABN (**C**) and BBN (**D**) in mixed sugar medium of 50 g/L glucose and 50 g/L xylose containing 3 g/L acetate. Fermentation profile of A1 (**E**) and A2 (**F**) in YP medium containing 3 g/L acetate, 80 g/L glucose, and 40 g/L xylose. Each experiment was repeated three times, and two parallel controls were set at the same time.

industrial diploid yeasts from two individual ethanol companies, *S. cerevisiae* Angel and Henderson, were selected as the starting strains for the following genetic modification and evolution. As expected, neither of the two yeasts could consume xylose. During a 96-h fermentation in the medium containing 50 g/L glucose, 50 g/L xylose, and 3 g/L acetate, both strains consumed all of the glucose within the initial 12 h, and ethanol productions reached the maximum of 27.4 g/L for Angel and 24.8 g/L for Henderson (Figures 1A,B). Henderson formed a slightly higher level of xylitol in this process, with 1.80 g/L xylitol production, whereas 1.36 g/L was produced by strain Angel. No significant difference in glycerol accumulation was observed, and both strains exhibited high capabilities of acetate consumption, with 2.3 and 1.2 g/L residue within 48 h, respectively.

Construction of Diploid Xylose Assimilating Yeast Strains ABN and BBN and Their Fermentation Analysis

To enhance xylose utilization in yeast, diploid xylose assimilating yeast strains ABN and BBN were constructed by incorporating the two sets of gene clusters involved with xylose metabolism *XYL1/XYL2/XKS1* and *TAL1/TKL1/RKII/RPE1* into the strains of Angel and Henderson, respectively. The fermentation performance of these strains was evaluated by growing them separately in a medium added with mixed sugars and external acetate, same as before. Both strains consumed all of glucose in the medium within 12 h. In addition, strain ABN converted 50 g/L glucose and 21.2 g/L xylose into 27.4 g/L ethanol in 96 h, whereas BBN consumed 50 g/L glucose and 10.9 g/L xylose yielding 25.0 g/L ethanol within the same duration (Figures 1C,D). Compared to BBN, strain ABN displayed better xylose metabolic efficiency with a similar glycerol accumulation and lower xylitol accumulation (Figures 1C,D). Therefore, ABN was selected for further evolutionary engineering. Unexpectedly, the acetate utilization of these two engineered strains reduced significantly compared to those of their original strains, indicating that the metabolism of acetate was inhibited after the introduction of the xylose metabolic pathway.

The Generation of Strain A21Z and Fermentation Performances of This Strain and Its Ancestors A1 and A2

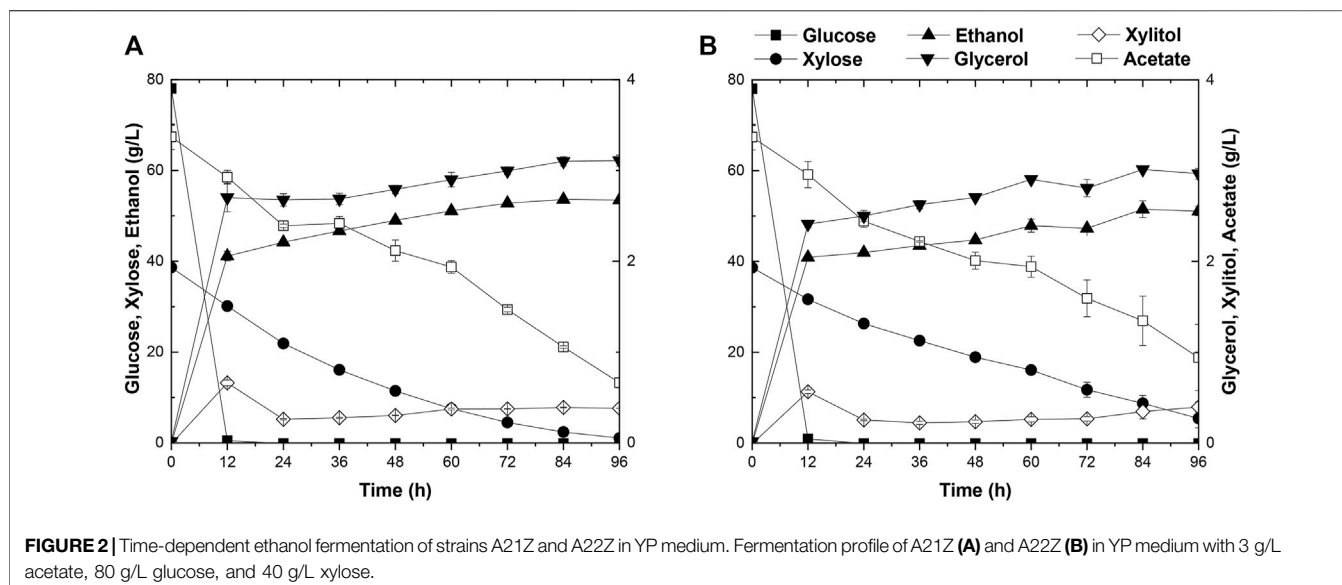
Toxic substances are always accumulated in the hydrolysates of lignocellulosic materials to some extent, which brings about great hindrance to the cell growth of yeasts due to the intracellular acidification, resulting in poor xylose utilization and 2G ethanol formation. Two approaches, by acetate catabolism or by mechanisms of acetate tolerance, were prompted to counteract the negative effects of acetate in the media (Zhang et al., 2019). Here, adaptive evolution was adopted to increase the metabolic efficiency of mixed sugars in the presence of acetate. Initially, the diploid strain ABN was subjected to adaptive evolution, resulting in strain A1 in YPAX domestication medium using a previous method (Zhang et al., 2019). Then an A2 strain was obtained by growing strain A1 in the YPAX medium for another round of

adaptation. Fermentation of A1 and A2 was separately performed in the medium containing 80 g/L glucose, 40 g/L xylose, and 3 g/L acetate (Figures 1E,F). Both strains A1 and A2 showed significantly higher xylose consumption capacities than ABN. They consumed the entire glucose in the medium within 12 h, leading to ethanol yields of 88.1 and 88.2% of the theoretical values (0.51 g ethanol/g total sugars), respectively (Tran et al., 2020). Compared with strain ABN, strain A1 totally yielded 43.6 g/L of ethanol by consumption of 80 g/L glucose and 17.9 g/L more of xylose, and 45.2 g/L from A2 finally by consumption of 80 g/L glucose and an additional 21.4 g/L of xylose. Furthermore, A1 and A2 displayed increased acetate consumptions compared to ABN.

Strain A2 consumed a 3.5 g/L more xylose with a 1.6 g/L higher ethanol production than strain A1. The superior performance of this strain may likely lie in the more favorable mutations accumulated during the two-round evolutionary engineering in this strain (Figures 1E,F). A2 was then selected for subsequent engineering. To further improve the xylose metabolism, the six gene clusters, *1z-e7*, (*XYL1(K270R)-XYL2-TAL1-PYK1-MGT05196-PYK1-MGT05196*) with the characteristics of redox balance, and *2z-e7*, (*XYL1(K270R)-XYL2-TAL1-klPYK1-MGT05196-klPYK1-MGT05196*) with an exogenous gene *PYK1* from *Kluyveromyces lactis* were introduced into the strain A2 to obtain strain A21Z and A22Z, respectively, according to previous studies (Zhang et al., 2019). After 96 h, the xylose consumption and ethanol production of A21Z were shown to be 37.5 g/L and 53.5 g/L (Figure 2A), respectively, reaching a yield of 87.4% of the theoretical ethanol production, whereas 33.2 g/L and 51.1 g/L for the strain A22Z were observed (Figure 2B), respectively, with a 83.5% theoretical yield of ethanol production. Within 96 h, most xylose in the medium (with 1.1 g/L xylose remained) was consumed by strain A21Z, producing 8.3 g/L more ethanol than that of A2. Overall, A21Z showed a superior performance in xylose consumption, ethanol yield, and sugar-to-alcohol conversion (Figures 2A,B) compared with its ancestors and A22Z, which therefore encouraged using this strain for the subsequent evolutionary engineering further.

A31Z Strain Evolved by Adapting Strain A21Z in the Hydrolysate of Wheat Straw Stover With 15% Solid Loading

Currently, wheat straw is the most abundant lignocellulosic biomasses among agricultural residues. However, intractable compositions accumulated in the hydrolysates, such as acetate, severely impede the cell growth in the subsequent fermentation procedures. To overcome these difficulties, adaptive evolution was broadly employed to customize a target strain in stressful industrial pretreated products (Zhang et al., 2019). In this study, solid wheat straw stover pretreated product was added to the cultural medium at a 15% (w/v) proportion for domestication of A21Z by serial passages (Figures 3A,B). The seed culture of A21Z was inoculated into the wheat straw pretreated products at 10.0% (v/v); the initial concentration of glucose, xylose, ethanol, and glycerol in the medium for evolution was 45.85 g/L, 17.07 g/L,



1.84 g/L, and 1.01 g/L, respectively. Yeast cells initially underwent a lag in growth upon inoculation in the fresh wheat straw-pretreated products medium and did not manifest efficient utilization of the pretreated products immediately for ethanol production. After passages in the medium, the strain A31Z was evolved, displaying robust growth in the medium (Figure 3B), even though the xylose consumption and ethanol production did not show significant increases across the passages, which suggested that the strain A31Z had adapted to the cultural medium, and could proceed to the simultaneous saccharification and co-fermentation (SSCF).

Simultaneous Saccharification and Co-Fermentation of Strain A31Z Using Wheat Straw

Prior to SSCF, the wheat straw was subjected to hydrolysis with concentrated acid and bio-detoxification (Zhang et al., 2019), and then the resultant hydrolysates were used to evaluate the fermentation efficiency of strain A31Z. During the process of simultaneous saccharification, with the addition of 9.71% (w/w) of cellulase, the content of glucose increased along with the process of pretreated products fermentation. However, the concentration of xylose remained unchanged. It was likely that most of xylan had already been hydrolyzed into xylose or oligo-xylan during the pretreatment step, which might lead to the release of the maximum level of xylose in the medium at this point resulting in the failure of further increase in the subsequent saccharification. After 12 h, the concentration of free glucose and xylose in the medium achieved 77.08 g/L and 35.95 g/L, respectively. During the following co-fermentation stage, the conversion of free glucose into ethanol occurred within 24 h after the strain A31Z was inoculated, and then the cells continued to utilize glucose released from cellulase hydrolysis and xylose. In the presence of 15 mg cellulase per gram of dry wheat straw, strain A31Z could produce 56.68 g/L ethanol with a 63.13%

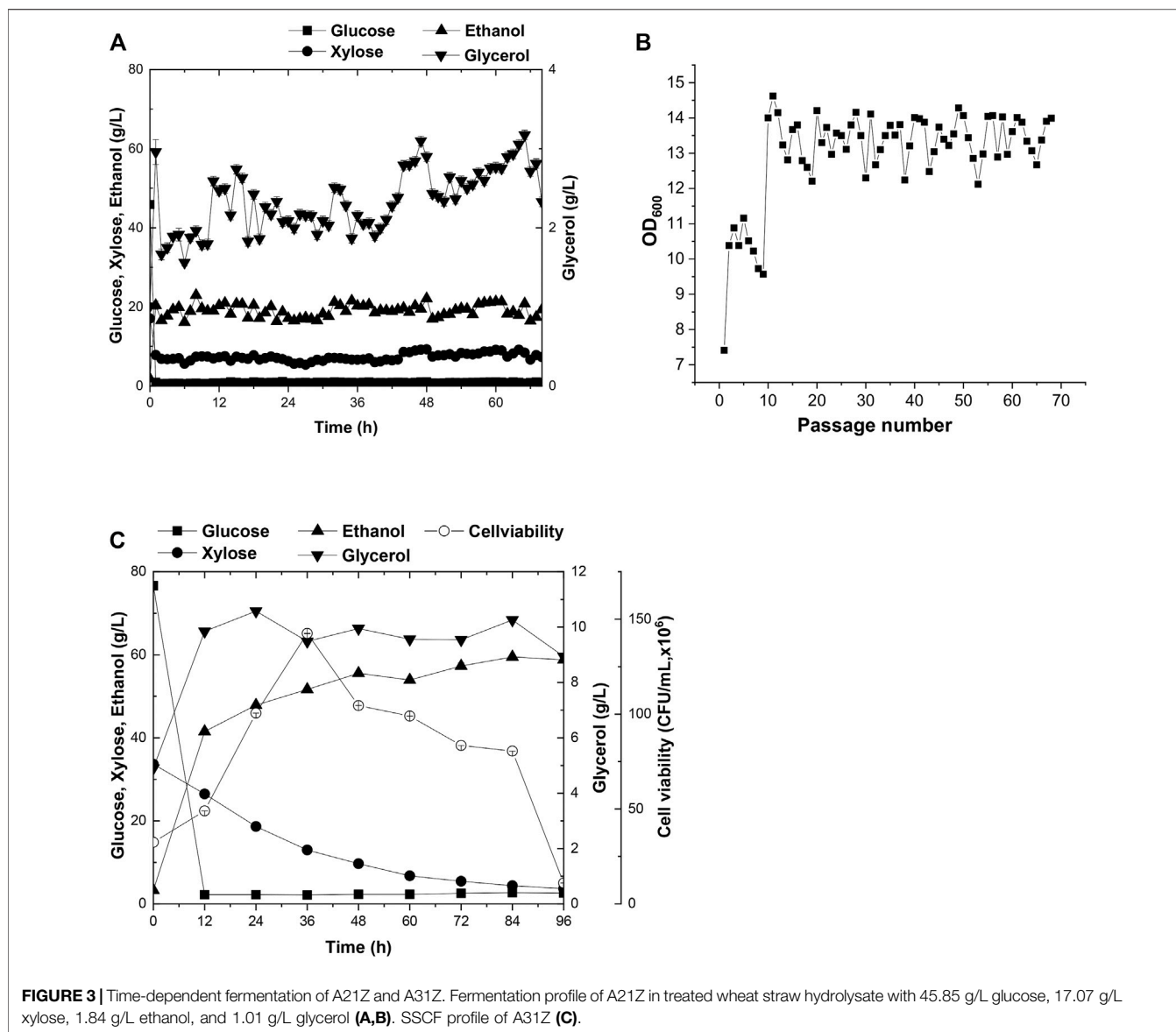
sugar-to-alcohol conversion rate (Figure 3C). Approximately, partial ethanol of this conversion came from the initial free glucose released from the pretreatment of hydrolysis, and the rest was from xylose and the glucose released during the SSCF (Liu et al., 2018).

Fermentation of A31Z in Hydrolysate From Enzymatic Hydrolysis of Engineered *Miscanthus*, Maize, and Wheat Straw

Lignocellulosic biomasses such as *Miscanthus*, maize, and wheat straw were the major feedstocks for 2G bioethanol. Hydrolysates from *Miscanthus*, maize, and wheat straw were used as the substrates for ethanol production. As shown in Figure 4, the commercial strain Angel from Wuhan and one of our previous reported strains CE7 were used as controls in this study for the evaluation of the fermentation performance of A31Z at 37°C (Zhang et al., 2019). It was shown that strain A31Z exhibited an ethanol yield of 10.51% of dry matter, which was slightly higher than that of Angel (9.80%) and CE7 (7.82%) from the hydrolysate of *Miscanthus*, while no difference from hydrolysates of maize and wheat straw under the same conditions (Table 1) was observed. However, the xylose utilization of A31Z in the aforementioned three hydrolysates was significantly improved compared to that of the other two strains (Table 2).

Fermentation of A31Z Using Corn and Dried Distillers Grains With Soluble as Feedstocks

The capacity of strain A31Z in first-generation yeast-based ethanol production from corn starch was evaluated. Strain Angel was used as the control. Corn contained approximately two-thirds of starch, and the corn starch was hydrolyzed into glucose prior to fermentation. Strain A31Z could produce 122.32 g/L ethanol, about 2.92 g/L more than that of the



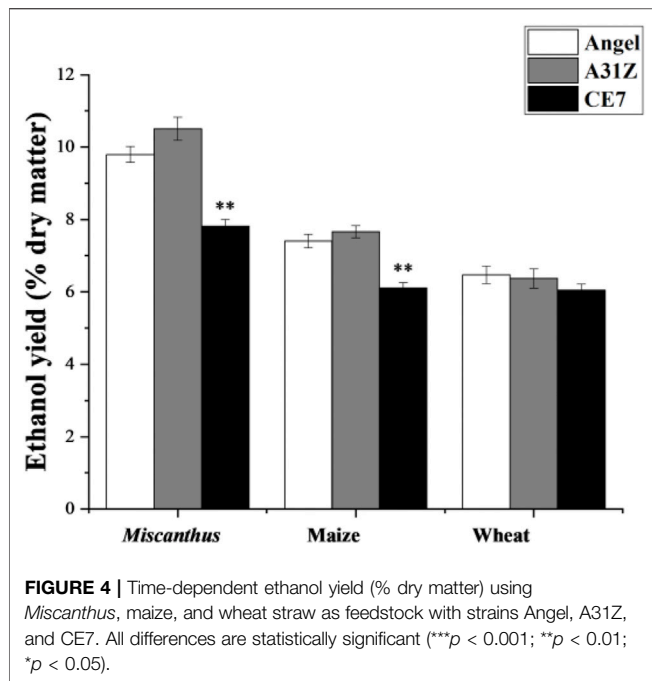
control strain after 48 h of fermentation (Figures 5A,B). Besides, its by-product glycerol was about 20% less than that of Angel, which was likely due to the increase in the ethanol production, consistent with a previous study of Scanes et al. (1998) that the level of glycerol was inversely related to that of ethanol (Scanes et al., 1998).

The residues of corn and cells from the 1G ethanol fermentation, known as DDGS, were rich in glucose and xylose and could be used as the feedstock, for further ethanol production. Here, we also evaluated the fermentation performances of Angel and A31Z using a mixture of 100 g/L glucose and 50 g/L xylose as a mimic DDGS hydrolysis (Figures 5C,D). Strain A31Z exhibited both notably higher xylose consuming capacity and ethanol production than those of Angel, with 46.21 g/L and 8.06 g/L for their xylose conversions, and 63.33 g/L and 45.98 g/L for the ethanol productions of the two strains, respectively.

When using the DDGS hydrolysate for fermentation, a slightly higher ethanol production was achieved by A31Z. As shown in Figure 5F, strain A31Z produced an ethanol titer of 5.54 g/L from a total sugar of 11.17 g/L (7.84 g/L glucose and 3.33 g/L xylose) feedstock, and strain Angel produced 4.94 g/L ethanol from 9.56 g/L sugar (6.74 g/L glucose and 2.82 g/L xylose) (Figure 5E). Our fermentation results showed that strain A31Z with a slightly higher ethanol production is superior to strain Angel.

Simultaneous Saccharification and Co-fermentation of Integrated 1G and 2G Feedstock for Ethanol Production Using A31Z

As mentioned before, the evolved strain A31Z had shown its excellence in fermentation using various types of substrates. It had been reported that the integrative utilization of whole corn



fermentation (Figures 6A,B). Both strains, Angel and A31Z, consumed glucose completely within 24 h, and the xylose consumption were shown to be 9.42 g/L and 17.93 g/L with ethanol productions of 60.73 g/L and 67.18 g/L within 72 h, respectively. It had been proved that the application of integrative 1G and 2G feedstocks for ethanol industrial production yielded a better economic profit than the standalone of 1G or 2G plant (Dias et al., 2012).

DISCUSSION

The capacity of monosaccharide utilization is crucial for the yield of ethanol production using lignocellulose biomasses as fermentation feedstock by yeasts. This study provided a roadmap on how to improve cellulosic ethanol production in a diploid yeast strain by progressively optimizing the xylose metabolic pathway via the combination of metabolic genetic engineering and adaptive evolution. Our previous studies demonstrated that imbalanced expression of the set of xylose metabolic enzymes and/or their activities might lead to the disproportion of xylose metabolism in yeasts, thus increasing the accumulation of massive xylitol, an intermediate product of

TABLE 1 | Ethanol yield (% dry matter) and concentration (g/L) of different yeast using the hydrolysis of *Miscanthus*, maize, and wheat straw.

Strain	Hydrolysis								
	<i>Miscanthus</i>			Maize			Wheat straw		
Ethanol yield (% dry matter)									
Angel	9.80	±	0.22	7.41	±	0.19	6.47	±	0.24
CE7	7.82	±	0.19	6.11	±	0.15	6.05	±	0.16
A31Z	10.51	±	0.32	7.66	±	0.17	6.37	±	0.27
Ethanol concentration (g/L)									
Angel	4.73	±	0.11	3.57	±	0.09	3.12	±	0.12
CE7	3.77	±	0.09	2.95	±	0.07	2.92	±	0.08
A31Z	5.07	±	0.16	3.70	±	0.08	3.07	±	0.13

TABLE 2 | Sugar-ethanol conversion rate (%) and pentose utilization rate (%) of different yeast using the hydrolysis of *Miscanthus*, maize, and wheat straw.

Strain	Hydrolysis								
	<i>Miscanthus</i>			Maize			Wheat straw		
Sugar-to-ethanol conversion rate (%)									
Angel	60.88	±	1.85	66.07	±	2.01	71.26	±	2.17
CE7	56.91	±	1.26	61.76	±	1.37	66.61	±	1.48
A31Z	59.94	±	2.07	65.05	±	2.25	70.16	±	2.42
Pentose utilization rate (%)									
Angel	38.38	±	0.95	22.45	±	1.46	39.65	±	1.19
CE7	28.01	±	1.21	21.15	±	1.43	37.67	±	0.86
A31Z	45.81	±	1.11	34.53	±	1.43	51.86	±	0.89

for fermentation could result in a higher ethanol titer and accelerates the application of the 2G technology in ethanol industry (Erdei et al., 2013; Kim et al., 2017). The SSCF data in this study showed that there was a significant improvement in xylose utilization and ethanol production in strain A31Z using the integrated carbon sources of 1G + 2G feedstocks for

xylose metabolism, resulting in the reduction of the yield of ethanol eventually (Zhang et al., 2019). The rate-limiting gene *TAL1* was identified to play a key role in the balance of metabolites in the pentose phosphate pathway (Zhang et al., 2019). The elevation of *TAL1* expression against an *XYL1(K270R)-XYL2-XKS1* overexpressed background could

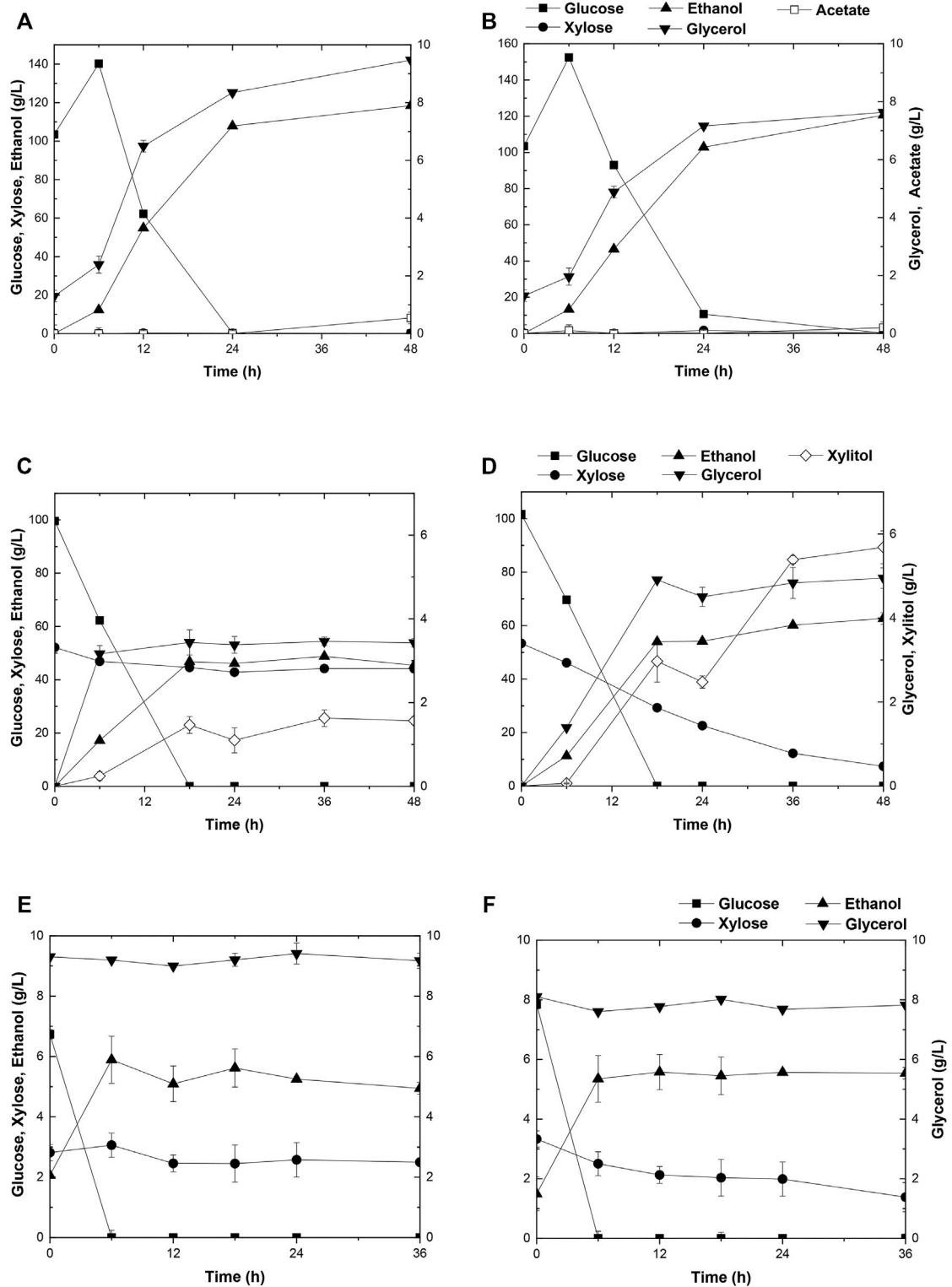
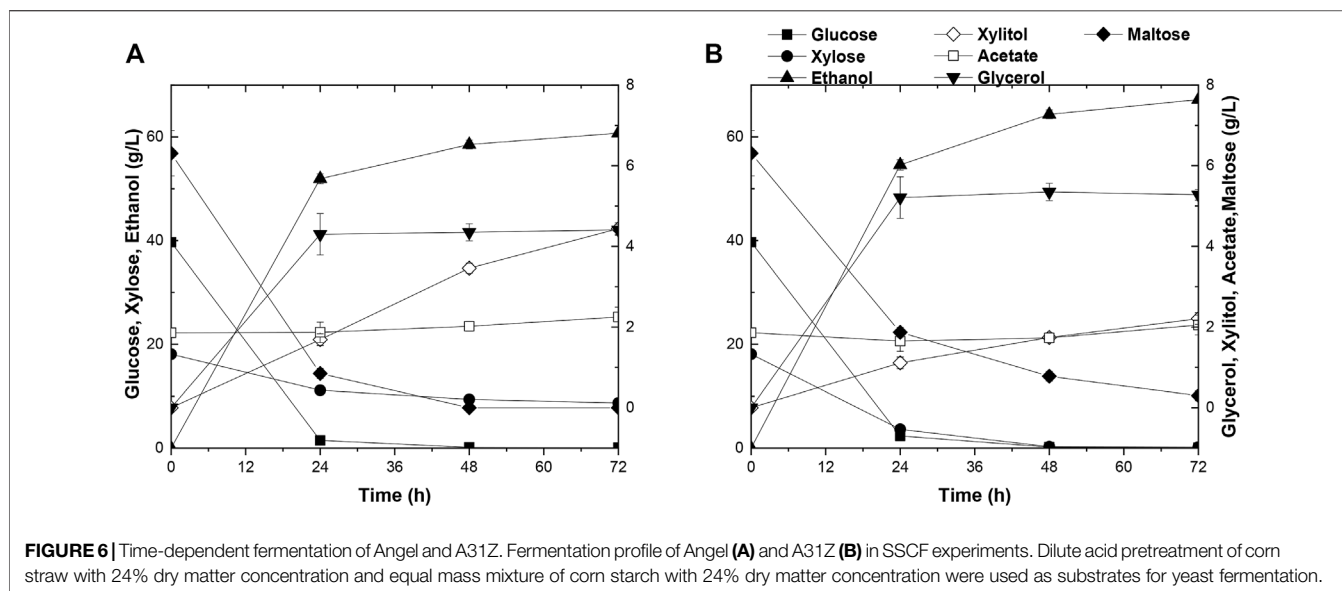


FIGURE 5 | Time-dependent fermentation of Angel and A31Z. Fermentation profile of Angel (A) and A31Z (B) in corn starch medium. The fermentation profile of Angel (C) and A31Z (D) in mixed sugar medium of 100 g/L glucose and 50 g/L xylose. The fermentation profile of Angel (E) and A31Z (F) from DDGS.



promote the xylose metabolism, as well as lessen the glycerol and xylitol accumulation (Cao et al., 2014). The overexpression of the gene *PYK1* could facilitate the of improvement the sugar-to-ethanol conversion ratio (Gruning et al., 2011; Gruning et al., 2014). Moreover, the upregulation of the xylose transporter *MGT05196* resulted in a stronger xylose uptake flux, which consequently led to an improvement in its utilization efficiency (Wang et al., 2015). A previous study by Zhang et al. (2019) revealed constitutive promoters of genes in the Embden–Meyerhof–Parnas (EMP) pathway, the tricarboxylic acid cycle (TCA), and stress–response gene family were involved in driving the expression of the xylose metabolic gene cluster in a haploid evolved strain CE7, which accelerated the consumption rate of xylose, and promoted subsequent ethanol production (Zhang et al., 2019). These promoters, involved in different fermentation stages (glucose and xylose stage), played a key role in the xylose metabolism, especially in the presence of acetate (Cao et al., 2014). Kim et al. (2013) constructed an efficient xylose-fermenting diploid yeast strain by mating two engineered haploid yeasts capable of xylose assimilation (Kim et al., 2013). And, it was believed that diploid yeasts were more suitable for the fermentation of industrial hydrolysates (Kim et al., 2013).

All of these previous publications were summarized, which gives a clue to construct a yeast strain via combining the metabolic engineering and adaptive evolution for an improvement of the growth and consequent 2G ethanol production from xylose. The ethanol production in this study was improved from 53.7 to 87.4% of the theoretical yield (from ABN to A21Z), and the obtained yeast A21Z was subjected to genetic modification and evolutionary adaptation. In our work, a highly efficient and stable xylose metabolic pathway was constructed in diploid yeast, paving the path for the 2G bioethanol production.

The numerous inhibitors presented in the lignocellulose hydrolysate created a barrier for yeast fermentation as they severely restricted cell growth. A biorefining approach starting

from dry acid pretreatment, disk milling, and biodetoxification of lignocellulose feedstock was employed to counteract the inhibitory effects that occurred in the process of SSCF (Liu et al., 2018). The anti-inhibitory properties of the adaptive strain A31Z manifested in hydrolysates of *Miscanthus*, DDGS, and whole corn could be attributed to the accumulated favorable mutations in its genome. Three strains produced more ethanol yield and volume concentration in the hydrolysate of *Miscanthus* than the other two materials maize and wheat straw; this, in turn, suggests that the hydrolysis of *Miscanthus* can release more mixed glucose and xylose. In *Miscanthus* hydrolysate, A31Z can convert more xylose and glucose into ethanol compared to Angel, indicating that it has better fermentation performance. When total sugars are relatively high, the conversion of sugar to alcohol may differ little, even though ethanol is slightly higher. It would be beneficial in the future to evaluate the contribution of potential target mutations in A31Z by genome sequencing and genetic engineering, and novel gene variants which could be discovered that are responsible for the functional variations related to stress responses, acetate metabolism, and detoxification. Since multiple genes were rationally introduced and integrated in the genome of A31Z, gene expression analysis is required to quantitatively identify the expression ratio of these genes in the PPP, xylose utilization, and transport pathways. Understanding this, it may reveal the quantitative contribution of each enzyme for yeast fermentation on xylose. In this study, 56.7 g/L ethanol was produced by evolved strain A31Z with an overall yield of 63.1% from cellulose and xylose using wheat straw as the feedstock, and a higher xylose conversion ratio (84.9%) was achieved. Higher xylose conversion efficiency in SSCF fermentation accompanied by the generation of minimum amount of wastewater suggested that A31Z was superior to its ancestors.

In addition, our study demonstrated that a xylose-consuming strain for fermentation with hydrolysates from 1G/2G feedstocks was developed, laying the foundation for academic research and industrial large-scale application.

DATA AVAILABILITY STATEMENT

The original contributions presented in the study are included in the article/**Supplementary Material**, further inquiries can be directed to the corresponding authors.

AUTHOR CONTRIBUTIONS

All authors listed have made a substantial, direct, and intellectual contribution to the work and approved it for publication.

FUNDING

This study was funded by the National Natural Science Foundation of China (Grant No. 31570044) and the Fundamental Research Funds for the Central Universities.

REFERENCES

- Abo, B. O., Gao, M., Wang, Y., Wu, C., Ma, H., and Wang, Q. (2019). Lignocellulosic Biomass for Bioethanol: an Overview on Pretreatment, Hydrolysis and Fermentation Processes. *Rev. Environ. Health* 34 (1), 57–68. doi:10.1515/reveh-2018-0054
- Alam, A., Zhang, R., Liu, P., Huang, J., Wang, Y., Hu, Z., et al. (2019). A Finalized Determinant for Complete Lignocellulose Enzymatic Saccharification Potential to Maximize Bioethanol Production in Bioenergy Miscanthus. *Biotechnol. Biofuels* 12, 99. doi:10.1186/s13068-019-1437-4
- Antunes, F. A. F., Chandel, A. K., Terán-Hilares, R., Ingle, A. P., Rai, M., Milessi, T. S. D. S., et al. (2019). Overcoming Challenges in Lignocellulosic Biomass Pretreatment for Second-Generation (2G) Sugar Production: Emerging Role of Nano, Biotechnological and Promising Approaches. *3 Biotech.* 9 (6), 230. doi:10.1007/s13205-019-1761-1
- Baruah, J., Nath, B. K., Sharma, R., Kumar, S., Deka, R. C., Baruah, D. C., et al. (2018). Recent Trends in the Pretreatment of Lignocellulosic Biomass for Value-Added Products. *Front. Energ. Res.* 6, 141. doi:10.3389/fenrg.2018.00141
- Cao, L., Tang, X., Zhang, X., Zhang, J., Tian, X., Wang, J., et al. (2014). Two-stage Transcriptional Reprogramming in *Saccharomyces cerevisiae* for Optimizing Ethanol Production from Xylose. *Metab. Eng.* 24, 150–159. doi:10.1016/j.ymben.2014.05.001
- Chandel, A. K., Garlapati, V. K., Singh, A. K., Antunes, F. A. F., and da Silva, S. S. (2018). The Path Forward for Lignocellulose Biorefineries: Bottlenecks, Solutions, and Perspective on Commercialization. *Bioresour. Technol.* 264, 370–381. doi:10.1016/j.biortech.2018.06.004
- Deparis, Q., Claes, A., Foulquié-Moreno, M. R., and Thevelein, J. M. (2017). Engineering Tolerance to Industrially Relevant Stress Factors in Yeast Cell Factories. *FEMS Yeast Res.* 17 (4), fox036. doi:10.1093/femsyr/fox036
- Dias, M. O. S., Junqueira, T. L., Cavalett, O., Cunha, M. P., Jesus, C. D. F., Rossell, C. E. V., et al. (2012). Integrated versus Stand-Alone Second Generation Ethanol Production from Sugarcane Bagasse and Trash. *Bioresour. Technol.* 103 (1), 152–161. doi:10.1016/j.biortech.2011.09.120
- Erdei, B., Galbe, M., and Zacchi, G. (2013). Simultaneous Saccharification and Co-fermentation of Whole Wheat in Integrated Ethanol Production. *Biomass and Bioenergy* 56, 506–514. doi:10.1016/j.biombioe.2013.05.032
- Fatma, S., Hameed, A., Noman, M., Ahmed, T., Shahid, M., Tariq, M., et al. (2018). Lignocellulosic Biomass: A Sustainable Bioenergy Source for the Future. *Protein Pept. Lett.* 25 (2), 148–163. doi:10.2174/0929866525666180122144504
- Gietz, R. D., and Schiestl, R. H. (2007). High-efficiency Yeast Transformation Using the LiAc/SS Carrier DNA/PEG Method. *Nat. Protoc.* 2 (1), 31–34. doi:10.1038/nprot.2007.13
- Grüning, N.-M., Du, D., Keller, M. A., Luisi, B. F., and Ralser, M. (2014). Inhibition of Triosephosphate Isomerase by Phosphoenolpyruvate in the Feedback-Regulation of Glycolysis. *Open Biol.* 4, 130232. doi:10.1098/rsob.130232

ACKNOWLEDGMENTS

We sincerely thank Bao Jie, Peng Liangcai, Jin Mingjie, He Boyang, and Xu Zhaoxian for comparative fermentation experiments to evaluate our proposed A31Z. We thank Jingyu Wang for his valuable assistance and discussions. We also acknowledge the support from the Beijing Advanced Innovation Center for Soft Matter Science and Engineering.

SUPPLEMENTARY MATERIAL

The Supplementary Material for this article can be found online at: <https://www.frontiersin.org/articles/10.3389/fbioe.2021.835928/full#supplementary-material>

- Grüning, N.-M., Rinnerthaler, M., Bluemlein, K., Mülleider, M., Wamelink, M. M. C., Lehrach, H., et al. (2011). Pyruvate Kinase Triggers a Metabolic Feedback Loop that Controls Redox Metabolism in Respiring Cells. *Cel Metab.* 14 (3), 415–427. doi:10.1016/j.cmet.2011.06.017
- Gutierrez-Macias, T., and Nacheva, P. M. (2015). Clofibrilic Acid and Gemfibrozil Removal in Membrane Bioreactors. *Water Sci. Technol.* 71 (8), 1143–1150. doi:10.2166/wst.2015.079
- Kim, D., Orrego, D., Ximenes, E. A., and Ladisch, M. R. (2017). Cellulose Conversion of Corn Pericarp without Pretreatment. *Bioresour. Technol.* 245 (Pt A), 511–517. doi:10.1016/j.biortech.2017.08.156
- Kim, S. R., Lee, K.-S., Kong, I., Lesmana, A., Lee, W.-H., Seo, J.-H., et al. (2013). Construction of an Efficient Xylose-Fermenting Diploid *Saccharomyces cerevisiae* Strain through Mating of Two Engineered Haploid Strains Capable of Xylose Assimilation. *J. Biotechnol.* 164 (1), 105–111. doi:10.1016/j.jbiotec.2012.12.012
- Klinke, H. B., Thomsen, A. B., and Ahring, B. K. (2004). Inhibition of Ethanol-Producing Yeast and Bacteria by Degradation Products Produced during Pretreatment of Biomass. *Appl. Microbiol. Biotechnol.* 66 (1), 10–26. doi:10.1007/s00253-004-1642-2
- Koppram, R., and Olsson, L. (2014). Combined Substrate, Enzyme and Yeast Feed in Simultaneous Saccharification and Fermentation Allow Bioethanol Production from Pretreated spruce Biomass at High Solids Loadings. *Biotechnol. Biofuels* 7 (1), 54. doi:10.1186/1754-6834-7-54
- Kwak, S., Jo, J. H., Yun, E. J., Jin, Y.-S., and Seo, J.-H. (2019). Production of Biofuels and Chemicals from Xylose Using Native and Engineered Yeast Strains. *Biotechnol. Adv.* 37 (2), 271–283. doi:10.1016/j.biotechadv.2018.12.003
- Li, H., Chen, X., Xiong, L., Zhang, L., Chen, X., Wang, C., et al. (2019). Production, Separation, and Characterization of High-Purity Xylobiose from Enzymatic Hydrolysis of Alkaline Oxidation Pretreated Sugarcane Bagasse. *Bioresour. Technol.* 299, 122625. doi:10.1016/j.biortech.2019.122625
- Li, X., Chen, Y., and Nielsen, J. (2019). Harnessing Xylose Pathways for Biofuels Production. *Curr. Opin. Biotechnol.* 57, 56–65. doi:10.1016/j.copbio.2019.01.006
- Liu, G., Zhang, Q., Li, H., Qureshi, A. S., Zhang, J., Bao, X., et al. (2018). Dry Biorefining Maximizes the Potentials of Simultaneous Saccharification and Co-fermentation for Cellulosic Ethanol Production. *Biotechnol. Bioeng.* 115 (1), 60–69. doi:10.1002/bit.26444
- Rempel, A., de Souza Sossella, F., Margarites, A. C., Astolfi, A. L., Steinmetz, R. L. R., Kunz, A., et al. (2019). Bioethanol from *Spirulina Platensis* Biomass and the Use of Residuals to Produce Biomethane: An Energy Efficient Approach. *Bioresour. Technol.* 288, 121588. doi:10.1016/j.biortech.2019.121588
- Sambrook, J., and Russel, D. J. I. (2001). *Molecular Cloning: A Laboratory Manual*. 3rd ed. 49. New York: Cold Spring Harbor Laboratory Press, 895–909.
- Scanes, K. T., Hohmann, S., and Prior, B. A. (1998). Glycerol Production by the Yeast *Saccharomyces cerevisiae* and its Relevance to Wine. *A Rev.* 19 (1), 17–24. doi:10.21548/19-1-2239

- Tian, G., Ding, M., Xu, B., He, Y., Lyu, W., Jin, M., et al. (2018). A Novel Electrochemical Biosensor for Ultrasensitive Detection of Serum Total Bile Acids Based on Enzymatic Reaction Combined with the Double Oxidation Circular Amplification Strategy. *Biosens. Bioelectron.* 118, 31–35. doi:10.1016/j.bios.2018.07.030
- Tran, P. H. N., Ko, J. K., Gong, G., Um, Y., and Lee, S.-M. (2020). Improved Simultaneous Co-fermentation of Glucose and Xylose by *Saccharomyces cerevisiae* for Efficient Lignocellulosic Biorefinery. *Biotechnol. Biofuels* 13, 12. doi:10.1186/s13068-019-1641-2
- Wang, C., Bao, X., Li, Y., Jiao, C., Hou, J., Zhang, Q., et al. (2015). Data Set for Cloning and Characterization of Heterologous Transporters in *Saccharomyces cerevisiae* and Identification of Important Amino Acids for Xylose Utilization. *Data in brief* 4, 119–126. doi:10.1016/j.dib.2015.05.005
- Wang, X., Wang, G., Yu, X., Chen, H., Sun, Y., and Chen, G. (2017). Pretreatment of Corn stover by Solid Acid for D -lactic Acid Fermentation. *Bioresour. Technol.* 239, 490–495. doi:10.1016/j.biortech.2017.04.089
- Watanabe, K., Tachibana, S., and Konishi, M. (2019). Modeling Growth and Fermentation Inhibition during Bioethanol Production Using Component Profiles Obtained by Performing Comprehensive Targeted and Non-targeted Analyses. *Bioresour. Technol.* 281, 260–268. doi:10.1016/j.biortech.2019.02.081
- Wu, L., Feng, S., Deng, J., Yu, B., Wang, Y., He, B., et al. (2019). Altered Carbon Assimilation and Cellulose Accessibility to Maximize Bioethanol Yield under Low-Cost Biomass Processing in Corn Brittle Stalk. *Green. Chem.* 21 (16), 4388–4399. doi:10.1039/C9GC01237K
- Xiong, M., Chen, G., and Barford, J. (2011). Alteration of Xylose Reductase Coenzyme Preference to Improve Ethanol Production by *Saccharomyces cerevisiae* from High Xylose Concentrations. *Bioresour. Technol.* 102 (19), 9206–9215. doi:10.1016/j.biortech.2011.06.058
- Xu, H., Kim, S., Sorek, H., Lee, Y., Jeong, D., Kim, J., et al. (2016). *PHO13* Deletion-Induced Transcriptional Activation Prevents Sedoheptulose Accumulation during Xylose Metabolism in Engineered *Saccharomyces cerevisiae*. *Metab. Eng.* 34, 88–96. doi:10.1016/j.ymben.2015.12.007
- Zhang, C., Xue, Q., Hou, J., Mohsin, A., Zhang, M., Guo, M., et al. (2019). In-depth Two-Stage Transcriptional Reprogramming and Evolutionary Engineering of *Saccharomyces cerevisiae* for Efficient Bioethanol Production from Xylose with Acetate. *J. Agric. Food Chem.* 67 (43), 12002–12012. doi:10.1021/acs.jafc.9b05095
- Zhang, X., Wang, J., Zhang, W., Hou, J. y., Xiao, W., and Cao, L. (2018). Optimizing the Coordinated Transcription of central Xylose-Metabolism Genes in *Saccharomyces cerevisiae*. *Appl. Microbiol. Biotechnol.* 102 (16), 7207–7217. doi:10.1007/s00253-018-9172-5

Conflict of Interest: The authors declare that the research was conducted in the absence of any commercial or financial relationships that could be construed as a potential conflict of interest.

Publisher's Note: All claims expressed in this article are solely those of the authors and do not necessarily represent those of their affiliated organizations, or those of the publisher, the editors, and the reviewers. Any product that may be evaluated in this article, or claim that may be made by its manufacturer, is not guaranteed or endorsed by the publisher.

Copyright © 2022 Sun, Kong, Li, Li, Xue, Hou, Jia, Lei, Xiao, Shi and Cao. This is an open-access article distributed under the terms of the Creative Commons Attribution License (CC BY). The use, distribution or reproduction in other forums is permitted, provided the original author(s) and the copyright owner(s) are credited and that the original publication in this journal is cited, in accordance with accepted academic practice. No use, distribution or reproduction is permitted which does not comply with these terms.



Effects of Microwave-Assisted Liquid Hot Water Pretreatment on Chemical Composition and Structure of Moso Bamboo

Jie-Yu Cui¹, Ning Zhang^{2,3,4,5,6*} and Jian-Chun Jiang^{2,3,4,5,6*}

¹College of Chemical Engineering, Nanjing Forestry University, Nanjing, China, ²Institute of Chemical Industry of Forest Products, Chinese Academy of Forestry, Nanjing, China, ³National Engineering Laboratory for Biomass Chemical Utilization, Nanjing, China, ⁴Key Laboratory of Chemical Engineering of Forest Products, National Forestry and Grassland Administration, Nanjing, China, ⁵Key Laboratory of Biomass Energy and Material, Nanjing, China, ⁶Co-Innovation Center of Efficient Processing and Utilization of Forest Resources, Nanjing Forestry University, Nanjing, China

OPEN ACCESS

Edited by:

Lei Wang,
Ocean University of China, China

Reviewed by:

Quan Bu,
Jiangsu University, China
Yifeng Chen,
Luleå University of Technology,
Sweden

*Correspondence:

Ning Zhang
ningzhangemail@126.com
Jian-Chun Jiang
linhs_bioenergy@126.com

Specialty section:

This article was submitted to
Bioprocess Engineering,
a section of the journal
Frontiers in Bioengineering and
Biotechnology

Received: 25 November 2021

Accepted: 27 December 2021

Published: 07 February 2022

Citation:

Cui J-Y, Zhang N and Jiang J-C (2022)
Effects of Microwave-Assisted Liquid
Hot Water Pretreatment on Chemical
Composition and Structure of
Moso Bamboo.
Front. Bioeng. Biotechnol. 9:821982.
doi: 10.3389/fbioe.2021.821982

The effects of microwave assisted liquid hot water (MA-LHW) pretreatment on the chemical composition of Moso bamboo were investigated, and the fiber structure of pretreated residues were studied. The results showed that MA-LHW pretreatment had high selectivity for the degradation of hemicellulose in Moso bamboo, and the extracted hemicellulose could be used to prepare xylooligosaccharide through enzyme depolymerization. The degradation rates of cellulose and lignin after MA-LHW pretreatment were only 14.73% and 7.18%, which were significantly lower than those of LHW pretreatment; 155.0 mg/g xylobiose and 61.0 mg/g xylotrisoe can be obtained after enzymatic hydrolysis, and the yield of xylo-oligosaccharide reached 80.59% of the theoretical conversion rate. MA-LHW pretreatment increased the removal of hemicellulose, lignin, and other non-crystalline parts in bamboo materials, and more cellulose with crystalline structure was retained, which increased the CrI value of Moso bamboo by 14.84%. FTIR spectra showed that the characteristic peak intensity of hemicellulose was significantly reduced after MA-LHW pretreatment, which confirmed the selective degradation of hemicellulose by MA-LAW pretreatment. Moreover, MA-LHW pretreatment also destroyed O-H, C-H, C-O-C, and β -glucoside bonds in Moso bamboo fiber, caused by the recombination and synthesis of some groups (-CH₂ and C=O) of cellulose, hemicellulose, and lignin destroyed under pretreatment conditions.

Keywords: Moso bamboo, microwave assisted liquid hot water, pretreatment, structure, hemicellulose

1 INTRODUCTION

With the increasing shortage of petrochemical resources and the global energy crisis, the use of renewable biomass resources to produce new materials, fuels, and chemicals has become a research hotspot of many researchers. Moso bamboo is a perennial evergreen plant of Poaceae and Bambusoideae, which is widely distributed in tropical, sub-tropical, and warm temperate regions (Liu et al., 2019). It is one of the most valuable biomasses in the world and has the highest economic value. In addition, it has the advantages of fast growth, strong reproductive capacity, great development, and utilization potential (Wang et al., 2013). In China, Moso bamboo accounts for

more than 70% of the country's forest area, with a total area of 2.92 million hectares and an annual output value of nearly 5.85 billion yuan.

Like other lignocellulosic raw materials, bamboo is composed of cellulose, hemicellulose, and lignin, which interweave with each other to form a complex and dense structure and it is difficult to degrade. The structural system determines that the degradation of any kind of components is bound to be restricted by other components, resulting in the low hydrolysis efficiency of cellulose (Singh et al., 2015). Therefore, it is necessary to pretreat the raw materials, cut off the cellulose structure with cellulose degrading enzyme, release the sugar needed for fermentation, and then use these sugars to further produce bio alcohol liquid fuels such as fuel ethanol, butanol and pentanol, and high value-added chemicals such as xylitol, lactic acid, and so on. One of the difficulties is to find efficient and low-cost pretreatment technology. In contrast, the content of cellulose and lignin in bamboo is higher than that in straw, and it has the higher density and hardness than the straw.

The commonly used pretreatment methods include physical method, chemical method, and biological method (Zhang et al., 2016). Chemical method is widely used because of its advantages of high efficiency and easy industrialization. Like the dilute acid method, it mainly overcomes the obstacle of hemicellulose on the enzymatic hydrolysis in acidic environment such as sulfuric acid, formic acid, and acetic acid by interrupting the molecular chemical bond of polysaccharide. Dilute alkali method mainly uses NaOH, ammonia water, and lime water to dissolve lignin components in the cell wall, so as to increase the contact opportunity between raw cellulose and enzyme and improve the enzymatic hydrolysis rate of cellulose. The liquid hot water (LHW) pretreatment (Zhuang et al., 2016) process uses water as the reaction medium, does not need to add any chemical reagent, and has higher yield of hemicellulose derived sugar (including xylo-oligosaccharides and xylose), higher cellulase hydrolysis rate, and lower yield of degradation products. Compared with supercritical water (temperature higher than 374°C, pressure higher than 22 Mpa), liquid hot water (compressed liquid water between 160°C and 280°C, pressure higher than its saturated vapor pressure) also has good mass transfer performance (low viscosity and high diffusion coefficient). The ion product of liquid hot water is three orders of magnitude larger than that of normal state, which is 10^{-11} , that is, the concentration of H^+ and OH^- in neutral water is about 100 times higher than that of normal state (Wang et al., 2016). In this way, the liquid hot water itself will have the function of acid catalysis and alkali catalysis. In addition, its reaction conditions are more mild, are easier to control, and achieve large-scale production.

Microwave-assisted liquid hot water (MA-LHW) method developed on this basis is to use microwave as a heating tool, which can overcome the shortcomings of uneven heating of water, shorten the reaction time, improve the work efficiency, and have the advantages of fast heating speed, uniform heating, no temperature gradient, no lag effect, and so on (Luo et al., 2017). Microwave treatment of materials can produce physical and thermal effects. The physical effect is that microwave radiation produces a continuously changing magnetic field, which leads to the vibration of polar bonds in biomass

corresponding to the magnetic field and then provides internal heat to biomass (Chen et al., 2012). This distribution and vibration of polar bonds can accelerate physical, biological, and chemical processes (Ha et al., 2011). Thermal effect is that acetic acid is produced by heat treatment of materials in aqueous solution, which leads to spontaneous hydrolysis of materials in acidic environment. Microwave irradiation can change the ultrastructure of cellulose, remove lignin and hemicellulose, and improve the enzymatic hydrolysis efficiency of cellulose. In this research, the effects of MA-LHW pretreatment on the chemical composition and the structure of Moso bamboo were studied and the extracted hemicellulose was used to produce xylooligosaccharide through further enzyme depolymerization.

2 MATERIALS AND METHODS

2.1 Experimental Material

Experimental Moso bamboo powder was supplied by China National Bamboo Research Center. The bamboo powder was sieved through a 0.45 mm mesh screen and dried naturally.

2.2 Pretreatment Methods

LHW pretreatment method (Suriyachai et al., 2020): 10 g dried bamboo powder and 100 ml water were mixed into a 250 ml high-pressure reaction kettle. The reaction was run at 200°C for 30 min. After reaction, the mixture was centrifuged, and then the filter cake was washed with distilled water and dried at 105°C until a constant weight.

MA-LHW pretreatment method (Passos et al., 2013): Microwave-assisted liquid hot water pretreatment was carried out with the MWD-520 microwave digestion system which was produced by Shanghai Metash Instruments Co., Ltd.; 1 g dried bamboo powder and 20 ml water were mixed into a 50 ml microwave digestion tube. The reaction was run in the microwave digestion system at 200°C for 30 min. The microwave power was 1,000 W. After reaction, the mixture was centrifuged, and then the filter cake was washed with distilled water and dried at 105°C until a constant weight.

2.3 Analysis Method

2.3.1 Composition Analysis

The contents of cellulose, hemicellulose, and lignin in raw materials and pretreated materials were determined according to the method of NREL (Sluiter et al., 2010).

2.3.2 X-Ray Diffraction Analysis

The D8 Focus X-ray Diffractometer (XRD) produced by Brooke company in Germany was used to determine the relative crystallinity of the samples. The detection wavelength was 0.15406 nm and the sampling interval was 0.02°. The crystallinity is then calculated according to the formula proposed by Segal et al. (1959):

$$C_{rl}(\%) = [(I_{002} - I_{am})/I_{002}] \times 100 \quad (1)$$

where $C_{rl}(\%)$ is the percentage of relative crystallinity; I_{002} is the maximum intensity of (002) lattice diffraction angle (any unit);

TABLE 1 | Chemical composition change after different pretreatments.

Samples	Solid remain (%)	Glucan (%)		Xylan(%)		Klason lignin (%)	
		Content	Removal	Content	Removal	Content	Removal
Raw material	100.00	48.59	—	22.71	—	22.35	—
LHW	62.50	52.84	32.03	0.55	98.49	23.26	34.96
MA-LHW	63.83	64.91	14.73	5.28	85.16	32.50	7.18

and I_{am} is the scattering intensity of amorphous background diffraction (same as I_{002} unit) when 2θ is close to 18° .

2.3.3 Infrared Spectroscopic Analysis

The change of fiber structure was detected by Nicolet IS10 Fourier transform infrared spectrometer produced by American Nicolet company. The scanning wave number range was $4,000\text{--}500\text{ cm}^{-1}$. The calculation method of the relative intensity of the absorption peak is the ratio of the absorbance of the corresponding characteristic absorption peak to the absorbance of $1,372\text{ cm}^{-1}$; $1,372\text{ cm}^{-1}$ is only found in the IR of crystalline cellulose, which is a band related to crystallization (Chandel et al., 2014). The experimental results are the average of the three experimental results.

2.3.4 Scanning Electron Microscope Analysis

The morphological changes of Moso bamboo samples were observed by 3400-I scanning electron microscope (SEM) produced by Hitachi, Japanese. The magnification was 500 and 1,000 times.

3 RESULTS AND DISCUSSION

3.1 Chemical Composition Analysis After Different Pretreatment

The chemical components of Moso bamboo before and after pretreatment were determined with three samples. The results in this table were the average of the three samples.

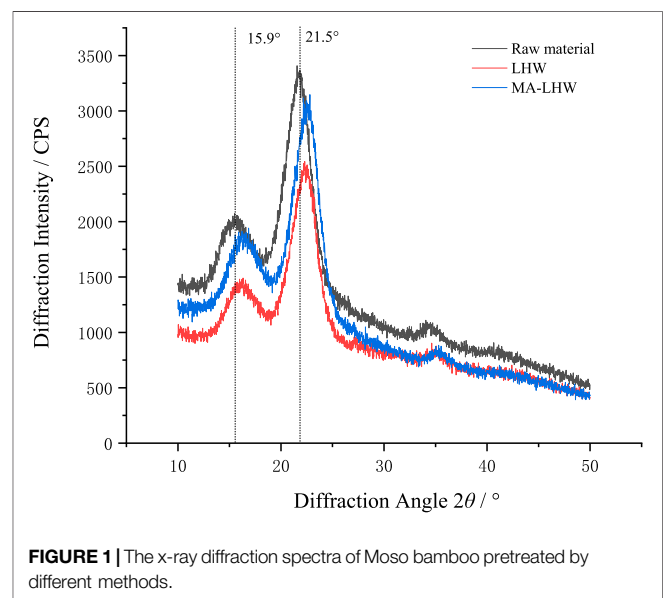
The content of cellulose, hemicellulose, and lignin (Table 1) of Moso bamboo material were 48.59, 22.71, and 22.35%, respectively. After the LHW and MA-LHW pretreatment, the composition of cellulose, hemicellulose, and lignin in Moso bamboo has changed greatly. The percentage of cellulose in remained materials after pretreatment increased significantly, especially pretreated by MA-LHW, which has high recovery of 85.27%, making the percentage of cellulose reach 64.91%. It can be seen from the results that both LHW and MA-LHW pretreatment can effectively hydrolyze hemicellulose in Moso bamboo. After LHW pretreatment, 98.49% of hemicellulose was hydrolyzed, while 32.03% of cellulose and 34.96% of lignin were also removed. The hydrolysis rate of hemicellulose was 85.16% after MA-LHW pretreatment, but under this condition, the lignin removal rate was only 7.18%, and the cellulose recovery rate was 22.84% higher than that of LHW pretreatment.

3.2 Effects of Different Pretreatment Methods on X-Ray Diffraction

The crystallinity of lignocellulosic was once thought to be a major obstacle to its enzymatic digestibility (Puri, 2004), and some other

TABLE 2 | Effect of different methods on relative crystallinity of Moso bamboo.

Sample	$2\theta = 22^\circ$	$2\theta = 18.4^\circ$	Crystallization index (%)
Raw material	3,367	1,699	49.53
LHW	3,353	1,598	52.33
MA-LHW	3,147	1,357	56.88

**FIGURE 1** | The x-ray diffraction spectra of Moso bamboo pretreated by different methods.

learners think that it was a remark of the extent of material destruction (Gao et al., 2013). As show in Table 2, after being pretreated by LHW, the CrI value of Moso bamboo increased by 5.65%, and after being pretreated by MA-LHW, it increased by 14.84%. This indicates that after pretreatment by LHW and MA-LHW, most hemicellulose and part of amorphous cellulose in Moso bamboo raw materials were removed, and the proportion of cellulose with crystalline structure increased accordingly, which was consistent with previous component analysis results (Mohan et al., 2015).

Generally, there are two types of natural cellulose, I_α and I_β . Cellulose I_α and I_β are triclinic cells with one chain and triclinic cells with two chains, respectively (Hinterstoisser and Salmén, 1999). Figure 1 shows that the pretreatment did not change the crystal types of Moso bamboo, which all belonged to typical cellulose I_α . At $2\theta = 15.9^\circ$, the non-crystalline part is mainly hemicellulose and lignin peak, and at $2\theta = 21.5^\circ$, the crystalline part is mainly I_α cellulose peak. However, after pretreatment with LHW and MA-LHW, the diffraction peak of Moso bamboo fiber

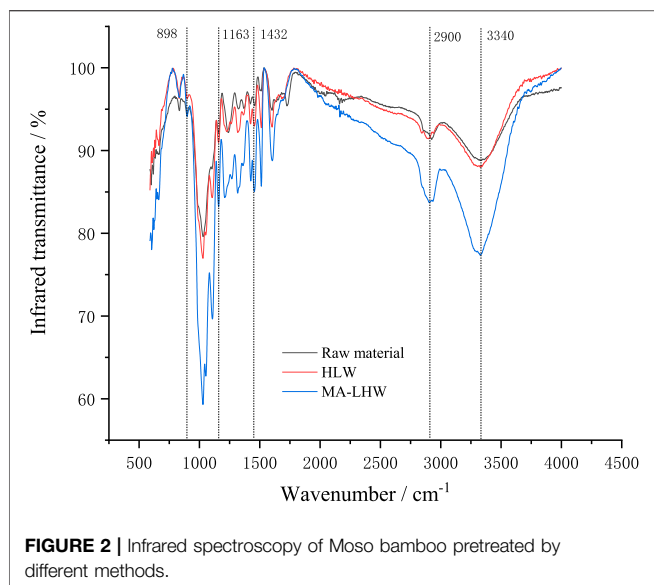


FIGURE 2 | Infrared spectroscopy of Moso bamboo pretreated by different methods.

at 21.5° shifted to 22.4°, and the peak width decreased slightly. This was also the result of the increase of the CrI value (Puri,2004).

3.3 Effects of Different Pretreatment Methods on Infrared Absorption

The changes in the chemical structure of materials before and after pretreatment cannot be completely identified by x-ray diffraction method alone, and other methods were needed to assist in observing the changes of other chemical groups. Moso bamboo samples being pretreated by LHW and MA-LHW were scanned by infrared spectroscopy. The results are shown in **Figure 2**. The structure attribution and the relative absorption intensity of the absorption peaks in infrared spectra are listed in **Table 3**. As can be seen from the changes of the relative absorption peak intensity, the pretreatment of MA-LHW has a more significant effect on the structure of Moso bamboo samples, which may be the result of the combined effect of physical effect and thermal effect from microwave.

The wider absorption peak near 3,340 cm^{-1} is the O-H characteristic absorption peak, which mainly comes from the glucose ring on cellulose (Sang et al., 2005). The peak near 2,900 cm^{-1} is the stretching vibration of C-H. After

pretreatment with LHW and MA-LHW, these absorption peaks intensity all decreased, which indicated that the pretreatment caused a certain degree of damage to the hydrogen and methyl bonds in Moso bamboo fiber, and cellulose molecules were more likely to fracture and hydrolyze after being pretreated by MA-LHW.

Moreover, the intensities of absorption peaks at 1,163 and 898 cm^{-1} also decreased after MA-LHW pretreatment, which suggests that C-O-C bonds and β -glycosidic bonds were damaged to the same extent by MA-LHW pretreatment. C-O-C bonds and β -glycosidic bonds were the main bonds in the supramolecular chain of cellulose and glucan, and their rupture meant that the degree of polymerization of cellulose molecule decreased and this can facilitate the subsequent hydrolysis (Lino et al., 2013).

In the Moso bamboo raw material, there was an obvious absorption peak of carboxyl group at 1,730 cm^{-1} , and its strength decreased significantly after pretreatment. The group was mainly the characteristic peak of hemicellulose (Schwanninger et al., 2004), so this indicated that most hemicellulose has been deacetylated, and the hemicellulose was easily damaged and degraded due to its low degree of polymerization.

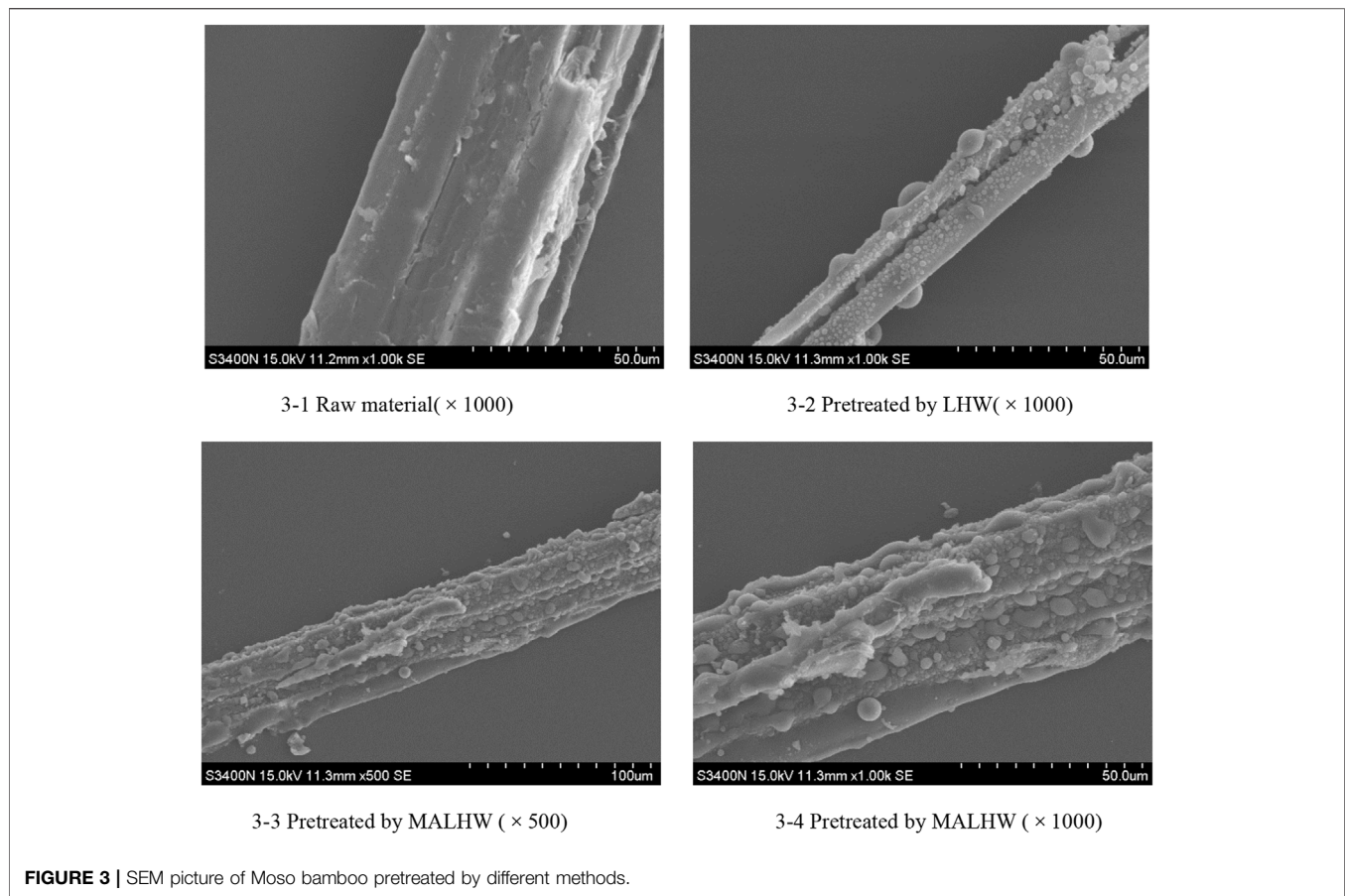
However, the relative absorption peak intensity at 1,432 cm^{-1} increased after pretreatment, in which the intensity increased significantly after pretreatment of MA-LHW. This indicated that the destruction of the carbon chain structure of sample fiber generated more methylene bonds, which was a highly active reaction intermediate (Abidi et al., 2008). From **Figure 2**, we also noticed that C=O stretching vibration peaks of cellulose, hemicellulose, and lignin were generated at 1,050 cm^{-1} after pretreatment, which may be caused by the recondensation of some groups of cellulose, hemicellulose, and lignin destroyed under pretreatment conditions. Therefore, the pretreatment process of LHW and MA-LHW was not only a degradation process, but also caused the recombination and synthesis of some groups.

3.4 Effects of Different Pretreatment Methods on Surface Morphology of Moso Bamboo

It can be seen from **Figure 3** of the scanning electron microscope that there are obvious differences between the surface morphology of the untreated raw materials and the treated materials, and there are also some connections. The

TABLE 3 | Structure attribution and relative strength of absorption peaks in IR spectra (Kim and Lee, 2005).

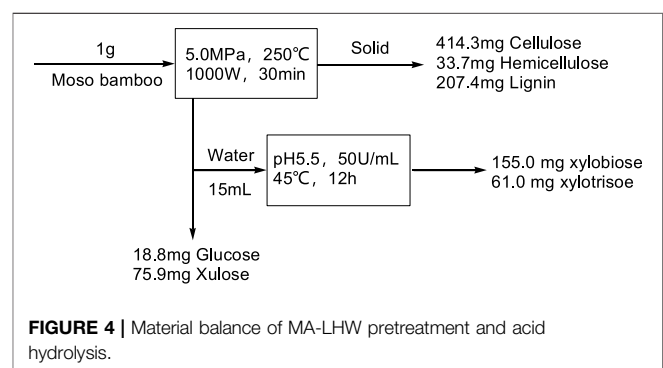
Wave number/ cm^{-1}	Response peak	Pretreatment methods		
		Raw material	Pretreated by LHW	Pretreated by MA-LHW
3,600–3,000	O-H stretching vibration	2.366	2.234	2.211
2,900	C-H stretching vibration	1.750	1.527	1.465
1,432	Cellulose CH ₂ bending vibration and shear vibration	0.757	1.006	1.099
1,730	Hemicellulose C=O stretching vibration	0.919	0.285	0.174
1,372	Cellulose and hemicellulose-CH bending vibration	1.000	1.000	1.000
1,163	Cellulose and hemicellulose C-O-C stretching vibration	1.577	1.578	1.429
898	β -glucoside bond vibration	1.197	0.668	0.504



raw material of Moso bamboo has bundle structure, which is relatively flat under the electron microscope, and there are obvious gullies, but it seems that the fibers are arranged as orderly, dense, and hard. After LHW and MA-LHW pretreatment, the structure of the whole Moso bamboo changed significantly due to the removal of hemicellulose. The smooth and orderly surface showed irregular bubbles like protrusions, which indicated that LHW and MA-LHW pretreatment had a strong erosion effect on Moso bamboo. Combined with the material composition analysis, x-ray diffraction crystallinity analysis, and IR spectrum analysis, the mass loss of Moso bamboo after MA-LHW pretreatment was more, and the changes of chemical bonds are more significant, reflecting the material morphology is more disorganized.

3.5 Enzyme Depolymerization of the Extracted Hemicellulose to Xylooligosaccharide

The detailed material balance of MA-LHW pretreatment and enzyme depolymerization are shown in **Figure 4**. There was 36.17% solid loss in the whole process, and the removal rate of hemicellulose reached 85.16%. After MA-LHW pretreatment (solid-liquid ratio 5%, w/V, hydrolysis at 250°C for 30 min,



power 1,000 W, pressure 5.0 MPa), 18.8 mg glucose and 75.9 mg xylose were obtained from each gram of Moso bamboo raw material. For the further depolymerization of extracted hemicellulose to obtain xylooligosaccharide, the xylanase was added into the hydrolysate with the concentration of 50 U/ml. After enzymatic hydrolysis for 20 h, the hydrolysis contained 10.33 g/L xylobiose and 4.07 g/L xylotriose. The yield of xylo-oligosaccharide reached 80.59%.

4 CONCLUSION

MA-LHW pretreatment of Moso bamboo can separate hemicellulose from lignocellulose through deacetylation reaction and enter the hydrolysate, which cannot only relieve the polymerization of hemicellulose on the structure of Moso bamboo but also facilitate the further enzymatic hydrolysis reaction. In our study, the final yield of xylooligosaccharide reached 80.59% of the theoretical yield, and the main products were xylobiose (11.83 g/L) and xylotriose (4.59 g/L). Additionally, MA-LHW pretreatment did not change the crystal types of Moso bamboo, but it caused an increase in crystallinity because most hemicellulose and part of amorphous cellulose in Moso bamboo raw materials were removed, and the proportion of cellulose with crystalline structure increased. At the same time, MA-LHW pretreatment destroyed O-H, C-H, C-O-C, and β -glucoside bonds in Moso bamboo fiber, caused by the recombination and synthesis of some groups (-CH₂ and C=O) of cellulose, hemicellulose, and lignin destroyed under pretreatment conditions.

REFERENCES

- Abidi, N., Hequet, E., Cabrales, L., Gannaway, J., Wilkins, T., and Wells, L. W. (2008). Evaluating Cell Wall Structure and Composition of Developing Cotton Fibers Using Fourier Transform Infrared Spectroscopy and Thermogravimetric Analysis. *J. Appl. Polym. Sci.* 107, 476–486. doi:10.1002/app.27100
- Chandel, A. K., Antunes, F. A., Anjos, V., Bell, M. J., Rodrigues, L. N., Polikarpov, I., et al. (2014). Multi-scale Structural and Chemical Analysis of Sugarcane Bagasse in the Process of Sequential Acid-Base Pretreatment and Ethanol Production by *Scheffersomyces Shehatae* and *Saccharomyces cerevisiae*. *Biotechnol. Biofuels* 7, 63–79. doi:10.1186/1754-6834-7-63
- Chen, W.-H., Ye, S.-C., and Sheen, H.-K. (2012). Hydrolysis Characteristics of Sugarcane Bagasse Pretreated by Dilute Acid Solution in a Microwave Irradiation Environment. *Appl. Energy* 93, 237–244. doi:10.1016/j.apenergy.2011.12.014
- Gao, Y., Xu, J., Zhang, Y., Yu, Q., Yuan, Z., and Liu, Y. (2013). Effects of Different Pretreatment Methods on Chemical Composition of Sugarcane Bagasse and Enzymatic Hydrolysis. *Bioresour. Tech.* 144, 396–400. doi:10.1016/j.biortech.2013.06.036
- Ha, S. H., Mai, N. L., An, G., and Koo, Y.-M. (2011). Microwave-Assisted Pretreatment of Cellulose in Ionic Liquid for Accelerated Enzymatic Hydrolysis. *Bioresour. Tech.* 102, 1214–1219. doi:10.1016/j.biortech.2010.07.108
- Hinterstoisser, B., and Salmén, L. (1999). Two-Dimensional Step-Scan FTIR: A Tool to Unravel the OH-Valency-range of the Spectrum of Cellulose I. *Cellulose* 6, 251–263. doi:10.1023/A:1009225815913
- Kim, T. H., and Lee, Y. Y. (2005). Pretreatment and Fractionation of Corn Stover by Ammonia Recycle Percolation Process. *Bioresour. Tech.* 96, 2007–2013. doi:10.1016/j.biortech.2005.01.015
- Liu, X., Guan, X., and Guo, M. (2019). Chemical Composts of Moso Bamboo (*Phyllostachys heterocycla* var. *Pubescens*) Culm at Different Ages and Heights. *Appl. Ecol. Env. Res.* 17, 4193–4203. doi:10.15666/aer/1702_41934203
- Luo, Y., Fan, J., Budarin, V. L., Hu, C., and Clark, J. H. (2017). Microwave-assisted Hydrothermal Selective Dissolution and Utilisation of Hemicellulose in *Phyllostachys heterocycla* Cv. *Pubescens*. *Green. Chem.* 19, 4889–4899. doi:10.15666/aer/1702_4193420310.1039/c7gc02300f
- Mohan, M., Banerjee, T., and Goud, V. V. (2015). Hydrolysis of Bamboo Biomass by Subcritical Water Treatment. *Bioresour. Tech.* 191, 244–252. doi:10.1016/j.biortech.2015.05.010
- Oh, S. Y., Yoo, D. I., Shin, Y., Kim, H. C., Kim, H. Y., Chung, Y. S., et al. (2005). Crystalline Structure Analysis of Cellulose Treated with Sodium Hydroxide and

DATA AVAILABILITY STATEMENT

The raw data supporting the conclusion of this article will be made available by the authors, without undue reservation.

AUTHOR CONTRIBUTIONS

JJ and NZ conceived and designed the experiments. J-yC performed the experiments and analyzed the data. J-yC wrote the manuscript. J-yC, NZ, and JJ revised and approved the final version of the manuscript.

ACKNOWLEDGMENTS

The authors acknowledge a research grant support by the National Natural Science Foundation of China (No. 31770636).

- Carbon Dioxide by Means of X-ray Diffraction and FTIR Spectroscopy. *Carbohydr. Res.* 340, 2376–2391. doi:10.1016/j.carres.2005.08.007
- Passos, F., Solé, M., García, J., and Ferrer, I. (2013). Biogas Production from Microalgae Grown in Wastewater: Effect of Microwave Pretreatment. *Appl. Energy* 108, 168–175. doi:10.1016/j.apenergy.2013.02.042
- Puri, V. P. (1984). Effect of Crystallinity and Degree of Polymerization of Cellulose on Enzymatic Saccharification. *Biotechnol. Bioeng.* 26, 1219–1222. doi:10.1002/bit.260261010
- Schwanninger, M., Rodrigues, J. C., Pereira, H., and Hinterstoisser, B. (2004). Effects of Short-Time Vibratory ball Milling on the Shape of FT-IR Spectra of wood and Cellulose. *Vib. Spectrosc.* 36, 23–40. doi:10.1016/j.vibspec.2004.02.003
- Segal, L., Creely, J. J., Martin, A. E., and Conrad, C. M. (1959). An Empirical Method for Estimating the Degree of Crystallinity of Native Cellulose Using the X-Ray Diffractometer. *Textile Res. J.* 29, 786–794. doi:10.1177/004051755902901003
- Singh, S., Cheng, G., Sathitsuksanoh, N., Wu, D., Varanasi, P., George, A., et al. (2015). Comparison of Different Biomass Pretreatment Techniques and Their Impact on Chemistry and Structure. *Front. Energy Res.* 2, 1–12. doi:10.3389/fenrg.2014.00062
- Sluiter, J. B., Ruiz, R. O., Scarlata, C. J., Sluiter, A. D., and Templeton, D. W. (2010). Compositional Analysis of Lignocellulosic Feedstocks. 1. Review and Description of Methods. *J. Agric. Food Chem.* 58, 9043–9053. doi:10.1021/jf1008023
- Soares Júnior, F. L., Dias, A. C. F., Fasanella, C. C., Taketani, R. G., Lima, A. O. d. S., Melo, I. S., et al. (2013). Endo- and Exoglucanase Activities in Bacteria from Mangrove Sediment. *Braz. J. Microbiol.* 44, 969–976. doi:10.1590/S1517-83822013000300048
- Suriyachai, N., Weerasai, K., Upajak, S., Khongchamnan, P., Wanmolee, W., Laosiripojana, N., et al. (2020). Efficiency of Catalytic Liquid Hot Water Pretreatment for Conversion of Corn stover to Bioethanol. *ACS Omega* 5 (46), 29872–29881. doi:10.1021/acsomega.0c04054
- Wang, B., Wei, W. J., Liu, C. J., You, W. Z., and Man, R. Z. (2013). Biomass and Carbon Stock in Moso Bamboo Forests in Subtropical China: Characteristics and Implications. *J. Trop. Sci.* 25, 137–148. doi:10.1515/hf-2011-0247
- Wang, W., Zhuang, X., Yuan, Z., Qi, W., Yu, Q., and Wang, Q. (2016). Structural Changes of Lignin after Liquid Hot Water Pretreatment and its Effect on the Enzymatic Hydrolysis. *Biomed. Res. Int.* 2016, 1–7. doi:10.1155/2016/8568604
- Zhang, K., Pei, Z., and Wang, D. (2016). Organic Solvent Pretreatment of Lignocellulosic Biomass for Biofuels and Biochemicals: A Review. *Bioresour. Tech.* 199, 21–33. doi:10.1016/j.biortech.2015.08.102

Zhuang, X., Wang, W., Yu, Q., Qi, W., Wang, Q., Tan, X., et al. (2016). Liquid Hot Water Pretreatment of Lignocellulosic Biomass for Bioethanol Production Accompanying with High Valuable Products. *Bioresour. Tech.* 199, 68–75. doi:10.1016/j.biortech.2015.08.051

Conflict of Interest: The authors declare that the research was conducted in the absence of any commercial or financial relationships that could be construed as a potential conflict of interest.

Publisher's Note: All claims expressed in this article are solely those of the authors and do not necessarily represent those of their affiliated organizations, or those of the publisher,

the editors, and the reviewers. Any product that may be evaluated in this article, or claim that may be made by its manufacturer, is not guaranteed or endorsed by the publisher.

Copyright © 2022 Cui, Zhang and Jiang. This is an open-access article distributed under the terms of the Creative Commons Attribution License (CC BY). The use, distribution or reproduction in other forums is permitted, provided the original author(s) and the copyright owner(s) are credited and that the original publication in this journal is cited, in accordance with accepted academic practice. No use, distribution or reproduction is permitted which does not comply with these terms.



Biochemical and Molecular Dynamics Study of a Novel GH 43 α -L-Arabinofuranosidase/ β -Xylosidase From *Caldicellulosiruptor saccharolyticus* DSM8903

Md. Abu Saleh^{1*}, Shafi Mahmud¹, Sarah Albogami², Ahmed M El-Shehawi², Gobindo Kumar Paul¹, Shirmin Islam¹, Amit Kumar Dutta³, Md. Salah Uddin¹ and Shahriar Zaman¹

¹Microbiology Laboratory, Department of Genetic Engineering and Biotechnology, University of Rajshahi, Rajshahi, Bangladesh, ²Department of Biotechnology, College of Science, Taif University, Taif, Saudi Arabia, ³Department of Microbiology, University of Rajshahi, Rajshahi, Bangladesh

OPEN ACCESS

Edited by:

Xin Zhou,
Nanjing Forestry University, China

Reviewed by:

Kankan Jiang,
Hangzhou Medical College, China
Limin Cao,
Capital Normal University, China

*Correspondence:

Md. Abu Saleh
saleh@ru.ac.bd

Specialty section:

This article was submitted to
Industrial Biotechnology,
a section of the journal
Frontiers in Bioengineering and
Biotechnology

Received: 07 November 2021

Accepted: 07 January 2022

Published: 11 February 2022

Citation:

Saleh MA, Mahmud S, Albogami S, El-Shehawi AM, Paul GK, Islam S, Dutta AK, Uddin MS and Zaman S (2022) Biochemical and Molecular Dynamics Study of a Novel GH 43 α -L-Arabinofuranosidase/ β -Xylosidase From *Caldicellulosiruptor saccharolyticus* DSM8903. *Front. Bioeng. Biotechnol.* 10:810542. doi: 10.3389/fbioe.2022.810542

The complete hydrolysis of xylan can be facilitated by the coordinated action of xylanase and other de-branching enzymes. Here, a GH43 α -L-arabinofuranosidase/ β -xylosidase (CAX43) from *Caldicellulosiruptor saccharolyticus* was cloned, sequenced, and biochemically investigated. The interaction of the enzyme with various substrates was also studied. With a half-life of 120 h at 70°C, the produced protein performed maximum activity at pH 6.0 and 70°C. The enzyme demonstrated a higher activity (271.062 ± 4.83 U/mg) against *para* nitrophenol (*p*NP) α -L-arabinofuranosides. With xylanase (XynA), the enzyme had a higher degree of synergy (2.30) in a molar ratio of 10:10 (nM). The interaction of the enzyme with three substrates, *p*NP α -L-arabinofuranosides, *p*NP β -D-xylopyranosides, and sugar beet arabinan, was investigated using protein modeling, molecular docking, and molecular dynamics (MD) simulation. During the simulation time, the root mean square deviation (RMSD) of the enzyme was below 2.5 Å, demonstrating structural stability. Six, five, and seven binding-interacting residues were confirmed against *p*NP α -L-arabinofuranosides, *p*NP β -D-xylopyranosides, and arabinan, respectively, in molecular docking experiments. This biochemical and *in silico* study gives a new window for understanding the GH43 family's structural stability and substrate recognition, potentially leading to biological insights and rational enzyme engineering for a new generation of enzymes that perform better and have greater biorefinery utilization.

Keywords: β -xylosidase, α -L-arabinofuranosidase, *Caldicellulosiruptor saccharolyticus*, biochemical characterization, molecular dynamics

INTRODUCTION

Xylan, the most prominent hemicellulose in plant biomass, is made up of a repeating β 1, four xylose residue backbone with modified galacturonic acid or acetyl group, rhamnose, and other substituents that vary depending on the other sources (Yen et al., 2015). Although the metabolic process and the molecular mechanism underlying the biosynthesis of xylan are not fully understood, β -D-xylosidase

works as a rate-limiting enzyme to hydrolyze xylan (Wierzbicki et al., 2019; Xu et al., 2019). Xylose is coupled to the arabinose substituents *via* α -1,2- or α -1,3-glycosidic linkages (De Vries and Visser, 2001).

Arabinose, the second most abundant pentose in nature, is found in varieties of plant cell wall polymers. Arabinoxylan, arabinan, and arabinogalactan are arabinose-containing polysaccharides that are significant components of plants' cell walls. The first chain of this heteropolysaccharide is created from β -1,4-linked D-xylopyranosyl sugar with L-arabinose scattered randomly. Furthermore, the backbone of arabinan and arabinogalactan consists of a linear 1,5-linked L-arabinofuranosyl polymer and 1,6-glycosidically connected D-galactopyranose residues, respectively (Liu et al., 2021).

Arabinoxylan degradation requires the coordinated action of endo-1,4- β -xylanases (EC 3.2.1.8), α -L-arabinofuranosidase (EC 3.2.1.55), α -glucuronidase (EC 3.2.1.139), acetyl (xylan) esterase (EC 3.1.1.72), ferulic acid esterase (EC 3.1.1.73), and β -xylosidase (EC 3.2.1.37) (De Vries et al., 2000; Sørensen et al., 2003). Side-chain substitution of L-arabinofuranoside is additionally found in xylans, and also, the alteration of those side chains can inhibit enzymatic degradation by xylanases and pectinases (Shallom et al., 2002; Rahman et al., 2003). The α -L-arabinofuranosidase catalyzes the hydrolysis of a terminal non-reducing α -1,2-, α -1,3-, and α -1,5-L-arabinofuranosyl residues from arabinoxylan and other polysaccharides containing L-arabinose (Saha 2000; Sozzi et al., 2002; Zhang et al., 2021). This enzyme acts in tandem with endo-1,5- α -L-arabinanases to convert polysaccharides or L-arabinose oligosaccharides to L-arabinose. L-arabinose holds back sucrose and glucose increase caused by sucrose consumption (Osaki et al., 2001; İlğü et al., 2018). As a result, it has the power to scale back obesity and forestall disorders linked to high glucose.

CAZy classified arabinofuranosidases in seven distinct glycoside hydrolase families (GH 1, 3, 10, 43, 51, 54, and 62), for knowing their structural and mechanical activities and evolutionary relationship according to the similarities of their protein sequences (Limsakul et al., 2021). Compared with most active catalytically potent xylosidases, GH 43 is categorized into GH-F clan for having no transglycosylation activity (Jordan and Li, 2007). According to the CAZy database (<http://www.cazy.org>), three putative β -xylosidases were assigned to this GH family. Various arabinofuranosidases from both fungal and bacterial origins have recently been found, offering essential information for understanding the enzymes. Thermotolerant biomass-degrading enzymes often perform well due to their higher stability and potentiality, and thermophilic bacteria are one of the finest sources of arabinofuranosidases (Hu et al., 2018; Long et al., 2020).

Although only a few publications deal with β -xylosidase from a couple of bacterial strains, no paper was found for β -xylosidase from *Caldicellulosiruptor saccharolyticus* DSM8903 (Xu et al., 2019). *C. saccharolyticus* is a thermophilic bacterium; hence, the enzyme produced by it would be thermostable. This enzyme can act in extreme environmental conditions and is crucial for biotechnological operations that require harsh settings (Friedrich and Antranikian, 1996). Furthermore, higher temperatures result in faster reaction speeds, reduced

contamination risk, and enhanced substrate solubility (Béguin and Aubert, 1994). Thus, thermotolerant α -L-arabinofuranosidase/ β -xylosidase has a great deal of commercial potential (Zurawski et al., 2015). GH families have varied substrate specificities for arabinofuranosidases. Individual members' substrate specificity could vary; the GH 51 and 54 AFs had a wide range of substrate specificity (Yang et al., 2015).

It is difficult to determine the regularity in the substrate specificity of enzymes with cost and labor intensity since a sufficient amount of xylosidase enzymes are required to conduct multiple tests. Furthermore, for mass production of the enzyme, biological stability, and characterization are critical (Ebert and Pelletier, 2017). Bioinformatics is becoming a prominent technique in this regard, since it provides user-friendly algorithms for gaining insights into protein-substrate interactions in a short amount of time and at a low cost (Ebert and Pelletier, 2017). Autodock is a software program that can be used to determine substrate specificity. In this study, we investigated the structural stability, substrate specificity, and potential of the GH43 family enzyme using biochemical and *in silico* methods, leading to biological insights and rational enzyme engineering to develop a new generation of enzymes.

MATERIALS AND METHODS

Bacterial Strains, Plasmid, and Culture Conditions

C. saccharolyticus DSM8903 was used as a source of genomic DNA. The expression vector *pEASY* blunt E_2 was used to produce a recombinant enzyme with six His-tags in its carboxy-terminus. Trans1-T1 phage-resistant chemically competent cells and *E. coli* BL21 (C43) were employed for recombinant plasmid maintenance and protein production, respectively. The recombinants were cultured in Luria-Bertani (LB) medium supplemented with ampicillin (100 μ g/ml) at 37°C. *C. saccharolyticus* DSM8903 genome was obtained from Molecular Microbial Engineering Group, Qingdao Institute of Bioenergy and Bioprocess Technology, China. Vector was obtained from TransGen Biotech Co. Ltd., China. All the used substrates were purchased from Megazyme; plasmid extraction kit and PCR purification kit from QIAGEN Shanghai Co. Ltd; and SDS, APS, DNA marker, protein marker, DNA loading dye, TEMED, etc. were purchased from Promega United States. All other used chemicals were of analytical grade.

Cloning and Expression

The gene (1586; *C. sac*-0359)-encoding region was amplified by PCR using pfu DNA polymerase for expression and purification of the α -L-arabinofuranosidase/ β -xylosidase from *C. saccharolyticus* in *E. coli*. The primers were designed so that they could be cloned in-frame into the *pEASY* blunt E_2 expression vector.

Recombinant vector (*pEASY* blunt E_2 and CAX43) (Supplementary Figure S1) was transformed to Trans1-T1 component cells and poured on LB agar with ampicillin (100 μ g/ml). Ampicillin-resistant clones were chosen, and

therefore, the accuracy of the inserts was confirmed by sequencing. Plasmid was extracted by using a TransGen plasmid purification kit and transformed into BL21 (C43) for protein expression.

Induction and Purification of Protein

After overnight incubation, one colony was injected in 10 ml of LB liquid and shaken at 37°C. The pre-culture was then transformed to a 1-L LB medium with ampicillin (100 μ g/ml) and incubated at 37°C. When the optical density at 600 nm reached 0.6 to 0.8, isopropyl-beta-D-thiogalactopyranoside (IPTG) was added at a concentration of 0.3 mM to induce protein, and also, the cells were shaken for an additional 7 h at 30°C.

The cells were collected after centrifuging (4,000 \times g) at 4°C for 30 min and resuspended to 15 ml washing buffer (Tris—30 mM and NaCl—500 mM, pH—8). By ultrasonication, the cells were then disrupted, and debris was removed by centrifugation (7,500 rpm) for 30 min at 4°C. Since the proteins expressed by *Caldicellulosiruptor* sp. are thermostable, the recombinant proteins were heated in an exceeding water bath at 70°C for 15 min before being chilled on ice. The cells were again centrifuged at 4°C (7,500 rpm for 15 min) to precipitate the other co-eluting thermostable host proteins. After loading the supernatant onto a nickel-nitrilotriacetic acid (Ni-NTA)-sefinose column (Sangon, Shanghai, China), it was washed with washing buffer and binding buffer (Tris—30 mM, NaCl—500 mM, and imidazole—40 mM; pH—8), then eluted with elution buffer (Tris—30 mM, NaCl—500 mM, and imidazole—300 mM; pH—8). By using a 10-kDa cutoff membrane, the active fractions were identified and reconstituted with protein storage buffer (Tris—30 mM, NaCl—100 mM, and 15% glycerol; pH—7). SDS-PAGE was carried out to separate the purified protein, and the Bradford method was used to determine the concentration with bovine serum albumin as a standard (Bradford, 1976).

Enzyme Activity Assay

The activity of α -L-arabinofuranosidase and β -xylosidase was measured using *p*NP α -L-arabinofuranosides and *p*NP β -D-xylopyranosides as substrates, according to the Beer-Lambert law. At optimum pH and temperature, one unit of enzyme activity was defined as the quantity of enzyme that released 1 μ mol of *p*-nitrophenol per minute. The reactions were as follows: 100 μ l of an enzyme (0.0002 mg/ml) in citric acid phosphate buffer (pH 6) and 100 μ l of 2 mM substrate in citric acid phosphate buffer (pH 6) were mixed and heated at 70°C for 10 min; 1 ml of 0.2 mM Na₂CO₃ was added to stop the reaction, and the absorbance was measured at 415 nm (Margolles and de los Reyes-Gavilán, 2003).

The Effect of pH and Temperature on the Enzyme Activity

The optimum pH for α -L-arabinofuranosidase/ β -xylosidase activity was measured by incubating at 70°C for 10 min in

citric acid phosphate buffer with pH ranging from 4 to 8. The effect of temperature on enzyme activity was also measured in the same buffer (pH 6) at different temperatures ranging from 40°C to 90°C. The findings were reported as relative activity (%).

By incubating the enzyme solutions at various temperatures (60°C, 70°C, 75°C, and 80°C), the half-life of thermal inactivation of the enzyme was determined as a function of incubation time. At various periods, aliquots of samples were extracted at appropriate intervals, and the activity of enzyme was assessed immediately. The time it took for the relative activity on the best-fitting line to decline by half was the enzyme's half-life.

Substrate Specificity and Kinetic Parameters

The substrate specificity of purified enzyme was also tested using *p*NP α -L-arabinofuranosides, *p*NP β -D-xylopyranosides, and a variety of different polysaccharides (1%) like beechwood xylan, insoluble wheat arabinoxylan, sugar beet arabinan, and debranched sugar beet arabinan. In the case of *p*NP α -L-arabinofuranosides and *p*NP β -D-xylopyranoside, the activity was measured by above description, but when using 1% polysaccharides (beechwood xylan, insoluble wheat arabinoxylan, sugar beet arabinan, and debranched sugar beet arabinan), the reaction mixtures (6 μ g enzyme and substrate) were incubated at 70°C for 14 h, and therefore, the reducing sugar was measured by the dinitrosalicylic acid method (Miller, 1959) with xylose and L-arabinose as a regular. Kinetic parameters of purified enzyme were examined against *p*NP α -L-arabinofuranosides with various concentrations (from 0.5 to 3.5 mM/l). By employing non-linear regression, K_m (mmol/L) and k_{cat} (/sec) were measured from the Michaelis-Menten equation with GraphPad Prism nine software (San Diego, CA) (Su et al., 2012).

Determination of Synergistic Effects

The enzyme XynA (xylanase, isolated from the *C. saccharolyticus*) was employed to explore the synergistic effects of the enzyme. The reactions were allotted at pH 6 and 70°C in citrate buffer. After incubation, the mixture was centrifuged, and therefore, the reducing sugar within the supernatant was quantified using the DNS technique (Miller, 1959). The synergy calculated supported the ratio between the reducing sugars liberated by the combined actions of enzymes to the sum of the sugar liberated by each enzyme (Iakiviak et al., 2011; Yang et al., 2016).

Ligand Preparation

The 3D structure of the *p*NP α -L-arabinofuranosides, *p*NP β -D-xylopyranosides, and arabinan was collected from the PubChem database (Kim et al., 2019). The structure was energy minimized using Avogadro software package in mmff94 force field with steepest gradient algorithms (Halgren, 1996).

Protein Preparation

The enzyme's 3D structure has yet to be explored, and we used a homology modeling approach to anticipate the hypothetical model structure of the protein. The sequence was obtained

from NCBI (Federhen, 2012) with the accession number (ABP66000.1) and entered into Phyre2 tools (Kelley et al., 2015) as Fasta format. The D chain of bifunctional GH43-CE from *Bacteriodes eggerthii* (PDB ID: 6MLY) was used as a template. The alignment coverage was 96% (13–522), and the confidence score was 100. The protein model was energy minimized in a short molecular dynamics simulation. After the minimization process, the accuracy and geometry of the model protein were checked in Ramachandran plot (Sheik et al., 2002), ERRAT (Hasan et al., 2015), and Verify3D (Eisenberg et al., 1997) model. The model structure was further used for docking and molecular dynamics simulation.

Active Site Prediction

The active sites of the modeled protein were predicted from the Computed Atlas of Surface Topology of protein (CASTp) webserver (<http://sts.bioe.uic.edu/castp>), which provides the pockets on the protein surface by molecular surface and solvent-accessible surface models. The webserver can predict the active sites/catalytic sites precisely along with the surface and functional features of the protein (Binkowski et al., 2003).

Molecular Docking

The docking study was conducted to search out the interaction dynamics of the glycosidase hydrolase and ligand molecules. The docking study was employed in AutoDock Vina (Trott and Olson, 2010). The ligand was converted into the PDBQT format because AutoDock Vina (Trott and Olson, 2019) only accepts this format. The grid box's center was X: 67.996, Y: 11.53, and Z: 21.38 Å, whereas the scales were X: 230, Y: 139, and Z: 161 Å. The binding energy of the docked complex was calculated in kilocalorie/mole unit. Also, the ligand molecules and protein were separated from PDB ID: 6MLY by the Discovery Studio and docked in AutoDock Vina to compare with the other docked complexes. The docked pose was combined in Pymol package (DeLano, 2002), and the interactions were also investigated in Discovery studio (Miyata, 2015).

Molecular Dynamics

The docked complexes were simulated by YASARA dynamics to analyze the conformational variety and stability of the complexes in AMBER14 force field. The systems were initially cleaned and hydrogen bonds were optimized. The linear constraint solver (LINCS) was used to limit all bond lengths, and SETTLE was employed to constrain water molecules. SHAKE algorithms were used to fix the chemical bond length in hydrogen bonds. The initial energy-minimization approach was carried out using the simulated annealing method by steepest gradient algorithms (5,000 cycles) (Krieger and Vriend, 2015). In all cases, a cubic simulation cell was formed with periodic boundary conditions by extending 20 Å and TIP3P water model with a solvent density of 0.997 g/cm³. The acid equilibrium constant for each amino acid within the protein was computed during the solvation process. The SCWRL algorithms were used in conjunction with hydrogen bonding network optimization to keep each amino acid residue in the correct protonation state. The Berendsen thermostat kept the simulation temperature constant. The system was neutralized by adding 0.9%

NaCl, pH 7.4, at 36.85°C temperature. The long-range electrostatic interaction was calculated using particle meshes Ewald algorithms with a cut-off radius of 8 Å (Krieger et al., 2006). The time was set as 2.0 fs for simulation. Finally, the simulation was run for 100 ns using the Berendsen thermostat and constant pressure, with each trajectory saved after a 100-ps interval. Root mean square deviation, root mean square fluctuation, a radius of gyration, solvent accessible surface area, hydrogen bond, and MM-PBSA were all calculated using simulated trajectories (Swargiary et al., 2020; Mahmud et al., 2021a; Mahmud et al., 2021b; Mahmud et al., 2021c; Mahmud et al., 2021d; Mahmud et al., 2021e; Mahmud et al., 2021f).

Statistical Analysis

For each biological sample, three independent replications were used in all studies. In SPSS statistics 20 software, the significance of each group's data was analyzed statistically at $p \leq 0.05$ using one-way ANOVA followed by Duncan's multiple range test (DMRT). Confidence of interval (CI) of the value was calculated using the following formula: $CI = \text{mean} \pm SE$. Z / \sqrt{n} . Here, SE is for sample standard error; n stands for sample size; Z stands for confidence level value. Graphical figures were prepared using GraphPad Prism 8.

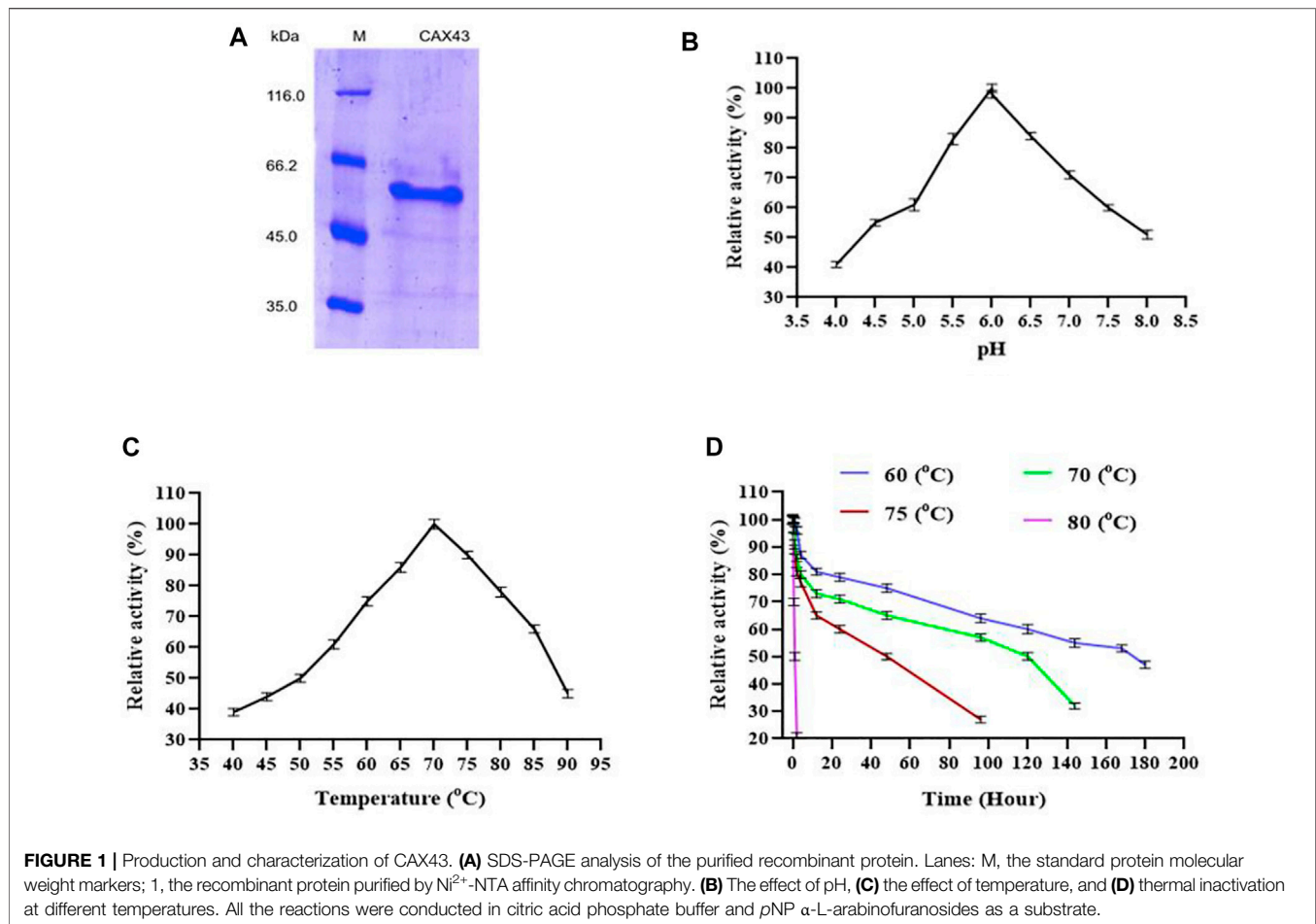
RESULTS

Gene Cloning and Sequencing

PCR was used to extract a 1,586-kb gene fragment from *C. saccharolyticus*. This gene encodes 528 amino acids, predicting a molecular weight of 60.59 kDa. We investigated the phylogenetic relationship (Supplementary Figure S2) of this enzyme with other GH43 family enzymes from different bacterial species. The deduced amino acid had 99.05% similarity with the GH43 from *Caldicellulosiruptor* sp. F32. No signal peptide was predicted by using the signal IP-5. Based on substrate specificity, the α -L-arabinofuranosidases have been classified into two glycoside hydrolase families (EC 3.2.1.55 and EC 3.2.1.99) and to five glycoside hydrolase families, 3, 43, 51, 54, and 62 based on sequence homology.

Expression, Purification, and Biochemical Characterization of Recombinant Protein

For purification of recombinant protein, a histidine tag was appended to the c-terminus of the protein. This His-tagged protein was purified using a nickel affinity chromatography (Figure 1A) and demonstrated a molecular weight of 60.59 kDa. The biochemical characteristics of purified α -L-arabinofuranosidase/ β -xylosidase were investigated using pNP α -L-arabinofuranosides and β -D-xylopyranosides as a substrate at 70°C. The enzyme activity was examined by covering the range between pH 4 to eight at 70°C. CAX43 showed its highest level of activity at pH 6 (Figure 1B). The activity of the recombinant enzyme was also examined at different temperatures ranging from 40°C to 90°C, and the higher activity was recorded at 70°C (Figure 1C). To observe the thermostability, the enzyme was incubated at 60°C, 70°C, 75°C, and 80°C for various periods



with pNP α -L-arabinofuranosides as a substrate. The enzyme had a half-life over 160 h at 60°C, but at 80°C, the enzyme lost its activity rapidly (**Figure 1D**).

The enzyme was active against different synthetic (pNP α -L-arabinofuranosides and β -D-xylopyranosides) and natural (wheat arabinoxylan, sugar beet arabinan, and debranched sugar beet arabinan) substrates. The specific activity of the enzyme (U/mg) was 271.061 ± 4.83 , 111.822 ± 3.23 , 0.693 ± 0.08 , 2.672 ± 0.83 , and 1.061 ± 0.33 for pNP α -L-arabinofuranosides, pNP- β -D-xylopyranoside, wheat arabinoxylan, sugar beet arabinan, and debranched sugar beet arabinan, respectively. The kinetic parameters of the recombinant enzyme were determined by using pNP α -L-arabinofuranosides. The Michaelis–Menten constant (K_m), turn over number (k_{cat}), and the catalytic efficiencies (k_{cat}/K_m) of the enzyme were $1.071 \text{ mmol l}^{-1}$, 234.674 s^{-1} , and $219.323 \text{ m (mol l}^{-1})^{-1} \text{ s}^{-1}$, respectively.

Substrate Specificity and Interaction With an Endo-Xylanase

CAX43 exhibited a wide range of substrate specificity. The enzyme's ability to liberate sugar from beechwood xylan, wheat arabinoxylan, sugar beet arabinan, and debranched arabinan was tested for up to 14 h, and the results are

presented in **Supplementary Figure S3**. The highest activity was observed against sugar beet arabinan. The enzyme had a lower activity against beechwood xylan and wheat arabinoxylan than sugar beet arabinan and debranched arabinan.

The dinitrosalicylic acid method was used to investigate the synergistic effects of CAX43 with an endo-xylanase (XynA) against wheat arabinoxylan (WAX) (Miller, 1959). Various molar ratios were used to investigate the synergistic effects (**Figure 2**). The higher (corresponding to a score of 2.301) degree of synergy (DOS) was observed with XynA and CAX43 in a ratio of 10:10 (**Table 1**). The confidence of interval of these values was 1.604 and 2.221.

Protein Modeling and Active Site Prediction

The 3D structure of the hypothetical model of the enzyme was predicted from Phyre2 tools. The protein model was energy minimized in brief dynamics simulation, where the secondary structure (helix, sheet, turn, and coil) from the hypothetical protein maintained its integrity (**Supplementary Figure S4A**). The root mean square deviation of the C-alpha atoms had a steady profile and did not deviate excessively. The root mean square deviation (RMSD) was below 2.5 Å during the whole simulation period, which indicates the conformational stability of the hypothetical protein (**Figure 3A**). The root mean square

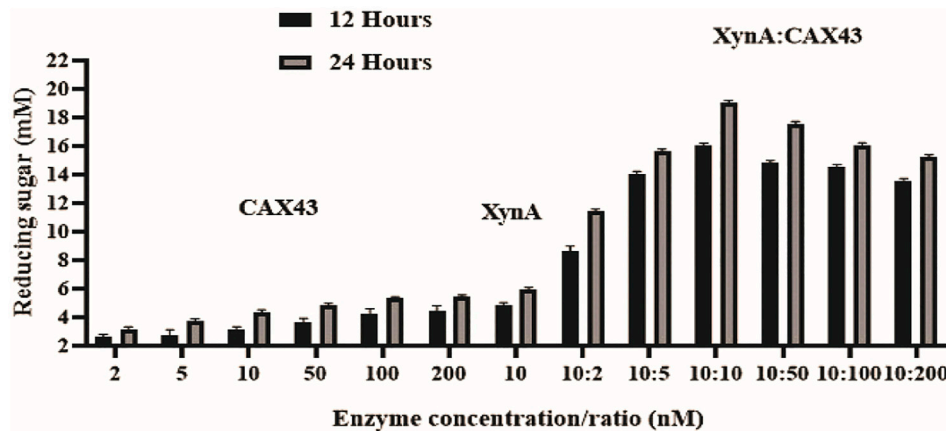


FIGURE 2 | Synergistic effects of CAX43 with XynA. A series of enzyme combinations (molar ratio) were used. All reactions were performed at pH 6 and 70°C against wheat arabinoxylan for two different time durations (12 and 24 h). Reducing sugars were measured by DNS method.

TABLE 1 | Synergistic effect of XynA and CAX43 in various combinations (nM) on wheat arabinoxylan. Data were recorded after 24 h of incubation.

Enzyme ratio (nM) XynA/CAX43	Amount of sugars released (mM) \pm SD	Degree of synergy
10:2	11.403 \pm 0.295	1.228 ^a
10:5	15.310 \pm 0.335	1.820 ^b
10:10	18.806 \pm 0.310	2.301 ^d
10:50	17.606 \pm 0.203	2.212 ^d
10:100	15.311 \pm 0.401	2.036 ^c
10:200	14.703 \pm 0.500	1.866 ^b

*Different letters indicate significant differences between mean \pm SD of treatments (n = 3) at a p < 0.05 significance level.

fluctuation of the amino acid residues of the model protein had a lower RMSF profile for maximum amino acid, which denotes the proteins' stable nature (**Figure 3B**). Therefore, the ERRAT score

of the minimized protein was greater than 80%, indicating the structural accurateness of the model protein (**Supplementary Figure S4B**). Moreover, Ramachandran plot analysis of the protein model revealed that 97% of residues were in the core region, which coincides with the complex accuracy (**Supplementary Figure S5**). We chose this structure for further investigation based on the projected protein model's quality rating (**Figure 4A, B**).

The CASTp webserver predicts the active sites of the modeled protein, and about 56 catalytic sites were obtained from the server. Those active points are Phe43, Asn44, Cys45, Val46, Gly48, Val67, Glu68, Arg69, Leu70, Pro71, Ser72, Pro73, Glu74, Tyr75, Thr77, Pro78, Gln79, Ile80, Lys82, Gly83, Ile84, Trp85, Ala86, Ser101, Met102, Pro103, Asp104, Gly130, Ile132, Asp133, Pro134, Ala149, Phe150, Ala151, Phe157, Ser159, Thr189, Glu191, Trp334, His335, Ala336, Asn337, Pro338,

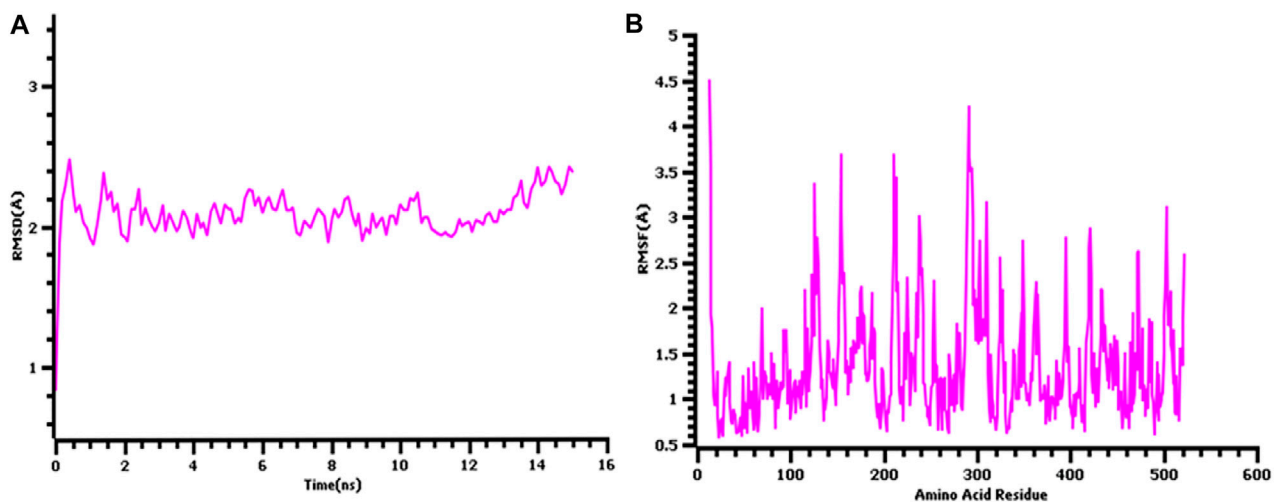


FIGURE 3 | The quality assessment of the hypothetical protein (**A**) root mean square deviation of the model protein and (**B**) the root mean square fluctuation of the hypothetical model.

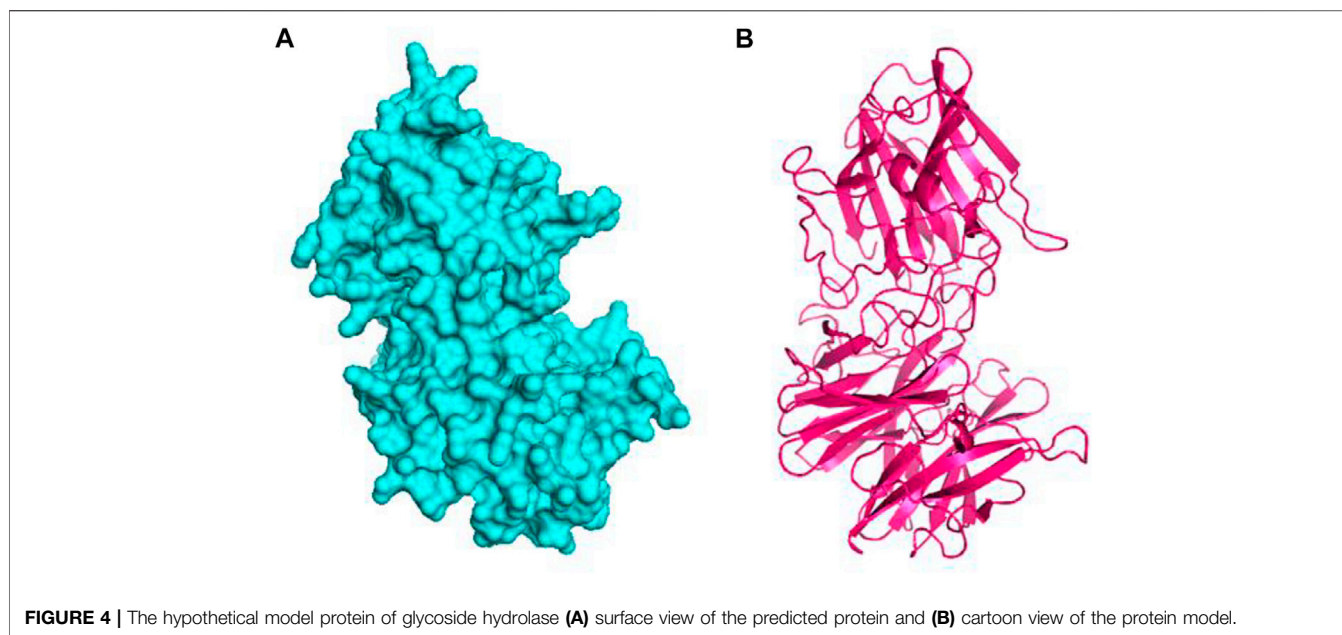


TABLE 2 | The binding interactions of the docked complexes. The binding residues were analyzed in Discovery Studio software package.

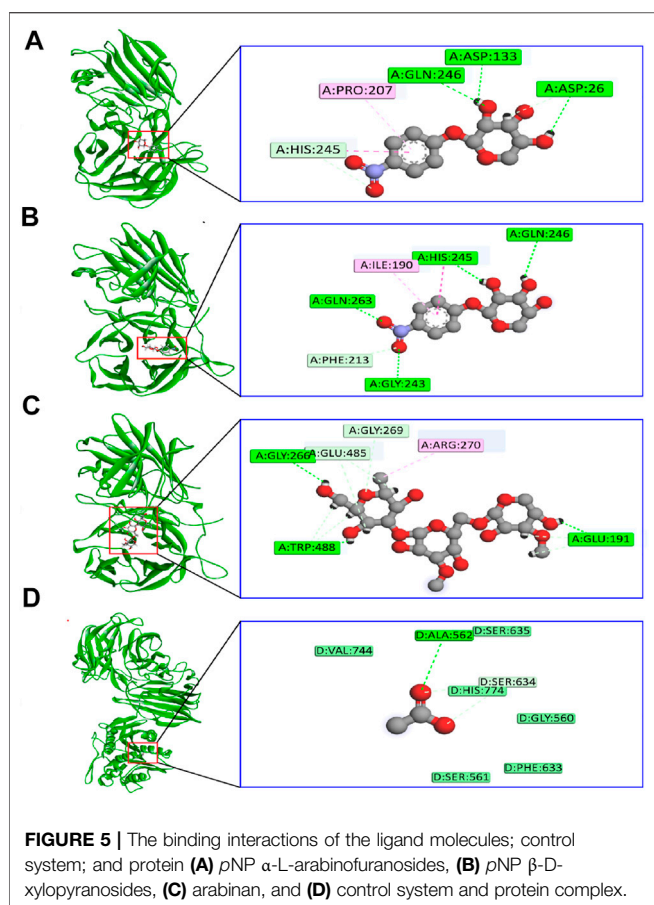
Complex	Residues	Bond type	Distance (Å)	Energy (Kcal/mol)
<i>p</i> NP α -L-arabinofuranosides	Asp26	Hydrogen bond	2.46	-8.7
	Asp133	Hydrogen bond	2.70	
	Glu191	Hydrogen bond	2.76	
	Gly209	Hydrogen bond	3.09	
	Ile190	Pi-alkyl	5.21	
	Pro207	Pi-alkyl	4.67	
<i>p</i> NP β -D-xylopyranosides	Gln246	Hydrogen bond	2.16	-7.8
	Glu191	Hydrogen bond	2.34	
	Gly214	Hydrogen bond	2.95	
	Asp133	Hydrogen bond	2.36	
	Gly209	Hydrogen bond	2.94	
	His245	Pi-Pi stacked	4.89	
Arabinan	Ile487	Hydrogen bond	2.92	-8.3
	Glu485	Hydrogen bond	2.31	
	Asp133	Hydrogen bond	2.77	
	Gly266	Hydrogen bond	3.06	
	Gly81	Hydrogen bond	2.85	
	Gly269	Hydrogen bond	2.49	
	Arg270	Hydrogen bond	3.08	

Gln339, Asn364, Ile369, Phe370, Phe371, Met372, Pro373, Asn374, Leu375, Ile405, Phe496, Cys497, and Ile498.

Molecular Docking

The binding interactions of protein and ligand complexes were studied. The *p*NP α -L-arabinofuranosides, *p*NP β -D-xylopyranosides, and arabinan had a binding energy of -8.7 kcal/mol, -7.8 kcal/mol, and -8.3 kcal/mol, respectively (Table 2). The control system had -7.6 kcal/mol energy in the molecular docking study. The *p*NP α -L-arabinofuranosides had three hydrogen bonds at the Gln246, Asp133, and Asp26 positions; one carbon hydrogen bond at His245; and one pi-alkyl bond at the Pro207 position (Figure 5A). This

compound interacts in the active site of the modeled protein at Asp133 position. *p*NP β -D-xylopyranosides formed four hydrogen bonds at the Gly243, Gln263, His245, and Gln246 positions; one carbon hydrogen bond at the Phe213 position, and one pi-alkyl bond at the Ile190 position (Figure 5B). The arabinan had three hydrogen bonds at the Glu191, Trp488, and Gly266 positions; two carbon hydrogen bonds at the Gly269 and Glu485 positions; and one pi-alkyl bond at the Arg270 position (Figure 5C), whereas it interacts in the active site of the modeled protein at the Glu191 position. Moreover, the control system had one hydrogen bond at the Ala562 position and one carbon hydrogen bond at the Ser634 position (Figure 5D).



Molecular Dynamics

The dynamics simulation was conducted to confirm the docking and structural stability of the complexes (**Supplementary Figure S6**). The root mean square deviations of the complexes were depicted in **Supplementary Figure S6A**. The RMSD value of the three docked complexes had an initial upper trend from 0 to 30 ns, but they did not rise sharply. The RMSD profile of these complexes tends to be stable at that phase and maintain the constancy. pNP α -L-arabinofuranosides and pNP β -D-xylopyranosides had more RMSD profile at that phase than arabinan, but they did not fluctuate much. This trend correlates with the structural stability of the complexes.

Therefore, the solvent-accessible expanse of the complexes was analyzed (**Supplementary Figure S6B**) to know the change within the protein surface area, where a higher SASA profile indicated the expansion in protein volume and a lower SASA profile indicates the truncated nature of the protein. Although pNP-L-arabinofuranosides had a reduced surface area throughout the remainder of the simulation time, the SASA values of the three complexes followed a similar pattern from 0 to 20-ns simulation times. Although the complex had a fluctuation in SASA profile, it was small, and the complex's profile remained steady. The pNP β -D-xylopyranosides had a higher SASA profile than other complexes, indicating that the complex had expanded in volume. The arabinan experienced some changes as well, but they did not diverge significantly in SASA.

The radius of gyration of the complexes was analyzed (**Supplementary Figure S6C**) to grasp the complex's liability and motions. The arabinan had a lower RG profile than the other two complexes during the entire simulation time. This trend is related to the structural compactness of the other two complexes. The pNP α -L-arabinofuranosides and pNP β -D-xylopyranosides had a higher RG profile than arabinan as they are more mobile in simulating conditions. However, these two complexes had lower deviation, indicating that they were more rigid. Moreover, the hydrogen bond of the system defines the stable nature of the complex, and any change in hydrogen bond number can lead to flexibility (**Supplementary Figure S6D**). The three complexes had less hydrogen bond at the start, but they had a gentle trend within the entire simulation trajectory.

The root mean square fluctuations of the complexes indicate the flexibility across the amino acid residues of the complexes. From **Supplementary Figure S7**, the RMSF profile of the complexes was much lower than most of the amino acid residues. The maximum amino acid residues exhibited an RMSF value of less than 2.5 Å, except Glu13 (2.70 Å), Arg154 (4.05 Å), Ile155 (2.92 Å), Glu176 (2.91 Å), Lys212 (3.21 Å), Thr186 (2.54 Å), Thr239 (2.53 Å), Asp291 (2.72 Å), Gly292 (3.38 Å), Lys310 (2.61 Å), Lys367 (2.64), Lys503 (3.226 Å), and Phe522 (2.62 Å), indicating less flexibility.

DISCUSSION

All *Caldicellulosiruptor* species are extremely thermophilic and purely anaerobic, allowing them to degrade plant biomass without any physical and chemical intervention (Yang et al., 2009). Knowing the functions of novel cellulolytic enzymes is crucial for reaching higher quantities of fermentable sugars (Blumer-Schuette et al., 2008). The GH43 is a large family with over 10,000 sequences organized into 37 subfamilies. The CAZy database contains three enzymes from *C. saccharolyticus* that have the GH43 domain. Bifunctional activity with both β -xylosidase and α -L-arabinofuranosidase activity has also been reported (Mai et al., 2000; Canakei et al., 2007; Morana et al., 2008).

Over 80°C, α -L-arabinofuranosidases from *Thermotoga maritima* (Miyazaki, 2005), *Sulfolobus solfataricus* (Morana et al., 2007), and *Clostridium thermocellum* (Taylor et al., 2006) exhibited higher activity. The half-lives of α -L-arabinofuranosidases from *T. maritima* (Miyazaki, 2005), *S. solfataricus* (Morana et al., 2007), *Thermotoga thermarum* DSM 5069 (Xie et al., 2016), and *Thermobacillus xylanilyticus* (Debeche et al., 2002) were 2, 7, 2, and 2 h, respectively at 90°C. However, *C. saccharolyticus* depicted a half-life of 49 h at 75°C (Lim et al., 2010). A multimodular XynF containing GH43 from *C. saccharolyticus* was described (Saleh et al., 2017) and demonstrated maximal activity at pH 6.5 and 70°C temperature. In this study, the recombinant enzyme exhibited higher activity at pH 6.0 and 70°C temperatures. Among all the tested substrates, the enzyme exhibited higher activity against the synthetic substrate pNPA. The enzyme demonstrated no activity against beechwood xylan and had a reduced level of activity against wheat arabinoxylan. The result reflects that CAX43 is more

effective against synthetic substances than natural ones, which is justified by previous research (de Camargo et al., 2018). Sugar beet arabinan and debranched arabinan contain α -1-2, 1-3, and 1-5 glycosidic bonds. CAX43 showed 2.52 times higher activity against sugar beet arabinan than debranched arabinan. This result indicated that it preferred α 1-2 and α 1-3 bonds over α 1-5 bonds.

Prior researches showed that combining hydrolytic enzymes was a beneficial strategy for enhancing sugar releases at a low cost (Taylor et al., 2006; Canakei et al., 2007; Morana et al., 2007; Limsakul et al., 2021). Synergic action was often assessed because the combined effect was greater than the sum of the individual effects. CAX43 was incubated with one extracellular protein XynA from *Caldicellulosiruptor* sp. in various combinations of molar ratio since the molar ratio is important for successful saccharification (Kim et al., 2014). CAX43 showed a substantial synergistic impact against wheat arabinoxylan when incubated with XynA. Among different molar ratios, 10:10 exhibited a higher DOS. This DOS is significantly different from other DOS values except 10:50 ratio (Table 1). Similar results were obtained when XynF was combined with XynA against wheat arabinoxylan (Saleh et al., 2017). Moreover, Mroueh et al. (2019) combined RcAbf62Am2,3 and RcAbf43Ad2,3 with arabinoxylan and got a synergistic factor of 1.53. However, endoxylanases are unable to cleave substrates containing large amounts of arabinoxylan without prior or simultaneous incubation with arabinofuranosidases (Sornyotha et al., 2007; Teeravivattanakit et al., 2017; Mroueh et al., 2019). So, the synergistic potentiality of the CAX43 may open a new dimension in this regard.

Different indicators were used to assess synergy in various systems. In protein-protein interaction, synergy is defined by the value of DOS > 1 indicates synergism, DOS < 1 indicates antagonism, and DOS = 1 indicates indifference, but in the case of plant extracts and antibiotics interaction, synergy is suggested by FIC index (Silva et al., 2019). FIC between 0.5 and 1 indicates synergy, FIC \geq 4.0 indicates antagonism, and between 4.0 and 1.0 indicates indifference.

As the substrates include over 30 different 4-nitrophenol (PNP)-glycosides, oligosaccharides, and polysaccharides, traditional substrate-specificity analysis for arabinofuranosidase is time-consuming and expensive. Nowadays, molecular mechanisms of substrate binding and catalysis are deciphered using structure-based molecular dynamics simulations, allowing for the rational design of the enzyme to improve its catalytic efficiency and stability (Chen et al., 2015; Yang et al., 2015). Here, we performed an all-atom molecular dynamics simulation for confirming the docking stability of the docked complexes. Also, the docked complexes interacted at the active sites of the protein, which is crucial for the targeted inhibitions or disrupting the function of the target protein. Therefore, the binding energy of the control was lower than the other three complexes, which indicates much better favorable binding of the ligand molecules. Our findings revealed that all three docked complexes are stable with upper trends of RMSD value within 0–30 ns. Molecular dynamics (MD) simulations of β -xylosidase from *Thermomyces lanuginosus* also showed stable nature in 20 ns (Gramany et al., 2016). During the simulations, the radius of gyration (Rg) study revealed the protein's compactness (Lobanov et al., 2008). Even though arabinan had a lower Rg profile than the

other two substrates, all of the complexes were stiff. At pH 7, β -xylosidase showed substantial fluctuations between residues 150 and 200 (Gramany et al., 2016), but CAX43 enzyme showed reduced flexibility across the board. The surface area of the complexes was also analyzed where the stable and lesser degree of fluctuations were observed for the complexes indicating the lower degree of changes in the surface area. Therefore, the hydrogen bond pattern was also similar in the simulation trajectories, which defines the rigid conformations of the docked complexes. The flexibility across the amino acid residues was also observed for very small number of residues, which defines the stable nature, and maximum residues had lower RMSF than 2.5 Å.

CONCLUSION

In this study, a GH43 α -L-arabinofuranosidase/ β -xylosidase from thermophilic *C. saccharolyticus* DSM8903 was cloned and purified. Our findings show that it can adapt to harsh environments while also possessing desired features such as increased specific and synergistic activity. Molecular dynamics simulation studies revealed major information on binding this enzyme with respective substrates. This study also indicated similar and higher stability in the form of protein-ligand complexes. The docked complexes were validated through the stable profile from the multiple simulation descriptors of the simulation trajectories. As a result, it can be used in the industrial production of L-arabinose in conjunction with endoarabinanase and/or xylanase. The combined findings suggest this enzyme is stable and that it could be used for rational enzyme engineering for improved biorefineries.

DATA AVAILABILITY STATEMENT

The original contributions presented in the study are included in the article/Supplementary Material; further inquiries can be directed to the corresponding author.

AUTHOR CONTRIBUTIONS

MAS contributed in the conceptualization, investigation, writing, editing and supervision. SM contributed in the investigation, validation, data curation, and drafting. SA and AME contributed in the fund acquisition for publication and editing. GKP contributed in the investigation, validation, and data curation. SI contributed in the drafting, resources gathering, and methodology. AKD contributed resources and in the methodology. MSU and SZ contributed in the review and editing. All authors contributed to the article and approved the submitted version.

FUNDING

This work was supported by the Grant for Advanced Research in Education (No. LS2018758), Ministry of Education, Government

of the People's Republic of Bangladesh and Taif University Researchers Supporting Project number (TURSP-2020/202), Taif University, Taif, Saudi Arabia.

and Bioprocess Technology, Shandong, China) for providing the genome and vector.

ACKNOWLEDGMENTS

The authors are grateful to FuLi Li and Ming Lu (Molecular microbial Engineering Group, Qingdao Institute of Bioenergy

SUPPLEMENTARY MATERIAL

The Supplementary Material for this article can be found online at: <https://www.frontiersin.org/articles/10.3389/fbioe.2022.810542/full#supplementary-material>

REFERENCES

- Béguin, P., and Aubert, J.-P. (1994). The Biological Degradation of Cellulose. *Fems Microbiol. Rev.* 13 (3), 25–58. doi:10.1111/j.1574-6976.1994.tb00033.x
- Binkowski, T. A., Naghibzadeh, S., and Liang, J. (2003). CASTp: Computed Atlas of Surface Topography of Proteins. *Nucleic Acids Res.* 31, 3352–3355. doi:10.1093/nar/gkg512
- Blumer-Schuetz, S. E., Kataeva, I., Westpheling, J., Adams, M. W., and Kelly, R. M. (2008). Extremely Thermophilic Microorganisms for Biomass Conversion: Status and Prospects. *Curr. Opin. Biotechnol.* 19 (3), 210–217. doi:10.1016/j.copbio.2008.04.007
- Bradford, M. M. (1976). A Rapid and Sensitive Method for the Quantitation of Microgram Quantities of Protein Utilizing the Principle of Protein-Dye Binding. *Anal. Biochem.* 72 (2), 248–254. doi:10.1006/abio.1976.9999
- Canakci, S., Belduz, A. O., Saha, B. C., Yasar, A., Ayaz, F. A., and Yayli, N. (2007). Purification and Characterization of a Highly Thermostable α -L-Arabinofuranosidase from *Geobacillus Caldoxylolyticus* TK4. *Appl. Microbiol. Biotechnol.* 75, 813–820. doi:10.1007/s00253-007-0884-1
- Chen, Q., Luan, Z.-J., Cheng, X., and Xu, J.-H. (2015). Molecular Dynamics Investigation of the Substrate Binding Mechanism in Carboxylesterase. *Biochemistry* 54 (9), 1841–1848. doi:10.1021/bi5015612
- de Camargo, B. R., Claassens, N. J., Quirino, B. F., Noronha, E. F., and Kengen, S. W. M. (2018). Heterologous Expression and Characterization of a Putative Glycoside Hydrolase Family 43 Arabinofuranosidase from *Clostridium Thermocellum* B8. *Enzyme Microb. Technol.* 109, 74–83. doi:10.1016/j.enzmictec.2017.09.014
- De Vries, R. P., and Visser, J. (2001). *Aspergillus* Enzymes Involved in Degradation of Plant Cell Wall Polysaccharides. *Microbiol. Mol. Biol. Rev.* 65 (4), 497–522. doi:10.1128/MMBR.65.4.497-522.2001
- De Vries, R. P., Kester, H. C. M., Poulsen, C. H., Benen, J. A. E., and Visser, J. (2000). Synergy between Enzymes from *Aspergillus* Involved in the Degradation of Plant Cell wall Polysaccharides. *Carbohydr. Res.* 327 (4), 401–410. doi:10.1016/s0008-6215(00)00066-5
- Debeche, T., Bliard, C., Debeire, P., and O'Donohue, M. J. (2002). Probing the Catalytically Essential Residues of the α -L-arabinofuranosidase from *Thermobacillus Xylanilyticus*. *Protein Eng.* 15 (1), 21–28. doi:10.1093/protein/15.1.21
- DeLano, W. L. (2002). Pymol: An Open-Source Molecular Graphics Tool. *CCP4 Newsl. Protein Crystallogr.* 40, 82–92. Available at: https://www.ccp4.ac.uk/newsletters/newsletter40/11_pymol.pdf
- Ebert, M. C., and Pelletier, J. N. (2017). Computational Tools for Enzyme Improvement: Why Everyone Can - and Should - Use Them. *Curr. Opin. Chem. Biol.* 37, 89–96. doi:10.1016/j.cbpa.2017.01.021
- Eisenberg, D., Lüthy, R., and Bowie, J. U. (1997). VERIFY3D: Assessment of Protein Models with Three-Dimensional Profiles. *Methods Enzymol.* 277, 396–404. doi:10.1016/s0076-6879(97)77022-8
- Federhen, S. (2012). The NCBI Taxonomy Database. *Nucleic Acids Res.* 40, D136–D143. doi:10.1093/nar/gkr1178
- Friedrich, A. B., and Antranikian, G. (1996). Keratin Degradation by *Fervidobacterium Pennavorans*, a Novel Thermophilic Anaerobic Species of the Order Thermotogales. *Appl. Environ. Microbiol.* 62 (8), 2875–2882. doi:10.1128/aem.62.8.2875-2882.1996
- Gramany, V., Khan, F. I., Govender, A., Bisetty, K., Singh, S., and Permaul, K. (2016). Cloning, Expression, and Molecular Dynamics Simulations of a Xylosidase Obtained from *Thermomyces Lanuginosus*. *J. Biomol. Struct. Dyn.* 34, 1681–1692. doi:10.1080/07391102.2015.1089186
- Halgren, T. A. (1996). Merck molecular force field. II. MMFF94 van der Waals and electrostatic parameters for intermolecular interactions. *J. Comput. Chem.* 17, 520–552. doi:10.1002/(sici)1096-987x(199604)17:5/6<520:aid-jcc2>3.0.co;2-w
- Hasan, M. A., Mazumder, M. H. H., Chowdhury, A. S., Datta, A., and Khan, M. A. (2015). Molecular-docking Study of Malaria Drug Target Enzyme Transketolase in *Plasmodium Falciparum* 3D7 Portends the Novel Approach to its Treatment. *Source Code Biol. Med.* 10, 7. doi:10.1186/s13029-015-0037-3
- Hu, Y., Zhao, Y., Tian, S., Zhang, G., Li, Y., Li, Q., et al. (2018). Screening of a Novel Glycoside Hydrolase Family 51 α -L-Arabinofuranosidase from *Paenibacillus Polymyxa* KF-1: Cloning, Expression, and Characterization. *Catalysts* 8 (12), 589. doi:10.3390/catal8120589
- Iakiviak, M., Mackie, R. I., and Cann, I. K. O. (2011). Functional Analyses of Multiple Lichenin-Degrading Enzymes from the Rumen Bacterium *Ruminococcus Albus* 8. *Appl. Environ. Microbiol.* 77, 7541–7550. doi:10.1128/AEM.06088-11
- İlgü, H., Sürmeli, Y., and Şanlı-Mohamed, G. (2018). A Thermophilic α -L-Arabinofuranosidase from *Geobacillus Vulcani* GS90: Heterologous Expression, Biochemical Characterization, and its Synergistic Action in Fruit Juice Enrichment. *Eur. Food Res. Technol.* 244 (9), 1627–1636. doi:10.1007/s00217-018-3075-7
- Jordan, D. B., and Li, X.-L. (2007). Variation in Relative Substrate Specificity of Bifunctional β -D-xylosidase/ α -L-arabinofuranosidase by Single-Site Mutations: Roles of Substrate Distortion and Recognition. *Biochim. Biophys. Acta Proteins Proteomics* 1774 (9), 1192–1198. doi:10.1016/j.bbapap.2007.06.010
- Kelley, L. A., Mezulis, S., Yates, C. M., Wass, M. N., and Sternberg, M. J. E. (2015). The Pyre2 Web portal for Protein Modeling, Prediction and Analysis. *Nat. Protoc.* 10, 845–858. doi:10.1038/nprot.2015.053
- Kim, I. J., Lee, H. J., Choi, I.-G., and Kim, K. H. (2014). Synergistic Proteins for the Enhanced Enzymatic Hydrolysis of Cellulose by Cellulase. *Appl. Microbiol. Biotechnol.* 98, 8469–8480. doi:10.1007/s00253-014-6001-3
- Kim, S., Chen, J., Cheng, T., Gindulyte, A., He, J., He, S., et al. (2019). PubChem 2019 Update: Improved Access to Chemical Data. *Nucleic Acids Res.* 47, D1102–D1109. doi:10.1093/nar/gky1033
- Krieger, E., and Vriend, G. (2015). New Ways to Boost Molecular Dynamics Simulations. *J. Comput. Chem.* 36, 996–1007. doi:10.1002/jcc.23899
- Krieger, E., Nielsen, J. E., Spronk, C. A. E. M., and Vriend, G. (2006). Fast Empirical pKa Prediction by Ewald Summation. *J. Mol. Graph. Model.* 25, 481–486. doi:10.1016/j.jmkgm.2006.02.009
- Lim, Y.-R., Yoon, R.-Y., Seo, E.-S., Kim, Y.-S., Park, C.-S., and Oh, D.-K. (2010). Hydrolytic Properties of a Thermostable α -L-arabinofuranosidase from *Caldicellulosirupter Saccharolyticus*. *J. Appl. Microbiol.* 109 (4), 1188–1197. doi:10.1111/j.1365-2672.2010.04744.x
- Limsakul, P., Phitsuwon, P., Waeonukul, R., Pason, P., Tachaapaikoon, C., Poomputsa, K., et al. (2021). A Novel Multifunctional Arabinofuranosidase/Endoxylanase/ β -Xylosidase GH43 Enzyme from *Paenibacillus Curdlanolyticus* B-6 and its Synergistic Action to Produce Arabinose and Xylose from Cereal Arabinoxylan. *Appl. Environ. Microbiol.* 87 (24), e0173021. doi:10.1128/aem.01730-21
- Liu, Y., Vanderhaeghen, S., Feiler, W., Angelov, A., Baudrexel, M., Zverlov, V., et al. (2021). Characterization of Two α -L-Arabinofuranosidases from *Acetivibrio Mesophilus* and Their Synergistic Effect in Degradation of Arabinose-

- Containing Substrates. *Microorganisms* 9 (7), 1467. doi:10.3390/microorganisms9071467
- Lobanov, M. Y., Bogatyreva, N. S., and Galzitskaya, O. V. (2008). Radius of Gyration as an Indicator of Protein Structure Compactness. *Mol. Biol.* 42, 623–628. doi:10.1134/S0026893308040195
- Long, L., Sun, L., Lin, Q., Ding, S., and St John, F. J. (2020). Characterization and Functional Analysis of Two Novel Thermotolerant α -L-arabinofuranosidases Belonging to Glycoside Hydrolase Family 51 from *Thielavia terrestris* and Family 62 from *Eupenicillium parvum*. *Appl. Microbiol. Biotechnol.* 104 (20), 8719–8733. doi:10.1007/s00253-020-10867-7
- Mahmud, S., Paul, G. K., Afroze, M., Islam, S., Gupta, S. B. R., Razu, M. H., et al. (2021a). Efficacy of Phytochemicals Derived from *avicennia officinalis* for the Management of Covid-19: A Combined In Silico and Biochemical Study. *Molecules* 26, 2210. doi:10.3390/molecules26082210
- Mahmud, S., Paul, G. K., Biswas, S., Afroze, S., Mita, M. A., Hasan, M. R., et al. (2021b). Prospective Role of Peptide-Based Antiviral Therapy against the Main Protease of SARS-CoV-2. *Front. Mol. Biosci.* 8, 1–11. doi:10.3389/fmolb.2021.628585
- Mahmud, S., Rafi, M. O., Paul, G. K., Promi, M. M., Shimu, M. S. S., Biswas, S., et al. (2021c). Designing a Multi-Epitope Vaccine Candidate to Combat MERS-CoV by Employing an Immunoinformatics Approach. *Sci. Rep.* 11, 1–21. doi:10.1038/s41598-021-92176-1
- Mahmud, S., Biswas, S., Paul, G. K., Mita, M. A., Promi, M. M., Afroze, S., et al. (2021d). Plant-based Phytochemical Screening by Targeting Main Protease of Sars-Cov-2 to Design Effective Potent Inhibitors. *Biology* 10, 589–618. doi:10.3390/biology10070589
- Mahmud, S., Biswas, S., Kumar Paul, G., Mita, M. A., Afroze, S., Robiul Hasan, M., et al. (2021e). Antiviral Peptides against the Main Protease of SARS-CoV-2: A Molecular Docking and Dynamics Study. *Arabian J. Chem.* 14, 103315. doi:10.1016/j.arabjc.2021.103315
- Mahmud, S., Mita, M. A., Biswas, S., Paul, G. K., Promi, M. M., AfrozeHasan, S. R., et al. (2021f). Molecular Docking and Dynamics Study to Explore Phytochemical Ligand Molecules against the Main Protease of SARS-CoV-2 from Extensive Phytochemical Datasets. *Expert Rev. Clin. Pharmacol.* 14, 1305–1315. doi:10.1080/17512433.2021.1959318
- Mai, V., Wiegel, J., and Lorenz, W. W. (2000). Cloning, Sequencing, and Characterization of the Bifunctional Xylosidase-Arabinosidase from the Anaerobic Thermophile *Thermoanaerobacter ethanolicus*. *Gene* 247, 137–143. doi:10.1016/s0378-1119(00)00106-2
- Margolles, A., and de los Reyes-Gavilán, C. G. (2003). Purification and Functional Characterization of a Novel α -L-Arabinofuranosidase from *Bifidobacterium longum* B667. *Appl. Environ. Microbiol.* 69, 5096–5103. doi:10.1128/AEM.69.9.5096-5103.2003
- Miller, G. L. (1959). Use of Dinitrosalicylic Acid Reagent for Determination of Reducing Sugar. *Anal. Chem.* 31, 426–428. doi:10.1021/ac60147a030
- Miyata, T. (2015). Discovery Studio Modeling Environment. *Ensemble* 17, 98–104.
- Miyazaki, K. (2005). Hyperthermophilic α -L-arabinofuranosidase from *Thermotoga maritima* MSB8: Molecular Cloning, Gene Expression, and Characterization of the Recombinant Protein. *Extremophiles* 9, 399–406. doi:10.1007/s00792-005-0455-2
- Morana, A., Paris, O., Maurelli, L., Rossi, M., and Cannio, R. (2007). Gene Cloning and Expression in *Escherichia coli* of a Bi-functional β -D-xylosidase/ α -L-arabinosidase from *Sulfolobus solfataricus* Involved in Xylan Degradation. *Extremophiles* 11, 123–132. doi:10.1007/s00792-006-0020-7
- Morana, A., Paris, O., Maurelli, L., Rossi, M., and Cannio, R. (2008). Gene Cloning and Expression in *Escherichia coli* of a Bi-functional β -D-xylosidase/ α -L-arabinosidase from *Sulfolobus solfataricus* Involved in Xylan Degradation. *Extremophiles* 11, 123–132. doi:10.1007/s00792-006-0020-7
- Mroueh, M., Aruanno, M., Borne, R., De Philip, P., Fierobe, H.-P., Tardif, C., et al. (2019). The Xyl-Doc Gene Cluster of *Ruminiclostridium cellulolyticum* Encodes GH43- and GH62- α -L-Arabinofuranosidases with Complementary Modes of Action. *Biotechnol. Biofuels* 12 (1), 144. doi:10.1186/s13068-019-1483-y
- Osaki, S., Kimura, T., Sugimoto, T., Hizukuri, S., and Iritani, N. (2001). L-arabinose Feeding Prevents Increases Due to Dietary Sucrose in Lipogenic Enzymes and Triacylglycerol Levels in Rats. *J. Nutr.* 131, 796–799. doi:10.1093/jn/131.3.796
- Rahman, A. K. M., Kato, K., Kawai, S., and Takamizawa, K. (2003). Substrate Specificity of the α -L-arabinofuranosidase from *Rhizomucor pusillus* HHT-1. *Carbohydr. Res.* 338, 1469–1476. doi:10.1016/s0008-6215(03)00203-9
- Saha, B. C. (2000). α -L-Arabinofuranosidases. *Biotechnol. Adv.* 18, 403–423. doi:10.1016/s0734-9750(00)00044-6
- Saleh, M. A., Han, W.-J., Lu, M., Wang, B., Li, H., Kelly, R. M., et al. (2017). Two Distinct α -L-Arabinofuranosidases in *Caldicellulosiruptor* Species Drive Degradation of Arabinose-Based Polysaccharides. *Appl. Environ. Microbiol.* 83, e00574–17. doi:10.1128/AEM.00574-17
- Shallom, D., Belakhov, V., Solomon, D., Gilead-Gropper, S., Baasov, T., Shoham, G., et al. (2002). The Identification of the Acid-Base Catalyst of α -Arabinofuranosidase from *Geobacillus stearothermophilus*T-6, a Family 51 Glycoside Hydrolase. *FEBS Lett.* 514, 163–167. doi:10.1016/s0014-5793(02)02343-8
- Sheik, S. S., Sundararajan, P., Hussain, A. S. Z., and Sekar, K. (2002). Ramachandran Plot on the Web. *Bioinformatics* 18, 1548–1549. doi:10.1093/bioinformatics/18.11.1548
- Silva, D. M., Costa, P. A. D., Ribon, A. O. B., Purgato, G. A., Gaspar, D.-M., and Diaz, M. A. N. (2019). Plant Extracts Display Synergism with Different Classes of Antibiotics. *Acad. Bras. Ciênc.* 91, e20180117. doi:10.1590/0001-3765201920180117
- Sørensen, H. R., Meyer, A. S., and Pedersen, S. (2003). Enzymatic Hydrolysis of Water-Soluble Wheat Arabinoxylan. I. Synergy between α -L-Arabinofuranosidases, Endo-1,4- β -Xylanases, and β -xylosidase Activities. *Biotechnol. Bioeng.* 81, 726–731. doi:10.1002/bit.10519
- Sornyotha, S., Kyu, K., and Ratanakhanokchai, K. (2007). Purification and Detection of Linamarin from Cassava Root Cortex by High Performance Liquid Chromatography. *Food Chem.* 104 (4), 1750–1754. doi:10.1016/j.foodchem.2006.10.071
- Sozzi, G. O., Greve, L. C., Prody, G. A., and Labavitch, J. M. (2002). Gibberellic Acid, Synthetic Auxins, and Ethylene Differentially Modulate α -L-Arabinofuranosidase Activities in Antisense 1-Aminocyclopropane-1-Carboxylic Acid Synthase Tomato Pericarp Discs. *Plant Physiol.* 129, 1330–1340. doi:10.1104/pp.001180
- Su, X., Mackie, R. I., and Cann, I. K. O. (2012). Biochemical and Mutational Analyses of a Multidomain Cellulase/mannanase from *Caldicellulosiruptor besicii*. *Appl. Environ. Microbiol.* 78, 2230–2240. doi:10.1128/AEM.06814-11
- Swargiary, A., Mahmud, S., and Saleh, M. A. (2020). Screening of Phytochemicals as Potent Inhibitor of 3-chymotrypsin and Papain-like Proteases of SARS-CoV2: an In Silico Approach to Combat COVID-19. *J. Biomol. Struct. Dyn.*, 1–15. doi:10.1080/07391102.2020.1835729
- Taylor, E. J., Smith, N. L., Turkenburg, J. P., D'Souza, S., Gilbert, H. J., and Davies, G. J. (2006). Structural Insight into the Ligand Specificity of a Thermostable Family 51 Arabinofuranosidase, Araf51, from *Clostridium thermocellum*. *Biochem. J.* 395, 31–37. doi:10.1042/BJ20051780
- Teeravivattanakit, T., Baramee, S., Pitsuwan, P., Sornyotha, S., Waeonukul, R., Pason, P., et al. (2017). Chemical Pretreatment-independent Saccharifications of Xylan and Cellulose of rice Straw by Bacterial Weak Lignin-Binding Xylanolytic and Cellulolytic Enzymes. *Appl. Environ. Microbiol.* 83 (22), e01522. doi:10.1128/AEM.01522-17
- Trott, O., and Olson, A. J. (2010). AutoDock Vina: Improving the Speed and Accuracy of Docking with a New Scoring Function, Efficient Optimization, and Multithreading. *J. Comput. Chem.* 31, 455. doi:10.1002/jcc.21334
- Trott, O., and Olson, A. J. (2019). AutoDock Vina: Improving the Speed and Accuracy of Docking with a New Scoring Function, Efficient Optimization, and Multithreading. *J. Comput. Chem.* 31, 455–461. doi:10.1002/jcc.21334
- Wierzbicki, M. P., Maloney, V., Mizrachi, E., and Myburg, A. A. (2019). Xylan in the Middle: Understanding Xylan Biosynthesis and its Metabolic Dependencies toward Improving wood Fiber for Industrial Processing. *Front. Plant Sci.* 10, 1–29. doi:10.3389/fpls.2019.00176
- Xie, J., Zhao, D., Zhao, L., Pei, J., Xiao, W., Ding, G., et al. (2016). Characterization of a Novel Arabinose-Tolerant α -L-Arabinofuranosidase with High Ginsenoside Rc to Ginsenoside Rd Bioconversion Productivity. *J. Appl. Microbiol.* 120 (3), 647–660. doi:10.1111/jam.13040
- Xu, B., Dai, L., Zhang, W., Yang, Y., Wu, Q., Li, J., et al. (2019). Characterization of a Novel Salt-, Xylose- and Alkali-Tolerant GH43 Bifunctional β -xylosidase/ α -L-arabinofuranosidase from the Gut Bacterial Genome. *J. Biosci. Bioeng.* 128 (4), 429–437. doi:10.1016/j.jbiosc.2019.03.018

- Yang, S.-J., Kataeva, I., Hamilton-Brehm, S. D., Engle, N. L., Tschaplinski, T. J., Doepcke, C., et al. (2009). Efficient Degradation of Lignocellulosic Plant Biomass, without Pretreatment, by the Thermophilic Anaerobe "Anaerocellum Thermophilum" DSM 6725. *Appl. Environ. Microbiol.* 75, 4762–4769. doi:10.1128/AEM.00236-09
- Yang, Y., Zhang, L., Guo, M., Sun, J., Matsukawa, S., Xie, J., et al. (2015). Novel α -L-Arabinofuranosidase from *Cellulomonas Fimi* ATCC 484 and its Substrate-Specificity Analysis with the Aid of Computer. *J. Agric. Food Chem.* 63 (14), 3725–3733. doi:10.1021/jf5059683
- Yang, M., Zhang, K.-D., Zhang, P.-Y., Zhou, X., Ma, X.-Q., and Li, F.-L. (2016). Synergistic Cellulose Hydrolysis Dominated by a Multi-Modular Processive Endoglucanase from *Clostridium Cellulosi*. *Front. Microbiol.* 7, 932. doi:10.3389/fmicb.2016.00932
- Yen, J., Gillaspay, G., and Senger, R. (2015). Systems Metabolic Engineering of *Arabidopsis* for Increased Cellulose Production. *FASEB J.* 29 (S1). doi:10.1096/fasebj.29.1_supplement.887.26
- Zhang, X. J., Wang, L., Wang, S., Chen, Z. L., and Li, Y. H. (2021). Contributions and Characteristics of Two Bifunctional GH43 β -xylosidase/ α -L-Arabinofuranosidases with Different Structures on the Xylan Degradation of *Paenibacillus Physcomitrellae* Strain XB. *Microbiol. Res.* 253, 126886. doi:10.1016/j.micres.2021.126886
- Zurawski, J. V., Conway, J. M., Lee, L. L., Simpson, H. J., Izquierdo, J. A., Blumer-Schuette, S., et al. (2015). Comparative Analysis of Extremely Thermophilic Caldicellulosiruptor Species Reveals Common and Unique Cellular Strategies for Plant Biomass Utilization. *AEM* 81, 7159–7170. doi:10.1128/AEM.01622-15

Conflict of Interest: The authors declare that the research was conducted in the absence of any commercial or financial relationships that could be construed as a potential conflict of interest.

Publisher's Note: All claims expressed in this article are solely those of the authors and do not necessarily represent those of their affiliated organizations, or those of the publisher, the editors and the reviewers. Any product that may be evaluated in this article, or claim that may be made by its manufacturer, is not guaranteed or endorsed by the publisher.

Copyright © 2022 Saleh, Mahmud, Albogami, El-Shehawi, Paul, Islam, Dutta, Uddin and Zaman. This is an open-access article distributed under the terms of the Creative Commons Attribution License (CC BY). The use, distribution or reproduction in other forums is permitted, provided the original author(s) and the copyright owner(s) are credited and that the original publication in this journal is cited, in accordance with accepted academic practice. No use, distribution or reproduction is permitted which does not comply with these terms.



Enhanced Mechanical Properties of Polyvinyl Chloride-Based Wood–Plastic Composites With Pretreated Corn Stalk

Tao Shen^{1,2}, Minghui Li¹, Bo Zhang¹, Lingxia Zhong¹, Xiran Lin¹, Pengpeng Yang¹, Ming Li^{1*}, Wei Zhuang^{1*}, Chenjie Zhu¹ and Hanjie Ying^{1,3}

¹College of Biotechnology and Pharmaceutical Engineering, Nanjing Tech University, Nanjing, China, ²College of Food Science and Light Industry, Nanjing Tech University, Nanjing, China, ³School of Chemical Engineering, Zhengzhou University, Zhengzhou, China

OPEN ACCESS

Edited by:

Caoxing Huang,
Nanjing Forestry University, China

Reviewed by:

Rijia Lin,
The University of Queensland,
Australia
Rongxian Ou,
South China Agricultural University,
China
Xuefei Cao,
Beijing Forestry University, China

*Correspondence:

Ming Li
m.li@njtech.edu.cn
Wei Zhuang
weizhuang@njtech.edu.cn

Specialty section:

This article was submitted to
Bioprocess Engineering,
a section of the journal
Frontiers in Bioengineering and
Biotechnology

Received: 06 December 2021

Accepted: 20 December 2021

Published: 24 January 2022

Citation:

Shen T, Li M, Zhang B, Zhong L, Lin X, Yang P, Li M, Zhuang W, Zhu C and Ying H (2022) Enhanced Mechanical Properties of Polyvinyl Chloride-Based Wood–Plastic Composites With Pretreated Corn Stalk. *Front. Bioeng. Biotechnol.* 9:829821. doi: 10.3389/fbioe.2021.829821

Wood–plastic composites (WPCs) are a type of environmentally friendly materials widely used in daily life. This paper selected low-value biomass, corn stalk (CS), as the lignocellulosic resource for polyvinyl chloride (PVC)-based WPCs. To depict the relationship between lignocellulosic composition (cellulose, hemicellulose, and lignin) and mechanical performance of WPCs, pretreatments have been optimized to selective removal of lignin using an alkaline-EtOH stewing process and selective removal of hemicellulose using an acid stewing process. The α C sample, in which both lignin and hemicellulose were removed, shows the highest degree of crystallinity (72.60%) as estimated from X-ray diffraction analysis results and fibrous morphology with the highest aspect ratio as seen in scanning electron microscopy images. Compared with PVC/CS, PVC/ α C gives a substantial increase in tensile strength and modulus by 37.21 and 21.66% and flexural strength and modulus by 29.98 and 34.88%, respectively. These improvements lie in the reinforcing effect of a fibrous structure and the improved interfacial compatibility as proven by scanning electron microscopy and dynamic mechanical analyzer results. Considering the extracted lignin and hemicellulose can be further developed to valuable biochemicals, the pretreatment to CS adds value to both WPC materials and biorefinery products.

Keywords: wood–plastic composites, polyvinyl chloride, lignocellulose, pretreatment, mechanical properties

INTRODUCTION

The environmental and climate problems caused by massive petroleum consumption have accumulated to a stage where people have to respond quickly. The global plastic demands are approximately 300 Mt/year nowadays (Liminana et al., 2018) and are still dominantly fulfilled by petroleum-based plastics. To replace petroleum-based plastics, at least partially, with materials from renewable resources or bio-based wastes is one practical approach to reduce the carbon footprint (Tahir et al., 2017; Andreeßen and Steinbüchel, 2019; Quiles-Carrillo et al., 2019). Wood–plastic composites (WPCs) composed of thermoplastics and wood powders have been developed since the 1990s and are nowadays widely applied as furniture and domestic/outdoor building materials (Liu et al., 2019; Sun et al., 2019; Mu et al., 2021). WPCs are generally regarded as a type of

environmentally friendly materials due to their partial biomass origin. Low-value lignocellulosic biomass, e.g., corn stalk (CS), and recycled thermoplastics, can also be involved to minimize carbon footprint.

High-density polyethylene and polypropylene were most exploited as the thermoplastic matrix for WPCs due to their high production amount, high durability, and ease of processing (Tserki et al., 2005; Hao et al., 2020). Lignocellulose is mainly composed of cellulose, hemicellulose, and lignin, each playing a particular structural role and self-assembled to support the plant (Boerjan et al., 2003). Their compositions vary depending on the origin of the resource and therefore impose influences on the properties of the resulting WPCs (Nourbakhsh and Ashori, 2010). WPCs filled with highly crystalline lignocellulosic fibers showed significantly improved tensile, flexural, and impact properties (Michell et al., 1976; Tian et al., 2009; Ashori and Nourbakhsh, 2010). Filling with hemicellulose-extracted lignocellulose could improve the tensile strength and water resistance of the composites (Enayati et al., 2009; Hosseinaei et al., 2012). Incorporation of lignin or modified lignin into WPCs has found improvement in weatherability and thermal stability (Kharade and Kale 1999; Maldhure et al., 2012).

Lignocellulose contains large amounts of polar functionalities (e.g., -OH), especially in the cellulose and hemicellulose components. Therefore, the lignocellulose is basically incompatible with the hydrophobic polyolefin matrix (Alvarez-Valencia et al., 2010; Ayrlimis et al., 2011) and results in poor interfacial adhesion between the lignocellulose and thermoplastics domains and inefficient stress transfer from the ductile matrix to the rigid lignocellulose reinforcements (Kazayawok et al., 1999; Chaharmahali et al., 2008). To enhance the mechanical properties of the composites, compatibilizers such as ethylene-acrylic acid copolymer (Szabo et al., 2018), ethylene-vinyl acetate copolymer (Alexy et al., 2004), maleic anhydride (Cazacu et al., 2004), and grafting modifiers (Casenave et al., 1995) were explored as functional additives.

Polyvinyl chloride (PVC) is another type of thermoplastics extensively used in daily life. Compared with high-density polyethylene and polypropylene, it contains non-protonic polar C-Cl bonds in its macromolecules, which impart higher compatibility with the lignocellulosic fillers. Due to the intrinsic flame retardance of PVC, PVC-based WPCs are especially suitable for domestic applications. Researchers studied a few PVC-based WPCs with various lignocellulose resources, including eucalyptus wood, rice husk, bamboo, CS, and sisal (Petchwattana et al., 2012; Chen et al., 2017; Chen J. et al., 2018; Zong et al., 2020; Qi et al., 2021). Wood flour treated with an aminosilane modifier was reported to provide improved mechanical properties (Yim and Kim, 2012). However, the research about PVC-based WPCs is far less intensive compared with that for polyolefin-based WPCs. It is still unclear how the composition in lignocellulose plays a role in the mechanical performance of PVC-based WPCs.

In this paper, low-value biomass, CS, has been selected as the lignocellulosic resource for PVC-based WPCs. To distinguish the contribution of the components (cellulose, hemicellulose, and lignin), pretreatments have been optimized to selective removal of

hemicellulose or/and lignin from CS. The raw CS and the residue compounds have been examined to analyze their composition, structure, and morphology. PVC-based WPCs have been prepared with the raw CS and the residue compounds as fillers and characterized to depict the relationship between lignocellulosic composition and mechanical performance of the resulting WPCs.

EXPERIMENTAL AND MATERIALS

Materials

Pretreatment reagents and processing additives were purchased from Aladdin Company. PVC was purchased from Tianye Group, China. CS was obtained from a local factory in Lianyungang, China, which was smashed and screened to 40–60 mesh and dried at 100°C to constant weight. The composition of the raw CS (on a dry weight basis) is 35.90 wt% of cellulose, 24.8 wt% of hemicellulose, 19.7 wt% of lignin, 3.9 wt% of ash, and 15.7 wt% of unknown components.

Methods

Characterization of Lignocellulose

The composition of lignocellulose samples was analyzed according to National Renewable Energy Laboratory procedures (Sluiter et al., 2008). The acid hydrolysate was quantified by high-performance liquid chromatography (Waters 1525–2414) with a refractive index detector, using an Aminex HPX-87H ion exclusion column (300 × 7.8 mm; Bio-Rad Laboratories, Hercules, CA, USA). The mobile phase was 5.0-mM H₂SO₄ at a flow rate of 0.6 ml min⁻¹; the temperature of the column was 55°C. Lignin was determined by gravimetric analysis (calcined acid-insoluble residue at 575°C for 24 h) and ultraviolet–visible spectroscopy.

Fourier-transform infrared spectroscopy (FT-IR) analysis was conducted using Thermo Scientific IS-5 with a universal attenuated total reflection accessory. FT-IR spectra were collected from 4,000 to 500 cm⁻¹ for 16 scans. Morphology analysis was conducted using a scanning electron microscope (SEM, FEI Quanta 200 FEG SEM) at 2 kV and 5,000 magnification. Thermogravimetric analysis (Netzsch STA 449F3) of lignocellulosic samples was conducted from 25 to 600°C at 10°C min⁻¹ under nitrogen flow (40 ml min⁻¹). The crystallinity of lignocellulosic samples was characterized by an X-ray diffractometer (Bruker D8). The samples of particle size less than 100 mesh were scanned from 10 to 40 at a speed of 10° min⁻¹ in the 40-kV voltage and 40-mA current.

Characterization of Wood–Plastic Composites

The dynamic mechanical properties of WPCs were characterized by the dynamic mechanical analyzer (DMA 450, France, Metravib). The samples (20 × 8 × 3 mm) were scanned in a tensile mode at 1 Hz with a strain amplitude of 15 μm, in a temperature range from 25 to 140°C at 3°C min⁻¹. The tensile and flexural properties of WPCs were characterized using a universal testing machine according to the GB/T 1040.2–2006. The dumbbell tensile samples (160 × 20 × 4 mm) were tested at a tensile rate of 5 mm min⁻¹. The flexural samples (80 × 10 × 4 mm) were tested at a rate of 2 mm min⁻¹.

TABLE 1 | Delignification conditions and the corresponding composition analysis.

Entries	Pretreating conditions			Residue/ %	Composition/%			Delignification rate/%	Retention rate/%	
	NaOH/ w%	EtOH/H ₂ O v%	Temp./ °C		Cellulose	Hemicellulose	Lignin		Cellulose	Hemicellulose
1	0	60/40	130	74.8	45.82	28.04	15.63	40.66	95.46	84.56
2	4	60/40	130	64.2	52.16	30.56	6.47	78.93	93.27	79.12
3	8	60/40	130	52.4	60.82	28.54	4.84	83.78	88.77	60.31
4	8	80/20	130	53.6	61.63	33.77	1.54	87.23	92.01	72.98
5	8	80/20	150	57.8	56.63	23.18	0.75	91.01	91.17	54.03
6 ^a	8	80/20	130	58.5	58.15	34.92	0.26	89.98	94.69	82.32

^a1 wt% anthraquinone added.

TABLE 2 | Acid stewing conditions and the corresponding composition analysis.

Entries	Conditions		Residue/%	Composition/%			Removal rate of hemicellulose/%	Retention rate/%	
	pH	Time/min		Cellulose	Hemicellulose	Lignin		Cellulose	Lignin
1	5.0	30	60.2	56.12	14.19	28.88	65.55	94.11	88.25
2	5.5	30	58.4	59.30	17.57	29.45	58.63	96.46	87.29
3	5.5	60	50.8	66.46	6.19	34.02	87.32	94.04	87.72

Experimental Pretreatment of Corn Stalk

Typically, 1-kg CS was placed in a 10-L autoclave with 6 L of 80/20 v/v ethanol/water, 8 wt% NaOH, and 1 wt% anthraquinone and pretreated at 130°C for 60 min under stirring to selectively remove the lignin component. Afterward, the mixture was filtrated and washed with deionized water to be neutral, and the residue was dried and labeled as HC.

Typically, 1-kg CS was placed in a 10-L autoclave with 6 L of deionized water. The pH of the mixture was adjusted to 5.5 using 72 wt% H₂SO₄. The mixture was stirred at 150°C for 60 min to selectively remove the hemicellulose component. Afterward, the mixture was filtrated and washed with deionized water to be neutral, and the residues were dried and labeled as HR.

Preparation of Wood-Plastic Composites

Typically, the CS was dried at 105°C for 24 h before use. WPC was prepared according to the following formulation: 1,000 g of PVC, 200 g of CS, 60 g of Ca-Zn stearate, 30 g of acrylate copolymer, 100 g of chlorinated polyethylene, 5 g of stearic acid, and 4 g of polyethylene wax. The components mentioned earlier were first mixed in a high-speed blender, then melt-compounded using a twin-roll miller at 175°C for 5–10 min, and finally, compression-molded at 185°C for 5 min.

RESULTS AND DISCUSSION

Pretreatment of Corn Stalk

To selectively delignify CS with maximum removal of lignin and highest retention of cellulose and hemicellulose, we explored the delignification of CS using alkaline-organic solvent stewing method as inspired by previous studies (Tang et al., 2017;

Chen X. et al., 2018; Zhong et al., 2018; Chen et al., 2019). As shown in **Table 1**, pretreatment systems with different concentrations of NaOH and EtOH were evaluated in removal rate of lignin and retention rate of cellulose and hemicellulose. The residue compound, labeled as HC, were examined using the National Renewable Energy Laboratory procedures to quantify each component (cellulose, hemicellulose, and lignin). As shown in Entries 1–3, simply increasing the concentration of NaOH from 0% to 8 w% led to a higher delignification rate, but the retention rate of cellulose and hemicellulose decreased rapidly, which is not desirable. In Entry 4, the amount of EtOH was increased to 80 v% compared with that in Entry 3 (60 v%). The delignification rate was improved to 87.23%, whereas the retention rate of cellulose and hemicellulose also moderately increased. When we elevated the stewing temperature to 150°C, as shown in Entry 5, the delignification rate reached a maximum, but the retention rate of hemicellulose significantly decreased, suggesting that hemicellulose is more sensitive to harsher temperatures. Anthraquinone has been reported to be able to oxidize the aldehyde end-groups of cellulose and hemicellulose and to retard the exfoliation of the carbohydrate components during the pretreatment (Nascimento et al., 2016). To further improve the retention rate of cellulose and hemicellulose, we added 1 wt% anthraquinone to the stewing system of Entry 4 and achieved a delignification rate of 89.98%, and the retention rates of cellulose and hemicellulose were 94.69 and 82.32%, respectively. Therefore, the optimal delignification conditions can be regarded as 8 wt% NaOH, 80 v% ethanol solution, and 1% anthraquinone at 130°C for 60 min.

Hemicellulose is one of the main components in lignocellulose and can be hydrolyzed to pentose under acid stewing conditions (Li et al., 2020; Shen et al., 2020; Sun et al., 2021). To selectively remove the hemicellulose component, CS was pretreated *via* acid

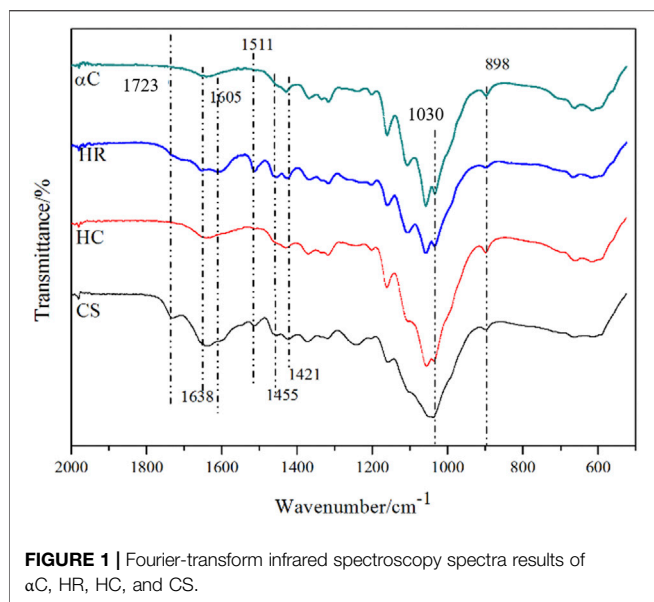


FIGURE 1 | Fourier-transform infrared spectroscopy spectra results of α C, HR, HC, and CS.

stewing at 150°C with different pH and stewing times, and the resulting residue compound was labeled as HR. **Table 2** shows the pretreatment conditions and the corresponding results of composition analysis. Compared with a pretreating system of pH 5.0 (Entry 1), the system of pH 5.5 (Entry 2) gave an inferior decrease in removing hemicellulose but a slightly higher retention rate of cellulose. When we extended the stewing time from 30 to 60 min (Entry 3), the removal rate of hemicellulose dramatically increased to 87.32%, and meanwhile, a reasonably high retention rate of cellulose (94.04%) and lignin (87.72%) was still obtained. Also, considering the corrosion to equipment and difficulty in dealing with acidic wastewater, a higher pH is preferable. Therefore, the optimal condition for selective removal of hemicellulose was regarded as acid stewing at pH 5.5 for 60 min. To obtain both lignin- and hemicellulose-removed samples, CS was pretreated consecutively with the conditions of Entry 6 in **Table 1** and the conditions of Entry 3 in **Table 2**. The resulted compound was labeled as α C and examined to contain 78.27 wt% of cellulose, 2.97 wt% of hemicellulose, and 5.52 wt% of lignin.

Analysis of Pretreated Corn Stalk

FT-IR was used to characterize CS, HC, HR, and α C as shown in **Figure 1**, and the attribution of characteristic peaks is

summarized in **Table 3**. The spectra for HC and α C are highly similar because these two samples are mainly composed of polysaccharides. The characteristic peaks for lignin at 1,723 (C=O), 1,605, 1,511, and 1,455 cm^{-1} (aromatic ring skeleton vibration in lignin) are obviously found in CS and HR but vanish for HC and α C, indicating that in these two samples, lignin was effectively removed. These results are consistent with the composition analysis data (**Tables 1** and **2**).

The morphology of CS, HC, HR, and α C was characterized by SEM, as shown in **Figure 2**. The original CS sample shows large sheets or blocks, whereas the pretreated samples exhibit cylindrical or fibrous shapes with smaller sizes and higher aspect ratios, especially for the α C sample revealing thin fiber-like morphology with the highest aspect ratio. Lignin and hemicellulose are generally regarded as adhesives to glue the cellulose fibrils in the plant cell walls, and the removal of these components leaves more cellulose fibrils exposed, as presented in the SEM image of α C. Because lignin is not directly bonded to cellulose molecules, the HC sample with selective removal of lignin still presents thick sheets and blocks rather than thin fibers.

The crystal form of cellulose in all these samples was detected and analyzed by X-ray diffraction analysis, as shown in **Figure 3**. As previously reported, the crystal type I of cellulose gives characteristic 2θ diffractions at 16.5 and 22.5° (Segal et al., 1959), which can also be seen in all samples, suggesting that the crystal form of cellulose did not change during the pretreatment. The degree of crystallinity (Cr I) for each sample was estimated based on the intensity of characteristic diffractions (**Eq. 1**) (Segal et al., 1959).

$$Cr I (\%) = (I_{002} - I_{am}) / I_{002} \times 100\% \quad (1)$$

where I_{002} is the intensity for the 2θ diffraction at 22.5°; I_{am} is the intensity for the 2θ diffraction at 16.5°. The α C sample shows the highest degree of crystallinity (72.60%), which is in line with its highest content of cellulose and the highest aspect ratio (Oujai and Shanks, 2005). HR exhibits a degree of crystallinity of 53.90%, higher than that for CS (42.18%). These results confirm that removing the amorphous lignin and hemicellulose components enriches cellulose in the residue compounds, leading to a higher degree of crystallinity. However, HC contains 58.15 wt% of cellulose, much higher than that for CS (35.90 wt%), but shows a similar degree of crystallinity (42.23%), suggesting that a large proportion of crystalline cellulose has been disordered and turned into amorphous cellulose during the alkaline-organic solvent stewing process.

TABLE 3 | Assignment of Fourier-transform infrared spectroscopy absorption.

Wavelength/ cm^{-1}	Peak assignments	Corresponding the components of lignocellulose
1,723	Unconjugated carbonyl C=O stretching	Lignin
1,638	O-H	Bound H_2O
1,605, 1,511, and 1,455	Aromatic ring skeleton vibration	Lignin
1,421	C-H bending	Lignin and polysaccharides
1,030	C-O-C stretching	Polysaccharides
898	β -glycosidic bond stretching	Cellulose

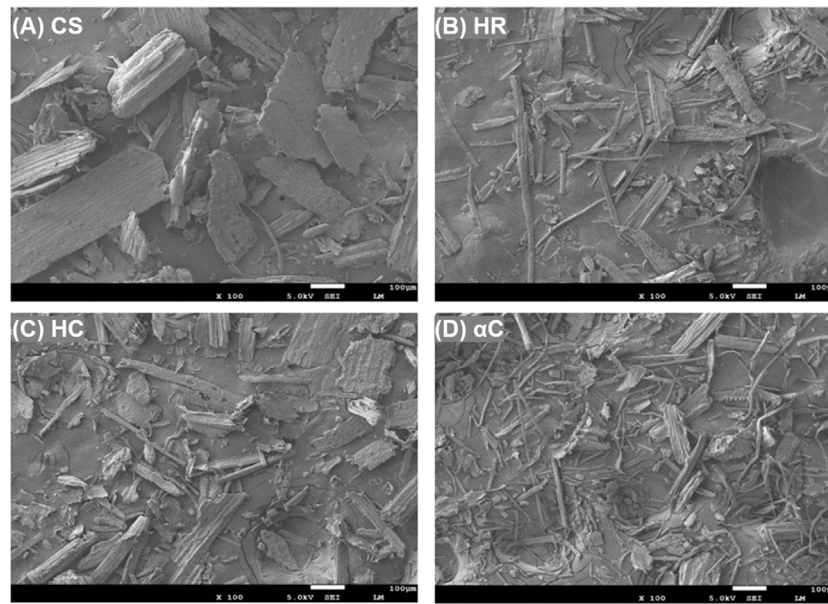


FIGURE 2 | SEM of different lignocellulose components (A) CS, (B) HC, (C) HR, and (D) α C.

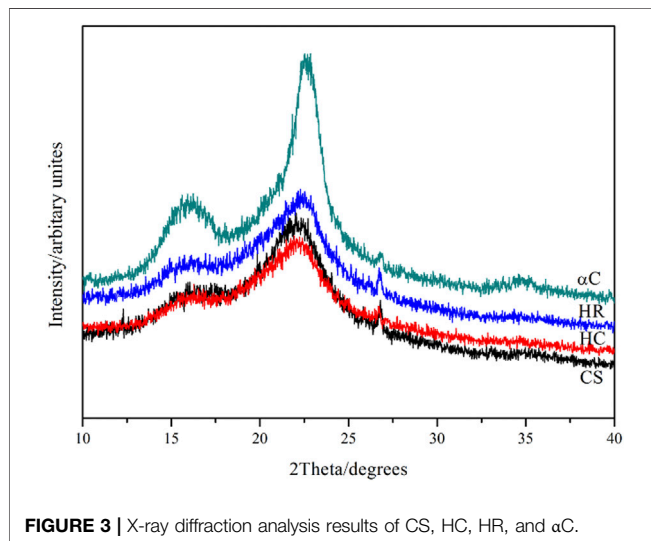


FIGURE 3 | X-ray diffraction analysis results of CS, HC, HR, and α C.

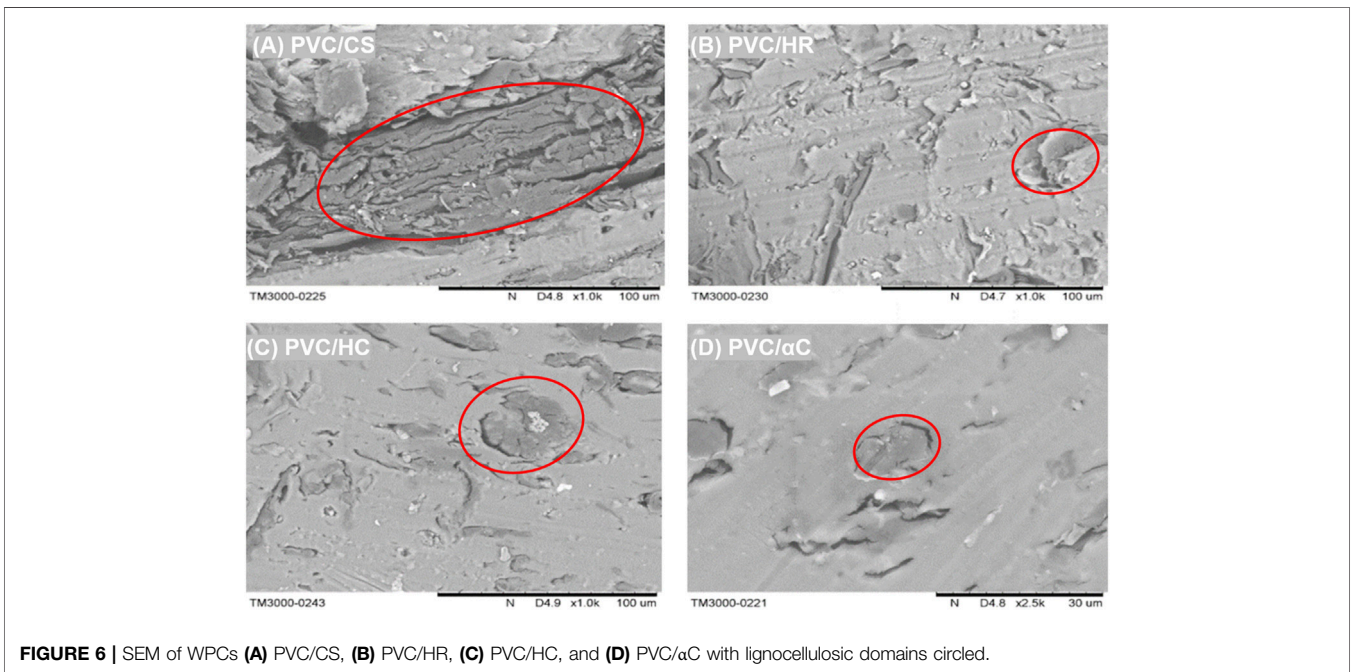
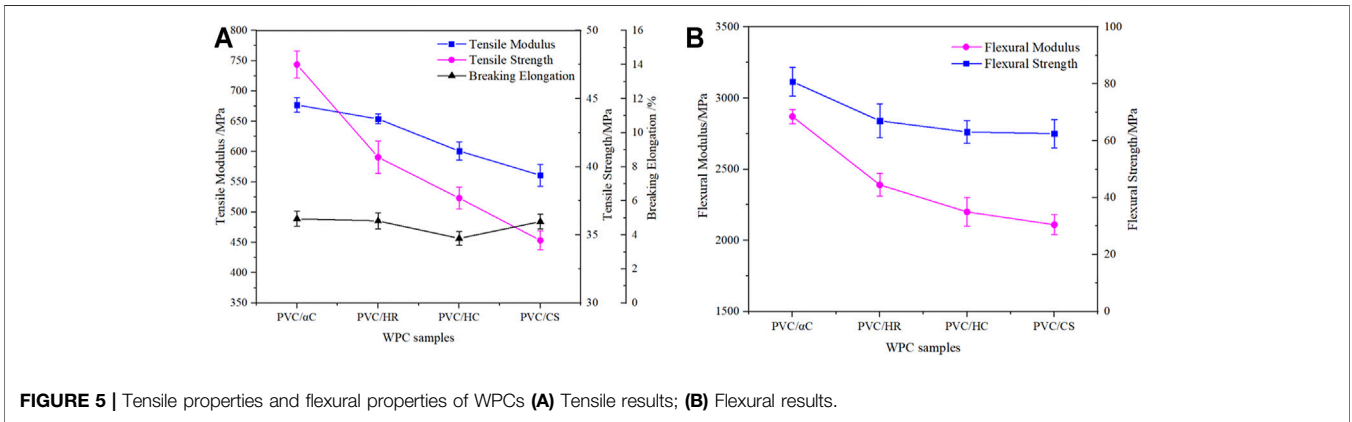
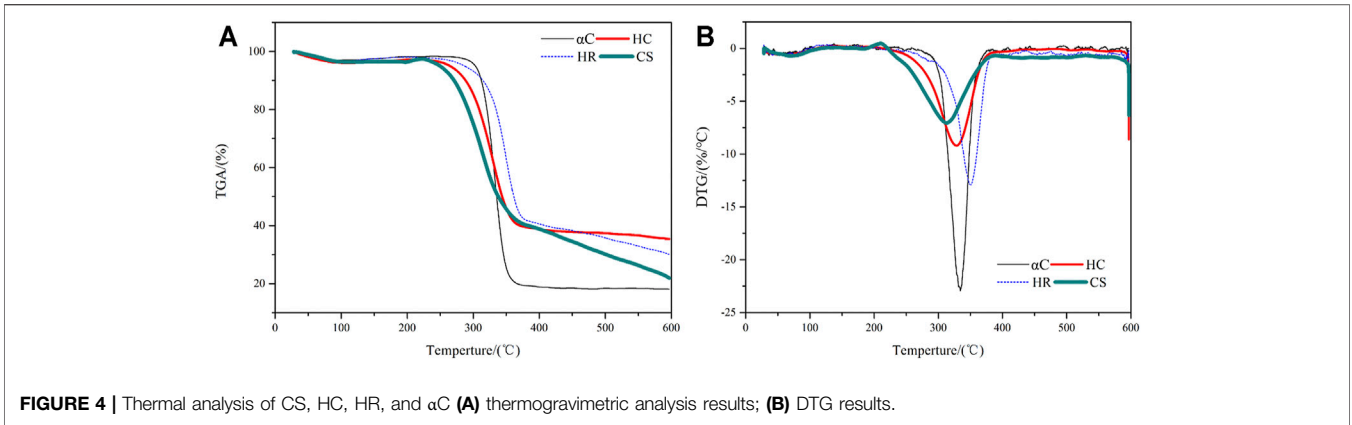
The thermal stability of CS, HC, HR, and α C was studied by thermogravimetric analysis, as shown in **Figure 4**. All samples give a slight weight loss at $<100^{\circ}\text{C}$, which was attributed to moisture evaporation. When the temperature reaches above 200°C , the decomposition process gradually speeds up as hemicellulose and low molecular weight component such as phytowax; oligosaccharides start to degrade and leave. This is especially prominent for the CS sample because it was not pretreated and retains a higher amount of low molecular weight components. This decomposition stage for the HC sample took place at a lower temperature than those for the HR and α C samples because it was delignified and contained a higher amount of hemicellulose than

the other two. When the temperature reached $270\text{--}380^{\circ}\text{C}$, the glycosidic bond in cellulose cleaves and the C-O bond in lignin also breaks up, resulting in rapid weight loss for all samples (Gibson, 2016), reaching a maximum loss rate at 315°C for the CS sample, 331°C for the HC and α C sample, and 351°C for the HR sample. The residue weight reached a plateau at $>380^{\circ}\text{C}$ for the HC and α C samples, whereas the weight loss for HR and CS is still slowly taking place. This weight loss is attributed to the ongoing degradation of the lignin component where the C-C backbone breaks up at this temperature range. The HR sample with selective removal of hemicellulose has the highest content of lignin, and therefore, its DTG peak shifted to a higher temperature range.

Morphology and Mechanical Properties of Wood-Plastic Composites

To investigate the effect of lignocellulosic compositions on the properties of PVC-based composites, WPC samples filled with CS, HC, HR, and α C were prepared by traditional thermal compounding and compression molding techniques (Liu et al., 2014). The mass ratio of the PVC matrix and the filler was controlled to be 100:20. Necessary functional additives such as thermal stabilizer (Ca-Zn stearate), lubricants (stearic acid and polyethylene wax), and toughening modifiers (acrylate copolymer and chlorinated polyethylene) were blended in before thermal compounding.

The tensile and flexural properties of WPCs are shown in **Figure 5**. Compared with the PVC/CS sample, the WPC samples with HC, HR, and α C show similar elongation at break (3.80–4.95%) but higher tensile and bending performance in both strength and modulus. The reinforcing effect in the PVC/ α C sample is especially prominent, showing a significant increase in tensile strength and modulus by 37.21 and 21.66% and in flexural strength and modulus by 29.98 and 34.88%, respectively.



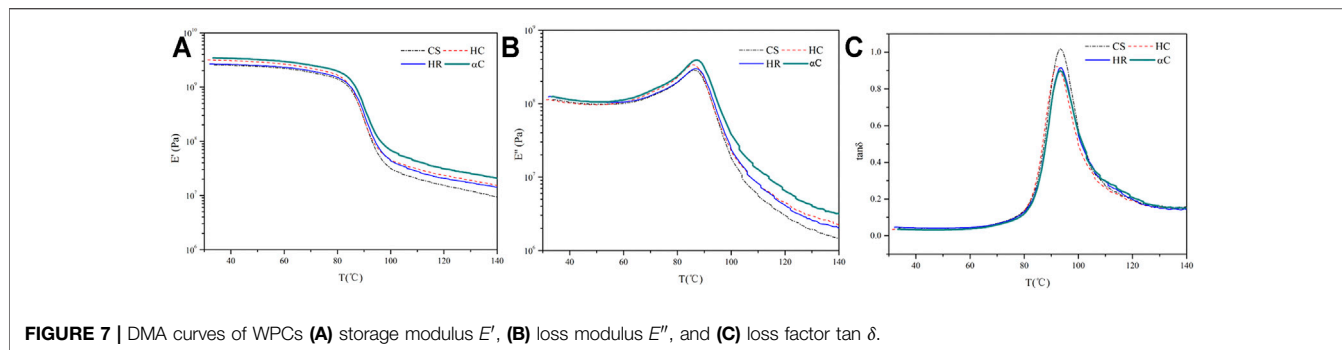


TABLE 4 | Dynamic mechanical analysis data of WPC.

	PVC/CS	PVC/HC	PVC/HR	PVC/ α C
T_g (°C)	93.2	92.1	93.0	93.0
$\tan \delta_{\max}$	1.01	0.93	0.92	0.89

These improvements are highly related to the morphology of the fillers, as observed in **Figure 4**. α C has the highest content of crystalline cellulose and shows fibrous appearance with the highest aspect ratio and therefore acts as the most efficient reinforcement for stress transfer and load-bearing (Gibson, 2016). The PVC/HR sample gives superior mechanical properties than the PVC/HC sample because HR has more fibrous structures, although not as fine and regular as α C.

We also studied the morphology of the lignocellulosic fillers in WPCs by SEM (**Figure 6**). The PVC/CS sample shows a coarse cross-section where a large block of CS can be found as circled in **Figure 6A**, whereas the rest samples, especially for the PVC/ α C sample, present smoother appearance with smaller filler domains, which suggests enhanced interfacial interactions between the lignocellulosic reinforcements and the PVC matrix, and this is crucial for the reinforcing effect in polymer composites. Lignin has been reported to have better compatibility with non-protonic polymers than the carbohydrate components due to its higher hydrophobicity (Li et al., 2021). The leftover lignin after pretreatment was more exposed rather than well-assembled inside the origin lignocellulosic structure and therefore may perform as a compatibilizer to improve the interfacial adhesion. This may also explain why PVC/HC gives a relatively weak reinforcing effect, as in HC, the lignin component is almost completely removed.

The dynamic mechanical properties of WPCs were studied *via* DMA, as shown in **Figure 7**. The storage modulus (E') for all samples shows the same trend, which is staying relatively stable at the low-temperature range and decreasing rapidly at $>80^\circ\text{C}$ due to the glass transition of PVC macromolecules. The loss modulus (E'') and the loss factor ($\tan \delta$) curves give a peak at the glass transition, and the peaked temperature (T_g) and maximum values for the $\tan \delta$ curves are listed in **Table 4**. The T_g for all samples appears at 92.1–93.2°C, demonstrating that these micro-sized lignocellulosic fillers impose little influence on the glass transition behavior of PVC. The $\tan \delta_{\max}$ for PVC/CS is apparently higher than those for the rest samples, which

confirms the poorer interfacial adhesion between PVC and CS as also presented in the SEM image (**Figure 6**). The friction at the interface of lower compatibility consumes more energy during dynamic stress–strain movement and therefore leads to a higher loss factor (Schirp and Wolcott, 2006; Fang et al., 2014).

CONCLUSION

In summary, we have optimized the alkaline-EtOH stewing process to selectively remove lignin from CS, achieving the HC sample, and explored the acid stewing process to selectively remove hemicellulose achieving the HR sample. These optimal processes were combined to pretreat CS obtaining the α C sample with both lignin and hemicellulose removed. The α C sample shows the highest degree of crystallinity (72.60%) as estimated from X-ray diffraction analysis results and fibrous morphology with the highest aspect ratio as seen in SEM images. PVC-based WPCs with CS, HC, HR, and α C fillers were prepared using the traditional thermal compounding process. Compared with PVC/CS, PVC/ α C gives a substantial increase in tensile strength and modulus by 37.21 and 21.66% and flexural strength and modulus by 29.98 and 34.88%, respectively. PVC/HR and PVC/HC also present superior mechanical properties than the PVC/CS sample. These improvements in mechanical properties lie in the reinforcing effect of a fibrous structure and the improved interfacial compatibility as proven by SEM and DMA results. Therefore, better than nature, the removal of lignin and hemicellulose can be one potential approach to prepare efficient reinforcements for PVC-based WPCs, and the extracted lignin and hemicellulose can be further developed to valuable biochemicals, which adds value into both WPC materials and biorefinery products.

DATA AVAILABILITY STATEMENT

The original contributions presented in the study are included in the article/Supplementary Material; further inquiries can be directed to the corresponding authors.

AUTHOR CONTRIBUTIONS

All authors listed have made a substantial, direct, and intellectual contribution to the work and approved it for publication.

FUNDING

We would like to thank all the authors and the financial support by the National Key Research and Development Program of China (grant no. 2019YFD1101202), Jiangsu Province Natural Science Foundation for Young Scholars (grant no. SBK2021040275), Natural Science Foundation for Distinguished Young Scholars

(grant no. SBK20190035), Program of National Natural Science Foundation of China (grant nos. 22178170, 21878142, 22008119, and 21908100), Key Research and Development Plan of Jiangsu Province (grant no. BE2020712 and BE2019001), Six Talent Peaks Project in Jiangsu Province (SWYY-045), and High-Level Innovation and Entrepreneurship Talents Introduction Program of Jiangsu Province.

REFERENCES

- Alexy, P., Košíková, B., Crkonová, G., Gregorová, A., and Martiš, P. (2004). Modification of Lignin-Polyethylene Blends with High Lignin Content Using Ethylene-Vinylacetate Copolymer as Modifier. *J. Appl. Polym. Sci.* 94, 1855–1860. doi:10.1002/app.20716
- Alvarez-Valencia, D., Dagher, H. J., Davids, W. G., Lopez-Anido, R. A., and Gardner, D. J. (2010). Structural Performance of Wood Plastic Composite Sheet Piling. *J. Mater. Civ. Eng.* 22 (12), 1235–1243. doi:10.1061/(ASCE)MT.1943-5533.0000132
- Andreeßen, C., and Steinbüchel, A. (2019). Recent Developments in Non-biodegradable Biopolymers: Precursors, Production Processes, and Future Perspectives. *Appl. Microbiol. Biotechnol.* 103, 143–157. doi:10.1007/s00253-018-9483-6
- Ashori, A., and Nourbakhsh, A. (2010). Performance Properties of Microcrystalline Cellulose as a Reinforcing Agent in Wood Plastic Composites. *Compos. B. Eng. Comp.* 41, 578–581. doi:10.1016/j.compositesb.2010.05.004
- Ayrlimis, N., Jarusombuti, S., Fueangvivat, V., and Bauchongkol, P. (2011). Effect of Thermal-Treatment of Wood Fibres on Properties of Flat-Pressed Wood Plastic Composites. *Polym. Degrad. Stab.* 96, 818–822. doi:10.1016/j.polydegradstab.2011.02.005
- Boerjan, W., Ralph, J., and Baucher, M. (2003). Lignin Biosynthesis. *Annu. Rev. Plant Biol.* 54, 519–546. doi:10.1146/annurev.arplant.54.031902.134938
- Casenave, S., Ait-Kadi, A., and Brahimi, B. (1995). Properties of Highly Filled Lignin-Polyethylene Composite Materials Made by Catalytic Grafting. *Annu. Tech. Conf. Soc. Plast. Eng.* 53, 1438–1442.
- Cazacu, G., Mihaies, M., Pascu, M. C., Profire, L., Kowarskik, A. L., and Vasile, C. (2004). Polyolefin/Lignosulfonate Blends. *Macromol. Mater. Eng.* 289, 880–889. doi:10.1002/mame.200300378
- Chaharmahali, M., Tajvidi, M., and Najafi, S. K. (2008). Mechanical Properties of Wood Plastic Composite Panels Made from Waste Fiberboard and Particleboard. *Polym. Compos.* 29, 606–610. doi:10.1002/pc.20434
- Chen, J., Teng, Z., and Wu, J. (2017). Recycling of Waste FRP and Corn Straw in Wood Plastic Composite. *Polym. Compos.* 38, 2140–2145. doi:10.1002/pc.23789
- Chen, X., Cao, X., Sun, S., Yuan, T., Wang, S., Shi, Q., et al. (2019). Hydrothermal Acid Hydrolysis for Highly Efficient Separation of Lignin and Xylose from Pre-Hydrolysis Liquor of Kraft Pulp Process. *Sep. Purif. Tech.* 209, 741–747. doi:10.1016/j.seppur.2018.09.032
- Chen, J., Zou, Y., Ge, H., Cui, Z., and Liu, S. (2018). Mechanical and Water Absorption Behaviors of Corn Stalk/Sisal Fiber-Reinforced Hybrid Composites. *J. Appl. Polym. Sci.* 135, 46405. doi:10.1002/app.46405
- Chen, X., Li, H., Sun, S., Cao, X., and Sun, R. (2018). Co-Production of Oligosaccharides and Fermentable Sugar from Wheat Straw by Hydrothermal Pretreatment Combined with Alkaline Ethanol Extraction. *Ind. Crops Prod.* 111, 78–85. doi:10.1016/j.indcrop.2017.10.014
- Enayati, A. A., Hosseinaei, O., Wang, S., Mirshokraie, S. A., and Tajvidi, M. (2009). Thermal Properties of Wood-plastic Composites Prepared from Hemicellulose-Extracted Wood Flour. *Iran. J. Polym. Sci. Technol.* 22, 171–181. doi:10.22063/JIPST.2013.633
- Fang, L., Chang, L., Guo, W.-j., Chen, Y., and Wang, Z. (2014). Influence of Silane Surface Modification of Veneer on Interfacial Adhesion of Wood-Plastic Plywood. *Appl. Surf. Sci.* 288, 682–689. doi:10.1016/j.apsusc.2013.10.098
- Gibson, R. F. (2016). *Principles of Composite Material Mechanics*. 4th Eds. Florida: CRC Press.
- Hao, X., Zhou, H., Mu, B., Chen, L., Guo, Q., Yi, X., et al. (2020). Effects of Fiber Geometry and Orientation Distribution on the Anisotropy of Mechanical Properties, Creep Behavior, and Thermal Expansion of Natural Fiber/HDPE Composites. *Composites B: Eng.* 185, 107778. doi:10.1016/j.compositesb.2020.107778
- Hosseinaei, O., Wang, S., Enayati, A. A., and Rials, T. G. (2012). Effects of Hemicellulose Extraction on Properties of Wood Flour and Wood-Plastic Composites. *Composites A: Appl. Sci. Manufacturing* 43, 686–694. doi:10.1016/j.compositesa.2012.01.007
- Kazayawoko, M., Balatinecz, J. J., and Matuana, L. M. (1999). Surface Modification and Adhesion Mechanisms in Wood Fiber-Polypropylene Composites. *J. Mater. Sci.* 34, 6189–6199. doi:10.1023/A:1004790409158
- Kharade, A. Y., and Kale, D. D. (1999). Lignin-Filled Polyolefins. *J. Appl. Polym. Sci.* 72, 1321–1326. doi:10.1002/(sici)1097-4628(19990606)72:10<1321::aid-app12>3.0.co;2-9
- Li, M., Sun, X., Chen, Y., Shen, T., Tan, Z., Tang, C., et al. (2020). Effect of Xylan Sulfate on the Responsive Swelling Behavior of Poly(Methacrylateoethyl Trimethyl Ammonium Chloride)-Based Composite Hydrogels. *Cellulose* 27, 8745–8756. doi:10.1007/s10570-020-03402-4
- Li, M., Jia, Y., Shen, X., Shen, T., Tan, Z., Zhuang, W., et al. (2021). Investigation into Lignin Modified PBAT/Thermoplastic Starch Composites: Thermal, Mechanical, Rheological and Water Absorption Properties. *Ind. Crops Prod.* 171, 113916. doi:10.1016/j.indcrop.2021.113916
- Liminana, P., Garcia-Sanoguera, D., Quiles-Carrillo, L., Balart, R., and Montanes, N. (2018). Development and Characterization of Environmentally Friendly Composites from Poly(butylene Succinate) (PBS) and almond Shell Flour with Different Compatibilizers. *Composites Part B: Eng.* 144, 153–162. doi:10.1016/j.compositesb.2018.02.031
- Liu, R., Cao, J., and Peng, Y. (2014). Influences of Wood Components on the Property of Wood-Plastic Composites. *Chem. Ind. Eng. Prog.* 33, 2072–2083. doi:10.3969/j.issn.1000-6613.2014.08.023
- Liu, Y., Guo, L., Wang, W., Sun, Y., and Wang, H. (2019). Modifying Wood Veneer with Silane Coupling Agent for Decorating Wood Fiber/High-Density Polyethylene Composite. *Construction Building Mater.* 224, 691–699. doi:10.1016/j.conbuildmat.2019.07.090
- Maldhure, A. V., Ekke, J. D., and Deenadayalan, E. (2012). Mechanical Properties of Polypropylene Blended with Esterified and Alkylated Lignin. *J. Appl. Polym. Sci.* 125, 1701–1712. doi:10.1002/app.35633
- Michell, A. J., Vaughan, J. E., and Willis, D. (1978). Wood Fiber-Synthetic Polymer Composites. II. Laminates of Treated Fibers and Polyolefins. *J. Appl. Polym. Sci.* 22, 2047–2061. doi:10.1002/app.1978.070220724
- Mu, B., Tang, W., Liu, T., Hao, X., Wang, Q., and Ou, R. (2021). Comparative Study of High-Density Polyethylene-Based Biocomposites Reinforced with Various Agricultural Residue Fibers. *Ind. Crops Prod.* 172, 114053. doi:10.1016/j.indcrop.2021.114053
- Nascimento, V. M., Nakanishi, S. C., Rocha, G. J. M., Rabelo, S. C., Pimenta, M. T. B., and Rossell, C. E. V. (2016). Effect of Anthraquinone on Alkaline Pretreatment and Enzymatic Kinetics of Sugarcane Bagasse Saccharification: Laboratory and Pilot Scale Approach. *ACS Sust. Chem. Eng.* 4, 3609–3617. doi:10.1021/acsschemeng.5b01433
- Nourbakhsh, A., and Ashori, A. (2010). Wood Plastic Composites from Agro-Waste Materials: Analysis of Mechanical Properties. *Bioresour. Tech.* 101, 2525–2528. doi:10.1016/j.biortech.2009.11.040
- Ouajai, S., and Shanks, R. A. (2005). Composition, Structure and Thermal Degradation of Hemp Cellulose after Chemical Treatments. *Polym. Degrad. Stab.* 89, 327–335. doi:10.1016/j.polydegradstab.2005.01.016
- Petchwattana, N., Covavisaruch, S., and Sanetuntikul, J. (2012). Recycling of Wood-Plastic Composites Prepared from Poly(Vinyl Chloride) and Wood Flour. *Construction Building Mater.* 28, 557–560. doi:10.1016/j.conbuildmat.2011.08.024
- Qi, R., He, C., and Jin, Q. (2021). Accelerated Weathering of Polyvinyl Chloride-Based Wood-Plastic Composites: Effect of Plant Species. *BioRes* 16, 5261–5271. doi:10.15376/biores.16.3.5261-5271

- Quiles-Carrillo, L., Montanes, N., Jorda-Vilaplana, A., Balart, R., and Torres-Giner, S. (2019). A Comparative Study on the Effect of Different Reactive Compatibilizers on Injection-Molded Pieces of Bio-Based High-Density Polyethylene/Poly lactide Blends. *J. Appl. Polym. Sci.* 136, 47396. doi:10.1002/APP.47396S1361
- Schirp, A., and Wolcott, M. P. (2006). Fungal Degradation of Wood-Plastic Composites and Evaluation Using Dynamic Mechanical Analysis. *J. Appl. Polym. Sci.* 99, 3138–3146. doi:10.1002/app.22945
- Segal, L., Creely, J. J., Martin, A. E., Jr., and Conrad, C. M. (1959). An Empirical Method for Estimating the Degree of Crystallinity of Native Cellulose Using the X-Ray Diffractometer. *Textile Res. J.* 29, 786–794. doi:10.1177/004051755902901003
- Shen, T., Hu, Y., Hu, R., Zhuang, W., Li, M., Niu, H., et al. (2020). Continuous Production of Furfural from Pulp Prehydrolysate in a Vaporization Reactor. *Ind. Crops Prod.* 153, 112565. doi:10.1016/j.indcrop.2020.112565
- Sluiter, A., Hames, B., Ruiz, R., Scarlata, C., Sluiter, J., Templeton, D., et al. (2008). Determination of Structural Carbohydrates and Lignin in Biomass. Technical report of Laboratory Analytical Procedure NREL/TP-510-42618.
- Sun, Y., Guo, L., Liu, Y., Wang, W., and Song, Y. (2019). Glue Wood Veneer to Wood-Fiber-High-Density-Polyethylene Composite. *Int. J. Adhes. Adhesives* 95, 102444. doi:10.1016/j.ijadhadh.2019.102444
- Sun, S.-C., Sun, D., Li, H.-Y., Cao, X.-F., Sun, S.-N., and Wen, J.-L. (2021). Revealing the Topochemical and Structural Changes of Poplar Lignin during a Two-Step Hydrothermal Pretreatment Combined with Alkali Extraction. *Ind. Crops Prod.* 168, 113588. doi:10.1016/j.indcrop.2021.113588
- Szabó, G., Kun, D., Renner, K., and Pukánszky, B. (2018). Structure, Properties and Interactions in Ionomer/Lignin Blends. *Mater. Des.* 152, 129–139. doi:10.1016/j.matdes.2018.04.050
- Tahir, N., Bhatti, H. N., Iqbal, M., and Noreen, S. (2017). Biopolymers Composites with Peanut Hull Waste Biomass and Application for Crystal Violet Adsorption. *Int. J. Biol. Macromolecules* 94, 210–220. doi:10.1016/j.ijbiomac.2016.10.013
- Tang, C., Shan, J., Chen, Y., Zhong, L., Shen, T., Zhu, C., et al. (2017). Organic Amine Catalytic Organosolv Pretreatment of Corn stover for Enzymatic Saccharification and High-Quality Lignin. *Bioresour. Tech.* 232, 222–228. doi:10.1016/j.biortech.2017.02.041
- Tian, G., Zhuang, J., Fu, Y., Wang, Z., and Li, Q. (2009). Enhanced Mechanical Strength of Polyethylene-Based Lignocellulosic-Plastic Composites by Cellulose Fibers. *BioResources* 14, 1668–1678. doi:10.15376/biores.14.1.1668-1678
- Tserki, V., Zafeiropoulos, N. E., Simon, F., and Panayiotou, C. (2005). A Study of the Effect of Acetylation and Propionylation Surface Treatments on Natural Fibres. *Composites Part A: Appl. Sci. Manufacturing* 36 (8), 1110–1118. doi:10.1016/j.compositesa.2005.01.004
- Yim, H., and Kim, D. S. (2012). Physical Properties of PVC/Aminosilane-Treated Wood Flour/Organoclay Composites. *Polym. Adv. Technol.* 23, 1441–1445. doi:10.1002/pat.2065
- Zhong, L., Zhang, X., Tang, C., Chen, Y., Shen, T., Zhu, C., et al. (2018). Hydrazine Hydrate and Organosolv Synergetic Pretreatment of Corn Stover to Enhance Enzymatic Saccharification and Co-Production of High-Quality Antioxidant Lignin. *Bioresour. Tech.* 268, 677–683. doi:10.1016/j.biortech.2018.08.063
- Zong, G., Hao, X., Hao, J., Tang, W., Fang, Y., Ou, R., et al. (2020). High-Strength, Lightweight, Co-Extruded Wood Flour-Polyvinyl Chloride/lumber Composites: Effects of Wood Content in Shell Layer on Mechanical Properties, Creep Resistance, and Dimensional Stability. *J. Clean. Prod.* 244, 118860. doi:10.1016/j.jclepro.2019.118860

Conflict of Interest: The authors declare that the research was conducted in the absence of any commercial or financial relationships that could be construed as a potential conflict of interest.

Publisher's Note: All claims expressed in this article are solely those of the authors and do not necessarily represent those of their affiliated organizations, or those of the publisher, the editors and the reviewers. Any product that may be evaluated in this article, or claim that may be made by its manufacturer, is not guaranteed or endorsed by the publisher.

Copyright © 2022 Shen, Li, Zhang, Zhong, Lin, Yang, Li, Zhuang, Zhu and Ying. This is an open-access article distributed under the terms of the Creative Commons Attribution License (CC BY). The use, distribution or reproduction in other forums is permitted, provided the original author(s) and the copyright owner(s) are credited and that the original publication in this journal is cited, in accordance with accepted academic practice. No use, distribution or reproduction is permitted which does not comply with these terms.

Advantages of publishing in Frontiers



OPEN ACCESS

Articles are free to read for greatest visibility and readership



FAST PUBLICATION

Around 90 days from submission to decision



HIGH QUALITY PEER-REVIEW

Rigorous, collaborative, and constructive peer-review



TRANSPARENT PEER-REVIEW

Editors and reviewers acknowledged by name on published articles

Frontiers

Avenue du Tribunal-Fédéral 34
1005 Lausanne | Switzerland

Visit us: www.frontiersin.org

Contact us: frontiersin.org/about/contact



REPRODUCIBILITY OF RESEARCH

Support open data and methods to enhance research reproducibility



DIGITAL PUBLISHING

Articles designed for optimal readership across devices



FOLLOW US

@frontiersin



IMPACT METRICS

Advanced article metrics track visibility across digital media



EXTENSIVE PROMOTION

Marketing and promotion of impactful research



LOOP RESEARCH NETWORK

Our network increases your article's readership